RTO-MP-8
AC/323(AVT)TP/9

RTO-MP-8

NORTH ATLANTIC TREATY ORGANIZATION

RESEARCH AND TECHNOLOGY ORGANIZATION

BP 25, 7 RUE ANCELLE, F-92201 NEUILLY-SUR-SEINE CEDEX, FRANCE

RTO MEETING PROCEEDINGS 8

Design Principles and Methods for Aircraft Gas Turbine Engines

(les Principes et méthodes de conception des turbomoteurs)

Papers presented at the RTO Applied Vehicle Technology Panel (AVT) Symposium - organized by the former AGARD Propulsion and Energetics Panel (PEP) - held in Toulouse, France, 11-15 May 1998.

Published February 1999

Distribution and Availability on Back Cover

Groupe Communication Canada
Membre de la Corporation St-Joseph

Canada Communication Group
A St. Joseph Corporation Company

March 1999

ERRATUM NOTICE – RTO-MP-8

Paper 21 – "Numerical Simulation of Multi-Stage Turbomachinery Flows"

To all recipients of RTO publication MP-8, "Design Principles and Methods for Aircraft Gas Turbine Engines", printed this month.

This is to inform you that the printed version of the above mentioned paper has been replaced by the version attached to this erratum letter. Please disregard the text for Paper 21 in the bound publication, as the pages were not printed in sequence.

We apologise for any inconvenience caused.

Kelly Edwards
Project Manager RTO Publications
Canada Communication Group Inc.

45, boulevard Sacré-Coeur
Hull (Québec) K1A 0S7

45 Sacré-Coeur Boulevard
Hull, Quebec K1A 0S7

Numerical Simulation of Multi-Stage Turbomachinery Flows

John J. Adamczyk
NASA Lewis Research Center
M.S. 5-9
Cleveland, Ohio 44135, USA

Michael D. Hathaway c/o Adamczyk

Aamir Shabbir c/o Adamczyk

Steven R. Wellborn c/o Adamczyk

ABSTRACT

A comprehensive assessment is made of the predictive capability of the average passage flow model as applied to multi-stage axial flow compressors. The average passage flow model describes the time average flow field within a typical passage of a blade row embedded in a multi-stage configuration. In this work data taken within a four and one-half stage large low speed compressor will be used to assess the weakness and strengths of the predictive capabilities of the average passage flow model. The low speed compressor blading is of modern design and employs stators with end-bends. Measurements were made with slow and high response instrumentation. The high response measurements revealed the velocity components of both the rotor and stator wakes. Based on the measured wake profiles it will be argued that blade boundary layer transition is playing an important role in setting compressor performance. A model which mimics the effects of blade boundary layer transition within the frame work of the average passage model will be presented. Simulations which incorporated this model showed a dramatic improvement in agreement with data.

Paper presented at the RTO AVT Symposium on "Design Principles and Methods for Aircraft Gas Turbine Engines", held in Toulouse, France, 11-15 May 1998, and published in RTO MP-8.

INTRODUCTION

The challenge today for turbomachinery flow analysts is the development of mathematical models which provide a greater degree of resolution of the flow field within multi-stage turbomachinery than today's through flow models. Implied, is the notion that increased resolution will enhance our understanding of the flow processes which control the performance, stability and durability of turbomachinery. It is argued that the enhanced understanding will lead to improved turbomachinery with reduced development time and costs. The increase in flow resolution afforded by any proposed model must be weighted against the computer resources (i.e. measured in terms of CPU time, memory size and costs) associated with executing a CFD simulation and the costs of supporting the empirical data base required to underpin the model. Furthermore these resources must be compatible and readily available to support the design of turbomachinery. The development of such a model is thus a very formidable challenge.

To start the development of a CFD based model for multi-stage turbomachinery one can look to the evolution of CFD models for isolated blade row configurations. The literature on this subject is extensive and its review is far beyond the scope of this paper. However, it is clear that CFD based flow models have had a dramatic and positive impact on the performance of fan rotors for aero-engines. Today fan rotors are designed using viscous 3D CFD models. Based on simulations performed using these models the blade geometry is tailored to control shock location, boundary layer growth and end-wall blockage. It would be highly desirable if such a model could be evolved for multi-stage configurations.

The direct extension of the CFD isolated blade row model to multi-stage configurations is enormously complicated by the fact that neither in the stator nor rotor frame of reference is the deterministic flow steady in time. In addition at a given instant in time the deterministic flow is spatially aperiodic from one passage to another within a wheel. The development of a CFD model capable of capturing all of the time and spacial scales associated with the deterministic flow state within multi-stage turbomachinery is in its infancy and it will be a number of years before such models are used routinely in support of aero-design.

A means of circumventing the problems associated with directly simulating the deterministic flow state within multi-stage machinery is to restrict the resolution capabilities of the model to only those length and time scales associated with flow processes that are explicitly addressed during design. Examples being the build-up of flow blockage, mixing associated with radial transport, and various forms of leakage including bleed and purge. Historically this has been the approach adopted by turbomachinery flow analysts. The classic example being the through flow models in which all time and circumferential length scales have been suppressed by assuming each blade row to have an infinite number of blades. The resulting flow description is axisymmetric and is often referred to as an actuator duct.The effect of a blade row on the flow is introduced through a body force and

an energy source (sink).Cascade models are used to link the incoming flow field to the body force and energy source (sink), and supplemented by rig data to correct for end-wall effects.Through flow models are the backbone of todays multi-stage design systems and have been used very effectively in design. However, the costs and time to acquire the data needed to support through flow models is becoming excessive as requirements for turbomachinery are being extended far beyond the bounds of existing data bases. This extrapolation of the data bases could result in significant development costs over runs. There is a clear need for a true three dimensional flow model capable of providing new insight into the flow process within multi-stage machinery whose computing requirements is compatible with the design environment. Hopefully the empirical data base needed to underpin a three-dimensional model will be less costly to support than that associated with existing through flow models.

It has been proposed that a model of the three-dimensional time average flow field within a typical passage of a blade row embedded in a multi-stage configuration address some of the short-falls of the through-flow models. This three-dimensional flow model governs the conceptional flow field designers have historically designed to and is referred to as the average-passage flow model, Ref. 1. From simulations based on the average-passage model performance parameters such as blade loss, deviation angle, and flow blockage can be derived. This is not the case with the through flow model where explicit models supported by an empirical data base are required specifically for these parameters.

The average-passage flow model can be derived directly from the Navier-Stokes equations through a systematic application of temporal and spacial averaging. The resulting system of equations contain more unknowns than there are equations and thus as with the through flow models additional modeling is required in order to solve the equations. This additional modeling is associated with the mathematical issue of closure and is analogous to the modeling of the turbulent stress which appears in the Reynolds form of the Navier-Stokes equation. The usefulness of the average-passage equation in supporting the design of turbomachinery in-part will depend on the ability to derive closure models which capture the effect of the unsteady aperiodic flow field on the average-passage flow state. The issue of closure is beyond the scope of this work, however the model used in the present study is outlined in Ref. 2. The closure model accounts for the effect of radial mixing associated with the deterministic flow field and that due to turbulence. The mixing associated with the deterministic flow field accounts for the flow physics outlined by Adkins and Smith Ref. 3., while that associated with turbulence accounts for the mixing process outlined by Galmore and Cumpty, Ref. 4.

The objective of this paper is to present a status report of the development of the average-passage flow model including the closure models currently being implemented. To accomplish the stated objective an experimental data set is required against which the accuracy of the model can be assessed in addition to revealing shortcomings in the closure models. It must be remembered that the issue is not whether the average-passage model is correct but the ability to develop closure models which can capture the effects of the

unsteady aperiodic flow field on the average-passage flow state.

EXPERIMENT VERSUS NUMERICAL SIMULATION

Experimental Configuration

The experimental data to be used in this study came from measurements taken in the NASA Lewis Large Low Speed Research Compressor. The compressor has four repeating stages plus an inlet guide vane. The geometry of the compressor is outlined in Ref. 5. Both the rotor and stator geometry is representative of modern day aero-engines. The third stage rotor and stator diffusion factor at mid-span are 0.45. The stator design employed end-bends to control the flow field at the hub and shroud. Casing treatment was used over the first stage rotor and was not accounted for in the simulations which are presented. From measurements taken with the casing treatment sealed and unsealed it appears that the casing treatment impacts the performance of the machine at operating conditions near and above peak pressure. Near peak efficiency the impact of the first rotor casing treatment on performance appears to be negligible. The simulated hub flow path was of constant radius while in the compressor only the rotor hubs are of constant radius. The simulations also did not account for the effect of leakage from beneath the stator foot-rings.

Data taken with slow response instrumentation as well as data taken with high response hot-film instrumentation will be presented. In addition some data taken with the leakage gaps beneath the stator foot-rings sealed will be used to supplement the data set taken with the foot-rings unsealed. Flow variables derived from data taken with the foot rings sealed will be noted as such.

Compressor and Stage Static Pressure Rise Characteristic

The compressor static pressure rise characteristic per stage is shown in Fig. 1 with all the stator foot-rings unsealed and sealed with the stator disk cavities closed to the primary flow stream. The characteristic was determined from static pressure taps located on the outer casing. At a fixed flow coefficient the pressure rise is slightly higher with the foot rings sealed and the cavities closed than with them unsealed and the stator cavities open. Maximum efficiency is achieved at a flow coefficient of 0.395. Its value is estimated to be between 90 and 90.5%. Superimposed on Fig. 1. are two points derived from simulations. One of these points is at a flow coefficient corresponding to peak efficiency (i.e. flow coefficient of 0.395) while the other is at flow coefficient of 0.375, midway between peak pressure and peak efficiency. At the simulated flow coefficients the pressure rise per stage is less than that measured. The difference is approximately 6%. The predicted efficiency at a flow coefficient of 0.395 is 89%, which is 1 to 1.5% less than that based on experimental estimates. The measured pressure rise characteristics (determined from outer casing pressure taps) for each of the stages is shown in Fig. 2 along with the results obtained from the two simulations. The data are from cases with the foot rings sealed and the stator disk cavities closed and with the foot rings unsealed and the stator disk cavities

opened to the primary flow stream. The characteristics with the foot-rings sealed and the cavities closed are slightly higher than those with the foot-ring unsealed and the cavities open. Figure 2 shows that the predicted pressure rise of the first stage at a flow coefficient of 0.395 is 6% less than that measured. At this same flow coefficient, the predicted pressure rise for the second and third stage is approximately 7% less than that measured. For the fourth stage the predicted pressure rise is 5% less than that measured.

The agreement with measurements is encouraging. However, the disagreement between the predicted pressure rise and that measured needs to be reduced before the model can be fully utilized in support of design.

Axisymmetric Flow Variables

To understand the reasons for the shortfall in the predicted pressure rise of the second and third stage, a comparison of the axisymmetric flow variables derived from measurement and simulation are presented for the flow coefficient of 0.395. The plots are for an axial position between the exit of the second stator and the inlet of the third rotor, between the exit of the third rotor and the inlet of the third stator, and between the exit of the third stator and the inlet of the fourth rotor. These three axial positions are referred to as station 3,3.5 and 4 respectively and their location is given in the cross-section layout of the compressor, Fig. 3.

The total and static pressure coefficient, axial and tangential velocity, absolute and relative flow angle, as derived from the experimental measurements are shown in Fig. 4 for station 3. The experimental results are annotated as to the configuration of the stator foot-rings and the stator disk cavities. Also shown on this figure are the corresponding variables derived from the numerical simulation. The total pressure and static pressure coefficient are referenced to the plenum total pressure and normalized with respect to the dynamic head based on plenum total density and the rotor tip speed squared. The velocity components are normalized with respect to the rotor tip speed.

Both the total and static pressure coefficient as derived from the data are greater than those derived from the numerical simulation. At midspan the experimental total pressure coefficient is 5% greater than that predicted by the numerical simulation. The shape of the predicted total pressure coefficient curve is very similar to that measured, both showing a bulge near 90% per cent of span.

The velocity components derived from the measurements are in reasonable agreement with those derived from the simulation. This agreement is consistent with the agreement seen in the flow angle comparison. With the exception of the hub region (i.e. below 10% span) the velocity triangles determined from the experimental data and the simulation are in reasonable agreement with each other. The disagreement near the hub is in part associated with the stator leakage.

Figure 5 shows the total and static pressure coefficient, axial and tangential velocity, absolute and relative flow angle at station 3.5 (at the exit of the third rotor) as a function of span. The measured total pressure rise at mid-span across the third rotor is 6.3% greater than that predicted. The measured static pressure rise across the third rotor is also greater than that predicted. The axial velocity component derived from the experimental data is in reasonable agreement with that derived from the numerical simulation as is the tangential velocity component.

The axisymmetric flow conditions at the exit of the third stage stator are shown in Fig. 6. Plotted as a function of span are the measured and predicted total and static pressure coefficient, axial and tangential velocity components, absolute and relative flow angles. Once again the measured total and static pressure coefficients are greater than that predicted. The measured and predicted flow angles and velocity components exiting the stator are in good agreement with each other. The velocity components at the exit of the third stage stator are nearly identical to their counterparts exiting the second stage stator (Fig. 4). The machine is operating in a repeating stage condition.

Rotor and stator blade element loss estimates obtained from either the simulation or from measurements taken with slow response instrumentation failed to provide any additional information as to the cause in the shortfall in predicted compressor pressure rise. The explanation for the shortfall was deduced from an analysis of the hot-film data taken downstream of the second stage stator and third stage rotor. Figure 7 shows the pitch-wise distribution of the time average axial velocity component at 15,50,85 and 92.5% of span exiting the second stage stator. Both measured and predicted results are shown. Also shown is the envelope of the unsteady axial velocity component at these locations. The stator wake is quite evident in these plots. These plots show that the predicted stator wake is deeper than that measured. Analysis of the axial velocity contour plots for station 3, Fig. 8, shows that the predicted stator wake is deeper than that measured nearly over the entire span. Analysis of the measured and predicted time average tangential velocity field exiting the second stator yielded a similar conclusion, the predicted stator wake is deeper than that measured.

Figure 9 shows the measured and predicted time average axial velocity component in the rotor frame of reference exiting the third rotor. The axial velocity component is plotted as a function of pitch for four span-wise locations. There is an error in the experimental results presented in Fig. 9 caused by a shift in the probe position which was found after the data was taken. This shift caused a 2 deg. error in the measured absolute flow angle. This shift affected the measurements between 20 and 80% of span. The actual axial velocity component at mid-span is thus slightly less than that plotted. However, the shift in the probe alignment did not affect the shape of the measured pitch-wise variation of the axial velocity component. Once again the predicted blade wake depth is greater than that measured. Figure 10, which is a contour plot of the measured and predicted time average axial velocity component in the rotor frame of reference, shows that the predicted wake is deeper than that measured over nearly the entire span.

The simulations assumed the boundary layers on the blade surfaces to be fully turbulent starting at the leading edge. Test of a similar compressor configuration, Hallstead and Weisler Ref. 6, have shown the blade boundary layers to be transitional. The turbulence model that was used in the simulations presented thus far was an average passage form of a high Reynolds number standard $k-\epsilon$ model. For an isolated blade row this model reduces to that of Launder and Spalding, Ref. 7. It is well known that this turbulence model over estimates the turbulent viscosity near flow stagnation. Such is the case in the simulations presented. It is conjectured that the large values of turbulent viscosity at the leading edge of a blade leads to the development of a boundary layer which is thicker over the entire blade surface than what actually exits. A thicker boundary layer implies more flow blockage, hence less diffusion, hence less pressure rise.

HINDSIGHT - A Case For Transition Modeling

In the previous section it was shown that the predicted blade wakes were deeper than those measured. It was argued that the deeper wakes were the result of the blade boundary layers being assumed turbulent from the leading edge on. Because there is strong evidence to suggest that the blade boundary layers are transitional, the actual blade boundary layers are thinner than predicted. The result is an under-prediction of the pressure rise of the compressor.

In an attempt to improve the agreement with measurements, simulations were executed using an improved $k-\epsilon$ model developed by Shih et. al., Ref. 8, and applied to turbomachinery configuration by Shabbir, Zhu and Celestina, Ref. 9. The Shih model is not a transition model, however unlike the $k-\epsilon$ model of Launder and Spalding, Ref. 7, it does not produce unrealistically high levels of turbulent eddy viscosity in regions of high strain rates. Thus the Shih model suppresses the growth of eddy viscosity at the leading edge of a blade and along the blade surface where the pressure gradient is favorable. The eddy viscosity begins to grow in value when the flow locally begins to diffuse. The Shih model approximately mimics the growth of the turbulent eddy viscosity in a transitional boundary layer.

The average stage pressure rise predicted using the Shih model at a flow coefficient of 0.395 and 0.375 is shown in Fig. 11 along with the measured characteristic. At a flow coefficient of 0.395 the predicted pressure rise is 0.505 while that measured with the stator foot-rings sealed and the stator disk cavity closed to the primary flow is 0.512. For the same configuration, at a flow coefficient of 0.375 the predicted pressure rise is 0.541, while that measured is 0.538. The predicted efficiency at 0.395 flow coefficient is 90.1%, an increase of one point over the previous prediction. Figure 12 shows the measured pressure rise characteristic for each stage along with the results obtained from the simulations using the Shih model. The agreement is excellent compared to the results presented in Fig. 3. Further confirmation of the improvements gained by using the Shih model is shown in Fig. 13. Figure 13 shows plots of the postdicted and measured total and static pressure coefficient, axial and absolute tangential velocity component, absolute

and relative flow angle at station 3 as a function of span. The flow coefficient is 0.395. The postdicted velocity components and flow angles are nearly the same as those shown in Fig. 4. However, the postdicted total and static pressure coefficient are in better agreement with the measurements than their counter-parts in Fig. 4. The slight difference between the postdicted total pressure coefficient and that measured in board of 40% of span is unknown.

Figure 14 shows the measured and postdicted total and static pressure coefficient, axial and absolute tangential velocity component, absolute and relative flow angle at station 3.5 (downstream of the third stage rotor) as a function of span. The agreement between the postdicted results and those obtained experimentally is excellent. The detailed shape of the experimental curves is captured by the postdicted results. These results clearly indicate the improvements gained by using the Shih turbulence model. The corresponding plots for axial station 4.0, which is downstream of the third stage stator yield results comparable to those shown in Fig. 13.

Figures 15 and 16, show the cross passage time average axial velocity field at the exit of the second stage stator and the third stage rotor. The third stage rotor contour plot is with respect to the rotor frame of reference. Results are shown as derived from the simulation and measurements. What is clearly evident is that the depth of the postdicted wakes are less than those shown in Figs. 8 and 10 and that the depth of these wakes are in much better agreement with the measurements.

Finally, the loss coefficient for the third stage rotor and stator derived from the simulations which used the Shih turbulence model is shown in Fig. 17. The figure shows that the loss associated with both blade rows is less when the Shih model is used. The reduction in blade loss is the primary reason for the improved agreement with data.

CONCLUSIONS

The objective of this paper was to document the status of the development of the average passage flow model for multi-stage axial flow compressors. This model describes the time average flow field in a typical passage of a blade row embedded in a multi-stage machine. The configuration analyzed was the NASA Lewis 4 1/2 stage large low speed compressor whose blading is representative of todays aero-engines. Detailed aero survey data exists which documents the axisymmetric flow field exiting the second stage stator, third stage rotor and third stage stator at flow coefficients corresponding to peak efficiency and peak pressure. In addition the pressure rise of each stage as a function of flow coefficient has been documented.

The performance estimates associated with the first series of simulations fell short of that measured. Based on hot-film data it was deduced that the predicted blade wakes were deeper than that measured, the result of the blade boundary layers being assumed turbulent from the leading edge on. It is highly likely that the blade boundary layers in

the low speed compressor simulated are transitional. If these transitional boundary layers were to remain attached they would produce less loss than a turbulent boundary layer. Less loss would result in more flow diffusion and hence an increase in compressor rise. Although no direct measurement of the state of the blade boundary layer exists, evidence of laminar flow regions on the blades of a similiar low speed multi-stage compressor exits. The existence of a transitional blade boundary layer would explain the shortcoming in the predictions.

To test the sensitivity of the prediction to the assumed state of the blade boundary layers a second series of simulations were executed where in the turbulence model used allowed the turbulent eddy viscosity to be a local function of the flow strain rate. The dependence of the turbulent viscosity on local strain rate suppresses the growth of the turbulent viscosity in regions of flow stagnation and in regions along a blade surface for which the pressure gradient is favorable. Although this turbulence model is not a transition model it does yield a boundary layer which has many of the traits of a transitional boundary layer. Using such a turbulence model greatly improved the accuracy of the simulation. The compressor pressure rise as well as the pressure rise of each stage was predicted to within 2%. The span-wise distribution of the absolute total and static pressure coefficient, the axisymmetric components of axial and tangential velocity, and the absolute and relative flow angles at the exit of the second stage stator, and the third stage rotor were all in excellent agreement with results derived from measurements. The improvements gained in predicting compressor performance using a turbulence model where-in the eddy viscosity is a direct function of the local flow strain rate is very encouraging and is strongly recommended. The present study clearly indicates the need for incorporating a transition model of some form when simulating multi-stage axial flow compressors.

REFERENCES

1. Adamczyk, J.J., "Model Equation for Simulating Flows in Multistage Turbomachinery," *ASME Paper 85-GT-220*, 1985.

2. Adamczyk, J.J., Celestina, M.L., Beach, T.A., and Barnett M., "Simulation of Three-Dimensional Viscous Flow Within a Multistage Turbine", *ASME J. of Turbomachinery*, Vol. 112, 1990

3. Adkins, G.G. and Smith Jr. L. H., "Spanwise Mixing in Axial-Flow Turbomachines," *J. Eng. Power*, Vol. 104, No. 1 1982.

4. Gallimore S.J. and Cumsty N.A., "Spanwise Mixing in Multistage Axial Flow Compressors", *ASME. J. of Turbomachinery*, Vol. 108, 1986.

5. Wellborn, S. and Okiishi, T., 1996, "Effects of Shrouded Stator Cavity Flows on Multistage Axial Compressor Aerodynamic Performance", NASA CR 198536.

6. Halstead, D.E., Wisler, D.C., Okiishi, T.H., Walker, G.J., Hodson, H.P., and Shin, H.W., "Boundary Layer Development in Axial Compressors and Turbines", *ASME papers*, 95-GT-461, 95-GT-462 95-GT-463, 95-GT-464, 1995.

7. Launder, B.E., and Spalding, D.B., 1974, "The Numerical Computation of Turbulent Flows", *Comp. Math. Appl. Mech. Engg.*, 3, 269-289.

8. Shih, T.-H., Liou, W.W., Shabbir, A. , Zhu, J., and Yang, Z., 1995, "A New $k-\epsilon$ Eddy Viscosity Model for High Reynolds Number Turbulent Flows", *Computers Fluids*, 24, 3, 227-238.

9. Shabbir, A., Zhu, J., and Celestina, M.L. 1996, " Assessment of Three Turbulence Models in a Compressor Rotor", Paper 96-GT-198, *ASME/IGTI International Gas Turbine Conference*, Birmingham, UK.

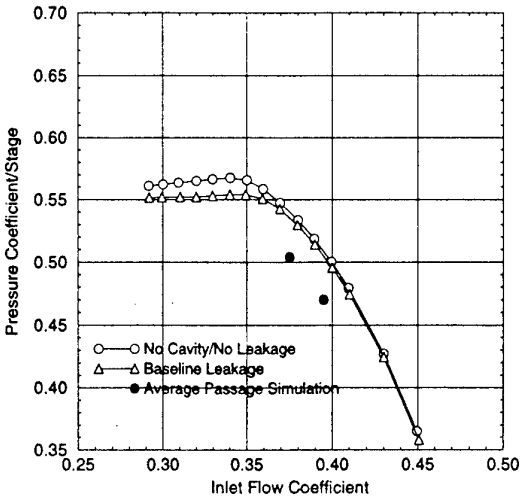

Fig. 1. Overall pressure coefficient as a function of inlet flow coefficient.

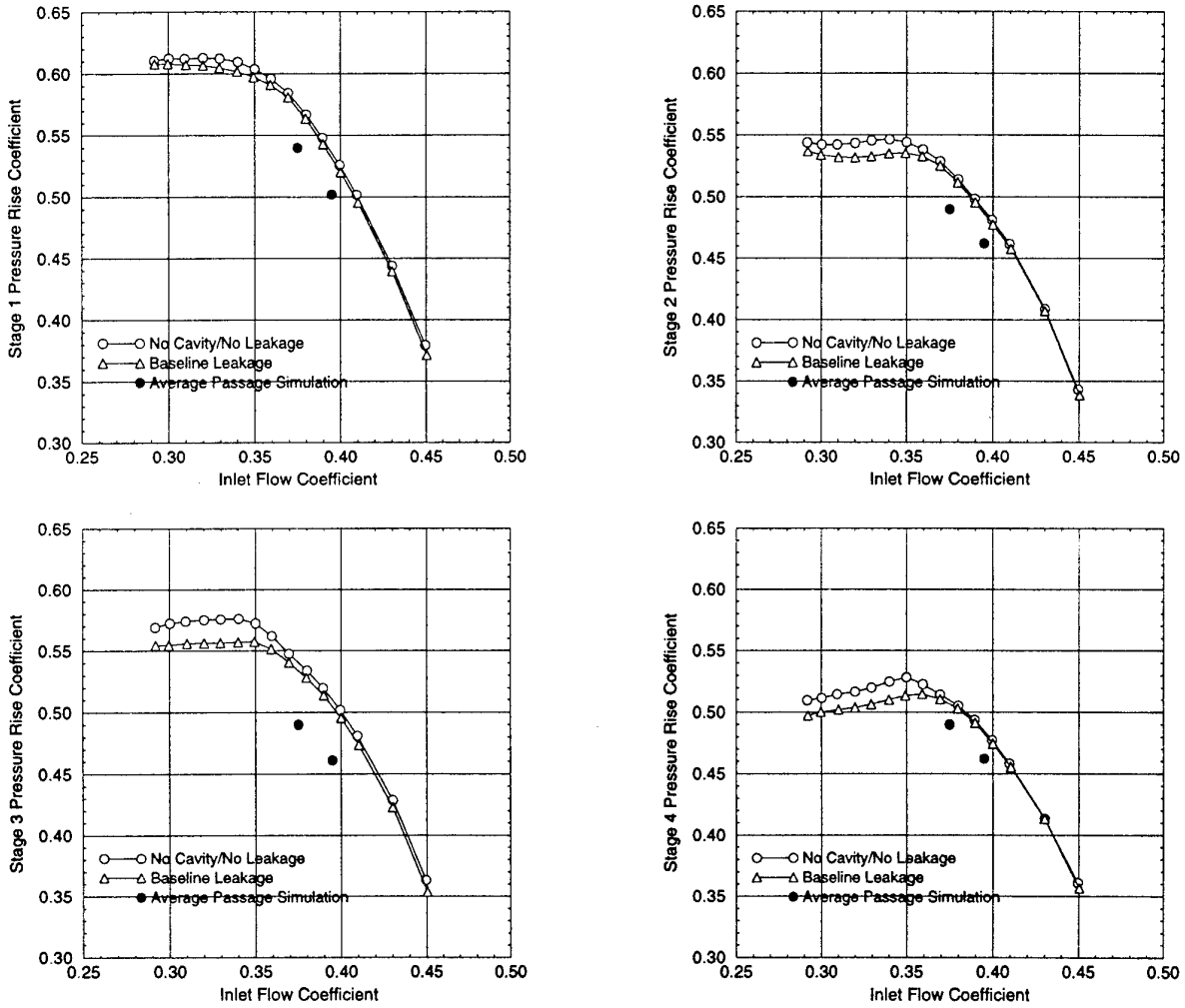

Fig. 2. Individual stage pressure rise coefficient as a function of inlet flow coefficient.

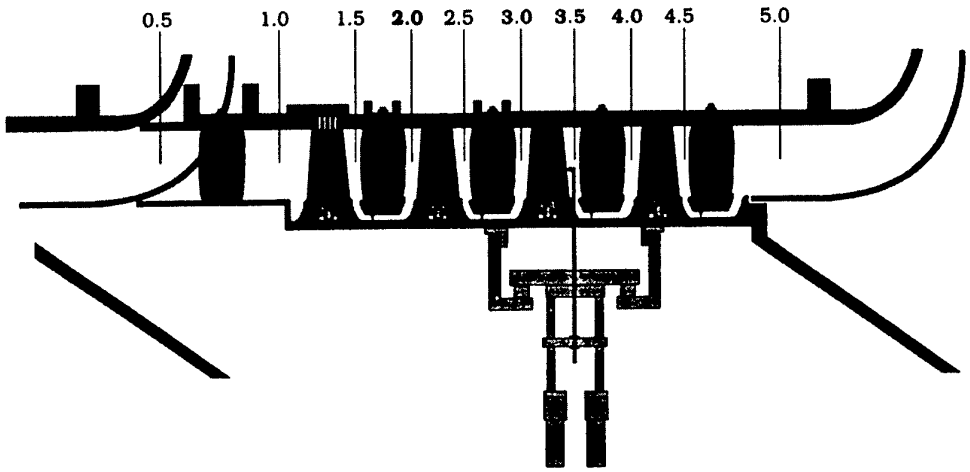

Fig. 3. Schematic of the Low Speed Axial Compressor.

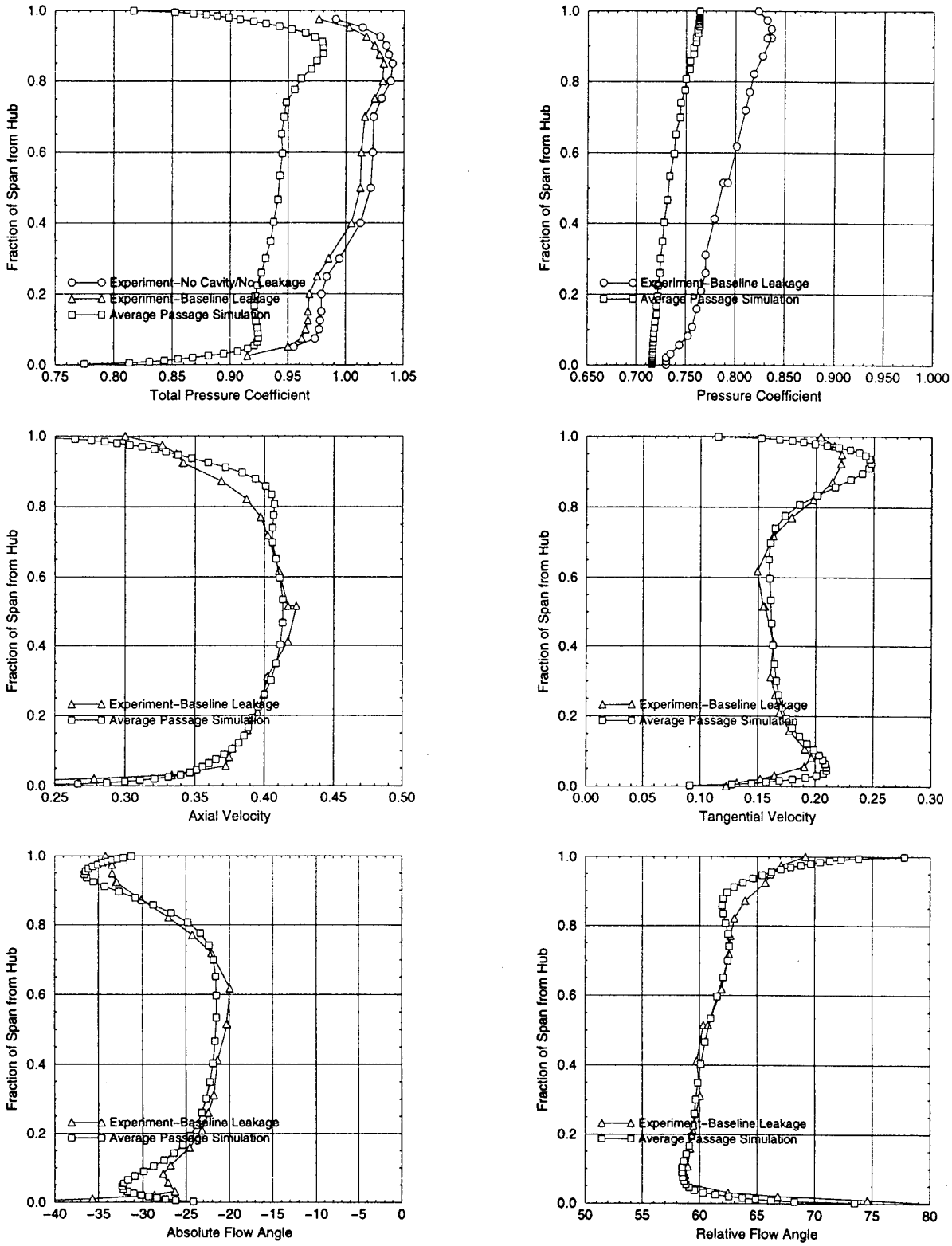

Fig. 4. Axisymmetric flow variables at Station 3.0.

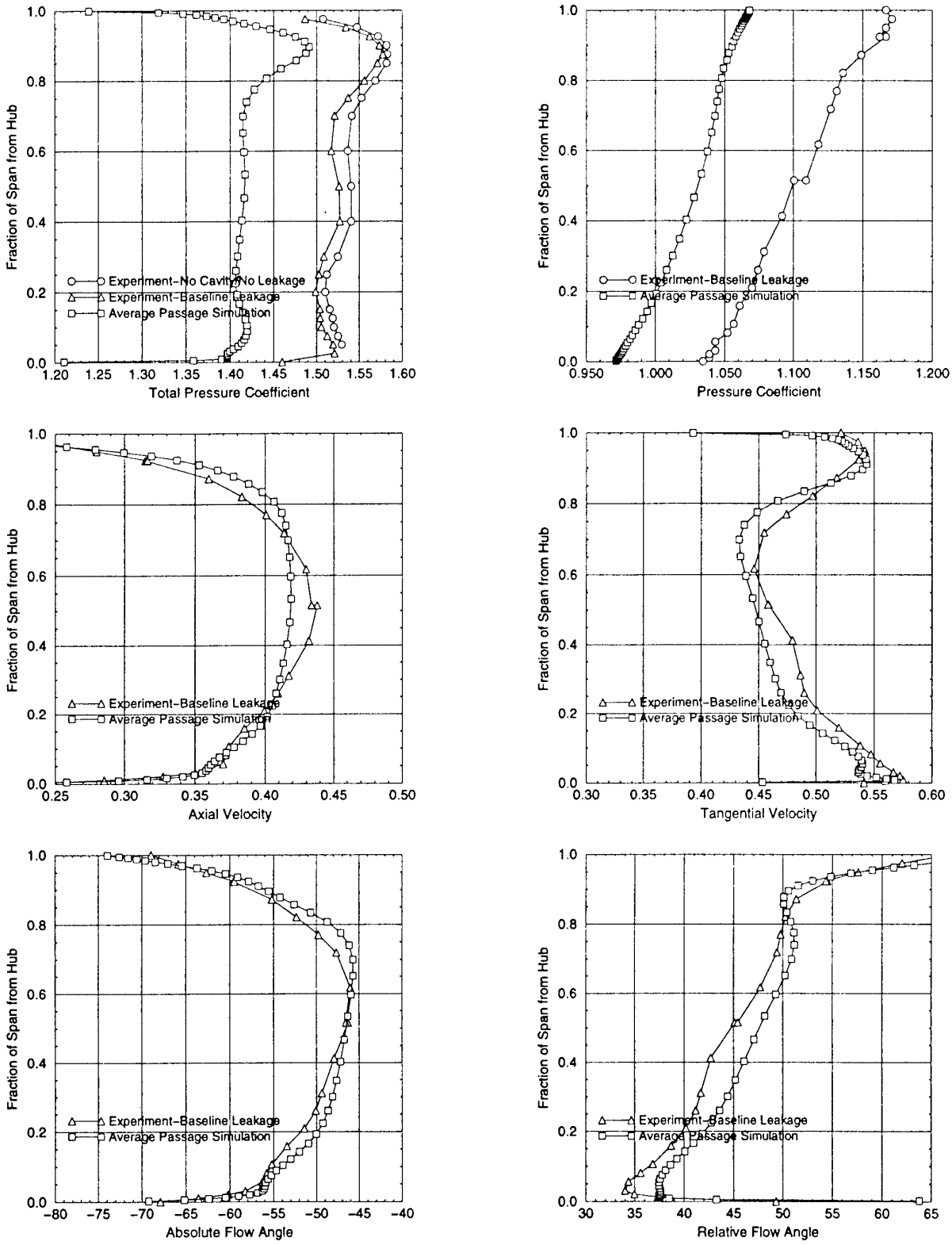

Fig. 5. Axisymmetric flow variables at Station 3.5.

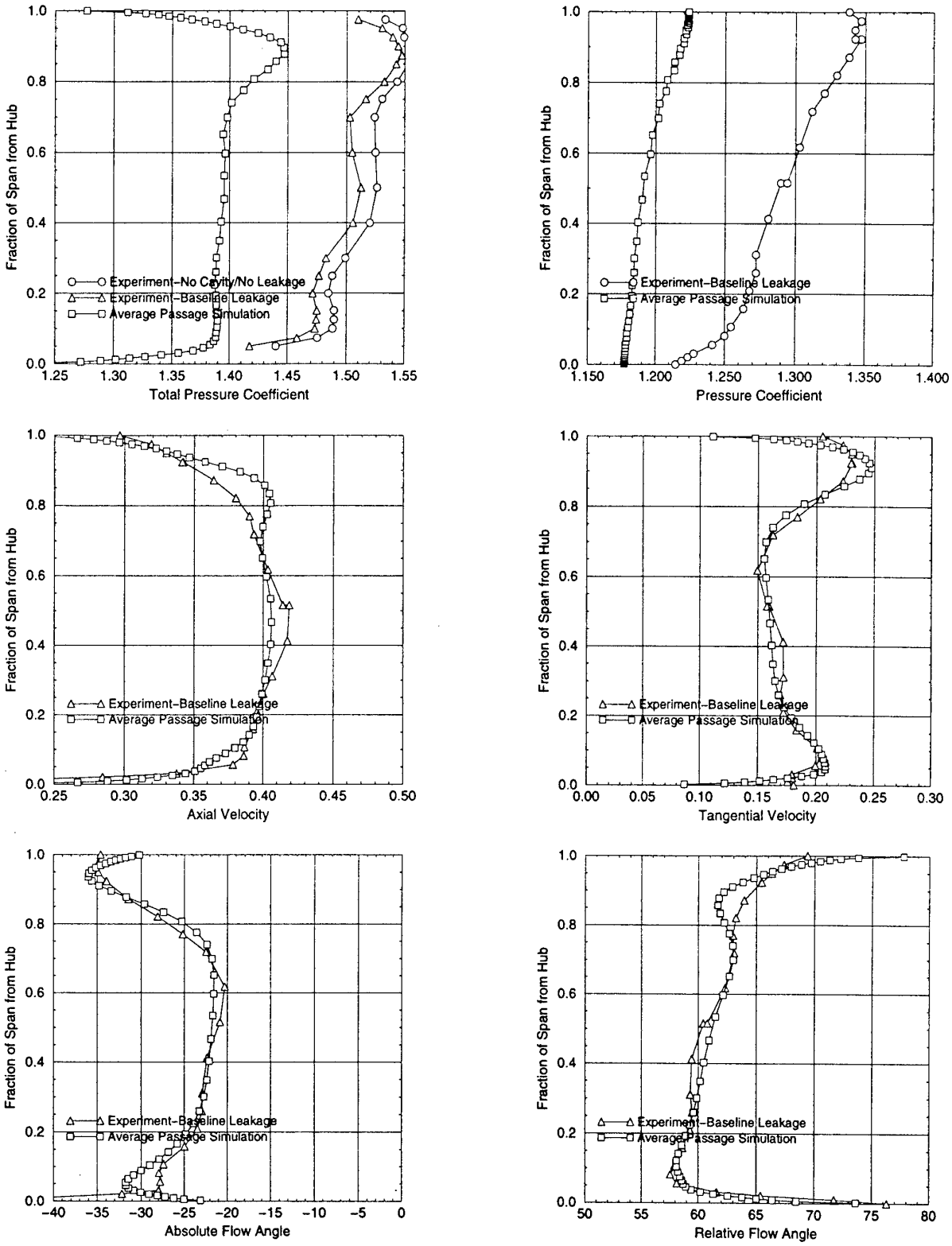

Fig. 6. Axisymmetric flow variables at Station 4.0.

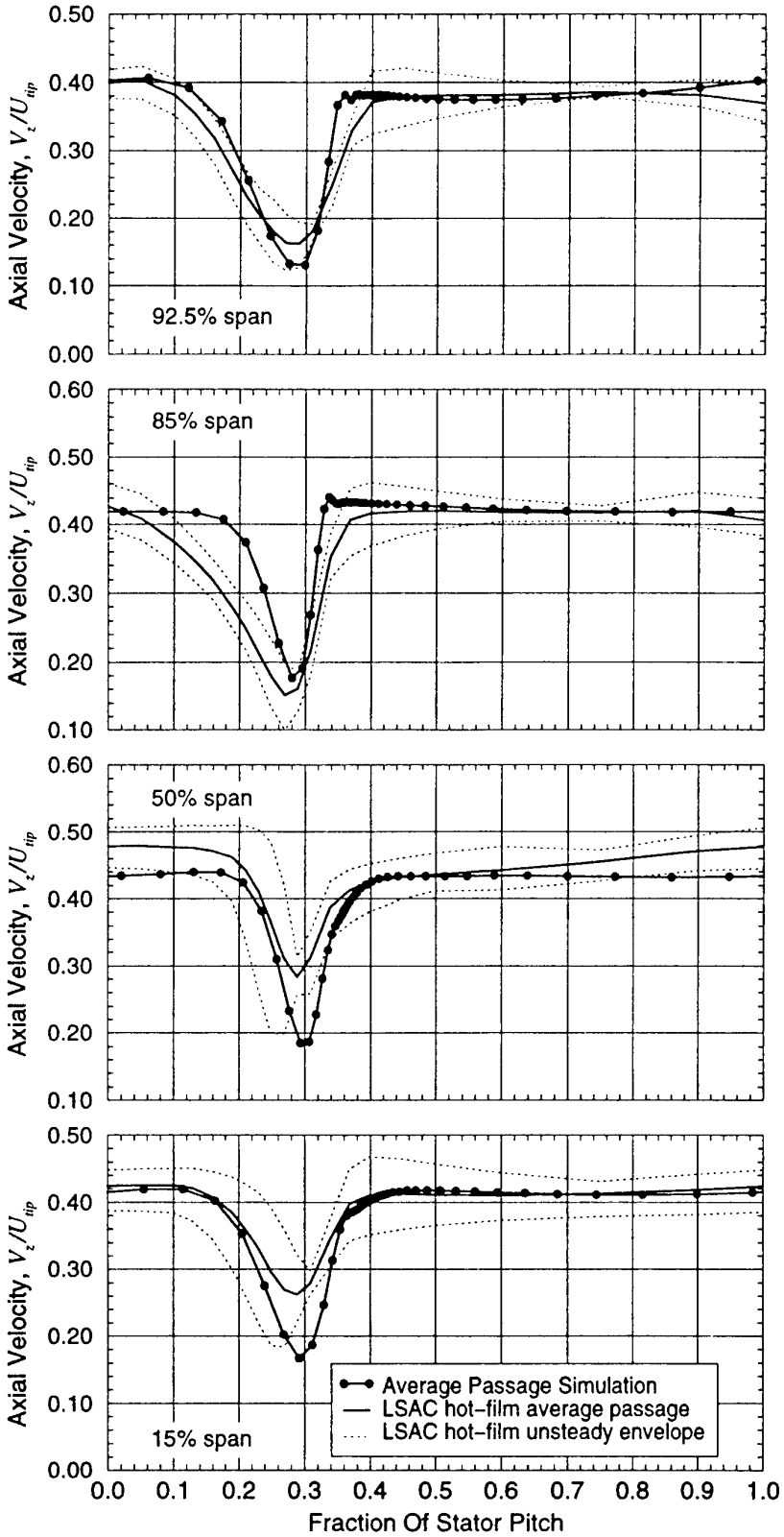

Figure 7. Measured and simulated LSAC axial velocity (Vz / Utip) distributions at ST 3.0

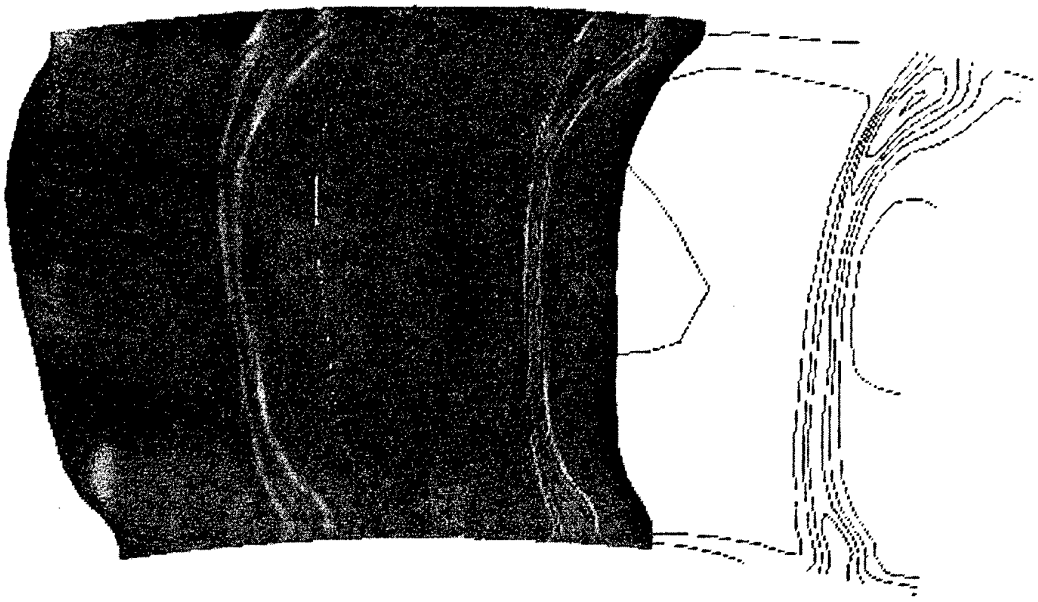

Measured (hot-film) average passage (ensembled and time averaged across the rotor pitch) axial velocity (Vz / Utip) at ST 3.0. Contour minimum level is 0.10, contour maximum level is 0.45, contour increment is 0.05.

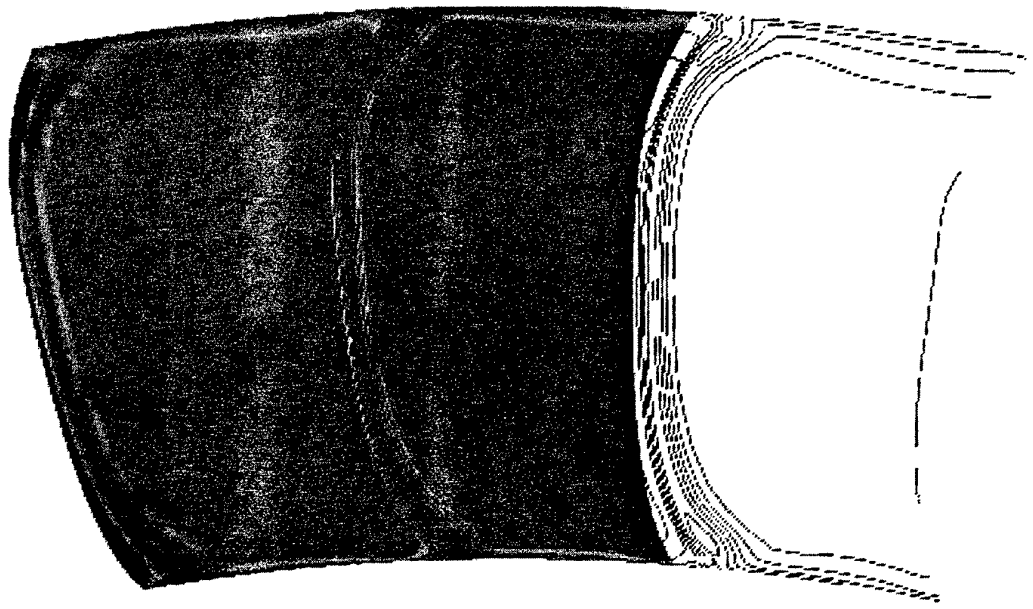

Average passage simulated axial velocity (Vz / Utip) at ST 3.0 (solution interpolated to match axial location of ST 3.0). Contour minimum level is 0.10, contour maximum level is 0.45, contour increment is 0.05.

Figure 8

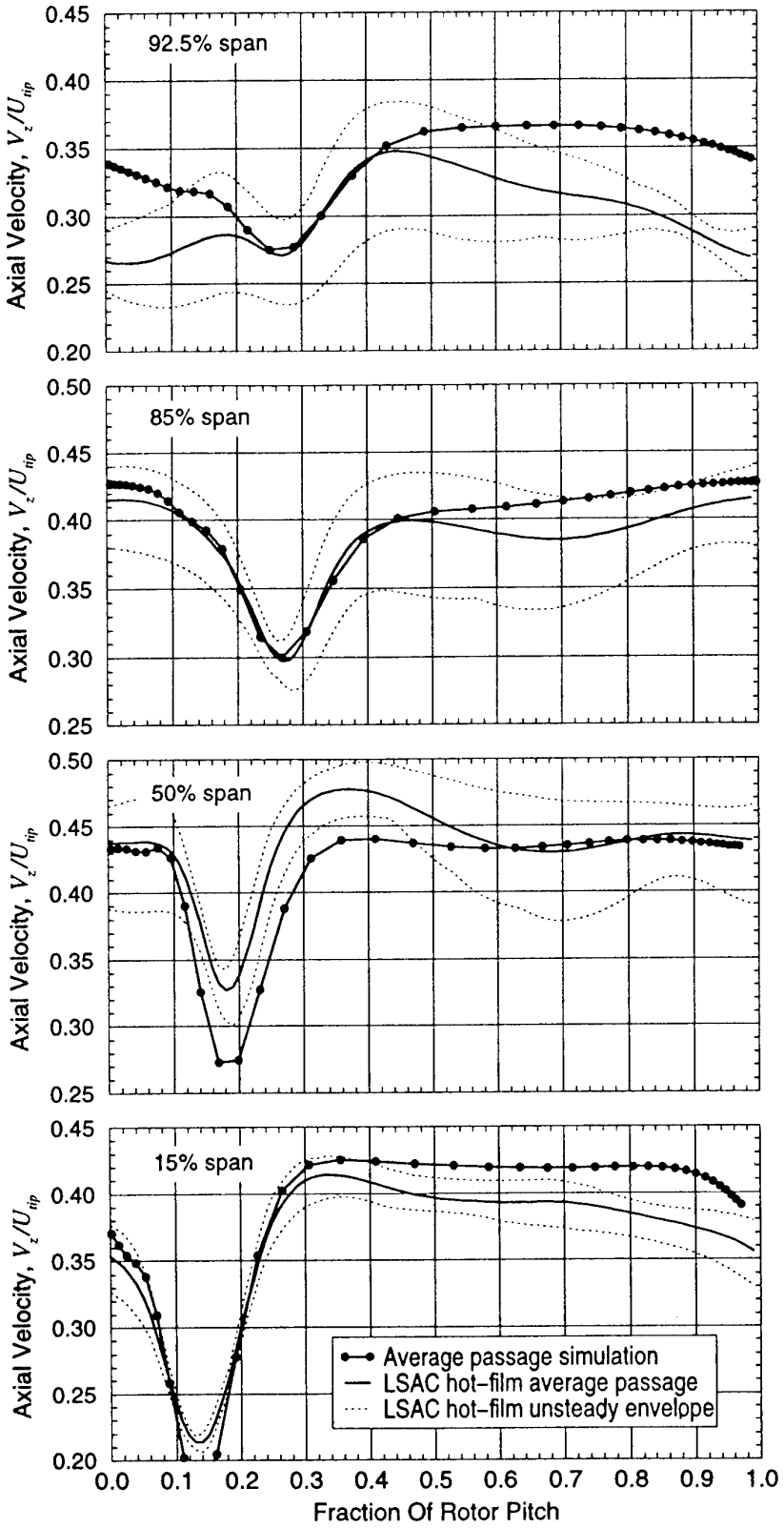

Figure 9. Measured and simulated LSAC axial velocity (Vz / Utip) distributions at ST 3.5 for 15, 50, 85 and 92.5% span. Simulation data are denoted by filled circles, average passage data are represented by solid lines and the unsteady envelope data are depicted by dotted lines.

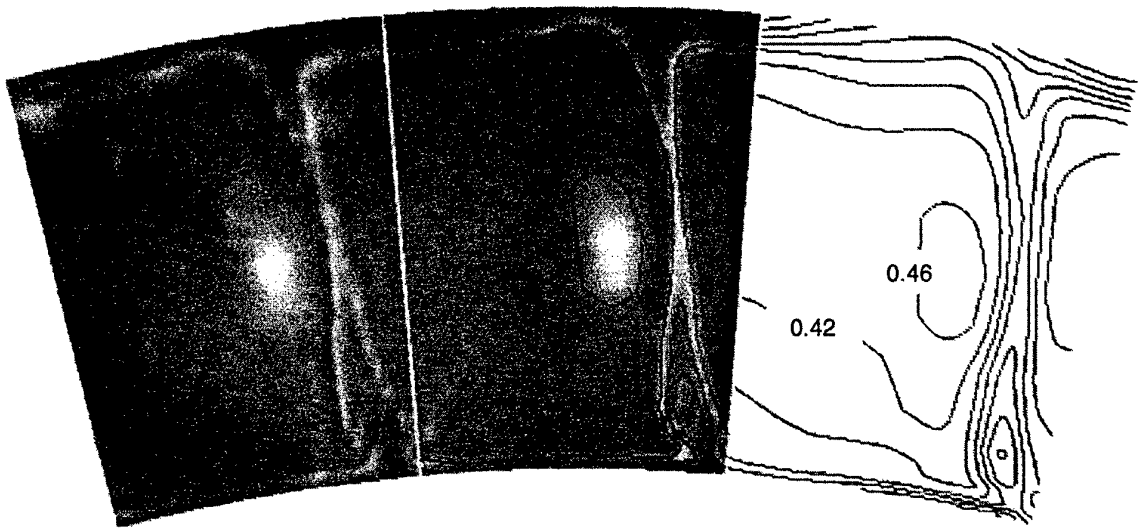

Measured (hot–film) average passage (ensembled and time averaged across the stator pitch) axial velocity (Vz / Utip) at the discharge of rotor 3 (ST 3.5). Contour minimum level is 0.14, contour maximum level is 0.46, contour increment is 0.04.

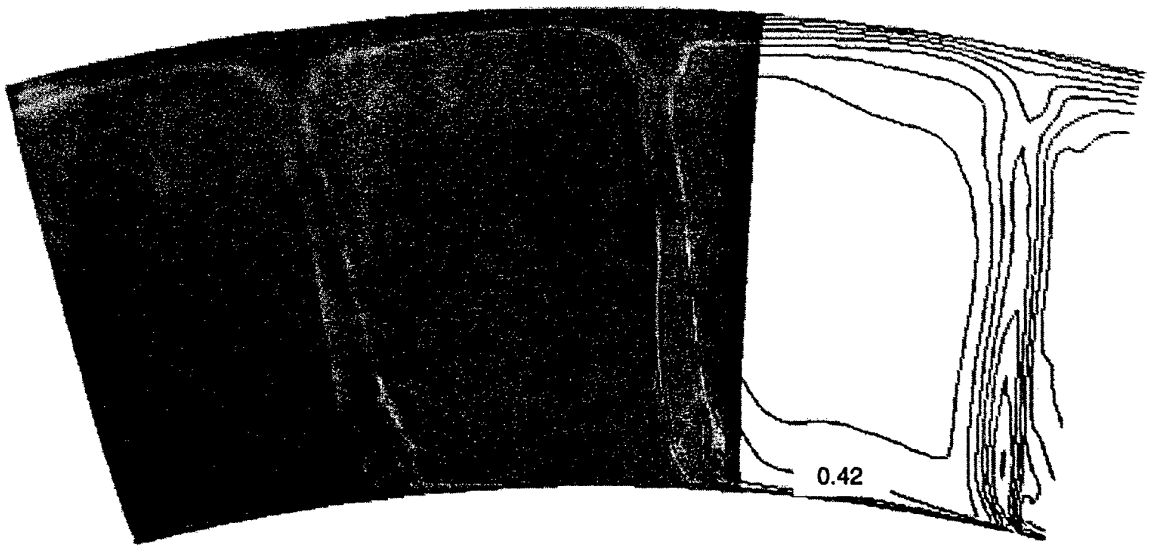

APNASA simulated axial velocity (Vz / Utip) at the discharge of rotor 3 (solution interpolated to match axial location of ST 3.5). Contour minimum level is 0.14, contour maximum level is 0.42, contour increment is 0.04.

Figure 10

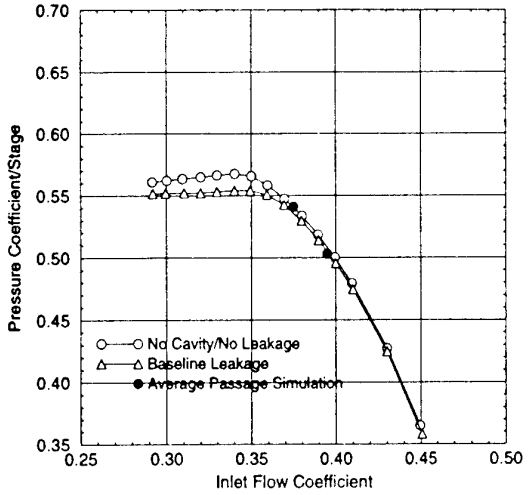

Fig. 11. Overall pressure coefficient as a function of inlet flow coefficient.

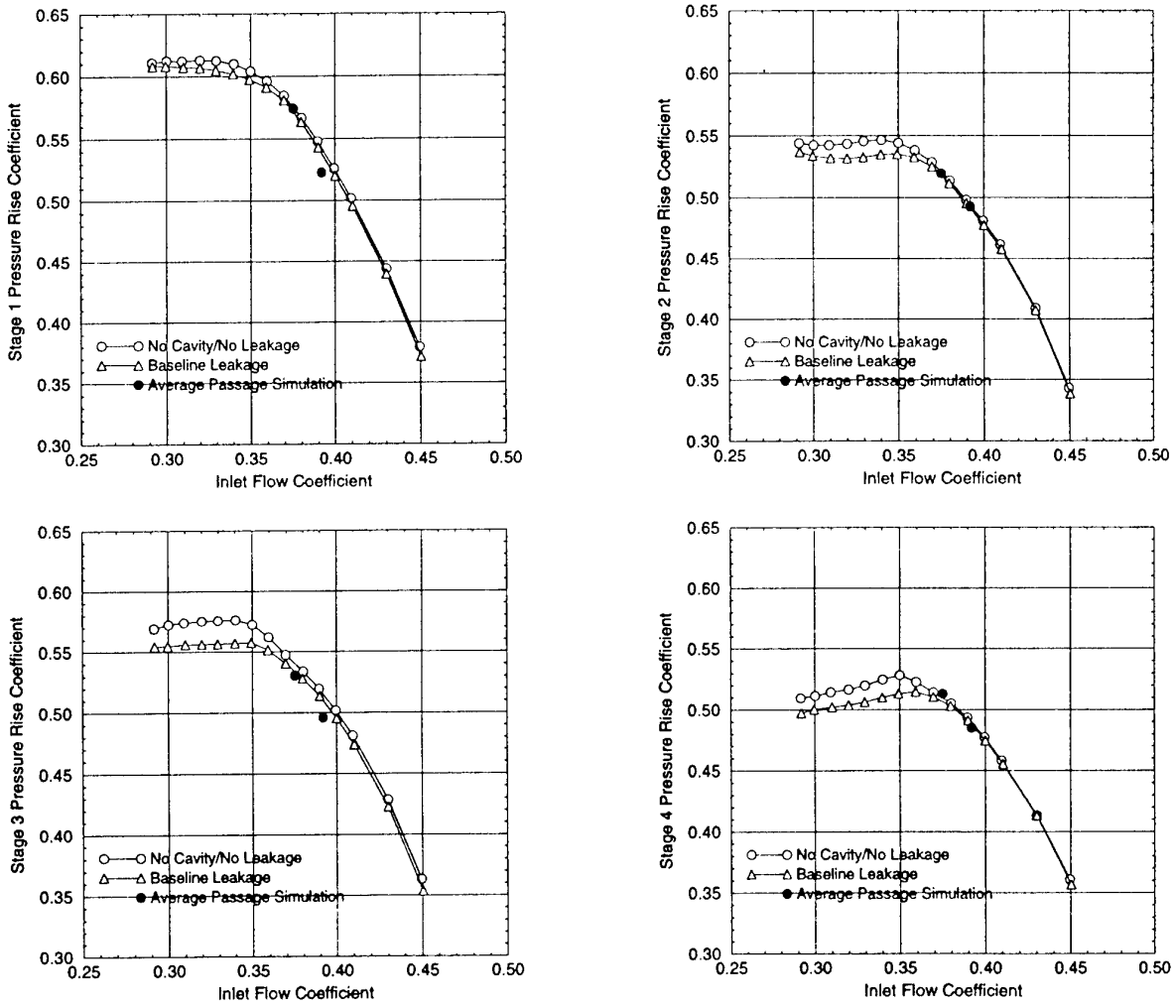

Fig. 12. Individual stage pressure rise coefficient as a function of inlet flow coefficient.

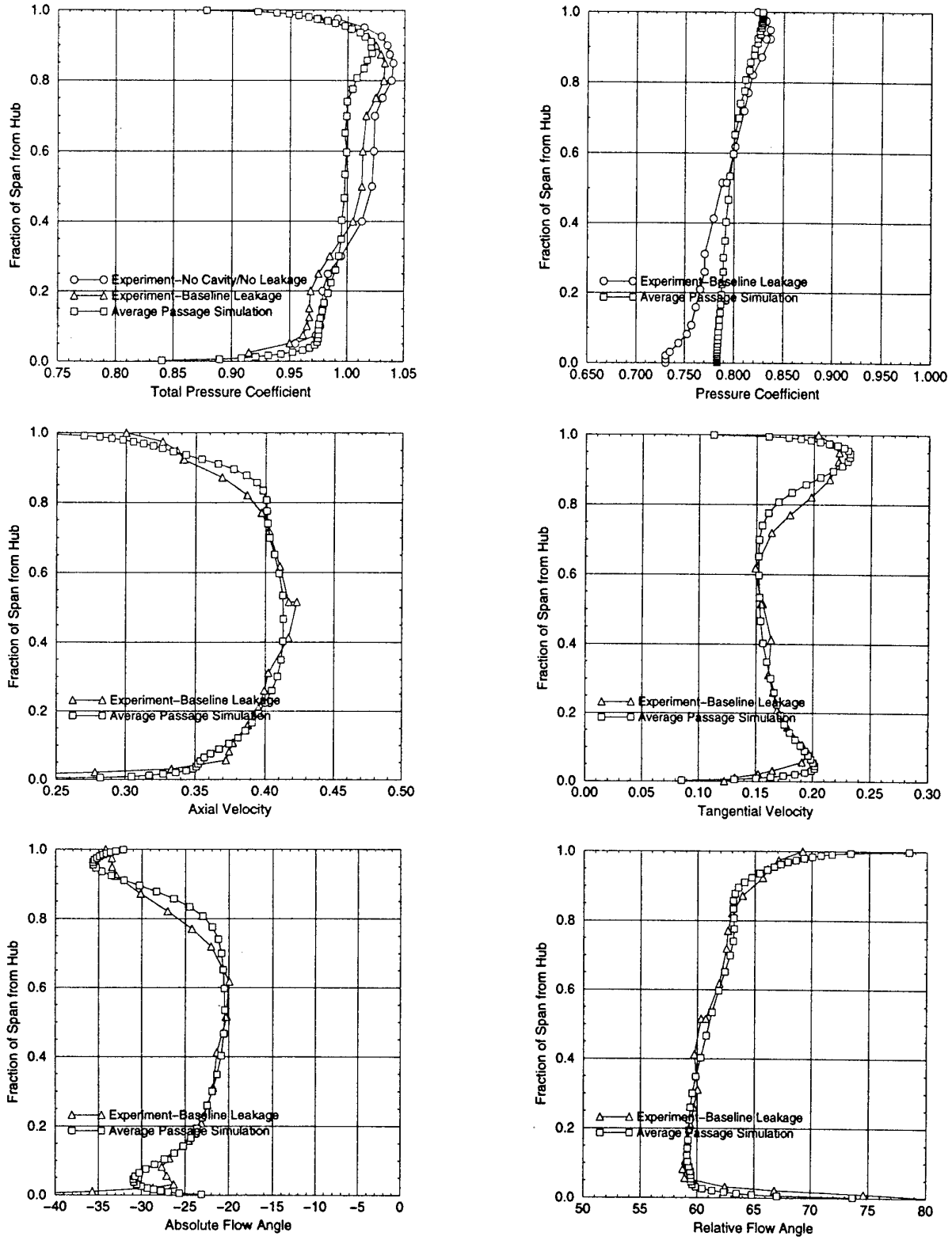

Fig. 13. Axisymmetric flow variables at Station 3.0 using the improved $k - \epsilon$ turbulence model of Shih et al.[8].

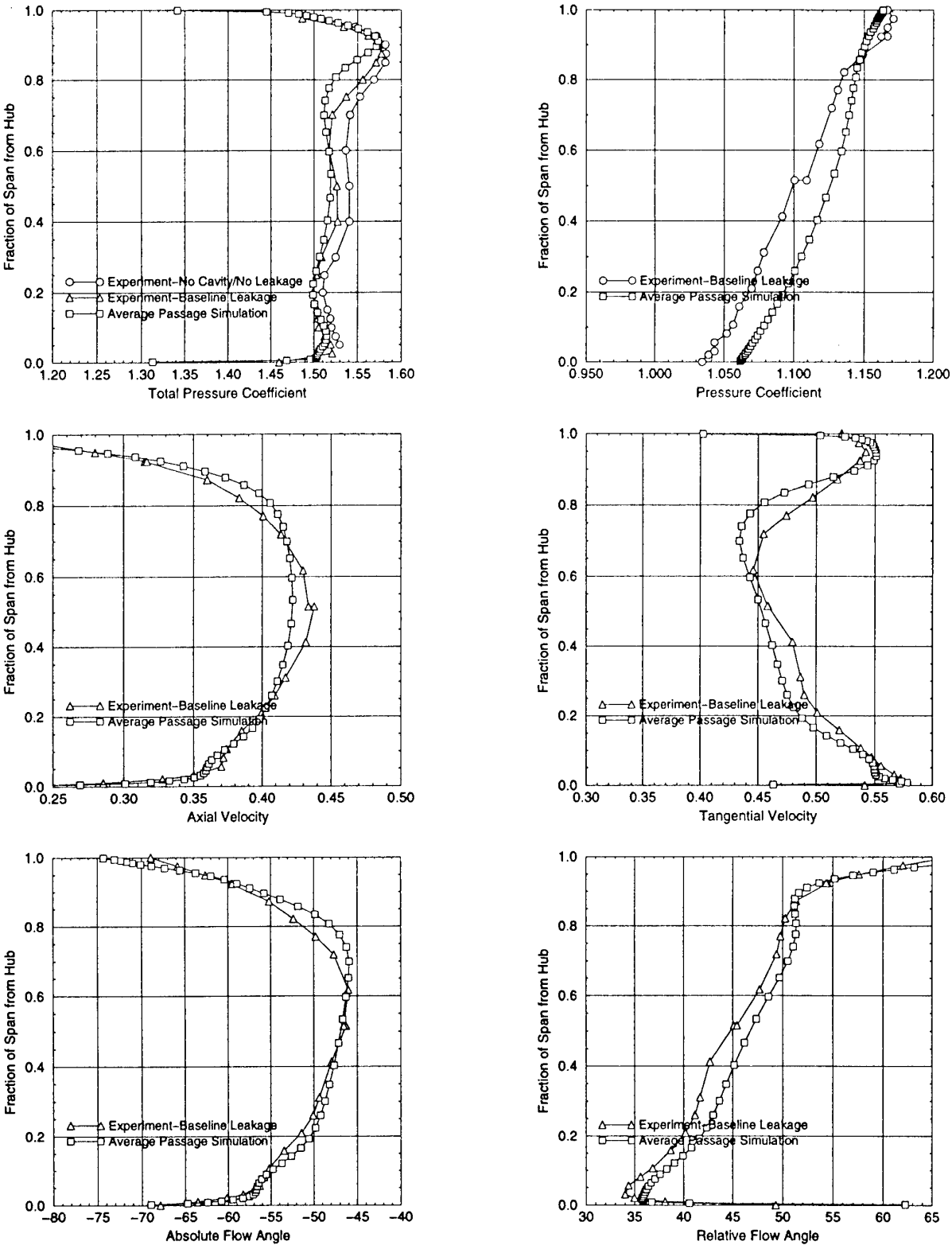

Fig. 14. Axisymmetric flow variables at Station 3.5 using the improved $k - \epsilon$ turbulence model of Shih et al.[8].

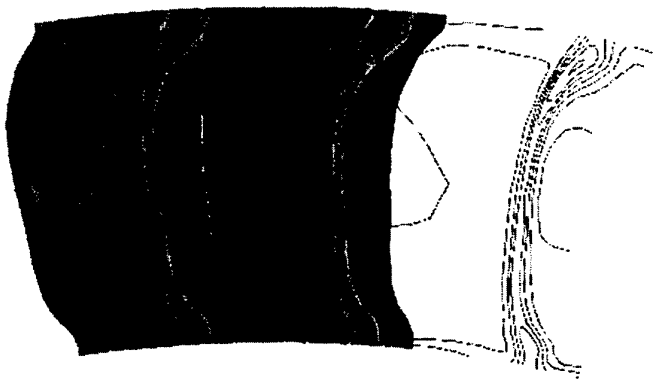

Measured (hot–film) average passage (ensembled and time averaged across the rotor pitch) axial velocity (Vz / Utip) at ST 3.0. Contour minimum level is 0.10, contour maximum level is 0.45, contour increment is 0.05.

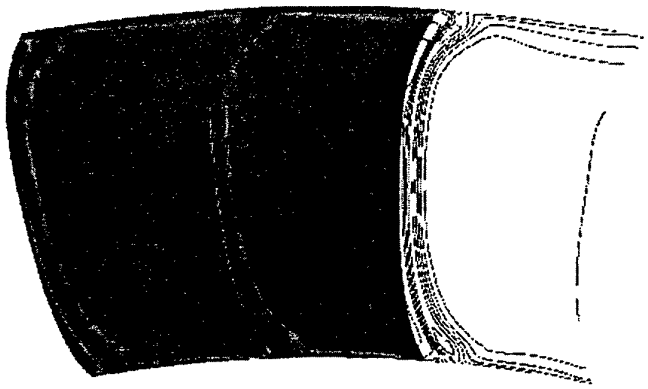

Average–passage (standard k–ε) simulated axial velocity (Vz / Utip) at ST 3.0 (solution interpolated to match axial location of ST 3.0). Contour minimum level is 0.10, contour maximum level is 0.45, contour increment is 0.05.

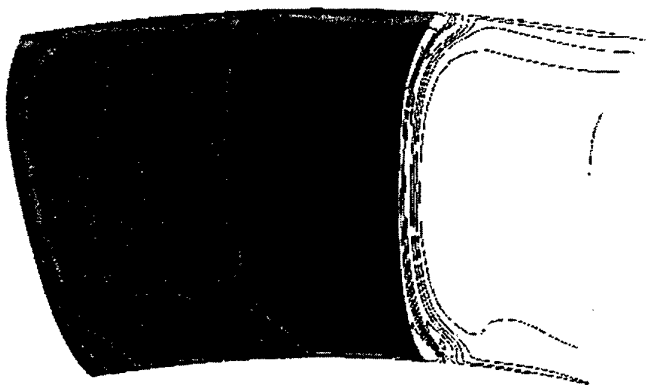

Average–passage (Shih k–ε) simulated axial velocity (Vz / Utip) at ST 3.0 (solution interpolated to match axial location of ST 3.0). Contour minimum level is 0.10, contour maximum level is 0.45, contour increment is 0.05.

Figure 15

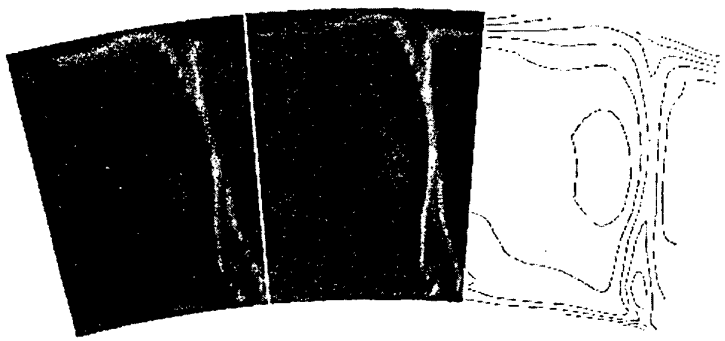

Measured (hot–film) average passage (ensembled and time averaged across the stator pitch) axial velocity (Vz / Utip) at ST 3.5. Contour minimum level is 0.10, contour maximum level is 0.45, contour increment is 0.05.

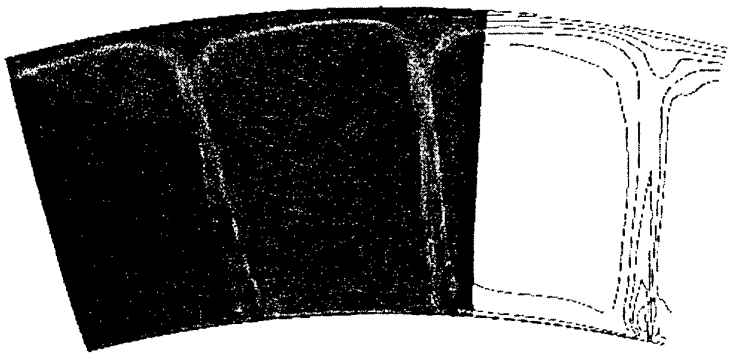

Average–passage (standard k–ε) simulated axial velocity (Vz / Utip) at ST 3.5 (solution interpolated to match axial location of ST 3.5). Contour minimum level is 0.10, contour maximum level is 0.45, contour increment is 0.05.

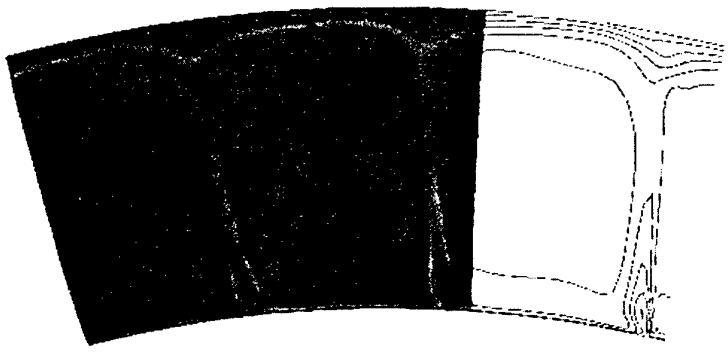

Average–passage (Shih k–ε) simulated axial velocity (Vz / Utip) at ST 3.5 (solution interpolated to match axial location of ST 3.5). Contour minimum level is 0.10, contour maximum level is 0.45, contour increment is 0.05.

Figure 16

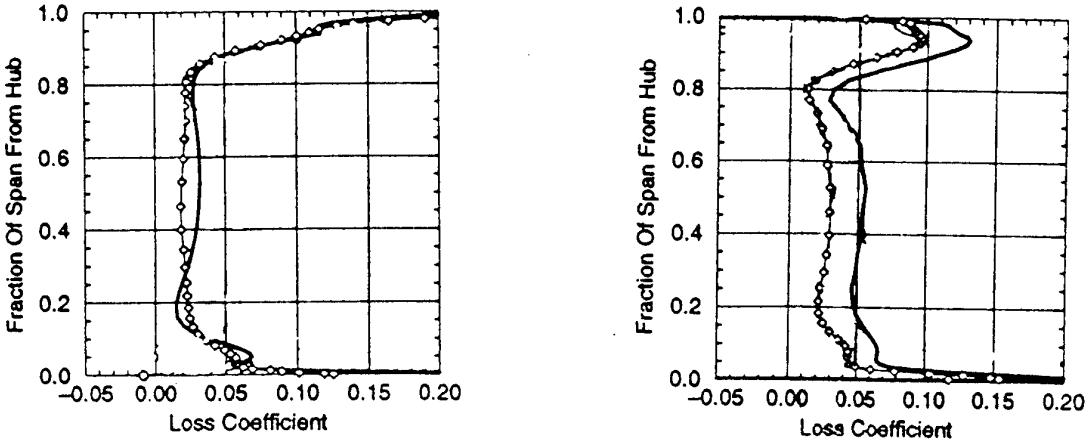

Fig. 17. Loss coefficient at Station 3.5 and Station 4.0 as obtained from the Average Passage simulations. Soild corresponds to standard $k-\epsilon$ model and diamonds correspond to improved $k-\epsilon$ model of Shih et al.[8]

RTO-MP-8
AC/323(AVT)TP/9

NORTH ATLANTIC TREATY ORGANIZATION

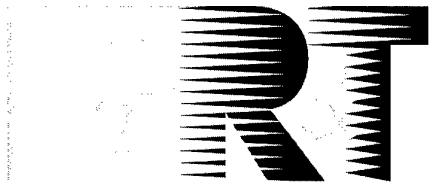

RESEARCH AND TECHNOLOGY ORGANIZATION

BP 25, 7 RUE ANCELLE, F-92201 NEUILLY-SUR-SEINE CEDEX, FRANCE

RTO MEETING PROCEEDINGS 8

Design Principles and Methods for Aircraft Gas Turbine Engines

(les Principes et méthodes de conception des turbomoteurs)

Papers presented at the RTO Applied Vehicle Technology Panel (AVT) Symposium - organized by the former AGARD Propulsion and Energetics Panel (PEP) - held in Toulouse, France, 11-15 May 1998.

The Research and Technology Organization (RTO) of NATO

RTO is the single focus in NATO for Defence Research and Technology activities. Its mission is to conduct and promote cooperative research and information exchange. The objective is to support the development and effective use of national defence research and technology and to meet the military needs of the Alliance, to maintain a technological lead, and to provide advice to NATO and national decision makers. The RTO performs its mission with the support of an extensive network of national experts. It also ensures effective coordination with other NATO bodies involved in R&T activities.

RTO reports both to the Military Committee of NATO and to the Conference of National Armament Directors. It comprises a Research and Technology Board (RTB) as the highest level of national representation and the Research and Technology Agency (RTA), a dedicated staff with its headquarters in Neuilly, near Paris, France. In order to facilitate contacts with the military users and other NATO activities, a small part of the RTA staff is located in NATO Headquarters in Brussels. The Brussels staff also coordinates RTO's cooperation with nations in Middle and Eastern Europe, to which RTO attaches particular importance especially as working together in the field of research is one of the more promising areas of initial cooperation.

The total spectrum of R&T activities is covered by 6 Panels, dealing with:

- SAS Studies, Analysis and Simulation
- SCI Systems Concepts and Integration
- SET Sensors and Electronics Technology
- IST Information Systems Technology
- AVT Applied Vehicle Technology
- HFM Human Factors and Medicine

These Panels are made up of national representatives as well as generally recognised 'world class' scientists. The Panels also provide a communication link to military users and other NATO bodies. RTO's scientific and technological work is carried out by Technical Teams, created for specific activities and with a specific duration. Such Technical Teams can organise workshops, symposia, field trials, lecture series and training courses. An important function of these Technical Teams is to ensure the continuity of the expert networks.

RTO builds upon earlier cooperation in defence research and technology as set-up under the Advisory Group for Aerospace Research and Development (AGARD) and the Defence Research Group (DRG). AGARD and the DRG share common roots in that they were both established at the initiative of Dr Theodore von Kármán, a leading aerospace scientist, who early on recognised the importance of scientific support for the Allied Armed Forces. RTO is capitalising on these common roots in order to provide the Alliance and the NATO nations with a strong scientific and technological basis that will guarantee a solid base for the future.

Printed on recycled paper

Published February 1999

ISBN 92-837-0005-8

Printed by Canada Communication Group Inc.
(A St. Joseph Corporation Company)
45 Sacré-Cœur Blvd., Hull (Québec), Canada K1A 0S7

Design Principles and Methods for Aircraft Gas Turbine Engines

(RTO MP-8)

Executive Summary

After more than half a century of operational use of gas turbine engines to power military aircraft, this symposium sets the focus on highlights of today's achievements in research and development of aircraft engine technology.

Future military aircraft will require significant performance gains from the propulsion system to provide enhanced operational flexibility, longer range, better fuel efficiency and improved affordability.

Gas turbine engines combine disciplines from all major engineering sciences in a most interdependent way. The energy concentration in engine components is permanently increasing. Aerodynamic loads, materials, cooling techniques, structural components, mechanical systems, combustors, augmentors and nozzles are equally designed to the limit of know-how. Sophisticated methods and design tools are used, relying on electronic control and monitoring systems, which safely operate engines close to their boundaries of flow stability and their mechanical integrity, at the same time pushing further the useable life span and reducing life cycle cost (LCC). The symposium addressed gas turbine design aspects for all classes of engines, including turbofan/turbojet, turboprops/turboshaft and turboramjet engines for tactical, transport, helicopter and expendable aircraft applications. The results will permit the military user to better understand the limit and options of any gas turbine engine in performance and use. They will also allow the industries of the NATO countries to better meet the design goals and other requirements set by the military customer thus improving NATO's defense and peace keeping capability while respecting today's budget constraints.

Les principes et méthodes de conception des turbomoteurs

(RTO MP-8)

Synthèse

Après plus d'un demi-siècle d'exploitation opérationnelle des turbomoteurs pour la propulsion d'avions militaires, ce symposium met en lumière les principales avancées réalisées dans le domaine de la recherche et du développement des technologies des moteurs d'avion.

Les propulseurs des avions militaires du futur devront assurer des gains de performances sensibles afin de permettre une plus grande souplesse opérationnelle, une autonomie plus grande, un meilleur rendement du carburant et un coût d'acquisition plus acceptable.

La technologie des turbomoteurs couvre des disciplines représentatives de l'ensemble des sciences de l'ingénieur, qui sont fortement imbriquées. La concentration des efforts sur les organes moteur ne cesse de s'accroître. Aussi, le calcul des charges aérodynamiques, des matériaux, des techniques de refroidissement, des éléments structuraux, des systèmes mécaniques, des chambres de combustion, des augmenteurs de poussée et des tuyères touche, aujourd'hui, aux limites des connaissances techniques. Il est fait appel à des méthodes et des outils de conception sophistiqués, qui sont tributaires de systèmes électroniques de contrôle et de surveillance. Ces systèmes permettent d'exploiter les moteurs dans des conditions proches des limites de stabilité de la veine et de l'intégrité mécanique, en toute sécurité, tout en prolongeant leur durée de vie et en diminuant leur coût global de possession (LCC). Le symposium a examiné les différents aspects de la conception des turbomoteurs pour toutes catégories de propulseur, y compris les réacteurs à double flux/turboréacteurs, les turbopropulseurs/turbomoteurs et les turbo-statoréacteurs pour des applications tactiques, de transport, hélicoptère et avions non-réutilisables. Les conclusions du symposium permettront à l'utilisateur militaire de mieux comprendre les limites de performance et les options offertes par tout turbomoteur. Elles permettront également aux industriels des pays membres de l'OTAN de mieux répondre aux objectifs de conception et aux autres exigences annoncées par le client militaire, afin d'améliorer les capacités de défense et de maintien de la paix de l'OTAN, tout en respectant les contraintes budgétaires actuelles.

Contents

SESSION II: MECHANICAL SYSTEMS

SESSION III: CONTROLS

SESSION IV: COMBUSTORS/AUGMENTORS

SESSION V: COMPRESSION SYSTEMS PART I

SESSION IX: ENGINE DESIGN AND ANALYSIS PART II

Theme

Future aircraft will require significant performance gains from the propulsion system to provide enhanced operational flexibility, longer range, better fuel efficiency and improved affordability. Gas turbine engines will be required to provide excellent performance and durability with minimum weight over a wide range of operating conditions. Improvements in aerodynamics, cooling technology, materials, structures and mechanical systems will offer the prospect of significantly improved performance and mechanical integrity within affordability constraints. Full progress can only be realized by the incorporation of advanced systems and component design methods utilising sophisticated mathematical models of flows, thermal behaviour, stresses, vibration, etc. This symposium will address gas turbine design aspects for all classes of engines, including turbofan/turbojet, turboprops/turboshaft and turboramjet engines for tactical, transport, helicopter and expendable aircraft applications.

Thème

Les propulseurs des avions futurs devront réaliser des gains en performances considérables afin de permettre une meilleure souplesse opérationnelle, une plus grande autonomie, une diminution de la consommation spécifique et un coût d'acquisition plus acceptable. Les turbomoteurs devront fournir d'excellentes performances et faire preuve de durabilité pour une masse minimale dans un large éventail de conditions opérationnelles. Des améliorations dans le domaine de l'aérodynamique, des technologies de refroidissement, des matériaux, des structures et des systèmes mécaniques, offrent des perspectives d'amélioration considérables au niveau des performances et des caractéristiques d'intégrité mécanique, tout en permettant de respecter les contraintes budgétaires imposées. Cependant, aucun progrès véritable ne pourra être réalisé sans l'incorporation de systèmes avancés et de méthodes de conception de composants faisant appel à des modèles mathématiques sophistiqués d'écoulements, de comportements thermiques, de contraintes, de vibrations etc. Ce symposium examinera les différents aspects de la conception des turbomoteurs pour toutes les catégories de moteurs, y compris les turboréacteurs/réacteurs à double flux, les turbopropulseurs/turbomoteurs et les turbo-statoréacteurs, pour applications tactiques, ainsi que pour les avions de transport, hélicoptères et aéronefs non réutilisables.

Recent Publications of the Former AGARD Propulsion and Energetics Panel

CONFERENCE PROCEEDINGS (CP)

Engine Response to Distorted Inflow Conditions
AGARD CP 400, March 1987

Transonic and Supersonic Phenomena in Turbomachines
AGARD CP 401, March 1987

Advanced Technology for Aero Engine Components
AGARD CP 421, September 1987

Combustion and Fuels in Gas Turbine Engines
AGARD CP 422, June 1988

Engine Condition Monitoring — Technology and Experience
AGARD CP 448, October 1988

Application of Advanced Material for Turbomachinery and Rocket Propulsion
AGARD CP 449, March 1989

Combustion Instabilities in Liquid-Fuelled Propulsion Systems
AGARD CP 450, April 1989

Aircraft Fire Safety
AGARD CP 467, October 1989

Unsteady Aerodynamic Phenomena in Turbomachines
AGARD CP 468, February 1990

Secondary Flows in Turbomachines
AGARD CP 469, February 1990

Hypersonic Combined Cycle Propulsion
AGARD CP 479, December 1990

Low Temperature Environment Operations of Turboengines (Design and User's Problems)
AGARD CP 480, May 1991

CFD Techniques for Propulsion Applications
AGARD CP 510, February 1992

Insensitive Munitions
AGARD CP 511, July 1992

Combat Aircraft Noise
AGARD CP 512, April 1992

Airbreathing Propulsion for Missiles and Projectiles
AGARD CP 526, September 1992

Heat Transfer and Cooling in Gas Turbines
AGARD CP 527, February 1993

Fuels and Combustion Technology for Advanced Aircraft Engines
AGARD CP 536, September 1993

Technology Requirements for Small Gas Turbines
AGARD CP 537, March 1994

Erosion, Corrosion and Foreign Object Damage Effects in Gas Turbines
AGARD CP 558, February 1995

Environmental Aspects of Rocket and Gun Propulsion
AGARD CP 559, February 1995

Loss Mechanisms and Unsteady Flows in Turbomachines
AGARD CP 571, January 1996

Advanced Aero-Engine Concepts and Controls
AGARD CP 572, June 1996

Service Life of Solid Rocket Propellants
AGARD CP 586, May 1997

Aircraft Fire Safety
AGARD CP 587, September 1997

Future Aerospace Technology in the Service of the Alliance — Sustained Hypersonic Flight
AGARD CP 600, Volume 3, December 1997

Advanced Non-Intrusive Instrumentation for Propulsion Engines
AGARD CP 598, May 1998

ADVISORY REPORTS (AR)

The Uniform Engine Test Programme *(Results of Working Group 15)*
AGARD AR 248, February 1990

Test Cases for Computation of Internal Flows in Aero Engine Components *(Results of Working Group 18)*
AGARD AR 275, July 1990

Test Cases for Engine Life Assessment Technology *(Results of Working Group 20)*
AGARD AR 308, September 1992

Terminology and Assessment Methods of Solid Propellant Rocket Exhaust Signatures *(Results of Working Group 21)*
AGARD AR 287, February 1993

Guide to the Measurement of the Transient Performance of Aircraft Turbine Engines and Components *(Results of Working Group 23)*
AGARD AR 320, March 1994

Experimental and Analytical Methods for the Determination of Connected — Pipe Ramjet and Ducted Rocket Internal Performance *(Results of Working Group 22)*
AGARD AR 323, July 1994

Recommended Practices for the Assessment of the Effects of Atmospheric Water Ingestion on the Performance and Operability of Gas Turbine Engines *(Results of Working Group 24)*
AGARD AR 332, September 1995

Structural Assessment of Solid Propellant Grains *(Results of Working Group 25)*
AGARD AR 350, December 1997

CFD Validation for Propulsion System Components *(Results of Working Group 26)*
AGARD AR 355, May 1998

LECTURE SERIES (LS)

Blading Design for Axial Turbomachines
AGARD LS 167, June 1989

Comparative Engine Performance Measurements
AGARD LS 169, May 1990

Combustion of Solid Propellants
AGARD LS 180, July 1991

Steady and Transient Performance Prediction of Gas Turbine Engines
AGARD LS 183, May 1992

Rocket Motor Plume Technology
AGARD LS 188, June 1993

Research and Development of Ram/Scramjets and Turboramjets in Russia
AGARD LS 194, December 1993

Turbomachinery Design Using CFD
AGARD LS 195, May 1994

Mathematical Models of Gas Turbine Engines and their Components
AGARD LS 198, December 1994

Integrated Multidisciplinary Design of High Pressure Multistage Compressor Systems (LS-211)
published as RTO EN 1, September 1998

AGARDOGRAPHS (AG)

Measurement Uncertainty within the Uniform Engine Test Programme
AGARD AG 307, May 1989

Hazard Studies for Solid Propellant Rocket Motors
AGARD AG 316, September 1990

Advanced Methods for Cascade Testing
AGARD AG 328, August 1993

REPORTS (R)

Application of Modified Loss and Deviation Correlations to Transonik Axial Compressors
AGARD R 745, June 1990

Rotorcraft Drivetrain Life Safety and Reliability
AGARD R 775, June 1990

Propulsion and Energy Issues for the 21st Century
AGARD R 824, March 1997

Impact Study on the use of JET A Fuel in Military Aircraft during Operations in Europe
AGARD R 801, January 1997

The Single Fuel Concept and Operation Desert Shield/Storm
AGARD R 810, January 1997 (*NATO Unclassified*)

Active Combustion Control for Propulsion Systems
AGARD R 820, September 1997

Programme Committee

Programme Committee Chairman

Mr. A. Cifone
Head, Planning and Operations
Propulsion and Power Engineering
Bldg 106 NAWCAD
22195 Elmer Road Unit 4
Patuxent River, MD 20670-1534, USA

BELGIUM

Prof. C. Hirsch
Vrije Universiteit Brussel
Dienst Stromingsmechanica
Pleinlaan 2
1050 Brussel

CANADA

Mr. D. Rudnitski
Head, Engine Laboratory
Institute for Aerospace Research
National Research Council of Canada
Ottawa, Ontario K1A 0R6

FRANCE

Prof. F. Leboeuf
Directeur Scientifique à l'Ecole Centrale
de Lyon
ECL, 36 avenue Guy de Collongue
69131 Ecully Cedex

GERMANY

Prof. H. Weyer
Direktor
Institut für Antriebstechnik
DLR
Postfach 90 60 58
51140 Köln

ITALY

Mr. C. Vinci
FIATAVIO s.p.a.
Tecnologie
via Nizza 312
10127 Torino

NORWAY

Mr. I. Skoe
IA-T
Kristian Sonjusvei 20
N-3600 Kongsberg

TURKEY

Mr. N. Sen
TUSAS Motor San A.S.
P.K. 610 Eskisehir

UNITED KINGDOM

Prof. R.S. Fletcher
Deputy Vice Chancellor
Cranfield Institute of Technology
Cranfield, Bedford MK43 OAL

Mr. K. Garwood
Rolls Royce plc.
P.O. Box 3
Mail Drop 0S6
Filton, BRISTOL BS12 7QE

UNITED STATES

Dr. C. Russo
Director of Aeronautics
NASA Lewis Research Center
MS 3-8
21000 Brookpark Road
Cleveland, Ohio 44135

HOST NATION COORDINATOR
Dr. G. Meauzé

PANEL EXECUTIVE OFFICE

From Europe
AVT - OTAN
7, Rue Ancelle
92201 Neuilly-sur-Seine

Mail from USA and Canada
AVT - OTAN
PSC 116
APO AE 09777

Tel: 33 (1) 55 61 22 85/87 Telefax: 33 (1) 55 61 22 98/99
e-mail: tonnp@rta.nato.int/cheynes@rta.nato.int

Technical Evaluation Report

Applied Vehicle Technology Panel Symposium on
DESIGN PRINCIPLES AND METHODS FOR AIRCRAFT GAS TURBINE ENGINES

Ludwig Schweikl
MTU Motoren- und Turbinen-Union München GmbH
Dachauer Str. 665
80995 München, Germany

1. INTRODUCTION

After more than half a century of operational use of gas turbine engines to power military aircraft, this symposium set the focus on highlights of today's achievements in research and development of aircraft engine technology.

Gas turbine engines combine disciplines from all major engineering sciences in a most interactive, interdependent and optimized way. As performance and thrust to weight ratios keep going up, the energy concentration in engine components is increasing accordingly. In today's newly developed engines, aerodynamic loadings, materials, cooling techniques, structural components, mechanical systems, combustors, augmentors and nozzles are equally designed to the limit of our present know-how. Sophisticated methods and design tools are used, relying on electronic control and monitoring systems, which safely operate engines close to their boundaries of flow stability and their mechanical integrity.

Consequently, this symposium did not concentrate on highly specialised subjects in specific areas only, but the papers, presented during this symposium, covered highlights and developments almost over the whole range of aircraft gas turbine design. The authors described recent achievements of their intensive work, to stretch the present state of the art in their particular fields.

2. KEYNOTE SPEAKER

The keynote speaker, Mr. J. P. Herteman, Directeur Technique, SNECMA, set the scene by pointing out, how the race after highest technology continues, but under new requirements. Not high technology as such is the goal anymore, but achievements in high technology at an affordable cost. This holds true for the development of engines as well as for production- and in service costs of whole aircraft systems, throughout their lifetime.

The traditional primary criteria to describe engine performance, like specific fuel consumption, thrust to weight ratio, acceleration, deceleration, range, reliability and their optimization according to missions requirements are no longer seen as the only major elements. They have to be complemented by new objectives, which are low cost of ownership and stealth capability.

What this means is that one has to look at engine developments in a global way, taking into account systems integration rather than optimizing engine components in isolation. There is a need to minimize risks by getting well prepared in generic technology programs, which take into account the impact of mechanical engine behaviour on their aerothermodynamic performance, as well as the interaction between individual engine modules.

Modeling engine components three dimensionally in their transient and dynamic environment in the early design stages and concurrent engineering, including manufacturers, suppliers and customers, are ways to keep cost down and shorten development times. Mr. Herteman presented impressive examples how this is being accomplished at SNECMA.

3. SYMPOSIUM OVERVIEW

The symposium was structured into nine sessions covering: Engine Design and Analysis, Mechanical Systems, Controls, Compression Systems, Combustors/Augmentors and Turbines. The papers that were presented in these sessions can be summarized under the following topics:

- Systems Integration
- Safety and Reliability
- Safe Engine Operation
- CFD and 3D Modelling
- Inverse Design Methods
- Cooling of Turbine Blades and Vanes
- Noise and NOx Emissions
- Materials and Mechanical Components

For an overview of the symposium and as a guide to how these topics were addressed by the authors, this is a brief summary:

3.1 Systems Integration

There is a critical phase right at the beginning of an engine development, when it comes to define the aircraft mission, the engine performance requirements and associated guarantee points. If performance specifications are incomplete or poorly defined or keep changing when engine design and development has started, then, as a consequence, boundary and operating conditions for engine components are fluid. Costly redesigns will be the consequence. Therefore, right at the beginning, the overall aircraft and engine definition as a global system is a mandatory requirement. The engine and aircraft companies have to get involved in creating such specifications. They know best what technology is available, what risk levels can be accepted and they know best what needs to be specified, in what detail, and when.
Papers 1, 2 and 46 give good examples how this can be accomplished.

3.2 Safety and Reliability

There are papers on reliability and safety. Paper 3 points out, in general terms, the importance of building in reliability and safety into engine designs. Paper 13 explains an interesting methodology that can be followed to generate faultless control software.

3.3 Safe Engine Operation

Flight safety under conditions of heavy inlet distortions can be secured by early detection of compressor stall onset in order to initiate countermeasures fast enough, to regain and maintain stable engine operation. Papers 14, 28 and 29 show that there are ways to detect stall onset but stall prevention by rapid counteraction could not yet be demonstrated.

Two papers address flow induced mechanical forces on blades.
Paper 26: With transonic fans, sufficient flutter-margin can become a very difficult problem to solve. Progress has been made towards reliable prediction methods, available during the design phase of fan blades.
Paper 34: Compressor and turbine blades are never free from wake and backpressure induced vibrations. Prediction methods for amplitudes of turbine blades are described in order to safeguard their integrity.

Another topic to be seen under „Safe Engine Operation" is crack propagation in rotor discs. Engine operators ask for life extensions in excess of original design targets.

Safe life extension can only be granted if a good understanding of crack onset and crack propagation exist. Two papers were presented, paper 33 covers this subject analytically, paper 38 uses a statistical approach to keep crack propagation under control.

3.4 CFD and 3D Modelling

Three dimensional viscous flow calculations, including transient conditions, have become a standard throughout the engine industry and some remarkable results have been presented of flow visualisation in engine components. CFD not only helps to understand where aerodynamic losses occur and therefore, how efficiencies can be increased, but to investigate aerodynamic interaction between components in order to optimize engine stability and overall performance. Keynote-paper and papers 18, 21, 22, 26, 31, 32, 35.

Transient 3D analyses of mechanical structures in combination with transient thermal analyses are used to study total engine behaviour under maneuvres with extreme load conditions. Keynote-paper and papers 4, 33, 34.

3.5 Inverse Design Methods

Inverse design methods, based on latest up to date codes in aerodynamic flow field prediction, heat transfer and internal cooling flow calculations are an excellent tool to shorten the highly iterative design process for turbine blades and vanes and, at the same time, generate optimum design solutions at acceptable costs, which under conventional sequentual design procedures can hardly be achieved. Papers 23 and 30 show how optimized blade and vane profiles can be obtained by inverse design. Paper 35 goes one step further and includes an internal cooling configuration that conforms to specified boundary conditions.

3.6 Cooling of Turbine Blades and Vanes

Besides analytical tools to determine the right aerodynamic shape of blades and vanes with their cooling configuration, there is a need to proof that what has been predicted theoretically, holds true when it comes to use the parts in an engine. A testfacility, providing a controlled environment for that purpose, is described in Paper 37.

There are ways of intelligent simulations to reduce the cost of heat transfer testing, for instance on a film cooled blade. Paper 39 presents the basic thermodynamic equations for an approximate procedure, using gas with suitable molecular properties.

3.7 Noise and NOx Emissions

An interesting Paper 15 was given on noise suppression of large turbofan engines, which demonstrates that by artificially generating additional noise at the right frequencies and with 180 degrees out of phase, one can actually substantially cancel out far field noise, generated by fan rotor and stator interaction.

A numerical 3D method was presented in Paper 18 on the subject of flow field prediction of jet cross-flows in the primary zone of Rich-Quench-Lean-combustors. Theoretical results, supported by jet air concentration measurements, correlated well with isothermal test results. The target is to generate flow fields with adverse fuel/air ratios to avoid NOx formation.

An intentionally much simpler combustor model that can be installed on desktop computers to study unsteady flow conditions including flame out and incorporating most elements of modern gas turbine burners, was presented in paper 17.

3.8 Materials and Mechanical Components

In contrast to traditional bearing life predictions, where it is assumed that bearing life is limited, there is now, with advanced bearing materials, a theory that under well defined conditions, bearings can be expected to last infinitely long even if small inclusions exist below the bearing surface. Details are given in paper 8.

A deep nitrided Chrome Molybdenium Vanadium steel, Paper 10, shows superior properties over conventional bearing materials. This new material can be used for bearing applications with higher speeds and complex shapes.

There was a presentation on the state of the art on vapor lubrication of bearings in paper 9, showing advantages over solid and powder lubricants at elevated temperatures.

Papers 27 and 42 deal with new composit metal matrix materials. These materials are ideally suited for rotating components, where high tangential stresses are present and offer a further step in circumferential speeds or alternatively lighter designs of engine compressors.

The impact of critical seal effectiveness on engine performance is part of a NASA funded technology program. A preliminary design study on advanced film-riding seals in the turbine region is the subject of paper 11.

4. TECHNICAL EVALUATION

SESSION I - Engine Design and Analysis - Part I

Paper 1 - The Gas Turbine Engine Conceptual Design Process - An Integrated Approach

Conceptual Design of a new engine has become an increasingly complex and sophisticated task. The designer is faced with conflicting targets and an overwhelming number of parameters to be considered, when engine performance and the whole aircraft system under its mission requirements are to be optomized.

How this problem can be attacked in the early design phase is the subject of this paper. It describes an approach, where aircraft performance goals are investigated first, in order to deduct main parameters of compatible engine cycles, which in turn are selected, taking into account constraints, such as available engine technology, weight, space and cost. In a next step it is shown, how engine integration with the aircraft can be handled and how installation losses are to be bookkept. The downselect process continues with the component flowpath and mechanical definition of candidate engine cycles. As a final step, aircraft mission analyses with trade off studies lead to the best compromise and final engine definition.

The paper offers a well structured methodology and a comprehensive overview of elements which need to be addressed in the conceptual design process of gas turbine engines.

Paper 2 - Design of a New Fighter Engine - The Dream in an Engine Man's Life

Fighter engines in Europe are designed in international cooperations, adding complexity to the decision making process. At the same time the whole knowledge base of European engine companies can be applied.

Task requirements are complex, because different goals exist between nations. Many different missions and hence performance guarantee-points are to be met. Cost and weight is paramount, which leads to the need to minimize number of parts, but demands highest technology at an acceptable risk level. Optimising a design means bringing conflicting requirements together, even at a time when many open questions cannot yet be answered.

There is a human element in this paper, speaking about the „Art of Engineering". The message is that well balanced judgements can only be obtained with the technical background and knowledge of senior engineers, accumulated over many years of experience in engine development.

Paper 3 - Designing for Reliability - the Rolls-Royce Approach
One of the primary objectives of RR is described as the „provision of reliable and safe products and services which meet the expectations and specified requirements of its customers". Safety, maintenance cost and fleet availability are main drivers to reliability. For civil engines, ETOPS regulations are additional factors.

The paper gives a good definition of reliability and explains the RR-methodology how to achieve reliability by paying special attention to the design and manufacturing process of engine components.

Paper 4 - The PW100 Engine: 20 Years of Gas Turbine Technology Evolution
The evolution of the PW100 engine is presented. Technical details of engine components are illustrated and performance numbers, as a result of continuous improvement in component technology, are quoted.

Besides telling the success story of the PW100 engine family in general, this paper is a good example, how 3D-analyses, for aerodynamic flow fields as well as on structural components, can lead to higher power concentration and lower fuel consumption. Advanced analytical tools enable higher aerodynamic loading of compressors and turbines with their associated flow ducts and higher specific energy release in combustors. Modeling static and rotating parts and studying their transient movements and deflections under thermal exposure and mechanical loads, is essential to keep parasitic losses under control. It also is the key to minimize rig and engine testing, which pays off in short development times and lower cost.

Paper 5 - Withdrawn

Paper 6 - Process Optimization in Advanced Compressor Design
Integrated product design and integrated product development in teams have become standard processes in the engine industry. MTU's experience is that teamwork can benefit if, in the early stages of a design process, one person acts as the focal point and team members contribute mainly outside meetings and on request only.

As the paper points out, the number of team meetings can be reduced and routine work can be kept off experts. This, however, is no longer valid, when fine tuning between specialists is necessary, to arrive at optimum design solutions.

Paper 7 - Actuation System for Variable Exhaust Nozzle and Inlet Guide Vanes on an Advanced Gas Turbine Engine
Hydraulic actuation systems for exhaust nozzles and variable compressor vanes are well known systems with similar basic components and functions. The system, presented in this paper, is unique insofar as it features a hydraulic pump, where the output volume is not controlled at a constant pressure, but where volume and pressure are adjusted to the momentary demand of hydraulic load by the convergent divergent nozzle. With only little additional complexity, heat rejection is thus minimized and power, extracted from the gearbox to drive the pump, is constantly adjusted to the operating mode of the engine. The paper describes in great detail the operation, reliability and maintainability of the various components and explains a mathematical model, used as a development tool, to simulate, during the design phase, the systems steady state and transient performance.

Paper 8 - La fiabilité des roulements aéronautiques et le comportement en fatigue
In contrast to earlier conventional bearing life predictions, where it was assumed that bearing life is always limted, there is now with advanced bearing materials, a theory that under well defined conditions bearings can be expected to last infinitely long, even if small inclusions exist below the bearing surface. This theory has been proven by extensive metallurgical research as well as bearing endurance tests and it is shown that in fact there is a threshold load condition, below which high speed bearings can be expected infinitely long not to fail.

It is important to note that this statement relates to bearings that might have small undetected internal defects below a certain size. The object of the research program was not to deal with external impurities, such as corrosion or foreign particals on bearing tracks.

Paper 9 - Computer Modeling of Heat Generation in Vapor Lubricated Bearings for Gas Turbines
Progress has been made to replace liquid lubrication systems for bearings by vapor lubricants. The driving idea behind it is to eliminate complex and heavy conventional oil-system components.

Although it cannot be expected that, for heat balance reasons, bearings for high performance gas tubine engines can ever be vapor lubricated, there seems to be an opportunity for short duration applications at temperatures around 400°C and above in cruise missile engines.

Paper 10 - Caracterisation metallurgique et tribologique de l'acier à roulement 32CrMoV13 nitruré profond pour roulements aéronautiques
The paper reports on the development targets, characteristics and endurance test results of a new deep nitrided material that is superior over conventional through hardened and surface hardened bearing materials.
By careful dimensional control of the nitrided zone in the bearing races, porous and brittle layers in critical areas are eliminated. Major requirements of advanced gas turbine bearings, such as high bearing loads at elevated temperatures and speeds, small cross sections with complex shapes, insensitiveness to deflections, pollution and limitted lubrication, can be met.

Paper 11 - Advanced Seal Technonolgy Role in Meeting Next Generation Turbine Engine Goals
Air leakage in secondary air systems is a major contributor to the loss in engine efficiency and hence to the increase in DOC. It is obvious that improvements in secondary air system seal technology are essential, if pressures and temperatures in engines continue to rise. Relatively few locations in the turbine rim area account for the majority of total air leakage losses. Consequently in the study, presented in this paper, the rim cavities between turbine disks were selected, to replace conventional labyrinth seals by film-riding face seals.

In total, the paper gives a good overview of current and future seal technology with its impact on engine performance and operating cost. However, the investigated film-riding face seal design will need careful attention in its detailed design, and convincing reliability demonstrations under adverse engine running conditions will be necessary, before it can be regarded as a possible solution for flight engines.

Paper 12 - Fuel/Oil System Management in Aircraft Turbine Engines
Fuel cooled oil coolers, assisted by air cooled oil coolers are used to keep maximum temperatures in engine oil systems within limits. The total fuel capacity on board of an aircraft, serving as a heat sink, may be limited at adverse flight missions, therefore a circuit of heat flows in an engine is used to predict critical conditions covering a full flight envelope.

The computer program, which was developed for this purpose, is not yet capable to simulate accurately enough the complete heat flux system without additional adjustments through engine tests. Oil churning is one of the phenomena, which at present is not included in the program.

Paper 13 - Fault Tolerant Design Methodology in Software for Safety Related Systems
Errors in safety related software can, with an acceptable probabilty, only be detected by a well organised systematic review process, which takes into account dependancies and retrospective effects of changes between individual software elements.
The described methodology, which is still under development, brakes the software creating process down to fundamental input and output elements of a network and allocates probabilities of errors to its nodes, which are based on past experience. The overall probability of errors can then be computed.

The paper also refers to limitations of this methodology. As it stands, it is considered to be quite feasible for assessing the integrity of software by project managers prior to its delivery, but a large amount of data is required and statistical results obtained are not yet completeley satisfactory.

Paper 14 - Monitoring and Control of Helicopter Engines at Abnormal Operating Conditions
An Allison 250-C20B engine, equipped with a slave electronic control system, a bleed valve and throttle device was used to study its compressor behaviour close to and beyond surge onset. Pressure and temperature signals, taken from the compressor were analysed in an attempt to detect unstable operation early enough to offload the compressor by opening a bleed valve. The test showed that, above idle conditions, the time from stall onset detection to full stall was too short to initiate countermeasures and regain stable engine operation.

One could argue that the results obtained are not generic but are closely related to the particular engine setup and its compressor characteristic. Therefore, for different engine installations, the signal processing under investigation may well be considered as a valid concept for a surge avoidance system.

Paper 15 - Simultaneous Active Source Control of Blade Row Interaction Generated Discrete Tones
The paper reports on the theory and successful demonstration of active noise control to cancel out discrete frequency tones, propagating upstream and downstream of interacting fan blade and vane rows into the far-field. This is accomplished by superimposing out of phase acoustic waves, generated by sources that can be mounted in engine centerbodies.

It seems that active noise treatment, as demonstrated, can be designed for incorporation into large fan engines. It adds complexity and cost, but may have to complement today's passive treatments, if noise regulations become more stringent in the future.

16 - Improved Gas Turbine Response using LQR Control
The investigation presented in this paper refers to a control system of a low bypass turbofan engine for a U.S.Navy aircraft. By using the linear quadratic regulator technique the response time to fuel flow inputs stepwise and transiently as well as the performance stability of the engine used as an example could be improved.

The paper explaines how LQR functions are derived and shows the basic equations, which can serve as a guide to the design of linear quadratic regulators for any other application, where fast response characeristics and good stability of a control system are required.

Paper 17 - Unsteady, Finite-Rate Model for Application in the Design of Complete Gas Turbine Combustor Configurations.
In contrast to Computational Fluid Dynamic methods, which are frequently used to analyse gas turbine combustors, this paper predicts combustor performance by a one-dimensional, finite-rate, unsteady combustor model which is capable of describing transient flow-fields in combination with non-equilibrium chemical reactions.

By running a reverse-flow combustor on a desktop computer during the presentation of the paper, it was demonstrated that the overall combustion process could, with some calibration for pressure losses, well be predicted. Flow dilution, flow- and temperature fields, flame blowout was visualised under steady state and oszillating combustor inlet-conditions.

Paper 18 - Design Principles for the Quench Zone of Rich-Quench-Lean Combustors
This paper describes in much detail experimental work carried out to optimize jet row configurations for crossflow mixing of secondary air behind the primary zone of a combustor in order to quickly overcome NOx producing stochiometric conditions. It shows that, by using isothermal mixing in combination with a numerical method to account for heat release effects and by comparing gas analysis of a combustor with light sheet results of the same combustor, valid results can be obtained.

The technique described can be a very usefull tool to determine the basic configuration of a combustor in the initial design phase without extensive combustion testing. Although it is aimed at visualising and optimising cross flow patterns in RQL combustors, it could well be adapted to study flow fields in other areas of interest in an engine where flow mixing takes place.

Paper 19 - Afterburner Design and Development
The paper presents a comprehensive description of a state of the art afterburner system for an advanced fighter aircraft. It starts out with the fundamental requirements, an afterburner system has to fullfill and explains the major steps of the design process. Each individual component and subsystem is addressed, with sufficient background to understand why a particular solution was chosen. It also gives an overview and explanation of problems encountered during the development and how these problems were solved.

Besides the descriptive part of the presentation, the paper also points out the benefits of complementing an empirical approach with advanced computational methods, which are used to analyse flows and temperature distributions under reheat and non reheat conditions.

Paper 20 - A Mixed Flow Turbofan Afterburner Simulation for the Definition of Reheat Fuel Control Laws
To secure fan stability under unintentional afterburner ignition delays, closed loop systems, where there is a pressure feedback signal to control the nozzle position, are replaced by open loop systems without a direct link between nozzle area and afterburner pressure. Open loop control systems rely solely on a simulation of the engine performance to calculate the required fuel flow for selected nozzle areas in order to build up the associtiated pressures in the afterburner, which in turn relate to corresponding thrust levels.

This task is highly dependent on a precise knowledge of nozzle areas under operating conditions where temperatures, loads and leakages influence the effective nozzle flow. The paper concentrates on modeling the afterburner and nozzle by describing effects that have to be taken into account and on calibration and verification with engine results.

Paper 21 - Numerical Simulation of Multi-Stage Turbomachinery Flows
A four and one-half stage large low speed compressor was used to assess the predictive capabilities of an average passage flow model despite the fact that, between cascades, the deterministic flow is unsteady in time and spatially aperiodic. Although predicted stage characteristics were close in shape, there was a clear shortfall in the computed pressure rise, which could be attributed to stator wakes that were predicted to be deeper than they were measured. Using an improved model that yielded thinner boundary layers along the blade surface, where pressure gradients are favorable, resulted in an excellent agreement between measurement and prediction.

Paper 22 - Performance Analysis of Centifugal Compressor Stage, by Means of Numerical and Experimental Investigation of Rotor-Stator Interactions

The paper deals with the computation of the highly distorted flow field in the vaneless space between the impeller outlet and diffusor inlet of a radial compressor. So far, matching a diffusor with the flow out of an impeller, passing through a vaneless space, was only accomplished through mono-dimensional considerations.

In this presentation, results out of Laser Two Focus measurements are shown and interpreted, giving an insight to the flow phenomena in this area. At the same time an outline of a Navier-Stokes based numerical method is explained, which, customised through a special data reduction technique, allows design time affordable calculations. Unsteady and steady flow calculations show a high degree of conformance with measured data.

Paper 23 - Three-Dimensional Inverse Design Method for Turbine and Compressor Blades

Blade designs have to conform to velocity or pressure distributions along their surface that are determined by efficiency requirements. Usually successive modifications are performed by the designer, backed up by rig testing, to fullfill all aerodynamic and mechanical design targets, which is time consuming and does not necessarily lead to the best possible solution.

The method, introduced by this paper, follows a procedure in which three-dimensional blade shapes are optimized numerically, based on prescribed velocity or pressure distributions and mechanical boundaries. The method uses time steps to an iterative solution of three-dimensional Euler equations, by assuming permeable wall boundaries and updating of the flow field until the flux through wall boundaries is zero and prescribed conditions are met.

Paper 24 - Withdrawn

Paper 25 - A One Dimensional, Time Dependent Inlet / Engine Numerical Simulation for Aircraft Propulsion Systems

Tests, carried out to study the interaction between a supersonic inlet and a turbojet engine, were analysed by a closely coupled, high frequency simulation that solved one dimensional Euler equations. This was accomplished by combining two existing codes to model the intake and the engine. Results compare reasonably well. The simulation had to be tuned somewhat to conform to test data, since accurate compressor and turbine maps of the tested engine standard were not available.

Paper 26 - Part Speed Flutter of Transonic Fans

The window for flutter free operation of fan blades is sometimes small, therefore their flutter characteristic must be predictable in the early design phase, if costly redesigns are to be avoided. The paper describes a linear, unsteady calculation, performed on an inviscid flow mesh for two typical fan blades. It demonstrates that the results are in fair agreement with the results from a model that includes non-linear, unsteady effects and confirms the utility of a linear approach, taking considerable less time to calculate than for a steady state, viscous flow solution.

A number of effects, not included in the model, which are addressed in the papers conclusions, may well be of importance to flutter onset in a marginal situation and may need to be accounted for.

Paper 27 - The Introduction of Reinforced TMC Materials into Rotating Machinery - The Safe Approach

Significant progress has been made with regard to the quality of titanium metal matrix composites. One fundamental issue, the uniform fibre distribution inside the matrix, has reached a near perfect stage, suitable for the design of rotating components under tangential stress or for parts where high stiffness is a requirement. There are other quality related topics to be further improved, which are mainly concerning the manufacturing process and which are dealt with in the paper.

A stable manufacturing process will, with this kind of material, always be related to specific part configurations. Therefore, the development of individual control methods in all stages of the manufacturing process for a part will be as important as reliable non destructive inspection techniques for the final component.

Paper 28 - Design of an Active Stall Avoidance System for a Subsonic Axial Compressor

The paper presents test results that were obtained by operating a single stage compressor rig close to and in surge. The purpose of the test was to detect and analyse the onset of static pressure fluctuations at the wall in front of the rotor, as rotating stall evolves and to define and test a robust closed-loop control system which is fast enough to prevent full rotating stall.

So far, the goal of stall prevention could not yet be achieved. But by means of a modified two-step controller, unloading the compressor temporarily after rotating stall onset and inspite returning close to the operating point where rotating stall initiated, the compressor could be stabilised again within five revolutions at 3700 rpm.

Paper 29 - Rotating Pip Detection and Stall Warning in High-Speed Compressors Using Structure Function

The focus of this paper is set on a method to detect rotating pressure spikes prior to stall in experimental high speed compressors. Pressure signals are processed statistically by introduction of a so-called structure function, which is used to predict the onset of instabilities that lead to stall. It is shown that this method can reliably be applied by using a single pressure trace only. An online implementation in conjunction with an active controller will, according to the paper, be a next step after further work on signal conditioning.

Paper 30 - Turbomachinery Blade Design Using a Navier-Stokes Solver and Artificial Neural Network

Two-dimensional blade sections are geometrically defined by an automatic approximation method, based on the known performance and its boundary conditions of previously investigated blades, stored in a database. The new blade sections undergo a Navier-Stokes analysis and its characteristic data are added to the existing database as a new input. The approximation is a self optimising interpolation process, with blade shapes from the database which conform closest to the given requirements. This cycle is repeated, until the design goals are met.

A key feature of an automatic optimization method is its capability to judge the quality of its results and to introduce improvements for the following step. This has particularly been accomplished in paying attention to the Mach number distribution on the blade surface and in determining the transition point from laminar to turbulent flow in order to adjust the calculation method for the momentum thickness of the boundary layer.

Paper 31 - Advanced CFD Tools for Multi-Stage Turbine Analysis

Results of an improved CFD code are presented in this paper. The algorithm to solve the governing equations for compressible fluid problems is used to predict the impact of rotor tip leakages on a single stage high pressure turbine and to analyze a four stage low pressure turbine, taking into account the influence of adjacent blade rows.

The numerical results are in good agreement with the experimental data from cold flow rig tests. The shapes of the radial distribution of total pressures and swirl angles are well predicted for both turbines. The same applies for the absolute values of the static pressures at hub and tip of the low pressure turbine.

Paper 32 - Advanced Computational Fluid Dynamics in the Design of Military Turbines

In designing high lift shroudless turbine blades, it is essential to keep additional losses incurred under control. A thorough investigation has been carried out of how well losses from secondary flows and overtip leakages can be predicted by various codes currently in use or still in development at RR.

The paper compares codes for isolated blade rows with codes for multistage steady overlapping grids and describes, what can be expected from code, aimed at calculating 3D unsteady viscous flow through a whole turbomachine. Special attention is given to the convergence of solutions, run time and the influence of coarse versus fine grids on the quality of loss prediction and shock resolution.

Paper 33 - Automatic Three-Dimensional Cyclic Crack Propagation Predictions with Finite Elements at the Design Stage of an Aircraft Engine

Numerical crack propagation calculations depend on the knowledge of the three dimensional crack geometry as it develops under cyclic stress. The method described in this paper starts with an arbirarily shaped crack and calculates three dimensional crack increments after determining a mixed-mode stress intensity factor.

The remarkable feature outlined in this paper is the ability of the code to automatically replace an existing mesh in front of the crack by a mesh that corresponds to the developing crack shape. The crack shape establishes itself during propagation in equilibrium with the prevailing stress fields and calculated local stress intensity factors. Predicted crack shapes and observed cracks from tests were in good agreement.

Paper 34 - Forced Response Predictions for a HP Turbine Rotor Blade

Unsteady aerodynamic forces, due to wake passing from upstream blades, the potential field of upstream and downstream bladerows, or due to fluctuating backpressures may cause excessive vibration levels in rotating blades, if resonances with their natural frequences occur within the running range of an engine. In most cases it is not possible to avoid such resonances due to the wide range of speeds and conditions in engine operation. If resonances occur, then actual vibration amplitudes need to be predicted, to determine the blades lives under these conditions.

Two methods to compute forced responses of rotor blades are discussed in this paper. Both methods are in good agreement with measured data. One method in particular is quoted to be an efficient and accurate tool for use within design cycle times.

Paper 35 - Aero-Thermo-Structural Design Optimization of Internally Cooled Turbine Blades
There is a strong interaction of engineering disciplines in designing cooled gas turbine blades. To determine the best blade design the traditional way that fullfills aerodynamic, thermal and structural requirements under given boundary conditions, is time consuming and therefore is usually terminated at some point, hoping that the design is not too far away from the optimum solution. The paper describes a methodology that makes use of existing proven disciplinary analysis codes that may have been written in different programming languages and with different types of solving algorithms. A hybrid optimization process is incorporated with a logic for automatic switching between the codes in order to arrive at the global optimum.

The chosen sequentially coupled computation is an approach with a high potential to efficiently speed up the design process and to arrive at better results for internally cooled turbine blades using state of the art technology in the disciplines involved.

Paper 36 - Withdrawn

Paper 37 - The Benefits of a Rotating Rig for Research into Advanced Turbine Cooling Systems
Traditional design methods for cooled turbine blades neglect the influence of rotation on heat transfer coefficients. Coriolis and buoyancy forces in modern multipass turbine blade designs create radial secondary and cross flows that have a significant effect on heat transfer, which is indispensable to know as future designs aim at higher gas temperatures with less cooling flow and longer blade lives.

For this reason and because CFD calculations so far are unreliable in predicting heat transfer levels in highly turbulent flows, a large scale rotating rig as presented in this paper, can yield valuable data to obtain a comprehensive experimental data-base to accurately predict heat transfer coefficients and to calibrate CFD codes.

Paper 38 - Simulation of Crack Propagation in Engine Rotating Components under Variable Amplitude Loading
This paper deals with a new life management philosophy for life limited critical rotating components in engines. The used life is calculated on a statistical basis simulating a probable mission mix for an engine over its lifetime. Initial flaws are assumed to exist on a life limiting component location just below the detection threshold of a chosen inspection technique and the crack propagation life to a fracture critical size is then calculated under variable loads, corresponding to the randomly selected mission mix. Planned inspections of these critical locations are set to a fraction of the calculated lives to ensure that all propagating cracks are found well before they might cause component failure.

If accurate accounting of the actual life usage by means of an on board engine monitoring system is not available, then this method can maximize the use of undamaged components and at the same time safely detect damaged components in time.

Paper 39 - Theory for the Use of Foreign Gas in Simulating Film Cooling
For gas turbine film cooling experiments at small temperature differences between the coolant and the free gas-stream the coolant density and the mass flow need to be simulated if the resulting turbulent flow field should reflect the real situation in an engine environment.

The paper derives the fundamental equations that apply if gas of higher density than air is used as a coolant and prooves that for carbon dioxide little correction is necessary to obtain the correct film cooling effectiveness and heat transfer coefficients.

Paper 40 - Withdrawn

Paper 41 - Withdrawn

Paper 42 - The Potential of Advanced Materials on Structural Design of Future Aircraft Engines
A significant part of gas turbine engine operating costs, in terms of low fuel consumption, depend on high component efficiencies within a high pressure and high temperature thermodynamic cycle, whereby the available material technology is a dominant factor. This paper covers latest titanium alloys for increased temperature applications, titanium matrix technology for high circumferencial speed compressors, thermal barrier coatings for turbines and ceramic matrix composites for combustors.

Characteristic differences and possible applications of the materials are well covered. Mechanical and physical data are compared and explanations are given how chemical composition, microstructure and processing techniques influence the material properties. The paper contains a comprehensive list of references for backup information.

Paper 43 - Withdrawn

Paper 44 - Cycle-match Engine Models used in Functional Engine Design - an Overview
As in the past, steady state engine performance is predicted by modeling the thermodynamic cycle.
Cycle-match typically is achieved by iteration under given boundary conditions of interest. Transient

simulation follows a numerical integration method of selected state variables. Besides this performance engineers approach, the control engineer tries to meet performance requirements by suitable control laws, using a different computing environment. The paper emphasises the need for a common functional working relationship in the future by means of a common engine model and outlines an iterative solution method for the time dependant behaviour of an engine.

The use of an iterative thermodynamic engine model offers the capability to account for dynamic effects that influence engine behaviour, like heat soakage, shaft dynamics or unsteady gasflow. These effects can be a major factor, if engines are running close to stability limits, or if high transient engine response is a requirement.

Paper 45 - Smart Flow Control in Aircraft Engine Components & Component Interactions
Vortex generators are known as devices that can reduce drag in areas where subsonic or supersonic flow separation is occurring. A typical area of interest in engine installations is the aircraft inlet system which may, under flight maneuvers, deliver distorted flow to the compressors. With exhaust system, afterbody drag and noise can be a problem. In addition there are regions inside an engine, where flow separation is causing losses. In contrast to passive vortex generators, which may be the only possibility for rotating components, the paper deals with active systems, which adjust their geometry to the local requirements as they arise via feed back signals from sensors and actuator systems.

The tests carried out so far in laboratories prove the feasibility of the concept. Before implementing active vortex generators in new aircraft and engine installations, suitable sensors, actuators and controllers need to be developed that are reliable and robust enough to withstand in field environments.

Paper 46 - F/A-18 E/F Aircraft Engine (F414-GE-400) Design and Development Methodology
This paper describes background, methodology and experience with a new team-approach to design and develop an aircraft/engine system, with the focus on engine development. The key elements behind this successful program are addressed, which center around full and open communication to the highest level and into every detail in all phases of the program.

Technical details of the engine are presented but the main topic of the paper is how to implement and operate an efficient program management system, taking into account risk management, risk balance, concurrent engineering and lessons learned.

5. CONCLUSIONS

This symposium gave an overview on the state of the art for a wide range of engineering disciplines that make up current engine technology.

Future progress is increasingly difficult to achieve. The computational effort, to calculate and visualise true flow fields in aerodynamic components or to predict deflections, temperature and stress distributions in critical parts is constantly rising with the need to model three-dimensional phenomena in great detail and under transient conditions. Due to the fact that the design of engine components encompasses a wide range of variables under unsteady boundary conditions, optimum solutions can only be obtained in reasonable time with the help of intelligent self-learning software.

To follow environmental regulations with regard to engine noise is well under control. To design combustors for low NOx emission is still a highly empirical process, where full numerical simulation of the combustion process is an unsolved problem.

Critical rotating parts are designed to operate close to their mechanical limits with little margin. The capability to predict crack propagation, originating from unknown defects, is essential for flight safety and cost efficient life management.

It is evident that new materials are a key element in future engine designs. The availability of titanium aluminides and titanium matrix composites is imminent. However, there is a need for proven design systems, with faultless manufacturing processes, damage tolerant lifing systems and design rules that guarantee reliability and conformance to the special properties of these materials.

6. RECOMMENDATIONS

Out of many important technology programs that were covered in this symposium, three major issues are to be mentioned:

- To develope efficient codes, to model the global performance of an engine and its components, three-dimensionally under transient and dynamic conditions, is of paramount importance.

- Inverse design methods require increasing attention. They need to be available as common tools to design engineers for optimum results.

- New light weight, high temperature alloys and metal matrix composites are to be introduced together with safe design systems. They are the key to higher specific engine performance.

LES PRINCIPES ET LES METHODES DE CONCEPTION DES TURBOREACTEURS AERONAUTIQUES MILITAIRES

J.P. HERTEMAN, Directeur Technique
M. GOUTINES, Directeur Adjoint des Recherches
Snecma Villaroche
77556 MOISSY CRAMAYEL
France

1. INTRODUCTION

La conception des turboréacteurs d'avions militaires connaît actuellement une transformation due, entre autres, à l'évolution des demandes de leurs clients qui, soit modifient les priorités entre les performances demandées, soit introduisent de nouvelles spécifications. De ce classement il peut être tiré la liste des technologies, méthodes ou savoir-faire sur lesquels il convient de faire porter l'effort de recherche et de développement.

En ce qui concerne les avions militaires, il faut tout d'abord noter que les cinq critères de performances habituelles, à savoir, la consommation spécifique de carburant, le rapport poussée au décollage/masse du moteur, les temps d'accélération et de décélération, l'étendue du domaine de vol et la fiabilité peuvent se pondérer de différentes façons pour constituer un critère de performance globale. Les poids de ces diverses performances varient suivant la ou les missions de l'aéronef, ce qui peut conduire à des architectures moteur différentes.
Ces dernières années, les armées et Services Officiels ont souvent mis au premier plan de leurs préoccupations deux besoins qui auparavant apparaissaient peut-être moins critiques, à savoir :

- la réduction de tous les coûts, depuis le coût de production jusqu'au coût de maintenance des systèmes depuis longtemps en service
- la contribution du moteur à la discrétion électromagnétique des aéronefs, à la fois en infra-rouge et dans les bandes Radar.

En ce qui concerne les coûts, il s'agit maintenant de concevoir des moteurs de haute technologie à faible coût . Concrètement cela veut dire que les technologies désirables sont celles qui procurent simultanément des performances élevées et des coûts réduits et pas forcément le maximum des performances. Il faut noter qu'un même progrès technologique (par exemple, l'aérodynamique des aubes) peut être décliné de plusieurs manières (on peut maximiser le rendement de la turbomachine, réduire le nombre d'aubes ou distribuer le gain sur ces deux postes).

2. AMELIORATION DE L'ARCHITECTURE DES MOTEURS ET DE L'INTEGRATION DE LEURS COMPOSANTS

2.1. Composants de technologie avancée pour moteurs à cycle thermodynamique conventionnel

Le couplage fort entre les différents modules conduit généralement à un dessin optimal différent de celui que l'on obtiendrait par assemblage des optimums de chaque module. Cela est évident pour la conception des compresseurs et des turbines liés sur un même arbre.
L'accent mis sur les coûts, la discrétion électromagnétique et des qualités telles que la fiabilité conduit maintenant à effectuer des optimisations fondées sur des critères globaux, multi-dimensionnels et exprimés au niveau du moteur ou du système avion/moteur.

Il existe de fortes interactions aérothermodynamiques entre modules. Par exemple, on doit s'assurer que les distorsions instationnaires de pression d'arrêt et du vecteur vitesse, délivrées par l'entrée d'air lors des manœuvres à haute incidence, restent compatibles avec le niveau de détérioration acceptable de la ligne de pompage du compresseur basse pression. L'avion optimal n'est atteint qu'au travers d'une répartition judicieuse des spécifications entre l'entrée d'air (distorsion maximale admissible) et le compresseur BP (marge au pompage minimale à assurer). La figure 1 illustre l'ensemble des moyens de simulation, mesures et calculs aérodynamiques développés pour s'assurer, au stade de la conception (calcul) et avant les essais en vol (essais sur banc sol de moteur ou de compresseur BP), de la compatibilité entrée d'air/moteur.
De la même manière, il existe un couplage aérothermique évident entre la chambre de combustion et la turbine HP.

Les jeux radiaux entre les carters et le sommet des aubes d'un rotor, ou ceux entre les léchettes d'un labyrinthe et l'anneau en regard, ont une influence critique sur les performances des turbomachines. Ces jeux et leur évolution sont fortement conditionnés par le comportement dynamique et thermique du moteur considéré dans sa globalité. De plus, dans les conditions d'opération réelle les moteurs sont soumis à des efforts transitoires de diverses origines. : balourd, appontage, manœuvre sous forte charge, etc... La figure 2 illustre un modèle dynamique d'un moteur complet et l'utilisation qui peut en être faite pour réduire les efforts sur une attache de moteur dus aux chocs à l'appontage. Ce type de calcul est nécessaire pour s'assurer que le moteur conçu est à la fois le plus léger possible et apte à assurer sans détérioration significative un nombre de cycles suffisant en service dans les armées.

Enfin, l'assemblage, le montage-démontage d'un moteur et de ses très nombreux accessoires et tuyauteries peuvent être des opérations coûteuses et longues si l'effort de rationalisation et de simplification n'est pas fait dès la conception. Celle-ci reposait auparavant sur des maquettes matérielles, qui par ailleurs se prêtaient mal à l'obtention d'une configuration optimale dans un délai raisonnable. L'utilisation de maquettes numériques à l'aide de logiciels de conception et de visualisation 3D du type CATIA V4 et autres a permis des réductions spectaculaires des temps de dépose/repose aussi bien que des coûts de conception de l'habillage. La figure 3 montre le maquettage numérique d'un sous-ensemble d'un moteur militaire .

Paper presented at the RTO AVT Symposium on "Design Principles and Methods for Aircraft Gas Turbine Engines", held in Toulouse, France, 11-15 May 1998, and published in RTO MP-8.

2.2. Cycles thermodynamiques avancés et architectures complexes

De nouveaux concepts sont étudiés pour améliorer les performances ou les qualités opérationnelles. Citons par exemple le cycle variable (ou hybride) qui conduit à un compresseur HP à dilution variable, la gestion des prélèvements d'air ou de puissance, la poussée vectorielle, et à plus long terme le distributeur de turbine basse pression à calage ou à perméabilité variable.

Le principal défi posé par ces techniques nouvelles est le maintien des coûts et de la fiabilité au même niveau que celui atteint sur les moteurs conventionnels. En particulier, une des principales difficultés est la gestion et le contrôle du moteur à l'aide d'un système de régulation de complexité acceptable. De la même manière, l'intégration des différents modules dans des moteurs de ce type sera rendue plus complexe.

L'avenir des moteurs d'architecture avancée dépendra de la capacité des concepteurs à maintenir un coût global d'exploitation (« Life Cycle Cost ») proche de celui des moteurs conventionnels .

3. TECHNOLOGIES DES STRUCTURES ET DES SYSTEMES MECANIQUES

Des progrès devront être réalisés afin de réduire les coûts et d'augmenter la fiabilité des systèmes de commande des organes à géométrie variable. Cela concernera la dilution variable des compresseurs, les tuyères à deux paramètres (et/ou vectorielles), la confluence variable, etc...

De nouveaux concepts matériaux structuraux, intégrant de façon plus poussée différentes fonctions mécaniques et thermiques, seront retenus afin de diminuer la masse des moteurs. La figure 4 montre l'utilisation de composite à matrice organique (carbone/résine « PMR15 ») pour le canal flux froid du moteur M88-2 du Rafale. Cette figure illustre aussi l'emploi de composites thermostructuraux à matrice céramique (carbone/SiC) pour construire les volets extérieurs de la tuyère du SNECMA M88-2. A terme, les matériaux composites de type « CERASEP » (SiC/SiC), grâce à leur tenue à haute température, seront utilisés pour la construction des volets chauds divergents des tuyères et autres éléments constitutifs des chambres et systèmes de réchauffe..

Des paliers d'arbres, roulements et systèmes d'étanchéité plus avancés seront utilisés dans les turboréacteurs. Il s'agira de diminuer les fuites tout en réduisant la génération de chaleur et bien sûr d'augmenter la durée de vie de ces composants.

4. SYSTEMES DE REGULATION

4.1. Systèmes numériques

les régulations numériques pleine autorité sont adoptées sur tous les projets récents. Les impératifs de sécurité et de fiabilité feront dans le futur appel à des techniques de distribution du « cœur numérique » plutôt qu'à la muliplication de canaux de traitements indépendants. Ces technologies permettront de reconfigurer les calculateurs et de s'affranchir ainsi des conséquences des pannes localisées. Les spécifications de sécurité et de fiabilité pourront donc être réalisées à un coût inférieur à celui des architectures actuelles, ou bien, pour un coût équivalent, procurer un taux de disponibilité plus élevé.

Les codes de régulation les plus avancés simulent le fonctionnement thermodynamique global du moteur en temps réel. Cela permet de mettre en œuvre des régulations multivariables, qui se distinguent des simples techniques de régulation de variables indépendantes et qui procurent des améliorations significatives dans les domaines suivants :

- Réduction des temps d'accélération et de décélération. La figure 5 montre que le temps pour atteindre 95 % de la pleine poussée a pu être réduit de 17 % toutes choses égales par ailleurs
- Implantation de modes de régulation adaptés aux différentes missions de l'avion. On peut par exemple envisager des modes de régulations minimisant les émissions infra-rouge dues aux produits de combustion et à la température du jet, ou bien des modes dits « temps de paix » réduisant l'endommagement des pièces par fatigue thermomécanique
- Réduction du temps et du coût de mise au point du système de régulation

Le modèle numérique du moteur, embarqué dans le calculateur permet aussi de détecter les pannes des capteurs décrivant l'état du moteur (vitesses de rotation, pressions, températures). Dans une certaine mesure, une « alternative » à la régulation de base peut être mise en œuvre pour atténuer les effets de ces pannes et améliorer drastiquement la disponibilité opérationnelle. La figure 5 illustre la « compensation » d'une dérive de la mesure de la température T23 (sortie du compresseur BP) au cours d'une accélération. On constatera que la pertubation visible est très modérée et que le régime de rotation du compresseur HP (XN25) augmente de manière quasi linéaire, comme souhaité.

4.2. Systèmes mécaniques et hydrauliques

Les études en cours visent à réduire le nombre des pièces, les coûts et les masses des systèmes commandant l'injection de carburant et le mouvement des organes mobiles. Il est par exemple envisagé d'utiliser une pompe à carburant unique (au lieu d'une pompe principale et d'une pompe pour la réchauffe). Des efforts devront également être faits pour simplifier de manière générale les systèmes mécaniques mettant en mouvement les stators à calage variable, les vannes et les volets mobiles des tuyères (vérins, systèmes de synchronisation, etc...)

5. COMPRESSEURS

5.1. Méthodes de conception et d'analyse

L'analyse aérodynamique utilisant la résolution des équations de Navier-Stokes 3D dans lesquelles les phénomènes turbulents sont représentés en moyenne temporelle par des modèles évolués (κ- ε, etc...) se généralise. Les compresseurs actuels sont optimisés en utilisant des codes, traitant toujours des écoulements stationnaires, mais capables de résoudre l'écoulement au travers d'un ensemble de grilles mobiles et fixes. Le transfert des conditions limites aux interfaces entre grilles utilise une simplification demandant de moyenner circonférentiellement l'écoulement. La figure 6 visualise le champ du nombre de Mach relatif aux grilles dans le premier étage d'un compresseur HP (roue directrice d'entrée + roue mobile + redresseur). Ces résultats sont très utiles, non seulement pour optimiser les profils, mais aussi pour adapter chaque aubage à l'écoulement délivré par la grille qui se situe en amont. Les compresseurs modernes étant de plus en plus chargés aérodynamiquement, il convient de tenir compte dans ces analyses numériques des effets dits de petite échelle, tels que jeux radiaux en sommet de pale, fuites au travers des parois de la veine, ressauts, etc... La figure 7 illustre une quantification de l'influence du jeu radial au sommet d'une aube chargée, qui, en permettant au fluide sous pression du côté intrados de fuir vers l'extrados du canal voisin, induit un tourbillon de dimension non négligeable et diminue le rendement de compression.

Les versions « instationnaires » de ces codes de calcul Navier-Stokes 3D font l'objet de mises au point et de tests de manière à atteindre rapidement un niveau d'utilisation industriel. L'enjeu est de prévoir, dès le stade de la conception, les domaines de flottement des aubages ainsi que les caractéristiques dynamiques de l'excitation aérodynamique sillages stator/aubes rotor et vice versa. Le dimensionnement structural sera plus sûr et la probabilité de ne pas avoir à retoucher la conception du compresseur plus grande.
Enfin, la mise à disposition de calculs aérodynamiques prenant en compte les phénomènes non stationnaires devraient améliorer la prévision des rendements et surtout des limites de décrochage ou de pompage des compresseurs. Les technologies de contrôle actif du pompage pourraient aussi bénéficier des progrès réalisés dans les méthodes de calcul d'aérodynamique instationnaire.

En ce qui concerne le dimensionnement structural des rotors et des stators, des efforts particuliers sont faits dans les deux voies suivantes :

- Modélisation du dommage causé par l'ingestion de corps étrangers (pierres, oiseaux, ...). Il s'agit de savoir évaluer correctement les conséquences de chocs en termes de déformation plastique, ruptures et rétention des débris,
- Prévision de la durée de vie des rotors dans l'environnement opérationnel réel et en tenant compte des imprécisions et des imperfections mineures de fabrication. Il s'agit de bien connaître le comportement des matériaux sollicités durant de longues périodes en présence de petites singularités localisées (rayures, zones soudées, etc...)

5.2. Matériaux et procédés de construction avancés

L'augmentation du rapport de pression et donc de la température de sortie des compresseurs conduit à adopter des parties aval de rotor en alliages à base nickel élaborés en métallurgie des poudres. Il est aussi envisagé d'utiliser des aluminures de titane pour construire les portions de carters et les redresseurs à température moyenne pour lesquels on utilise aujourd'hui les aciers. L'objectif principal est la réduction des masses.
Pour le moyen terme, des développements sont en cours sur les composites à matrice métallique (CMM) du type Sic/Ti. Ces matériaux, à haut rapport contrainte à la limite élastique/masse volumique, permettront une forte réduction de la masse. Dans ce type d'architecture, les disques conventionnels sont remplacés par de minces anneaux en CMM qui supportent l'effort centrifuge des aubes mobiles. L'ensemble anneau + pales forme finalement une partie monobloc.
A plus long terme, il est envisagé d'employer des composites à matrice constituée de matériaux intermétalliques (CMIM), ce qui conduirait à des performances structurales sans égal. Une des difficultés majeures réside dans la mise au point de procédés de fabrication reproductibles présentant un coût acceptable.

5.3. Tendances des conceptions des futurs compresseurs

Les exigences de réduction des coûts conduisent dès aujourd'hui à réduire le nombre d'étages sans diminuer le rendement. Cela conduit à utiliser les avancées en aérodynamique pour augmenter le facteur de charge aérodynamique, $\Delta H/U^2$, qui est compris entre 0.5 et 0.6 sur les machines récentes. Un compresseur HP expérimental SNECMA récent réalisant un rapport de pression de 11.4 en 5 étages est une bonne illustration des tendances actuelles (cf. figure 8). Ce compresseur, par rapport à l'état de l'art, présente une charge aérodynamique ($\Delta H/U^2$) augmentée de 20 % à même rendement, ou bien un gain de rendement de 2 points à même charge aérodynamique.
Enfin, les matériaux avancés décrits au paragraphe précédent seront employés, soit pour réduire les masses, soit pour autoriser une vitesse de rotation plus élevée sans pénalité de poids.

6. CHAMBRE DE COMBUSTION ET RECHAUFFE

6.1. Méthode de conception et d'analyse

Alors que par le passé il était largement fait appel à l'empirisme, les chambres de combustion sont aujourd'hui conçues en utilisant des codes de simulation numérique 3D des écoulements de fluides visqueux, chimiquement réactifs. La bonne simulation des phénomènes de combustion du kérosène demande à ce que soient traités les écoulements diphasiques (gouttelettes de carburant/gaz brûlés et air) et que les modèles de turbulence soient bien adaptés à ce problème. La figure 9 montre les cartes de température obtenues dans trois sections méridiennes différentes d'une chambre de combustion à deux têtes. Ce type de calcul est utilisé pour obtenir, à l'aide d'une étude paramétrique, un dessin minimisant les hétérogénéités de température. Il est important que l'utilisation de ce type de calcul aille jusqu'à la prise en compte de tous les organes de refroidissement de petite échelle (perforations, fentes générant des films froids, etc...), car la prévision des flux thermiques est un élément essentiel du dimensionnement structural des peaux constituant la chambre.
Des travaux de recherches sont en cours pour mettre au point des codes de combustion instationnaires capables de prédire les domaines d'instabilité. Cela sera très utile pour le dimensionnement des systèmes de réchauffe dont une des exigences doit être l'absence d'instabilité due au couplage acoustique/réactions de combustion (« screech »).

En ce qui concerne les méthodes de dimensionnement structural des organes de combustion, l'effort doit porter sur la généralisation des modélisations du comportement viscoplastique des peaux et en final sur la prévision des durées de vie.

6.2. Tendances des conceptions des futures chambres de combustion

Afin de diminuer la taille et les masses des futurs moteurs, la température en fin de combustion sera augmentée pour atteindre typiquement 2100 K à la sortie du distributeur de turbine HP. Les exigences de discrétion infrarouge conduiront à des réductions des émissions de fumées et d'autres produits secondaires de la combustion (NOx, etc...). Une des architectures permettant de satisfaire ces spécifications est la chambre à deux têtes (deux injecteurs) axialement décalés. (cf. figure 9). Ces technologies de la chambre seront associées à des systèmes d'injection de nouvelles technologies améliorant la qualité des brouillards de carburant et la distribution spatiale du carburant.
La réduction des débits de refroidissement des parois de chambre (ou l'augmentation des durées de vie à même débit) est obtenue par utilisation de technologies avancées (multiperforations, tuiles à picots, etc...) associées à des revêtements en zirconate faisant office de barrières thermiques. L'utilisation de composites à matrice céramique (SiC/SiC) pour construire les parois de chambre est aussi une voie digne d'intérêt.

7. TURBINES

7.1. Méthodes de conception et d'analyse

De la même manière que pour la conception des compresseurs, le dessin des turbines fait appel à des codes de résolution des équations de Navier Stokes 3D associées à un modèle de turbulence évolué. Des progrès importants ont été réalisés lorsque il a été possible de calculer simultanément plusieurs grilles d'aubes (par exemple distributeur + roue mobile) et de prendre en compte le jeu radial en tête des aubes. La figure 10 illustre le champ de nombre de Mach relatif obtenu sur un étage de turbine HP ; la compatibilité des conditions limites à l'interface distributeur/roue mobile n'est assurée que pour les valeurs moyennées circonférentiellement. La description précise des films de refroidissement et de toutes les réintroductions sera bientôt introduite dans les codes Navier stokes 3D afin de modéliser en détail les flux de chaleur dans les aubages.

Les progrès en cours concernant les méthodes de dimensionnement structural portent essentiellement sur la mise en œuvre des méthodes de calcul de l'endommagement viscoplastique afin d'accéder à une meilleure prévision des durées de vie.

7.2. Technologies de refroidissement et matériaux

Les technologies de refroidissement jouent un rôle essentiel dans la conception des turbines HP. On ne pourra en effet accéder à des hautes températures que si l'on dispose de circuits de refroidissement très efficaces afin de limiter les débits de ventilation et éviter une dégradation des rendements qui annuleraient le gain réalisé sur le cycle thermodynamique. Les technologies étudiées pour les futurs moteurs sont entre autres :

- Circuits de refroidissement constitués de canaux de dimensions réduites placés près des parois extrados et intrados,
- Utilisation des perturbateurs internes sophistiqués permettant d'augmenter la convection thermique turbulente à l'intérieur des aubes,
- Profilage et évasement des trous d'émission des films « froids » afin d'améliorer leur qualité,
- Amélioration des propriétés des alliages monocristallins et des barrières thermiques céramiques .

La figure 11 illustre un prototype de noyau de fonderie de nouvelle génération dont l'objectif est une amélioration de 8 % de l'efficacité thermique, à même débit de ventilation, et par rapport à l'état de l'art actuel.

7.3. Tendances des conceptions des futures turbines

L'obtention de poussées spécifiques élevées et de consommations de carburant réduites conduit à adopter des températures élevées à l'entrée turbine (typiquement 2100K), ce qui exige, comme on l'a déjà mentionné, de maintenir les débits de refroidissements à des niveaux acceptables.

L'accroissement des rapports de pression des compresseurs HP, tout en maintenant la vitesse de rotation à des valeurs modérées pour ne pas pénaliser la masse, va conduire à des facteurs de charge aérodynamique élevés pour la turbine HP, typiquement $\Delta H/U^2 > 2$.

Les progrès en aérodynamique seront utilisés pour réduire les nombres de pales mobiles et des aubages distributeurs. On vise typiquement à augmenter les pas relatifs de 20 % par rapport à ceux issus des critères conventionnels. Pour cela on utilisera des conceptions 3D prenant en compte le comportement des couches limites des profils dans l'environnement instationnaire dû à l'alternance des rotors et des stators.

Notons finalement que la réduction du nombre des aubes de la roue mobile du rotor de turbine HP, ainsi que de leur coût unitaire, jointe à une augmentation de la durée de vie de cette pale, sont des facteurs déterminants de la réduction du coût de maintenance. Le remplacement ou réparation des ces pièces lors des opérations de révision du moteur constitue en effet une part majeure des frais de maintenance.

8. LES TENDANCES FUTURES DANS LA CONDUITE DES PROJETS DE TURBOREACTEURS MILITAIRES – CONCLUSIONS

La meilleure des technologies peut s'avérer tout à fait inopérante si elle n'est pas mise en œuvre dans le cadre d'un Processus de Développement –Industrialisation du moteur, qui soit convenablement maîtrisé et optimisé

A cet égard, la conception multidisciplinaire intégrée gagne à être appliquée aux Développements de Moteurs Militaires, même si certaines contraintes particulières, budgétaires ou autres peuvent en compliquer le déroulement. Les résultats essentiels sont une meilleure satisfaction des attentes client, une réduction de 30% à 40% des coûts non récurrents et des délais de développement/industrialisation du moteur.

Les trois facteurs principaux facteurs clés de succès d'une telle démarche sont :

- une gestion rigoureuse du projet : Tableau de bord, phasage, identification des risques, etc
- une colocation des équipes opérationnelles dès la première phase de conception. Ces équipes comprennent des membres des équipes de conception, de production, d'après-vente et support logistique , etc.
- une forte intégration avionneur/motoriste.

D'un point de vue technique, il n'est plus envisageable aujourd'hui de libérer un dessin sans avoir procédé à des évaluations tridimensionnelles complètes en mécanique des fluides et des structures.

La réduction drastique des délais de développement n'est possible que si sont mis en place des programmes de maturation technologique (ou « développements exploratoires ») destinés à lever les risques majeurs avant le lancement d'un programme moteur. La figure 12 donne un calendrier d'un moteur militaire dérivé qui est développé et industrialisé selon ce type d'approche. On constate que la première rotation du moteur intervient 16 mois après le début des études de conception et la qualification en vol après un total de 36 mois.

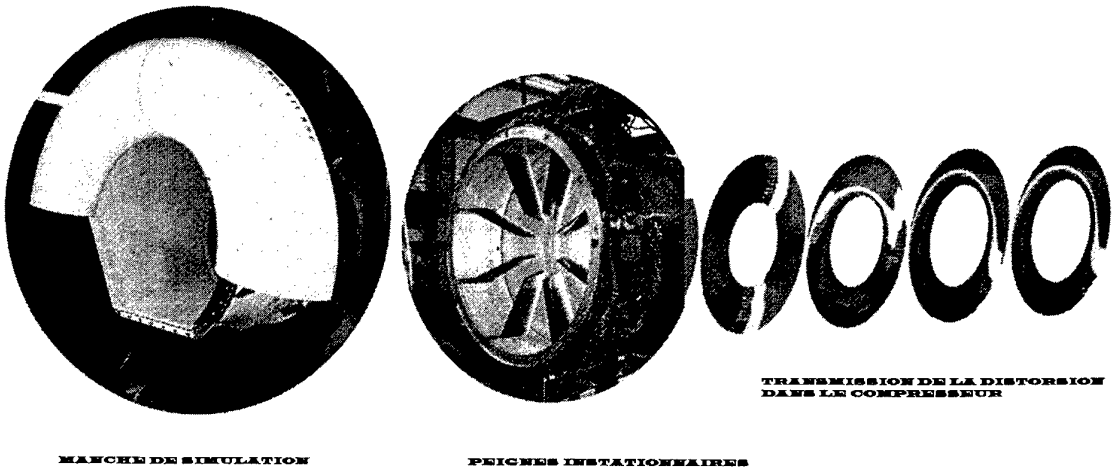

Fig. 1 : Compatibilité entrée d'air/moteur
Moyens de simulation, mesures et calculs aérodynamiques

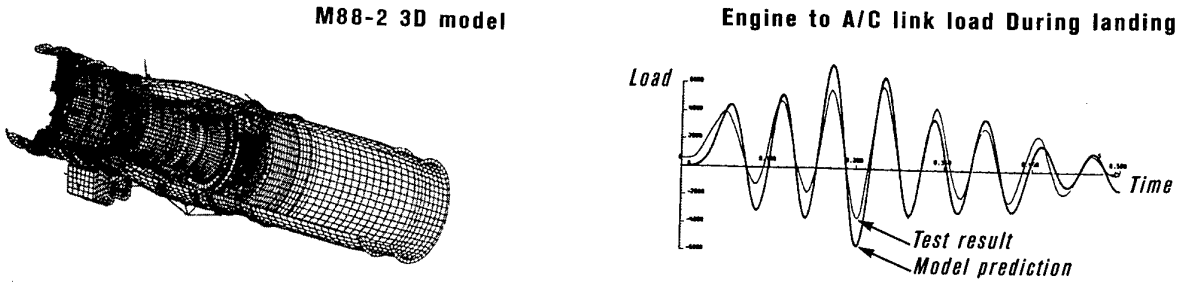

Fig 2 : Dynamique d'ensemble : modèle d'un moteur complet
et application au calcul d'un choc à l'appontage

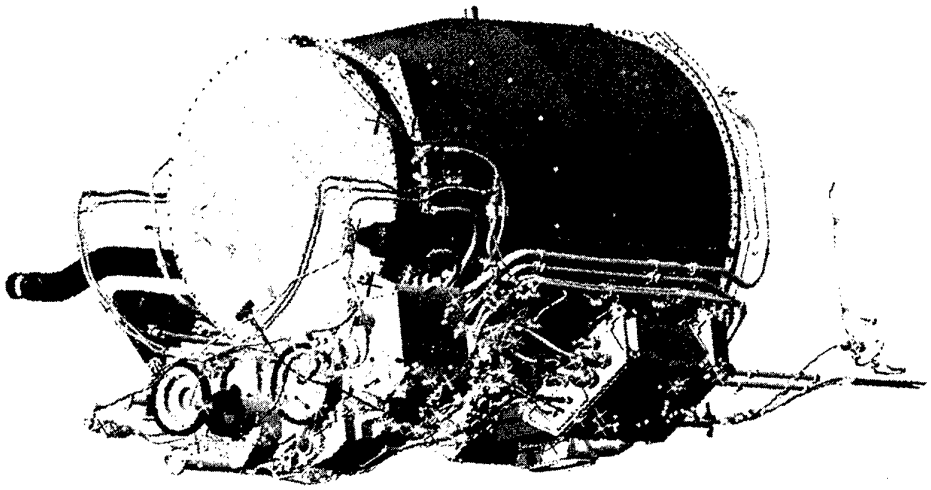

Fig 3 : Maquettage numérique des accessoires et tuyauteries
autour des parties « turbomachines » d'un moteur militaire

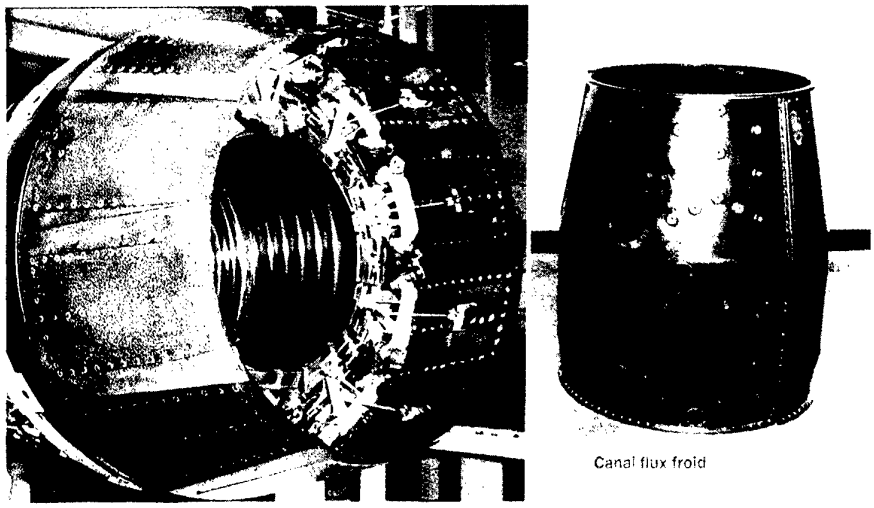

Fig 4 : Application de matériaux composites (carbone/SiC et carbone/PMR15) au moteur M88-2

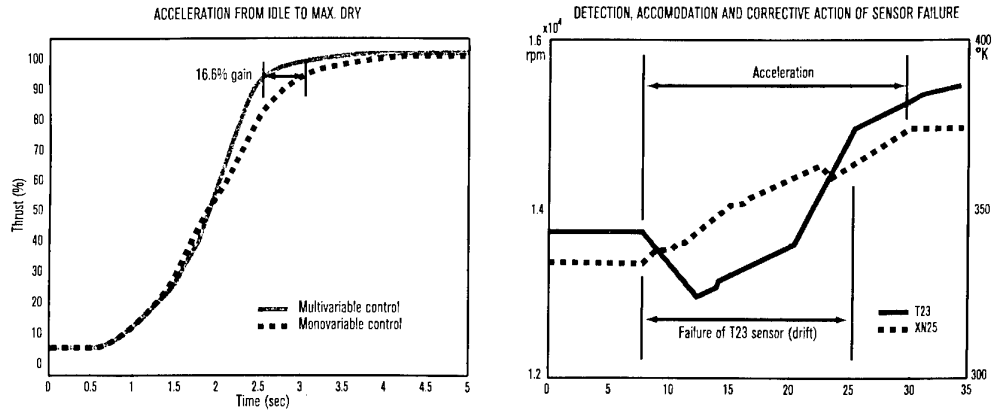

Fig 5 : Illustration des avantages des techniques de régulation multi-variables :
temps d'accélération réduit, atténuation des effets de pannes

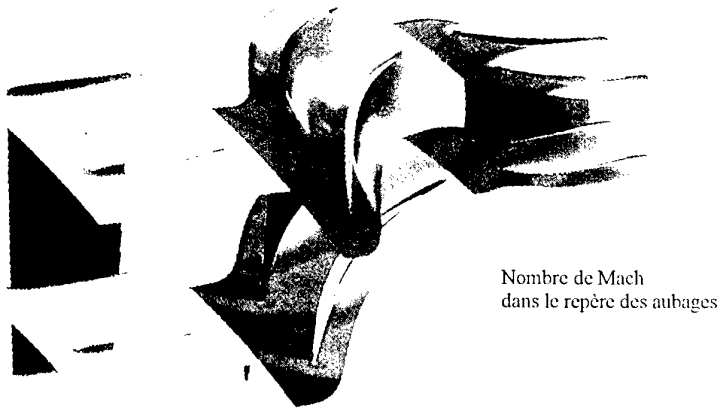

Nombre de Mach
dans le repère des aubages

Fig 6 : Calcul NS3D sur le 1er étage complet d'un compresseur HP.
Sections proches du moyeu et du carter

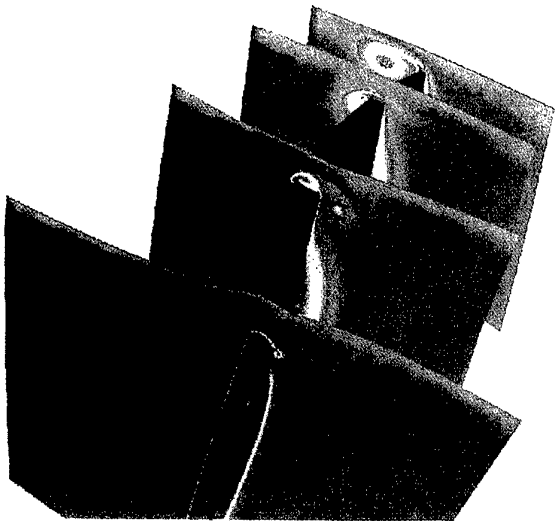

Fig. 7 : Calcul NS3D. Tourbillon créé par le jeu en tête d'une aube mobile

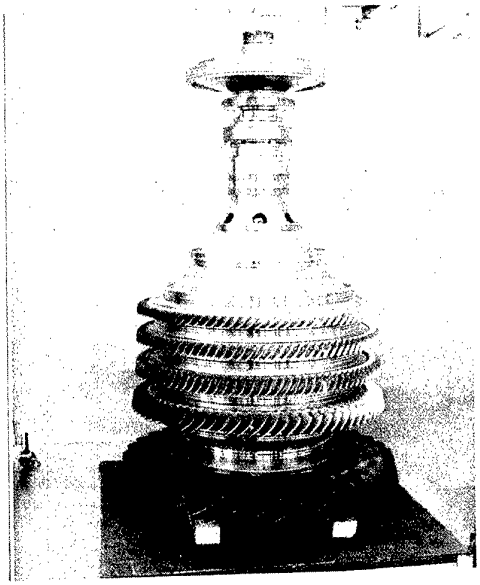

Fig 8 : Rotor de compresseur HP expérimental testé en 1997. Architecture hybride à P/P = 11.4 en 5 étages

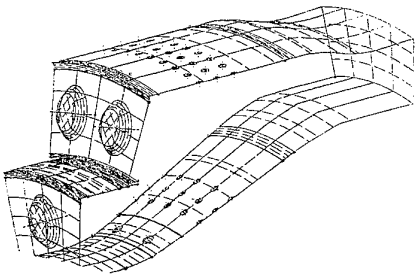

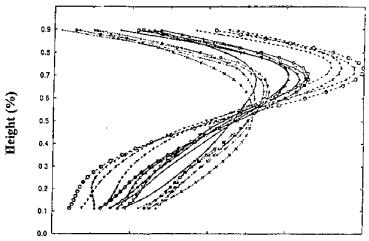

TEMPERATURE PROFILES VARIATION DURING PARAMETRIC STUDIES

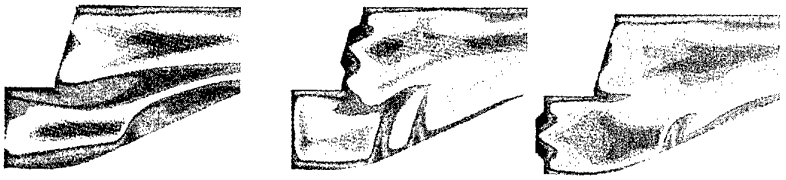

TEMPERATURE MAPS AT 3 DIFFERENT SECTIONS

Fig 9 : Exemple d'utilisation de calculs NS3D réactifs pour dimensionner une chambre de combustion à 2 têtes axialement décalées

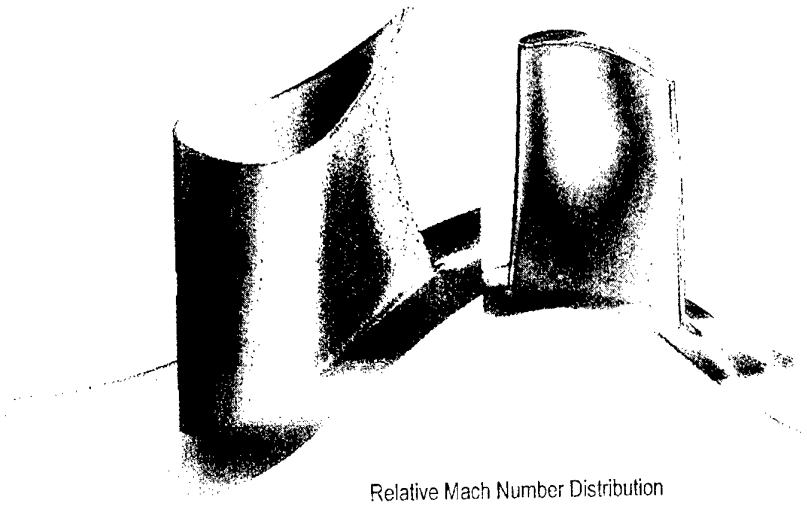

Fig 10 : Calcul NS3D sur la turbine HP du M88-2
Distribution du nombre de Mach relatif près des parois des aubes

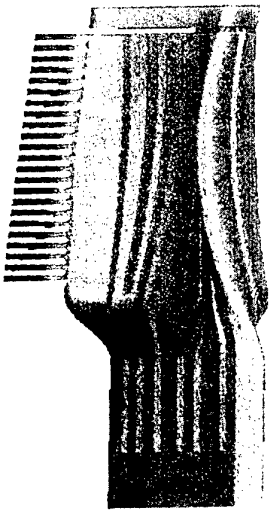

Fig 11 : Noyau de fonderie
d'aube de turbine HP
à circuits de refroidissement avancés

Task	Year 1	Year 2	Year 3	Year 4
Aeromechanical design				
Industrialization & toolings				
HP compressor manufacturing & bench test				
HP turbine manufacturing & bench test				
First engine test		V		
Engine # 2				
Engine # 3				
Flight tests (engines # 2 to 5)			V	
Qualification for entry in service				

Fig 12 : Calendrier typique de développement d'un moteur militaire dérivé

DESIGN PRINCIPLES AND METHODS FOR MILITARY TURBOJET ENGINES

J.P. HERTEMAN, Technical Director
M. GOUTINES, Assistant Director for Research
SNECMA Villaroche
77556 MOISSY CRAMAYEL
France

1. INTRODUCTION

The design of turbojet engines for military aircraft is at present undergoing a transformation, due among other things to changing demands from customers, who are either modifying their initial performance priorities, or introducing new specifications. Basing ourselves on this new order, we can draw up a list of those technologies, methods, or know-how areas which require research and development effort.

As far as military aircraft are concerned, the first thing to note is that the usual five performance criteria, i.e. specific fuel consumption, thrust to weight ratio on take-off, acceleration and deceleration times, flight envelope limits and reliability, can be weighted in different ways to produce a global performance criterion. The individual weights of the different performances will vary, depending on the mission or missions assigned to the aircraft, and this can produce different engine architectures.

In recent years, armed forces and government departments have frequently been concerned with two requirements which initially appeared less critical, i.e.

- the reduction of costs of all types, from production costs to the costs of maintaining equipment with a long service history;
- the contribution of the aircraft engine to electromagnetic stealth, both infra-red and in the radar bands.

As far as costs are concerned, the requirement is to design hi-tech engines at low cost. In practice this means that the desirable technologies are those which provide high performance at low cost, and not necessarily those which provide maximum performance. It should be noted that a given technological advance, for example, improved blade aerodynamics, can be used in different ways; to maximise engine efficiency, to reduce the number of blades, or as a trade off between the two.

2. ENGINE ARCHITECTURE ENHANCEMENT AND COMPONENT INTEGRATION

2.1 Advanced technology components for conventional thermodynamic cycle engines

The high level of coupling between the different modules generally means that the optimum design is not simply an assembly of the optimum designs of each module. This is obviously true for the design of compressors and turbines linked on the same shaft.

The emphasis placed on cost, electromagnetic stealth and qualities such as reliability, means that optimisation work is now based on overall multidimensional criteria and

The figures are in the French version of this Address

Paper presented at the RTO AVT Symposium on "Design Principles and Methods for Aircraft Gas Turbine Engines", held in Toulouse, France, 11-15 May 1998, and published in RTO MP-8.

expressed in terms of the engine or aircraft/engine system.

There is a considerable amount of aerothermodynamic interaction between modules. For example, care should be taken to ensure that the unsteady distortions of stagnation pressure and velocity vector produced by the air inlet during high angle of attack manoeuvres remain compatible with an acceptable level of deterioration of the surge line of the low pressure compressor. The optimum aircraft can only be achieved by a judicious trade-off of specifications between the air inlet (maximum permissible distorsion) and the LP compressor (minimum surge margin to be ensured). Figure 1 shows the aerodynamic simulation, measurement and computation facilities developed to ensure air inlet/engine compatibility both at the design stage (computation) and prior to flight testing (engine or LP compressor tested on a ground test rig). The radial clearance between the casing and the blade tips of a rotor, or between the rub strip of a honey comb structure and its sealing fins can have a critical influence on turbojet engine performance. This type of interaction and the way in which it develops is conditioned to a great extent by the dynamic and thermal behaviour of the engine considered as a whole. In addition, under real operating conditions, engines are subjected to various types of transient effects : imbalance, deck landings, high-g manoeuvres etc...
Figure 2 shows a dynamic model of a complete engine and illustrates how it can be used to reduce the strain on an engine fastener during deck landings.This type of calculation is necessary to ensure that the resulting engine is both as light as possible and capable of running for a sufficient number of cycles under military operating conditions.

Finally, the assembly-disassembly of an engine and its many accessories and hoses can be long and costly operations if efforts towards rationalisation and simplification are not made right from the design stage. Previously, this was achieved by means of scale mock-ups, which in fact were ill-suited to the job of obtaining an optimal configuration within a reasonable time frame. The use of numerical mock-ups produced by CATIA V4 type 3D design and display software has enabled spectacular reductions in removal/installation times as well as in design costs of the build-up. Figure 3 shows the numerical mock-up of a subassembly of a military engine.

2.2 Advanced thermodynamic cycles and complex architectures

New concepts are being examined to enable improvements in of performance and operational qualities. Among others are the variable cycle or hybrid concepts, which can be used to produce a variable by-pass ratio HP compressor, air or power bleeds, vectored thrust, and in the longer term a fixed or variable area turbine nozzle. The main difficulty presented by these new techniques is to keep costs and reliability at the same levels as those achieved on conventional engines. In particular, one of the major problems is to obtain an acceptable degree of complexity for the regulation system responsible for engine management and control. In the same way, integration of the different modules into this type of engine will become more complex.

The future of advanced architecture engines will depend on the ability of designers to keep life cycle costs close to those of conventional engines.

3. TECHNOLOGIES FOR STRUCTURES AND MECHANICAL SYSTEMS

Progress needs to be made to reduce the costs and improve the reliability of control systems for variable geometry control surfaces. We

are concerned here with the variable by-pass ratio of compressors, twin parameter nozzles (and/or vectoring), variable mixing etc..

New structural materials concepts, with greater incorporation of different thermal and mechanical functions, will be used to reduce engine weight. Figure 4 shows the use of an organic matrix composite ("PMR 15" carbon/resin) for the fan duct of the Rafale M88-2 engine. This figure also shows the use of ceramic matrix thermostructural composites (carbon/SiC) for the outboard flaps of the nozzle of the SNECMA M 88-2. Eventually, thanks to their high temperature tolerance properties, composite materials such as CERASEP (SiC/SiC), will be used for hot divergent nozzle flaps and other component elements of afterburners and afterburner systems.

More advanced bearing shaft bearings, bearings and sealing systems will be used in turbojet engines. The aim will be to stop leaks while reducing heat generation and of course, extending the lifetime of these components.

4. REGULATION SYSTEMS

4.1 Numerical systems

Full authority numerical regulation has been adopted on all recent projects. In the future, safety and reliability requirements will necessitate the use of "numerical core" distribution techniques in preference to the proliferation of separate processing channels. These technologies will enable us to reconfigure computers and thus avoid the consequences of localised failures. It will therefore be possible to meet safety and reliability specifications at a lower cost than is the case with present day architectures, or alternatively, achieve a higher availability rate for an equivalent cost.

The most advanced regulation codes simulate overall thermodynamic operation of the engine in real time. This enables the use of mutivariable regulations, which are not the same as independent variable regulation techniques and which enable significant improvements in the following fields :

- reduction of acceleration and deceleration times. Figure 5 shows that the time required to achieve 95% of full thrust has been reduced by 17%, all other conditions being equal.

- use of regulation modes adapted to different aircraft missions. For example, regulation modes which minimise the infrared emission created by combustion products and the temperature of the jet, or so-called "peacetime modes" which reduce part damage caused by thermomechanical fatigue.

- reduction of the cost and time required for debugging regulation systems.

The numerical model of the engine stored in the onboard computer can also be used to detect the failure of sensors which monitor engine status (rotation speeds, pressures, temperatures etc..). To a certain extent, an "alternative" to the basic regulation system can be implemented to lessen the effects of these failures and to provide a dramatic improvement in operational availability. Figure 5 shows the "compensation" for a temperature measurement drift T23 (outlet from LP compressor) during an acceleration. It will be noted that the visible disturbance is very moderate and that the rotation speed of the HP compressor (XN25) increases in quasi-linear fashion, as required.

4.2 Mechanical and hydraulic systems

Current research work aims at reducing the weight, cost and the number of parts in the systems which control the injection of fuel and actuate engine components. It is, for example, planned to use a single fuel pump (instead of a main pump and a pump for the

afterburner) . Effort is also being put into generally simplifying the mechanical systems which drive the variable setting stators, and the nozzle valves and mobile flaps (actuators, synchronisation systems etc..)

5. COMPRESSORS

5.1 Design and analysis methods

Aerodynamic analysis shows a general tendency to use 3D Navier-Stokes equations in which turbulent phenomena are represented as a temporal average by means of sophisticated models (κ, ε etc...). Modern compressors are optimised using codes which are always applied to steady flows, but which are capable of solving flow through a series of fixed and variable cascades.Transfer of the boundary conditions obtaining at the interfaces between cascades makes use of a simplification involving circumferential averaging of the flow. Figure 6 shows the field of the Mach number for the cascades in the first stage of an HP compressor (inlet guide vane + rotor + outlet guide vane). These results are very useful, not only for optimising the profiles but also for adapting each blading to the flow produced by the upstream cascade. As modern compressors are subject to increasing aerodynamic loads, it is important when carrying out digital analyses to allow for the so-called small scale effects such as blade tip radial clearance, leaks through the walls of the duct, hydraulic jumps etc..Figure 7 gives an example of quantification of the influence of radial clearance at the tip of a loaded blade which, while allowing the fluid under pressure from the pressure side to escape to suction side of the neighbouring channel, induces a significant eddy and reduces compression efficiency.

The "unsteady" versions of these 3D Navier-Stokes calculation codes are being developed and tested with the aim of rapidly qualifying them for industrial applications. The aim is to be able to make provision for blading flutter envelopes and for the dynamic characteristics of stator wake/rotor blade aerodynamic excitation and vice versa. Structural sizing will be more accurate and the probability of not having to go back and alter the compressor design will be much greater.

Finally, the provision of aerodynamic calculations which allow for unsteady phenomena should improve compressor efficiency predictions particularly with regard to stall and surge limits. The technologies used for active control of compressor surge could also benefit from the advances made in unsteady aerodynamics design methods.

In so far as concerns the structural sizing of rotors and stators, special efforts are being made in the fields of :

- modelling of the damage caused by the intake of foreign bodies (stones, birds etc..) . The objective here is to be able to correctly assess the consequences of impacts in terms of plastic deformation, fracture and retention of debris,

- prediction of rotor lifetimes under real operating conditions and allowing for minor manufacturing inaccuracies and imperfections. The aim is to fully understand the behaviour of materials which are loaded for long periods in the presence of small localised irregularities (scratches, welded areas etc..)

5.2 Advanced materials and manufacturing processes

The increase in pressure ratio and therefore in compressor outlet temperatures explains the adoption of powder metallurgy nickel based alloys for parts downstream of the rotor. It is also planned to use titanium aluminides for the medium temperature parts of the casings

and guide vanes which are at present made of steel. The main aim is to reduce weight.

In the medium term, there are some developments on Sic/Ti type metal matrix compound materials (CMM). These materials, which have a high stress to elastic limit/density ratio, will enable considerable weight reduction. In this type of architecture, the conventional disks are replaced by thin CMM rings which take up the centifugal strain of the rotating vanes.The ring + blade assembly forms a one-piece unit.

In the longer term, it is planned to use intermetallic matrix compound materials (CMIM), which would produce unequalled structural performances. One of the major difficulties lies in the development of reproducible production processes at acceptable cost.

5.3 Design trends for future compressors

Cost reduction constraints mean that today's compressors must achieve the same efficiency with less stages. This is accomplished by using the advances made in aerodynamics to increase the aerodynamic load factor $\Delta H/U^2$, which is between 0.5 and 0.6 on recent machines. A good illustration of present trends is the recently produced SNECMA experimental HP compressor with a pressure ration of 11.4, in 5 stages (cf. Fig 8). Compared to the state-of-the-art, this compressor presents an aerodynamic load ($\Delta H/U^2$) increased by 20% with the same efficiency, or alternatively an increase in efficiency of 2 points with the same aerodynamic load.

Finally, the advanced materials described in the above paragraph will be used either to reduce weight or to increase rotational speed without any weight penalty.

6. COMBUSTION CHAMBER AND AFTERBURNER

6.1 Design and analysis methods

Whereas in the past empirical methods were widely used, today's combustion chambers are designed using 3D numerical codes to simulate the flow of viscous, chemically reactive fluids. The realistic simulation of jet fuel combustion phenomena means looking at two-phase flows (fuel droplets/burnt gases and air) and ensuring that the turbulence models are suited to the problem. Figure 9 shows the temperature maps obtained in three different throughflow sections of a double headed combustion chamber. This type of calculation is used in conjunction with a parametric study to produce a design which minimises temperature irregularities. It is important that the use of this type of calculation includes all the small cooling devices (perforations, slots generating cold films etc..), as the prediction of heat flows is an essential element in the sizing of the walls which make up the chamber. Research is under way to develop unsteady combustion codes capable of predicting the instability domains. This will be very useful for sizing afterburner systems, one of the requirements of which should be the absence of instability caused by acoustic coupling/combustion reactions, or "screech".

Concerning the design of combustion devices, an effort should be made to generalise modelling of the viscoplastic behaviour of the walls, as well as lifetime prediction.

6.2 Design trends for future combustion chambers

In order to reduce the size and weight of future engines, combustion exit temperature will be increased to typically 2100K on outlet from the HP turbine nozzle. Infrared discretion requirements will lead to reductions in the emission of smoke and other secondary combustion products (NOx etc..). One of the architectures which meets these

specifications is the double headed combustion chamber (two axially offset injectors) (cf fig. 9). These combustor technologies will be combined with new technology injection systems which will improve the quality of fuel spray and the spatial distribution of fuel.

Reduction in chamber wall cooling rates (or increased lifetime with the same cooling air) will be achieved by the use of advanced technologies (multi-perforations, pin tiles etc..) associated with zirconate coatings acting as thermal barriers. The use of ceramic matrix compound materials (SiC/SiC) for the chamber walls is another area worthy of interest.

7. TURBINES

7.1 Design and analysis methods

In the same way as for the design of compressors, turbine design uses 3D Navier-Stokes equations with sophisticated turbulence models. Considerable progress was made when it became possible to do the design calculations for several cascades simultaneously (for example nozzle guide vane + rotor) and allow for radial clearance at the blade tips. Figure 10 illustrates the relative Mach number profile obtained from an HP turbine stage; the compatibility of boundary conditions at the guide vane/rotor interface can only be achieved for circumferentially averaged values. An accurate description of cooling fins and internal flow distributions will shortly be included in the 3D Navier-Stokes codes to enable detailed modelling of heat flows in the guide vanes.

Current research into structural design methods essentially concerns the use of viscoplastic damage calculation methods for improved life cycle prediction.

7.2 Cooling technologies and materials

Cooling technologies play an essential role in the design of HP compressors. High temperatures could not in fact be achieved without very efficient cooling systems to limit the ventilation flow rates and prevent any fall-off in efficiency which would otherwise cancel out the gain achieved on the thermodynamic cycle. Among the technologies being considered for future engines are :

- cooling systems composed of small channels located near the pressure side and suction side walls,
- the use of sophisticated internal disturbance devices producing an increase in turbulent thermal convection inside the blades,

- fairing and flare-out of the "cold" film effusion holes in order to improve their quality,

- improvement of the properties of monocrystalline alloys and ceramic thermal barriers.

Figure 11 shows a prototype of a new generation casting designed to achieve an 8% improvement in thermal efficiency on present state-of-the-art, at the same ventilation flow rate.

7.3 Design trends for future turbines

The achievement of high specific thrust and reduced fuel consumption requires high turbine inlet temperatures (2100K), which, as we have already menioned, means that cooling flow rates must be kept to acceptable levels. The increase in HP compressor pressure ratios, while keeping rotation speeds at moderate levels so as not to penalise weight, will lead to high aerodynamic load factors for the HP turbine, typically $\Delta H/U^2>2$.

Advances in aerodynamics will be used to reduce the number of moving blades and guide vanes. The objective is typically to increase pitch-to-chord ratios by 20% compared to those produced using conventional criteria. Three dimensional designs will be used, with allowance for the behaviour of the blade boundary layers in the unsteady environment created by the alternation of stators and rotors.

Finally, we note that a reduction in the number of blades on the HP turbine rotor, together with their unit cost, and an increased blade lifetime, are decisive factors in the reduction of maintenance costs. In fact, the replacement or repair of these parts during engine overhaul operations represents a major percentage of maintenance costs.

8. FUTURE TRENDS IN THE MANAGEMENT OF MILITARY TURBOJET PROJECTS - CONCLUSIONS

Even the best technologies can prove quite worthless unless they are implemented as part of a suitably controlled and optimised engine development-production process.

In this respect, the application of integrated multidisciplinary design is of benefit to the development of military engines, even though certain constraints, budgetary or otherwise, may complicate the situation. The essential results are improved customer satisfaction, a 30% to 40% reduction in non-recurrent costs and better development/production lead times.

The three key success factors in such an approach are :

- stringent project management : progress charts, phasing, risk identification etc...

- colocation of operational teams right from the initial design phase. These teams are made up of members of design, production, after-sales and logistics support teams.

- a high level of integration between engine and aircraft manufacturers.

From a technical point of view, we can no longer release a design without making full three-dimensional fluid mechanics and structures evaluations.

No significant reduction of development lead times can be achieved without the creation of "technology nurturing" programmes or exploratory developments designed to remove the major risks before the launch of an engine programme. Figure 12 gives the schedule for a derived military engine which is being developed and manufactured in accordance with this type of approach. It should be noted that the first engine turn-over is previewed 16 months after the start of the design studies and flight qualification after a total of 36 months.

THE GAS TURBINE ENGINE CONCEPTUAL DESIGN PROCESS - AN INTEGRATED APPROACH

Jeffrey M. Stricker
Propulsion Directorate
Air Force Research Laboratory
1950 Fifth Street
Wright-Patterson AFB, OH 45433-7251, USA

1.0 SUMMARY

The conceptual design process of gas turbine engines is complex, involving many engineering disciplines. Aerodynamics, thermodynamics, heat transfer, materials science, component design, and structural analysis are a few of the fields employed when down selecting an appropriate engine configuration. Because of the complexity involved, it is critical to have a process that narrows engine options without missing the "optimum". The following paper describes a typical process used at the conceptual design level. The various steps that will be described include propulsion requirements definition, engine cycle analysis, component design, flowpath/weight prediction, installation, and engine design influence on aircraft size and performance. The engine design process is not completely linear since the steps listed above are highly interdependent. A number of iterations are usually necessary in selecting a final engine configuration. This paper will describe several of the inter-relationships between the various steps.

Frequently, a particular aircraft system has special requirements that influence the design selection process. Some modern day examples of these criteria include reduced observables and cost reduction. How these variations are incorporated into the conceptual design process will be discussed.

2.0 LIST OF SYMBOLS

FN/Wa	Specific Thrust (lbf/lbm/sec)
TSFC	Thrust Specific Fuel Consumption (lbm/lbf-hr)
FN	Net Thrust (lbf)
Wa	Total Engine Airflow (lbm/sec)
W_{ft}	Total Engine Fuel Flow (lbm/hr)
TOGW	Takeoff Gross Weight (lbm)
FF	Aircraft Fuel Weight Fraction
L/D	Lift-to-Drag Ratio
T/Waircraft	Aircraft Thrust-to-Weight Ratio
Wa_{spec}	Specific Corrected Flow (lbm/sec-ft2)
θ	Theta Temperature Correction (TT/519°R)
δ	Delta Pressure Correction (PT/14.696 psi)
R_{hub}/r_{tip}	Fan or Compressor Inlet Radius Ratio
ξ_{cool}	Cooling Effectiveness
T_{gas}	Gas Path Temperature (°R)
$T_{mat'l}$	Average Bulk Material Temperature (°R)
T_{cool}	Cooling Air Temperature (°R)
Cd_{inlet}	Inlet Drag Coeff. (Referenced to Capture Area)
Cd_{aft}	Aftbody Drag Coeff. (Referenced to Aircraft Aft Area)
CFG	Nozzle Gross Thrust Coefficient
P_{T8}/P_9	Nozzle Pressure Ratio
A_9/A_8	Nozzle Area Ratio
$GJ\Delta H/U^2$	Compressor or Turbine Aerodynamic Loading

3.0 INTRODUCTION

The advent of the computer has made early examination of numerous propulsion characteristics possible. Figure 1 notionally illustrates when various computerized techniques became widely available. In the early years of computers, engine selection was based primarily on cycle trade studies and the design engineer's experience. Other elements such as installed performance, flowpath, and weight have to be put off for the detailed design part of the overall engine development process. This could result in the selection of an engine configuration, which was not fully optimized.

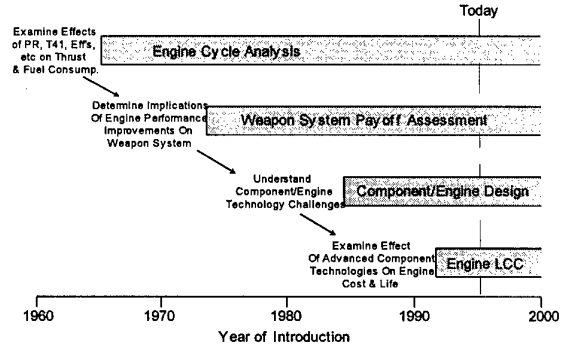

Figure 1 - Historical Trends In Computerized Analysis Capability

In the worst case, the selected engine could not satisfy the aircraft requirements, necessitating a costly and time-consuming redesign. Today, many computerized tools are at the design engineer's disposal to consider component/engine design characteristics, weapon system tradeoffs, and most recently, life cycle cost.

The computer has been a mixed blessing. Because of many different design characteristics that can now be considered at the very early stages of the engine selection process, it is much more difficult to provide a process that can properly address their interdependency. Obviously, many viable approaches exist to conduct a conceptual engine design. The methodology described in this paper is summarized in Figure 2. Each step is covered in more detail in the following sections.

4.0 PROPULSION REQUIREMENTS DEFINITION

Perhaps the most critical phase of any development process is right at the beginning -- the definition of requirements. An over constrained or poorly defined set of requirements can lead the design team on a wild goose chase, focusing on the wrong criteria. Unfortunately, at the early stages of an aircraft's conceptual design, the requirements are hard to quantify. Oftentimes, the aircraft user

Paper presented at the RTO AVT Symposium on "Design Principles and Methods for Aircraft Gas Turbine Engines", held in Toulouse, France, 11-15 May 1998, and published in RTO MP-8.

has only a vague idea of what he or she is looking for, i.e., reduced acquisition and maintenance cost, longer range, greater survivability, etc. However, for a successful design, a clearly defined set of requirements right up-front is critical.

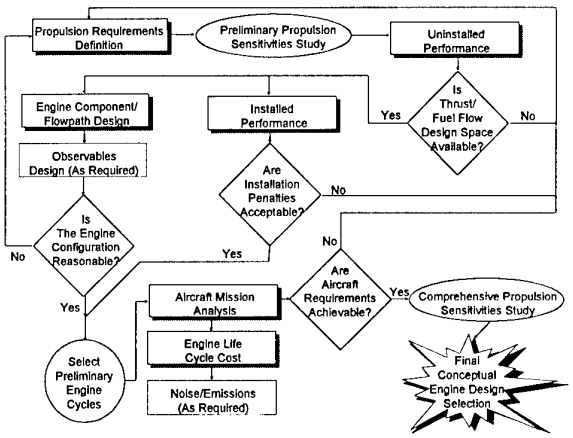

Figure 2 - Engine Conceptual Design Process

In many respects, the requirements definition phase is a mini-conceptual design process. Preliminary propulsion constraints such as combat thrust and cruise fuel consumption need to be established for the rest of the design process to be accomplished. Mission requirements such as range, payload, cruise speed, point performance, endurance, and takeoff and landing restrictions (conventional/short/vertical) must be set. Aircraft weight and dimensional restrictions must be considered. For example, a Navy aircraft is constrained not only by carrier takeoff and landing distance limits, but by the ability to store the aircraft below deck. Elevator weight limits and door opening size place restrictions on aircraft weight and dimensions. These in turn impact the allowable size and dimensions of the propulsion unit. For low observable (LO) aircraft, the engine is a major contributor to the overall aircraft signature. Radar cross section (RCS), infrared (IR), and noise reduction need to be considered in the engine conceptual design process.

A valuable tool to the engine designer is an aircraft sensitivity analysis to engine performance parameters. This provides very preliminary estimates of the impact of thrust, fuel consumption, and engine weight on aircraft range and/or takeoff gross weight. The propulsion designer can use this information to assess engine cycle and flowpath tradeoffs prior to the aircraft mission analysis. The number of potential engine configurations can be narrowed earlier in the process, resulting in shorter overall analysis time.

With reduced resources available to the military, affordability is becoming *the* primary propulsion design criteria for the 90's. Although up front costs associated with research, development, and acquisition are currently the most significant concern relative to affordability, major emphasis is being placed on support and maintenance aspects of life cycle cost as well. There is a strong desire to utilize existing propulsion systems for future aircraft because of the minimal research and development required as well as the acquisition benefits associated with higher production runs.

As far as maintenance is concerned, the US Air Force is presently going through a fairly radical transition from a three-level to a two-level system. What this means is that if an engine cannot be repaired on the flight line in a relatively short period of time, it is returned to the depot. Obviously, improvements in the ability to maintain future engines will be even more important under this new maintenance system.

Historically, environmental concerns have significantly influenced propulsion design for commercial aviation. The Federal Aviation Agency (FAA) has issued regulations which limit both noise and combustion emissions on commercial aircraft. Increasingly, the military is being asked to give consideration to these issues. Even if regulations are not extended to include military systems, good neighbor policies with local and state governments will likely drive future propulsion designers to consider their impact on the environment.

Figure 3 summarizes the myriad of potential propulsion requirements which should be included in the definition of a given propulsion system. Clearly, a great deal of communication between aircraft and propulsion designers is crucial. Unfortunately, because of the lack of information available at this point, most preliminary requirements are set by historical trends and back-of-the-envelope calculations. Updates are necessary throughout the design process as more detailed information becomes available. However, clear requirements definition is key to a successful engine conceptual design.

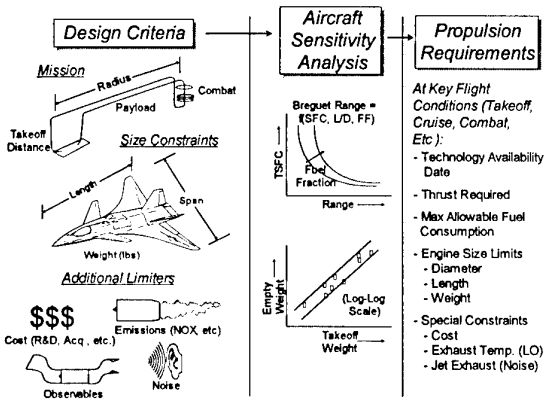

Figure 3 - Propulsion Requirements Definition

5.0 UNINSTALLED PERFORMANCE PREDICTION

Once a reasonable definition of propulsion requirements has been accomplished, the designer can begin to assess the thermodynamic cycle characteristics. For the most common turbine engine type in use today, the turbofan, major cycle characteristics include overall pressure ratio, fan pressure ratio, turbine inlet temperature, and bypass ratio (bypass airflow/core airflow). These parameters have the most significant impact on engine performance. The key performance indicators used by the turbine engine community are specific thrust (FN/WA) and specific fuel consumption (SFC), which are defined as

$$FN/Wa = \frac{Net\ Thrust}{Airflow}(lbf/lbm/\sec)$$

$$TSFC = \frac{Fuel\ Flow}{Net\ Thrust}(lbm/hr-lbf)$$

The larger the specific thrust, the smaller the engine size needed. A small value for specific fuel consumption is desirable, for obvious resasons.

A distinction should be made between uninstalled and installed performance. At this point in the design process, the engine designer will wish to examine a wide array of potential engine cycles. There could be as many as several hundred combinations of overall pressure ratio, fan pressure ratio, turbine inlet temperature and bypass ratio. Because of the large number of cycles involved, it is not feasible to perform a detailed inlet and exhaust system installation for each. Therefore, an uninstalled assessment is performed with standard assumptions made to correct for inlet and exhaust losses. To account for inlet losses, a standard ram pressure loss is assumed as (based on Mil-E-5007D),

$$Ram\ Recovery\ (\eta_{ram}) = 1.0 \quad (Subsonic)$$

$$Ram\ Recovery\ (\eta_{ram}) = 1.00 - 0.076(Mn-1)^{1.35} \quad (Supersonic)$$

Internal nozzle losses are based on past experience with similar type nozzles such as axisymmetric or two-dimensional. These losses are a function of nozzle pressure ratio and area ratio. Sometimes exhaust area is limited to a maximum based on aircraft aftbody constraints.

To perform the uninstalled performance analysis, a one-dimensional thermodynamic model is used. "Design" point inputs include the cycle characteristics mentioned above as well as component efficiencies, pressure losses, and cooling flows. Oftentimes, more than one flight condition is considered, such as take-off, cruise, and combat. A methodology is needed to determine component "off-design" performance. This is done through the use of compressor, combustor, turbine, and nozzle performance maps that are scaled to account for variations in airflow size and pressure ratio.

To illustrate the uninstalled cycle selection process, consider an example - the Global Strike Aircraft (GSA). This is a future aircraft system with a Technology Availability Date of 2010 (or an Initial Operational Capability of 2020). The preliminary design criteria for GSA is shown in Figure 4. The mission objectives are to achieve 5000 nautical miles radius unrefueled at a supercruise speed of Mach 1.5. Point performance is not critical for the GSA, so combat capability need not be considered. However, takeoff field length and the ability to cruise unaugmented at Mach 1.5 are thrust sizing constraints. . The thrust required at takeoff and cruise is found using the following

$$FNsls = (T/W)aircraft(TOGW)$$

$$FN1.5Mn = TOGW(\frac{L}{D})$$

Note that for both cases, aircraft gross weight is used. Although not strictly correct, this calculation should predict within a reasonable level of accuracy the minimum thrust required.

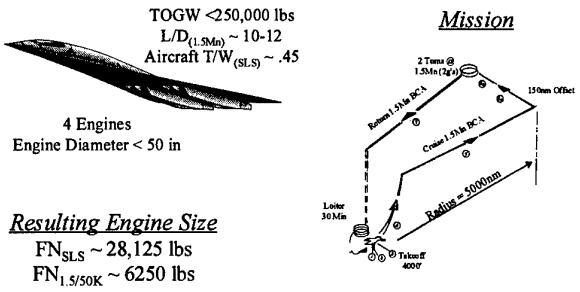

Figure 4 - Global Strike Aircraft Requirements Definition

A simple aircraft analysis provides estimates for takeoff gross weight vs. fuel fraction and Breguet radius vs. TSFC, which is used to define aircraft size and fuel consumption limits. In this case, the vehicle takeoff gross weight should not exceed 250,000 lbs to keep aircraft cost down. Referring to Figure 5, the takeoff gross weight vs. fuel fraction curve, the maximum allowable fuel fraction is estimated to be 0.64. Cross plotting the fuel fraction limit on the Breguet radius vs. TSFC, and given the desire for 5000 nautical miles radius capability, the TSFC needs to be 0.85 or less.

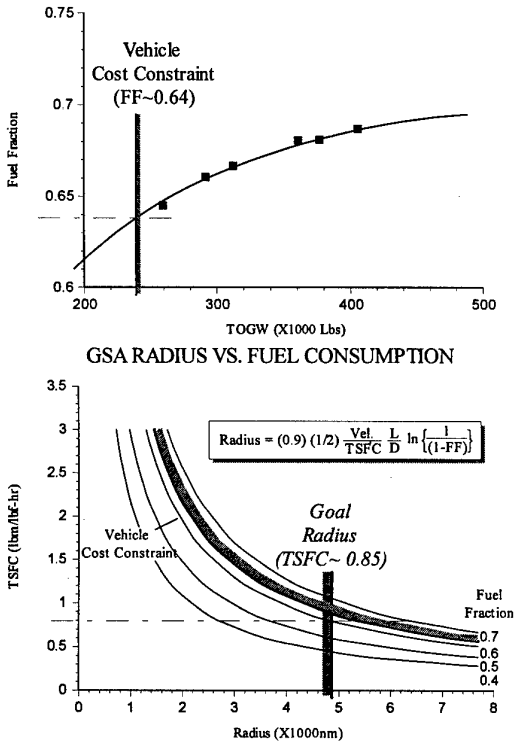

Figure 5 - Global Strike Aircraft Sensitivity Analysis

The uninstalled cycle trades associated with the GSA propulsion system are shown in Figure 6. Specific thrust is plotted versus specific fuel consumption for lines of constant overall pressure ratio and turbine inlet temperature. The data is grouped according to bypass ratio.

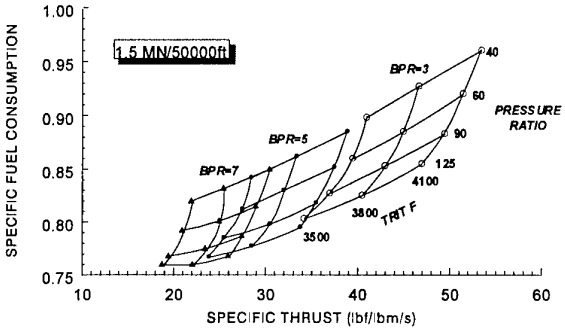

Figure 6 - GSA Uninstalled Performance Trades

Using rough order-of-magnitude estimates for various engine parameters and aircraft limits, a cycle design space is defined. Assuming fan specific flow (i.e., Corrected flow per annulus area) and inlet radius ratio (r_{hub}/r_{tip}), the engine maximum diameter and thrust required (at both takeoff and cruise) can be converted into a minimum allowable specific thrust

$$FN/Wa = \frac{FN\sqrt{\theta}}{Waspec(\delta)\pi(rtip)^2(1-(\frac{rhub}{rtip})^2)}$$

For the GSA, specific flow and radius ratio are assumed to be 40 lbs/sec-ft^2 and 0.3, respectively. The next step is to check both takeoff and cruise conditions to determine the most stringent constraint. For fighter aircraft, where point performance is important, a similar approach can be used to determine thrust required during combat.

Reasonable materials limits define a maximum compressor exit temperature, and hence, overall pressure ratio. Combined turbine bulk average blade material temperature ($T_{mat'l}$) and cooling effectiveness define an additional constraint to the design space. For this example, cooling effectiveness is defined as

$$\varepsilon cool = \frac{Tgas - Tmat'l}{Tgas - Tcool}$$

Returning to the GSA example case, Figure 7 is a repeat of Figure 6 with the design constraints applied. Maximum allowable SFC is based on required aircraft radius. Technology constraints on cycle pressure ratio and turbine inlet temperature further limit the design space. Cost concerns can also play a role in setting the design space. At this point, this is addressed by limiting the compressor and turbine stage count. Hopefully, with all the propulsion limitations applied, there exists a reasonable design space. If there is no design space available, it will be necessary to re-evaluate propulsion design requirements.

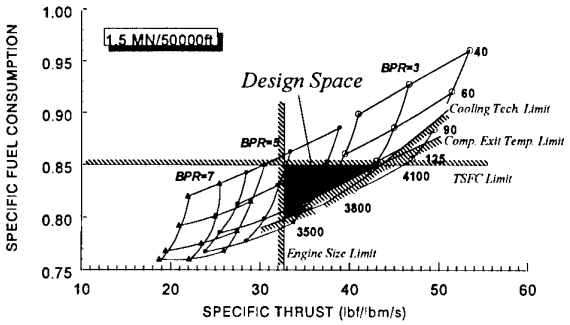

Figure 6 - GSA Uninstalled Performance Trades (With Constraints)

It is important to note that because of the assumptions involved, there may be viable designs outside the predicted design space. Some cycle points outside the design space should be carried through the analysis for completeness. However, the number of viable propulsion options has been narrowed substantially. With this more manageable number of propulsion options, a more detailed assessment can be performed. The installed performance, component/flowpath design, and observable performance prediction (as required) can be analyzed simultaneously (see Figure 2). This is typically executed by a number of designers who must interact with each other on a regular basis. Each of these design steps will be described separately with the understanding that they have a high amount of interdependency.

6.0 INSTALLED PERFORMANCE PREDICTION

With the number of cycles narrowed, the designer can perform a more detailed assessment of the performance losses associated with integrating the engine with the aircraft. Installation losses cover the effects of the engine/aircraft interaction on the propulsion performance. The installation penalties are typically categorized into inlet, nozzle internal, and aftbody (or boattail) losses. Inlet loss mechanisms include: (1) ram recovery, which includes the pressure losses due to friction, shocks, and flow separation inside the inlet; (2) spillage, which addresses the mismatch between airflow the engine wants and the inlet delivers; (3) wave drag, which accounts for the external shock losses associated with the inlet lip; and, (4) bleed, which covers inlet bleed penalties due to boundary layer and bypass bleed flows. Internal nozzle losses include: (1) friction; (2) over-expanded or under-expanded flow due to non-optimum exhaust area; (3) shock losses; and, (4) separation, which can cause severe penalties and is caused by excessive ramp angles or under-expansion. Aftbody drag is probably the most difficult to predict because it is most closely tied to the airframe. It is influenced by aftbody length, boattail angle, and exhaust jet flowfield interaction with the rest of the aircraft. Nozzle type (axisymmetric or two-dimensional), number of engines, and their proximity to each other also play a part in defining the aftbody penalties.

There are several ways to adjust uninstalled performance values to account for installation losses. The method described in this paper uses a series of inlet and exhaust system tables to correct for the engine integration penalties. Figure 8 provides an overview of the process. The inputs include uninstalled performance parameters (thrust, airflow, fuel flow, nozzle pressure ratio, and exhaust area), inlet and exhaust system maps, and inlet/airframe reference areas.

The designer will likely look at the installed performance of a variety of inlets and aftbody configurations before making a final selection. Tradeoffs based on engine flight envelope are required to select the appropriate inlet capture and exhaust nozzle areas. The final output for this step is a definition of installed thrust, airflow, and fuel flow at all the necessary flight conditions.

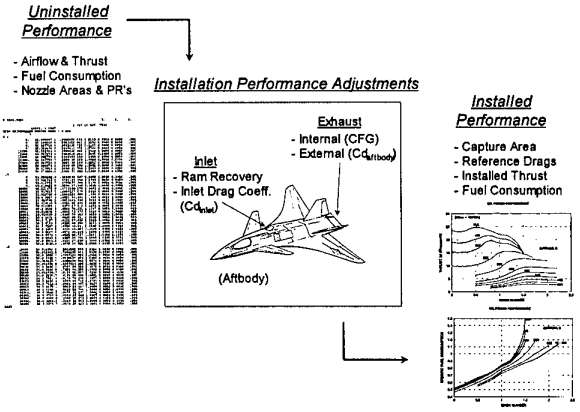

Figure 8 - Engine Installation Process

For inlet loss modeling, the most rigorous approach would be to account for the various penalties separately. However, a simplified approach can be used which combines all the loss elements except ram recovery. Figure 9 illustrates the format of the two inlet loss curves. Once inlet capture area is selected, the combined spillage/bypass/bleed/external wave drag losses can be determined based on corrected flow per capture area. This method has been found to be reasonably accurate, particularly for early engine analyses. For the exhaust nozzle, both internal and external aftbody must be considered. As shown in Figure 9, an adjustment to the gross thrust coefficient (CFG) is made to account for internal losses. This correction is a function of nozzle pressure ratio (P_{T8}/P_9) and area ratio (A_9/A_8). The aftbody installation penalty is accounted for in the aftbody drag coefficient, which uses the aircraft aft area (A_{10}) as a reference area. It too is a function of nozzle pressure ratio and area ratio, as well as flight Mach number.

One more point should be made before moving to the next propulsion design step. The installation losses can be applied to either the engine thrust or aircraft drag. Because of the interdependency between the aircraft and its propulsion system, a methodology is required so that no penalties are overlooked or double book kept. The standard practice is to include a reference maximum power loss with the aircraft drag and apply any additional losses to the installed engine performance. The portion included with the aircraft drag is commonly referred to as "throttle independent drag". The remainder, which is treated as an installed thrust decrement, is the "throttle dependent drag". Proper bookkeeping of installation penalties can be a sticky issue, particularly if a vehicle does not perform as anticipated. Oftentimes, the customer assesses large economic penalties on the airframe or engine manufacturer for shortfalls in both commercial or military aircraft performance. It is critical that an agreed upon thrust and drag bookkeeping methodology be established and adhered to throughout the design process.

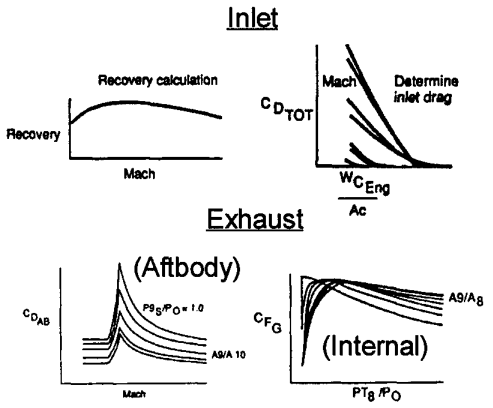

Figure 9 – Installation Map Format

7.0 ENGINE COMPONENT/FLOWPATH DESIGN

Overall component cycle characteristics have been defined, but a more detailed assessment is required to determine engine dimensions and weight. A preliminary look at individual components and how they fit together into an engine flowpath is necessary. Because the component design is largely independent of the installation analysis, both can be performed concurrently. If observables requirements exist, they can have a major impact on the component design. The interaction between observable and performance requirements must be addressed within the component design process. This could result in several iterations within the step.

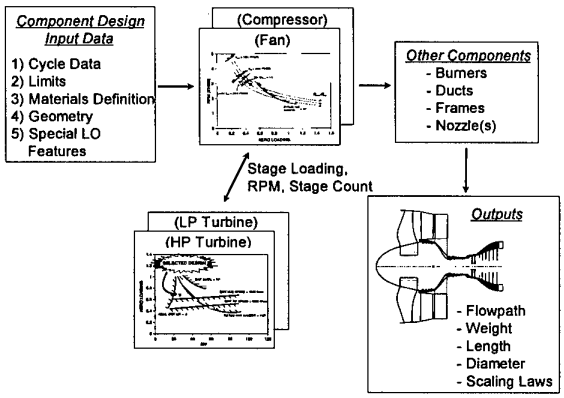

Figure 10 - Generalized Engine Component/Flowpath Design

Figure 10 illustrates the generalized component/engine flowpath design process. Specific inputs for each of the engine components include:

1) Inlet and exit pressures, temperatures, flows, and fuel/air ratios
2) Design limits (tip speed, hub speed, blade height, exit swirl, aerodynamic loading, etc.)
3) Material definition (type, strength, density, etc.)
4) Geometry (aspect ratio, solidity, combustor

length/diameter ratio, etc.)
5) Low observable features, as required (coatings, added cooling, shaping, etc)

The various components which make up a given engine configuration must be matched in terms of airflows, speeds, and work levels. In order to proceed, the design must begin with one component. For the methodology described in this paper, the fan and compressor are laid out first. The fan and compressor define turbine speeds (RPM) and work requirements.

To illustrate the methodology, the GSA high pressure compressor and turbine are examined. The inlet and exit pressures, temperatures, and mass flows from the cycle analysis establish the overall compressor thermodynamic requirements. A matrix of compressor designs are examined at varying aerodynamic loading ($gJ\Delta H/U^2$) and stage counts (Figure 11a). Limits are set which

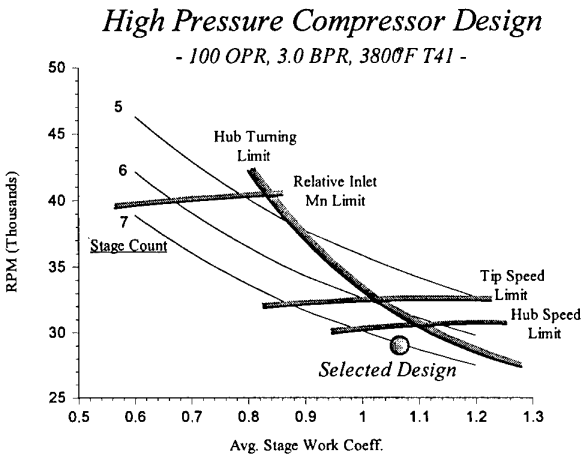

(11a)

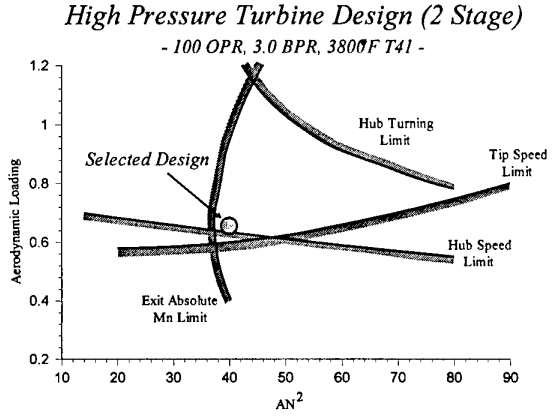

(11b)

Figure 11 - GSA High Pressure Spool Design Space

establish the compression system's design space. Usually a compressor is selected based on minimum stage count while not exceeding any design limits. This typically results in the lightest weight and lowest parts count configuration. For this example, the GSA compressor is primarily constrained by hub speed and stator hub turning, requiring 7 stages at 29,000 RPM. With the compression system configuration selected, the turbines can be analyzed. As in the compressor, turbine limits are applied to establish available design space. For the turbine design, stage count is assumed and design space determined based on AN^2 and aerodynamic loading ($2gJ\Delta H/U^2$). If no turbine solution space is available, more turbine stages can be added or the compressor design iterated upon. A two stage high pressure turbine was needed for the GSA engine. Figure 11b shows the design space. Note that the design constraints are exit swirl, hub speed, tip speed and absolute exit Mach number. Minimizing turbine stage count is even more important because added turbine stages seriously impact weight, cost, and cooling flow requirements. In addition to loading limits, the high pressure turbine radius should be reasonably close to the compressor radius to align the combustor inlet and exit. The inlet radius of the low pressure turbine should be closely matched to the high pressure turbine exit for similar reasons. Matching high and low pressure turbine radii can result in iterations of the compression system design. Once the high and low spool components are established, the rest of the engine flowpath is defined with appropriate design limits.

Once the engine flowpath is defined, weights can be computed for the various components. Materials are selected down to the engine piece part level (blades, vanes, disks, cases, etc). Airfoil volume is set by the flowpath analysis, blade solidity (chord/spacing), thickness/chord ratio, and leading and trailing edge thickness. Input rim and bore allowable stresses define the disk size. Empirical methods based on case diameter and pressure load are used to establish case thickness. Overall engine weight is determined using the density of the material and predicted component volumes. Weight adders based on empirical data are applied to account for additional features such as variable geometry and cooling.

Results of the engine configuration analysis to this point include overall engine flowpath definition, weight, and dimensions. Since the precise engine size is unknown at this stage in the analysis, scaling laws are required. The scaling laws provide the ability to resize the engine without having to repeat the component design analysis. The final overall engine design must be run through a range of flow sizes to provide scaling laws.

At this point, the number of acceptable engine configurations will likely be further narrowed. Additional engine configurations may have been eliminated because of poor installed performance, excessive weight, or perhaps an undesirable compressor or turbine stage count. As a result, the remaining designs are ready for the next step - the aircraft mission analysis.

8.0 AIRCRAFT MISSION ANALYSIS

At the same time the engine installation and flowpath analysis is being performed, the aircraft and mission have likely been sufficiently refined for propulsion trade studies. The overall aircraft mission analysis process is shown in Figure 12. An Aircraft figure-of-merit is selected such as range, operating empty weight, takeoff gross weight, or endurance. This will be used as a tradeoff parameter, with all other aircraft design parameters held constant, so that the optimum engine configuration can be established. For

example, if takeoff gross weight is to be used as a figure-of-merit, the mission range or radius will be held constant.

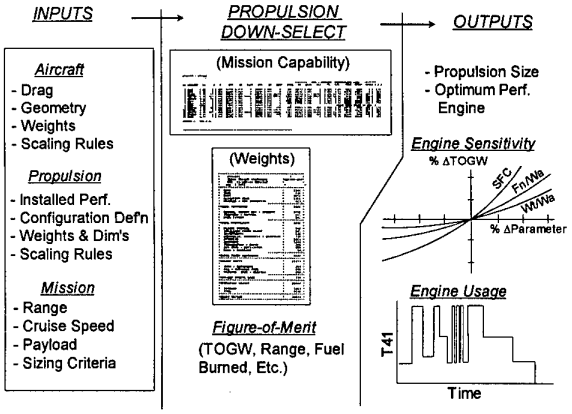

Figure 12 - Aircraft Mission Analysis

The mission is broken into segments such as taxi, takeoff, acceleration, climb, and cruise. Each segment must be defined in detail, including such parameters as initial and final Mach number and altitude. Wing area and propulsion thrust sizing criteria are normally set by a number of aircraft performance requirements including specific excess power (P_s), load factor (n), acceleration time and climb rate at key points throughout the flight envelope. Different engines have different sizing criteria due to what is commonly referred to as "lapse rate." Lapse rate is defined as the rate of thrust roll off associated with increasing Mach Number and/or altitude from sea level static to some pre-defined condition. Higher bypass ratio, higher overall pressure ratio, and lower turbine inlet temperature designs will typically have a higher lapse rate, and hence, poorer performance at increased Mach and altitude. The result is that a larger engine is needed for higher lapse rate designs to satisfy the aircraft's performance requirements.

The aircraft geometry, weights, and drag must be determined as well. Normally, aircraft characteristics are determined by breaking the aircraft into major subassemblies including the fuselage, wing, tail and engine nacelles (if applicable). Geometry calculations are used to verify that sufficient volume exists for avionics, payload, propulsion, crew compartment, etc. With the aircraft geometry defined, the weights of various aircraft parts can be predicted. Overall drag is the sum of induced, parasite, wave, and trim drag. Also, the throttle independent drag, as described in the Installed Performance Prediction section, is included in the overall aircraft drag.

A number of important propulsion characteristics can be derived from the aircraft analysis. In addition to down-selecting the optimum engine design, required engine size is established. A propulsion sensitivity analysis can be performed to determine the effect of variations in thrust, fuel consumption, engine size and weight on the specified figure-of-merit. A refinement to the optimum engine design may result from the sensitivity analysis. Also, this analysis is helpful when the designer moves into the propulsion detailed design phase. Sometimes the detailed engine design analysis indicates that the selected engine must be compromised. The tradeoff analysis can provide the necessary information to determine which propulsion parameter to trade off which will minimize aircraft impact.

Another important piece of information resulting from the aircraft mission analysis is engine usage definition. Throttle excursions, and their impact on compressor exit temperature, turbine inlet temperature, and TAC cycles is critical to predict engine maintenance requirements and life. With engine usage defined, the operations and support cost element of the propulsion Life Cycle Cost (LCC) can be analyzed.

9.0 SPECIAL CONSIDERATIONS

In the past, the selected engine would be ready to transition into the preliminary design phase of development. Recent developments in the world brought on by the perceived diminished threat to national security have resulted in a tremendous change in the military aerospace community. Resources dedicated to national defense are in decline, and as a result, future systems have cost reduction as a key design criteria. The overall Life Cycle Cost (LCC) of an engine can be subdivided into the following categories:

1) Research & Development (R&D)
2) Acquisition
3) Operations & Support (O&S)
4) Disposal

R&D cost encompasses the expenses associated with bringing the engine into production. Acquisition cost includes the actual production costs to build the fleet. O&S cost covers the fuel and maintenance cost. Disposal cost addresses the costs to remove an engine from the fleet, and is normally not included in the conceptual analysis. The generalized cost prediction process is discussed in the following paragraphs.

From an overall life cycle cost standpoint, R&D cost is comparatively small. However, since the R&D must be accomplished at the beginning of the program, it represents a major up-front investment. Because of the high cost of R&D (typically greater than $1B for large man-rated engines), there is the inclination to use off-the-shelf or derivative engines that require minimum development. In addition, technical and manufacturing development problems are largely unpredictable. At the conceptual design stage, R&D costs are typically determined based on past experience corrected to account for engine technology maturity. Anticipated engine testing requirements play a role in defining R&D costs as well. Perhaps in the future, design tools will have progressed to the point where the need for development testing will be reduced. This would offer the added benefit of reducing the number of development engine required, which are quite expensive.

Acquisition cost is the other half of the up-front cost of a new system. This is an ideal opportunity for the manufacturing engineer to impact the engine configuration at the very early stages of the design process. There is a spectrum of approaches to predict acquisition cost (Figure 13). The simplest method is purely empirically based using general cycle parameters such as airflow, overall pressure ratio, turbine inlet temperature, and bypass ratio. On the other end of the spectrum is a prediction of cost based on individual component manufacturing processes. This involves adding the raw material, fabrication, and man-hour costs for each piece part. Although this methodology provides a more accurate

prediction, the complexity of the analysis makes this approach impractical unless the various manufacturing processes are well understood. A bottoms-up analysis also requires more detailed analysis, and therefore, more time. An alternative approach melds some of the advantages of both. This method is based on attributes such as part size, shape, and material machining characteristics. A database is used to represent a wide variety of component and material manufacturing processes. The designer picks a part's manufacturing process from this database and uses scaling relations to represent the configuration being designed. Regardless of the approach taken, the number of engines to be purchased has a large impact on acquisition cost. In general, the more engines a company manufactures, the greater the opportunity to learn better ways to produce an engine. In order to account for this, learning curves are used to account for the number of engines to be purchased.

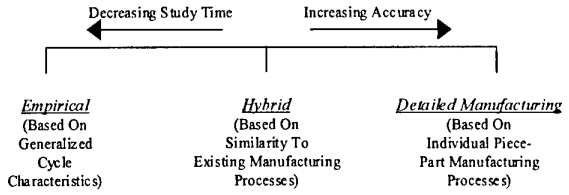

Figure 13 - Spectrum of Acquisition Cost Prediction Methods

Engine operations and support (O&S) costs are highly dependent on average flight time and/or TAC cycles during peacetime training, and to a lesser extent, wartime operation. Usage impacts O&S cost both directly through fuel cost, and indirectly through consumption of engine life. Usage is very difficult to predict for a system that has not even been designed beyond the conceptual level. Even if engine performance and life are accurately predicted, how an aircraft is flown is often different than how it was designed to operate. As a result, O&S cost prediction at the conceptual design phase is unlikely to match very well with the actual O&S cost. However, O&S cost predictions can be a valuable tool in comparing various potential engine designs. It can also be helpful in comparing new systems to existing aircraft performing similar missions.

To predict O&S cost, several system level assumptions must be made. These assumptions include aircraft fleet size, aircraft life, and usage per month in terms of flight time and/or TAC cycles. To determine cost, the designer essentially adds up the total engine usage. Scheduled and unscheduled maintenance actions are predicted from this usage estimate, and total number of engines required (including spares) is determined. It should be kept in mind that fuel cost is a major portion of engine O&S cost, typically over 50%.

For the design process described in this paper, the assumption has been that cost analysis is accomplished after the aircraft mission analysis. Recent development of computerized tools will likely move cost analysis forward in the design process. This is particularly true in the case of R&D and acquisition cost, which is not as dependent on overall aircraft system usage and force structure. It is anticipated that up front costs will become an integral part of the component/flowpath analysis.

One other item deserves a brief mention - Engine emissions. For the purposes of this discussion, emissions include both noise and combustion products (smoke, NOX, CO, and hydrocarbons). Local communities have become increasingly critical of the military's environmental impact. Although it is unlikely the military will give up their performance edge, future designs will have to give consideration towards reduced noise and combustion emissions. Emissions could well become the next element to be incorporated in the engine conceptual design process.

10.0 CONCLUDING REMARKS

This brief synopsis is intended to provide an overview of the interrelationships between various propulsion conceptual design steps. Computerized conceptual design tools exist to analyze uninstalled performance, installed performance, component/flowpath design, aircraft tradeoffs, and engine life cycle cost. Noise and combustion emissions could very well become the next elements to be integrated into the process. Whole books have been written to address each of these steps, so this paper cannot possible cover all issues. Hopefully it has at least introduced the reader to tools that are currently available.

Many different methods exist to integrate various design elements into an overall process. Ideally, designers like to perform all design steps concurrently in order to minimize the overall time required to conduct a study. However, several steps must be performed in series since results of one must feed into the next. Installation and component design analyses can be performed simultaneously, and the hope is that up-front costs (R&D and acquisition) can be integrated into the process at an earlier stage.

11.0 REFERENCES

1. Stricker, J.M., Norden, C.M., "Computerized Preliminary Design of Turbomachinery", ASME No. 91-GT-391, June 1991.

2. Widdison, C.A., Schreffler, E.S., Hosking, C.W., "Aircraft Synthesis with Propulsion Installation Effects", AIAA No. 88-4404, Sept 1988.

3. Zarchan, Paul, Jensen, Gordon E., Netzer, David W., "Tactical Missile Propulsion", AIAA Progress in Astronautics and Aeronautics, Volume 170, 1996

4. Mattingly, Jack D., "Elements Of Gas Turbine Propulsion, McGraw Hill, 1996

5. Mattingly, Jack D., Heiser, William H., Daley, Daniel H., "Aircraft Engine Design", AIAA Education Series, 1987

6. Nicolai, Leland M. "Fundamentals of Aircraft Design", METS, Inc., 1984

Meeting Discussions

Paper 1: **The Gas Turbine Engine Conceptual Design Process - An Integrated Approach**
Author: Jeffrey M. Stricker

Discussor: Bruce M. Steinetz

Question: Was there any particular reason that draws you to use a 100 OPR?

Author's reply: The purpose of this paper was to describe the conceptual design process used in my organization to assess advanced technologies. The Global Strike Aircraft is merely used as an example to illustrate the methodology. However, the US Air Force is considering higher overall pressure ratio cycles in its long range planning studies, because of the significant fuel con-sumption benefits to future aircraft.

Design of a new Fighter Engine - the dream in an engine man's life

A. Schäffler
W. Lauer

MTU Motoren- und Turbinen-Union
München GmbH
Dachauer Str. 665
80995 München, Germany

1. Introduction

In 1984-85 a feasibility study between 5 European Nations France, Germany, Italy, Spain and United Kingdom for a common air superiority fighter was pursued which ended in 4 Nations to step into the Definition Phase in autumn 85. For us this was the beginning of an exciting experience in various roles as MTU Chief Engineers and Technical Directors of Eurojet Turbo GmbH, i.e. Chairmen of the Chief Engineers' meeting.

Designing a brand new fighter engine at the very edge of technology is an occasion so seldom that given the opportunity to take a lead function in such a multi-billion dollar project is a dream, which only few enjoy once a life.

2. International Cooperation

A four Nation project is a delicate task. It is however of great help if 3 of the 4 partners have known each other for a long time as in case of Eurojet where Fiat, Rolls-Royce (RR) and MTU already had a long experience in the Tornado/RB199 engine project and could integrate the Spanish ITP Company easily. Cooperation can have 2 distinct difficulties:

- The way of cooperation
- The work share and split of responsibilities

Eurojet agreed to operate to the principle of joint working groups and unanimous decisions in groups and subgroups - a not convenient system but one which forces everybody to convince rather than to dictate and that improves the quality of a decision.

The work share and component/responsibility distribution is very important and sometimes very difficult to achieve to all partners' satisfaction because it contains the strong element of technology transfer. In most cases, however, it is a question of the available technology background and if one looks at the work share eventually found in the EJ200 it follows this line with one big exception:

the convergent/divergent nozzle for which no background existed was given to the newcomer SENER, later ITP, and they solved it admirably well.

As can be seen from Fig. 1, the responsibilities are split as follows along the engine:

MTU	Low pressure compressor
	High pressure compressor
	Digital Control System
RR	Inter Duct casing
	Combustor
	High pressure turbine
Fiat	Low pressure turbine
	Afterburner
	Gearbox
SENER / ITP	Convergent - divergent nozzle
	external Dressing

To integrate four responsible companies to an overall success requires continuous preparedness to really cooperate, to accept other than own ideas, to respect and appreciate the partners efforts and to develop a feeling for the partners sensitive areas - it is likely to fail on a „shear power" situation in an environment of the european type, namely several similarly strong partners.

3. The Task - Requirements and Assumptions

The new engine should be:

- optimised for the fighter role
- outperform existing engines at lowest possible weight
- be designed equally well for low cost of ownership (LCC), as for high performance
- set new standards on life, maintainability and testability

Paper presented at the RTO AVT Symposium on "Design Principles and Methods for Aircraft Gas Turbine Engines", held in Toulouse, France, 11-15 May 1998, and published in RTO MP-8.

- provide carefree handling everywhere in the flight envelope
- Built in 15 % thrust growth potential

Fig. 2 summarises is in short the task given to the engine companies. It is written down in a document called the European Staff Requirement ESR-D in which the Joint Air Staffs described what the four Air Forces expect the new Weapon System and as part of it - the engine - should provide. Europe may look small - nevertheless the requirements of the 4 Air Forces were different enough that Eurofighter and Eurojet had to design the aircraft for

11 different missions

8 performance guarantee points

Out of the 11 missions 2 were design driving namely the:

- Air superiority mission
- Supersonic minimum time intercept mission

which each burns about 75 % of the fuel either at subsonic speed in dry engine mode or at high supersonic speed in afterburning operation. It is obvious that these 2 conditions are the shear opposite with regards to the dominating overall engine parameter specific thrust.

Dry specific thrust directly reflects itself in the nozzle pressure ratio and nozzle entry temperature and for an optimised mixed turbo fan cycle the nozzle pressure ratio closely correlates with the fan pressure ratio.

Therefore, the dominating engine cycle design parameter is the fan pressure ratio with the bypass ratio resulting from the available technology level as shown in Fig. 3.

Reheat specific thrust depends almost exclusively on the afterburner temperature, in particular at supersonic flight conditions. Highest possible reheat temperature gives smallest engine mass flow and engine size to achieve the demanding aircraft point performance requirements. However, due to the steep increase in specific fuel consumption, when increasing the afterburner temperature towards the stoichiometric limits the reheat temperature has been carefully selected to achieve the best compromise between high specific reheat thrust and low specific fuel consumption during aircraft combat manoeuvres at full power.

Amongst a careful cycle optimisation, high engine technology is mandatory to achieve the weapon system requirements.

Highest engine technology for a given optimum specific thrust results in

- the smallest core and hence the lightest engine
- the lowest specific fuel consumption and hence lowest fuel tank size and mass.

The task of the Eurofighter engine design was to optimise the engine specific thrust and to provide the adequate engine technology to achieve the partially conflicting aircraft performance and mission requirements with lowest possible procurement and operating costs.

4. The Optimisation Process of the Engine Cycle

4.1 General Approach

As stated above the customer required a Weapon System with lowest possible investment and operating cost, which fully achieves the mission and performance requirements. In general - not in every detail - aircraft cost does correlate well with its basic mass. Aircraft design experience shows that a multitude of requirements can usually be fulfilled at a given level of technology by increasing the size of the aircraft - resulting in higher overall cost and cost of ownership and that was the strictly forbidden way forward. „Mass" was the undoubtedly most quoted word during the first phase of the project and remained there most of the time.

Starting from this hard condition with the basic thermodynamics, shown on Fig. 3, the engine design proceeded in closest possible co-operation with the aircraft companies over several iterative steps which are sketched in Fig. 4.

The iterative process of cycle selection

The following approach was used:

- Fixing of a nominal thrust size (90 kN)
- Variation of fan pressure ratio and turbine rotor inlet temperature within a sensible range
- Selection, decision and proof of feasibility of the engine architecture - the most challenging part
- Evaluation of outer dimensions, mass and performance data for all variants
- Scaling factors for different thrust size engines

➢ Final optimisation process out of the most promising variants

How engine design affects the required minimum aircraft basic mass empty is sketched on Fig. 5 as a function of fan pressure ratio (i.e. dry specific thrust) as the governing parameter and engine technology level.

4.2 Definition of Optimum Specific Thrust

The optimum specific thrust i.e. the optimum fan pressure ratio was investigated in the initial part of the definition phase.

The optimum fan pressure ratio is the intersection of two mirror image functions which result either from the Air Superiority or the Minimum Time Intercept missions.

The optimum fan pressure ratio for the air superiority mission is well below 4. The optimum fan pressure ratio for the supersonic min time intercept mission is above 4.5.

The minimum aircraft mass in case of the conflicting Eurofighter requirements resulted at a fan pressure ratio of 4.2. The absolute level of aircraft mass required can then only be influenced by the engine technology level applied. The really interesting result is that the optimum fan pressure ratio does actually change very little with technology level.

4.3 Selection of Technology Level

The technology level to be applied was the highest available or achievable in time within the four partner nations based on existing technology or demonstrator programs.

The design philosophy followed the principle:

- Simple rugged design with a minimum number of turbomachinery stages and parts
- high component efficiencies by advanced 3-D design and high rotational speeds
- Acceptable risk level, no new exotic materials
- Optimised performance to fulfil all missions/ guarantees
- Lowest Cost of Ownership

Engine design technology level expresses itself essentially in 2 parameters:

- compressor exit temperature
- turbine rotor inlet temperature

The excellent supersonic performance capability of the Eurofighter resulted in the need of unrestricted engine operation at high compressor inlet temperatures. The overall compression ratio was selected such that material property limits in the HP spool were not exceeded. Fig. 6 illustrates that within the temperature limit optimum dry specific thrust at minimum dry specific fuel consumption is achieved.

The choice of turbine inlet temperature is illustrated in Fig. 7, which shows a number of limits to be considered in a plot of bypass ratio vs fan pressure ratio:

- 4.8 maximum fan pressure ratio for a growth version
- Maximum RIT level for life requirement
- Max 0.6 bypass ratio for a single stage low pressure turbine
- 0.25 - 0.30 minimum bypass ratio for afterburning of the bypass air.

The last element is very important as it strongly affects the supersonic thrust potential. In order to keep this potential also for a growth version which at given outside maximum diameter results in higher fan flow and fan pressure ratio at reduced bypass ratio, a bypass ratio clearly above 0.3 is required for the initial variant. This means that at optimum fan pressure ratio the turbine inlet temperature can not be reduced below the selected level.

A smaller bypass ratio would also increase the engine mass due to the bigger core and worsen the dry SFC i.e. result in a heavier aircraft. An increase above the selected level would further reduce the size of the aircraft, but would not leave the required growth margin in the engine design.

4.4 Selection of Nozzle Concept

The optimised cycle did not fulfil the minimum time intercept missions. So far a simple convergent nozzle was used in the design process. In order to reduce the fuel consumption during the supersonic cruise phase the effect of a convergent/divergent nozzle was studied.

The application of the supersonic nozzle was at the time a fiercefully fought decision as no real data base existed in Europe. However the additional mass at the back end - and this was the main mental block under the overall mass limit - is a very good investment as it brought the break through in a stalled situation by improving the available combat time by 25 % to a satisfactory level (see Fig. 8). In fact the reduced back end drag even slightly improved the Air superiority mission as well.

4.5 Final Cycle Choice

The best cycle design solution was an engine with the following overall parameters:

FAN PR 4.2
BPR 0.4
Overall PR 25.6
Con/di nozzle, single parameter control

5. FIXING THE ENGINE ARCHITECTURE

In parallel to the consecutive cycle selection process the engine companies went through the core process of engine design:

Design rationale and decision on the engine architecture

It is the most challenging step as it requires a systematic decision process on very fundamental elements in a floating environment and it requires partially very deep investigations, which take a certain time to achieve conclusive results. It is this phase where the Chief Engineer's capability to judge the directions without having everything in black and white is required most. He must be able to go forward and keep enough flexibility to react to outside changes or look for solutions which allow correction without changing the basic decisions. This is what we call the „Art of Engineering".

The basic decisions in the EJ200 design were:

- Fan with or without variable inlet guide vanes
- Fan bearing arrangement - overhung or straddle mounted design
- Rear bearing arrangement - hot interturbine duct or turbine exit case strut/intershaft bearing
- Co - or contra rotating spools
- Convergent or convergent/divergent nozzle

Decision Rationale

Fig. 9 sketches schematically the basic options with respect to bearing arrangement and fan design.

5.1 Variable IGV's or no IGV's

This question actually remained open for some time as it was very difficult to answer. The attraction of not having a complicated, expensive and bird strike sensitive element as a variable inlet guide vane is very high with respect to life cycle cost and mass. This is specifically true against the very demanding bird strike resistance requirements imposed on to the EJ200, which are drastically above comparable engines. However elimination of the variable IGV's implies the problem of aerodynamic matching over the whole speed range and avoidance of dangerous mechanical resonances over the large range of fan speeds as the required flow range can only be covered by fan speed.

The fan is the component in an engine which operates over the by far widest speed and flow range between idle and transonic flight, i.e. something between 35 % and 105 % speed. The whole range of the characteristics is covered with performance guarantee points due to the different missions and point performance requirements written down in the ESR-D document. It was not really known whether or not all these conditions can be met with a wide chord 3-stage fan of fixed geometry at 4.2 pressure ratio until additional test data became available from a very similar 3-stage rig. The solution was to strive for a design which could eventually apply variable IGV's without changing the bearing arrangement but leave the way open for a very simple design.

5.2 Fan bearing arrangement - overhung vs straddle mounted design

This decision was probably the most difficult to make as it implies a limitation on the maximum fan tip speed.

The investigations covered:

- general shaft dynamics
- manoeuvre loads
- unbalance forces and shaft deflections in case of blade loss
- mass trade off

It was concluded that an overhung fan can be designed with the wide chord aerodynamics required for the 4.2 pressure ratio at a certain tip speed limit.

This actually paved the way for the **simplest possible** design of a top performance supersonic fighter engine of unprecedented appearance. **The EJ200 design is unique as no other engine of similar capability has such a low number of parts.**

5.3 Rear bearing arrangement

The design logic for the interturbine strut vs turbine exit strut/intershaft bearing was a minimal shaft dynamic interference between low and high pressure system, both being directly supported against the casing via the hot strut structure.

- lower mass
- no intershaft seals
- lower life cycle costs

5.4 Co - or Contra rotating shafts

There are 4 arguments for the contra-rotating arrangement:

- reduced gyroscopic forces under manoeuvres
- minimal tip clearances under manoeuvre loads in conjunction with inter turbine duct arrangement
- reduced aerodynamic loading on the low pressure turbine stator vanes
- reduced aerodynamic sensitivity of the high pressure compressor against rotating stall cell distortions emanating from the fan.

5.5 Number of HP-Compressor stages

With the choice of a 4.2 fan pressure ratio a 5-stage HPC appeared compatible with the available data base.

Figs. 10 and 11 recall the engine architecture decision which in case of the fan bearing arrangement is driven on simplicity reasons.

6. Design to Life Cycle Costs

Minimum Life cycle cost was a basic requirement in the ESR-D. The evaluation and comparison of the various options showed that the basic elements where the EJ200 differs from comparable high performance fighter engines is the NON IGV and the turbine interduct bearing support. These 2 elements reduce life cycle cost by about 2,4 % - which may sound small. It is, however, a very big sum of money for the airforces.

Fig. 12 shows the essential summary of the life cycle cost study.

7. Basic Programme Philosophy, Development Process and Results

„The engine program must be of an acceptable risk level and the design principle is to be demonstrated in a Design Verification Program". From this philosophy an overall program was defined which followed the phases shown on Fig. 13.

The engine development process followed the prescribed procedure to build 3 Design Verification Engines, which actually were designed and built parallel to the Definition Phase and DVE 01 did run only 2 weeks after signature of the Main Development Contract without fan IGV's and achieved within 2 test hours 95 % of the dry design thrust. After a deep investigation into the design principles and overall engine architecture the „Full Scale Development Engine" design started and run first in October 90. The contract asked for continuous thrust increase and flight envelope expansions over a 3 years period and Eurojet reacted to this requirement with 2 basic engine standards, the 01 and the 03 line, which started with 80 % nominal thrust followed by 100 % thrust for the 03 standard engines.

The engine up to now has undergone an extensive test program with

- 5.600 hours bench testing
- 3.100 hours in altitude test facility
- 500 hours in the aircraft

The engine has been exposed to most severe intake distortion testing with different types of distortion gauzes simulating distortion levels up to DC 60 ~ 1.0. The engine is highly responsive and has achieved all the specification handling times. During its total flight testing the engine never experienced a surge in flight. The engine does have a very good track record and the pilots like it as reliable, responsive and powerful.

Fig. 14 shows the experience gained in altitude test facilities all over the flight envelope.

8. New Elements

Parallel to the main program Eurojet developed advanced elements for the engine and will introduce these into the production engine standard.

The most obvious changes are the so called „All Blisk Fan" and the new advanced Digital Control Unit although there are advanced features like better material turbines for even longer life and the change of the vaporiser combustor to an airspray design in the 03 Standard.

The blisk fan became a viable solution when the linear friction welding technique developed into a stable process allowing the repair of big diameter blisks and hence make them cost effective for the combustor.

MTU started development of the linear friction welding process together with Rolls-Royce and eventually brought it to a standard that now blisk fans can be introduced into the latest 03 Standard engines. The engine does achieve its specification mass and performance and it is undoubtedly one of the „hottest" and highest performance engines anywhere in the world - it is a European Success Story.

9. Concluding Remarks

The design of a new fighter engine is a personal experience one will never forget. It is an effort full of technical excitement and interesting interaction. In a phase where there are unknowns which by no means can be answered in all and every detail it always happens that some decisions must eventually be taken by engineering judgement after intense debates with good friends and colleagues. One of the deepest experiences I enjoyed during my activities in this project was the friendship and continuous assistance of the late Rolls-Royce EJ200 Chief Engineer R. J. Lane who is no longer amongst us. The fact that we can present this paper on a successful engine program is much to his credit.

Acknowledgement

The authors wish to express their thanks for permission to publish this paper to NETMA, EUROJET and the Management of MTU.

EJ200 – Production Workshare

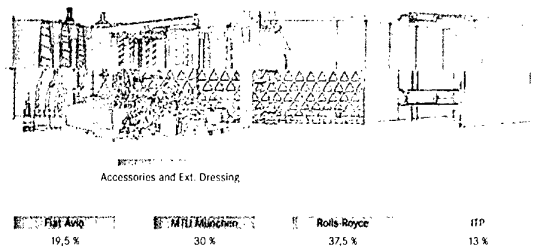

Figure 1

EJ200 –Engine Requirement (ESR-D)

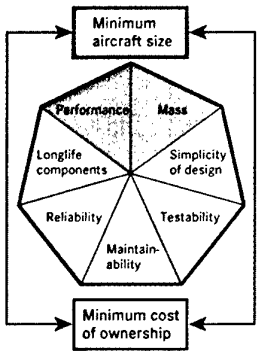

- ☐ 11 Missions
- ☐ 8 Aircraft point performance requirements
- ☐ 22 Engine guarantee points
- ☐ Optimized for fighter
- ☐ Superior supersonic performance
- ☐ Minimum cost of ownership
- ☐ Excellent reliability, maintainability and testability

Figure 2

EJ200 Effect of Fan Pressure Ratio and Turbine Inlet Temperature on Engine Performance

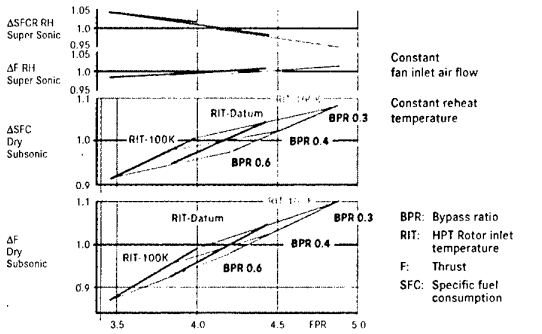

Figure 3

EJ200 – Definition

1. Cycle selection — **Feasibility study**

0,25 < BPR < 0.8 → BPR = 0.5 / BPR = 24

2. Cycle selection study

BPR = 0.3 - 0.6
PR Fan < 4.8

- ■ Fixing of engine architecture
- ■ Parameter data

BRR 0.3 0.4 0.5 0.6
RIT - 50 K NOM + 50 K — PR Fan < 4.8

- ■ Overall dimensions
- ■ Mass
- ■ Performance (F, SFC)

Definition phase

☐ Engine/Scaling factors (Size, Mass = f (F))

3. Cycle selection/Final optimisation

BPR 0.35 0.375 0.4
Nozzle type con vs con/di — PR Fan ≤ 4.2

Figure 4

EJ200 – Selection of Fan Pressure Ratio

Missions with high proportion of engine fuel burn

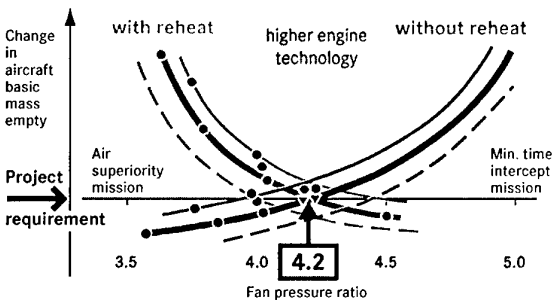

Figure 5

EJ200 – Cycle Selection

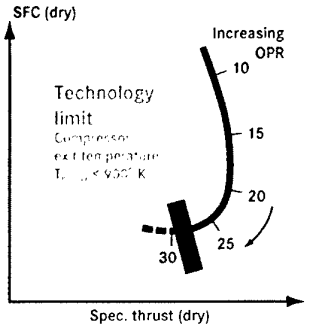

Max overall pressure ratio:

☐ limited by compressor exit temperature
i.e. cooling requirements for disks/vanes/blades resulting in

- ☐ high dry spec. thrust
- ☐ min dry SFC

Figure 6

EJ200 – Cycle Selection

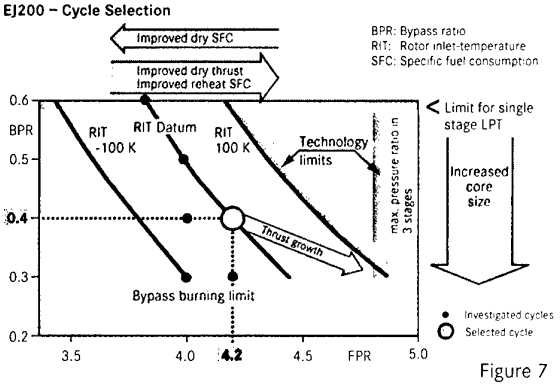

Figure 7

EJ200 – Effect of Convergent/Divergent Nozzle on Aircraft performance

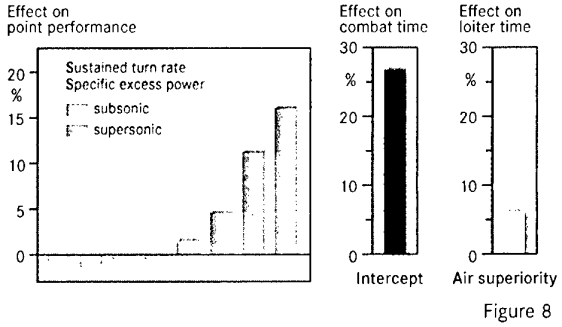

Figure 8

EJ200 – Engine Architecture · Bearing Arrangement Configuration

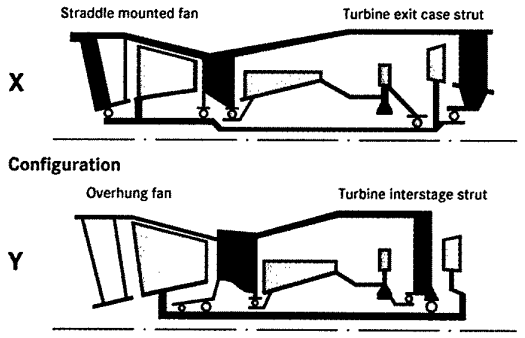

Figure 9

EJ200 Design Rationale on Engine Architecture

TOPIC	Arguments	Weighting	Rationale
Fan variable IGV's	aerodynamic performance	+	strive for non IGV
	aerodynamic stability	+	
	mechanical blade vibration/ resonance tuning	+	keep decision open until aero results available
	simplicity	--	
	mass	-	
	bird strike capability	-	
	Life cycle cost	--	
Fan bearing arrangement	shaft dynamics	0	go for overhung fan
	manoeuvre deflections	0	
overhung fan	unbalance forces/blade of case	-	keep non IGV solution
	mass	0	open
	simplicity	+	
	maintainability	+	

Figure 10

EJ200 Design Rationale on Engine Architecture

TOPIC	Arguments	Weighting	Rationale
Rear bearing arrangement	shaft coupling	+ +	
	minimum tip clearance change	+	
Inter Turbine Strut vs Intershaft bearing	Life cycle cost	+	Inter Turbine strut
	maintainability	+	
Co-Contra-Rotation	Reduced gyroscopic loads	+	
	Minimum tip clearance changes	+	Contral Rotation best for
	LP Turbine efficiency	+	overhung fan
Con-/divergent nozzle	Supersonic performance	++	con/di single parameter
	single control parameter	-	for mass reasons
	two control parameters	+	

Figure 11

EJ200 – Design to Life Cycle Cost

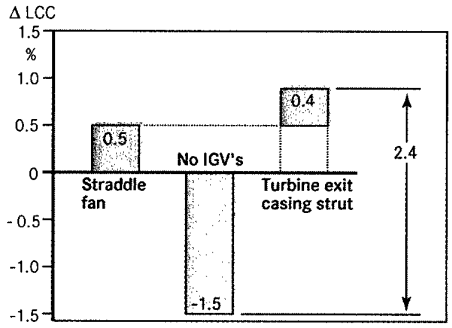

Figure 12

EJ200 – Programme Phases

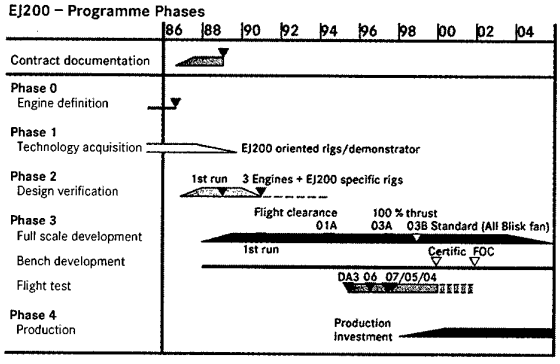

Figure 13

ATF Experience with FSD Engines

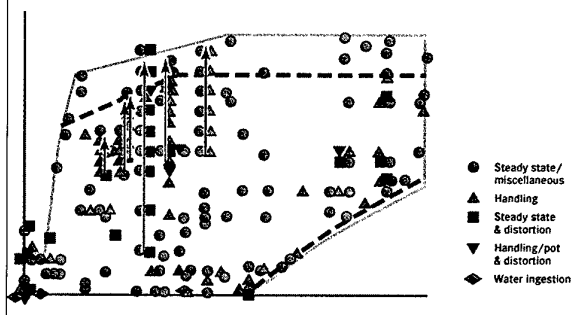

Figure 14

Designing for Reliability - the Rolls-Royce Approach.

P.J. Hopper
Senior Reliability and Safety Engineer
Rolls-Royce Military Aero Engines Limited
PO Box 3, Filton
Bristol, BS12 7QE
United Kingdom

Introduction.

In today's highly competitive world market, where safety, reliability and operating costs of equipment are often paramount, there are many drivers to maintaining a viable, and economic, operation. This is as true in the world of aerospace as in any other. Aircraft on the ground neither win wars for armed forces nor earn revenue for civil operators.

It is against this background that the Rolls-Royce Aerospace Group has as one of its primary objectives the "provision of reliable, and safe products and services which meet the expectations and specified requirements" of its various customers. These include both military and civil operators, and various regulatory authorities.

The task of the Company is therefore to realise the challenge in meeting these safety and reliability requirements in both the civil and military markets at the entry into service of its projects.

Reliability Drivers.

The Company finds that the drivers to safety and reliability are many and various. These include, but are not limited to reducing the cost of ownership.

For example the unscheduled maintenance costs on a wide-bodied aircraft can be ten times the capital outlay over the operating life of the aircraft. Similarly, but at a reduced level, this is estimated to be two to three times for a military "fast jet".

Another heavy burden is the cost of changing a "big fan" engine away from the aircraft's main base. This has been estimated to be of the order of £500,000 sterling. One medium sized British charter airline estimates that "unreliability" costs it about £1million per aircraft per year. Again, it has been officially estimated that unreliability costs the RAF in excess of £500 million per year.

An exercise by the Company has indicated that, typically, a Rolls-Royce military engine undergoes an unscheduled maintenance action every three minutes. The average "hands on" time for these actions is 20 hours. This however includes major activities such as engine removal and repair for FOD (foreign object damage). It has also been estimated that some 30% of a fast jet fleet is not available at any one time.

All of these have an indirect, if not direct, impact on aircraft operations and effectiveness.

The Company is also fully aware of its responsibilities with regards to safety. Sometimes quite small and apparently innocuous shortcomings can lead to spectacular failures. Examples of this include the space shuttle Challenger with its inadequate seal design; the Turkish Airlines DC10 crash near Paris when the cargo door came open; and the Ariane accident caused by software validation problems. Closer to home for engine manufacturers is the Sioux City accident when a DC10 was lost due to a small, almost invisible, imperfection in the fan disc of the centre engine.

A major driver towards greater reliability is the greater use of ETOPS (Extended range Twin OPerationS) for civil wide-bodied twinjets where this regulation has steadily been increased from 60 minutes to 180 minutes. This allows aircraft to fly for up to 3 hours on only one engine.

Rolls-Royce also finds itself increasingly involved in contracts where the engines are leased by operators on a "power by the hour" basis. These operate in a similar way to renting a car and paying for it on a daily and/or mileage basis.

Rolls-Royce has also been involved in several programmes to improve reliability and maintainability (R&M) such as the USAF's R&M 2000, where the aim is to double reliability and halve the maintenance hours. The RR Aerospace Group is currently engaged with other UK companies in a collaborative programme to improve R&M - the Ultra Reliable Aircraft project.

The company also finds itself being increasingly required to meet increasingly stringent contractual R&M requirements for both military and civil projects, as well as the well-established civil certification airworthiness requirements of several different authorities.

Reliability Methodology.

It is with this in mind that RR recognises that reliability is not an isolated or optional extra, an afterthought. Neither is it the province solely of "experts", nor is it the inevitable consequence of "good" design. Rather, that reliability is no accident. It must be recognised from the very start of a project and addressed all the way through

Paper presented at the RTO AVT Symposium on "Design Principles and Methods for Aircraft Gas Turbine Engines", held in Toulouse, France, 11-15 May 1998, and published in RTO MP-8.

its life. It is also the result of good engineering incorporating the best of practices and procedures, especially during both the design and the manufacturing processes.

With regards the mathematical and statistical side of reliability, there are two schools of thought. Firstly that it is common sense with mathematical aids, or, secondly, it is the reverse. The Company recognises both, but generally prefers the former. As part of the numerical aspects of reliability, the company uses such tools as Weibull Analysis, Bayesian statistics and Monte Carlo.

It is also important that everyone concerned, either directly or indirectly with a project recognises that they can influence the reliability of that project. As a result reliability can be influenced by the many, and often varied decisions that are made throughout the whole life cycle of a project, even when it has been in service for many years. A well-engineered design, well made is not the end of the story.

Reliability is a subject that is often not understood very well and is often inadequately specified in a variety of ways. Dictionaries for example deal with abstract qualities and concepts, eg. Goodness, honesty, integrity. Generally, **Reliability** can be defined as " the ability of a product not to break down when in operation. Even this, though is inadequate.

RR believes, along with many others, that it is important that any definition of

Reliability contains four specific criteria. These are that the product, whether aircraft, line replacement unit (LRU), engine, module or component will:

- perform a required function,
- under specified conditions (environment, use, etc.),
- without failure
- for a specified period of time.

In addition, it is also important that the definition of failure is clear and unambiguous. Here there are two main criteria:

- a deviation beyond the limits of acceptability, or

- a cessation of operation (functional failure).

Either of these can cause an inability to accomplish the intended function.

Reliability is a characteristic that can impact and have an influence upon a number of other characteristics. These include, but are not necessarily limited to:

- safety,
- maintainability,
- cost of ownership (life cycle costs),
- availability,
- mission reliability.

Unreliable equipment can, and does, lead to safety critical situations due to their frequency of occurrence. These can result in death or a loss of the system, ie. aircraft. Every effort is therefore made to eliminate potentially safety critical failure modes and their effects. If this cannot be done the probability of occurrence is made acceptably small by stringently controlling the whole design and manufacturing process. This, usually makes for a safer, but more expensive, product.

Similarly, maintainability costs, and the cost of ownership can be reduced by addressing those aspects that most frequently give rise to unscheduled maintenance action or require frequent, scheduled maintenance.

More reliable equipment also means that more aircraft are available as and when required. This means that fewer aircraft need to be purchased or deployed to undertake a given commitment.

In addition, more reliable equipment also means that once deployed there is a greater probability that the mission will be completed successfully.

It can thus be seen that reliable equipment is essential if a minimum sized fleet of aircraft is to be operated in the most effective and profitable manner.

Reliability Approach.

There are two essential approaches to producing reliable products. Reliability can either be "screened" in, or it can be "built" in.

In the former, the product is designed, built and tested. During the test phase when a failure occurs and, if it is considered to be unacceptable, a redesign is undertaken of that particular feature which caused the failure, the product modified, and testing continued until the product appears to reach the level of reliability sought. This approach, which is iterative, is expensive, time consuming and often ineffective.

The second approach, which views reliability as an investment, is far more effective, quicker and less costly. It involves defining all the design parameters required, including safety, reliability and maintainability, right at the start of the

programme. If this cannot be achieved, then it must be done at the earliest possible opportunity. Simply, the sooner the better. These parameters, typically, can include for instance mean times between unscheduled engine maintenance actions, engine removal rates (scheduled and unscheduled), and maintenance (failure) free operating periods.

As the design is evolved and finalised, it is continuously analysed and modelled using various tools and methodologies, such as Failure Mode, Effects and Criticality Analysis (FMECA) and Fault Tree Analysis

(FTA), to ensure that the specified reliability parameters are likely to be met when the product enters service. The design, which must be as close to the intended production standard as possible, is then tested and validated against the various specified design parameters. Finally, it is verified that the design will indeed perform as specified, and the product certified by the civil authorities or given technical approval by the military authorities concerned.

It is worth noting that the Rolls-Royce Aerospace approach to the design and manufacture engines is essentially the same whether a civil or military engine is concerned, or whatever the number of engines the aircraft application has.

From a safety point of view, there is only one real distinction. For multiple-engined aircraft, ie. two or more engines, the objective is continued safe flight and landing. For single-engined aircraft the objective is a stable ejection platform to allow the aircrew to abandon the aircraft safely. Apart from that the engineering approaches, both design and manufacturing methods and processes, are essentially the same.

Major reliability, safety and maintainability, issues addressed by RR Aerospace include, but are not limited to:

- in flight shut down rates,
- unscheduled maintenance action rates
- unscheduled engine removal rates
- mission abort rates,
- engine caused aircraft attrition (loss) rates,
- overspeed protection, especially turbines,
- loss of containment, especially discs and blades,
- fires - fuel, oil and titanium.

In addressing and achieving these there are two essential, and key factors that have the greatest influence upon reliability, and hence the other parameters. These are that:

- the design must be as right as is feasibly possible from the very start, and continued throughout the whole life of the programme, and

- the manufacturing process must be to as high and consistent a standard as economically possible, whilst meeting the desired design intent.

These two paramount factors form the basis of the RR Aerospace design methodology. Experience and research, show that there is a number of best practices that when incorporated in a programme, can, and will lead to a more reliable product being produced.

The Design Process.

These best practices, which are incorporated in the RR aerospace propulsion system definition (design) process, include, but again are not limited to the following. This definition process is shown in pictorial form in Figure 1.

- Specification of requirements, including reliability, eg. Mean Time Between Failures (MTBF) and/or maintenance Free Operating period (MFOP). This should be done as an input to STAGE 1: Preliminary Concept Definition, and can be at whole engine, module, assembly or component level.
- As part of the preparation for STAGE 2: Full Concept definition, the Reliability Programme Plan is formulated, a preliminary Failure Mode and Effects Analysis (FMEA) prepared, and any reliability modelling and/or predictions of the envisaged product undertaken.

- Following Stage 2, a series of design reviews is held, a detailed FMECA is prepared, plus, if required, a FTA, and all designs are "bought off" to ensure that the manufacturing process can deliver products that meet the design intent. In addition, the product is adequately tested and validated to ensure that the original specification requirements are met. This testing, can, and often does, include reliability growth testing, eg. Accelerated Simulated Mission Endurance Testing (ASMET).

  Where it is deemed appropriate, stress screening or "burn-in" is undertaken. New methods such as Highly Accelerated Life Testing (HALT) and Highly Accelerated Stress Screening (HASS) are also being evaluated. Where appropriate airworthiness issues such as bird and water ingestion, in addition to fan blade release testing, etc. is undertaken. A rigorous flight test programme is also operated. Alongside the engine bench and flight test programmes, and often preceding them, are extensive technology demonstration and rig testing programmes.

  As part of this activity a rigorous Failure Reporting, Analysis and Corrective Action System (FRACAS) is operated, and a reliability "lessons learnt" database established.

- Finally, prior to STAGE 3: Product Realisation being achieved, the whole engine, module, assembly or component is "standardised". This is the process whereby the technical, engineering case is presented to substantiate that the design intent has been achieved.

- At this point, and not before, the civil Certification or military Approval process is commenced, and the product released for full production and entry into service.

- Following entry into service a FRACAS is again operated and the reliability of the product monitored.

- This experience is then fed back in the form once again of a "lessons learnt" database for use on future projects.

The Design Approach.

With regards specifically to the design approach, it is important that mistakes made in the past are avoided. These are costly, time consuming, and can be embarrassing. This avoidance of past mistakes is where the operation of a good, effective and user-friendly database comes into its own. It must be accessible to all, and also have an effective read-across to all current and future projects.

It is important that all design proposals are rigorously evaluated by undertaking FMECAs, FTAs, reliability modelling and predictions, etc.

When the design details have been finalised, and possibly even earlier, before any hardware is produced, it is important that each feature of the design is fully assessed for all the possible risks involved. These should not only involve technical and commercial risks in achieving the design intent, but also safety and manufacturing risks. The sooner any undesirable feature is identified, the easier and cheaper it is to effect any corrective actions, whether these are to change the design or manufacturing process.

Even when the design has been finalised, the manufacturing aspects of creating the product must not be overlooked. You can have the finest design in the world, but if it is badly made the whole process can be undermined. It is also considered that inadequate maintainability activities and abuse of the equipment can also have a significant effect upon the reliability of a product.

When producing a design, it should be remembered that the design intent not only includes producing the actual design and how it is to be made, but also flown and maintained. Such aspects should not be overlooked.

The Manufacturing Approach.

It is therefore important that components are capable of being produced to the highest, practical and economic standard within the capabilities of the manufacturing process.

It is generally recognised that components which are difficult to make usually have the highest rate of non-conformance, resulting in high scrap rates. These components also tend to have high problem rates in service due to manufacturing variations that have gone undetected, thereby resulting in premature failures.

Earlier, the manufacturing "buy off" of designs was mentioned. This is where, before the design is released for manufacture, whether development or production, the manufacturing people agree that they can produce components that will consistently meet the intent of the design in a timely and cost effective manner.

Experience has shown that producing designs and hardware to "development" standards is costly, time-consuming and frequently leads to problems. It is now the policy of RR Aerospace that all designs, whenever possible and feasible, are produced with production in mind, and that all hardware is manufactured in production facilities to production processes.

Conclusion.

Designing for reliability, safety, maintainability, and low life cycle costs is something that must be done at the earliest opportunity in the design process. It is essential that this approach be continued throughout the whole life cycle of the project.

To summarise, and it may seem trite to say it, but:

- DESIGN IT RIGHT!
- MAKE IT RIGHT!
- MAINTAIN IT RIGHT!
- FLY IT RIGHT!

If that is done, especially the first two, then you have every chance of producing reliable, safe and cost effective products.

FIGURE 1.

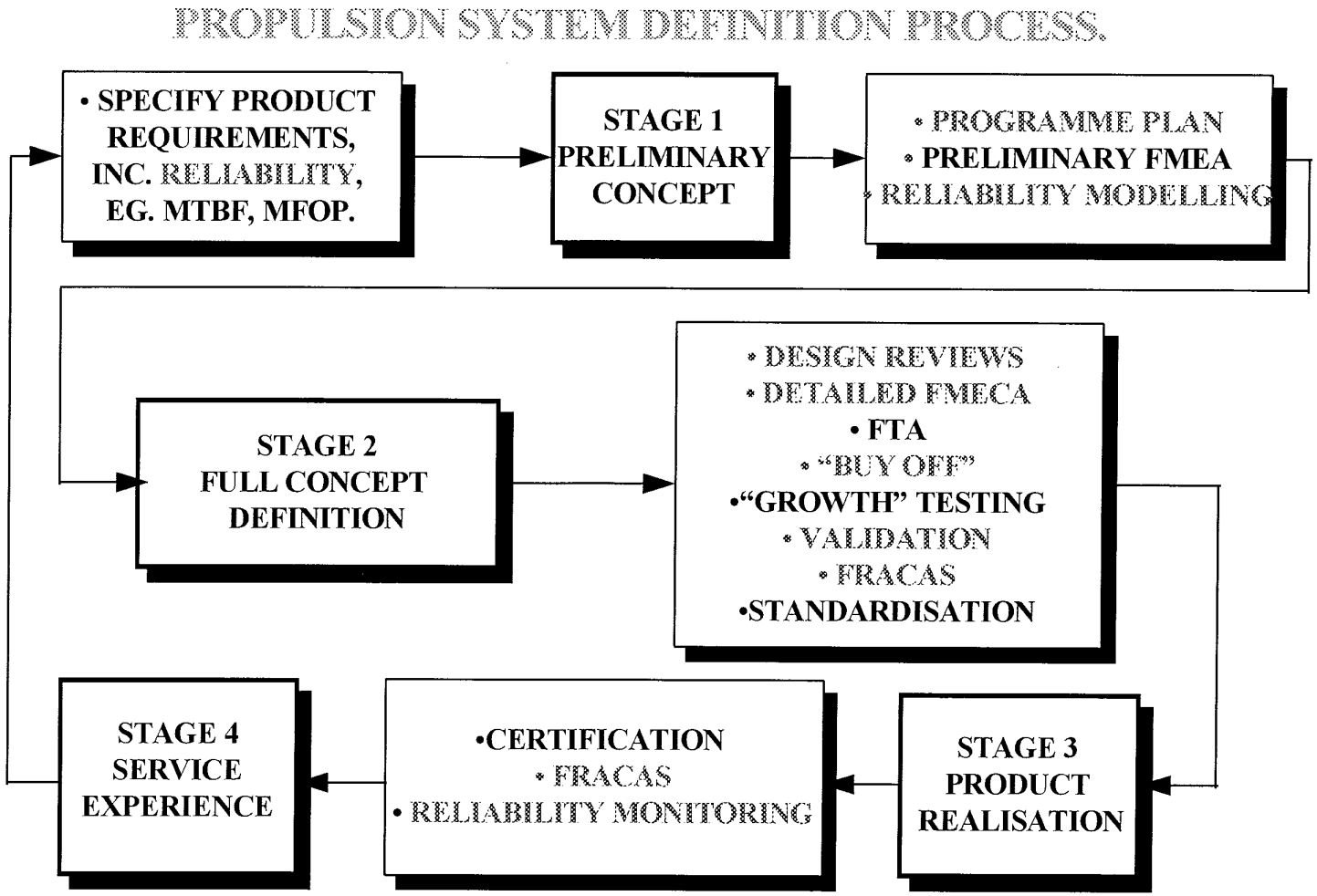
PROPULSION SYSTEM DEFINITION PROCESS.
• SPECIFY PRODUCT REQUIREMENTS, INC. RELIABILITY, EG. MTBF, MFOP.
STAGE 1 PRELIMINARY CONCEPT
• PROGRAMME PLAN
• PRELIMINARY FMEA
• RELIABILITY MODELLING
STAGE 2 FULL CONCEPT DEFINITION
• DESIGN REVIEWS
• DETAILED FMECA
• FTA
• "BUY OFF"
•"GROWTH" TESTING
• VALIDATION
• FRACAS
•STANDARDISATION
STAGE 3 PRODUCT REALISATION
•CERTIFICATION
• FRACAS
• RELIABILITY MONITORING
STAGE 4 SERVICE EXPERIENCE

The PW100 Engine: 20 Years of Gas Turbine Technology Evolution

E. Hosking, D. P. Kenny, R. I. McCormick
S. H. Moustapha, P. Sampath, A. A. Smailys

Pratt & Whitney Canada Inc.,
1000 Marie Victorin
Longueuil, Quebec J4G 1A1
Canada

Summary

The PW100 three-spool turboprop engine family has been designed for the commuter, utility and executive aircraft markets. The first PW100 engine, with a thermal power rating of 1780 Kw, entered service in the mid-1980s. Growth through increased pressure ratio and turbine inlet temperature as well as application of new technology has allowed the power of the engine to reach 4980 Kw for the latest PW150. This paper will highlight examples of this technical evolution covering the cold and hot end, gearbox, installation and control systems and the application of the latest three-dimensional aerodynamic and stress analysis to the design of the different components.

Introduction

The first PW100 entered service in 1985. Since then the family has grown to over thirty models and has accumulated in excess of forty three million hours of operational experience. The principle application of the engine has been in the regional aircraft market although the engine has also been modified to suit a water-bomber, industrial applications and it has been adapted to super charge a piston engine in a high altitude aircraft. A few statistics on the engine are presented in Figure 1. Installations include the DeHavilland Dash 8 series of regional aircraft, Avions de Transport Regional ATR 42 and ATR 72 series of regional aircraft, the Dornier Do328 and Embraer's EMB 120 regional aircraft.

Engine Delivered	4,325
Certified aircraft applications	12
Different operators	249
Regional operators	203
Aircraft	1,827
Countries of operation	88
Fleet operating time (hrs)	43,112,700
High time engine (hrs)	29,260
Highest time between overhaul	12,000

Fig. 1 PW100 engine statistics

The general configuration has been constant throughout the life of the engine program. It features a three shaft layout comprising the high pressure rotor, the low pressure rotor and the power turbine rotor. Growth through evolution and application of technology has allowed the power of the engine to grow from 1780 Kw to 4980 Kw (Figure 2).

Since inception, the engines have been controlled electronically. The earlier models incorporate supervisory electronic systems with hydro-mechanical back-up. Later versions have progressed from full authority electronic systems with hydro-mechanical back-up to a full authority, dual channel electronic control on the PW150 engine. The electronic control supports multiple rating structures in some variants.

Engine Model	PW120	PW127	PW150
Year (Program Launch)	1979	1990	1995
Weight (Kg)	417	481	690
Thermal Power (Kw)	1782	2457	4981
Power/Weight (Kw/Kg)	4.27	5.11	7.22
Max. gearbox power (Kw)	1491	2050	3781
ESFC (Kg/Kw/hr)	.286	.273	.255
Turbine Inlet Temp. (°C)	X	X+58°	X+187°
Compressor Flow Kg/sec	6.70	8.49	14.44
Pressure ratio	12.14	15.77	17.97
Control	Supervisory digital electronic control with mechanical back up	Full authority digital electronic control with hydro mechanical back up	Full authority digital electronic dual channel control
Initial Installation	DeHavilland Dash8-100	ATR-72	Bombardier Dash8-400

Fig. 2 Evolution of the PW100 engine

PW120 to PW127 Power Growth

In order to achieve power growth within the same engine size as the original PW100, advancements have been made in all relevant engineering specialist technologies including compressor and turbine aerodynamics, materials and structural analysis of rotating components and of the static structure of the whole engine. Increased cycle temperature has been made possible, in particular, by better nickel-based alloys. This combined with a 50% increase in the engine mass flow has enabled the power growth (Figure 3)

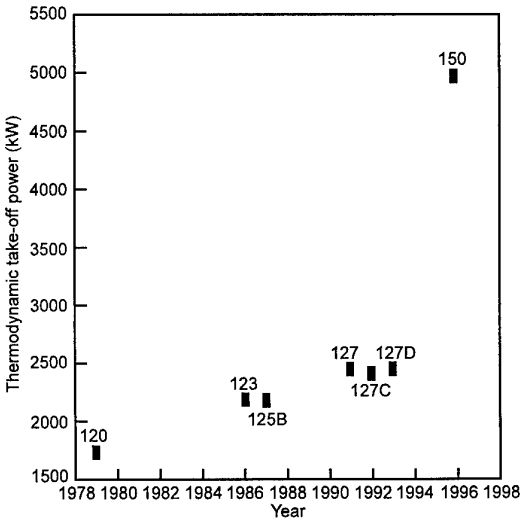

Fig. 3 PW100 power growth

Paper presented at the RTO AVT Symposium on "Design Principles and Methods for Aircraft Gas Turbine Engines", held in Toulouse, France, 11-15 May 1998, and published in RTO MP-8.

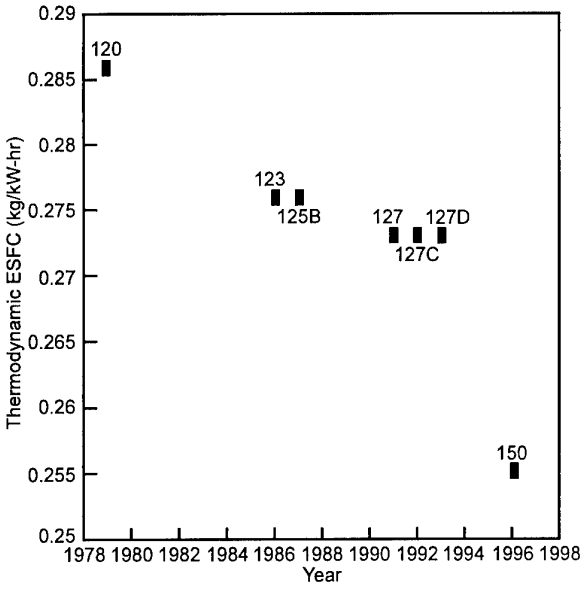

Fig. 4 PW100 fuel comsumption evolution

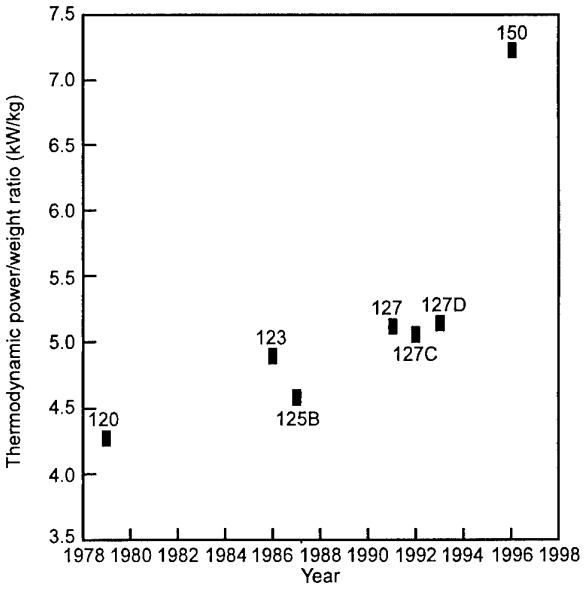

Fig. 5 PW100 specific power evolution

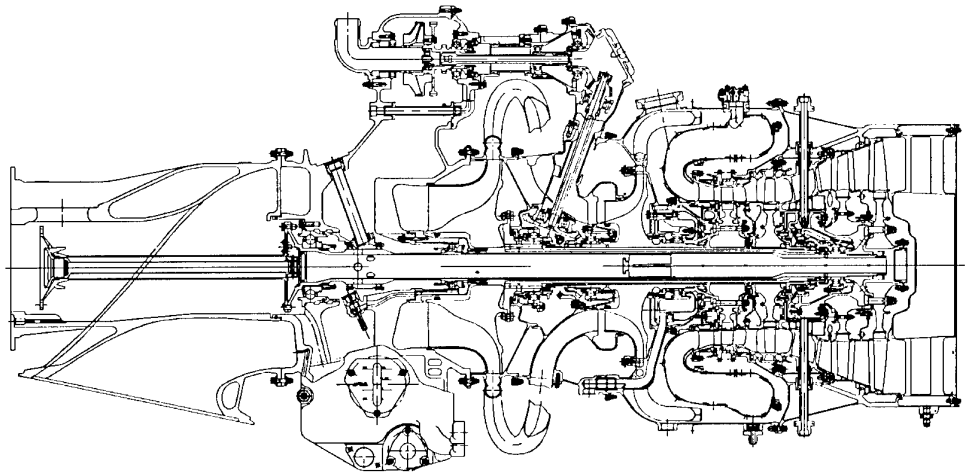

Fig. 6 PW120 gas turbine

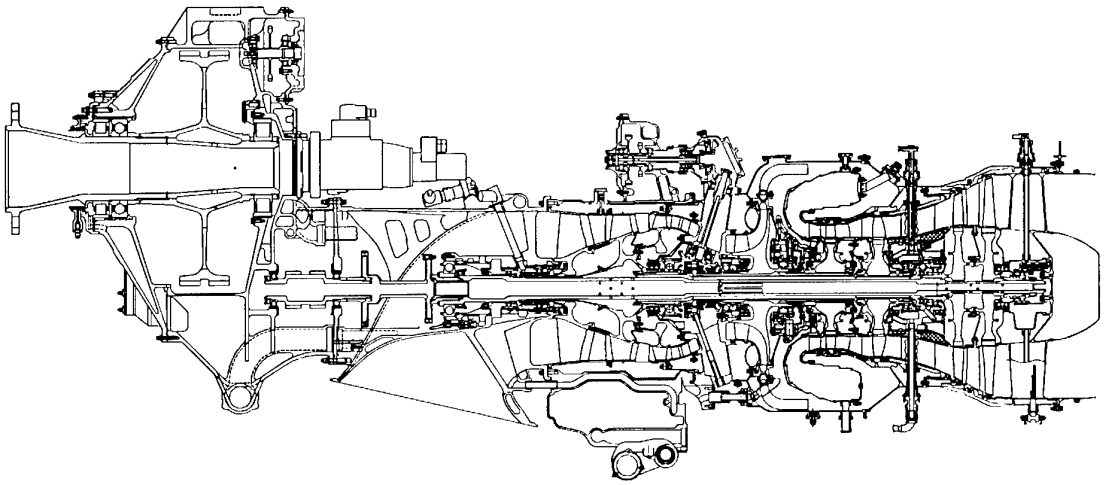

Fig. 7 PW150 gas turbine

while specific fuel consumption improvement (Figure 4) has resulted from increased cycle pressure ratio and improved component efficiencies. Increasing mass flow and pressure ratio have resulted in higher relative Mach numbers along with higher blade loading. Power to weight ratios have improved while maintaining high durability (Figure 5).

The high pressure rotor carries a centrifugal compressor and a single stage cooled turbine (Figure 6). The low pressure rotor carries a centrifugal compressor and a single stage turbine. In the low power versions of the engine this turbine is completely uncooled. In the high power variants the turbine vane is cooled. The higher power variants require some form of shroud bleed on the compressor and an electronically controlled handling bleed valve. The power turbine rotor features a two stage shrouded turbine which delivers power to a reduction gearbox featuring two stages of speed reduction. The reduction ratio varies from 15.4:1 to 17.2:1 depending on the model.

PW127 to PW150 Power Growth

The year 1995 saw the start of the PW150 engine model development with a goal to certify the engine in mid 1998. This engine rated at nearly 5000 Kw thermally (Figure 2) uses the general layout of the PW100 series engines. Again a three spool configuration has been used with the following significant configuration changes (Figure 7): the low pressure compressor features three axial stages, and the low pressure turbine vane and blade are cooled. Overall the engine is much larger than the PW100 series accommodating a 75% increase in mass flow through the gas path while delivering 80% more mechanical power through an uprated gearbox. A 130 degree C increase in turbine inlet temperature has been realized through the use of advanced alloys and advanced cooling technology in the combustor and the turbines. To accommodate the length increase while maintaining acceptable dynamic characteristics, the power turbine shaft has been fitted with an additional bearing supporting the rear of the power turbine assembly. The engine also features a two channel FADEC control without mechanical back-up.

Compressor Technology

The PW100 compressor has evolved through twenty years of research and development. The original arrangement of two contra-rotating centrifugal compressor stages on concentric shafts has grown to a family of four different low-pressure stages, all with a common high-pressure stage. The higher specific speed demands of the PW150 engine have recently lead to the introduction of a three stage axial low-pressure compressor, in combination with a centrifugal high-pressure compressor stage. All PW100 models use pipe diffuser, first introduced on PT6 engines, because of its demonstrated superior performance and compactness (Kenny, 1973). The fundamental qualities of high performance, ruggedness, and reliability with long-life critical parts, have been maintained on all models.

Compressor performance has been developed by testing in a gas generator facility, in which the power turbine is replaced by an adjustable valve to obtain individual stage maps. Compressor intake performance has also been verified in an intake and exhaust facility, which permits detailed instrumentation to be installed.

Aerodynamic analysis codes have advanced dramatically in twenty years. Beginning with blade-to-blade Euler analyses linked to a robust finite-element throughflow code, and progressing via a three-dimensional Euler program, today a three-dimensional viscous code (Habashi et al, 1992) is in routine use in the design of centrifugal impellers and diffusers.

The air induction system of the PW100 turboprop family of engines is characterized by an S-shaped intake providing a transition from a quasi-rectangular cross-section at the nacelle inlet to an annular cross-section at the entry to the low pressure compressor (Figure 8). Such a duct is considered ideal for high ram recov-

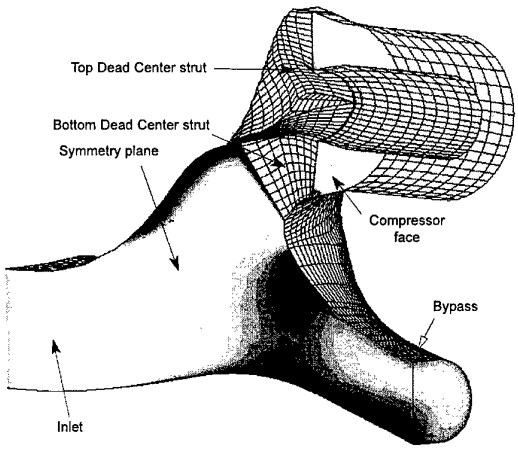

Fig. 8 PW100 inlet system

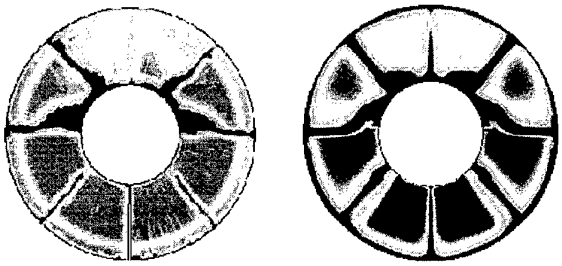

Fig. 9 PW150 intake total pressure profiles

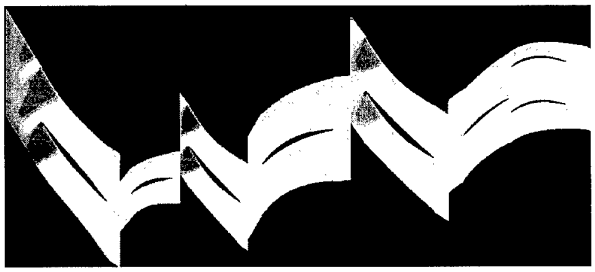

Fig. 10 3D multistage viscous analysis for PW150 low pressure compressor

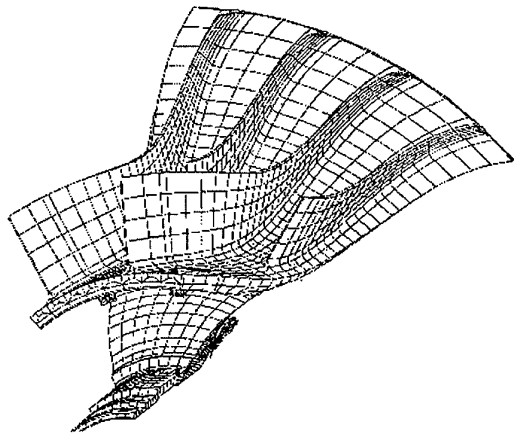

Fig. 11 3D finite element model of PW127 impeller

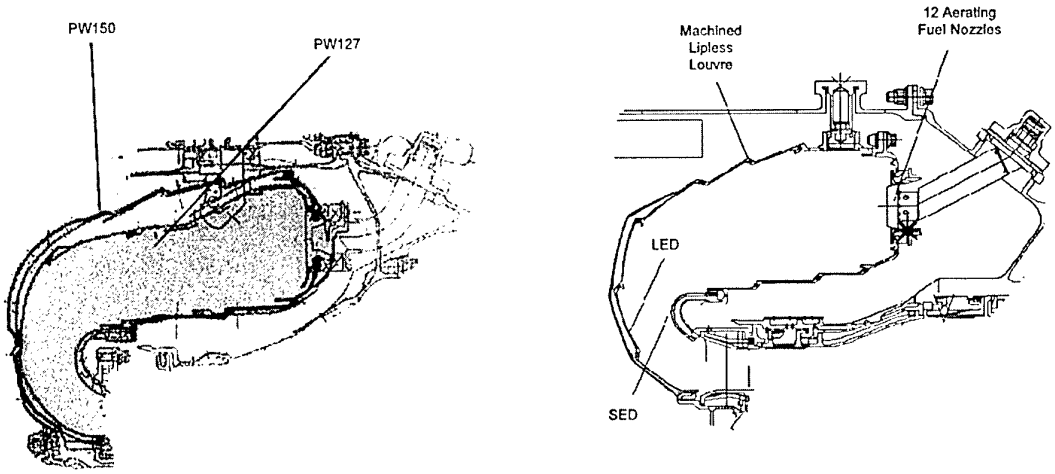

Fig. 12 PW150 combustor compared to PW127

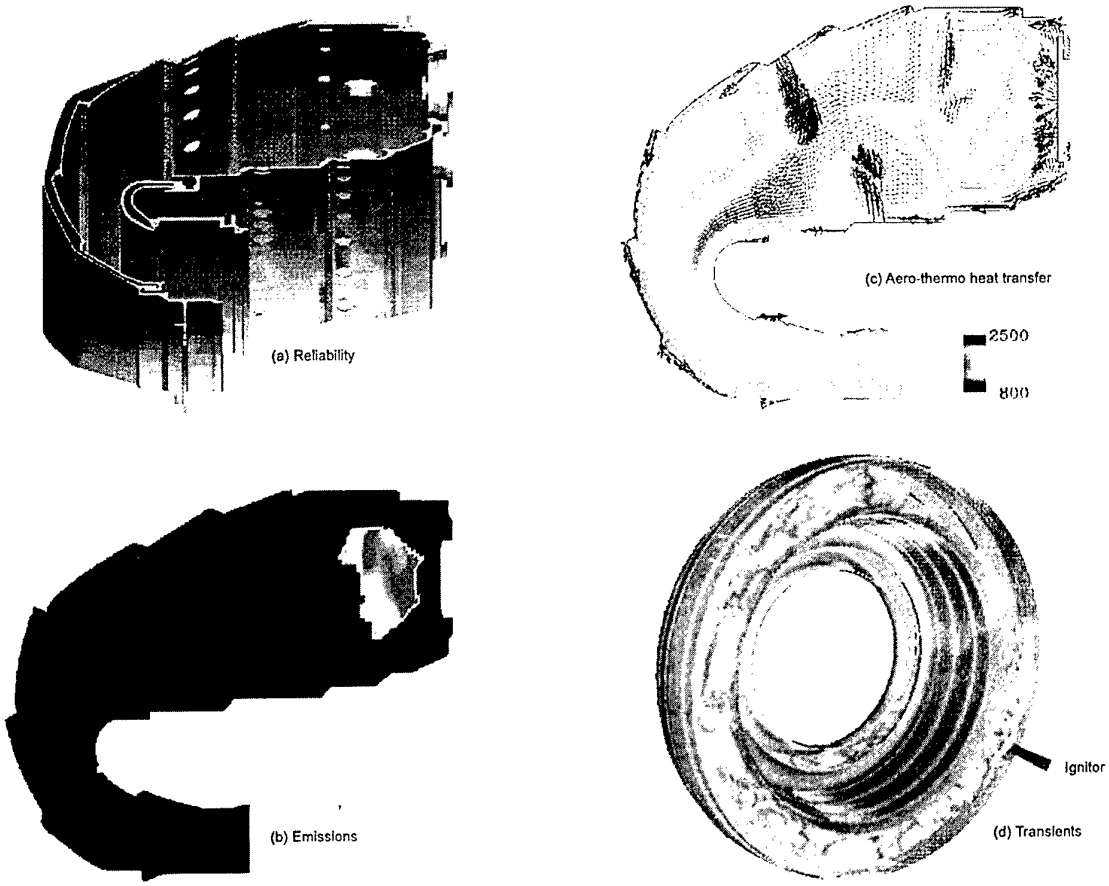

Fig. 13 PW150 combustor numerical modelling

ery and, coupled with a bypassing portion, for good ice and foreign object damage protection. Since its inception in early PW100 applications, the inlet system concept has undergone some refinements to improve performance and separation efficiency. Ice protection of the customer supplied nacelle inlet is accomplished using either pneumatic boots or electrical de-icing systems. Both have been successfully implemented in revenue service. Viscous 3D code has been used recently in the design of the intake for the PW150 compressor, with excellent results as shown in Figure 9 (Robichaud et al., 1997). The design of the axial low-pressure compressor of the PW150 engine has also benefitted from the application of a three-dimensional multi-stage Navier-Stokes solver (Rhie et al., 1995), as illustrated in Figure 10.

On early PW100 engines, rotating stall produced a loud, low-frequency tone accompanied by a large amount of broadband

noise. The combination of these could, in some instances, have resulted in aircraft noise exceeding regulatory limits. Since the low-frequency tone could not be effectively attenuated by sound treatment, it was eliminated by modifying the low-pressure impeller design and the bleed valve schedule. Building on the experience from previous models, the PW150 low pressure compressor incorporates features that eliminated rotating stall from the outset.

Structural analysis of the compressor is conducted with three-dimensional finite element codes as shown in Figure 11, using temperature distributions obtained from both steady-state and transient thermal analyses. The complete compressor assembly is analyzed over the mission cycle to study the changes in tip clearances with changes in centrifugal and thermal loads. Compressor geometry is optimized to give the best Low Cycle Fatigue (LCF) life, while satisfying often-conflicting dynamic, aerodynamic, and weight requirements. The predicted LCF life is substantiated by thorough spin-pit testing, while rotor forgings are continuously monitored for the required quality. This process ensures the reliability of published LCF lives.

State-of-the-art technology is used to manufacture the compressor rotors. The design and manufacture of rotors has been integrated to allow the flank of a conical cutter to finish a blade surface in one pass (Wu, 1994). The compressor of the PW150 engine incorporates such flank-milled Integrally Bladed Rotors to improve LCF life and reduce part count. Rotor blades are extrude-honed after machining to improve surface texture, and critical regions are peened to enhance LCF life.

Combustion Technology

In recent years, major strides have been made in making combustors small, to ensure compact installation in engines. The combustor for the PW150 represents a very compact design, with the overall size only slightly larger than the PW100, yet capable of more than twice the power (Figure 12). This higher loading has been facilitated by the use of advanced numerical tools, which enable more efficient use of combustor space. Lessons learned from PW100 have been applied to this design. The demands from the combustion system include combustion efficiencies exceeding 99.5% over most of the operating range, exit conditions matching turbine requirements, cold starts down to -45°C, low exhaust smoke, good stability and relight characteristics. With the use of highly sophisticated numerical simulation methods, such as steady state and unsteady CFD, the performance of the PW150 was optimized without resorting to any rig testing, a first in the entire industry (Figure 13). Combustor exit profiles were optimized by 3D viscous methods and the hardware has shown performance consistant with the predicted temperature profiles. The PW150 was designed with 12 aerating fuel nozzles, two fewer than in the PW100 family. To ensure good integration with the combustor flow fields, the fuel nozzle design was undertaken in house , a first at P&WC. These nozzles have fuel flow passages exceeding 0.46 mm thus minimizing coke formation, and the atomization characteristics meet the requirements for good combustion efficiency as well as low smoke.

The combustor has been designed for 10000 hour field life. Since the combustor exit temperatures are significantly higher than that of the top model of the PW100 family, advanced wall cooling methods have been employed. These include double pass (impingement backside convection with front side film) cooling for the large entry duct, impingement film on the skin for the small entry duct and machined louvres elsewhere in the combustor. The machined louvres have eliminated the hot side filming skirts (like in PW100) which are known to buckle. Uniform wall films are produced by use of multi-layored rows of cooling jets. In addition, thermal barrier coating has been incorporated throughout the combustor. Testing to date has shown promising results with this design. All the performance goals have been met and the engine is demonstrating state-of-the art emission levels consistant with an environmentally friendly turbomachine (Sampath and Eatock, 1993). In addition, work is underway on the industrial derivative of the PW150-ST30 which will eventually have dry low emission technology for both liquid and gaseous fuels.

Turbine Technology

Figure 14 shows the improvement in the turbine efficiency of the PW100 models over the last 20 years. Compressor turbine efficiencies have, on average, increased despite the increased cooling flow, requirements for higher turbine temperatures and higher aerofoil Mach number. The PW150 design used a full hot end 3D multistage viscous simulation compared with the component or stage analyses performed on early PW100s. These codes, coupled with research, have allowed, for example, the optimization of vane end wall contouring (Moustapha and Williamson, 1986) and aerofoil leans that have reduced secondary flow vortical strength and radial pressure gradients. This has also resulted in better integration with downstream blade rows. Blade tip geometries and loadings have been analyzed in recent designs with 3D viscous solvers to optimize the tip leakage loss and downstream incidence effects on vanes. Research on optimal aerofoil loading (Moustapha et al., 1987) has helped increase blade loading coefficients throughout the compressor turbines so reduced aerofoil counts are achieved, with little or no efficiency penalties. Cooled aerofoils in the more recent engines have been optimized with an integrated approach. Aerodynamics and durability considerations have resulted in more optimal vane leading edge shapes for heat load and reduced cooling flows and losses. The feasibility of reducing aerofoil unsteadiness, through aerofoil spacing and/or clocking, was for the first time introduced in the design process.

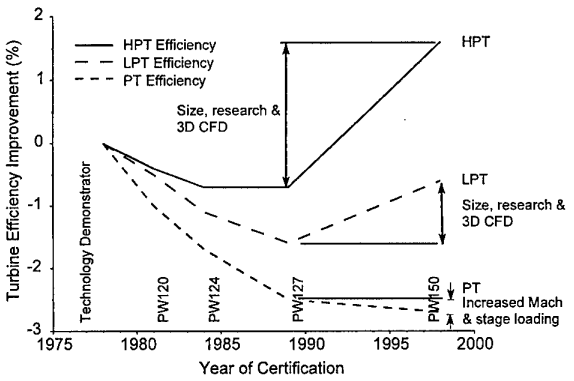

Fig. 14 Evolution of PW100 turbine efficiency

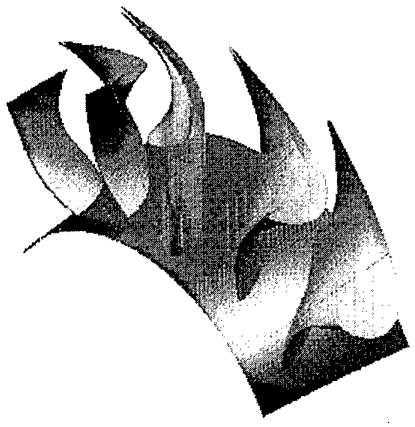

Fig. 15 PW150 inter-turbine vane

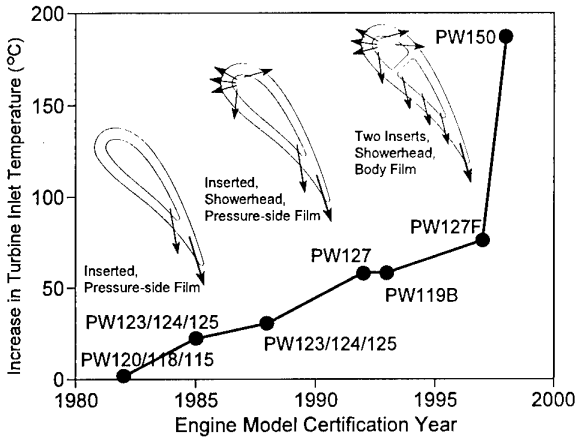

Fig. 16 Evolution of PW100 turbine inlet temperature

The Inter-Turbine-Duct has evolved from a 3 thick/3 thin struts uncooled configuration to the present strutless duct with an Inter-Turbine-Vane (ITV), (Figure 15), benefitting from full 3D viscous analyses. A special version of the cooling scheme was designed for the two thick vanes which must accommodate bearing oil flow transfer tubes. Minimizing the performance loss of this low aspect ratio aerofoil allowed for the reduction in parts count, cost and weight .

Cooling technology (Arora and Abdel-Messeh, 1985, 1990) has been directed at improved cooling effectiveness to cater for increased turbine inlet temperatures. On early engine models, PW115/118/120, the High Pressure Turbine (HPT) vane is segmented and uses an internal cooling scheme with an insert (Figure 16). The early HPT blade design uses an internal multi-pass scheme and directionally solidified material. The Low Pressure Turbine (LPT) vane is uncooled. With the introduction of the PW123/124/125 series engine models, showerhead cooling was added to the HPT vane to cater for an increase in turbine inlet temperature. The HPT blade was re-designed to improve the cooling effectiveness and the material was changed to advanced single crystal. The LPT vane was changed to an internally cooled multi-pass design. A further increase in turbine inlet temperature has been accomplished in the PW127 series of engine models through development.

The PW150 engine operates at significantly higher turbine inlet temperatures than the PW127, and incorporates more advanced cooling technology to provide this higher temperature capability. The HPT vane is segmented and has a purpose-designed showerhead and body film cooling scheme. The HPT blade uses advanced single crystal alloy and has a more advanced internal cooling scheme with showerhead, body and tip film cooling. The LPT vane is also segmented and uses an internal multi-pass cooling scheme with some film cooling. The LPT blade is cooled and uses advanced single crystal and an internal, multi-pass cooling scheme.

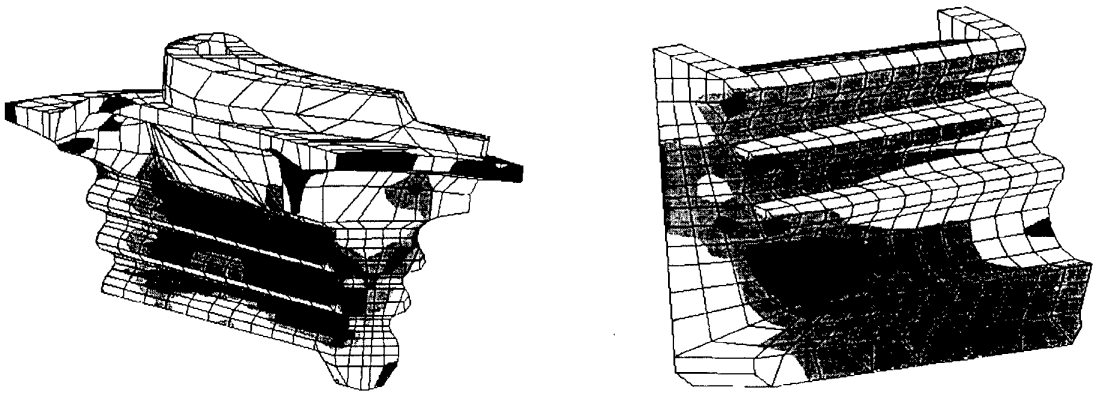

Blade fixing

Disc fixing

Fig. 17 PW150 low pressure turbine 3D stress distribution

The power turbine (PT) efficiencies have not shown the general improvement expected with the advancement of years and technology (Figure 14). This can however be explained by the mass flow increase through basically the same hot end and stage loading increases. The PW150 PT aerofoils have elliptic leading edges to increase incidence tolerance at off-design conditions (Benner et al., 1997).

The PW100 exhaust system is of the axial type. Turbomachinery exhaust gases are deswirled through an exhaust cascade and are then channeled through an airframe supplied exhaust duct to expel the exhaust gas from the engine. The gases are expelled rearwards to maximize the recovery of thrust and avoid potential impingement of the exhaust plume on aircraft structures. The exhaust gases are also used to drive an ejector for nacelle ventilation. The design of the PW150 exhaust system was facilitated using full 3D viscous analyses, which allowed for the easier integration of thick struts (for oil tubes) and thin struts. The estimated duct loss is less than any previous PW100, even with the increased mass flow of the larger engine.

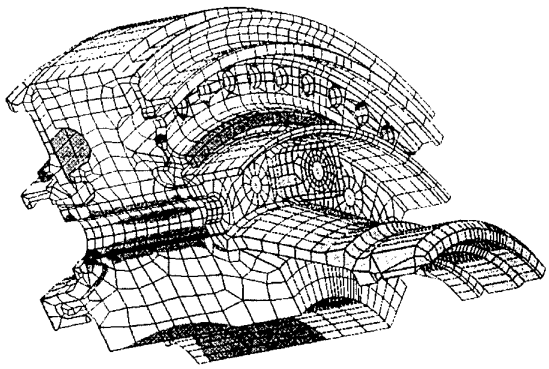

Fig. 18 PW100 high turbine centrifugal stresses

Detailed 2D and 3D stress analyses have been used to optimize the life of the turbine discs and fixings (Figure 17). Transient analyses have been used to determine the correct fits and stresses on the rotor assembly at all engine conditions. The predictions were correlated with heat transfer rig, engine temperature surveys and extensive spin pit rotor tests. The disc attachment profile has been optimized to achieve a high service life and the blade fixing fatigue life has been enhanced by high intensity shot peening of the fir-tree necks. The low pressure turbine was designed for failure sequence by blade release and the power turbine overspeed protection was achieved by airfoil burst. This intrinsically safe overspeed protection design philosophy was validated by extensive high energy spin pit tests and full engine testing. Calibration of 3D tools (Figure 18) permits single pass designs with target speeds reached with an accuracy better than 4%. Cover plate design evolved to low loss aerodynamic profiles while maintaining adequate strength margin. 3D creep effects were successfully analyzed and resolved. 3D dynamic effects can be modeled to permit the design of large blades without dampers.

High pressure turbine tip clearance control and power turbine blade containment were also subjected to sophisticated 3D analysis at the detail design stage, resulting in predicted clearances, materials and thicknesses remaining unchanged following all of the appropriate development and certification testing.

System and Structure Technology

Improvements in air and oil systems have been achieved through research and concept development which have led to great enhancements in analysis capability and to the introduction of improved air/oil system components. The PW150 engine has largely benefited from this evolution.

The use of non-contacting control gap carbon seals on all bearing chambers has reduced by 65% the non usable air thrown overboard through the breather (engine air/oil separator) and has therefore, diminished the amount of heat rejected to the oil. At suitable locations, labyrinth seals have been supplanted by brush seals due to their compactness, their superior sealing performance and their ability to sustain occasional shaft radial excursion. This has contributed to minimize air system consumption and, consequently, to improve engine performance.

In order to minimize oil tank size, a more efficient air/oil separator has been used. The "Retimet" breather has demonstrated a 40-50% reduction in oil consumption relative to a conventional double pass centrifugal breather. Further tank size reduction has been obtained with the introduction of a cyclonic deaerator located at the tank inlet.

To avoid flooding at sub-idle conditions, the PW100 requires two valves : a switching valve and a minimum oil pressure relief valve . These two valves have been eliminated on the PW150. Each bearing cavity has a dedicated scavenge pump which has been sized to create a partial vacuum at sub-idle conditions. Oil is then introduced at first spin without flooding. To minimize scavenge pump sizes, special care has been taken to optimize the bearing cavity pressure balance at sub-idle conditions.

All PW100 models from PW119 to PW150 have a 5 mount configuration with rubber vibration isolators. The five mounts allow for continued safe operation with one mount link failed. The PW118 model has four mounts with a catcher mount to cover any single link failure. For total installed weight reduction and improved noise suppression, the PW150 has a hydraulic torque restraint system replacing the torque tube system of all previous models.

Three dimensional finite element modelling of the structural casings has been applied since the earliest PW100 models. For the PW150, a full engine model (Figure 19), including both static and rotating parts, was made to study mount reactions, carcass deflections and clearance control. Advanced steady state and transient thermal analysis techniques have been applied to all the engine static components. The internally-cooled ITV, which is both an aerodynamic component and a structural load path for two bearing supports, experiences high temperature gradients, but was designed with the appropriate analytical tools to achieve the high service lives required by the commuter market.

Gearbox and Bearing Technology

The PW100 reduction gearbox is a two stage offset design for turboprop applications with reduction ratios varying from 15.4:1 to 17.16:1. The low turbine input speeds combined with these high reduction ratios allow the use of slower larger diameter propellers for quieter operation. The offset design of the gearbox provides easy access to the rear of the propeller shaft for propeller controls. This basic gearbox configuration has been maintained throughout the evolution of the PW100 from the original PW115, rated for 1119 Kw, to the newest PW150 reduction gearbox rated

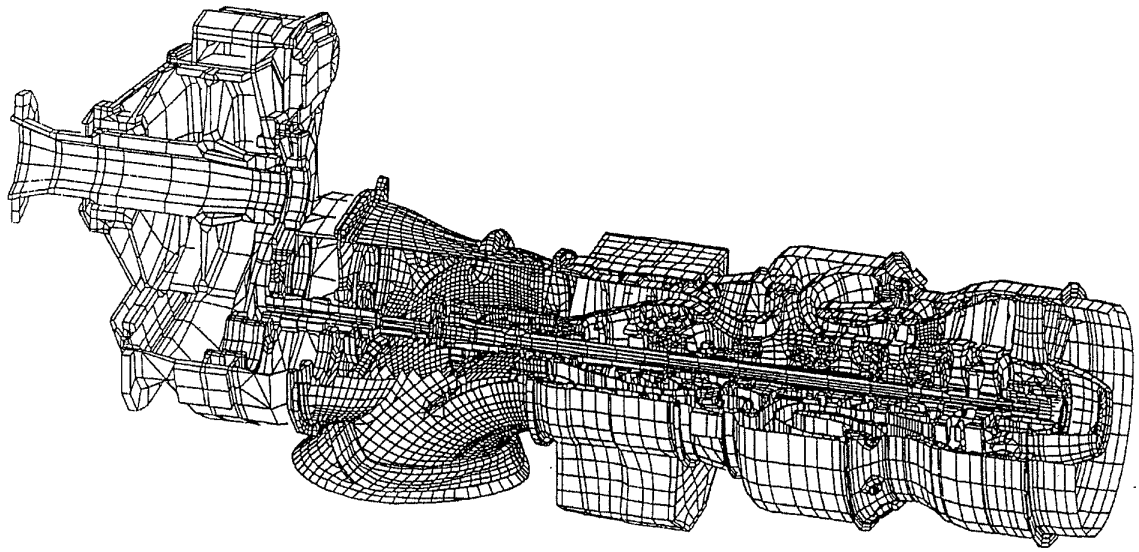

Fig. 19 PW150 full engine finite element model

for 3783 Kw. The development and application of technology to this gearbox design has enabled this growth without a corresponding increase in weight.

The first stage gears of all PW100 gearbox designs incorporate double helical gears for increased capacity and smoother running. The first stage torque from the input pinion is shared between two gears on opposite sides of the pinion. This reduces the loading on each gear mesh and balances the load on the input pinion bearings for increased life and reliability. The use of a double helical gear arrangement with the split torque path means that the torque in the first stage is shared by four gear meshes. The torque is transferred from the first stage to the second stage gearing by means of two layshafts which provide both torsional and lateral flexibility to ensure equalized gear load sharing and accommodating any misalignments. The torsional flexibility of the layshafts also allows them to be used for torque measurement on the large PW100 engine models (PW124 and larger).

The two second stage pinions drive a bullgear mounted directly on the propeller shaft. These are high contact ratio straight spur gears, which means that at least two gear teeth carry the load at any instant in time, to provide high load capacity combined with smooth running.

The gear designs on PW100 gearboxes have benefited from the latest technology in 3D finite element gear tooth contact analysis (FEA), developed in house. The FEA model of the complete geartrain and casing includes details such as tooth profile modifications, crowning, tooth lead errors, manufacturing tolerances and engine distortion effects on each gear mesh (Figure 20 and 21). This detailed analysis is used to optimize the gear design for minimum stress which is compared to gear fatigue rig testing and extensive field experience.

Propellers impose once-per-revolution (1P) aerodynamic loads on the gearbox, which result from non-axisymetric air flow into the propeller, that must be considered in the design of propshafts, bearings, gears and casings. To address this, aircraft and propeller aerodynamic modeling techniques have been developed and calibrated, with flight tests, to predict the air flow into the propeller and resulting loads on the engine (Gates and Smailys, 1989). The 1P load is a cyclic load on the propeller flange and contributes to the loads between the bullgear and propshaft which, if not addressed, can lead to problems. A design method, based on 3D FE contact analysis, has been developed to avoid types of interface problems (Smailys and Brownridge, 1987).

In addition, the thorough characterization of materials and more precise shaft lifing techniques, accounting for HCF/LCF interaction, combined with FEA of loads due to misalignment has resulted in reliable yet lightweight shaft and coupling designs.

The bearings used in PW100 gearboxes and mainshafts are all designed using the latest state-of-the-art techniques. Bearings are designed to minimize skidding, skewing and internal stresses, in addition to achieving life. Extensive field experience has been used to calibrate the bearing lifing methods to ensure their life and reliability.

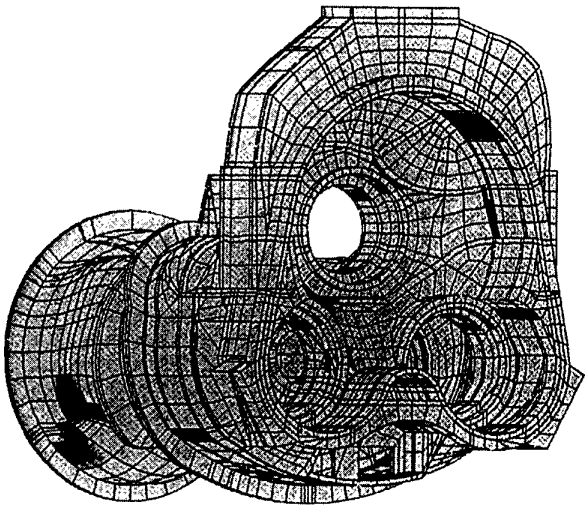

Fig. 20 PW127 reduction gearbox finite element model

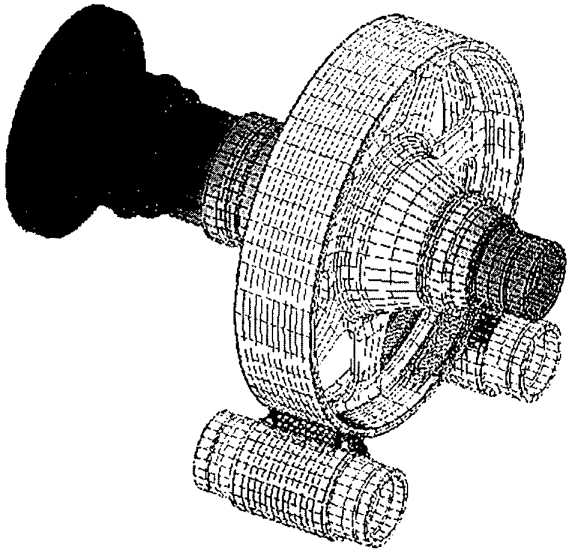

Fig. 21 PW100 gearbox second stage finite element analysis

Control Technology

From the outset of the PW100 program there has been a desire to take advantage of the benefits of electronic control technology to improve the operability of the engines and to reduce the pilot workload. The low power models of the engine incorporate a simple electronic control derived from the JT15-D family of engines. This control comprises an 8 bit processor and 8k bytes of memory. It is configured to act in a supervisory arrangement acting through a torque motor in a hydro-mechanical control capable of providing complete mechanical back-up. Failure of the electronic control results in fuel schedule enrichment during the transition.

Later variants of the engine benefit from a more powerful 16 bit processor and a quadrupling of memory available for control laws and fault accommodation. The underlying mechanical control is a derivative of the PT6 pneumatic DPF-2 control fitted with a stepper motor interface. This allows full authority control in the electronic control mode and full mechanical back-up. Failure of the electronic control results in fixed fuel flow until the manual control is selected by the pilot.

Development of the software is a shared responsibility with Hamilton Standard Division of United Technologies, the supplier of the electronic control. Control laws are defined using a Pictures to Code utility and passed to HSD. Validation of the engine control system including software includes bench, engine and flight testing consistent with industry standards such as DO178B.

As the engine has grown, the demand on the control system has grown to include more sophisticated monitoring of engine parameters, fault accommodation and control of the engine. Early controls were based on the rate of change of high compressor rotor

speed. Later models followed with closed loop on torque and ultimately closed loop on power. Rating algorithms were added to drive bug torque indicators in the cockpit and now some models have multi-rating software to allow customers to buy one engine suited to many variants of the aircraft. Both Arinc 429 and RS 422 data busses are available for communication with the cockpit, electronic prop controls and the ground based diagnostic systems. The latest versions of the electronic control also support field loadable software. To address the bleed requirements of the larger engines, the control modulates the handling bleed valve through a torque motor interface.

The PW150 uses a two channel FADEC to control the engine. As there is no mechanical backup in this control, the architecture has been modified extensively to provide redundant inputs and effectors. The fault accommodation has been extensively modified to use the redundant channel, the redundant effectors and to use redundant inputs or synthesized parameters. The configuration supports the use of Time Limited Dispatch in the event of certain classes of uncorrected system faults.

The FADEC communicates with an engine monitoring unit (EMU) that records engine data for uses such as trend analysis, trouble shooting, event analysis, parameter exceedences and life cycle factor counting. The EMU is the prime interface with ground based diagnostics systems. The EMU also interfaces with cockpit for display of engine parameters in the cockpit.

Conclusion

The PW100 series of engines has become the engine of choice in the regional aircraft sector through the effective application of appropriate technology. The basic layout provided a rugged turbomachine with few rotating components which was relatively easy to control and grow. The application of new technology as it became available provided the means to increase operating temperatures and loads without sacrificing durability. Improved analytical tools have provided the means to increase flow and pressure ratio as well as component efficiencies.

The large number of variants reflect the diversity of applications and the need to satisfy a wide range of customer needs. The three shaft modular layout of the engine has facilitated this diversity in that modules can be combined in many ways and can be upgraded independently.

First engine run of the recent PW150 model was achieved within a year from program launch. PW150 certification will be after 36 months from program launch compared to 60 months for early PW100 models. This reduction in elapsed time is mainly attributed to the integrated product development, advanced design and analytical tools, early interaction with manufacturing and concurrent engineering.

The PW100 engine family has gained wide acceptance for its reliability, low operating cost and broad range of power over the past two decades and like the PT6 before it will serve the industry for decades to come.

Acknowledgments

Industry, Science and Technology Canada and Technology Partnership Canada have participated in the support of the different phases of the PW100 engine development programs. The authors wish to extend their sincere appreciation to all personnel at Pratt & Whitney Canada who have worked on the PW100 engine throughout its 20 years of research, design and development. Special thanks also go to the personnel who have contributed to this paper.

References

Arora, S.C., and Abdel-Messeh, W., 1985, "Pressure Drop and Heat Transfer Characteristics of Circular and Oblong Low Aspect Ratio Pin Fins", AGARD Conference Proceedings 390, PEP Symposium, Bergen, Norway.

Arora, S.C., and Abdel-Messeh, W., 1990, "Characteristics of Partial Length Circular Pin Fins as Heat Transfer Augmentors for Airfoil Internal Cooling Passages", ASME Journal of Turbomachinery, Vol. 112, No. 3.

Benner M.W., Sjolander S.A. and Moustapha S.H., 1997, "Influence of Leading Edge Geometry on Profile Losses in Turbines at Off-Design Incidence : Experimental Results and an Improved Correlation", ASME Journal of Turbomachinery, January 1997.

Gates, F., and Smailys, A., 1989, "Prediction of 1-P Aerodynamic Loads on Tractor Aircraft Engine Installations", AIAA/ASME/SAE/ASEE 25th Joint Propulsion Conference.

Habashi, W.G., Peeters, M.P., Robichaud, M.P., Nguyen, V.-N.,and Bhat, M.V., 1992, "Finite Element Solution of Viscous Compressible Flows in Gas Turbine Ducts and Diffusers", AGARD Proceedings 510, CRD Techniques for Propulsion Applications, Feb. 1992.

Kenny, D.P., 1973 "A Comparison of the Predicted and Measured Performance of High Pressure Ratio Centrifugal Compressor Diffuser" , ASME Paper No. 72-GT-54.

Moustapha S.H., and Williamson R.G. , 1986, "Effect of Two Endwall Contours on the Performance of an Annular Nozzle Cascade", AIAA Journal, Sept. 1986.

Moustapha S.H., Okapuu U. and Williamson R.G. , 1987, "The Influence of Rotor Blade Aerodynamic Loading on the Performance of a Highly Loaded Turbine Stage", ASME Journal of Turbomachinery, April 1987.

Sampath P., and Eatock, H.C., 1993, "Low emissions Combustor Technology for Small Aircraft Gas Turbines", AGARD 82nd Symposium on Technology Requirements for Small Gas Turbines, October 1993.

Smailys, A., and Brownridge, C., 1987, "Designing for Fretting Fatigue Free Joints in Turboprop Engine Gearboxes", Paper No. AIAA-87-2046

Rhie, Chae M., Glexiner, Aaron J., Spear, David A., Fishbeg, Craig J., and Zacharias, Robert M., 1995, "Development and Application of a Multistage Navier-Stokes Solver", Paper No. ASME 95-GT-342.

Robichaud, M.P., DiBartolomeo, W., Heikurinen, K., and Habahsi, W.G., 1997, "Turboprop Air Intake Design Using 3D Viscous Analysis", 35th AIAA Aerospace Sciences Meeting, Paper No. AIAA 97-0171.

Wu, Chung, 1994, "Arbitrary Surface Flank Milling of Fan Compressor and Impeller Blades", Paper No. ASME-94-GT-426, 1994.

PROCESS OPTIMIZATION IN ADVANCED COMPRESSOR DESIGN

Gisbert Schulze, Helmut A. Geidel, Klaus Pirker
Daimler Benz Aerospace - MTU Muenchen
Postfach 50 60 40 80976 Muenchen, Germany

1 Abstract

After an overview of MTU's current compressor projects, this paper focuses towards the fundamentals of the team oriented integrated product design process (IPD) and a new approach to its goals, the advanced multi-disciplinary design process. The new idea behind this process is the focus on the integration of the most important design skills in one person. Most of the compressor design work is performed by the same person with the support of a team of specialists of the different disciplines rather than carrying out the different tasks by different members of the team. The goal of this process is a further reduction in development lead time and cost and a better focus on project requirements rather than on certain discipline requirements. In order to achieve a viable multi - disciplinary design process three major conditions have to be fulfilled:

1. The last generation of very user friendly design and analysis tool have to be available and accessible from one desk top and the data exchange must be trouble free
2. Broad minded generalistic oriented individuals have to train to use these tools while focusing on the project goals
3. Strong support from the different disciplines is necessary to avoid misleading designs

Based on the experience with the design of a new technology high speed compressor rotor the advantages of this process are proven. Up to a high level of design maturity, most of design tasks can be performed by a single individual.

2 Introduction

MTU is Germany's leading company in aeroengine design and manufacturing. As a competent partner in international cooperative engine programs one of MTU's core businesses is the development, procurement and in service support of world class high and low compressors. Beside technological leadership, one important reason for MTU's success in that field is the integration of these skills with design process optimization (1), (5). Technology programs are not just used to improve the technical characteristics of tomorrow's compressors, they are also used to evaluate the capability and the potential of optimized design processes. The size of these projects are much smaller than entire engine compressor development programs. It turned out to be highly efficient to combine technical and process emphasizes rather than only focusing on the technological achievement.

2.1 MTU's Compressor Projects

The basics of MTU's compressor design have been established in the RB199 3-shaft engine, the propulsion system for the Tornado Multi Role Combat Aircraft. More than 2500 engines have been delivered with MTU having design and manufacturing responsibility for both the intermediate pressure and the high pressure compressor.

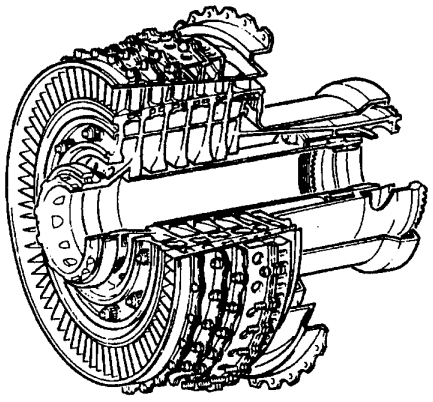

Figure 1: RB199 6-Stage HP-Compressor

Paper presented at the RTO AVT Symposium on "Design Principles and Methods for Aircraft Gas Turbine Engines", held in Toulouse, France, 11-15 May 1998, and published in RTO MP-8.

These two in the early seventies designed compressors have accumulated several million engine flight hours thus forming a sound basis of experience for upcoming new designs. Figure 1 shows the six stage high pressure compressor of that engine.

The evolutionary progress can be demonstrated by comparing the RB199 compressors against the latest design actually being flight tested in the EJ200, the engine for the Eurofighter aircraft. Within that engine MTU has design responsibility the for HP-compressor and for the 3-stage fan. figure 2 shows a schematic cross section of the five stage HPC and figure 3 a photo of the rotor.

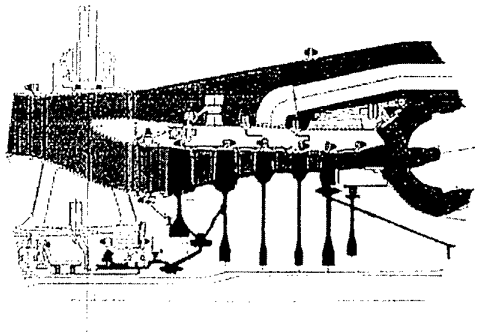

Figure 2: EJ200 5-Stage HP-Compressor, Schematic Cross Section

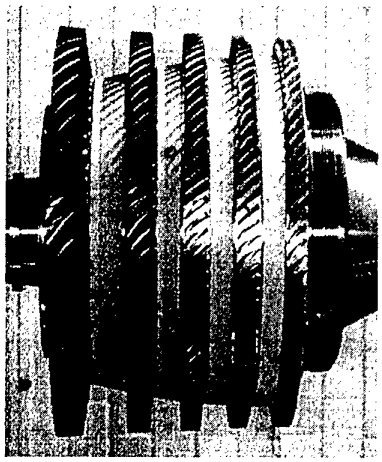

Figure 3: EJ200 5-Stage HP-Compressor, Bladed Rotor

With the design of the three stage fan for the EJ200 MTU verified the integrated development effort in an all-blisk configuration, which required most intensive joining of disciplines from aeromechanics through structures into reparability. Figure 4 shows the first stage of that all blisk rotor.

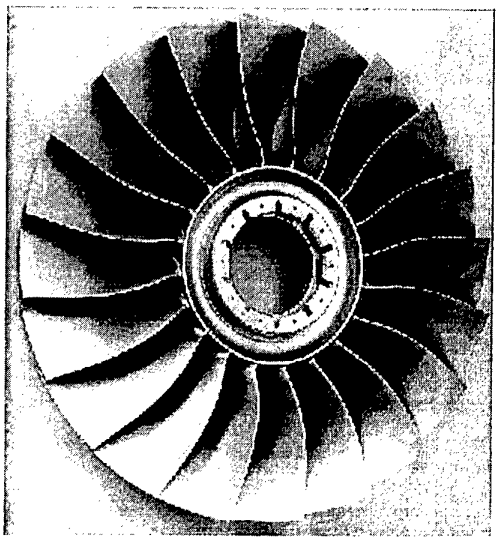

Figure 4: EJ200 3-Stage All Blisk Fan, First Rotor Stage

To further indicate the versatility in applying interdisciplinary design efforts, figure 5 shows a 15-stage compressor for a stationary gas turbine for power plant application.

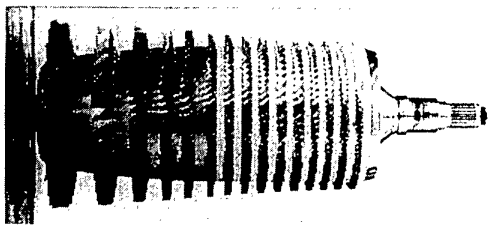

Figure 5: 15-stage compressor for stationary gas turbine application

It is MTU's intention to further exploit the background and experience in successful compressor design by other potential applications, i.e. in commercial aircraft engines.

To highlight a specific technology program example, in close cooperation with the Technical University in Darmstadt, Germany a research compressor test facility was designed, built and put into operation in a very short time frame on a minimum budget. The design includes a blisk rotor and composite guide vanes (figures 6 & 7). It is now one of MTU's test vehicle for the calibration of flow prediction tools and is used to proof the concept of new materials. Descriptions can be found in (2), (3) & (4).

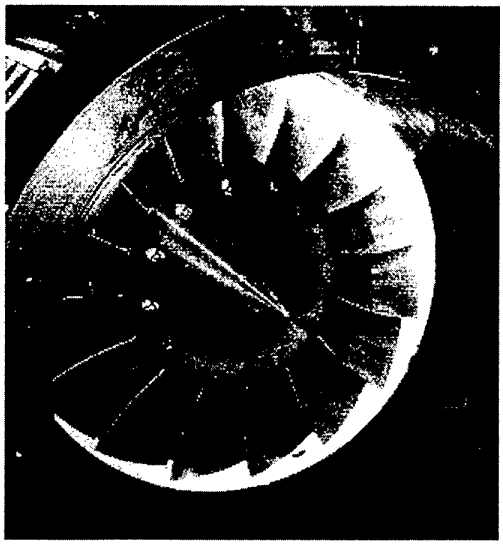

Figure 6: Single Stage High Speed Compressor Test Rig

The most recent achievement is the testing of a new high speed high compressor module. It demonstrates MTU's capability of designing world class compressors for both commercial and military engine applications in the future as mentioned before.

4 The Advanced Multi-disciplinary Design Process

4.1 The Idea

The above described compressor projects prove MTU's integrated product design process (IPD) to be a powerful method to achieve technical world class products within continuously shortening development lead times. The process is described in (1). It is based on the involvement of teamwork in every step of the design with the team members from all disciplines including engineering and manufacturing. The different design and analysis tasks are carried out by specialists of the different disciplines. With the ongoing improvements of the computer based tools heading towards better user friendliness, these tools become more available to less specialized individuals.

The design of a compressor is iterative by its nature. Beginning with a first design proposal, most often from the aero discipline, it goes through a series of analysis tasks (structures, systems, cost, manufacturing...). Proposals for alterations as a result of these analyses are the base for a next iteration towards convergence. Despite the analytical character of these tasks, usually the designer is the individual to bring the diverging requirements of the different disciplines to a synthesis.

Up to a certain level of design maturity it is neither necessary to use the highest level of analytical tools nor to have the highest level of skills. In combination with the above mentioned improved availability of the design tools the idea of letting one person carry out the entire design and analysis work came up.

4.2 The Task

The task was to pick up a research & development project and demonstrate the advantages of such an advanced design process. Since a compressor rotor design was chosen as the appropriate project the process was soon called the "one man one blade" process.

As a first step, the most recent design and analysis tools, as described later, needed to be integrated on a single work station platform. Despite the software industry's claims the data exchange between the programs sometimes can be challenging and the participation of skilled computer people turned out to be very helpful.

Second step was the training of an all-rounder on the software as well as on the technical backgrounds behind the tools. This person becomes the focal point of the project and can be referred to as the design team leader. This person is solely responsible for the progress and the level of involvement of specialists.

4.3 The Project

The project picked up to evaluate the advanced multi-disciplinary design process is a new design for the above mentioned single stage research compressor. Figure 6 shows the current rotor, figure 7 a cross section of the test rig. The goal of this technology project was to demonstrate a significant improvement in compressor efficiency by taking advantage of the yet unknown design freedom that composite material provides in combination with using the most advanced 3D aero and structure analysis tools. The compressor rotor has a tip diameter of 380mm, a rotor tip relative inlet Mach number of 1.35 and design pressure ratio of 1.5.

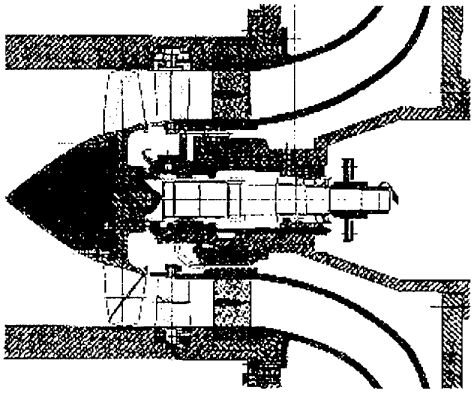

Figure 7: Single Stage High Speed Compressor Test Rig, Cross Section

4.4 The Tools

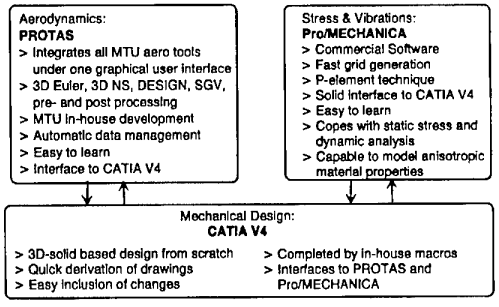

Figure 8: The Tools used in the Design Process

The tools can be divided in three groups (figure 8): Aerodynamics, structures and mechanical design. Aerodynamics: PROTAS, a user friendly in-house development integrates all MTU aero tools under one graphical user interface. These are: pre- design tools (1D, 2D), airfoil design tools, Quasi-3D analysis tools, 2D & 3D Euler and Navier Stokes analysis tools etc. plus all necessary pre- and post processing programs. It features an automated, project oriented data management system and an interface for geometrical data exchange with CATIA.

Structures: Pro/Mechanica, a commercial software package was chosen. It features fast grid generation, the p-element technique and copes with static and dynamic stress analysis. It is capable to model anisotropic material properties (composites), can be used for optimization tasks, has a solid based geometry interface with CATIA.

Mechanical design: CATIA V4. Since it has interfaces to both the other groups of tools, its 3D solid modeller is the core of the iterative geometry definition. It is completed by in-house developed macros, custom designed to make blade design very efficient. Drawings can be derived very quickly, so design iteration changes can be communicated to all participating members of the design team on a daily basis.

4.5 The Team

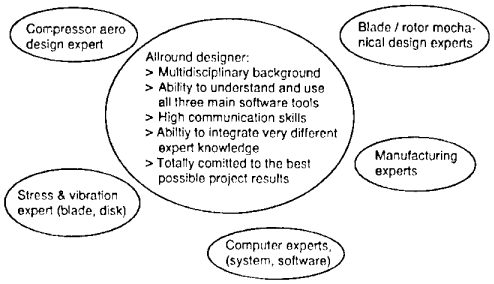

Figure 9: The Team involved in the Design Process

Focal point of the team is the all-round designer or team leader. He needs to have a strong multi-disciplinary turbomachinery background and the ability to use and understand all the three main software tools. He is supported by experts of the different disciplines, for this project people with

the following background: compressor aero, blade / disk structures, materials, mechanical design, manufacturing and the computer experts.

4.6 The Process

Figure 10 visualizes the iterative design process graphically. Squares with fillet corners represent part processes like aero design & analysis, 3D modeling etc. and hexagons represent events. The squares above the part processes are labeled with the information in- and output (top left and right respectively). Below the part processes are squares with the people carrying out the task (left) and the tools used (right). The level of the participant's contribution to the part process is indicated with the letters D(Decides), C(Carries out), A(Advises).

As it can be seen, the entire process is not just controlled by the design team leader, he is the person who carries out most of the work himself. The relation between this person and the experts contributing advice to the process is crucial to the success of the design. Frequent discussions with the experts are important. These discussions are more bilateral rather than team meetings. The number of necessary team meetings therefore can be reduced. Advising can be anything from helping the tools getting started to discussion of results. Since the entire data is in the hand of one person, many discussion can be held at the work place by using on screen data. This reduces the amount of paper work.

This process does neither enable one person to design a blade all on its own nor does it make experts obsolete. It is changing the way how the team works towards a mature design. Up to a level of a certain maturity it is not necessary to involve the full expertise and the highest sophisticated tools.

Since one person is controlling the entire work, a quick convergence can be achieved. From this level on expert work is necessary to achieve the final design quality. The point where the work is handed over entirely to experts varies from discipline to discipline and depends upon the practice of the design team leader. From this moment the process changes more and more to a classical integrated development team work.

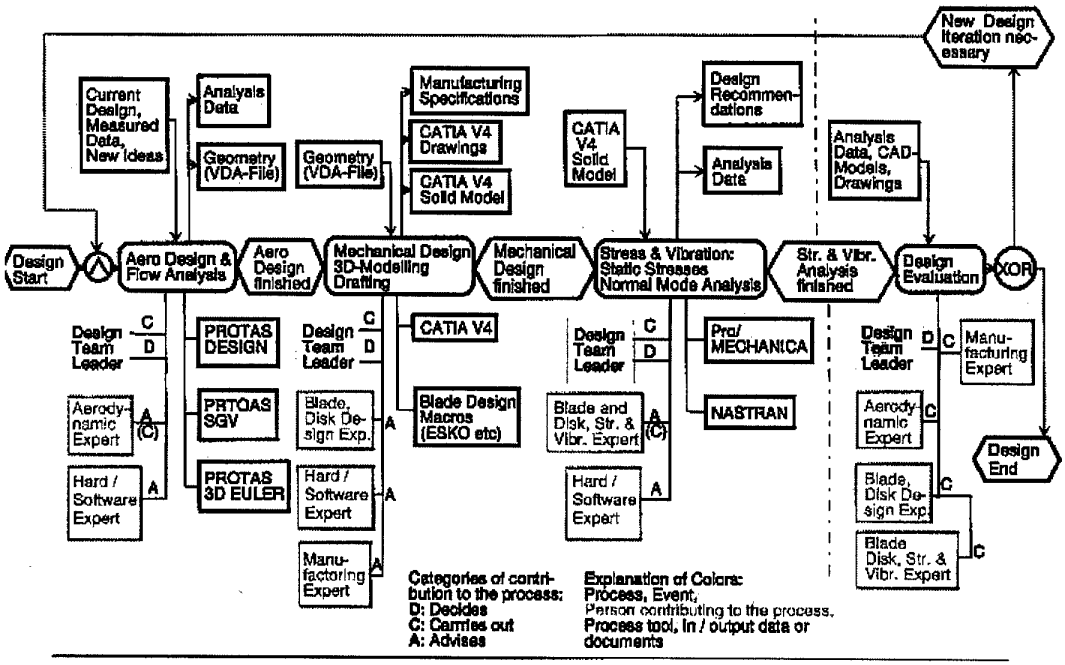

Figure 10: Advanced Mulit-Disciplinary Process Visualization

4.7 Technical Results

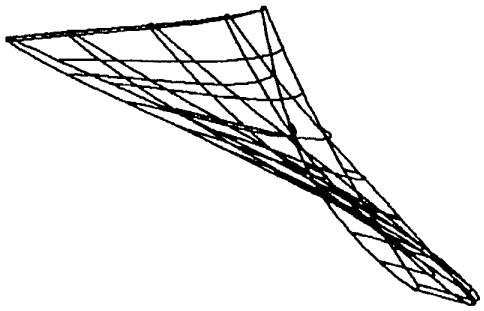

Figure 11: Blade Geometry as Defined with the Aero Design Tool (PROTAS - DESIGN)

Figure 11 shows the final blade geometry as a view from the blade tip to the hub. The geometry is generated by using the DESIGN module of PROTAS. DESIGN uses a set of aerodynamically relevant parameters to define the geometry. This geometry is used as the input to the 3D flow solver. Its pre-processor is capable of generating the grid automatically. Usually about a dozen different geometries per day can be generated, meshed and analyzed.

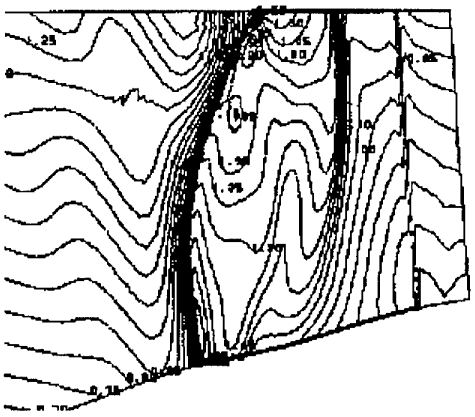

Figure 12: Predicted Mach Number Distribution, Blade Suction Side

Figure 12 shows the Mach number distribution on the blade suction side. The results are the output of a 3D Euler solver. When an a geometry is found, which meets the required flow properties, an interface transfers the data into CATIA V4. There a 3D solid model of the entire blade is created with the help of special macros developed for blade design. This can be done within a day.

Figure 13: CAD Solid Model of the Compressor Rotor Assembly

Figure 13 shows the result of this effort. Beside the blade geometry the adjacent parts of the rotor assembly are defined in the same model and parameters are driving changes consistently. Drawings can be derived from this kind of solid models within minutes.
Using the CATIA V4 - Mechanica solid interface, a 3D FE-model can be created within a few hours when the auto mesher is applied or within a day for manual meshing. The latter is necessary for optimization tasks. This feature was used in order to optimize chordwise blade thickness distribution for resonance tuning. Dynamic stress distributions for a certain resonance mode are shown in figure 14.

Figure 14: Calculated Blade Vibration Stress

4.8 Time / Cost Improvements

- The team leader drives the process and is able to carry out most of the work, so delays due to poor team member availability becomes less an issue
- The entire design data is in one hand, interface delays are reduced.
- One all-rounder agrees faster to an interdisciplinary compromise than a team of individual specialists, a fact that reduces the number of iterations
- A reduced number of team members are involved in the development process
- The number of team meetings are reduced and replaced by shorter and more efficient meetings with particular experts leading to significant less meeting man hours. These items together proved to cause a significant reduction in lead time and development cost.

4.9 Quality Aspects

Design quality could be considered an issue looking at 'laymen' doing expert design work. The key to success however is the right level of expert advice. The designer has to develop a good sense of when to ask the expert in order to prevent wasting time working on less promising design options. An important advantage of the multi-disciplinary design process is the high motivation of the designer due to his high level of responsibility. This leads to a commitment to the best project results. Since he is not committed to any particular engineering discipline, a compromise will be found faster and the design quality will be as high as necessary rather than as high as possible.

The experts are less loaded with routine work, but they keep on being exposed to the daily design work results and decisions. They gain extra time to improve the level of expertise and ensure the increasing level of quality of future projects.

4.10 Necessary Investment

To introduce the multi-disciplinary design process two different areas of necessary investment are to be considered. First the employee training. This is basically user training on software tools and technical backgrounds. With the help of good material and experts capable to teach, most of this can be done as training on the job. Some training has to be invested in the understanding of the ideas behind the process. The experiences showed the need of cultural changes in the engineering community.

The other area of necessary investment is information technology. Depending on the already available opportunities to run all the tools and to exchange data between them, one has to consider to invest in computers, networks and software updates.

6 Conclusions

The idea of getting most of the analysis and design work for a compressor rotor carried out by the same individual turned out to be a powerful tool to reduce the lead time and the development cost without sacrificing product quality. It can not replace the contribution of experts. Once a certain level of design maturity is achieved, it is necessary, that the experts take over the work and transform the process into a conventional integrated design process.

This advanced multi-disciplinary design process has been tested with a small scale development project. It is recommended to apply it to larger scale projects. To achieve this, it is important to focus on training of the people as well as on investing in information technology.

Testing new ideas for design processes on a small scale by using technology development projects is an important contribution to ensuring

MTU's leadership in the design of world class compressors for jet engines.

List of References

(1). H.A. Geidel, C. Prodehl: Quality Design - *Evolution in Aircraft Engine Mechanical Design*, ISABE 95, 12th International Symposium in Air Breathing Engines, Melbourne, September 1995

(2). G. Schulze, C. Blaha, D.K. Hennecke, J. Henne: *The Performance of a New Transonic Axial Single Stage Compressor,* ISABE 95, 12th International Symposium in Air Breathing Engines, Melbourne, September 1995

(3). G. Schulze, D.K. Hennecke, J. Frischbier, S. Sikorski: *Entwicklung einer Verdichterleitschaufel aus kohlefaserverstaerktem Kunststoff (CFK),* DGLR 94, Deutscher Luft- und Raumfahrtkongress, Erlangen Oktober 1994

(4). J. Frischbier, G. Schulze et al: Blade Vibrations of a High Speed Compressor Blisk-Rotor, ASME 96-GT-24

(5). H.A.Geidel et al:. *Axial flow compressors - Mechanical Design Trends,* ISABE 93, 11th International Symposium in Air Breathing Engines, Tokyo, September 1993

ACTUATION SYSTEM FOR VARIABLE EXHAUST NOZZLE AND INLET GUIDE VANES ON AN ADVANCED GAS TURBINE ENGINE

G. BARDONE
S. MARCHETTI
A. TROVATI
Fiat Avio S.p.A.,Direzione Tecnica,C.so Ferrucci 112, 10138 Torino, Italy

ABSTRACT

Aircraft engines with afterburner need to have variable exhaust nozzle and inlet guide vanes in order to control the air flow.

Different types of actuation systems provide the force to move such variable geometry devices.

The paper describes the architecture of a hydraulic actuation system installed on a military engine of the last generation, paying particular attention to the technical solutions chosen to keep at minimum mass and heat rejection and to the dynamic mathematical model used during the development to predict the nozzle area behaviour, inlet guide vanes position, hydraulic oil flows and pressures as functions of external loads, engine rating and commanded positions.

SUMMARY

The paper deals with the development of the Air Flow Control System (AFCS) for a reheated turbofan engine installed on an advanced fighter aircraft.

The very severe design requirements of the engine, with very short transient times required for the response to pilot power demand, i. e. Idle to Max Dry, Max Dry to Combat and Idle to Max Dry throttle slams, set very stringent requirements also to the engine control system both in terms of control hardware and software.

In particular, a very quick and very precise control of Variable Inlet Guide Vanes (VIGV) and of the variable geometry convergent - divergent nozzle is essential to accommodate for sudden variations of air flow, pressure and temperature, as required by pilot throttle requests, keeping the engine within the safe operation, preventing, for example, any risk of a stall of fan and high pressure compressor.

LIST OF ACRONYMS

AFCS Air Flow Control System
FADEC Full Authority Digital Engine Control
FCOC Fuel Cooled Oil Cooler
HPGU Hydraulic Power Generation Unit
LRI Line Repleceable Item
LVDT Linear Variable Displacement Transducer
MAOS Master Actuator Output Shaft
MAR Moving Actuation Ring
NACU Nozzle Actuation and Control Unit
PLA Pilot Lever Angle
RVDT Rotary Variable Displacement Transducer
VIGV Variable Inlet Guide Vane
VACU Variable Guide Vanes Actuation and Control Unit

1. INTRODUCTION

This paper describes the main characteristics of the Air Flow Control System (AFCS), installed on a reheated turbofan engine equipping an advanced fighter aircraft.

This system, specified by FiatAvio to meet the requirements defined in the engine Accessory Control Specification, was designed by one of the European leader companies producing hydraulic systems and jointly developed together FiatAvio.

The joint work of many European companies involved in the development of the engine and of its accessories and sub-systems, aiming to ensure the best technological base available for the project, resulted in a very successful design.

2. SYSTEM DESCRIPTION

The Air Flow Control System (AFCS) is a self contained system, supplying high pressure oil to control the four synchronised hydraulic actuators operating the variable convergent divergent exhaust nozzle, to control nozzle throat area and to control the HP compressor variable inlet guide vane angle.

The required hydraulic power is generated by the AFCS by means of a gearbox mounted pump. This power is supplied to the actuators which control the position of the moving actuator ring (MAR) of the engine exhaust convergent - divergent nozzle and control the variable inlet guide vane (VIGV) position through the vane synchronisation ring.

Nozzle throat area and VIGV position are scheduled by the Full Authority Digital Engine Control (FADEC) as a function of pilot throttle position (PLA) to control thrust, inlet air mass flow rate, as well as fuel consumption at engine low power settings.
The system is therefore equipped with position transducers to monitor the position of these two synchronisation rings, which are under control of the Full Authority Digital Engine Control (FADEC).
This is achieved acquiring the electrical signal from a linear position transducer for the nozzle actuators and a rotary transducer for the HP compressor inlet guide vane.
These signals provide the feedback to the FADEC to close the system control loop.

Paper presented at the RTO AVT Symposium on "Design Principles and Methods for Aircraft Gas Turbine Engines", held in Toulouse, France, 11-15 May 1998, and published in RTO MP-8.

3. SYSTEM REQUIREMENTS

As mentioned, the system requirements were tailored around the engine design, in order to comply with the Engine Specification and the Accessory Control Specification.
The most significant system requirements are collected in this chapter.

Moreover, the possible increase of engine thrust was also considered since the beginning of the AFCS development.
Therefore, the system was designed to be able to match the foreseen requirements of an engine growth version without major modifications.

3.1. System Loads

The system is designed to operate nozzle and VIGV actuation within the whole engine flight envelope.
During operations the nozzle control actuators may be subjected either to negative loads or to asymmetric loads.
The system is therefore designed to withstand :

- Negative load up to ~ 18% of max. operating load
- Asymmetric load up to ~ 8% of max. operating load

3.2. System Accuracy and Response

System requirements for accuracy of position (in steady state conditions) and response times were specified in agreement with engine control requirements, as follows :

- MAR position accuracy ± 0.6% of actuators full travel
- MAR settling time ≤ 0.2 s
- NACU response time 1 ÷ 2.5 s (full actuator travel)
- MAOS position accuracy ± 0.3% of actuators full travel
- VACU response time 1.5 ÷ 3 s (full actuator travel)

3.3. System Reliability and Maintainability

The AFCS is designed to satisfy the engine reliability and maintainability targets.

The following requirements were also specified :

- No external leakage allowed.
- Explosion proof system
- Fire resistant system
- Testability features for the following electrical components :
  - Reservoir Oil Level Switch
  - Filters Impending Blockage Indicators
  - Servovalves electrical parts
  - Position Transducers (LVDT and RVDT)

3.4. Environmental Conditions

According to engine specification, the AFCS is designed to withstand the following adverse environmental conditions :

- Acceleration
- Fungus
- Humidity
- Salt fog
- Sand and Dust
- Shock
- Low / High Temperature
- Vibration

4. SYSTEM ARCHITECTURE

The architecture of the AFCS hydraulic system (fig. 1) is based on a valve controlled system, with a variable delivery / variable pressure pump, which was selected in order to minimise system mass and size.
The hydraulic power is fed to the actuators by throttling the flow to the jacks through a control valve which changes the flow restrictions according to the signal received from the FADEC.
An additional feature is the regenerative oil control flow applied to the nozzle actuators, which prevents oil overheating.

In the variable delivery and variable pressure pump, the displacement is controlled by a hydromechanical pressure compensator.
Since the load on nozzle actuators is a function of engine operating conditions (altitude and thrust), the same pressure compensator controls the pump discharge pressure, in order to keep the nozzle actuators at the required position.

In the regenerative hydraulic system, the rod end side of the actuators is connected to the supply pressure line, while the head end side is connected to the control valve (fig. 2).
This solution is particularly convenient because it allows to have the actuators subjected to large tensile loads and small compressive loads.
Moreover, it was also preferred because it requires a smaller pump.

5. COMPONENT DESCRIPTION

The major components of the AFCS include the following functional sub-system :

- HYDRAULIC POWER GENERATION UNIT (HPGU)
- NOZZLE ACTUATION AND CONTROL UNIT (NACU)
- VARIABLE GUIDE VANES ACTUATION AND CONTROL UNIT (VACU)

5.1. Hydraulic Power Generation Unit (HPGU)

The HPGU, designed to supply high pressure oil to the NACU and VACU, is mechanically driven from the rear face of the main engine gearbox.
The HPGU components are integrated into a hydraulic package which performs the following tasks :

- filtering the hydraulic oil
- controlling the oil flow to the sub-systems (according to FADEC requests)
- ensuring the safety of the circuit.

An integral pressurised reservoir is also provided to feed the oil to the pump.

The unit is composed of the following items :

1. Hydraulic Pump
2. Reservoir
3. Hydraulic Filter module
4. Pressure Relief Valve
5. Check Valve (pump crossport)
6. Non Return Check Valve
7. Bypass Valve (heat exchanger line)
8. Overfill Overtemperature Protection Device
9. Low Pressure Bypass Valve
10. Electrohydraulic Servo Valve for Nozzle Control
11. Electrohydraulic Servo Valve for VIGV Control

5.1.1. Hydraulic Pump

Four alternative designs were considered before starting the system design, considering advantages and disadvantages (fig. 3).
Although the *fixed delivery pump* (fig. 3a) is the simplest solution, it works at constant flow rate requiring a bypass line for the excess fluid and generating a very large amount of heat, which was not acceptable for this system.
The *variable delivery pump - constant pressure* (fig. 3b) solution, avoiding the bypass line, is used in most aircraft hydraulic system, where constant pressure has to be guaranteed.
The above mentioned solution, however, can be improved with a *variable delivery pump - variable pressure* system (fig. 3c), where system pressure is adapted to the load, minimising the heat generation and the mechanical power required at the pump drive shaft.
A *pump controlled* system (fig. 3d) requires an additional pump and it was therefore excluded.

On the basis of the above mentioned reasons, the pump is a variable delivery, variable pressure one, with a build-in pressure compensator on the pump supply line.
This choice allows to avoid oversizing of system components, particularly the oil reservoir, therefore minimising system mass and size.

The pump is driven by the engine gearbox.
The insertion of the pressure compensator allows to vary the pump reference pressure according to the load on nozzle actuators.
The system is operated with a reduced pressure when nozzle loads are relatively low, while at higher loads higher oil pressure is provided, as required to contrast nozzle thrust loads.
The main benefit obtained from this arrangement is the reduction of system heat rejection (see fig. 4).
Moreover, by reducing the time of full pressure operation, a benefit in terms of system life is also obtained.

The pump is designed for no external leakage, the few drops per hour out of the pump shaft rotating seal are collected in a chamber of the gearbox.

5.1.2. Reservoir

A pressurised *reservoir*, integral with the unit, ensures that a minimum pump inlet pressure is always available during system operations, independently of operating conditions.
At system start this is obtained with a spring loaded piston, whereas a connection with the nozzle actuator bleed line provides the pressure during operations : the required force is set in order to maintain an oil pressure level which is sufficient to prevent transient cavitation of the pump.

The reservoir contains an on/off switch, to give a "low oil level" signal to the FADEC.
The open switch position corresponds to low oil level : the design is therefore inherently safe, since a switch failure would result in an undue alarm but not in system operations with low oil level.
Moreover, a visual indicator is provided, allowing to check the oil level during maintenance operations.

Finally, a safety disc is designed for thermal expansion protection against excess of pressure.

5.1.3. Filter Module

The HPGU contains both high and low pressure *filters*, which are integrated into one single module.
The high pressure filter, at pump outlet, cleans all the fluid supplied by the pump before it is distributed to the system.
The low pressure filter, on the pump return line, has a very fine degree of filtration and cleans the continuous fluid flow from all the drains and bleeds.
This arrangement was selected because the actuator flow is quite large but it is limited to very short periods, while the small bleed flow is continuous : therefore the highest level of fluid contamination is found in the fluid out of drains.

With the selected design it is then possible to get the following benefits :

- very high degree of filtration of the hydraulic fluid
- small difference between pump case and suction pressures
- minimum pressure losses from actuator return to reservoir

To monitor the need of filter maintenance, each filter is equipped with an electrical switch giving the indication of filter impending blockage to the FADEC.
The electrical switch is set in the open position when the differential pressure limit is exceed : this design is conservative, since a switch failure would result in an undue alarm but not in system operations with a clogged filter.

When clogging results in an excessive pressure drop across the filter, both filters contain a by-pass valve which opens to allow oil flow through a bypass line : therefore the system will temporarily operate without hydraulic oil filtration until filter maintenance is carried out.
A latched visual (pop-out) indicator will extend when the by-pass valve has operated : system operations are no more allowed until this indicator is manually reset after having maintained the filter.
In order to avoid false indications, a thermal lock-out device inhibits the indication at low oil temperatures (< 40 °C), when the high pressure drop is caused by the high oil viscosity rather than by filter clogging.

5.1.4. Pressure Relief Valve

Under normal operating conditions, the system maximum working pressure is controlled by the pressure compensator of the hydraulic pump.

In case of any malfunctions of the variable delivery mechanism of the pump, however, a *pressure relief valve*, located at the pump outlet, acts as a protective device to avoid system overloading.
When the supply pressure exceeds the maximum pressure safety limit, the relief valve bypasses the excess hydraulic flow directly to the return line.

5.1.5. Check Valve

The *check valve*, located across the interconnection of pump inlet and outlet, acts to balance system pressures avoiding damages of the pump due to cavitation as well as preventing the reservoir from overpressurisation during engine windmilling.

5.1.6. Non Return Check Valve

A *check valve* is located in the case drain line downstream of the low pressure filter.
This valve acts to prevent any reverse flow from the reservoir through the filters, which could occur during ground operations, when the nozzle actuation system is manually operated with the handwind.

5.1.7. Bypass Valve (Heat Exchanger line)

Hydraulic oil cooling is obtained exploiting the engine Fuel Cooled Oil Cooler (FCOC) heat exchanger.

A *bypass valve* is located just upstream of the check valve, on the drain line connecting the HPGU case drain to the return line.
This valve operates to relieve case drain pressure in the event of an excessive pressure drop across the FCOC.

5.1.8. Overfill and Overtemperature Relief Valve

The HPGU also contains an *overfill* and *overtemperature* protection device consisting of a *relief valve*, a burst diaphragm visual indicator and a protection cap.
This device protects the reservoir against inadvertent overfill during ground maintenance and against high pressure resulting from excessive volumetric expansion of the fluid caused by high temperature, as a result of a failure of the variable pump mechanism.

During ground maintenance, if the reservoir is inadvertently overfilled and the reservoir piston reaches its upper position, the relief valve opens and the hydraulic fluid flows back to the maintenance unit through an auxiliary passage.

If the oil pressure exceeds the diaphragm cracking pressure, the diaphragm will burst, thus conveying fluid to the chamber of the gearbox which collects leakage from the pump shaft rotating seal.
This occurrence is indicated by a permanent visual indication.

5.1.9. Low Pressure Bypass Valve

This is a *spring actuated valve* : when the system is running the valve is kept closed by the hydraulic oil pressure, while when the engine is not running (static conditions) and the hydraulic pump is not operating, the valve opens connecting the supply line to the return line.
By reducing flow resistance, this helps to move the nozzle actuators using the handwind for ground maintenance and to perform nozzle setting procedures.

5.1.10. Electrohydraulic Servo Valve for Nozzle Control

The nozzle control valve is a *two stages, three ways servovalve* (fig. 5) which modulates the oil flow to the NACU hydraulic jacks in order to translate the nozzle MAR according to the FADEC demand signal.

The electrical input from the FADEC acts on the control valve torque motor.
The torque motor operates the valve such that the hydraulic pump delivery flow is applied to the appropriate side of the hydraulic jacks to obtain the required direction of travel of the nozzle MAR.

The electrical part of the valve is fully duplicated and each lane is electrically independent.
During normal functioning only one coil is driven by the selected lane of the FADEC, whereas the other lane remains in active stand-by mode until the FADEC initiates a lane change.

5.1.11. Electrohydraulic Servo Valve for VIGV Control

The VIGV control valve is a *two stages, four ways servovalve* (fig. 6) which modulates the oil flow to the VACU hydraulic actuators in order to rotate the VIGV according to the FADEC demand signal.

The electrical input from the FADEC acts on the control valve torque motor.
The torque motor operates the valve such that the hydraulic pump delivery flow is applied to the appropriate side of the hydraulic actuators to obtain the required direction of rotation of the guide vanes.

The electrical part of the valve is fully duplicated and each lane is electrically independent.
During normal functioning only one coil is driven by the selected lane of the FADEC, the other lane remains in active stand-by mode until the FADEC initiates a lane change.

5.2. Nozzle Actuation and Control Unit (NACU)

The NACU comprises the following parts :

1. Nozzle Actuation System
2. Nozzle MAR Position Transducer

5.2.1. Nozzle Actuation System

The four *nozzle actuators* are mounted on and supported by the aft end of the afterburner casing.
These actuators are unbalanced areas piston jacks with the rod ends connected to the Moving Actuator Ring (MAR) of the nozzle.

The function of these actuators is to provide a stroking motion with sufficient force to position the variable exhaust nozzle within the response time required by the FADEC for each engine flight condition.

There are two hydraulic connections on each side of the actuators : the forward hydraulic connection is called the head end and the aft hydraulic connection is called the rod end.
Oil pressure supplied to the head end of the actuators will extend the piston and open the nozzle.
Oil pressure supplied to the rod end of the actuators will retract the piston and close the nozzle.

At the head end there are mechanical flexible synchronising cables, connecting the four actuators to prevent any misalignment of the actuating ring when its position is changing.
These flexible cables are installed inside of the hydraulic lines, therefore reducing the system envelope and saving mass.

One of the rod end tubes is provided with two calibrated bleed orifices into the each end for the following purposes :

- remove heat transferred by conduction
- remove contaminated fluid
- remove the entrained air during ground maintenance operations.

The jacks incorporate a mechanical end stop to limit MAR overtravel, irrespectively of engine control input demand.
These jack stops are able to withstand the system full loads.

5.2.2. Nozzle MAR Position Transducer

A *Linear Variable Displacement Transducer* (LVDT) is mounted between the jet pipe and the MAR.
The core of the Transducer is attached to the actuating ring, the movement of the core has a linear relationship to output voltage, therefore, output voltage from LVDT can be measured and converted to linear motion in the FADEC logic.
So that the MAR position is directly related to actual nozzle area, the LVDT detects and transmits this linear motion and feedbacks the signal to the FADEC.
Two independent sets of coils are connected to the LVDT, to feed signals to the two independent lanes of the FADEC.

5.3. Variable Inlet Guide Vanes Actuation and Control Unit

The VACU comprises the following parts:

1. Hydraulic Actuators (Master and Slave)
2. Master Actuator Position transducer

5.3.1. VIGV Actuation System

The two *hydraulic actuators*, with equal area pistons, operate the rotary output shafts connected to the levers which actuate, through a synchronising (unison) ring, the HP compressor Variable Inlet Guide Vanes (VIGV).

Both actuators are fed by the VACU electrohydraulic servovalve, located on the HPGU, according to the FADEC demand.
The actuators incorporate mechanical end stops to limit the vanes overtravel irrespectively of the electrical control input demand.
The actuator overtravel stops are able to withstand the system full dynamic loads.
As for the nozzle actuators, calibrated bleed orifices are provided to remove heat generation, to remove the contaminated fluid and to remove the entrained air during ground maintenance operations.

The master actuator is equipped with a handwind device to manually move the rotary output shaft : a counterclockwise (looking from the master actuator top) rotation of the handwind closes the VIGV ring.

5.3.3. Master Actuator Position Transducer

The master actuator output shaft position, directly related to the vane angle, is measured by a *rotary variable displacement transducer* (RVDT) and transmitted to the FADEC.
The RVDT is a part of the master hydraulic actuator unit and its excitation is supplied by the FADEC.
The RVDT provides two independent electrical signals of the Master Actuator Output Shaft (MAOS) position, one for each lane of the FADEC.

6. SYSTEM RELIABILITY AND MAINTAINABILITY

6.1. HPGU Reliability and Maintainability

The HPGU design incorporates many features to improve system reliability and maintainability.

- The HPGU hydraulic fluid is the same as for the engine lubrication system, improving engine logistic. However, the two oil systems are completely separated, so that an oil leakage in a system will not affect the other system, therefore improving engine reliability and flight safety.
- The hydraulic oil absolute filtration level is 15 µm, in order to prevent particles to enters the system servovalves. To improve reliability, the servovalve flapper gap at null position is 0.05 mm, quite larger than the filtration level.

- The oil filters are equipped with impending blockage indicators and bypass valves to avoid reliability problems due to filter clogging. The visual indicator of the bypass valve opening prevents from operating the system with a bypassed oil filter.
- The unit is designed, so that in case of an electrical failure (input signal to servovalve = 0 mA) the HPGU will deliver the oil flow in the direction to open the engine variable exhaust nozzle and close the compressor VIGV, i. e. in the safe mode to prevent the engine from either overspeeding or stalling.
- Quick disconnect self-sealing fittings are used for oil pressure fill from ground equipment for maintenance.
- Filter cartridges can be removed without discharging the HPGU system, therefore reducing maintainability times.
- Many components (the two servovalves, the two oil filters, the two filter impending blockage indicators, the oil level switch and all the plastic metal cover plates) are Line Replaceable Items (LRI's) and can be replaced on the field with the engine installed on the aircraft.

6.2. NACU Reliability and Maintainability

The nozzle actuation system was designed with the following features to improve reliability and maintainability.

- A double dynamic seal is provided to avoid external leakages of the actuators.
- The installation of the synchronising flexible cables inside the hydraulic tubes minimises the number of fittings, optimising maintainability, and reduces the potential risks of leakage.
- Each actuator features an adjuster on the rod end side. This adjuster performs the following tasks :
  - it allows to adjust the rod length to the correct position, in order to avoid any misalignment of the nozzle actuation ring
  - it allows to replace an actuator on an aircraft installed engine, avoiding engine removal from aircraft.
- A handwind is available to manually actuate the NACU during system oil filling, in order to eliminate air bubbles and to make the filling easier.

6.3. VIGV Reliability and Maintainability

The VIGV actuation system design incorporates some features to improve reliability and maintainability, too.

- As for the NACU, the master actuator embodies a handwind device which allows to manually move the rotary output shaft during the system oil filling, in order to eliminate air bubbles and to make the filling easier.
- Both the master actuator female gear and the actuation ring male gear have a missing tooth : this simple feature ensures the correct alignment of the master actuator with the actuation ring. This alignment is made easier by the utilisation of the handwind.

7. AFCS SIMULATION

A FORTRAN 77 mathematical model of the AFCS has been developed with the aim of predicting steady-state and transient performance of the system up to a frequency of 20 Hz.

This model is a non-linear one and provides the values of all variables versus time, starting from the following independent variables :

- MAR position command
- VIGV position command
- Nozzle axial loads
- VIGV torque load
- Engine rating (pump speed)

Oil temperature is accepted as a parameter, allowing to evaluate the relevant resistance and capacitance of the hydraulic components.
The model accuracy, expressed in terms of actuators full travel, is :

- steady-state performance ± 2%
- transient performance ± 10%

The dynamic simulation model is composed of three sub-models :

- a linear model of the NACU
- a linear model of the VACU
- a non-linear model of the whole AFCS

The linear models are mainly used for frequency response and stability analysis.

7.1. NACU Linear Model

The system diagram used to build this model is shown in fig. 7a, while fig. 7b depicts the corresponding mathematical model.

Since no high pressure accumulator is present in the hydraulic system, the dynamic response of the NACU servoloop is affected by the dynamics of the variable delivery pump : the pump is therefore included in the model.
No dynamic effects were considered in the feedback line because of the high frequency response of the transducer.

Computed closed loop and open loop performance are shown, respectively, in figs. 8a - 8b and 9a - 9b.
The system has very good stability margins and they are only slightly affected by the system pressure.

7.2. VACU Linear Model

For the transient performance analysis of the VACU a model was prepared, and the corresponding mathematical model is presented in fig. 10.

Differently from the NACU model, in this model the pump dynamics is not considered.
As a matter of fact, considering the very small flow required by the vane actuators and the relatively large hydraulic capacitance of the pressurised portion of the system, the dynamics of the VACU servoloop is practically unaffected by the pump dynamics.
No dynamic effects were considered in the feedback line because of the high frequency response of the transducer.

Computed closed loop and open loop performance are shown, respectively, in figs. 11a - 11b and 12a - 12b.
As for the NACU, the system has very good stability margins and they are only slightly affected by the system pressure.

7.3. AFCS Non-Linear Model

The non-linear model is essentially organised in 6 blocks :

- Master block
- Control block
- Pump and Compensator block
- Servovalve block
- Actuator block
- Reservoir block

7.3.1. Master Block

The *master block* reads the input variables and data, manages the simulation and evaluates variables (like piping pressure drop) not computed by the other blocks.
It also stores output values at each simulation time interval.

7.3.2. Control Block

The *control block* evaluates the 3-way and 4-way servovalve currents, as a function of the position error on the basis of the control laws.
It also evaluates the values of the commands and of the loads acting on the actuators as a function of time : the variation of command and load may be either linear or sinusoidal.

7.3.3. Pump and Compensator Block

The *pump and compensator block* simulates the dynamic behaviour of the HPGU, evaluating the pump flow rate and supply pressure as a function of system operating conditions.
The model accounts for variable delivery mechanism, gearbox speed, masses, stiffnesses, overlaps and clearances of the pressure compensator moving elements, considering damping effect of orifices and hydraulic compliances within unit.
Pressure drops, either laminar or turbulent, through the passage ways and the high pressure filter are also computed.

7.3.4. Servovalve Block

The *servovalve block* derives the position of the two stages of both AFCS hydraulic servovalves as a function of the current input, and subsequently evaluates the flow rates as a function of the second stage spool position and of upstream and downstream pressures.
This model takes into account servovalve hysteresis and offset, servovalve internal leakages, servovalve pressure drop (laminar or turbulent) and overlaps and radial clearances.

7.3.5. Actuator Block

The *hydraulic actuator block* simulates the dynamic behaviour of the hydraulic actuators, accounting for the hydraulic compliances of the actuator chambers, the stiffness of mounting points, the mass of the pistons and of the connected elements, the external loads and the friction losses.

7.3.6. Reservoir Block

The *reservoir block* evaluates the position of the reservoir moving elements, on the basis of reservoir geometry, spring pre-load and stiffness, piston mass, chamber compliances and pressure drops in the passage ways.

7.4. AFCS Non-Linear Model Output

Main outputs of AFCS non-linear model are the following :

- Pump flow rate and supply pressure, high pressure filter pressure drop, hydraulic package inlet and outlet pressure drops, piston position, flow rate through the pressure compensator and position of the pressure compensator moving elements.
- Currents of the servovalves, servovalve stages position, supply, return and control flow rates and pressures and servovalve leakages.
- Position and speed of the hydraulic actuators, actuator flow rates and chamber pressures.
- Position of reservoir piston, flow rates and internal pressure drops
- Pressure drops and flow rates in pipes connecting the hydraulic package to the actuators.

8. CONCLUSIONS

The variable nozzle and variable inlet guide vanes hydraulic actuation system was successfully designed, developed and engine tested, in front of very stringent design requirements.

The design trade-off allowed to optimise the system in terms of performance, mass and size.
Maintainability and reliability requirements have also been duly taken into account in the design phase, introducing special features to enhance these characteristics.

A non-linear dynamic model of the whole system was also implemented and set in front of experimental evidences.
This mathematical model has been used to evaluate the initial system design and to correlate the system behaviour with engine FADEC logic.
The same model has been exploited to evaluate system development modifications and for the interpretation of system test results, proving to be a very important development tool.

9. ACKNOWLEDGEMENTS

On behalf of FiatAvio the authors would like to acknowledge the joint effort of Microtecnica design and test departments in the design and development of this actuation system.

We would also like to thank Microtecnica personnel for the information provided for the preparation of this paper.

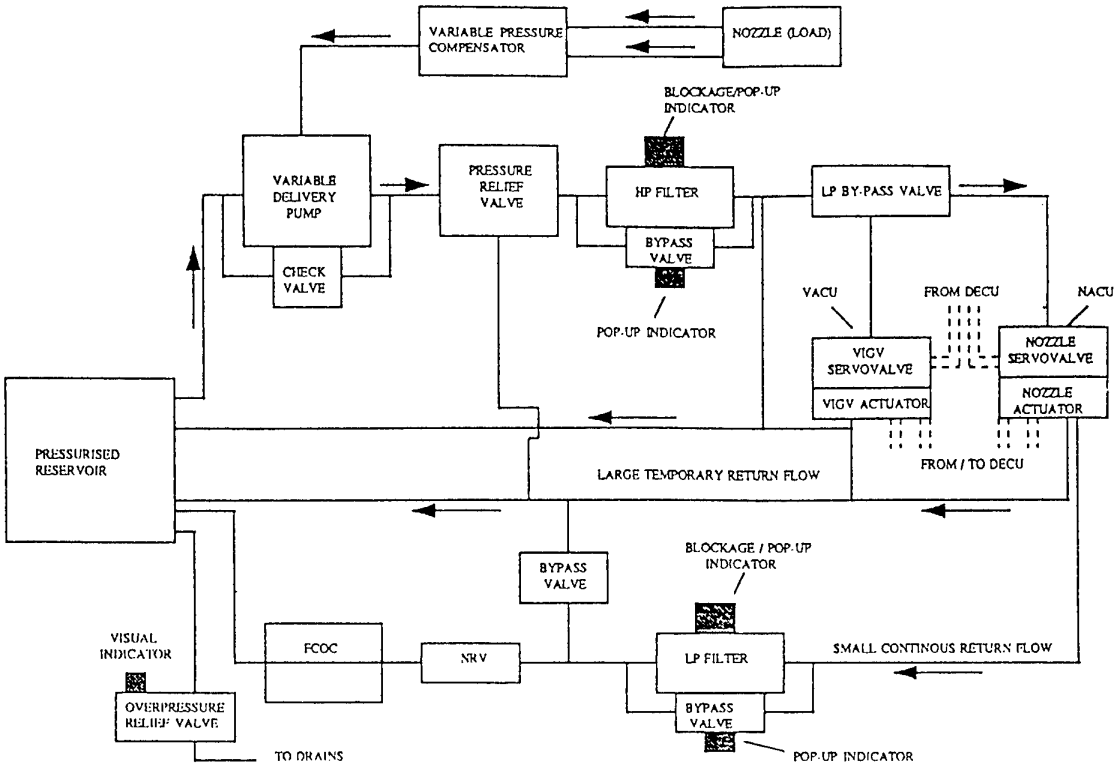

Fig. 1 - Air Flow Control System

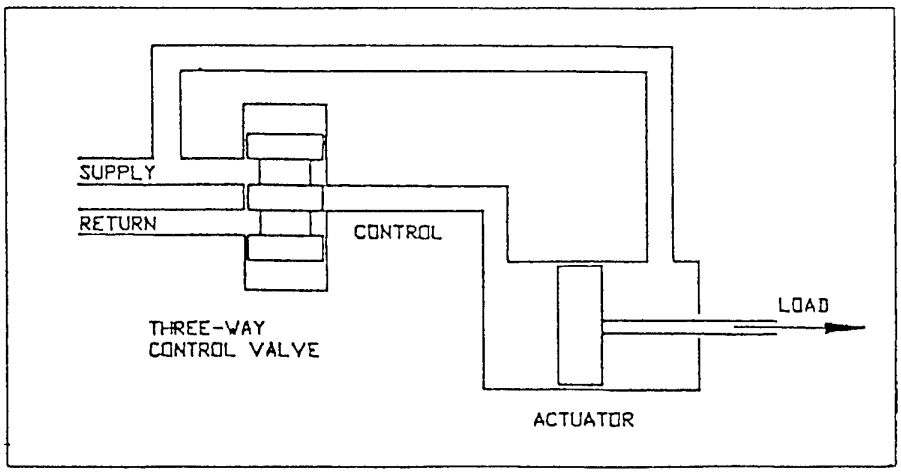

Fig. 2 - Regenerative Flow Configuration

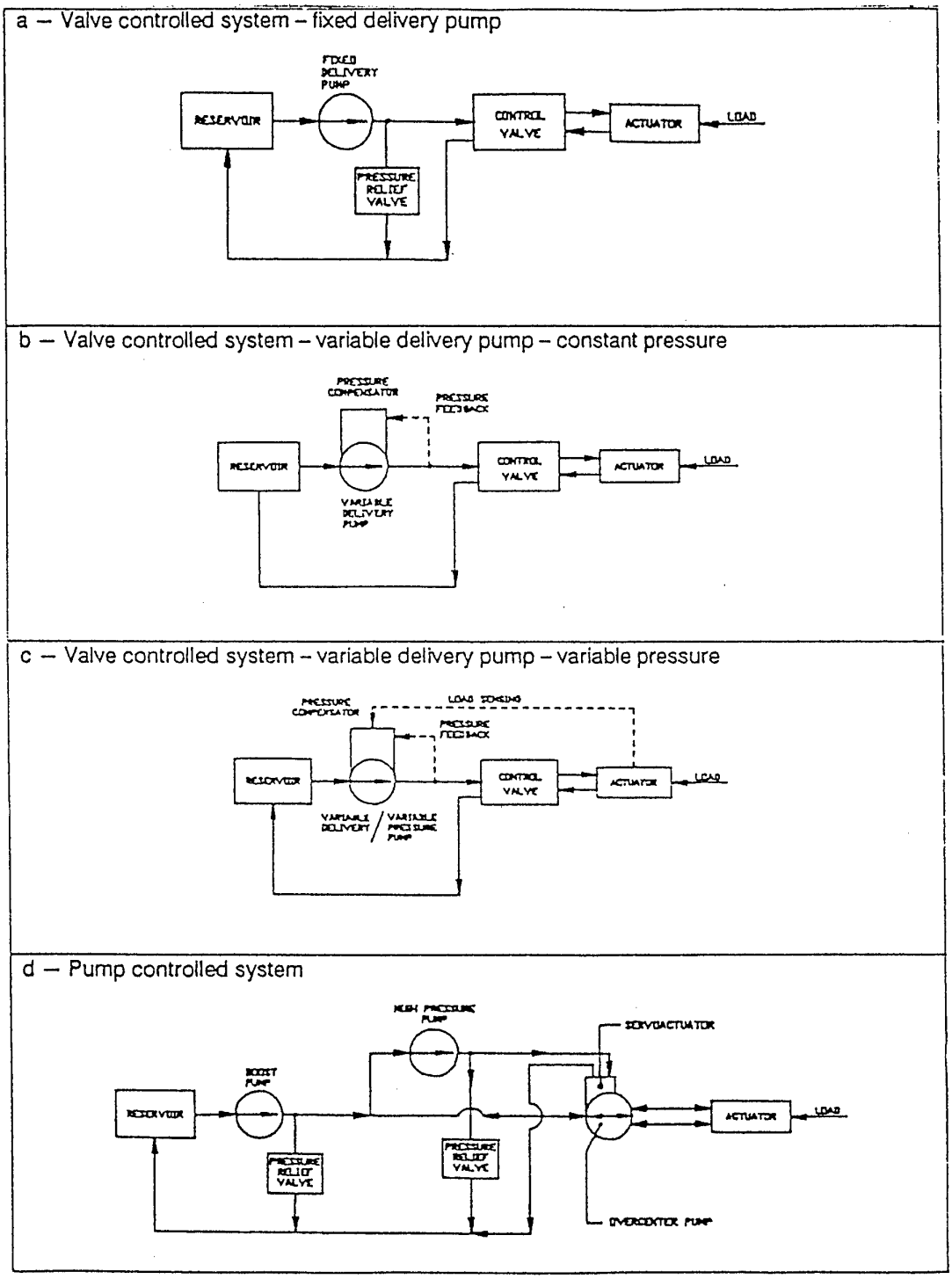

Fig. 3 - AFCS Alternative Configurations

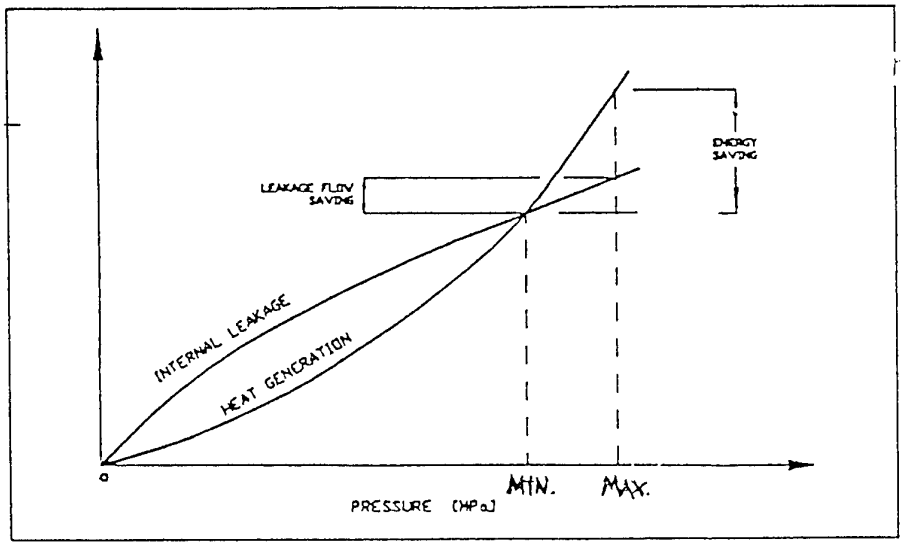

Fig. 4 - Energy Saving for a Variable Pressure System

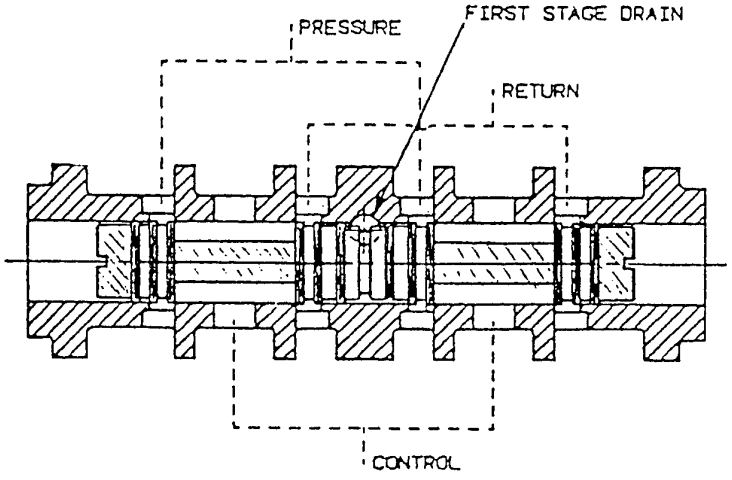

Fig. 5 - 3-way servovalve for Nozzle Control - Second Stage Schematic

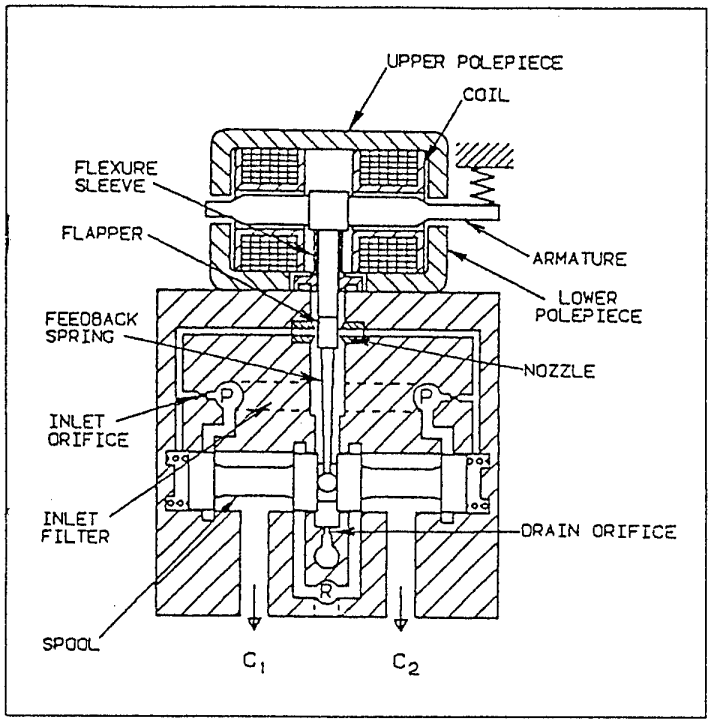

Fig. 6 - VACU 4-way Servovalve Schematic

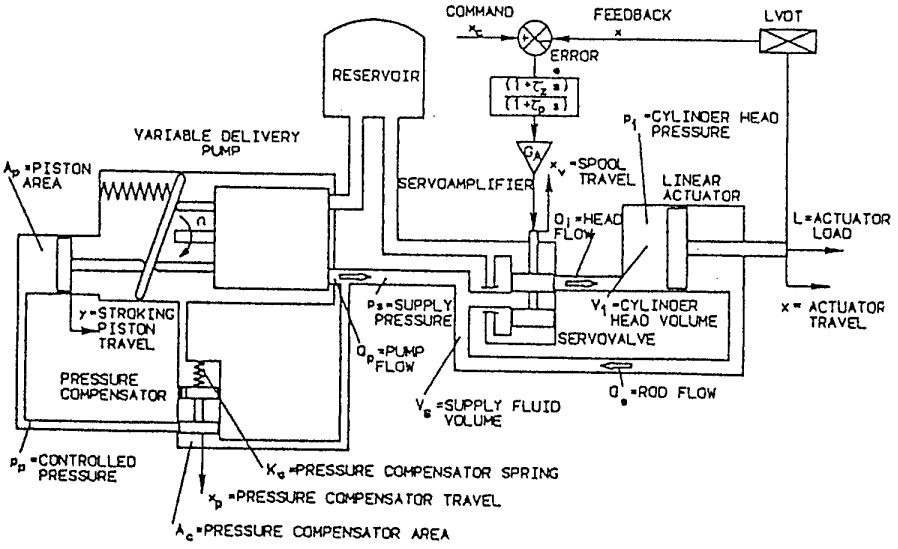

Fig. 7a - NACU Diagram for Linear Model Calculations

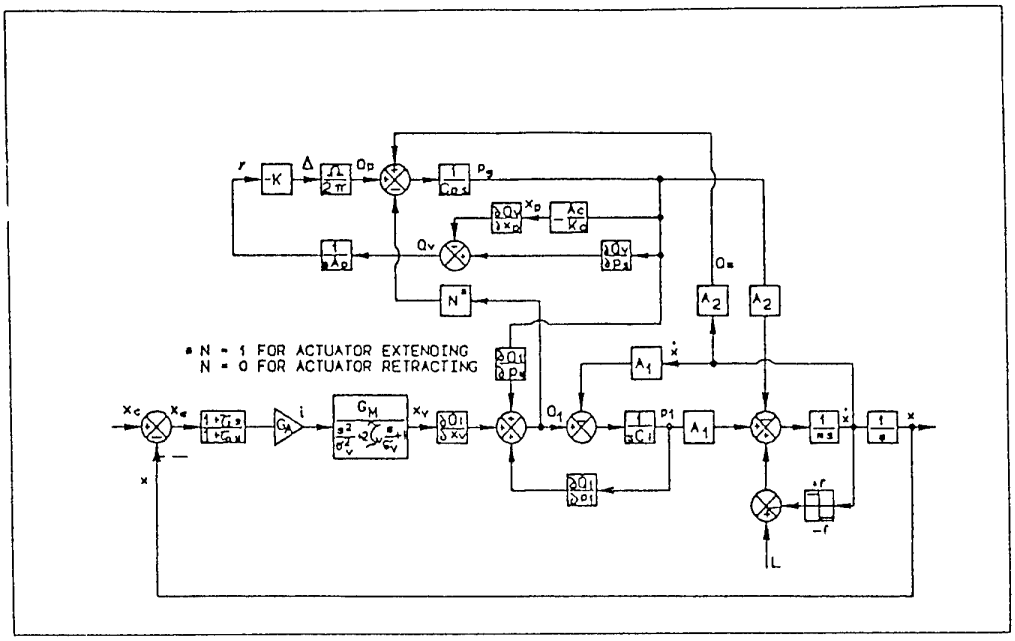

Fig. 7b - NACU Block Diagram

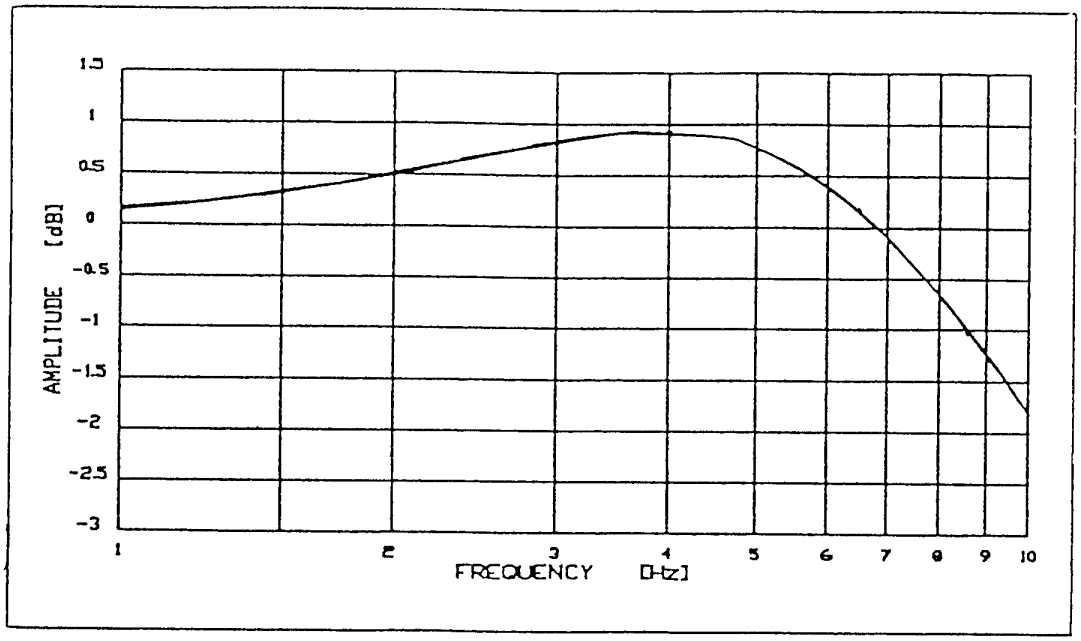

Fig. 8a - NACU Servoloop : Closed Loop Frequency Response at Maximum Pressure

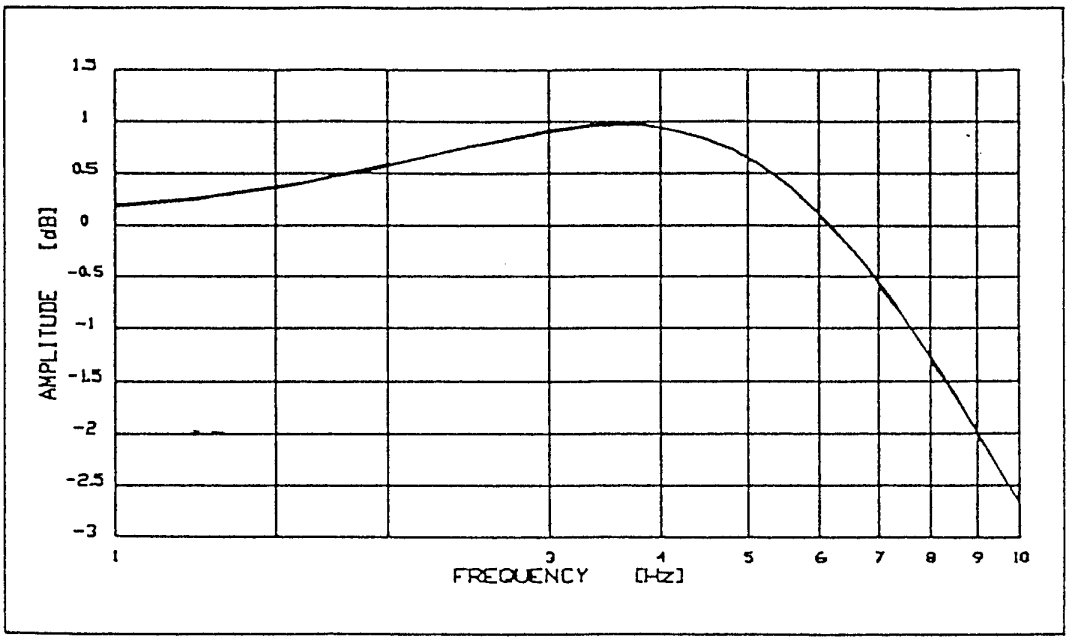

Fig. 8b - NACU Servoloop : Closed Loop Frequency Response at Minimum Pressure

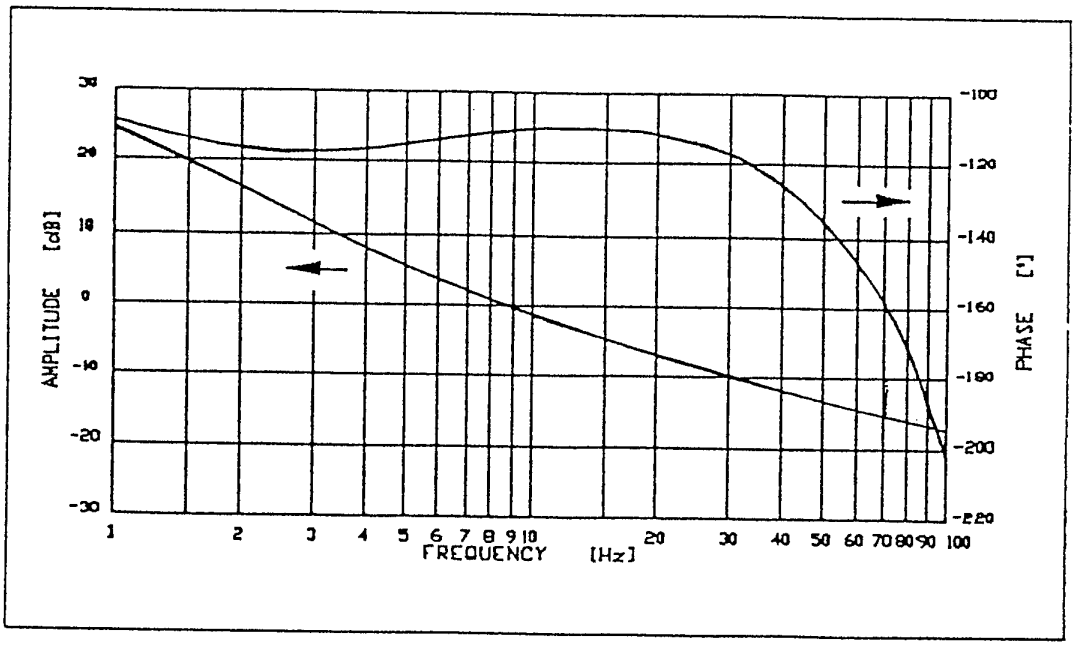

Fig. 9a - NACU Servoloop : Open Loop Frequency Response at Maximum Pressure

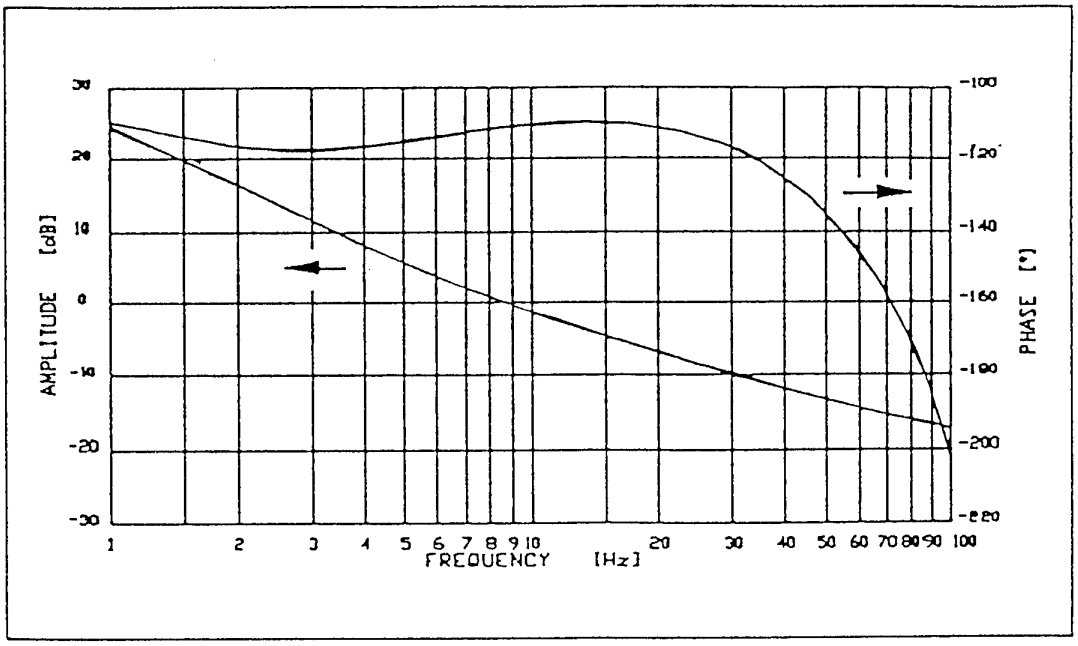

Fig. 9b - NACU Servoloop : Open Loop Frequency Response at Minimum Pressure

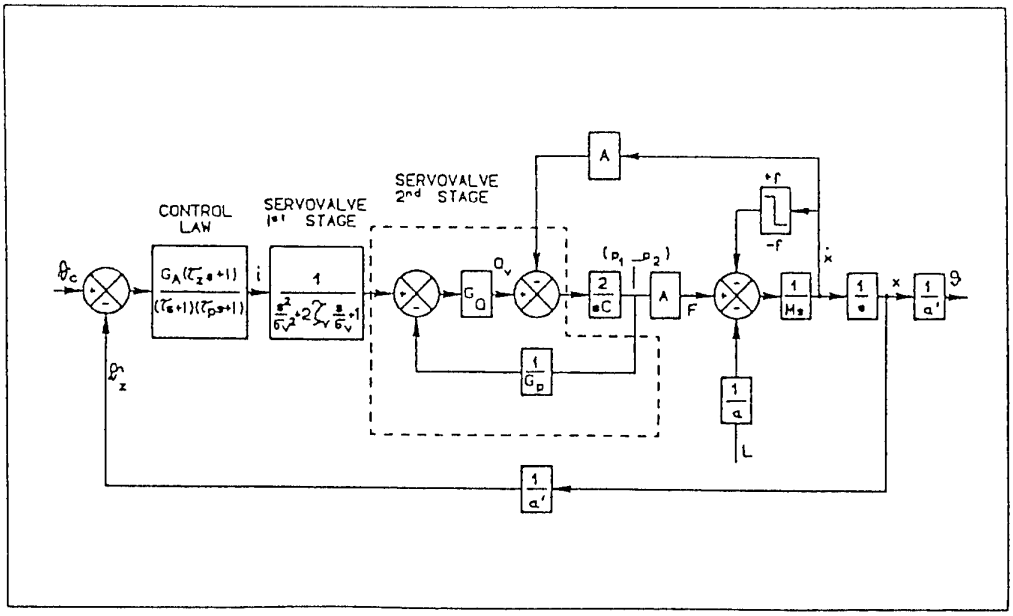

Fig. 10 - VACU Servoloop Block Diagram

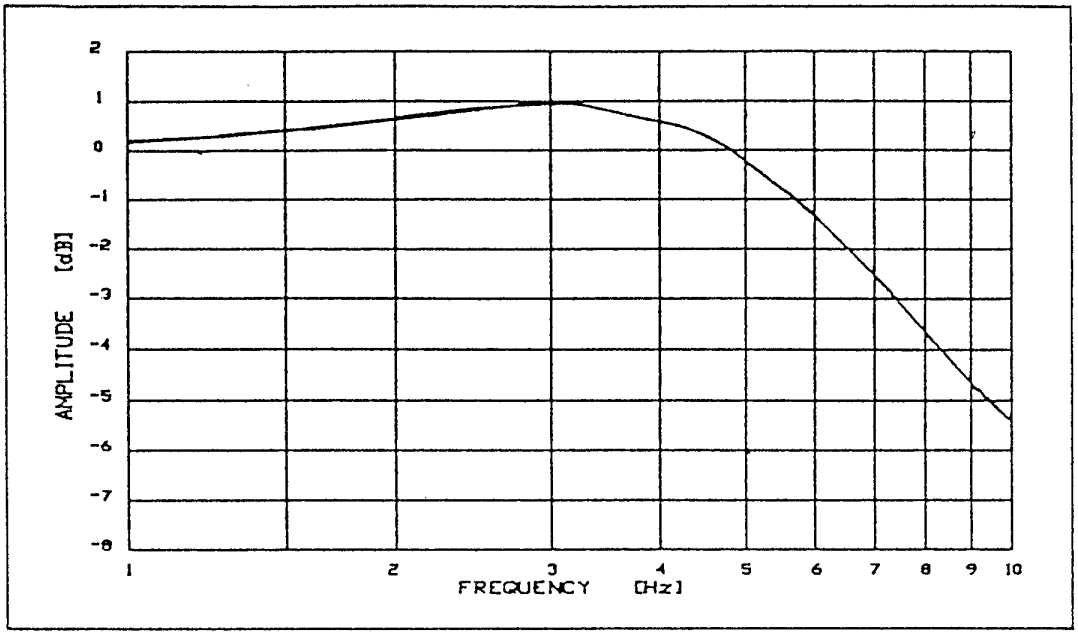

Fig. 11a - VACU : Closed Loop Frequency Response at Maximum Pressure

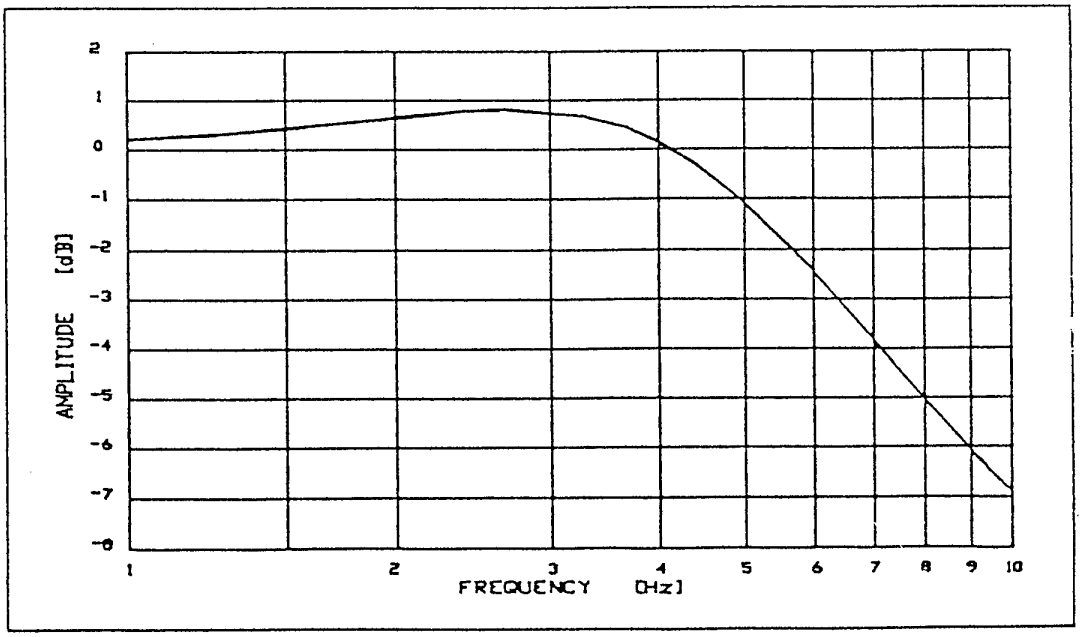

Fig. 11b - VACU : Closed Loop Frequency Response at Minimum Pressure

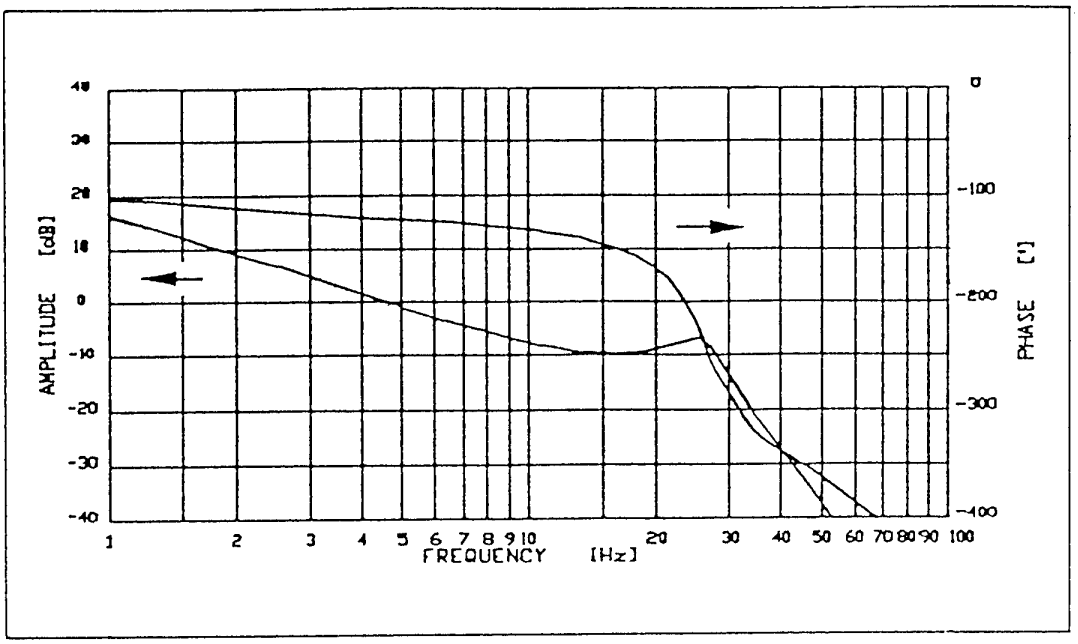

Fig. 12a - VACU : Open Loop Frequency Response at Maximum Pressure

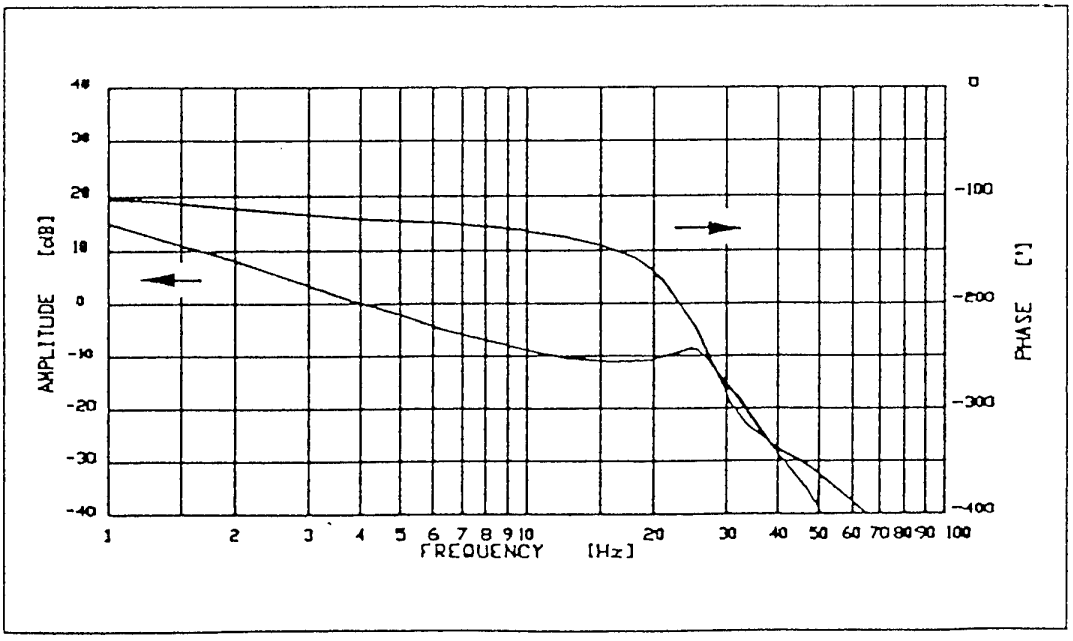

Fig. 12b - VACU : Open Loop Frequency Response at Minimum Pressure

Meeting Discussions

Paper 7: **Actuation System for Variable Exhaust Nozzle and Inlet Guide Vanes on an Advanced Gas Turbine Engine**

Authors: G. Bardone; S. Marchetti; A. Trovati

Discussor: Ludwig Schweikl

Question: The point was made that the pump delivery pressure is adjusted to the load demand by the nozzle via a feed back signal. It was also stated that the nozzle goes through a zero load condition. How is the variable inlet guide vane operation affected under these circumstances? Is there an effect to the disadvantage of that system?

Author's reply: It is true that pump delivery pressure is adjusted, according to nozzle loads. However, this ajustment is limited: Minimum working pressure (even when nozzle loads are around zero) is still approximately 2/3 of maximum working pressure. This limitation of pressure variation, together with closed loop control of nozzle and VIGV actuator positions, keeps the effect on VIGV operation to the minimum. Engine rig and flight tests have confirmed that pump delivery pressure variations do not alter significantly VIGV operation.

La fiabilité des roulements aéronautiques et le comportement en fatigue

Brigitte CHEFTEL/Gérard PATY
TURBOMECA - 64511 BORDES CEDEX FRANCE

0. ABSTRACT

Gas turbine bearings are mechanical components which influence engine performance through this reliability. They link rotating parts to stationnary ones. A bearing failure may have serious consequences such as engine out of order or aeroship manœuvrability losses.

Engine improvements through SFC and weight/power ratio lead to increase rotationnal speeds and other parameters such as applied loads and bulk temperature.

The figure 1 shows the N.Dm evolution of the bearings applied on TURBOMECA gas generators from the 60's year up to future generation.

As other engine manufacturers, TURBOMECA use to design bearings such to prevent typical failures observed on field.

The fatigue defect is the most important to be addressed. In this context, it has been raised that an endurance limit under which no fatigue is developped exists.

A research programme named "ELABOMM" involving bearings and turbine engines Manufacturers and University and funded by the CEC was conducted during four years in order to identify the influencing parameters and the threshold of this endurance limit in dependance of their value.

It resulted a model and a databank available at the engine manufacturer offices which can be used to design bearings with confidence relatively to the expected fatigue behaviour.

1. INTRODUCTION

Les roulements de turbines à gaz font partie de ces composants mécaniques qui contribuent directement aux performances des moteurs aéronautiques au travers de leur fiabilité. Leur rôle de liaison entre les parties fixes et mobiles fait que toute défaillance peut avoir des conséquences catastrophiques telles que pertes d'usage du moteur et de la manœuvrabilité de l'aéronef.

L'évolution constante des turbines visant à l'amélioration des rapports poids/puissance et consommation spécifique conduit bien souvent à augmenter la vitesse de rotation et les autres conditions de service telles que charges appliquées et températures ambiantes.

Il est d'usage d'utiliser le N.Dm (produit de la vitesse par le diamètre primitif du roulement) pour exprimer le niveau de sévérité de fonctionnement.

Le diagramme ci-dessous montre l'évolution du N.Dm des roulements à billes de butée générateur des turbomoteurs TURBOMECA au cours de quatre décennies.

En fait, le N.Dm est un paramètre incomplet puisqu'à valeur égale il peut correspondre à des vitesses très différentes et ne pas traduire les facteurs dépendant du carré de la vitesse.

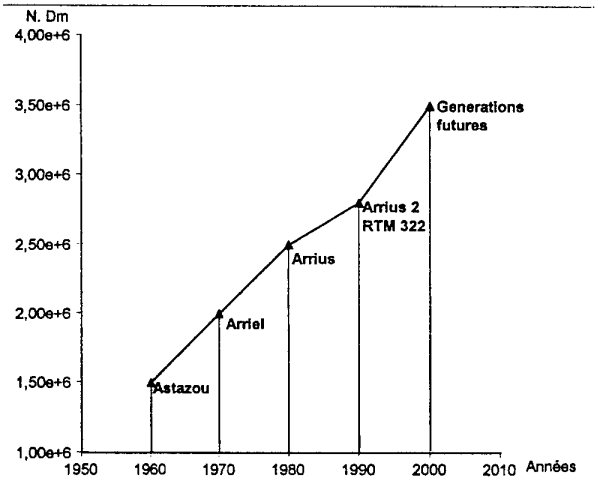

Figure 1 : TURBOMECA Gas Generator bearing N.Dm versus year

Les règlementations de navigabilité évoluent aussi en imposant une plus grande survavibilité en cas de dommages externes ou internes subis par la turbine. Les roulements doivent supporter ces conditions limites.

L'observation des modes de dégradation en service fait que TURBOMECA comme tous les autres motoristes, a identifié les modes de défaillances pouvant intervenir sur ses produits et applique des règles de conception visant à prévenir leur occurence.

Les lignes qui suivent précisent quel rôle est joué par la maîtrise de la fatigue des roulements parmi les règles appliquées et les modèles utilisés lors de la conception des roulements.

Paper presented at the RTO AVT Symposium on "Design Principles and Methods for Aircraft Gas Turbine Engines", held in Toulouse, France, 11-15 May 1998, and published in RTO MP-8.

2. LA FATIGUE DES ROULEMENTS

Ce sont les bagues des roulements dont les pistes sont soumises au passage répété des corps roulants qui subissent principalement les contraintes de fatigue (pression de Hertz).

Les fréquences de passage élevées provoquent des accumulations importantes de cycles en des temps très réduits, comme le montre l'exemple ci-dessous :

Roulement :

Diamètre primitif : 52 mm
Nombre de billes : 15
Diamètre des billes : 8,731 mm

A la vitesse de rotation de 54 100 tr/min, on atteint 10^7 cycles pour :

Bague intérieure : 22 min
Bague exérieure : 28 min

Une durée de fonctionnement de 5000 h correspond donc pour la bague intérieure de cet exemple à $1,35 \times 10^{11}$ cycles.

Cette situation et l'objectif de fiabilité placé à un très haut niveau font de la maîtrise de la fatigue un point-clé de la conception des roulements.

3. LA NOTION DE "LIMITE D'ENDURANCE" - LES PARAMETRES INFLUENTS

Pendant très longtemps les modèles et codes de calculs ont prévu des durées de vie finies quelles que soient les conditions de fonctionnement. Cette situation était réelle mais a évolué avec l'amélioration de la qualité des aciers utilisés.

Désormais, il existe des conditions qui permettent d'espérer une durée de vie infinie. Le concepteur a donc comme objectif de prévoir une définition de composant telle que les conditions de travail resteront à l'intérieur de ce domaine sous limite d'endurance.

Afin de le satisfaire, il est primordial de connaître

- l'étendue du domaine d'utilisation des roulements avec précision
- la limite d'endurance des aciers utilisés et les paramètres qui influent sur cette limite

Ce dernier point a fait l'objet du programme de recherche Brite "ELABOMM" de 4 ans financé par la CEC et impliquant tous les motoristes européens (BMW-RR, MTU, HISPANO-SUIZA, RR, SNECMA, et TURBOMECA), deux fabricants de roulements (FAG, SNR) et deux université (INSA Lyon et CETRIB/INEGI de Porto).

Les paramètres influents qui ont été évalués sont :

- le matériau utilisé
- la pression de Hertz
- les contraintes tangentielles dues au frettage des bagues et à la vitesse
- la température
- les contraintes résiduelles de surface
- la pollution du lubrifiant
- le glissement dans les contacts

4. L'ANALYSE MICROSCOPIQUE

Le projet "ELABOMM" s'est donné comme objectif d'approfondir le processus de fatigue intervenant au cœur du matériau, d'en connaître l'initiation et le développement afin de le modéliser et mieux le maîtriser. Parallèlement, une série importante d'essais appliqués sur une grande variété de matériaux a permis d'apprécier les valeurs pratiques utiles et à les corréler au modèle développé.

Le stade ultime et endommageant de la fatigue des roulements est l'écaillage provoquant la perte de matière. C'est l'aboutissement d'un phénomène initié autour d'une hétérogénéité présente dans le matériau.

Le volume de matière est soumis à un champ de contraintes qui dépend en premier lieu du contact entre deux corps.

4.1. Nature des contacts - Tribologie

Afin de déterminer un champ de contrainte réaliste, il est utile de préciser la géométrie des contacts (topographie réelle).

Les surfaces de frottements et les températures interviennent aussi dans l'élaboration des contraintes.

Enfin, une particule de pollution contenue dans le lubrifiant et circulant dans le contact contribuera aussi à déterminer une surtension locale.

C'est l'ensemble de ces paramètres qui a été pris en compte dans le modèle d'"ELABOMM" par l'INSA pour aboutir à la prédiction du champ de contrainte généré dans un contact de roulement.

4.2. Initiation et développement des fissures

L'expérience montre que les fissures se développent dans le massif soumis à une contrainte dans la zone qui contient une hétérogénéité . En effet l'inclusion (carbure par exemple) et la matrice ont des propriétés mécaniques différentes et donc des comportements sous charge différents. Ces incompatibilités de déformation sont accommodées élastiquement jusqu'à un certain seuil. Au-delà, des dislocations sont générées et se développent pour aboutir aux endommagements par fatigue.

Les laboratoires de l'INSA Lyon ont particulièrement bien mis en évidence les phénomènes que l'on observe sur les applications aéronautiques des roulements, que ce soit par méthode analytique ou par essai sur machine bi-disque.

On retiendra en particulier :

- la forme dite en papillon (voir fig. 2) observable autour d'une hétérogénéité soumise à un champ de contrainte et que l'on observe sur un grand nombre de roulements, que ce soit après quelques centaines d'heures en opération sur moteur ou bien après plusieurs milliers d'heures

Une analyse très fine du processus de formation du papillon et de son développement a permis à l'INSA Lyon d'établir que quatre étapes existent qui ont été identifiées comme des seuils successifs, H1, H2, H3 et H4.

Seuil H1 :

C'est l'état de contrainte autour de l'inclusion en dessous duquel aucune évolution ne se produit (pas de déformation plastique)

Seuil H2 :

Au-delà de H1, il y a déformation plastique autour de l'inclusion. De plus, le caractère cyclique de la sollicitation conduit à une transformation de phase (papillon de fatigue), dans le domaine où se produit cette déformation plastique. Le seuil H2 représente le niveau qui va permettre l'initiation d'une fissure le long du papillon, la déformation plastique ne permettant plus l'accommodation locale.

Seuil H3 :

Entre H2 et H3, la fissure ne se propage pas. En revanche, le dépassement du seuil H3 entraîne la propagation de la fissure qui aboutira à terme à l'écaillage.

Seuil H4 :

C'est le niveau qui entraîne la propagation de la fissure qui aboutira à terme à l'écaillage.

- L'autre point à retenir est la matérialisation de la profondeur de la contrainte maxi et sa dépendance du frottement.

  La profondeur moyenne à laquelle se situe la contrainte maxi est ~ 0,7 a_0 (a_0 étant le 1/2 petit axe de la surface de contact). Les essais sur machines bi-disques sur du matériau M50 ont confirmé ce fait.

  L'INSA Lyon a utilisé une technique d'échographie ultrasons pour détecter les fissures générées au cours d'essais avec et sans glissement dans les contacts (et pour identifier leur progression avec les cycles).

  La figure 3 représente la densité de papillons/fissures détectés en fonction de la profondeur. En particulier, la zone de densité maxi est localisée à la profondeur prévue pour le calcul, de même qu'il se confirme que ce maxi se déplace vers la surface en présence de contraintes tangentielles de surface.

On retiendra de ce chapitre les points suivants :

- la limite d'endurance en fatigue d'un matériau de roulement existe
- la présence de papillons de fatigue dans le matériau représente un niveau de contrainte appliqué qui n'aboutit pas à l'écaillage si le seuil H3 n'est pas dépassé
- on peut analytiquement connaître l'influence de paramètres extérieurs sur la limite d'endurance si on sait les prendre en compte à la fois dans le champ de contrainte et dans les caractéristiques mécaniques de la matrice et des hétérogénéités (l'effet de la température par exemple a été étudié au cours du projet "ELABOMM").

5. L'ANALYSE MACROSCOPIQUE

Afin de créér une banque de données fiable et d'usage pratique pour les concepteurs, des essais de roulements ont été entrepris sur une population importante (principalement par FAG).

Les matériaux suivants ont fait l'objet d'investigations :

- 100 Cr6 (AISI 52 100)
- M 50
- M 50 - NIL
- Cronidur 30

Le tableau 1 en annexe précise le détail des essais conduits par FAG. La démarche retenue fut de soumettre chaque roulement à une durée de fonctionnement équivalente à 5 x 10^6 cycles, sachant que cette durée est suffisante pour générer les déformations plastiques qui sont une condition minimum de l'initiation du processus de fatigue.

Par suite, chaque roulement a été l'objet d'une mesure de contrainte résiduelle en fonction de la profondeur sous la surface de la piste de travail de la bague intérieure.

Afin de pouvoir exploiter ces résultats de manière simple et fiable, FAG a créé le paramètre intitulé : "Characteristic deformation number" (voir fig. 4). Il consiste à utiliser le profil des contraintes résiduelles d'une bague neuve en référence par rapport à celui du specimen testé et d'intégrer numériquement sur une étendue suffisante les valeurs mesurées afin de fournir une image fidèle du domaine soumis au changement d'état.

La figure 5 en annexe illustre l'influence de la pression de Hertz sur la distribution des contraintes résiduelles pour la matière 100 Cr 6 à faible vitesse. On constate l'accroissement des valeurs de contraintes de compression ainsi que le déplacement en profondeur avec l'augmentation de pression de Hertz imposée au cours de l'essai.

Ce type d'essai converti en paramètre "Charactéristic deformation number" ainsi que les essais concernant les autres matériaux se résument sur la figure 6.

Un des enseignements de ce diagramme concerne l'influence de la température sur la tenue en fatigue. Il est d'usage de lier son évolution à celle de la dureté. Or, la figure 6 montre que l'hypothèse utilisée jusqu'à ce jour est fausse.

En plus de ces travaux exécutés par FAG, d'autres partenaires du programme "ELABOMM" ont effectué des essais de roulement d'application aéronautique dans leurs conditions de service (MTU,BMW-RR, SNECMA, SNR).

L'ensemble de ces travaux cumulés a permis de déterminer avec précision les limites d'endurance des matériaux sujets de l'étude ainsi que l'effet des paramètres les plus influents.

Par exemple, l'étude a conclu que la limite d'endurance du M50 si situe entre 2100 et 2250 MPa pour une température de 180/200° C.

6. CONCLUSION

L'industrie aéronautique est de celles qui ont le plus besoin de connaître les limites des matériaux qu'elle utilise afin de toujours mieux optimiser ses produits.

L'application des roulements aux turbines suppose que tous les modes de défaillances sont connus et que leur conception est dirigée pour s'écarter au maximum des conditions qui les exposent à ces risques.

Dans le domaine de la fatigue, la connaissance du seuil d'endurance en dessous duquel aucune rupture ne se développe est essentielle.

Au cours de ces 5 dernières années, les motoristes européens se sont associés avec le support de la CEC afin de faire évoluer leurs connaissances dans ce domaine et ont obtenu des valeurs de référence primordiales pour concevoir les roulements d'applications futures avec un maximum de confiance.

REMERCIEMENTS

Ces travaux ont été effectués dans le cadre du projet BRITE "ELABOMM", Contrat BRE 2 - CT 92 - 0209, financé par la CEC.

Les partenaires de ce programme sont remerciés pour l'autorisation donnée aux auteurs de présenter leurs résultats, en particulier FAG et l'INSA Lyon, ainsi que BMW-RR, HISPANO-SUIZA, MTU, RR, SNECMA et le CETRIB/INEGI de PORTO.

7. REFERENCES

[1] P. LAMAGNERE, R. FOUGERES, G. LORMAND, A. VINCENT, D. GIRODIN, G. DUDRAGNE, F. VERGNE "A Physically Based Model for Endurance Limit of Bearing Steels", ASME Journal of Tribology, January 1998, Vol. 120, p. 1-6.

[2] D. NELIAS, M.L. DUMONT, F. CHAMPIOT, A. VINCENT, D. GIRODIN, R. FOUGERES, L. FLAMAND "Role of Surface Roughness and Operating Conditions on Rolling Contact Fatigue", soumis pour publication dans ASME, Journal of Tribology, 1998.

Type of experiment	Rotational speed	D*N [mm/min]	Hoop stresses	Oil-in temp.	M50	M50 NIL	Cronidur 30	100 Cr 6	Total
Not loaded	-	-		-	1	1	1	1	4
Basic	2500 rpm	$0,42*10^6$	60 MPa	80°C	8	8	8	6	30
Basic	2500 rpm	$0,42*10^6$	60 MPa	160°C	8	8	8	6	30
Basic	2500 rpm	$0,42*10^6$	60 MPa	185°C	8	8	8	6	30
Basic	2500 rpm	$0,42*10^6$	60 MPa	210°C	8	8	8	0	24
Tight interference fit	2500 rpm	$0,42*10^6$	350 MPa	185°C	5	5	6	6	22
High speed	14000 rpm	$2,36*10^6$	110 MPa	70°C	6	6	8	6	26
High speed	14000 rpm	$2,36*10^6$	110 MPa	110°C	6	6	8	0	20
				Total	50	50	55	31	186

Table 1 : Overview of the performed test runs

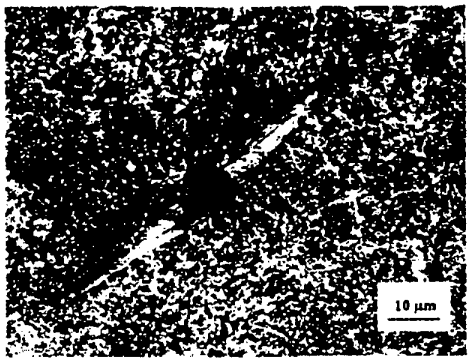

a) Optical micrograph of the W.E.A. observed around an aluminum oxide inclusion found at 0.6 mm beneath the surface (the shear stress is maximum at 0.38 mm beneath the surface)

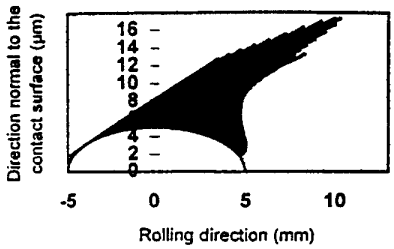

b) Calculated domain (only half of the system is represented)

Figure 2 : Comparison between an experimental W.E.A. and the corresponding calculated domain swept by dislocations (P_H = 4.5 GPa ; 52 100 steel)

(a) Example of inclusion (alumina-calcium aluminate)/W.E.A./microcrack observed by S.E.M. at the location where an ultrasonic echo was detected (depth 1100 µm); M50 steel

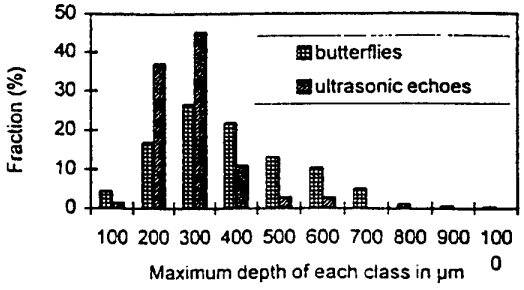

(b) Comparison between distributions of butterflies (optical microscopy) and ultrasonic echoes versus depth; Hertzian pressure 3.5 GPa; 5 10^7 cycles; M50 steel

Figure 3 : Butterflies and ultrasonic echoes versus depth

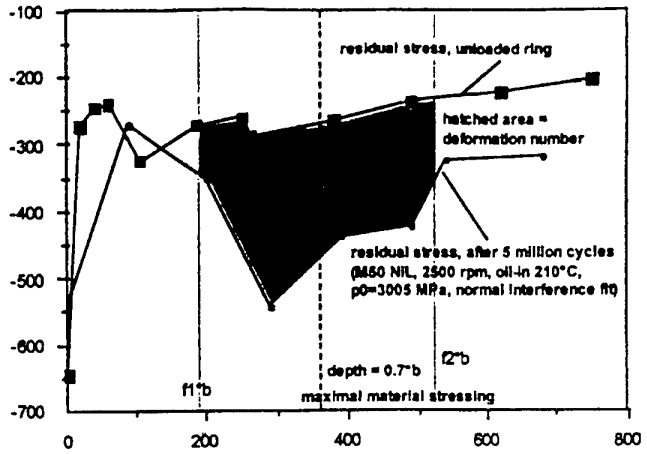

Figure 4 : Definition of the characteristic deformation number

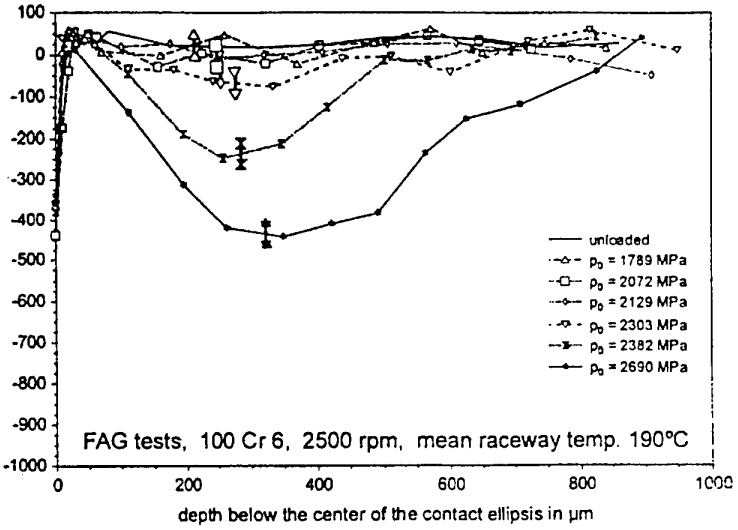

Figure 5 : Changes in residual stress
(FAG tests, 100Cr6, 2500 RPM, 190° C)

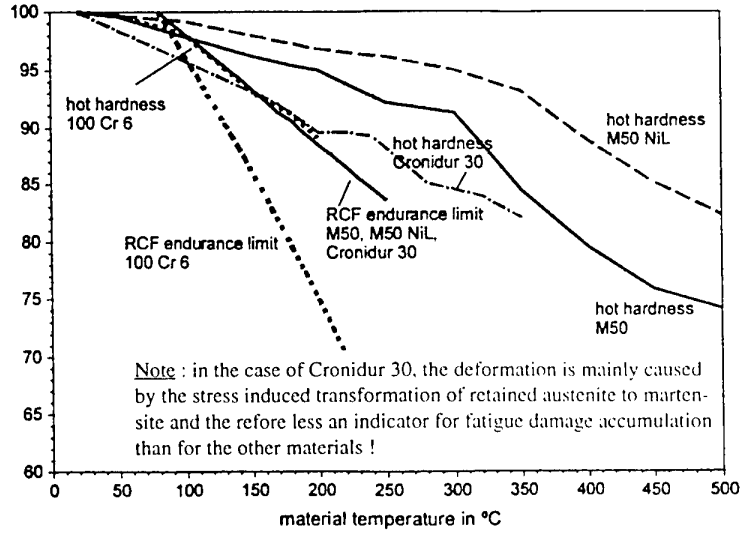

Figure 6 : Influence of the operational temperature on the material strength

Computer Modeling of Heat Generation in Vapor Lubricated Bearings for Gas Turbines

Nelson H. Forster
and
Garry D. Givan

Propulsion Sciences and Advanced Concepts Division
Propulsion Directorate
Air Force Research Laboratory
1790 Loop Road North
Wright Patterson AFB, OH 45433-7103

SUMMARY

Analytical and experimental data are presented for a 30 mm bore ball bearing operating at 31,000 rpm (0.93 MDN where MDN=10^{-6} x shaft diameter x shaft rpm), applied thrust load of 445 N (1.0 GPa maximum Hertzian contact stress), and a steady-state bulk outer race temperature of 425°C (135°C above the initial static temperature of 290°C). The bearing was lubricated with a tertiary-butyl phenyl phosphate (TBPP) delivered from the vapor phase at 325°C. The steady-state bearing torque, at the conditions described above, was 0.07 N-m, resulting in a bearing power loss of 227 W. The major advantage of vapor lubrication in gas turbines is the potential to eliminate the conventional liquid lubrication system, resulting in considerable weight and cost savings benefits. The major disadvantage of vapor lubrication, is the inability to remove the bearing heat generation due to loss of the recirculating liquid lubricant. Although heat transfer poses potential problems, the higher temperature capability of the TBPP vapor lubricant, 600°C compared to 200°C for a recirculating polyolester liquid lubricant, may enable the vapor lubricant to withstand this higher heat generation. This paper takes a first look at examining heat generation in vapor lubricated bearings. To accomplish this, friction measurements were made in a single bearing contact under controlled conditions of rolling and sliding. The lubricant was delivered as vapor to the bearing contact. Friction measurements were made at ball temperatures of 300°C and 400°C; stress loads of 0.75 GPa, 1.00 GPa, 1.25 GPa, and 1.50 GPa; and rolling speeds of 10 m/s and 15 m/s. Using the friction measurement as input data, analysis of the bearing was performed at the experimental test conditions using the bearing computer program ADORE. After validating the computer model to match the experimental bearing heat generation, parametric computer runs were made for the bearing geometry operating at conditions of 1.0 MDN to 2.0 MDN, and applied contact loads of 1.0 GPa and 2.0 GPa. Under the most severe case, 2.0 MDN and 2.0 GPa of contact stress, the 30 mm bore test bearing is expected to generate 3742 watts of heat. Additional analysis is required to convert this heat input to the expected operational bearing temperature, but the results suggest that improved heat transfer will be required to meet the conditions at 2.0 MDN and 2.0 GPa of Hertzian contact stress.

NOMENCLATURE

Symbols

ω	=	Rotation (rad/s)
η	=	Coefficient of friction
T	=	Torque (N-m)
L	=	Load (N)
r	=	Radius (m)
S	=	Slide to roll ratio
u	=	Surface speed (m/s)
c	=	Empirical constants
Q	=	Total bearing heat generation or power loss (W)
M	=	Bearing torque (N-m)
q	=	Heat generation in an individual bearing contact (W)
$\vec{f}$	=	Friction force vector (N)
$\vec{v}$	=	Velocity vector (m/s)
x	=	Coordinate system transverse to the rolling direction (m)
a	=	Hertzian major contact ellipse axis (m)
b	=	Hertzian minor contact ellipse axis (m)

Subscripts

m	=	Number of contacts
n	=	Number of time steps
B	=	Ball
D	=	Disk
S	=	Bearing shaft
i	=	Bearing contact

1. INTRODUCTION

The development of gas turbines operating without a conventional liquid lubrication system has been a research objective for several decades. Potential benefits of eliminating the liquid lubrication system include reductions in cost, weight, and maintenance. Additional benefits are possible if the lubrication method also increases the operating temperature of the mainshaft bearings. Currently, bearing temperatures in gas turbines

Paper presented at the RTO AVT Symposium on "Design Principles and Methods for Aircraft Gas Turbine Engines", held in Toulouse, France, 11-15 May 1998, and published in RTO MP-8.

are limited to approximately 200°C due to thermal limitations of the liquid lubricant. To maintain a 200°C operating temperature, the bearing compartment is cooled with compressor air, heat shielding is added to critical locations, and the lubricant is cooled with an oil to fuel heat exchanger.

Since the 1950's, several approaches have been investigated to develop oil-free bearings; including, powder lubrication (1-4), solid film lubrication (5-7), and more recently vapor phase lubrication (8-14). Of these concepts, vapor phase lubrication has shown the most promise as a high temperature lubricant for high speed rolling element bearings. To accomplish vapor phase lubrication, a small quantity of lubricant is vaporized and transported to the bearing surface (15). After screening several classes of synthetic lubricants (9,12,13), the organophosphates have shown the best overall performance for use in a gas turbine environment (11,14). Our efforts have focused on a tertiary-butyl phenyl phosphate (TBPP) compound to minimize toxicity concerns (11). At temperatures below the vapor point of the lubricant, the organophosphorus compound condenses and functions as a conventional liquid lubricant (13, 16). As the bearing temperature approaches the vapor point, chemical reactions occur between the lubricant and the bearing substrate to form a solid lubricant film (11,16). Although similar to conventional solid lubrication, vapor lubrication possesses a significant advantage, in that the reactivity of the lubricant vapor allows the lubricating film to be rapidly replaced under dynamic conditions (11,16,17). Conventional solid lubricants do not posses this property, and typically the solid lubricated bearing fails shortly after the coating wears away. Analyses of the post-condition of bearing surfaces lubricated with the TBPP lubricant indicates that the reaction film is a complex mixture of inorganic polyphosphate, metal from the substrate, and graphite (11). Phosphate ions liberated during thermal decomposition of the lubricant are thought to serve as a catalyst for the chemical reactions, which generate and replenish the deposition film (11). After deposition, the phosphate structure serves as an anti-oxidant and as a binder for the bearing substrate and graphite (11).

Vapor lubrication in a gas turbine environment is envisioned as a once pass through system (14). This eliminates most of the hardware associated with the lubrication system, including the oil tank, supply and scavenge pumps, heat exchanger, and most of the plumbing hardware. Although this provides significant advantages in reducing engine weight and cost, it also poses significant challenges in handling the heat generation of the mainshaft bearings. Normally, a significant amount of heat is carried away from the bearing by flow of liquid lubricant. Thus, thermal management becomes a significant issue for the practical implementation of vapor lubrication in a gas turbine engine.

This paper outlines an analytical approach for the analysis of the heat generated in a vapor lubricated bearing. The approach involves friction testing and data modeling for vapor lubrication in concentrated contacts; measurement of the experimental bearing torque to calculate the power loss at high speed conditions; and computer modeling of the bearing to match the experimental power loss to the predicted results. Afterwards, the validated model can be used in the analyses of high speed rotating machinery, or for optimizing the bearing internal geometry for improved performance in future systems. As a demonstration, parametric analyses were performed using the test bearing geometry to predict the heat generation under increased rolling speed and higher load conditions. The approach is broadly applicable to all types of lubricants.

2. EXPERIMENTAL

2.1 Lubricant Delivery System

The lubricant delivery system used in the friction measurements and the full-scale bearing test, is shown in Figure 1. The vapor was generated by introducing liquid TBPP into a heated stainless steel tube, 25 mm in diameter by 200 mm long. A syringe pump regulated the flow rate of the lubricant into the heated tube. The lubricant supply rate was maintained at 2.4 ml/hr for the friction testing and at 5.0 ml/hr in the bearing test. Shop air was used as the carrier gas for the vaporized lubricant. The flow rate of air was 283 l/hr for both the friction and bearing evaluation. A thermocouple on the downstream side of the heated tube was used to monitor and control the vapor delivery temperature. The temperature was set at 325°C for the friction measurements and the high speed bearing test. The quantity of lubricant delivered, is sufficiently low, that reclamation of the lubricant is not required, i.e., a once pass through system.

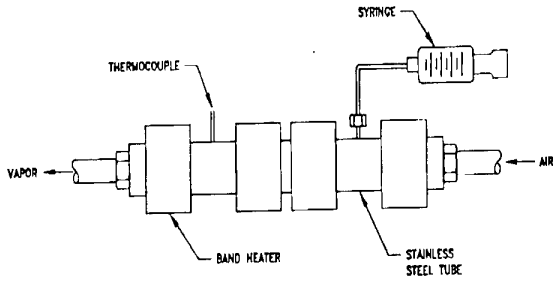

Figure 1. Delivery system for the lubricant vapor. The lubricant is introduced into a heated tube by a commercially available syringe pump. The vapor temperature, measured by the thermocouple in the figure, was controlled at 325°C for the friction and bearing testing.

2.2 Friction Testing

Experimental friction data were obtained with the test rig shown in Figure 2. The friction is generated between a 30 mm ball loaded against a flat disk under dynamic conditions. A torque sensor connected to the drive shaft of the rotating ball measures the moment due to friction. Load is applied to the bearing contact by a pneumatic cylinder, which loads the rotating disk against the rotating ball. The friction coefficient is calculated using the following relation:

$$\eta = \frac{T}{Lr_B} \qquad (1)$$

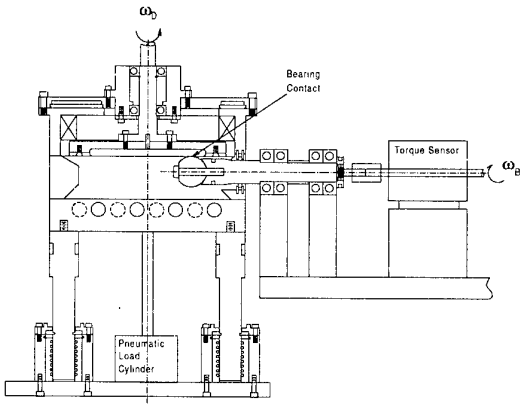

Figure 2. Cross section of the Rolling Contact Friction Tester. Rotations of the disk shaft and ball shaft are depicted by ω. The torque sensor measures the friction in the bearing contact under a combination of rolling and sliding conditions. Load is applied to the bearing contact through the pneumatic cylinder.

The surface speed of the ball and disk are independently computer controlled by two DC servomotors. After reaching a rolling condition, S = 0, slip is introduced into the contact by varying the speed of the ball and disk above and below the rolling speed. The rotational speeds of the ball and disk are sampled during a test to calculate the slide to roll ratio, S. Where S is defined by the amount of slip in the contact, divided by the average rolling speed:

$$S = \frac{u_B - u_D}{\frac{1}{2}[u_B + u_D]} \qquad (2)$$

The experimental friction data were modeled using the following empirical relationship (19):

$$\eta = (c_1 + c_2 S)\exp(-c_3 S) + c_4 \qquad (3)$$

The empirical constants, c_1 through c_4, were determined using a Marquardt-Levenberg nonlinear regression algorithm (20). Equation 3 allows the friction coefficient to be calculated for any combination of rolling and sliding conditions. To calculate the friction coefficient for negative values of the slide to roll ratio, requires using absolute values for S and η.

2.3 High Speed Bearing Testing

A cross section of the High Speed Bearing Tester is shown in Figure 3. The test bearing is mounted on a shaft, driven by an integral air turbine. The lubricant was delivered to the bearing through a 6.35 mm diameter tube as shown in the figure. Thrust load was applied to the bearing through an annulus containing the bearing outer race. A moment arm connected to a load transducer restricted rotation of the annulus. The applied moment, transferred from the outer race of the bearing to the load transducer, was used to calculate the bearing torque. The mass of the annulus is 2.39 kg, which contributes an additional 23.4 N radial load to the bearing. Also, vibration of the annulus contributes dynamic forces and applied moments to the bearing, which are not accounted for in the reported bearing loads. The bearing power loss, which is equivalent to the total heat generated by the bearing, was calculated by the following equation:

$$Q = M\omega_S \qquad (4)$$

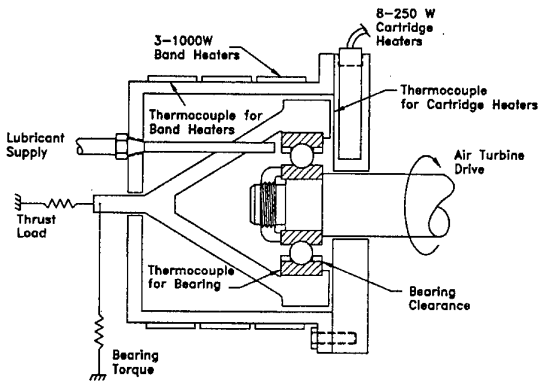

Figure 3. Cross section of the High Speed Bearing Tester. The shaft speed is controlled by an air turbine drive. The vapor delivery system was connected to the tube labeled lubricant supply. The bearing temperature was taken from the thermocouple mounted to the bearing outer race.

2.4 Bearing Geometry, Cage Selection, and Material Properties

The internal geometry of the test bearings is summarized in Table 1. The bearing envelope geometry conforms to the Anti-Friction Bearing Manufacturers Association (AFBMA) standard for 206 size bearings. The bearings were machined to an ABEC 5 tolerance, which is considered a precision class ball bearing.

Table 1. - Bearing Geometry	
Class: 206, ABEC 5, Outer Land Guided Cage	
Contact Angle	24°
Outer Race Curvature	0.515
Inner Race Curvature	0.527
Pitch Diameter (m)	4.618×10^{-2}
Radial Clearance (m)	6.10×10^{-5}
End Play (m)	3.05×10^{-4}
Ball Diameter (m)	9.52×10^{-3}
Cage Land Clearance (m)	2.54×10^{-4}
Cage Width (m)	1.45×10^{-2}
No. of Balls	13

The material properties of the bearing components are summarized in Table 2. M50 tool steel was selected as the bearing race material. NBD 200 Si_3N_4 ceramic was used for the rolling elements. The cage was made form AISI 4340 steel with approximately 50 μm of silver plating. The silver plating is used as a boundary lubricant for the high sliding conditions.

Table 2. – Bearing Material Properties at 400°C

Material	4340	M50	Si3N4
Yield Strength (MPa)	500	1300	
Elastic Modulus (GPa)	170	175	320
Poisson's Ratio	0.30	0.29	0.26
Coef. Of Thermal Expansion (μm/°C)	15.0	11.0	2.0
Thermal Conductivity (w/m k)	34	25	21
Density (kg/m^3)	7750	8190	3160

2.5 Computer Modeling of the Bearing

The test bearing was modeled using the computer program, Advanced Dynamics of Rolling Elements (ADORE) (19). The input data for the computer model consists of: friction data, bearing geometry, bearing material properties, shaft speed, and bearing load. Internal to the bearing solution are the differential equations of motion for each bearing element. The equations are expressed in six degrees of freedom, and are interdependent on the solutions of neighboring elements. The program marches forward in time, and the derivative vector output of velocity and acceleration for each element is used as the input vector for the solution in the next time step. The output of the program consists of several parameters including, contact stresses, dynamic collision forces, friction, and heat generation of each bearing element. The following relation calculates the heat generation in a single contact, at a particular time step:

$$q_i = \frac{1}{2a}\int_{-a}^{a} \vec{f} \bullet \vec{v}\, dx \qquad (5)$$

The summation of all of the individual power losses provides the total power loss for a specific time step. The time averaged value of the total power loss, shown in Equation 6, is equal to the power loss determined shown in Equation 4.

$$Q = \frac{1}{t_n}\int_0^{t_n} \sum_1^m q_i\, dt = M\omega_s \qquad (6)$$

3. RESULTS

3.1 Friction Data

The experimental friction data for a ball temperature of 300 °C and 400°C, rolling speeds of 10 m/s and 15 m/s, and maximum Hertzian contact stress of 0.75 GPa, 1.00 GPa, and 1.25 GPa are shown in Figures 4(a-d). The vertical-axis in the figures is the friction coefficient defined by Equation 1. The horizontal-axis is the slide to roll ratio as defined by Equation 2. Typical of friction measurements in rolling contacts, the slope of the curve is very steep near rolling conditions. Low slip conditions are particularly relevant for the friction between the rolling elements and the bearing raceway. Under high slip conditions the friction levels off and in many cases starts to decrease with increasing slip. The high slip region is pertinent to the sliding cage surfaces. It is also interesting to note that the friction coefficient decreases at 400°C compared to 300 °C, this is consistent with the bearing torque measured in sub-scale bearing tests (13). Also, the friction coefficient is relatively unaffected by increasing speed and decreases with increasing load. This is opposite of the trend expected for liquid lubricants (21). This result is attributed to the solid nature of the lubricating film.

Also shown in Figures 4(a-d), are the empirical solutions obtained from regression analysis using Equation 3. The empirical solutions are shown as solid lines. In general the empirical solution does a good job of fitting the experimental data. The constants c_1 through c_4 are summarized in Table 3.

Based on the trends with speed, load, and temperature in the experimental friction data, a friction curve was generated for the operating conditions of the bearing. For the inner race conditions of 425°C, 39 m/s

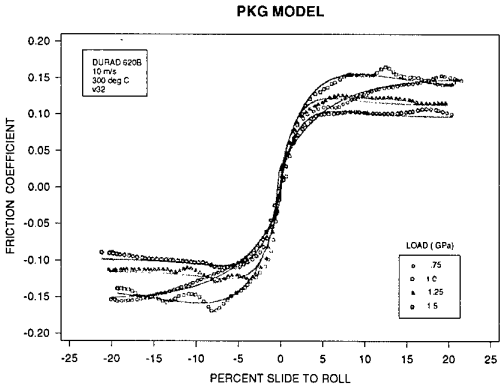

Fig 4(a), 10 m/s rolling speed and ball temperature of 300°C

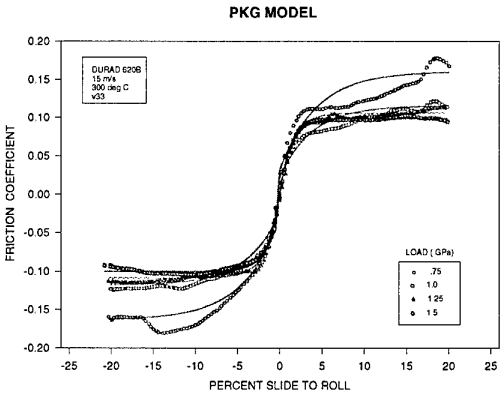

Fig 4(b), 15 m/s rolling speed and ball temperature of 300°C

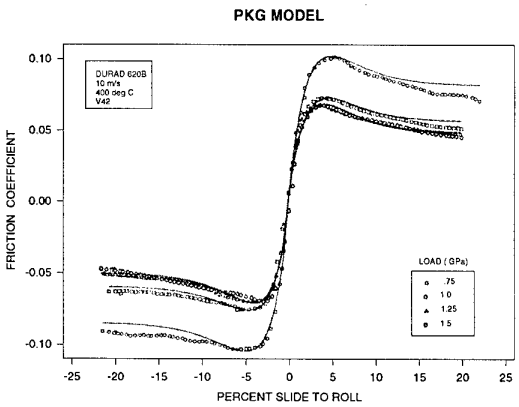

Fig 4(c), 10 m/s rolling speed and ball temperature of 400°C

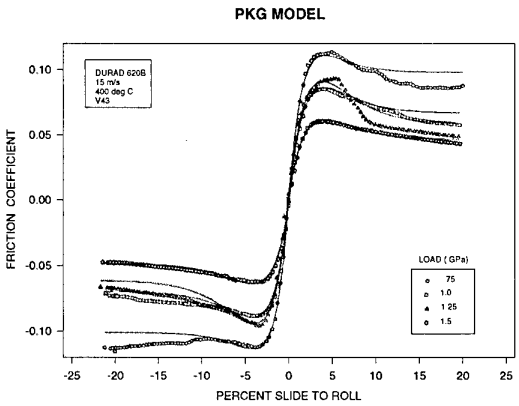

Fig 4(d), 15 m/s rolling speed and ball temperature of 400°C

Figure 4 (a-d). Friction coefficient as a function of the slide to roll ratio. Each curve represents a different maximum Hertzian stress condition; 0.75, 1.00, 1.25, and 1.5 GPa. Experimental data are shown as symbols. Empirical solutions from the friction model are shown as solid lines.

rolling speed, and 1.0 GPa of Hertzian stress, the maximum traction coefficient was estimated to be 0.11. For the lightly loaded, high sliding conditions of the cage-land and cage-pocket contacts, the maximum traction coefficient was estimated to be 0.22. The higher friction coefficient for the lightly loaded cage contacts is consistent with the trends in the experimental data where the friction coefficient increases with decreasing load. It is also evident from the experimental results that the friction was higher at the cage-land surface. Small adjustments were made to the friction values to match the computer predicted power loss to the experimental power loss. The final results are the estimated friction curves for the ball-race and the cage-race contacts, as shown in Figure 5. The coefficients c_1 through c_4 for the friction solution are also summarized in Table 3. These conditions were used as the friction input in the bearing heat generation analysis.

3.2 High Speed Bearing Testing

A plot of the bearing torque, speed, and temperature versus operating time is shown in Figure 6. The bearing reached a steady-state temperature of 425°C, 135 °C above the initial static bearing temperature. The bearing also reached a steady-state torque condition of approximately 0.07 N-m. Using the shaft rpm of 31,000 rpm, the total bearing power loss is 227 watts. The condition of the bearing is shown in Figure 7. Aside from wear on the sliding surfaces of the cage, the bearing is in good shape.

Table 3. – Equation (3) constants for empirical solution and generated friction solution

Speed (m/s)	Temperature (°C)	Load (GPa)	c_1	c_2	c_3	c_4
10	300	0.75	-0.1305	4.308e-5	-0.2307	0.1625
		1.00	-0.0942	1.123e-12	-0.2611	0.1171
		1.25	-0.1051	6.394e-5	-0.6455	0.1075
		1.50	-0.0980	2.434e-5	-0.7314	0.0994
15	300	0.75	-0.0627	0.0269	-0.3221	0.0751
		1.00	-0.0539	0.0163	-0.3240	0.0587
		1.25	-0.0495	0.0189	-0.2829	0.0514
		1.50	-0.0384	0.0172	-0.2943	0.0420
10	400	0.75	-0.0794	0.0390	-0.3486	0.0830
		1.00	-0.0544	0.0306	-0.3590	0.0577
		1.25	-0.0453	0.0332	-0.3761	0.0503
		1.50	-0.0438	0.0332	-0.3670	0.0490
15	400	0.75	-0.1029	0.0483	-0.4924	0.0993
		1.00	-0.0683	0.0414	-0.4018	0.0680
		1.25	-0.0640	0.0524	-0.3730	0.0595
		1.50	-0.0448	0.0290	-0.3835	0.0472
39	425	Ball Race	-0.1035	0.0371	-0.4405	0.1036
		Cage Race	-0.2139	0.0314	-0.2140	0.2111

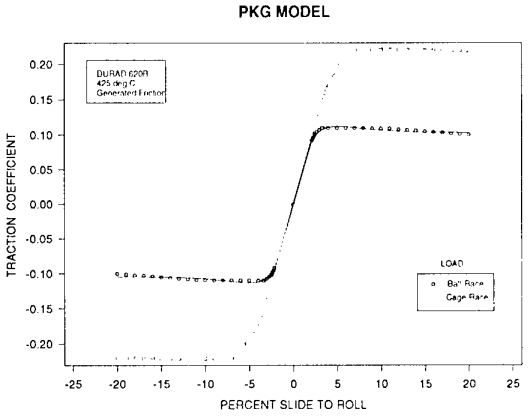

Figure 5. Friction curves for modeling heat generation in a vapor lubricated bearing. The maximum friction coefficient for the lightly loaded cage is 0.22 and 0.11 for the ball/race contact.

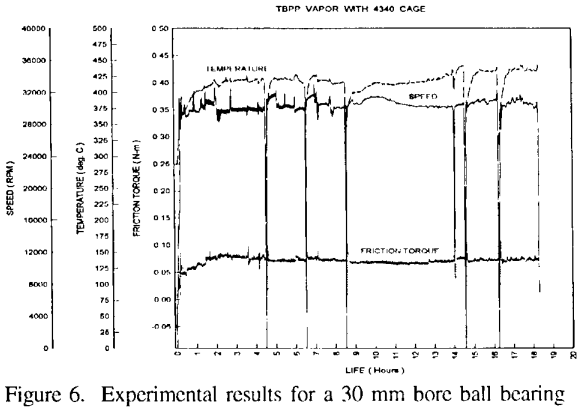

Figure 6. Experimental results for a 30 mm bore ball bearing lubricated with a tertiary-butyl phenyl phosphate lubricant delivered as a vapor at a temperature of 325°C. Test conditions: 425°C outer race temperature, 31,000 shaft rpm, and 445 N axial load.

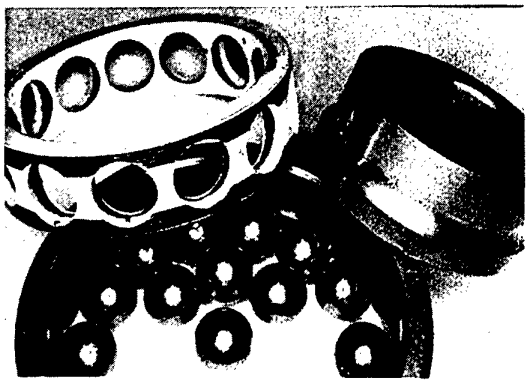

Figure 7. Condition of the test bearing after nineteen hours of testing at 425°C outer race temperature, 31,000 shaft rpm, and 445 N axial load. The rolling elements and bearing race are still in good shape. There is considerable wear in the sliding surfaces of the cage.

3.3 Bearing Computer Modeling

Output from the computer program ADORE are summarized in Table 4. The first condition of 31,000 rpm and 445 N thrust load corresponds to the experimental test conditions. The total time average power loss of 226 W, compares favorably to the experimental value of 227 W. At the 31,000 rpm, 445 N thrust load condition, the outer and inner race contact angles change form the initial value of 24°, to 16.8° and 37.6°, respectively. The contact angles formed between the rolling element and the outer and inner race are defined in Figure 8. The change in contact angles is due to centrifugal force on the rolling elements, which tends to throw the elements towards the center of the outer race. When the contact angles are different, a common axis of rotation does not exist, and the ball will have a combined motion of spinning and rolling. The slip from spinning is accounted for in the spin/roll ratio and the slip from rolling

Table 4. – Analytical Results for Bearing Performance and Heat Generation - Analytical Solution for Time Step n=5000

Shaft Speed (rpm)	31,000	66,700	66,700
Applied Thrust Load (N)	445	445	3002
Applied Radial Load (N)	23.4	23.4	23.4
Cage Unbalance (gm-cm)	0.23	0.23	0.23
Contact Angle (Deg)			
Outer Race	16.8	4.74	20.4
Inner Race	37.6	39.5	38.1
Hertzian Contact Stress (GPa)			
Outer Race	0.97	1.43	1.72
Inner Race	1.04	1.07	1.93
Rolling Element / Race Contact Load (N)			
Outer Race	123	398	667
Inner Race	64.9	68.9	409
Rolling Element / Race Slip Velocity (m/s)			
Outer Race	0.47	1.60	2.82
Inner Race	2.11	7.06	8.05
Spin / Roll Ratio			
Outer Race	-0.024	-0.0135	-0.054
Inner Race	0.473	0.717	0.410
Friction Coefficient			
Outer Race	0.071	0.091	0.108
Inner Race	0.109	0.104	0.103
Cage – Land Parameters			
Sliding Speed (m/s)	36.5	83.7	77.6
Centrifugal Load on Land 1 (N)	6.36	42.3	32.1
Centrifugal Load on Land 2 (N)	6.98	42.3	33.6
Contact Losses – q_i (W)			
(1)-Outer Race/Cage Land 1	38.4	781.8	549.4
(2)-Outer Race/Cage Land 2	56.1	780.4	575.8
(3)-Outer Race/Elements	24.7	121.0	561.4
(4)-Inner Race/Elements	68.2	236.1	1549.5
(5)-Elements / Cage Pocket	22.9	304.4	407.3
Time Average Total Power Loss – Q(W)	226	2515	3742

is accounted for in the rolling element slip velocity. The values listed in Table 4 are the average values of the thirteen rolling elements. The friction coefficient in Table 4 is the value derived from the dynamic slip conditions, and the friction curve for the ball-race contact shown in Figure 5. The individual contact losses, q_i, are calculated using the analytical slip profile and the friction force as the independent variables in equation 5. The various contacts labeled (1) through (5) in Table 4 are defined in Figure 8. The time average value at the bottom of Table 4 represents the total power loss, Q, as calculated by equation 6.

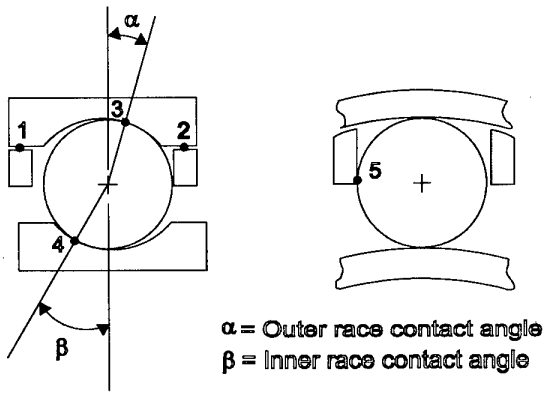

Figure 8. Contacts in a ball bearing: (1) Outer Race / Cage-land 1 (2) Outer Race / Cage-land 2 (3) Outer Race / Rolling element contact (4) Inner Race / Rolling element contact (5) Rolling element / Cage contact.

This total value at a particular time step varies about the total time average value, depending on the dynamic interactions for that particular time step. The time average value is the computer model estimate of the power loss from bearing torque.

The middle column in Table 4 shows the effect of speed on bearing performance. The contact angle at the outer race is substantially reduced due to increased centrifugal force. Similarly, the contact load and stress between the rolling element and bearing race has significantly increased due to centrifugal force. The increased sliding, with higher loads, leads to higher friction in the sliding contacts. Additionally, the rate at which frictional energy is generated increases at higher speed conditions. These factors combine to increase the bearing heat generation by over one order of magnitude in going from the 31,000 rpm to 66,667 rpm, under the same thrust load condition. For a 30 mm bore bearing, the 31,000 rpm and 66,667 rpm shaft speeds corresponds to bearing speeds of 0.93 MDN and 2.0 MDN.

The third column in Table 4 list results for a bearing speed of 66,667 rpm and 3002 N of applied thrust load. The increased thrust load increases the outer race contact angle. This should reduce slip in the bearing. However, the slip remains unusually high for this particular bearing geometry. The friction coefficient between the rolling elements and the outer and inner race, 0.108 and 0.103, are near the maximum value of 0.11. Redesigning the internal geometry for high speed conditions could substantially reduce the heat generation for this particular bearing. This represents another potential application of how computer modeling of bearing performance can be used.

The effect of speed and load, where load is defined by the contact stress at the rolling element-inner race contact, is shown in Figure 9. Speed has the dominant effect on heat generation in high DN bearings.

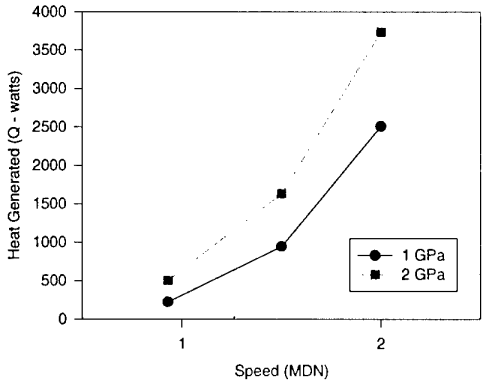

Figure 9. ADORE heat generation values predicted at speeds of 0.97, 1.5, and 2.0 MDN with inner race Hertzian stresses of 1 and 2 GPa

4. CONCLUSIONS

The friction coefficients obtained with vapor lubrication are approximately half the values obtained with powder lubrication (22), and are approximately one order of magnitude higher than values obtained with a high quality synthetic liquid lubricant used in aviation gas turbines (21). Even so, the experimental results indicate that vapor lubrication can maintain steady-state operation in rolling element bearings operating at speeds near 1.0 MDN and Hertzian contact stress of 1.0 GPa. We have not been successful in obtaining equivalent performance with metal bearings operating with solid lubricants, or with powder lubricants, at these bearing conditions.

The improved results with vapor lubrication are attributed to the quick replenishment of the lubricating film due to chemical reactions with the vapor lubricant.

Using the friction curves shown in Figure 5, the computer program ADORE predicts 226 W of heat at the experimental bearing conditions. This agrees closely with the experimental value of 227 W, providing confidence that the model can be extrapolated to approximate the bearing heat generation under different operating conditions. Using this approach, ADORE predicts 3742 W of heat at the maximum condition of 2.0 MDN and 1.92 GPa of Hertzian contact stress. While specific analysis have not been performed to convert this power loss to bearing temperature, the 3742 W level raises concern that vapor lubrication will not be able to handle the upper end bearing conditions in high performance gas turbines.

The analytical results also indicate that the primary driver in bearing heat generation is the bearing speed. Mathematically this can be seen from equation 6, where the total power loss is equal to the bearing torque multiplied by the bearing speed. Bearing torque increases with increasing speed, so the net effect is that power loss increases in a near quadratic fashion. The increase in torque with increasing bearing speed is in part, due to the centrifugal effects on the ball, which induce higher ball spin. Changing the race curvatures to reduce the difference in contact angle under dynamic conditions can reduce ball spin. Another application of the validated computer model, is to optimize the internal geometry of the bearing for a given speed condition, to minimize the ball spin, and hence, reduce the bearing heat generation.

The following is a list of tasks, which are now either planned, or are underway, as follow on work to the research described in this paper.

1. Finite element modeling of the heat generation to predict temperatures of the bearing elements under dynamic conditions.
2. Improved lubrication of the sliding surfaces of the cage.
3. Optimizing the bearing internal geometry to reduce ball spin.
4. Experimental bearing testing at higher speeds and load conditions to validate the model over a range of operating conditions.
5. Investigating composite cage materials to improve heat transfer, and reduce centrifugal loading effects.
6. Friction testing of the cage specimens under lightly loaded conditions to improving friction model of the bearing cage.

ACKNOWLEDGMENTS

The authors wish to thank the U.S. Air Force for permission to publish this work, with particular emphasis in the support and encouragement of Major Hugh C. DeLong, Air Force Office of Scientific Research, Bolling AFB, Washington D.C. They also wish to acknowledge the contributions of John Murry and David Gerardi of UES Inc. for performing the traction and high speed bearing testing.

REFERENCES

1. Macks, E.F., Nemeth, Z.N., Anderson, W.J., "Preliminary Investigation of Molybdenum Disulfide – Air-Mist Lubrication of Roller Bearings Operating to DN Values of $1x10^6$ and Ball Bearings Operating to Temperatures of 1000°F," NACA RM ES1 631 (1951).
2. Anderson, W.J., "Advanced Bearing Technology," NASA SP-38 (1965), Eds. Bisson, E.E., Anderson W.J., pp 309-370.
3. Wilson, D.S., "Powdered and Gaseous Lubricants for Use in Ball Bearings at Temperatures from Room Temperature to 1200°F," ASD-TDR-62-465 (1962), Eds. Beane, G.A., Berkey, K.L., pp 201-209.
4. Wallerstein, S., "Application of a Gas Powder Lubrication System to a Gas Turbine Engine," AFAPL-TR-65-43 (1965).
5. Devine, M.J., Lamson, E.R., Bowen, J.H., "The Lubrication of Ball Bearings with Solid Films," ASME 61-UBS-11, (1961).
6. Dayton, R.D., "Experimental Investigation of Ag-Hg-WTFE-$MoSe_2$ Solid Lubricated Ball Bearings for High Speed, High Temperature, and High Load Applications," AFAPL-TR-71-100 (1971).
7. Boes, D., "Development of Light Weight Solid Lubricated Bearing Retainers," Air Force AFAPL-TR-78-72 (1978).
8. Graham, E.E., Nesarikar, A., Forster, N.H., Givan, G.D., "Vapor Phase Lubrication of High Temperature Bearings," Lubr. Eng., **49**, 9, pp 713-718 (1993).

9. Rao, A.M.N., "Identification of an Alternative Lubricant for Vapour Phase Lubrication," M.S. Thesis, Cleveland State University, (1993).
10. Forster, N.H., "Rolling Contact Testing of Vapor Phase Lubricants," AGARD-CP-589, pp 15-1-15-8, (1996).
11. Forster, N.H., "High Temperature Lubrication of Rolling Contacts with Lubricants Delivered from the Vapor Phase and as Oil-Mists," Ph.D. Dissertation, University of Dayton (1996).
12. Forster, N.H. and Trivedi, H.K, "Rolling Contact Testing of Vapor Phase Lubricants: Part I - Material Evaluation," Trib. Trans., **40**, 3, pp 421-428 (1997).
13. Forster, N.H. and Trivedi, H.K, "Rolling Contact Testing of Vapor Phase Lubricants: Part II - System Performance Evaluation," Trib. Trans., **40**, 3, pp 493-499 (1997).
14. Van Treuren, K.W., Barlow, Heiser, W.H., Wagner, M.J., Forster, N.H., "Investigation of Vapor Phase Lubrication in a Gas Turbine Engine," J. of Engineering for Gas Turbines and Power, **120**, pp 1-6 (1998).
15. Graham, E.E., and Klaus, E.E., "Lubrication from the Vapor Phase at High Temperatures," ASLE Trans., **29**, pp 229-234 (1985).
16. Klaus, and E.E. Duda, J.L., "Vapor Phase Lubrication Development for Engines," SAE Publ. SP-256, pp 541-550 (1991).
17. Maki, J.F. and Graham, E.E., "Vapor Phase Deposition on High Temperature Surfaces," Trib. Trans., **33**, 4, pp 595-603 (1990).
18. Gupta, P.K, Advanced Dynamics of Rolling Elements, Springer-Verlag, New York, pp 123-127 (1984).
19. Gupta, P.K, Advanced Dynamics of Rolling Elements, Springer-Verlag, New York, pp. 79-80 (1984).
20. Marquardt, D.W., "An Algorithm for Least Squares Estimation of Nonlinear Parameters," J. Soc. Indust. Appl. Math., **11**, 2, pp 431-441 (1962).
21. Forster, N.H., Schrand, J.B., Gupta, P.K., "Viscoelastic Effects in Mil-L-7808 Type Lubricant, Part II: Experimental Data Correlations," Trib. Trans., **35**, 2, pp 275-280 (1992).
22. Heshmat, H, "Rolling and Sliding Characteristics of Powder-Lubricated Ceramics at High Temperature and Speed," Lubr. Eng., **49**, 10, pp. 791-797 (1993).

Meeting Discussions

Paper 9: Computer Modeling of Heat Generation in Vapor Lubricated Bearings for Gas Turbines

Authors: Nelson H. Forster, Garry D. Givan

Discussor: Saeed Farokhi

Question: Where does the magnetic bearing fit in the picture?

Author's reply: In the near-term, the primary application for vapor lubrication is the expendable engine. Magnetic bearings are being developed for man operated engines, which typically require 4000 hours of life from the bearings before overhaul. However, even in magnetic bearings, vapor lubrication may play a role as the lubricant for a back-up bearing, used to assist in overload or power out situations.

Discussor: G. T. Cook

Question: Are there potential applications for low speed/sliding applications, such as variable stator vane or variable nozzle spindles? Does TBPP show better characteristics to existing materials? Could such a surface treatment be replenished or reactivated as a maintenance activity on overhaul?

Author's reply: TBPP should be an effective lubricant for variable stator vanes or spindles. However, its primary advantage over conventional solid lubricants, is the material's ability to chemically react with a metal substrate to form a vapor deposited lubricant film. The reaction rates can be set to match the wear rate of the film to maintain steady-state film characteristics. To accomplish this, requires supplying the lubricant at a flow-rate of a few ml/hr. This may not be practical for variable stator vanes.

Advanced Seal Technology Role in Meeting Next Generation Turbine Engine Goals

Bruce M. Steinetz and Robert C. Hendricks
National Aeronautics and Space Administration
Lewis Research Center
MS 23-3
21000 Brookpark Road
Cleveland, Ohio 44135, USA

John Munson
Allison Engine Company
Indianapolis, IN 46206-0420, USA

Abstract

Cycle studies have shown the benefits of increasing engine pressure ratios and cycle temperatures to decrease engine weight and improve performance in next generation turbine engines. Advanced seals have been identified as critical in meeting engine goals for specific fuel consumption, thrust-to-weight, emissions, durability and operating costs. NASA and the industry are identifying and developing engine and sealing technologies that will result in dramatic improvements and address the goals for engines entering service in the 2005-2007 time frame.

This paper provides an overview of advanced seal technology requirements and highlights the results of a preliminary design effort to implement advanced seals into a regional aircraft turbine engine. This study examines in great detail the benefits of applying advanced seals in the high pressure turbine region of the engine. Low leakage film-riding seals can cut in half the estimated 4% cycle air currently used to purge the high pressure turbine cavities. These savings can be applied in one of several ways. Holding rotor inlet temperature (RIT) constant the engine specific fuel consumption can be reduced 0.9%, or thrust could be increased 2.5%, or mission fuel burn could be reduced 1.3%. Alternatively, RIT could be lowered 20 °F resulting in a 50% increase in turbine blade life reducing overall regional aircraft maintenance and fuel burn direct operating costs by nearly 1%. Thermal, structural, secondary-air systems, safety (seal failure and effect), and emissions analyses have shown the proposed design is feasible.

Introduction

Recognizing the need to reduce costs, NASA has put in place several programs to improve both engine and vehicle performances and lower direct operating costs (DOC). General program goals include:

1. Reduce commercial aircraft direct operating costs including interest by: 3% (large engines) and 5% (regional engines).
2. Reduce engine fuel burn up to 10%.
3. Reduce engine oxides of nitrogen (NO_x) emissions by greater than 50%.
4. Reduce airport noise by 7 dB, or about three-quarters reduction in acoustic energy.

Meeting these aggressive goals for engines to be certified early in the next century (2005-2007) requires significant advancements in each of the primary component technologies—including the supporting mechanical component technologies such as seals. Airlines have become increasingly cost-conscience. As a result, the NASA/industry team is pursuing technologies that show promise of high performance-to-cost benefit ratios. Technologies are being considered that increase engine and vehicle performance, lower acquisition and lifetime costs and reduce engine maintenance.

Advanced engine seals show promise of reducing engine losses and maintaining these performance benefits over the service interval of the engine. New seals coupled with improved analysis codes give the designer better control of engine secondary flows—critical in extracting the maximum useful work out of the engine. Because of their high performance payoff and their relatively low development costs, seals have repeatedly shown high performance-to-cost benefit ratios in recent studies (Smith, 1994; Munson, 1994).

The objective of this paper is to provide an overview of the future engine development trends, provide an overview of the advanced seal technology requirements and highlight results of a detailed case study showing specific benefits of implementing advanced seals.

Advanced Subsonic Technology Program Goals

Operating Cost Reduction: Cost-conscious airline operators continue to demand lower operating costs including reduced fuel burn. Starting with a "clean sheet" aircraft/engine design, reduced engine weight translates into reduced overall system weight (engine and airframe weight). Reducing airplane weight and

Paper presented at the RTO AVT Symposium on "Design Principles and Methods for Aircraft Gas Turbine Engines", held in Toulouse, France, 11-15 May 1998, and published in RTO MP-8.

size reduces acquisition costs including interest. Costs to operate a 50 passenger regional aircraft are broken down as a percentage of total DOC in Fig. 1, showing that engine and airframe acquisition costs are 42% of the total costs. Engine maintenance costs amount to about half of the 22% total engine + airframe maintenance costs shown. Fuel burn amounts to about 19% of DOC, therefore reducing fuel burn results in additional savings over the life of the aircraft. Reduced fuel burn also helps lower emissions throughout the mission - key to a cleaner environment.

Specific fuel consumption (SFC) has continued to decrease over the course of turbine engine history, as shown in Fig. 2. In this chart a number of turbojet and turbofan engine SFC are shown versus engine certification date. Reducing SFC by 8% from current baseline engines will result in engines with SFC values for large engines to about 0.48.

Engine Pressure Ratio: For both engine classes, the goal is to increase pressure ratio roughly 50% from engines currently being certified for flight. For instance, the PW4084 now certified for the Boeing 777 has an overall pressure ratio of 38. Pressure ratios for large engines are targeted to increase to 50 or 60 to 1. Regional aircraft engines pressure ratios are expected to climb to 35 to 45. Engines decrease in size with increasing pressure ratios. Reducing engine size again reduces weight and acquisition costs.

As a result of the increasing pressure ratios, engine compressor discharge temperatures are expected to reach 1300 °F and higher, requiring compressor materials with 1450 °F operating temperatures (considering margin requirements). Turbine inlet temperatures are expected to be several hundred degrees over today's, requiring improved materials and thermal barrier coatings in the turbine hot section. Seal material temperatures will increase in proportion to the compressor and turbine material temperatures.

NASA/industry studies have indicated that improving engine performance and reducing operating costs would result in airline economies over the life of the engine fleet 20 times the total development cost (Smith, 1994)—a strong motivation for implementing advanced technologies that are cost effective.

Motivation for Advanced Seal Development

Source of Engine Efficiency Gains: Overall engine efficiency, the useful work produced by the engine divided by the fuel energy, can be determined by the product of the three efficiencies illustrated in Fig. 3, (Smith, 1993). Plotting the historical trends of core efficiency versus the product of transmission and propulsive efficiencies, (Fig. 4), one sees that relatively more progress has been made recently in advancing the propulsive efficiency (e.g., fan) and low-pressure turbine than has been made in the core. This is illustrated by the "historical trend" line. To obtain the low SFC desired for the advanced engines, more progress must be made in increasing core efficiencies, as illustrated by the "future trend" line. As can be seen comparing the slopes of these two lines, reaching the SFC goal requires proportional, or balanced, increases in core and the product of propulsive and transmission efficiencies.

Increasing core efficiencies will be obtained by high cycle pressure ratios and compressor exit temperature, higher turbine inlet temperature, and improved component efficiencies including better sealing and secondary air flow management. Higher propulsive efficiencies will be obtained through increased bypass ratio and reduced installation drags and losses. Higher transmission efficiency will be achieved through improved fan system efficiencies and improved low-pressure turbine efficiencies.

Benefits: In addition to the strong case made for improving core efficiencies by reducing leakage and better managing secondary air flow systems, there are several other compelling reasons to advance seal technology to meet advanced engine goals. There is a strong correlation between the percentage reduction in seal leakage and either the percentage decrease in SFC or the percentage increase in thrust—all other things held constant. Advancements in seal technology generally are made with investments much smaller than those required for a compressor or turbine stage redesign and qualification. Studies performed by Stocker (1977) and corroborated by Smith (1994) estimated that making the same performance improvements with compressors or turbines would come at a cost a minimum of 4 to 5 times higher than the same improvements made by improving seal technology. Limited technology development budgets are compelling NASA and the engine community to exploit technologies such as seals with a high return on technology dollar invested.

Seal Technology: Current and Advanced Requirements

In examining seal requirements for advanced engines it is instructive to review current engine seal capabilities (Steinetz and Hendricks, 1997). Table 1 provides an overview of current engine seal capabilities in terms of pressures, speeds, temperatures, and materials. Table 2 summarizes expected seal operating requirements for next generation turbine engines

including some military applications. Seals will generally be expected to operate hotter, seal higher pressures (to accommodate higher pressure ratios), and operate with higher surface speeds.

Carbon Face Seals: Face seals play a vital role in sealing bearing locations in turbine engines and auxiliary power units. Carbon face seals have low leakage and can seal pressures up to 150 psid. They currently operate reliably to speeds of 475 ft/s with acceptable friction and wear rates. These seals operate reliably with low leakage and cost less than labyrinth seals and therefore will continue to play a role in advanced aircraft engines. Even more will be asked of carbon face seals in future engines. Carbon face seal speeds will likely rise to 600 ft/s for advanced engines.

Research efforts are being directed at overcoming problems of face seal coking and blistering. AlliedSignal has had success replacing the carbon face seal with a ceramic ring seal overcoming the coking problems, eliminating oil odor in the cabin, and significantly increasing seal life (Ullah, 1997).

Labyrinth Seals: Perhaps the single most common flow path seal used over turbine engine history is the labyrinth seal. The labyrinth seal consists of multiple knife edges (typically 5) run in close clearance (0.01-0.02 in.), depending on location. Labyrinth seals can be configured in many ways including stepped and straight. Labyrinth seals are clearance type seals and therefore have high leakage rates. Furthermore, labyrinth seal leakage increases over time. Clearances open when shaft excursions force the labyrinth teeth into the adjoining rub-strips. Labyrinth seals are used as shaft seals, turbine rim seals, and as inner air seals—sealing the vane-to-drum inter-stage locations.

Brush Seals: Significant efforts are underway to develop brush seals (Arora, Proctor, 1997; Short et al., 1996; Hendricks et al., 1994a; Chupp, Nelson, 1990; Holle, Krishnan, 1990). Brush seals consist of a dense pack of bristles sandwiched between a face plate and a backing plate (Ferguson, 1988). A primary attribute of the brush seal is its ability to accommodate transient shaft excursions and return to small running clearances, unlike labyrinth seals that wear to the full radial excursion. Brush bristles are oriented to the shaft at a lay angle (generally 45 to 55 degrees) that point in the direction of rotation. Brush seals are designed initially with a small radial interference $\leq$0.004 in. Starting with a small radial interference allows seal to accommodate seal-to-shaft centerline manufacturing variations providing a good seal. Leakage rates on initial run can be as little as 10-20% of comparable labyrinth seals. Seal temperatures are generally 1300 °F or less and surface speeds are generally 1000 ft/s or less.

Experience has shown that during engine operation, brush seal flow rates do increase due to wear. PW has entered revenue service with brush seals in three locations on the PW 4168 (see Fig. 5) for Airbus aircraft and on the PW4084 for the Boeing 777. PW has made leakage comparisons of new and aircraft-engine-tested brush seals and concluded that performance did not deteriorate significantly for periods approaching one engine overhaul cycle of 3000 hr. (Mahler and Boyes (1995)). Of the three brush seals examined, the "worst-case" brush seal's leakage doubled compared to a new brush seal. Even so, brush seal leakage was still less than half the leakage of the labyrinth seal.

Standard single stage brush seals typically are manufactured using 0.0028 in. diameter bristle wires. Bristle pack widths are usually maintained around 0.03 in. and the backplate is in contact with the last row of downstream bristles. Multiple brush seals are generally used where large pressure drops ($\geq$80 psid) must be accommodated. The primary reason for using multiple seals is not to improve sealing but to reduce pressure-induced distortions in the brush pack, namely axial brush distortions under the backing ring, which cause wear. Also, researchers have noticed greater wear on the downstream brush if the flow jet coming from the upstream brush is not deflected away from the downstream brush-rotor contact. Single stage brush seals made of larger diameter wires and thicker pack widths are showing promise of overcoming this effect.

Brush seal designs for higher pressure applications require bristle packs that have higher axial stiffness to prevent the bristles from blowing under the backing ring. Recently Short et al., (1996) amongst others have developed brush seals rated for pressure differentials of 120 psid and above using 0.006 in. diameter wire bristles, a thicker brush pack width (0.05 in.), and a front flexi-plate to limit bristle blowdown.

Brush seals will continue to evolve to meet the ever more demanding conditions required of them. Surface speeds will continue to increase in advanced engines. Surface speeds may climb as high as 1500+ ft/s in advanced engines, at temperatures up to 1500 °F. Under these extreme conditions, designs that would significantly limit the irrecoverable bristle wear are highly desirable. Other proprietary designs are also being investigated. Ceramic brush seals are also being investigated by a number of researchers including Hendricks et al., (1994b) and Howe (1994). Though

not yet proven, hard ceramic bristles may be more wear resistant and may offer longer term wear lives.

Film-Riding Seals: Film riding seals rely on a thin film of air to separate the seal faces and show promise of reducing wear and leakage to its practical limit. Film riding face seals can be designed to operate at the high pressures and temperatures anticipated for next-generation gas turbine engines. There are two classes of film riding seals being developed for gas turbines: hydrostatic and hydrodynamic seals. Hydrostatic face seals port high pressure fluid to the sealing face to induce opening force and maintain controlled face separation (see Steinetz, 1998 review article). Changes in the design clearance results in an increase or decrease of the opening force in a stabilizing sense. Converging faces are used to provide seal stability. Hydrostatic seals are not applicable to lower pressure differential applications. Hydrostatic face seals suffer from contact during startup, requiring faces made of rub-tolerant materials.

The aspirating hydrostatic seal under development by GE and Stein Seal provides a unique fail-safe feature (Hwang et al., 1995, Wolfe et al., 1996, Bagepalli, 1996). The seal is designed to be open during initial rotation and after system shutdown—the two periods during which potentially damaging rubs are most common. Upon system pressurization, the aspirating teeth set-up an initial pressure drop across the seal that generates a closing force to overcome the retraction spring force causing the seal to close to its operating clearance (nominal 0.0025 in.). System pressure is ported to the face seal to prevent touchdown and provide good film stiffness during operation. At engine shutdown, the seal pressure across the seal drops and the springs retract the seal away from the rotor preventing contact.

Hydrodynamic or self-acting face seals incorporate lift pockets to generate a hydrodynamic film between the two faces to prevent seal contact. Munson (1992a,b, 1993) has developed a compressor discharge face seal for high-pressure, high speed applications and follows the early work of Ludwig (1978). A number of lift pocket configurations are employed including shrouded Rayleigh step, spiral groove, circular grooves and annular grooves (Steinetz, 1998). In these designs, hydrodynamic lift is independent of the seal pressure; it is proportional to the rotation speed and to the fluid viscosity. Therefore a minimum speed is required to develop sufficient lift force for face separation. Hydrodynamic seals operate on small ($\leq$0.0005 in. nominal) clearances resulting in very low leakage compared to labyrinth, or brush seals as shown in Fig. 6, (Munson, 1993). Because rubbing occurs during start-up and shut-down, seal faces are made of rub-tolerant materials.

Outer Air/Blade Tip Seals: Better management of blade tip leakage improves engine designs in several ways. Reduced compressor blade tip leakage improves compressor efficiency and improves stall/surge margins, improving engine operability. Maintaining tighter clearances over the life of the engine addresses a key observation that 80-90% of engine performance degradation is caused by blade tip clearance increase (O'Sullivan, 1994). In a limited number of commercial engines, blade tip clearance control is used. Blade tip clearance control is performed by preferentially cooling the turbine case during cruise operation. This has been successful in greatly reducing turbine blade clearances in the PW4000 series of engines and has resulted in handsome turbine efficiency gains (O'Sullivan, 1994).

Currently the industry does not use active feedback control. Adding feedback control by sensing average blade tip clearances and regulating case coolant will provide extra benefits, including allowing use of clearance control for other than cruise-only conditions, as is the case today. Mechanical control techniques are also being examined. Allison has demonstrated centrifugal compressor efficiency gains up to 1% using an experimental electromagnetic actuator to control compressor clearances (Weimer, 1992). For both active feedback control techniques, a pacing technical issue that is being worked is the development of reliable, high temperatures sensors.

Loss of design clearances results in a loss of thrust, requiring an increase throttle setting to achieve the same engine performance. The increase throttle setting, however, increases the exhaust gas temperature (EGT) and thus reduces the life of the hot turbine components. When EGT exceeds a Federal Aviation Administration (FAA) certified limit, engine overhaul is required costing typically over $1 million (1998 dollars). Manufacturers will continue to develop techniques to combat this performance degradation to serve their cost-conscious airline customers.

Allison Engine 3007 Advanced Seal Study

The engine used for the advanced seal/secondary air management study was the Allison AE3007, 7000 pound thrust class turbofan engine, shown in Fig. 7. Although this is a modern engine in every respect, the secondary airflow system differs little from what is typical within the industry. In other words, very little has changed with regard to the management of the secondary airflow system in gas turbine engines. Over the same time period vast resources have been spent on materials development programs and investment in compressor, combustor, and turbine

development programs. The reward has been steady improvement in overall engine performance.

More aggressive engine cycles place increasingly more severe demands on the secondary airflow systems and seals which will be used in these and future advanced engines. Even though the operating environment for these seals is becoming more severe, better performance from the overall secondary flow systems is needed so as not to erode performance gained by going to higher pressures and temperatures.

Study Goals: The study which is described in this paper serves to demonstrate that investment in sealing technology can provide substantial engine performance benefits. The goals of this program are to:

- Estimate SFC and other increased performance benefits possible as a result of incorporating advanced seal technology into advanced turbofan engines.
- Examine limitations in the current state of the art sealing technology for high compression ratio regional transport engines.

After many years of little progress, there is renewed interest in development of improved gas turbine sealing systems. These efforts have successfully demonstrated advanced sealing concepts which are ready for further development and incorporation in advanced engine demonstration programs. These and other sealing technologies provide a relatively low cost way to greatly increase engine performance.

Approach

Several engine analysis groups contributed to this study to evaluate system level performance benefits and to investigate the feasibility of the approaches considered. Using the engine layout and cycles provided by the performance group, the flow systems group constructed an analytical model of the entire secondary airflow system. The model was then used to determine the airflow distribution within the engine. Turbine and compressor aerodynamic groups determined component efficiency versus seal clearances. The next step was to convert change in engine performance into change in overall aircraft performance. This is done by constructing a so-called "rubber" airframe model using Allison's mission analysis computer code. Mission studies were performed for a 50 passenger regional jet, powered by two AE3007 engines.

The relative sensitivity of an engine to the effects of leakage air is dependent on the particular cycle selected for the engine as well as the particular operating point selected. Results have been reported based on a hypothetical "mission," that was condensed from several different missions and operating points into a few typical power settings (See Table 3). For example idle is meant to represent ground idle, taxi, flight idle and descent. Maximum power represents both climb and takeoff.

The next step was to define which secondary airflows constituted a leak. A consistent definition was required to enable comparison between baseline and advanced engines, particularly where there were differences in the secondary flow system. For this study, a leak was defined as any airflow which exits or enters from the main flow stream. Deliberate compressor bleeds were ignored, as well as all airflows which were associated with turbine blade or vane cooling. It was assumed that these cooling airflows had been sized exactly to perform their necessary functions. This results in a definition which allows engine comparisons to be made regardless of the configuration of the secondary flow system.

Operational concerns enter into this decision as well. All present secondary flow systems bleed air from the compressor to provide pressurized air to the turbine interstage cavities. This air is used to prevent the ingress of hot flowpath gasses, to cool the disks and blades, and to balance thrust. Air is metered into the interstage cavities by the secondary seals which are located inboard, towards the disk hubs, and thus meter air up-stream of the blade/vane gap outboard at the disk rims. These vane/blade gaps then represent the real leak in the system.

Using the leakage definition, the engine was evaluated stage-by-stage to rank the relative sizes of the leaks. Thirty total locations were investigated. Table 4 provides the relative size of the various leakage flows, for those flows amounting to greater than 5% of the total weighted leakage. The mission ranking was obtained by dividing all the leakage flows by the highest leakage obtained for a particular operating point. These individual rankings were then multiplied by the percent of the mission spent at that particular point, then the weighted rankings were summed to obtain the overall mission ranking. The mission weighted percent represents the weighted fraction of total leakage that each individual leak represents. Compressor inner-band and turbine and compressor blade tip leakages effect component efficiency, but the leakage flows remain in the main flow stream. Design data was used to estimate engine blade tip and compressor inner band clearances throughout the operating range represented by the selected mission. These leakages did not fit the leakage definition as previously stated. They do impact performance and so were treated separately.

One notices from Table 4 that relatively few locations, primarily the turbine rim seal locations, are

responsible for the majority of the total leakage. The top five locations are responsible for 75% of the total leakage. Table 4 also presents the "ideal SFC benefits" for each of the leaks. To attain these full benefits a "clean-sheet" design would be required. The preliminary design performed herein accepted as a ground-rule that there would be no changes allowed to the blade air flow circuit (e.g., no redesign of the blades). A "clean-sheet" or full hot-section redesign exploiting all of the benefits of advanced seals would have yielded even greater benefits than those indicated in the Benefits Section below.

Advanced Sealing Systems: Preliminary Design

Small Change Coefficients: Using the Allison mission analysis computer model and the engine cycle information small change coefficients were generated for all the engine bleed flows. These were used to determine the effect on overall aircraft/engine performance caused by changes in seal leakages. Component (compressor and turbine) small change coefficients were also generated to enable the effects of compressor inner band leakage, and blade tip leakage to be assessed. The compressor and turbine aerodynamic groups used analytical and test data from developmental engine testing to define the effect that these seals had on overall component efficiency. The small change coefficients are shown in Table 5. As an example how to use this table, a one percent change in compressor discharge to high pressure turbine airflow results in a 0.7% change in SFC.

Based on the results of the previous steps it was possible to rank the various leakage locations to determine where the largest performance gains could be obtained for several approaches considered.

Approaches Considered: Several proposed designs were analyzed using a proprietary compressible flow computer code to analyze secondary air flows. Four turbine rim seals were planned initially (Fig. 8, iteration A). These were placed into the secondary flow model with no other adjustments made to the flow system relative to the existing AE3007. This iteration resulted in a net leakage reduction of 0.75% of core flow. Representative film-riding seal flow characteristics derived from experimental and analytical data were provided to the secondary flow code. It was clear more gain could be realized. The cavity pressures increased due to more effective rim seals. This caused large air leakage in places which previously had ingress from the gas path. In addition, a large amount of high pressure air was leaking into the low pressure cooling circuit. Adjustments were made to reduce airflow into the HP turbine cooling circuit, as well as changing from segmented to solid turbine blade cover plates.

A second major iteration (B) removed the second-blade-third-vane (2B-3V) rim seal and added two film riding face seals. This was an effort to prevent leakage of the HP air into the LP cooling circuit. This produced an overall leakage reduction of 2.75% and did totally separate the HP and LP cooling circuits. Unfortunately the amount of air required through the compressor ID rotor bleed to feed the LP circuit was excessive. A third iteration (C) was considered to solve the compressor problem. Although this probably would have resulted in even greater leakage reduction the proposal was not evaluated due to flight safety concerns, and the sheer complexity and risk trying to introduce so many advanced seals at one time into the engine.

Mechanical Configuration Selected: The fourth configuration (D) was selected that uses 3 advanced film riding face seals to seal the 1V-1B, 1B-2V, and the 2V-2B locations. This configuration balances complexity and risk against the benefits of reduced leakage and increased performance. Sealing just the 3 locations saves 2% in total leakage flow (1.2% chargeable; 0.8% recoverable). Using existing proprietary design methodology Allison developed space claims for the proposed seals which were located as close to the main flow path as possible. The resulting mechanical arrangement is shown in Fig. 9. Notice that there are still very small cavities outboard of the seals. These must be purged with some cooling flow. While no cavity is the most desirable situation, this is the best that could realistically be accomplished.

For this preliminary design exercise, candidate film riding face seals were designed based on the expected operational requirements which include: operating temperature, pressure, speed, relative thermal growths of rotor and stator, part tolerances, and anticipated thermal and mechanical deflections. All of these parameters effect the seal design and in particular the required space envelope. The size of the seal determines to a large extent how close to the flow path the seal can be physically be located. Allison and NASA seal codes (Shapiro and Athavale, 1994) were used to develop preliminary designs for the candidate advanced seals used for these studies.

Every attempt was made to ensure that the seal substitution was being performed in a realistic manner. Heat transfer work was done to verify that turbine metal temperatures remained within presently accepted maximum operating temperatures. The effects of advanced seals were evaluated by substituting flow characteristics for the advanced seals in selected sealing locations. In most cases this required some

additional rebalancing of the secondary flow systems because of the large reductions in leakage. During this process it was evident that as a result of improved sealing of the secondary flow systems, the engine could be redesigned to reduce fuel burn or increase thrust; or by reducing rotor inlet temperature, increase engine life.

Analytical Studies and Discussion

After selecting the mechanical configuration, a number of more detailed analytical studies were performed to assess the feasibility of the approach.

Heat Transfer Analysis: The purpose of these studies was threefold: fine tune the air flows, make sure that predicted metal temperatures were within acceptable limits, and prepare temperature files for subsequent use by stress analysis. Temperatures were calculated initially for a steady state power point, and then later for transient operating conditions.

Several studies were used to determine if the small cavities above the seals had to be completely purged or if some ingress could be tolerated. When leakage was adjusted to completely eliminate ingress, most of our gains disappeared. This produced metal temperatures below current AE3007 values and the cavities were being overcooled. Next we tried leakage flows halfway between the first trial and the low value possible for film riding seals. These results also indicated that we were closer to the AE3007, but still overcooling in some locations. Finally we tried the film riding seal leakage values. The team agreed that these results were acceptable from an operational standpoint with one exception, the 2V-2B cavity. This cavity was running slightly hot. The reason was due to leakage through a segmented blade cover on the aft side of the second rotor. This was changed to solid, and the problem was eliminated.

Results of the thermal analysis for the maximum power point are shown in Figure 10. This figure plots temperature *differences* of the advanced engine relative to the current AE3007. There are a umber of interesting results presented which bear pointing out. There was less than a 10 °F change in turbine wheel bore and web temperatures indicating that the new seals have almost no effect on the bulk of the rotor.

Figure 10 shows that the aft first vane platform and the first blade platform forward are considerably hotter (e.g., 270 °F shown) than on the existing AE3007. However, the actual peak first vane metal temperature is only 35 °F hotter than the existing AE3007. This temperature rise is well within the present capability of the existing vane. Peak metal temperatures for the first blade are almost identical between the existing AE3007 and the new engine. What Figure 10 is showing is essentially a redistribution of temperatures in the first blade.

The reason for these temperature differences can be traced both to an overall reduction in airflow, and changes in the leakage pathways brought about by the increased effectiveness of the new 1V-1B seal. The new seal is much more effective than the existing labyrinth seal at restricting flow through the 1V-1B gap. By providing such an effective seal at this location we reduce the amount of air which can flow through this gap. Temperatures thus rise outboard of the seal as expected, accounting for the higher blade and vane platform temperature in the vicinity of the small cavity outboard of the first advanced seal.

Despite the fact that the differential pressure across this seal is small, airflow through the current labyrinth is substantial. In effect this leakage flow presently provides more cooling than is needed at this location. We also found that we needed to reduce airflow to this inter stage cavity by approximately 0.8%, and to provide solid blade cover plates. If this was not done the air had a tendency to flow through the blade attachment regions outward in the main flow path, and axially into the 1B-2V cavity. Figure 10 shows that the 1B attachment is much cooler with the new system than the existing AE3007. This is the effect of the remaining residual airflow through the first blade attachments. Thus, temperatures of the first vane platform aft, first blade platform forward, and first blade attachments are linked to both the magnitude and the direction of the leakage flows from this inter-stage cavity.

Failed Seal Scenario: The next step in the thermal analysis was to look at the effect of failed seals. This study was also done at maximum power, having the highest boundary temperatures. We had considered the possibility of single or multiple seal failures when conducting the secondary flow studies. A design guideline followed was that any failed seal scenario would not effect the flow of cooling air to the blades and vanes. As stated previously however, the fact that the total air flow to the seals had been reduced meant the possibility of ingress existed at these locations in the event of a failed seal. We simulated failed seals by substituting leakage flows of conventional labyrinth seals in place of the advanced seal flows. The labyrinth seal gap modeled is consistent with what the AE3007 presently runs with existing hardware. This could easily be provided by a back-up seal which would control flow to these similar levels.

Failure of the first stage seal had an almost negligible effect since the differential pressure at this location is only slightly biased in favor of flow out of

the inter-stage cavity into the flow path. Failure of the 1B-2V-2B seal results in considerable ingress to the 1-2 cavity outboard of the spacer. However no change in blade cooling flow was observed. Rotor and blade attachment temperatures showed only a slight rise in temperature due to the mitigating effects of the blade cooling flows. A 300 °F rise in temperature of the second stage vane inner band and turbine 1-2 spacer was observed. While this is not an immediate concern, it would require engine removal and overhaul at some point. Failure would be detectable by a drop in power and a rise in maximum measured gas temperature. By adding monitoring thermocouples on the second stage vane, an additional indication of failure would also be provided. Gas temperature is currently measured near this location, so this approach is feasible.

Structural Analysis: A thermal-structural finite-element analysis was performed on the HP rotor systems. At this preliminary design stage, some of the parts did not quite meet Allison's life criterion. However in the judgment of the design and analytical groups involved the results are close enough that the parts could be easily modified during a detailed design. Design changes would involve material substitution, adjusted fillet radii, and other similar minor details.

Seal Tracking: Using finite element analysis coupled with engine limit stack and tolerance data we were able to predict relative axial, radial, and angular deflections between the rotor and stator. These are presented in Table 6. The deflections must be held relatively small so that the proposed seal designs are able to track. For long life and high reliability the seals must be able to operate in a non-contacting manner, with the possible exception of startup and shutdown.

Proprietary hydrodynamic seals are being developed at Allison and within the seal community that show promise of meeting the demanding seal operating conditions. A key feature of all of these seals will be seal compliance, namely the ability to accommodate and dynamically track thermal coning and circumferential out-of-flatness of adjacent seal surfaces. Depending on how this idea is implemented, a slight increase in leakage could be possible.

Reliability: Greater than 99% reliability as demonstrated through test programs is required before these seals would be considered for use on an engine. Component reliability problems are direct drivers of unscheduled maintenance. Unscheduled maintenance is a large driver of direct operating cost. Seals that are ultimately developed for this application will be designed based on the need for extreme reliability.

Another key goal is flight safety. No matter how reliable the individual components that comprise the engine, the total system needs to be designed such that the failure of any one component does not result in catastrophic failures of any other part of, or the total engine. It is also important that any failure also be immediately detectable. Based on the nature of the failure the pilot can then make the determination to continue running till the plane can be landed safely, or shut down the engine so that secondary failures do not occur.

Benefits

As a result of installing the advanced seals in the HP turbine, secondary airflows were reduced by 2%. Of this 1.2% was chargeable providing for significant performance benefits. This savings in leakage can be used in several ways.

Increased Engine Power: For the same turbine inlet temperature and fuel burn, the reduced leakage can be used to provide more power from the same engine. Using the small change coefficients in Table 5 (CDP->HPT row), one can attain 2.5% (e.g., 2.1 x 1.2%=2.5%) higher engine thrust-to-weight ratio or 0.24% lower take-off gross weight.

Increased Operating Margin: In this case the maximum power output remains fixed. Lower leakage allows this power to be obtained using less fuel, and at a lower maximum cycle temperature. The sensitivity coefficients presented in Table 5 do not apply in this case—a new turbine map is developed and implemented in the performance computer code. Then the performance deck was run to match thrust levels between the original and the modified engines. These runs made it possible to compare fuel flow rates, specific fuel consumption, rotor inlet temperature, etc. and were directly attributable to the reduction in leakage.

The net result was a 0.9% reduction in SFC, and an approximately 20 °F average reduction in turbine inlet temperature across the range of operating points from idle to maximum power. This result was input into a detailed turbine blade life model which was itself based on a very detailed regional mission. The result of this was a greater than 50% increase in both first and second stage blade life. This in turn would result in a 6.6% decrease in engine maintenance costs associated with flying the 50 passenger regional aircraft mission.

Since engine maintenance costs are 11% of total operating costs, Fig. 1, this reduces direct operating costs by approximately 0.73%. Adding the contribution of SFC reduction (0.9% times 19% Fuel component, Fig. 1), brings the total reduction in direct operating costs to 0.89%, or 18% of the NASA AST goal, with just 3 seals.

Emissions: Reducing fuel burn and making the other cycle changes had a generally positive effect on emissions, using the ICAO standards for emissions calculations. Due to longer combustor residence time and higher compressor discharge temperature, a very slight 0.7%, increase in oxides of nitrogen (NO_x) was observed. Starting with a "clean sheet" design NO_x emissions would have been reduced. Carbon monoxide (CO) emissions were reduced 3.47% and unburned hydrocarbons were reduced 2.91%.

Summary and Conclusions

Engine designers are re-evaluating all aspects of turbine engines to meet the efficiency, performance and operating cost goals set for next generation turbine engines. A comprehensive survey was made of cycle losses in terms of leakages of a modern regional jet engine, the Allison Engine AE3007. The survey identified the largest performance gains come from applying advanced seals within the gasifier section of the engine. This is because energetic compressor discharge air must be used to purge the majority of the gasifier turbine. The study demonstrated applying advanced seals will lead to large reductions in specific fuel consumption and ultimately direct operating costs. Based on the investigations performed the following points are clear.

1. Incorporating just three advanced sealing devices, (e.g., mechanical face seals), in a gas turbine engine should improve engine SFC by approximately 0.9%. Use of additional advanced seals would provide even greater benefit with somewhat greater complexity.
2. Advanced sealing devices pay very large dividends. Just three advanced face seals installed at appropriate locations in the current AE3007 should reduce direct operating costs of the regional aircraft by approximately 0.89% or 18% of NASA's stated goal.
3. Analytically it was shown that the advanced seals could be incorporated into the gasifier section of a gas turbine engine. The resulting design required no compromise to the main flow path and the design meets all criterion for flight safety. During a detailed design, minor design modifications are possible to allow the hardware to meet all Allison design criterion for hot section life.

References

Arora, G.K., Proctor, M.P., 1997, "JTAGG II Brush Seal Test Results," AIAA-97-2632, July.

Bagepalli, B., Imam, I., Wolfe, C.E., Tseng, T. Shapiro, W., Steinetz, B.M., 1996, "Dynamic Analysis of an Aspirating Face Seal for Aircraft-Engine Applications," AIAA 96-2803.

Chupp, R.E. and Nelson, P., 1990, "Evaluation of Brush Seals for Limited-Life Engines," AIAA 90-2140, July 16-18.

Ferguson, J.G., 1988, "Brushes as High Performance Gas Turbine Seals," ASME paper 88-GT-182, June.

Hendricks, et.al., 1994a, "Relative Performance Comparison Between Baseline Labyrinth and Dual-Brush Compressor Discharge Seals in a T-700 Engine Test," NASA TM-106360, June 1994

Hendricks, R.C., Flower, R., and Howe, H., 1994b, "Development of a Brush Seal Program Leading to Ceramic Brush Seals," Seal Flow Code Development '93; NASA CP-10136.

Holle, G.F. and Krishnan, M.R., 1990, "Gas Turbine Engine Brush Seal Applications," AIAA 90-2142, July 16-18.

Howe, H., 1994, "Ceramic Brush Seals," Seal Flow Code Development '93; NASA CP-10136.

Hwang et al., 1995, "Advanced Seal for Engine Secondary Flowpath", AIAA-95-2618.

Ludwig, L. 1978, "Self-Acting Shaft Seals, " *Seal Technology in Gas Turbine Engines,* AGARD, Conference Proc. No.-237.

Mahler, F.; Boyes, E.; 1995, "The Application of Brush Seals in Large Commercial Jet Engines," AIAA 95-2617.

Munson, J., 1992a, "Development of Film Riding Face Seals for a Gas Turbine Engine," STLE Tribology Transactions, Vol 35, pp. 65-70.

Munson, J., 1992b, "Development of a High Performance Compressor Discharge Seal," AIAA 92-3714, July

Munson, J., 1993, "Testing of a High Performance Compressor Discharge Seals," AIAA 93-1997, June.

Munson, J. and Steinetz, B.M., 1994, "Specific Fuel Consumption and Increased Thrust Performance Benefits Possible with Advanced Seal Technology," AIAA-94-2700, June.

O'Sullivan, J. 1994, "PW Turbine Engine Fundamentals Course," NASA Lewis Research Center, March.

Shapiro, W. and Athavale, M.M., 1994, "Seal Analysis Computer Codes," SAE 941206, presented at Aerospace Atlantic Conference, April.

Short, J.F., Basu, P., Datta, A. Loewenthal, R.G., Prior, R.J., 1996, "Advanced Brush Seal Development," AIAA-96-2907.

Smith, C. 1993, Technical Discussion, General Electric Aircraft Engines, Evandale, OH.

Smith, C.J., 1994: "Unique Propulsion Systems Advanced Subsonic Technologies Evaluation and Analysis," Task 14-Interim Oral Report, Contract NAS3-25953, January.

Steinetz, B.M., Hendricks, R.C., 1994, "Engine Seal Technology Requirements to Meet NASA's Advanced Subsonic Technology Program Goals, NASA TM-106582, AIAA-94-2698.

Steinetz, B.M., Hendricks, R.C., 1997, "Aircraft Engine Seals," Chapter 9 of *Tribology for Aerospace Applications*, STLE Special Publication SP-37.

Steinetz, B.M. 1998, "Seal Technology," Chapter 22 of Mechanical Engineer's Handbook, M. Kutz Editor; Wiley Pub.

Stocker, H.L.; Cox, D.M.; and Holle, G.G., 1977, "Aerodynamic Performance of Conventional and Advanced Design Labyrinth Seals with Solid Smooth, Abradable, and Honeycomb Lands - Gas Turbine Engines", NASA CR-135307.

Ullah, R.M., 1997, "Air-Oil Seals R&D at AlliedSignal," presented at the NASA Lewis Seals/Secondary Flow Workshop, NASA Lewis Research Center, Cleveland, OH. October.

Weimer, M., 1992, "Development and Test of an Active Tip Clearance System for Centrifugal Compressors," AIAA 92-3189, July.

Wolfe, C.E., Bagepalli, B.S., Turnquist, N.A., Tseng, T.W., NcNickel, A.D., Hwang, M.F., Steinetz, B.M., 1996, "Full Scale Testing and Analytical Validation of an Aspirating Face Seal," AIAA 96-2802.

Table 1.—Current Turbine Engine Seal Technology

Seal	ΔP (psid)	Temp (F)	Surf. Speed (ft/s)	Materials
Face	150	1000	475	Carbon
Labyrinth	250-400	1300	1500	Ni Superalloy Teeth + Abradable
Brush	80-100/ stage	1300	1000	Cobalt Superalloy
Outer Air Seals: Compressor HP Turbine	 Stage ΔP	 1200 2000+	 1200 1500	Abrasive Tipped Blades vs: Abradable Graded Ceramic

Table 2.—Advanced Turbine Engine Seal Technology

Seal	ΔP (psid)	Temp (F)	Surf. Speed (ft/s)	Materials
Face: Single Rot. Counter-Rot.	 60 60	 1000 1000	 600 1000	 Carbon Carbon
Film Riding Seal	800	1500	1200+	Ceramic + Superalloy
Labyrinth	250-400	1300	1650	Ni Superalloy Teeth w/Abrasive Tips + Abradable
Brush	140/ stage	1500	1500	Superalloy or Ceramic

Table 3—Performance Results are Reported on the Basis of a Generic Regional Aircraft Mission

Operating Point	Condition	Duration (% of total)
Idle	SLS 103°F	34%
Cruise	20,000 ft, Mach = 0.7	33%
Max.	SLS (ISA+18°F)	33%

SLS = Sea Level Static
ISA = International Standard Atmosphere

Table 4.—Seal leakages accounting for more than 5% of total weighted leakage

Leakage Location	Mission Weighted Ranking	Weighted % of Total Leakage	Ideal SFC Benefit
1V-1B Inner	0.96	25	1.25
2V-2B "	0.98	25	0.97
2B-3V "	0.39	10	0.46
3V-3B "	0.41	10	0.42
4V-4B "	0.24	6	0.19
2B-3V "	0.25	6	0.01
Total		82	3.30

Note: 1V-1B = first stage vane -first stage blade rim seal interface

Table 5.—Small change coefficients used to evaluate the effect of leakage on overall regional aircraft performance

	ΔSFC %/PT	ΔFn/Wgt %/PT	ΔTOGW %/PT	ΔMFB %/PT
CDP -> o/b	+1.5	-2.8	+0.4	+2.0
CDP -> HPT	+0.7	-2.1	+0.2	+1.1
INT -> HPT	+0.3	-1.6	+0.2	+0.6
η HPC	+1.0	-1.9	+0.2	+1.3
η HPT	+0.8	-0.9	+0.1	+1.0
η LPT	+0.8	-0.9	+0.1	+1.0

CDP = Compressor discharge
o/b= overboard
η = efficiency
HPC = High pressure compressor
LPT = Low pressure turbine
HPT = High pressure turbine
SFC = Specific fuel consumption
PT = percentage point
Fn/Wgt = Thrust/weight
TOGW = Take-off gross weight
MFB = Missionized fuel burn
INT = Compressor Interstage (10^{th})

Table 6.—Anticipated run-out and deflections, operational requirements at the proposed advanced rim seal locations

Location	1V-1B	1B-2V	2V-2B
Radial (in)	.04 to .09	.08 to .13	.02 to .10
Axial (in)	-0.04 to +.02	-.03 to +.13	-.04 to +.19
Angular (ID to OD) deg.	.13	.32	.52
Circumferential (TIR) (in)	.004	.006	.008
Max. Speed (ft/sec)	1150	1050	1050
ΔP (max. psid)	0.2	8.5	60
ΔP (min. psid)	0	0.5	6.3
Temp. (max. metal) °F	1200 - 1500	1100 - 1400	1100 - 1400

Note: 1V-1B = first stage vane - first stage blade rim seal interface

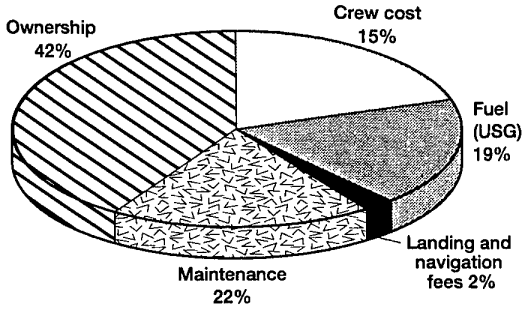

Figure 1.—Direct operating cost breakdown for a 50 passenger regional jet, 800 nautical mile mission.

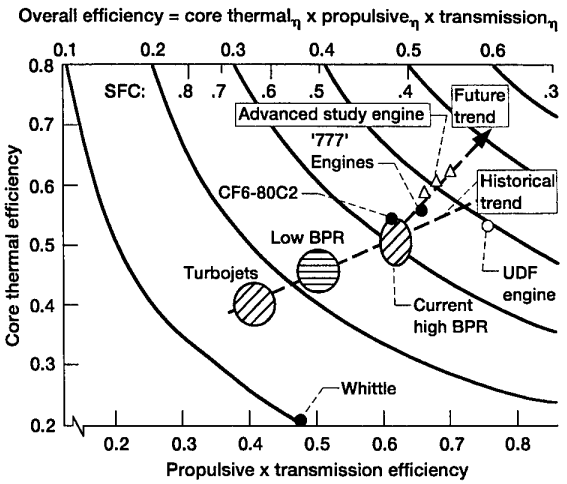

Figure 4.—Historical turbine engine overall efficiency as a function of core thermal efficiency and propulsive x transmission efficiency showing required improvements in core efficiency (Smith, 1993).

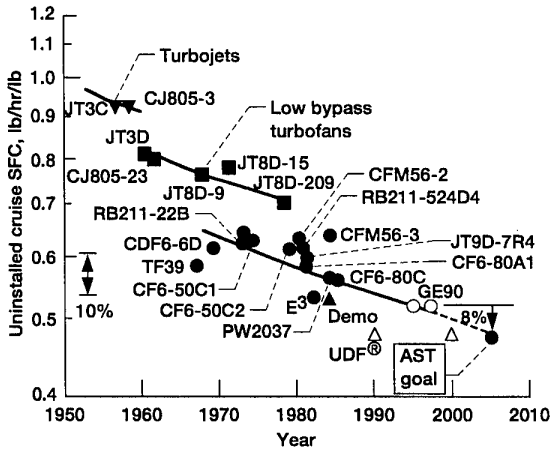

Figure 2.—Subsonic engine historical trend and program goal specific fuel consumption (Steinetz and Hendricks, 1994).

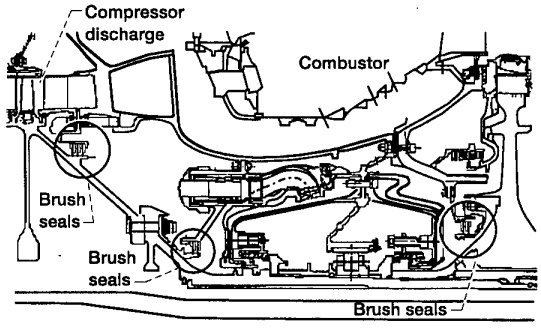

Figure 5.—Brush seals used in PW4168 engine. (Mahler and Boyes, 1995).

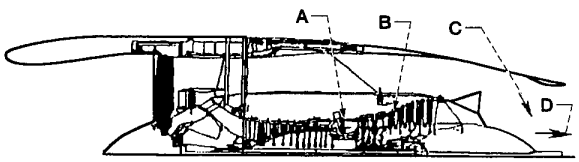

Core thermal efficiency = Energy at the LP turbine entry / Energy of fuel (B)/(A)

Transmission efficiency = Energy at the nozzle / Energy at the LP turbine entry (C)/(B)

Propulsive efficiency = Useful work produced by engine / Energy at the nozzle (D)/(C)

Overall efficiency = Core thermal x transmission x propulsive efficiency

Figure 3.—Breakdown of engine efficiencies (Smith, 1993).

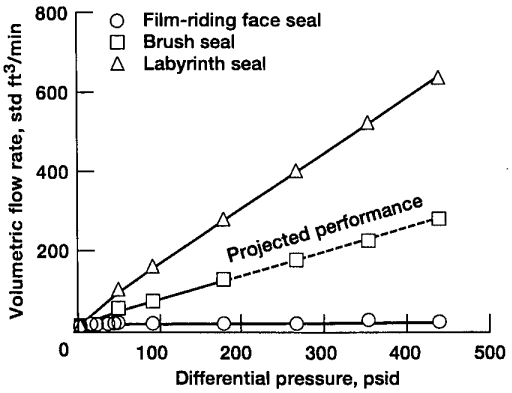

Figure 6.—Comparison of seal leakage rates as a function of differential pressure. Seal diameter 5.84 in. (148 mm). (Munson, 1993).

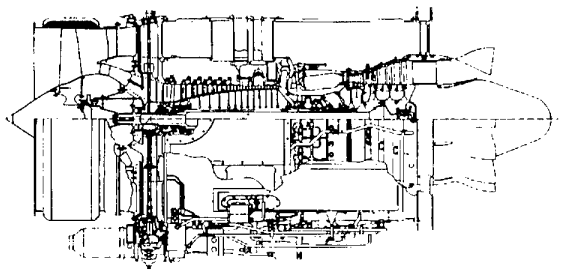

Figure 7.—Allison AE 3007 regional transport engine used to evaluate benefits of advanced seal technology.

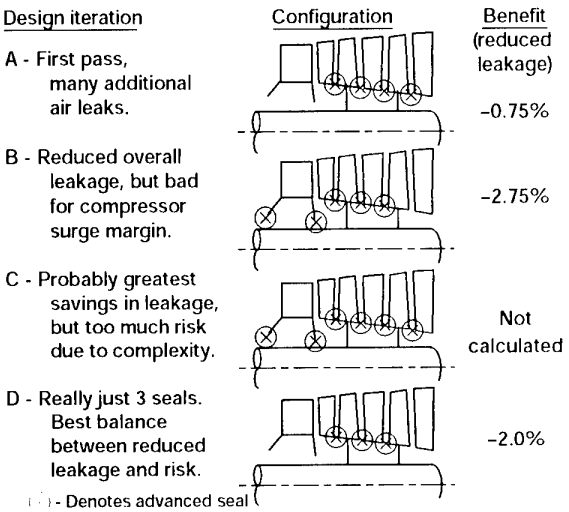

Figure 8.—Several different advanced sealing configurations were studied before selecting one for further analysis.

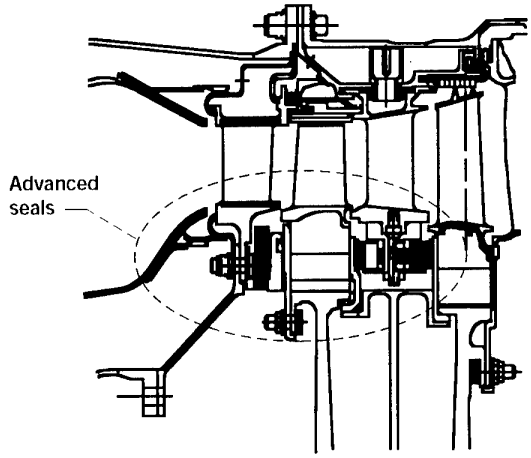

Figure 9.—Turbine rim seal mechanical configuration.

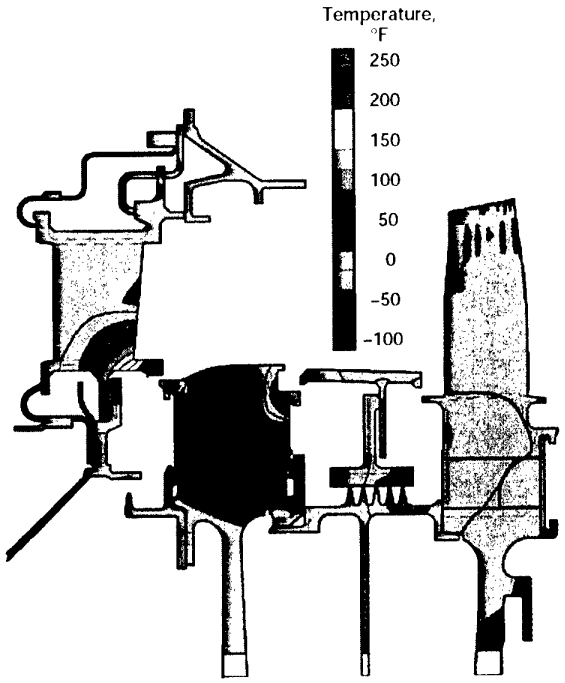

Figure 10.—Advanced HP Turbine temperatures with film-riding face seals minus AE 3007 temperatures. Conditions: steady-state Max T/O; 73 °F; 175 KCAS.

Meeting Discussions

Paper 11: **Advanced Seal Technology Role in Meeting Next Generation Turbine Engine Goals**

Authors: Bruce M. Steinetz, Robert C. Hendricks

Discussor: G. T. Cook

Question 1: a — NASA Program sets different DOC targets for large commercial and regional engines. Is this function of the different engine scales or different levels of technology offering less margin for improvement?

Authors's reply: NASA set a more aggressive cost goal for regional jets, based on two factors:

a) Industry demands in regional jets, for lower costs, are more strict
b) The current NASA advanced subsonic technology program is one of four programs that have targeted the small regional jets and NASA believes there is a greater margin for improvement.

Question 2: Does the NASA program address the power generation sector?

Author's reply: The NASA program does not directly address power generation. This is handled by US Dept. of Energy. However, much of the seal development work does make it to power generation with minor to adaption.

Fuel/Oil System Thermal Management in Aircraft Turbine Engines

Helmut Streifinger
MTU München GmbH
Dachauer Str. 665
80995 München
Germany

1. Introduction

The fuel consumed by an aircraft turbine engine is the preferred heat sink for its lubrication, hydraulic, and integrated drive generator oil systems. Reasons for this are, that a fuel/oil heat exchanger is more compact, if compared with an air/oil cooler, and causes no drag increase and no engine performance loss from air bleed or loss of momentum of the air. Furthermore, the energy exchanged in the fuel/oil cooler is conserved in the thermodynamic cycle. The capacity of the fuel as a heat sink is temperature limited, however, and the fuel pumps contribute to the fuel heating as well. Integration of the fuel and oil systems to a thermal management system is required, which performs its functions without exceeding fuel or oil temperature limits within the aircraft flight envelope. To make this possible, reduction of the oil system heat rejection, as well as the installation of air/oil heat exchangers, has to be considered early in the engine development programme (Ref. 1). A continuous analysis of the heat loads from fuel and oil systems is required, until sufficient test evidence proves that the design meets the requirements.

2. Fuel/Oil Cooling Systems

2.1 System Schematics

The term "thermal management" is used for a system which connects the fuel and lubrication oil systems via the fuel cooled oil cooler (FCOC). Other systems and components, like an engine hydraulic system or an integrated drive generator (IDG), may also use FCOCs and belong to the thermal management system as well. Shown in figure 1 is a schematic diagram of a typical heat management system. It includes a simplified fuel system scheme and an FCOC for lubrication oil cooling. The lube oil circuit is shown together with an air cooled oil cooler (ACOC). Because such an ACOC is not installed in all engines, it is indicated in dotted lines, like the other components which may not always be included. Instead of the simple lubrication oil system circuit indicated in figure 1, a more detailed scheme is presented in figure 2, which shows the main components and the air and oil flows between them. A brief description of the individual systems of the thermal management system will help to better understand their effects on the fuel and oil temperatures.

2.2 Engine Fuel Inlet Temperature

Although not part of the thermal management system of the engine, the fuel delivered from the aircraft tank to the engine fuel interface of a subsonic transport aircraft may have been heated already on the ground by the ambient air and by radiation. The ambient temperature is often used as a limit for thermal calculations. On a hot day (ISA + 40 °C), the maximum engine fuel inlet temperature may reach 55 °C, therefore. At cold day conditions on the ground and during a long cruise at altitude, the fuel temperature at the engine interface may decrease to less than 0 °C. At such a condition, a fuel heater is required to avoid blockage of the engine fuel filter by ice particles.

The fuel system of a combat aircraft is used as a heat sink for its hydraulic systems, secondary power system, the integrated drive generators, and, in some cases, the environmental control system. An air cooled fuel cooler may also be included. The engine fuel inlet temperature depends on the heat generation of these aircraft systems and on the fuel tank temperature, which is determined by the same factors as that of a transport aircraft, but also by kinetic heating during high Mach number flight conditions. A maximum engine fuel inlet temperature of 80 °C or more is typical for modern combat aircraft.

Paper presented at the RTO AVT Symposium on "Design Principles and Methods for Aircraft Gas Turbine Engines", held in Toulouse, France, 11-15 May 1998, and published in RTO MP-8.

2.3 Engine Fuel System

Energy is added to the fuel in the low pressure first stage fuel pump, which typically is a centrifugal pump, in the high pressure second stage pump, which now is a gear pump in most engines, and in the reheat pump, which is a special type of centrifugal pump. Most fuel pumps are driven by the high pressure (HP) spool via the accessory gearbox, and their pumping capacities vary with the HP speed. During normal engine operation, the fuel flow of the centrifugal first stage pump is throttled by the back pressure. The gear pump fuel flow rate only depends on its shaft speed, and excess fuel is recirculated in the fuel system. In some engines, the FCOC is installed upstream of the fuel filter to avoid filter blockage by ice particles when the fuel is cold.

Heat generation of the fuel system is determined by the pump speeds and by the fuel flow rate, by pump efficiencies, the pressure rise through the pumps, and by additional friction losses of bearings and carbon seals.

2.4 Engine Lubrication Oil System

In the lubrication oil system, oil is pumped from the tank to the oil nozzles and squeeze film dampers in the bearing chambers and accessory gearbox, where it lubricates and cools bearings, gears, and carbon seals and removes vibration energy. Scavenge pumps are used to return the oil to the tank. The sealing air flow to the bearing chambers is vented to the centrifugal breather, where oil droplets and oil mist are separated and scavenged to the tank, while the air can flow overboard.

Heat in the lubrication oil system is generated by bearings, squeeze film dampers, gears, carbon seals, oil pumps, as well as by churning and windage in the bearing chambers and gearbox housing. Heat flux through bearing chamber and gearbox walls and through pipes, as well as mixing of sealing air with the bearing chamber oil, adds or removes heat from the system, depending on the local oil and air temperatures. A calculated break-down of this heat to oil is presented in figure 3, for a take-off condition of a projected civil turbofan engine with 18 klbs. thrust.

2.5 Engine Hydraulic System

Many afterburner engines use a hydraulic system for nozzle area variation. The hydraulic pump is driven by the accessory gearbox. If a variable flow pump is used, the engine speed has only a relatively small effect on the heat generation. More important are the nozzle loads on the hydraulic actuators and the convection of the oil pipes between the gearbox mounted hydraulic pump and tank and the actuators close to the nozzle petals. The heat rejection of the system is small and varies only little with the flight conditions.

2.6 Integrated Drive Generator

In transport aircraft, the IDG is installed on the engine accessory gearbox. It has a hydrostatic constant speed drive. Oil from this drive is also used for generator cooling. Heat to oil depends mainly on the electrical power demand and on the drive speed. Data for a typical 90 kVA generator is presented in figure 4.

2.7 Oil Coolers

Fuel cooled oil coolers are relatively compact, because of the high density, specific heat, and thermal conductivity of the fluids. They can be installed within the engine bay or nacelle as required and cause no particular integration problems.

The integration of an air cooled oil cooler is more difficult. It either requires engine bleed air, an ejector system, a mechanically or electrically driven fan, or it is a ram air cooler with bypass air or ambient air. An external ram air cooler causes an additional interface with the aircraft. The ACOC has a negative effect on engine performance (bleed air, loss of momentum of the cooler or ejector air flow, mechanical power loss for fan drive), or increases the aircraft drag (ram air cooler).

In a fighter aircraft flying at a high supersonic Mach number, the air flow through the cooler is choked and the high ram air temperature reduces the temperature difference between air and oil. At high altitude, the low air temperature increases the ACOC effectiveness, but the low air density reduces the air mass flow and, hence, cooling effectiveness. The interactions of these effects are demonstrated in figure 5 for different Mach numbers and altitudes, where the calculated oil temperature reduction across a ram air ACOC is shown for a fixed oil inlet temperature and oil flow. An ACOC position in the bypass duct is even more problematic, because the bypass air temperature will rise to 300 °C at high supersonic Mach numbers.

2.8 Fuel and Oil Temperature Limits

Because of the disadvantages of air/oil heat exchangers, the fuel is the preferred heat sink in a turbofan engine. Its capacity is limited by the maximum permissible temperature, at which fuel degradation and other problems are still acceptable. Fuel coking is a major problem in the fuel nozzles of some fighter engines. Fuel lubricity is worse at high temperatures and degrades the reliability of fuel pumps and fuel servo valves. Boiling of overheated fuel at the fuel pump entry may cause vapour locking, while boiling at the engine burners can cause a combustion instability.

If the oil would not be cooled sufficiently, damage could result to bearings, gears and seals. Because of the reduced viscosity, the load carrying capability of oil becomes lower at high oil temperatures. Its lubricity is worse, and the high oil temperature will cause higher temperatures of bearings, gears, and carbon seals. Oil coking on hot surfaces could start, as well as oil fire, if there are suitable local conditions. The evaporation oil loss through the centrifugal breather will increase as well (Ref. 2).

Figure 6 lists some approximate fuel and oil temperature limits typical for existing engines. Because of the long intervals between engine removals from the aircraft, the limits for civil turbofans are conservative. The cooling problems associated with supersonic and

high altitude flights are reasons for the higher fuel and oil temperature limits, which have to be accepted for fighter engines.

2.9 Fuel System Heat Sink Capacity

The discussion shows, that the fuel system heat sink capacity available for other engine components is limited by high engine fuel inlet temperatures and by heat generation in the fuel pumps. Because of the high turn-down ratios at low fuel flows, the highest temperatures are expected at these conditions, if combined with a high HP spool speed, i.e., during cruise at high altitudes and during an idle descent. It depends on the fuel inlet temperature and on the heat rejection characteristics of the other systems integrated in the heat management system, whether the fuel and oil temperatures will remain below their respective limits. These effects are indicated in figure 7, which compares the change of fuel flow and heat generation for ground idle and for a high altitude flight condition, relative to the data at max. dry, sea level static. The data is representative for a typical fighter engine,

In figure 8, fuel temperatures are plotted for the same flight conditions, instead of heat loads. The largest temperature rise happens at high altitude, with a low fuel flow rate and a high HP spool speed. The high fuel flow at the sea level static, max. dry, running condition causes only a small fuel temperature rise. At extreme altitudes, the combination of high fuel temperatures and low fuel flows is also responsible for very high FCOC oil outlet (feed oil) temperatures.

3. Prediction of Heat to Fuel and Oil

3.1 Heat to Fuel/Oil Computer Programme

The many variables which influence the fuel and oil temperatures in the heat management system make it difficult to define simple correlations for a prediction of the worst conditions. The physical integration of the fuel and oil systems in the thermal management system makes insulated calculations of oil or fuel temperatures useless. This has been the motivation for the development of a modular heat to fuel/oil programme by MTU. The programme combines the effects from the performance, secondary air system, lubrication oil system, hydraulic system, and fuel system, to calculate heat balances and fuel and oil temperatures. The interactions are illustrated in figure 9. Performance data is required as input, while the data of the other systems is calculated in the computer programme for steady-state and transient engine running conditions.

The programme has been developed from the Modular Performance Synthesis Programme described in Ref. 3 (a similar approach is also reported in Ref. 4). It has been used in an international engine programme, where Rolls-Royce have provided all fuel system modules and are responsible for the fuel system, including the FCOC. MTU has programmed the oil system modules and analysed oil system test data for model verification and improvements.

3.2 Physical Models

The heat to oil modules simulate the functions of the respective engine components. They calculate secondary air system boundary conditions, oil and air flows, compartment pressures, and oil exit flow distributions. Heat to oil is computed from power losses of bearings, gears, seals, pumps, as well as from windage, churning, oil pressure drop, heat flux, and from mixing of oil and air flows in components. For transient calculations, the air/oil exit temperatures of the bearing chambers and of the gearbox are modified with time constants.

3.3 Lubrication Oil System Analysis

The computer programme is also used for the lubrication oil system analysis. The measured FCOC oil outlet temperature replaces the calculated data. Heat is added to or subtracted from the individual oil system components, until the calculated scavenge and vent temperatures agree with the actual measurements. This "additional heat" represents the errors of the models used in the heat to oil computer programme. If churning losses have not already been considered in the model, this additional heat gives a good indication, whether oil churning exists at the analysed condition.

3.4 Comparison with Engine Test Results

Heat to oil analysis results have been used to improve the computer model. Boundary conditions, oil flow loss coefficients, seal clearances, and "additional heat" correlations have been updated, and the data of the theoretical model has been compared with measured engine temperatures and heat to oil of the lubrication system. If agreement with test data is reasonable, this permits to use the model for steady-state and transient temperature predictions.

The engine bay model has been improved with flight test data. Calculation of the engine bay air flow and its local distribution is quite complex, and the flow distribution varies with the flight conditions, presumably. It is difficult, therefore, to simulate this in a simple one-dimensional flow model. The engine bay model can be trimmed to give good agreement for a particular flight condition, but if the flight condition changes considerably, the discrepancy may increase again. In figure 10, this is visible during the idle descent, where the calculation over-predicts the scavenge pump exit oil temperature. In general, however, the analysis of flight test data has proven that the model is accurate enough to use it for the prediction of the oil temperatures throughout the flight envelope.

4. Heat to Oil Research

Although it has been demonstrated that reasonable accuracy can be reached with the heat to oil programme, the accuracy relies on the input of "additional heat" for churning, which has to be estimated from the experience of other engine programmes, or from engine and rig test analysis. To improve the heat to oil prediction and to eliminate or reduce churning in bearing chambers and gearboxes, European and German research programmes

deal with this subject. This will eventually lead to the development of CFD codes which can calculate the complex two-phase flows in bearing chambers and gearboxes.

5. Future Performance Improvements

5.1 Reduction of Heat Generation

It is difficult to reduce the heat generated by the fuel and oil systems of an engine without detrimental effects on performance or reliability. In the fuel system, variable-stroke plunger-type pumps have been used in the past. Because their capacity can be adjusted to the engine fuel flow demand, they produce less heat at low fuel flows. Because high pressure gear pumps are mechanically simpler and more reliable, they have replaced the variable displacement pumps in most engines. Recent developments investigate vane pumps with variable capacities. A fuel pump driven by an electrical motor or by an air turbine motor could run at variable speed, but would cause weight and performance penalties, and would be less reliable, presumably. Fuel systems with one or two centrifugal pumps have been investigated as well, but their overall performance does not promise much benefits for heat management. One possibility to avoid high reheat fuel temperatures at high altitudes would be to bypass the reheat pump and to supply the main and reheat fuel flows from the high pressure gear pump. Its capacity is sufficient for high altitude flight conditions.

In the lubrication oil system, the introduction of air riding carbon seals could help to avoid the friction losses of conventional carbon seals. Replacing labyrinth seals by brush seals or clearance seals can reduce the bearing chamber pressure and the windage losses. Carbon seals, meshes, and baffles can be installed to reduce churning. Gears should be designed for the lowest speed compatible with weight and space considerations, and the number of gearboxes and gears should be as low as possible. Elimination of the external centrifugal breather by a center vent breather would remove at least one high-speed gear and reduce the bearing chamber pressure, with advantages for windage and churning. The separation of lubrication and cooling in bearings, as well as the introduction of ceramic bearings, could reduce their heat generation. The feed oil flows should be as low as possible and just sufficient for component lubrication and cooling, to limit the churning and windage losses. This requires to use a full flow (non-regulated) feed oil supply, running with only a small margin over the oil pressure warning condition. With a suitable metering system, the low heat rejection at low engine speeds would permit to reduce the feed oil flows considerably more than it is the case with a full flow system. This would help to reduce the fuel and feed oil temperatures at critical low fuel flow conditions.

5.2 Integration with Aircraft Fuel System

Fuel recirculation to the aircraft tank increases the fuel flow through pumps and coolers and can be used to limit the fuel and oil temperatures. For many years and without problems, such a system has been used in a European combat aircraft. In the MD-90 airliner, it is used to heat the fuel in the tanks to avoid wing icing. The subject of thermal management becomes even more complex, however, because aircraft and engine fuel systems form one integrated heat management system.

If fuel recirculates only for a short period of time to avoid peak fuel and oil temperatures, or only when required by the aircraft, this is no problem. If the engine relies on recirculation for longer periods of time, however, the heat stored in the tanks may even limit the aircraft range, because tank temperature limits will be reached when the tank fuel contents is low and recirculation continues. One of the worst conditions for such a system is a long range idle descent at the end of a flight, when the tank contents and the engine fuel consumption are low.

5.3 Higher Fuel and Oil Temperatures

In the United States, JP8+100 fuel will replace all military jet fuels. It has a higher resistance to thermal degradation and will permit higher fuel temperatures or better engine reliability.

The specification MIL-PFR-7808L, which replaces MIL-L-7808J, is for oils with a low temperature limit of -51 °C. It includes a new 4 cSt oil with a better thermal stability than the 3 cSt oil (Type I), which is retained in the specification as well. The thermal stability of the 4 cSt oil is similar to that of the 5 cSt (Type II) oil of MIL-L-23699, which can be used down to a temperature of -40 °C. Research is ongoing for oils with higher temperature stability, which can cope with the thermal effects of increased oil system heat rejection and improved fuel consumption, as expected as a result of the IHPTET research programme (Ref. 4).

6. Summary

The heat generation mechanisms of fuel and oil systems are discussed. It is shown that low fuel flow conditions, combined with relatively high HP spool speeds, are the most demanding conditions for the heat management system. If the oil temperature is high, an air cooled oil cooler may be used. Its performance constraints and size, as well as the problems at high Mach numbers and high flight altitudes, make it a difficult choice for fighter engines, however.

Interactions between all components of the thermal management system require that oil and fuel temperatures are considered together. A heat to fuel/oil computer programme is presented, which is suitable to fulfil this requirement. This is demonstrated by comparison of a calculated scavenge oil temperature with test data, and the suitability of the programme for oil system analysis is discussed. Oil churning has often to be included to the computer model to simulate the measured oil temperatures. The churning models rely on experience from other engine programmes or on analysis of engine and rig test data of the actual engine type.

European and German research programmes are ongoing, which aim on the reduction of churning and on a better understanding of the physics. The paper briefly presents some other possible methods to reduce the heat generation in fuel and lubrication oil systems and to limit the fuel and oil temperatures. One possibility is an integrated aircraft/engine thermal management system, and the advantages and risks of this approach are discussed. The introduction of better fuels and oils in the United States, which will permit to design engines with increased fuel and oil temperatures, is mentioned.

Acknowledgements

The author would like to thank all colleagues who have contributed to the development of the heat to fuel/oil computer programme, and who have worked with him on the subject of thermal management over the years and on different projects. This also includes colleagues from Rolls-Royce, FiatAvio, STN ATLAS Elektronik, DASA, Pratt & Whitney and Snecma. My special thanks go to Peter Harding from Rolls-Royce Bristol, whose co-operation has made it possible to successfully use a common heat to fuel/oil computer programme in a joint engine project.

References

1 Heat Management in Advanced Aircraft Gas Turbine Engines
G. L. Brines, D. E. Gray
ASME Paper 86-GT-76, 1986

2 In-service Engine Oil Problems
K. Maier
Symposium Aviation Turbine Oils
Technische Akademie Esslingen
December 14th-16th, 1988

3 Calculation of installation effects within performance computer programs
J. Kurzke in
"Steady and Transient Performance Prediction of Gas Turbine Engines
AGARD Lecture Series 183, 1992

4 High Temperature Liquid Lubricant Requirements For Advanced High Performance Gas Turbine Engines
G. Pezzella, P.A. Warner
AIAA/SAE/ASME/ASEE
26th Joint Propulsion Conference Orlando,
July 16-18, 1990

Figure 1: Heat Management System

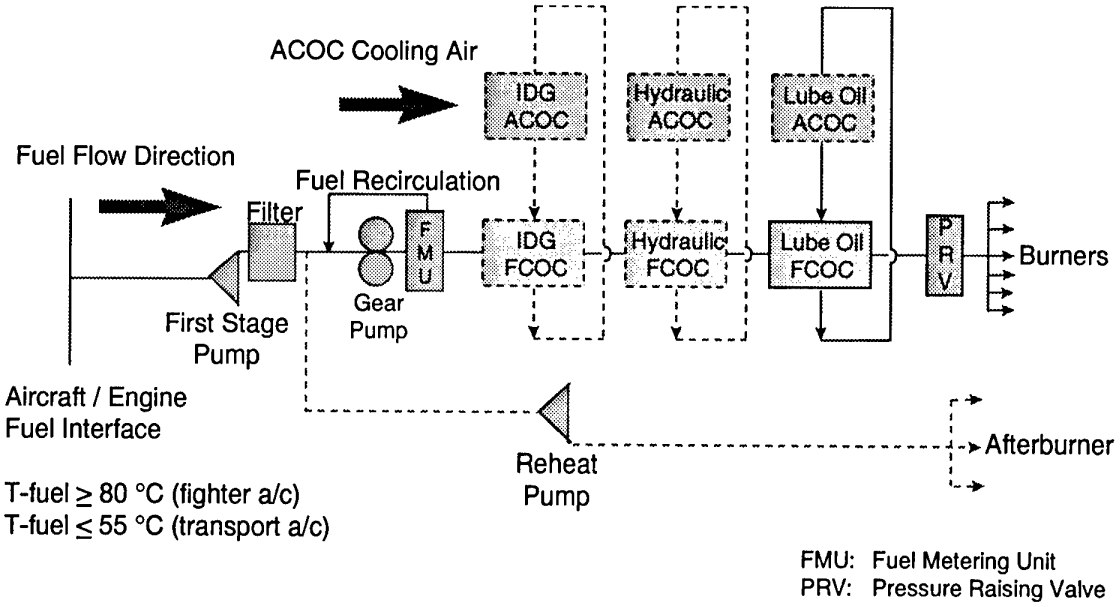

Figure 2: Simplified Lubrication Oil System

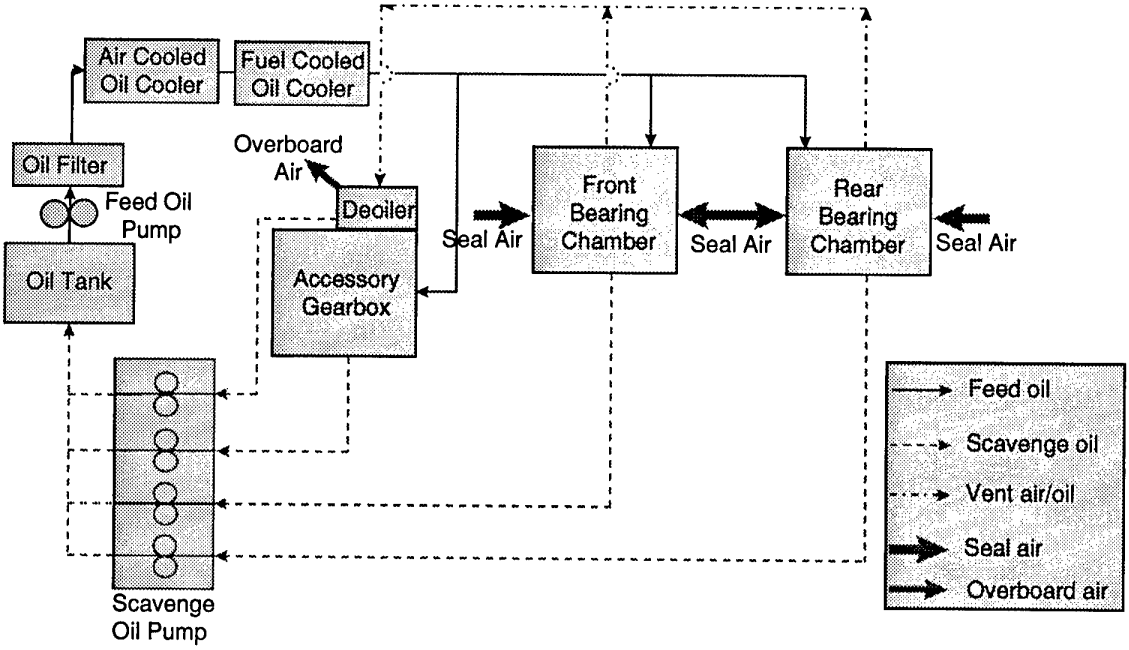

Figure 3: Heat to Oil Break-down for an 18 klbs. Engine Project - Take-off Condition

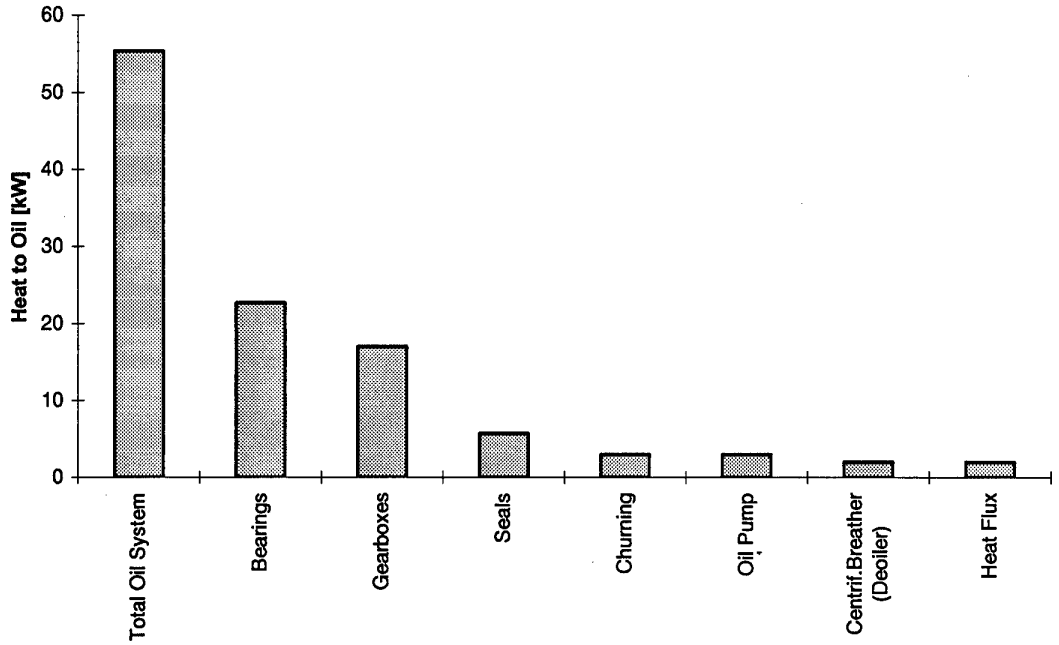

Figure 4: Integrated Drive Generator Heat Rejection

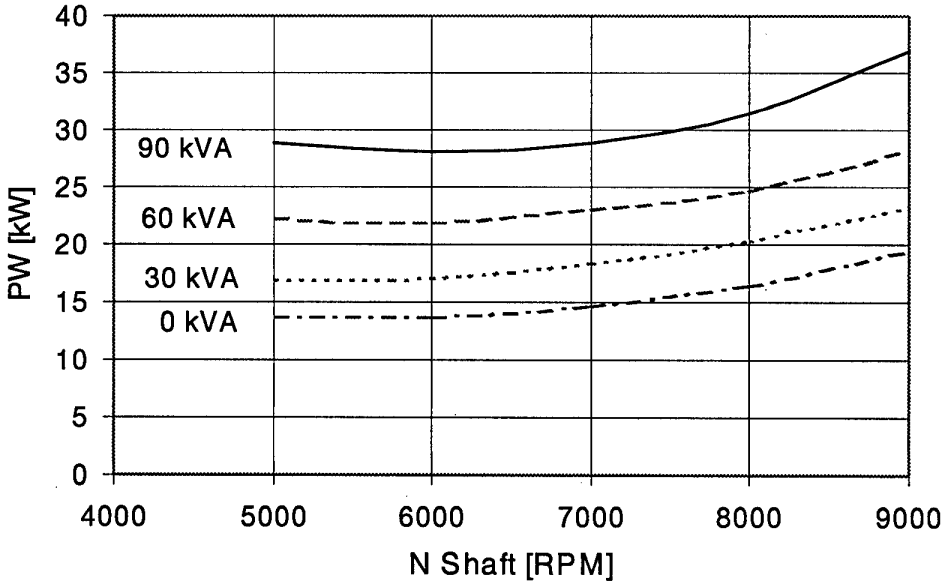

Figure 5: Air Cooled Oil Cooler Performance

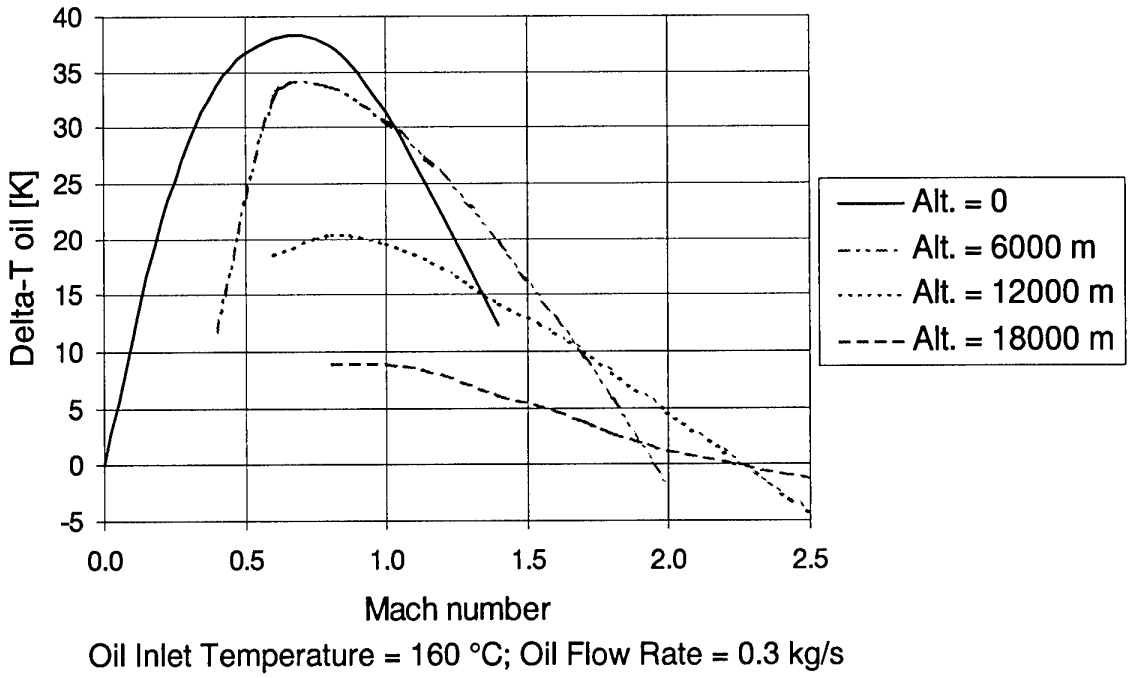

Figure 6: Typical Fuel and Oil System Temperature Limits

	Turboprop/Turboshaft	Turbofan/Transport	Turbofan/Fighter
Fuel Temperatures			
fuel filter in - minimum	0 °C	0 °C	anti-icing additive
Burner in - maximum steady state	130 °C	130 °C	160 °C
Burner in - maximum transient	140 °C	140 °C	180 °C
IDG Oil Temperatures			
Oil cooler out - maximum	100 °C	100 °C	-
Oil cooler in - maximum	135 °C	135 °C	-
Hydraulic Oil Temperatures			
Oil cooler out - maximum	-	-	135 °C
Oil cooler in - maximum	-	-	165 °C
Lubrication Oil System Temperatures			
Oil cooler out (feed oil) - steady-state	110 °C	135 °C	160 °C
Oil cooler out (feed oil) - transient	125 °C	160 °C	180 °C
Scavenge pump out - steady-state	165 °C	165 °C	200 °C
Scavenge pump out - transient	180 °C	180 °C	220 °C

Figure 7: Change of Engine Fuel Flow and Systems Heat Generation with Flight Condition

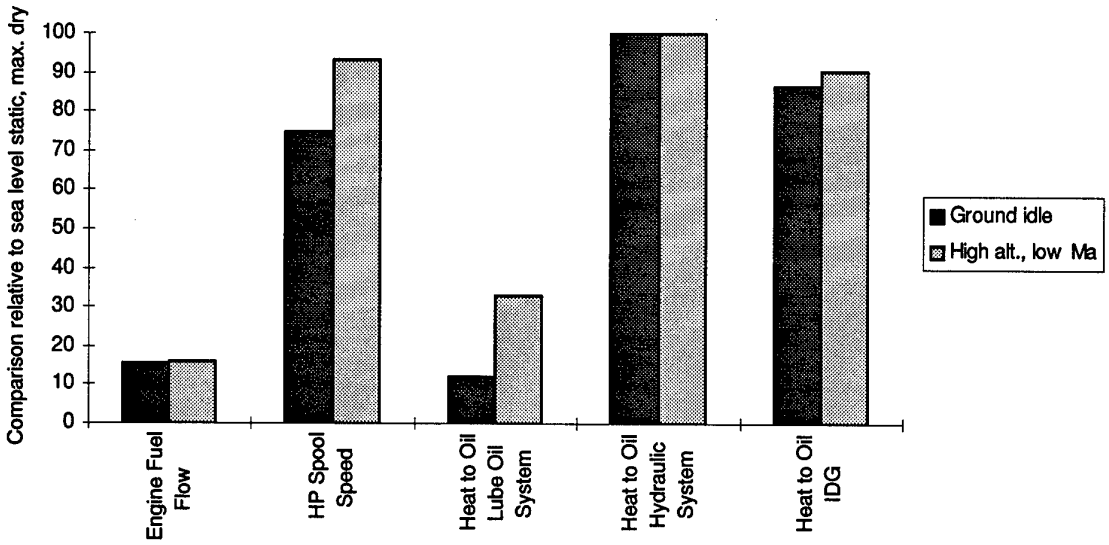

Figure 8: Fuel Temperature Rise From Engine Interface to Burners

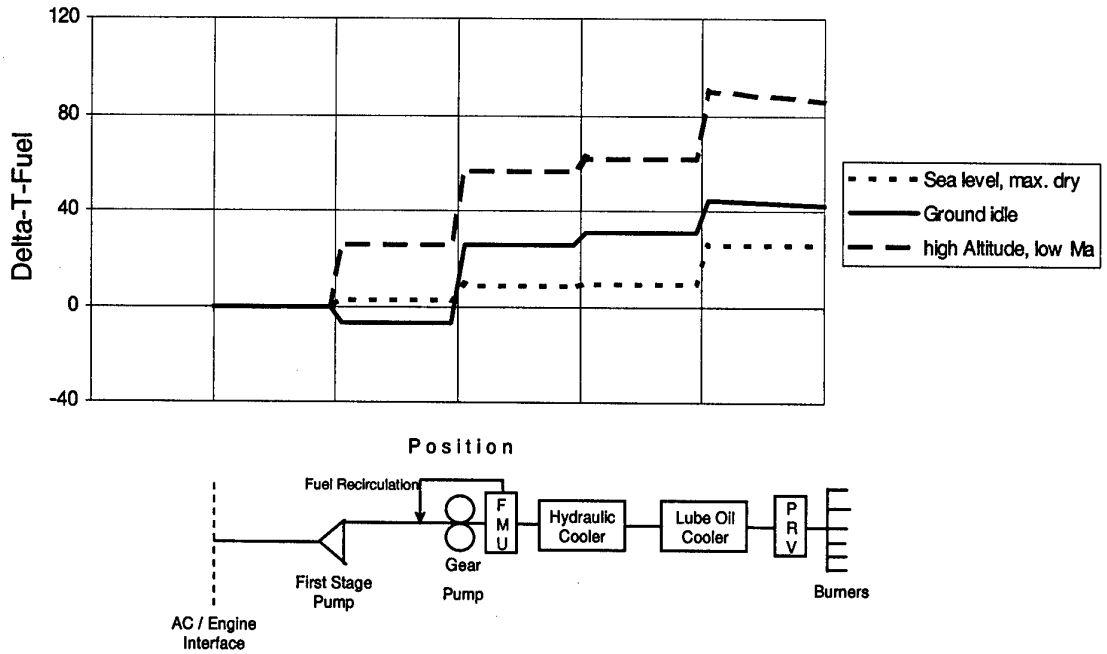

Figure 9: Interaction of Components in the Heat to Fuel/Oil Computer Programme

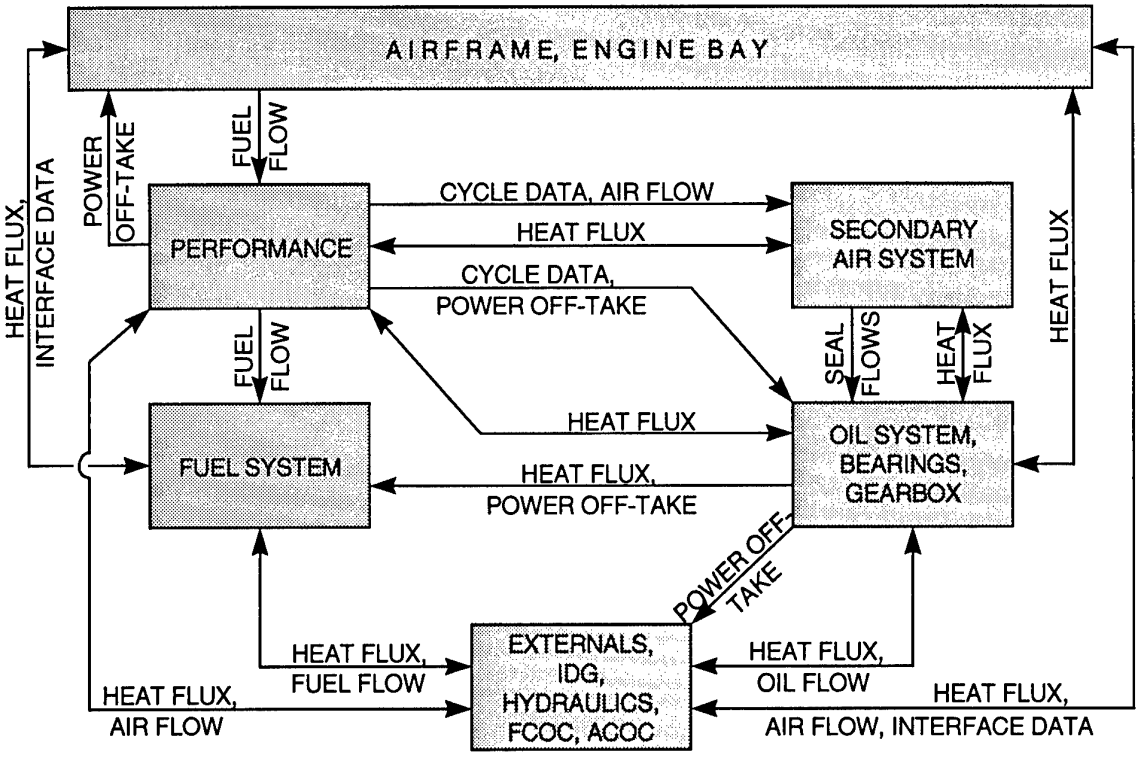

Figure 10: Comparison of Calculated Scavenge Return Temperature and Flight Test Data

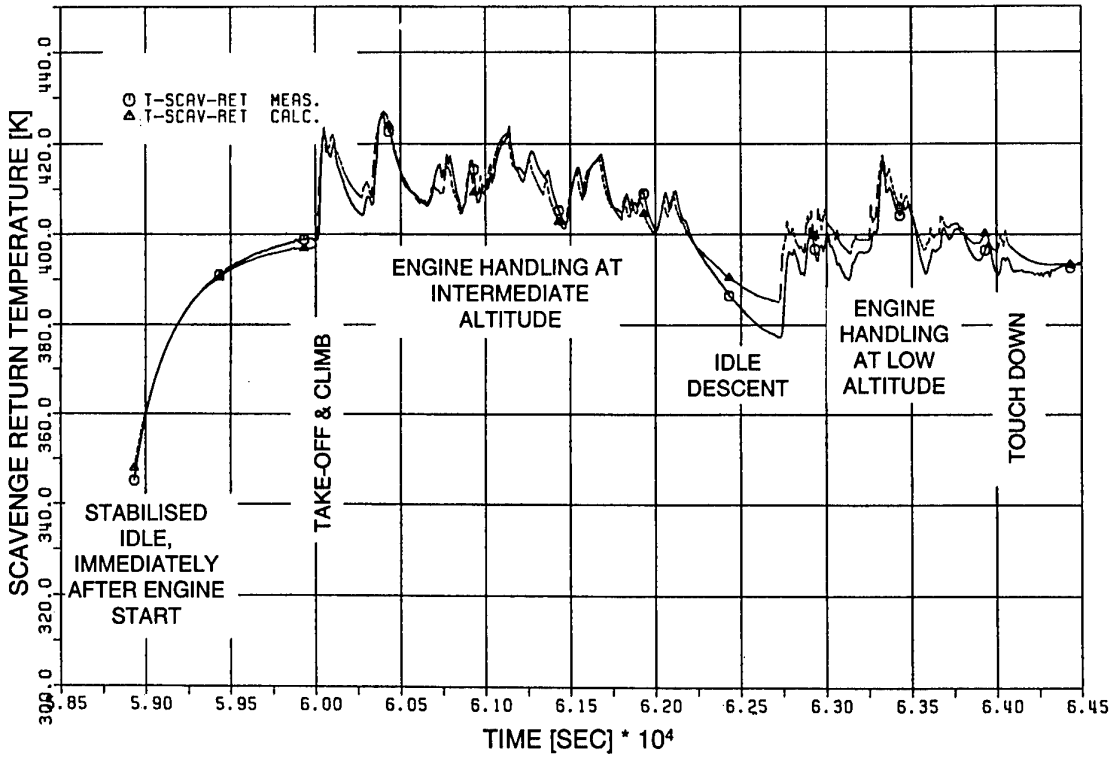

Fault tolerant design methodology in software for safety related systems

Trevor Cockram
Rolls-Royce Military Aero Engines Limited
PO Box 3
Filton
Bristol BS34 7QE
UNITED KINGDOM

1. SUMMARY

System failures caused by software are not caused by wear out; they are due to errors in the design or specification of the software. Most activities during the software development process have the potential to cause errors in the final software code. An important mechanism in this type of systematic error is human error, both as individuals and within groups.

Adherence to procedures or standards implies a kind of fault tolerant design. However, in order to judge whether practices are effective at achieving the required integrity of the product, a measurement based approach to software design is required.

The methodology described has been developed to provide project managers with a means to assess the integrity of the software product at any stage prior to delivery. The product integrity is described in terms of the probability distribution for the numbers of errors that exist in any product or set of products. The approach is equally applicable to determine the effectiveness of the quality assurance processes and of any error correction mechanism including software maintenance.

The methodology is supported by a tool that uses graphical probability models to describe each atomic development or review process, defining the dependencies between the process attributes. Bayesian statistics are then used to calculate the integrity prediction using *a priori* experience together with evidence.

2. INTRODUCTION

The wear-out mechanism that occurs with hardware cannot occur in software. Software errors are systematic errors; i.e. they are built into the software. An important mechanism for this type of error introduction is human error which results both from our nature as individuals and in the way in which engineers act and communicate in groups [PRICES 1997]. Traditionally with safety related systems reliance is placed on a managed development process and testing to find faults within the software. The problem with this approach is that the errors are found at the end of the development process. It is known, however, that a high proportion of software errors are introduced at the start of the development lifecycle during the requirements phase. For example [Lutz R.1993] found that some 70% of software faults in mission critical space systems, were due to requirements errors.

Software faults can also be introduced during any of the subsequent stages of development. Software faults when detected, lead to re-work. When detection occurs later in the process, e.g. testing, then the re-work of the previous development stages is often at considerable expense. The error correction process, however, is not perfect and further faults may be introduced by the re-work.

The FASGEP (Fault Analysis of the software generation process) project [FASGEP 1997] set out to identify the factors that influence the number of faults introduced into a safety related software system and to provide a basis for computing numerically the number of faults that could be present in a software product.

A software fault will only be manifested as a failure of the system when a particular input sequence, exercising the portion of the software code containing the fault is presented to the system. This set of inputs may never occur during the operation of the software and the fault remains dormant for the life of the system. It is therefore not possible to consider software in conventional reliability terms. This is confirmed by considering the profile of integrity against time. With conventional reliability growth it is assumed that integrity will improve over time, however a "Christmas tree" profile is often seen [Sommerville I, 1992].

The approach taken was to predict the probability distribution for the number of faults that exist in any product or set of products in terms of its fault propensity. This is defined as the probability that there being no faults, one fault two faults and so on in the product.

Paper presented at the RTO AVT Symposium on "Design Principles and Methods for Aircraft Gas Turbine Engines", held in Toulouse, France, 11-15 May 1998, and published in RTO MP-8.

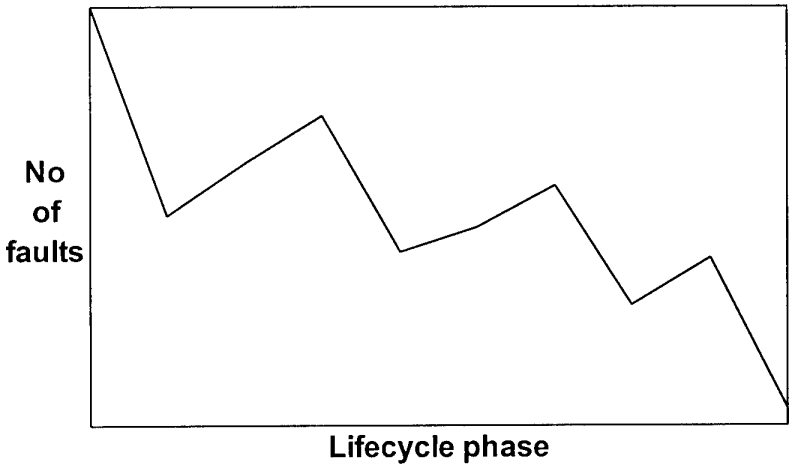

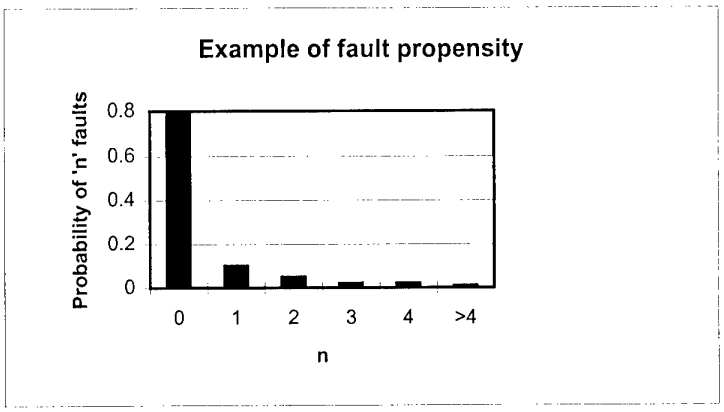

3. SOFTWARE DEVELOPMENT PROCESS

Adherence to procedures or standards for example IEC1508 implies a kind of fault tolerant design. However, in order to judge whether the practices adopted, to comply with the standard, are effective at achieving the required integrity of the product, a measurement based approach to software design is required.

To provide a framework for the measurement it is necessary to characterise the software development process. Conventional lifecycle or process models are not appropriate as they often described the ideal or intended process [Parnas DL & Clements PC. 1986].

It is necessary to describe the actual process used to develop the software in a sufficiently generic way in order to provide a realistic estimate of the number of software faults in a product. The approach taken was to use the concept of an "atomic process" which can be considered as a single activity or task undertaken by an individual. The atomic process is decomposed into its lowest level entities:

i.e.

- an input product (or set of products)
- a process (or activity or task)
- an output product (or set of products)

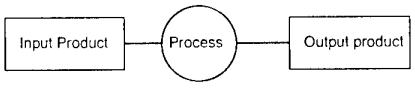

Atomic process

The complete development process can be described by linking processes via the products, the output product of one atomic process being the input product of another, either sequentially in series or concurrently in parallel which can be represented in a linear diagram or directed acyclic graph (DAG).

In general terms two types of atomic process have been characterised:

- Development processes, i.e. specification, design or coding including re-work
- Review processes, e.g. Reviews, Walkthroughs, Inspections

Development processes (indicated as D in the DAGs) can be regarded as a potential source of fault introduction, and

review processes (indicated as R in the DAGs) as potential means of identifying faults. (To complete the process description, the combination of process elements is indicated by I.)

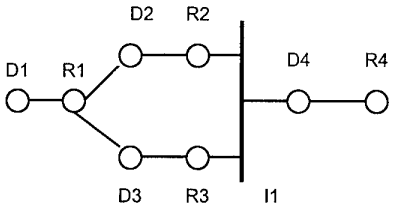

A simple DAG

2.1 Modelling of review effects

Reviews can be considered as not affecting their input products directly. It is the consequent development process that corrects any software faults that have been identified by the review. Reviews cannot be assumed, however, to identify all of the faults present in the input product, so in the model it is necessary to identify the remaining fault propensity in the product. The removal of faults results is a denuded development atom (which is indicated as D') and a reduction of the scope of the review to only the unmodified portion of the development atom (which is indicated by R'). As an example, when faults are found by review R1 in development atom D1, the process model is modified to become:

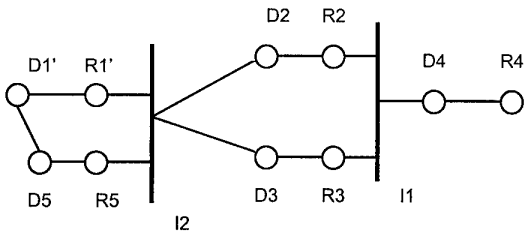

DAG showing the effect of faults found in D1

As a result of identifying faults through-out the software development a complete picture of the process is built up using these constructs. Although the concept of combining process elements is relatively simple, as the fault propensities for each atom are probability distributions the mathematics is more complex requiring convolution of fault propensity functions. A full description of the mathematics is given in [May et al. 1993]

2.2 Process attributes

It is assumed that there is a correlation between the attributes of the atomic process and the number of faults introduced during the development. For each development process, attributes have been identified:

- Human factors attributes
  - person related: training, experience, motivation, role
  - task related: organisation, workload, familiarity,

    concurrency, variability, complexity

    environment related: physical, management, social
- Product attributes
  - size, complexity, format, formality, usability, faults
- Project attributes
  - management of: business, team, resources, project, process, quality configuration
- Tools & methods attributes
  -availability, support, maturity, applicability, usability, flexibility, robustness, efficiency, compatibility
- Unidentified process attributes
  - which is a recognition that in any software development process there are likely to be several processes that are hidden or not thought as processes in their own right.

Attributes for the review process have been similarly identified to determine the effectiveness of the review:

- Product attributes
  - size, complexity, fault propensity
- Effectiveness of pre-meeting
  - adequate time, experience, availability of check lists
- Quality of review meeting
  - quality of chairperson; size of team; experience of reviews, application and domain.
- Quality of reviewing process
  - formality, scope, evaluation criteria, preparation time.

Data is collected from each project using a standard questionnaire which is applied during the software development.

Sample of the questionnaire

How many algorithms are implemented in the product?

..... [Integer]

How many outputs are there from each section of product?

..... [Integer]

How many inputs into each section of the product?

..... [Integer]

Or What is the cyclomatic complexity of the finished code? (McCabes)

.....[Integer]

This section is only applicable to packages and the main program

Is the product structured in a modular form? e.g document sections, functions, packages

☐Yes ☐ No

What is the maximum depth of module nesting?

.....[Integer]

How many modular sections constitute the product?

.....[Integer]

What is the average (mean) no. of lines in a modular section, package or subunit?

..... [Integer]

4. BAYESIAN PROBABILITY MODEL

To determine the fault propensity of a development atomic process or the review effectiveness of a review process type of Bayesian probability model known as a graphical probability model (GPM) or causal network is required.

Causal networks provide a framework for performing uncertain inference [Pearl J. 1988]. A causal net consists of a number of nodes which represent variables which can take discrete values linked together by links which represent the dependencies between the variables. Each link represents the influence which the value of one variable has on the value of another (if the influence is zero then there is no link). The influence is not necessarily linear: in general if one node can take n values and the other m values, the influence of one node on the other is an nxm matrix

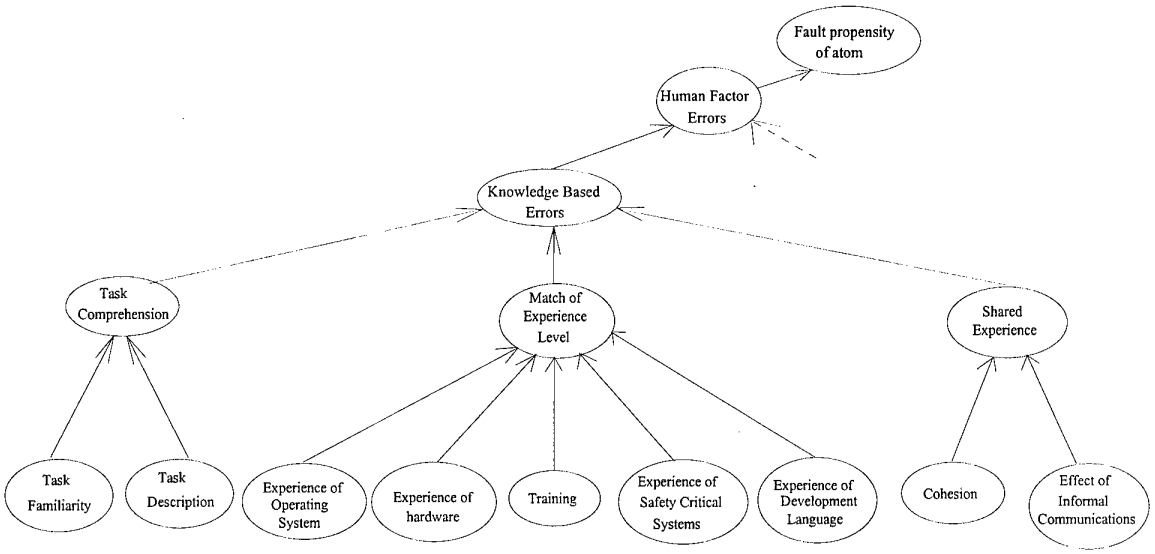

Example of a causal network

Experience is used to provide a priori conditional probability values for each node matrix. If values are then supplied for the lowest level nodes, which are provided from the metrics derived from the questionnaire, then it is possible using Bayesian inference calculations to compute the probability for each value in the top level node.

```
n13 "SHARED_EXPERIENCE" %% Node name and
label
1030.62 798.258      %% Node position
( "poor" "good" )    %% State vector
 n21 n68             %% Parents
((( 1 0 )            %  poor  poor
  ( 0.8 0.2 )        %  poor  fair
  ( 0.5 0.5 ))       %  poor  good
 (( 0.8 0.2 )        %  fair  poor
  ( 0.5 0.5 )        %  fair  fair
  ( 0.3 0.7 ))       %  fair  good
 (( 0.6 0.4 )        %  good  poor
  ( 0.4 0.6 )        %  good  fair
  ( 0 1 )))          %  good  good
```

Example of conditional probability table in Hugin format

As data from a number of projects becomes available is it possible to improve the conditional probability values for the link matrices, by feeding both evidence and actual results into the network. The resulting new experience can be taken into account. This provides some limited form of artificial intelligence within the model.

Ideally, all the influences feeding into a node should be independent pieces of evidence. In practice, however, this is not always possible, and the dependencies that do exist are difficult to measure or even determine. If too many incorrect independence assumptions are made, then the quality of the network will be degraded. The problem has been addressed by deriving an orthogonality rule, drawn from related ideas in measurement theory [Fenton N 1991].

The application of causal network requires three types of knowledge:

1. The structure of the network showing the node dependencies
2. A matrix giving the conditional probability distribution for each link
3. Evidence at some nodes.

Evidence is applied to the network either as direct measurement of the variables or as a probability distribution to describe the effect at a single node with uncertainty. The level of confidence in the resulting prediction can then be measured by observing the variance of the final distribution. A low variance will indicate high confidence and a high variance - low confidence. By this means it is still possible to make some form of prediction (with lower confidence) even when some metrics data is missing or not available.

4.1 Model verification

Verification of the model is difficult, as although the model will predict a distribution for the fault propensity of an atom or the effectiveness of a review, the absolute number of faults present in the product cannot be found. What can be found, however, is the number of findable faults given that with safety related systems, the process of reviews and testing will result in software to an acceptable standard, This view is supported by data from Adam's experiment [Adams EN. 1984] which suggested that above a certain level of fault finding effort, the number of fault found is altered little.

By using data from actual projects is therefore possible to assign all the faults found to particular atomic processes and compare the actual results found with the predicted values.

5. PROTOTYPE TOOL

The methodology described above can be applied, to provide project managers with a means to assess the integrity of the software product at any stage of development prior to delivery. The methodology is supported by a prototype tool which applies the graphical probability models for each atomic development or review process according to the atomic process model.

The tool provides the user to apply the method in full, with the ability to:

- complete the questionnaire on-line and to validate the responses.
- to create the atomic process model.
- a Bayesian inference engine (inner model).
- to compute the predicted fault propensities in accordance with the process model (outer model).

The tool was developed in conjunction with my colleagues at Nuclear Electric and Lucas Aerospace. The tool is implemented on UNIX workstation, using an X windows emulation to interface with a spreadsheet package application which allows the questionnaire validation and data manipulation to be completed. Bespoke software was written in 'C' and is used for the process model definition and for the fault propensity computation. The main Bayesian inference engine is the Hugin tool [Olesen KG, et al. 1993], which was developed as part of an ESPRIT program. The tool has been applied to a number of safety related projects in both the Aerospace and Nuclear industries.

It must be recognised, however, that the amount of data required by the method as a whole is large and the results obtained, although encouraging are not statistically sufficient to claim the method as completely successful yet. Application of parts of the method, particularly in determining the quality of design reviews, have shown the potential for the method and work in developing a more limited application in this field is continuing.

ACKNOWLEDGEMENTS

Much of this work was developed as part of the DTI funded FASGEP project ref. IED4/1/9004. I am also grateful for the valuable contributions made to the project by : Lloyd's Register, Lucas Aerospace, CSC Computer Sciences Ltd, Nuclear Electric, Open University, Bristol University, Dr M Falla and my colleagues in Rolls-Royce plc.

REFERENCES

[PRICES 1997] Tomlison C, Cockram TJ, Griffyth J, Merrett P, Smith L, Summers R, West J, Whytock S, Winsborrow L. *PRICES Code of Practice*
available from Department of Trade and Industry SafeIT Distribution Centre 35 Benbrook Way, Macclesfield, Cheshire, UK, SK11 9RT 1997

[Lutz R.1993] Lutz R. Analyzing Software Requirements Errors in Safety-Critical Embedded Systems, *Proceedings of the IEEE international symposium on requirements engineering. San Diego 1993* p126-133

[FASGEP 1997] Fault Analysis of the Software Generation Process (*various reports*) available from Department of Trade and Industry SafeIT Distribution Centre 35 Benbrook Way, Macclesfield, Cheshire, UK, SK11 9RT 1997

[Sommerville I, 1992] Sommervile I. *Software Engineering* - Fourth Edition
Addison-Wesley Wokingham ISBN 0 201 56529 - 3

[Parnas DL & Clements PC. 1986] Parnas DL, Clements PC. A rational design process: how and why to fake it. *IEEE Trans Software Engineering Vol SE-12 No2, February 1986* p251-257

[May et al. 1993] May J, Hall P, Zhu H, Cockram T, Bird N, Winsborrow L. Fault Prediction for Software development processes in *Mathematics of Dependable Systems,* based on the proceeding of a conference on Mathematics of Dependable Systems organised by The Institute of Mathematics and its Applications and held at Royal Holloway, University of London in September 1993
ed. C Mitchell and V Stavridou
Oxford University Press 1995 ISBN 0 19 853491 4

[Pearl J. 1988]. Pearl J. *Probabilistic reasoning in Intelligent Systems: Networks of plausible inference.* Morgan Kaufmann, San Mateo, California 1988

[Fenton N 1991]. Fenton NE. *Software Metrics - A rigorous approach*
Chapman and Hall London 1991 ISBN 0 412 40440 - 0

[Adams EN. 1984] Adams EN. Optimizing preventative service of software products *IBM Journal Vol 28 No 1* p2-14 1984

[Olesen KG, et al. 1993], Olesen KG, Lauritzen SL, Jensen FV. aHUGIN: A system creating adaptive causal probabilistic networks
Technical report, Aalborg University Denmark 1993

Monitoring and Control of Helicopter Engines at Abnormal Operating Conditions

W. Erhard, R. Gabler, A. Preiss, H. Rick

Technische Universität München
Lehrstuhl für Flugantriebe
D-85748 Garching, Boltzmannstraße 15

1 ABSTRACT

A digital non-flight standard control system for the helicopter engine ALLISON 250-C20B has been developed. It is used as a development slave system at the institute's test bed for various research projects. The topics to be presented in this paper cover control and monitoring aspects for these types of engines in the presence of abnormal operating conditions. Investigated are compressor rotating stall and surge due to engine failure, control system failure, inlet distortion, as well as water ingestion problems.

To get control over the operating line of the engine and to avoid, respectively to abort a surge condition an appropriate bleed valve can be used. Therefore the original valve is replaced by a newly developed simple and cost effective one which is integrated into the electronic control system and can be controlled by software.

The software itself is developed with means of an object oriented tool and runs on a rapid prototyping real-time computer. To detect stall and surge onset as early as possible different methods of signal analysis are applied and investigated. The wavelet method as a relatively new one proved to be very interesting for such applications.

But it emerged that in many cases, particularly at slam accelerations, it was not possible to avoid surge entirely with the developed system, because of insufficient actuator dynamics. Therefore a special control mode was developed to abort surge immediately and recover to normal operation.

2 INTRODUCTION

Safety aspects are of major importance for aircraft engines. Therefore any instabilities in operation that will cause loss of performance or mechanical damage have strictly to be avoided. Gas turbines are the most commonly used propulsion systems for fixed wing as well as for rotary wing aircraft. There are some reasons that can lead to instabilities respectively abnormal operating conditions of such engines. The Federal Aviation Authorities FAA [1] describe possible reasons for reduced stability margins as for instance, inlet distortion, water, snow or ice intake, adverse adjustment of the control system or engine deterioration.

In particular the component compressor is limited in its stable operating range. When the aerodynamic load of the compressor exceeds a certain limit then the flow stalls at the blade suction side and that ends in a non-stable operation. Both the rotating stall condition and the surge condition cause an immediate loss of performance and high mechanical stress for the engine. Whereas rotating stall is localised on the compressor, surge is an instability of the entire engine [2,3,4].

Especially slam accelerations decrease the stability reserve because of the thermal compressor throttling. That is the reason for compromises in the gas turbine design to implement a sufficient stability reserve which implicate a lower performance and overall efficiency. In most cases additional control devices such as bleed valves or variable stator vanes are used to extend the stability reserve in the low power operating region.

Now it is easy to understand that many investigations concerning aerodynamic compressor instabilities have been done in the past decades. The following main focuses have emerged:

- fundamental investigations on the global behaviour of turbo machines near the stability margin
- development of control concepts to influence the position of the compressor operating point or to extend the stable operating range
- investigations of parameters which influence the position of the stability margin.

The present paper makes a contribution to the first two items whereas the experimental part was done on the 300 kW turbo-shaft engine ALLISON 250-C20B. In contrast to many other publications concerning investigations on compressor rigs the present paper deals with tests on a complete production engine. The ALLISON engine itself was only marginally modified for additional instrumentation, but the hydro-mechanical control system was replaced by a newly developed lab-FADEC. Comparable publications among others are [5,6,7,8].

The major task was to develop a monitoring and control system to detect stall onset as early as possible and to avoid compressor surge as far as possible. At least to minimise the surge time, abort surge and recover as soon as possible to the required operating point.

3 EXPERIMENTAL SET-UP

3.1 Test Engine

The test bed engine is an Allison 250 turbo-shaft gas turbine used in various helicopters and aircraft. It is a series -C20B model that was originally installed in a German Army Bo105 helicopter, which is equipped with two power plants each delivering 300 kW maximum continuous power. With more

Paper presented at the RTO AVT Symposium on "Design Principles and Methods for Aircraft Gas Turbine Engines", held in Toulouse, France, 11-15 May 1998, and published in RTO MP-8.

than 26,000 units built, the engine still is in production for several applications.

The engine is equipped with a combined 7-stage axial/radial flow compressor. The air mass flow is led via two ducts into a single reverse-flow combustion chamber. The exhaust gas partially expands through a two-stage axial flow turbine which drives the compressor and auxiliary devices. After the high pressure turbine, the exhaust gas enters a two-stage axial flow low pressure turbine (LPT) and expands to ambient pressure. The LPT drives, through the engine's gearbox, the output shaft that is connected to the main gearbox in a helicopter application.

In the test facility environment, an eddy current brake is connected to the engine's drive shaft. The brake is electronically controlled, providing a fast torque load response. Thus it is possible to simulate the dynamic behaviour of a helicopter rotor system throughout the entire flight envelope.

3.2 Special Test Set Up

In order to run the engine under operating conditions different from those usually found in normal flight operations, the test facility and engine were fitted with supplementary devices. The modifications focused on the compressor and its close environment. As shown in figure 1 the engine is equipped with electronically controlled valves to regulate the air mass flow leaving the compressor. Those valves will be described in detail in the following paragraphs.

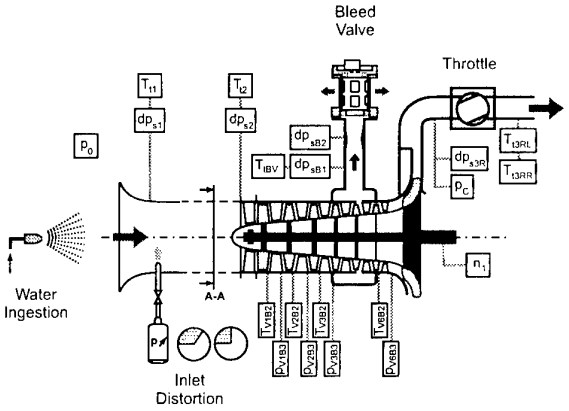

Figure 1: Compressor and facility set up

To thoroughly investigate the inherent aerodynamic instabilities the compressor was equipped with a number of pressure and temperature sensors providing signals for the first three and the sixth axial-flow compressor stages and the radial-flow end stage. The inlet flow can be distorted with means of apertures, pressurised air injection or water ingestion.

3.3 Bleed Valve

The design of the Allison 250-C20B compressor provides a bleed air port at the 5th axial-flow compressor stage. Production engines are equipped with a pneumatically operated handling bleed valve which schedules the over-board bleed air flow according to the compressor outlet pressure (p_c). In order to ensure sufficient compressor surge margin during engine acceleration, the bleed valve schedule must ensure that the valve is open at low power and starts to close when the N1-rotational speed exceeds 72 % and is fully closed when the N1 speed reaches 94 %.

To improve the operational behaviour of the engine and for reasons of compressor stability control, it was decided to implement the control of the bleed air flow into the existing experimental FADEC system [9]. Therefore a digitally controlled bleed valve was developed and manufactured in the department's shop.

The valve, as shown in figure 2, comprises an aluminium casing with eight rectangular discharge areas. A cylindrical valve body is mounted on bearings inside the casing. The valve body also has eight discharge areas that can be aligned with the discharge areas in the casing. By rotating the valve body the effective discharge area can be varied from fully closed to a maximum area of 2500 mm². The maximum area is significantly larger than the one of the pneumatically controlled valve, allowing the simulation of customer bleed air off take.

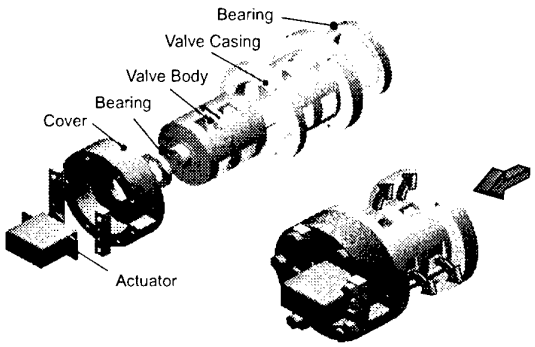

Figure 2: New bleed valve

The actuator used to control the valve body was an off-the-shelf device, that was originally used in remote controlled aeroplane models. This device provides a fast and accurate response to the control input at low actuator cost. The discharge area of the bleed valve is directly commanded by the FADEC system. There is a dead response time of approximately 10 ms caused by the control electronics. The slew rate of the actuator is 480 degrees/s, which means about 40 ms additional time to fully open or close the valve.

3.4 Compressor Throttling Device

Generating an entire compressor map from engine experiment data is usually not possible, since the position of the steady-state working line is determined by the interaction with other engine components like combustion chamber and turbine nozzle areas and cannot be varied significantly. To allow the determination of a compressor map of the installed compressor, the department's test engine was modified with valves in the ducts leading the compressed air to the combustion chamber (fig. 1). The blockage of the airflow through the valves can be used to shift the working line of the compressor towards the surge line and gather information on the compressor map. These throttling valves also give the possibility to bring the compressor to its stability limits and to simulate reduced compressor efficiency due to ageing.

3.5 Fuel System

The engine is originally equipped with a hydro-mechanically operating Bendix fuel flow governor and an engine-driven high pressure fuel pump. Additionally the department's test engine was fitted with a second, digitally controlled fuel supply system [9]. This system is used in combination with the departments experimental FADEC system for development and research purposes (see fig. 3).

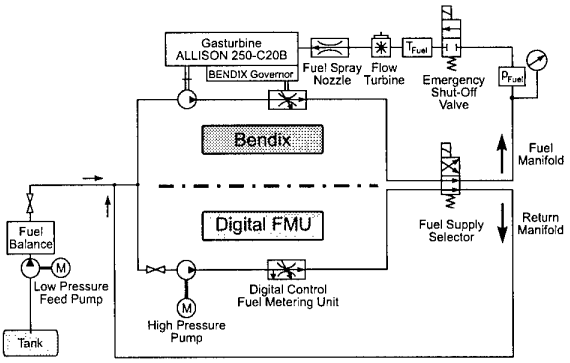

Figure 3: Schematic of the fuel system

Both fuel systems can be operated in parallel and transition between the two systems is possible at idle power setting without the need of an engine shut down. Furthermore, under all operating conditions a safe transition from the digitally controlled system back to the Bendix governor, acting as a safety back-up in case of a FADEC system failure, is possible and can be commanded by the operator.

3.6 Experimental FADEC System

The test engine is equipped with an experimental full authority digital engine control (FADEC) system. The schematic of the system is described in the following paragraph and shown in figure 4. The control software includes basic control laws and a number of limitation functions.

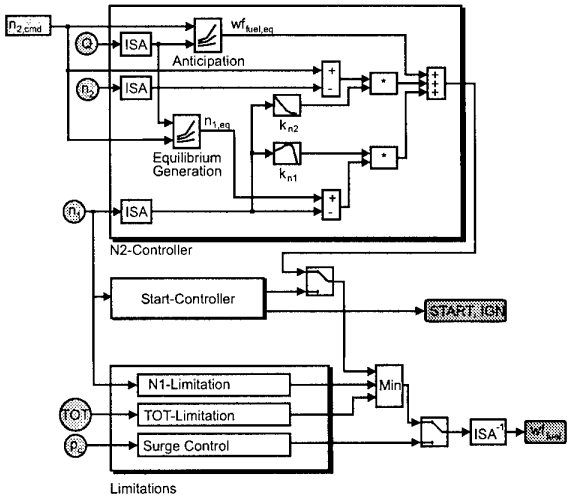

Figure 4: Schematic of the engine control

The start controller's task is to start the engine and bring it into a stable idle power condition. Therefore the starter motor, ignition and fuel flow are deployed by the controller. During the starting sequence engine parameters are closely monitored to avoid any exceeding of operational limits.

Once the engine is stabilised in idle power, the operator can activate the normal control law. This control law's aim is to maintain a constant pre-set power turbine speed (N2), i.e. a constant main rotor speed in a helicopter application. The N2-control law comprises a steady-state equilibrium generation. For a given set of control input values (commanded power turbine speed $n_{2,cmd}$ and engine torque load Q) the equilibrium gas generator speed $n_{1,eq}$ and fuel flow wf_{fuel} are determined. Using variable rotational speed dependent gain factors for the actual N1- and N2 offset the metered fuel flow is calculated.

To ensure safe engine operation over the entire range of flight conditions, several limitations are included into the control system. A N1-speed limiter limits the maximum gas generator rotational speed to a pre-set value in order to avoid damage of the engine due to mechanical and pressure forces. The turbine-outlet-temperature (TOT) is also constantly monitored and the fuel flow is limited to avoid an exceeding of the TOT limit.

Additionally an active surge control and abort system is included. The surge control is described in detail in the following paragraphs.

3.7 Software Development for the Experimental FADEC System [10]

The hardware used for the experimental control system, was a dSPACE multiprocessor system equipped with a 300 MHz DEC-alpha-CPU and a Texas Instruments C40-DSP. This system provides sufficient computation performance for very time critical applications such as surge-control.

A crucial point for shortening the development cycle-time is the effort spent on creating a validated, real-time software for the FADEC system. Here an approach using rapid prototyping tools was chosen to bring down the time for the pure programming tasks. The software development, with the possibility of intensive off-line testing, was performed on a PC in a graphical environment using MATLAB and SIMULINK. Once verified, C-code was automatically generated by MATLAB and with the use of cross compilers loaded onto the target hardware.

The development system comprises several software tools which allow easy on-line data logging and monitoring during testing. Recorded data is immediately available in MATLAB for analysing. A graphical user interface (GUI) provides easy control of the entire FADEC system and allowes on-line parameter changes within the control software during engine operation.

3.8 Data Acquisition

The test engine was dressed with a large number of sensors, in order to acquire complete details of the engine operating cycle. Shown in figure 5 are the locations of the various sensors mounted on the engine. The dark shading depicts the FADEC instrumentation. The data acquisition system, which consists of VME-Bus based hardware, is functionally divided into two separate tasks for steady-state and dynamic measurement.

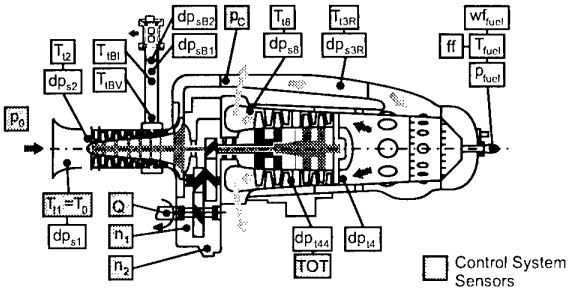

Figure 5: Engine instrumentation

The steady-state data acquisition, i.e. 96 channels, 16-Bit, 35µs conversion time focuses on a high resolution and accuracy of the measurement. The dynamic data acquisition system's aim is to provide very high sampling rates for recording transient engine operations, i.e. 40 channels, 12-Bit, 4µs conversion time. A separate data acquisition system records internal parameters of the control system.

4 COMPRESSOR INSTABILITIES

4.1 Compressor Map

The compressor behaviour is of great importance for the operating range of the whole engine, in particular the stability margins. For the investigated engine there was only a compressor map from the manufacturer 'ALLISON' available. This map was obtained by compressor rig tests without a bleed valve. Therefore it was decided to get the missing information from the engine under test, using throttle valves installed between the compressor outlet and the combustion chamber inlet.

To perform such an experimental compressor map measurement a special control mode was implemented. The task of the controller was to hold the gas generator speed constant during compressor throttling, via fuel metering. The power turbine speed was held constant via load control. A separate bleed valve controller was designed to get a constant bleed air ratio for the tests.

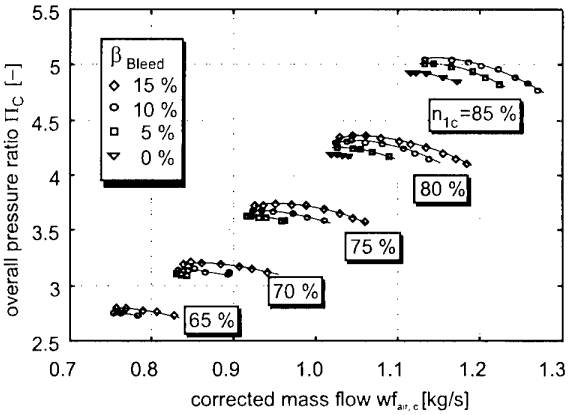

Figure 6: Measured engine compressor map

Figure 6 depicts the measured compressor map with different bleed air ratios. The right margin of the speed lines is obtained with fully opened throttle valves, i.e. these points are part of the normal steady state working line. The left margin is the last stable compressor operating point before surge. Note the decrease of stability reserve towards lower speed.

4.2 Surge caused by throttling at Quasi Steady State

The measured data in figure 7 depict a surge event which is initiated by slowly closing the bleed valve starting near the stability margin. The fuel flow was held constant throughout the entire recording. The left diagrams show the pressures at different stations for the first three surge cycles. The measurement stations are (top-down): radial compressor outlet (air ducts to combustion section), axial compressor outlet, third stage, first stage stator at two different circumferential positions. The right side shows a zoomed region of the surge inception phase.

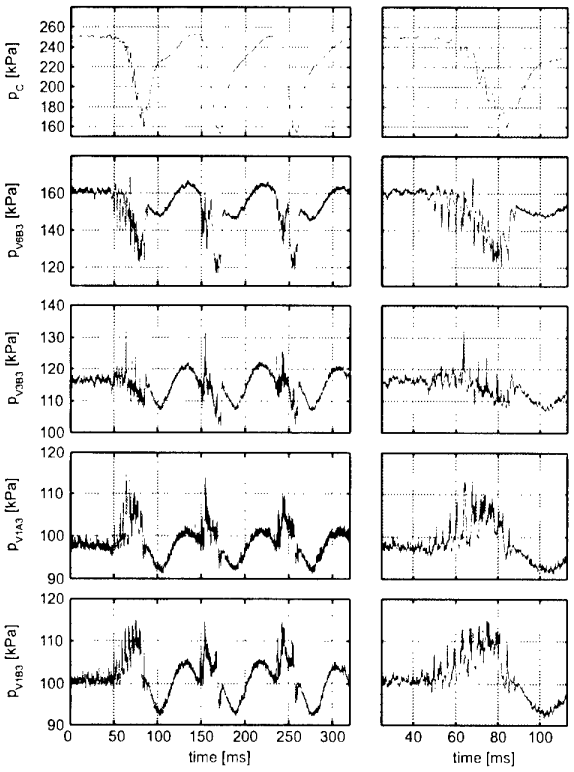

Figure 7: Surge caused by throttling at quasi steady state conditions

With the pressure signals of the first compressor stage the inception mechanism of an aerodynamic instability can be studied. Starting at 48 ms one can see periodically occurring small pressure peaks. The peaks in the signals p_{V1A3} and p_{V1B3}, measured along two different circumferential positions at the first stage stator exit, show a time delay. This is an indication for a rotating stall cell, i.e. a local region of separated flow propagating along the annulus. At the same time sharp, distinct pressure drops are discernible in the axial compressor outlet signal (p_{V6B3}). At the radial compressor outlet there is virtually no indication for the formation of a flow separation in the axial compressor.

The pressure increase at the first stages is due to the lower velocity in the stall region and hence a higher static pressure. The following stages are more or less screened along this region and without through flow that causes the pressure drop there.

At about 65 ms a local flow reversal of compressed air commences which causes a pressure peak in the third stage. At 68 ms the flow back from the radial compressor is indicated by the pressure peak at the outlet of the axial compressor. This deflation process lasts about 20 ms and causes the overall pressure drop at the compressor outlet. The reverse flow ceases at 86 ms and a stabilization phase starts until the normal operating condition is reached. Without a change of the bleed valve position, the compressor once again reaches the stability margin, triggering the next surge cycle.

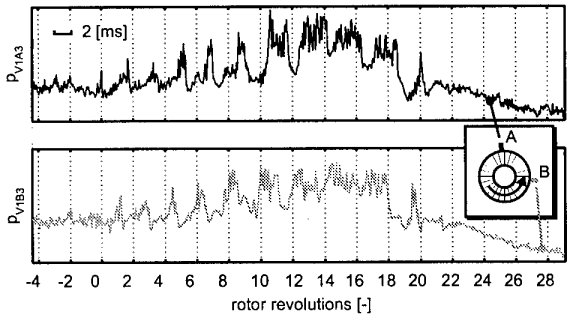

Figure 8: Pressures at the stator of the first compressor stage

In figure 8 the presence of a local rotating stall cell can be seen. Shown are the pressure signals of the first compressor stage stator versus rotor revolutions. The stall cell rotates at approximately 62 % of the rotor speed.

4.3 Rotating Stall Condition in Engine Steady State

With the developed control system it is possible to operate the engine below its normal idle point with reduced bleed air and keep the compressor in a continuous rotating stall condition.

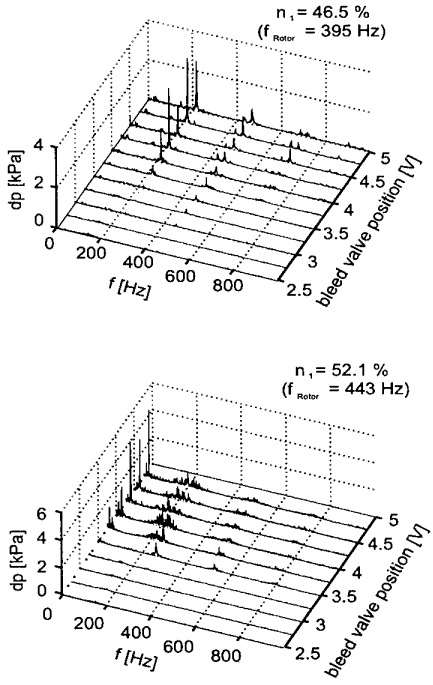

Figure 9: FFT-Analysis of the axial flow compressor outlet pressure

In figure 9 a Fast Fourier Transform of the compressor outlet pressure for different bleed valve positions and compressor speeds is depicted.

For a rotor frequency of 395 Hz first there are two stall cells observable with 230 Hz rotating frequency. With increasing throttling - decreasing of bleed air - there alternately is a one cell and two cell configuration observable. With the bleed valve almost being closed, partly even a three cell configuration is present. At higher speed (443 Hz), with increased throttling, it starts with a two cell configuration and changes to a one cell configuration.

4.4 Surge during Acceleration

During an engine acceleration there is a temporary reduction of compressor stability margin due to thermal throttling and hence a heightened threat of engine surge. At the test bed two different procedures were available to induce surge during an engine acceleration. For the standard control mode (constant power turbine speed), the bleed air off-take was reduced to start the acceleration with reduced stability margin.

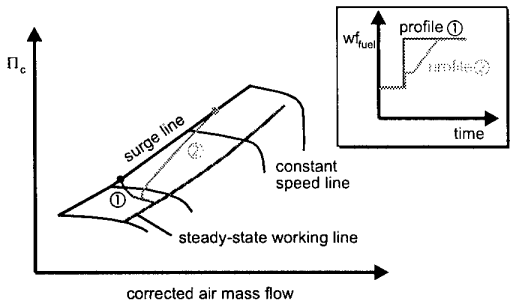

Figure 10: Fuel profiles to bring the engine in surge condition

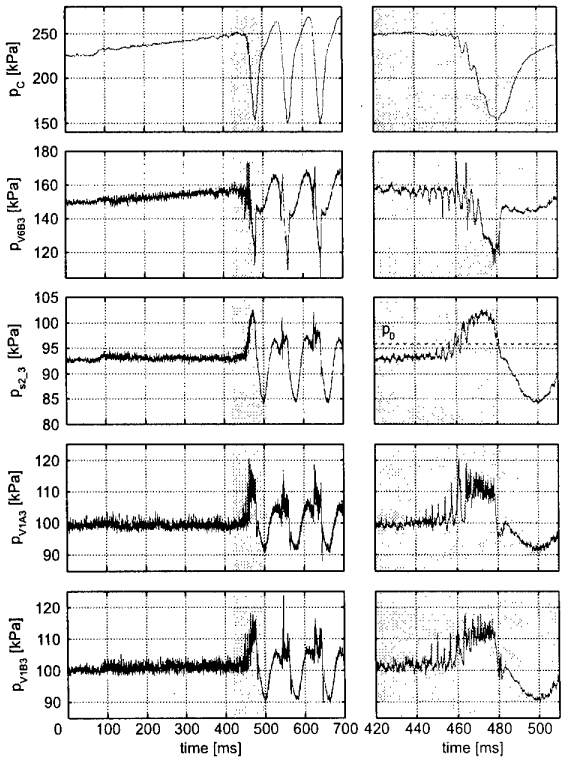

Figure 11: Surge during moderate acceleration

Alternatively a direct fuel control mode was available allowing the use of predefined fuel flow schedules. Type 1 profiles would almost immediately lead to surge. For type 2 profiles the engine would initially reach a stabilised acceleration until the surge line is approached during the fuel flow ramp (fig. 10).

Figure 11 shows a surge event induced by a type 2 fuel flow schedule. Note the thermal throttling starting at 80 ms, indicated by the rise in static inlet pressure (p_{s2_3}). This is related to a decrease in flow velocity and hence a reduction of compressor mass flow.

4.4 Wavelet Signal Analysis

To avoid surge that can cause mechanical damage due to the high pressure peaks it is necessary to detect rotating stall as early as possible and then react with appropriate control actions. There are different analysis methods known for this type of problem. We investigated several and found the relatively new method of so called Wavelets best fitted to the problem of real-time recognition of stall inception.

The wavelet analysis is implemented in form of discrete FIR filters. There are already proven wavelet families available and mathematical tools to design the filters for those. Investigations showed that the "Daubechies 2" wavelet brought good results for the given problem.

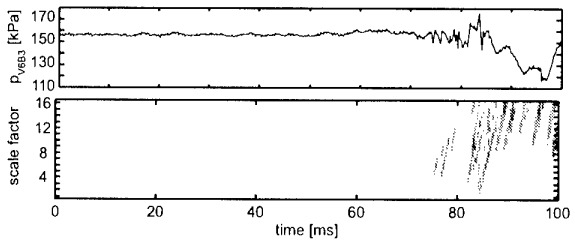

Figure 12: Wavelet analysis of compressor stall

Figure 12 shall demonstrate the applicability of the wavelet method for stall recognition. The analysis is performed with a Daubechies 2 wavelet and one can see the possibility of stall identification within a reasonable time delay.

4.5 Water Intake

There are certain circumstances for water intake into helicopter engines for instance, flying in heavy rain or hovering closely above a water surface. Such water ingestion leads generally to engine mismatch and a reduction of the compressor surge margin [11]. For large amount of water intake there is the danger of flame out in the combustion chamber which has to be avoided in any circumstances. The control system must cope with that and has to assure safe operation.

The general aim of the present paper was as mentioned before, to develop a lab-FADEC system for such abnormal operating conditions. External circumstances allowed only a few restricted tests with water ingestion into the compressor intake at different water/air ratios, water droplet diameters and control modes. Figure 13 shows as an example of some measured engine parameters during water ingestion. The water to air ratio was 4 % and the mean Sauter diameter was about 500 µm.

The torque load was held constant. When the water ingestion commences, after about a second, the corrected gas generator speed n_{1c} immediately drops and the power turbine speed n_{2c} rises. The decrease of the gas generator speed is mainly due to the higher load of the compressor. The steep rise of the shaft power is caused by the increase of the pressure and mass flow in the power turbine despite the temperature drop.

The controller was in constant corrected power turbine speed mode. Therefore its first reaction is to reduce the fuel flow wf_{fuel} for speed stabilization. Afterwards the fuel flow rises up due to the gas generator speed drop and stabilizes at about 10% higher flow.

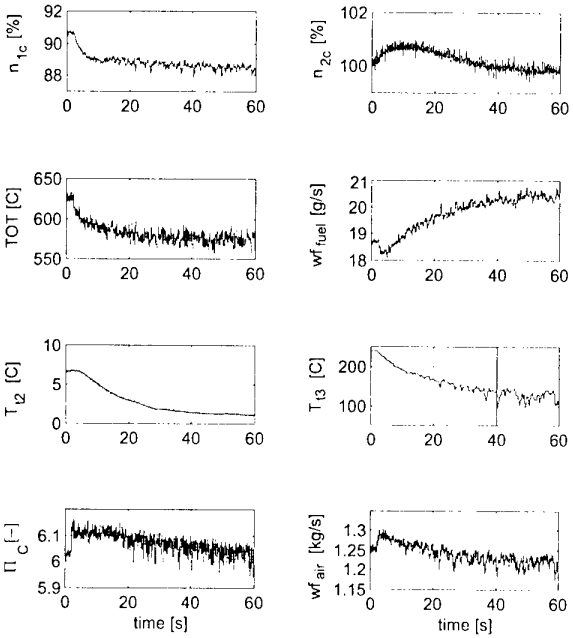

Figure 13: Engine parameters during water ingestion

Because of the partly vaporisation of the ingested water droplets the inlet temperature T_{t2} decreases. The same is for the compressor outlet temperature T_{t3}. Looking at the air mass flow wf_{air} an immediate rise starting with the water ingestion can be seen at first. This is due to the steep temperature drop and hence a de-throttling effect. After that the influence of the compressor speed change leads to a lower flow rate. A similar behaviour can be observed for the overall pressure ratio Π_c.

Increasing the water to air ratio up to 6.1 %, by using a spray nozzle with higher flow number and a higher injection pressure, led to an immediate flame out. This could be avoided by bleed valve opening. The test results shown in figure 14 were obtained by water ingestion starting with fully opened bleed valve and then slowly continuous closing the valve.

The speed signals as well as the turbine outlet temperature TOT and the fuel flow wf_{fuel} do not show any significant pre-warnings for flame out. The compressor outlet temperature T_{t3} drops about 100 °C in the first 20 seconds after water ingestion start. Then it stabilizes for the next 20 s, but with spikes in the signal, probably because of boiling droplet impingement on the shielded thermocouple sensors. After 40 s when the bleed valve is almost closed, the temperature drops a further 30 °C and the signal becomes more noisy.

In the last diagram the calculated polytropic exponent n_{poly} is depicted. The starting value at dry conditions corresponds to an isentropic efficiency of $\eta_{is} = 0.8$. That polytropic exponent seems to be a significant signal for identification of the combustion instability margin due to the water air ratio. The monitoring system could detect a limit exceeding and the control system then would open the bleed valve. Unfortunately this could not be further investigated, because our test bed had to be moved and it is not ready for testing up to now.

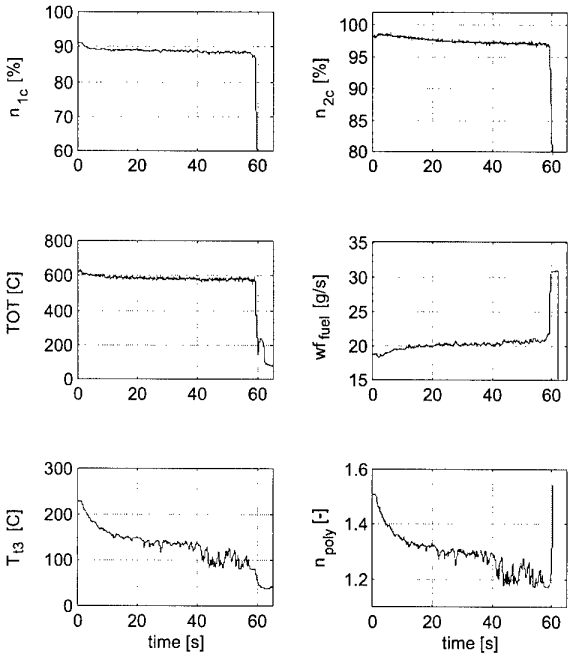

Figure 14: Water intake and bleed valve closing

5 MONITORING AND CONTROL SYSTEM

5.1 Sensor Configuration for Stall Recognition

The acceptance to incorporate a compressor instability recognition and avoidance system into the control system for production engines depends to a large extent on the complexity, reliability and cost. For that reason only one or maximum of two sensors are acceptable. A key requirement for the pressure sensors is good dynamic response and that means they have to be installed as near as possible to the measurement point. Of course this location should be the one providing the best signal information for stall inception.

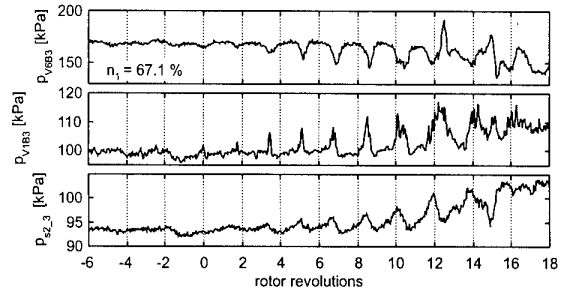

Figure 15: Pressure signals for stall detection

Figure 15 depicts an example of the various investigated pressure signals during rotating stall onset. Generally the first two stages showed best results in pressure peaks (p_{V1B3}) because of the high loading of the first stages of a multi stage axial compressor at low speed. The pressure signal p_{V6B3} at the outlet of the axial part shows distinct pressure drops concurrently to the stall cells at the inlet. It is also suitable for identification but with the disadvantage of a higher temperature load on the sensor. With respect to mechanical installation the inlet sensors p_{s2_3} would possibly be preferred. However, the inlet station signals indicate an impending compressor stall later and less distinct than signals from stations within the compressor.

5.2 Surge Detection at Low Signal Sampling Frequency

Today's engine control systems typically operate with cycle times in the order of about 20 ms. Obviously it is not possible to detect stall onset and prevent surge within this time frame. That means the task in the normal control loop is to detect surge and abort that state as fast as possible.

One solution to the problem could be to run an observer model of the engine parallel to the real engine and compare model outputs to measured parameters. In figure 16 some measured parameters are depicted once for engine in surge state and once without surge. It is obvious that an extremely high model quality is necessary to detect surge in an early stage using other parameters than pressures. The pressure signals are significantly different in dynamic during surge to the normal engine operation. They show a typical oscillation which can be identified by a filter.

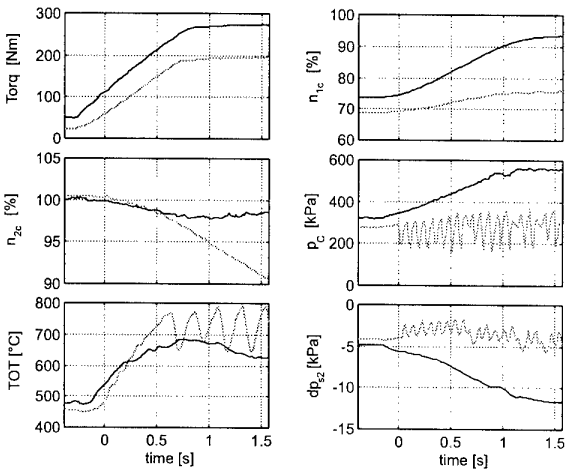

Figure 16: Parameters for surge detection

The requirement for such a filter is a small time delay. The developed controller runs in 60 Hz frequency. A third order Butterworth high pass filter with 10 Hz cut off frequency for compressor inlet and outlet pressure signals was chosen for surge detection. In figure 17 the filter outputs during surge, as well as the predefined thresholds are depicted.

5.4 Stall Recognition at High Signal Sampling Frequency

For early stall detection a much higher sampling frequency is required. Two different algorithms based on a sampling frequency of 6 kHz were developed.

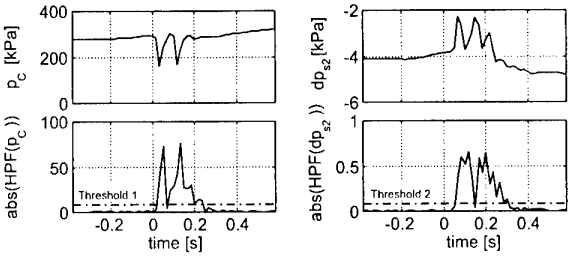

Figure 17: High-pass filtered pressure signals during surge

5.4.1 Correlation method with pressures from two different circumferential positions

The similarity of two signals can be rated by the mathematical correlation function. A rotating stall cell causes similar pressure peaks at the sensors with a time delay due to the rotational frequency and the displacement angle. Continuous monitoring of the correlation between the two signals shows an considerable increase when a stall cell develops.

5.4.2 Wavelet analysis for the axial compressor outlet pressure

Chosen for the wavelet algorithm was a Debauchie 2 wavelet with scales 3 to 7 to get a small filter delay. The stall onset shows also a considerable analysis output increase. A time integrator is used for the robustness of the algorithm. Only when a limit is exceeded a certain lapse of time then the stall flag in the software is set to true.

5.5 Experimental Verification

To verify the algorithms, many experiments were performed. For that the compressor was first brought near the instability margin by closing the bleed valve at low power. Then pressurised air was injected into the compressor inlet to induce stall (see fig. 1). This is a commonly used method to simulate inlet disturbances.

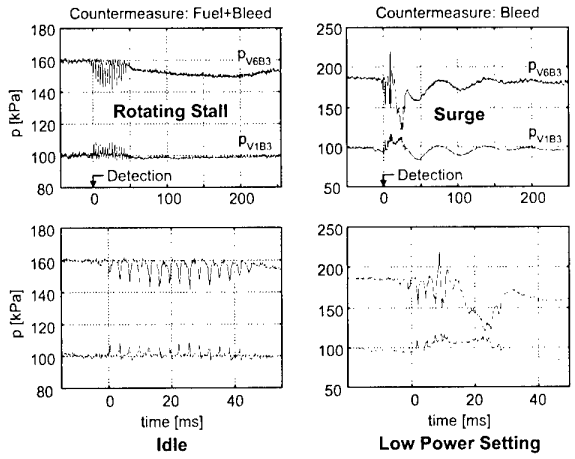

Figure 18: Rotating stall and surge detection

For all performed experiments, rotating stall was detected within the first rotation. Figure 18 shows two examples, one at idle and one at low power. In the first case it was possible to avoid surge with means of bleed valve opening after stall detection.

At higher loads it was not possible to avoid the first surge cycle neither with bleed air nor with fuel flow, nor with a combination of both. The reason for that is the insufficient response time of the actuators. The time between rotating stall onset and surge was often only 15 ms, that is in the range of the dead time of the used actuators.

Using the fuel flow for de-throttling the compressor has not only the response time problem of the metering valve, but also the thermodynamic behaviour of combustion. Figure 19 shows the compressor outlet pressure related to the injection pressure of the fuel. One can recognise a time delay of more than 20 ms of the compressor pressure reaction due to vaporisation and ignition delay.

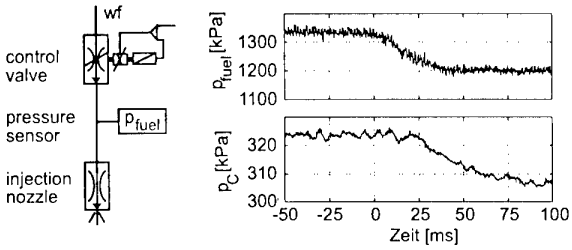

Figure 19: Reaction of the compressor pressure to the fuel flow drop

5.6 Engine Recovery from Surge

After a surge event it is not immediately admissible to switch back to the normal power turbine speed control mode. Due to the drop in power turbine speed during the surge event, this control law would command an excessive fuel flow due to the high feedback gain. Consequently the compressor would again be throttled to the stability limit and the engine would surge once again.

To avoid such limit cycles the engine control algorithm was supplemented by a gas generator stabilization and a gas generator acceleration control mode. Figure 20 gives an overview of the surge abort and re-stabilization control.

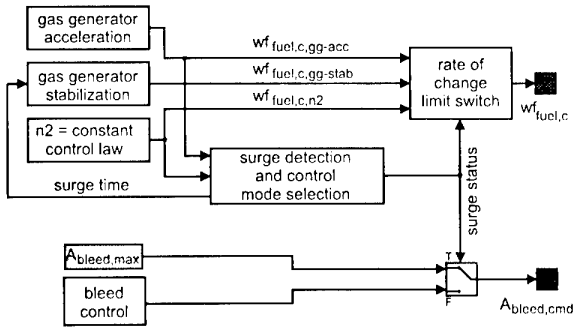

Figure 20: Scheme of control functions to abort surge and re-stabilize engine operation

5.6.1 Gas generator stabilization

After surge detection the first objective is to stabilize the gas generator in disregard of a drop in power turbine speed. This is accomplished by fully opening the bleed valve and a reduction of the metered fuel flow. The algorithm schedules the steady-state fuel flow pertaining to the N1-Speed immediately prior to surge detection. If the surge event does not cease after a predefined time span of 0.5 s then the fuel flow will be ramped down to a combustor flame out minimum. The latter was never in action for the performed test series. Figure 21 depicts the control scheme of the gas generator stabilization function.

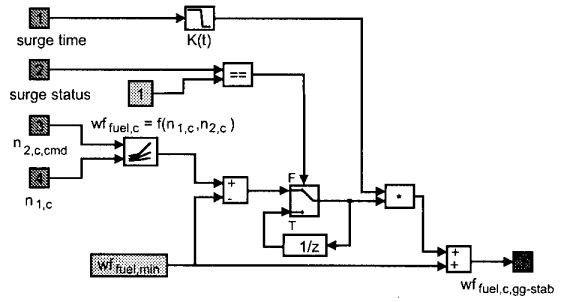

Figure 21: Control scheme of gas generator stabilization

5.6.2 Gas Generator Acceleration

After a successful gas generator stabilization, the engine has to be brought back to the required power setting. This demands a rapid, yet stable, gas generator acceleration. First of all the commanded acceleration is calculated (fig.22).

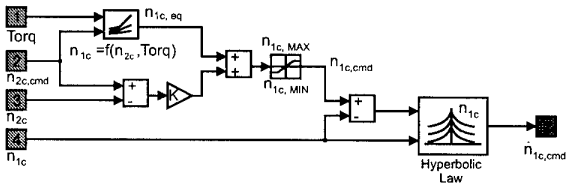

Figure 22: Generation of set points for the acceleration

The algorithm computes an equilibrium gas generator speed based on actual torque load and power turbine speed drop. A hyperbolic function is then utilised to derive the commanded acceleration depending on the difference between equilibrium and actual gas generator speed. The parameters of the hyperbolic function itself vary with engine speed to take full advantage of the available acceleration potential at different speeds.

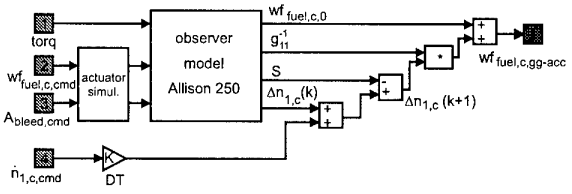

Figure 23: Dynamic model based pre-compensation of the gas generator acceleration control

The determined set point for the speed acceleration is fed into an on-line engine and actuator observer model [12] and results in a required fuel flow (fig. 23).

The uncertainties of the model based calculation are compensated by a PI-algorithm which becomes active as soon as a stabilized acceleration is accomplished. In figure 24 the signal flow of the entire acceleration controller is depicted.

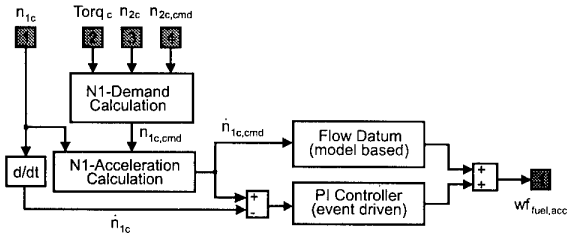

Figure 24: Flow diagram of the acceleration controller

Figure 25 shows an example of a re-stabilisation process after engine surge. Surge was initiated with a almost closed bleed valve and a slam acceleration from idle condition. The first surge cycle was detected and after a second cycle the gas generator was stabilised. Then the acceleration mode is active first with an active rate limiter and then tracking the set point changing. About two seconds after surge detection the controller switches back to normal constant power turbine speed law.

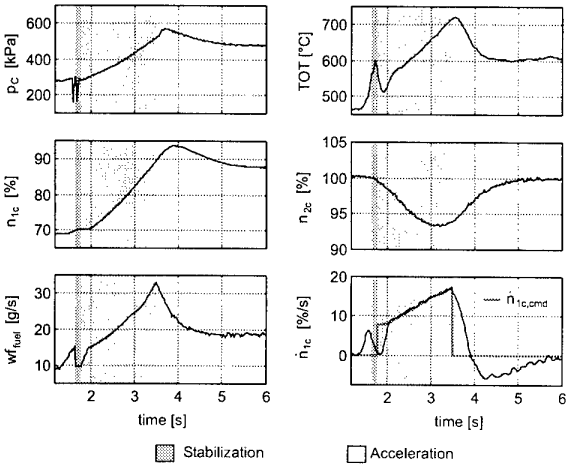

Figure 25: Example of a surge recovery

6 CONCLUSION AND SUMMARY

The aim of the present work was to investigate the possibilities for avoiding compressor surge of turbo-shaft engines with means of an engine electronic monitoring and control system. The experimental verification was done on the helicopter engine ALLISON 250-C20B with a sensor and actuator configuration which seems to be appropriate for such types of engines.

The task required some mechanical changes for the engine. First the installation of throttle valves into the air ducts between compressor outlet and combustion chamber inlet. This allowed to shift the operating line towards the surge margin and to measure the part of the compressor map above

the normal steady state line. Second the outer axial compressor casing was slightly modified to accommodate additional sensor equipment. Third a new bleed valve has been developed which can be controlled electronically and allows fast discharging of the compressor. In an earlier work the engine fuel system was modified to use electronic controlled fuel flow [9] .

For the development of an engine electronic controller a rapid prototyping tool has been used. The tool consists of a special real-time computer and Mathwork's Simulink software for graphical symbolic programming.

Different approaches like throttle valves, modified bleed schedule, inlet distortion, slam acceleration were made to bring the engine into a non-stable, abnormal operating condition. Unfortunately there was only time left for one preliminary water ingestion test run and without an appropriate sensor configuration, before the tests had to stop because of the required test bed move.

The investigations in general have shown that only beyond idle it was possible to keep the compressor in continuos rotating stall condition. In the normal area of operation after a couple of stall rotations the engine surged with partly considerable reverse flow. The time between first stall inception and surge was often less than 20 ms. Different analysing methods were applied to the measured data, but there was no indication of any signal anomaly before stall inception.

With the developed surge avoidance system it was only possible to protect the engine from surge at or near idle. At higher power levels the available response time of the actuators - bleed valve and fuel metering unit - was too slow for fast compressor discharging. The effectiveness of the fuel decrease is delayed not only by the metering unit itself but also considerably by the vaporisation and ignition delay in the combustion chamber.

The developed re-stabilisation function recovers the engine from surge status automatically. This function in the controller reduces considerably the workload of the pilot particular in the critical state of the engine. That is a contribution for a safer engine operation.

The first test with water ingestion showed that flame out could be avoided at certain water/air ratios by opening the bleed valve. The polytropic exponent, calculated with means of the compressor inlet and outlet temperature and the pressure ratio, could be monitored and used as an indicator to open the bleed valve. Further investigations in that field are planned for the near future.

7 REFERENCES

[1] N.N.: FAA-Airworthiness Standards: Aircraft Engines - Surge and stall characteristics. Federal Aviation Regularity, FAR 33.65

[2] Greitzer E.M.: The Stability of Pumping Systems - The 1980 Freeman Scholar Lecture. ASME Journal of Fluids Engineering, Vol. 103

[3] Greitzer E.M.: Surge and Rotating Stall in Axial Flow Compressors, Part I: Theoretical Compression System Model. Gas Turbine Conference, ASME 75-GT-9, Houston, USA, 1975

[4] Day I.J., Freeman C.: The Unstable Behavior of Low and High Speed Compressors. ASME International Gas Turbine and Aeroengine Congress, 93-GT-26, Cincinnati, USA, 1993

[5] Herpel T.: Untersuchung zum dynamischen Leistungsverhalten von Turboluftstrahltriebwerken unter Berücksichtigung instationärer Verdichterströmungen nahe der Stabilitätsgrenze. Institutsbericht LRT-WE12-95/07, 1995

[6] Wilson G.W., Freeman C.: Stall Inception and Development in an Axial Flow Aeroengine. ASME International Gas Turbine and Aeroengine Congress, 93-GT-2, Cincinnati, USA, 1993

[7] Freeman C., Wilson A.G., Day I.J., Swinbanks M.A.: Experiments in Active Control of Stall on an Aeroengine Gas Turbine. ASME International Gas Turbine and Aeroengine Congress, 97-GT-280, Orlando, USA,1997

[8] Gallops G.W., Roadinger T.J., French J.V.: Stall Testing and Analysis of Two Mixed Flow Turbofans. ASME International Gas Turbine and Aeroengine Congress, 93-GT-62, Cincinnati, USA, 1993

[9] Auer E.J.: Modellbildung, Simulation und Entwicklung eines digitalen Reglers für eine Hubschraubergasturbine. VDI-Fortschrittsbericht, Reihe 8, Nr. 581, VDI Verlag Düsseldorf, Dissertation, Lehrstuhl für Flugantriebe, TU München, 1996

[10] Preiß A., Gabler R., Erhard W.: Entwicklung eines Labor FADEC-Systems zur Regelung von Gasturbinen. DGLR Jahrestagung, München, 1997

[11] N.N.: Recommended Practices for the Assesment of the Effects of Atmospheric Water Ingestion on the Performance and Operability of Gas Turbine Engines. AGARD-Advisory Report 332, France, 1995.

[12] Gabler R., Auer E., Erhard W., Rick H.: Turboshaft Engine Monitoring System Including Contingency Operation. 5th European Propulsion Forum, EPF95-17, Pisa, Italien, 1995

Simultaneous Active Source Control Of Blade Row Interaction Generated Discrete Tones

Scott Sawyer and Sanford Fleeter
School of Mechanical Engineering
Purdue University
West Lafayette, Indiana 47907

1. ABSTRACT

Unsteady blade row interactions in turbomachines generate discrete-frequency tones at blade pass frequency and its harmonics. Specific circumferential acoustic modes are generated. However, only certain of these modes propagate upstream and downstream to the far field, with these the discrete frequency noise received by an observer. This paper is directed at experimentally demonstrating the viability of active noise control utilizing active airfoils to generate propagating spatial modes that interact with and simultaneously cancel the upstream and downstream propagating acoustic modes. This is accomplished by means of fundamental experiments performed in the Purdue Annular Cascade Research Facility configured with 16 rotor blades and 18 stator vanes. At blade pass frequency, only the k_θ = -2 spatial mode propagates. Significant simultaneous noise reductions are achieved for these upstream and downstream propagating spatial modes over a wide range of operating conditions.

2. INTRODUCTION

The design of an aircraft engine to be quiet is by nature a necessary technical evil. This is because it adds no performance value. Rather, current state-of-the-art methods for reducing engine noise often add weight, reduce performance, and increase engine complexity. However, aeroacoustics has become an increasingly important design issue. This is because in addition to meeting the long-term performance requirements of increased fuel efficiency, decreased weight, improved reliability and maintainability, and being competitively priced, engine certification requires meeting prevailing noise regulations. Also, more stringent noise level guarantees are often required of the engine manufacturer by airlines to meet tougher local airport noise requirements. In addition, there is a near certainty that more stringent Stage 4 requirements will require an additional reduction of 5-10 EPNLdB.

As engines with higher bypass ratios have been introduced, turbomachinery noise, i.e., fan, compressor, and turbine generated noise, has become more important, with jet exhaust mixing noise contributing less to the total engine noise signature. For current high bypass ratio engines (bypass ratios of 5:1 to 6:1), fan noise dominates the total noise on approach and takeoff. The new ultra high bypass ratio ducted fan engines (bypass ratios greater than 10:1) have an even greater fan noise component at lower frequencies, with little jet noise contribution to the total engine noise signature

The primary noise sources for a high bypass turbofan engine are the fan, the low-pressure compressor, and the low-pressure turbine [1,2], Figure 1. Their noise signatures include a broadband noise level with large spikes or tones at multiples of blade passing frequencies, Figure 2. The discrete-frequency tones are generated by periodic blade row unsteady aerodynamic interactions. Namely, turbomachine blade rows are subject to spatially nonuniform inlet flow fields resulting from either potential or viscous wake interactions. For subsonic fans, the acoustic spectrum discrete tones are usually 10-15 dB above the broadband level. . These discrete tones may not contribute significantly to the overall noise level but are the main source of irritating screech noise at take-off and landing.

Current noise control and reduction methods for high-bypass turbofan engines are a combination of turbomachinery noise source control and suppression. Source control is accomplished by increasing the axial spacing between adjacent blade rows and by selecting blade and vane number combinations to produce "cut-off", whereby the highest-energy blade pass frequency acoustic modes decay exponentially with distance along the ducting. Source suppression is achieved with acoustic liners in the fan inlet and exhaust ducts and the core exhaust duct.

The increasing bypass ratios of turbofan engines means increased fan diameter. However, nacelle length is kept at the current bypass ratio size - not scaled with diameter. Thus, inlet and exhaust duct length-to-diameter ratios must be smaller, with current liner design techniques providing less noise suppression. Also, as the fan diameter increases, the blading becomes larger, and maintaining acoustically desired axial spacing becomes a severe weight penalty. Further, the trend toward low blade number, wide-chord fan designs is a further deterrence to maintaining large spacing/chord ratios. Larger diameters, lower blade numbers, and lower tip speeds all produce lower blade-passing frequencies which require deeper treatment liners to achieve comparable suppression. To provide low drag, however, large diameter nacelles must be thin. Consequently, current liner treatment designs will provide significantly less source suppression.

Higher bypass ratio engines thus require more source noise control by design, not liner suppression, to even maintain current engine noise levels, let alone reduce

Paper presented at the RTO AVT Symposium on "Design Principles and Methods for Aircraft Gas Turbine Engines", held in Toulouse, France, 11-15 May 1998, and published in RTO MP-8.

noise levels significantly below those of current engines. Therefore, progress in gas turbine noise reduction is dependent on a better understanding of turbomachinery noise, specifically far-field discrete-frequency noise, and after exhausting passive techniques, the designer is left to the active control of noise.

Active noise control has been analytically modeled and experimentally demonstrated. Thomas et al. [3] applied a three channel active control system to reduce fan noise radiating from the inlet of a JT15D turbofan engine. Large area microphones placed outside the inlet in the acoustic far field provided the error signals. The control sound field was generated by an array of 12 horns and 24 loudspeakers mounted on the circumference of the inlet. The control system utilized a feed-forward adaptive filtered-x LMS algorithm. The 28 bladed rotor was excited by 28 rods mounted upstream of the rotor which generated a plane wave spatial mode. With the three error microphones placed outside the engine, noise control was achieved within a 30° arc. However, there was an overall increase in the measured discrete-frequency noise.

Another approach to active noise control considers the reduction of the unsteady forces acting on the blade row [4]. This reduction in the unsteady lift translates into a decrease in noise generation. This was demonstrated by Simonich et al. [12] on an isolated airfoil with a moveable trailing edge flap that represented the active aerodynamic element. The flap was actuated by a servomotor and its motion controlled to reduce the unsteady lift generated by a periodic disturbance. The peak-to-peak acoustic dipole pressure was reduced by a factor of two and the sound pressure level was reduced by 10 dB over portions of the spectrum.

A third approach combines the anti-noise and source control techniques with the generation of anti-noise at the noise source. This active airfoil source control technique minimizes actuator power requirements and maximizes control authority. Kousen and Verdon [6] developed a computational model based on the linearized unsteady potential flow analysis LINFLO. The model considered blade surface mounted pistons as a source of anti-sound. Complete cancellation of all propagating waves required one surface actuator per acoustic wave. The amplitude and phase of the actuators was determined through the solution of a set of complex linear equations. Kousen [7] was also able to minimize the sound generation through a least-squares minimization procedure when the number of actuators was less than the number of propagating acoustic waves.

Using on-airfoil source control and in-duct spatial mode measurements, both Minter et al. [7], and McCarthy and Fleeter [8] demonstrated active control of propagating spatial modes generated by a 16 bladed rotor and a 3 vaned stator. Minter et al. used piezoelectric crystals to actuate airfoil surface pistons and oscillating flaps to realize maximum noise reductions of 6-dB upstream and 8 dB downstream. McCarthy and Fleeter used a compression driver-horn combination in a speaker-dipole arrangement for near source control of either the upstream or the downstream going acoustic wave. Maximum reductions of 17.1 dB upstream and 15 dB downstream were obtained.

In summary, the effectiveness of current passive discrete tone control is limited by high bypass ratio designs. Active airfoil source control has been analytically conceived, but demonstrated for only upstream control or downstream control. Active noise control techniques have not been demonstrated over a range of operating conditions. Finally, there has been no experimental demonstration of the viability of active airfoil source control for the simultaneous control of upstream and downstream propagating acoustic modes.

This paper is directed at experimentally demonstrating the viability of active airfoil source control for discrete frequency tones. Specific objectives include the simultaneous reduction of the upstream and downstream going propagating spatial modes generated by rotor-stator interactions using active discrete-frequency noise source control techniques, i.e., combining anti-noise and source control techniques through the generation of anti-noise at the source. This is accomplished utilizing active airfoils to generate propagating spatial modes that interact with and simultaneously cancel the upstream and downstream propagating acoustic modes.

The technical approach is centered on fundamental experiments performed in a single-stage turbomachine. The far-field discrete-frequency tones are characterized by the modal structure in the duct both upstream and downstream of the airfoil rows. The active noise control system cancels or reduces the propagating acoustic modes in the duct, i.e. before the modes are radiated to the far field. The active noise control system utilizes active airfoil source control that mimics the rotor-stator interaction and is optimized for control of the propagating acoustic modes generated by the rotor-stator interactions. Additionally, on-airfoil actuators minimize the actuator power requirements. The simultaneous cancellation of one rotor-stator interaction generated propagating spatial mode both upstream and downstream of the airfoil rows requires two sets of acoustic sources. Each set of acoustic sources produces upstream and downstream going spatial modes. Driving each set of acoustic sources at the proper amplitude and phase results in the simultaneous cancellation of both propagating waves.

3. DISCRETE TONE GENERATION & CONTROL

In a multistage turbomachine, the periodic wakes of an upstream rotor blade row and the potential fields of upstream and downstream rotor blade rows generate unsteady pressures on stator rows. These unsteady stator vane surface pressures are the source of the discrete-frequency noise. The stator row responds to these periodic excitations by generating fluctuating periodic lift forces at multiples of the rotor blade pass frequency. This stator row unsteady loading then couples to the duct to produce acoustic waves.

The acoustic response of the stator row is characterized as the superposition of spatial modes, where the generated spatial modes are a function of the number of rotor blades and stator vanes. A spatial mode is described as a lobed pressure pattern where the spatial mode order is equal to the number of lobes. The propagation, resonance, or decay of a spatial mode is given by the axial wave number. Of the generated modes, only certain modes propagate to the far field. It is these propagating modes which represent the discrete-frequency noise received by an observer. These acoustic response characteristics are important to properly explain the measured acoustic response due to rotor-stator interactions and to provide the necessary understanding of the basic concepts of an active discrete-frequency noise control system.

3.1 Annular Duct Acoustics

The classical model of discrete-frequency noise considers a rotor and stator in an annular duct. The unsteady flow is described by the wave equation for a uniform axial flow, derived by considering the flow to be inviscid and compressible with small unsteady perturbations.

$$\left(\frac{\partial}{\partial t}+U_\infty\frac{\partial}{\partial \xi}\right)^2 p = A_\infty^2\left(\frac{1}{r}\frac{\partial}{\partial r}\left(r\frac{\partial}{\partial r}\right)+\frac{1}{r^2}\frac{\partial^2}{\partial \theta^2}+\frac{\partial^2}{\partial \xi^2}\right)p \quad (1)$$

where p is the acoustic pressure, A_∞ is the freestream sound speed, U_∞ is the freestream axial velocity, and ξ, r and θ are the axial, radial and circumferential coordinates.

The acoustic pressure is a function of radius and is harmonic in time, axial distance and polar angle.

$$p(\xi,r,\theta,t)=\bar{p}(k_\mu r)e^{i\left(k_\xi\xi+k_\theta\theta-nN_{Blades}\Omega t\right)} \quad (2)$$

where $\omega = nN_{Blades}\Omega$ is a multiple of blade passage frequency, n is the rotor harmonic, k_μ is an eigenvalue determined from the flow tangency conditions at the inner and outer duct radii, k_ξ is the axial wave number and k_θ is the tangential wave number or mode order, corresponding to the number of nodal diameters of the pressure pattern.

To determine the generated spatial modes, a rotor and stator in a duct is considered. The spatial modes in the duct are produced by the unsteady pressures on N_{Vanes} stator vanes that are downstream of and excited by N_{Blades} rotor blades rotating at speed Ω. The unsteady pressure pattern is the superposition of spatial modes that are generated at multiples of blade passage frequency $nN_{Blades}\Omega$.

The stator circumferential vane spacing $\Delta\theta$, as shown in Figure 3, is equal to $\Delta\theta = 2\pi/N_{Vanes}$. In time $\Delta t = \Delta\theta/\Omega$, the rotor moves $\Delta\theta$, traversing one stator passage. The excitation on the zeroth vane at time t = t equals the excitation on the first vane at time $t = t+\Delta t$. Therefore the response of the zeroth vane at time t = t equals the response of the first vane at time $t = t+\Delta t$.

$$\bar{p}(k_\mu r)e^{i\left(k_\xi\xi+k_\theta\theta-nN_{Blades}\Omega t\right)} = \bar{p}(k_\mu r)e^{i\left(k_\xi\xi+k_\theta(\theta+\Delta\theta)-nN_{Blades}\Omega(t+\Delta t)\right)}$$

Canceling terms leads to the following solution for k_θ

$$k_\theta = nN_{Blades}+mN_{Vanes} \qquad m=\pm1,\pm2,\ldots \quad (3)$$

where m is any arbitrary integer.

Thus, the only modes generated by the rotor-stator interaction are specified by these values of k_θ. The frequencies are the harmonics of blade pass $\omega = nN_{Blades}\Omega$, with the acoustic duct modes also responding at these frequencies.

The spatial mode order is related to the interblade phase angle $\sigma = -\frac{2\pi N_{Blades}}{N_{Vanes}}$ that defines the unsteady loading of airfoils with reference to the zeroth airfoil.

Although all of the acoustic pressure circumferential modes of order $k_\theta = nN_{Blades}+mN_{Vanes}$ are generated by the rotor-stator interaction at the harmonics of blade passage frequency $\omega = nN_{Blades}\Omega$, only certain of these modes propagate to the far field, with the rest decaying before reaching the far field. Thus it is only those circumferential modes that propagate to the far field that represent the discrete-frequency noise received by an observer.

Substituting the assumed solution into Equation 1 yields the axial wave number k_ξ.

$$k_\xi = \frac{k_\omega M}{1-M^2}\pm\sqrt{\left(\frac{k_\omega M}{1-M^2}\right)^2+\frac{k_\omega^2-k_\mu^2}{1-M^2}} \quad (4)$$

3.2 Far-Field Discrete-Frequency Noise

Although an infinite number of spatial modes are generated by the rotor-stator interaction at the harmonics of blade passage frequency, only certain of these modes propagate to the far-field, with the rest decaying before reaching the far-field. Thus it is only those spatial modes that propagate to the far field that represent the discrete-frequency noise received by an observer. The propagation of the acoustic pressure modes is specified by the expression under the radical of k_ξ.

* $k_\omega^2 - k_\mu^2\left(1-M^2\right) > 0$ - Two real k_ξ values corresponding to two propagating pressure waves, one upstream and the other downstream.
* $k_\omega^2 - k_\mu^2\left(1-M^2\right) < 0$ - Two complex k_ξ values corresponding to two decaying waves, one upstream and the other downstream.
* $k_\omega^2 - k_\mu^2\left(1-M^2\right) = 0$ - This is resonance or cut-off.

4. ACTIVE NOISE SOURCE CONTROL

The far-field discrete-frequency noise is composed of spatial modes generated at multiples of the rotor blade pass frequency which have propagated in the duct and have radiated to the acoustic far field. These discrete-frequency tones are generated by the rotor-stator interaction at multiples of blade pass frequency, with these spatial modes specified by the number of rotor blades and stator vanes $k_\theta = nN_{Blades} + mN_{Vanes}$.

The function of the active noise control system is the reduction of these propagating acoustic modes in the duct before the modes are radiated to the far field. The ideal active control system will produce the same propagating acoustic waves as those generated by the rotor-stator interaction. As the acoustic pressure of the propagating mode is equal to the superposition of the rotor-stator noise with the active control system, having the control generated acoustic waves out-of-phase results in the active control system canceling the rotor-stator generated propagating waves.

The active noise control concept considered herein utilizes active airfoil source control which mimics the rotor-stator interaction and is optimized for control of the propagating acoustic modes generated by the rotor-stator interaction. The source of the discrete-frequency noise is the unsteady loading on the stator airfoils, where the unsteady loading of adjacent airfoils is equal in magnitude and shifted in phase by the interblade phase angle. Placing an acoustic source on each stator vane and driving adjacent sources by signals that are equal in magnitude and shifted in phase by the interblade phase angle, the active control system and the rotor-stator interaction will generate the same spatial modes. These spatial modes generated by the active control system propagate or decay upstream and downstream of the blade rows in the same manner as the spatial modes generated by a rotor-stator interaction.

Note that the cancellation of one propagating spatial mode generated by the rotor-stator interaction both upstream and downstream of the cascade requires two sets of sources. Each set will produce upstream and downstream going acoustic modes. When each set is driven at the proper amplitude and phase, cancellation of both propagating waves is possible.

5. FACILITY & INSTRUMENTATION

The experiments are performed on the Purdue Rotating Annular Cascade Research Facility, Figure 4. This facility is an open loop draw through type wind tunnel capable of test section velocities of 220 ft/sec. The flow, conditioned by a honeycomb section and an acoustically treated inlet plenum, accelerates though a bellmouth inlet to the constant area annular test section. The flow exiting the test section is diffused into a large acoustically treated exit plenum. The flow is drawn through the facility by a 300-hp centrifugal fan located downstream of the exit plenum.

The annular test section is configured with a rotor with 16 perforated plates upstream of a stator with 18 NACA 65A012 airfoils with a 15.24 cm (6.00 in.) chord, Figure 5. An optical pickup on the rotor shaft is utilized to determine the rotor shaft speed. The perforated plates, fabricated from 56% porosity aluminum sheet mounted on the rotor such that the plate width is normal to the rotor axis, generate large vortical gusts, thereby corresponding to forcing functions considered in mathematical models of rotor-stator interaction generated discrete tones.

The 16 rotor blades and 18 stator vanes in the test section generate $k_\theta = n16 + m18$ spatial modes where n is the rotor harmonic and m is an arbitrary integer. Therefore, the spatial modes k_θ = ..., -20, -2, 16, ... are generated at blade pass frequency. At twice blade pass frequency, the spatial modes k_θ = ..., -22, -4, 14, ... are generated by the rotor-stator interaction. For operating conditions from 800 to 1000 rpm, only the k_θ = -2 mode at blade pass frequency and the k_θ = -4 at twice blade pass frequency are cut-on and generated by the rotor-stator interaction. Figure 6 shows the acoustic response as a function of frequency and spatial mode. As predicted, significant acoustic pressure is measured for the propagating spatial modes generated by the rotor-stator interaction at the multiples of blade pass frequency.

Two arrays of 10 Piezotronics PCB 103A piezoelectric microphones with uniform circumferential spacing are mounted via static pressure taps in the outer wall of the inlet annulus. The Nyquist critical mode $k_{\theta,\,critical}$ is 5 for the ten microphone array, with all spatial modes above the Nyquist critical mode aliased below the Nyquist mode.

6. SIGNAL PROCESSING & ACTIVE CONTROL

A primary component of the active noise control system is the measurement of the propagating spatial modes generated by both the rotor-stator interaction and the active airfoil source control system. The measured spatial modes not only characterize the baseline rotor-stator response, but also quantify the effectiveness of the active noise control system.

The discrete-frequency acoustic response is the superposition of spatial modes generated at the multiples of rotor blade pass frequency, with the acoustic modes at blade pass and twice blade pass frequency of primary concern. An array of microphones is required to determine the measured acoustic response as a function of both frequency and spatial mode. This temporal-spatial transform is accomplished using two discrete Fourier transforms. The first determines the frequency content of the microphone signals, and the second determines the amplitude of spatial modes at each frequency. The spatial transform, operating on the temporal Fourier transform, is a function of frequency separates the forward and backward spinning modes.

The signal processing and active control system is depicted schematically in Figure 7. The rotor-stator interaction acoustic response is determined as a function of frequency and spatial mode from the measured acoustic pressure by the inlet array of microphones. This dual transform is accomplished using two discrete Fourier transforms, one in time and the other in space.

Discretely sampling the pressure from the j'th microphone $p_j(t)$ at rate $1/\Delta t$, $N_{\Delta t}$ times over one rotor revolution, $p_j(t)$ becomes $p_{j,1}$ where 1 is the sampling index. The temporal discrete Fourier transform is

$$P_j(f_m) = \frac{2}{N_{\Delta t}} \sum_{1=0}^{N_{\Delta t}-1} p_{j,l}\ e^{-i2\pi lm/N_{\Delta t}} \qquad (6)$$

where $P_j(f_m)$ is the discrete Fourier transform of the j'th microphone found at frequency $f_m = \frac{m}{N_{\Delta t}\Delta t}$ and the arbitrary integer m = 0, 1, 2, $\cdots$, $N_{\Delta t}/2$. Acquiring data over one rotor revolution. the transform of the pressure is determined at multiples of rotor pass frequency.

The spatial Fourier transform operating on the complex output of the temporal transform separates the forward and backward spinning modes, i.e., spatial modes greater and less than zero are uniquely determined.

$$P(f_m, k_\theta) = \frac{1}{N} \sum_{j=0}^{N-1} P_j(f_m)\ e^{-i2\pi k_\theta j/N} \qquad (7)$$

where $P(f_m,k_\theta)$ is the dual temporal-spatial transformation of the acoustic pressure in the duct, N is the number of microphones in the circumferential array, and k_θ = -N/2, -N/2+1, $\cdots$, 0, 1, $\cdots$, N/2-1.

Thus, the acoustic pressure is determined as a function of frequency and spatial mode. Combining Equations 6 and 7 yields the temporal-spatial transform.

$$P(f_m, k_\theta) = \frac{1}{N}\frac{2}{N_{\Delta t}} \sum_{j=0}^{N-1} \sum_{1=0}^{N_{\Delta t}-1} p_{j,l}\ e^{-i2\pi lm/N_{\Delta t}}\, e^{-i2\pi k_\theta j/N} \qquad (8)$$

7. ACTIVE AIRFOIL SOURCE CONTROL

The simultaneous cancellation of one propagating spatial mode both upstream and downstream of the rotor-stator requires a vane row of active airfoils with each airfoil having two independent acoustic sources. The acoustic sources of the active airfoils are organized into two sets, each set having one acoustic source per active airfoil. Each set of acoustic sources produces upstream and downstream propagating spatial modes. When each set of acoustic sources is driven at the proper amplitude and phase, simultaneous cancellation of the upstream and downstream propagating spatial modes is possible.

In these experiments, only the k_θ = -2 mode propagates to the far field. Thus, the spatial modes propagating upstream and downstream due to the rotor-stator interaction are characterized by the complex amplitudes $P_{up,\,\mathrm{gust}}(k_\theta = -2)$ and $P_{down,\,\mathrm{gust}}(k_\theta = -2)$. It is these modes that will be canceled through active control.

The control system is assumed to be linear with the control signal input amplitude. Therefore, the active control system is characterized by the generated complex amplitudes $P_{up,\,A_1}(k_\theta = -2)A_1$, $P_{up,\,A_2}(k_\theta = -2)A_2$, $P_{down,\,A_1}(k_\theta = -2)A_1$ and $P_{down,\,A_2}(k_\theta = -2)A_2$ where these are the influence coefficients of the active control and A_1 and A_2 are the complex amplitude of the control signals. The measured response of the active control system and the rotor stator interaction expressed in matrix form is

$$\begin{bmatrix} P_{up,A_1} & P_{up,A_2} \\ P_{down,A_1} & P_{down,A_2} \end{bmatrix} \begin{bmatrix} A_1 \\ A_2 \end{bmatrix} = \begin{bmatrix} P_{up,\,measured} - P_{up,\,\mathrm{gust}} \\ P_{down,\,measured} - P_{down,\,\mathrm{gust}} \end{bmatrix} \qquad (9)$$

where P_{up,A_2} and P_{down,A_2} are the influence coefficients of the second set of acoustic drivers and A_2 is the complex amplitude of the control signal.

The active control system will cancel the measured acoustic response, i.e., $P_{up,\,measured} = P_{down,\,measured} = 0$. From Equation 9, the required control signals are

$$\begin{bmatrix} A_1 \\ A_2 \end{bmatrix} = \begin{bmatrix} P_{up,A_1} & P_{up,A_2} \\ P_{down,A_1} & P_{down,A_2} \end{bmatrix}^{-1} \begin{bmatrix} -P_{up,\,\mathrm{gust}} \\ -P_{down,\,\mathrm{gust}} \end{bmatrix} \qquad (10)$$

The central component of this active noise control system is the active stator airfoils that generate propagating spatial modes analogous to those of the rotor-stator interaction. The simultaneous cancellation of one rotor-stator interaction generated propagating

spatial mode both upstream and downstream of the airfoil rows requires two sets of acoustic sources. This is accomplished with twin-cavity active stator airfoils, with perspective and chordwise cross section views shown in Figures 8 and 9. The cavity access ports located on the airfoil hub allow the airfoil to be driven by a remote centerbody-mounted acoustic source. The microperforated sheathing minimizes the disturbance of the stator vane aerodynamics while providing only minor resistance to the acoustic radiation from the cavity. The dimensions of the connector and vane cavity were selected such that the cavity and the tube formed a resonator tuned to the rotor blade pass frequency at 1,000 rotor shaft rpm (267 Hz). This resonator configuration provided an amplification of 12 dB relative to the compression driver alone. This configuration is also characterized by a sufficiently broad bandwidth that is necessary to achieve a useful operating range specified for the experiments.

Both the upper and lower surface actuators generate upstream and downstream going propagating spatial modes. When the two sets of actuators are driven in concert by signals of proper amplitude and phase, the active airfoils of the stator vane row cancel the upstream and downstream propagating spatial modes. The active control system naturally mimics the rotor-stator interaction noise, with the physics that governs the rotor-stator interaction also applying to the active noise control system. The magnitude and phase of two reference signals characterize the control signal generation. The reference signals drive the zeroth stator vane of the cascade, with successive stator vanes driven by the same magnitude signal shifted in phase by the interblade phase angle. The amplitude and phase of the reference signals are set to reduce the measured propagating acoustic wave both upstream and downstream of the rotor-stator.

8. RESULTS

Active discrete-frequency noise control is accomplished using active airfoil source control and in-duct spatial mode measurement. The propagating spatial mode generated by the rotor-stator interaction represents both the error signal of the control system and the discrete-frequency noise radiated to an observer. The goal of the active noise control system is to measure and cancel the rotor-stator generated propagating spatial modes before they are radiated to the far field.

A rotor with 16 perforated plates upstream of a stator with 18 active symmetric airfoils were installed in the annular test section of the Purdue Rotating Annular Cascade, with circumferential arrays of microphones in the inlet and outlet used for spatial mode measurement. At blade pass frequency, the k_θ = -2 spatial mode propagates both upstream and downstream. As the k_θ = -2 spatial mode represents the discrete-frequency noise produced by the rotor-stator interaction, the control system was designed to minimize the amplitude of that spatial mode.

The effectiveness of the control system is seen in Figure 10 where the upstream and downstream modal amplitudes are shown for the baseline rotor-stator interaction and the simultaneous upstream and downstream active control. Noise reductions of nearly 20 dB upstream and over 20 dB downstream are realized.

Figure 11 shows the controlled and uncontrolled amplitudes of the k_θ = -2 spatial mode as a function of rotor shaft rotation, with simultaneous control of this spatial mode both upstream and downstream of the rotor-stator. Significant control authority is demonstrated over the entire operating range.

The reduction of the generated discrete-frequency noise relative to the noise generated by the rotor-stator interaction is presented in Figure 12. Reductions of over 10 dB were achieved over nearly the entire range of operating conditions, and maximum reductions of 30 to 40 dB were demonstrated for specific conditions.

Figure 13 shows the amplitude and phase of the control signals required to realize the simultaneous control of the upstream and downstream propagating discrete-frequency noise as a function of rotor shaft rotation. Fortunately, the required control signals are nearly in phase and of comparable amplitude. This allows the drivers to complement each other, and represents the minimum power consumption of the system.

The simultaneous upstream and downstream control of a propagating spatial mode can also be modeled analytically. Using this model for the unsteady flow, the measured propagating spatial mode can be compared with the corresponding calculated value. In addition, for simultaneous control of the upstream and downstream propagating spatial mode, the experimentally determined control voltages can be compared to the calculated piston displacements.

Active noise control techniques can be modeled computationally using the linearized unsteady flow solver LINFLO. The model considers two dimensional, inviscid, adiabatic, attached, compressible, subsonic flow of a perfect gas. The unsteady flow field is considered as a small perturbation superimposed on the steady flow field where the steady flow field is determined using the steady potential flow solver SFLOW. The steady flow field is calculated for a given airfoil geometry, cascade stagger angle, cascade solidity, inlet flow angle and Mach number. The unsteady flow is then determined for a given upwash condition, reduced frequency and interblade phase angle in addition to the airfoil geometry and flow conditions used in the steady analysis. Thus, this analysis is used to determine the airfoil unsteady loading and acoustic response generated by any combination of airfoil motion, vortical gust excitation or potential gust excitation.

The model has been extended to determine the acoustic response generated by oscillating blade-mounted surface pistons [6]. Using anti-sound theory, the upstream and

downstream sound fields of the rotor-stator interaction are completely canceled by the superimposed anti-sound fields of the active blade mounted pistons.

To predict the acoustic response of the rotor-stator interaction with LINFLO, the vortical gust excitation provided by the rotor must be known. The vortical excitation provided by an isolated rotor was measured at the location corresponding to the stator leading edge, with the transverse velocity or upwash generated by the vortical gust is determined directly. With LINFLO, the simultaneous upstream and downstream control of the propagating spatial mode is accomplished using upper and lower surface pistons. The location and extent of the surface pistons corresponds to the location and extent of the actuators of the active airfoils. This allows the comparison of the predicted surface piston velocity and the experimental control voltage.

Figure 14 provides a direct comparison of the measured and predicted propagating spatial mode generated by the rotor-stator interaction as a function of rotor shaft rotation where the acoustic influence coefficients generated by LINFLO for the vortical gust are dimensionalized using the experimentally determined isolated rotor transverse velocity excitation. In general, reasonable agreement is obtained. The acoustic response is predicted somewhat better in the downstream duct. For nearly all operating conditions, the acoustic response is under predicted in the upstream duct. It is evident that the measured acoustic response has maxima and minima due to acoustic reflections at the duct inlet and exit. These acoustic reflections are in no way modeled by LINFLO. Especially in the downstream duct, the predicted response seems to represent the "average" measured response.

9. SUMMARY & CONCLUSIONS

Advanced high bypass turbomachines generate prominent discrete-frequency tones. These tones are generated by rotor-stator interactions, with specific spatial modes generated. However, only certain of these modes propagate to the far field, with these the far-field discrete-frequency noise. High bypass turbomachines limit the effectiveness of current state-of-the-art acoustic treatments for suppression and source control. As prevailing noise regulations become ever more stringent, innovative control of turbomachine noise sources is increasingly important. Thus, a series of fundamental experiments was performed to demonstrate the effectiveness of active simultaneous control of upstream and downstream propagating discrete-frequency noise using active airfoil source control.

In the active airfoil source control technique, the upstream and downstream propagating modes, i.e., the far field tone noise, are simultaneously canceled through the generation of control propagating waves which interact with and cancel those modes generated by the rotor-stator interaction. The active airfoil source control is optimized for the control of propagating spatial modes. The active noise control system incorporates active airfoil source control with in-duct spatial mode measurements and real time rotor phase referenced control signal generation. The active airfoil source control system was successfully demonstrated, with noise reductions of nearly 20 dB upstream and over 20 dB downstream realized simultaneously.

ACKNOWLEDGMENTS

This research was sponsored, in part, by NASA Lewis Research Center. The technical interactions with Dan Buffum, Larry Heidelberg and John Simonich (UTRC) as well as the financial support are most gratefully acknowledged.

REFERENCES

1. Gliebe, P.R., "Aeroacoustics in Turbomachines and Propellers - Future Research Needs," 6th International Symposium on Unsteady Aerodynamics, Aeroacoustics, and Aeroelasticity of Turbomachines and Propellers, Editor H.F. Atassi, Springer-Verlag, 1992.

2. Groeneweg, J.F. and Rice, E.J., "Aircraft Turbofan Noise," *ASME Journal of Turbomachinery*, Vol. 109, No. 1, January 1987, pp. 130-141

3. Thomas, R. H., Burdisso, R. A., Fuller, C. R., and W. F. O'Brien "Preliminary Experiments on Active Control of Fan Noise From a JT15D Turbofan Engine," *Journal of Sound and Vibration*, Vol. 161, No. 3, 1993, pp. 532-537.

4. Goldstein, M., *Aeroacoustics*, McGraw-Hill, New York, 1975.

5. Simonich, J., Lavrich, P., Sofrin, T., and Topal, D., "Active Aerodynamic Control of Wake-Airfoil Interaction Noise-Experiment," *AIAA Paper 92-02-038*, May 1992.

6. Kousen, K.A., and Verdon, J.M., "Active Control of Wake/Blade Row Interaction Noise," *AIAA Paper 93-4351*, October 1993.

7. Minter, J., Hoyniak, D., and Fleeter, S., "Oscillating Flaps for Control of Turbomachine Wake Generated Discrete Frequency Noise," *International Journal of Turbo & Jet Engines*, Vol. 11, Nos. 2-3, 1994, pp. 249-261.

8. McCarthy, S.M., and Fleeter, S., "Dipole Active Control of Wake-Blade Row Interaction Noise," *AIAA Paper 96-1783*, May 1996.

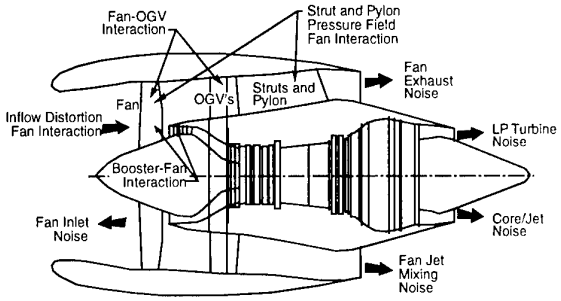

Figure 1. Sources of turbomachine noise

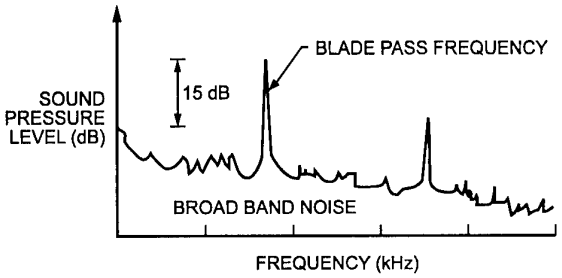

Figure 2. Typical turbomachine noise spectrum

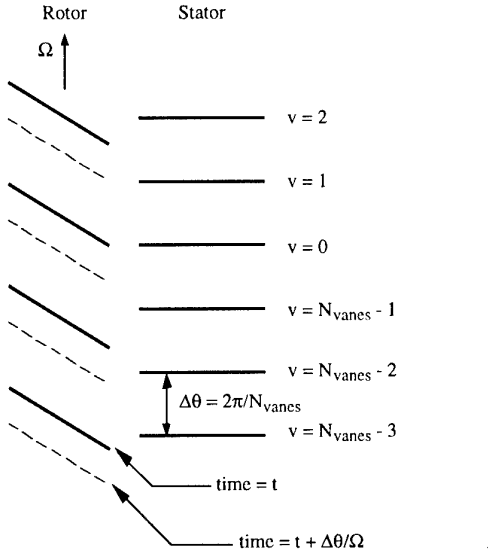

Figure 3. Rotor moves one stator passage in $t = \Delta\theta/\Omega$

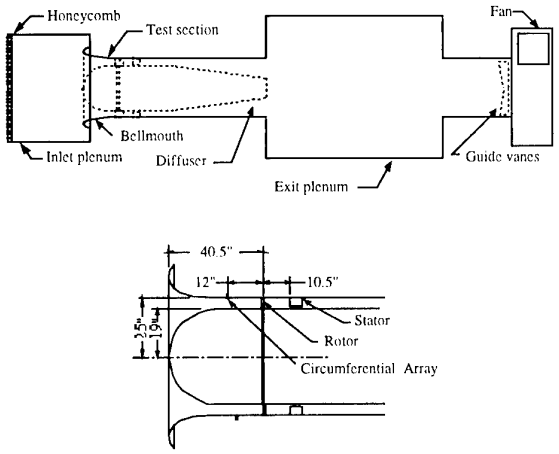

Figure 4. Purdue Annular Cascade Facility

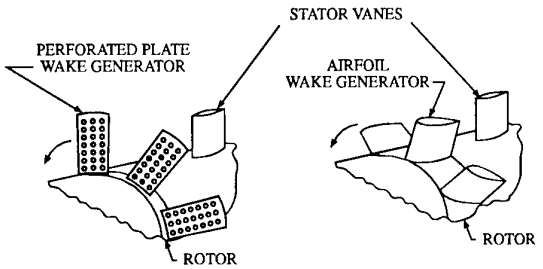

Figure 5. Rotor and stator and representative gust.

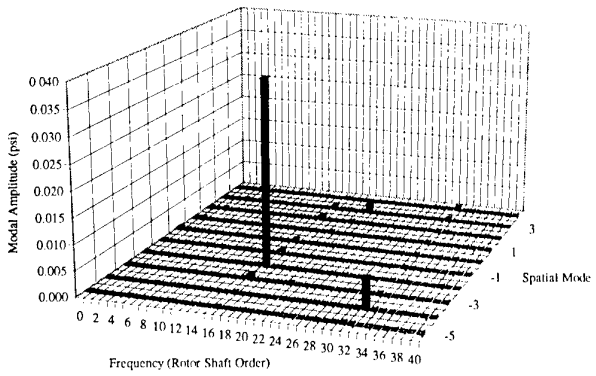

Figure 6. Rotor-stator interaction spatial modes

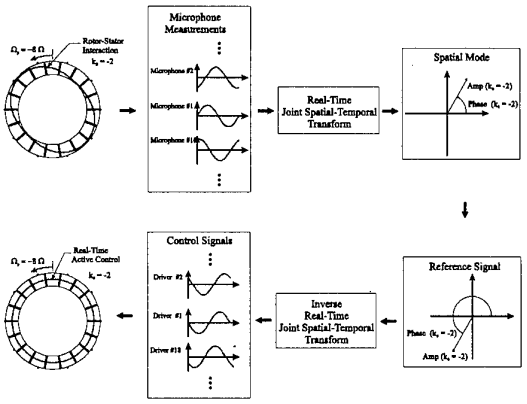

Figure 7. Active noise control system

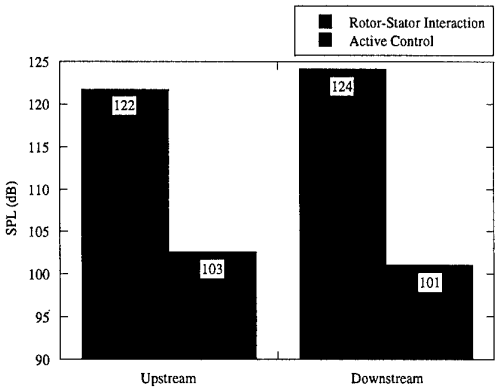

Figure 10. Simultaneous up & downstream control

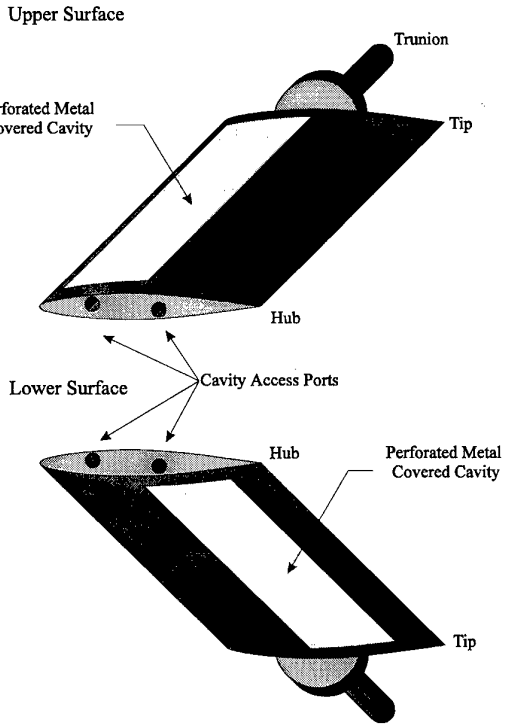

Figure 8. Active stator airfoil

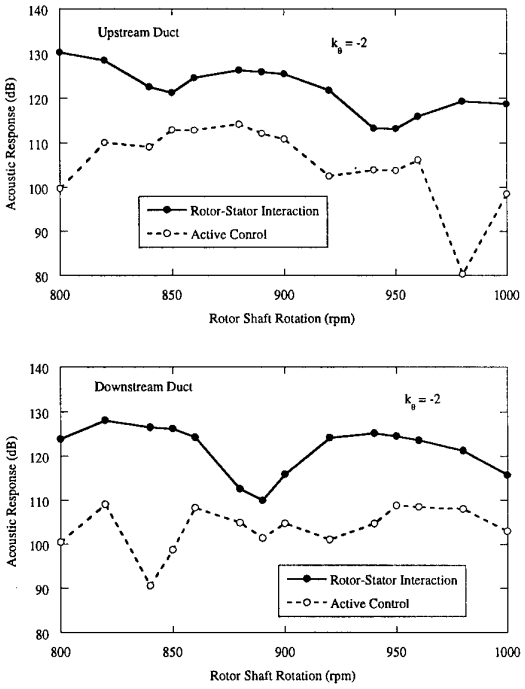

Figure 11. Simultaneous control of upstream and downstream propagating discrete-frequency noise

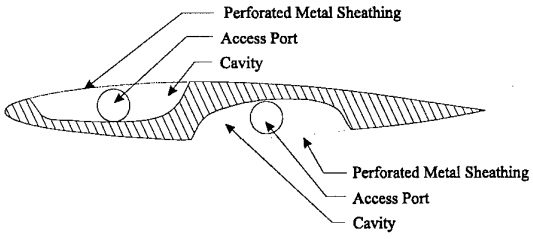

Figure 9. Active airfoil chordwise cross-section

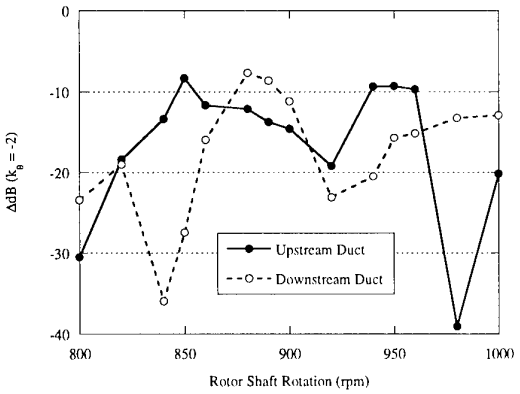

Figure 12. Control authority over wide range of operating conditions

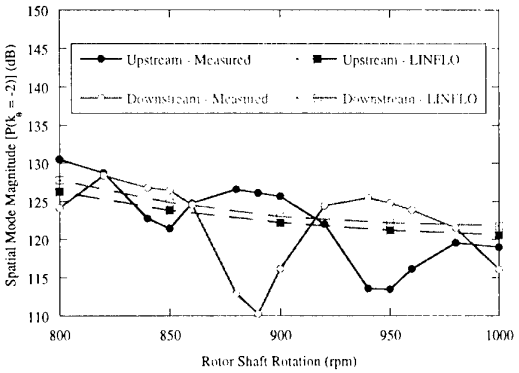

Figure 14. Comparison of measured and predicted rotor-stator acoustic response

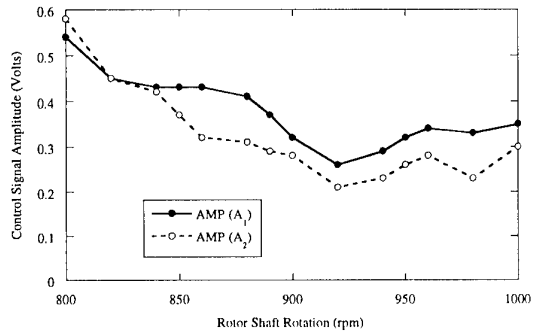

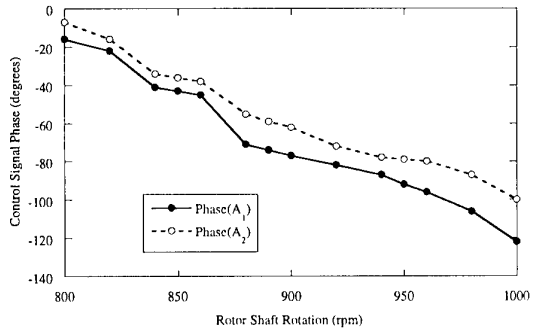

Figure 13. Control signal voltage amplitude and phase as a function of rotor shaft rotation

Meeting Discussions

Paper 15: Simultaneous Active Source Control of Blade Row Interaction Generated Discrete Tones

Authors: S. Fleeter, S. Sawyer

Discussor: George S. Dulikravich

Question: In transonic flows with shock waves impinging on a blade with a porous surface and a cavity underneath, there could be a substantial improvement in the aerodynamic performance of the blade because of the diffusion of the shock foot and the consequent prevention of the shock-induced boundary layer separation. Research in this area has been active for almost 20 years. If the surface porosity distribution is not appropriately specified, the aero dynamic performance of the blade can actually be worsened. So, my comment is actually a positive comment.

Authors's reply: Several interesting points regarding the interaction of a shock and a porous cavity were raised. As this system would most likely be implemented in a fan where flow mach numbers are not transonic, these factors would not be applicable in the design process.

Discussor: Jürgen Broede

Question 1: You mentioned that cavities in the vanes are necessary for active noise control. Those cavities weaken the mechanical strength of the vanes. Could you comment on the actions needed to recover the mechanical strength of the vanes?

Authors reply: Vane cavities will weaken the vanes. This would definitely be a concern for solid vanes. If the system is applied to hollow core vanes or struts, certainly the vane could be stiffened using standard techniques.

Question 2: For active noise control you need additional equipment for the engine which add weight to the propulsion system. What is this additional weight relative to the engine weight?

Authors's reply: Engine weight versus active control system weight. Estimated weights of the research system are 2 lbm/speaker (36 speakers), 40 lbm/amplifier (3 amplifiers), and a 25 lbm computer for control. Obviously, application would require optimization of the design.

- Speaker weight will be reduced by an increase in blade pass frequency. High frequency drivers will have minimal weight compared to midrange drivers.
- Use of high voltage power supply will drastically reduce amplifier weight, as the majority of amplifier weight is due to the transformer.
- Finally, development of a dedicated control system will also drastically reduce the weight of the control computer.

Thus, the flight ready system will have negligible weight.

Discussor: R. Van dem Braembussche

Question: Could you please comment on the influence of such a system on the stator performance and how much power is needed to drive the system in comparison to the compressor power?

Author's reply:1. The airfoil cavities will certinly effect the steady aerodynamics of the vane. The microperforated sheathing should minimize the disturbance to the steady flow, but the influence of the cavities must be determined before application.

2. The maximum power output by the speaker is 30W. Thus, the total power is 1.08 kW (1.45hp). This is negligible power consumption campared to the power required to drive the compressor.

Improved Gas Turbine Response using LQR Control

Mike Richman, Dr. Vernon Gordon
Propulsion Fuel Systems, Controls and Diagnostics
Bldg 106, Naval Air Warfare Center Aircraft Division
22196 Elmer Road Unit, Code 4.4.2
Patuxent River, MD 20670-1534, USA

1. Summary

This paper develops a design methodology for a full state feedback controller using linear quadratic regulator (LQR) multivariable control techniques. The result is a controller that will perform with the quickest settle time, containing optimal stability margin while minimizing the feedback gains to realistic real world values. A correlation will be established between the weighting parameters used in a typical LQR design and their effect on steady state settle time and maximum feedback gain.

The entire investigation uses MATLAB with Simulink, including an assortment of control system toolboxes, to design, trend, and evaluate the system with and without the full state feedback controller. A Simulink block diagram was used to design and test a full-state feedback controller. Settle time, maximum feedback gain, and steady-state values were plotted as a function of LQR design parameters Q and R. These parameters weight either the state or control energy for optimization. Choosing a Q identity matrix of 10 and R identity matrix of 0.1 the system was evaluated with both a step input and a sine wave input. The controlled system reduced the steady state settle time by .5 seconds over the open loop step response.

LIST OF SYMBOLS

A	System matrix
B	Input coupling matrix
C	Output matrix
D	Feedforward matrix
X	State vector
Y	Output vector
U	Input vector
Q	LQR State vector weight
R	LQR Control vector weight

2. Introduction

Naval Aviation dictates unique requirements and operating conditions on aircraft and especially their power plants. Landing a state-of-the-art supersonic fighter/attack aircraft on the deck of a rolling and pitching carrier is no easy task for pilot or vehicle. The demand on the propulsion system is very high as are the expectations that it will perform when and where the pilot wants it to.

Engine control system design is crucial in a successful landing aboard a carrier. The propulsion system must reliably provide maximum thrust at the given conditions in the shortest amount of time. Pilots constantly adjust throttle position during landing to maintain proper glide slope and the engine must follow these demands. The key is to design a system with fast response characteristics while maintaining good stability margins without stepping out of the engine operating parameters such as overspeed limits, combustor and turbine temperature limits. Add to this, the uncertainties in accurately modeling the fluid dynamics within the engine as well as the inlet distortion effects and the control system begins to take on a new role of maintaining a happy medium between disaster and success.

Many design techniques provide solutions to either the performance or the robustness issues. Few give insight as to how the one affects the other (performance Vs robustness). The challenge is to design a robust full-state feedback controller based on the optimum performance of the system.

Robustness is a key parameter in designing a control system for a turbo-fan engine enduring the

Paper presented at the RTO AVT Symposium on "Design Principles and Methods for Aircraft Gas Turbine Engines", held in Toulouse, France, 11-15 May 1998, and published in RTO MP-8.

high demand levels of a carrier approach. The control system must operate properly in realistic situations. Modeling the system with all of these realistic variables is not an exact science. Models are not 100% accurate. The control system must account for the uncertainties in the model with which it was designed. It must perform not only for the plant it was designed, but for a whole set of plants. (Shahian and Hassul) The controller must be capable of stabilizing the system which does not have a distinct set of poles and zeros but a range over which each of the poles and zeros might lie.

Multi-variable control system design techniques lend themselves to gas turbine engine control systems. The turbofan engine is a multi-input multi-output (MIMO) system. Common inputs are: fuel flow, compressor variable geometry, fan variable geometry, nozzle area, inlet area, bypass and bleed air control, etc. As technology advances the knowledge of the fluid dynamics and combustion characteristics of the system, many more methods for actively controlling every aspect of the operation will be introduced. Therefore, the complexity of the system necessitates the control system designer understand how each design parameter affects the entire engine.

The system to be investigated is a modern turbo-fan gas turbine engine for an existing U.S. Navy aircraft. The low bypass turbofan produces approximately 20,000 lbf thrust with full augmentation. The engine is controlled via four parameters: fuel flow, exhaust area, core guide vanes, and fan guide vanes. Rather than using the current controller, this investigation will develop a linear quadratic regulator (LQR) based on the systems response to a step input in fuel flow. The steady-state settle time will be correlated with the design parameters used in LQR to provide a optimal multi-variable control system with guaranteed stability margins and the highest performance. The design algorithm will produce trend plots which will illustrate the effect that robustness has on performance.

3. LQR Design

A regulator is designed to keep a stationary system within an acceptable deviation from a reference condition using acceptable amounts of control. The regulator moves the system from an initial state $x(t_o)$ to a terminal state, using acceptable levels of control $u(t)$ without exceeding acceptable levels of the state.

Linear Quadratic Control (LQ) refers to a body of techniques, using optimal control, developed for control system design. The plant is assumed to be a linear system in state space form, and the cost function is a quadratic functional of the plant states and control inputs. The objective is to minimize the quadratic (cost) functional with respect to the control inputs subject to the linear system constraints.

System Configuration (regulator)

$$\dot{x} = Ax + Bu$$

$$y = Cx + Du$$

$$J = \frac{1}{2}\left(x^T S_f x\right)_{t=t_f} + \frac{1}{2}\int_0^T \left(x^T Q x + u^T R u\right) dt$$

Q = symmetric positive semidefinite

R = symmetric positive definite

$\frac{1}{2}\left(x^T S_f x\right)_{t=t_f} \rightarrow$ quadratic form in the terminal state

S_f = P in the algebraic Riccati equation

The cost function J represents the weighted sum of energy of the state and control. The weighting matrices Q and R control the characteristics of the system. By weighting R more than Q the control energy is penalized heavily translating into smaller actuators, motors and gains required to implement the control law. By weighting Q much larger than R the state is similarly affected resulting in a damped system which avoids large fluctuations or overshoots in system states. An appropriate choice of Q and R must be made to obtain acceptable levels of $x(t_f), x(t)$, and $u(t)$. (Bryson and Ho)

Possible choices might be diagonal matrices with:

$$1/A_{ii} = (t_f - t_o)X \quad \text{max acceptable } [x_i(t)]^2$$

$$1/B_{ii} = (t_f - t_o)X \quad \text{max acceptable } [u_i(t)]^2$$

The objective is to minimize the affects of disturbances on the system.

Optimizing a cost function, which relates key parameters of the system, provides a design method for the system to operate with maximum efficiency and performance with respect to these key parameters. This study will optimize a cost function comprised of state and input matrices. The cost function is optimized for a given importance placed either on the states or the inputs. This optimal point shifts with the relative importance placed on Q and R.

To solve the LQR problem the following assumptions are made. First, the entire state vector x(t) is available for feedback. Thus, a Kalman estimator is not needed. Second, the system is stabilizable. Stabilizable systems contain unstable modes which are all controllable. If matrix A and B are controllable then the system is stabilizable. The system is controllable if the states can be moved in any direction in the state space. If the system is controllable, then full state feedback can be used for this. Controllability is a function of the A and B matrix and can be determined by the controllability matrix. A system is controllable if and only if the rank of the controllability matrix is equal to the system order or the dimension of the plant matrix A. The controllability matrix is given by the following equation:

$$C = \begin{bmatrix} B & AB & A^2B & \dots & A^{n-1}B \end{bmatrix}$$

The final assumption is that the system is detectable. Detectability is the dual notion of stabilizability. A system is detectable if the unstable modes are observable or equivalently the unobservable modes are stable. If matrix A and C are observable then the system is detectable. Observability is the ability to uniquely determine the state of a free linear dynamic system from observations of linear combinations of the output of the system in finite time. (Bryson and Ho) Observability can be mathematically tested by checking the rank of the observability matrix.

$$O = \begin{bmatrix} C \\ CA \\ CA^2 \\ \cdot \\ \cdot \\ CA^{n-1} \end{bmatrix}$$

If the rank of O is equal to the dimension of O then the system is observable.

One method used to solve for the control law is Pontryagin's minimum principle. (Shahian and Hassul)

Hamiltonian:

$$H(x,\lambda,t) = \frac{1}{2}(x'Qx + u'Ru) + \lambda'(Ax + Bu)$$

The optimal control and state trajectories must satisfy the following three equations:

$$\dot{x} = \frac{\partial H}{\partial \lambda} \quad x(0) = x_0 \text{ state equations}$$

$$-\dot{\lambda} = \frac{\partial H}{\partial x} \quad \lambda(T) = 0 \text{ costate of adjoint equations}$$

$$\frac{\partial H}{\partial u} = 0$$

By differentiating the Hamiltonian with respect to $\lambda, x,$ and u:

$$\dot{x} = Ax + Bu \quad x(0) = x_0$$

$$-\dot{\lambda} = Qx + A'\lambda \quad \lambda(T) = 0$$

$$u^* = -R^{-1}B'\lambda \quad u^* \text{ is the optimal control}$$

These equations form a two point boundary value problem which is difficult to solve numerically due to the mixed boundary condition. A Hamiltonian matrix is formed by substituting the optimal control (u^*) into the original state equation.

$$\begin{bmatrix} \dot{x} \\ \dot{\lambda} \end{bmatrix} = \begin{bmatrix} A & -BR^{-1}B' \\ -Q & -A' \end{bmatrix} \begin{bmatrix} x \\ \lambda \end{bmatrix} \stackrel{\Delta}{=} H \begin{bmatrix} x \\ \lambda \end{bmatrix}$$

By differentiating an assumed solution for

$\lambda\ (\lambda = Px)$ with respect to time and substituting

$$\frac{d\lambda}{dt} = \frac{dP}{dt}x + P\frac{dx}{dt} = \frac{dP}{dt}x + PAx - PBR^{-1}B'Px = -Qx - A'Px$$

This must hold for any x and P must satisfy following the Riccati Differential Equation (RDE) for optimal control.

$$-\frac{dP}{dt} = A'P + PA + Q - PBR^{-1}B'P, \quad P(T) = 0$$

(Riccati Differential Equation)

The Riccati equation is a nonlinear first order differential equation that must be solved backwards in time. The solution to the Riccati equation results in a linear time varying feedback controller:

$$u(t) = -K(t)x(t)$$

$$K(t) = R^{-1}B'P(t)$$

Even if the RDE converges and the optimal control exists it does not necessarily result in a stable closed loop system. However, under mild conditions, P(t) approaches a constant matrix P $\left(\frac{dP}{dt}\right) \to 0$ and the positive definite solution of the algebraic Riccati equation (ARE) results in an asymptotically stable closed loop system.

$$A'P + PA + Q - PBR^{-1}B'P = 0$$

$$u = -Kx, \qquad K = R^{-1}B'P$$

ARE assumptions are (A,B) are stabilizable and R > 0 and Q can be factored as $Q = C_q'C_q$ where C_q is any matrix such that $(C_q, A$ is detectable. The ARE and it's assumptions are sufficient for the existence and uniqueness of an optimal controller that will asymptotically stabilize the system.

An initial controller design is easily obtained via the LQR methodology. However, the implications of the input and state variable weights must be accounted for properly to guarantee a proper and realistic control system.

4. Engine State Model

The system to be investigated is a modern turbo-fan gas turbine engine for an existing U.S. Navy aircraft. The low bypass engine produces approximately 20,000 lbf thrust with full augmentation (afterburner). The engine is controlled via four parameters: fuel flow, exhaust area, core guide vanes, and fan guide vanes. The state parameters are fan speed and core speed. The linear model was developed at the flight conditions of:

Mach = 0.4
Tambient = 390.31 Rankine
Pambient = 3.30 psi

The model was developed by Mr. Jim Vincent president of Control Application Inc. The linear engine state model used in this investigation was developed via a MATLAB m-file which generates a set of initial conditions, rotor inertia's, and partial derivatives calculated from a detailed non-linear engine transient cycle simulation. The details of this simulation will not be discussed in this investigation due to the proprietary nature of the data. The m-file produces the following linear state model.

$$aeng = \begin{bmatrix} -2.7273 & 1.4554 \\ 0.0408 & -1.5112 \end{bmatrix}$$

$$beng = \begin{bmatrix} 0.0106 & 0.1683 & -0.3728 & 0.2930 \\ 0.0118 & 0.0174 & 0.0029 & -0.3711 \end{bmatrix}$$

$$ceng = \begin{bmatrix} 1 & 0 \\ 0 & 0.7983 \\ 81.05 & 4.969 \\ 1.135 & 1.289 \\ 6.4661 & -2.0016 \\ -7.453 & -13.04 \\ 1.215 & 0.1901 \\ -1.084 & 1.539 \end{bmatrix}$$

$$deng = \begin{bmatrix} 0 & 0 & 0 & 0 \\ 0 & 0 & 0 & 0 \\ .5008 & -5.483 & 10.27 & 1.682 \\ 0.0137 & -0.0768 & 0.1433 & 0.2557 \\ 0.0103 & -0.3716 & 0.8899 & -0.2919 \\ 0.4042 & -0.2203 & -0.7865 & -1.8060 \\ -0.0149 & -0.0682 & 0.1671 & 0.0215 \\ -0.0081 & 0.3003 & -0.443 & 0.2188 \end{bmatrix}$$

This model is used in conjunction with the Simulink block diagram shown in figure 1. The system consists of three major parts. The first is the input generator. The four input parameters are initialized and combined into matrix form. Fuel flow is the only input that is exercised. The three other inputs, exhaust area, fan and core guide vane angles are simply generated via lookup tables based upon the fuel demand. However, these commands are sent through limit blocks which restrict the inputs within predetermined boundaries. These limits are set to prevent component failures caused by overspeeding the turbine and compressor or overtemping the hot section of the engine. After the four inputs are bounded by their limits they go through a system which simulates the individual component dynamics. The second component of the block diagram is the state-space linear engine model linking the A, B, C, and D matrices as well as the feedback control. The third component produces the systems eight outputs: fan speed (%), core speed(%), gross thrust (lbf), net thrust (lbf), p21 (psia), p25 (psia), ps3 (psia), and p56 (psia).

6. Controller Design and Evaluation

Multi-input/multi-output (MIMO) control systems do not allow the level of insight into the design process that single-input/single-output (SISO) system algorithms furnish. The complexity involved in the multiple differential equations which make up a MIMO system makes it hard to evaluate the design based on simple tools such as root locus and bode plots. For this reason, the controller for the turbofan engine will be designed via LQR techniques using classical design parameters such as a step response and steady-state settle time. Using these simplistic methods to design a linear quadratic controller will correlate MIMO system design parameters to that of a more classical SISO.

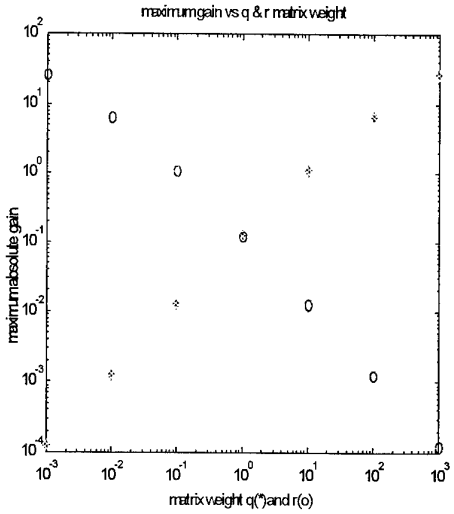

Figure 2

The outputs of interest are fan and core speed, gross and net thrust. Fan and core speed are the primary outputs which indicate how the engine is responding to the input and the controller. The gross and net thrust outputs are merely empirical calculations which give insight to the system performance. They are functions of both core and fan speeds.

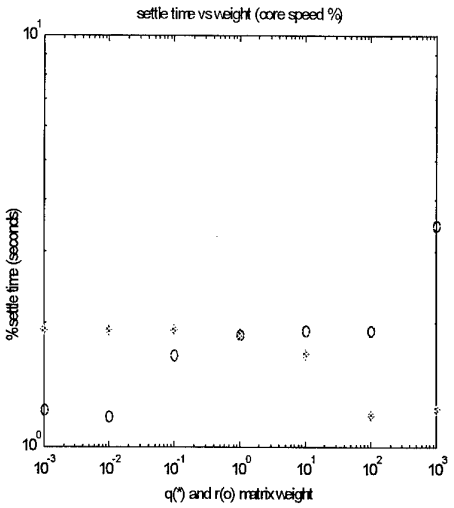

Figure 3

Figures 2 and 3 are two trend plots developed by the MATLAB m-file created for this project. These plots illustrate the correlation between the weighting matrices and the performance considerations of settle time and maximum gain. Figure 2 illustrates that the maximum feedback gain is essentially a linear function of Q and an inverse linear function of R. These plots were developed by iterating Q and R as follows:

$$Q^* = s[Q]$$
$$R^* = s[R]$$
$$s = 0.001 \rightarrow 1000$$

These results correspond to the LQR equations presented in section 3 where the feedback gain K is proportional to the solution of the algebraic Riccati equation which is a function of Q and R. Therefore, as the states are more heavily weighted the feedback gain increases. Conversely, as the input weighting is increased the maximum feedback gain decreases.

Figure 3 illustrates the steady-state settle time for engine core speed response to a step input fuel flow (magnitude equal to 50lb/hr step). The figure shows that as the magnitude of Q increased the core speed steady-state settle time decreased in a non-linear fashion. The converse action is true for the R matrix. The minimum settle time occurs when $Q^* = 100[Q]$ and $R^* = 0.01[R]$. This nonlinear relationship is characteristic of the system dynamics and the linear state model used in this investigation.

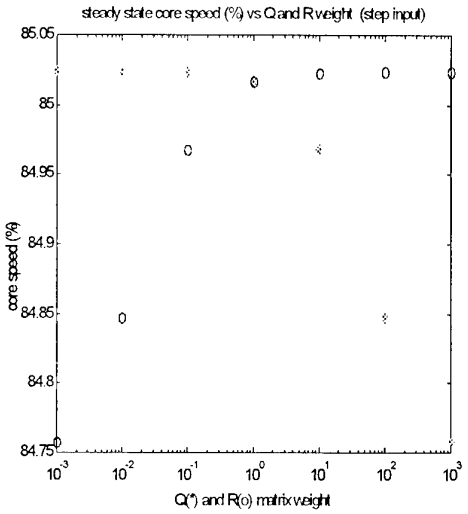

Figure 4

Figure 4 shows the affect that Q and R have on the steady state core speed (step response). By increasing Q from identity up to 1000 times the identity matrix, the core speed changes drastically. However, with Q less than the identity matrix the core speed is maximized. Conversely, as R is increased from 0.001 to identity the core speed changes drastically maximizing when R is greater than the identity matrix. Note the mirror images for the Q and R effects on steady-state core speed trend plots. Similar plots were developed for the remaining 7 outputs of the model. Due to size limitations they are not included in this paper. However, the trends are similar. Both gross thrust and fan speed give the same characteristic steady-state increase as R increases. Conversely, these outputs decrease with as Q increases.

7. Performance and Robustness

The primary objective of this investigation was to develop a correlation between the linear quadratic regulator design parameters and the turbofan performance, and, by doing so, design a control system which optimizes the turbofan performance with a guaranteed stability. Given the trends shown in section 6, a LQR was chosen based on the steady-state system response to a step input. Key parameters such as steady-state settle time and

maximum feedback gain were chosen as design constraints.

The LQR was chosen to optimize the cost function (J) of section 3 with weighting matrices as follows:

$$Q = \begin{bmatrix} 10 & 0 \\ 0 & 10 \end{bmatrix}$$

$$R = \begin{bmatrix} .1 & 0 & 0 & 0 \\ 0 & .1 & 0 & 0 \\ 0 & 0 & .1 & 0 \\ 0 & 0 & 0 & .1 \end{bmatrix}$$

Next, the system was evaluated with a step input of 50 lb/hr applied at t = 1 sec. Figure 5 shows the comparison between the baseline open loop system and the closed loop system with a LQR. The dashed line is the open loop system, while the solid line is the closed loop system. Once again, the primary outputs of interest are fan and core speed as well as gross and net thrust levels. As indicated by this figure the closed loop system, with LQR in place, yields slightly reduced output. However, the settle time on each is significantly quicker. The system response has been improved with very little degradation in steady-state output. Specifically the fan and core speed reduced by only .2%, which is insignificant compared to the almost .5 sec reduction in settle time.

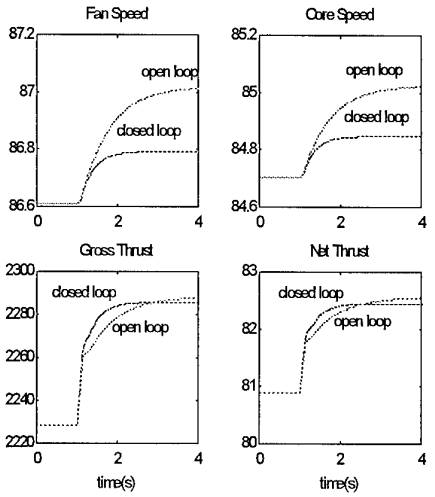

Figure 5

The LQR has produced a significant improvement in steady-state response to a step input. However, the real test is the system's response to a transient fuel flow input. Figures 6 and 7 contain non-dimensionalized plots of the input, fan speed, core speed, gross thrust, and net thrust response to a 5Hz sine wave in fuel flow with 100 lb/hr amplitude.

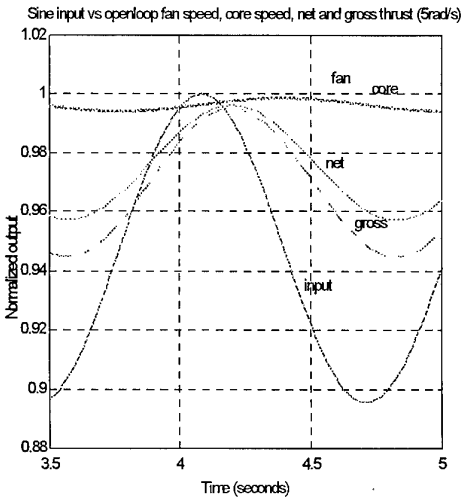

Figure 6

Figure 6 shows the baseline transient response. This output snapshot is taken from 3.5 to 5 seconds at which time the system has reached a steady response state. This figure illustrates that after four seconds the fan and core speed is almost 90 deg out of phase from the input (approx. .3 sec behind the input wave). This occurs with a slow 5 rad/s sine wave input.

Comparatively, figure 7 shows that with the same input wave, the LQR system is only .25 seconds behind the input wave. This can be attributed to the characteristic found in the steady-state step response i.e. a .5 second settle time improvement. Additionally, the step response and sine response (5 rad/s) indicate that the system does not grow unstable during the simulation as guaranteed by the LQR design.

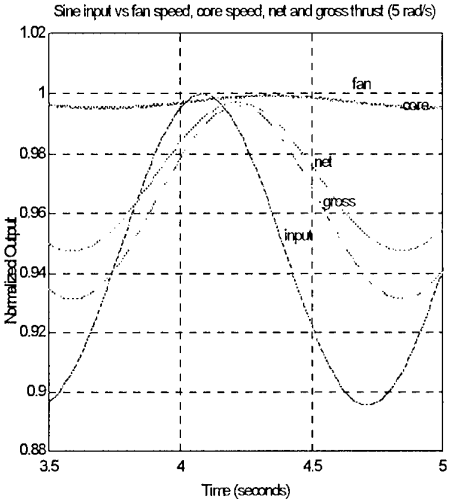

Figure 7

Similar plots were generated for an input of 20 rad/s at which point the system falls 180 deg out of phase from the input. However, the system model is only valid for small fluctuations around the design point.

8. Conclusion

This investigation provides simple trend plots correlating the linear quadratic regulator design parameters to the system performance aiding in the design of a robust controller with good response time. The models response to a step input can be improved by as much as .5 seconds using this design technique. The data indicated that an increase in the Q weighting matrix would result in a non-linear decline in steady-state settle time for both core speed and gross thrust with similar trends in the steady-state value of each of these parameters. An increase in Q did provide an increase in the maximum feedback gain as expected. By increasing R the results produced an opposing effect on the system. Settle time and steady-state values for both core speed and gross thrust increased non-linearly as a function of increasing R. The maximum gain decreased with increasing R as expected. Choosing a Q identity matrix of 10 and R identity matrix of 0.1 the system was evaluated with both a step input and a sine wave input. The controlled system reduced the steady state settle time by .5 seconds over the open loop step response. Accordingly, the system was able to respond with smaller transient phase shift.

The settle time and maximum feedback gain trends found in this investigation are a function of the LQR design algorithm and the optimal cost function. The correlation between Q and R and the system performance will be the same regardless of the A, B, C, and D matrices used. This paper can be used as a design guide for the development of a linear quadratic regulator using MATLAB with Simulink. The m-files used to iterate the LQR feedback gain are general in nature. Little modification is needed to duplicate this investigation for other state-space linear models.

REFERENCES

1. Bryson, Arthur E., and Yu-Chi Ho. *Applied Optimal Control.* New York: Hemmispere Publishing Corporation, 1975.

2. Kwakernaak, Huibert., and Raphael Sivan. *Linear Optimal Control Systems.* New York: Wiley-Interscience, 1972.

3. Maciejowski, J.M. *Multivariable Feedback Design.* New York: Addison-Wesley, 1989.

4. Ogata, Katsuhiko. *Solving Control Engineering Problems with MATLAB.* New Jersey: Prentice Hall, 1994

5. Shahian, Bahram., and Michael Hassul. *Control System Design using MATLAB.* New Jersey: Prentice Hall, 1993.

6. Stengel, Robert F. *Stochastic Optimal Control.* New York: Wiley-Interscience, 1986.

7. Zhou, Kemmin., with John C. Doyle and Keith Glover. *Robust and Optimal Control.* New Jersey: Prentice Hall, 1996.

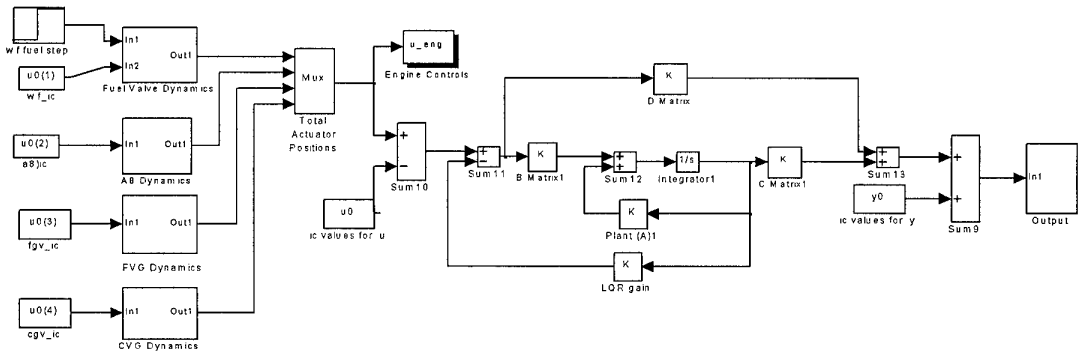

Figure 1

UNSTEADY, FINITE-RATE MODEL FOR APPLICATION IN THE DESIGN OF COMPLETE GAS-TURBINE COMBUSTOR CONFIGURATIONS

Carlos G. Rodriguez*
Walter F. O'Brien†

Mechanical Engineering Department
Virginia Polytechnic Institute and State University
Blacksburg, VA 24061-0238

ABSTRACT

Design methods for gas-turbine engine combustors require mathematical models that satisfy two simultaneous and often conflicting requirements: to provide an accurate description of the highly complex geometry and physics involved, and be sufficiently inexpensive in computational requirements as to allow its incorporation in a design cycle involving the evaluation of a great number of operating conditions.

For these reasons a one-dimensional, finite-rate, unsteady combustor model has been developed that incorporates most elements found in modern gas-turbine burners, and yet is simple enough to be implemented in desktop computers. The model includes the division of the flow-path into annular and primary streams, finite-rate effects within the primary flow, and interaction between hot and cold gases though dilution holes. Examples show predictions of flow distribution within complete burner configurations, blowout predictions, and the effects of perturbations in boundary and operating conditions.

1. INTRODUCTION

Computational Fluid dynamic (CFD) methods are an indispensable tool in the analysis of modern gas-turbine combustors. They can provide both a qualitative understanding of the complex phenomena within the burner and reasonable quantitative results. They are also used in design applications, either to improve existing designs (Crocker and Smith, 1993; Lawson, 1994), or to predict the performance of completely new layouts (Davis et al., 1996).

However, there are limitations in their use for industrial design. First, limitations in turbulence and chemistry models involve a degree of uncertainty in any practical application. As a result, a fair amount of "tuning" is needed on a case-by-case basis. Additionally, there are limits in the size of the physical domain to be solved due to the intensive computational effort required. As a result, practical gas-turbine combustors designs have to be analyzed on a sequential basis (McGuirk and Spencer, 1996): the external flows around and into the primary are solved first, and the resulting mass flow-splits are imposed on the primary flow; the interaction between the different flow-paths is almost never attempted. Furthermore, most available solutions are steady-state; transient simulation of blow-out or changes in boundary and/or operating conditions are rarely if ever performed.

Therefore, CFD is usually complemented with lower-order methods based on first principles and empirical information in order to handle some of the issues raised in the previous discussion. Some (though not all) of these methods can handle complete combustor configurations including all the mass flow-splits; examples include Samuel (1961) and Stuttaford and Rubini (1996). On the other hand, the vast majority are steady-state solvers.

To address some of these issues the authors started the development of one-dimensional methods based on first principles which tried to minimize the amount of empirical (usually user-given) information. The first of these models (Rodriguez and O'Brien, 1997) was a steady, complete-configuration, calorically-perfect model which used chemical-equilibrium calculations to estimate the heat-release in the energy equation. It was followed by a steady infinite-rate model (Rodriguez and O'Brien, 1998) which calculated the heat-release by a mixture-fraction equation and allowed for variable specific heats.

The present model improves on the previous ones by being fully unsteady (allowing for transient solutions to be obtained) and by using finite-rate chemistry to account for

---

* Research Associate
† J. Bernard Jones Professor and Department Head

Paper presented at the RTO AVT Symposium on "Design Principles and Methods for Aircraft Gas Turbine Engines", held in Toulouse, France, 11-15 May 1998, and published in RTO MP-8.

flammability limits. A complete description can be found elsewhere (Rodriguez, 1997). Only the basic elements will be presented here, followed by some applications.

2. THEORETICAL BACKGROUND

2.1. Equations at the Control-Volume Level

The domain is discretized into finite- or control-volumes (CVs), in whose interior the governing equations in integral form are solved. Figure 1 shows a generic CV i with some of the elements to be described next. In the usual CFD notation the complete system of one-dimensional equations for multi-component, reacting mixtures is:

$$\Delta V(i)\frac{\partial}{\partial t}\vec{Q}(i) + \vec{F}(i)\,A(i) - \vec{F}(i-1)\,A(i-1) = \vec{W}(i) \qquad (1)$$

where $\vec{Q}(i)$ is the vector of conservative variables defined in the interior of the CV. $\vec{F}(i)$ represents the fluxes through the flow-area A(i) of the conserved properties associated with $\vec{Q}(i)$. $\vec{W}(i)$ is the vector of source-terms, i.e., additional fluxes of properties coming through the walls or created within the CV itself; this vector is also evaluated inside the CV. The expressions for these vectors are given by

$$\vec{Q} = \begin{bmatrix} \rho \\ \rho u \\ \rho e_t \\ \rho y_j \end{bmatrix} \qquad \vec{F} = \begin{bmatrix} \rho u \\ \rho u^2 + p \\ \rho u h_t \\ \rho u y_j \end{bmatrix} \qquad (j = 1, \ldots, N_s - 1) \qquad (2)$$

where ρ is the density, u the axial or mean-flow velocity, θ_t the absolute (formation plus sensible) total internal energy, y_j the mass-fraction of species j, p the static pressure and h_t the absolute total enthalpy. N_s is the number of species being present.

The above is a system of N_s+2 equations in the N_s+2 unknowns

$$\vec{q} = \begin{bmatrix} \rho \\ u \\ p \\ \rho y_j \end{bmatrix} \quad (j = 1, \ldots, N_s - 1) \qquad (3)$$

known as primitive variables ($\vec{q}$ being the primitive-variables vector). To close the system it is necessary to relate e_t and h_t to the primitive variables by means of the temperature T:

$$h_t \equiv e_t + \frac{p}{\rho} \qquad (4)$$

$$e_t \equiv \sum_{k=1}^{N_s} y_k\, e_k(T) + \frac{1}{2}u^2 \qquad (5)$$

where e_k is the static energy of species k, given by

$$e_k(T) = \left(h_f^0\right)_k + \int_0^T C_{v_k}(\tau)\,d\tau \qquad (6)$$

with $\left(h_f^0\right)_k$ being the energy of formation of species k at 0 K. The constant-volume specific heat of species k, C_{vk} is usually given in terms of empirical polynomial correlations.

The system is closed by relating T to the main variables via the equation of state for a mixture of gases:

$$p = \rho\left[\sum_{k=1}^{N_s} y_k R_k\right] T \qquad (7)$$

where R_k is the specific gas-constant of species k.

Finally the remaining mass-fraction is obtained from

$$y_{N_s} = 1 - \sum_{k=1}^{N_s - 1} y_k \qquad (8)$$

2.2. Source Terms - Chemistry Model

The source terms allow for the application of the previous generic system 1 to a particular case. As already mentioned these sources represent additional mass, momentum, energy and species **into** the CV, either as fluxes through the solid boundaries or created within the CV itself.

Figure 2 shows the source terms that may be present in a typical CV as could be found in combustor applications. Through the solid walls there may be mass flow-rates w_k of species k (k= 1, ..., N_S) with associated axial velocity u_k and absolute enthalpy h_k. The solid walls themselves will in general exert an axial-component force F_{wall} and may have a heat-transfer $\dot{Q}_{wall}$ into the CV. Within the CV itself there could be a force F_{CV} due to obstacles that may be present inside the CV. Energy $\dot{H}_{CV}$ may also be produced (**not** including energy released during chemical reactions). Finally there may be production of species k due to chemical reactions, represented by the mass production-rate per unit volume $\dot{\omega}_k$ within the CV volume ΔV.

Therefore the source vector $\vec{W}$ in equation 1 will look like

$$\vec{W} = \begin{bmatrix} \sum_{k=1}^{N_s} w_k \\ \sum_{k=1}^{N_s} w_k u_k + F_{wall} + F_{CV} \\ \sum_{k=1}^{N_s} w_k h_k + \dot{Q}_{wall} + \dot{H}_{CV} \\ w_k + \dot{\omega}_k \Delta V \end{bmatrix} \quad (9)$$

In the context of a single CV, the flow-rates w_K and associated properties may be assumed as given. The remaining terms will in general be functions of the main variables $\vec{q}$. A full account of their calculation can be found in Rodriguez (1997). Only a brief description for the chemistry source-term $\dot{\omega}_K$ will be presented here.

The present paper deals with hydrocarbon (HC) fuels reacting with air to produce the heat-release in a combustion chamber. The reaction mechanism involved will be approximated by a global, single-step irreversible reaction. For a generic hydrocarbon C_xH_y the reaction equation on a molar basis will be

$$C_xH_y + (x + y/4)(O_2 + 3.76N_2) \Rightarrow x CO_2 + y/2\ H_2O + 3.76(x + y/4)N_2 \quad (10)$$

Note that the above assumes stoichiometric reaction, i.e., no fuel or molecular oxygen among the products. For the reaction rate of equation 10 Westbrook and Dryer (1981) propose

$$q = A \exp\left(-\frac{E_a/R_u}{T}\right)\left[C_xH_y\right]^m\left[O_2\right]^n \quad (11)$$

where the authors tabulated values for A, E_a/R_u, m and n for several fuels in order to provide the best possible agreement with experimental and predicted flame-speeds and flammability limits.

The present model is assumed to consist of three species (N_s = 3): fuel, air and products of combustion. Consequently two species equations are required, and those for fuel and air are chosen. It can be shown that the **mass** production rates of fuel and air are given by

$$\dot{\omega}_{fuel} = -\dot{\omega}\ ; \qquad \dot{\omega}_{air} = -\nu\,\dot{\omega} \quad (12a)$$

where

$$\dot{\omega} = MW_{fuel}\, q \quad (12b)$$

with q given by equation 11, and where

$$\nu = 4.76(x + y/4)\frac{MW_{air}}{MW_{fuel}} \quad (13)$$

is the stoichiometric air/fuel mass ratio, which gives rise to the equivalence ratio:

$$\phi = \frac{f/a}{1/\nu} \quad (14)$$

where f/a is the actual or local fuel/air mass ratio. In the above expressions, MW represents the molecular weights.

2.3. Overall Solution for a Simply-Connected Domain

This section summarizes the overall solution procedure for a simply-connected domain discretized as shown in Figure 3. Again, the details can be found in Rodriguez (1997).

For an assumedly given vector $\vec{q}$ inside the CV, it is necessary to evaluate the fluxes $\vec{F}$ at the faces. This is done in two successive steps: first, the main variables within the CV are extrapolated to the faces, and then the fluxes are evaluated from these. The extrapolation is done by means of MUSCL schemes (Hirsch, 1990). Roe's method for reacting flows (Grossman and Cinnella, 1990) is used for the fluxes.

To evaluate the fluxes at the inlet and exit faces of the domain shown in Figure 3, boundary conditions have to be applied. For subsonic flows, total conditions $(p_t)_{inlet}$ and $(T_t)_{inlet}$ and static pressure p_{exit} are imposed at inlet and exit faces, respectively. These conditions are in general user-given functions of time. The remaining variables at the boundaries are calculated by extrapolation from the interior domain.

Once the fluxes are known as functions of $\vec{q}$ and boundary conditions, the system of equations 1 ends up being a parabolic ordinary differential equation in time. Starting with a known solution at time t^n the system can be marched in time to obtain the solution at $t^{n+1} = t^n + \Delta t$. The integration in time can be performed by either semi-implicit Runge-Kutta or fully-implicit schemes. Calculations are initialized at time t = 0 by means of a steady-state calculation (Rodriguez and O'Brien, 1998).

2.4. Multiply-Connected Domains

Figure 4 and 5 show the discretization of generic straight- and reverse-flow designs, typical of gas-turbine combustors. The main issues associated with these layouts, from the point of view of a one-dimensional theory, are:

- division of main flow into primary and annular paths,
- interaction between flow-paths through the presence of dilution holes.

As before, only the outline of the method will be presented here, with the details to be found in the previously-mentioned reference.

2.4.1. Flow division

Figure 6 shows the details of a straight-flow division interface. In order to estimate the three separate fluxes Fu, Fc, F_l a single average flux is calculated first, using area-averages of the MUSCL-extrapolated variables. The flux is then redistributed among the flow-paths based, among other things, on the ratio:

$$\beta_{u,l} = \frac{(p_t)_c}{(p_t)_{u,l}} \qquad (15)$$

This ratio is estimated based on available data for a given combustor, or experience with similar combustors.

For a reverse-flow combustor (Figure 7), the flow-division CV is solved by assuming quasi two-dimensional conditions.

2.4.2. Dilution

Figure 8 shows two superimposed CVs connected through a dilution hole. It is assumed that flow will go from the higher-pressure CV ("duct" CV) to the lower-pressure one ("primary" CV). The dilution flow-rate is estimated as

$$w_{dil} = C_D A_h \sqrt{\frac{2}{\rho_d}\left((p_t)_d - p\right)} \qquad (16)$$

where C_D is the discharge coefficient, and the meaning of the remaining variables is given in the figure.

This is essentially a mass transfer between CVs, with associated momentum and energy transfers. These transfers appear as the terms w_k, u_k, h_k in equation 9. They will be added with plus sign in the primary CV, and minus sign in the duct CV.

3. RESULTS

3.1. Steady-State Calculations

Figure 9 presents an early Rolls-Royce design for a straight-flow design, together with the discretization used for the calculations.

To obtain realistic results, and due to the lack of reliable and universal correlations for viscous pressure-losses (**excluding** dilution, heat-release and sudden expansions), additional data has to be provided to the model. For the present calculations discrete data obtained from a Rolls-Royce proprietary code ("RR code") was used (Weeks, 1997).

Figure 10 shows the RR-code calculations and those of the present method, the latter without friction losses (i.e., in "inviscid" mode). Without additional data, the losses before the dome or in the lower-annular path can not be captured. It should be noted that the RR calculations were aided by empirical information (Weeks, 1997).

The pressure-loss deviations (mainly between flow-division and start of dilution) were fed back into the model by means of the procedure described in Rodriguez (1997). The resulting actual pressure appears in Figure 11. The additional information allows the method to reach the level of pressure predicted by the RR-code. It also enables for the total mass flow-rate and the different flow-splits to be adequately predicted (Figure 12). On the other hand, total temperature appears overpredicted in the reaction region (Figure 13). The RR code uses a proprietary efficiency correlation which may account for at least some of the difference (Weeks, 1997).

3.2. Unsteady Blowout Prediction

A constant-area cylindrical tube was used to demonstrate blowout (Figure 15). For these calculations the inlet total pressure and temperature were held constant at the values shown in the figure. The fuel (C_3H_8) flow-rate and the exit static pressure were varied until the desired inlet flow-rate and overall equivalence ratio were achieved. Calculations were initialized with the infinite-rate steady-state solution corresponding to the desired operating condition. Although in all cases steady-state conditions were achieved, for blowout the final solution is radically different from the initial; therefore the present case was considered "unsteady".

Figure 15 shows how the blow-out limits, in the form of maximum and minimum values of equivalence-ratio ϕ change with inlet flow-rate. It is apparent that the "loop"

does not close at $\phi = 1$, as it commonly occurs in the literature. Several explanations may be attempted. As the limit is approached, calculations become "unstable", i.e., small changes in parameters, initial conditions, etc., may push results one way or the other. This is particularly true for the small inlet Mach numbers encountered here (of the order of 0.01). Furthermore the curves in Figure 15 consist of points where there is still a flame inside the duct and therefore do not represent actual blow-out. Finally most stability curves in the literature correspond to single "well-stirred reactors", which assume perfect mixing. The current approach is more akin to a succession of elemental "plug-flow reactors" where there is no mixing at all.

3.3. Unsteady Perturbation in Operating and Initial Conditions

A generic reverse-flow combustor, like the one shown in Figure 16, was subjected to perturbations in boundary and operating conditions. Specifically, starting from steady-state conditions corresponding to the conditions shown in the figure, oscillations were introduced separately to the fuel flow-rate and the inlet total pressure in order to determine the ability of the model to respond to controlled dynamic events.

Figure 17 shows the oscillations imposed on the fuel flow-rate: 50% above and below the steady-state flow-rate, at a frequency of 100 Hz. Figures 18 and 19 register the effects of these oscillations in the mass flow-rates and temperatures in the combustor respectively. As the fuel increases from a lean steady-state condition, so does the heat release and therefore the load on the combustor, reducing the entire flow-rate; the decrease in fuel has obviously opposite effects. There is an upper-limit in the heat-release though, corresponding to stoichiometric conditions; for this reason the maximum amplitude of the temperature appears to reach a ceiling at approximately the maximum adiabatic temperature. The effects of these changes in the combustor and primary-flow inlets are almost simultaneous. This can be attributed to the upper-liner dilution flow-rate which links the combustor inlet to the primary zone ;the magnitude of this dilution is almost as big as the flow-rate coming into the primary.

The oscillations in inlet total pressure and its effects are shown in Fig 20-22. These oscillations are of magnitude 50% above and below the steady-state value and with a frequency of 50 Hz. The main effect of the pressure rise is to increase the flow-rate into the combustor (at constant exit pressure), reducing the overall equivalence ratio and therefore the heat-release and temperature; the opposite occurs during the downward part of the cycle. These effects are felt immediately at the inlet of the combustor, but with some delay (about a quarter cycle) at the primary inlet. Note that in this case there is flow reversal at the combustor inlet. This situation is handled by the model as if the inlet were an "exit": the imposed total pressure becomes static pressure and all the other variables are extrapolated from the interior. The delay or inertia mentioned above may account for the fact that there is still some flow into the primary even when the inlet flow is reversed. This may also explain the asymmetry in the exit temperature.

4. CONCLUSIONS

An unsteady model was developed for complete gas-turbine configurations, based on the fundamental governing equations for flows with non-equilibrium chemistry. The chosen approach was to solve the one-dimensional integral conservation equations for multi-species flows with chemical reactions. All the effects that could not be handled by the usual one-dimensional ideal-flow (Euler) equations (i.e., area-changes, friction) were included in source terms on the right-hand side of the system. A one-step chemistry sub-model has been adopted for the calculation of the species production terms.

The model can provide steady-state and dynamic results. For the first type the model was compared to the results of an industrial code on a production burner. The results from the present method were satisfactory, but showed some of the limitations of any one-dimensional approach in that pressure losses that could not be modeled by simple fluid-dynamic effects had to be provided to the model. This is not considered as serious as it may appear. More sophisticated tools also have to be "calibrated" in order to give adequate agreement with known results. It is expected that once this calibration is obtained for one operating condition it can be held fixed for most other conditions.

For the unsteady part of the validation the main effect of finite-rate chemistry, i.e., blowout due to lean and rich mixtures, was tested. Results show that the model can predict blow-out outside certain limits which are functions of operating conditions. The main effects of the blow-out phenomenon appear to be physically captured.

Finally, perturbations were introduced in boundary and operating conditions for the previously-mentioned reverse burner. The response of the model to these perturbations seems to be fundamentally correct.

References

Crocker, D.S., and Smith, C.E. (1993) "Numerical Investigation of Enhanced Dilution Zone Mixing in a Reverse Flow Gas Turbine Combustor", ASME Paper 93-GT-129.

Danis, A.M., Burrus, D.L. and Mongia, H.C. (1996) "Anchored CCD for Gas Turbine Combustors Design and Data Correlation", ASME Paper 96-GT-143.

Grossman, B. and Cinnella, P. (1990) "Flux-Split Algorithms for Flows with Non-equilibrium Chemistry and Vibrational Relaxation", *Journal of Computational Physics*, 88, 131-168.

Hirsch, C. (1990) *Numerical Computations of Internal and External Flows*, John Wiley and Sons.

Lawson, R.J. (1993) "Computational Modeling of an Aircraft Engine Combustor to Achieve Target Exit Temperature Profiles", ASME Paper 93-GT-164.

McGuirk, J.J. and Spencer, A. (1995) "Computational Methods for Modeling Port Flows in Gas-Turbine Combustors", ASME Paper 95-GT-414.

Rodriguez, C.G. (1997) "One-Dimensional, Finite-Rate Model for Gas-Turbine Combustors", Ph.D. Dissertation, Virginia Polytechnic Institute and State University, Blacksburg, Virginia (http://scolar.lib.vt.edu/theses/materials/public/etd-7197-151428/etd-title.html).

Rodriguez, C.G. and O'Brien. W.F. (1997) "One-Dimensional, Steady Model for Straight- and Reverse-Flow Gas-Turbine Combustors", AIAA Paper 97-0289.

Rodriguez, C.G. and O'Brien. W.F. (1998) "Validation of a One-Dimensional, Steady, Infinite-Rate Model for Gas-Turbine Combustors", AIAA Paper 98-1068.

Samuel, B.P. (1961) "A Jet Engine Combustor Design Analysis Suitable for Electronic Computers", AMSE Paper 61-WA-305.

Stuttaford, P.J. and Rubini, P.A. (1996) "Preliminary Gas Turbine Combustor Design Using a Network Approach", ASME Paper 96-GT-135.

Weeks, S.A. (1997) Private Communication, Rolls-Royce plc, Filton Bristol, UK.

Westbrook, C. and Dryer, F. (1981) "Simplified Reaction Mechanisms for the Oxidation of Hydrocarbon Fuels in Flames", *Combustion Science and Technology*, 27, 31-43.

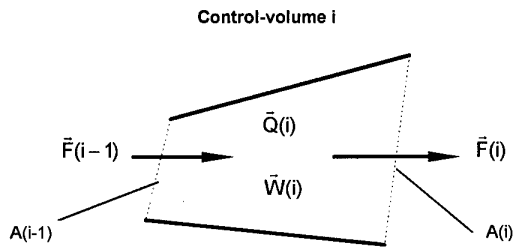

Figure 1: Elements of a generic CV i

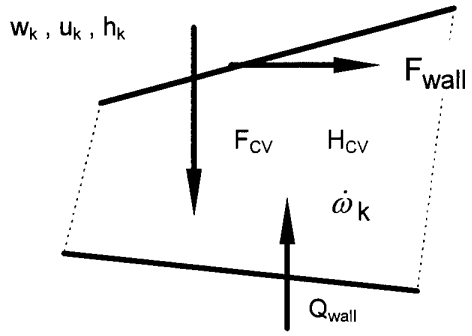

Figure 2: Sources for CV i

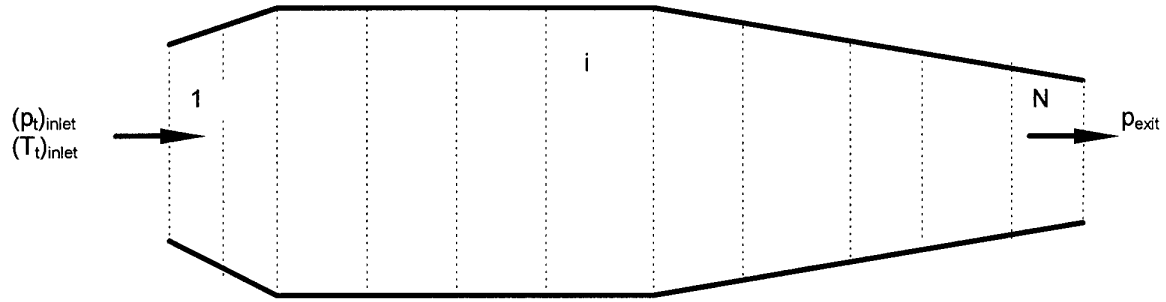

Figure 3: Discretization of a simply-connected domain

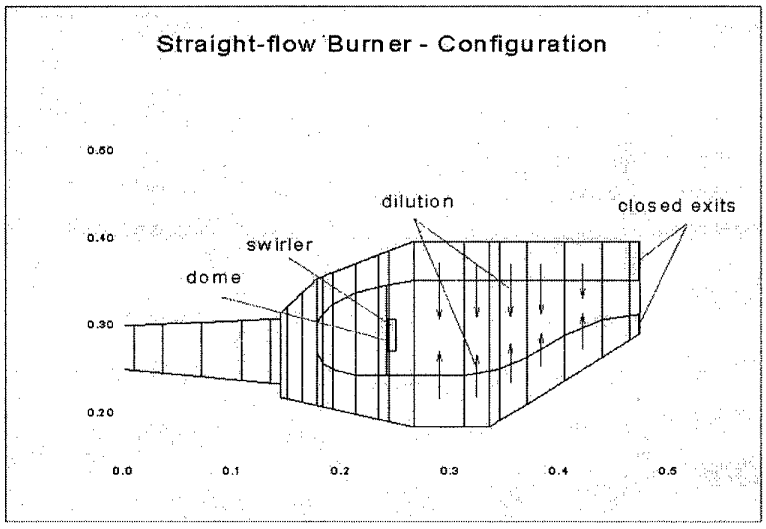

Figure 4: Discretization of a straight-flow annular combustor

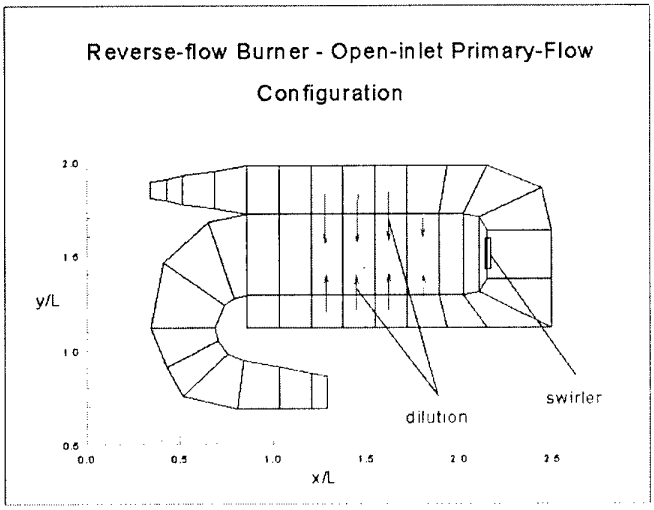

Figure 5: Discretization of a reverse-flow combustor

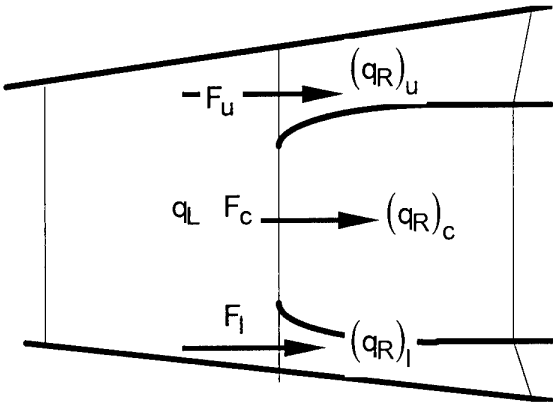

Figure 6: Straight-flow flow-division

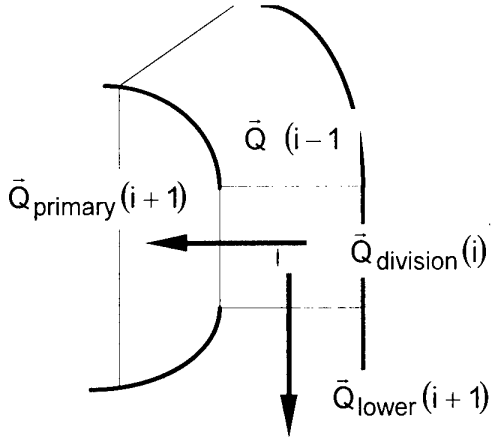

Figure 7: Reverse-flow flow-division

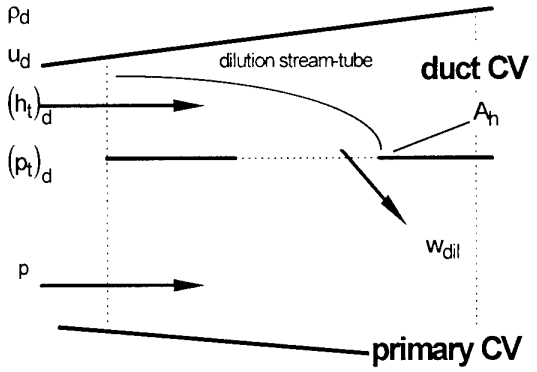

Figure 8: Dilution characteristics

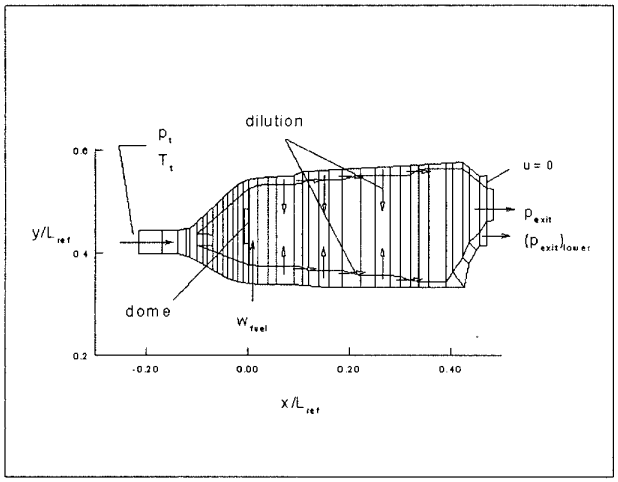

Figure 9: Straight-flow burner - Configuration and discretization

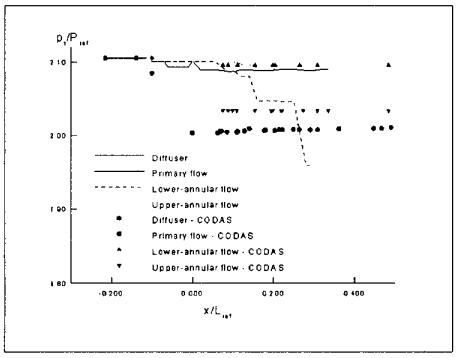

Figure 10: Total pressure - "Inviscid"

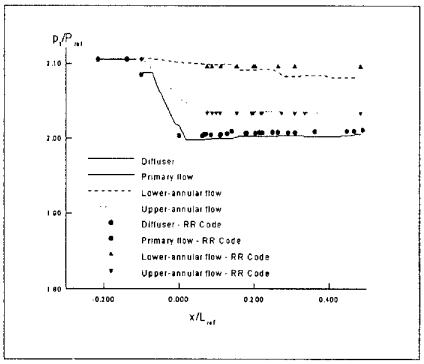

Figure 11: Total pressure - Actual

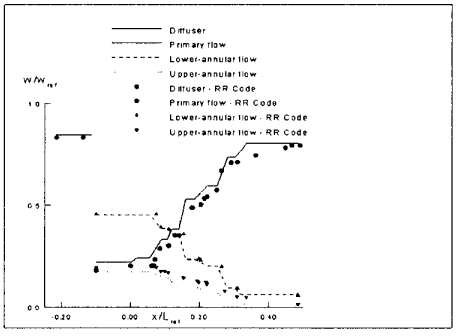

Figure 12: Mass flow-rates

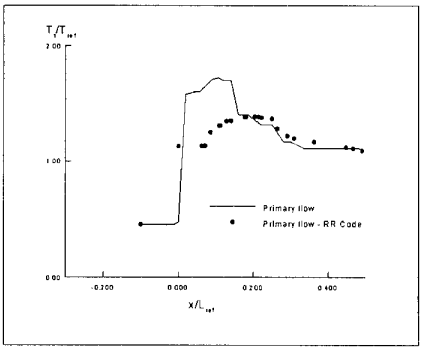

Figure 13: Total temperature

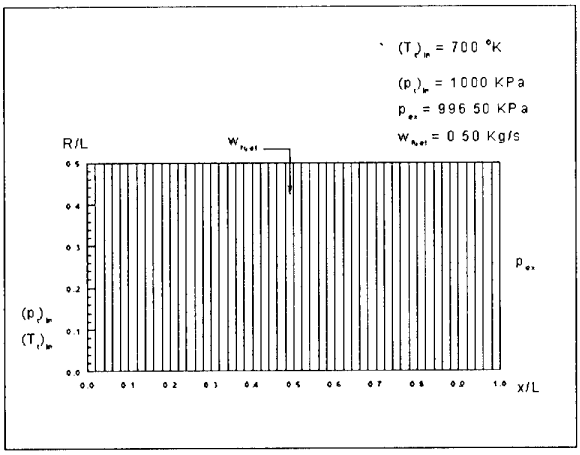

Figure 14: Constant-area duct

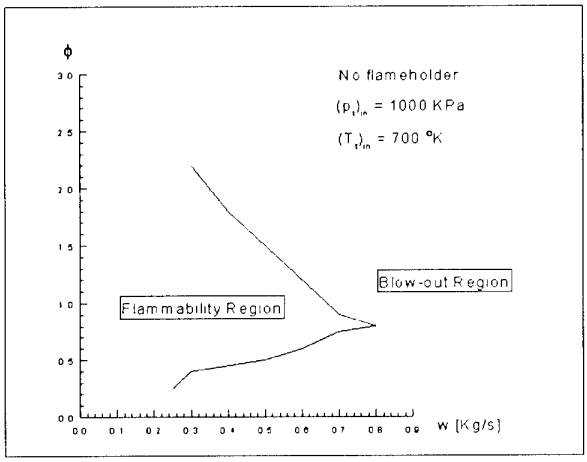

Figure 15: Constant-area duct - Blowout limits

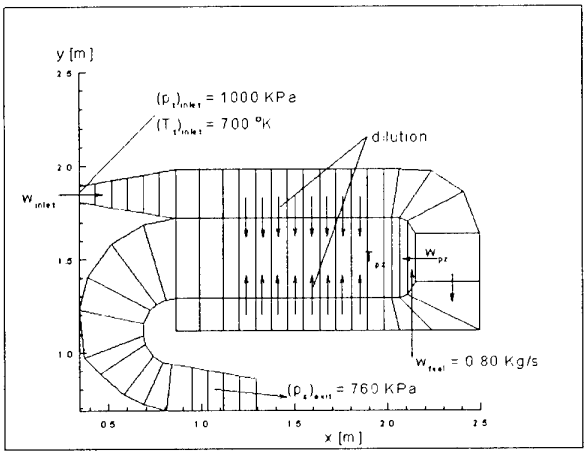

Figure 16: Reverse-flow burner configuration

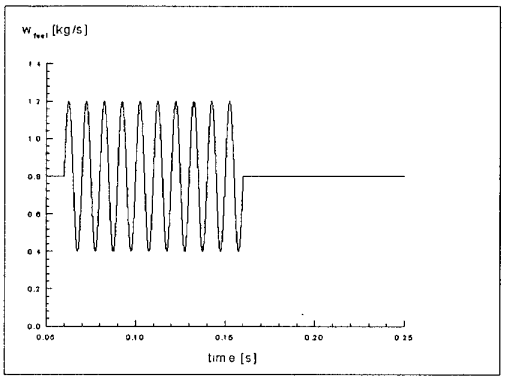

Figure 17: Oscillations in fuel flow-rate

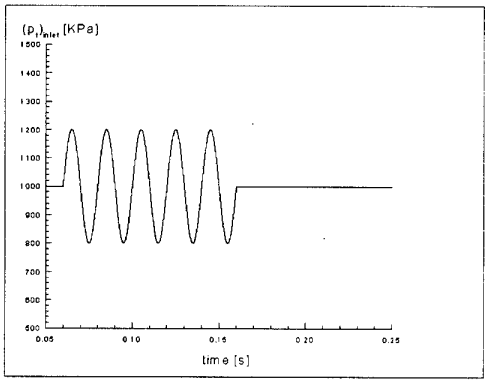

Figure 20: Oscillations in inlet p_t

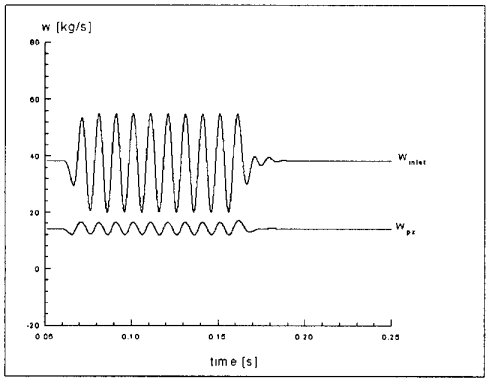

Figure 18: Effect in mass flow-rates

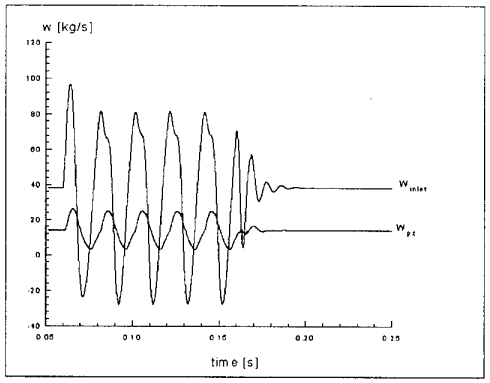

Figure 21: Effect in mass flow-rates

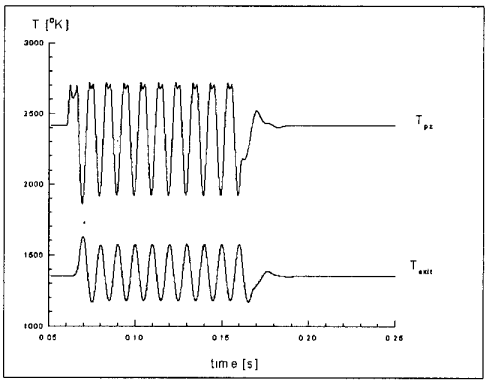

Figure 19: Effects in temperatures

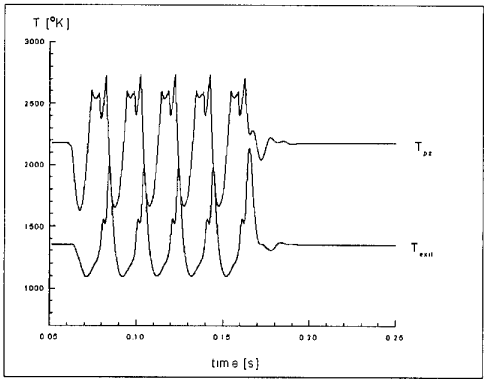

Figure 22: Effects in temperatures

Design Principles for the Quench Zone of Rich-Quench-Lean Combustors

C. Hassa, C.E. Migueis*, P. Voigt
German Aerospace Center,
DLR
P.P. Box 90 60 58
Institute for Propulsion Technology,
D-51170 Köln,
Germany

1. Summary

Isothermal experiments on the mixing of jet rows in crossflow with particular attention to the quench zone mixing of RQL combustors have been carried out. Comparing mixing with combusting and isothermal mixing, it could be demonstrated, that with the combination of jet air concentration measurements and numerical calculations of the flow, medium pressure combustion tests with 3-D probe measurements can be bypassed for the jet row optimization.

The study with homogenuous crossflow for RQL combustors without cooling air in the primary zone showed optimum mixing with two staggered rows with close axial spacing.

The light sheet technique could be demonstrated to give good quantitative results with higher spatial resolution than any other competing technique if applied with the appropriate care. Its application clearly revealed the influence of swirling, recirculating primary zone flow on the jet mixing.

2. Introduction

2.1 Motivation

The aerothermal design and development of combustors for aircraft gas turbine engines poses more hurdles to the application of numerical simulation than other components, because of the dominant influence of turbulence on combustor aerodynamics and the coupling of the highly nonlinear processes in combustion to the flow. Hence in practice, a combined approach of CFD and experimental tests with ascending complexity is always used. This contribution describes work, that has been performed with the goal of shortcutting expensive medium pressure sector tests and 3-D gas analysis with a combination of atmospheric, isothermal tests and CFD. The accuracy of the concentration measurement with Laser light sheets, an efficient measuring technique for isothermal testing, has been improved and its application is demonstrated with two examples.

The work was performed as a part of the general effort of laying groundwork for the practical design of low emission aeroengine combustors, and is attached to the work on Rich Quench Lean (RQL) combustion. That concept has been successfully applied in other applications for nitrogen oxide reduction and is studied in research and technology programmes in the US and Europe for supersonic and subsonic civil transport. The basic idea is to burn the fuel under rich conditions in the primary zone, where nitrogen oxide formation is inhibited by the lack of O atoms, and then quickly mix in the remaining combustion air for lean combustion in the secondary zone, proceeding at temperatures, that keep thermal NOx production at low levels.

*Present adress: INPE-LCP 12630 Cachoeira Paulista, Brasil

One fundamental problem of the method is the transition from the rich to the lean zone, which necessarily implies stoichiometric combustion, giving the highest temperatures and thus producing the highest amount of thermal NO_x. Therefore, the mixing of the secondary air has to be so quick as to beat the thermal NOx formation rate even at the high combustor inlet temperatures and pressures of modern gas turbines. Although there are many results available for the jet mixing from liner holes, the RQL specific design constraints necessitate additional investigations. Since, given by chemical considerations, the amount of air to be mixed is more than the incoming flow, designs with more than one row of holes are under consideration, such that there is not only reciprocating action in the jet mixing from neighbouring holes but also between the rows of holes.

In the remainder of the paper, the isothermal mixing experiment, the measuring technique and the used CFD tool will be described. The applicability of the isothermal experiment is checked with a comparison of flowfield calculations with and without combustion and with an experimental comparison of the isothermal quench zone mixing with the evolution of mixture fraction in combustion. Results of the investigations with uniform primary flow for combustors without primary zone film cooling are presented and finally the application of the light sheet technique to a practical RQL combustor model incorporating a swirled primary zone is demonstrated.

2.2 Jet mixing in combustors

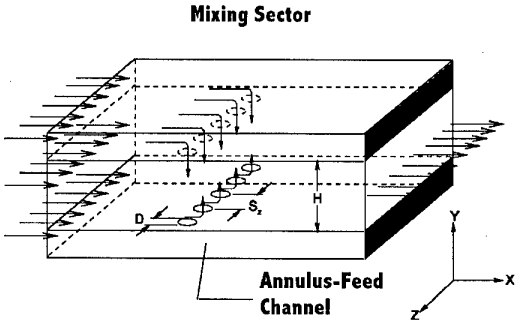

Fig. 2.1: Experimental model of RQL mixing section with geometrical parameters

Since the early times of aviation gasturbines, jets in crossflow have been the subject of investigation, due to their widespread use in combustion chamber design, e.g. to adjust the zonal air/fuel ratio or to aerodynamically stabilize combustion. At the begining most of the studies were limited to the calculation of discharge coefficients and jet penetration. Modern engines

Paper presented at the RTO AVT Symposium on "Design Principles and Methods for Aircraft Gas Turbine Engines", held in Toulouse, France, 11-15 May 1998, and published in RTO MP-8.

with higher temperature rise combustors have created the need for better temperature patterns at the turbine inlet. For that reason, significant research on dilution jet design has been undertaken, considering the large number of aerodynamic and geometric parameters that define the process, see fig. 2.1.

A comprehensive study on this subject was conducted at NASA Lewis by *Holdeman, 1993*, in wich a useful empirical relation was worked out to achieve the desired temperature patterns. Unfortunately, this empirical relation is not directly applicable to the design of RQL combustors due to the different operating conditions. In conventional aeroengine combustors, the mass flow ratio between injected fresh air and primary zone is typically about 0.30, but for RQL combustors it is between 1.5 and 3. The air staging is governed by combustion chemistry, showing optimum NO_x reduction at primary zone equivalence ratios of 1.4 to 1.7 and secondary zone temperatures well below 2000 K, necessitating equivalence ratios of at least 0.5. For jet to mainstream ratios above 2, previous studies showed, that it is necessary to use at least two rows of jets on the in- and outboard combustor wall. In this case the injected jets may create a strong interaction between them, which can produce a nonnegligible effect on the mixing process. Another difference between conventional and RQL combustors is a rather high Mach number in the primary zone annulus, in the case where film cooling is not used and high heat exchange rates are necessary on the outside of the liner. Then a plenum chamber condition for the flow to the mixing holes, as usually assumed, doesn't exist anymore and the flow dynamics of the annulus play an important role for the injection process, *Migueis, 1996.*

2.3 RQL mixing design study

In RQL combustors the transition from rich to lean combustion must be done very quickly to avoid long residence times under high temperatures in order to produce less thermal NO_x. For the jet mixing process it means that, instead of the pattern factor as its ultimate result, the mixing speed is of major importance. In this contribution, the mixing process is investigated with an array of two rows of opposite jets, in which the geometrical parameters were varied to evaluate the effects of jet interaction on the mixing. As one goal, an efficient configuration for a specific RQL chamber had to be generated. To that end, we used a set of RQL design data communicated by the MTU - Motoren und Turbinen Union, Munich, Germany as a part of a joint effort to investigate the emissions reduction potential of RQL combustion in aeroengines, *Zarzalis, 1996.* The maximum potential can only be reached without filmcooling the primary zone, because the cooling films create a large stoichiometric interface. Hence the case of a fixed jet-to-mainstream momentum ratio of 180 for the first row was considered, corresponding for the jets to the full pressure differential of 3% across the liner. For this investigation, 16 different arrays of jets, or mixer configurations were chosen following two criteria for good RQL-mixing:

- no backward flow of injected air into the primary zone, because this causes stoiciometric zones;
- quickest possible transition from rich to lean combustion.

From previous investigations, *Doerr, 1995,* it became apparent, that with one row of holes, the first condition can only be met with difficulty, hence only configurations with two rows were investigated.

To design the mixer configurations, the empirical relations by *Gueroui, 1982* for the calculation of the hole discharge coefficients were used. These empirical correlations are not valid in the parameter range used here, but for the lack of anything better, were used as a first order method.

The mixing study was done experimentally and numerically, considering only isothermal flows. To assure its validity, effects of heat release on the mixing were analysed numerically and by exemplary comparison of gas analysis from one combustor with light sheet results of the same combustor at isothermal operation. In the same way swirling flow upstream of the mixing sector was not considered systematically, due to the enormous variety of possible boundary conditions, but again this was analysed numerically and with the application of the light sheet technique to a model combustor.

3. Description of Methods

3.1 Similarity between mixing with combustion and isothermal experiment

As explained in section 2.3, the mixing study was without combustion using two inert cold flows. In doing so, full similarity between real and inert isothermal mixing isn't achievable, nevertheless some important characteristics can be simulated. Dimensional analysis, *Doerr, 1995*, showed that the most important parameters, besides the nondimensional geometric parameters **S/D**, **H/D**, and **X/H** (see fig. 2.1) defining the jet array, are the Strouhal number **Sr**, the jet to crossflow momentum ration **J**, the crossflow Reynolds number $\mathbf{Re_{\infty}}$ and the ratios of density and kinematic viscosity of the two flows. *Kamotani & Greber, 1972* and many other workers prooved, that the density ratio plays a minor role on the mixing in such flows and it seems to be reasonable that the molecular viscosity ratio has no dominant effect in such strongly turbulent flows. *Fric & Roshko, 1989*, studying the jet wake formed behind a single jet in crossflow, concluded that a clear relationship between the Strouhal number and vortex shedding frequency of the jet is quickly lost after the injection port. The jet to crossflow momentum ratio is considered to be the dominant parameter in this kind of problem, so that in order to perform a good simulation, the same **J** value as encountered in the real situation must be retained, which ensures similarity of the jet path. This is the reason, why the **J** value given by the MTU design wasn't changed. Other geometric characteristics from that design, like the height of main channel and the annulus feed were also preserved.

Following the work of *Gueroui, 1982* on injection hole discharge coefficients we could verify that for the simulation of the injection through liner holes, the local pressure loss must have the same value as in the real case. This assures that the ratio between static to dynamic pressure is the same and consequently the initial jet angle, which then means that jet path will be similar.

The isothermal simulation of the RQL mixing sector causes a change in the annulus-feed to crossflow density ratio. To have the same axial momentum, the flow velocity **V** must be corrected as follows:

$$V_{an,sim} = V_{an,real} * \sqrt{T_{an,sim} / T_{an,real}} \quad (1)$$

$$V_{pz,sim} = V_{pz,real} * \sqrt{T_{pz,sim} / T_{pz,real}} \quad (2)$$

where the subscripts **an** and **pz** are related to the conditions of the annulus-feed flow and the primary zone flow respectively, while **sim** and **real** means the condition of the simulation or of the real situation. Unfortunately

$$\left[T_{an}/T_{pz}\right]_{sim} \neq \left[T_{an}/T_{pz}\right]_{real} . \quad (3)$$

This results in a proportional distortion of the massflow ratio

$$\left[\dot{m}_{an}/\dot{m}_{cr}\right]_{sim} \neq \left[\dot{m}_{an}/\dot{m}_{cr}\right]_{real} . \quad (4)$$

The effect of this distortion on the validity of our investigation is not so obvious and was checked by means of a CFD simulation, as shown in section 4.1. This also causes the Reynolds number not to be simulated, which constitutes a problem of atmospheric testing of gasturbine combustors where Reynolds number independence cannot always be assumed. But since the Reynolds number of the isothermal experiment is similar to what is encountered in medium pressure combustion tests with air preheat, the present study complies with common engineering practice.

3.2 Quality of a mixture

To give a quantitative idea about the mixture homogenity the parameter called "Spatial Unmixedness" was used, which was originally defined by *Dancwerts, 1952* and later re-defined by *Liscinsky et al., 1993,* being the ratio between the standard deviation and the mean value of the spatial distribution of a passive scalar like temperature:

$$U = \sigma / \overline{T} \quad (5)$$

For this purpose the jet flow was at ambient temperature and the crossflow was heated by 50° C. The temperature field was normalized as follows:

$$\theta_{ijk} = \left|T_{ijk} - T_{an}\right| / \left|T_{pz} - T_{an}\right| \quad (6)$$

so that inside the jet $\theta_{ijk} = 0$ and upstream in the primary zone flow $\theta_{ijk} = 1$. T_{ijk} is a local temperature of the flow field, T_{an} and T_{pz} are the constant temperature values of the jet and the primary zone flows, respectively. In our work, due to the strong three dimensionality of the flow near the jet injection, the standard deviation of the spatial distribution of the temperature was calculated using the local massflow as a weighting factor:

$$\sigma_{mw,i} = \sqrt{\frac{\sum_{j=1}^{m}\sum_{k=1}^{n} \dot{m}_{ijk} * \left[\theta_{ijk} - \theta_{avg}\right]^2}{1/n \, 1/m \sum_{j=1}^{m}\sum_{k=1}^{n} \dot{m}_{ijk}}} \quad (7)$$

where $\dot{m}_{ijk}$ is the local massflow and θ_{avg} is the final temperature of the mixture, which is given by

$$\theta_{avg} = \frac{\dot{m}_{jets}}{\dot{m}_{pz} + \dot{m}_{jets}} \quad (8)$$

where $\dot{m}_{jets}$ is the sum of all jet massflows and $\dot{m}_{pz}$ the primary zone flow. The massflow weighted unmixedness $\hat{U}_{mw}(x)$ is then calculated by

$$\hat{U}_{mw} = \frac{\sigma_{mw,i}}{\theta_{avg}} \quad (9)$$

and is a function of the axial position inside the RQL-combustor. It can be shown that, using the dimensionless form of the temperature defined in (6), the maximun value of the standard deviation is still a function of the injected and primary zone massflows. This means that it is not possible to compare different mixers having differents massflow ratios. To avoid this problem we normalized $\hat{U}_{mw}$ by its maximum value $\sigma_{mw,i,max}$:

$$U_{mw} = \frac{\hat{U}_{mw}}{(\sigma_{mw,i})_{max}} \quad (10)$$

where $(\sigma_{mw,i})_{max} = \sqrt{\frac{\dot{m}_{jets}}{\dot{m}_{pz}}}$. (11)

To gain a qualitative understanding of the turbulent mixing, we defined an integral value of the specific kinetic energy of turbulence **k** in each axial cross section, which was only available from the validated numerical results. Its mathematical definition is given by

$$\overline{k}_i = \frac{\sum_j \sum_k k_{ijk} * A_{ij}}{\sum_j \sum_k A_{ij}} \quad (12)$$

where k_{ijk} is the local specific kinetic energy of turbulence, *Hinze, 1975*, and A_{ij} is the local cross section of each grid cell of the numerical simulation. We also defined another auxiliary parameter, which indicates in each cross section of the mixing sector the percentage of massflow having an equivalence ratio in the range of $0.66 < \phi < 1.11$. In this nearstoichiometric range, most of the thermal NO_x is produced. The calculation of this parameter is only possible because we are dealing with a non-reacting flow, so that there exists a relationship between equivalence ratio and the temperature field given by (13).

$$\theta = \left[1 + \frac{FA_{sto}}{\phi_{pz}}\right] \Big/ \left[1 + \frac{FA_{sto}}{\phi_{ijk}}\right] \quad (13)$$

where FA_{sto} is the stochiometric kerosine-air ratio, ϕ_{pz} the mean equivalence ratio in the primary zone and ϕ_{ijk} the local value. The percentage of massflow under near stoichiometric condition is then calculated as follows:

$$M_{ns} = \frac{\sum_j \sum_k \dot{m}_{ns,ijk}}{\sum_j \sum_k \dot{m}_{ijk}} \quad (14)$$

$\dot{m}_{ns,ijk} = \dot{m}_{ijk}$ if at the same point *ijk* $0.66 < \phi_{ijk} < 1.11$

otherwise $\dot{m}_{ns,ijk} = 0$.

3.3 Experimental Setup

The experimental setup is shown in Fig. 3.1, in which both side walls were made up with 6 mm glass, to assure optical access for non-intrusive measurements to most parts of the mixing sector. The design provides also easy changeability of the hole plates, so that a lot of different jet arrays could be investigated without any work. The mixing sector is 180 mm wide and 70 mm high, the secondary channel height is only 15 mm, giving the high velocities needed for convective primary zone cooling. Both primary zone and secondary massflow where controlled by two independent critical nozzles upstream of the measuring section. At the end of the secondary channel, a valve and a flowmeter were positioned to adjust the desired bleed flow through the secondary channel. The liner pressure loss was monitored on both sides with pressure gauges. The primary zone flow was heated up to 50° C by a heater upstream of the primary zone.

3.4 Measurement techniques

In order to quantify mixing quality, three different variables were measured: flow velocity, temperature and mixing air concentration. The local flow velocity distribution was measured using LDA and is described in *Migueis, 1996.*

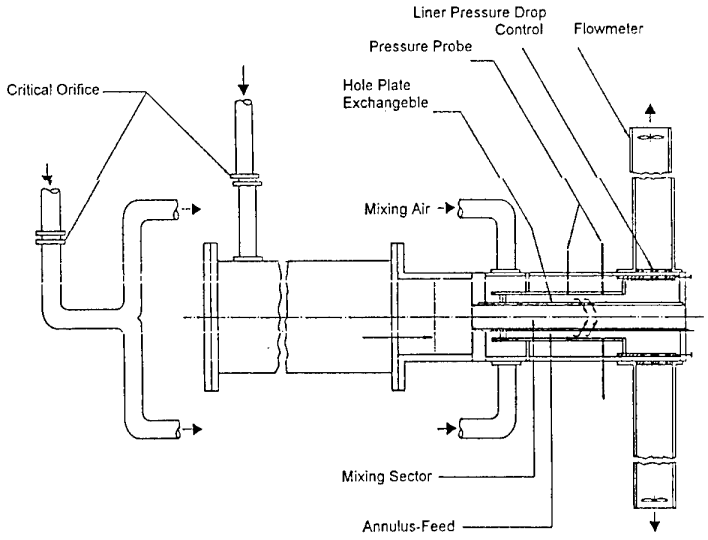

Fig.3.1: Scheme of experimental rig

Velocity measurements were only done for a subset of measuring points. They were mainly used to validate the numerical flowfield calculations. The temperature measurements were done using a thermistor from Fenwal Electronics, type GA51SM2, having 0.4 mm diameter and a time constant in flowing air of 1.1 sec. The attached electronic bridge was developed to give a resolution of 0.1° C and together with probe and cable were calibrated between 0° C and 100° C. For the measurements an IBM-PC based 12 bit data acquisition system was used, having a resolution of 0.048° C. The integration time in each measurement point was 10 secs.

By comparison of thermistor and light sheet results, a systematic error of the temperature measurements in the flow region near the jet injection point was identified. This error occured due to heat conduction through the temperature probe. This situation was simulated in laboratory, and we could estimate an deviation of about 7.5% from the correct value. In the flow region downstream of the injection, where temperature measurements were used to quantify mixing quality, such errors didn't occur. Everywhere else, the temperature error was estimated to be below 0.3 °C.

3.5 Computational fluid dynamic calculations

In the RQL research program, we used a DLR code named MUG3D, *Eickhoff 1985*, which solves the three-dimensional steady-state Navier-Stokes equations, with a standard **k-ε** model. In the energy transport equation, effects of flow turbulence are also simulated by a Boussinesq approximation. The influence of heat release is simulated by a combined Arrhenius/Eddy-Break-Up combustion model. The diffusive part of the transport equations was discretized by a central differencing scheme, which gives very accurate results. The discretization of the convective part is a little bit more demanding, because in some applications it causes numerical instabilities. For the discretization of convective terms simple schemes like Hybrid or Upwind, *Anderson et al., 1984*, are numerically stable, but can smear the solution by numerical diffusion. Higher order schemes reproduce sharp gradients better, but are prone to numerical instabilities. Therefore the Monotonized Linearized Upwind Scheme from *Noll 1992*, was implemented, which is a modern second order scheme without any numerical instability and false diffusion.

The computational domain was discretized in rectilinear finite volumes, where in each volume a balance of mass, momentum, energy and the other transported variables was reached iteratively using the SIMPLE-algorithm, *Patankar, 1980*. The grid was non-staggered, so that every variable was solved on the same grid, *Rachner, 1992*. MUG3D gives the option to use two or more overlapping grids. This feature was very helpful in the calculations, because it enabled the inclusion of the secondary channel flow.

A typical grid, considering an array of two rows of opposite, staggered jets had about 250.000 gridpoints. Such a job, running on an IBM RISC-6000 Unix Workstation, spend about 73 hours to reach a relative error level of 10^{-3} in the residuals of momentum equations. This jobtime could not be reduced, due to problems in the vectorization. That is the reason, why only a performance of 33 MFlops was attained in a typical run using the highest level of optimization.

The MUG3D code was validated for this application by comparing its results with many temperature, and axial mean and fluctuating velocity measurements. The calculations turned out to be quantitatively good and useful for design phase calculations. The quality of the results were less good only when the injected jets were very close to each other, triggering unsteady jet fluctuations.

3.6 Quantitative Laser Light Sheet QLS

Most of the existing techniques for concentration measurements are based on pointwise measurements, like chemical or thermal probe sampling. It is obvious that probe sampling underlies severe drawbacks in combustion research, since the method is time consuming and the probe influences the mixing process where it is most intense: in the high gradient regions. Optical techniques are promising, since they have the potential to give planar information about the mixing process without disturbing the flow field.

The light sheet method uses scattering of light by small particles marking the flow. The underlying Mie theory is covered in a number of basic works, cf. *Bohren and Huffman, 1983*. The inflow must consist of at least two separate streams, allowing to inject tracer particles to only one of them. Then a stationary particle size distribution and -production rate are required.

The particle concentration inside the mixing zone is proportional to the measured scattering light and hence equivalent to the volume flow ratio thus:

$$I_{sca}(\vec{r}) \propto c(\vec{r}) = \frac{\dot{\boldsymbol{v}}_1(\vec{r})}{\dot{\boldsymbol{v}}_1(\vec{r}) + \dot{\boldsymbol{v}}_2(\vec{r})} \qquad (15)$$

where $\dot{\boldsymbol{v}}_1$ is the mass flow of the seeded component, whereas $\dot{\boldsymbol{v}}_2$ remains unseeded. A typical setup is shown in fig.3.3.

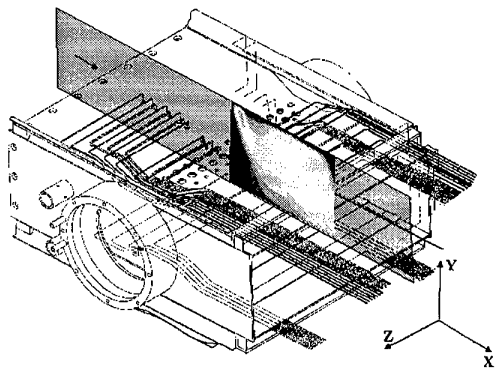

Fig 3.2: Typical setup of a longitudinal light sheet for concentration measurements in a RQL combustion chamber

However, in order to get a sufficient accuracy, most of the system components must be analyzed and optimized, cf. *Voigt,1996.*

The main influencing parameters are:

- Choice of particles
- Background reflections
- Light sheet intensity distribution
- Scattering direction
- Polarization
- Extinction
- Multiple Scattering

Choice of particles

Marker particles in laser velocimetry are usually very small (below 1 μ m) to closely follow the flow. When applying the QLS-method, particles should be larger in order to scatter sufficient light energy. However a particle diameter exists that gives the maximum signal for a given fluid particle volume. It is supposed for computational convenience that all N particles possess the same diameter d_p. The whole fluid volume will than be the sum over all particle volumes:

$$V = N \cdot \frac{\pi}{6} \cdot d_p^3 \qquad (16)$$

In the diameter range of the Mie theory, the scattering cross section is very irregular but approximately proportional to the fourth power of the diameter, whereas in geometrical optics it is proportional to the square of the diameter and the particle volume increases with the third power of d_p. With I_L as the laser intensity and c_{sca} as the scattering cross section, the total scattering power is given by:

$$P = I_L \cdot c_{sca}(d_p) \cdot N \qquad (17)$$

The maximum scattering power from a given fluid volume can now be estimated by differentiating equation (17) with respect to d_p, yielding an optimum diameter of: $d_{opt} = 1.85 \mu m$.

This approximation was made with a Mie computation, using the algorithm given in *Bohren and Huffman, 1983.*

Reflection suppression

Whenever the QLS method is applied in turbo machines, the problem of surface reflections arises. Reflected light is in general several orders of magnitude more intense than the light scattered by particles, hence it spoils the measurement whereever it enters the imaging region. If reflections cannot be avoided, there is a possibility to suppress them. One technique is to cover the reflecting material with a thin sheet of fluorescent paint. To that effect a specific coating consisting of a mix of rhodamine dye 610 in ethanol was created, having strong absorption bands for argon ion lines. The next step is to place the appropriate laser line filter in front of the camera, cutting all wavelengths but the laser line. When the light touches the painted surface, the reflections will be wavelength shifted and thus filtered by the laser line filter.

Another wide spread suppression technique is the use of black or soot painting. In fig. 3.3 it can be seen that the decision if to use fluorescent paint is strongly angular dependant. The study has been carried out with a metal plate, covered with 3 different surfaces. The first was the blank metal, the second a soot painting and the third the fluorescent paint. The laser beam as well as the camera were mounted stationary. While turning the plate, the scattered signal was recorded by the ccd camera. It turned out, that for large angles α, which is the angle between the optical axis of the camera and the direction of the plate surface, soot painting is recommended. As can be seen in fig. 3.3, there exists a break even point at $\alpha = 40°$.

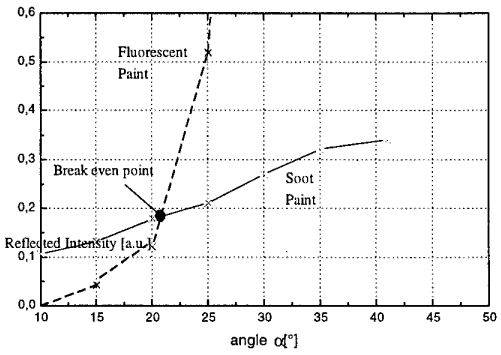

Fig. 3.3: Break even point in suppression efficiency

When turning to smaller angles, the filtering capacity of the fluorescent paint turns out to be nearly 100%, whereas the efficiency of the soot suppression remains unchanged. For light sheet experiments, the reflection angle α is generally very small. Therefore fluorescent paint is recommended.

Scattering direction

Mie scattering is strongly influenced by the scattering direction. One very simple way of overcoming the problem of scattering direction experimentally is the so called *Double Pass Cell.* By reflecting the light sheet back into the measurement volume, effects of direction and extinction are reduced. This technique works best with low seeding levels.

Polarization

Since Mie scattering is dipole scattering, it is partly polarization conserving. Compared to the scattering direction its influence is almost negligible with a maximum influence in the order of 10 %. The effect can be compensated easily by inserting a $\lambda/4$-plate in the beam path, circularly polarizing the light.

Extinction

Whenever light is scattered by particles, the incident light will be attenuated. This effect, called *extinction* comprises absorption and scattering. The loss of intensity along a line

can be formalized by the Lambert-Beer-law in differential form,

$$dI(x) = -\sigma_{sca} \cdot c(x) \cdot I(x)dx \qquad (19)$$

where σ_{sca} is the scattering efficiency and the absorption efficiency is set to zero. c(x) is the local concentration in the direction of the laser beam. I(x) denotes the local laser intensity. Only for the very special case of homogeneous particle distribution the well-known Lambert-Beer law in its integral form holds:

$$I(x) = I_0 \cdot e^{-\sigma_{sca} x} \qquad (20)$$

It is possible to correct for this effect of intensity loss by applying a numerical technique based on shooting. Other methods such as relaxation can also be used but as mentioned by *Press et al.* shooting should be preferred, if the convergence properties are satisfying.

In *Voigt, 1996* a technique to compensate the extinction effect for arbitrary particle distributions is implemented. In the case of light sheet measurements, the boundary conditions are given by the laser intensity on both sides of the probe volume. Shooting means starting from the left boundary and integrating the differential equation until the right boundary is reached. It is necessary to measure the integral extinction along each line in the image. This means that apart from the flow image, there must be a second camera or line array saving the intensity profile.

This knowledge must be correlated with the content of the mixing image. It is important to keep in mind that this technique allows the correction of extinction for arbitrary particle distributions and it is not restricted to QLS-measurements.

The potential of this method is demonstrated with a test case with three gaussian concentration distributions. The integral intensity loss was 50%. In fig. 3.4, a result is shown including a profile through the original image as well as the corrected profile.

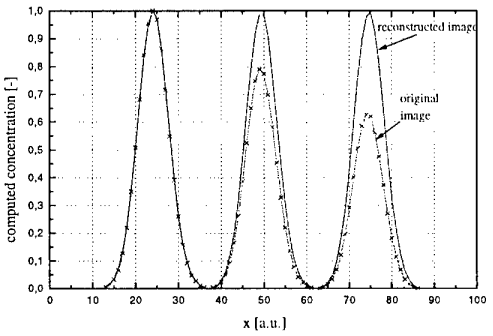

Fig.3.4: Extinction correction of 3 equally spaced gaussian concentration peaks

Multiple Scattering

Multiple scattering is a secondary effect in scattering experiments. It denotes the fact that scattering particles can be light sources for adjacent particles. This effect depends on the particle load. The existence of secondary scattering has been proven in a number of experiments and different aspects have been simulated numerically.Fig. 3.5 shows the virtual thickening of a laser beam.

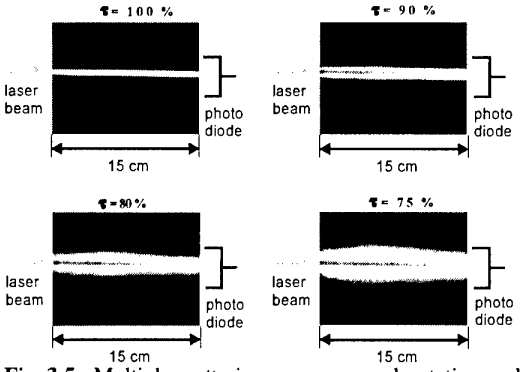

Fig. 3.5: Multiple scattering corona around a stationary laser beam

A stationary laser beam passes through a laboratory combustion chamber with homogeneous seeding. The incident beam enters the plane on the left side and leaves after a total distance of 15 cm. On the outlet side the transmission ratio τ is measured by a photo diode. The chamber is seeded with four different particle loads. In the upper left image no extinction could be measured. The beam was thin. For the following experiments the seeding was intensified successively. On the upper right image the overall extinction was 10 % and a small increase in the beam thickness can be recognized. In the lower column both images show an increase in radial direction. But this expansion is not constant along the beam. In the first quarter of the path the expansion increases, due to the strong secondary scattering in the forward direction. After reaching the maximum diameter, the expansion decreases, caused by the coexisting extinction effect on the centerline.

The correction of multiple scattering is the most challenging part of the post processing, since the effects are fully three dimensional. A number of different approches have been tested already, but none of them with sufficient results yet.

Accuracy of QLS measurements

A detailed discussion of measurement accuracy is beyond the scope of this contribution. A thorough analysis will be reported in *Voigt, 1998*. It is obvious though, that secondary scattering effects are the dominant remaining error source. It could be shown, *Voigt & Schodl, 1997,* that for practical seeding levels, the error due to secondary scattering is limited to the order of 5%. It is important to keep in mind that this value depends on local particle concentration. Consequently, errors caused by secondary scattering are locally different and it is strictly recommended to use the lowest seeding level possible.

4 Results and Discussion

4.1 Isothermal Mixing Study

Fig. 4.1: Geometrical parameters defining an array with two rows.

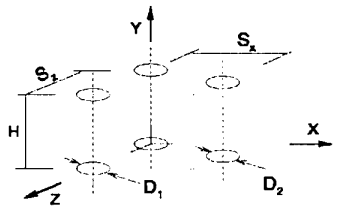

The following characteristica of the jet array were investigated, cf. fig. 4.1:

a) staggered and inline arrangement of the opposed jets;
b) the distance between the holes S_z,
c) the hole diameter, D,
d) the distance between the jet rows, S_x, and
e) the first to second row hole diameter ratio, D_1/D_2.

At the beginning were changes in the value of S_z and D in both *inline* and *staggered* configurations, fig. 4.2, so we could compare the following effects on both:

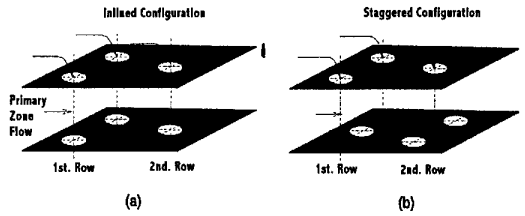

Fig. 4.2: Inlined and staggered mixer configurations

- The variation of $\mathbf{S_z}$ and **D** with constant total hole area;
- The variation of $\mathbf{S_z}$ and **D** with constant $\mathbf{S_z/D}$ ratio;
- The variation of **D** with constant $\mathbf{S_z}$ and
- The variation of $\mathbf{S_z}$ **with** constant **D**.

At this step we considered the ratios S_x/S_z and D_1/D_2 as constant, but later their influence was separately investigated.

For the design of the staggered configurations, values of $\mathbf{S_z/D}$ between 2 and 4 and values of Holdeman's C-parameter, $C = S_Z/H * \sqrt{J}$, *Holdeman, 1991,* were varied between 2.2 and 8.8, such that the dimensionless hole diameter varied in the range 5.5 < H/D < 15.5. Fig. 3.3 resumes all those configurations. The ordinate gives the number of holes in each row, having a direct relationship to the parameter C, because the channel width was constant (= 180 mm). The abscissa shows the relative massflow through all holes (here 100% means the total available air for mixing in the RQL combustor defined in the MTU design data).

8 *staggered* configurations were investigated experimentally and 3 numerically. Altough the parameters were varied widely, the unmixedness changed only about 10%. This insensitivity was probably due to the weak variance of the jet penetration from the first row, resulting from the opposite influence of the parameters **D** and $\mathbf{S_z}$. Considering a certain number of holes per row, augmenting the hole diameter enhances the jet penetration into the crossflow, but automatically reduces the space between the jets, which causes a higher pressure loss of the crossflow, decreasing the local momentum ratio **J** and consequently a diminution of the jet penetration. The *staggered* configuration showed no marked tendency of backflow into the primary zone. Only when $\mathbf{S_z/D}$ was about 2.1 or less the injected jets blocked the mixing sector causing a backflow of the primary zone stream. The configuration [S_z/D=3, C=7] proved be the best suited for a use in the RQL mixing sector.

For the *inline* arragement the jet arrays had a C parameter between 1.25 and 2.5, following *Holdeman, 1991* and *Licinsky et al., 1993*. The ratio $\mathbf{S_z/D}$ was between 1.5 and 2 and the dimensionless hole diameter 8.4 < **H/D** < 29.1. Seven

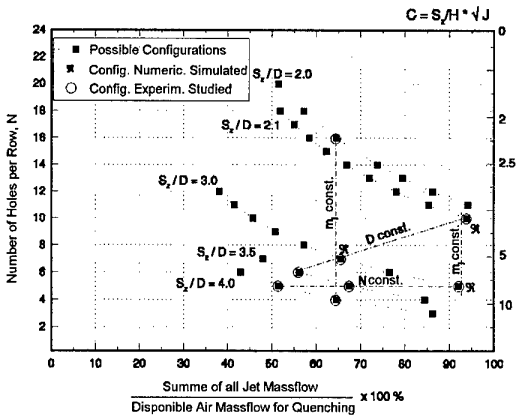

Fig. 4.3: Measurement points in parameter range

configurations were investigated numerically and three of them experimentally. By this arrangement, small changes in $\mathbf{S_z}$ or **D** caused under- or overpenetration of the jets, in both cases resulting in a poor mixing rate. Moreover, the results showed that, to inject 100 % of the design mass flow, it is necessary to have at least three rows of opposed jets, with the risk of relatively long residence times at high temperature.

In the next step, the distance $\mathbf{S_x}$ between the jet rows was varied for the more promising staggered case. The ratio S_x/S_z was adjusted to 0.5, 1.0 and 1.4, for the following row parameters:
1) $S_z/D = 3$, C = 7, 2) $S_z/D = 3$, C = 5, 3) $S_z/D = 4$, C=7, so that the influence of S_x/S_z was tested for configurations having the same S_z/D ratio or same C parameter. All nine cases were studied experimentally and four of them numerically. Fig. 4.4 summarizes the influence of S_x/S_z on the unmixedness for configuration 1. It shows, that $S_x/S_z = 1$ has

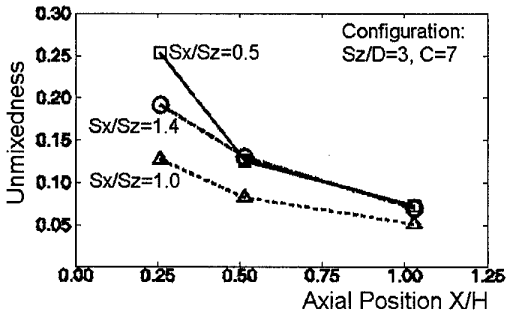

Fig. 4.4: Effect of row spacing on mixture homogeneity

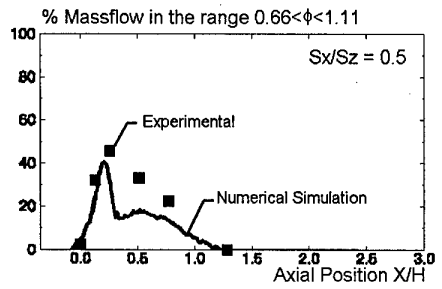

Fig. 4.5: Effect of row spacing on percentage of nearstoichiometric flow

the best relative mixture homogenity. $S_x/S_z = 0.5$ showed the worst homogenity behind the 2nd. row (at X/H = 0.25).

However looking at the development of the nearstoichiometric percentage of the flow M_{ns} in fig. 4.5 gives a different picture. For the wide spacing, 100% of the mixture lies in the nearstoichiometric interval of $0.66 < \phi < 1.1$ after 1st. row injection at X/H = 0.5. With S_x/S_z=1.0 (not shown), this amount reduces to about 90%, whereas for S_x/S_z= 0.5 only 50% is in the interval, indicating a "dilution effect", such that the short spacing gives better RQL mixing even without having the lowest unmixedness. This seeming contradiction is a simple effect of the partition of the mixing air on two rows. After the 1st row injection, jet and crossflow begin to mix together and if there is space or time enough before the 2nd injection takes place, this mixture achieves an intermediate equilibrium condition, which, in the RQL case, will probably assume a value near stoichiometry. Hence, for more than one row, it is essential to overcome this range quickly and inject the 2nd jet row as close as possible to the 1st row.

Some results from the numerical simulation of the configuration 1 are presented to enable the understanding of the detailed fluid mechanics leading to those findings. The XY-plane through the middle of a 1st row hole at the botton and through the middle of a 2nd row hole at the top of the mixing sector is shown in fig. 4.6. The vectors depict the velocity field for S_x/S_z = 0.5. The jet from the 1st row collides with the one from the 2nd. The mixture homogenity in terms of temperature and velocity profiles is achieved very fast. In fig. 3.6 b six different cross sections from X/H = 0 to 0.5 show the strong interaction between both rows of jets. The jet penetration provoces in the YZ-plane a clockwise rotating movement. At X/H = 0.4 the 2nd injection causes a counterclockwise rotation, that works against the rotation from the 1st row, enhancing the mixing process: The secondary flows originating from the first and second row are destroyed, producing a high level of turbulence, the reduction of local mixing scale and ultimately an acceleration of homogenisation by the lateral mixing of jet fluid.

Finally we studied also the influence of the ratio D_1/D_2 preserving the total hole area. For this investigation, the best configuration for equal hole diameters, S_z/D = 3, C = 7 with S_x/S_z=0.5 was used. The other S_x/S_z were not useful for this variation, because their 1st row jets already reached the opposite wall and an augmentation of D_1 would cause a backflow to the primary zone. D_1/D_2 were adjusted to 0.7 and 1.5 and investigated numerically, due to the good agreement of the simulations for the staggered arrangements, *Migueis, 1996*. The setting D_1/D_2 = 1.5 showed a small change in the flowfield, having a marginal reduction in the amount of massflow under near stoichiometric condition. For D_1/D_2 = 0.7 the flowfield experienced a tremendous change. The interaction between 1st and 2nd row jets was stronger as for D_1/D_2 = 1, so that the mixing channel was partially blocked, and augmented the pressure loss. This was enough to create a backflow in the middle of the channel.

4.2 Similarity between isothermal mixing and mixing with heat release

As mentioned before, the mixing problem of the RQL quench zone was investigated without combustion. To investigate the similarity between both mixing processes, a numerical study was undertaken using the configuration S_z/D=3, C=7, described with its isothermal results in the previous chapter. In this investigation, the variation of the S_x/S_z ratio was repeated for combustion.

As initial condition, a fully pre-mixed, homogeneous flow in thermochemical equilibrium was taken for the crossflow, where gaseous n-Dodecan fuel was burned with a global equivalence ratio of ϕ=1.81. According to *Griebel, 1995,* this is a suitable rich zone value for RQL combustion. In the primary zone as well as in the secondary channel, air was pre-heated to a temperature of 850 K. For the simulation of combustion effects, a two-step reaction mechanism was used, which accounts the oxidation of hydrocarbons and carbon monoxide. With such a simple combustion model, calculation times could be held under praticable limits, showing qualitative accuracy in the results.

A comparison between the flow fields of both, isothermal and combusting mixtures, *Migueis, 1996,* demonstrated a qualitatively good agreement, i.e. both flow fields showed the same jet paths, -wakes and most importantly, the same secondary flow phenomena described in the section 4.1, which is responsable for the enhancement of the mixing rate. In the fig. 4.7 the amount of massflow under near stoichiometric conditions is shown in each cross section.

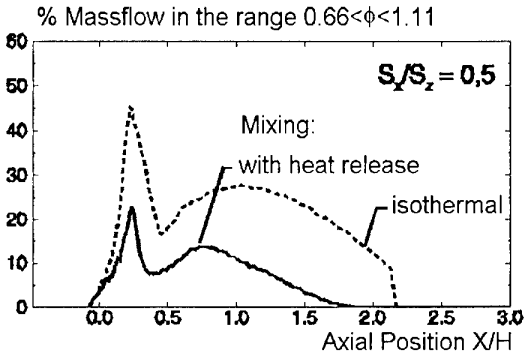

Fig. 4.7: Effect of heat release on the mixing

In this graph, two aspects can be discerned: a) both curves have the same form, which means that there exists a similarity between both mixing processes; b) the flow overcomes the near stoichiometric region quicker, because, due to the chosen similarity, the pimary massflow is a larger part of the total flow for the isothermal case as compared with the combusting case, c.f. eqs 2 and 4. The same analysis was one for the variation of the S_x/S_z ratio, fig. 4.8.

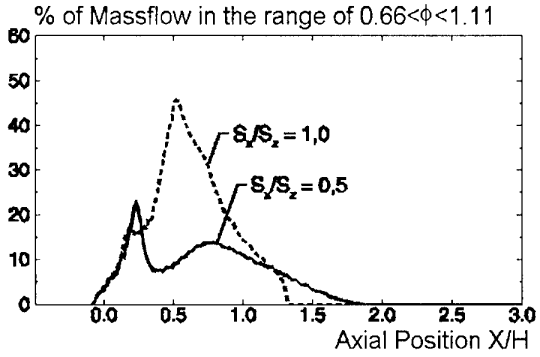

Fig. 4.8: Effect of S_x/S_z ratio on the mixing when heat release is considered

We can see that, with combustion, the reduction of S_x/S_z also accelerates the transition of the near stoichiometric zone. Comparing the area under both curves, we obtain a reduction of 30% of the mass under the conditions where most of thermal NO_x is produced.

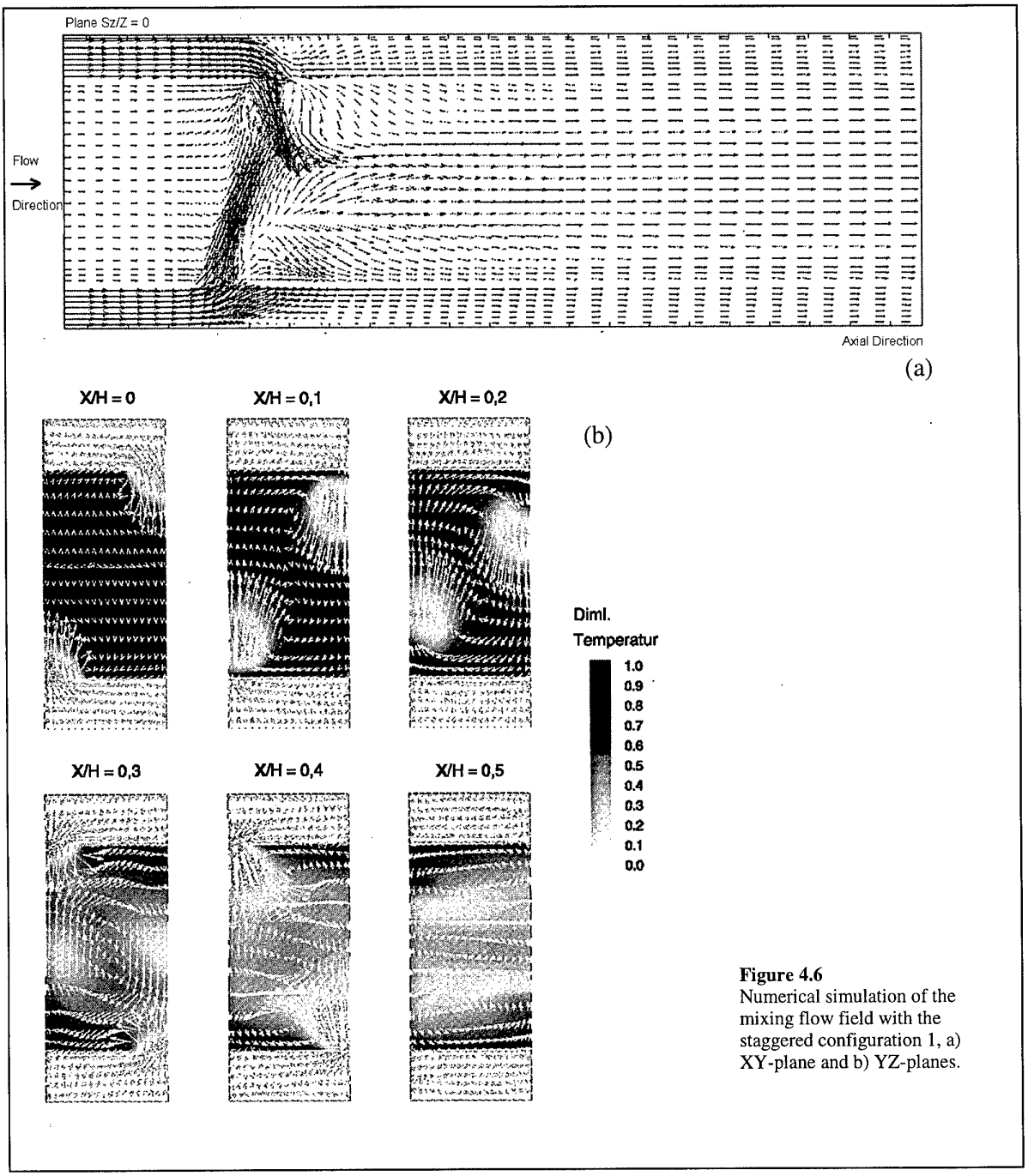

Figure 4.6
Numerical simulation of the mixing flow field with the staggered configuration 1, a) XY-plane and b) YZ-planes.

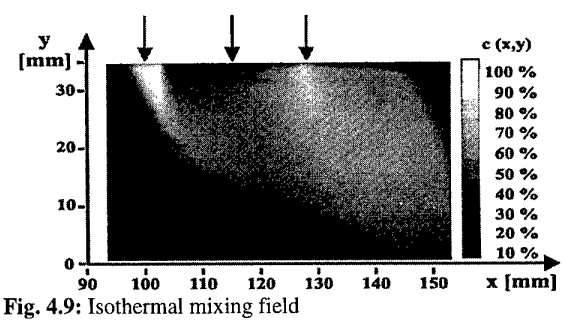

Fig. 4.9: Isothermal mixing field

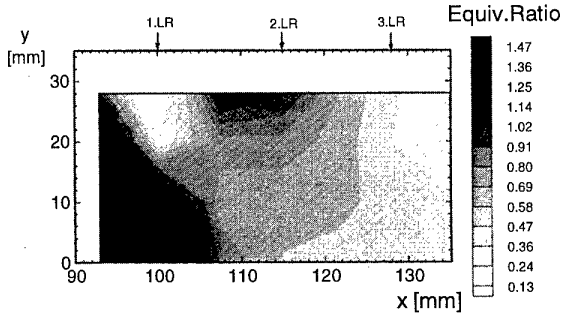

Fig. 4.10: Chemically reacting mixing field

To confirm this similarity between isothermal and chemically reacting mixing processes, a comparison of some isothermal and combusting experimental results described in *Griebel, 1997,* are shown. In this work, a research RQL combustor sector was investigated. Multiple airblast atomizers at the chamber head produced good primary zone homogeneity, the mixing sector had an *inline* configuration with three rows. The research combustor is shown in fig. 3.2. Figure 4.9 shows the isothermal mixing field at the XY-plane, which passes through a hole of the first and of the third row. The grey scale is directly related to the light intensity recorded using the Light Sheet Technique (LST), i.e. it is related to the mixing air concentration. Figure 4.10 shows at the same XY-plane the equivalence ratio distribution calculated from species measurements performed with suction probes and gas analysis in the combusting sector. The low spatial resolution of the gas samples allows only a rough comparison of both figures. It is however clearly visible that some important flow characteristica, like the jet injection angle, the penetration depth into the crossflow and also the wake after the first row are quite similar. These results confirm the jet-to-crossflow momentum ratio as the most important parameter in the mixing process.

The success of the isothermal simulation in the prediction of the basic features of the jet mixing is at first surprising. However, the isothermal mixing study shows, that the jet path and most importantly the jet penetration depth steer all the entailing mixing phenomena, like the described secondary flow. Although the quench and secondary zone combustion accounts for about one third of the overall heat release and the density ratio simulated with the applied similarity rules ultimately goes to zero, the density field around the portion of the jet deciding its penetration is not substantially changed. Fig. 4.9 shows, that the cold jet core is preserved until y=20mm, and CARS temperature measurements performed in the mixing field don't exhibit temperature peaks in the reaction zone around the jets, such that the density gradients are not substantially changed. The latter result may be specific to the slower chemistry of atmospheric combustion as compared with full pressure, however the first condition, i.e. that the penetration is decided by the extent of the unmixed jet core will be often met for jet mixing problems in combustion.

4.3 Quantitative Laser Light Sheet Investigation of a swirled isothermal combustor model

Having demonstrated the applicability of isothermal mixing investigations for design studies of combustor aerodynamics and having validated the quantitative light sheet technique as an efficient measuring technique for that purpose, the technique was used in the next step for a more applied combustor. MTU built a rectangular RQL combustor model with three swirl nozzles The mixing section had 3 rows of staggered holes and one goal was to quantify, how the inhomogenuous primary zone would influence the jet penetration and hence the mixing. Fig. 4.11 shows a section of the mixing zone after the first row between the centrelines of the two outer nozzles. The different penetration of the jets corresponding to different jet angles can be clearly seen. It corresponds well to the variation of the primary zone flow with recirculating zones on the nozzle centrelines leading to steeper jet angles and stronger forward velocities in between leading to smaller jet angles respectively lower penetration. The results can be used in two ways: Since the interaction of a swirling flow with wall jets are not easily predicted by standart turbulence models it can be used for validation purposes but also to design jet rows with differing diameters to equalize the penetration and mixing disturbance of the swirling flow.

5. Conclusions

From the results shown and discussed in the previous chapter it can be concluded, that it is possible to use the isothermal mixing investigation as a means to test the mixing of rich primary zone gas and wall jet rows, thereby bypassing to some extent medium pressure sector tests with 3-D gas sampling measurements. Ist use is particularly appropriate for RQL as validated design correlations for jet rows don't exist.

Fig. 4.11: Concentration of secondary air after first jet row in RQL combustor model with three swirling primary nozzles

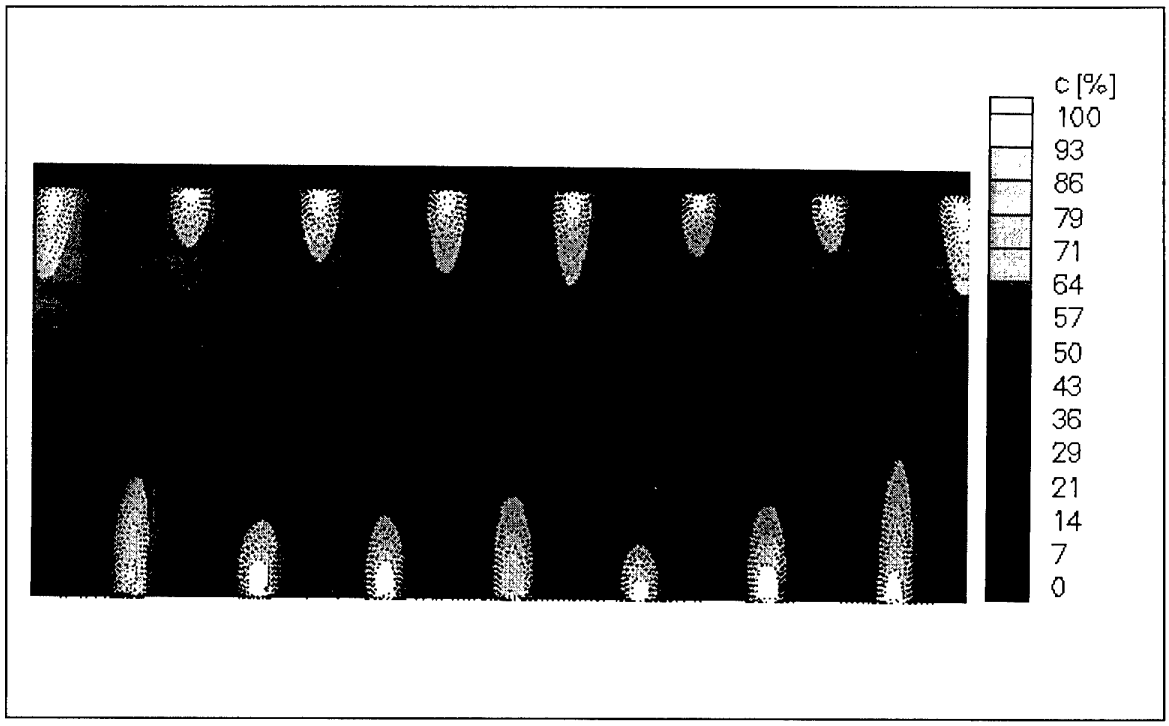

The computational and experimental comparison with combusting flow show surprising similarity, which is partially attributed to the fact, that the secondary zone heat release was slow enough not to change the density field around the jets fundamentally where they still exhibit significant vertical velocity.

The isothermal mixing study with homogenuous cross flow for RQL combustors without cooling flow into the primary zone showed that at least two rows of holes are necessary to avoid recirculating the secondary flow. Staggered row arrangements are preferable, because secondary flow patterns can be set up, which promote quick mixing. Since for the suppression of thermal NO_x formation, the mixing time to reach an equivalence ratio of 0.66 is decisive, it is not sufficient to identify the configuration which gives the best ultimate homogeneity, but in contrast to dilution jet studies, the mixing speed in the early phase has to be monitored also, because different optimum configurations for the two criteria can exist.

The light sheet technique for concentration measurements in mixing flows could be demonstrated to give reliable quantitative information with a much higher spatial resolution as any other competing technique, however it also requires a careful setup and appropriate correction techniques. The application in the RQL combustor model with primary swirl enabled clear identification of the influence of the swirl and the recirculation of the primary zone on the jet mixing.

The potential of the technique will be further augmented by application of the planar Doppler Global Velocimetry, then giving together the full description of the mixing field and its dynamics. It is planned as the next step of the investigations.

6. Acknowledgements

C.E.M. thanks CNPq of Brazil and the BMBF of Germany for financial support while undertaking the research at DLR, as well as M. Rachner for the continuous support of MUG3D calculations. The design and built of the combustor model of chapt. 4.3 by MTU as well as the fruitful collaboration during the course of the RQL research are gratefully acknowledged.

7. References

Holdeman, J.D., " Mixing of multiple jets with a confined crossflow", AIAA-91-2485, 1991.

Migueis, C. E., "Untersuchungen zur Optimierung der Mischzone einer fett-mager gestuften Ringbrennkammer", Forschungsbericht 96-33, Deutsches Forschungsanstalt für Luft- und Raumfahrt e.V. ISSN 0939-2963, 1996

Zarzalis, N., „Rectangular RQL Combustor", Brite/Euram Low-Emission Combustor Technology Research Programme, Task 1.2, Final Report, 1996

Dörr, Th., "Ein Beitrag zur Reduzierung des Stickstoffausstosses von Gasturbinenbrennkammern - Die Optimierung des Mischungsprozesses der Fett-Mager-Stufenverbrennung", Dissertation, T.H. Darmstadt, 1995.

Gueroui, D., "The performance of combustor-liner air-admission holes in uniform and distortet flows", M.Sc. Thesis, Cranfield Institute, 1982.

Kamotani, Y. and Greber, I., " Experiments on a turbulent jet in a crossflow, AIAA J., vol. 10, no.11, pp. 1425, 1972.

Fric, T.F. and Roshko, A., " Structure in the near field of the transverse jet", Proc. 7th. Symposium on Turbulent Shear Flows, vol. 1, pp. 6.4.1, 1989.

Danckwerts, P.V., " The definition and measurements of some characteristics of mixtures", Appl. Sci. Res., Sec. A, vol. 3, pp.279, 1952.

Liscinsky, D.S., True,B., and Holdeman, J.D., " Experimental investigation of crossflow jet mixing in a rectangular duct", AIAA-93-2037, 1993.

Hinze, J.O.,"Turbulence", 2nd.Edition, Mc-Graw-Hill Inc., 1975.

Eickhoff, H., Koopman, J., Neuberger, W., Rachner,M.,"Entwicklung eines Berechnungsverfahrens zur Bestimmung der dreidimensionalen Strömungs- und Verbrennungsvorgänge in Gasturbinenbrennkammer", FVV-Abschlussbericht Gasturbine-Brennkammern, Vorhaben nr. 300, Heft 363, 1985.

Noll, B.E., "Möglichkeiten und Grenzen der numerischen Beschreibung von Strömungen in hoch belasteten Brennräumen, Habl.Schrift., Lehrstuhl und Inst. für Thermische Strömungsmaschinen, Univ. Karlsruhe, 1992.

Patankar, S.V., Basu, D.K., Alpay, S.A., "Prediction of the three-dimensional velocity field of a deflected turbulent jet", J.Fluid Engng., vol.99, no.4, pp.758, 1977.

Rachner, M., "Flow computation in combustion chambers using a zonal non-staggered grids", AGARD CP-510, pp.37-1, 1992.

Voigt, P., Schodl, R., Using the Laser Light Sheet Technique in Combustion Research, AGARD - PEP 90th Symposium on "Advanced Non-Intrusive Instrumentation for Propulsion Engines", Brussels, Belgium, 20-24.October 1997

Bohren, C.F., Huffman, D.R., Absorption and Scattering of Light by Small Particles, John Wiley and Sons, 1983

W.H.Press, S.A.Teukolsky, W.T.Vetterling and B.P.Flannery, Numerical Recipes in C, chapter 17

Voigt, P. Entwicklung und Einsatz eines flächenhaften Meßverfahrens zur Bestimmung der Volumenstrom-konzentration im Mischungsgebiet von Zweikomponenten-strömungen, Dissertation Ruhr Universität Bochum, to be published, 1998

Griebel, P., Behrendt, T., Hassa, C., Lückerath, R., Bergman, V., Stricker, W., Zarzalis, N., "Untersuchung eines atmosphärischen Fett-Mager-Brennkammersektors für Flugriebwerke", VDI-Berichte Nr. 1193, pp. 589, 1995.

Griebel, P., "Untersuchung zur schadstoffarmen, atmosphärischen Verbrennung in einem Fett-Mager-Brennkammersektor für Flugtriebwerke", Forschungsbericht 97-48, Deutsche Zentrum für Luft- und Raumfahrt, ISSN 1434-8454, 1997.

AFTERBURNER DESIGN AND DEVELOPMENT

A. TROVATI
F. TURRINI
C. VINCI
Fiat Avio S.p.A., Direzione Tecnica, Corso Ferrucci 112, 10138 Torino, Italy

ABSTRACT

The paper deals with the design and the development of the afterburner system for an advanced fighter aircraft.
The design background of the system and its major components is given, in front of design requirements.

The design process is described, outlining most important design tools, with particular attention to CFD and aerothermal modelling.

The principal experimental evidences are also presented, showing the most significant achievements of system development and giving a survey of major problems and relevant solutions during the system development and optimisation process.

SUMMARY

The realisation of the afterburner system for an advanced fighter aircraft is described herewith, giving a survey of the development process from specification requirements to flight tests.

Since the very challenging design requirements asked to start the design already introducing the most updated available technology features, the development process was initially largely based on experimental activities, with the exploitation of dedicated technology rigs.
This was certainly justified at the beginning of the development phase, when the state of art of combustion theoretical modelling was still quite poor and an empirical approach was the traditional way to develop combustion chambers and afterburners, while the analytical approach was mainly adopted for stress calculations, only.

However, the very quick development of more and more advanced computational tools and the parallel evolution of combustion modelling, allowed by these tools, gradually shifted some of the design activity from empiricism to a more balanced mixture of analytical activities and confirmatory tests.
This new approach has been gradually introduced, starting from more detailed heat transfer calculation, then proceeding to simple flow-dynamic models and finally approaching CFD models, for both non-reacting flow ("dry conditions") aerodynamic simulation and for reacting flow ("reheat conditions").
Therefore, rig and engine tests weren't the only tools for the component development, any more.
On the contrary, they were used to confirm new design solutions or modifications which had been already analytically evaluated, in order to correctly set the computational tools, to verify the assumptions used for design calculations and, finally, to validate design improvements.

The paper gives a survey of this design process, highlighting the most important achievements and describing some of the most interesting problems encountered during the afterburner development and the relevant solutions.

LIST OF ACRONYMS

ABFMU Afterburner Fuel Metering Unit
CFD Computational Fluid-Dynamics
DECU Digital Engine Control Unit
DVE Design Verification Engine
FAR Fuel - Air Ratio
FEA Finite Element Analysis
FSR Full Scale Rig
HPT High Pressure Turbine
LPT Low Pressure Turbine
PFR Pre-Flight Release
R/H Re-heat
SLS Sea Level Static
TBC Thermal Barrier Coating

1. INTRODUCTION

The realisation of this afterburner module, herewith described, went through a rather long sequence of development phases from specification requirements to flight tests.

The initial design, starting from the experiences available from older engines service data and from technological demonstrator engines tests, was validated at the beginning of the programme in the "Design Verification Engine" (DVE) phase.

The experience from technological rig and DVE's testing was then exploited in the following "Pre Flight Release" (PFR) phase, which led to a configuration close to the first flight engine one.

Though this configuration was already quite satisfactory, the full achievement of all the specification requirements asked for additional improvements and design adjustments, which were gradually introduced in the process towards the "Production Standard" final module configuration.

This design process is described in this paper, with particular attention to design criteria and advanced modelling.

Paper presented at the RTO AVT Symposium on "Design Principles and Methods for Aircraft Gas Turbine Engines", held in Toulouse, France, 11-15 May 1998, and published in RTO MP-8.

2. SYSTEM REQUIREMENTS

The afterburner, or reheat (R/H) system is obviously expected to be used for a limited portion of the flight mission, corresponding to intercept and fight.
However, the consideration that in the intercept missions 80% to 90% of the total fuel consumption is burned in reheat led to the requirement of the highest possible burning efficiencies at both full R/H and part R/H (about 70% of maximum combat thrust) operation.
At full R/H (Combat) the required R/H combustion efficiencies, within most of the flight envelope, range from 90% to 95%, while efficiency equal to or higher than 80% is requested for partial afterburning.

The afterburner system "dry" pressure loss (i. e. friction and mixing aerodynamic loss, not considering combustion "fundamental" losses) are required not to exceed 3% at SLS flight condition.

Another requirement is the ability to operate the afterburner within the whole steady-state flight envelope, whereas R/H flame-out is accepted only in the top left-hand corner of the extended (transient) envelope (see fig. 1).

Engine handling times are also fundamental to give to the aircraft the required flexibility in operations, to achieve a very good combat capability.
Expected times to achieve full thrust slamming the engine from Idle to Max R/H are therefore lower than 5 seconds at "high ram conditions" (either low altitude or high aircraft speed) and lower than 10 seconds at the top left-hand side of the flight envelope.
The satisfaction of those handling times required a proper design of afterburner fuel system, nozzle control [1] as well as engine digital control unit (DECU).

Furthermore, the afterburner system is required to operate without significant combustion instabilities (buzz or screech) within the whole flight envelope.

As far as the thermo-mechanical design is concerned, the engine targets of a high reliability and a low maintenance were the basis for the specification.
With specific address to the afterburner system, the most significant reason to fail is thermal fatigue, related the very high thermal gradient from "dry" to "reheated" conditions, at every R/H selection.
Therefore, life requirements can be more significantly expressed in terms of R/H selections, rather than Flight Hours.
The consideration of engine specification life requirements and of the required operational mission mixes led to an overall figure of 16000 R/H selections to be achieved by afterburner components.
This requirements is reduced to 12000 selections for the thermal liner (screech damper and heat shield) which is the most critical component for thermal stress.
On the other hand, can be quite easily replaced on the engine without major disassembling, beside of the removal of the variable nozzle module.
A further structural requirement of the module is the capability to withstand buckling loads in case of afterburner flame-out.

3. SYSTEM ARCHITECTURE

The overall arrangement of the afterburner system is presented in fig. 2.

Upstream of the afterburning region, a duct separates the turbine exit and the bypass streams.
For this design, the "mix/burn" arrangement was selected : fuel is separately injected in the various air flow streams, but the mixing process of the core and bypass streams is simultaneous with the combustion process.
This option allows to minimise the system length and also reduce the tendency of the afterburner system to low frequency combustion instability [2].
The area ratio is set in accordance with the ratio of mass flow rates, in order to have, for both flows, a Mach number no higher than 0.3, sufficiently low to obtain good mixing of the two flows and to good flame stability.
This bypass duct is supported by 6 tangential and 6 radial links (fig. 3) connecting it with the engine jet-pipe and carrying inertial loads (since pressure loads on the duct are very small, most important loads come from engine "g-loads" during aircraft manoeuvres).

The primary zone is provided with an annulus of individual vaporisers, located between the core and the bypass streams.
This location provides the required heat release to sustain the core stream flame at afterburner light up.
On the other hand, the recirculation region downstream of the vaporiser shells acts as a flame stabilisation zone also for the bypass stream combustion.

As far as the core stream is concerned, in previous engine designs the flameholders were typically made of V-shaped uncooled metal rings.
However, the evolution of engine performance, requiring the increase of the hot gas temperature at the exit of the LP turbine, made the uncooled solution particularly critical for this application.
Since at the time of the initial design the introduction of exotic materials (e. g. high temperature composites) was not considered reliable enough, the alternative solution was a different arrangement with radial flameholders, capable to be cooled by a small amount of cold bypass air.
This design also led to the choice of radial core fuel injectors, in line with the flameholders downstream (see fig. 2).
Fuel is injected in the bypass stream by means of fan spray jets to provide the best fuel preparation and distribution in the relatively cold bypass air, achieving high efficiency also for the bypass fuel combustion.

Core and bypass stream fuel injectors are fuelled by external fuel manifolds with pressurising valves to feed groups of burners.
This arrangement allows the majority of the manifolds to be kept full of fuel at all times, greatly reducing the volumes to be primed during R/H selection and reducing selection / deselection times.
On the contrary, primary fuel is fed through a single valve manifold located within the bypass duct, to reduce manifold volumes and, therefore, system mass.

In the core stream, combustion obviously develops in the wake of the flameholders.

The primary zone (vaporisers) is located at the same axial plane, to optimise ignition performance.
The shape of vaporisers is selected in order to create a recirculation region where primary fuel is lit and burns.
The same wake region, expanding outwards, helps to maintain stable combustion of bypass stream, too.

Considering the very high temperature and the pressure of LPT exit flow, ignition of the reheat flow is practically guaranteed at low altitude flight points.
At high altitude conditions, however, R/H light-up must be enhanced by an external energy source.
This is provided by a short time (about 1 - 2 seconds) fuel injection upstream of the high pressure turbine, which produce a "hot shot" able to ensure the ignition of afterburner fuel.
Even if this system is certainly increasing the thermal stress, particularly on the HPT, it was preferred to other systems (like an additional electrical igniter, which requires also electrical cables, conditioning box, and so on to be installed) because of its simplicity, reliability and reduced mass.

At R/H entry the bypass stream splits into two flows : one flow directly enters the combustion region, while the second flow is through the liner annulus to provide R/H and nozzle cooling (see fig. 2).
The inlet areas of both flows are set in order to optimise engine matching (a variation of these pressure loss directly affects fan backpressure and, therefore, turbomachinery working line) and, at the same time, to have the necessary cooling flow for the liner and the nozzle.

The length of the screech damper section has been also optimised to ensure that the required operating margins with respect to screech are achieved.
The following section of the annulus duct has a double function : it acts as a thermal shield for the jet-pipe, which is insulated from flame radiation, and also provides cooling air flow to the convergent - divergent nozzle.
Effusion cooling holes distributed along the heat shield length provides the necessary cooling of the shield itself.
The "wavy" shape of this liner not only allows to optimise the distribution and the effectiveness of the cooling flow, but it also increase the component structural stiffness allowing to reduce its thickness and saving mass (fig. 4).

4. SYSTEM FUNCTIONAL DESCRIPTION

In order to achieve the required burning efficiencies, the afterburner was designed with the ability to separately control fuel burning in the engine hot (core) and bypass streams.

A separated fuelled primary zone is provided between the core and bypass stream to provide reliable light up and flame stability in low pressure - low temperature operating points (top left-hand corner of the flight envelope).
To optimise efficiency a fuel staging strategy is adopted, with the following steps :

- For a given flight point, primary fuel is kept constant at the ignition value;
- At low R/H setting, fuel is supplied to the turbine exit flow only, since burning in the hot temperature gas stream gives the best efficiency;
- At high R/H setting, if the total required fuel flow was injected in the core stream it would approach or exceed the stoichiometric mixture ratio with a drop in efficiency : therefore part of the afterburner fuel is injected to the bypass stream, when fresh air is available for combustion.

The three fuel flows are metered by the Afterburner Fuel Metering Unit (ABFMU) and individual metering valves, with a strict tolerance.
The metering valves are located very close to the fuel injection points, allowing to reduce the afterburning priming time and to obtain the required operating times.
For the core and the bypass fuel flows, a further reduction of the priming time is obtained by using 5 metering valves for each flow, with a very small volume between valves and injectors.

Reheat ignition is driven by the "hot shot" coming from the turbine flow.
This system, avoiding the use of a R/H igniter and a dedicated electrical box, gives a definite advantage in terms of installed mass and, above all, successfully proved to be very reliable.

The relatively high speed of the core stream air flow required the introduction of flameholders to obtain the time residence necessary to achieve the required flame stability, as it is typical for all afterburning systems.

On the contrary, flame stabilisation in the bypass stream is provided by the primary zone combustion, not requiring the design of ad-hoc flame stabilisers.

Fuel - air mixture ratios (FAR) were selected in order to achieve maximum thrust and stability.
Primary FAR was designed to be fuel rich within the vaporisers, being the excess fuel a cooling medium to avoid vaporiser overheating.
However, when the recirculation of air flows (both cold air from the bypass duct and hot gas from behind the flameholders) is considered, the resulting fuel - air mixture in the wakes of the vaporiser shells is about stoichiometric, giving maximum flame stability.

Core stream fuel flow was also designed to be stoichiometric, taking into account that the hot gas stream at LP turbine exit is already vitiated by the main engine fuel flow.
In such a way, maximum thrust is extracted from engine core flow.

Finally, the bypass additional fuel flow, which is selected only when Combat thrust is required, was basically set by the maximum R/H temperature compatible with afterburner and nozzle materials.

A final optimisation of afterburner fuel schedules, in terms of split between hot and cold stream fuel flows, for a given flight point, was carried out in order to minimise the possibility of encountering R/H instabilities, i. e. either buzz in the top left-hand corner of the flight envelope or screech in the right-hand side of the same flight envelope.

The overall length of the afterburning system was dictated by the required combustion efficiency, with particular reference to the high altitude flight points, while the jet pipe inner

diameter is a compromise between best R/H performance and lowest aircraft drag, also considering the requirement on aerodynamic losses.
The afterburner jet pipe is protected from overheating by a liner.
This upstream portion of this liner acts also as a screech damper, while the downstream portion is a heat shield.
Furthermore, the liner has the function to supply cooling air to the convergent - divergent nozzle.

5. SYSTEM CONTROL

The ABFMU is controlled by the engine digital control unit (DECU) which computes the required fuel mass flow to the primary, core and bypass stream burners as a function of achieved nozzle area, flight condition and engine rating (fig. 5).

Afterburner selection is initiated by action of the pilot on engine throttle lever.
At afterburner selection, the control system performs the following actions :

- to avoid the risk of reducing the compressor stall margin at R/H ignition, pre-opening the variable nozzle throat area to a value set as a function of the engine operating point (inlet pressure and temperature);
- selecting the minimum afterburner flow for primary ignition, as a function of engine operating point;
- after a set delay time, firing the hot shot;
- increasing nozzle area and afterburner fuel flow up to the value corresponding to pilot's throttle selection (also this fuel value is a function of engine operating point).

At pilot's reheat cancellation, the control system immediately shuts off the fuel flow, then the appropriate "dry" nozzle throat area is selected.

6. COMPONENT DESIGN PRINCIPLES

In this chapters the most important components of the afterburner systems are described, giving a survey of relevant design principles and design methods.

6.1. Afterburner Fuel System

Afterburner fuel system piping was sized considering the fuel mass flow turn-down ratio, within the whole operating range (from "min R/H" to "Combat") and within the whole flight envelope and considering engine specification requirements in terms of afterburner "handling" times (i. e. time to accelerate / decelerate from "dry" conditions to "Combat").

The reduction of handling times can be obtained by reducing the piping volumes, i. e. pipe sizes; in fact, for given fuel flow and fuel density :

$$t = \frac{\rho_f * Vol}{W_f} = \frac{\rho_f * L * \pi * \phi^2}{W_f}, \text{ where}$$

t = time to fill (or void) the volume,
ρ_f = fuel density,
L = pipe length,
ϕ = pipe diameter,
W_f = fuel mass flow rate.

However, the reduction of pipe diameter has the obvious drawback of largely increasing fuel pressure drop at higher mass flows, with heavy impact on pump sizing :

$$\Delta p \approx 0.5\, k * \rho_f * V^2 \approx \frac{8\, W_f^2}{\rho_f * \pi^2 * \phi^4}.$$

As a result of a trade-off analysis, it was selected to reduce piping volume by designing a system with fuel valves located around the afterburner jet-pipe section.
Fuel pipes upstream of the valves are kept full of fuel, therefore the time required to inject fuel in the R/H system is corresponding to the short length between valve ports and fuel injectors.
For core and bypass stream fuel flows, the selection of multiple R/H fuel valves improved the design; while for the primary fuel it was preferred to have only one fuel valve (to reduce engine mass), by having a fuel manifold internal to the bypass stream (reducing both engine mass and handling time).

The adoption of this internal manifold required the evaluation of the operating envelope, in terms of bypass air temperature and fuel pressure, temperature and flow rate, to be sure that, even in the worst conditions with light fuel, hot temperature and low pressure and flow, fuel boiling within the manifold is avoided.
Moreover, the adoption of a single valve required the flow check not only of each fuel injector, as it requested all (primary, core and bypass) fuel injectors, but also of the half manifold carrying the fuel from the primary valve to the vaporisers, to guarantee the necessary uniformity of fuel feeding.

This arrangement allows to obtain handling times equal to or lower than engine spec. requirements.

6.2. Turbine Exhaust Diffuser

This component, placed downstream of Low Pressure Turbine (LPT) exit, has different purposes :

- to recover the residual flow swirl at the turbine exit, in order to ideally feed the afterburner "core" section with a no-swirl flow,
- to reduce flow velocity at R/H entry, in order to make combustion in the core stream stable,
- to straighten the flow in order to obtain a flow ideally parallel to engine centreline, maximising engine thrust.

The first of these functions is obtained with a row of vanes located upstream of the conical diffuser and giving a "counter-swirl" angle to the flow.
Since the design of this component is more related to the design of the LPT rather than of the afterburner, it will not be described here.

The two other functions are performed by a conical diffuser, whose aerodynamic has been carefully designed and verified.
The overall geometry of the conical diffuser is basically dictated by the desired flow Mach number upstream of the

flame stabilisers section : at the reheat design point, this Mach number has been selected in the 0.2 - 0.25 range.
The calculation of the inlet-to-outlet area ratio of the diffuser is therefore straightforward on the basis of continuity equation; however the diffusion angle and length required for this area ratio have to be determined.
A shorter diffuser is, of course, preferable to reduce engine length and mass, however a too sharp diffusion angle could result, in some operative conditions, in a separation of the diffuser flow and an unacceptable reduction of pressure recovery capability.
This issue is even more important for the design of this diffuser, which can not be symmetrical.
As a matter of fact, the outer wall of the annular diffuser is also the inner wall of the bypass duct, hence it has to be cylindrical to avoid drawback effects on the bypass flow : therefore, all the flow diffusion has to be obtained on the diffuser inner side, making the problems of flow separation more stringent (see fig. 2).
A 2D computer simulation of the diffuser boundary layer at different flight conditions was therefore carried out, identifying the maximum diffusion angle to be 15.5°.

The above mentioned steps allowed to define the diffuser geometry (area ratio, diffusion angle and, hence, length).
The final check is the comparison of diffuser expected performance with acceptable pressure losses, considering diffusion losses and friction losses.
For the annular diffuser case, this can be derived from fig. 6 plot, where the diffuser effectiveness is the pressure recovery factor, defined as :

$$C_p = \frac{p_2 - p_1}{p_{tot1} - p_1} .$$

Even if this plot was derived for annular (symmetrical) diffusers, it has been used also for the initial design of this asymmetrical configuration with good results.

6.3. Core Stream Flameholders

As it usual for afterburning systems, flame stabilisers are necessary to get the required flame stability in the core stream, where flow velocity at the exit section of the diffuser is still relatively high.
As already mentioned, the necessity to provide air cooling for the flame stabilisers led to the selection of radial flameholders with closed (triangular) section, with cooling air taken from the bypass stream.

Flame stability is controlled by the shape and size of the flameholders, which determine the dimensions of the wake region downstream of the flameholders themselves and therefore the gas residence time inside this wake : higher the residence time, better the flame stability.
On the other hand, a larger blockage also implies, for a given geometry of the flame tube, a higher velocity of the gas flow in the free stream around the flameholders, which is detrimental for flame stability [3] : a trade-off analysis was therefore carried out to obtain the optimum blockage ratio of approximately 1 : 3.

This blockage ratio also allows to keep the flameholder pressure drop, at the afterburner design point, within the 3% design target.

To take into account the effect of flow variables within the whole flight envelope, flame stability was finally rated with the introduction of a "stability parameter" S, defined as :

$$S \approx \frac{M}{P^x * W^y * T^z} , \text{ where}$$

M = flameholder throat Mach number,
P = flameholder throat static pressure,
W = flameholder width,
T = gas temperature at R/H inlet.

The exponents x, y, z and the limit value of the stability parameter S were derived from previous experiences on similar engines.

6.4. Core Stream Fuel Injectors

Having chosen a radial configuration with the core stream flame stabilisers, the same radial configuration was also selected to inject afterburner fuel in the LPT core stream flow.
Fuel injectors are therefore radial bars (spraybars), upstream of flameholders and in the same angular positions, injecting fuel normally to the air flow through plain injection holes.

To achieve the better flow distribution, increasing combustion efficiency and reducing the risk of combustion instability, the fuel injection holes are distributed on both sides of the spraybars and are centered in equal area flow annuli.
The injection direction, normal to air flow, is a compromise between the requirement of having good fuel atomisation in a short length (which is obtained by the aerodynamic effect of the incoming air flow) and improving the uniformity of fuel distribution.

6.5. Bypass Stream Fuel Injectors

To have a fuel distribution as uniform as possible in the bypass stream, the module design features a large number of injection points, circumferentially equispaced around the colander throat section.
For a given fuel mass flow, the number of injection points is limited, obviously, by geometrical constraints and also by the minimum size of the injection holes, to avoid injector clogging : a 0.6 mm diameter was estimated to be the minimum acceptable hole size.
To improve fuel atomisation, which is much worse than for core injectors because the bypass flow is much cooler and the velocity in the colander section is higher, fan spray fuel jets have been selected.

6.6. Afterburner Liner

The afterburner liner has the primary functions to shield the engine jet-pipe from the afterburner hot gas and to carry the nozzle cooling flow.
Additionally, the first portion of the liner is used as a damper to minimise eventual high frequency combustion oscillations ("screech").

The screech damper portion is a cylindrical drum with rather large holes which alter the reflection patterns of combustion pressure waves and give the damping effect.
This screech damper was initially designed on the basis of past experience, to select damping hole size, distribution and length of the damping section.

The second portion of the liner, the "heat shield", was designed initially as a sequence of conical metal sheets with forged "Z-rings" carrying the air for film cooling (figs 7a and 7b).
The most important parameters to design the liner are the metal temperature and, consequently, the resistance to thermal cycling.
Being the metal sheets very thin, the metal temperature can be computed by balancing radiation and convection on both surfaces of the liner, i. e. from hot gas to metal and from metal to cooling air flowing in the annulus.
Even if this calculation is theoretically a simple one, in reality there are big uncertainties related to :

- not uniform distribution of liner cooling flow pressure and temperature, with the creation of "hot streaks" : the effect of these hot streaks proved to be, in worst cases, in the order of a 150 °C - 300 °C increase of metal temperature,
- characterisation of cooling device effectiveness, as a function of geometry and operating conditions.

As a matter of fact, the optimisation of the liner was the most painful task in the whole afterburner development, requiring a large number of rig and engine tests with dedicated hardware.

7. COMPONENT DEVELOPMENT

This chapters describes the most significant modifications and improvements which were introduce to the afterburner components as a consequence of development testing and evolution of analysis methodologies.

7.1. Reheat Efficiency Analysis

R/H combustion efficiency is defined as the ratio between the "burnt" fuel flow divided by the total afterburning flow :

$$\eta_{R/H} = \frac{(W_{fR/H})_{burnt}}{(W_{fR/H})},$$

however the measurement of this quantity is not easy, since it requires a chemical analysis of gas sampled from the flow at the afterburner exit section.
Many these tests were performed on a Full Scale Reheat Rig (FSR), allowing to identify the better disposition of fuel spraybar injection holes [4] and confirming that a very high quantity of fuel (more than 99% at SLS) is actually "burnt", i. e. converted into combustion products (CO_2 and water) : this can be identified as a "chemical" reheat efficiency.

On the other hand, the engine thrust boost provided by the afterburner is given by the sharp increase of the gas flow temperature, therefore another interpretation of the efficiency definition can be derived from these thermodynamical considerations.
As a matter of fact, by knowing the thermodynamic flow parameters (mass flow rate, pressure and temperature) at the afterburner inlet and at the nozzle throat section, it is possible to compute the value of the "burnt" fuel, which is, in this case, defined as the "ideal" fuel quantity necessary to obtain the nozzle throat gas total temperature.
"Ideal" in this case means that this is the fuel mass flow obtained from combustion charts (including combustion fundamental losses and dissociation effects), without other losses (like aerodynamic mixing effects, mixing with reheat cooling flows, not uniform gas temperature distribution, etc.).

Efficiency data consistent with this latter definition, which can be called reheat "propulsive" efficiency, were also computed from R/H FSR tests and their analysis, compared with the results of gas sampling, gave a very important guideline for the development of the afterburner module.
At Combat conditions, the aerodynamic mixing between the core and bypass stream is enhanced by combustion turbulence and it is rather good.
The effect of the injection on reheat liner cooling flow is also negligible, since this is a small quantity of fresh air which is distributed along the liner length and is able to quickly mix with the main stream gas flow and participate to the combustion process.
On the contrary, a more important cooling flow is the nozzle cooling flow, which is injected tangentially to the main gas stream at the nozzle entry section (refer to fig. 2).
A lip divides this flow in two streams, the outer one (Nozzle Cooling Flow) is tangential to the nozzle convergent petal, to provided a good film up to the nozzle throat and to the divergent section.
The inner flow (the so-called "Z-ring" Flow, from the geometry of the ring which carries the cooling holes) is tangential to the lip surface to cool the lip itself.

These cooling flows are obviously necessary to guarantee the nozzle integrity, however they generate a cold air annulus around the hot core flow, which is detrimental for engine thrust boost.
In order to correctly evaluate their effect on the reheat "propulsive" efficiency, a careful analysis of test data was necessary and the following conclusion were apparent :

- the Nozzle Cooling Flow behaves as separate stream, not mixing with the main stream upstream of the nozzle throat, and creates a cold fresh air layer around the main stream :
  - equivalent thrust is computed as a mass flow weighted average of gas temperature square root

$$w\sqrt{T} = w_1\sqrt{T_1} + w_2\sqrt{T_2};$$

- the "Z-ring" Flow mixes with the main stream upstream of the nozzle throat, however the residence time is too short to complete the combustion of the fuel entrained in this

flow : no combustion in this flow is assumed for efficiency analysis :
- equivalent gas temperature is computed by enthalpy balance

$$w*C_p*T = w_1*C_{p1}*T_{11} + w_2*C_{p2}*T_2 .$$

The results of these analyses, together with test data about R/H liner and nozzle metal temperatures, have been fundamental for the optimisation of the cooling flow quantities and distribution to get the specified thrust boost.

7.2. Turbine Exhaust Diffuser Development

This component didn't suffer any particular problem during the engine development.
However, the analysis of the computed air static pressure profile along the diffuser cone, confirmed by engine experimental measurements, highlighted that the downstream portion of the diffuser was quite ineffective to recover the static pressure.
This observation, together with the requirement to minimise engine mass, led to a series of back-to-back tests (at SLS and altitude simulated conditions) with reduced length diffuser, basically to verify the eventual effect of this shortened configuration on R/H stability.
After this verification, a shorter version of the exhaust diffuser, with the same diffusion angle, has been introduced on the engine.

7.3. Bypass Duct Optimisation

The original design of the bypass duct was basically set on the grounds of required flow areas.
Core stream and bypass stream flows were considered to define the bypass duct diameter obtaining the required engine bypass ratio.
As for the bypass duct exit areas, the colander throat section, where the bypass fuel sprayers are located, was defined by the limit Mach number acceptable for combustion in the bypass stream, whereas the annulus inlet of the liner cooling duct was designed on the basis of the required cooling flows for the liner itself and to the nozzle.

However, during the engine development, it was discovered a very strong impact of bypass "secondary" flow on engine turbomachinery and, therefore, on overall performance.
In particular, all the leakages of air from the bypass duct to the core stream, give an uncontrolled alteration (increase) of the engine bypass ratio : to reduce this effect, special seal arrangement have been introduced at the bypass duct inlet interface and around the fuel spraybar (fig. 8).
More significantly, a large and quite unpredictable bypass flow enters the liner annulus and is then re-injected into the main afterburner stream through the large holes of the screech damper : this flow immediately mix with the main stream and its effect on reheat combustion performance is negligible, however the variation on the fan backpressure is, on the contrary, very important for engine overall performance.

In order to minimise this flow, without impairing afterburner and nozzle cooling, many different kind of "bluff bodies" (like flat plates or vanes) were designed and tested on the Full Scale Rig and on engines.
CFD detailed studies were also exploited to have a better comprehension of the problem and find out the best solution.

On the mechanical side, even if the bypass duct is a quite simple component and it is normally subject to relatively low loads, some criticalities were discovered in case of R/H flame-out.
As a matter of fact, during normal operations the static pressures of core and bypass stream are very similar and the pressure load on the duct is almost negligible.
On the contrary, in case of a flame-out, being the variable nozzle throat area still open to the afterburning value, the pressure in the core stream suddenly drops, whereas the bypass pressure is much slower to react : this cause a sharp increase of the pressure drop applied to the bypass duct and results in component buckling.
In the original design, the probability of a R/H flame-out at high pressure (low altitude) conditions was estimated, on the basis of combustion stability margins, very low and this eventuality was not considered.
Development experience however showed that other engine failures, like either an erroneous control input from engine DECU to nozzle actuation system or a nozzle actuation system hydraulic failure, can be the cause for reheat flame-out.
The bypass duct has been therefore strengthened to get the necessary resistance against buckling (fig. 8).

7.4. Flameholder Development

The very first testing phase already put into evidence the high criticality on thermal cycling on the flameholder structure, particularly because of the large thermal gradient occurring between the relatively cold leading edge and the extremely hot downstream face.
A long development process, implying the optimisation of air cooling and the optimisation of mechanical structure, has been therefore necessary to reach the required life expectancy.

As far as air cooling is concerned, a first action has been the insertion of turbulence promoters (ribs) within the cooling duct, in order to improve the convective heat transfer.
Since these ribs have the obvious drawback of increasing pressure drop, limiting the cooling air mass flow, a 1-D heat transfer computer code was prepared to trade-off various rib orientations and sizes.
As a result of this trade-off, which was confirmed by dedicated component rig tests, a rib orientation of 30° was selected as the most beneficial configuration [4, 5] (figs. 9a and 9b).
The higher pressure drop was partially compensated by a simplification of the flameholder air intake, limiting inlet loss.

On the mechanical side, first of all a significant benefit was given by the application of thermal barrier coating (TBC) on the flameholder rear wall.
With the application of the TBC, the heat transfer global coefficient can be evaluated combining heat conduction and convection with the classical formulation [6]:

$$H = \left[\frac{1}{h_1*A} + \frac{1}{L/(k*A)} + \frac{1}{L'/(k'*A)} + \frac{1}{h_2*A} \right], \text{ where}$$

H = heat transfer global coefficient,
h_1 = convective heat transfer coefficient (hot gas side),
h_2= convective heat transfer coefficient (cooling air side),
A = heat transfer surface area,
L = metal thickness,
L' = TBC thickness,
k = metal thermal conductivity,
k' = TBC thermal conductivity.
Since this was still insufficient to adequately limit the thermal gradient, a lighter internal structure was finally designed to reduce the differential thermal expansion and the deformations.

7.5. Bypass Fuel Sprayer Re-design

Even if the original design of bypass fuel injectors was perfectly sound for combustion purposes, giving satisfactory combustion efficiency and good fuel distribution, a mechanical problem forced the review of the design of these components.
In fact, these Titanium made bypass fuel sprayers went satisfactorily through the initial engine development phase but, with the evolution of engine development standards, a series of engine tests at many different engine operating points, with measurements of sprayers temperature, stress and vibrations, in parallel with a survey of jet pipe vibration, demonstrated that the lightened version of the engine jet pipe had a typical vibration mode with frequency coincident, at least in some operating points, with the sprayer natural frequency.
This observation led to a brand new design of the sprayers to avoid resonance.
Considering also the previously described issues about turbomachinery matching, the new design also incorporates a new shape giving the required blockage of the colander throat section, avoiding the introduction of flat plates and then reducing the pressure losses (fig. 10).

7.6. Screech Damper Development

The original version of the screech damper had plain damping holes.
This configuration demonstrated to fully achieve the required damping capabilities, however the very small static pressure drop across the liner resulted in a very small cooling air flow or, in some instances, even in reversed flow with ingestion of the combustion hot gas in the cooling annulus and consequent overheating of the screech damper rear portion.
This was immediately cured by introducing some "tipping" of the damping holes : with such a configuration, the effective pressure upstream of the damping holes is not a pure static one but it recovers some of the flow dynamic pressure, and a positive flow from the cooling annulus to the main stream is always guaranteed [4] (fig. 11).
In the successive engine development, the already mentioned effort to improve the turbomachinery matching by reducing the flow through the screech damper led to a series of tests with reduced screech damper lengths.
While the elimination of the upstream portion (1/3 of total length) resulted in a significant loss of damping capability, the same length reduction applied to the rear portion didn't show any adverse effect, neither at SLS nor in altitude rig and engine tests.
This modification was then introduced in the current afterburner configuration, reducing the screech damper length and moving upstream the heat shield interface.
This not only provides a better engine matching, but it also allows to remove the hotter part of the screech damper and replace it with the heat shield, which is more effective cooled.

7.7. Heat Shield Development

The original heat shield design, with "Z-rings" to provide film cooling, appeared to be critically hot and very much prone to exhibit heavy distortions and thermal fatigue cracks.
After some attempt to improve the situation with relative small design changes, a completely different arrangement has been deemed necessary to fix this very significant problem.

With respect to the initial configuration, the new design incorporates a lot of innovative features (figs. 2 and 4) :

- Discrete cooling injection through the Z-rings is replaced by an almost continuous cooling air injection through effusion holes distributed along the liner length. Only the last Z-ring to carry the nozzle cooling flow is maintained in present design.
- Since the original thick forged Z-rings had also a structural function, a corrugated ("wavy") shape has been adopted in order to maintain the required liner stiffness. This configuration helps to improve the effectiveness of the effusion cooling holes, too.
- Dedicated CFD studies and rig tested have been carried out to optimise the shape of the corrugated liner and the distribution of the effusion cooling holes.
- Thermal barrier coating is applied to the hottest regions, in the rear portion of the heat shield, to further mitigate metal temperature.
- The geometry of the nozzle cooling Z-ring have been also optimised by means of detailed FEA calculations, in order to make it more flexible and reduce the stress gradient existing between the very thin (and hot) liner and the relatively thick and rigid (and cooler) Z-ring, which was the primary reason for thermal fatigue crack initiation and propagation.

8. CFD AFTERBURNER MODELLING

Computational Fluid-Dynamic (CFD) analysis has been carried out creating a whole afterburner model and some more detailed local models.
This models were successfully checked against experimental data and then used to evaluate design improvements and optimisations.

8.1. Afterburner CFD Model

Being the afterburner a symmetric module, a CFD model of the reheat and nozzle system has been prepared, reproducing the hardware geometry of a 3-D sector comprised between the flameholder centreline and the vaporiser centreline, extended from reheat inlet to nozzle divergent exit section (fig. 12)

The computer code used for this study is CFX [7], which is able to solve Navier-Stokes equations in a body-fitted, multiblock, structured computational grid.
The computed flow-field is steady-state, fully viscous, fully compressible and turbulent (k-ε turbulence model), with an upwind differencing scheme.
To have a better convergence, particularly in the supersonic region downstream of nozzle throat, a "false-time-stepping" technique is applied, with time stepping adaptation of the local time stepping to the flow velocity in each computational cell (constant Courant number).
Symmetry conditions are applied at the sector sides, i. e. no swirling flow crossing the boundaries is assumed.
Heat transfer equations are solved to allow the calculation of enthalpy balance for core and bypass stream mixing.
Model internal walls are assumed to be adiabatic, beside of the R/H liner, which is thermally conductive to allow heat transfer from the combustion main stream to the annulus cooling air : velocity and temperature profiles in wall boundary layers are computed with a code built-in logarithmic law.
Gutter cooling flow and air flow through the vaporisers were computed with a simplified 1-D flow network and imposed to the CFD simulations as boundary conditions (mass sources).
For the simulation of reacting flow (combustion) conditions, a model of fuel vaporisation and a 1-step combustion model are also implemented in the CFD code.

The CFD analysis have been carried out for both the aerodynamic (dry conditions) and reacting flow (afterburning conditions) cases, at two engine operating points, i. e. : SLS and z = 36000 ft / Mach = 1.8.
The computational mesh was adapted to each operating condition to match actual nozzle throat area.

8.1. Afterburner CFD Model Results

Some examples of static pressure fields computed are shown in figs. 13 and 14 [8].
Fig. 13 : SLS - Combat - Pressure field along the plane between two flame stabilisers
Fig. 14 : z = 36000 ft, M = 1.8 - Combat - Pressure field along the flame stabiliser plane.

Beside of the blockage effects of core stream fuel spraybars and flame stabilisers, a clearly visible feature is the small low pressure region at the downstream end of the exhaust diffuser cone.
Since no flow separation is there, this effect is due to the flow curvature around the cone tip : the same pressure behaviour was experimentally measured.
The static pressure balancing plane between the two streams (core and bypass) is also clearly visible : this plane is located somehow downstream of the flamaholder edge / colander throat plane.

Figs. 15a to 15d show a comparison between measured and computes static pressure profiles in the four mentioned operating points.
A rather good agreement of the results with the test data is confirmed.
Figs. 16 and 17 give an example of the computed fuel distribution and total temperature fields.

The first picture refers to the simulation of fuel injection without chemical reaction.
Since in reality the injected fuel reacts with air and burns, this is obviously a non-realistic case, however it provides information about the fuel distribution within the flowfield.
The results are in good agreement with gas analysis results obtained from a 2-D combustion rig and from the Reheat Full Scale Rig.

The second picture depicts the total temperature field in a Max R/H case.
Again, the overall pattern is qualitatively in line (fig. 18) with experimental observations (test data refer to a previous afterburner configuration, therefore perfect correspondence can't be expected).
In particular, the engine development showed the necessity to avoid fuel recirculation downstream of the exhaust diffuser cone prevent from injecting fuel from core sprayers at a too low radius.
This caution obviously result in a low gas temperature region where almost no fuel is injected : this kind of plots allows to evaluate the importance of this region and to evaluate the impact on component efficiency.
condition to match actual nozzle throat area.

8.2. Local CFD Models

In addition to the above mentioned model of the whole afterburner module, local models have been prepared for detail investigations.
In particular, the criticality of liner metal temperature, with local "hot streak", much hotter than the average temperature, was the reasons for detailed studies of the flow within the cooling annulus, to evaluate the effect of local changes of the cooling system and to investigate the impact of obstacles present in the annulus duct which are a potential source of hot streaks.

Some example of those activities are presented in the following [9], [10].
Fig. 19 depicts the flow velocity distribution in the cooling annulus, giving evidence of the effect of bypass fuel sprayers, annulus inlet vanes, instrumentation and assembly bosses.

Fig. 20 shows the pressure field generated by the wavy shape of the liner, with a low pressure region where cooling flow injection is not possible.
This was confirmed by 2-D combustion rig tests, where the presence on cooling holes on the top of liner waves resulted in

hot gas ingestion in the cooling annulus rather than in an injection of cooling flow into the main stream.
Alternative configurations, with a different distribution of the cooling holes and a plate to avoid the hot gas ingestion was studied with CFD (fig. 21).
The potential benefits for this modified configuration are showed in fig. 22.

9. CONCLUSIONS

The afterburner design described in this paper allowed to obtain a very satisfactory component, able to satisfy engine design requirements.

To achieve this result, many studies and tests have been necessary, with a continuous process of gradual improvement and optimisation.
CFD studies also gave an important contribution to this optimisation process.

The most important improvements which have been incorporated to the original design are the following :

- shortened exhaust diffuser to save mass
- flameholder duct stiffening to carry buckling loads
- flameholder duct and core fuel spraybar interface sealing to improve turbomachinery matching and engine performance
- new bypass fuel sprayer design to avoid resonance with jet pipe natural frequency
- adjustment of bypass exit flow areas to improve turbomachinery matching and engine performance
- flameholder cooling improvement with turbulence promoters and optimisation of mechanical structure to overcome thermal cycling stress
- tipping of screech damper holes to avoid hot gas ingestion
- new design of "wavy" heat shield to save mass, improve cooling and overcome thermal cycling stress
- adjustment of nozzle cooling ring interface to optimise mechanical behaviour and engine performance
- application of thermal barrier coating on flameholder back face and on afterburner liner.

10. ACKNOWLEDGEMENTS

The authors would like to thank all people who were involved and gave their valuable contribution to the development of this afterburner : FiatAvio Engineering and Testing Departments, RR Combustion Technology Department who co-operated with FiatAvio in a common design effort, the operators of DRA (Pyestock) test cell, where Reheat Full Scale Rig tests are performed as well as all test engineers of Eurojet partners companies involved in engine bench and flight testing.

11. REFERENCES

[1] Bardone, G., Marchetti, S., Trovati, A.,. "Actuation System for Variable Exhaust Nozzle and Inlet Guide Vanes on an Advanced Gas Turbine Engine", AVT - Propulsion and Power Systems (PPS) 1st Meeting on "Design Principles and Methods for Aircraft Gas Turbine Engines", Toulouse, France, 11th - 15th May 1998.

[2] Sotheran, A., "High Performance Turbofan Afterburner Systems", AGARD Propulsion and Energetics Panel 70th Symposium on "Combustion and Fuels in Gas Turbine Engines", Chania, Crete, Greece, 19th - 23rd October 1987.

[3] Lefebvre, A. H., "Gas Turbine Combustion", McGraw-Hill, 1983.

[4] Riccardi, G., Tasselli, A., Trovati, A., "Technology Rigs - A Tool for Afterburner Development", AGARD Meeting on "Fuels and Combustion Technology for Advanced Aircraft Engines", Fiuggi, Italy, 10th - 14th May 1993.

[5] Han, J. C., Park, J. S. and Lei C. K. , "Heat Transfer and Pressure Drop in Blade Cooling Channels with Turbulence Promoters", NASA Contractor Report 3837, 1984.

[6] Kreith, F., "Principi di Trasmissione del Calore" (Principles of Heat Transfer), Liguori, 1981.

[7] CFX 4.2, User Manuals, CFX International, Didcot (UK), December 1997.

[8] Gallo, A., Turrini, F., "CFD analisi del campo di pressione del post-bruciatore EJ200 in condizioni Dry e Reheat" (CFD Analysis of EJ200 afterburner pressure field in Dry and Reheat conditions), FiatAvio internal report PMMA97022EJR, July1997 (in Italian).

[9] Coutandin, D., Gallo, A., Turrini, F., "Riduzione temperature metallo H/S" (H/S metal temperature reduction), FiatAvio internal memo 187/97, May 1997 (in Italian).

[10] Gallo, A., "Analisi CFD del Campo di Moto nell'annulus del Liner del Reheat EJ200 per l'Indagine dei Problemi di Surriscaldamento" (CFD Analysis of the Flow Field in EJ200 Reheat Liner Annulus for the Investigation of Overheating Problems), FiatAvio internal report PMMA97033EJR, November 1997 (in Italian).

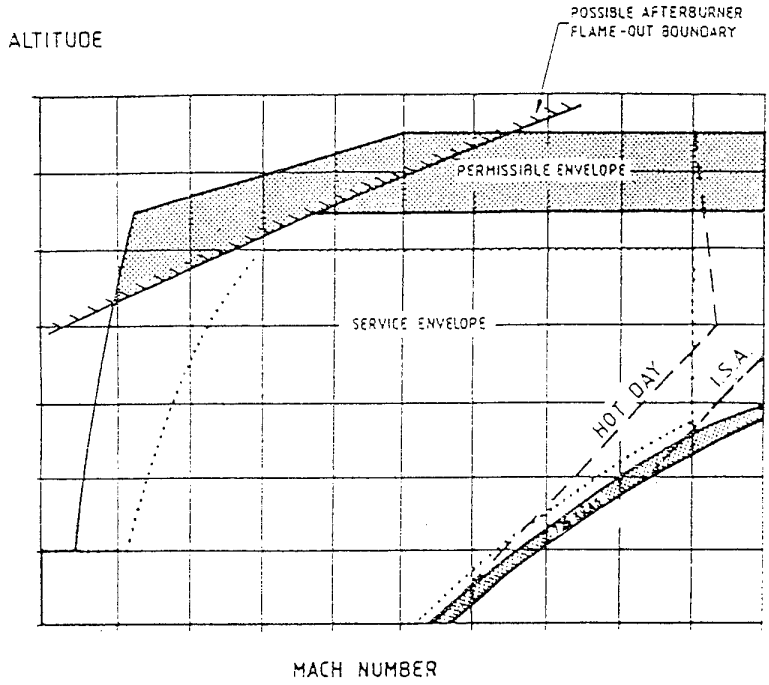

Fig. 1 - Engine Flight Envelope

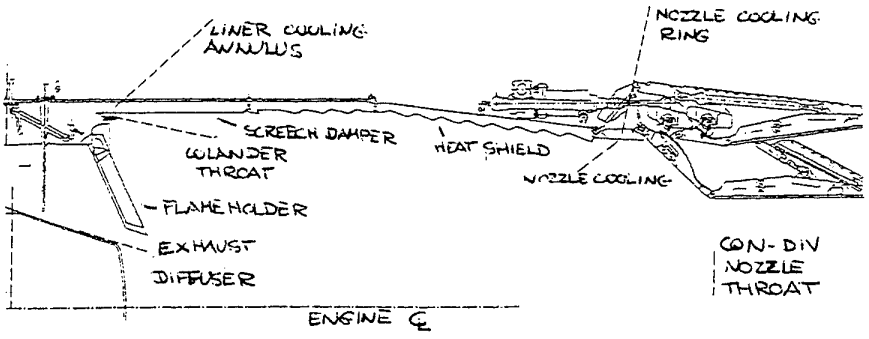

Fig. 2 - Afterburner System

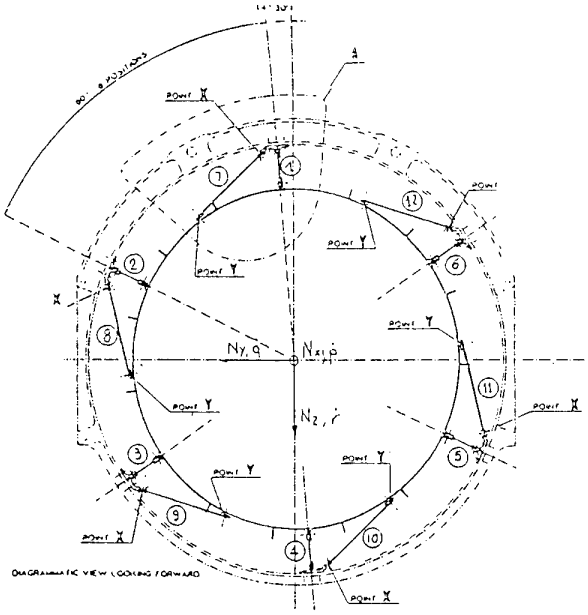

Fig. 3 - Bypass Duct Links Arrangement

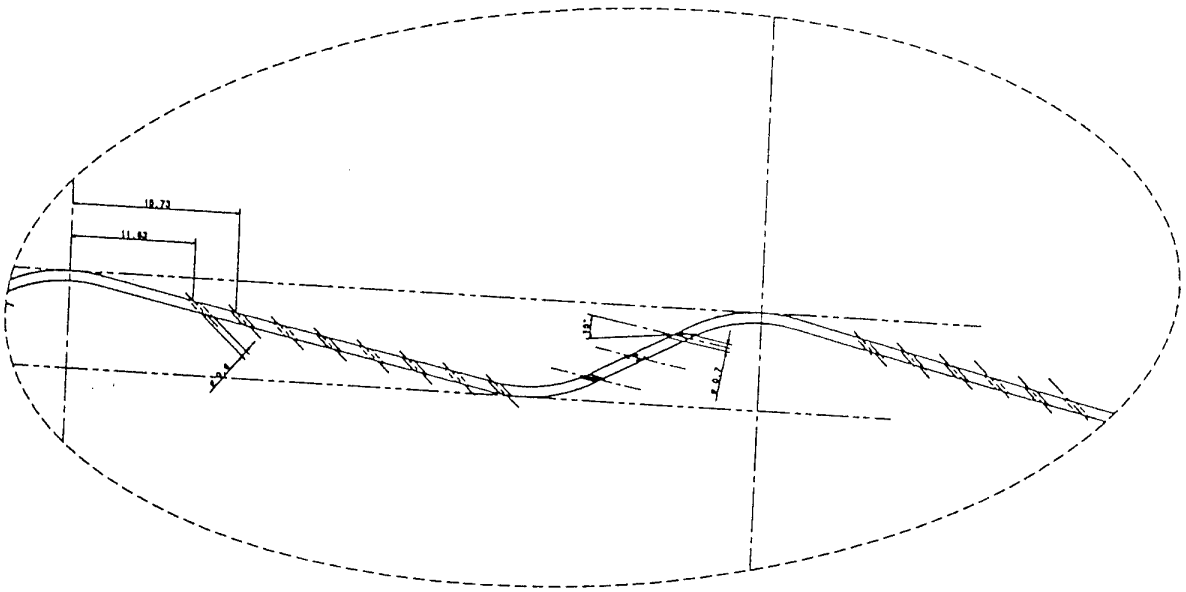

Fig. 4 - Corrugated ("Wavy") Heat Shield Cooling Holes

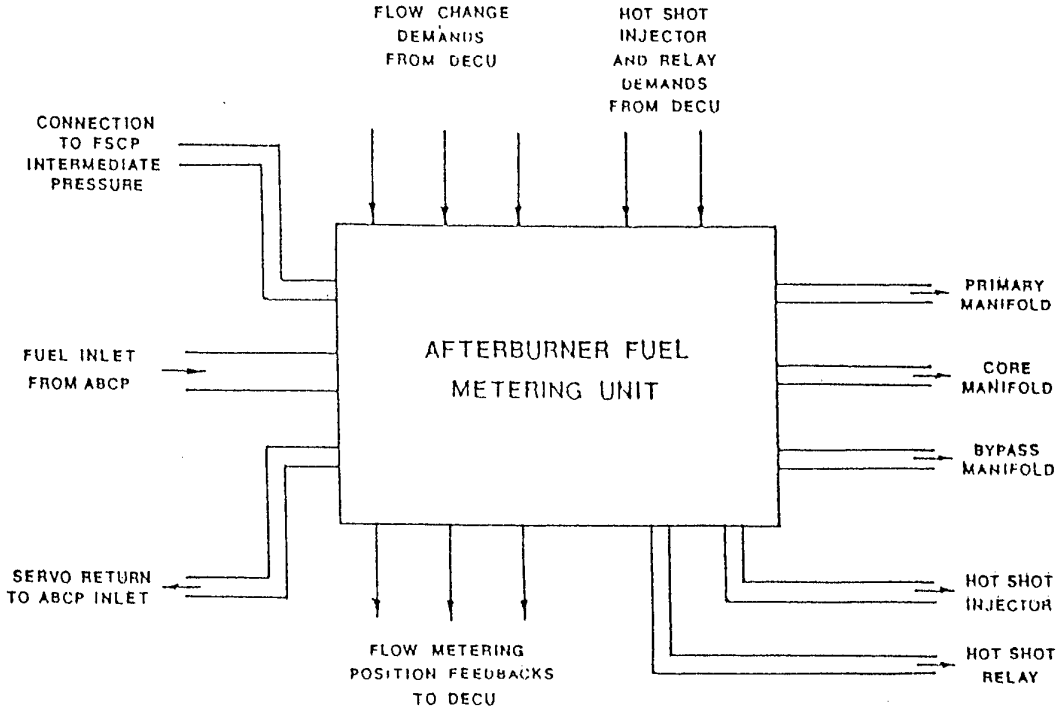

Fig. 5 - Afterburner Fuel Metering Unit Interface

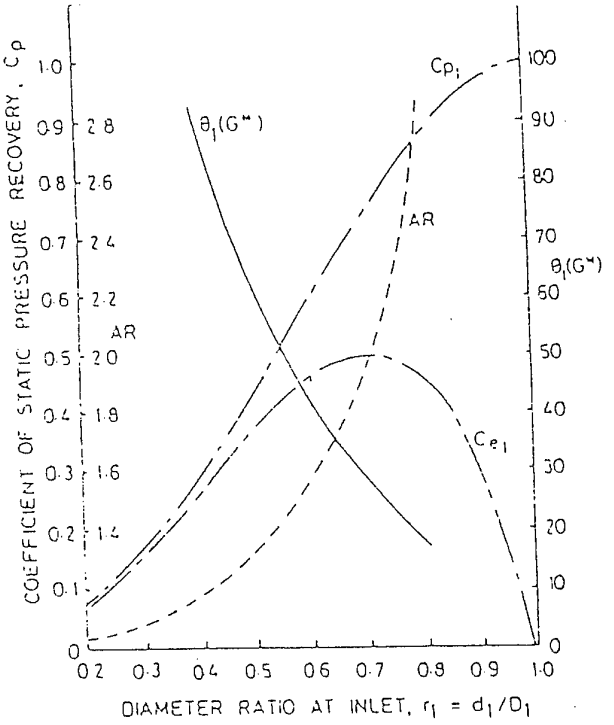

Fig. 6 - Annular Diffuser Pressure Recovery Plot

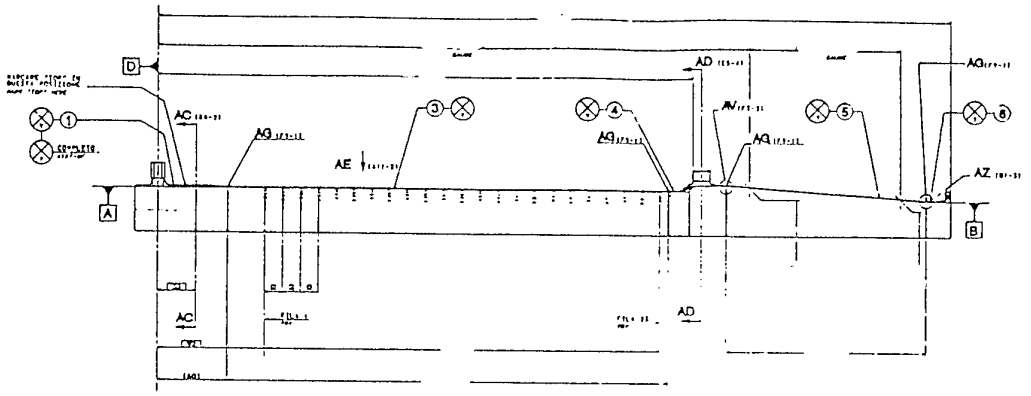

Fig. 7a - Screech Damper Original Design

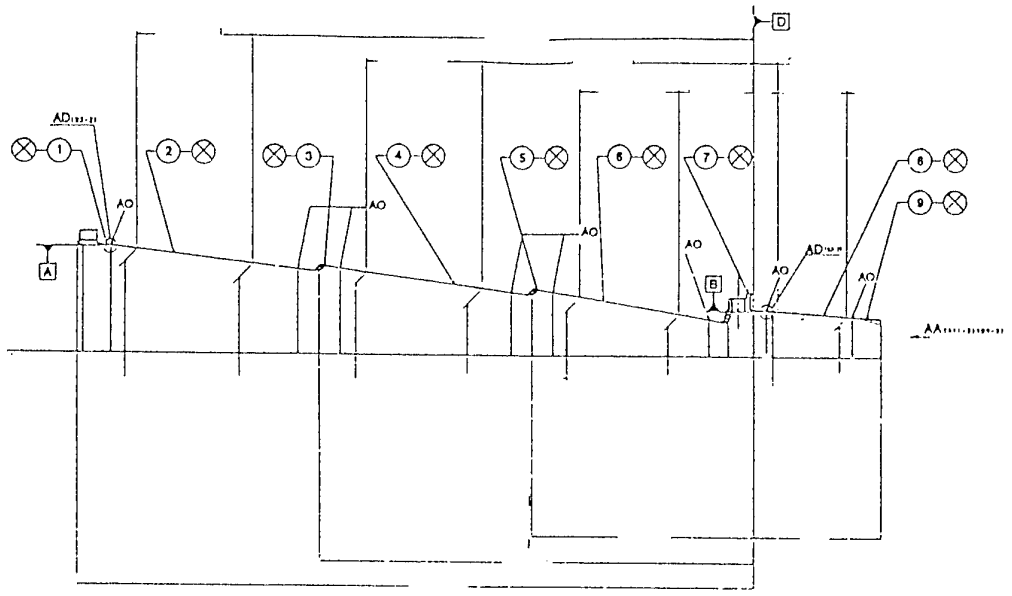

Fig. 7b - Heat Shield Original Design

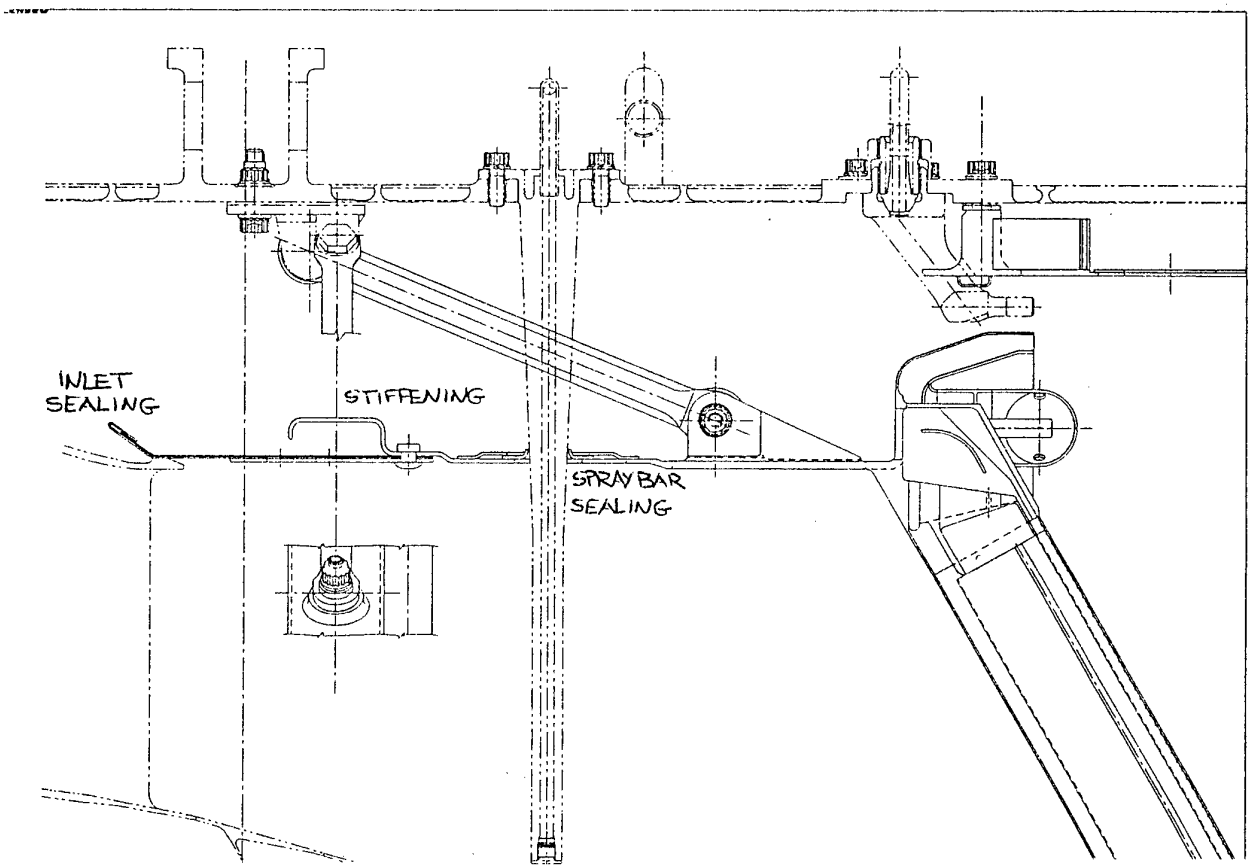

Fig. 8 - Stiffened Flameholder Duct and Sealed Core Fuel Spraybar

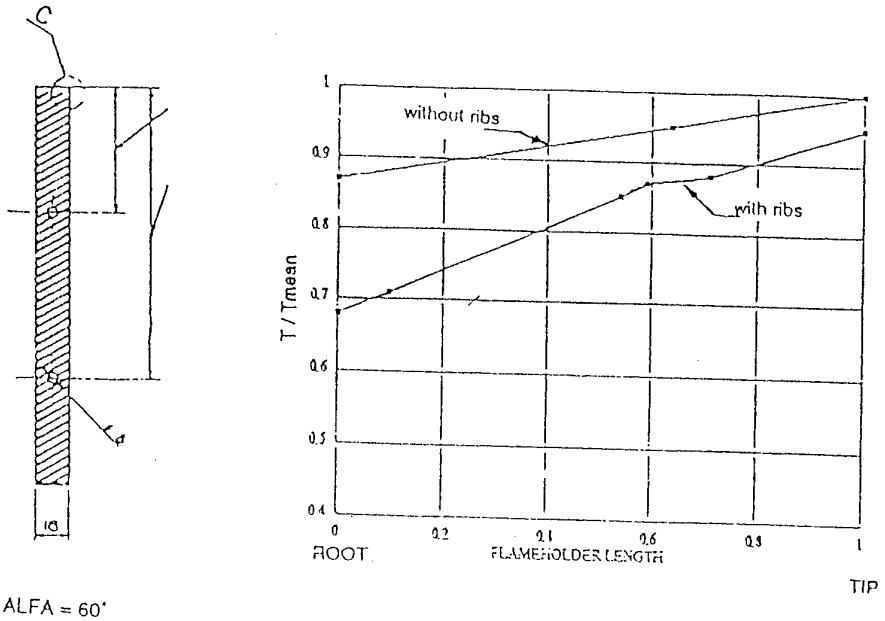

Figs. 9a - Flameholder Cooling Duct with 60° oriented Turbulence Promoters
Fig. 9b - Flameholder Temperature : Effect of Turbulence Promoters

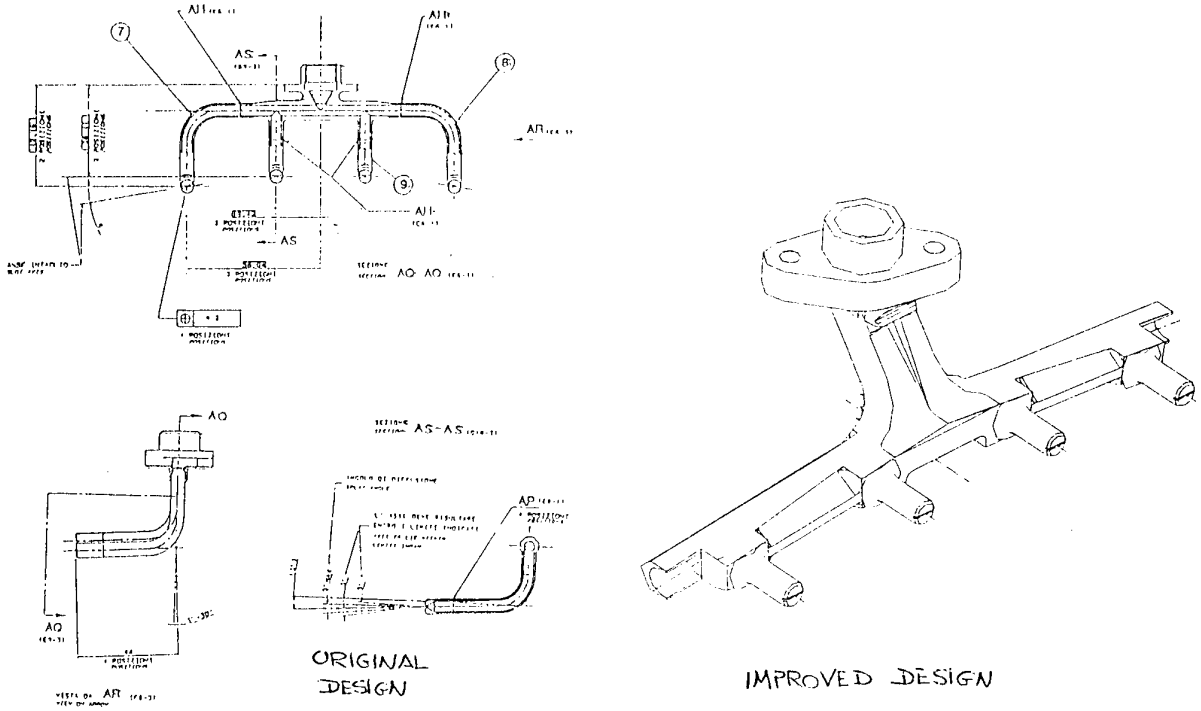

Fig. 10 - New Bypass Fuel Sprayer Design (compared with original design)

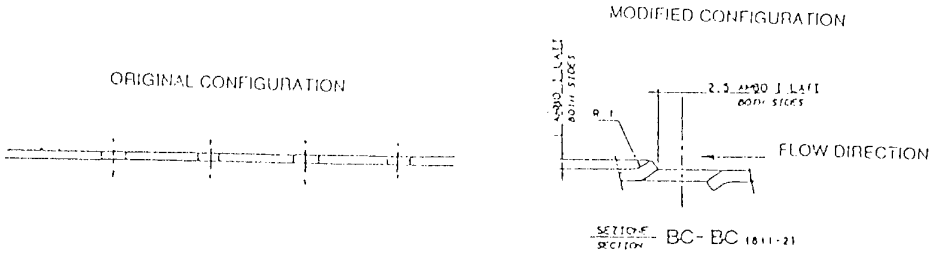

Fig. 11 - Screech Damper : Modification of Damping Hole Geometry

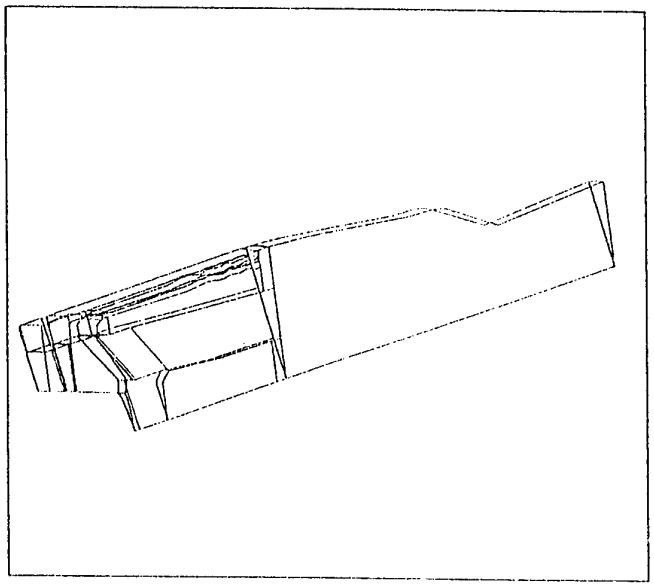

Fig. 12 - CFD : Afterburner 3 D Model Outline

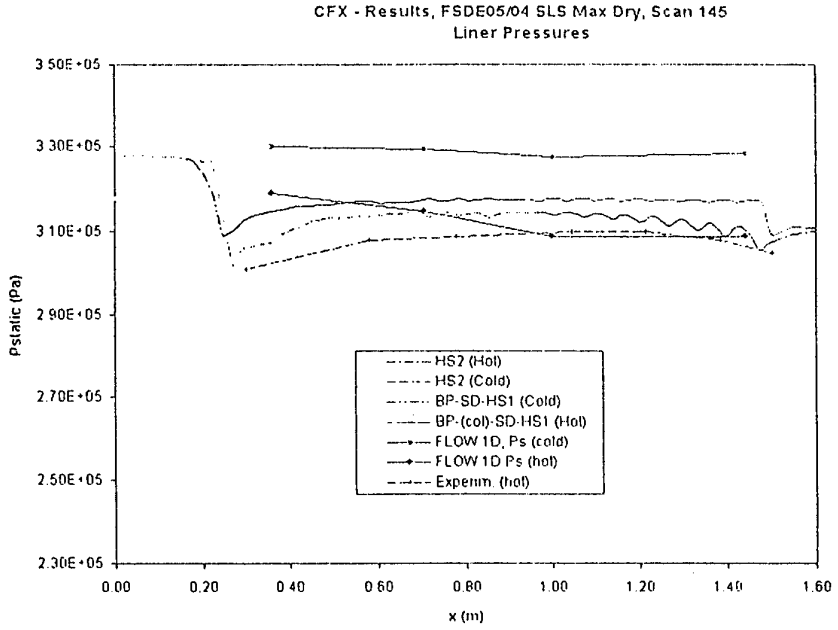

Fig. 15a - SLS - Max Dry - CFD computed static pressure vs. Engine measured static pressure

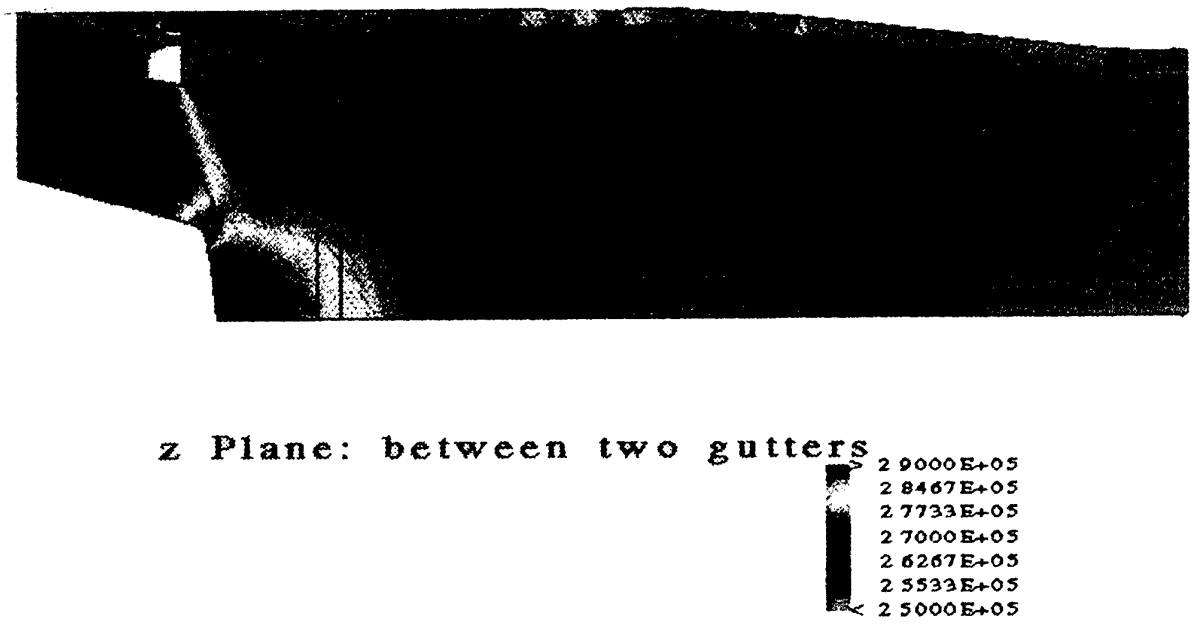

Fig. 13 - SLS - Combat - Pressure field along the plane between two flame stabilisers

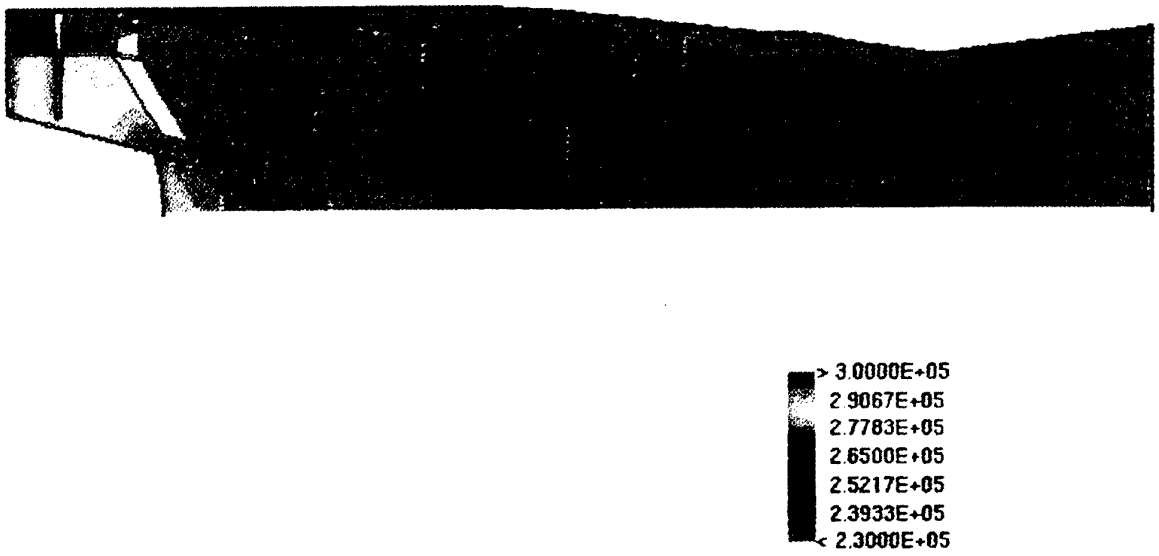

Fig. 14 - z = 36000 ft, M = 1.8 - Pressure field along the flame stabiliser plane

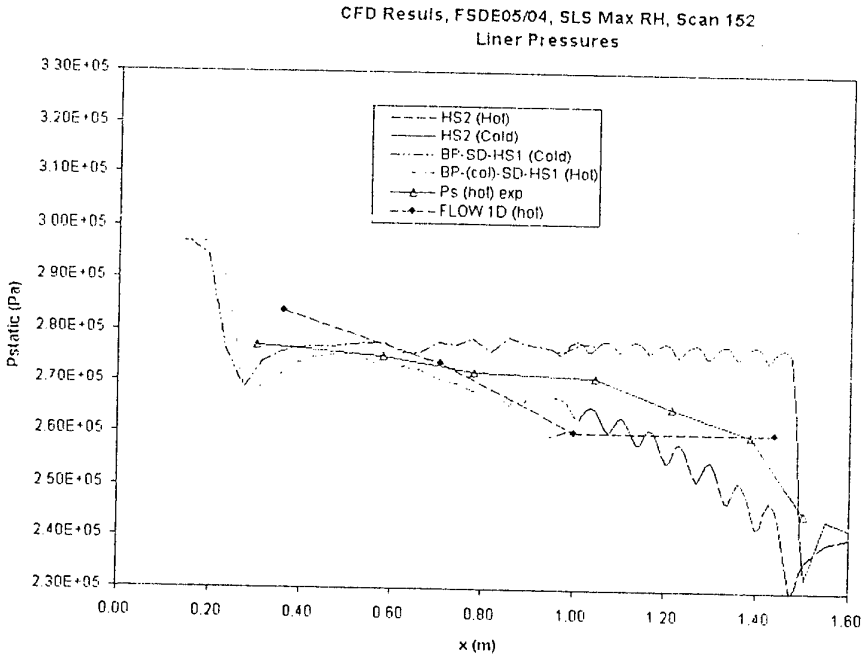

Fig. 15b - SLS - Max R/H - CFD computed static pressure vs. Engine measured static pressure

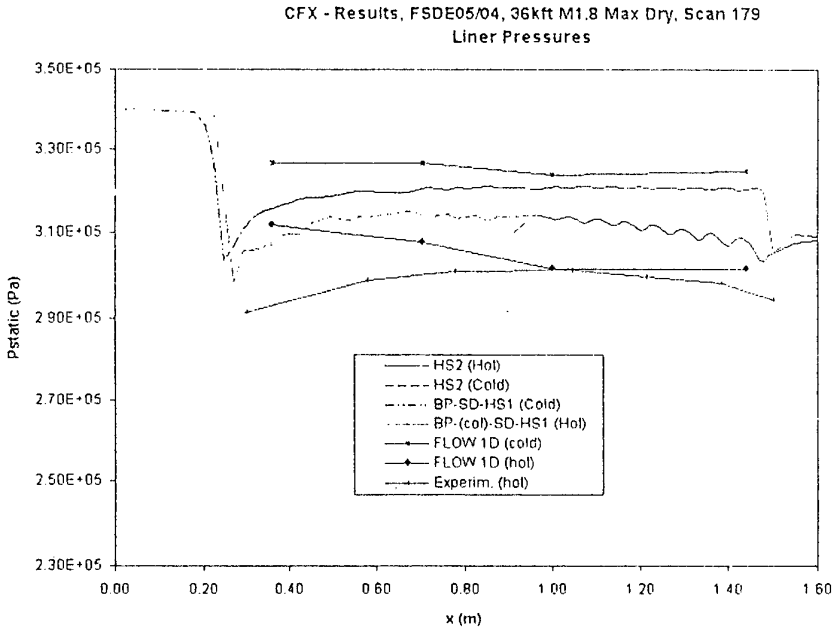

Fig. 15c - 36kft/1.8-Max Dry - CFD computed static pressure vs. Engine measured static pressure

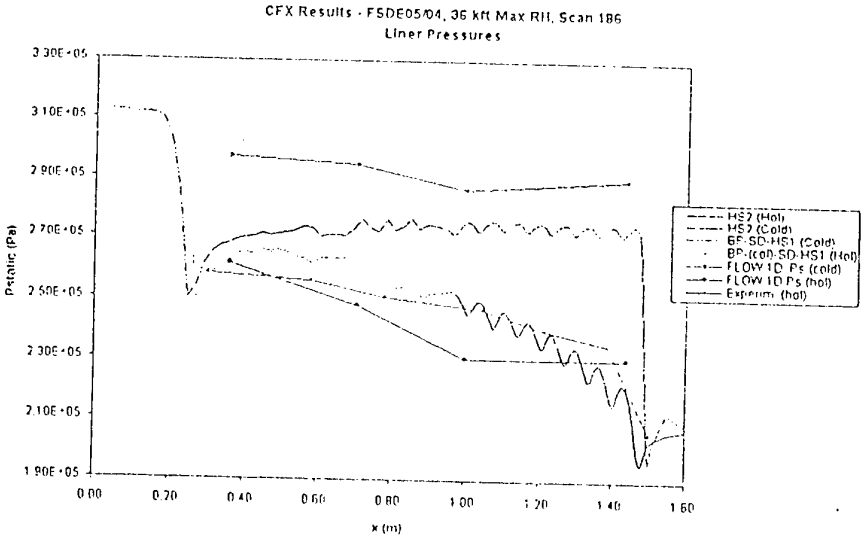

Fig. 15d - 36kft/1.8-Max R/H - CFD computed static pressure vs. Engine measured static pressure

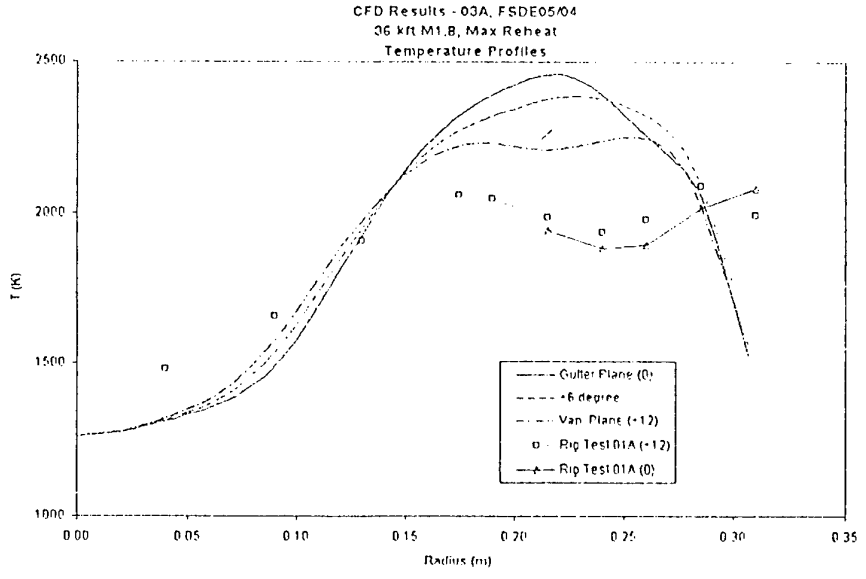

Fig. 18 - 36kft / M=1.8 - Max Reheat - CFD computed vs. Engine measured temperature profiles

36 kft M1.8, RH, Scan 186

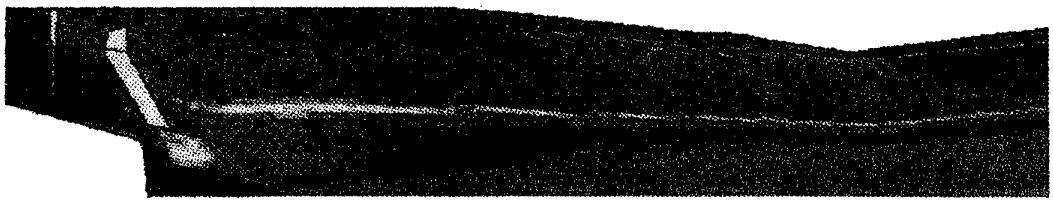

Evaporated Fuel Field

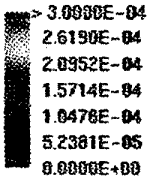

Fig. 16 - 36kft / M=1.8 - Max Reheat - CFD computed evaporated fuel distribution

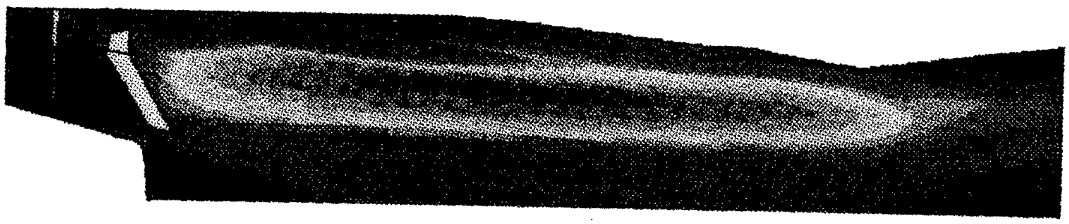

Temperature Field (K)

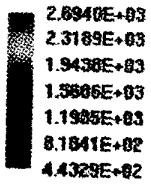

Fig. 17 - 36kft / M=1.8 - Max Reheat - CFD computed temperature field

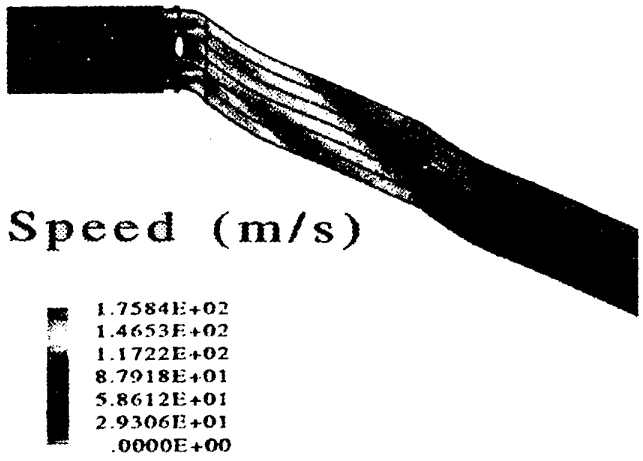

Fig. 19 - Liner Cooling Annulus - CFD computed flow velocity field

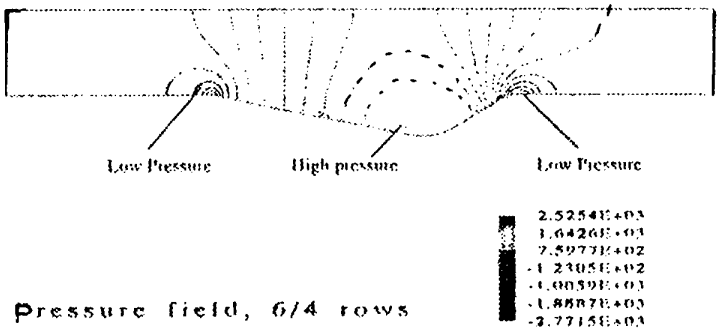

Fig. 20 - Corrugated Heat Shield - CFD computed static pressure distribution

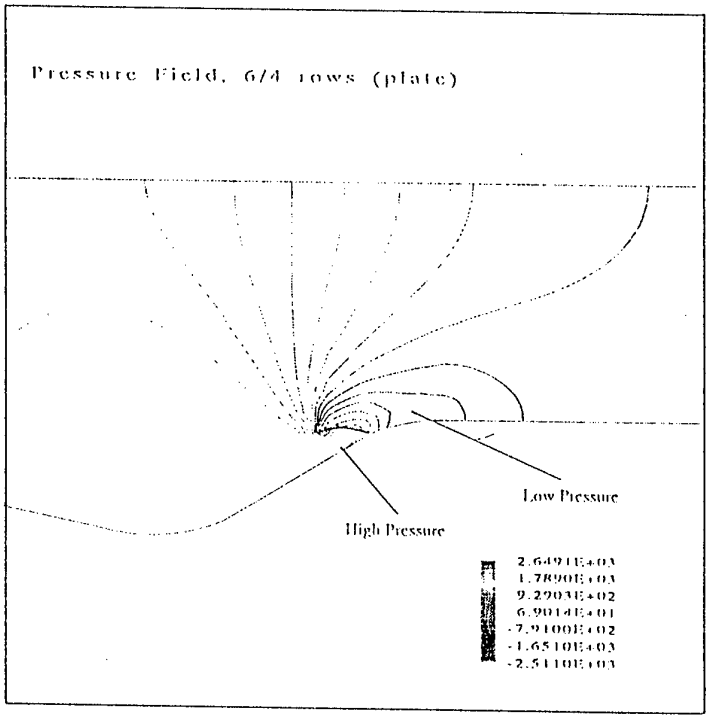

Fig. 21 - Modified Heat Shield Cooling - CFD computed static pressure distribution

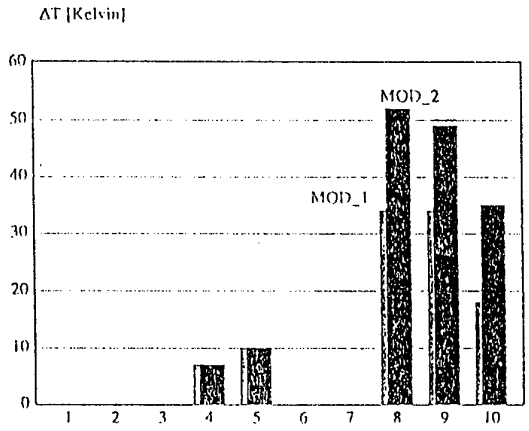

Fig. 22 - Heat Shield - Computed Metal Temperature reduction with modified configurations

Meeting Discussions

Paper 19: **Afterburner Design and Development**

Authors: A. Trovati, F. Turrini, C. Vinci

Discussor: B. Steinetz

Question: What is your liner material?
Are you using a thermal barrier coating?
What thermal barrier coating?

Author's reply: Liner material is Cobalt/Nickel alloy.
Thermal barrier coating is ZrO_2 based with NiCoCrALy type anchoring layer.
It is used on flameholder rear wall and on screech damper and heat shield hottest zones (Mass penalty prevented to apply thermal barrier coating all along the liner).

Discussor: Saeed Farokhi

Question: The effect of stagger angle on cooling effectiveness is due to streamwise vortex generation which would be absent in unstaggered ribs. Is that right?

Author's reply: Yes, the staggered vortex rows generated by the ribs give the best effects in terms of flow turbulence and convective heat transfer.

A mixed flow turbofan afterburner simulation for the definition of reheat fuel control laws

Joachim Kurzke
MTU München GmbH
Engine System Simulation TPSZ
Dachauer Str. 665
80995 München
Germany

Claus Riegler
Deutsches Zentrum für Luft- und Raumfahrt e.V.
Institut für Antriebstechnik
Linder Höhe
51147 Köln
Germany
Presently working at MTU München, TPSZ

1 Motivation

The afterburner fuel flow control for mixed flow turbofan engines is a complex task. At a given nozzle area, burning too much afterburner fuel can throttle the fan until it surges. On the contrary - when not enough heat is released - the fan pressure ratio will decrease, and the gas velocity in the jet pipe will rise with the danger of blowing out the flame. Ideally, the operating point of the fan in its map should not be affected by the afterburner operation.

Two different methods are in use to achieve this at least approximately. In some engines the afterburner fuel flow is controlled 'closed loop' so that a prescribed fan pressure ratio is achieved. The problem with this approach is that in case of an unexpected afterburner ignition delay the nozzle will close with the aim to keep the fan pressure ratio at the target level. When the afterburner fuel ignites in such a situation unexpectedly the nozzle probably cannot open quickly enough and therefore the pressure in the afterburner will rise sharply. This can result in a fan surge.

The problem described can be avoided from principle with an 'open loop' afterburner fuel control. With this system the pilot selects a nozzle area and the afterburner fuel flow is calculated within the control system as a function of the measured nozzle position. The fuel injected into the afterburner will heat the exhaust gas so that the desired fan pressure ratio is achieved. However, there is no feedback of a pressure signal into the afterburner fuel flow control. Therefore an ignition delay will not cause the nozzle to close, and there is no danger of a fan surge when the fuel finally ignites.

With the open loop afterburner fuel control one obviously needs a precise method to calculate the fuel flow from the control system inputs. When the heat release of the injected afterburner fuel is too high then the fan surge margin will be less than wanted. On the other side, when the heat release is lower than desired then this can cause a loss of thrust. Any inaccuracy of the fuel schedules and the fuel metering units will directly affect the thrust, specific fuel consumption and fan surge margin.

Deducing the afterburner control laws from sea level and altitude tests with an engine is neither practical nor economic. Therefore, the nozzle area and fuel flow schedules must be derived from a simulation model. Any deficit in this model requires an additional fan surge margin for safety reasons in some flight conditions, and - in other flight conditions - an additional turbine inlet temperature margin to compensate for potential thrust losses.

The first aim of the control system must be safe operation of the engine and consequently the simulation model must predict the fan operating point as precisely as possible.

Setting up a good simulation model requires much more than an accurate description of the afterburner burning efficiency. In fact, all elements of the model have a direct or an indirect impact on the calculated fan surge margin. In a paper like this there is not enough room to go through all elements of a mixed turbofan simulation model in detail. We concentrate here on the component models for afterburner and nozzle, and describe their calibration and verification with engine test results.

Paper presented at the RTO AVT Symposium on "Design Principles and Methods for Aircraft Gas Turbine Engines", held in Toulouse, France, 11-15 May 1998, and published in RTO MP-8.

2 Design of the simulation model

Within the Eurojet consortium, MTU has the lead for the development of the Digital Engine Control Unit (DECU) of the EJ200, a mixed flow turbofan engine for the Eurofighter aircraft (ref. 1). The afterburner fuel control is designed in such a way, that the pilot lever sets the nozzle position, and the DECU calculates the suitable amount of fuel injected into the afterburner. There is no pressure feedback signal, and we have an "open loop" afterburner fuel control system. The algorithms within the DECU are derived from an engine simulation and verified with engine tests.

At MTU we use the **M**odular **P**erformance **S**ynthesis program MOPS for the performance simulation of all engines in development (ref. 2). This program allows to build a model of any engine from a set of program modules. For each engine module we have a corresponding module in our simulation program.

2.1 Turbomachinery

The models of the turbomachines use component maps as primary description of their behaviour. Corrections to the values read from the maps are applied for Reynolds number effects. The component maps are valid for known tip clearances and nominal guide vane settings. The differences between the rig and the in-engine tip clearances are taken into account, and equally the differences between the Variable Guide Vane (VGV) setting for which the rig map is valid and the VGV setting in the engine. Other elements of the model are a mathematical description of the external gearbox power requirements and the secondary air system.

2.2 Afterburner

A schematic longitudinal section of the EJ200 afterburner is shown in figure 1. The thermodynamic station 6 is downstream of the low pressure turbine (LPT) exit guide vanes. Along the exhaust cone upstream of the radial gutters the flow is decelerated. The black bars show the position of the core stream fuel injectors.

Bypass fuel injectors are in the 'colander' throat area (station 161). The term 'colander' was inherited by the EJ200 from an early design feature of the RB199 afterburner. Just upstream of the station number 161 there is the third fuel injection location which is called 'primary'.

Along the afterburner wall the screech damper is followed by the liner.

2.2.1 Flow distribution

The air entering behind the liner is a significant portion of the bypass flow in station 16. One part of it flows through the screech damper (W_{168}), and another part flows through the cooling air holes of the liner. The rest serves as nozzle cooling air (W_{169}). The gutter cooling air W_{611} is mixed with the core flow W_{61} and this yields W_{63}. W_{63} and W_{163} are combined to the single stream W_{64}. In the simulation model, all three afterburner fuel flows are burned together between stations 64 and 7.

When the afterburner is lit, then the static pressure on the mainstream side of the liner is lower than in dry operation and therefore the cooling air flow through the screech damper and the liner increases compared with dry operation.

2.2.2 Pressure losses

The pressure losses in the afterburner have an impact on the fan surge margin for a given nozzle area. Getting this element of the simulation right is important.

2.2.2.1 Dry

The pressure losses of the LPT exit guide vanes, and the exhaust diffusor with the fuel injectors and the gutters depend only on the LPT exit flow Mach number and the flow angle. Both these quantities are directly related to the operating point in the LPT map. It is assumed, that all the core stream pressure losses have happened upstream of station 63.

The pressure losses in the bypass stream are more difficult to describe. They depend on the corrected flow through the colander throat and through the screech damper. In station 163 the mass flows through the colander and the screech damper are combined. Similarly to the core stream assumption, all pressure losses are included in P163.

The conditions in station 64 are found from calculations assuming conservation of momentum, energy and mass flow in a frictionless duct with constant flow area. We have no pressure losses in our model downstream of the mixing plane 64 when the afterburner is not lit.

2.2.2.2 Reheat

Heat addition in a duct causes a loss in total pressure. Assuming a constant effective burning area makes it easy to calculate this fundamental pressure loss from conservation of momentum, mass flow and energy.

2.2.3 Heat addition

In three locations fuel is injected into the EJ200 afterburner. During a thrust modulation from minimum to maximum reheat first the primary zone is ignited. Next the fuel to the gutter region (i.e. the core stream) is added and the amount is increased to a certain level. Last, the colander fuel injectors start to operate and supply an increasing portion of fuel to the bypass stream.

In the simulation, we describe the reheat burning efficiency without going into the details of the three different burning zones. However, we make a difference between low and high fuel-air-ratios. At the lower end reheat efficiency depends on the injected reheat fuel-air-ratio, and at the upper end it varies with the total fuel-air-ratio.

Other factors with influence on the reheat efficiency in our simulations are the bypass ratio and the pressure P_{s64} in the jetpipe.

In the model, the heat addition commences with the fully mixed temperature T_{64}. From the total injected fuel flow only the part $\eta_{RH}*W_{RH,inj}$ is releasing heat.

2.3 Nozzle

Understanding and simulating the nozzle correctly is most important for a high quality model. The effective flow area is directly related to the fan surge margin. Furthermore, the nozzle thrust performance assumptions influence the analysis result for the afterburner efficiency.

2.3.1 Geometry

When we want to understand the performance of a variable convergent-divergent nozzle, then we need a precise description of its geometry for all positions (fig. 2). The nozzle geometry model uses the primary petal angle, and the temperatures of the cooling air and of the main stream as input. Thermal expansion of the primary master petals causes opening of A_9 because the length of the strut that holds the divergent petals remains practically unaffected by the temperature of the gas inside the nozzle. The model gives the geometric values for the throat area A_8 and the exit area A_9, and thus the geometrical nozzle area ratio A_9/A_8, for any operating condition.

Once the geometry is found, the static pressure along the nozzle inside is calculated. In the convergent part the static pressure along the wall can be determined from the local area ratio with simple isentropic relationships. In the divergent part the wall pressure that is found from the isentropic formula needs some correction, see ref. 3.

The pressure differences between the inside and the outside of the nozzle are integrated along the petals. This yields the forces at the petals, the hinges, and in the struts that hold the secondary petals.

The leakage through the hinges and between the master and the slave petals depends on the difference between the pressures within and around the nozzle. As long as the pressure outside the nozzle is lower than inside, the effect of leakage is primarily a small loss of thrust. However, there are many operating conditions, as for example sea level static, where the static pressure in the nozzle throat and the divergent part of the nozzle is lower than the pressure outside and consequently air is sucked in.

During an engine test one can easily identify when inside the divergent part of the nozzle the pressure is lower than outside. Figure 3 shows that the slave petals are sucked in and a gap opens between the master and the slave petals. This has an impact on the effective nozzle area ratio $(A_9/A_8)_{eff}$ which in turn influences significantly the nozzle thrust.

2.3.2 Performance

There are several alternatives for describing the thrust performance of the mixer and the nozzle. Traditionally, the thrust loss due to incomplete mixing of the core and the bypass stream is described by mixing efficiency:

$$\eta_{mix} = \frac{F_G - F_{G,unmixed}}{F_{G,fullymixed} - F_{G,unmixed}}$$

The application of η_{mix} requires the calculation of the unmixed thrust, i.e. the separate expansion of the cold and the hot stream. This makes the nozzle calculation quite complex because first one has to find some artificial (unmixed) nozzle inlet condition. Second, one has to decide, how to divide the available effective nozzle throat area between the streams. Third, the result of this type of calculation is not consistent in itself.

Using the fully mixed flow at the nozzle entry as a reference is much simpler. Losses due to incomplete mixing are taken into account by correction factors to the reference flow conditions.

The performance of a convergent-divergent nozzle can be characterized by a suitably defined thrust coefficient. The ideal thrust coefficient C_{FGI} compares the actual thrust with the one produced by an ideal expansion to ambient pressure, whatever the nozzle area ratio is. C_{FGI} equals 1 only when there are no losses and the nozzle area ratio fits to the pressure ratio. This definition of a thrust coefficient is well suited for nozzle design studies, but not very practical when the nozzle geometry is given.

With given geometry, we cannot expect the nozzle to produce more thrust than that found from an ideal expansion to the present area ratio A_9/A_8. At the nozzle exit the static pressure may be higher (the flow is underexpanded) or lower (the flow is overexpanded) than the ambient pressure. When the nozzle pressure ratio is low, then the ideal expansion postulates a vertical shock in the divergent part, and at very low nozzle pressure ratios the flow becomes subsonic throughout the nozzle.

The flow conditions calculated for an ideal expansion to the given nozzle exit area A_9 serves in our simulation as a basis for the judgement of the nozzle performance. The gross thrust is calculated from

$$F_G = W_9 * C_A * C_f * C_{V9} * V_9 + (P_{s,9} - P_{amb}) * A_9$$

In this formula C_A is the angularity coefficient from ref.4, fig. 5.12 that takes the losses due to the non axial exit of the exhaust gases from the nozzle into account. The coefficient C_f from ref.4, fig. 5.13 accounts for the effects of boundary-layer momentum loss caused by friction in the nozzle. Both these coefficients depend on the nozzle area ratio and the primary petal angle.

We use the velocity coefficient C_{V9} as a measure for the nozzle efficiency. Note that this coefficient describes mainly the losses due to the incomplete mixing of the core and the bypass stream and the losses due to nozzle cooling.

2.3.3 Effective flow areas

For the calculation of the flow in the nozzle we need correlations between the geometric and the effective flow area. The nozzle throat flow coefficient $C_{D8}=A_{8,eff}/A_{8,geo}$ of a convergent-divergent nozzle varies only with the primary petal angle if the pressure ratio is above a certain limit, ref. 4, fig.5.7. This has been checked by our Spanish partner company ITP in the EJ200 project with comprehensive CFD calculations assuming different radial temperature and pressure profiles.

For high nozzle pressure ratios we assume that the nozzle exit flow coefficient C_{D9} is constant and equal to 0.995. When the nozzle pressure ratio is low, and the pressure inside the divergent part of the nozzle is lower than ambient pressure, the slave petals are sucked inwards and open slots between the master and the slave petals. Outside air flows into the nozzle and this affects both C_{D8} and C_{D9}.

A very important measurement used also for engine control purposes is the static wall pressure at the nozzle inlet $P_{s7,wall}$. Due to the local streamline curvature (which depends on the primary petal angle) the wall pressure does not show the representative mean static pressure in station 7. CFD calculations of our Spanish partners did produce correlations between $P_{s7,wall}$ and $P_{s7,mean}$ and also the flow area blockage coefficient C_{D7}, see figures 4 and 5. From this we can derive the mean total pressure P_7 at the nozzle inlet. It will be shown by comparison with measured data that P_7 derived from $P_{s7,wall}$ is a reliable, consistent and reasonable value.

3 Calibration of the simulation model

The simulation model described in chapter 2 is used to analyse engine test data resulting from dry and reheat operation at various flight conditions. The aim of the analysis work is to verify the modelling assumptions respectively to derive improved models fitting better to the test data. With the help of such an improved model reliable simulations may be carried out, for example, to define reheat fuel control laws.

3.1 Turbomachinery

For the compressors mean total pressure and temperature measurements are available upstream and downstream of the LPC and the HPC. In the turbine section of the engine, however, due to very high gas temperatures and due to severe pressure and temperature profiles measuring representative mean values is very difficult.

The total mass flow W_2 entering the engine is known from a venturi measurement upstream of the engine which is usually very precise. However, the mass flow W_{25} entering the core engine is not measured and thus has to be determined by any core flow analysis method.

3.1.1 Analysis by Synthesis

The main idea of Analysis by Synthesis (ANSYN) is to match an engine simulation model to test data automatically. This is done by scaling factors, which are applied to the component models to close the gap between calculated and measured component performance. For example the operating point of a compressor in its map is given by corrected spool speed $N/\sqrt{T}$ and specific work over speed squared dh/N^2, which both can be derived from measurement only. The corrected mass flow and the efficiency in the model are calculated using the compressor map and corrections for example for Reynolds number effects. The scaling factors then result as the particular ratio of measured to calculated value. Figure 6 shows as an example the scaling factor for the HPC efficiency versus corrected HPC spool speed resulting from the analysis of many scans. The small scatter of the scaling factor shows that the HPC efficiency model accounts for the most important physical phenomena and may be used for high quality performance predictions over a wide range of engine ratings and flight conditions.

3.1.2 Core flow

The flow W_{25} entering the core may be determined by several core flow analysis methods from which the "turbine capacity method" and the "heat balance method" are most common. In this paper the core flow is calculated using the known capacity of the HPT.

For the interpretation of analysis results one should keep in mind that all calculated quantities downstream of the HPT nozzle guide vane throat and downstream of the LPC in the bypass stream depend on the mass flow W_{25} entering the core and therefore on the core flow analysis method.

3.1.3 Afterburner inlet conditions

From the core mass flow, the burner fuel flow W_F and the measured burner inlet total temperature T_3 the HPT nozzle guide vane throat total temperature T_{41} results and with the known HPC power the interturbine total temperature T_{45} can be calculated. From the known capacity of the LPT the interturbine total pressure P_{45} is derived. For the LPT the power respectively the specific work is known from LPC yielding the total temperature T_5 downstream of the LPT. Due to the low accuracy of the measured total pressure P_5 this measurement is ignored and instead the LPT efficiency calculated from the map is used to derive P_5. The bypass mass flow is calculated from W_2 and W_{25}. The total pressure P_{161} and the total temperature T_{16} at bypass afterburner inlet are measured values. As can be seen from the description above most of the afterburner entry values depend on the core flow analysis method and on the LPT performance. Due to this fact for a precise afterburner and nozzle performance analysis a proper modelling of the turbomachinery, especially of the turbines, is very important.

3.2 Afterburner and Nozzle

3.2.1 Principle of the analysis method

There are many measurements in and around the afterburner. Not all of them give realistic mean values because sometimes there are only a few probes in regions with severe pressure and/or temperature profiles. For example, the measured total pressure P_5 downstream of the low pressure turbine (LPT) exit has a significant tolerance because the wakes of the relatively big LPT inlet guide vanes affect the probe readings.

One of the most consistent measurements is the static wall pressure $P_{s7,wall}$ at the nozzle inlet which allows to derive an accurate value for $P_7 = P_8$. Another high quality measurement is the total pressure P_{161} in the colander throat. This probe is in a region of accelerating flow which tends to level out any total pressure disturbance.

The test analysis uses P_7 and P_{161} as anchors for the calculation procedure. The measured mean value for P_5 is replaced in the test analysis by a calculated value that is consistent with the knowledge about the turbine performance. The mass flow and the total temperature at the inlet to the afterburner are known from the turbomachinery analysis.

With these assumptions we have values for the total pressures at the inlet and the exit of the afterburner. The core stream pressure loss can only depend on the LPT exit flow conditions. When we assume a loss characteristic for the core flow, then we have only one quantity left to reconcile the model with the measured pressures: this is the pressure loss coefficient of the colander flow.

We look simultaneously at many operating conditions of the engine. When the analysed colander pressure loss coefficient is the same for all test conditions then we have found a good simulation model. We can influence the analysis result by modifying the assumptions about the core stream pressure loss and by different interpretations of the turbine performance, i.e. using a different turbine exit pressure. The art of test analysis is to reconcile all various pieces of information from measurements and theoretical considerations.

The method we use is very sensitive because all uncertainties are shifted to the colander pressure loss coefficient. In the simulation this coefficient affects only a minor part of the

total afterburner mass flow. Therefore, a certain scatter in the analysed colander pressure loss coefficient is unavoidable.

3.2.2 Dry operation

When the afterburner is not lit then we can unambiguously calculate the nozzle inlet flow conditions. Applying the law of conservation of energy to the total engine inlet mass flow and the main burner fuel flow yields the nozzle inlet total temperature. Note that the result of this calculation does not depend on bypass ratio or turbomachinery performance.
The nozzle inlet total pressure P_7 can be found accurately from the static pressure measurement $P_{s7,wall}$ on the liner. From the known values W_8 (includes the nozzle cooling air W_{169}, see fig. 1), T_8 and $P_8 = P_7$ we can calculate the effective nozzle throat area $A_{8,eff}$. We know that when the nozzle pressure ratio is high enough the discharge coefficient C_{D8} depends only on the primary petal angle. Thus, we can unambiguously calculate the geometric nozzle throat area for all operating conditions with high nozzle pressure ratios.
There is also the control system input of the nozzle throat area ($A_{8,DECU}$) available for test analysis. This area is derived from the axial position of the moving actuator ring (see figure 1). In this area measurement chain are more unknowns than in the thermodynamic method described above. It will be shown, that there can be a significant deviation between the true and the indicated nozzle throat area.

3.2.2.1 Operation with high nozzle pressure ratios

Figure 7 shows the analysed nozzle velocity coefficient C_{V9} from engine tests over a wide range of engine ratings, altitudes and flight Mach numbers. When the nozzle pressure ratio is higher than 3.5, the velocity coefficient is a unique value of 0.99. The deviation from the ideal value of 1.0 describes the incomplete mixing of the core with the bypass stream and also losses due to nozzle cooling.

3.2.2.2 Operation with low nozzle pressure ratio

Why is C_{V9} increasing in figure 7 when the nozzle pressure ratio falls below around 3.5...4 ? The calculated force in the struts holding the secondary petals becomes negative, see figure 8. A negative strut force means that the divergent master petals are pulling on the struts because the pressure inside the divergent part of the nozzle becomes lower than ambient. Under these conditions the slave petals detach from the master petals. This can clearly be seen in figure 3. Air flows from outside into the nozzle and reduces the effective nozzle exit area. This leads to a better match of the effective nozzle area ratio to the low pressure ratio, and the nozzle performs better than calculated with the standard assumption C_{D9}=0.995.
In figure 9 this is illustrated with the help of the ideal thrust coefficient C_{FGI} mentioned in chapter 2.3.2. For example, when the flow would follow at a nozzle pressure ratio of 2.4 the geometric nozzle area ratio of 1.35, the ideal thrust coefficient C_{FGI} would be 0.95. In this situation a detachment of the flow in the divergent part of the nozzle leading to an effective area ratio of 1.20 would improve the thrust by 3%.
On some development engine nozzles we have a static pressure pickup (named S0565H) fitted near to the nozzle exit. Figure 10 shows $S0565H/P_{amb}$ plotted over the nozzle pressure ratio P_7/P_{amb}. There are also lines for A_9/A_8 = const. derived from the one-dimensional theory which extend to values of P_{s9}/P_{amb} well under 1.0. The measured pressure ratio $S0565H/P_{amb}$ is never lower than 0.91 in this set of data. One can use these data as a basis of an empirical correlation for C_{D9}. We make the hypothesis that the nozzle throat controls under all operating conditions the flow. We postulate thus that the effective nozzle area ratio is never lower than 1.0. The nozzle operates at pressure ratios less than 1.8 (i.e. the pressure ratio corresponding to sonic conditions) as a convergent nozzle does. This hypothesis fixes the point A in figure 10. At higher nozzle pressure ratios than 1.8 there is a trend in the measured data $S0565H/P_{amb}$ towards lower values. We follow this trend with the curve marked P_{s9L}/P_{amb} in figure 10. Along this curve we find unique values for A_9/A_8 as a function of nozzle pressure ratio P_7/P_{amb}.
The limiting curve $P_{s9L}/P_{amb} = f(P_7/P_{amb})$ in our simulation is applied as follows. First we calculate with the assumption of C_{D9}=0.995 a theoretical value for P_{s9}. When P_{s9}/P_{amb} is above the limiting line in figure 10, then we have found the solution for C_{D9}. When P_{s9}/P_{amb} is lower than P_{s9L}/P_{amb} we take $(A_9/A_8)_{eff}$ from the limiting curve, derive C_{D9} and recalculate the nozzle exit flow conditions.
With this procedure we get values for the static pressure at the nozzle exit that are never lower than those on the limiting curve. Therefore, we cannot simulate the measured values exactly. However, our primary goal is to describe the nozzle thrust performance. From the analysis of the same engine test data as in figure 7 we get with the revised calculation method for C_{D9} new results for the nozzle velocity coefficient C_{V9}, see figure 11. Now we get a very good collapse of all test analysis results over a very wide range of nozzle pressure ratios.

3.2.2.3 Pressure distribution in the afterburner

Several static pressure pickups are positioned on the mainstream side of the liner. S0568 is found at the end of the screech damper approximately where station 64 is marked in figure 1. Comparing this measured pressure with the static pressure P_{s64} which is found from the stream mixing calculation we find a perfect correlation with a low scatter throughout the dry operating range of the engine, see figure 12. Similar relationships could be shown for the other static wall pressure measurements fitted along the liner.
Thus it is proven, that the theoretically calculated static pressure P_{s64} is very well suited to correlate all static pressures within the jetpipe. It is also a confirmation, that the method of deriving P_7 from $P_{s7,wall}$ yields reasonable results. Moreover it proves indirectly, that the analysed nozzle throat area is correct.

3.2.3 Reheat operation

When the afterburner is lit, then we do no longer have a reliable value for the nozzle inlet total temperature since we do not know the reheat efficiency a priori. Actually, during test analysis we have to find a value for it.

3.2.3.1 Reheat efficiency

For engine test analysis we use the hypothesis, that the nozzle velocity coefficient C_{V9} is the same for dry and reheated operation. By iteration of the reheat efficiency we find T_7 from the measured thrust. Again, as during the test analysis of the dry engine operation, the nozzle area

measurement $A_{8,DECU}$ going into the control system is not directly used.
As a result we get the afterburner "thrust" efficiency $\eta_{RH,F}$ as an empirical correlation with fuel-air-ratio, bypass ratio and jet pipe pressure P_{s64}, see figure 13a-c. By virtue of its derivation, when used in the overall engine simulation $\eta_{RH,F}$ will yield the correct nozzle flow and also the correct gross thrust.
There are other definitions of reheat efficiencies in use. For example, from exhaust gas analysis the local burning efficiency may be found which is defined from chemistry. This definition is of use when the fuel distribution in the afterburner is to be optimized. On the reheat rig, there is no thrust measurement and therefore the reheat efficiency must be derived from the measured nozzle area $A_{8,DECU}$ instead.

3.2.3.2 Pressure distribution in the afterburner

Also when the afterburner is lit, the theoretically evaluated static pressure P_{s64} can serve as an excellent basis for estimating the mainstream static pressure along the liner. Due to the heat addition the gas velocity increases and this causes a drop in static pressure along the liner compared with the value without reheat. The pressure ratio $P_{s64}/S0568$ can be correlated with the temperature ratio T_7/T_{64} over the afterburner (figure 14).

3.2.4 Nozzle area measurement for control purposes

In the last two figures the ratio between $A_{8,DECU}$ and the correct, thermodynamically derived nozzle throat area A_8 is shown over nozzle position (15a) and the nozzle actuator force (15b). Obviously there exist correlations for the control system sensor indication error and it is easy to define an algorithm which corrects this error in the DECU.

4 Summary

The control schedules for a mixed flow turbofan with an 'open loop' afterburner fuel control system can only be derived from a performance model of the engine. Any inaccuracy of the simulation must be covered by safety margins in the afterburner fuel flow schedules. Poorly designed fuel schedules can cause a loss of thrust, and can require additional turbine inlet temperature clearance to compensate for that. However, the main objective of the simulation is to get the fan operating point right, since an inadequate fan surge margin is a safety issue.
All elements of the engine performance model affect the quality of the afterburner fuel flow schedules derived from it. This paper concentrates on the components afterburner and nozzle. The modelling approach is described in detail and verified with engine test data.
The key to a good simulation is a precise model of the convergent-divergent nozzle over the full range of pressure ratios encountered during flight. The nozzle flow characteristic has a big impact on the fan surge margin while understanding the thrust characteristics is a prerequisite for optimising the performance of the engine.

References

1 Design of a new fighter engine - The dream in an engine man's life
A. Schäffler
RTO - Applied Vehicle Technology Panel
Symposium on Design Principles and Methods for Aircraft Gas Turbine Engines
Toulouse, 1998

2 Calculation of installation effects within performance computer programs
J. Kurzke in
"Steady and Transient Performance Prediction of Gas Turbine Engines"
AGARD Lecture Series 183, 1992

3 Aerodynamics Design of Convergent-Divergent Nozzles
R. Rebolo, P. Arredondo, A. Matesanz, A. Velazquez and M. Rodriguez
AIAA-93-2574, 1993

4 Aircraft Propulsion Systems Technology and Design
Edited by Gordon C. Oates
AIAA Education Series, 1989

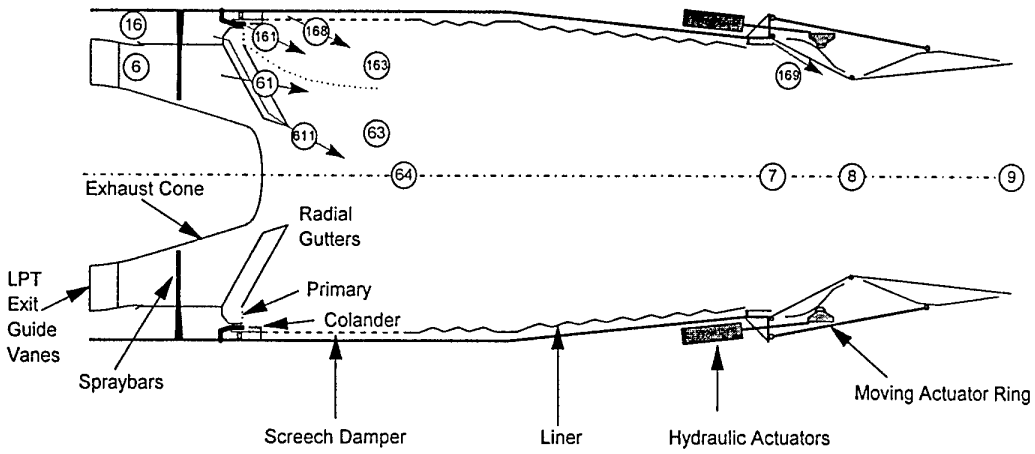

Fig. 1 Longitudinal section of the EJ200 afterburner and nozzle (schematic)

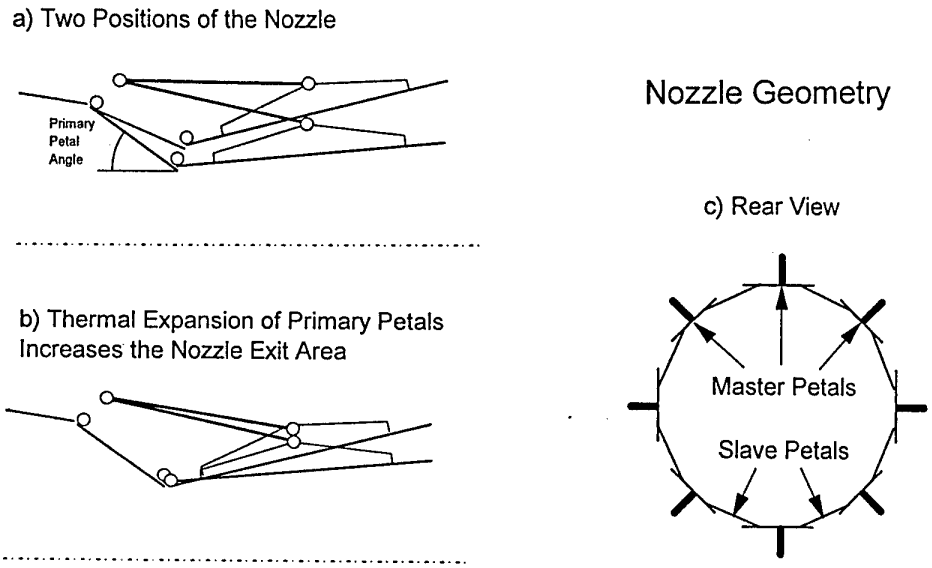

Fig. 2 Nozzle geometry

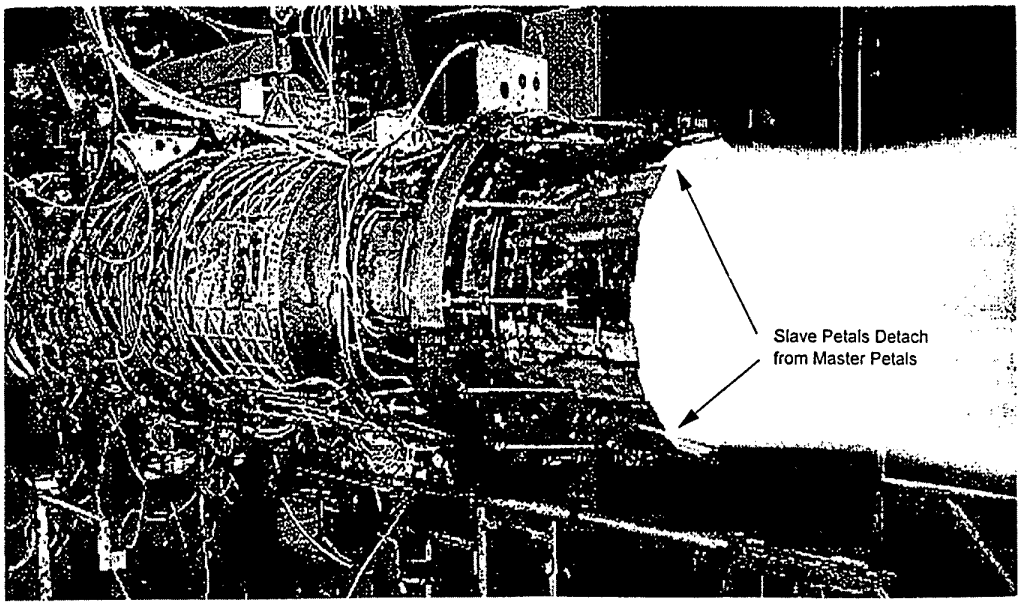

Fig. 3 EJ200 maximum reheat test on a sea level testbed

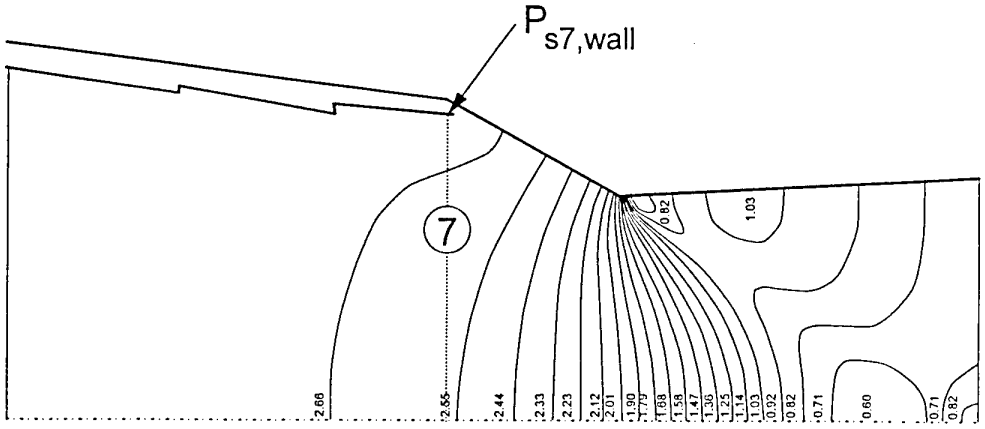

Fig. 4 Static pressure field at the nozzle inlet from CFD calculations

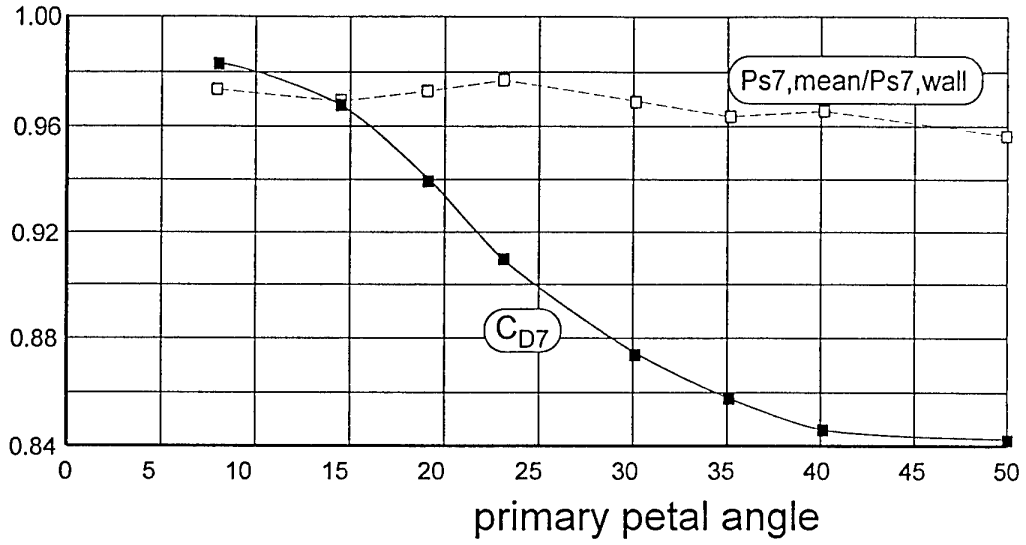

Fig. 5 CFD results for the nozzle inlet blockage coefficient C_{D7} and for $P_{s7,mean}/P_{s7,wall}$ (ref. ITP)

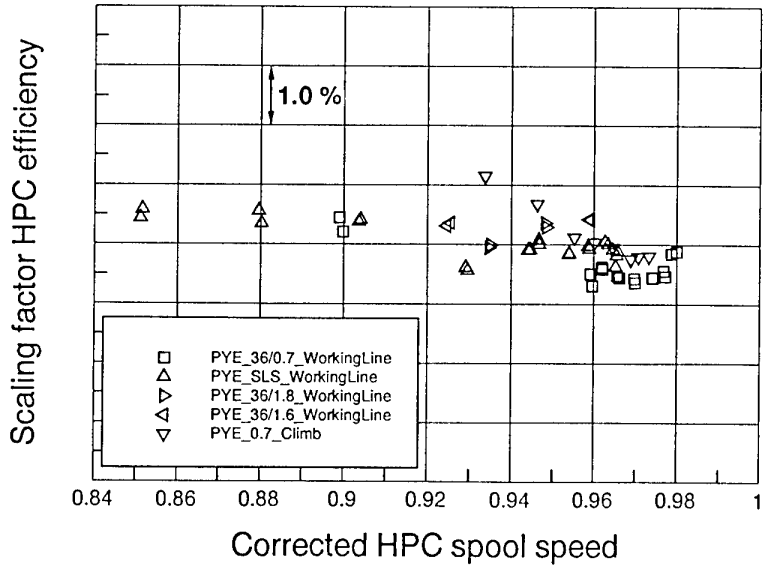

Fig. 6 Example for a component efficiency scaling factor found from engine test analysis

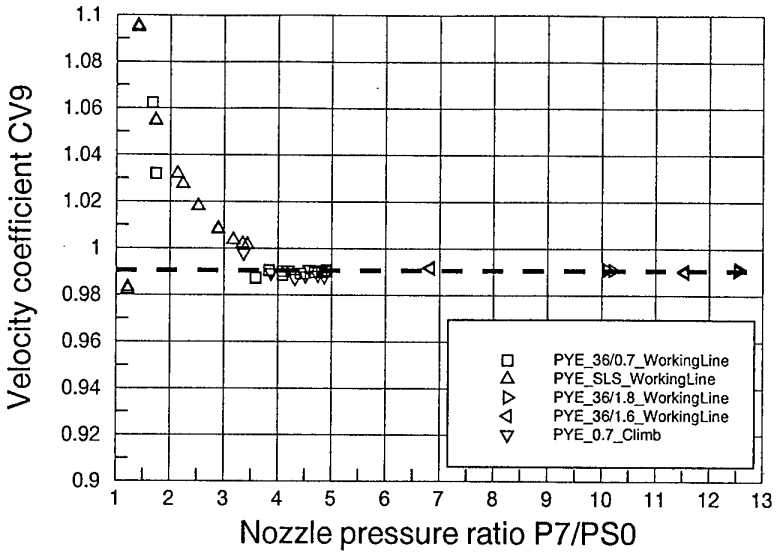

Fig. 7 Preliminary result for the nozzle velocity coefficient C_{V9}

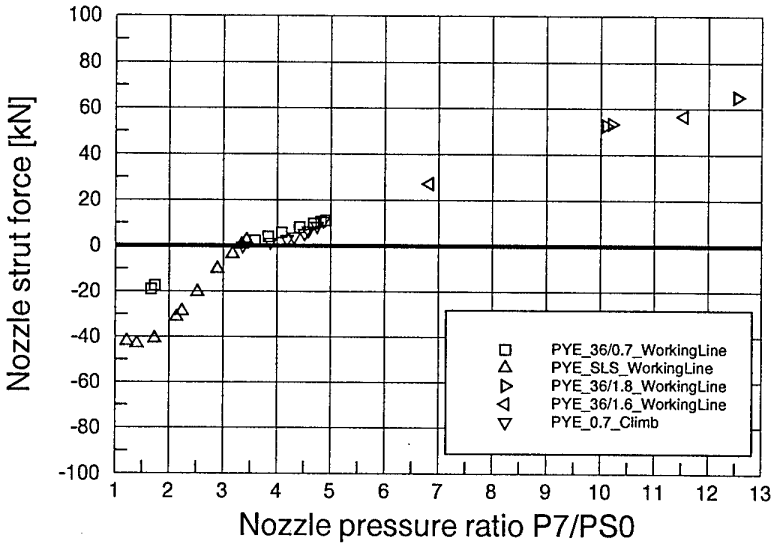

Fig. 8 Nozzle strut force (positive when struts are compressed)

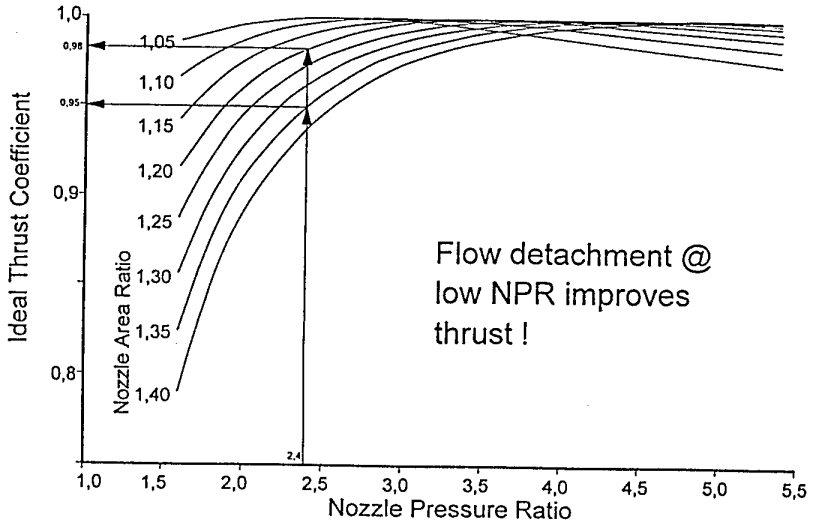

Fig. 9 Thrust gain due to flow detachment at low nozzle pressure ratio

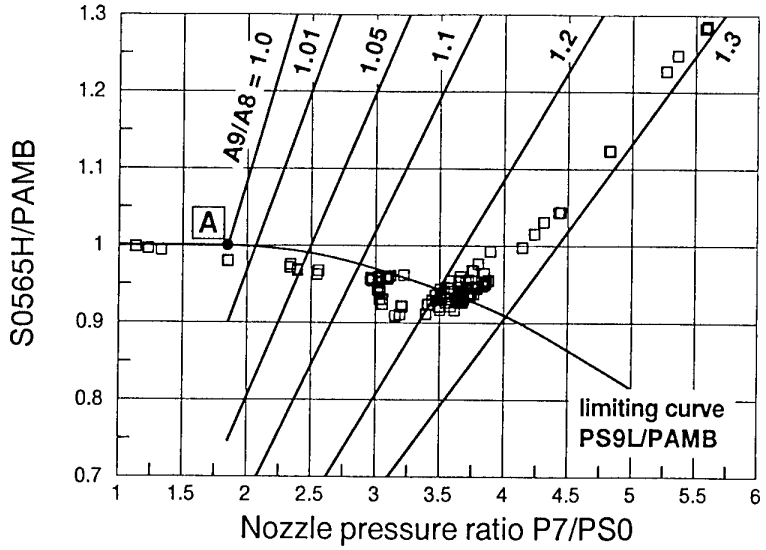

Fig. 10 Measured static pressure near to the nozzle exit

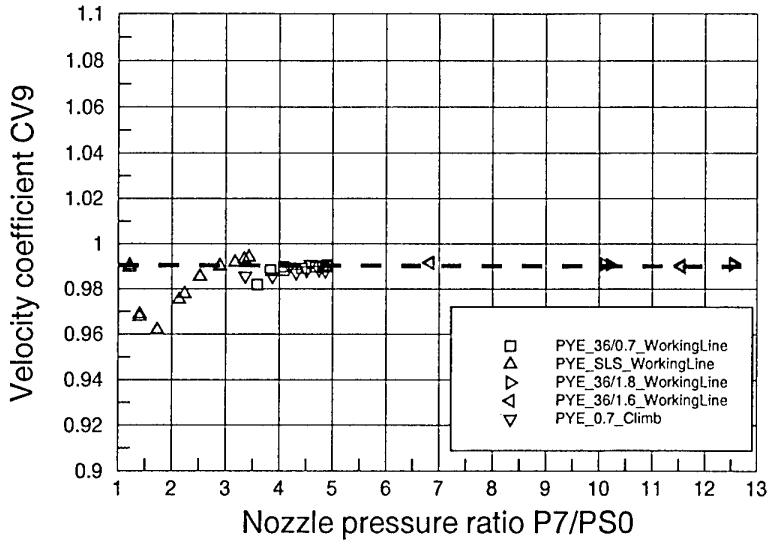

Fig. 11 Revised result for the nozzle velocity coefficient C_{V9}

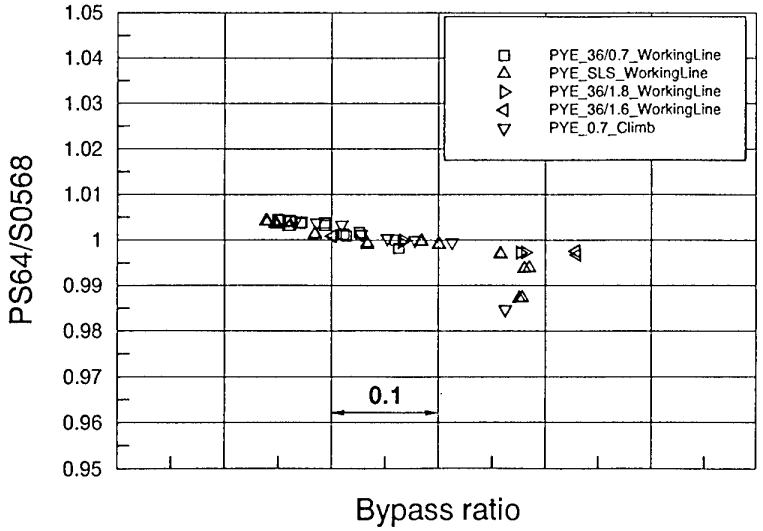

Fig. 12 Correlation between the calculated mixer pressure P_{s64} and the measured pressure S0568 (on the liner) in dry operation

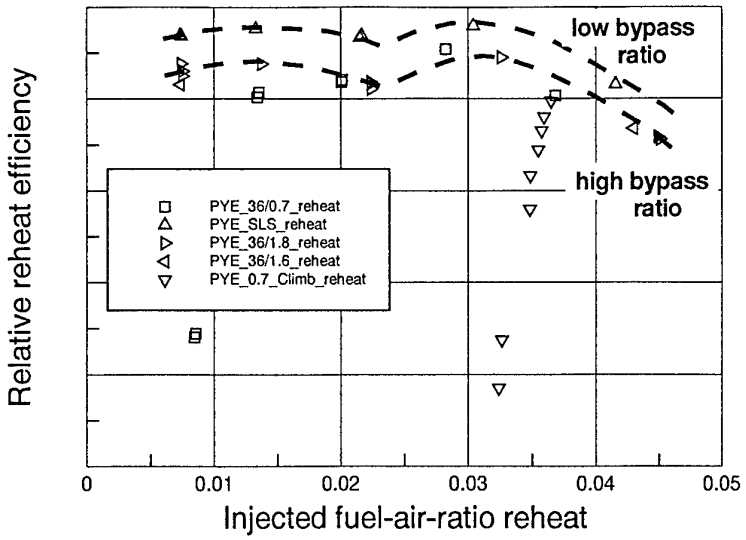

Fig. 13a Relative reheat efficiency: correlation with fuel-air-ratio. The lines for constant bypass ratio are both for the same pressure

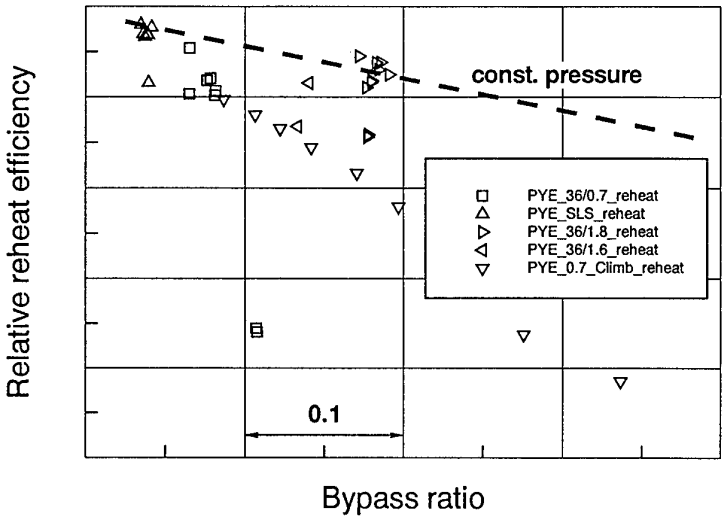

Fig. 13b Relative reheat efficiency: correlation with bypass ratio. Line is for constant pressure and fuel-air-ratio

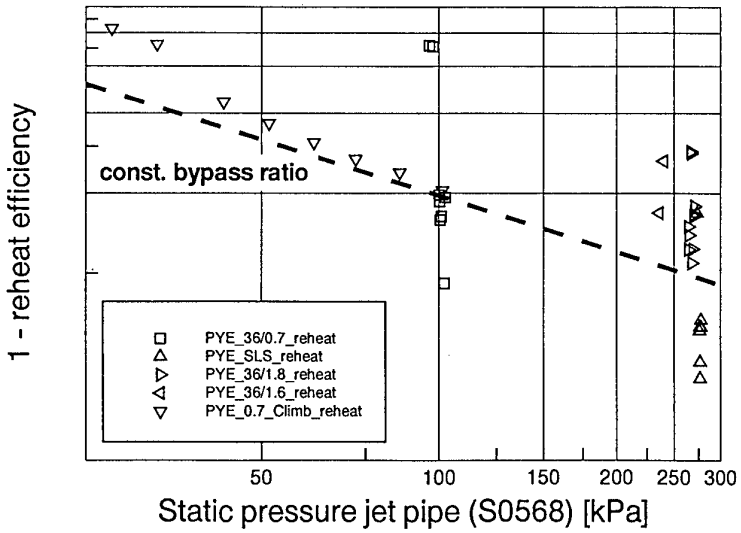

Fig. 13c Reheat efficiency: correlation with pressure. Line is for constant bypass ratio and fuel-air-ratio

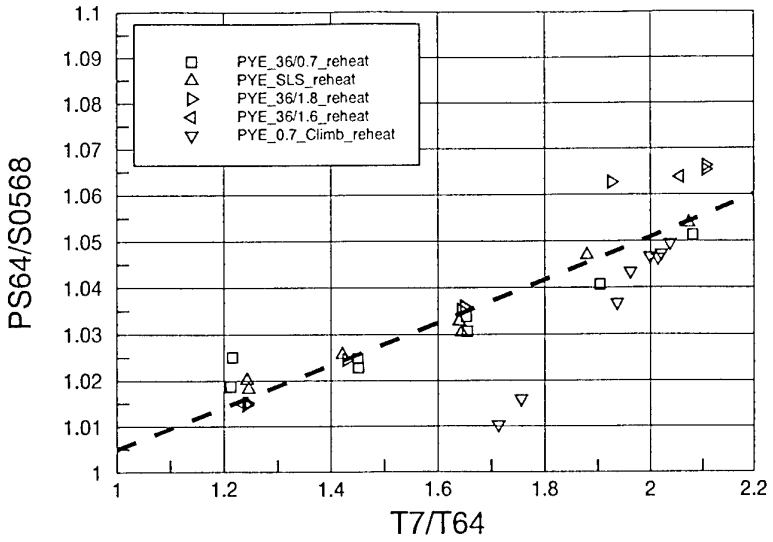

Fig. 14 Correlation between the calculated mixer pressure P_{s64} and the measured pressure S0568 (on the liner) in reheat operation

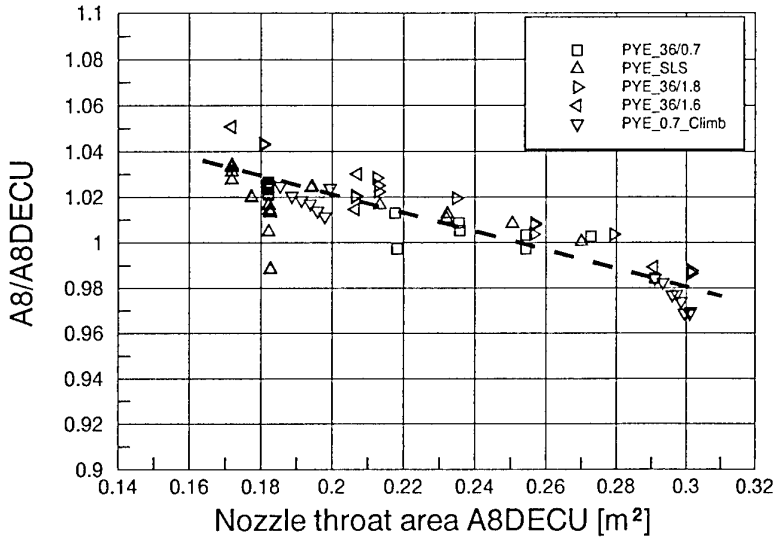

Fig.15a Deviation between the analysed nozzle area A_8 and the control system input $A_{8,DECU}$ correlated with nozzle position

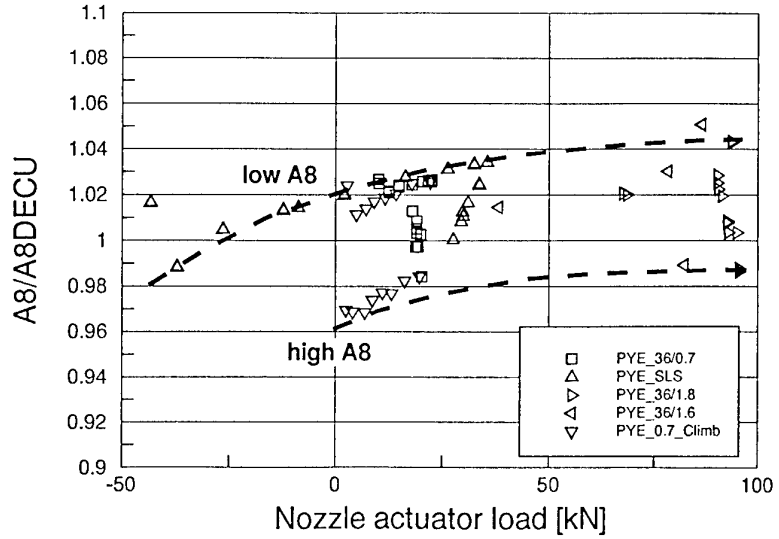

Fig.15b Deviation between the analysed nozzle area A_8 and the control system input $A_{8,DECU}$ correlated with nozzle actuator load

Numerical Simulation of Multi-Stage Turbomachinery Flows

John J. Adamczyk
NASA Lewis Research Center
M.S. 5-9
Cleveland, Ohio 44135, USA

Michael D. Hathaway c/o Adamczyk

Aamir Shabbir c/o Adamczyk

Steven R. Wellborn c/o Adamczyk

ABSTRACT

A comprehensive assessment is made of the predictive capability of the average passage flow model as applied to multi-stage axial flow compressors. The average passage flow model describes the time average flow field within a typical passage of a blade row embedded in a multi-stage configuration. In this work data taken within a four and one-half stage large low speed compressor will be used to assess the weakness and strengths of the predictive capabilities of the average passage flow model. The low speed compressor blading is of modern design and employs stators with end-bends. Measurements were made with slow and high response instrumentation. The high response measurements revealed the velocity components of both the rotor and stator wakes. Based on the measured wake profiles it will be argued that blade boundary layer transition is playing an important role in setting compressor performance. A model which mimics the effects of blade boundary layer transition within the frame work of the average passage model will be presented. Simulations which incorporated this model showed a dramatic improvement in agreement with data.

Paper presented at the RTO AVT Symposium on "Design Principles and Methods for Aircraft Gas Turbine Engines", held in Toulouse, France, 11-15 May 1998, and published in RTO MP-8.

INTRODUCTION

The challenge today for turbomachinery flow analysts is the development of mathematical models which provide a greater degree of resolution of the flow field within multi-stage turbomachinery than today's through flow models. Implied, is the notion that increased resolution will enhance our understanding of the flow processes which control the performance, stability and durability of turbomachinery. It is argued that the enhanced understanding will lead to improved turbomachinery with reduced development time and costs. The increase in flow resolution afforded by any proposed model must be weighted against the computer resources (i.e. measured in terms of CPU time, memory size and costs) associated with executing a CFD simulation and the costs of supporting the empirical data base required to underpin the model. Furthermore these resources must be compatible and readily available to support the design of turbomachinery. The development of such a model is thus a very formidable challenge.

To start the development of a CFD based model for multi-stage turbomachinery one can look to the evolution of CFD models for isolated blade row configurations. The literature on this subject is extensive and its review is far beyond the scope of this paper. However, it is clear that CFD based flow models have had a dramatic and positive impact on the performance of fan rotors for aero-engines. Today fan rotors are designed using viscous 3D CFD models. Based on simulations performed using these models the blade geometry is tailored to control shock location, boundary layer growth and end-wall blockage. It would be highly desirable if such a model could be evolved for multi-stage configurations.

The direct extension of the CFD isolated blade row model to multi-stage configurations is enormously complicated by the fact that neither in the stator nor rotor frame of reference is the deterministic flow steady in time. In addition at a given instant in time the deterministic flow is spatially aperiodic from one passage to another within a wheel. The development of a CFD model capable of capturing all of the time and spacial scales associated with the deterministic flow state within multi-stage turbomachinery is in its infancy and it will be a number of years before such models are used routinely in support of aero-design.

A means of circumventing the problems associated with directly simulating the deterministic flow state within multi-stage machinery is to restrict the resolution capabilities of the model to only those length and time scales associated with flow processes that are explicitly addressed during design. Examples being the build-up of flow blockage, mixing associated with radial transport, and various forms of leakage including bleed and purge. Historically this has been the approach adopted by turbomachinery flow analysts. The classic example being the through flow models in which all time and circumferential length scales have been suppressed by assuming each blade row to have an infinite number of blades. The resulting flow description is axisymmetric and is often referred to as an actuator duct.The effect of a blade row on the flow is introduced through a body force and

unsteady aperiodic flow field on the average-passage flow state.

EXPERIMENT VERSUS NUMERICAL SIMULATION

Experimental Configuration

The experimental data to be used in this study came from measurements taken in the NASA Lewis Large Low Speed Research Compressor. The compressor has four repeating stages plus an inlet guide vane. The geometry of the compressor is outlined in Ref. 5. Both the rotor and stator geometry is representative of modern day aero-engines. The third stage rotor and stator diffusion factor at mid-span are 0.45. The stator design employed end-bends to control the flow field at the hub and shroud. Casing treatment was used over the first stage rotor and was not accounted for in the simulations which are presented. From measurements taken with the casing treatment sealed and unsealed it appears that the casing treatment impacts the performance of the machine at operating conditions near and above peak pressure. Near peak efficiency the impact of the first rotor casing treatment on performance appears to be negligible. The simulated hub flow path was of constant radius while in the compressor only the rotor hubs are of constant radius. The simulations also did not account for the effect of leakage from beneath the stator foot-rings.

Data taken with slow response instrumentation as well as data taken with high response hot-film instrumentation will be presented. In addition some data taken with the leakage gaps beneath the stator foot-rings sealed will be used to supplement the data set taken with the foot-rings unsealed. Flow variables derived from data taken with the foot rings sealed will be noted as such.

Compressor and Stage Static Pressure Rise Characteristic

The compressor static pressure rise characteristic per stage is shown in Fig. 1 with all the stator foot-rings unsealed and sealed with the stator disk cavities closed to the primary flow stream. The characteristic was determined from static pressure taps located on the outer casing. At a fixed flow coefficient the pressure rise is slightly higher with the foot rings sealed and the cavities closed than with them unsealed and the stator cavities open. Maximum efficiency is achieved at a flow coefficient of 0.395. Its value is estimated to be between 90 and 90.5%. Superimposed on Fig. 1. are two points derived from simulations. One of these points is at a flow coefficient corresponding to peak efficiency (i.e. flow coefficient of 0.395) while the other is at flow coefficient of 0.375, midway between peak pressure and peak efficiency. At the simulated flow coefficients the pressure rise per stage is less than that measured. The difference is approximately 6%. The predicted efficiency at a flow coefficient of 0.395 is 89%, which is 1 to 1.5% less than that based on experimental estimates. The measured pressure rise characteristics (determined from outer casing pressure taps) for each of the stages is shown in Fig. 2 along with the results obtained from the two simulations. The data are from cases with the foot rings sealed and the stator disk cavities closed and with the foot rings unsealed and the stator disk cavities

an energy source (sink).Cascade models are used to link the incoming flow field to the body force and energy source (sink), and supplemented by rig data to correct for end-wall effects.Through flow models are the backbone of todays multi-stage design systems and have been used very effectively in design. However, the costs and time to acquire the data needed to support through flow models is becoming excessive as requirements for turbomachinery are being extended far beyond the bounds of existing data bases. This extrapolation of the data bases could result in significant development costs over runs. There is a clear need for a true three dimensional flow model capable of providing new insight into the flow process within multi-stage machinery whose computing requirements is compatible with the design environment. Hopefully the empirical data base needed to underpin a three-dimensional model will be less costly to support than that associated with existing through flow models.

It has been proposed that a model of the three-dimensional time average flow field within a typical passage of a blade row embedded in a multi-stage configuration address some of the short-falls of the through-flow models. This three-dimensional flow model governs the conceptional flow field designers have historically designed to and is referred to as the average-passage flow model, Ref. 1. From simulations based on the average-passage model performance parameters such as blade loss, deviation angle, and flow blockage can be derived. This is not the case with the through flow model where explicit models supported by an empirical data base are required specifically for these parameters.

The average-passage flow model can be derived directly from the Navier-Stokes equations through a systematic application of temporal and spacial averaging. The resulting system of equations contain more unknowns than there are equations and thus as with the through flow models additional modeling is required in order to solve the equations. This additional modeling is associated with the mathematical issue of closure and is analogous to the modeling of the turbulent stress which appears in the Reynolds form of the Navier-Stokes equation. The usefulness of the average-passage equation in supporting the design of turbomachinery in-part will depend on the ability to derive closure models which capture the effect of the unsteady aperiodic flow field on the average-passage flow state. The issue of closure is beyond the scope of this work, however the model used in the present study is outlined in Ref. 2. The closure model accounts for the effect of radial mixing associated with the deterministic flow field and that due to turbulence. The mixing associated with the deterministic flow field accounts for the flow physics outlined by Adkins and Smith Ref. 3., while that associated with turbulence accounts for the mixing process outlined by Galmore and Cumpty, Ref. 4.

The objective of this paper is to present a status report of the development of the average-passage flow model including the closure models currently being implemented. To accomplish the stated objective an experimental data set is required against which the accuracy of the model can be assessed in addition to revealing shortcomings in the closure models. It must be remembered that the issue is not whether the average-passage model is correct but the ability to develop closure models which can capture the effects of the

Figure 5 shows the total and static pressure coefficient, axial and tangential velocity, absolute and relative flow angle at station 3.5 (at the exit of the third rotor) as a function of span. The measured total pressure rise at mid-span across the third rotor is 6.3% greater than that predicted. The measured static pressure rise across the third rotor is also greater than that predicted. The axial velocity component derived from the experimental data is in reasonable agreement with that derived from the numerical simulation as is the tangential velocity component.

The axisymmetric flow conditions at the exit of the third stage stator are shown in Fig. 6. Plotted as a function of span are the measured and predicted total and static pressure coefficient, axial and tangential velocity components, absolute and relative flow angles. Once again the measured total and static pressure coefficients are greater than that predicted. The measured and predicted flow angles and velocity components exiting the stator are in good agreement with each other. The velocity components at the exit of the third stage stator are nearly identical to their counterparts exiting the second stage stator (Fig. 4). The machine is operating in a repeating stage condition.

Rotor and stator blade element loss estimates obtained from either the simulation or from measurements taken with slow response instrumentation failed to provide any additional information as to the cause in the shortfall in predicted compressor pressure rise. The explanation for the shortfall was deduced from an analysis of the hot-film data taken downstream of the second stage stator and third stage rotor. Figure 7 shows the pitch-wise distribution of the time average axial velocity component at 15,50,85 and 92.5% of span exiting the second stage stator. Both measured and predicted results are shown. Also shown is the envelope of the unsteady axial velocity component at these locations. The stator wake is quite evident in these plots. These plots show that the predicted stator wake is deeper than that measured. Analysis of the axial velocity contour plots for station 3, Fig. 8, shows that the predicted stator wake is deeper than that measured nearly over the entire span. Analysis of the measured and predicted time average tangential velocity field exiting the second stator yielded a similar conclusion, the predicted stator wake is deeper than that measured.

Figure 9 shows the measured and predicted time average axial velocity component in the rotor frame of reference exiting the third rotor. The axial velocity component is plotted as a function of pitch for four span-wise locations. There is an error in the experimental results presented in Fig. 9 caused by a shift in the probe position which was found after the data was taken. This shift caused a 2 deg. error in the measured absolute flow angle. This shift affected the measurements between 20 and 80% of span. The actual axial velocity component at mid-span is thus slightly less than that plotted. However, the shift in the probe alignment did not affect the shape of the measured pitch-wise variation of the axial velocity component. Once again the predicted blade wake depth is greater than that measured. Figure 10, which is a contour plot of the measured and predicted time average axial velocity component in the rotor frame of reference, shows that the predicted wake is deeper than that measured over nearly the entire span.

opened to the primary flow stream. The characteristics with the foot-rings sealed and the cavities closed are slightly higher than those with the foot-ring unsealed and the cavities open. Figure 2 shows that the predicted pressure rise of the first stage at a flow coefficient of 0.395 is 6% less than that measured. At this same flow coefficient, the predicted pressure rise for the second and third stage is approximately 7% less than that measured. For the fourth stage the predicted pressure rise is 5% less than that measured.

The agreement with measurements is encouraging. However, the disagreement between the predicted pressure rise and that measured needs to be reduced before the model can be fully utilized in support of design.

Axisymmetric Flow Variables

To understand the reasons for the shortfall in the predicted pressure rise of the second and third stage, a comparison of the axisymmetric flow variables derived from measurement and simulation are presented for the flow coefficient of 0.395. The plots are for an axial position between the exit of the second stator and the inlet of the third rotor, between the exit of the third rotor and the inlet of the third stator, and between the exit of the third stator and the inlet of the fourth rotor. These three axial positions are referred to as station 3,3.5 and 4 respectively and their location is given in the cross-section layout of the compressor, Fig. 3.

The total and static pressure coefficient, axial and tangential velocity, absolute and relative flow angle, as derived from the experimental measurements are shown in Fig. 4 for station 3. The experimental results are annotated as to the configuration of the stator foot-rings and the stator disk cavities. Also shown on this figure are the corresponding variables derived from the numerical simulation. The total pressure and static pressure coefficient are referenced to the plenum total pressure and normalized with respect to the dynamic head based on plenum total density and the rotor tip speed squared. The velocity components are normalized with respect to the rotor tip speed.

Both the total and static pressure coefficient as derived from the data are greater than those derived from the numerical simulation. At midspan the experimental total pressure coefficient is 5% greater than that predicted by the numerical simulation. The shape of the predicted total pressure coefficient curve is very similar to that measured, both showing a bulge near 90% per cent of span.

The velocity components derived from the measurements are in reasonable agreement with those derived from the simulation. This agreement is consistent with the agreement seen in the flow angle comparison. With the exception of the hub region (i.e. below 10% span) the velocity triangles determined from the experimental data and the simulation are in reasonable agreement with each other. The disagreement near the hub is in part associated with the stator leakage.

and relative flow angle at station 3 as a function of span. The flow coefficient is 0.395. The postdicted velocity components and flow angles are nearly the same as those shown in Fig. 4. However, the postdicted total and static pressure coefficient are in better agreement with the measurements than their counter-parts in Fig. 4. The slight difference between the postdicted total pressure coefficient and that measured in board of 40% of span is unknown.

Figure 14 shows the measured and postdicted total and static pressure coefficient, axial and absolute tangential velocity component, absolute and relative flow angle at station 3.5 (downstream of the third stage rotor) as a function of span. The agreement between the postdicted results and those obtained experimentally is excellent. The detailed shape of the experimental curves is captured by the postdicted results. These results clearly indicate the improvements gained by using the Shih turbulence model. The corresponding plots for axial station 4.0, which is downstream of the third stage stator yield results comparable to those shown in Fig. 13.

Figures 15 and 16, show the cross passage time average axial velocity field at the exit of the second stage stator and the third stage rotor. The third stage rotor contour plot is with respect to the rotor frame of reference. Results are shown as derived from the simulation and measurements. What is clearly evident is that the depth of the postdicted wakes are less than those shown in Figs. 8 and 10 and that the depth of these wakes are in much better agreement with the measurements.

Finally, the loss coefficient for the third stage rotor and stator derived from the simulations which used the Shih turbulence model is shown in Fig. 17. The figure shows that the loss associated with both blade rows is less when the Shih model is used. The reduction in blade loss is the primary reason for the improved agreement with data.

CONCLUSIONS

The objective of this paper was to document the status of the development of the average passage flow model for multi-stage axial flow compressors. This model describes the time average flow field in a typical passage of a blade row embedded in a multi-stage machine. The configuration analyzed was the NASA Lewis 4 1/2 stage large low speed compressor whose blading is representative of todays aero-engines. Detailed aero survey data exists which documents the axisymmetric flow field exiting the second stage stator, third stage rotor and third stage stator at flow coefficients corresponding to peak efficiency and peak pressure. In addition the pressure rise of each stage as a function of flow coefficient has been documented.

The performance estimates associated with the first series of simulations fell short of that measured. Based on hot-film data it was deduced that the predicted blade wakes were deeper than that measured, the result of the blade boundary layers being assumed turbulent from the leading edge on. It is highly likely that the blade boundary layers in

The simulations assumed the boundary layers on the blade surfaces to be fully turbulent starting at the leading edge. Test of a similar compressor configuration, Hallstead and Weisler Ref. 6, have shown the blade boundary layers to be transitional. The turbulence model that was used in the simulations presented thus far was an average passage form of a high Reynolds number standard $k-\epsilon$ model. For an isolated blade row this model reduces to that of Launder and Spalding, Ref. 7. It is well known that this turbulence model over estimates the turbulent viscosity near flow stagnation. Such is the case in the simulations presented. It is conjectured that the large values of turbulent viscosity at the leading edge of a blade leads to the development of a boundary layer which is thicker over the entire blade surface than what actually exits. A thicker boundary layer implies more flow blockage, hence less diffusion, hence less pressure rise.

HINDSIGHT - A Case For Transition Modeling

In the previous section it was shown that the predicted blade wakes were deeper than those measured. It was argued that the deeper wakes were the result of the blade boundary layers being assumed turbulent from the leading edge on. Because there is strong evidence to suggest that the blade boundary layers are transitional, the actual blade boundary layers are thinner than predicted. The result is an under-prediction of the pressure rise of the compressor.

In an attempt to improve the agreement with measurements, simulations were executed using an improved $k-\epsilon$ model developed by Shih et. al., Ref. 8, and applied to turbomachinery configuration by Shabbir, Zhu and Celestina, Ref. 9. The Shih model is not a transition model, however unlike the $k-\epsilon$ model of Launder and Spalding, Ref. 7, it does not produce unrealistically high levels of turbulent eddy viscosity in regions of high strain rates. Thus the Shih model suppresses the growth of eddy viscosity at the leading edge of a blade and along the blade surface where the pressure gradient is favorable. The eddy viscosity begins to grow in value when the flow locally begins to diffuse. The Shih model approximately mimics the growth of the turbulent eddy viscosity in a transitional boundary layer.

The average stage pressure rise predicted using the Shih model at a flow coefficient of 0.395 and 0.375 is shown in Fig. 11 along with the measured characteristic. At a flow coefficient of 0.395 the predicted pressure rise is 0.505 while that measured with the stator foot-rings sealed and the stator disk cavity closed to the primary flow is 0.512. For the same configuration, at a flow coefficient of 0.375 the predicted pressure rise is 0.541, while that measured is 0.538. The predicted efficiency at 0.395 flow coefficient is 90.1%, an increase of one point over the previous prediction. Figure 12 shows the measured pressure rise characteristic for each stage along with the results obtained from the simulations using the Shih model. The agreement is excellent compared to the results presented in Fig. 3. Further confirmation of the improvements gained by using the Shih model is shown in Fig. 13. Figure 13 shows plots of the postdicted and measured total and static pressure coefficient, axial and absolute tangential velocity component, absolute

REFERENCES

1. Adamczyk, J.J., "Model Equation for Simulating Flows in Multistage Turbomachinery," *ASME Paper 85-GT-220*, 1985.

2. Adamczyk, J.J., Celestina, M.L., Beach, T.A., and Barnett M., "Simulation of Three-Dimensional Viscous Flow Within a Multistage Turbine", *ASME J. of Turbomachinery*, Vol. 112, 1990

3. Adkins, G.G. and Smith Jr. L. H., "Spanwise Mixing in Axial-Flow Turbomachines," *J. Eng. Power*, Vol. 104, No. 1 1982.

4. Gallimore S.J. and Cumsty N.A., "Spanwise Mixing in Multistage Axial Flow Compressors", *ASME. J. of Turbomachinery*, Vol. 108, 1986.

5. Wellborn, S. and Okiishi, T., 1996, "Effects of Shrouded Stator Cavity Flows on Multistage Axial Compressor Aerodynamic Performance", NASA CR 198536.

6. Halstead, D.E., Wisler, D.C., Okiishi, T.H., Walker, G.J., Hodson, H.P., and Shin, H.W., "Boundary Layer Development in Axial Compressors and Turbines", *ASME papers*, 95-GT-461, 95-GT-462 95-GT-463, 95-GT-464, 1995.

7. Launder, B.E., and Spalding, D.B., 1974, "The Numerical Computation of Turbulent Flows", *Comp. Math. Appl. Mech. Engg.*, 3, 269-289.

8. Shih, T.-H., Liou, W.W., Shabbir, A. , Zhu, J., and Yang, Z., 1995, "A New $k-\epsilon$ Eddy Viscosity Model for High Reynolds Number Turbulent Flows", *Computers Fluids*, 24, 3, 227-238.

9. Shabbir, A., Zhu, J., and Celestina, M.L. 1996, " Assessment of Three Turbulence Models in a Compressor Rotor", Paper 96-GT-198, *ASME/IGTI International Gas Turbine Conference*, Birmingham, UK.

the low speed compressor simulated are transitional. If these transitional boundary layers were to remain attached they would produce less loss than a turbulent boundary layer. Less loss would result in more flow diffusion and hence an increase in compressor rise. Although no direct measurement of the state of the blade boundary layer exists, evidence of laminar flow regions on the blades of a similiar low speed multi-stage compressor exits. The existence of a transitional blade boundary layer would explain the shortcoming in the predictions.

To test the sensitivity of the prediction to the assumed state of the blade boundary layers a second series of simulations were executed where in the turbulence model used allowed the turbulent eddy viscosity to be a local function of the flow strain rate. The dependence of the turbulent viscosity on local strain rate suppresses the growth of the turbulent viscosity in regions of flow stagnation and in regions along a blade surface for which the pressure gradient is favorable. Although this turbulence model is not a transition model it does yield a boundary layer which has many of the traits of a transitional boundary layer. Using such a turbulence model greatly improved the accuracy of the simulation. The compressor pressure rise as well as the pressure rise of each stage was predicted to within 2%. The span-wise distribution of the absolute total and static pressure coefficient, the axisymmetric components of axial and tangential velocity, and the absolute and relative flow angles at the exit of the second stage stator, and the third stage rotor were all in excellent agreement with results derived from measurements. The improvements gained in predicting compressor performance using a turbulence model where-in the eddy viscosity is a direct function of the local flow strain rate is very encouraging and is strongly recommended. The present study clearly indicates the need for incorporating a transition model of some form when simulating multi-stage axial flow compressors.

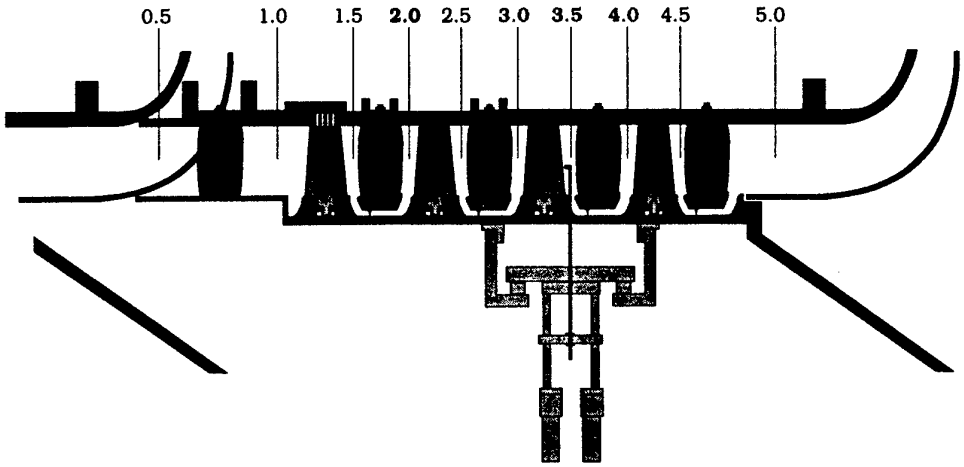

Fig. 3. Schematic of the Low Speed Axial Compressor.

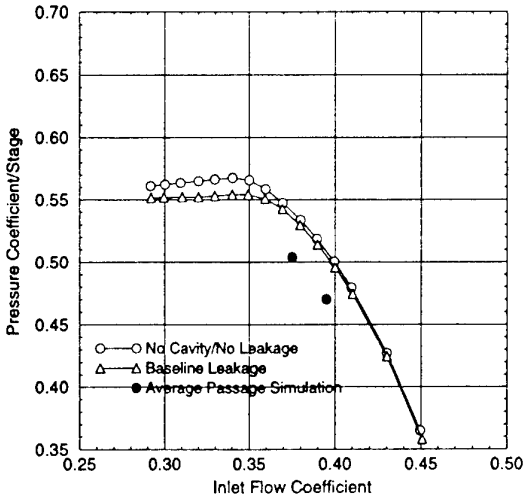

Fig. 1. Overall pressure coefficient as a function of inlet flow coefficient.

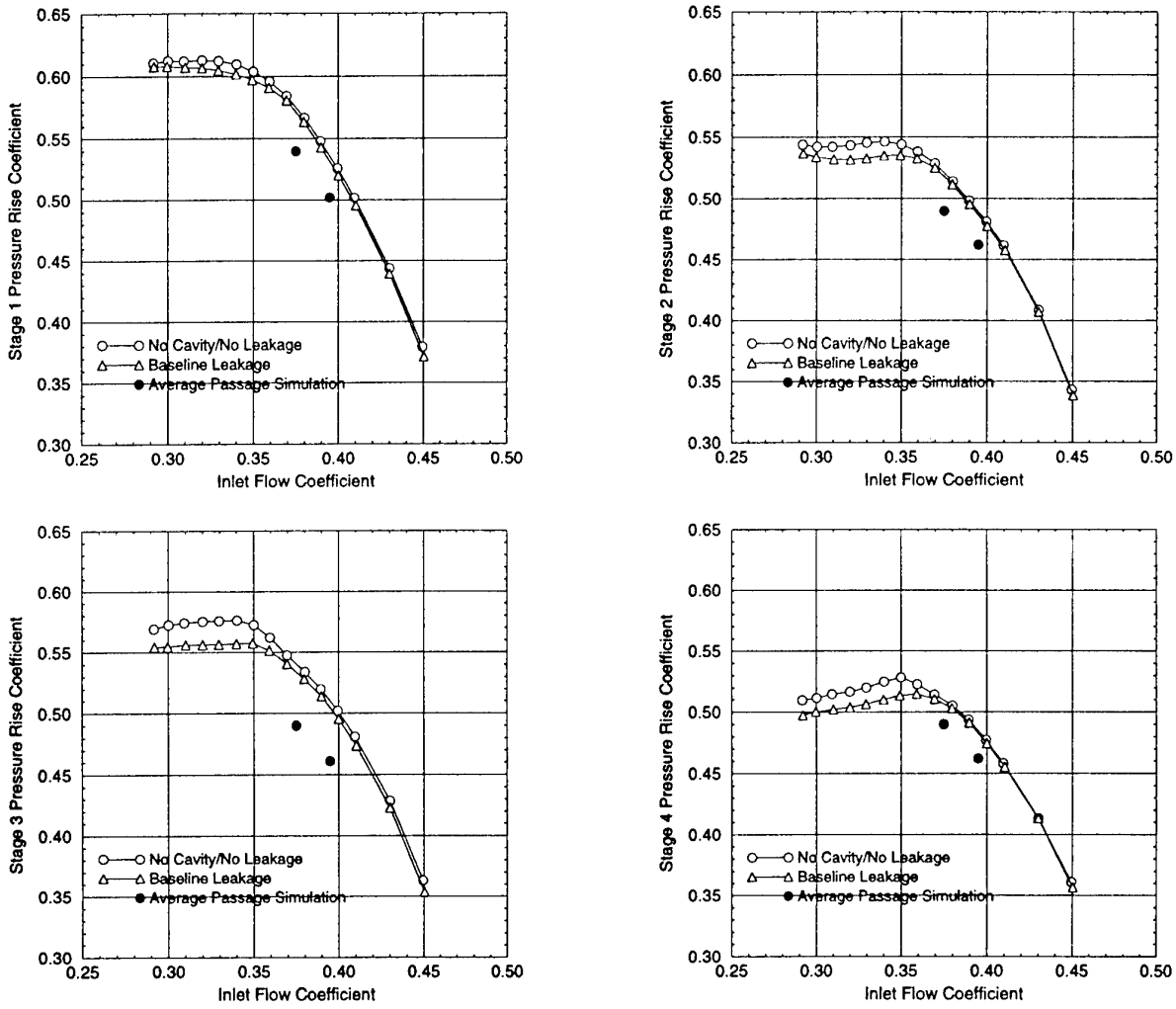

Fig. 2. Individual stage pressure rise coefficient as a function of inlet flow coefficient.

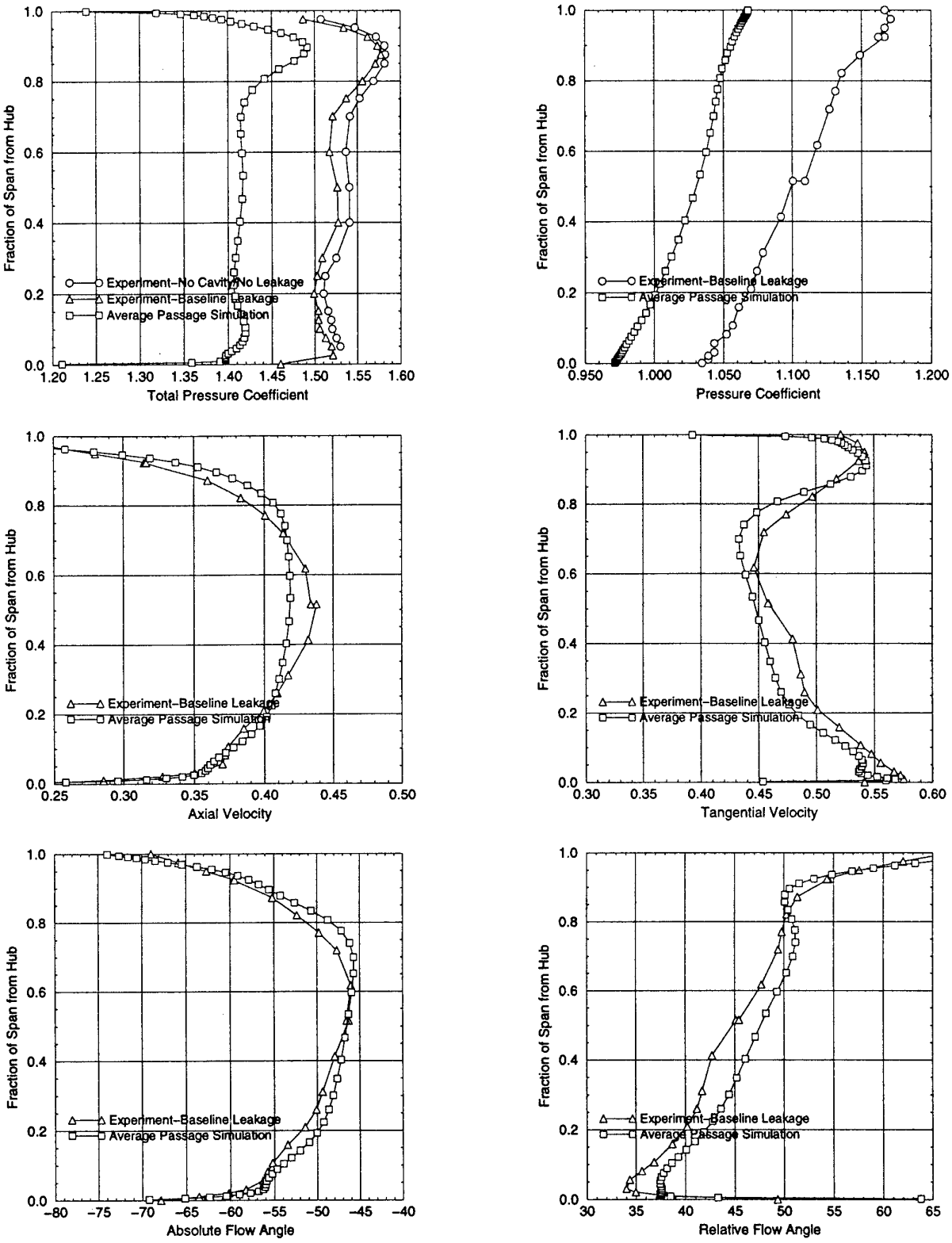

Fig. 5. Axisymmetric flow variables at Station 3.5.

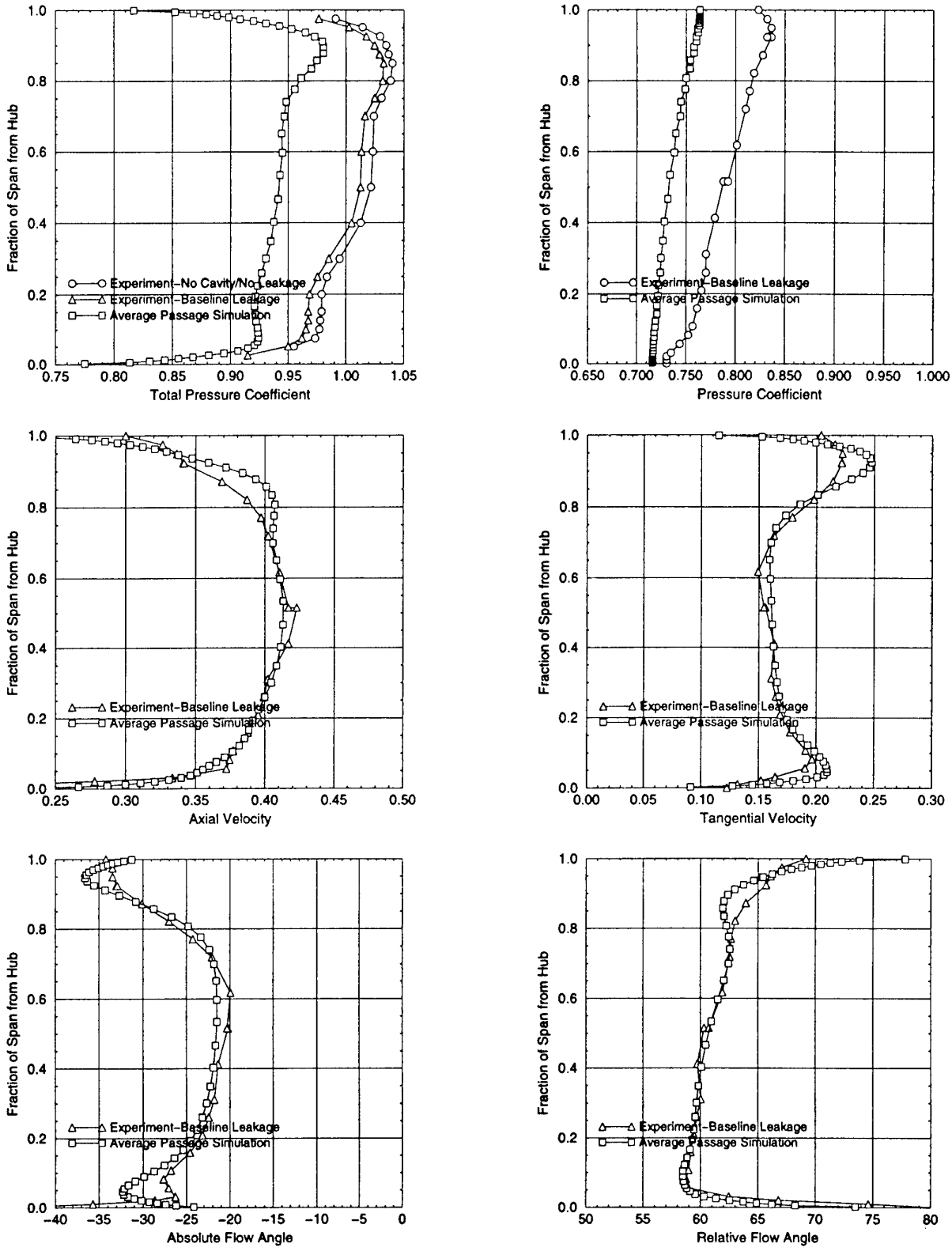

Fig. 4. Axisymmetric flow variables at Station 3.0.

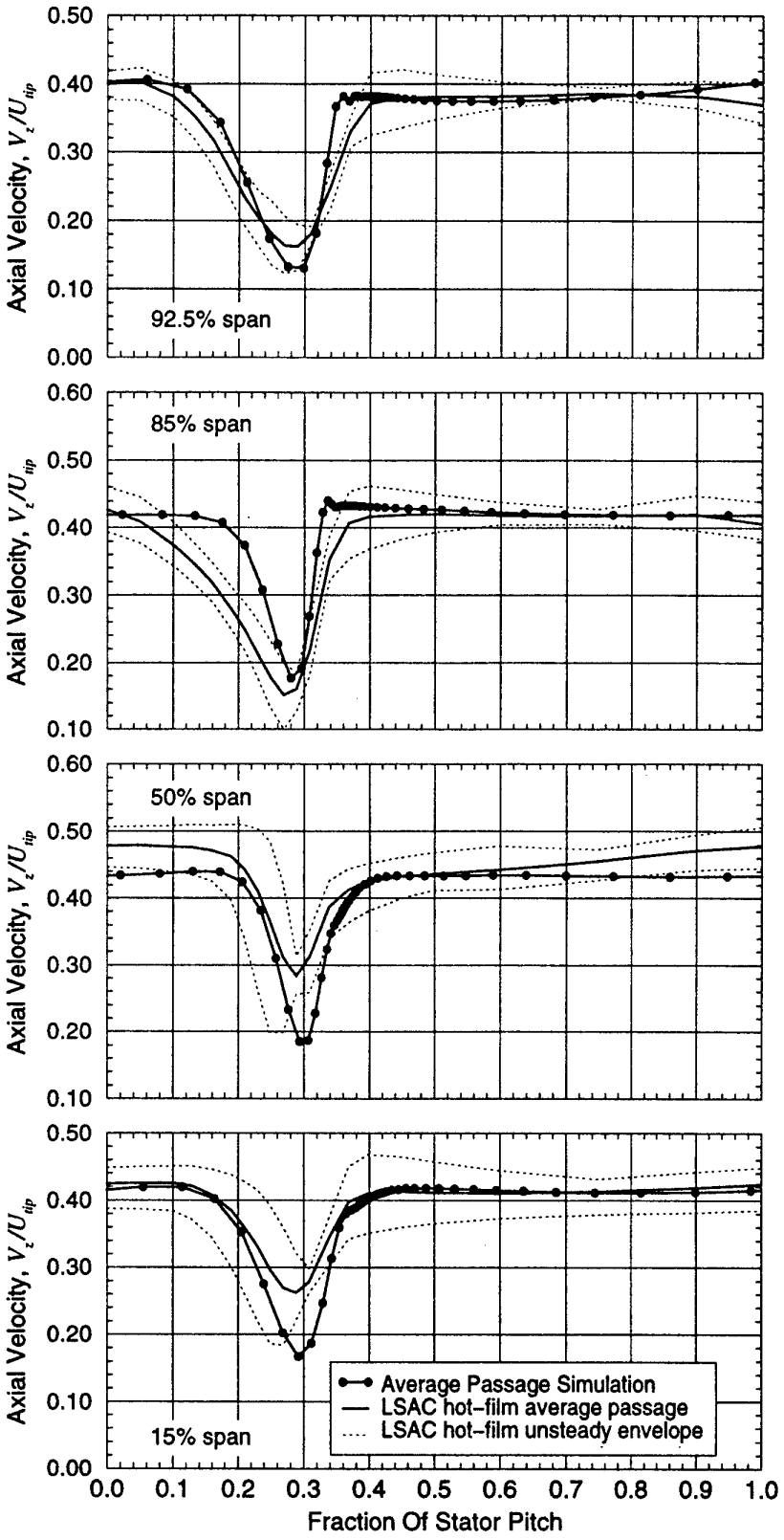

Figure 7. Measured and simulated LSAC axial velocity (Vz / Utip) distributions at ST 3.0

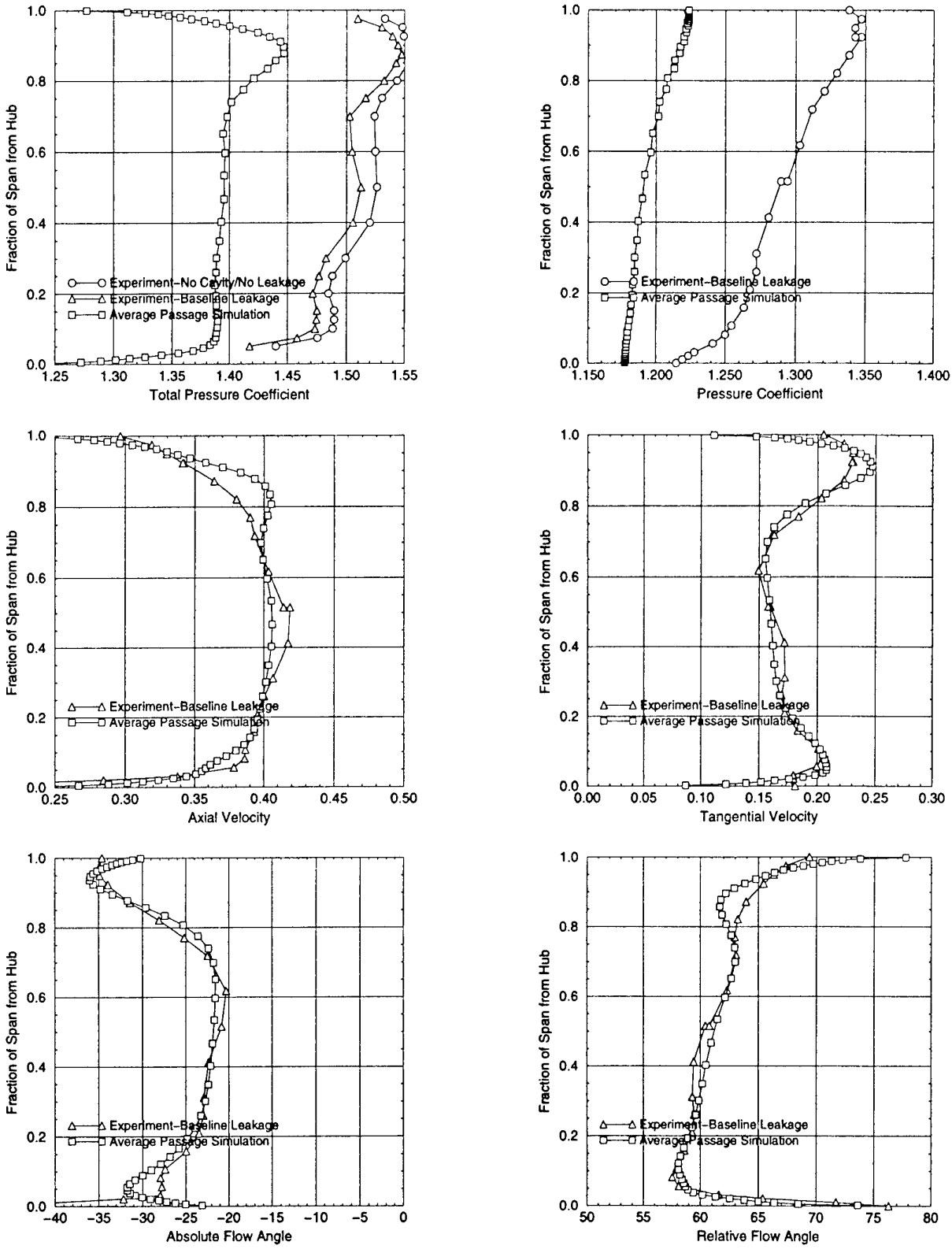

Fig. 6. Axisymmetric flow variables at Station 4.0.

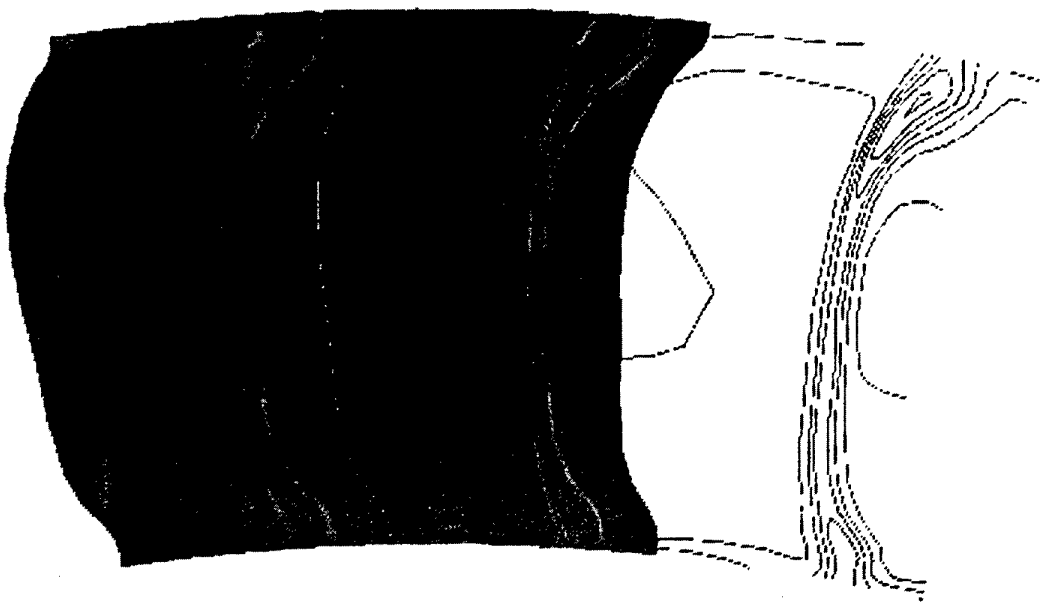

Measured (hot–film) average passage (ensembled and time averaged across the rotor pitch) axial velocity (Vz / Utip) at ST 3.0. Contour minimum level is 0.10, contour maximum level is 0.45, contour increment is 0.05.

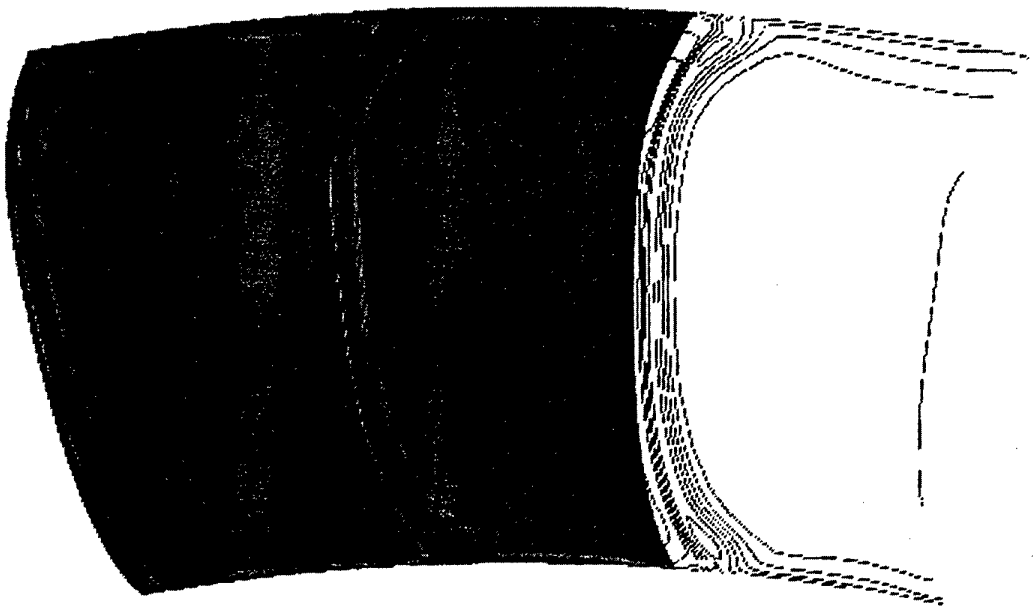

Average passage simulated axial velocity (Vz / Utip) at ST 3.0 (solution interpolated to match axial location of ST 3.0). Contour minimum level is 0.10, contour maximum level is 0.45, contour increment is 0.05.

Figure 8

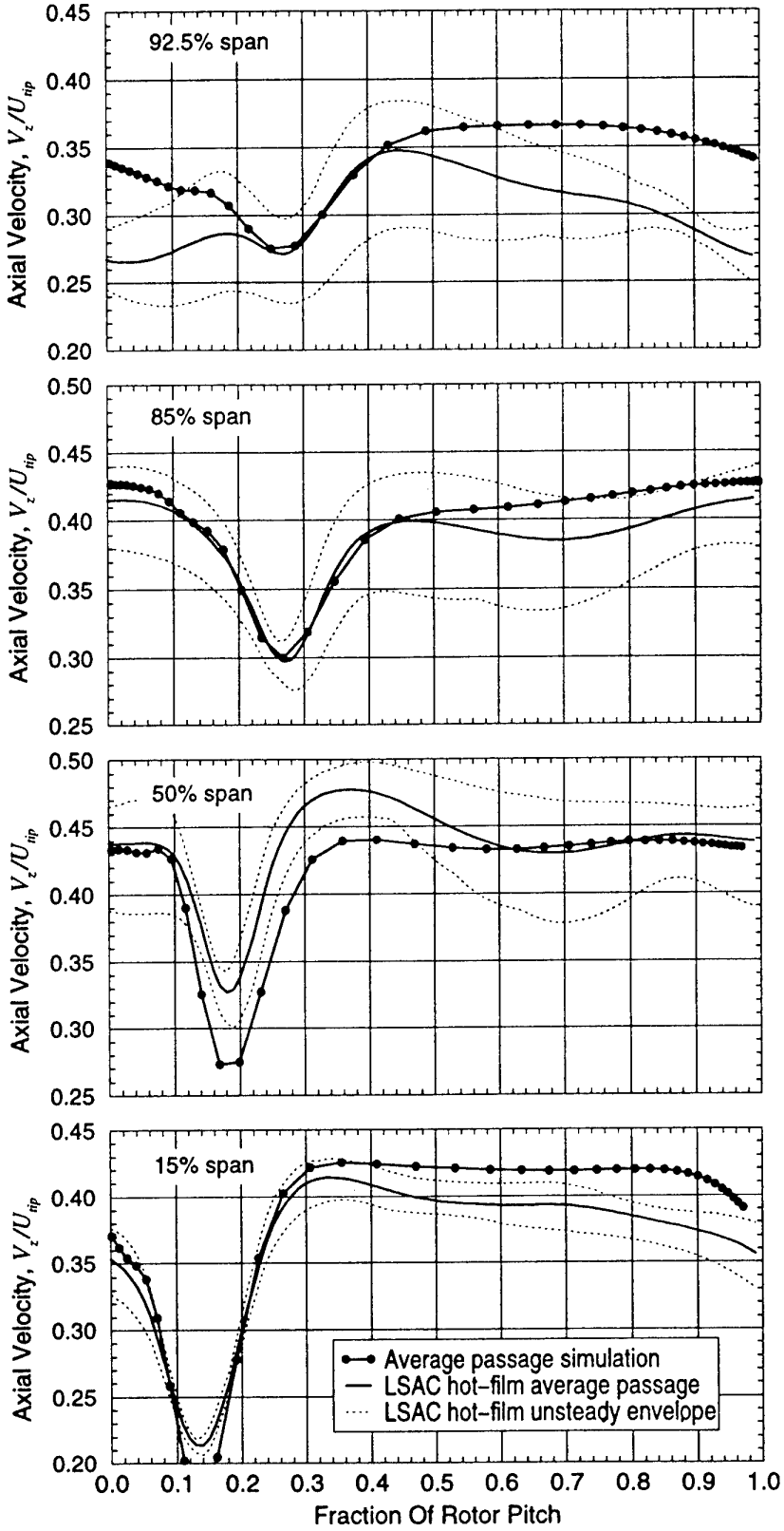

Figure 9. Measured and simulated LSAC axial velocity (Vz / Utip) distributions at ST 3.5 for 15, 50, 85 and 92.5% span. Simulation data are denoted by filled circles, average passage data are represented by solid lines and the unsteady envelope data are depicted by dotted lines.

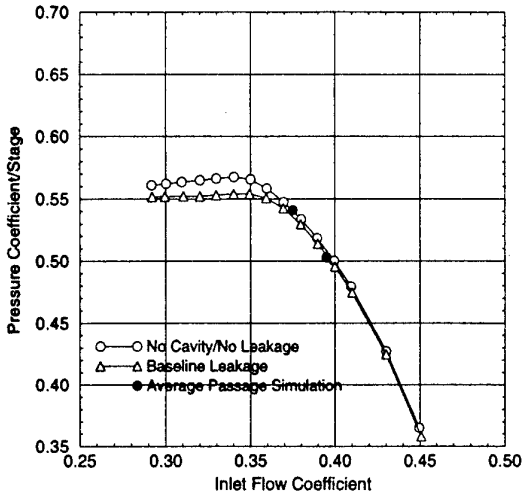

Fig. 11. Overall pressure coefficient as a function of inlet flow coefficient.

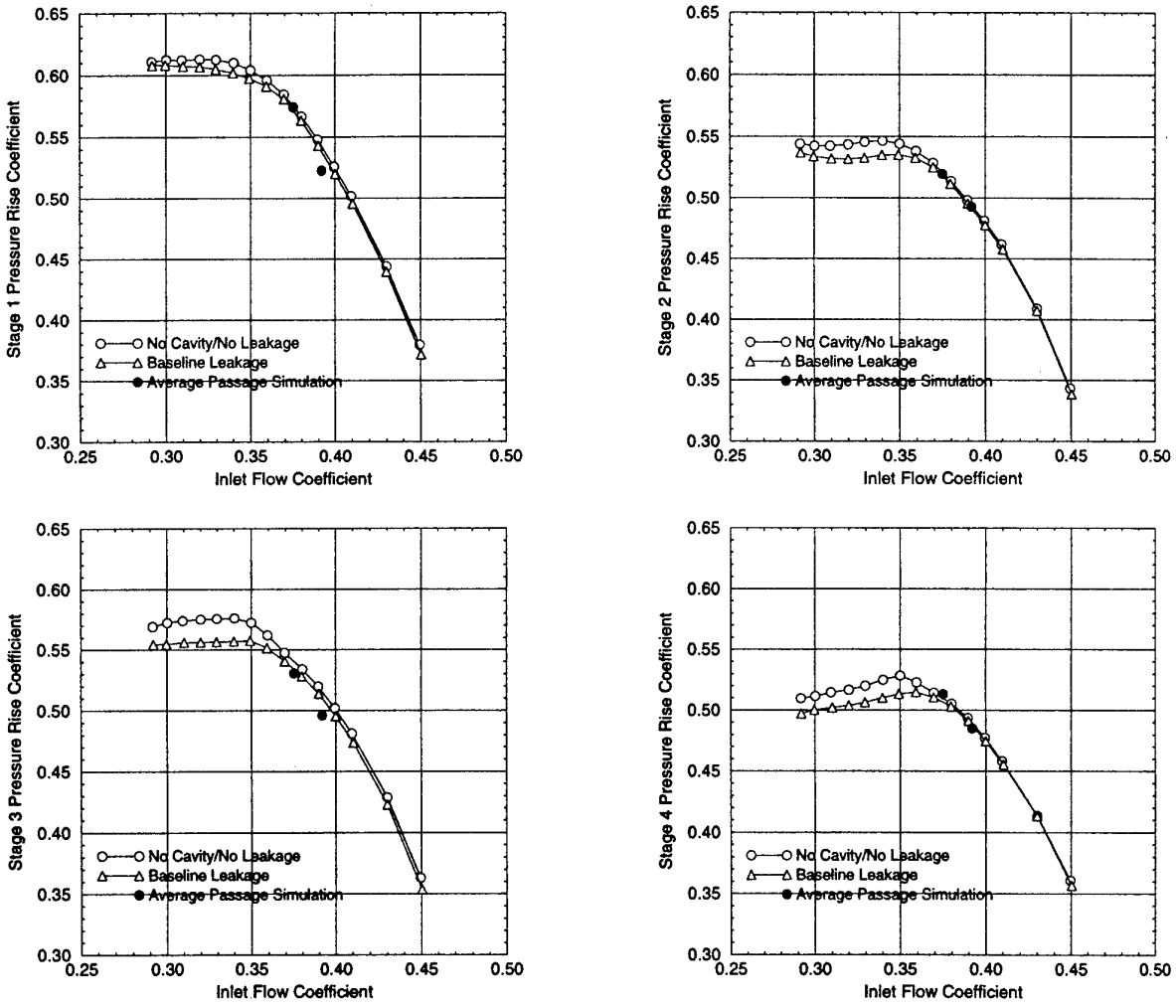

Fig. 12. Individual stage pressure rise coefficient as a function of inlet flow coefficient.

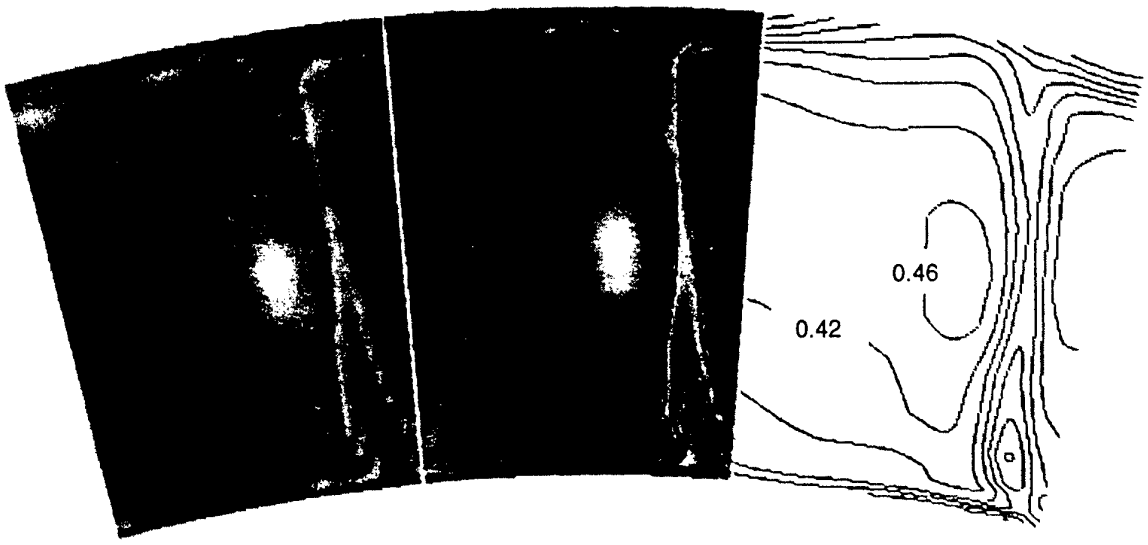

Measured (hot–film) average passage (ensembled and time averaged across the stator pitch) axial velocity (Vz / Utip) at the discharge of rotor 3 (ST 3.5). Contour minimum level is 0.14, contour maximum level is 0.46, contour increment is 0.04.

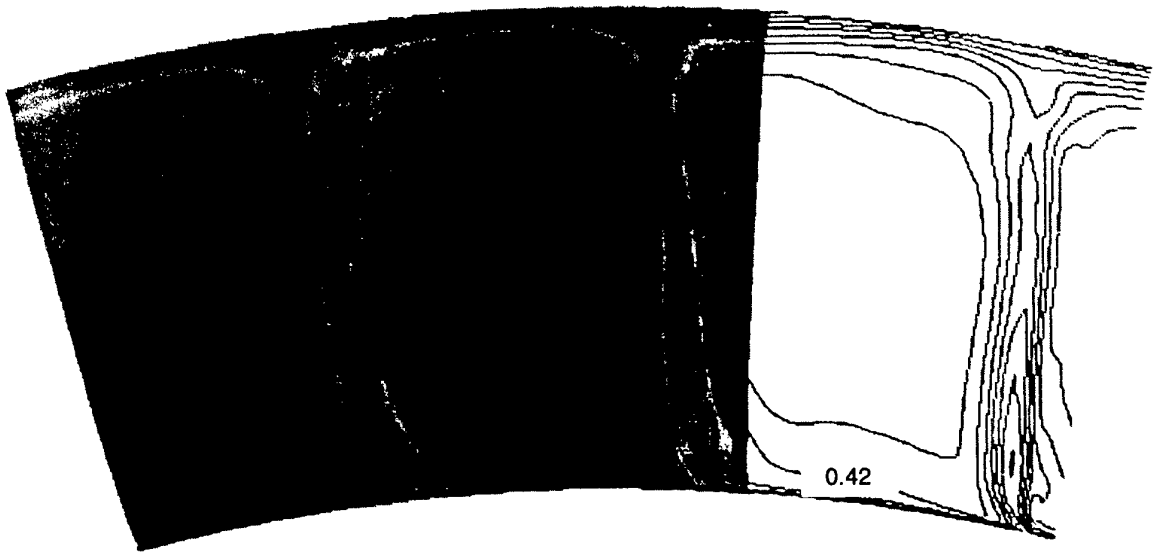

APNASA simulated axial velocity (Vz / Utip) at the discharge of rotor 3 (solution interpolated to match axial location of ST 3.5). Contour minimum level is 0.14, contour maximum level is 0.42, contour increment is 0.04.

Figure 10

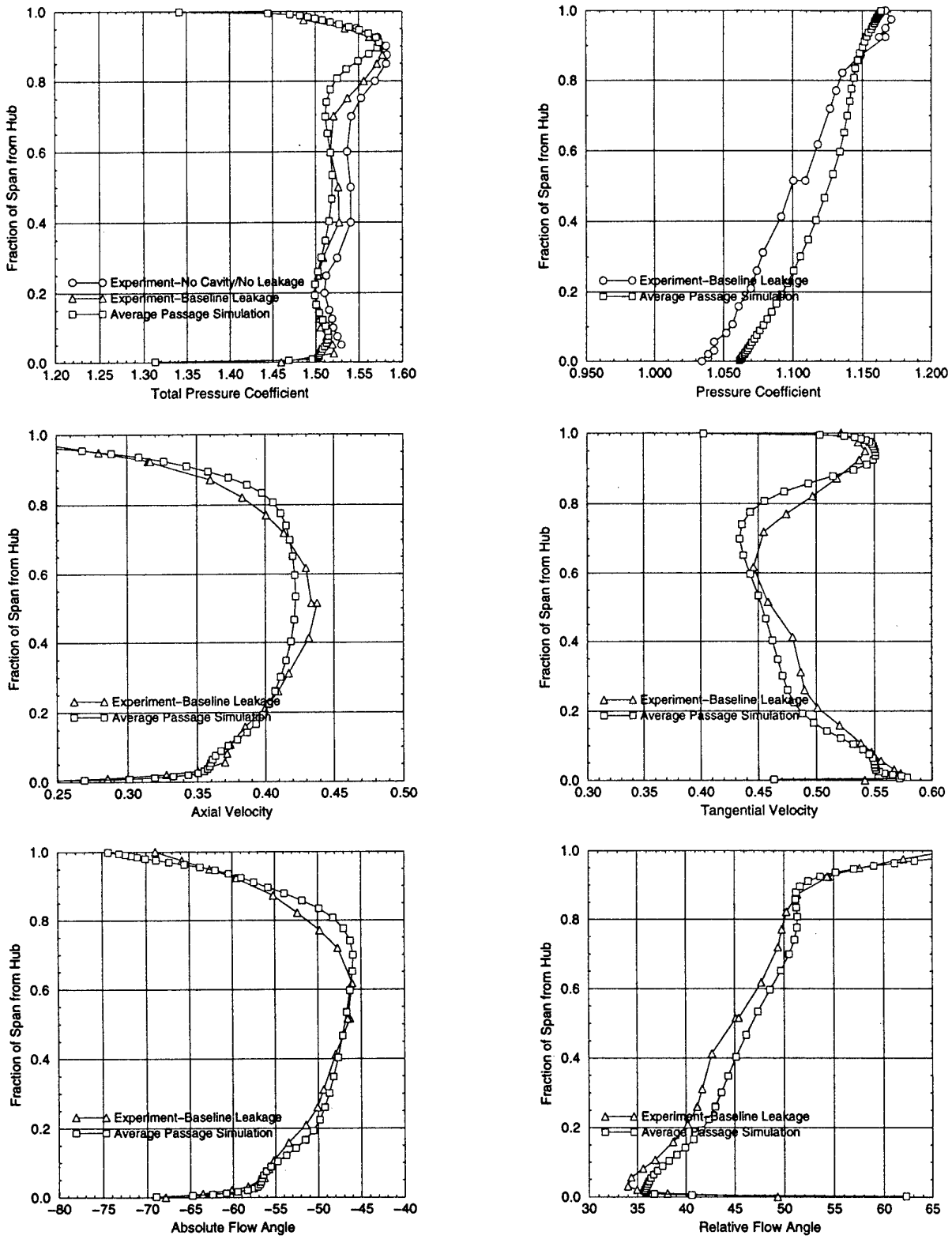

Fig. 14. Axisymmetric flow variables at Station 3.5 using the improved $k - \epsilon$ turbulence model of Shih et al.[8].

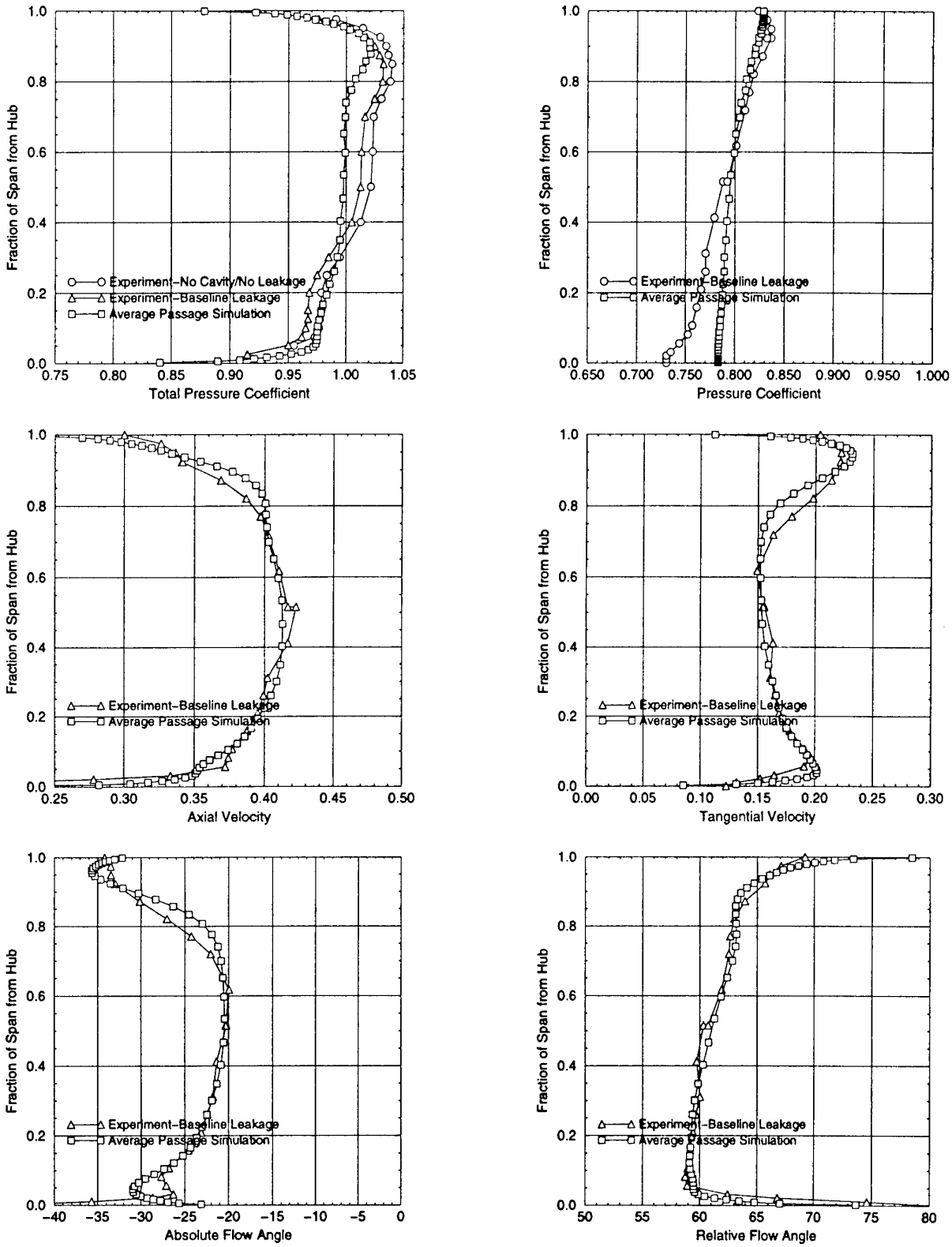

Fig. 13. Axisymmetric flow variables at Station 3.0 using the improved $k - \epsilon$ turbulence model of Shih et al.[8].

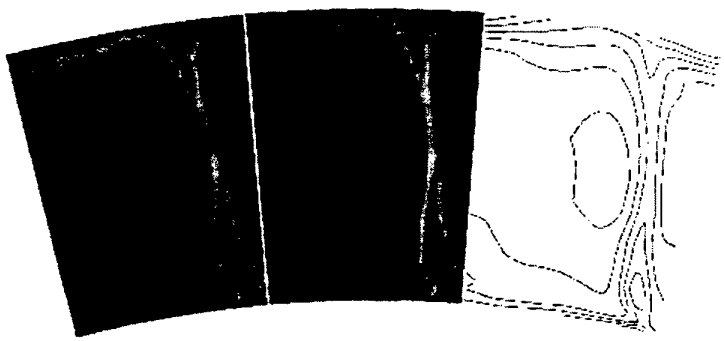

Measured (hot–film) average passage (ensembled and time averaged across the stator pitch) axial velocity (Vz / Utip) at ST 3.5. Contour minimum level is 0.10, contour maximum level is 0.45, contour increment is 0.05.

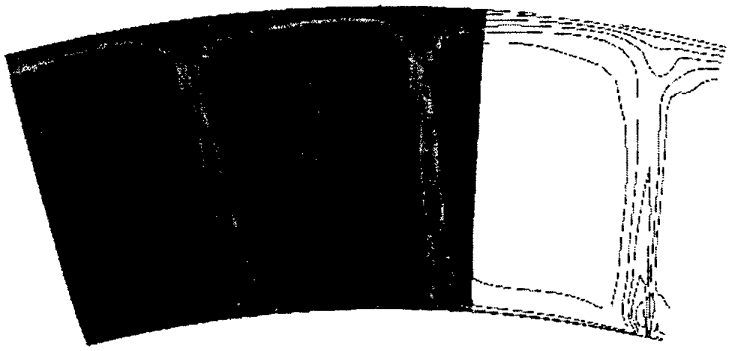

Average–passage (standard k–ε) simulated axial velocity (Vz / Utip) at ST 3.5 (solution interpolated to match axial location of ST 3.5). Contour minimum level is 0.10, contour maximum level is 0.45, contour increment is 0.05.

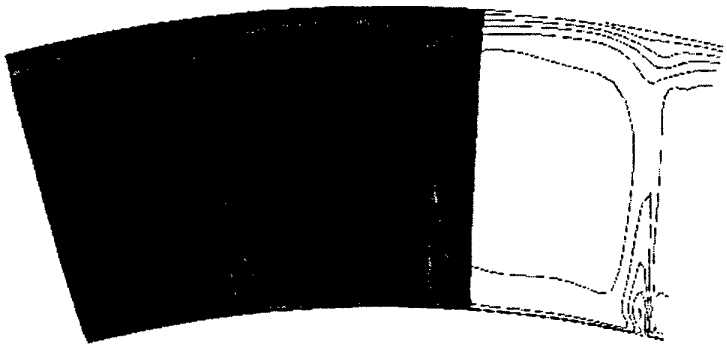

Average–passage (Shih k–ε) simulated axial velocity (Vz / Utip) at ST 3.5 (solution interpolated to match axial location of ST 3.5). Contour minimum level is 0.10, contour maximum level is 0.45, contour increment is 0.05.

Figure 16

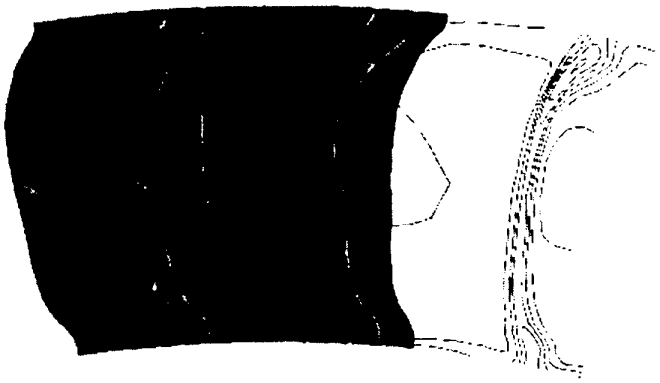

Measured (hot–film) average passage (ensembled and time averaged across the rotor pitch) axial velocity (Vz / Utip) at ST 3.0. Contour minimum level is 0.10, contour maximum level is 0.45, contour increment is 0.05.

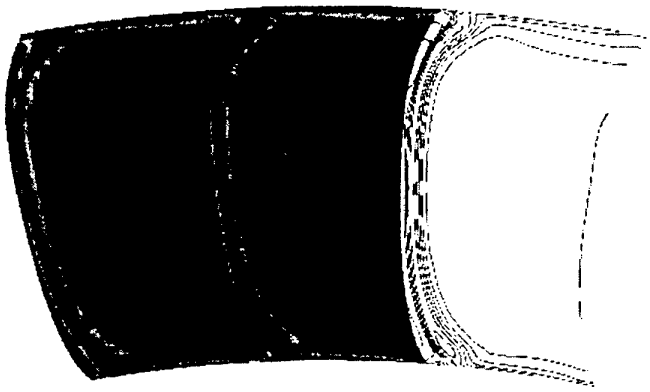

Average–passage (standard k–ε) simulated axial velocity (Vz / Utip) at ST 3.0 (solution interpolated to match axial location of ST 3.0). Contour minimum level is 0.10, contour maximum level is 0.45, contour increment is 0.05.

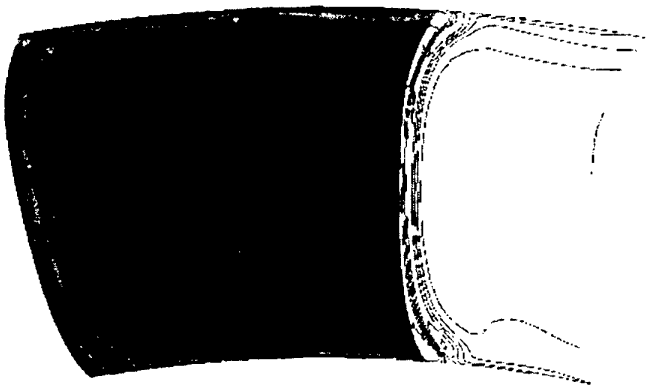

Average–passage (Shih k–ε) simulated axial velocity (Vz / Utip) at ST 3.0 (solution interpolated to match axial location of ST 3.0). Contour minimum level is 0.10, contour maximum level is 0.45, contour increment is 0.05.

Figure 15

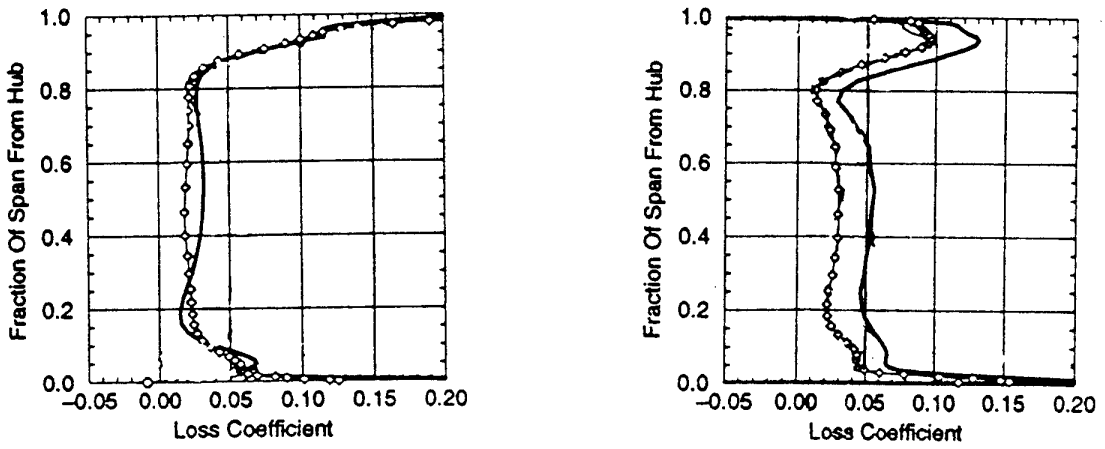

Fig. 17. Loss coefficient at Station 3.5 and Station 4.0 as obtained from the Average Passage simulations. Soild corresponds to standard $k-\epsilon$ model and diamonds correspond to improved $k-\epsilon$ model of Shih et al.[8]

PERFORMANCE ANALYSIS OF CENTRIFUGAL COMPRESSOR STAGE, BY MEANS OF NUMERICAL AND EXPERIMENTAL INVESTIGATION OF ROTOR-STATOR INTERACTIONS.

O.DOMERCQ
CIFRE Engineer,
Centrifugal compressors design,
Aerothermodynamic department,
Turbomeca - Boite 17
65411 Bordes, FRANCE.

R.THOMAS
Head of the turbine design team,
Aerothermodynamic department,
Turbomeca, Boite 17
65411 Bordes, FRANCE.

A. CARRERE
Professor at SUPAERO,
(Ecole Nationale Supérieure de l'Aéronautique et de l'Espace)
Thesis director,
31400 Toulouse, France.

1. ABSTRACT

This paper deals with numerical and experimental investigations of rotor-stator interactions between a backswept centrifugal impeller and its associated vaned diffuser. Experimental data were obtained by laser two focus velocimetry and fast response Kulite transducers. Computations were carried out thanks to a three-dimensional Navier-Stokes solver, customised by the authors, for the current purpose. Time-resolved simulations of the full stage with passages number reduction but respect to real geometry of components are then presented. Comparisons with experimental data lead to a code validation phase and critic investigations of rotor-stator interaction phenomena. Evidence of the existence of a strong interaction between the rotor and the stator flow fields are pointed out. In particular, an intense upstream influence of the vaned diffuser was observed. Finally, steady stage calculations, coupling the components by a mean interfacial treatment, are examined. The reasonable computational cost of this method now allows such numerical simulations of centrifugal stages to be part of design cycles.
The numerical part of the study was performed at Turbomeca, using the local software and hardware facilities, whereas the experimental campaign took place in the Propulsion Laboratory of SUPAERO, part of the LAMEP (Laboratoire Mixte en Energétique et Propulsion), which recently designed a test rig devoted to compressors.

Nomenclature :

Cp	Diffuser static pressure recovery coefficient
Q,E,F,G	Elements of Navier-Stokes equations in vectors form
G'	Corrected mass flow
J	Jacobian
M	Mach number
U,V,W	Contravariant velocity components
p, p_s	Static pressure
p_i	Total pressure
u, v, w	Absolute velocity cartesian coordinates
x, y, z	Cartesian coordinates

Greek symbols :

η	Efficiency
ρ	Density
τ	Shear stress tensor

Superscripts :

T	Transposed matrix or vector

Subscripts :

a	Absolute frame of reference
i	Total conditions
r	Relative frame
s	Static conditions
v	Viscous terms

2. INTRODUCTION

Advances made in the design of centrifugal compressors in the past thirty years, elevated that device to a key position in small and medium gas turbine engines[1]. Besides, aeroengines are required to be lighter and to involve reduced cost of ownership and maintenance. Considering compressors, those trends lead to more compact components with high level of aerodynamic loading, particularly for military applications. Then, the aim of first-attempt design with adequate performance and stability margin, becomes of rough achievement.
In the last decade, thanks to detailed flow investigations, the extensive use of 3D steady (Euler or Navier-Stokes) solvers and experience of designers gave birth to a high performance generation of centrifugal impellers. But, however efficient may be the rotor, the matching with its associated vaned diffuser remains a hard task, almost always obtained through mono-dimensional considerations. The flow generated by the impeller, entering the vaneless space and later the radial

Paper presented at the RTO AVT Symposium on "Design Principles and Methods for Aircraft Gas Turbine Engines", held in Toulouse, France, 11-15 May 1998, and published in RTO MP-8.

diffuser appears highly distorted in both circumferential and spanwise directions and subject to severe unsteady conditions. Among many aerodynamic causes, we can put emphasis on curvature, viscosity and compressibility effects as well as Coriolis force influence. Then the vaned diffuser aimed at static pressure recovery from the flow kinetic energy, receives strongly time-dependant inlet conditions, whose influence on its performances and stability is not yet accurately known but undoubtedly has undesirable adverse effects. Those assertions are indeed derived from experimental studies and industrial experience[2345,6]. Therefore future design methods will need to take into account aspects of the flow field currently ignored. In particular, the previously mentioned effects of the blade row proximity and unsteadiness. Some 3D Navier-Stokes codes, either in the form of commercial packages or research derived software, are now available to model those features. But the designer needs an estimation of the relevance of numerical results. Then, each constructor must assess his numerical design tools on unsteady data, obtained by detailed investigations on engine representative machines, by carrying out a code validation phase. TURBOMECA initiated such actions several years ago[7] and recently enhanced its data bases within a joint research program with the LAMEP (Toulouse, France) among others.

The present article is intended to give an outline of this process from the experimental work to the code validation phase and the modifications of the numerical package necessary to allow a design relevant use of such tools, regarding current hardware capabilities. The first part of the text will briefly describe the test compressor and the test rig, before examining the experimental data acquisition carried out by means of a Laser Two Focus velocimeter and fast response pressure transducers. In a second part, after a brief numerical background explanation, we will focus our attention on full unsteady simulations of the centrifugal stage flow field. Then, a steady mode of stage calculation, involving Riemann invariant theory, will be presented and assessed as an available design tool, already in use at TURBOMECA.

3. TEST STAGE AND MEANS OF INVESTIGATION.

3.1 Compressor and test rig.

The centrifugal compressor stage investigated in the present work is composed of a transonic backswept impeller matched with a vaned diffuser. The rotor has an equal number of full blades and splitter blades.

Close to the maximum efficiency point on the design speed curve, the impeller blade passing frequency is superior to 5000 Hz. The compressor stage pressure ratio and the mass flow rate are respectively around 4.0 and 2.0 kg/s. The impeller isentropic efficiency is then over 90%. This compressor and its experimental mounting were designed by Turbomeca company. In particular, the optical access is provided by a shroud inserted window allowing measurements situated in the vaneless diffuser and in the captation area (i.e. semi-vaneless space).

Experimental studies were performed in the Propulsion laboratory of the SUPAERO (part of the LAMEP, Toulouse, France). The compressors devoted test rig used is powered by an electric motor delivering 400kW. The air intake was precalibrated to ensure accurate mass flow measurement. The outflow enters a plenum chamber and the desired pressure ratio is reached by means of a butterfly valve motion. The operating point of the compressor is controlled with 42 pressure probes, inlet and outlet temperature probes. A computer linked to the rig allows on-the-fly storage of those data with a view to taking into account small operating point disturbances in experimental post-processing (for instance mass flow recovery calculation). Figure 1, shows the SUPAERO facility.

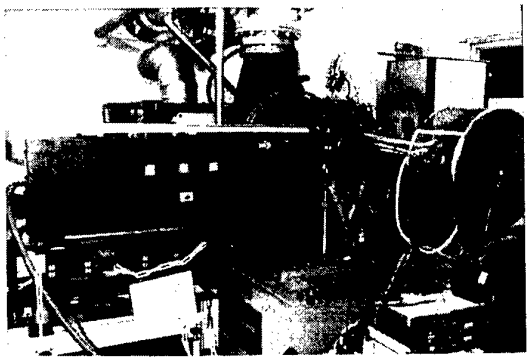

Figure 1- SUPAERO compressor test rig.

3.2 Laser Two Focus velocimeter.

3.2.1 General description.

The experimental approach had been carried out with a Laser Two Focus velocimeter. The present device is derived from DLR works and its main characteristics were given by Schold[8]. Briefly, the principle of L2F velocimetry consists in the measurement of the transit time of seeding particles, included in the flow, between two highly

focused laser spots. Histograms of particles detection as a function of spot alignment direction and time of flight (i.e. transit time) lead to flow velocity determination. The projection of the velocity vector on the plane perpendicular to the laser beams is obtained through its modulus, angle and turbulent rates by statistical calculations as described by Schold[8]. The measurement accuracy depends on the flow turbulence intensity. Considering our experimental facilities, the precision can be evaluated to +/- 1% on the absolute velocity and +/- 1° on the absolute flow angle, when turbulent rates are less than 5%.

Those measurements are intended to provide data for rotor-stator interaction mechanisms comprehension. Then, they have to be taken for various relative locations of the impeller main blade in front of the diffuser passage. A magnetic pick-up situated on the machine rotation axis allow the necessary data storage triggering.

The choice of L2F velocimeter instead of LDV (Laser Doppler) device was linked to the narrowness of the flow path and the restriction of flow accessibility to a single window. The need of high signal to noise ratio necessary for wall approaching investigations claimed in favour of the time of flight solution. Discussions on the technical aspects of this choice, as well as interesting developments on advantages and disadvantages of both devices applied to small high speed turbomachinery should be found in Fagan and Fleeter and Elder[9], Forster and Gill[10] publications.

3.2.2 Measurement positions.

Rotor-stator interaction influence on flow evolution has been investigated in three main test sections:

- the mean radius of the vaneless diffuser.
- the vaned diffuser leading edge.
- the throat of the vaned diffuser.

Each of the three main sections contains ten measurement locations. Several relative depths were investigated.

NB : Some results taken from a previous experimental campaign from the ONERA and conducted by Fradin[11] are added to our currently performed measurements with a view to increasing our validation data base.

3.2.3 Data analysis.

The flow in the mean vaneless space section appears to be dominated by a high level of time dependant heterogeneities. More precisely, a strong wake influence of the impeller passing blades is clearly observed. The wakes take the form of a high absolute speed and over-deflected flow feature. Velocity fluctuations up to 20% and flow angle variations of 15 to 20° are measured. However, the flow delivered by the rotor exhibits a relative smoothness, i.e. no jet/wake pattern in the sense of Dean and Krain[2] is observed. Turbulent rates reach 10 to 15% within the wake regions and are lower to 5% elsewhere.

The question then arise, to know to which extend these flow heterogeneities mix out before the radial diffuser leading edge as currently always assumed in design process. Considering the second measurement section, in terms of velocity magnitude, both the peak induced by the blade wake passing and the outer gradients have been reduced. However, large level of fluctuations, around 15% remain. The mixing hypothesis is then contradicted in our particular case. Similar observations can be drawn from the flow angle fluctuations remaining around 10 to 15°. Besides the discrepancies between turbulent rates obviously suggest that the mixing process is far to be completed at the radial diffuser leading edge.

At the throat section, the flow is still highly time-dependant and spatially heterogeneous. However, due to the differences in streampathes, adverse pressure gradients and in the influence of the leading edge stagnation area across the diffuser pitch, the time-organized blade passing feature has vanished.

3.3 Unsteady pressure measurement.

3.3.1 Transducers and measurements locations.

The transducers used for this application were Kulite pressure probes of the XCQ-093 serie. They fit the temperature and pressure conditions encountered in that flow region and present a bandwidth suitable for high frequency measurements. Each probe was calibrated in terms of transient response in a shock tube with its own protection screen, flush mounting device and acquisition facility used during later compressor runs. The measurement configuration is presented on Figure 2.

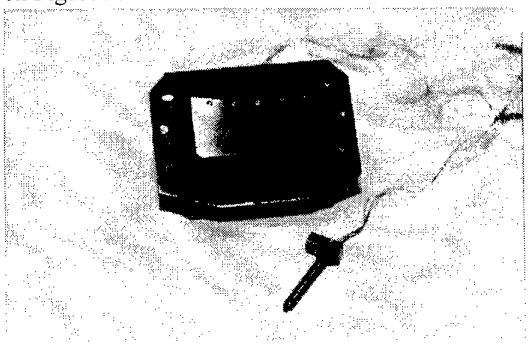

Figure 2 - Kulite flush mounting facility.

Sixteen measurement positions were distributed on the external wall of the radial diffuser (see later figures 5) :

- Four positions at the mean radius between impeller trailing edge and vaned diffuser leading edge at the reduced pitch ratios of 0., 0.25, 0.5 and 0.75.
- Three positions at the vaned diffuser leading edge, at reduced pitch ratios of 0.25, 0.5 and 0.75.
- Three positions in the captation area.
- Three positions at the diffuser throat section.
- Two positions downstream the diffuser throat situated on a mid-pitch line.

3.3.2 Data acquisition and processing.

The transducer signal is amplified via 4 channels of ANS-E300F4 and converted from analogic to digital through an 0X2000 Metrix Oscilloscope at a 500kHz rate. A pentium 90MHz PC is used to command the A/D converter and store the files via an RS232 serial link.

The acquired data consists in the raw signal obtained during five to ten impeller rotations. The synchronisation signal is given by a one per blade impulse allowing the initial time to be converted in a reduced time of the impeller blade passing in front of the diffuser pitch but preventing distinction between impeller passages. Then manufacturing differences between rotor passages will not be taken into account in our current study.

Those data are processed by a phase-locked averaging process, as described by Ainsworth[12] or Cicatelli and Sieverding[13]. Figure 3 represents the raw data obtained from position 1 for instance. The averaging consists in the following :

a) Ensemble averaged signal :

$$\overline{P(t)} = \frac{1}{N}\sum_{n=1}^{N} P(n,t)$$

b) Average random unsteadiness :

$$P(n,t) = \overline{P}(t) + p'(n,t)$$

$$T_p(t) = \sqrt{\frac{\overline{p'^2}}{\overline{P}^2}} = \frac{1}{\overline{P}}\sqrt{\frac{1}{N}\sum_{i=1}^{N}(P(n,t) - \overline{P(t)})^2}$$

where P(n,t) is the raw signal, N is the number of cycles acquired, t is the time, n is the index within the N cycles. A cycle corresponds to the rotation of an impeller passage in front of the probing position.

Figure 4 give the results of this procedure for position 1 for two different numbers of cycles, thus showing the independence of the solution when a sufficient number of cycles is described. In particular, no difference is observed between a five rotor rotations or ten rotor rotations acquisition. The accuracy in terms of reduced time dependency on synchronisation device can be evaluated to 2% of the cycle duration.

Nota : The unsteady pressures on the mean vaneless space radius and the throat section were treated to extract the time mean pressure ($\overline{P_s(t)} = \frac{1}{T}\int_0^T P(t)dt$) *which can be compared to static pressure tappings originally implemented on the test compressor. The comparisons showed some discrepancies between pressure probes. Correcting factors correlated for different operating points and assessed by swapping probe positions were then taken into account.*

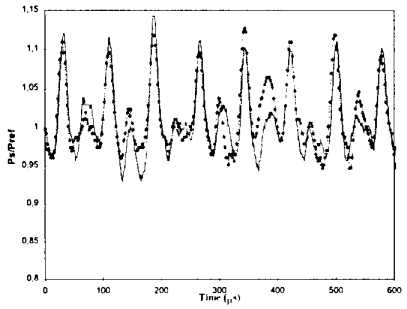

Figure 3 - Raw Data

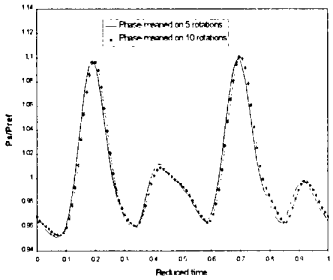

Figure 4 - Phase-meaned data

3.3.3 Data presentation.

Figure 5 represents the phase averaged period for the 4 experimental positions. The x-coordinate corresponds to the reduced period of rotor blade passing in front of the diffuser pitch, where 0. corresponds to a situation where the impeller trailing edge and the stator leading edge stands at the same azimuth.

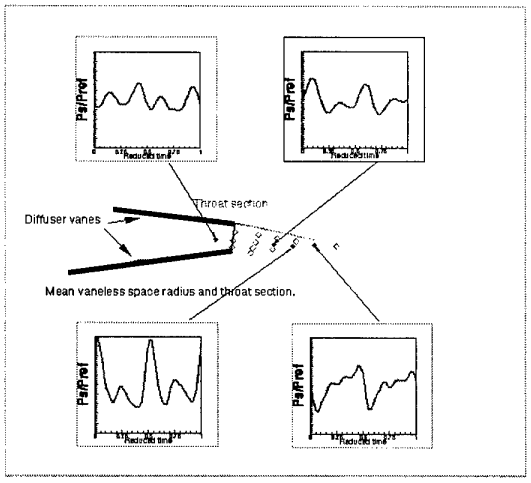

Figure 5 - Pressure evolutions (1).

4. THREE DIMENSIONAL NAVIER-STOKES SOLVER.

4.1 Foreword.

The NREC commercial software package VISIUN™ constituted the basis of this numerical study. This code, written for turbomachinery purpose solves the three-dimensional Navier-Stokes system of equations[14151617]. Pulliam and Steger works[18] give an overview of the implemented method. Developments were carried out by the authors wishing to closely examine rotor-stator interaction features. In particular, the treatment of interfacial areas and multi-channels domains had been customised, as well as the possibility to perform steady stage calculations.

4.2 Numerical background.

4.2.1 System of Equations.

The numerical approach of VISIUN™ is based upon a three dimensional Navier-Stokes code, written for turbomachinery purpose. The full system of equations expressed in strong conservation form is used herein. Its compact form can be expressed as follows in Cartesian coordinates[19].

$$\frac{\partial Q}{\partial t}+\frac{\partial(E-E_v)}{\partial x}+\frac{\partial(G-G_v)}{\partial y}+\frac{\partial(F-F_v)}{\partial z}=0$$

where vectors are given by :

$$Q=(\rho,\rho u,\rho v,\rho w,e)^T$$
$$E=(\rho u,\rho u^2+p,\rho uv,\rho uw,u(e+p))^T$$
$$F=(\rho v,\rho uv;\rho v^2+p,\rho vw,v(e+p))^T$$
$$G=(\rho u,\rho uw,\rho vw,\rho w^2+p,w(e+p))^T$$
$$E_v=(0,\tau_{xx},\tau_{xy},\tau_{xz},u\tau_{xx}+v\tau_{xy}+w\tau_{xz})^T$$
$$F_v=(0,\tau_{xy},\tau_{yy},\tau_{yz},u\tau_{xy}+v\tau_{yxy}+w\tau_{yxz})^T$$
$$G_v=(0,\tau_{xz},\tau_{yz},\tau_{zz},u\tau_{xz}+v\tau_{yz}+w\tau_{zz})^T$$

equations can be transformed to an arbitrary curvilinear space ξ,η,ζ,τ [18,19], while retaining strong conservation law form as:

$$\frac{\partial \hat{Q}}{\partial t}+\frac{\partial(\hat{E}-\hat{E}_v)}{\partial\xi}+\frac{\partial(\hat{G}-\hat{G}_v)}{\partial\eta}+\frac{\partial(\hat{F}-\hat{F}_v)}{\partial\zeta}=0$$

where the vectors are given by :

$$\hat{Q}=J^{-1}(\rho,\rho u,\rho v,\rho w,e)^T$$
$$\hat{E}=J^{-1}(\rho U,\rho uU+\xi_x p,\rho vU+\xi_y p,\rho wU+\xi_z p,(e+p)U-\xi_t p)^T$$
$$\hat{F}=J^{-1}(\rho V,\rho uV+\eta_x p,\rho vV+\eta_y p,\rho wV+\eta_z p,(e+p)V-\eta_t p)^T$$
$$\hat{G}=J^{-1}(\rho W,\rho uW+\zeta_x p,\rho vW+\zeta_y p,\rho wW+\zeta_{zx} p,(e+p)W-\zeta_t p)^T$$

and

$$U=\xi_t+\xi_x u+\xi_y v+\xi_z w$$
$$V=\eta_t+\eta_x u+\eta_y v+\eta_z w$$
$$W=\zeta_t+\zeta_x u+\zeta_y v+\zeta_z w$$

the viscous terms are transformed in the same way, their expression is given by Pulliam [18]

The metrics and the jacobian are :

$$\xi_x=J(y_\eta z_\zeta-y_\zeta z_\eta) \qquad \eta_x=J(z_\xi y_\zeta-y_\xi z_\zeta)$$
$$\xi_y=J(z_\eta x_\zeta-x_\eta z_\zeta) \qquad \eta_y=J(x_\xi z_\zeta-x_\zeta z_\xi)$$
$$\xi_z=J(x_\eta y_\zeta-x_\zeta y_\eta) \qquad \eta_z=J(y_\xi x_\zeta-x_\xi y_\zeta)$$
$$\zeta_x=J(y_\xi z_\eta-z_\xi y_\eta) \qquad \xi_t=-x_t\xi_x-y_t\xi_y-z_t\xi_z$$
$$\zeta_y=J(x_\eta z_\xi-x_\xi z_\eta) \qquad \eta_t=-x_t\eta_x-y_t\eta_y-z_t\eta_z$$
$$\zeta_z=J(x_\xi y_\eta-y_\xi x_\eta) \qquad \zeta_t=-x_t\zeta_x-y_t\zeta_y-z_t\zeta_z$$

$$J^{-1}=x_\xi y_\eta z_\zeta+x_\zeta y_\xi z_\eta+x_\eta y_\zeta z_\xi-x_\xi y_\zeta z_\eta-x_\eta y_\xi z_\zeta-x_\zeta y_\eta z_\xi$$

4.2.2 Turbulence modelling and solution algorithm.

The algebraic eddy viscosity model of Baldwin and Lomax[20] is implemented to take into account turbulence effects. Equations are solved numerically using a Beam and Warming type of algorithm[18,21]. At inflow boundary, total temperature, total pressure and two flow angles are

specified ; while static pressure is given at the outflow boundary.

4.2.3 Two frames of reference

The main difference between single blade row computations and stage simulations lies in the existence of two frames of reference, one for each component, separated by an interfacial area, through which numerical information has to be transferred in order to predict rotor/stator interaction effects. Several different approaches, either conservative or non conservative, have been used. The matching of the two frames retained in VISIUN™ is based on M. M. Rai [22] method. The grid is split into a rotating zone and a non-rotating zone with an interfacial overlay. Flux vectors are interpolated from one grid to the other in this overlaid area to obtain boundary conditions related to each component sub-domain. H-type meshes are used to model the geometry. Two overlaid grids are generated, one for each component. The interface area consists in a cylindrical surface situated at the mean radius between the impeller trailing edge and the vaned diffuser leading edge.

4.2.4 Unsteady stage calculations : a reduction of the computational domain.

Cpu time and memory necessary for unsteady stage numerical simulations make the use of a computational domain reduction unavoidable. A common approach consists in geometry modifications in order to obtain the same azimuthal extension in the rotor and in the stator modelled passages. This was basically used by VISIUN™, but also by Rai[22] and Dawes[6] among others.

In fact, geometrical transformations are, in the case of centrifugal compressors, mainly applied to the vaned diffuser considered passages. Therefore, the hub and/or shroud countours have to be ajusted to ensure the total design throat section conservation if an accurate simulation of stage performance is awaited. Then, in a code assessment contex, interpolations in the numerical flow field to probe the solution at the exact measurement locations have to bear reduced space considerations Moreover, some cases lead to a slightly diverging vaneless space which may adversly affect a commonly observed shroud recirculating region. Therefore, an alternative method was preferred by the authors with a view to computing the flow in the actual geometry thanks to minor numerical modifications. This reduction technique, developed by the ONERA (see for instance Fourmaux[23]), may be summarised as follows : let N1 and N2 be the real blade numbers of the rows to study, let K1 and K2 the number of passages considered in each stage component so that K1 and K2 are small but K1/K2 stays as close as possible to N1/N2. A periodic azimuthal condition is implemented in each row (I_{per} ad $I_{per'}$ lines for the impeller and D_{per} and $D_{per'}$ lines for the diffuser on Figure 6). This results in a time lag cancelling at the extreme azimuthal boundaries of each group of passages. The information transferred through the interfacial area from one grid to the opposite must be compatible with those spatially periodic conditions. Then we have to use an expansion/contraction step at the interface. Let $e_1=2\Pi K_1/N_1$, $e_2=2\Pi K_2/N_2$ be the respective azimuthal extension of each component grid on Figure 6 and $ec=(e_1+e_2)/2$. F1 is the downstream boundary of the first sub-domain related to e1, F2 is the upstream boundary of the second sub-domain related to e2. Fc is then a virtual frontier related to ec through which data are transferred by interpolation on an equal azimuthal extension ec thanks to previous expansion/contraction of the azimuthal gradient between F1 and Fc or between F2 and Fc as represented on Figure 6.

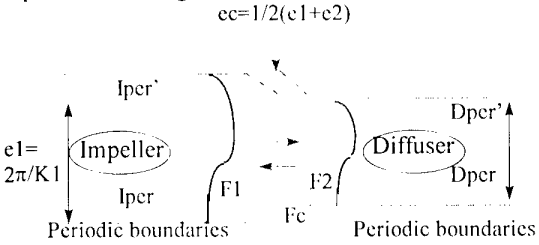

Figure 6 - Reduction of the computational domain.

The comparison between numerical results and experimental data presented in the following parts will give an outline of the level of description obtained with this method.

4.2.5 Steady stage calculations : an industrial necessity.

The previously described unsteady calculations involved a full time resolved interpolation process at the rotor-stator interface and a slow convergence towards a periodic numerical solution. Considering current hardware capabilities available to aeronautical design engineers, a time mean interfacial treatment becomes an industrial necessity. Such a calculation tool, taking into account rotor-stator coupling mainly in terms of hub to shroud distortions, is already in use during design cycles. For instance, three dimensional geometries of components, fitting intra-stage interactions, can be studied within short term development cycles.

The method implemented in VISIUN™ by the authors and presented herein is based on Riemann invariants theory and the derived compatibility relations. This approach comes from two considerations :

- Compatibility relations are a way to take into account the transport of flow properties by wave fronts[24].
- A grid point, steady in its own frame, receives informations from opposite points in the other frame points in the other frame rotating in front of him.

Then, the approach chosen consists in imposing interfacial boundary conditions through azimuthaly meaned compatibility relations. The French ONERA, first described this technique[25,26].

Let D be the computational domain and n an inward directed vector. The five compatibility relations obtained from the five eigenvalues $(V\cdot n-a, V\cdot n, V\cdot n+a)$ of the hyperbolic Euler system are :

$\lambda = V_n - a,$	$P'-(\rho a)\,V_n' = P^* - (\rho a)\,V_n^*$
$\lambda = V_n + a,$	$P'+(\rho a)\,V_n' = P^* + (\rho a)\,V_n^*$
$\lambda = V_n,$	$P'-(a^2)\,V_n' = P^* - (a^2)\,V_n^*$
$\lambda = V_n,$	$V_t' = V_t^*$ (Double relation)

where P is the static pressure, ρ the density, a the sound speed, V the speed vector, $V_n = V\cdot n$ and $V_t = V-(V\cdot n)\cdot n$. The superscript * indicates a scheme value and ' indicates the flow properties at the position receiving the corresponding characteristic.

The implementation for the interface mean treatment can be summarised as follows. The normal Mach number is supposed to be less than unity, inward and outward flow are distinguished. For exiting flow, $V\cdot n<0$, four compatibility relations are applied (four negative eigenvalues) and one boundary condition is necessary. This condition is similar to a non-reflection boundary condition. Then we have :

$$\begin{aligned}
&P'-(\rho a)\,V_n' = P^*-(\rho a)V_n^*\\
&P'-(a^2)\,V_n' = P^*-(a^2)V_n^*\\
&V_t' = V_t^*\\
&P'+(\rho a)\,V_n' = \overline{(P^*+(\rho a)V_n^*)_2} = I_1
\end{aligned}$$

where I1 is an azimuthaly averaged value calculated on the opposite domain. The averaging process is surface weighted and results in hub to shroud profile of I_1.

For inlet flows, $V\cdot n>0$, one compatibility relation is applied (one negative eigenvalue) and four boundary conditions are necessary. Then the relations are :

$$\begin{aligned}
&P'-(\rho a)\,V_n' = P^*-(\rho a)V_n^*\\
&P'-(a^2)\,V_n' = \overline{P^*-(a^2)V_n^*} = I_2\\
&\overline{V}_{t1}' = \overline{V}_{t1}^* = I_3\\
&\overline{V}_{t2}' = \overline{V}_{t2}^*\\
&P'+(\rho a)\,V_n' = \overline{(P^*+(\rho a)V_n^*)_1} = I_5
\end{aligned}$$

where I2,I3,I4 and I5 are averaged by the same previous process and result in hub to shroud varying boundary conditions.

Numerical flow fields obtained through this approach will be compared to experiments in the sixth part.

5. UNSTEADY FLOW CALCULATIONS AND ASSESMENT.

5.1 Numerical simulations conducted.

The real ratio of blade numbers between the wheel and the stator is surrounded by 1 and 1/2. Then, two basic mesh configurations were built : the first one contained one blade passage of each component and will be named case A, the second one matched one blade passage of the impeller with two passages of the vaned diffuser, named case B. In both cases an approximate number of 125000 nodes for each passage meshed was chosen which is quite low but planned to give an interesting compromise between accuracy and solution time. As will be stated later some fluctuations induced by impeller wakes were partly damped in those first cases, a third configuration was then meshed with an increased node number in the azimuthal direction. This case will be referred as case C.

	Impeller	Diffuser
Case A	82x61x24	74x69x24
Case B	82x61x24	2*(74x69x24)-1
Case C	82x82x24	2*(74x81x24)-1

Table 1- Node distribution.

For each configuration, the flow field of the peak efficiency point on the design speed curve has been computed. A time-periodic solution was obtained in all cases. Convergence was monitored by examining static pressure evolution in the most sensitive parts of the flow field i.e. the impeller trailing edge and the diffuser leading edge. An

approximate number of 10 to 15 blade passing period were necessary to obtain a periodic solution.

5.2 Mono-dimensional results.

From the designer point of view, the overall performance rendering capability of a code is of major importance, allowing him to evaluate a new designed release numerically without requiring intensive test rig campaign. The comparisons made on one-dimensional mean values can be summarised in the following chart. The values given are differences between experimental and numerical results expressed in percent.

	Case A	Case B	Case C
G'	+0.35	+1.22	+0.65
Pi_{stage}	+1.35	+1.86	+1.78
$Pi_{impeller}$	+0.26	-0.13	+0.44
Ps_{stage}	-2.32	-2.98	-0.88
$Ps_{impeller}$	+0.04	+0.96	+1.21
$Ti_{impeller}$	+0.82	+0.99	+1.01
$\eta_{impeller}$	-1.69	-1.65	-1.27
Cp	-1.78	-6.45	-2.28

Table 2- Mono-dimensionnal results.

The operating point is then quite accurately described in all cases. The efficiency lack generally observed is similar to the difference experienced in isolated wheel simulations. Moreover, it should be noted that previous simulations obtained by the sliding of impeller outflow conditions at the inlet of an isolated diffuser grid did not allow to reach such a level of description of the diffuser operating point. For instance the static pressure recovery coefficient was underestimated by more than 20%, thus suggesting, the importance of full stage coupling in a transonic configuration.

5.3 Two-dimensional results.

The first validation step consists in comparisons between measured and time averaged calculated spanwise evolution of the absolute flow angle and the absolute flow velocity. This phase will allow the evalution of the code capability to reproduce the hub-to-shroud distortions which, according to Dawes[6] are a key factor of rotor/stator interaction influence on stage performance. On Figure 7, the y-axis coordinate represents the hub-to-shroud reduced distance, where 0. corresponds to the hub. Either the absolute flow angle (counted between the velocity direction and the circumferencial direction), to which a reference angle is substracted or the absolute velocity modulus (reduced by the rotor tip speed) are given on the x-axis. Those evolutions are extracted at the mean vaneless space radius and here are given at a reduced pitch position of 0.3. More details are given by Domercq and Thomas[27].

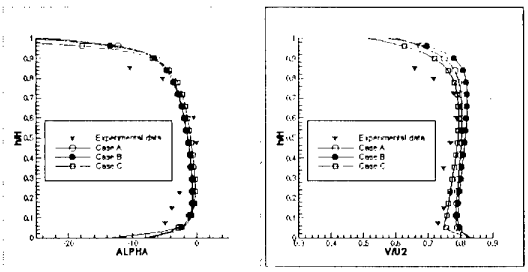

Figure 7 - Time averaged spanwise evolutions.

The two calculations performed on the A and B basic grids, restitute the same spanwise variation in terms of velocity and angle, thus illustrating their close one-dimensional behaviour. Besides, rather accurate descriptions of the hub to shroud experimental evolution are obtained. In particular, the gradient of velocity is shown by both (A and B) calculated profiles. The mean level difference is linked to the slight mass-flow discrepancies in calculations, see Table 2. Similarly, the calculated and measured flow angles denote an interesting agreement. The shroud area subdeflexion , known to result from a complex interaction between tip leakage vortex, passage vortex and horseshoe vortex (Kang and Hirsch[28]) is precisely given by both calculations. Concerning Case C, similar profiles are obtained with the increased node density. In particular, flow angle evolutions are identical to the previous (A and B) results

5.4 Unsteady assessment and unsteady flow invetsigation.

5.4.1 Unsteady assessment.

In the following part, we will focus our attention on case C results which, regarding the higher azimuthal node density, gave suitable results to face experiments. Figure 8 and Figure 9 represent the absolute flow angle and velocity at midspan for three reduced pitch positions of 0.3, 0.5 and 0.7. The measurement section considered is still section 1, i.e. the mean vaneless space radius.

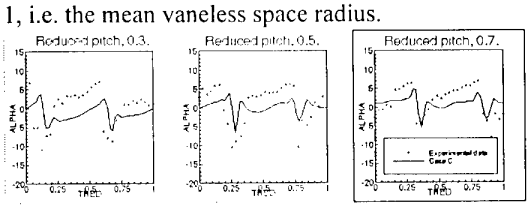

Figure 8 - Midspan unsteady evolution of the absolute flow angle.

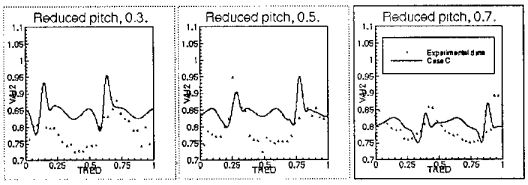

Figure 9 - Midspan unsteady evolution of the reduced absolute velocity.

A strong blade wake influence characterises the experimental results. This region is occupied by a low velocity fluid attached to the trailing edge in the rotating frame of reference. A speed triangle analysis shows that this results in a low, i.e. rather circumferencial, absolute flow angle and high speed pattern in the absolute frame of reference. Those wakes are indeed larger near the hub, since the trailing edge thickness increases from hub to shroud. Moreover, a steady point (i.e. a L2F measurement point in the diffuser frame of reference sees the pressure side of the backswept blade before its suction side. The experimental gradients observed thus suggest that the absolute speed magnitude decreases from suction side to pressure side while the absolute flow angle increases. Then, in the relative frame, the impeller delivers fluid of higher energy near the pressure side. Thus suggesting that the Coriolis effect that generally drags low energy particles to the suction side takes advantage, in our case, on the curvature effect, which on the contrary leads low energy fluid particles to the centre of curvature, that in our backswept case corresponds to the pressure side.

The comparison between experimental data and computational results shows that the wakes extensions are underestimated by the numerical simulations. However, the magnitude of the fluctuations is quite well estimated. A 10 to 12° angle fluctuation is obtained numerically whereas around 15° were measured. In terms of velocity, the predicted order of variation is situated between 17 to 25% where the corresponding L2F results range from 17 to 30 %. More precisely, despite the wake extension reduction, the flow angle and speed modulus blade-to-blade gradient, linked to secondary flow behaviour, are accurately rendered. Moreover, the speed modulus fluctuations are reduced in the same way with increasing reduced pitch position. Nonetheless, the downstream propagation of the numerical wake, thinner than the experimentally observed corresponding patterns will also be subject to faster mixing in the captation area.

Figure 10 presents the comparisons between case C and unsteady pressure measurements obtained with Kulite transducers. A fair agreement is obtained. The shape of the fluctuation is rendered for each position. Small structure of the pressure field are described with accuracy for locations 1 and 3. The evolution of the signal between location 1 and 2, consisting in the separation of the flat profile in a main and secondary peak is also captured. The description of this dual shape profile is confirmed by location 3 comparison. However, an inadequate numerical damping appears at location 4, since only half of the signal amplitude has been simulated numerically.

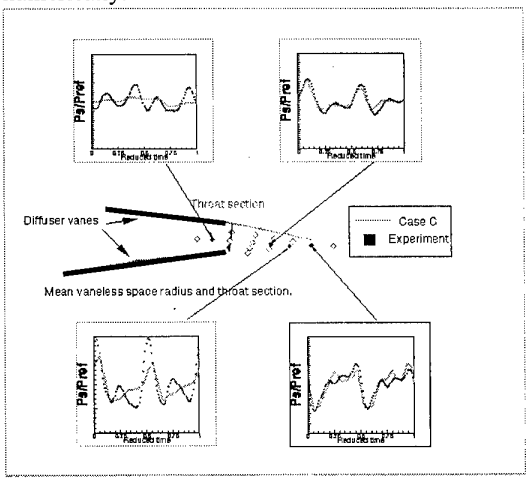

Figure 10 - Confrontation of pressure evolutions.

As a conclusion, the unsteady assessment reveals to be quite satisfactory, since the global behaviour of the matching between the impeller and its vaned diffuser is given by the code.

5.4.2 Unsteady flow investigation from impeller outlet to the captation area.

Figure 11 and Figure 12 give the time-resolved evolution of the unsteady flow field through its static pressure and absolute Mach for six positions across the blade passing period.

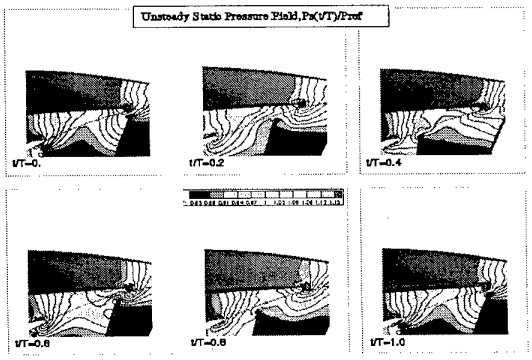

Figure 11 - Unsteady flow field, static pressure.

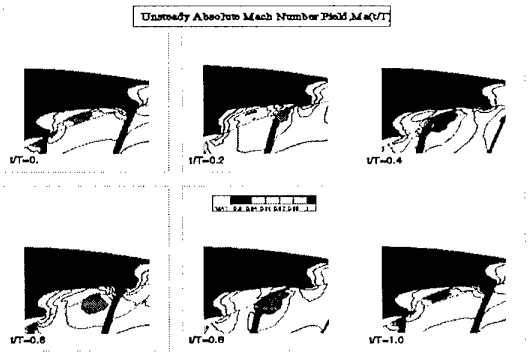

Figure 12 - Unsteady flow field, Mach number.

Those representations are given at midspan where experiment versus simulation agreement was interesting. The rotor/stator interaction appears to be reciprocal, the wheel indeed delivers pitch dependant flow conditions as discussed previously but the magnitude of stator vane counter effect reaches the same level. In fact, the pressure field representation, for instance, underlines the diffuser vane leading edge influence on the impeller outflow pressure condition through the existence of a high static pressure zone near the stagnation point situated on the leading edge. This leads to an approximate variation of 20% of static pressure on the pressure side of the impeller blades.

Moreover, the blade passing wakes have an obvious influence on the captation area flow field, in particular in the vane suction side nearby. The impeller blade trailing edge imposes a high absolute Mach number and low absolute angle flow pattern to the diffuser inlet. This zone has hardly no effect on the diffuser pressure side since its extend is reduced by the leading edge high pressure field, when impeller and diffuser blades face each other (t/T=0.).

Then, it affects the diffuser suction side by dragging a low Mach number fluid into the channel (t/T=0.2). The next step consists in the creation of a high Mach number flow region in the middle of the diffuser pitch (t/T=0.4), which stands in place of a similar pattern appeared at t/T=0 and observed whilst diffusing slightly downstream at this reduced time. Thus the captation area experiences a succession of high speed and low speed bulbs that mix downstream. The blade-to-blade flow dependence at the impeller outlet leads therefore to a fluctuation that follows the main flow direction.

6. STEADY SIMULATIONS OF BLADE ROW INTERACTIONS.

This part of the study will give an overview of the code capability to describe blade row interaction within the frame of steady coupling.

The geometry of the compressor previously investigated in an unsteady mode was submitted to a steady calculation involving the coupling process described in paragraph 4.2.5.

Table 3 sums up the discrepancies obtained between the time averaged flow field of case C and the steady simulation name case D. They are expressed in percent.

	(Case C - Case D) %
G'	+0.40
Pi_{stage}	-1.86
$Pi_{impeller}$	+2.18
Ps_{stage}	-1.37
$Ps_{impeller}$	+0.24
$Ti_{impeller}$	+0.5
$\eta_{impeller}$	+0.32
Cp	+1.96

Table 3 - Mono-dimensionnal comparison of case C (unsteady) and D (steady).

Close performance description is given by the two coupling techniques. An increased level of loss is predicted between the impeller trailing edge and the radial diffuser leading edge by the steady coupling calculation. This mainly results from slight discontinuities generated at the averaging plane.

Finally, spanwise evolutions of the absolute flow angle and absolute reduced speed of cases C and D are compared on Figure 13. The profiles are extracted at the leading edge radius of the stator.

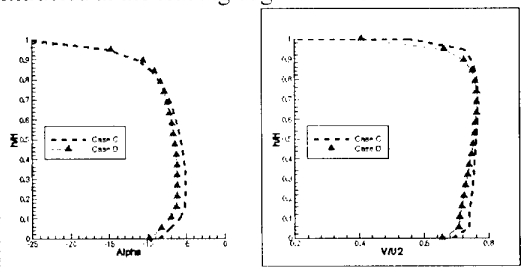

Figure 13 - Comparisons of spanwise evolutions.

The two profiles exhibit a good agreement. The hub to shroud gradients are accurately rendered. The discrepancy in terms of absolute flow angle is less than 1°. Thus a steady coupling calculation proves to be able to simulate the correct evolution of incidence angle and speed on the span of the radial diffuser. Then it can be considered as an interesting tool to take into account the coupling between the components of a centrifugal compressor stage thanks to calculations of a "design affordable" cost.

7. CONCLUSIONS.

The flow patterns that govern the rotor/stator interaction in a centrifugal compresssor stage have been investigated by means of experimental and numerical studies. The test stage representative of high speed and high performance turbomachinery devices, was known to be a rather severe aerodynamic case. The present paper yields to the following conclusions concerning the unsteady part of the study :

- An intense upstream influence of the vaned diffuser on the impeller flow field is observed. The performance of the compressor is then properly caculated by a full time-resolved simulation of the stage, whilst a method consisting in using impeller outflow as upstream boundary condition of the vaned diffuser reveals unsatisfactory.

- Unsteady variations measured thanks to a L2F device were qualitatively fairly described. The agreement in terms of blade to blade gradients, for instance, put emphasis on the code capability to reproduce secondary flows influence on the stage flow field. Moreover this gave an outline of the computational domain reduction as an acceptable representation.

- The interaction of the impeller blade leading edge and the vaned diffuser stagnation zone at midspan appeared to drive both the impeller outflow conditions and the unsteady flow patterns in the captation area.

Moreover, a method allowing design time-affordable calculations, which couples components thanks to a mean treatment of the interfacial area, using Riemann invariant theory, has been implemented in the Navier-Stokes code. The comparison made between the steady stage flow field and the time-averaged flow field of unsteady calculations underlines the capability of this tool to integrate rotor-stator interaction features in the calculations of the performance of a transonic centrifugal stage.

References :

[1] P.Belaygue, H.Vignau,
Le compresseur centrifuge, composant essentiel des turbomoteurs de petite et moyenne puissance.
AGARD-CP-537.

[2] Krain H.,
A study on centrifugal impeller and diffuser flow
ASME paper 81-GT-9, 1981.

[3] Krain H., Experimental observations of the flow in impellers and diffusers
VKI Lecture Series 1984-07, 1984.

[4] Bois G., Duchemin J.M., Vouillarmet A., Papaillou K.D.
Analyse expérimentale de l'écoulement dans un étage de compresseur centrifuge.
AGARD-CP-282, 1980.

[5] Hus H., Fradin Ch.
Influence de l'hétérogénéité de l'écoulement à la sortie du rotor sur les performances du diffuseur d'un compresseur centrifuge.
AGARD-CP-282, 1980.

[6] Dawes W.
A simulation of the unsteady interaction of a centrifugal impeller with its vaned diffuser : flow analysis.
ASME paper 94-GT-105.

[7] Bois G., Fradin Ch., Vignau H.
Problèmes de validation des codes Euler 3D pour compresseurs centrifuges.
Third European Propulsion Forum , November 13-15, 1991. AAAF/DGLR/RAeS.

[8] Schold R..
Laser Two Focus Velocimetry.
AGARD-CP 399, 1986.

[9] Fagan J.R., Fleeter S.
L2F & LDV velocimetry measurement and analysis of the 3D flow field in a centrifugal compressor.
AIAA-89-2572.

[10] Elder R.L., Forster C.P., Gill M.E.
Application of Doppler and Transit Laser Anemometry on small Turbomachines.
AGARD-CP-399.

[11] Fradin Ch.
Constitution d'une base de données relative a l'écoulement du fluide dans un compresseur centrifuge.
ONERA Report.

[12] R. W. Ainsworth
Unsteady Measurements Techniques.
VKI Lecture Series.

[13] G. Cicatelli, C.H.Sieverding
The Effect of Vortex Shedding on the Unsteady Pressure Distribution Around the Trailing Edge of a Turbine Blade.

Journal of Turbomachinery, Transaction of the ASME, Vol. 119, October 1997.

[14] User's Guide VISIUN-2FR™ Version 3.0,
Simultaneous three-dimensional CFD analysis of rotating and stationary bladed passages in turbomachinery, a computational system.
Northern Research and Engineering Corporation, Woburn, Massachusets, USA.

[15]Analysis of three-dimensional unsteady flow in centrifugal compressors.
Final report, phase one : diffuser performance.
Principal investigator : Oreper G.
Northern Research and Engineering Corporation, Woburn, Massachusets, USA.

[16] Analysis of three-dimensional unsteady flow in centrifugal compressors.
Final report, phase two : impeller performance.
Principal investigator : Oreper G.
Northern Research and Engineering Corporation, Woburn, Massachusets, USA.

[17]Analysis of three-dimensional unsteady flow in centrifugal compressors.
Final report, phase three : stage performance.
Principal investigator : Oreper G.
Northern Research and Engineering Corporation, Woburn, Massachusets, USA.

[18] Pulliam T.H., Steger J.L.
Implicit Finite-Difference Simulations of Three-Dimensional Compressible Flow.
AIAA Journal, Vol. 18, February 1980.

[19] Anderson D.A., Tannehill J.C., Plechter R.H.
Computational Fluid Mechanics and Heat Transfert.

[20] Baldwin B.S., Lomax H.,
Thin layer approximation and Algebraic Model for Separated Turbulent Flows.
AIAA paper 78-257, 1978.

[21] Beam R.M., Warming R.F.
An implicit factored scheme for the compressible Navier-Stokes Equations.
AIAA Journal, Vol. 16, April 1978.

[22] Rai M.M.
Navier-Stokes Simulations of Rotor-Stator Interaction using Patched and Overlaid Grids.
AIAA paper 85-1519.

[23] Fourmaux A.,
Assessment of a Low storage Technique for Multi-Stage Turbomachinery Navier-Stokes Computations.
ASME Winter Annual Meeting, Chicago, USA, November 6-11, 1994.

[24] JP Veuillot, G. Meauze
A 3D Euler Method for Internal Transonic Flows Computation with a Multi-domain Approach.
AGARD-LS-140

[25]A. LEMEUR
Calculs stationnaires et instationnaires dans un étage de turbine transsonique
AGARD - CP- 510.

[26] C. Toussaint, A. Fourmaux, G. Billonnet
Comparison of Steady and Unsteady 3D Viscous Flows Computations through a transsonic turbine stage.
ISABE, November 1997.

[27] O. Domercq, R. Thomas.
Unsteady Flow Investigation in a Transonic Centrifugal Compressor Stage.
AIAA-97-2877

[28] Hirsh Ch., Kang S., Pointel G.
A numerically supported investigation of the 3D Flow in Centrifugal Impellers, Part II : Secondary Flow Structure
ASME paper 96-GT-152

Three-Dimensional Inverse Design Method for Turbine and Compressor Blades

A. Demeulenaere * and R.A. Van den Braembussche

von Karman Institute for Fluid Dynamics, Turbomachinery Department
Chaussée de Waterloo, 72, B-1640 Rhode-Saint-Genese, Belgium

Abstract

An iterative procedure for turbomachinery blade design, in
which the three-dimensional blade shape is modified by means of a physical algorithm and the transpiration model, is presented. The transpiration flux is defined from the velocity normal to the wall, computed by means of a modified Euler solver when the target pressure distribution is imposed along the blade surfaces. This method is very efficient as it needs only a limited amount of computertime to obtain the required geometry.
After a short description of the method this paper focuses on some special features that have been introduced to enhance convergence and to facilitate compliance with required performances and mechanical constraints. Each of these techniques is illustrated with an example.

Keywords: inverse design, three-dimensional, compressor, turbine, transonic, Euler, lean, dihedral

LIST OF SYMBOLS

a	speed of sound
C_p	specific heat coefficient
E	total internal energy
F	flux
V	volume
W	relative velocity
P	pressure
Q_m	mass flow
s	streamwise length
S	volume surface
t	time
	spanwise length
T	temperature
th	blade thickness
β	relative flow angle
ρ	density
ξ	normal wall displacement

Subscripts

g	of the grid
i	axis of coordinate
in	at inlet
n	normal component
r	in relative frame
s	streamwise component
t	spanwise component
TE	at the trailing edge
out	at outlet
x	axial component
1	cascade inlet section
2	cascade outlet section
$*$	extrapolated value

Superscripts

n	time step
o	stagnation condition
k	spanwise position

* presently at NUMECA International, Avenue F. Roosevelt, 5, B-1050 Brussels, Belgium

1 INTRODUCTION

Blade design by successive modifications of the blade geometry and verifications by wind tunnel testing or flow calculations can be very time consuming and result in high design costs and delays. Furthermore as the outcome depends on the designers' experience it does not necessarily lead to the best possible blade shape required for improved efficiency of compressors and turbines. A more direct achievement of the design targets is possible by means of inverse methods defining directly the geometry corresponding to a prescribed velocity or pressure distribution.

A first generation of inverse design methods, based on the analytical solution of the flow equations, was limited to shock-free irrotational flows and difficult to extend to three dimensions [1,2,3] . Furthermore, these methods solve the flow equations in a non-physical plane which make it difficult to control the mechanical constraints during the design process.

These problems are avoided by solving the Euler or Navier-Stokes equations so that the method becomes applicable to three-dimensional rotational flows including shocks. Solving the equations directly in the physical domain, largely facilitates the control of the mechanical constraints. However, as the blade walls themself are the solution of the problem, the procedure must be iterative, requiring a first guess of the geometry to initialize the calculation.

The geometry modifications can be defined by a pure mathematical algorithm, minimizing the difference between the desired and present pressure distributions. Such an approach has the advantage that any flow solver can be used without modifying it. However these methods are very expensive in terms of CPU time because of the large number of flow analyses that are required [4,5].

The method presented here uses a physical model to define the geometry modifications required for achieving the prescribed performance. It has shown to be very efficient and applicable to a large variety of design problems [6,7,8,9,10]

Paper presented at the RTO AVT Symposium on "Design Principles and Methods for Aircraft Gas Turbine Engines", held in Toulouse, France, 11-15 May 1998, and published in RTO MP-8.

A major problem in inverse design is the definition of an optimum (minimum loss) velocity or pressure distribution , for which a blade exists, that provides the prescribed performance (turning) and satisfies the mechanical or other constraints.

This paper emphasizes on the different features, such as adjustable outlet pressure, hybrid design systems and parametrized target distributions, that have been introduced in order to facilitate compliance with the prescribed performances and/or mechanical constraints. Each of these features is illustrated by an example

2 BLADE DESIGN METHOD

The core of this design method is a time marching solution of the three-dimensional Euler equations in a domain of which the walls are moving during the transient part of the calculation [11].

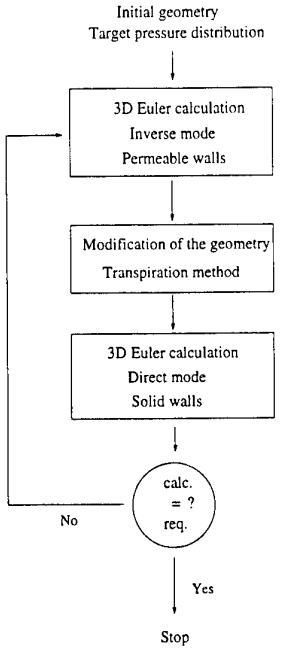

Fig. 1 : **Flow chart of moving wall inverse design method**

Two calculations are made at each time step (Fig. 1)

- In a first time step one calculates the flow corresponding to the required pressure distribution imposed on the blade walls of the present geometry. The calculated velocity will not be tangent to the walls, except when the imposed pressure distribution equals the one resulting from a direct calculation around the same geometry. Using permeable wall boundary conditions one can calculate a velocity normal to the blade walls which is then used to define a new blade geometry by means of the transpiration model.

- The second step makes an update of the flow field taking into account the movement of the walls and mesh. Experience shows that after each time step the pressure distribution on the new geometry is closer to the target one, provided that this target corresponds to a realistic geometry.

These two time steps are alternated in an iterative procedure until the normal velocity and hence the transpiration flux is zero i.e. when the pressure distribution obtained during the analysis step equals the required one. In this procedure the geometry converges to the desired one simultaneously with flow converging to the steady asymptotic solution. This facilitates a control of the blade geometry during the design process and allows for an eventual adjustment of the target pressure distribution.

A major advantage is that the method does not diverge when the constraints prevent reaching the target pressure distribution. It then converges to a geometry on which the pressure distribution is as close as possible to the target one.

2.1 The Euler solver

This type of inverse method can be based on any Euler solver. The validity of the results however clearly depends on the accuracy of the flow calculation. A high resolution three-dimensional solver has been developed for this purpose [10,11].

The cell centered finite volume approach uses a structured grid to discretize the numerical domain. The three-dimensional grid is composed of two-dimensional ones, defined on a series of axisymmetric surfaces, distributed between the hub and tip endwalls.

The unsteady three-dimensional Euler equations are integrated in time in an explicit way, with a four-step Runge-Kutta algorithm, until the steady solution is reached. The Flux Vector Splitting approach [12] is adopted for the computation of advective fluxes. This 'upwind' method respects the physics of supersonic flows, does not need any dissipation to ensure the convergence of the procedure, and guarantees the capturing of the grid-aligned shock waves in two or three discretization points. The fluxes are computed by the M.U.S.C.L. approach [13], which leads to third order accuracy for one-dimensional problems.

2.2 Boundary conditions

The only difference between the direct and inverse Euler solver lies in the way boundary conditions are applied along the blade walls. Each solution of the 3D Euler equations can be written as the superposition of 5 waves propagating in the numerical domain [14]. The 5 eigenvalues of the Jacobian matrix associated to the direction $\vec{n}$ and the corresponding compatibility relations are:

Eigenvalue	Compatibility relation
W_n^{n+1}	$\rho^{n+1} = \rho^* + \frac{P^{n+1}-P^*}{a^{n,2}}$
W_n^{n+1}	$W_t^{n+1} = W_t^*$
W_n^{n+1}	$W_s^{n+1} = W_s^*$
$W_n^{n+1} + a$	$W_n^{n+1} = W_n^* - \frac{P^{n+1}-P^*}{\rho^n a^n}$
$W_n^{n+1} - a$	$W_n^{n+1} = W_n^* + \frac{P^{n+1}-P^*}{\rho^n a^n}$

Where W_n, W_s and W_t are respectively the velocity component in the normal, streamwise and spanwise direction (figure 2) and the state * refers to the extrapolated values.

The compatibility relation can be used to calculate the unknown on the boundary of the numerical domain if the eigenvalue is positive. Three boundary condition are required when $W_n < 0.$. The first two are the total-temperature T_r° and pressure P_r° in the relative frame of

reference. One imposes the value obtained during the previous analysis step.

The static temperature can then be derived from the imposed static pressure by means of the isentropic flow equation. The magnitude of the relative velocity, as well as the velocity component tangent to the blade surface are defined by:

$$W^2 = 2C_p(T_r^{0,n} - T^{n+1})$$

$$W_s^2 + W_t^2 = W^2 - W_n^2 \quad (1)$$

The additional boundary condition to define W_s and W_t, is the ratio between the stream- and spanwise velocity components, which is also imposed at its local value during the previous analysis step:

$$\left(\frac{W_s}{W_t}\right)^{n+1} = \left(\frac{W_s}{W_t}\right)^n \quad (2)$$

Those three boundary conditions may not provide an exact solution at each iteration, they will not falsify the final results, as they are updated after each geometry modification. The final result is anyway obtained by an analysis step.

2.3 Transpiration model

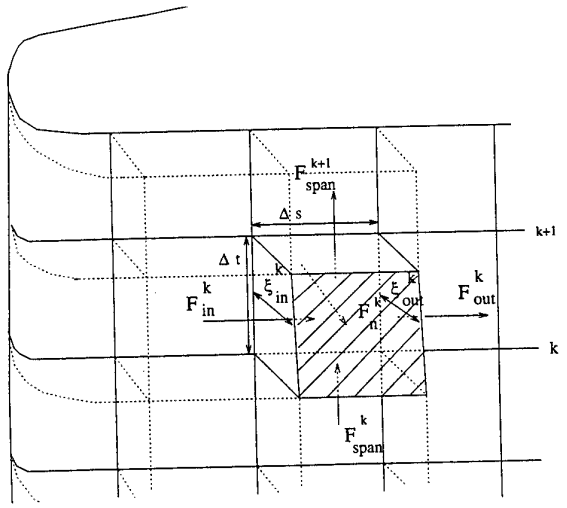

Fig. 2 : **3D transpiration**

The transpiration model defines a new blade geometry in function of the calculated normal and tangential velocity along the initial blade contour.

The method progresses separately along the pressure and suction surfaces, from the stagnation line to the trailing edge. One can keep the stagnation line on the blade unchanged or modify it to achieve the required lean and sweep. All mesh points, including those on the blade wall, are displaced in the axisymmetric surfaces which remain unchanged during the whole design.

The amplitude of the displacement is obtained by applying the mass equilibrium in the cells between the old and new blade walls (figure 2). The flux through an elementary surface ($\Delta s \Delta t$) of the old blade wall is defined by:

$$F_n^k = (\rho W_n \Delta s \Delta t)^k \quad (3)$$

where Δs and Δt are the dimensions of the face in the stream- and spanwise directions. Assuming that the new blade wall is a streamsurface, the streamwise fluxes are:

$$F_{in}^k = (\rho W_s \Delta t)_{in}^k \xi_{in}^k$$

$$F_{out}^k = (\rho W_s \Delta t)_{out}^k \xi_{out}^k \quad (4)$$

The spanwise mass fluxes F_t^k through the interior surfaces account for the interaction between the neighbouring cells:

$$F_t^k = (\rho W_t \Delta s)^k \frac{\xi_{in}^k + \xi_{out}^k + \xi_{in}^{k-1} + \xi_{out}^{k-1}}{4} \quad (5)$$

The hub and tip walls being impermeable, no mass flux can enter or leave the two extreme cells through them. The density and velocity components are obtained by interpolation, from the values at the calculation nodes. A three-dimensional grid, containing KM surfaces from hub to tip, results in a tri-diagonal system of $KM - 1$ equations, defining the unknowns ξ_{out}^k in function of the displacements ξ_{in}^k, the last one being already computed from the mass equilibrium of the upstream cells.

The displacement of the KM grid points are then derived from the displacements ξ_{out}^k, by interpolation for the interior points, and by extrapolation for the hub and tip points.

2.4 The flow field update

After the blade shape modification, a new mesh is generated around the new profile. The displacements of all mesh points over the time step are computed, from which a 'grid-point velocity' $\vec{W}_g$ is deduced.

The conservation of mass, momentum and energy is applied to control volumes V, whose faces are moving with the velocity $\vec{W}_g$:

$$\frac{d}{dt}\int_V \rho dV = \oint_S \rho(\vec{W} - \vec{W}_g)\vec{n}dS \quad (6)$$

$$\frac{d}{dt}\int_V \rho W_i dV = \oint_S [\rho W_i(\vec{W} - \vec{W}_g)\vec{n} + P n_i]dS + \int_V F_i dV$$

$$\frac{d}{dt}\int_V \rho E_r dV = \oint_S [\rho E_r(\vec{W} - \vec{W}_g) + \vec{W}P]\vec{n}dS$$

where $\vec{n}$ is the inward pointing normal vector.

The Euler solver with moving wall is different from an Euler solver with fixed walls only by the extra terms related to $\vec{W}_g$ and the variation of the cell volume with time. Attention must however be given to the relation between the time dependent change of the volume and the velocity of the faces.

$$\frac{d}{dt}\int_V dV + \oint_S \vec{W}_g \vec{n} dS = 0 \quad (7)$$

3 UNIQUENESS PROBLEM

The convergence of the iterative design procedure is closely related to the existence and uniqueness of the solution. In spite of a lot of theoretical work over the last 50 years [1] it has not yet been possible to define the necessary and sufficient conditions for a unique solution in compressible flows.

One of the convergence problems one has experienced results from imposing the inlet total pressure and temperature and outlet static pressure as boundary condition for the Euler solver. They define the outlet Mach number and together with the outlet flow angle, the axial velocity and hence the mass flow. Because the outlet angle for a given geometry is defined by the the Kutta condition (or equivalent), only the total inlet pressure and temperature and the static outlet pressure are needed for obtaining a unique solution of the analysis problem. The uniqueness of the solution is however no longer guaranteed when redesigning a blade with a prescribed pressure distribution because the outlet angle may change during the iterative procedure as shown by Zannetti et al. [15] .

Let's for simplicity assume that the flow is isentropic and irrotational so that the outlet Mach number and hence also the outlet velocity, is fixed for a given inlet total- pressure and temperature and outlet static pressure.
The axial velocity however is then changing with the outlet flow angle.
The tangential velocity $W_{2x}\ tg\beta_2$ is directly related to the pressure or velocity distribution imposed on the blade by the following relation:

$$\int W ds = W_{2x}(tg\beta_2 - tg\beta_1)\ pitch \qquad (8)$$

Any temporary increase of mass flow and hence axial velocity W_{2x} results in a decrease of $|\beta_2|$. At constant outlet velocity this results in a further increase of W_{2x} and according to (8) a decrease of $|\beta_2|$. As a consequence the procedure does not converge to the blade geometry corresponding to the desired outlet flow angle.

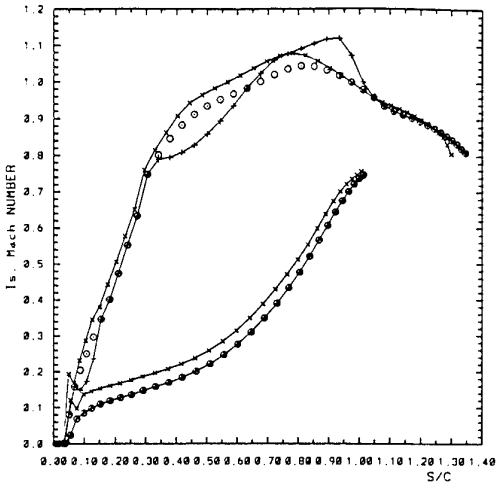

Fig. 3 : **Mach number distribution on the original blade (+), the imposed target Mach number distribution (o) and the one on the blade obtained after 600 iterations of the design procedure with fixed outlet static pressure (x)**

Following design illustrates the consequences of such a "divergence". The starting geometry is the VKI-LS89 turbine blade with inlet flow angle $\beta_1 = 0.$ and outlet static to inlet total pressure ratio of .5635 . Figure 3 compares the Mach number distribution corresponding to the original blade with the one imposed during the redesign and the one obtained after 600 time steps of the inverse design procedure where only the outlet static pressure has been imposed. The solution shown on figure 3 is a typical result of a design that did not fully converge to the required pressure distribution. It is about as close to the required one as one could get. During the iterative procedure the mass flow has increased by $\approx 30.\%$.

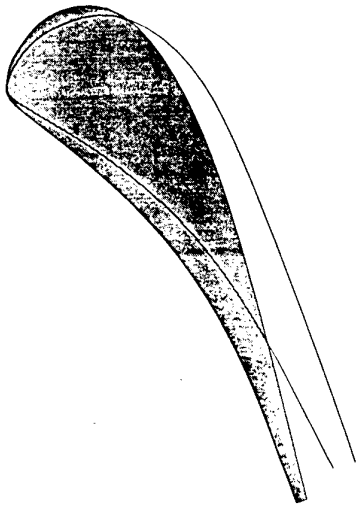

Fig. 4 : **Initial (grey) and redesigned blade (—) when imposing constant outlet pressure**

The redesigned blade geometry is compared to the initial one on figure 4. The very large change in geometry for the relatively small change in Mach number can be explained as follows. Keeping the same velocity distribution on the blade at increasing mass flow, requires a wider flow passage and hence results in a thinner blade as observed near the inlet. Having a smaller outlet flow angle results in a larger flow passage near the exit even at increased blade thickness. The design corresponding to each mass flow differs by the blade thickness and outlet flow angle.

During the design procedure it is therefore recommended to control the mass flow or to assure that the required outlet flow angle is respected. The latter one is difficult to control because it depends on the blade geometry and is in fact a result of the design. Constant mass flow can be obtained by calculating at each time step the exit mass flow and adjusting the outlet static pressure accordingly. Because of the long response time of the Euler calculation to outlet pressure modifications, an important underrelaxation factor is needed to stabilize this procedure.

The result shown on figure 5 compares the initial blade geometry with the one obtained by the constant mass flow design procedure, for which full agreement between imposed- and calculated pressure distribution could be obtained.

4 HYBRID DESIGN

Mechanical constraints are mostly related to blade thickness (maximum thickness at tip sections, minimum thickness at hub sections, prescribed trailing edge thickness, etc.). Imposing the velocity on the suction and pressure side does not necessarily provide the required blade thickness distribution. Imposing also the thickness distribution results in an overdetermined problem. This can be avoided by an hybrid design system in which the pressure is imposed only on the suction side together with the prescribed blade thickness distribution.

This procedure is illustrated by the design of a shock

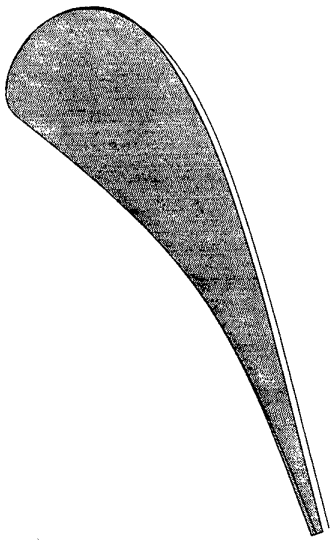

Fig. 5 : **Initial (grey) and redesigned blade (——) for constant mass flow**

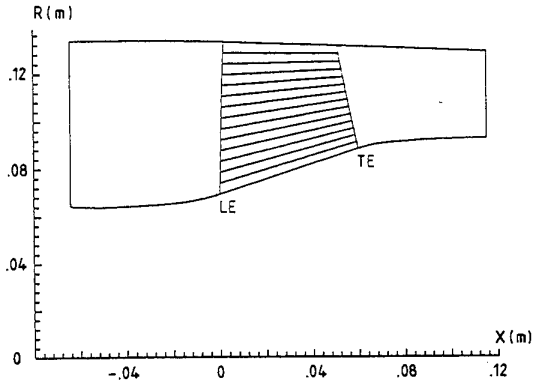

Fig. 6 : **Meridional view**

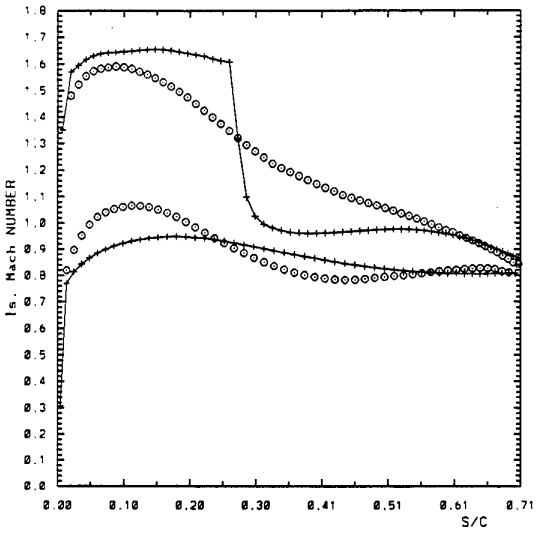

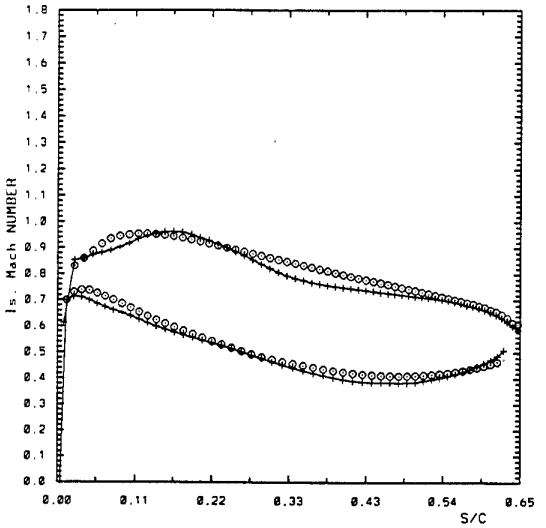

Fig. 7 : **Transonic compressor rotor - Calculated (+) and target (o) Mach number distribution at shroud and hub section**

free transonic axial compressor rotor with 14 twisted blades, rotating at 31264 RPM. The hub/tip diameter ratio is 0.5 at the inlet, and the meridional view shows a non negligible contraction of the passage (Fig. 6). Isentropic Mach number distributions along the hub and shroud section of the original blades are shown in figure 7.

The blade has been redesigned, to achieve a controlled diffusion with shock-free deceleration on the suction side. The last one is specified at five equidistant sections between the hub and shroud, and calculated at all grid points by interpolation between these sections. The prescribed distribution at hub and shroud is also shown on figure 7.

The local pressure distribution has not been prescribed on the pressure side but recalculated by the solver at each analysis step. Each time a new suction side is defined by the transpiration method, the pressure side is modified accordingly in order to keep the blade thickness distribution as prescribed. In this way the method itself predicts what pressure side Mach number is needed to satisfy the constraint. Once the solution approaches convergence (after 500 iterations) the calculation is continued with the normal design procedure whereby the newly calculated Mach number is imposed on the pressure side. An additional 1000 iterations have been made to obtain the fully converged solution with perfect agreement between the calculated and imposed pressure distributions.

The new pressure side Mach number distribution shows more diffusion than the initial one, and is therefore less optimum from the aerodynamic point of view. However, imposing an optimum pressure side Mach number as target, with less diffusion, would have resulted in a too thin (thick) front (rear) part of the blade shroud section as a consequence of the lower (higher) average velocity. Satisfying the thickness constraint by adjusting the suction side Mach number distribution should have resulted in a less efficient blade. The iso-density lines at the redesigned shroud section are shown in figure 8. The figure illustrates how the S shaped suction side generates compression waves, converging into a bow shock, which does no longer interact with the suction side boundary layer.

The initial and final blade geometries at hub, mean and tip are compared in figure 9. One observes that the blade thickness distribution is conserved at each cross section.

Euler solvers do not account for viscous effects, and the suction and pressure side boundary layer displacement thickness has to be subtracted from the designed blade to obtain the geometrical blade. This explains why the initial and final blade shapes shown in figure 9 have

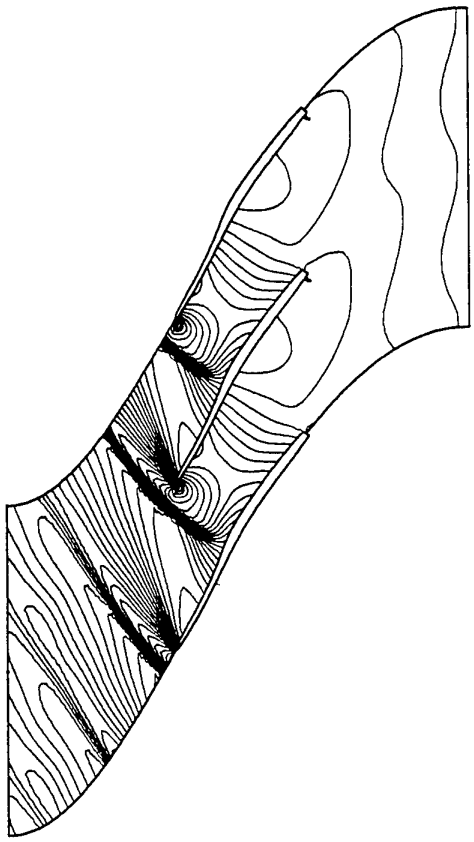

Fig. 8 : **Iso-density lines at shroud of the redesigned transonic compressor rotor**

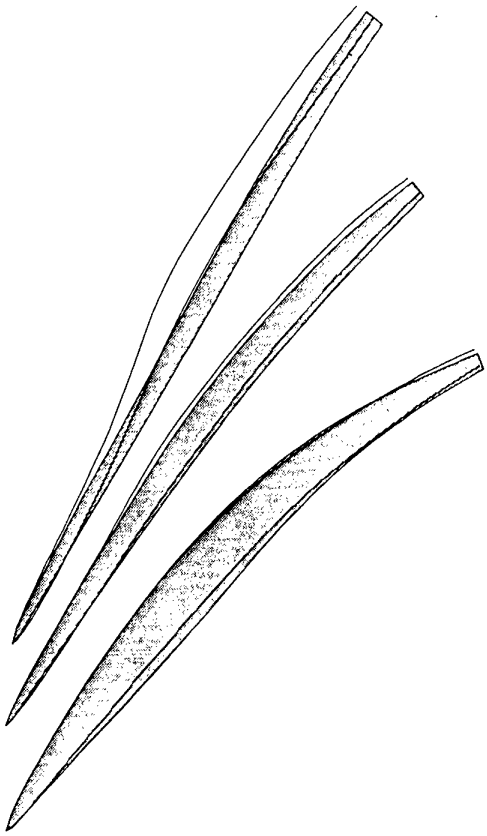

Fig. 9 : **Initial (grey) and modified blade geometry at hub, mean and shroud**

thick trailing edges. The required trailing edge thickness corresponds to the sum of the metal blade thickness and boundary layer displacement thicknesses. The later one can already be calculated from the imposed Mach number distribution, before the blade geometry is known. After completing the inverse design of the blade, the boundary layer displacement thickness must be subtracted, to obtain the shape of the metal blade (figure 10).

5 PARAMETRIZED TARGET

A third problem when redesigning blades is to specify a velocity or pressure distribution that guarantees the required performance in terms of turning and satisfies the mechanical constraints.

Following example illustrates the use of a parametrized target pressure distribution to control the outlet flow angle and trailing edge thickness. In fact both are closely related to the velocity prescribed at the trailing edge as shown by the following relation obtained from integrating the mass flow at the trailing edge plane.

$$Q_m = (\rho W)_{TE}\, cos\beta_{TE} \left(pitch - \frac{th_{TE}}{cos\beta_{TE}} \right) \qquad (9)$$

The flux $(\rho W)_{TE}$ being fixed by the velocity imposed on suction and pressure side at the trailing edge, one can conclude that any change of the angle β during the design process will result in a variation of the trailing edge thickness th_{TE}

Rotationality of the flow and three-dimensional flow effects prevent from using the two-dimensional irrotationality condition (8) to verify the turning in advance. A possible way of handling this problem is by specifying a parametrized pressure distribution and adjusting the parameters during the design until the constraints are satisfied.

This feature is illustrated by redesigning the blade section of a turbine annular cascade to correct for the

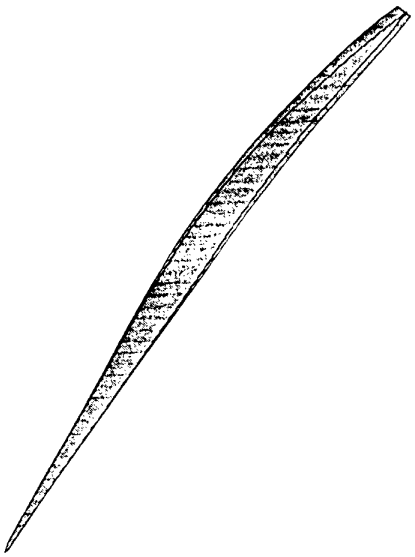

Fig. 10 : **Subtraction of the boundary layer - Mean section**

unfavorable effect of dihedral on the blade velocity distribution. The initial geometry has 21 blades with a constant VKI-LS89 profile from hub to tip, an aspect ratio of 0.7, and a pitch-to-chord ratio of 0.9 at midspan.

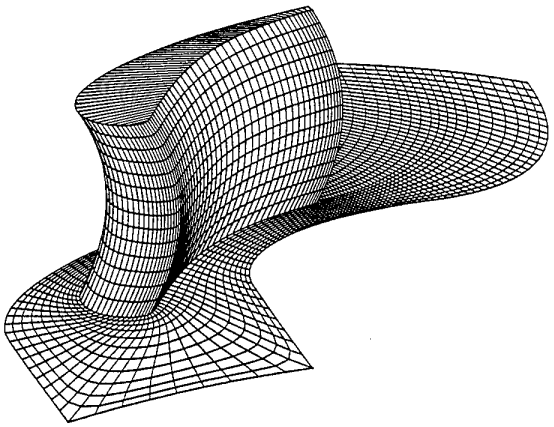

Fig. 11 : **3D view of the leaned blade**

The flow through such a low aspect ratio highly loaded turbine blade being dominated by secondary flows, one has introduced a 30 degrees positive compound lean to reduce the blade loading near the endwalls (fig. 11). However the Mach number distribution is definitely not optimal at midspan as shown on figure 12 and the outlet flow angle has changed as illustrated on figure 15.

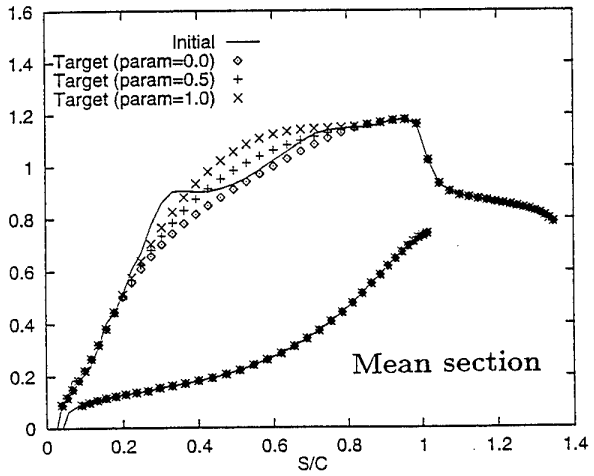

Fig. 12 : **Initial and prescribed is. Mach number distributions at mean section**

The leaned blade has been redesigned with the 3D inverse solver, to achieve a smooth acceleration along the suction side. Three different target Mach number distributions are imposed at each radial position on the suction side. Only the Mach number distributions at mid-section are shown in figure 12. They are function of a parameter between 0 and 1 that will be varied during the design process until the preset outlet flow angle and hence the required trailing edge thickness is obtained.

Full convergence inclusive adjustment of β_2 is obtained after 4000 iterations only. Figure 13 shows the evolution during the design process of the parameter at hub mean and tip together with the error on blade thickness.

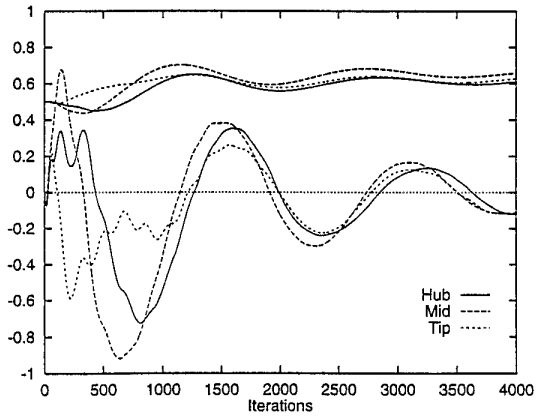

Fig. 13 : **Variation of velocity parameters (starting at .5) and variation of trailing edge thickness (starting at 0.)**

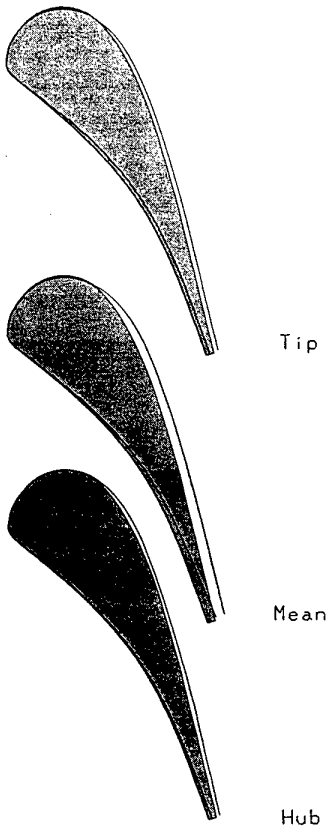

Fig. 14 : **Initial (grey) and modified blade shapes**

The initial and final blade shapes are compared at the hub, mean and tip sections in figure 14. The good agreement between initial and final spanwise distributions of pitchwise averaged outlet flow angle can also be observed in figure 15.

6 CONCLUSIONS

It has been shown how an analysis method can be transformed into an efficient design method by modifying the boundary conditions in combination with a transpi-

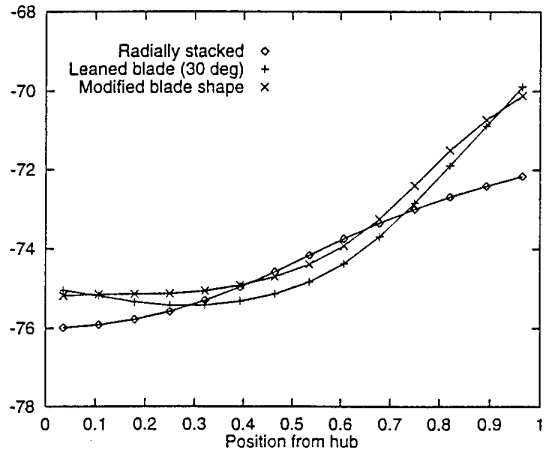

Fig. 15 : **Spanwise variation of outlet flow angle**

ration method. Once the target pressure distribution is defined the method converges to the required geometry in a time which is of the same order as the one needed for an analysis.

The features that have been introduced, such as constant mass flow design, hybrid design and parametrized target Mach number distribution, improve the convergence, facilitate achieving the required performances and respecting the mechanical constraints related to blade thickness.

7 ACKNOWLEDGEMENTS

The financial support of F.R.I.A. (Fonds pour la Formation á Recherche dans l'Industrie et l'Agriculture) is gratefully acknowledged.

8 REFERENCES

[1] Lighthill, J.M.: A new method of two dimensional aerodynamic design, ARC R&M 2112, (1945).

[2] Wang Zhengming, 1985, "Inverse Design Calculations for Transonic Cascades" ASME Paper 85-GT-6.

[3] Sanz J.M.: Automated design of controlled diffusion blades, ASME Journal of Turbomachinery, Vol. 110, No 4, pp 540-544, (1988)

[4] Vanderplaats, G.N.: Approximation concepts for numerical airfoils optimization, NASA TP-1370, (1979).

[5] Eyi, S. and Lee, D.: High-lift design optimization using the Navier-Stokes equations, AIAA paper 95-0477, (1995).

[6] Van den Braembussche, R.A., Léonard, O., Nekmouche, L.: Subsonic and transonic blade design by means of analysis codes. in: Computational Methods for Aerodynamic Design (Inverse) and Optimization, AGARD CP 463, Paper 9, (1989).

[7] Léonard, O. and Van den Braembussche, R.: "Design Method for Subsonic and Transonic Cascade with Prescribed Mach Number Distribution", Transactions of the ASME, Vol. 114, No. 3, pp 553-560, 1992.

[8] Léonard, O., and Van den Braembussche, R.: "Inverse Design of Compressor and Turbine Blades at Transonic Flow Conditions", ASME Paper 92-GT-430, 1992.

[9] Demeulenaere A., Léonard O. and Van den Braembussche R.A.: "A two-dimensional Navier-Stokes inverse solver for compressor and turbine blade design", Proc. Instn. Mech. Engrs., Vol 211, Part A, 1997.

[10] Demeulenaere A., Van den Braembussche R.A.: "Three-dimensional Inverse Method for Turbomachinery Blading Design", ASME Journal of Turbomachinery, Vol. 120, 1998.

[11] Demeulenaere A., Van den Braembussche R.A.: "A New Compressor and Turbine Blade Design Method Based on Three-Dimensional Euler Computations with Moving Boundaries", paper submitted for publication in "Inverse problems in engineering", Gordon and Breach Science publishers.

[12] Van Leer B.: "Flux Vector Splitting for the Euler Equations", ICASE, Report No 82-30 (1982).

[13] Van Leer B.: "Towards the Ultimate Conservative Difference Scheme, V: A Second Order Sequel to Godunov's Method", Journal of Computational Physics, 32:101-136 (1979).

[14] Hirsch, Ch.:"Numerical Computation of Internal and External Flows", Volumes 1 and 2, Chichester: Wiley-Interscience.

[15] Zannetti, L., Pandolfi, M.: "Inverse Design Technique for Cascades", NASA CR 3836, 1984.

Meeting Discussions

Paper 23: **Three-Dimensional Inverse Design Method for Turbine and Compressor Blades**

Authors: A. Demeulenaere and R.A.Van den Braembussche

Discussor: John W. Chew

Question: If I have understood correctly, the efficiency of your method is due to simultaneous advancement of the flow and geometry solutions. How does the method compare to linear design methods in which the optimized geometry is derived assuming a small perturbation from a „base solution"?

Author's reply: The efficiency of the method in terms of „easiness to design an acceptable blade" indeed results from the simultaneous advancement of the flow and geometry solution, because this allows a verification of the mechanical and other constraints during the design procedure.

The efficiency of the method in terms of convergence results from the first time step in which the required modification of the blade shape is defined from the solution of the flow equations without linearization. There is also no need to calculate any gradient of the objective function.
The step of the geometry modification is only limited by stability of the flow calculation.

It is difficult to compare with other methods on which I have no experience but I assume that the present method is faster. In cases where the required pressure distribution is fixed from the start of the design procedure, the present method needs about 50 % more iterations than a flow analysis calculation. Each iteration of the design procedure consists of two time steps, instead of one for the analysis, the total design takes nearly three to four times the time needed for an analysis.

A One Dimensional, Time Dependent Inlet / Engine Numerical Simulation for Aircraft Propulsion Systems*

Doug Garrard and Milt Davis, Jr.
Sverdrup Technology, Inc. / AEDC Group
1099 Avenue C
Arnold AFB, TN 37389-9013

Gary Cole
NASA Lewis Research Center
Cleveland, OH 44135

1. SUMMARY

The NASA Lewis Research Center (LeRC) and the Arnold Engineering Development Center (AEDC) have developed a closely coupled computer simulation system that provides a one dimensional, high frequency inlet / engine numerical simulation for aircraft propulsion systems. The simulation system, operating under the LeRC-developed Application Portable Parallel Library (APPL), closely coupled a supersonic inlet with a gas turbine engine. The supersonic inlet was modeled using the Large Perturbation Inlet (LAPIN) computer code, and the gas turbine engine was modeled using the Aerodynamic Turbine Engine Code (ATEC). Both LAPIN and ATEC provide a one dimensional, compressible, time dependent flow solution by solving the one dimensional Euler equations for the conservation of mass, momentum, and energy. Source terms are used to model features such as bleed flows, turbomachinery component characteristics, and inlet subsonic spillage while unstarted. High frequency events, such as compressor surge and inlet unstart, can be simulated with a high degree of fidelity. The simulation system was exercised using a supersonic inlet with sixty percent of the supersonic area contraction occurring internally, and a GE J85-13 turbojet engine.

2. NOMENCLATURE

ρ	Density
A	Cross Sectional Area
E	Total Energy
FX	Distributed Blade Force
H	Total Enthalpy
N	Engine Shaft Rotor Speed
P	Pressure
Q	Distributed Heat Addition
SW	Distributed Shaft Work
T	Temperature
U	Axial Velocity
V	Radial Velocity
W	Mass Flow Rate
x	Axial Coordinate

Subscript

B, b	Bleed
s	Static
t	Total
N	Maximum Node Number
x	Axial Coordinate
0	Free Stream Station
2	Compressor Inlet Station
3	Compressor Exit Station

3. INTRODUCTION

The economic viability of a commercial supersonic transport, such as the High Speed Civil Transport (HSCT, Ziemanski and Ball, 1993), is highly dependent on the development of a high-performance propulsion system. Typically these propulsion systems mate a supersonic mixed-compression inlet with a turbojet or turbofan engine. The nature of such propulsion systems offers the potential for undesirable component interactions which must be thoroughly understood to properly design the propulsion control system. Therefore, it is imperative to have tools that allow investigation of inlet-engine integration issues.

The inlet must provide the engine with the correct amount of mass flow rate at the highest possible pressure with minimum drag. Additionally, flow angularity and distortion must be minimized at the compressor face if the engine is to function appropriately. Maximum thrust with a minimum of fuel consumption will not be obtained without the inlet operating close to peak performance. Unfortunately, operating near peak performance can result in an inlet unstart (expulsion of the normal shock) followed by engine stall (Choby, et. al., 1971 and Cole, et. al., 1969) and possibly surge. When that happens, proper control action must be taken to recover the system as quickly as possible. Thus the operability of the overall system must also be addressed, as stable time dependent operation of the system must be ensured for both scheduled and nonscheduled events.

Because of the complexity of the inlet / engine systems and the resulting high cost of experimentally determining overall performance, numerical simulations of the components can be of significant benefit. For example, dynamic simulations provide a means for investigating the potential

* The research reported herein was performed by the Arnold Engineering Development Center (AEDC), Air Force Materiel Command and was partially funded under Interagency Agreement C-71064-E by NASA Lewis Research Center purchase order. Work and analysis for this research were done by personnel of Sverdrup Technology, Inc., AEDC Group, technical services contractor, and personnel of NASA Lewis Research Center.

Paper presented at the RTO AVT Symposium on "Design Principles and Methods for Aircraft Gas Turbine Engines", held in Toulouse, France, 11-15 May 1998, and published in RTO MP-8.

interactions mentioned above, as well as providing a test bed for guiding the design and testing/validation of propulsion controls. The NASA Lewis Research Center is pursuing a program to facilitate the use of CFD-based simulations by the controls community (Cole, et. al., 1994). This paper documents an effort undertaken to closely couple numerical simulations of both an inlet and an engine. In particular, the NASA LeRC developed Large Perturbation Inlet (LAPIN) code (Varner, et. al., 1984) has been coupled to the Arnold Engineering Development Center (AEDC) developed Aerodynamic Turbine Engine Code (ATEC) (Garrard, 1995). Both simulations provide a one dimensional, time dependent, compressible, inviscid flow field solution for internal flows by solving the Euler equations for the conservation of mass, momentum, and energy. Operational characteristics of the hardware are modeled using source terms. The two simulations are coupled together using the Application Portable Parallel Library (APPL) (Quealy, et al., 1993), a communications library for a variety of parallel/distributed computer systems. This paper will describe the general modeling techniques used in the simulations, the approach taken to implement the simulations under the APPL environment, and present results from selected test cases.

4. MODELING TECHNIQUES

Both the LAPIN and ATEC models and simulations solve the one dimensional Euler equations with source terms within a given domain of interest. The overall system under consideration is separated into individual, elemental control volumes, as sketched in Fig. 1. The governing equations are derived by the application of mass, momentum, and energy conservation to the elemental control volume:

$$\frac{\partial \mathbf{U}}{\partial t} + \frac{\partial \mathbf{F}}{\partial x} = \mathbf{G}$$

where:

$$\mathbf{U} = \begin{bmatrix} A\rho \\ \rho A u \\ AE \end{bmatrix}$$

$$\mathbf{F} = \begin{bmatrix} \rho A u \\ \rho A u^2 + AP \\ u(AE + AP) \end{bmatrix}$$

$$\mathbf{G} = \begin{bmatrix} -W_{Bx} \\ FX_x \\ Q_x + SW_x - H_{Bx} \end{bmatrix}$$

The specific flow variables are density ρ, static pressure P, total energy per unit volume E, and the axial flow velocity, u. The cross-sectional area of the flow path is defined as A. The inlet and engine domains each have their own source terms G. For ATEC the source term for the conservation of mass equation is the bleed flow rate distribution W_{Bx}. Compressor bleeds and turbine cooling bleeds are added through this term. The conservation of momentum equation source term is FX_x, which is the axial force distribution acting on the control volume. This term is used to represent the blade forces in such components as the compressor and turbine, and it is also used to implement wall friction losses. The conservation of energy equation source terms include the energy addition or extraction rate due to heat transfer or combustion into the control volume fluid Q_x, the shaft work distribution applied to the control volume SW_x, and the enthalpy change due to the bleed flow distribution H_{Bx}. LAPIN has similar source terms to account for bleed/bypass mass flow, subsonic spillage while unstarted, strut drag and skin friction, and area variation due to centerbody geometry variation.

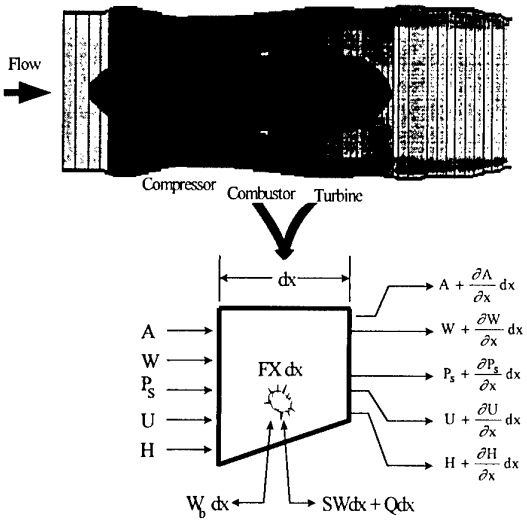

Figure 1. System Discretization into Elemental Control Volumes

To provide compressor and turbine stage force (FX_x) and shaft work (SW_x) inputs to the momentum and energy equations, sets of steady-state stage characteristics must be provided. A generic set of compressor pressure and temperature characteristics are shown in Fig. 2. Note that post-stall operation is allowed. The combustor heat addition (Q_x) to the energy equation uses a set of steady-state flammability limits and combustion efficiency maps. Inlet subsonic mass spillage during unstarted operation is modeled by the addition of incremental control volumes at the front of the inlet following the technique developed in Moeckel, 1949, and sketeched in Fig. 3. Several other equations are required to obtain closure of the equation set. These include the ideal gas equation of state and the isentropic flow relationships. A constant ratio of specific heats is also assumed.

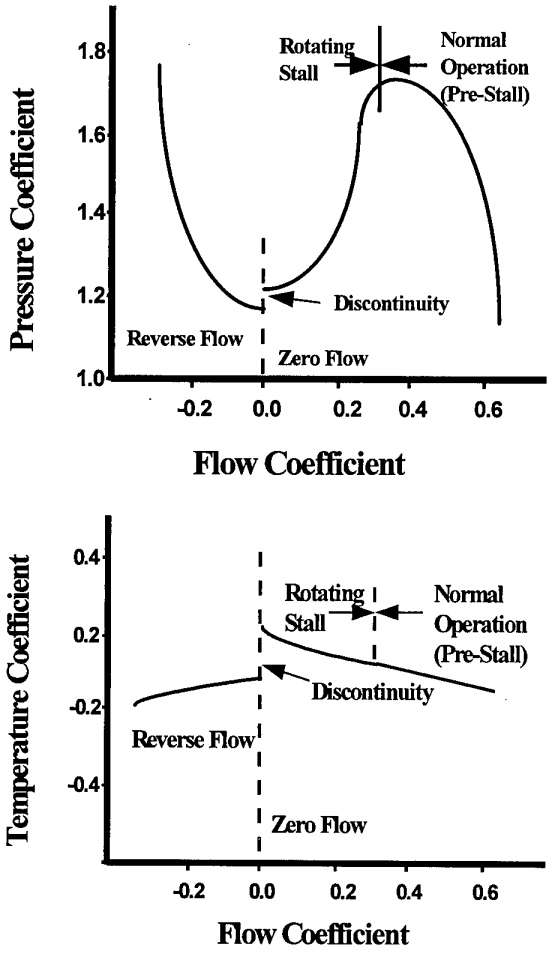

Fig. 2. Typical Compressor Pressure and Temperature Stage Characteristics Used in ATEC

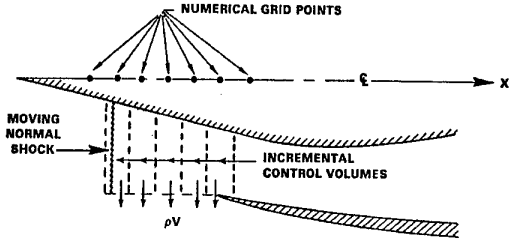

Figure 3. Mass Spillage Model Used in LAPIN (Varner, et al., 1984)

The models and simulations are formulated as initial condition boundary value problems. Initial conditions for the dependent variables ($\rho A, \rho Au, AE$) are provided by an internal calculation routine that assumes steady-state flow conditions. Major inputs for the LAPIN simulation include the free stream static conditions, the exit boundary condition type and magnitude, and whether the inlet is operating in the started regime. Bleed flows in the inlet are not accounted for during the initial-condition calculations, but are brought on-line during subsequent time steps. Thus, several thousand iterations may be required to reach a steady-state condition. The major inputs for the ATEC simulation include the corrected rotational speed of the rotor, the exit boundary condition type and magnitude, and fuel flow rate. A set of initial conditions for each control volume entrance is calculated using steady-state flow physics and pre-stall compressor stage characteristics. These routines develop steady-state initial condition sets of data from which the time dependent model solutions are initiated. Upon specification of boundary conditions, the simulations are ready for time marching.

The time dependent flow field within the system of interest is obtained by solving the time dependent system of equations using either an explicit or implicit numerical approach. Both simulations use a flux-difference splitting scheme based upon characteristic theory (Kneile, et al., 1995) expressed in both an explicit and implicit formulation to solve for the face fluxes. The explicit numerical solver uses a first order Euler method to integrate the solution from the current time step to the next time step. The implicit numerical solver uses a first order Runge-Kutta scheme for the time integration.

5. INTEGRATION OF SIMULATIONS

General Approach: To implement the LAPIN and ATEC simulations under the umbrella of the APPL environment, minor changes in coding in each of the simulations were required. Although not explicitly shown here, the changes involved adding the message passing calls and unit conversion calculations required for exchange of variables between LAPIN (non-dimensional) and ATEC (dimensional). The overall flow path of the two simulations during execution is outlined in Fig. 4. First, both simulations are initialized under the APPL environment. Input files are opened and read. Then, since it can take LAPIN several thousand iterations to converge to a steady state solution because of the bleed flows (as discussed above), the flow solution is determined on the inlet computational domain by marching through time until a converged, steady state solution is obtained. The constant corrected mass flow exit boundary condition is used during this time. Once the flow solution reaches steady state conditions, the LAPIN exit flow boundary conditions of total pressure, total temperature, and mass flow rate are then passed to the ATEC computational domain. The LAPIN conditions are passed from the N-1 node point of the LAPIN grid to the first node point of the ATEC grid, as sketched in Fig. 5. The reason for using the N-1 grid point rather than the N grid point will be discussed in the next paragraph. Initial conditions over the engine computational domain based on these inlet boundary conditions and component characteristics are then calculated. The engine flow field solution is then integrated in time until the engine computational domain time equals the inlet computational domain time. As with the LAPIN exit boundary conditions, the ATEC inlet boundary conditions are held constant during this time.

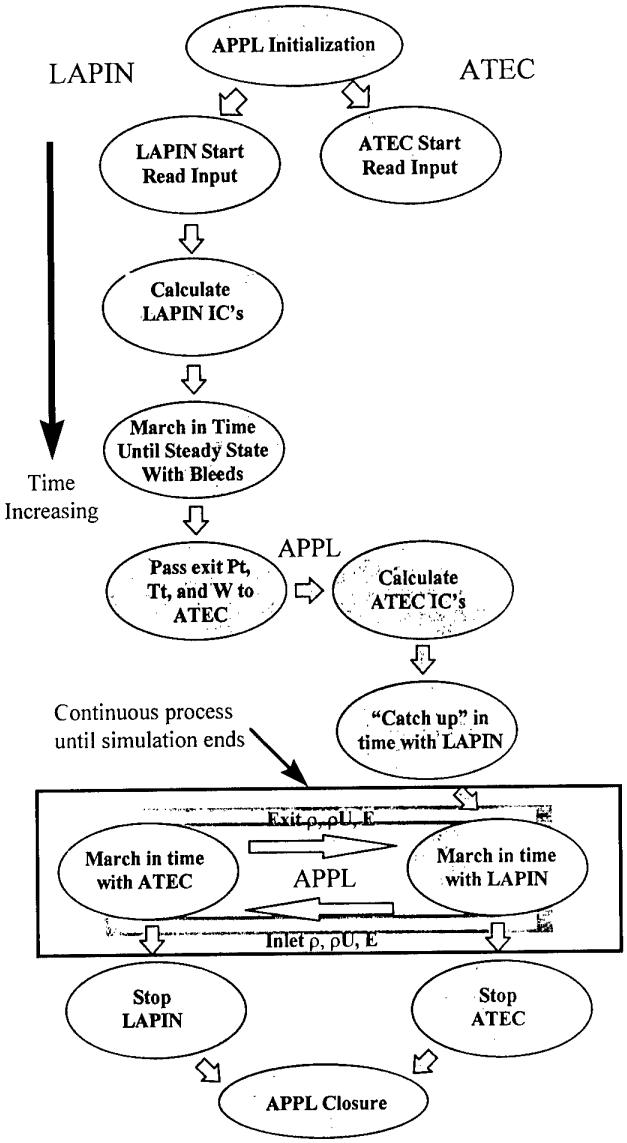

Figure 4. Flow Path of LAPIN and ATEC While Running Under the APPL Environment

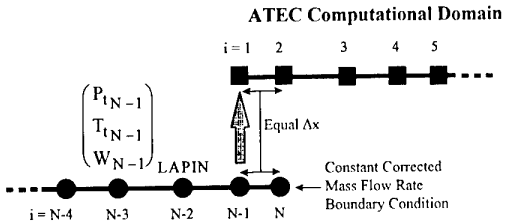

Figure 5. Passing of LAPIN Exit Boundary Conditions to ATEC Inlet Boundary Conditions After LAPIN Reaches Steady State Operation

Once both simulations are at the same computational time, the exit boundary condition routine in LAPIN and the inlet boundary condition routine in ATEC are not utilized. Rather, the two computational domains are coupled by passing the three conservative variables (ρA, ρAu, AE) from LAPIN to ATEC and visa-versa, as is shown in Fig. 6. (This approach is analogous to that of multiblock codes in which the conservative variables are exchanged at interfaces between blocks.) The last grid point in LAPIN obtains the required conservative variables from the second grid point on the ATEC computational domain, and the three conservative variables needed at the first grid point in ATEC are obtained from the N-1 grid point on the LAPIN computational domain. This process occurs at each time step during the simulation. An alternate approach could be used for coupling the inlet / engine simulations. This alternate approach would pass the inlet's total temperature and total pressure at the exit grid point to the engine as its inflow boundary condition, while the engine would pass the compressor face corrected mass flow rate at the inflow grid point to the inlet as its exit boundary condition. Because of the potential for reverse flow due to compressor surge, the passing of conservative variables was selected as the best approach for this effort.

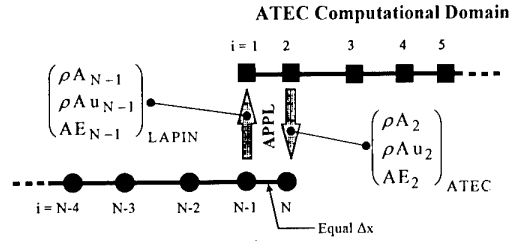

Figure 6. Passing of Conservative Variables Between Simulations During Time Marching

6. OPERATIONAL VERIFICATION

In order to demonstrate the capabilities of the coupled inlet / engine simulations, a representative test case has been selected from the available literature. The coupled LAPIN / ATEC simulation system has been exercised for a supersonic inlet with 60 percent internal compression (a 4060 Inlet) and a General Electric J85-13 turbojet. The inlet and engine have been actively tested at the LeRC since the mid-1960's, both

together and separately, and have been the subject of several technical reports (Cole, et al., 1969, Hager, 1977, Calogeras, 1969, Batterton and Gold, 1973, Costakis and Wenzel, 1975). The combined system is shown installed in the LeRC 10x10 supersonic wind tunnel in Fig. 7. A cross-sectional sketch is presented in Fig. 8.

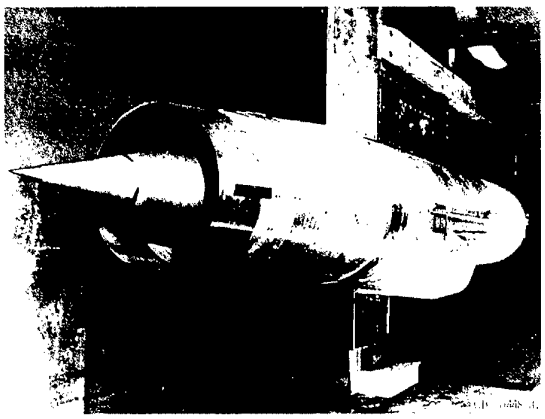

Figure 7. A 4060 Inlet and J85-13 Turbojet Installed in the LeRC 10x10 Supersonic Wind Tunnel (Calogeras, 1969)

The 4060 inlet is an axisymmetric mixed-compression inlet with 40 percent effective supersonic area contraction occurring externally and 60 percent supersonic area contraction occuring internally. The design free-stream Mach number is 2.5. The inlet has a translating centerbody to provide start/restart capability. High-response bypass doors were used for normal shock control by matching inlet airflow to engine airflow requirements. An ejector bypass provided air for engine cooling. The J85-13 turbojet consists of an eight stage axial flow compressor, a combustor, and a two stage axial turbine. An afterburner is attached to the engine. The compressor operates with a nominal pressure ratio of 7:1 at a design flow rate of 44 lbm/sec.

The purpose of the test case is to demonstrate the utility of the coupled simulation system. It is intended to exercise the system through an inlet unstart. Previously, a LAPIN simulation of the 4060 inlet was shown to give good agreement with experimental data (Varner, et. al., 1984) for both steady-state, transient, and dynamic operation. In those cases the effects of an engine were approximated by an appropriate time-varying exit boundary condition. The ATEC simulation has also been shown to accurately simulate this class of gas turbine engine (Garrard, 1996). For the J85-13, the ATEC simulation results have been compared to steady state cycle program output for a nominal J85-13 operating at sea level static conditions. The model was found to compare reasonably well, and the simulation was tuned until the maximum difference in the key parameters was less than 5 percent. Because of the many modifications that have been made to the specific LeRC J85-13 turbojet engine, adjustments to both the compressor and turbine characteristic maps were required to bring the simulation results in line with the test data. For example, it was stated in Cole, et. al., 1969, that the first stage nozzle of the axial flow turbine had been reduced to 86 percent of it's original value to move the engine operating point closer to the compressor surge limit. Several modifications to the compressor have also occurred, such as the various casing treatments reported in Hager, 1977. Because the available engine data for the configuration considered in the test case are limited, the tuning of the engine model was less accurate than for the steady state case. The simulation results presented herein will reflect this inaccuracy.

The test case selected for this study (Choby, et al., 1971, Figure 15) was conducted at a tunnel test section Mach number of 2.5 (called free stream Mach number in the test data). The engine shaft rotational speed was adjusted to 85 percent of the design corrected speed. Centerbody and bypass-door control loops (Cole, et al., 1969) were closed during the test. The transient event was initiated by pulsing the bypass doors in the closed direction. The result is an inlet unstart followed by an engine compression system stall. Upon sensing the inlet unstart, the control loop actions are to open the bypass doors and extend the centerbody. The centerbody continues to translate forward until the normal shock is re-ingested, after which the centerbody is retracted to its initial position. The bypass doors modulate continuously throughout the transient to maintain the commanded value of the control pressure (scheduled as a function of centerbody position). The inlet recovers from unstart to its initial condition in about 1.5 seconds. The control loops were not implemented in the simulation. Therefore, the bypass door area and centerbody position were scheduled as functions of time, as shown in Fig.'s 9 and 10, respectively, to approximate the control action.

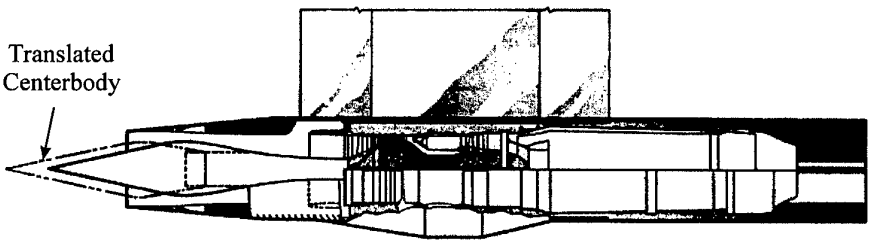

Figure 8. Cross-Sectional View of the 4060 Inlet and J85-13 Turbojet Installation (Calogeras, 1969)

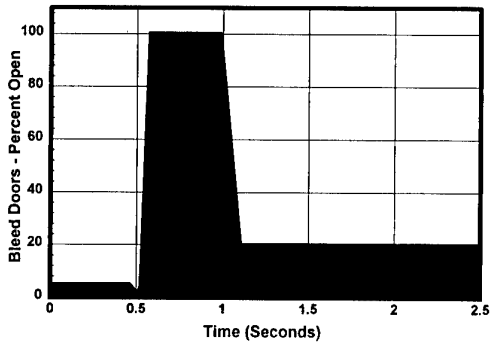

Figure 9. Bleed Bypass Doors Percent Open as a Function of Time

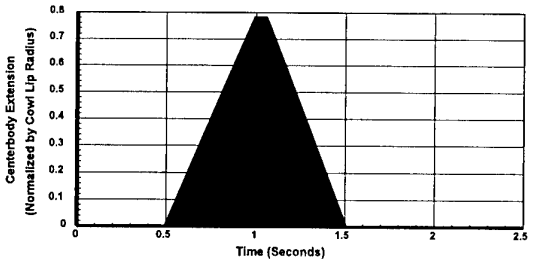

Figure 10. Centerbody Extension (Values Normalized by Cowl Lip Radius)

Before presenting the results of the computations, the test data will be discussed first. This will be done to establish the trends and characteristics that should also be present in the simulation results. The computational results for both the inlet and engine will then be presented. The presentation of the results will conclude with information from the computations that are not obtainable from the test data.

The first parameter that will be considered is the compressor inlet total pressure normalized by the free stream total pressure. This parameter provides a measure of how well the inlet provided total pressure recovery. Data for the test case are shown plotted as a function of time in Fig. 11. At the start of the transient, the total pressure recovery falls off significantly. The total pressure ratio across the inlet drops from an initial value of 0.93 to approximately 0.33. A 65 percent loss of total pressure recovery occurs during the inlet unstart. Only after the shock is reswallowed does the inlet total pressure ratio recover to the pre-transient level.

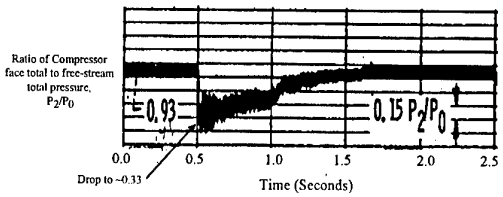

Figure 11. Test Data: Ratio of Compressor Inlet Total Pressure to Free Stream Total Pressure (Choby, et al., 1971)

The ratio of the compressor exit total pressure to free stream total pressure from test data is plotted in Fig. 12. The drop in compressor inlet total pressure forces the pressure ratio across the entire system from the inlet entrance to the compressor exit to drop dramatically. The ratio of compressor exit total pressure to free stream total pressure falls from an initial value of 3.58 to approximately 0.9. Recovery is obtained only after the shock is repositioned downstream of the inlet throat. Unlike the inlet, however, the engine compressor does not recover back to the original pre-transient level during the allotted time period due to the reduction in shaft rotational speed.

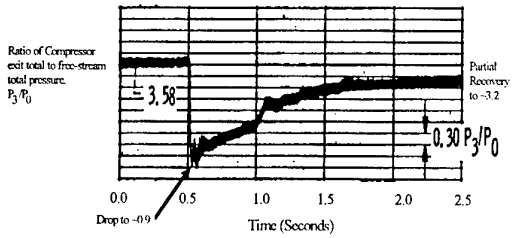

Figure 12. Test Data: Ratio of Compressor Exit Total Pressure to Free Stream Total Pressure (Choby, et al., 1971)

The shaft rotational speed of the engine during the transient is shown plotted as a function of time in Fig. 13. As would be expected, the engine speed decreases during the transient due to the flow instabilities. The original data shown in Choby, et al., 1971 indicated a drop in rotation speed of approximately 200 revolutions per minute. Data shown in Cole, et al., 1969, however, indicated that for the same transient event, the engine shaft rotational speed dropped by approximately 2000 revolutions per minute. It was judged by the authors that for the inlet to recover as shown in Fig. 11 with the bleed bypass door schedule as shown in Fig. 9, engine shaft rotation speed would be required to drop significantly more than 200 revolutions per minute. It was therefore concluded that by the end of the transient, the rotor speed had dropped from 14,335 rpm to approximately 12,050 rpm.

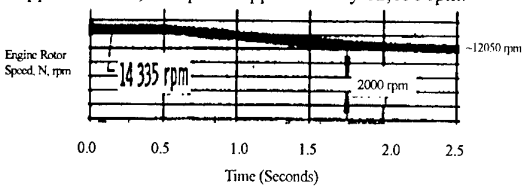

Figure 13. Test Data: Engine Shaft Rotational Speed (Choby, et al., 1971, with reference to Cole, et al., 1969)

Model results for the ratio of compressor face total pressure to free stream total pressure are shown in Fig. 14. Although the absolute values of the compressor face total pressure to free stream total pressure ratio are not exact, the overall trends of the test data and model do agree. As with the test data shown in Fig. 11, the model results show that the face total pressure recovery falls significantly as the shock is expelled from the inlet. Beginning with a pressure ratio of 0.94, the pressure ratio drops to 0.38 within a tenth of a

second. This is a loss of approximately 60 percent in total pressure recovery. After the inlet shock is reswallowed, the total pressure at the compressor face returns back to near its original level. Because of the previously discussed mismatch between the engine simulation performance and the actual test data, the model results show a reduction in inlet total pressure recovery as time progresses. Additional work is planned to investigate the differences between the test data and the simulation results.

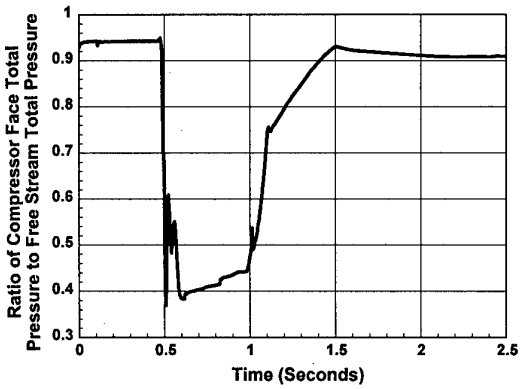

Figure 14. Model Predictions: Ratio of Compressor Face Total Pressure to Free Stream Total Pressure

Model results for the ratio of compressor exit total pressure to free stream total pressure are shown in Fig. 15. As is shown in the test data in Fig. 12, the inlet unstart forces the compressor exit total pressure to free stream total pressure to drop significantly. The model predicted a pressure ratio drop from 4.0 to approximately 0.3. As was shown in the test data, the engine compression system does not fully recover back to the original total pressure ratio. A maximum compressor exit total to free stream total pressure ratio of approximately 2.4 was reached at 1.5 seconds.

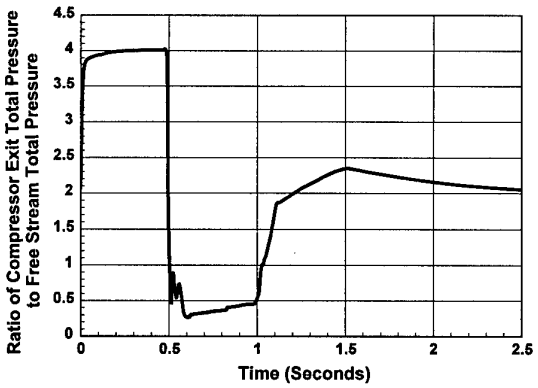

Figure 15. Model Predictions: Ratio of Compressor Exit Total Pressure to Free Stream Total Pressure

Model results for engine rotor speed are shown in Fig. 16. As with the test data shown in Fig. 13, the engine shaft rotational speed decreases in time. Over the two second time interval, the model rotation speed dropped by approximately 2000 revolutions per minute.

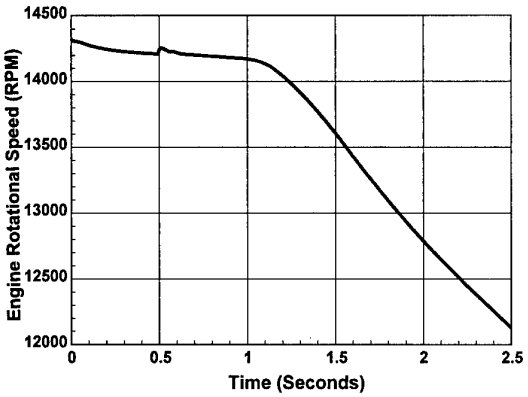

Figure 16. Model Predictions: Engine Rotational Speed

Although the above presentation does not represent a full validation of the coupled inlet / engine simulation system, it does demonstrate that the 4060 inlet and the GE J85-13 turbojet can be successfully represented by the given numerical simulations. The remainder of the paper will focus on presenting several parameters that were not presented in the test data, but provide an interesting view of the system operation.

During the given transient, the majority of the system instabilities can be traced to the fact that the normal shock, located initially downstream of the inlet throat, was expelled outside of the inlet. The location of the shock is plotted as a function of time in Fig. 17. The shock location is normalized by the inlet cowl lip radius, and referenced to the centerbody tip. The cowl lip is axially located two cowl lip radii downstream of the centerbody tip. The act of closing the bypass valve (shown in Fig. 9) forces the shock structure to be expelled from the inlet. Moving the centerbody forward in conjunction with proper modulation of the bypass doors allows the shock to be reingested.

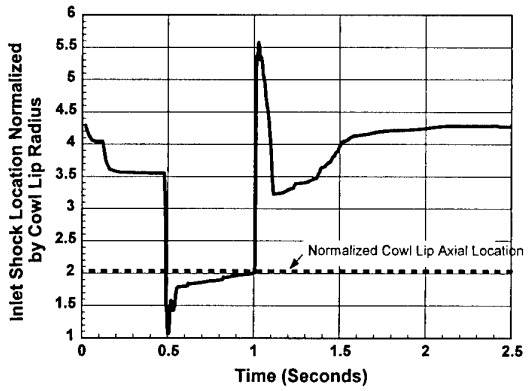

Figure 17. Inlet Shock Location Normalized by Cowl Lip Radius

The total pressure through the inlet during the transient is shown in Fig. 18. The data set is axially referenced to 0.0 at the inlet centerbody tip and is normalized by the distance from the centerbody tip to the inlet exit. The total pressure values are normalized by the maximum level obtained in the LAPIN computational domain. Three total pressure curves are shown, representing the axial distribution of total pressure through the system at times of 0.40 seconds, 0.75 seconds, and 1.75 seconds. These times correspond to instants before unstart, while unstarted, and after recovery of the initial started condition.. The total pressure falls dramatically during the unstarted portion of the transient due to the high losses associated with the expelled shock. It is interesting to note that the total pressure plot at 0.75 seconds indicates the presence of another shock structure in the inlet, located at approximately 85 percent distance. This is an expected result of opening the bypass doors which chokes the throat. Due to the closed-loop inlet control, the total pressure recovers to essentially the pre-transient level, while the engine speed is still undergoing changes.

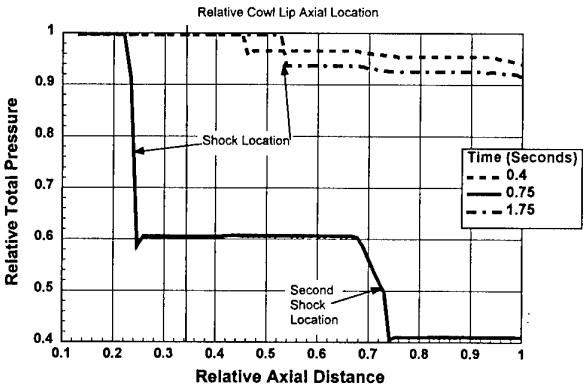

Figure 18. Relative Total Pressure in the Inlet at Three Different Times

The Mach number through the inlet is presented in Fig. 19 for the same three instants in time. The axial scale is the same as for Fig. 18. Note the jump in Mach number from supersonic to subsonic at the 85% axial location for the time plot at 0.75 seconds. This confirms the presence of the second normal shock that was indicated by the total pressure plot in Fig. 18..

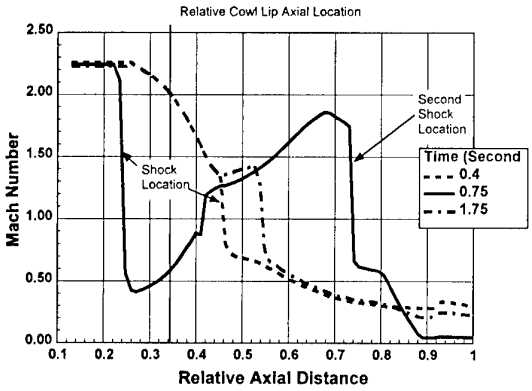

Figure 19. Mach Number in the Inlet at Three Different Times

The relative total pressure in the engine is presented in Fig. 20 for the same three instants of time that were used with the inlet. The axial distance is normalized by the overall length of the engine and pressure is normalized by the maximum level obtained in the ATEC computational domain. Total pressure across the compressor is lost once the inlet system unstarts. The compressor pressure ratio as a function of time is shown in Fig. 21. At the instant of unstart (time approx. .5 sec) there is as sharp spike in pressure ratio to value exceeding 5.0 which (probably) exceeds the steady-state stall line, resulting in stall. Although the system begins to recover the original level of compressor operating pressure ratio, the compressor total pressure ratio is lower.

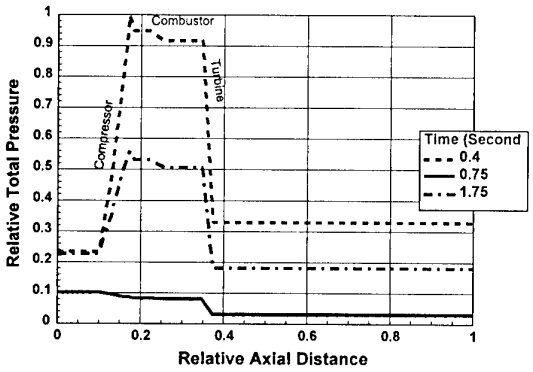

Figure 20. Relative Total Pressure in the J85-13 Turbojet at Three Different Times

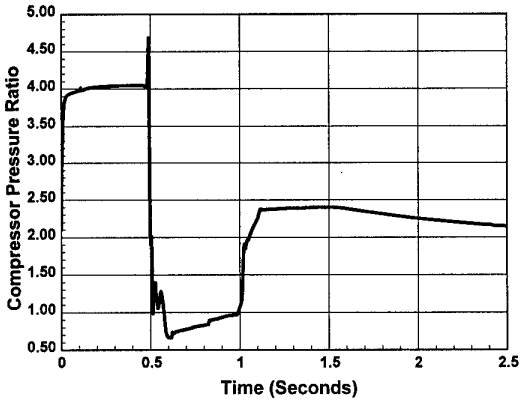

Figure 21. Compressor Pressure Ratio

The relative compressor pressure ratio is plotted as a function of the inlet corrected mass flow rate, expressed as a percentage of the design mass flow rate, in Fig. 22. It is evident from the figure that there is one engine surge cycle, with a rotating stall event. Recovery takes place at a lower corrected inlet mass flow rate due to the lower engine shaft speed..

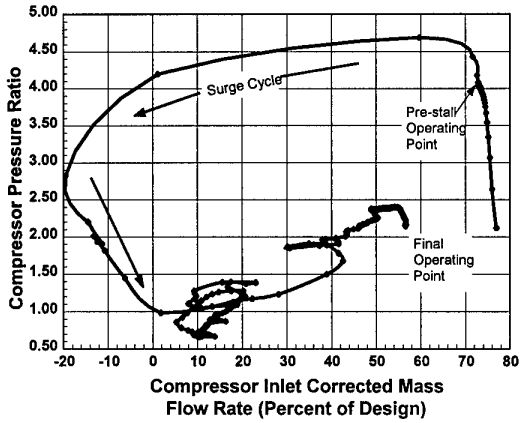

Figure 22. Compressor Pressure Ratio as a Function of Compressor Inlet Corrected Mass Flow Rate

7. SUMMARY

A closely coupled computer simulation system that provides a one dimensional, high frequency inlet / engine numerical simulation for aircraft propulsion systems has been developed. The simulation system uses the LAPIN simulation to represent the inlet system, and the ATEC simulation to represent the gas turbine engine. The LAPIN and ATEC simulations can simulate on- and off-design steady-state operation, as well as transient and dynamic engine responses to perturbations in a wide range of operational and control conditions. Operational verification of the simulation system has been conducted by comparing the trends and responses of the simulation system to test data. The system was exercised by imposing a sudden change in inlet overboard bypass conditions, resulting in an inlet unstart and engine surge cycle. The simulation showed reasonably good agreement with the data. Additional calibration of the simulations to additional test data is planned.

8. ACKNOWLEDGMENTS

The Aerodynamic Turbine Engine Code (ATEC) was developed under the direction of the Joint Dynamic Airbreathing Propulsion Simulations (JDAPS) partnership (Davis, et al., 1995). JDAPS is a partnership of government, university, and industry. The JDAPS partnership was formed for the purpose of developing and applying turbine engine and component numerical simulations to aid in the understanding of turbine engine behavior.

9. REFERENCES

Batterton, P. G., and Gold, H., "Experimental Test Results of a Generalized-Parameter Fuel Control," NASA TN D-7198, March 1973.

Calogeras, J. E., "Experimental Investigation of Dynamic Distortion in a Mach 2.50 Inlet with 60 Percent Internal Contraction and its Effect on Turbojet Stall Margin," NASA TM X-1842, October 1969.

Choby, D. A., Burstadt, P. L., and Calogeras, J. E., "Unstart and Stall Interactions Between a Turbojet Engine and an Axisymmetric Inlet with 60-Percent Internal-Area Contraction," NASA TM X-2192, March 1971.

Cole, G. L., Neiner, G. H., and Crosby, M. J., "An Automatic Restart Control System for an Axisymmetric Mixed-Compression Inlet," NASA TN D-5590, December 1969.

Costakis, W. G., and Wenzel, L. M., "An Experimental Investigation of Compressor Stall using an On-Line Distortion Indicator and Signal Conditioner," NASA TM X-3182, April 1975.

Davis, M. W., Jr., Owen, A. K., O'Brien, W. F., and Cousins, W. T., "Joint Dynamic Airbreathing Propulsion Simulations Partnership JDAPS," 95-GT-143 Presented at the 40th ASME International Gas Turbine and Aeroengine Congress and Exposition, Houston, TX, June 1995.

Garrard, G. D., "ATEC: The Aerodynamic Turbine Engine Code for the Analysis of Transient and Dynamic Turbine Engine System Operations," Ph. D. Dissertation, The University of Tennessee, Knoxville, August, 1995.

Hager, R. D., "Analysis of Internal Flow of J85-13 Multistage Compressor," NASA TM X-3513, April 1977.

Kneile, K. R., and Hale, A. A., "Appendix C: Numerical Solution to the Governing Equations," Appendix C in Garrard, G. D., "ATEC: The Aerodynamic Turbine Engine Code for the Analysis of Transient and Dynamic Turbine Engine System Operations," Ph. D. Dissertation, The University of Tennessee, Knoxville, August, 1995.

Moeckel, W. E., "Approximate Method for Predicting Form and Location of Detached Shock Waves Ahead of Plane or Axially Symmetric Bodies," NACA TN 1921, July 1949.

Quealy, A., Cole, G. L., and Blech, R. A., "Portable Programming on Parallel/Networked Computers Using the Application Portable Parallel Library (APPL)," NASA TM-106238, July 1993.

Varner, M. O., Martindale, W. R., Phares, W. J., Kneile, K. R., and Adams, J. C., Jr., "Large Perturbation Flow Field Analysis and Simulation for Supersonic Inlets," NASA CR 174676, September 1984.

Ziemianski, J. A., and Ball, C. L. "Propulsion Technology Challenges for Turn-of-the-Century Commercial Aircraft," NASA TM-106192, June 1993.

PART SPEED FLUTTER OF TRANSONIC FANS

J. W. Chew[+], R. J. Hamby[+], J. G. Marshall[+] and M. Vahdati[*]

[+]Rolls-Royce plc,
Technology Department
P.O. Box 31 - Moor Lane
Derby DB24 3BJ, U.K.

[*]Imperial College,
Mechanical Engineering,
Exhibition Road
London SW7 2BX, U.K.

1. SUMMARY

Until recently, only rudimentary methods have been available to assess designs for susceptibility to part speed flutter, but progress is now being made with more advanced CFD-based models. Earlier work has shown that coupled structural-fluid, non-linear methods may usefully be applied to this problem, but have also indicated that more computationally efficient linear methods have a role. One such linear approach is described in this paper and demonstrated on two research fans, representative of civil and military engines. Calculations are consistent with experimental observations in that the civil fan was found susceptible to flutter while the military fan was not. The results confirm the utility of the linear approach and give further insight into the physics of this type of flutter.

2. INTRODUCTION

Flutter can be a limiting factor in the design of fan blades with severe time and cost penalties involved if a redesign is necessary. While it is known that the occurrence of flutter depends on such parameters as inlet distortion and acoustics, aerodynamic and mechanical mistuning, and structural damping, the phenomenon has not been well understood. In this paper some recent developments in predictive methods and understanding of part speed flutter are described and illustrated.

Introductions and some background to the flutter problem are given by Cumpsty (1989) and Gostelow (1984). The main concern here is with part-speed flutter (which is sometimes referred to as stall flutter or loaded blade flutter). As described by Halliwell (1977), this is encountered in cantilevered fans (or other blade rows) and may be observed on a test rig as a blade instability excited when the exit throttle is closed at constant speed, and has been associated with a critical combination of local aerofoil stalling and blade frequency parameter. However, as noted by Gostelow, the view that so-called 'stall flutter' in blading rows depends on flow separation has been challenged by Carta and St Hillaire (1980). These authors argued that their experimental measurements show that blade stall is not essential for this class of flutter to occur. On the other hand, Szechenyi and Girault (1981) have, based on other experiments, concluded that blade flow separation is an essential component of this phenomenon.

Development of computational fluid dynamics (CFD)-based methods applicable to the flutter problem has received considerable attention in recent years. A review of this work will not be attempted here but the interested reader may like to refer to the paper by Marshall and Imregun (1996). However, it is appropriate to mention some of the most relevant previous work. In the present study use has been made of both linearised and non-linear CFD solvers for the unsteady flow. The linearised solver used is the SLiQ code which has been described and applied by Giles (1992) and Marshall and Giles (1997). The non-linear solver is the AU3D code described by Vahdati and Imregun (1994) and has been applied to wide chord blade fan flutter by Chew et al (1997 and 1998).

The study reported by Chew at al (1997) contains some comparison with measured data for the onset of flutter. While the work was not fully conclusive, it led to some important conclusions. It appears that the principal, driving mechanism for part-speed flutter in this case is essentially inviscid (so that boundary layer separation is not a necessary feature). It was further concluded that linearised, inviscid flow solvers would also be applicable to fan flutter. However, it is considered essential that viscous effects are modelled in the steady-state solution (about which the unsteady flow can be treated as a linear perturbation). This and other related research led to work reported below, which focuses on the linearised approach.

The following section gives a brief description of the mathematical model employed. Applications of the method are then described and discussed in sections 3 and 4. Two different research fans are considered; a high aspect ratio wide chord fan representative of modern civil engine fans and a low aspect ratio fan representative of military engines. The main conclusions from this work are then summarised in section 5.

Paper presented at the RTO AVT Symposium on "Design Principles and Methods for Aircraft Gas Turbine Engines", held in Toulouse, France, 11-15 May 1998, and published in RTO MP-8.

3. THE MATHEMATICAL MODEL

3.1 Structural Modelling

Blade vibrational frequencies and associated modeshapes are needed for the analysis. For the work described here these have been obtained using the proprietary finite element code SC03, early developments of which are described by Armstrong and Edmunds (1989). The same code was also used to calculate running blade geometries, as centrifugal and pressure loadings significantly affect the blade shape.

For use in the aeroelastic calculation the modeshapes are interpolated onto the aerodynamic, blade surface mesh. Since we use a linear approximation for the unsteady aerodynamics, interaction between modes is neglected and only one mode is included in each calculation. In practice this results in deflection vectors $\mathbf{s}_i$, being stored at each surface mesh point i. The contribution to the modal force per unit area at mesh point i is then $p_i \mathbf{n}_i . \mathbf{s}_i$ where p and **n** denote unsteady pressure and surface normal, respectively.

The modeshape and frequency define the input to the unsteady, aerodynamic calculation from the structural model, and the modal force distribution (as a function of time) is obtained from the aerodynamic solution. Integration of the product of modal force and velocity over the blade surface area for a complete vibration cycle then gives the work done on the blade by the air (W). From linear analysis, this is related to the logarithmic decrement through

$$\text{logdec} = -W/\omega^2 r^2$$

where ω and r denote the vibration frequency and mode amplitude. In the absence of mechanical damping, a negative value of logdec indicates instability. Logdec may also be related to the rate of change in amplitude of the vibration; if the amplitude reaches 1/R times its initial value after n cycles then logdec equals 1/n times the natural logarithm of R.

3.2 Steady-State Aerodynamic Modelling

The CFD code used to obtain the steady, aerodynamic solutions is the AU3D code referred to above. While this code has previously been used for non-linear, coupled flutter calculations by Chew et al (1997,1998), its main use here is solely to provide a steady solution. The code employs unstructured, tetrahedral meshes, a Baldwin-Barth (1991) turbulence model and implicit time stepping. It should be noted that the solutions presented below for the low aspect ratio fan were obtained using non-standard constants in the turbulence model. These changes have been found useful in improving the steady-state solutions near the stall boundary. Improvement of the turbulence model is an area which requires further attention. Further details of the code are given by Vahdati and Imregun (1994).

Inlet boundary conditions involve specified total pressure, total temperature and flow angle. Wall functions are used at the blade surfaces which are treated as no-slip boundaries in the viscous solutions and flow periodicity is imposed for these single passage calculations. The models do not include over-tip leakage and the end-wall boundary layers are treated as slip boundaries.

The calculation meshes used in the results described here had over 10^5 mesh points and were based on structured 'H' meshes. However, it may be noted that more recent calculations using this code make use of semi-structured meshes, as described by Sbardella et al (1997). The mesh resolution used is somewhat less than that currently employed in some aerodynamic, fan performance studies but is considered to give a fair estimate of the flow, within the limits of the modelling assumptions.

3.3 Unsteady Aerodynamic Modelling

The CFD code used to obtain unsteady aerodynamic solutions is the SLiQ code referred to in section 1 and described by Giles (1992) and Marshall and Giles (1997). The model is based on the assumption that departures from the steady solution are both periodic in time and small. This enables the solution to be written in terms of a Fourier series, and interaction between the different harmonics in the series to be neglected. Considering, for example, the first harmonic, each of the dependent variables is assumed to have the following form.

$$u(x,y,z,t) = \text{Re}[\hat{u}(x,y,z)e^{-i\omega t}] + \overline{u}(x,y,z)$$

Here u is any dependent variable, x, y and z are spatial co-ordinates, t denotes time, $\overline{u}$ is the steady-state value, $\hat{u}$ is the (complex) amplitude, i is the square root of -1, ω denotes frequency, and Re[ ] gives the real part of a complex function. With these assumptions, the governing equations are then rewritten, with higher order terms neglected and a factor $e^{-i\omega t}$ (which occurs as a multiple of the simplified equation) cancelling out. This results in a set of equations involving the complex amplitudes $\hat{u}$, but independent of time t. These can be solved efficiently using similar methods to those of steady-state CFD calculations.

It may be noted that the real part of $\hat{u}$ gives the solution at time t=0, and the imaginary part gives the solution at time $t=\pi/2\omega$. Similarly, splitting the linearised governing equations into real and imaginary parts recovers the governing equations at times t=0 and $\pi/2\omega$. Thus it is seen that with the linear method we essentially need make use of the governing equations at just two points in time, with the solution at all other time points given by the harmonic assumption. This results in large savings in computational times compared to time-marching solutions of the conventional non-linear equations. Although the use of complex variables is convenient and elegant, it is not essential, and need not obscure the physical interpretation of the equations.

SLiQ employs structured meshes (with mesh movement) and a time-marching algorithm to solve the linearised Euler equations. On solid walls, no-penetration boundary conditions are applied. The inlet and outlet boundary conditions are as formulated by Giles (1990), to avoid pressure wave reflections in 2D flows. It should be noted that this may not ensure no reflection for the 3D flows considered here. In all cases the calculation is performed on a single blade passage with the periodic boundary conditions being adjusted for the inter-blade phase angle. The inter-blade phase angle divided by the vibration frequency gives the time interval between the flow at one boundary being repeated at the other, and is given by ϕ =

$\pm 2\pi m/N$. Here N is the number of blades and m is the number of nodal diameters in the structural mode for the assembly. Positive values of ϕ correspond to forward travelling waves (relative to the fan) and negative values give backward travelling waves.

Although SLiQ is based on the Euler equations, it allows linearisation about an imported viscous solution. Essentially, this is equivalent to defining additional (steady) source terms in the Euler equation which ensure the steady solution matches that specified. This idea has been used in non-linear analyses (Chew et al, 1997, 1998) and was suggested by Giles (1995). The viscous AU3D solution is interpolated onto the SLiQ mesh, which has fewer points as it does not include resolution of the boundary layers. SLiQ meshes having about 46 000 points were used for the results presented below.

4. RESULTS FOR A WIDE-CHORD FAN

The research fan considered in this section is representative of modern civil engines. It is similar, but different in blade design, to the fan considered by Chew et al (1997). The assembly has 26 blades and, on test, exhibited part-speed flutter in forward travelling, first flap, assembly modes with low numbers of nodal diameters. The first flap mode is shown in fig. 1, and can be seen to involve axial and circumferential movements with relatively little twist. Results for just one operating point are given here. This corresponds to an 80% speed condition at a pressure ratio above the normal working line and close to the measured flutter boundary. The tip inlet relative Mach number at this position is about 1.25 and the frequency parameter (blade frequency times chord divided by relative inlet velocity) is 0.37.

The steady state solution is illustrated in fig. 2. This shows contours of static pressure on the blade surfaces and tip section, and velocity vectors close to the blade suction surface. The pressure contours show a shock, expelled from the passage. This intersects the suction surface at about half chord at the tip, and further forward at lower radii. The suction surface velocity vectors are of interest as they show 'radial migration' of the fluid in some regions with the vectors having a clear radial component. This effect is associated with thickening of the boundary layer and 'centrifuging' of the low axial momentum fluid. Note, however, there is no reversal of axial velocity which would indicate separation of the boundary layer. It may also be noted that the accuracy of the turbulence model for this boundary layer is open to some question.

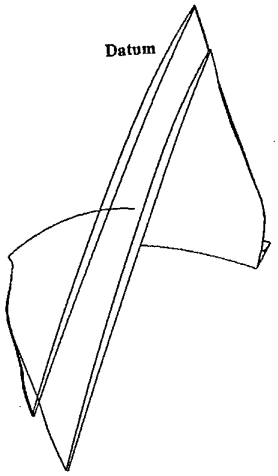

Figure 1: First flap modeshape, wide chord fan blade

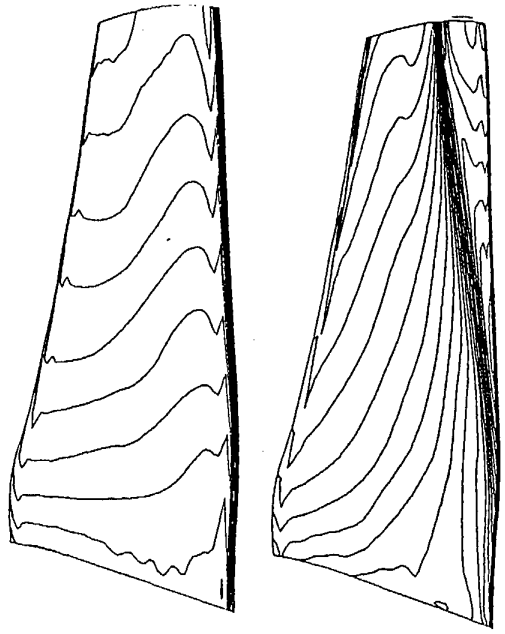

Pressure surface static pressure

Suction surface static pressure

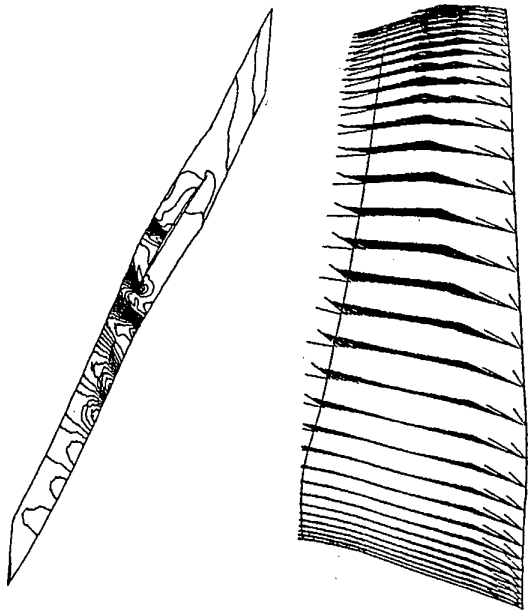

Tip static pressure

Suction surface velocity vectors

Figure 2: Steady state CFD solution, wide chord fan blade

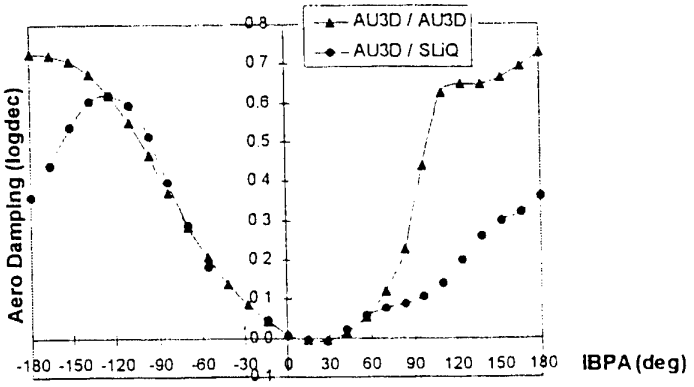

Figure 3: Stability analysis results, wide chord fan blade

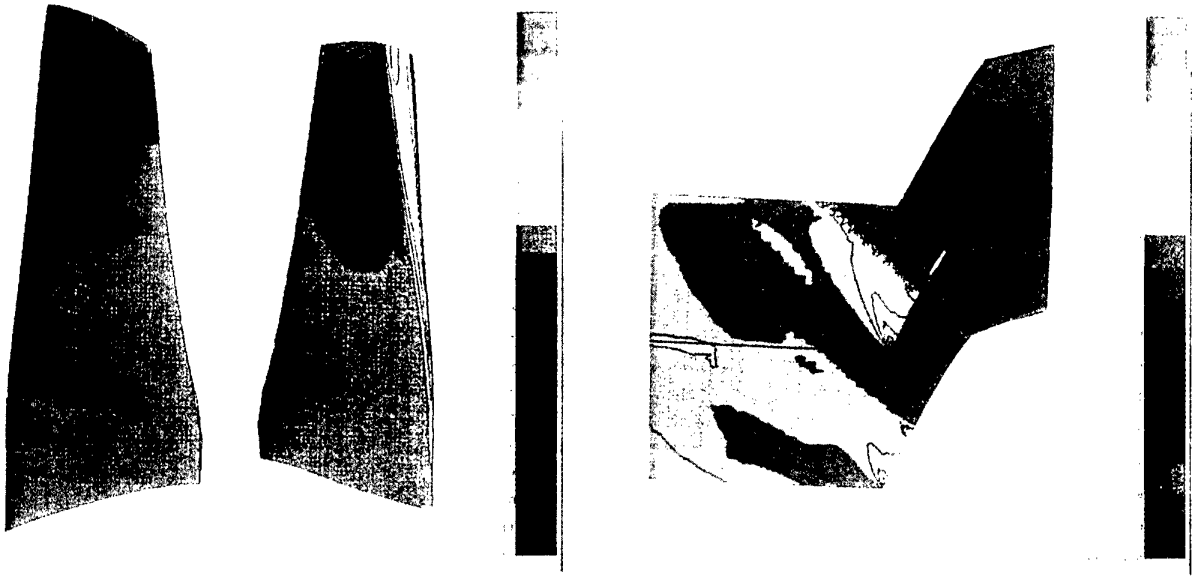

Real part
Pressure surface

Real part
Suction surface

Real part
Tip surface

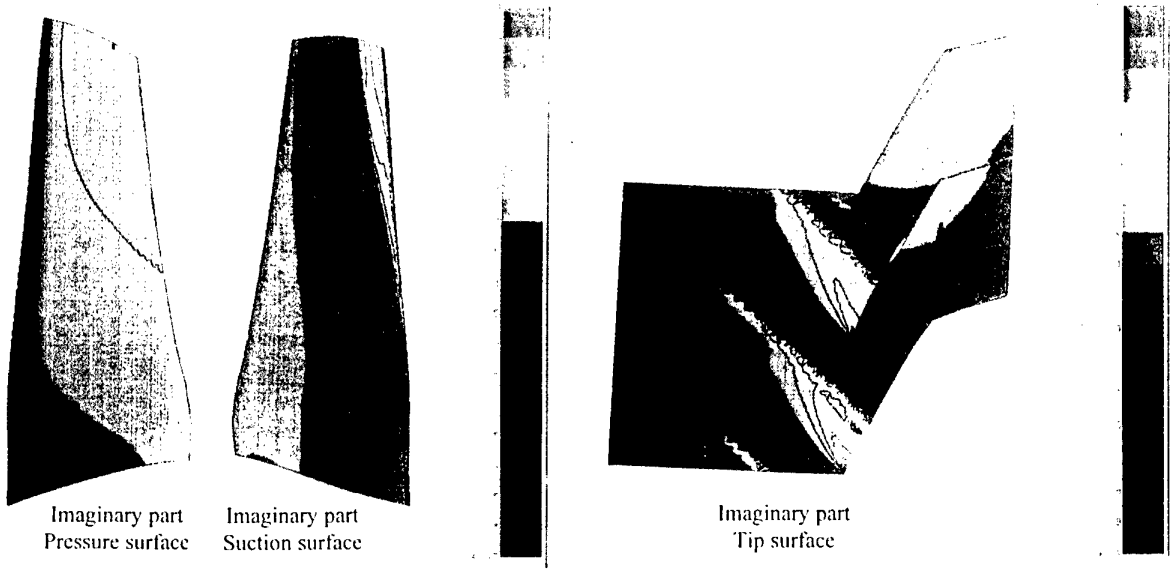

Imaginary part
Pressure surface

Imaginary part
Suction surface

Imaginary part
Tip surface

Figure 4: Real and imaginary components of pressure perturbation, wide chord fan blade, 2ND

The results of the stability analysis are summarised in fig. 3, which gives a plot of logdec against inter-blade phase angle. Calculations were performed at all the possible nodal diameters, but convergence difficulties were encountered for the backward travelling 1 and 2 nodal diameter cases, so these are not included. Predictions from a full AU3D coupled, non-linear analysis as described by Chew et al (1997) are also included on this graph. The AU3D solution was performed for a full fan assembly with all assembly modes excited simultaneously and using a relatively coarse mesh of about 11000 points per blade passage. The agreement between the two methods for the least stable modes is remarkably good and encouraging. The differences between the two results for the more stable modes might be attributed to a combination of the high decay rates in the high nodal diameter modes, non-linear effects, interaction between modes, and mesh dependency or other numerical inaccuracies. Both methods show marginal instability with AU3D giving the 1 nodal diameter mode and SLiQ giving the 2 nodal diameter mode as the most unstable.

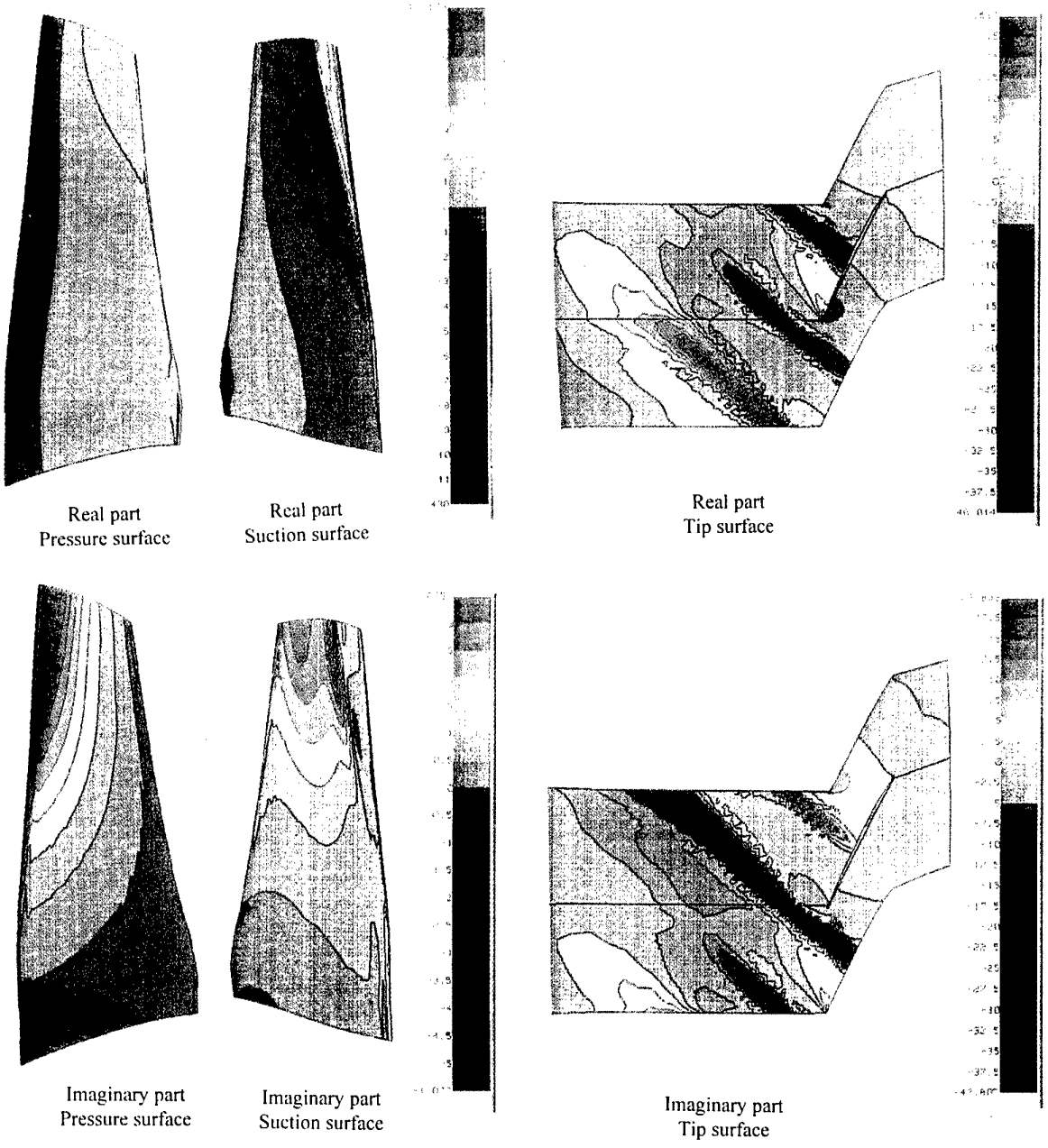

Figure 5: Real and imaginary components of pressure perturbation, wide chord fan blade, 6ND

From simple linear theory, assuming that the unsteady forces on a blade are a function of its own motion and and that of its immediately neighbouring blades only, it follows that the logdec versus inter-blade phase angle plot will be of sinusoidal form. However, as discussed by Cargill (1987), acoustic effects can disrupt this pattern. Given the uncertainty of the effect of reflections at the inlet and exit in the present calculation it is quite possible that reflections contribute to the departures from a sine wave in the current results. This point is to be investigated further. As shown by Chew et al (1998), it may also be noted that the intake acoustics can affect flutter behaviour.

The unsteady components of pressure are shown in figs 4 and 5 for the forward travelling 2 and 6 nodal diameter modes, corresponding to inter-blade phase angles of 27.7° and 83.1°. The domain for these unsteady calculations goes circumferentially from the pressure surface of one blade to the suction surface of another, so that the two blade surfaces will have different modal displacements at any instant. The real and imaginary components shown in the figure correspond to the actual pressure perturbations at times 0 and $\pi/2\omega$, respectively, where the phase is such that the suction surface has maximum displacement (in the downstream axial direction) at time 0. Since these are forward travelling waves the motion of the pressure surface leads that of the suction surface. Not surprisingly, the largest pressure fluctuations can be associated with shock motion. This is stronger for the 6 nodal diameter case. The zero nodal diameter case (not shown here), for which the blade displacements are in phase, shows relatively little shock motion.

Fig. 6 gives the distribution over the blade of the work done per unit area by the air on the blade. It is calculated from the integral over one vibration period of the product of the pressure perturbation force and the blade velocity. Note that there is some question as to the accuracy of these contours near the blade tip where, in contrast to the pressure plots, sharp radial gradients are observed. Negative values of this quantity indicate stabilising effects while positive values show areas of the blade contributing to instability. A summary of contributions from the pressure and suction surfaces are given in table 1. For the 2 nodal diameter case, the net instability arises from a delicate balance of stabilising and destabilising regions. The strongest stabilising region is upstream of the shock on the suction surface. This is balanced by destabilising forces downstream of the shock. The pressure surface also splits into stabilising and destabilising regions on the front and rear of the blade. For the 6 nodal diameter case the destabilising effects on the suction surface are considerably reduced with the shock motion now tending to stabilise the blade

fan	condition	ss logdec	ps logdec	total logdec
wide-chord	80% speed near-flutter 2 nodal diameter	-0.0316	0.0296	-.002
wide-chord	80% speed near-flutter 6 nodal diameter	0.1332	-0.0515	0.0818
low aspect ratio	80% speed near-stall 1 nodal diameter	-0.0053	0.0214	0.0161
low aspect ratio	80% speed near-stall 5 nodal diameter	0.0236	0.0290	0.0526

Table 1. Breakdown of contributions to logdec

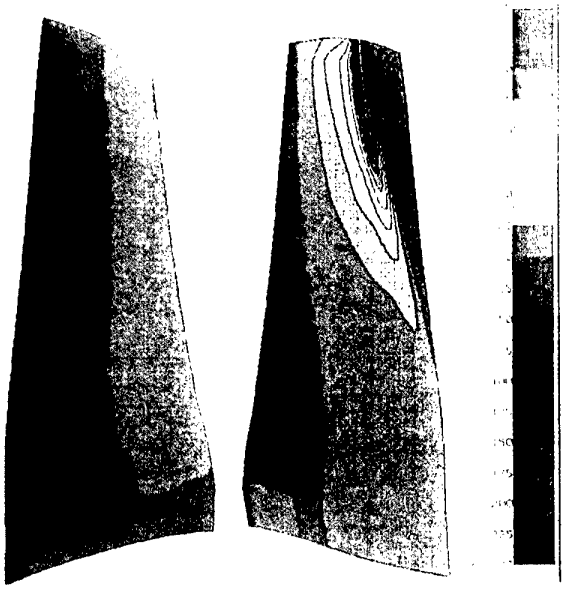

2ND, pressure surface 2ND, suction surface

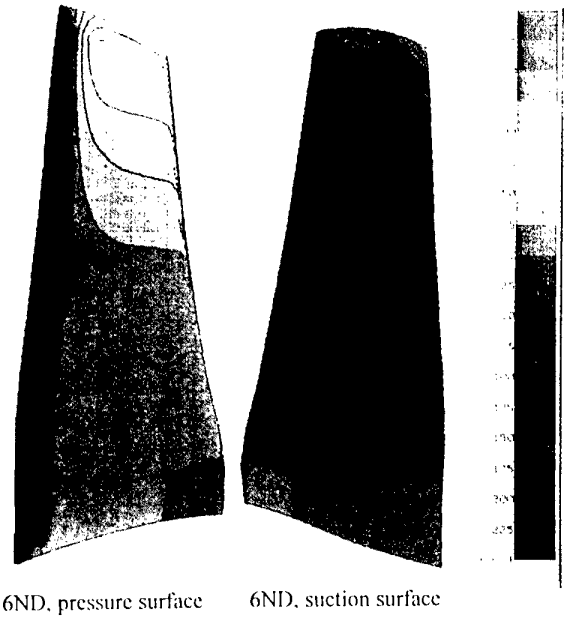

6ND, pressure surface 6ND, suction surface

Figure 6· Worksum, wide chord fan blade

5. RESULTS FOR A LOW ASPECT RATIO FAN

This research fan is more representative of modern military engine designs. It has 20 blades with a blisk construction. Prior to test there was some concern that the low mechanical damping of the blisk structure would lead to a flutter problem. However, on test, no flutter was observed. This might be due to the higher frequency of the blade, which at 80% speed, tip conditions gives a frequency parameter of about 0.8.

The first flap modeshape for this blade is shown in fig. 7. In this case a disc plus blade model was used to obtain the assembly modes. This gave slightly reduced frequencies for the 0 and 1 nodal diameter modes. For example, the 0 nodal diameter frequency for the 80% speed condition was 6.7% lower than that for the higher nodal diameter modes. Calculations were performed at three different fan speeds - 60%, 80% and 100% design speed. Two mass flow conditions - one on a working line and one near-stall - are considered at each speed. Tip inlet Mach numbers at these conditions are about 1.0, 1.3 and 1.6. Tip section pressure contours are shown in fig. 8. These show the expected trends of the shock moving forward and weakening as speed reduces. Note that there is a change in orientation between these aerodynamic results and the solid model in fig. 7.

Results from the stability analysis are given in fig. 9. All conditions were predicted to be stable, agreeing with experiment. The form of the logdec plots is similar to that for the wide-chord fan and is close to a sinusoid. Note that the magnitude of logdec is generally considerably less for this fan, indicating generally less significant aerodynamic damping. While converged solutions were obtained for all modes in this case, results for the backward travelling 1 and 2 nodal diameter modes do not seem to fit the general pattern very well. The forward travelling 1 nodal diameter mode is predicted to be the least stable.

Unsteady pressure and work-sum contours for the 80% speed, near-stall, 1 nodal diameter condition are shown in fig. 10 and 11. Comparing these with the results for the wide-chord fan, one can observe both similarities and differences. Towards the tip, both fans show a transition from stabilising forces to destabilising going from the front to the rear of the pressure surface. However, the stabilising forces dominate for the low aspect ratio fan as shown in table 1.

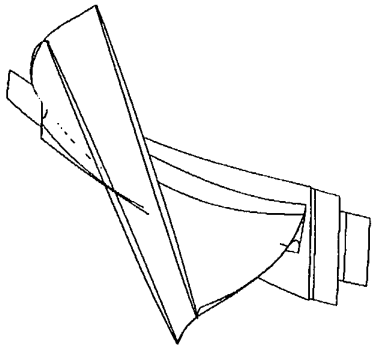

Figure 7: First flap modeshape, low aspect ratio fan

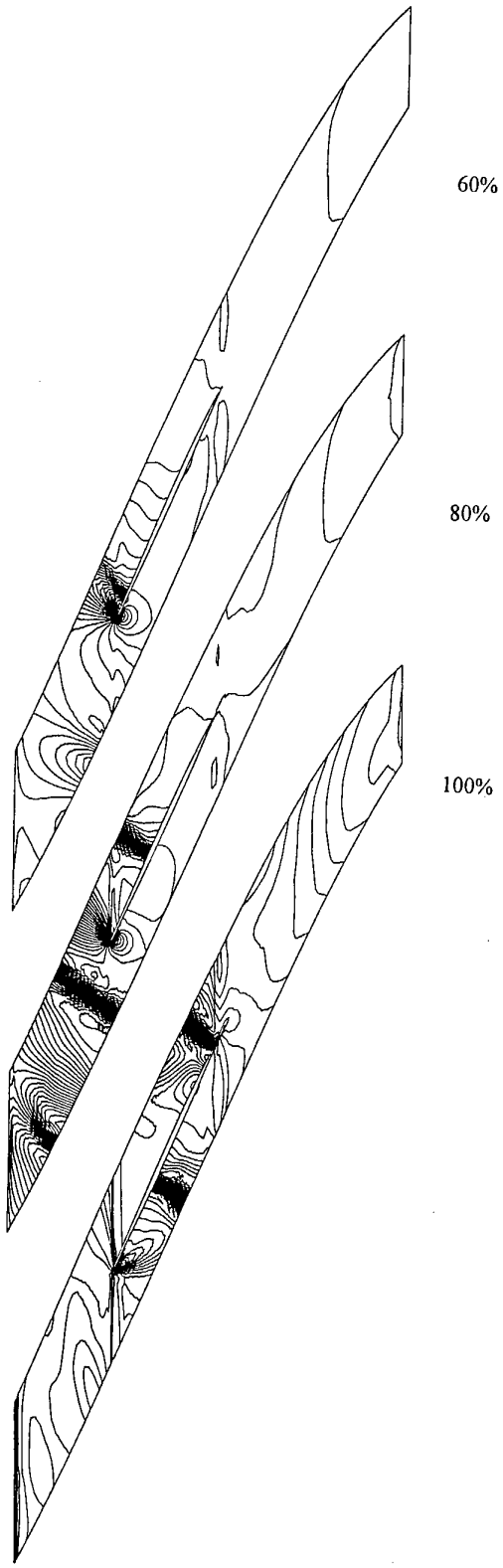

Figure 8: Static pressure at the tip section, low aspect ratio fan

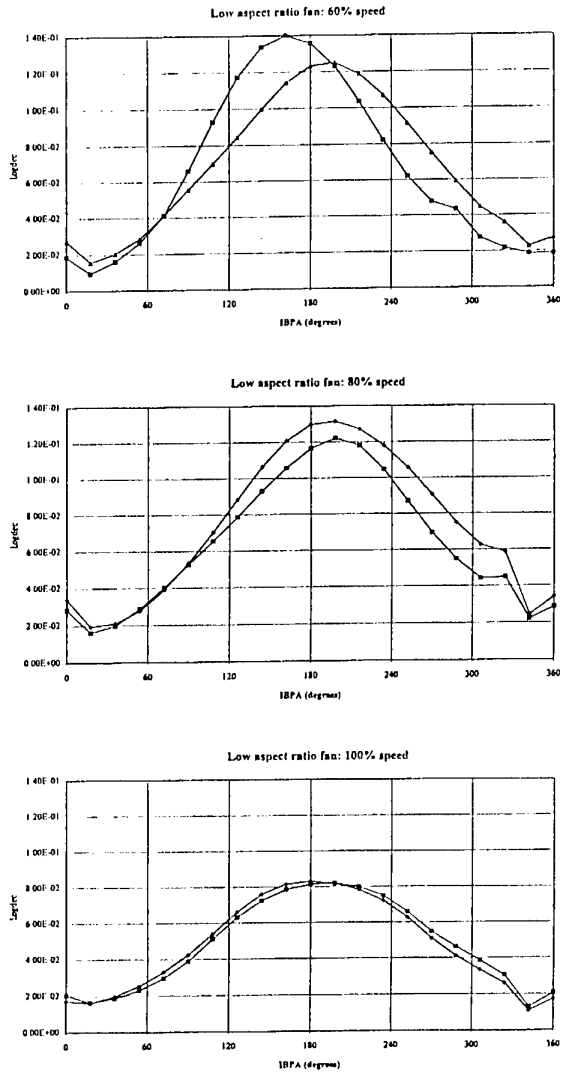

Figure 9: Stability analysis results, low aspect ratio fan

On the suction surface there is again a stabilising region upstream of the shock and a destabilising region downstream. For this fan there appears to be little net contribution to the work-sum from the shock movement for the least stable mode. Since the pressure contours do show evidence of shock movement this is evidently due to a change of phase. Such phase changes might well be attributable to the increased frequency parameter for this fan, and this would seem to be the underlying reason for its greater stability.

6. CONCLUSIONS

It has been demonstrated that the onset of flutter is predicted by a linear, inviscid, unsteady solution representing a perturbation from a viscous, steady solution. The results are in fair agreement with those from a model that includes non-linear, unsteady effects. The advantage of the linear method lies in its computational efficiency. Since the unsteady calculations are performed on an 'inviscid' mesh, the calculation for a single inter-blade phase angle takes considerably less time than the steady state, viscous solution.

Model predictions have been presented for two fans. The first fan had been observed to flutter on test, and the calculation at a near-flutter point indicated instability. The second fan did not show any signs of flutter experimentally and was predicted to be stable. Thus some agreement with experiment can be claimed, although the need for further verification is recognised. The results provide further support for the view that so-called 'stall flutter' in blade rows need not depend on flow separation, as has sometimes been supposed. Strong variation of aerodynamic damping with inter-blade phase angle is observed, which is consistent with experimental observations of flutter occurring in certain assembly modes. It appears that the different behaviour of the two fans is principally due to the higher frequency parameter of the second. This affects the phasing of the pressure fluctuations on the blade, so as to improve stability.

Examination of the model predictions shows the stability to depend on a delicate balance of forces. Thus it is not surprising that fan flutter is found to be very sensitive to the fan environment in practice. The shock position in the steady state solution appears particularly important, and so the analysis will be sensitive to the quality of the steady state solution. As prediction of near-stall conditions in fans is known to be difficult, this is considered a limiting aspect of the current model. The importance of accurate modelling of the suction surface boundary layer is emphasised here.

There are several aspects of the unsteady model that might be questioned. These include the neglect of viscous terms, end-wall boundary layers and tip clearance, and the rigour of the approach used here for modelling shock movement. It is expected that these will be investigated in due course. Despite these shortcomings it is considered that the model does capture much of the physics of flutter. One particular aspect of the unsteady analysis that is thought to need further attention, is the inlet and exit boundary conditions. There is some evidence that acoustic reflections are affecting the present results, and inclusion of the intake is needed for a more complete model.

ACKNOWLEDGEMENTS

This work has been carried out with the support of Ministry of Defence, Defence Evaluation and Research Agency and the Department of trade and Industry. The authors are grateful for this support and that from Rolls-Royce plc. Technical assistance from Professor Giles of Oxford University and our colleagues at Rolls-Royce and Imperial College is also gratefully acknowledged.

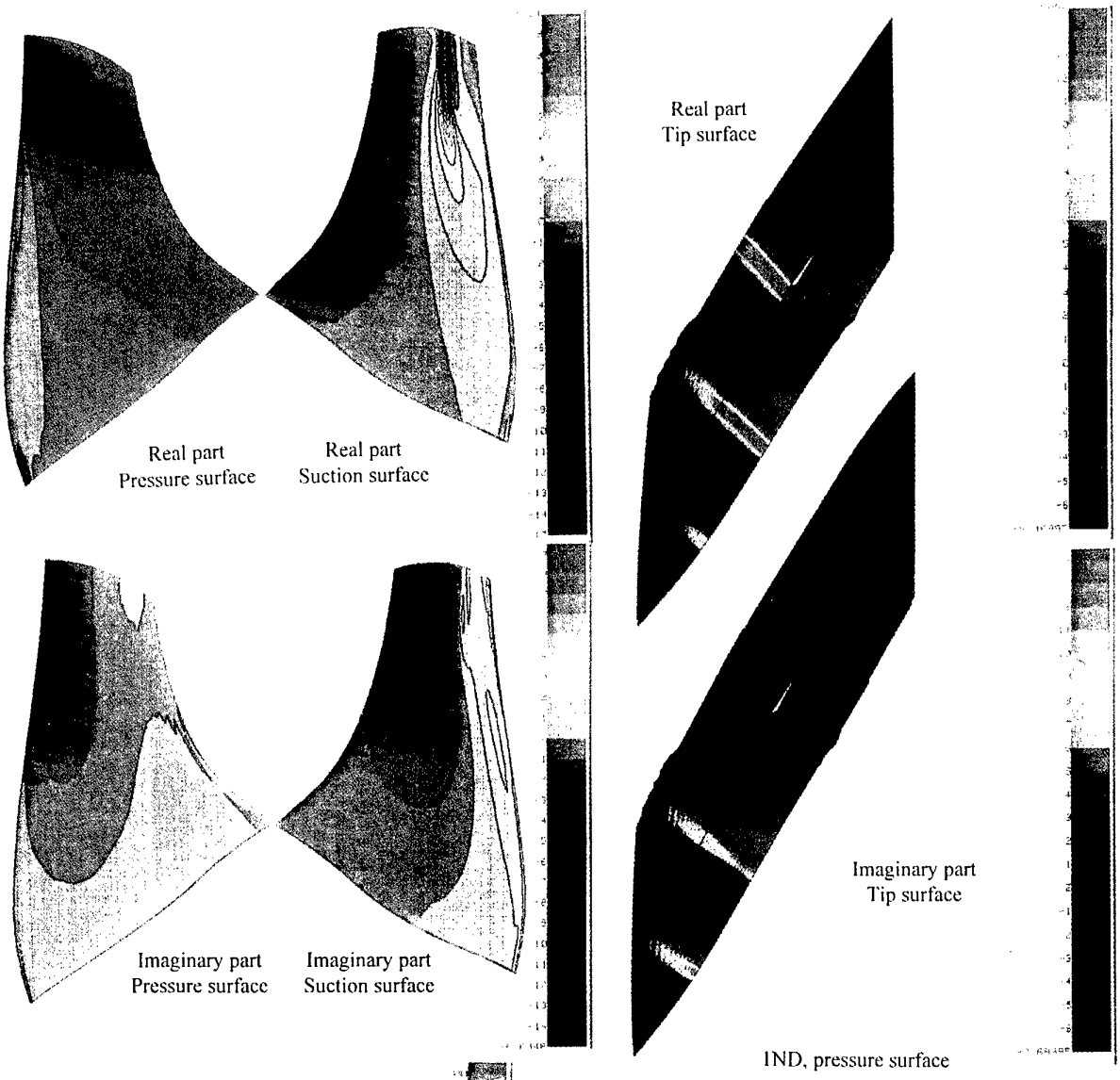

Figure 10:
Pressure perturbations for
low aspect ratio fan, 1ND

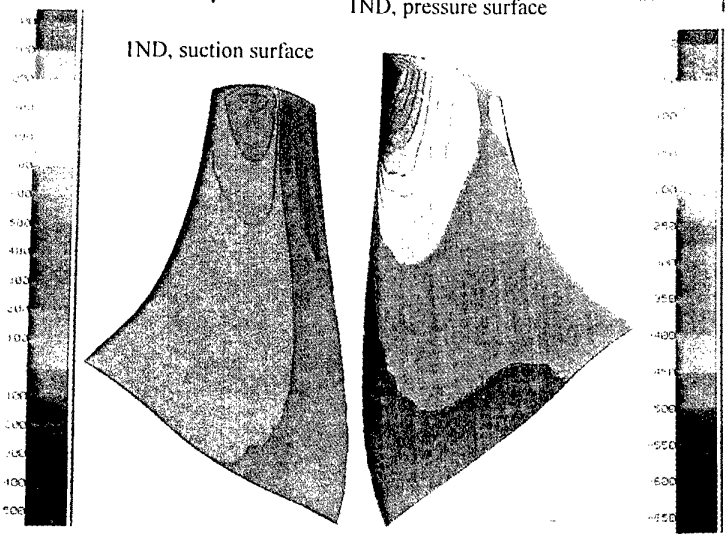

Figure 11: Worksum, low aspect ratio fan

REFERENCES

Armstrong, I. and Edmunds, T.M., 1989. Fully automatic analysis in the industrial environment. Proc. Second Int. Conf. On Quality Assurance and Standards in Finite Element Analysis, NAFEMS, 1989.

Baldwin, B.S. and Barth, T.J., 1991.A one equation turbulence transport model for high Reynolds number all-bounded flows. AIAA paper 91-0610.

Cargill, A.G., 1987. The role of acoustic resonances inunsteady turbomachinery aerodynamics. 4th Symp. Unsteady Aerodynamics and Aeroelasticity of Turbomachines and Propellors, Aachen, Germany.

Carta, F.O. and St Hillaire, A.O., 1980. Effect of inter-blade phase angle and incidence angle on cascade pitching stability. Trans. ASME J. Eng. Power, vol. 102, 391.

Chew, J.W., Marshall, J.G., Vahdati, M. And Imregun, M., 1997. Part-speed flutter analysis of a wide chord fan blade. Proc. eighth Int. Symp. On Unsteady Aerodynamics and Aeroelasticity of Turbomachines, Stockholm, Sweden.

Chew, J.W., Vahdati, M. And Imregun, M.,1998. Predicted influence of intake acoustics upon part-speed fan flutter. Submitted to ASME Gas Turbine Conference, Stockholm.

Cumpsty, N.A., 1989. Compressor Aerodynamics. Longman Scientific and Technical.

Giles, M.B., 1992. An approach for multi-stage calculations incorporating unsteadiness. ASME paper 92-GT-282.

Giles, M.B., 1990. Non-reflecting boundary conditions for Euler equation calculations. AIAA J, vol 28, 2050-2058.

Giles, M.B., 1995. Personal communication.

Gostelow, J.P., 1984. Cascade Aerodynamics. Pergammon Press.

Halliwell, D.G., 1977. Fan supersonic flutter: prediction and test analysis. Aeronautical research Council Reports and Memoranda No. 3789.

Marshall, J.G. and Giles, M.B., 1997. Some applications of a time-linearized Euler method to flutter and forced response in turbomachinery. Proc. eighth Int. Symp. On Unsteady Aerodynamics and Aeroelasticity of Turbomachines, Stockholm, Sweden

Marshall, J.G. and Imregun, M., 1996. A review of aeroelasticity methods with emphasis on turbomachinery applications. J. Fluids and Structures, vol 10, 237-267.

Sbardella, L., Sayma, A.I. and Imregun, M., 1997. A semi-unstructured mesh generator for flow calculations in axial turbomachinery blading. Proc. eighth Int. Symp. On Unsteady Aerodynamics and Aeroelasticity of Turbomachines, Stockholm, Sweden

Szechenyi, E. and Girault, J.P., 1981. A study of compressor blade stall flutter in a straight cascade wind tunnel. Aeroelasticity in Turbomachines, ed. P. Suter, Juris-Verlag, Zurich.

Vahdati, M. And Imregun, M., 1994. Non-linear aeroelastic analyses using unstructured dynamic meshes. Proc. seventh Int. Symp. On Unsteady Aerodynamics and Aeroelasticity of Turbomachines, Fukuoka, Japan.

The Introduction of Reinforced TMC Materials into Rotating Machinery - The Safe Approach

P J Doorbar
Rolls-Royce plc
P.O.Box 31
DERBY
DE24 8BJ

Abstract

Titanium metal matrix composites (TMCs) will play a significant role in the future of gas turbine aero-engine development, in particular when used for rotating disc/blade assemblies in axial flow compressors. This paper outlines the potential applications for TMCs and covers some of the main issues involved in the safe introduction of this relatively new class of composite material into critical engine components The key microstructural features which affect the mechanical performance of finished components are explained, (e.g. fibre damage, fibre placement, interfacial bonding and embrittlement etc.) and illustrations are given of how they can be controlled in the manufacturing process for a complex component.

Introduction

The aero-engine is one of the most hostile and demanding environments for any material system. When this is coupled with the ongoing industry requirements for higher thrust levels, lighter weight, and increased efficiency, all at reduced cost, it means that the introduction of an advanced composite material such as titanium metal matrix composite (TMC) will require an intensive and thorough development programme. Understanding component behaviour from the macro scale down to the micro material scale will be necessary to ensure that the leap from conventional monolithic metals to metal composites can be made safely.

Applications and Benefits of TMC in Gas Turbines

Operating temperature limitations are largely imposed by the matrix alloy, with Ti-6Al-4V composite limited to around 350°C and a Ti6242 composite reaching ≈500-550°C. Therefore, use is largely envisaged in the compressor section of the engine where blades, vanes, casings and discs are all potential applications. The high temperatures at the back end of the HP compressor currently dictate the use of heavy nickel base superalloys for discs and steel or nickel alloys for the casings. Future advances in the development of intermetallics such as the orthorhombic titanium aluminides, will provide a suitable matrix for reinforcement at the hot end of the HP compressor. Figure 1 illustrates these potential areas of application for a military engine.

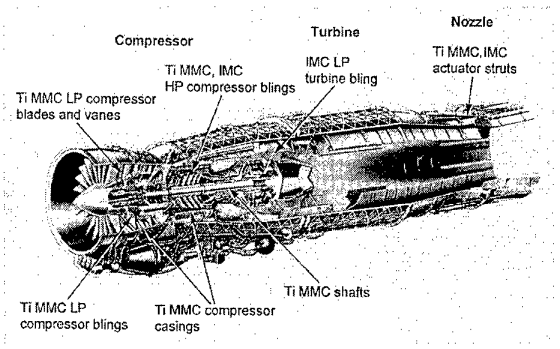

Figure 1 Potential Military Applications

Blades and Vanes

Titanium fan blades have long been considered as possible candidates for fibre reinforcement. Increasing the strength of the material could allow larger blades to be produced with higher rotational speeds thus generating increased thrust. A reduced number of lighter blades could also be envisaged. The increases in stiffness made possible through fibre reinforcement provides the blade designer with an opportunity to tune the performance of the blade under load. Increasing material stiffness also changes a blade's resonant frequency, allowing any damaging vibration modes to be removed from the engine running range without excessive section thickening and added weight. Reduced mass in the fan blades has a "knock-on" effect, allowing further weight savings in the discs, casings and containment structure.

The manufacturing technology for the reinforcement of hollow SPF/DB fan blades has been available for some time and is compatible with the wide chord titanium fan blade techniques pioneered by Rolls-Royce. This application has, however, not yet been taken up by engine manufacturers due to the present high cost of the composite parts. US programmes such as TMCTECC are addressing this issue and reducing costs through volume production of tape cast composite (which is well suited to blade manufacture). The long term cost goal of the TMCTECC initiative is ≈500$/lb. Even at this figure, however, a TMC fan blade may find it difficult to "buy" its way on to a future military engine programme through weight saving alone.

Paper presented at the RTO AVT Symposium on "Design Principles and Methods for Aircraft Gas Turbine Engines", held in Toulouse, France, 11-15 May 1998, and published in RTO MP-8.

Compressor Blings

This is the application which is seen to yield the greatest benefit from the use of TMCs. Weight savings of up to 40% have been predicted for a TMC compressor bling (bladed ring) when compared with conventional titanium alloy blisk (bladed disc) designs. This application is ideal for unidirectionally reinforced TMCs since the predominant loading is in the hoop direction. Radial loads in the transverse direction can be kept relatively low. The simple bling design (Figure 2) is therefore able to exploit fully the good longitudinal TMC properties whilst protecting the weakest transverse orientation.

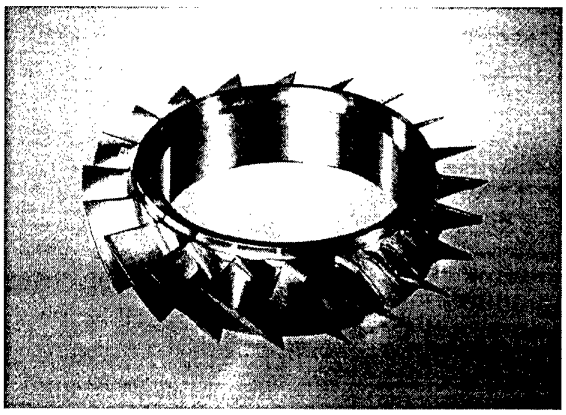

Figure 2 TMC Demonstration Bling

It is possible to utilise TMC in compressor blings and retain a replaceable blade design. Whilst blade replacement is easier, this results in a reduced weight saving, as the TMC is now carrying the extra parasitic weight of the blade root fixing.

Casings

Design studies for casing applications have shown weight savings in the region of 25-30% when nickel or steel parts are replaced by TMC. This saving is reduced significantly for engines where titanium itself can be used today. Gains in performance can, however, be predicted from the increased stiffness of a TMC casing. This would produce reduced distortion under aircraft manoeuvring loads, resulting in improved blade tip clearance control. Reduced thermal expansion coefficient, and the ability to tune the expansion (by varying fibre volume fraction) to better match the rotating structure, is also advantageous for the control of tip clearances.

The detailed design of a casing component in TMC will be critical to its success. Figure 3 shows the successful pressure test of a TMC Gem engine jet pipe. This type of component traditionally has numerous bosses, holes and flanges, all of which are difficult to accommodate in TMC. Novel design and manufacturing solutions will be needed before this type of application realises its full potential.

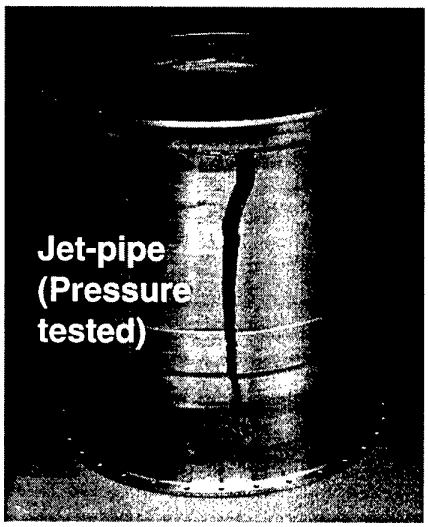

Figure 3 Successful Test of a Gem Jet Pipe

Shafts

TMC has the potential to replace steel in engine shafts. Its high stiffness and strength in the fibre direction coupled with the reduced density, can give weight reductions of around 20 - 30%, with improved whirling performance and torque capability. Shaft design is a major problem area, in particular the end fittings, where loads need to be transferred in and out of the shaft efficiently without adding excessive weight. Fibre orientation along the shaft requires careful consideration to retain high torque properties without sacrificing bending stiffness or axial tensile strength.

Struts and Links

These are often seen as lower risk parts, and hence ideal for the introduction of TMC into engines in order to gain experience in a service environment. Flight demonstrations of exhaust flap links have been undertaken successfully in the US, and TMC reinforced actuator piston rods have been specified for the P&W F119 engine in the No 5 F22 test aircraft (Ref 1). These applications generally show the greatest benefits, in terms of weight saving, where stiffness and compression strength are paramount, and where TMC is again able to replace heavy steel or nickel based components.

The overall simplicity of this type of component plus the maturity of conventional steel processing make this a difficult application to justify on a component cost basis. However, the position of these parts towards the rear of a military engine allows additional balancing mass to be removed from the front of the aircraft at no additional cost. This illustrates the point that in order to fully realise the benefits of TMC, the system as a whole needs to be considered.

Manufacturing Routes

The major manufacturing routes for TMC components are shown in figure 4.

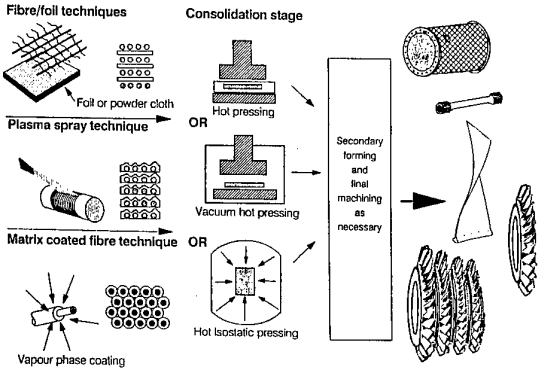

Figure 4 Manufacturing Routes for TMC

Fibre and Foil Type Methods

This is the most mature approach and has been used to manufacture a range of component forms. However, the high debulking during consolidation, and the relative inflexibility of the foil, limits the complexity of the shapes which can be considered. Foil cost is not insignificant and thus several efforts have been made to use different matrix forms. The most well developed is one utilising a powder matrix, whereby the powder is mixed with an organic binder and the resulting slurry is cast into a thin sheet or tape. This tape casting approach has many advantages for more complex shapes since an element of drape is now included in the preform. Initially fibre distribution from this process was poor. Process control has developed considerably, however, and high quality composite can now be made commercially by both Textron and ARC in the USA. This production scale development has allowed significant reductions in processing costs to be made. Debulking on consolidation is still high for this process largely restricting its use to "open-ended" type structures or thin rings.

To achieve the required fibre distribution for critical rotating ring applications, and minimise fibre damage on consolidation, debulking must be kept to a minimum. This has lead to the development by ARC of a wire/fibre co-winding technique where the matrix foil has been replaced by a fine wire. A reduced density preform is produced, which allows better control of fibre spacing and movement during consolidation, particularly in thick sections. Another advantage is that there is a physical barrier between each fibre, reducing the possibility of "touching fibre" defects in the consolidated composite. Automation should be relatively straight forward for this process, thus providing the potential for cost reduction in the future.

Metal Spray Processing

This process is capable of producing large sheets of single layer prepreg. Either a vacuum plasma or an induction plasma spray system is used to deposit titanium alloy powder directly onto a drum of wrapped fibre. The resulting sheets are stacked and then consolidated in a similar manner to the fibre foil process. Impact damage to the fibre and its coating during spraying has proven to be a problem with this technique, as is the limited flexibility of the prepreg sheets which restricts the type of component which can be manufactured.

Metal Coated Fibre Processing

With this technique, which has been developed independently by 3M in the US and DERA in the UK, the metal coating is applied directly to the silicon carbide fibre using an electron beam physical vapour deposition (EBPVD) process. Fibre is passed continuously through a vapour cloud above a molten pool of titanium alloy. The vapour condenses on to the moving fibre to form a continuous and uniform matrix coating (figure 5).

Figure 5 Matrix Coated Fibre

Although a slight variation in coating thickness can sometimes be seen, it is evident that the consolidated composite cannot contain touching fibres and has a near perfect fibre distribution (figure 6).

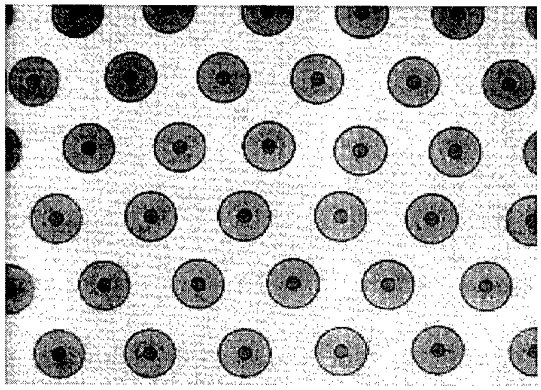

Figure 6 MCF Fibre Distribution

This process is particularly suitable for critical rotating components such as compressor blings (figure 2). Automation in both the coating process and the subsequent component manufacturing process will provide the basis for future cost reduction and process control monitoring

Microstructural Control

There are three key areas of TMC technology where evaluation at a micro-scale is needed in order to develop the required level of material understanding and process
control. These are:

evaluation of the fibre,
evaluation of the fibre/matrix interface,
evaluation of the composite as a result of processing.

Fibre

The SiC monofilament fibres are produced by chemical vapour deposition onto a heated tungsten or carbon core. This results in fine silicon carbide grains growing outwards radially from the core. A typical fibre structure is shown in the scanning electron image of a fibre fracture surface (figure 7).

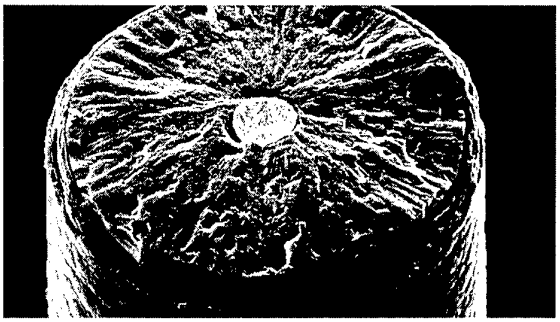

Figure 7 SEM Image of SiC Fibre

Contrast this uniform circular cross section with that seen in figure 8, where a growth defect has occurred near the fibre core causing secondary nucleation and subsequent grain growth. The resultant fibre surface shows a bulge emanating from the defect origin. The fracture surface in this case is dominated by this defect which has been the cause of the premature, low strength, failure. Minimising surface flaws is also critical to achieving good fibre strength. Commercial manufacturers use accurate laser surface roughness measurements to monitor and control their process.

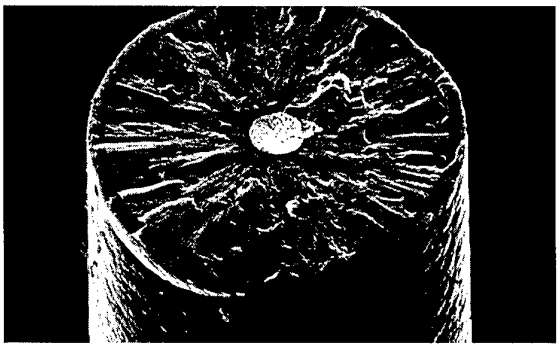

Figure 8 SiC Fibre Growth Defect

Tight control of CVD process parameters is crucial in order to minimise the occurrence of defects and obtain a narrow strength distribution. Reducing the population of low strength fibre breaks will result in improved minimum composite properties, with a reduced number of potential early/low strength fatigue crack initiation sites within the composite.

Fibre/Matrix Interaction

Attack of the reinforcing fibre by the titanium matrix has been extensively studied and the growth of interface reaction zones with extended time at temperature for both processing and service regimes can be accurately predicted. Figure 9 shows the typical micro-structure of an as processed Ti-6Al-4V/SCS-6 composite with a relatively small reaction zone ≈1μm thick, and the carbon-rich protective coating intact. The other extreme is illustrated in figure 10, where deliberately extended processing times have resulted in almost complete consumption of the carbon coating and a reaction zone several microns thick.

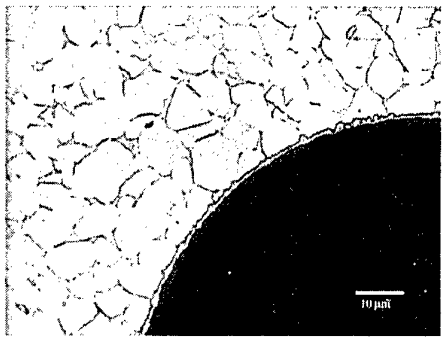

Figure 9 As Processed Ti-6Al-4V/SCS-6 Composite

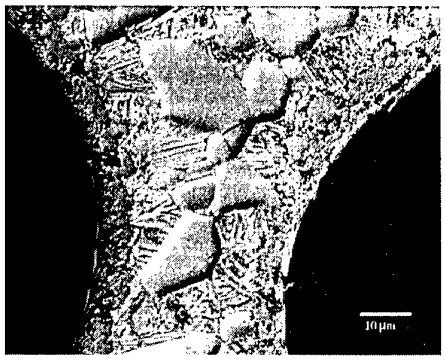

Figure 10 Extreme Interface Reaction

In order to maintain fibre and composite properties, therefore, the interfacial reaction zone needs to be controlled. The interface structure in a model composite manufactured from uncoated fibre is shown in figure 11. Many fibre surface flaw initiation sites can be seen generated by the angular TiC reaction zone grains. This material had low strength and was very brittle. The detailed nature of the interface region can also be clearly seen and consists of two distinct layers: fine titanium carbide grains adjacent to the fibre, with a coarser, mixed, carbide and silicide layer ($TiC + Ti_5Si_3$) next to the matrix.

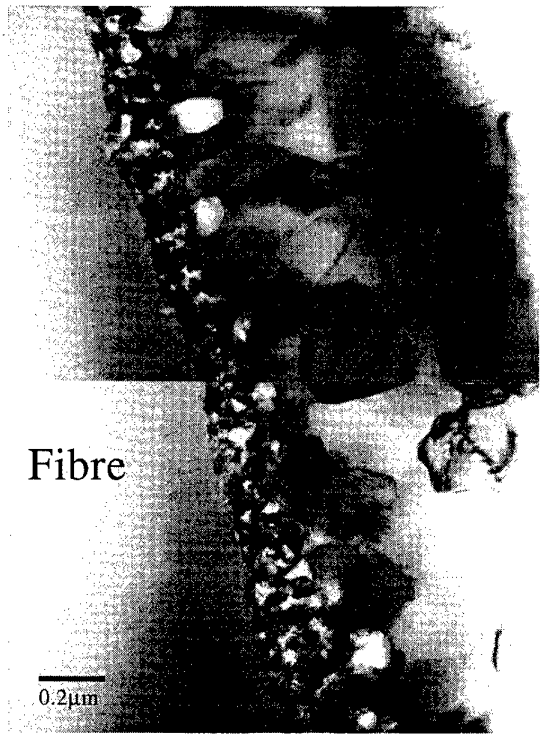

Figure 11 TEM Image of Fibre Matrix Interface

All the commercially available monofilament silicon carbide fibres have protective surface coatings, generally based on layers of carbon. The Textron SCS-6 fibre is shown in figure 12, illustrating the location of the reaction zone away from the critical SiC surface. The layers of carbon also provide a relatively weak interface, which aids in crack deflection thus allowing fibres to bridge growing fatigue cracks and therefore reduce propagation rates. A further benefit of carbon is that the reaction product is now primarily TiC. Removal of the silicide should ameliorate high temperature thermomechanical fatigue properties by reducing the propensity for interface cracking and crack initiation.

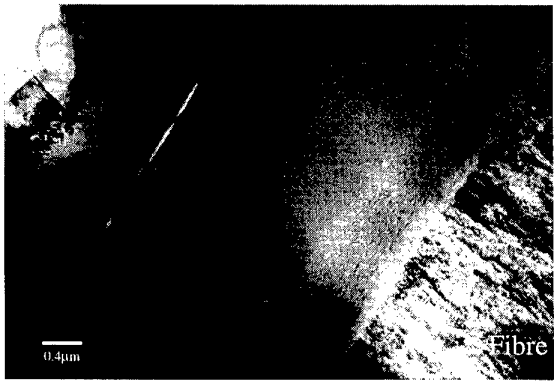

Figure 12 Textron SCS-6 Fibre Coating

Composite Process Control

There are several aspects of manufacturing process control, common to all the TMC processing routes, where detailed microstructural assessment is necessary. Some of these are outlined below.

Fibre damage during consolidation: The main reasons for fibre damage at this stage are;

- mishandling of the fibre preforms,
- excessive movement during consolidation causing buckling or tensile failure,
- pinching of fibres due to point contacts from badly stacked preforms or the inappropriate location of fibre ends.

Fibre distribution: Accurate control of fibre distribution is key to achieving consistent composite properties with low scatter. The higher the debulking required by the process the more difficult it is to maintain accurate positioning of fibres. In thick sections, the best fibre distributions to date have been achieved using the matrix coated fibre and wire winding routes

Fibre coating damage: Excessive damage during the preforming stages, such as particle impingement from metal spraying, or large movements during consolidation can remove the protective fibre coating resulting in mechanical property degradation.

Embrittlement of the matrix: This is generally due to inadequate cleaning or incomplete binder removal prior to consolidation. Very careful control of the cleaning and degassing stages of manufacture is necessary to eliminate this problem.

Poor diffusion bonding: Again this can be due to inadequate cleaning contaminating the bonding surfaces, or due simply to non optimum consolidation conditions.

Properties and Lifing

Until recently the mechanical properties of TMC material, have been significantly influenced by the manufacturing and processing defects described above. Low cycle fatigue properties tend to be the most sensitive to this, and a schematic representation is shown in figure 13.

The area on the left of figure 13 shows the effect of gross fibre defects where several fibre layers in close proximity are broken. This not surprisingly has the most detrimental effect on mechanical properties. Such defects, however, are readily found using today's x-ray or ultrasonic NDE techniques. The central region of localised fibre breaks and matrix defects is of more concern since NDE inspection in this region is unlikely to be able to locate all the defective parts without considerable technical development. Furthermore the cost of such detailed inspection would be prohibitive. Establishing high quality processing with adequate process control is therefore vital to the successful introduction of TMCs into engines.

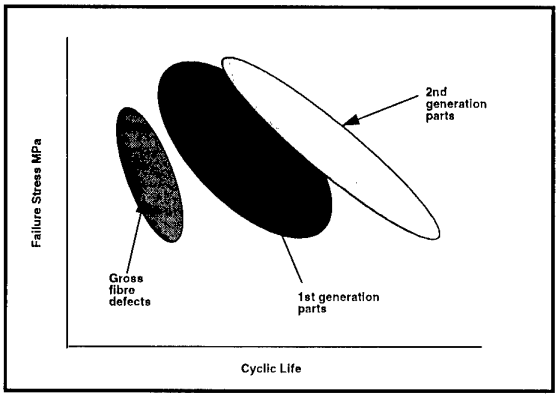

Figure 13 Schematic Fatigue Response of TMC

The significant improvement in composite quality demonstrated by the latest material forms (referred to as 2nd generation material) will enable the establishment of a predictive lifing capability. Future TMC components will be only partially reinforced and therefore will require a mix of lifing methods i.e. unreinforced areas will be able to use conventional monolithic rules. This will need considerable care in stress analysis to ensure that where changes from composite to non composite material occur the effect of potential defects can be correctly modelled. The key areas for lifing consideration on a TMC bling are shown in figure 14.

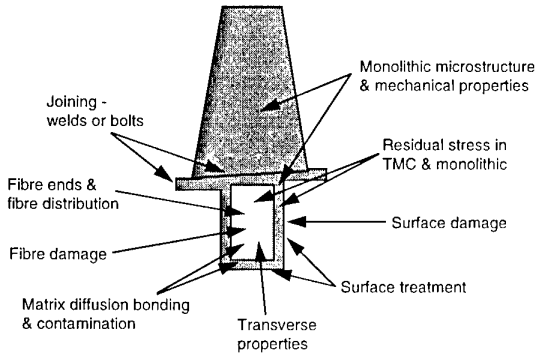

Figure 14 TMC bling key issues for lifing

Conclusions

This paper covers some of the key areas of TMC technology where it is necessary to control structure on a micro scale to safely introduce TMC components into aero-engines. The significant improvement in composite quality demonstrated by the latest processing techniques also promise improvements in performance and reliability. Programmes are in place to fully quantify this improvement.

Costs must also be acceptable and it is evident that significant effort is required to reduce the cost of today's best processes to meet future component cost targets. Integration of the manufacturing, design, and engineering activities through the use of integrated product development teams is the best way forward. Industry wide co-operation through collaborative programmes will also be crucial to the successful implementation of TMC technology in aero-engines.

References

1) Aviation Week & Space Technology May 12 1997

Meeting Discussions

Paper 27: **The Introduction of Reinforced TMC Materials into Rotating Machinery - The Safe Approach**

Author: P. J. Doorbar

Discussor: J. Kumpfert

Question: Did you calculate the transverse property requirements for the Bling Application?

Author's reply: Yes, the LP compressor application is well within the mechanical property limits in the transverse direction.

Design of an Active Stall Avoidance System for a Subsonic Axial Compressor

R. Schulze
D. K. Hennecke
Dept. of Gas Turbines and Flight Propulsion
Darmstadt University of Technology
Petersenstr. 30, D-64289 Darmstadt
Germany

Summary

A single-stage subsonic compressor was examined as a basis for an active stall avoidance system. The process of stall inception was investigated as well as the modes of unstable operation.

On the basis of the experimental results, a sensor/actuator scheme was choosen for the control system. A simple and robust stall detection system has been developed and implemented on a real-time computer.

The control system's capability of stabilizing the compressor was shown in first experiments. The experiments were analyzed in detail.

Nomenclature

A_{eff}	effective throttle area
$\dot{m}$	mass flow rate
$\dot{m}_{red}$	corrected mass flow
p_t	total pressure
PHI, Φ	compressor flow coefficient
PSI, Ψ	compressor pressure rise coefficient
Π	compressor pressure ratio
ρ	density

1 Introduction

The improvement of the compressor stability has been recognized as an important contribution to the enhancement of the performance of future aircraft engines. Efforts in research and development cover passive measures such as casing treatment [4] and the active suppression of compressor instabilities and their onset [1, 2, 3, 10].

The objective of the present work is to find an active stall avoidance system that allows the safe compressor operation near the stability line even in the presence of transient inlet distortions. The approach should be as simple and robust as possible as far as the actuator, the instrumentation and stall detection algorithms are concerned.

Most of the active control systems depend on the presence of small-amplitude rotating waves prior to the onset of rotating stall. However, pre-stall cursors of that kind are not always present prior to stall or may not be linked to the actual onset of compressor instabilities [5, 11]. Also the effect of transient inlet distortions on the occurrance of pre-stall waves is not yet examined. Several studies have shown that rotating stall occurs as the compressor becomes unstable even if the ultimate mode of unstable operation is surge [9, 2]. Also, rotating stall leads to flow perturbations that are much stronger than those induced by pre-stall waves [6] and hence can easily be detected.

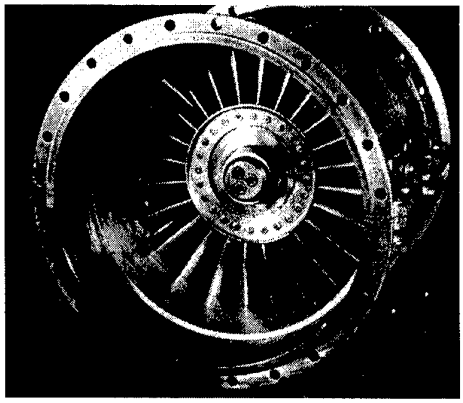

Figure 1: View of the compressor rotor (in flow direction)

It was shown that one-dimensional axissymmetric actuators can be applied for the enlargement of the domain of attraction of stable axissymmetric equilibria [2].

The above considerations lead to the following aim: A closed-loop control system shall be applied on an axial compressor in order to allow safe compressor operation near the stability line. The global operating point shall vary as little as possible even if the compressor becomes unstable due to transient distortions. The actuator shall be axissymmetric and one-dimensional. The detection of unstable compressor operation shall rely on the detection of evolving rotating stall rather than pre-stall waves thus allowing simple and robust instrumentation and algorithms.

For the design of the control system components (actuator, instrumentation, stall detection, controller) the knowledge of the unstable compressor behaviour in general and the onset of compressor stall is of great importance. Since no methods are available to quantitatively predict the stall inception process experiments for the determination of the compressor behaviour have to be performed.

The results of the experimental investigation of the test compressor's (see Fig. 1) unstable behaviour will be presented. On the basis of these results an instrumentation

Paper presented at the RTO AVT Symposium on "Design Principles and Methods for Aircraft Gas Turbine Engines", held in Toulouse, France, 11-15 May 1998, and published in RTO MP-8.

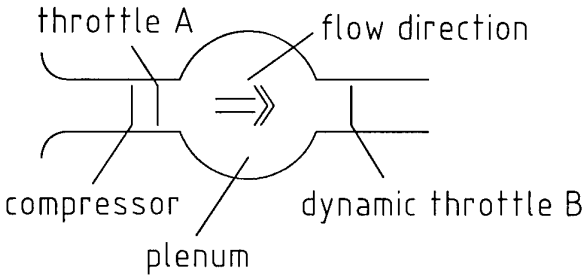

Figure 2: Schematic overview of the compression system

for the detection of unstable compressor operation will be introduced and its capability of detecting evolving compressor stall in connection with a simple and robust algorithm will be shown. A one-dimensional actuator will be described and incorporated into a one-dimensional model of the compression system. Finally, first results obtained from experiments with the closed-loop control system will be shown.

2 Experimental Setup

Figure 2 gives an overview of the compression system setup. The configuration is similar to that described in [7]. A cross section of the inlet duct with the test compressor and a downstream throttle can be seen in Fig. 3. Table 1 gives an overview of the compressor data. Figure 4 shows the test stand configuration. The compressor intakes air from the environment. A diffuser (see Fig. 3) connects the inlet duct with a downstream plenum. The diffuser exit can be narrowed with a ring-type throttle (see Fig. 3, Pos. A). This throttle was used to adjust the mass flow in the experiments for the system identification if not mentioned otherwise. The plenum discharges through an exit duct into the environment (see Fig. 4). Figure 1 gives an impression of the compressor rotor.

Figure 5 gives an overview of the pressure transducers and probes that were applied for the experiments. Position I shows a surface-mounted piezo-resistive sensor which is mounted on a traversable probe. In Position II a surface-mounted piezo-resistive sensor can be seen in the compressor casing. The surface-mounted probes resolve pressure fluctuations with frequencies up to 20 kHz. The sensors in Position III are also piezo-resistive sensors. Due to their configuration their maximum response frequency is about 1 kHz. However, they are very robust at a significantly lower price. The capability of the type-III sensors for serving in the control system was compared in [11] to that of the type-II sensors.

Figure 6 gives an overview of the circumferential (1...8) and axial (A...D) probe locations as well as an impression of the blade sections at mid-span.

3 Experimental System Identification

A more detailed presentation of the experimental results can be found in [11]. Here, the results will be resumed

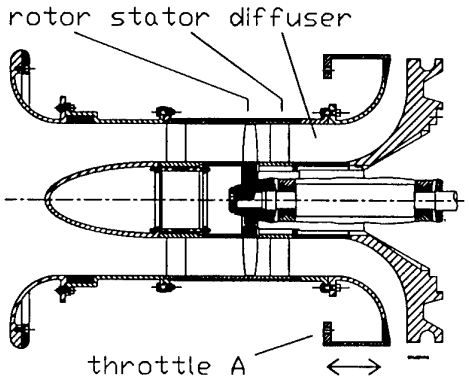

Figure 3: Cross section of the inlet duct with the compressor and the downstream ring-type throttle

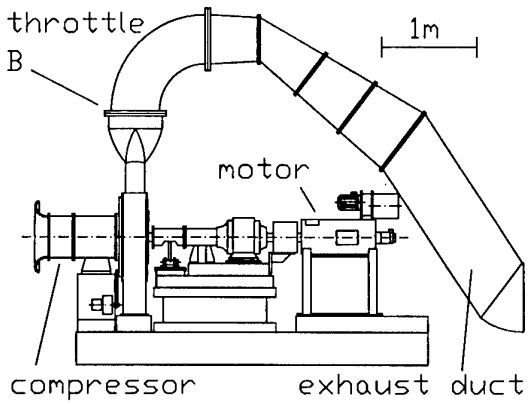

Figure 4: Overview of the test stand

Configuration:	axial: Rotor, Stator
No. of Blades:	24, 27
Blade Sections:	NACA 65, DCA
Hub-to-Tip Ratio:	0.5
Tip Diameter:	0.4 m
Speed:	3700 rpm

Table 1: Compressor data

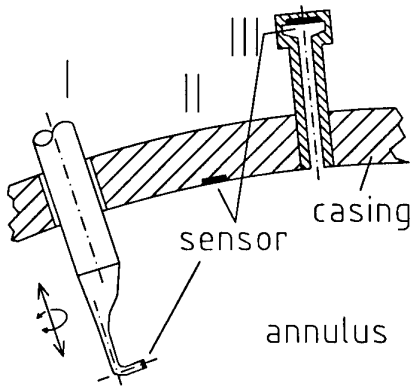

Figure 5: Dynamic pressure probes

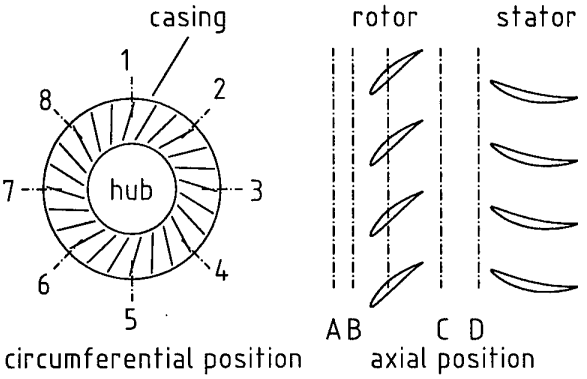

Figure 6: Probe locations and blade sections at mid-span

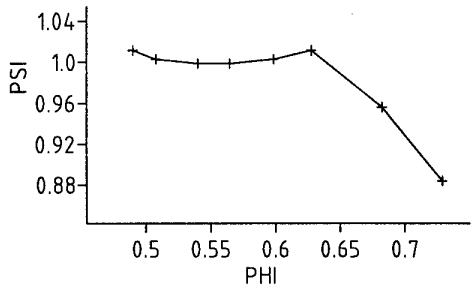

Figure 7: Characteristic of the stable operating regime

which have direct impact on the control system design.

3.1 Stable Operating Regime

Figure 7 shows the stable characteristic of the compressor at the speed of 3700 rpm. In [12, 14, 13, 8] the compressor properties as well as methods for the real-time operating point estimation are described for the stable operating regime.

3.2 Stall Inception

Figure 8 depicts the time after which stall can be seen with a traversable probe (Pos. I, Fig. 5) relativ to a type-II sensor at the casing in the same axial location (Pos. A, Fig. 6). The result clearly indicates that rotating stall develops at the blade tips thus allowing the application of wall static pressure sensors for the stall detection.

The development of the cell size after stall inception can be seen in Fig. 9. The stall cell development is completed after 10 rotor revolutions. In order to keep the control effort small the control system (including the actor) should react in a fraction of that time.

3.3 Unstable Operating Regime

Due to the small value for the B-parameter of 0.35 the ultimate mode of unstable operation is rotating stall. The B-parameter was introduced in [7] and it was shown that it has significant influence on the mode of unstable operation of a compressor. Depending on the mass flow rate

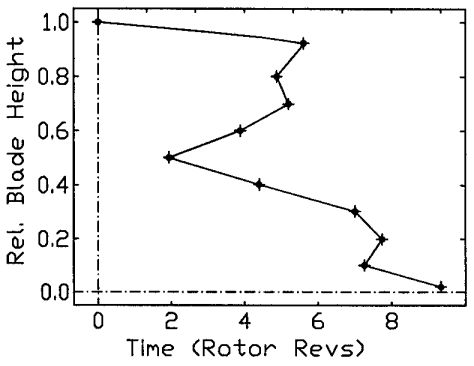

Figure 8: Delay of the stall detection at various radial locations

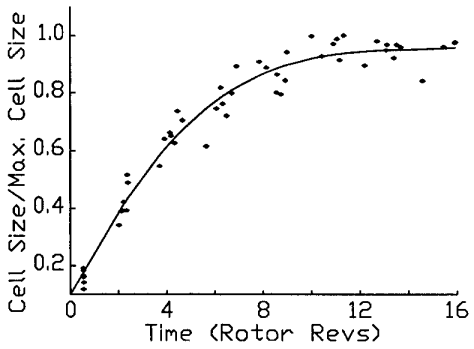

Figure 9: Time history of the cell size after stall initiation

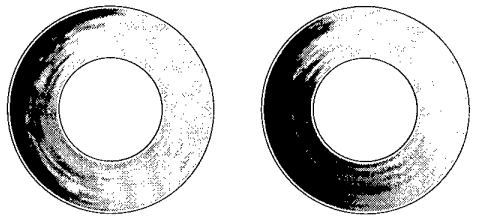

Figure 10: Fully developed part-span (left) and full-span (right) stall cells. The direction of rotation is clockwise.

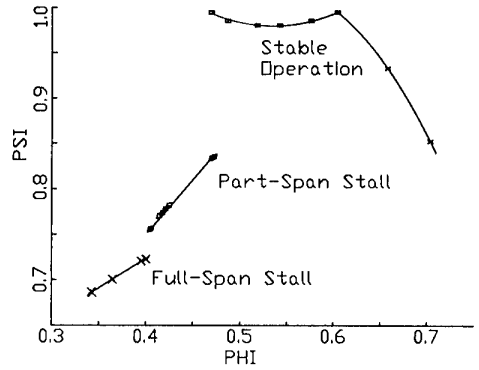

Figure 11: Characteristics of the various operating modes

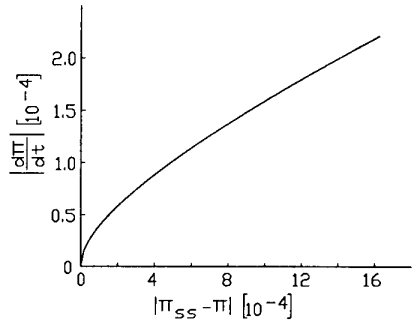

Figure 12: Transient post-stall compressor response

part-span stall or full-span stall occurs during unstable operation. Figure 10 gives an impression of the shape of the cells. The part-span stall cell rotates at 44 % of the rotor speed in the absolute frame of reference and the full-span stall cell at 31 %, respectively.

3.4 Transient Compressor Response

In [11] a model of transient post-stall compressor response was formed on the basis of experimental data. It describes the rate of change of pressure rise of the compressor as a function of the instantaneous pressure rise and the steady state pressure rise which can be derived from the instantaneous mass flow rate and the steady state characteristics.

The measured and modelled steady state characteristics of the operating modes *stable*, *part-span stall*, and *full-span stall* can be seen in Fig. 11. The model of the transient post-stall compressor response can be seen in Fig. 12.

3.5 Model of the Test Stand

On the basis of the lumped parameter model [7] a mathematical model of the test stand was developed in [11]. The model was optimized such that sufficient quantitative agreement with the test stand is given.

The dynamic throttle behaviour had to be integrated into the model because in terms of response time the throttle has to be regarded as a close-coupled actuator.

4 Stall Detection

An array of eight type-III sensors (see Fig. 5) in the locations A1...A8 (see Fig. 6) was applied for the detection of unstable compressor operation (compare Section 3.2).

Although pre-stall waves could be seen in the compressor annulus prior to stall [11] they were found not to be sufficiently reliable for the monitoring of the compressor stability (i.e. the detection of unstable compressor operation prior to stall). Also, as indicated in Section 1 it is the objective of this work to examine whether the compressor can be stabilized *after* the onset of rotating stall.

For the experiments shown here a modified version of the statistical method described in [11] was applied for the detection of upcoming rotating stall. Like the old statistical method, the modified (new) statistical method can be viewed as a band-pass filter [11]. From each sensor the two moving averages A_1 and A_2 are computed:

$$A_{i,t} = \frac{A_{i,t-1} \cdot W_i + p_t}{W_i + 1} \quad i = 1,2 \qquad (1)$$

W_1 and W_2 are the weighting factors, t is the time index and p_t is a sample of the pressure signal at the time t. When exceeding a fixed limit the difference $|A_1 - A_2|$ indicates upcoming stall.

Figure 13 illustrates the difference between the old and the new statistical method. The pressure signals from the eight transducers are shown during a stall inception process. The positions of stall detection with both the old and the new method are depicted for each pressure signal.

While the old method can detect upcoming stall in an earlier state than the new method it has a delay of up to 0.5 rotor revolutions between the passing of the stalled flow region and the stall detection. This is due to the integrating effect of the algorithm (compare [11]). The time delay is much smaller with the new method at the cost of a lower sensitivity. The passing of the stalled flow region which was detected by the old method in Signal 2 could be seen with the new method only when it passed the next sensor (Signal 3). However, due to the smaller time delay of the new method stall is detected 0.35 rotor revolutions earlier than with the old method. It must be noted that the benefit of the new method strongly depends on the number of sensors applied for stall detection and may even be negative when only few sensors are used.

Despite its simplicity and low cost of computation time, the algorithm's capability of reliably detecting upcoming stall shortly after the stall initiation was confirmed during many experiments.

5 Dynamic Throttle

As mentioned in Section 1 a one-dimensional, axissymmetric actuator shall be used for the control system. A dynamic throttle was installed downstream the plenum (see Figs 2, 4, Throttle B). The throttle can be seen in Fig. 14.

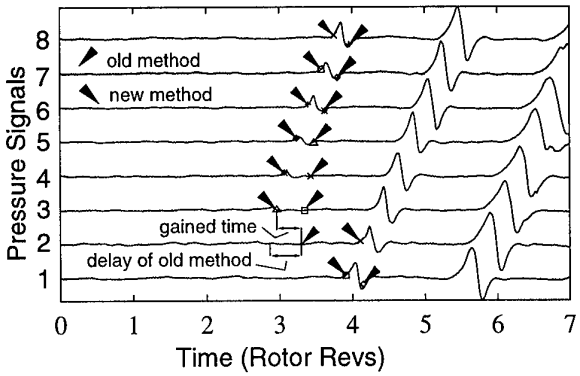

Figure 13: Comparison between the old and the modified statistical method

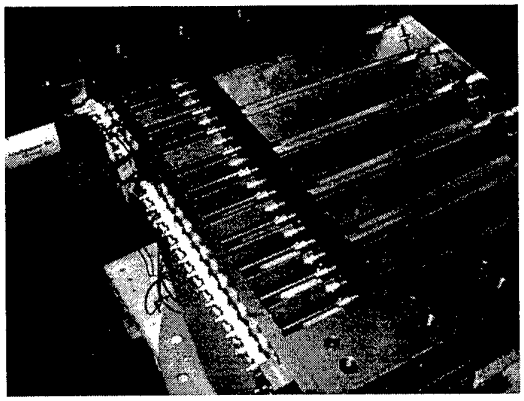

Figure 14: The dynamic throttle

It consists of two arrays of lamellas. The lamellas of each array can be collectively turned by a step motor. The functionality of the dynamic throttle is illustrated in Fig. 15. In the experiments both lamella arrays were moved simultaneously.

The dynamic throttle was integrated into the one-dimensional compression system model which was described in [11]. When incompressibility of the flow is assumed and the throttle is considered short in length the loss of total pressure over the throttle can be written as

$$\Delta p_t = \frac{\dot{m}^2}{2\rho} \cdot \frac{1}{A_{eff}^2}$$

where A_{eff} is the effective throttle area. The characteristic of the throttle was determined experimentally and the relation between the effective throttle area relative to the area of the compressor annulus and the angle of the lamellas is shown in Fig. 16.

The control algorithm generates a nominal value for the throttle position (i.e. a nominal angle position for the lamellas). The step motor controller has to take into account the inertia of the dynamic throttle and the step motors. Consequently, the dynamic behaviour of the throttle has to be

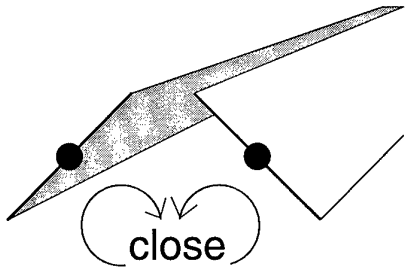

Figure 15: The functionality of the dynamic throttle

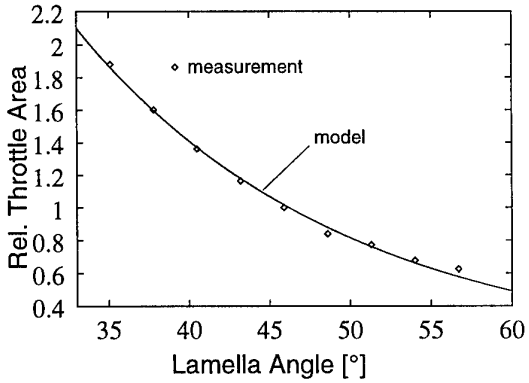

Figure 16: Characteristic of the dynamic throttle

integrated into the control system model. The maximum angular acceleration of the lamellas is $1.0 \cdot 10^4\, deg/sec^2$.

6 Real-Time Computer

A standard Digital Signal Processor (DSP) was applied as Real-Time Computer. The algorithms for the data acquisition, the stall detection, the controller, and for controlling the step motors of the dynamic throttle were implemented on the DSP.

High-level programming tools have proven to generate unefficient computer code that could not be run on the DSP in real-time. Consequently, the algorithms were implemented in the programming language *C* on the hardware level (register programming). This method proved to be simple and efficient in terms of both programming and computation time.

7 Experiments with the Control System

The aim of the experiments with the closed-loop control system was to estimate the control system's capability of stabilizing the compressor in an early state of upcoming stall thus allowing to maintain the pressure rise and mass flow rate.

A simple two step controller was implemented. The controller alternates the nominal throttle value between "open" and "closed". The position "open" corresponds to the position when the throttle is fully opened. The position "closed"

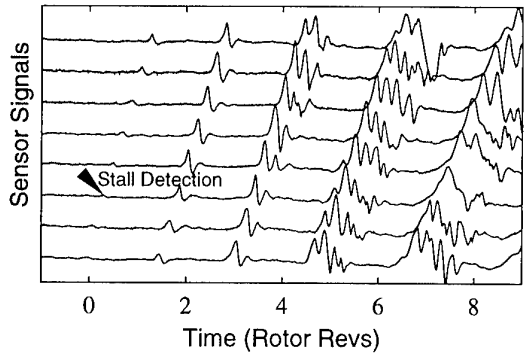

Figure 17: Stall evolution with no controller response

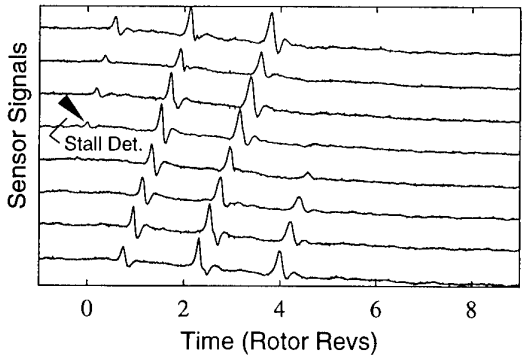

Figure 18: Stall evolution with the two-step controller

corresponds to the position immediately prior to the detection of compressor stall.

In the experiments the mass-flow was reduced gradually by slowly closing the dynamic throttle until the compressor became unstable. When upcoming rotating stall was detected the nominal throttle position was set according to three different control strategies. The experiments showed good reproducibility.

7.1 No Controller Response to Compressor Stall

Figure 17 shows the signal from the eight pressure transducers when the controller does not respond to the onset of rotating stall. Within roughly ten rotor revolutions a stall cell evolves as described in Section 3.2.

7.2 Simple Two-Step Controller

Experiments were performed where the throttle was fully opened after the onset of compressor stall was detected, i.e. the nominal throttle position was set to open and the actual throttle position followed at the maximum possible acceleration. The pressure signals from these experiments can be seen in Fig. 18.

After two rotor revolutions the growth process of the stall cell is stopped and after three more rotor revolutions the compressor is fully unstalled.

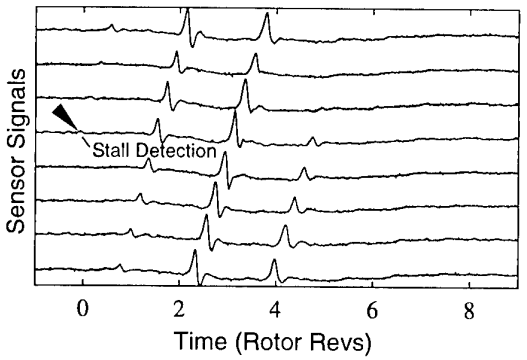

Figure 19: Stall evolution with the modified two-step controller

7.3 Modified Two-Step Controller

In order to keep the variation of the compressor operating point small after the stall inception, the experiments with the two-step controller were modified in such way that a short time after opening the throttle the nominal throttle position was set to a position close to the original value before the onset of stall. The pressure signals from these experiments can be seen in Fig. 19. Again, after five rotor revolutions the compressor is unstalled.

8 Analysis of the Experiments

In order to understand the process of active stabilization of the compressor the important process parameters such as pressure rise and mass flow rate have to be determined on the basis of the experimental data together with the mathematical model of the test stand.

8.1 Stall Cell Size

For the same experiment as shown in Fig. 18 the difference of each pressure signal to the average of all the signals is shown in Fig. 20. The figure gives an impression of the development of the pressure distortions due to the upcoming rotating stall during the active stabilization process.

When it is assumed that the development of the stall cell immediately responds to the compressor stability a rough estimate of the stability condition can be derived from the data shown in Fig. 20.

For further analysis of the experiments it is assumed that both the stall cell size and the drop of the pressure rise qualitatively behave like the model function also shown in Fig. 20.

8.2 Pressure Rise

The drop in compressor pressure rise due to upcoming stall could not be measured directly during the stall cell evolution process. Consequently, the pressure rise development during the experiments shown in Figs 18 and 19 had to be derived from both available measurement data and appropriate models of the transient compressor behaviour during the experiments.

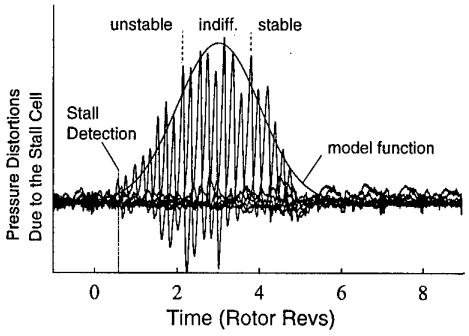

Figure 20: Pressure distortions of the eight signals due to the rotating stall cell during the experiment shown in Fig. 18. Model function for the qualitative description of the stall cell development during the experiment.

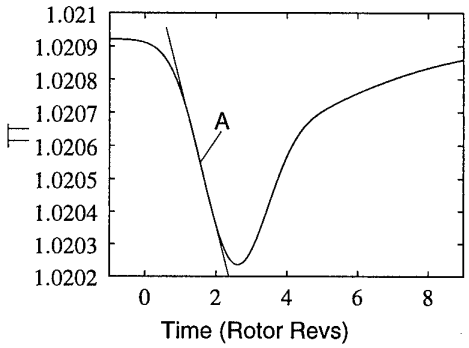

Figure 21: Compressor pressure rise transient during the experiment shown in Fig. 19. The qualitative trend conforms with the model function shown in Fig. 20 and the gradient of the pressure rise in Pos. A was obtained from the model shown in Fig. 12.

Since the transient compressor response model shown in Fig. 12 was obtained from experiments with uninterrupted stall inception it cannot predict the compressor pressure rise correctly for experiments where the stall cell growth is interrupted in an early state. The qualitative trend of the drop in pressure rise (i.e. the model function in Fig. 20) was combined with the quantitative information from the model shown in Fig. 12 in order to obtain useful information about the the transient compressor pressure rise. The modelled pressure rise transient during the experiment shown in Fig. 19 is depicted in Fig. 21.

It must be stressed that the method described above can only be applied for the off-line analysis of given experimental data. It is not a predictive model of the compressor behaviour.

8.3 Mass Flow Rate

When the pressure rise is given then the mass flow rate can be computed with the mathematical model of the test stand (see Section 3.5). The computed mass flow transient from the experiment shown in Fig. 19 is depicted in Fig. 22. The

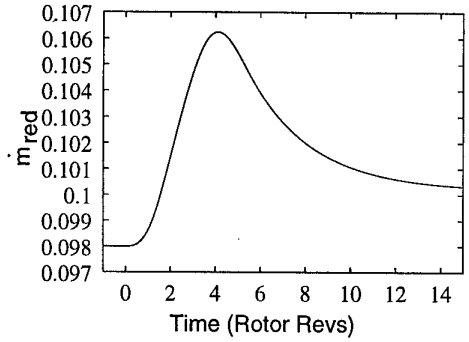

Figure 22: Mass flow transient of the experiment shown in Fig. 19 (mathematical model)

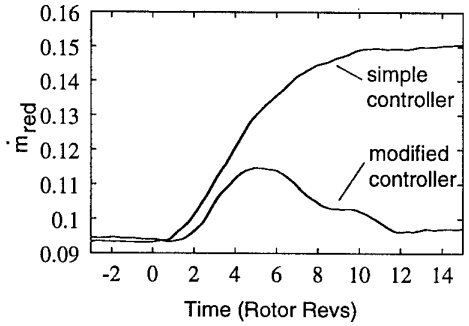

Figure 23: Measured mass flow transients from the experiments shown in Figs 18 and 19

mass flow rate is higher at the end of the experiment because the throttle was not closed all the way to its original value before the onset of rotating stall.

In order to compare the calculated mass flow transient with experimental data the mass flow rate was estimated by solving the unsteady Bernoulli equation with the wall static pressure which was measured with the sensor array (see Section 4). Only those sensors were considered which were not in the vicinity of the stall cell. Consequently the mass flow rate is overestimated whenever a stalled flow region is present. Fig. 23 shows the measured transients from the experiments presented in Figs 18 and 19. The trends are in good agreement with the results from the mathematical model.

8.4 Overview of the Experiments

Figures 24 and 25 show the compressor performance map with the trajectories of the compressor operating point during the three experiments shown in Figs 17, 18 and 19. The numbers in Fig. 25 give the time in rotor revolutions after stall inception at the according points of the trajectory paths.

The figures indicate that a hysteresis in mass flow exists between the stall inception point and the point of compressor stabilization.

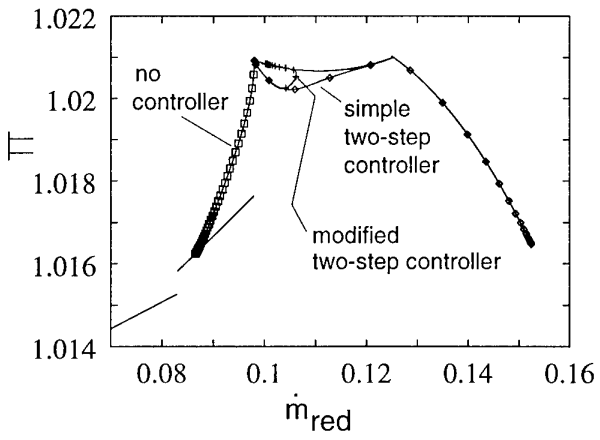

Figure 24: Operating point trajectories from the experiments shown in Figs 17, 18 and 19

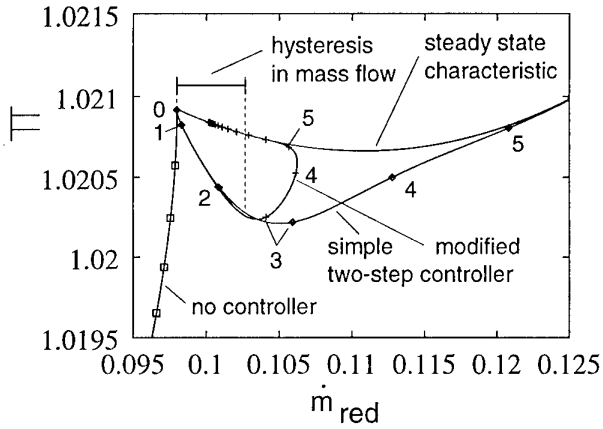

Figure 25: Operating point trajectories from the experiments shown in Figs 17, 18 and 19 (enlargement from Fig. 24)

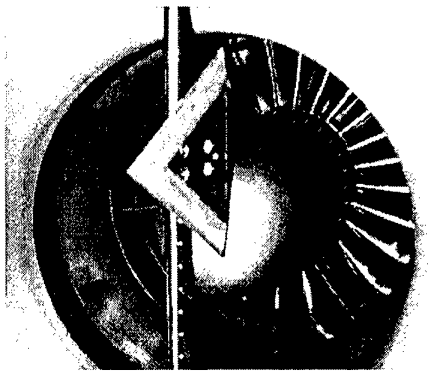

Figure 26: Delta wing for the generation of transient inlet distortions

9 Conclusions

It could be shown that the control system with the sensor array and the one-dimensional close-coupled actuator with the very simple control strategy is capable of stabilizing the compressor within a short time after stall inception. Even when unstable compressor operation is detected only after the onset of rotating stall (rather than using pre-stall waves) the variation of the operating point can be kept small during the stabilization process.

A hysteresis in mass flow exists between the onset of rotating stall and the point where stable compressor operation is reestablished. This hysteresis is of importance for the active stabilization because it has to be overcome with the one-dimensional actuator.

To the knowledge of the authors, the existing models for compressor instabilities are not capable of representing the stall evolution process shown in this paper. Consequently, the evaluation of the stall evolution process with the suppression of the stall cell growth can only be performed on the basis of existing experimental data.

10 Outlook

It is believed that the hysteresis in mass flow (compare Fig. 25) depends on the stage of the stall cell development thus making controller response a very critical factor. This dependency will be examined in further experiments.

The ultimate goal in any stall avoidance effort is the early detection of unstable compressor operation. The stall detection method will be modified such that the information in pre-stall waves will be used whenever available (compare [11]).

The availability of a model that is capable of describing the processes shown here is important for the development of stall avoidance systems in general. The development of such a model will be addressed in future work.

The benefit of improved control algorithms and actuator concepts will be studied in further experiments.

Figure 26 shows a delta wing that will be used for the generation of transient inlet distortions. Experiments for the comparison of the control system behaviour with clean and distorted inlet flow will be performed.

References

[1] O.O. Badmus, S. Chowdhury, K.M. Eveker, C.N. Nett, and C.J. Rivera. Simplified Approach for Control of Rotating Stall, Part 1: Theoretical Development. *Journal of Propulsion and Power*, 11(6):1195–1209, 1995.

[2] O.O. Badmus, S. Chowdhury, K.M. Eveker, C.N. Nett, and C.J. Rivera. Simplified Approach for Control of Rotating Stall, Part 2: Experimental Results. *Journal of Propulsion and Power*, 11(6):1210–1223, 1995.

[3] R.L. Behnken, R. D'Andrea, and R.M. Murray. Control of Rotating Stall in a Low-Speed Axial Flow Compressor Using Pulsed Air Injection: Modelling, Simulations, and Experimental Validation. In *Proceedings of the 35th Conference on Decision and Control*, pages 3056–3061, New Orleans, LA, 1995.

[4] N. A. Cumpsty. Part-Circumference Casing Treatment and the Effect on Compressor Stall. *ASME Paper, 89-GT-312*, 1989.

[5] I.J. Day. Active Suppression of Rotating Stall and Surge in Axial Compressors. *Journal of Turbomachinery*, 115:40–47, 1993.

[6] I.J. Day. Stall Inception in Axial Flow Compressors. *Journal of Turbomachinery*, 115:1–9, 1993.

[7] E.M. Greitzer. Surge and Rotating Stall in Axial Flow Compressors, Part I: Theoretical Compression System Model. *Journal of Engineering for Power*, 98:190–198, 1976.

[8] A. Koenig, P. Windirsch, M. Glesner, H. Wang, and D.K. Hennecke. An Approach to the Application of Neural Networks for Real-Time Operating Point Estimation in Turbojet Compressor Units. In *Proceedings of the IJCNN-'92, Vol. III, Beijing, China*, pages III 63 – III 69, 1992.

[9] C.A. Mansoux, D.L. Gysling, J.D. Setiawan, and J.D. Paduano. Distributed Nonlinear Modelling and Stability Analysis of Axial Compressor Stall and Surge. In *Proceedings of the 1994 American Control Conference*, pages 2305–2316, Baltimore, Maryland, 1994.

[10] J.D. Paduano, A.H. Epstein, L. Valavani, J.P. Longley, E.M. Greitzer, and G.R. Guenette. Active Control of Rotating Stall in a Low-Speed Axial Compressor. *Journal of Turbomachinery*, 115:48–56, 1993.

[11] R. Schulze, D.K. Hennecke, Th. Le, and M. Glesner. Experimental Examination of an Axial Compressor as a Basis for an Active Stall Avoidance System. In *Proceedings of the 1998 ISROMAC-7 Symposium, Vol. C, page 1265*, 1998.

[12] H. Wang and D.K. Hennecke. Grundlagenorientierte experimentelle Untersuchungen der Stallerkennung im Verdichter unter Echtzeitbedingungen. In *VDI Berichte Nr. 1109*, pages 681–702, 1994.

[13] H. Wang, D.K. Hennecke, A. König, P. Windirsch, and M. Glesner. An Approach to the Stall Monitoring in a Single Stage Axial Compressor. In *AIAA/SAE/ASME/ASEE 29th Joint Propulsion Conference and Exhibit*, number AIAA-93-1872, 1993.

[14] H. Wang, D.K. Hennecke, A. König, P. Windirsch, and M. Glesner. Method for Estimating Various Operating States in a Single-Stage Axial Compressor. *Journal of Propulsion and Power*, 11(2), 1995.

Meeting Discussions

Paper 28: **Design of an Active Stall Avoidance System for a Subsonic Axial Compressor**

Authors: R. Schulze, D. K. Hennecke

Discussor: G. William Gallops

Question: What was the nature of the post-stall model discussed and how was the in-stall compressor characteristic derived?

Author's reply: 2-D, with characteristics derived from measured data.

Discussor: George S. Dulikravich

Question: Your proposed system(s) seems to be quite simple and robust. What do you have to say to the people that are proposing the use of MEM's (Micro-Electro-Mechanical) devices for active control of blade shapes?

Author's reply: The intention of the application of the simple one-dimensional throttle was to investigate the possibility of stabilizing the compressor when rotating stall is already evolving, whereby the operation point shall be kept as steady as possible. Here, the aim is to allow safe compressoroperation at a reduced stall margin. It was shown that the stable operating regime of a compressor can be enlarged when rotating pre-stall waves in the compressor annulus are suppressed. To the author's knowledge, this requires less control efforts than unstalling a compressor, thus being a potential application for the MEM technology.

Discussor: Dr. K. K. Chan

Question: Does signal noise and other disturbance affect the effectiveness of the stall detection mechanism?

Author's reply: Yes, they do. The detection of upcoming rotating stall in an early state depends on the detection of small pressure perturbations which are caused by flow separations in the rotor. Signal noise and other distortions may lead to false stall detection. If this is the case, the limit for |A1-A2| (compare section 4) has to be increased which in turn leads to a less sensitive stall detection system and an increase in controller response time.

Rotating Pip Detection and Stall Warning in High-Speed Compressors Using Structure Function

Michelle M. Bright
NASA Lewis Research Center
Cleveland, Ohio 44135
email: mbright@lerc.nasa.gov

Helen Qammar, Hanif Vhora, Michael Schaffer
Department of Chemical Engineering
University of Akron
Akron, OH 44325, USA

1. SUMMARY

A statistic for both rotating pip and incipient stall detection, called Structure Function is introduced for use in high speed research compressor environments. Experimental studies on stall inception processes have long observed two types of pre-stall compressor activity. Presently there exist methods for indicating modal stall precursive events in the compressor. This is a first application of a new method to detect rotating pip activity prior to stall in research compressors. The algorithm requires a very short sample of data to distinguish pip activity prior to stall, and thus may be used in a real time application. Additionally, this Structure Function algorithm is also used as a single sensor stall warning method under a variety of operating conditions, including clean inlet conditions, radially and circumferentially distorted inlet conditions, and in examples of steady air injection along the casing, and controlled air injection conditions. Structure Function provides a potential advantage over linear spectral techniques and wavelet algorithms for stall detection due to the simplicity of the algorithm and because it does not rely on a priori knowledge of frequency content.

2. INTRODUCTION

Research in the area of compressor rotating stall has focused on three distinct areas: **modeling** the stall inception phenomenon to accurately capture fluid physical instabilities occurring prior to stall; **detecting** the stall inception phenomenon through knowledge of both the modeled characteristics of pre-stall behavior and observed experimental pre-stall events; and **controlling** stall through the fast and fervent application of knowledge from modeling and predicting. Since a recent emphasis has been placed on the fast identification and control of pre-stall disturbances, a reliable pre-stall indicator is necessary for future active stall control applications. Many of the present schemes for active stall control in experimental compressors are model based. This paper will focus on a prediction technique that is not model-based, but is robust in monitoring short length-scale rotating stall instabilities in experimental high speed compressors.

Models of the stall inception process have been documented by many authors. In a combined theoretical and experimental paper, Moore and Greitzer (1986) predict and detect stall inception patterns in low speed compressors. Their observations are of "modal" stall inception patterns of long length-scale circumferential velocity perturbations. These patterns are further documented by Hendricks (1993) and Day (1993). These modal patterns appear when the compressor stages are well matched, often during low speed operation in the front stages, and are affected by both inlet distortion and stage mismatch in their axial extent. (see Camp, 1997) These authors suggest that modal patterns occur at 50% or less of the fundamental rotational frequency of the compressor and grow in amplitude into rotating stall.

Observations of short length scale phenomenon in the compressor prior to stall have also been shown. In papers by Day (1993), Camp (1997) and Garnier (1991) there is evidence of "pip" stall inception patterns and combined modal and pip patterns prior to stall in several high speed compressor configurations. The formation of these pip instabilities is attributable to both stage mismatch and inlet conditions. These pip disturbances may grow in amplitude or change speed prior to rotating stall. Often these disturbances are localized to a particular blade row, however, they may propagate around the annulus. In papers by Spakovszky (1998) and Bright (1998), it is suggested that pips propagate around the circumference and then instigate modal stall during circumferential inlet distortion conditions.

In the area of detection, the existing methods to identify stall precursive events are often categorized based on the length scale of the disturbance, either long (modal) or short (pip). In a paper by Tryfonidis (1995), the emphasis is to study long length scale phenomenon that leads to rotating stall. Other investigations by Day (1993) and

Paper presented at the RTO AVT Symposium on "Design Principles and Methods for Aircraft Gas Turbine Engines", held in Toulouse, France, 11-15 May 1998, and published in RTO MP-8.

Park (1994) observe pip activity in the compressor, however, they do not provide schemes for detection of this pip activity.

It is in the area of controlling rotating stall that many recent contributions have been reported, specifically by Paduano (1993), Feulner (1994), and Haynes (1993). In a report by Weigl (1997) on the active stabilization of stall in high speed compressors, modal activity was suppressed through controlled air injection. However, it is suggested that subsequent pip activity instigated the controller to go unstable. Freeman (1997) describes the use of both air injection and controlled bleed in concert to actively suppress rotating stall in a high speed multistage compressor rig. It is specifically from evidence in these active control cases that a pip detection method would prove advantageous. Certainly, with these control capabilities in mind, it would be beneficial to have a pip detector working in concert with a modal stall detector to help stabilize the compressor.

In the present paper, we discuss such a prediction technique called Structure Function. This statistical method is used on a variety of experimental results from several compressor configurations. We will identify in these compressors the short length scale phenomenon present prior to rotating stall through visual inspection of the pressure traces. With this data we will then use the Structure Function algorithm to clearly show from a single pressure trace the onset of instabilities leading to stall. We will also show the growth and rotation of pip instabilities in data acquired from 8 equidistant pressure sensors at a single axial location. The Structure Function algorithm consistently predicts the onset of pip instabilities in all the compressors without any false positive results. The experimental results will include examples from single stage transonic compressors with clean and distorted inlet flow, with steady and controlled air injection upstream of the compressor face, and in an axi-centrifugal multistage rig experiment.

3. STRUCTURE FUNCTION

The structure function has historically been associated with the study of random variables. In particular, Kolmogorov (1941) has shown the use of structure function in random processes with stationary increments. It is a simple statistic which has been extensively used in turbulence research to measure moments in the spatial direction (Panchev, 1971). In this paper we consider a temporal structure function for two distinct applications: first, to detect the local amplitude bursts found in rotating pip instabilities using eight sensors and, in another application, to detect incipient stall using a single sensor. The temporal structure function, **SF** is:

$$SF = \frac{1}{N-t}\sum_{i=1}^{N-t}[x(i+t)-x(i)]^2$$

It is closely related to the RSS (reconstruction signal strength) statistic from chaotic dynamics and is also related to the correlation function. The SF is often more convenient to use than a correlation function in cases when one is concerned not with the absolute values of the quantities, but only with their differences at distinct instances in time. For example, in detecting a pip we are not concerned with monitoring the magnitude of the pressure rise as much as noting when there exists a noticeable local disturbance.

The statistic is the average squared difference between temporally separated points over a window **N**, which is the stationary increment. One way to view the SF is an amplitude enhancer. When a relatively large spike is located in the pressure signal, this spike will contribute a significant value to the SF as long as N and t are correctly chosen. To detect a rotating pip, we choose N to be small since we expect the amplitude rise to be very short-lived. If instead we want to detect incipient stall, we choose a much larger value for N, so that the statistic is not overly sensitive to local amplitude excursions and can react to the repetitive increases in amplitude found just prior to stall. The time delay, **t**, is selected to be approximately half the period of the oscillation of interest, that is approximately 70%-90% rotor speed for pip frequency detection or 35%-50% rotor speed for modal frequency detection in order to maximize the amplitude enhancing effect of the SF. With careful selection of N and t the SF does have the desired attributes of either a pip detector as discussed above or a single sensor stall warning technique.

4. EXPERIMENTAL CONFIGURATION

Experimental data to validate the use of structure function was recorded from several compressors in a series of experiments that occurred between 1994 and 1997. The data sets were collected on the high speed single stage compressor rig at NASA Lewis, running either stage 35 or stage 37. Configurations of the NASA stage 35 and 37 compressor included clean inlet conditions, radial distortion, circumferential distortion, steady air injection and controlled injected air upstream of the first rotor. These cases are further described in Spakovszky (1998). An additional data set is shown from the Allied Signal T-55 experimental compressor rig (as described in Owen,

1995). All the examples shown were transitioned into stall using a slow throttling maneuver.

In all the single stage test cases, data was acquired using 5 psi range a/c coupled pressure transducers at eight equally resolved locations around the annulus. The data was recorded at 3 Kilohertz sampling rate. All of the single stage results were taken from the NASA Lewis Research Center Single-Stage Axial Compressor Test Facility which is fully described in Weigl (1997). The NASA Stage 35 test compressor was originally designed as an inlet stage of an eight-stage 20:1 pressure ratio core compressor (Reid 1978, Moore 1980). The stage has a total pressure ratio of 1.82, a mass flow of 20.2 kg/s, a rotor tip speed of 455 m/s, and a rotation frequency of 286 Hz at design speed.

5. DETECTION OF ROTATING PIPS

Figure 1 shows the unfiltered pressure traces for stage 37 with radial inlet distortion. No modes are noticeable in this case but a rotating pip instability can be found two rotor revolutions prior to stall. Pips are also seen from 35 to 38 revolutions before stall. In either case, the cause of the pips is not obvious from the pressure traces. The SF was computed for each pressure transducer using a delay of 2 and a window length, N, of 4. The window is shifted one point and the next SF computed. When the SF is higher than the previous 20 values, a marker is placed on that sensor. Figure 2 shows the markers computed for the pressure traces entering stall. When a succession of eight sensors are marked within 1.8 rotor revolutions, a rotating pip is said to have occurred as indicated by the asterisks on the bottom of the figure. Our SF algorithm correctly detects the rotating pip in the same position as observed by Spakovszky (1998).

Figure 3 shows the SF analysis from 42 through 28 rotor revolutions before stall where pips are noticeable in the pressure traces. In our analysis, we find that the pip instability does not complete a full rotation as indicated by the dashed lines in Figure 3. The start of a rotating pip is seen at sensor 1 but is stopped at sensor 7 because no relatively significant increase in amplitude is found at that sensor. At 36 rotor revolutions another rotating pip appears to start at sensor 1 but does not continue past sensor 4. In this case, the pips of sensor 4 and 5 occur at the same time as the pip in sensor 3 and therefore are more indicative of a wave rather than a traveling pip instability.

Another example of local, pip instabilities was found in stage 37 with circumferential inlet distortion present. Figure 4 shows the unfiltered pressures traces for 50 rotor revolutions prior to stall. A rotating pip which precedes the development of traveling modes can be seen at approximately 33 rotor revolutions. At 33 rotor revolutions it then appears that modal waves are instigated. Evidence that a local instability such as a pip can trigger modal behavior in the compressor was also found by Garnier (1990). The SF with $N = 4$ and $t = 2$ was computed for each sensor. Figure 5 shows a rotating pip starting at sensor 4 and completing more than one full revolution. The SF does not detect any rotating behavior during the modal transition into stall primarily because the SF window is very small and does not respond to the low frequency oscillations.

6. DETECTION OF INCIPIENT STALL

The SF can also be used as a single sensor incipient stall warning technique. Rather than monitoring rotating characteristics in the compressor dynamic, this stall detection technique relies on the gradual increase in the amplitude of the oscillations found just prior to stall. Band pass filtering the data enhances the amplitude rise and in turn the SF values. In this off-line study, we found that a band-pass filter which encompasses one half of a prominent frequency band - as seen from a power spectrum - yields good results. An explanation for this is not available but may be related to the fact that the temporal SF can be equated to other signal processing concepts (Vhora, 1998). In all the cases that follow, we select a data window of 200 and a delay of 5 for the SF calculation.

Figure 6 shows the results of the structure function analysis for a single sensor of data from the radial distortion case of Figure 1. At the top of Figure 6 is shown the unfiltered pressure data. In the middle of Figure 6 is the normalized, zero averaged, filtered data used as input to the structure function. Both the unfiltered and filtered data are shown although the SF is computed only on the filtered data. The bottom figure shows the computed structure function value for the normalized data. At approximately 50 rotor revolutions before stall, the filtered data exhibits a series of oscillations, each with a higher amplitude than the previous oscillations. Because the window length is relatively long, the SF steadily increases rather than travel in phase with the oscillation. When the SF has passed some arbitrary limit, as indicated by the short horizontal line, we assume stall is imminent. In this case a stall warning results at 40 rotor revolutions before stall compared to two revolutions with the pip detector.

A similar result is obtained in the radial distortion with constant air injection case. A distinct rise in amplitude of the oscillations begins at 60 revolutions before stall in the filtered, normalized data, along with a corresponding rise

in the SF. Again the SF delivers a stall warning at 40 revolutions prior to stall.

We have experimented with the structure function as a stall warning technique on a wide variety of compressor data. A few additional examples are presented below to show the utility of this method. The SF stall warning technique yields good results when applied to a clean inlet stage as referenced from Weigl (1997). The results in Figure 8 show a distinct rise in SF value at 250 revolutions before stall. An additional result is shown in Figure 9 for a case with controlled air injection, also referenced from Weigl (1997). In this case, controlled air upstream of the rotor was actively stabilizing the first two harmonic modes and the surge mode while the compressor was throttled into stall. In this case the SF shows a distinct rise well before stall that is not attributed to modal stall onset. For this case the SF indicates when the modal controller is destabilizing at 500 revolutions before stall. In all cases given we find ample warning time to take action upon impending stall.

The final case involves a multi-stage T55 rig with a single sensor placed at the front of the first stage. Modal behavior is found throughout the pressure signal as shown in the top of Figure 10. When the signal is low-passed filtered, an obvious growth in the oscillation amplitude is found in the pre-stall region. SF makes use of this effect and shows a marked increase starting at 20 revolutions before stall. This is the first example of a stall warning method applied to a multi-stage rig which uses information from a single sensor.

7. CONCLUSIONS

The structure function is an effective statistical measure to detect both rotating pips and incipient stall. Although this statistic has been used extensively by the turbulence community, this is the first application of it for pip detection and incipient stall warning. From this off-line study, the structure function successfully detected traveling pip instabilities prior to stall in both a radially distorted experimental stage and in a circumferentially distorted stage.

Structure function also was used as a single sensor incipient stall detector. In the radial distortion case, the circumferential distortion case, the clean inlet case, and the controlled injection case, this technique warned of the onset of rotating stall at least 40 rotor revolutions in advance. In the clean inlet case the warning was 500 revolutions before stall. In the multi-stage T55 rig data, the warning was 20 rotor revolutions.

In order to most effectively use this method in conjunction with active control, we need to further examine the effects of signal conditioning the data before structure function is applied. Additionally, we will study the appropriate on-line selection of window length and time delay for stall or pip detection. This will lead to an on-line implementation in conjunction with an active controller.

This method should prove very useful in experimental rig or engine environments where it is not practical to install multiple sensors. While the structure function appears at first glance to be overly simplistic, it seems to be well suited to the task of on-line pip and incipient stall detection.

ACKNOWLEDGEMENTS

This research was funded in part through an Ohio Aerospace Institute Phase I Research Grant and a NSF Career Development Award (CTS - 9502327). The authors thank Tony Strazisar (NASA Lewis) for critical analysis and support and Ivor Day (Cambridge) for fruitful discussions on rotating pips. Additional thanks go to Faramarz Mossayebi (University of Wisconsin) for important information on the relationship between SF and other statistical quantities.

REFERENCES

Camp, T. R. and Day, I. J., "A Study of Spike and Modal Stall Phenomena in a Low-Speed Axial Compressor", in ASME Gas Turbine Conference, Orlando, FL, June, 1997.

Day, I. J., "Stall Inception in Axial Flow Compressors," Journal of Turbomachinery, Vol. 115, No. 1, January 1993.

Hoying, D. A., "Stall Inception in a Multistage High Speed Axial Compressor," ASME Journal of Propulsion and Power, Vol. 11, No. 5., September 1995.

Kolmogorov, A. N., "Dissipation of Energy in Locally Isotropic Turbulence", Doklady Acad. Sci., USSR 32, 1941.

Longley, J. P., "Calculating the Flowfield Behaviour of High-Speed Multi-Stage Compressors", Presented at the ASME IGTI, Orlando, Florida, 1997.

Moore, D. and Reid, L., "Performance of Single-Stage Axial-Flow Transonic Compressor with Rotor and Stator Aspect Ratios of 1.19 and 1.26, Respectively, and with Design Pressure Ratio of 2.05", NASA Technical Paper 1659, April 1980.

Paduano, J. D., Epstein, A.H., Valavani, L., Longley, J. P., Greitzer, E. M., and Guenette, G. R., "Active Control of Rotating Stall in a Low Speed Axial Compressor", Journal of Turbomachinery, Vol. 115, January 1993.

Panchev, S., Random Functions and Turbulence, Pergamum Press, Oxford, 1971.

Reid, L. and Moore, D., "Design and Overall Performance of Four Highly Loaded, High-Speed Inlet Stages for an Advanced High-Pressure-Ratio Core Compressor", NASA Technical Paper 1337, 1978.

Rosenstein, M., J. Collins, and C. DeLuca, "Reconstruction Expansion as a Geometry-Based Framework For Chosing Proper Delay Times", Physica D, 73, 82-98, 1994.

Spakovzsky, Z., Weigl, H., Paduano, J., Suder, K., Bright, M., "Rotating Stall Control in a High-Speed Stage with Inlet Distortion, Part I", presented at the ASME IGTI, Stockholm, 1998a.

Spakovzsky, Z., VanSchalkwyk, C., Paduano, J., Suder, K., Bright, M., "Rotating Stall Control in a High-Speed Stage with Inlet Distortion, Part II", presented at the ASME IGTI, Stockholm, 1998b.

Tryfonidis, M., Etchevers, O., Paduano, J. D., Epstein, A. H., and Hendricks, G. J., "Pre-Stall Behavior of Several High-Speed Compressors," Journal of Turbomachinery, Vol. 117, January 1995, p. 62.

Vhora, H., Master's Thesis, Department of Electrical Engineering, University of Akron, May 1998.

Weigl, H.J., Paduano, J. D., Frechette, L.G., Epstein, A.H., Greitzer, E. M., Bright, M. M., Strazisar, A.J., "Active Stabilization of Rotating Stall and Surge in a Transonic Single Stage Axial Compressor", accepted for publication in Journal of Turbomachinery, ASME Gas Turbine Conference, 1997.

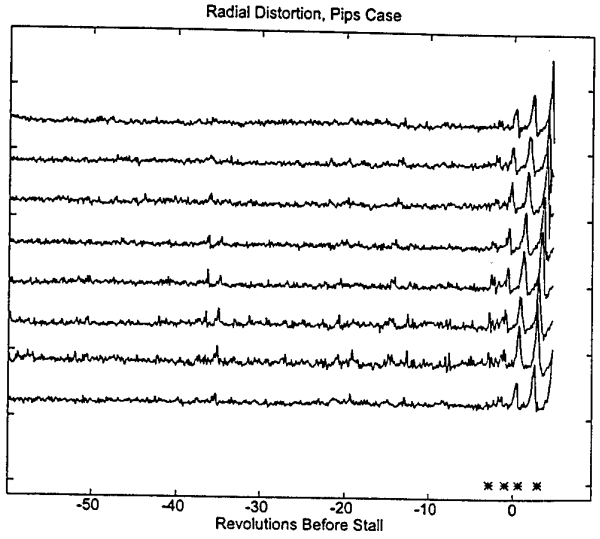

Figure 1. Pressure Traces for Radial Distortion

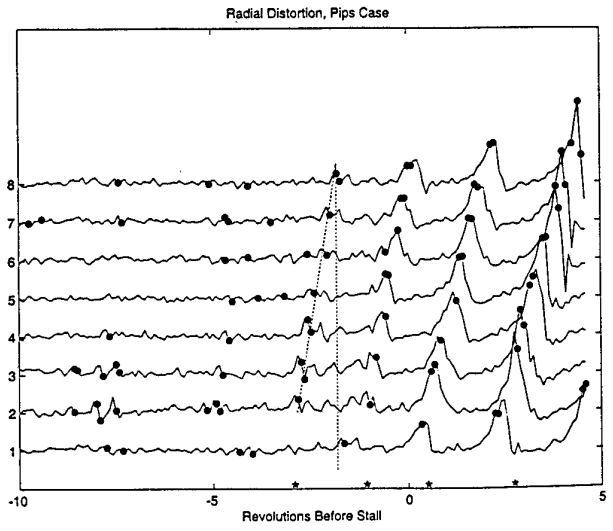

Figure 2. Pressure Traces 10 Revolutions Before Stall

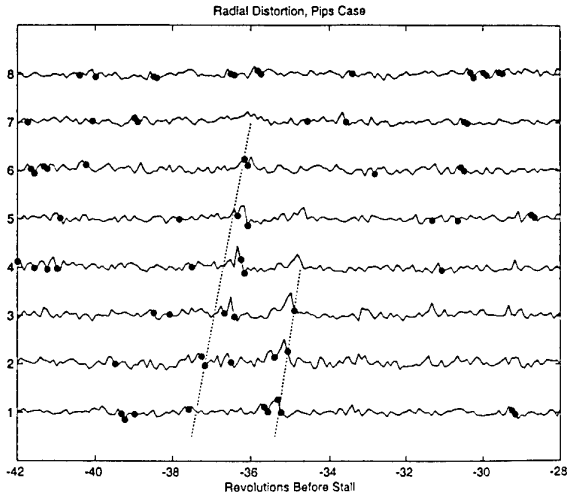

Figure 3. Pressure Traces 42 to 28 Revolutions

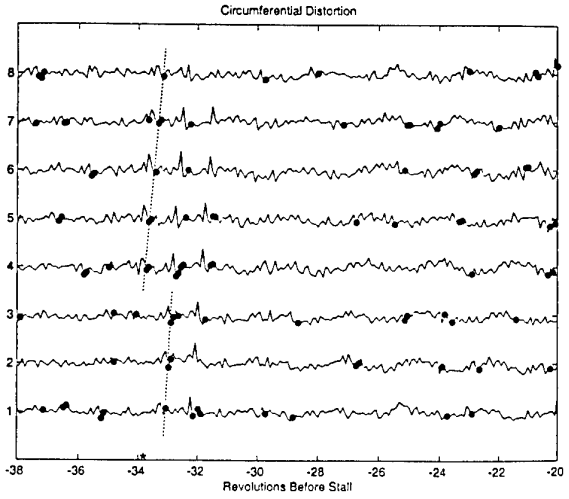

Figure 5. Pressure Traces for Circumferential Distortion 38 to 20 Revolutions before Stall

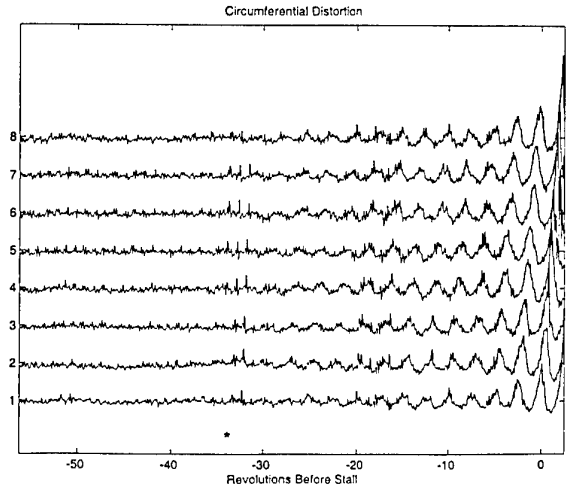

Figure 4. Pressure Traces for Circumferential Distortion

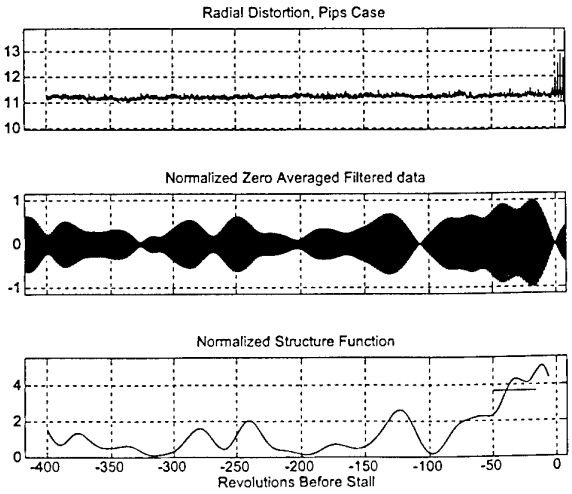

Figure 6. Structure Function Results Radial Distortion

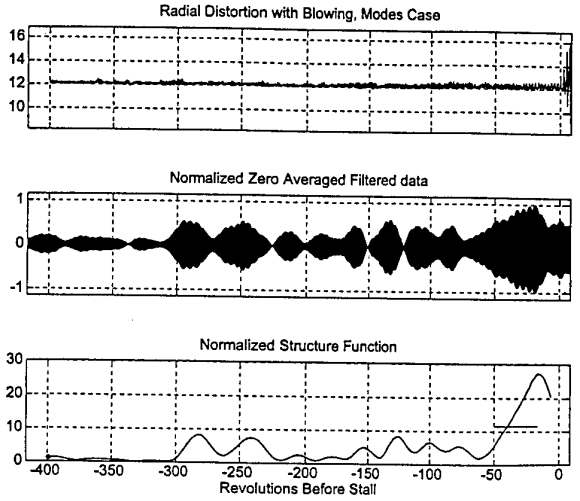

Figure 7. Structure Function Results Radial Distortion With Injection

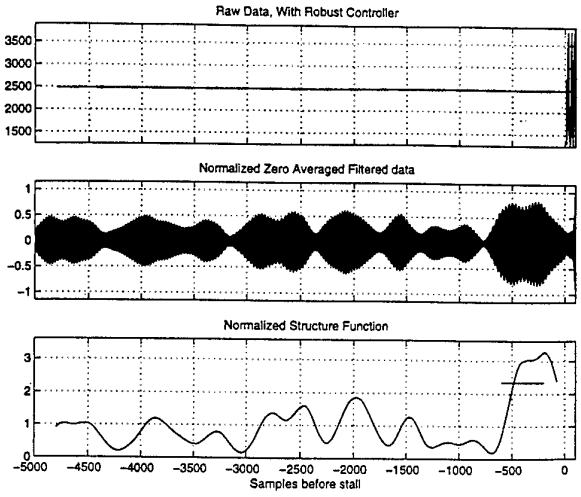

Figure 9. Structure Function Results Controlled Injection

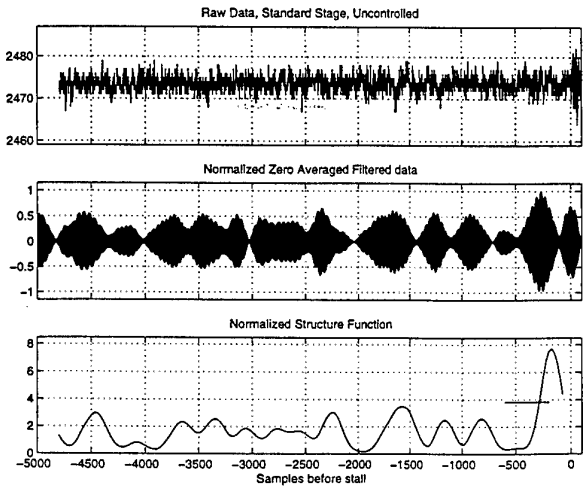

Figure 8. Structure Function Results Clean Inlet

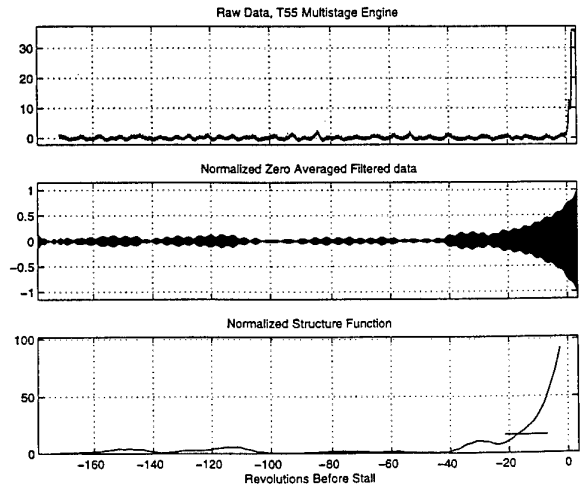

Figure 10. Structure Function Results T55 Rig

Turbomachinery Blade Design Using a Navier-Stokes Solver and Artificial Neural Network

S. Pierret and R.A. Van den Braembussche
von Karman Institute for Fluid Dynamics,
Turbomachinery department,
Chaussée de Waterloo, 72, B-1640 Rhode-Saint-Genese, Belgium

Abstract

This paper describes a knowledge-based method for the automated design of more efficient turbine blades.
Two-dimensional blade sections, defined by Bézier curves as a function of 15 parameters, are first optimized by means of Simulated Annealing (SA) and an Artificial Neural Network (ANN). The later one is an approximate model (response surface) of the 2D Navier-Stokes solutions of previous designs stored in a database. Depending on the performance predicted by a Navier Stokes analysis the procedure will be stopped or the design cycle will be repeated after the newly designed blade has been added to the database. This extended database allows a more reliable optimization of the blade at next iteration.
This procedure results in a considerable speed-up of the design process by reducing both the interventions of the operator and the computational effort. It is also shown how such a method allows the design of more efficient blades while satisfying both the aerodynamic and mechanical constraints.
In this paper, emphasis is put on the formulation of a new objective function and its validation by means of three different blade designs.

Keywords: blade design, optimization, turbine, objective function, Navier-Stokes, artificial neural network, response surface

1 INTRODUCTION

The main goal when designing turbines or compressors is to achieve light, compact and highly efficient systems while reducing the cost and the duration of the design cycle, to allow an easier adaptation of the machines to the high and rapidly changing demands of the market.

Further improvement of the machine performance requires a detailed knowledge of the flow which can only be provided by Navier-Stokes solvers. These solvers, which are now widely used in industry for the aerodynamic analysis of existing geometries, are time consuming and do not indicate what geometry modifications are required to improve the performance. The search for optimized blades must therefore be guided either by an experienced designer or by a numerical method [1]. This often requires a large number of Navier-Stokes computations, to evaluate many different blade geometries, before reaching a good solution satisfying both the aerodynamic and the mechanical requirements. Although this procedure allows the design of very efficient blades it is expensive in terms of computer- and/or designer time. In order to keep the cost and the duration of the design process within reasonable limits, the design is often stopped as soon as an acceptable solution has been found without guarantee that it is also the optimum.

The method described here intends to minimize the number of interventions of the designer and to minimize the design time, while guaranteeing optimum performance. This is achieved by using the knowledge (Navier-Stokes solutions) acquired during previous designs (evolutionary method).

After a short description of the method, of which more details can be found in [2], one will emphasize on a new objective function which is used to evaluate the different designs

2 DESIGN PROCEDURE

The basic idea of the present method, of which a flow chart is shown in Figure 1, is to accelerate the design of new blades using the knowledge acquired during previous designs of similar blades. The core of this knowledge-based design system is therefore a DATABASE containing the input and output of previous Navier-Stokes solutions i.e. the blade geometry ($\vec{G}$), the flow field boundary conditions ($\vec{BC}$) and the blade performance ($\vec{P}$) characterized by the efficiency, the turning and the Mach number distribution on the suction and pressure side of the blade.

The design of a new blade starts from the REQUIRED PERFORMANCES (aerodynamic and mechanical), as there are: inlet and outlet flow angles (β_1, β_2), the pressure ratio (P_2/P_{01}), the Reynolds number over axial chord ratio (Re/Cax), the blade cross-section area (Area), the trailing edge radius (R_{te}), the minimum and maximum moment of inertia (I_{min} and I_{max}) and the angle (alpha) between I_{max} and the axial direction (X), etc.

The first step of the design consists of defining a new optimized GEOMETRY that will have to be analyzed by the NAVIER-STOKES SOLVER. One starts by scanning the DATABASE to SELECT the sample that has a performance closest to the required one. This geometry is then adapted to the required performance, by means of an OPTIMIZATION procedure. The last one uses an heuristic search procedure, called "simulated annealing", and an approximate model for the performance evaluation of the modified blade geometries. The approximate model is derived from the information contained in the DATABASE by means of an Artificial Neural Network (ANN). The latter is an interpolator which builds the response surface by LEARNING the relation between per-

Paper presented at the RTO AVT Symposium on "Design Principles and Methods for Aircraft Gas Turbine Engines", held in Toulouse, France, 11-15 May 1998, and published in RTO MP-8.

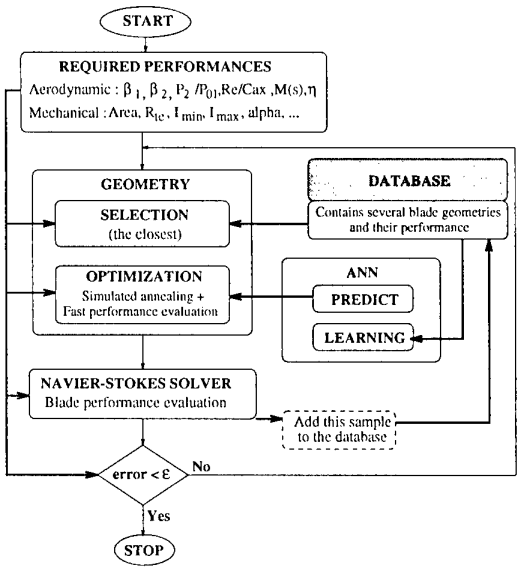

Fig. 1 : **General Algorithm of the Method**

formance $\vec{P}$, boundary conditions $\vec{BC}$ and geometry $\vec{G}$:

$$\vec{P} = \mathcal{N}(\vec{BC}, \vec{G}) \qquad (1)$$

After mapping the database samples, the ANN is able to generalize, meaning that it can PREDICT the performance of a new geometry, not present in the database.

During the second step, the new geometry, resulting from the OPTIMIZATION, is evaluated by means of a NAVIER-STOKES SOLVER. The geometrical parameters, the performance and the boundary conditions of this new sample are added to the DATABASE.

Finally, if the target performance has not been reached, a new iteration is started. Each new blade definition however has to be preceded by the LEARNING of the ANN using the new DATABASE. This one now contains a new geometry, closer to the requirements which allows an improvement of the relationship $\mathcal{N}$.

As the time for an ANN LEARNING is proportional to the number of training samples, it is of interest to build a sub-database (training database) containing only blade samples which are similar to the blade being designed. This "training database" is then used for the LEARNING of the ANN.

Next sections describe in more detail the main components of this procedure.

3 THE 2D NAVIER-STOKES SOLVER (TRAF2D)

The Navier-Stokes solver, used to predict the performance, is the TRAF2D/3D code developed by A. Arnone [3]. The Reynolds-averaged Navier-Stokes equations are solved using finite volumes and a Runge-Kutta time integration scheme in conjunction with accelerating techniques such as local time stepping, residual smoothing and Full-Approximation-Storage (FAS) multigrid. Two-dimensional computations are usually performed with 12,000 grid points requiring a memory of 3 MB and 6 minutes of computational time on an Alpha workstation (type 500/333).

4 GEOMETRY MODEL

A parametric definition of the blade geometry is needed to limit the number of unknown, characterizing the geometry $\vec{G}$ in the relation 1. Bézier curves are well suited for this purpose as they result in smooth curves and facilitate the control of the blade shape by restricting the design space.

Several models have been evaluated. The one presented hereafter turns out to be the one whose parameters have the best geometrical interpretation, avoiding the generation of unrealistic blades while having enough geometrical flexibility to represent all types of turbine blades. Moreover the velocity distributions obtained with this model are also very smooth.

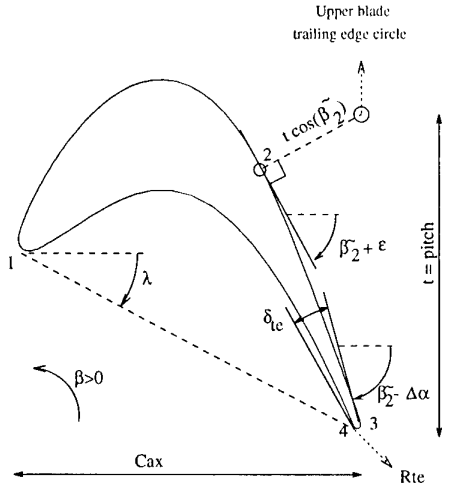

Fig. 2 : **Geometry model : basic parameters**

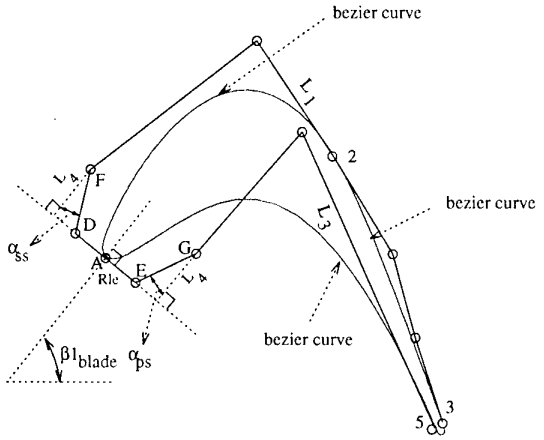

Fig. 3 : **Geometry model : Bézier curves**

The blade geometry is specified by four key points linked by four curves. These key points are fully defined by the following parameters : R_{te}, $\tilde{\beta}_2$, $\Delta\alpha$, δ_{te}, t, ϵ, Cax, λ as shown on figure 2. The key points 1 and 2 are linked by a Bézier curve defined by 3 additional polygon points whose location is a function of : β_{1blade}, R_{te}, L_4, α_{ss}, L_1 and the tangent at point 2 (see Figure 3). The key points 2 and 3 are linked by a Bézier curve defined by 2 additional polygon points. The last ones are located in such a way to ensure the continuity up to the third derivative at point 2 and continuity up to the first derivative at point 3. A Bézier curve with 3 additional polygon points defines the pressure side in the same way as the first part of the suction side. This curve is fully defined by the

parameters : β_{1blade}, R_{le}, L_4, α_{ps}, L_3 and the tangent at point 2. Using the same R_{le} and L_4 for both the suction and the pressure side guarantees the continuity of the curvature radius at the leading edge. The trailing edge is defined by part of a circle whose radius R_{te} is specified. The 2D blade geometry is thus fully defined by means of 15 parameters represented by $\vec{G}$(n) : n=1,15. It has been shown [2] that this geometry model is able to represent the various types of turbine blades encountered in industrial designs.

5 ARTIFICIAL NEURAL NETWORK

ANN are non-linear models that can be trained to map functions with multiple inputs/outputs [4], [5], [6]. Although the initial goal of artificial neural network is to imitate some brain functions, they can also be thought of as a very powerful interpolator.

An ANN (Fig. 4) is used here to PREDICT the performance (η, β_2 and the Mach number distribution in 20 points on both blade sides ($\vec{M}$(m) : m=1,40)) as a function of the geometrical parameters and the aerodynamic boundary conditions. An ANN is composed of several elementary processing units called neurons or nodes. These nodes are organized in layers and joined with connections (synapses) of different intensity, called the connection weight (W) to form a parallel architecture. Each node performs two operations : the first one is the summation of all the incoming signals and the second one is the transformation of the signal by using a transfer function, very often defined by a sigmoidal function : $F(x) = \frac{1}{1+e^{(-x)}}$. This function introduces power series (given implicitly in the form of an exponential term) which avoids to make any hypotheses concerning the type of relationship between the input and the output variables. A network is generally composed of several layers; an input layer, zero, one or several hidden layers and one output layer.

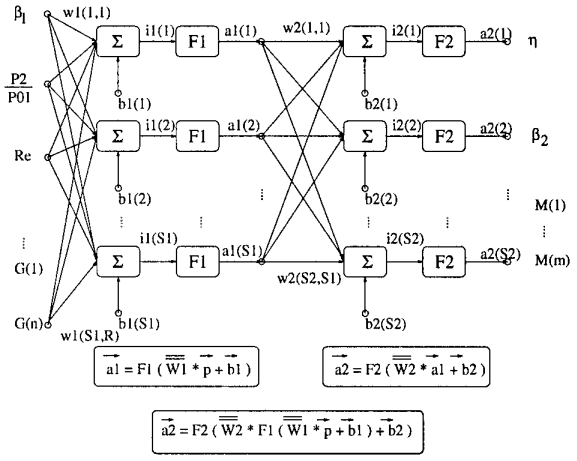

Fig. 4 : **A 2-layer artificial neural network**

Trained ANN are able to generalize which means that they give reasonable answers for input vectors that they have never seen. It is therefore possible to train an ANN on a representative set of input/output vectors without training the system on all possible cases.

The LEARNING process consists of adjusting the connection weights and the bias in order to make the calculated output vector ($\vec{a}$) coincide with the imposed output vector ($\vec{d}$), using the information contained in the DATABASE.

6 OBJECTIVE FUNCTION

A measure of the global performance of a blade geometry is needed at several steps in the design procedure, i.e.: for the blade selection from the database, during the optimization process and for the convergence check after the Navier-Stokes calculation.

Maximum efficiency is only one of the many design objectives. A good design must also respect the mechanical and manufacturing constraints and achieve the required performance (turning). The general approach to this problem is to build a single objective function (OF) by summing up penalty terms which are increasing when violating the constraints [1].

Following global objective function is defined:

$$OF_{2D} = P_{Meca} + P_{Perf} + P_{\xi} + P_{Mach} + P_{Geom}$$
$$= OF(\vec{P}, \vec{G}, \vec{BC}) \quad (2)$$

where P_{Meca} is the penalty for violation of the mechanical constraints, P_{Perf} stands for the penalty on the required performance, P_{ξ} is a penalty proportional to the loss coefficient, P_{Mach} stands for the penalty for non-optimum Mach number distribution and P_{Geom} is the penalty for violating geometrical constraints.

The penalty for a non optimum Mach number distribution is the most difficult to specify but is justified by the following arguments:

- Due to uncertainties in turbulence and transition modeling, the loss coefficient predicted by Navier-Stokes solvers is not accurate enough to be used blindly as the only measure of the quality of the flow. It is very important to verify also the Mach number distribution on the blade surface.
- The losses may have multiple local minima (several blades may have nearly the same losses) as well as discontinuous changes (when the boundary layer transition suddenly jumps from near leading edge to near trailing edge). However, blades having similar loss coefficient might have quite different Mach number distributions which can be used to decide which blade is the best.
- Blades need to perform also well at off-design conditions. One must therefore avoid to design blade geometries which have very good performance but are operating very close to separation and are likely to separate at slightly off-design conditions. It is therefore important to introduce in the design some constraints which account for changes on the Mach number distribution at off-design in order to ensure good performance of the blade over a wide range of operating conditions without the cost of several Navier-Stokes computations at off-design conditions.

Those three reasons explain why designers also use alternative objective function which very often measure the root-mean-square of the difference between a target pressure distribution specified by a knowledgeable designer and the one predicted by a CFD method. However a method in which an optimum pressure distribution must be defined doesn't fulfill one of our main objectives which is a method that can also be used by a non experienced designer. In order to reach that goal the Mach number distribution must be free to vary but a quality measure is needed. The purpose is to give high penalty to velocity distributions which are known of not being optimal such as distributions having a high probability of early transition, laminar or turbulent separation.

The penalty on the Mach number distribution is derived from the Mach number, predicted by the ANN or

the Navier-Stokes solver, in a limited number of points on the blade surface ($\vec{M}$(m), m=1,40). A continuous Mach number distribution is reconstructed using a cubic spline interpolation through these points. The evaluation of the penalty function is based on an estimation of the B.L. momentum thickness at the trailing edge on the pressure and suction side which is known to be proportional to the losses [7].

The momentum thickness of the **laminar boundary layer** is computed by the method of Thwaites [8] :

$$(\frac{\theta^2 U_e^6}{\nu})_s = 0.45 \int_{s_i}^{s} U_e^5 ds + (\theta^2 \frac{U_e^6}{\nu})_{s_i} \qquad (3)$$

θ can thus be computed at any curvilinear position along the blade surface (s) by a simple integration of the velocity at the edge of the boundary layer (U^5) along the curvilinear length starting at a point s_i being a stagnation or relaminarization point. This relation gives quite good results for favorable pressure gradients but less good results for adverse pressure gradients reflecting the breakdown of the assumption that the velocity profiles are uniparametric.

The momentum thickness of the **turbulent boundary layer** is computed by the method of Curle and Davies [9] :

$$(\theta(R_e)^{0.2})_s = \frac{0.0106}{U_e^4} \int_{s_i}^{s} U_e^4 ds + (\theta R_e^{0.2})_{s_i} \qquad (4)$$

at any curvilinear position along the blade surface.

Transition is assumed to be instantaneous when the Reynolds number, based on the local momentum thickness, Re_θ, exceeds a critical value, Re_{tr}, which is defined as [9] :

$$Re_{tr}(Tu, \lambda) = 163 + exp[F(\lambda) - \frac{F(\lambda)Tu}{6.91}] \qquad (5)$$

Where Tu is the free stream turbulence level, and :

$$F(\lambda) = 6.91 + 12.75\lambda + 63.64\lambda^2 \quad if \quad \lambda \leq 0 \qquad (6)$$

$$6.91 + \ 2.48\lambda - 12.27\lambda^2 \quad if \quad \lambda > 0$$

λ is the pressure gradient parameter (or Pohlhausen parameter) defined as :

$$\lambda = \frac{\theta^2 \frac{dU}{ds}}{\nu} \qquad (7)$$

Thwaites [8] assesses a quite reliable empirical value of $\lambda = -0.082$ below which a laminar boundary layer will separate. No modeling of the separated-flow transition is performed and therefore a laminar separation is supposed to induce immediately transition.

A similar approach for the turbulent boundary layer separation is proposed by Buri who defined the parameter:

$$Bu = R_e^{\frac{5}{4}} K \qquad (8)$$

where $K = \frac{\nu}{U_e^2} \frac{dU_e}{ds}$ is the acceleration parameter. The limit for separation can be approximated by $Bu = -0.05$.

Relaminarization (or reverse transition) is expected to take place if the acceleration parameter, K, is greater than 3.10^{-6} [10].

Due to the uncertainty in both the momentum thickness computation and transition onset prediction and because of the need for good off-design performance, it is preferable to define a set of points where the transition could take place and to start at each point a turbulent boundary layer computation.

The probability of transition is first defined as :

$$Pr_{transition}(s) = F(\frac{\Delta Re(s)}{Re_{ref}}) \qquad (9)$$

with $\Delta Re(s) = Re_\theta(s) - Re_{tr}(s)$, F is the sigmoidal function and Re_{ref} is a reference Reynolds number which ensures a correct scaling. It is defined as : 0.2 * the critical Reynolds number defined by (5) and $\lambda = 0$. Figure 5 gives the shape of this probability function and shows that if Re_θ is less than $Re_{tr} - 3 * Re_{ref}$ the probability of transition is very low. On the contrary for values of $Re_\theta > Re_{tr} + 3 * Re_{ref}$ this probability is almost 1.0.

Then the probability of transition, which ranges from 0 to 1, is divided into 10 intervals. If in 2 consecutive points along the blade surface, the probability of transition jumps from one interval to an interval of higher probability, this point is added to the set of points where a turbulent boundary layer computation is started.

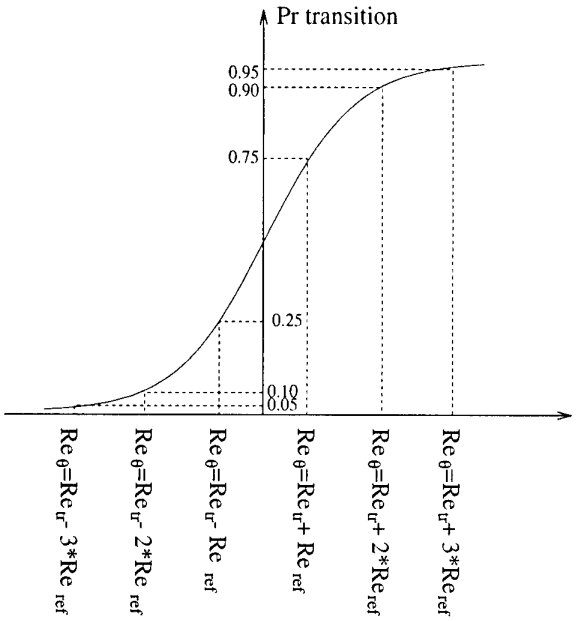

Fig. 5 : **Probability of having transition**

A probability is associated with each boundary layer computation. The laminar boundary layer starts with Pr(lam) = 1 at the stagnation point and its value decreases by Pr(turb) each time a turbulent boundary layer is started. The probability Pr(turb) associated to each turbulent boundary layer calculation equals Pr(lam) * Pr(tr) (the probability of having a laminar boundary layer upstream of this onset point multiplied by the probability of having transition at this location). This is illustrated on figure 6 where the upstream laminar boundary layer has a probability of 1 (as it is close to the stagnation point). If Pr(tr) =.2 at the first flagged point, the probability of the turbulent boundary layer starting at this point is .2. The probability of having a laminar boundary layer downstream of this point reduces by the value of Pr(turb) to .8. The probability of having turbulent boundary layer starting at the next flagged point, where $Pr(tr) = .3$, equals $.8 * .3 = .24$ and the probability

of having a laminar boundary layer downstream of that point reduces to $.8 - .24 = .56$.

In this way, the sum of the probabilities of all the boundary layer calculations is always 1 at each curvilinear position along the blade. A branch having a probability lower than 1% cannot be divided downstream.

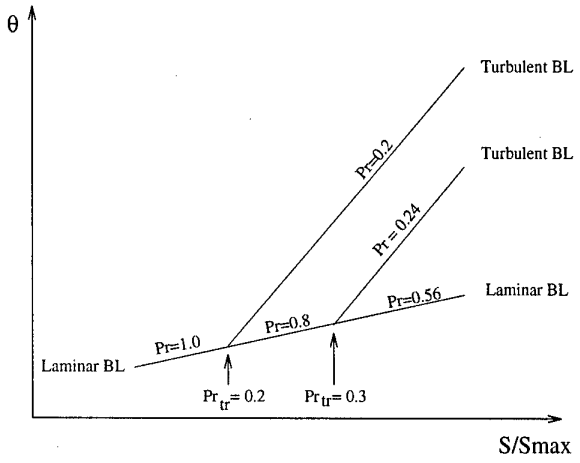

Fig. 6 : **Probability associated with each boundary computation**

Finally, the penalty of a velocity profile is defined as the the average of the momentum thicknesses at the trailing edge weighted by the probability of each boundary computation. An additional penalty is defined which account for the risk of turbulent separation using the Buri parameter.

A similar approach is used for relaminarization :

$$Pr_{relaminarization}(s) = F(\frac{\Delta K(s)}{K_{ref}}) \qquad (10)$$

where $\Delta K(s) = K(s) - K_{cr}(s)$, F is the sigmoidal function, K_{cr} is the critical acceleration parameter (3.10^{-6}) and K_{ref} is a reference acceleration parameter which ensure a correct scaling and is defined as : $K_{cr}/5$.

7 OPTIMIZATION

The goal of the optimization is to find the geometry which minimizes the objective function when the blade performance is evaluated with the simplified model $\vec{P} = \mathcal{N}(\vec{BC}, \vec{G})$ obtained from ANN.

The choice of the optimization algorithm is based on two considerations :
- the existence of many local optima in the design space poses problems for gradient type optimization methods.
- the number of function evaluations is of far less importance when using a simple and quick prediction model instead of a detailed but costly Navier-Stokes computation at each step of the optimization process.

Stochastic techniques are well suited for this type of optimization problems and a Simulated Annealing (SA) algorithm is used in present method.

It is based on the analogy with the annealing of solids (van Laarhoven and Aarts, 1987) but there is no clear definition. The only requirements are :
- sufficient randomness must be inherent in the point selection process so that a wide range of possible geometries can be covered
- more optimal points must be favored over less optimal points
- the degree of randomness must slowly decrease.

8 RESULTS

This design procedure has been successfully tested on a large number of designs and will be illustrated here by 3 examples for which the axial chord, the pitch and the trailing edge radius are imposed. In the second example, more emphasis is put on the results obtained by the penalty on the Mach number distribution.

8.1 Design of a reaction-type blade

The mechanical and aerodynamic requirements are summarized in Table 1 and compared to those obtained after 20 design cycles.

	Imposed	After 20 modif.
Inlet flow angle (β_1)	47.9^0	-
P_2/P_{01}	0.9415	-
Re/Cax (1/m)	$1.7\ 10^8$	-
$k = Cp/Cv$	1.2795	-
Cax (m)	0.029885	-
NB (number of blades)	170	-
Blade radial location (m)	0.7088	-
Trailing edge radius (m)	$3.0\ 10^{-4}$	-
Area (m^2)	$2.38\ 10^{-4}$	$2.40\ 10^{-4}$
I_{min} (m^4)	$3.31\ 10^{-9}$	$3.29\ 10^{-9}$
I_{max} (m^4)	$1.72\ 10^{-8}$	$1.71\ 10^{-8}$
alpha	-32.1^0	-32.4^0
Outlet flow angle (β_2)	-70.5^0	-70.5^0
Loss coefficient (ξ)	0.0 %	2.75 %

Table 1 : Mechanical and Aerodynamic requirements

This design started with a database containing 25 samples. The computational time needed to train the ANN and to run the optimization algorithm are respectively of 10% and 25% of the time needed by the Navier-Stokes solver. A full design cycle including blade design, optimization and verification by means of a Navier Stokes solver is only 35.% longer than one analysis.

The initial blade selected in the database (Fig. 7) is very different from the final one because the initial database does not contain any blade close to the required one. The initial blade was designed for a higher inlet flow angle and the pitch was much smaller than the one imposed.

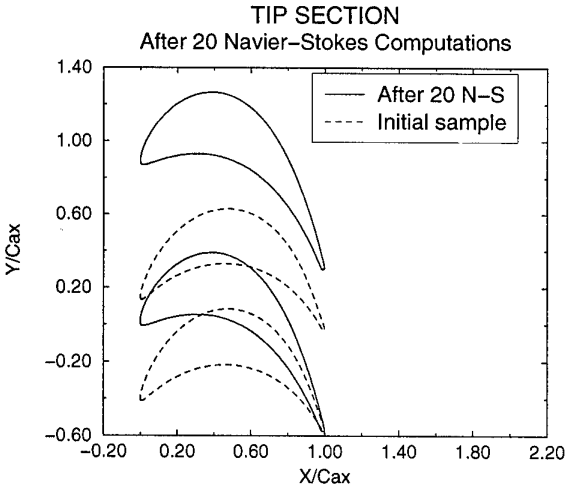

Fig. 7 : **Blade geometries : tip section**

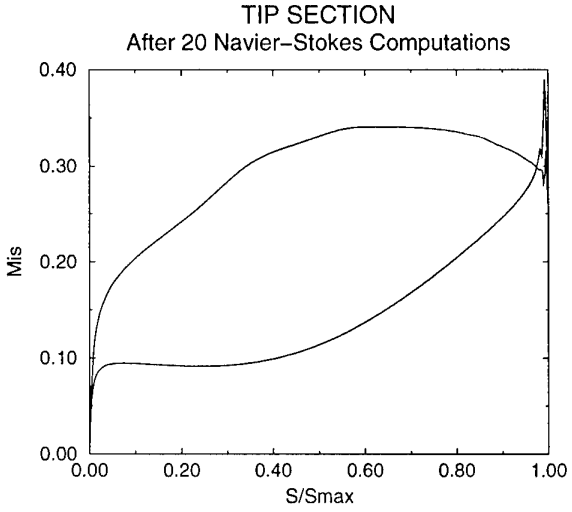

Fig. 8 : **Mach number distributions on the blade surface**

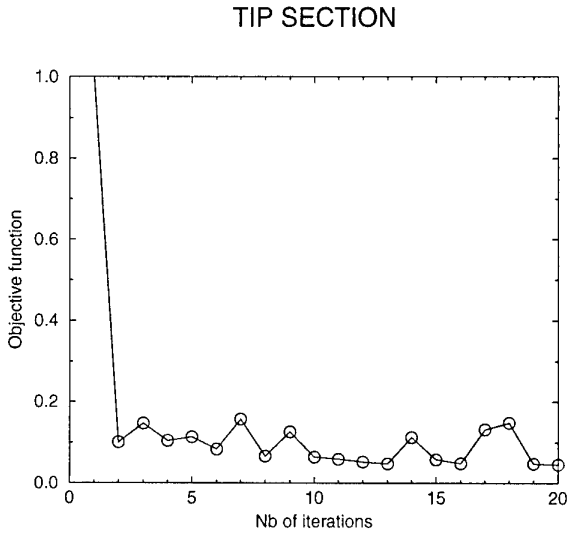

Fig. 9 : **Design convergence history**

This initial blade is then optimized by means of ANN and SA, taking into account the required performance specified in table 1. The geometry resulting from this optimization process is then analyzed by the Navier-Stokes solver. After each Navier-Stokes solution, the geometry, boundary conditions and performances are added to the database and used in a new learning of the ANN in order to recalibrate the approximate model before a new optimization loop is started. The convergence history of the process is show on figure 9. A low value of the objective function is already reached after 3 iterations however the solution is still slightly improving over 20 design cycles. The objective function doesn't continuously decrease because the blade shape analysed by the Navier-Stokes solver has been obtained by the approximate model. The isentropic Mach number distribution and the final blade are presented in figures 7 and 8. The Mach number distribution is smooth, the maximum Mach number is low resulting in a small diffusion near the trailing edge without risk of turbulent separation. The outlet flow angle (-70.52 deg.) is very close to the imposed value (-70.50 deg.) and the loss coefficient is low for this type of turbine blade (5.85 %). The error between the imposed and final mechanical constraints is lower than 1 %.

8.2 Design of an impulse-type blade

The design of impulse blades is usually very difficult because of the small pitch to axial chord ratio, resulting in a strong interaction between the velocity distributions on the pressure and suction side and because of the small acceleration of the fluid from the leading edge to the trailing edge.

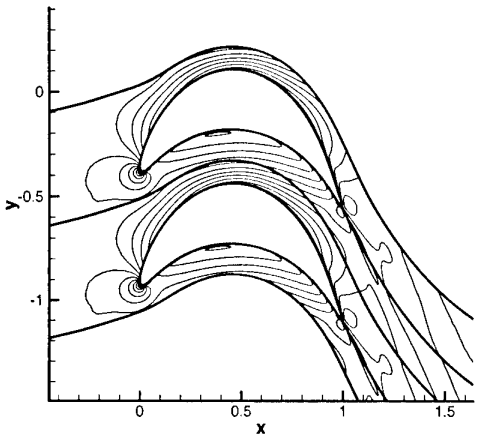

Fig. 10 : **Blade geometry : hub section**

The geometry obtained after 20 design cycles is presented on figure 10. The outlet flow angle (-66.60 deg.) is close to the imposed one (-66.3 deg.). The loss coefficient is only 4.18% and the mechanical constraints are satisfied within 1%. The Mach number distribution, represented on figure 11 is very smooth without unecessary accelerations and decelerations.

On figure 12 is represented the momentum thickness on the suction side for several boundary layer computations starting the turbulent computation at 12 different locations between $\frac{S}{S_{max}} = 0.175$ and 0.475. The turbulent boundary layer starts before the decelerating part and therefore limit the risk of laminar separation. On the pressure side (figures 13 a laminar separation occurs at $S/S_{max} = 0.1$ which has the consequence of triggering transition to the turbulent boundary layer at this points. Relaminarization takes place in between $S/S_{max} = 0.475$ and 0.55.

On figure 14 Re_θ is plotted for both the suction and pressure side when the boundary layer is laminar. From that figure $Re_{tr} = Re_\theta$ at $\frac{S}{S_{max}} = 0.375$.

On figure 15 is plotted, for the suction and pressure side, the Pohlhausen parameter when the boundary layer is laminar and the Buri parameter when the boundary layer is turbulent. This figure shows that the Buri parameter always remains far from the limit for turbulent separation (-0.02 instead of -0.05) on the rear part of the suction side.

On the pressure side 15) a laminar separation occurs at $S/S_{max} = 0.1$ (the Pohlhausen number is less than -0.08, which has the consequence of starting the turbulent

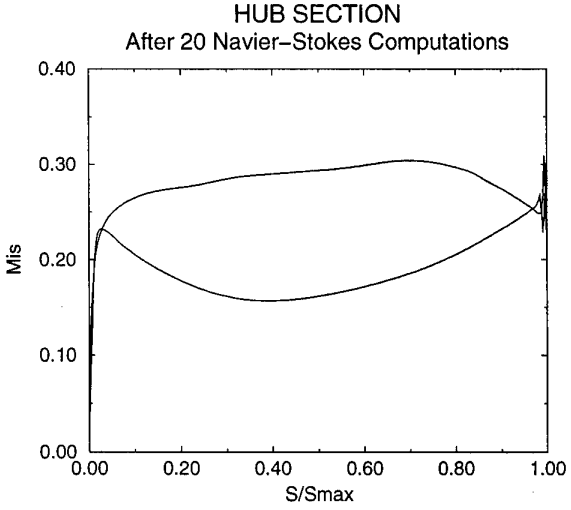

Fig. 11 : **Mach number distributions on the blade surface**

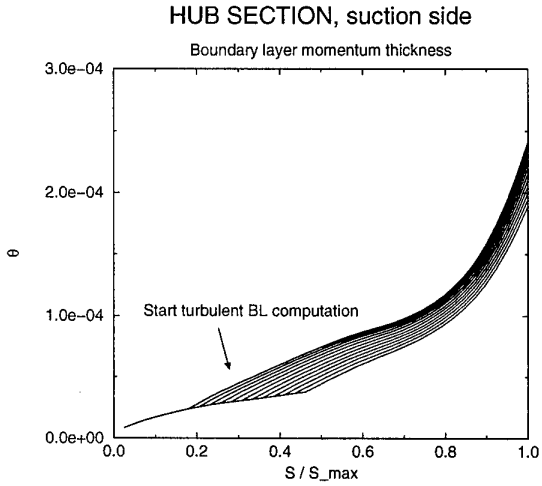

Fig. 12 : **Boundary layer momentum thickness (suction side)**

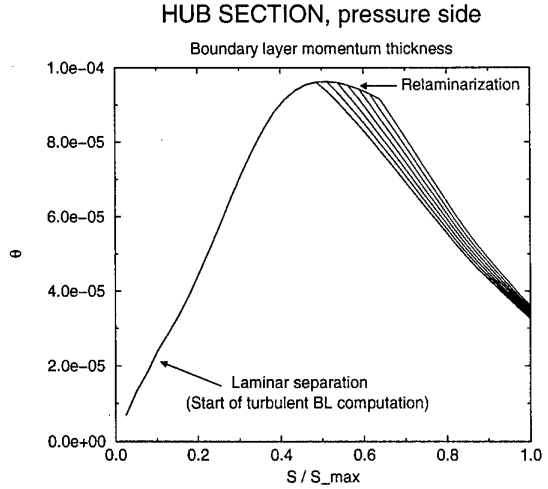

Fig. 13 : **Boundary layer momentum thickness (pressure side)**

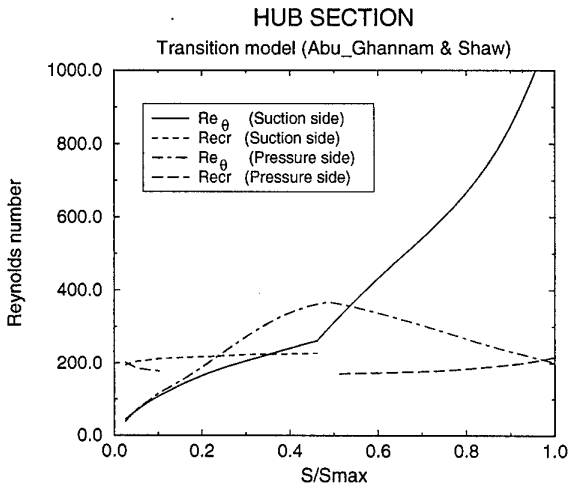

Fig. 14 : **Reynolds numbers**

boundary layer at this points. The Buri parameter is then computed and remains far from -0.05. When the relaminarization takes place the computed Pohlhausen is quite large (> 0.2).

8.3 Design of a high pressure nozzle blade

The third example illustrates the design of a high pressure nozzle blade. The major design problem are the large surface and moment of inertia required for such a blade.

The geometry obtained after 20 Navier-Stokes modifications is presented on figure 16. The real outlet flow angle is exactly the imposed one (-76.47 deg.). The loss coefficient equals 1.97% and the mechanical constraints are satisfied.

The corresponding isentropic Mach number distribution is shown on figure 17.

9 CONCLUSIONS

One has shown that the method presented in this paper requires only a few Navier-Stokes computations to define an optimized blade satisfying both the aerodynamic and the mechanical requirements.

This design method allows the exploration of more design options in a given period of time than with traditional methods and is applicable to any Navier-Stokes solver.

The effectiveness of the method results from :

- the use of a robust geometry model which avoids the generation of unrealistic blades but nevertheless has enough flexibility to generate a large number of different types of blade.
- the use of an artificial neural network and a database, able to gather experience from previous designs and efficiently use it for subsequent designs.
- A fully automated design procedure without operator intervention thanks to a reliable objective function capable of judging the quality of a solution in terms of per-

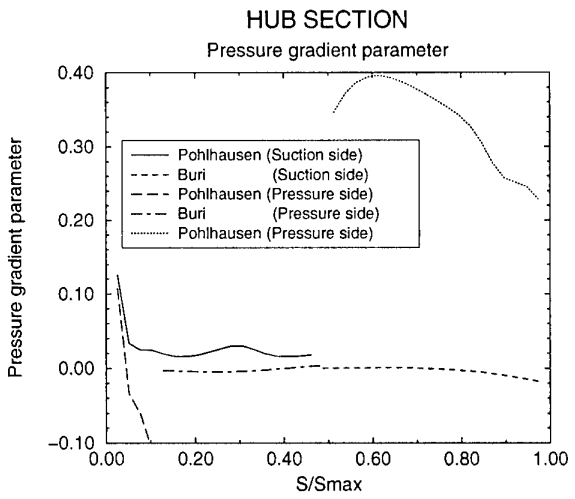

Fig. 15 : **Pressure gradient parameter**

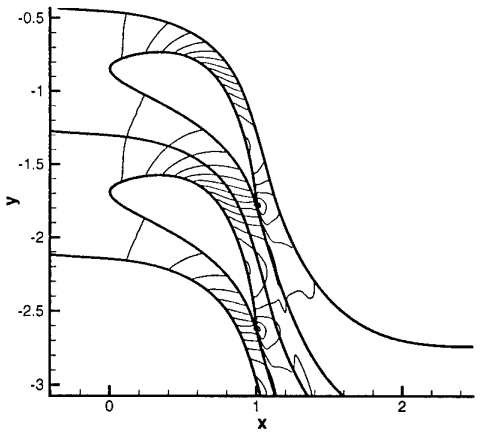

Fig. 16 : **Blade geometry : nozzle blade**

formance and mechanical constraints.
- The development of a penalty on the Mach number distribution allows taking advantage of some recent work on transition and greatly improves the confidence on the blade shape designed by means of Navier-Stokes solver.
- The optimization algorithm, based on simulated annealing, guarantees that the optimization system will not be trapped in a local minimum. From time to time new innovative designs are found and stored in the database.

Although this work has so far focused on two-dimensional turbine blades, the method can also be applied to the design of compressor blades.

ACKNOWLEDGMENTS

The first author gratefully acknowledge the financially support by the Belgian "Fonds pour la formation à la Recherche dans l'Industrie et l'Agriculture" (FRIA). The von Karman Institute acknowledges the computer support provided by Ansaldo Energia s.p.a. Special thanks also to Dr. A. Arnone for making his solver available.

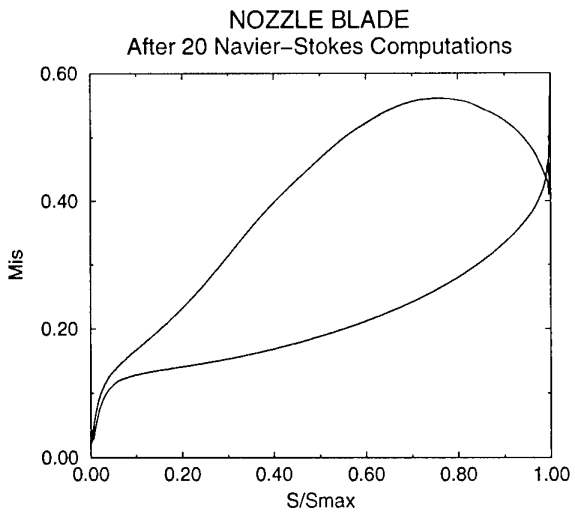

Fig. 17 : **Mach number distributions on the blade surface**

REFERENCES

[1] G.N. Vanderplaats. Numerical optimization techniques for engineering design. *McGraw-Hill*, 1984.

[2] S. Pierret and R.A. Van den Braembussche. Turbomachinery blade design using a Navier-Stokes solver and artificial neural network. *ASME paper*, 1998.

[3] A. Arnone. Viscous analysis of three-dimensional rotor flow using a multigrid method. *Journal of Turbomachinery*, pages 435–445, July 1994.

[4] A. Cichocki and R. Unbehauen. *Neural Networks for Optimization and Signal Processing.* John Wiley and Sons, 1994.

[5] B.J.A. Krose and P.P. van der Smagt. An introduction to neural-networks. *University of Amsterdam*, January 1993.

[6] T. Masters. *Advanced Algorithms for Neural Networks : a C++ Sourcebook.* John Wiley and Sons, 1995.

[7] J.D. Denton. Loss mechanisms in turbomachinery. *Journal of Turbomachinery*, pages 621–656, October 1993.

[8] A.D. Young. *Boundary Layers.* BSP Professional Books, 1989.

[9] B.J. Abu-Ghannam and R. Shaw. Natural transition of boundary layers - the effects of turbulence, pressure-gradient, and flow history. *Journal Mechanical Engineering Science*, pages 213–228, 1980.

[10] R.E. Mayle. The role of laminar-turbulent transition in gas turbine engines. *Journal of Turbomachinery*, pages 509–537, 1991.

Meeting Discussions

Paper 30: **Turbomachinery Blade Design Using a Navier-Stokes Solver and Artificial Neural Network**

Authors: S. Pierret, R.A.Van den Braembussche

Discussor: George S. Dulikravich

Question 1: It is a very nice design work. You have used boundary layer analysis in order to create an inexpensive training for the neural network. How much computing time does each batch of 1,000 (or so) boundary layer computations take as compared to a single Navier-Stokes computation?

Author's Reply: Typical computational times are:

- 1000 optimization loops take about 40 % of a Navier-Stokes computation,
- the training of the neural network takes about 20 % of a Navier-Stokes computation
- one Navier-Stokes computation takes about 6 minutes on a Digital alpha type workstation (500 Mhz)

Therefore, one complete design cycle in which the neural network training, the optimization and the Navier-Stokes computation are performed, takes about 1.5 times a simple Navier-Stokes analysis.

Question 2: Results that you have presented are for the subsonic flows. What do you plan to do with the boundary layer modeling in case of transonic and supersonic exit turbine flows?

Author's reply: Indeed, the boundary layer characteristics are computed using integral methods valid only for incompressible flows. Treating transonic and supersonic flows would require the use of a compressible boundary layer computation.

Discussor: T. V. Jones

Question: The conventional method of dealing with transition is by using an intermittancy model.Did your transition probability model act so, as to produce an equivalent result?

Authors's reply: Intermittancy functions for transition modeling are presently under development and start to be implemented in advanced Navier-Stokes solvers. The purpose of the transition probability is not to mimic an intermittancy function, but rather to measure the risk of having transition at some location on the blade surface. Better modeling for both the transition region and the laminar-separation region would, however, improve the results of the blades designed by this method.

ADVANCED CFD TOOLS FOR MULTI-STAGE TURBINE ANALYSIS

N. Liamis and J.-M. Duboué

Turbine Aero and Cooling Department
SNECMA
77550 Moissy Cramayel, France

ABSTRACT

The purpose of this contribution is to report on the aerodynamical performance calculations carried out around high and low pressure turbines. Two different turbine configurations are considered : a single stage high pressure turbine including rotor blade tip clearance effects and a four stage low pressure turbine. A multi-stage approach based on the ONERA-Snecma 3D Navier-Stokes code CANARI is used to investigate the turbine flow behavior. The computational results are compared with experimental data.

NOMENCLATURE

x, r, θ	spatial directions
ρ	density
p	static pressure
V	velocity
H	total enthalpy

INTRODUCTION

CFD tools represent a significant source of improvement in the design process of Snecma turbines, leading to higher performances, cost and cycle savings as well as to lower associated risks. Today, most of the CFD calculations used in the turbine design and analysis methodology are blade to blade calculations, carried out with quasi-3D and 3D Navier-Stokes codes ; the last Euler solver presently in use is applied to get the 3D unsteady aero-mechanical blade forced response due to wake excitation. These codes have been developed at ONERA and adapted for turbomachinery applications at Snecma.

During the last years, a significant effort has been devoted to the development of stable and fast running algorithms for solving the governing equations for compressible fluid problems. In addition to this development, the computer power has also increased tremendously. Therefore, turbomachinery designers are able to daily analyze 3D complex geometries with reasonable resolution of the flow domain ; interesting and complex flow phenomena can be studied by using numerical simulations, e.g. the influence of the rotor tip leakage on the turbine flowfield. Moreover, a designer is no longer restricted to an isolated blade row analysis when using 3D algorithms ; it is now possible to consider multiple-blade row configurations to take into account the influence of adjacent blade rows.

The present paper considers results from computations of the flow through high and low pressure axial flow turbine stages. The objective is to demonstrate the degree of reliability and maturity the 3D Navier-Stokes method used at Snecma has now reached for day-to-day application in turbine airfoil design and analysis. The first configuration deals with a single stage high pressure turbine ; the tip clearance was 1% of the rotor blade height. The second configuration deals with a four stage low pressure turbine. The results obtained from the simulations are compared to available experimental data.

NUMERICAL METHOD

The code used for the simulations presented hereafter is the code CANARI developed at ONERA (Vuillot et al, 1993, Liamis & Couaillier, 1994), and adapted for turbomachinery applications at Snecma (Heider et al, 1993). The present version of the code solves the 3D unsteady Reynolds averaged compressible Navier-Stokes equations using a cell-vertex approach for multi-domain structured meshes. The turbulent closure of the Navier-Stokes equations is obtained from the algebraic mixing-length turbulence model of Michel (Michel et al, 1969). The code does not use a wall law approach, therefore fine grids are required for the computations. For each row, the equations are formulated in a conservative manner and are solved in the frame of reference in which the blade is fixed. The numerical method is a finite volume, time marching, multi-step scheme.

The method having been presented in details (Liamis & Couaillier, 1994), it is only briefly mentioned here. The integration scheme is a four step

Paper presented at the RTO AVT Symposium on "Design Principles and Methods for Aircraft Gas Turbine Engines", held in Toulouse, France, 11-15 May 1998, and published in RTO MP-8.

scheme. Each step is a combination of three stages : an explicit stage, an artificial dissipation stage, and an implicit stage. The explicit stage is the space-centered explicit Runge-Kutta scheme introduced by Jameson (Jameson et al, 1981). The artificial dissipation stage being based on space-centered difference operators of second and fourth order is analogue to that introduced by Jameson (Jameson et al, 1981). The implicit stage is a variable coefficient residual smoothing obtained by an extension of the Lerat implicit stage (Lerat et al, 1982), allowing higher CFL numbers and accelerating the convergence to the steady state. The convergence of the steady-state flow simulations is also accelerated by a local time stepping technique. Furthermore, the wall clock time required for multiple-blade row computations is reduced by the capability to run the code in parallel by using a PVM type approach on a blade row by blade row basis.

The boundary condition treatment, the subdomain coupling and the multiple-blade row coupling are performed at each step. The boundary condition treatment is based on characteristic relations. The subdomain coupling is based on the use of an arithmetic average between the values of each domain (different before the coupling), these values being defined at mesh points or being interpolated.

Multiple-blade row simulations are carried out by using an interface plane technique to transfer the flow information between adjacent blade rows. In this approach averaged values for the governing flow quantities at the interface plane, which represent the new circumferentially homogenous inlet or outlet conditions at the upstream or downstream side of the interface plane, are used for the next step. The averaging procedure used for the blade row coupling is performed on the absolute frame and the averaged quantities are : ρV_x , ρV_x^2+p , $\rho V_x V_r$, $\rho V_x V_\theta$, $\rho V_x H$ (mixing plane approach). The values obtained with this averaging technique at one side of the interface plane are used to update the numerical scheme values on the other side of the interface plane by applying a treatment based on characteristic relations. In all cases presented hereafter, this blade row coupling treatment seems to be efficient ; the massflow error is always less than 0.07%.

All the calculations presented are performed using a CFL number equal to 8 which ensures a high convergence rate. A very good convergence of the global values (flow rate, losses, angles...) is reached within 2000 iterations. The code is written in standard FORTRAN 77 and requires approximately 4.5 μsec per grid point and per iteration on the VPP300 Snecma computer. For the single stage high pressure turbine configuration the code is running on two processors, while for the four stage low pressure turbine configuration the code is running on eight processors. By using this parallel approach, all computations are performed in approximately 3 hours of wall clock time.

EXPERIMENTAL SETUP

High Pressure Turbine

The test results presented in this part are issued from the 'Turbine Tip Clearance Studies' program which was conducted by Aachen University RWTH with the support of BMW RR, FIAT AVIO, MTU, Rolls-Royce, Snecma and Turboméca. The goal of the test program was to analyze secondary and tip-clearance flows in a high pressure axial turbine and to provide a database for CFD code validation.

The experiments were performed on a cold continuous test rig in which a single stage high pressure turbine was placed. The turbine is relatively small (33mm height) compared to a classical civil engine turbine ; this leads to important secondary flows as we will see during the rotor exit flowfield analysis.

The test program included the investigation of two blade tip geometries (flat/with groove), two blade tip-clearance heights (1%, 3%) and three cooling mass flows in the groove (0%, 1%, 3%). The tip clearance variation has been carried out by changing the outer casing. Only the flat uncooled blade 1% gap configuration is analyzed in this paper.

The nominal operating conditions are summarized in the following table :

Table 1. High pressure turbine nominal operating conditions

Inlet total pressure	2.1 bar
Inlet total temperature	355 K
Rotational speed	11482 RPM
Turbine work	192 J/Kg/K

Compared to original engine design conditions, reduced mass flow, reduced speed and reduced turbine work were kept constant. It has to be noticed the turbine work being low for a single stage high pressure turbine with a reaction degree of 0.35, the operating point provides high subsonic flowfield into the stator and rotor passages.

The test instrumentation is the following :

- upstream the stator, in the core region of the flow, a three hole probe is used to measure the total pressure and the flow angle ; the exact thickness and development of the boundary layers have been determined with hot wire probes for different axial positions,
- downstream the stator, a three hole probe and a five hole probe measure the total pressure and the flow angles ; measurements are taken less than half an axial chord upstream the rotor blade,
- downstream the rotor, a three hole probe allows to measure the total pressure and the flow angles ; measurements are taken roughly half an axial chord downstream the rotor blade,

- static pressure taps located at inner and outer rings are used in all measuring planes (defined by the probe heads) to measure static pressure.

Low Pressure Turbine

The experiments were performed on a cold continuous test rig in which an uncooled four stage low pressure turbine was placed downstream a pre-swirl blade row.

The nominal operating conditions are summarized in the following table :

Table 2. Low pressure turbine nominal operating conditions

Inlet total pressure	2.4 bar
Inlet total temperature	461.6 K
Rotational speed	3121 RPM
Turbine work	309 J/Kg/K

Compared to original engine design conditions reduced speed was kept constant, while the reduced turbine work was 9% less due to rig limitations. The operating point provides subsonic flowfield into the stator and rotor passages.

The test instrumentation is the following :
- upstream the stator 1, rakes are used to measure the total pressure and total temperature ; measurements are taken an axial chord upstream the vane,
- downstream the rotor 4, a three hole probe allows to measure the flow angle at 5%, 25% and 75% span, while arcrakes are used to measure the total pressure spanwise ; measurements are taken roughly an axial chord downstream the rotor blade,
- static pressure taps located at 15%, 50% and 85% span of the stator 1 are used to measure static pressure,
- static pressure taps located at inner and outer rings in planes upstream and downstream all stators are used to measure static pressure.

RESULTS AND DISCUSSION

In order to assess the method, the high and low pressure turbines presented previously are investigated.

The computational domain for each blade row is divided into subdomains. Each domain supports a structured grid, leading to a H-O-H mesh type for the blade row and to a O-H mesh type for the rotor tip clearance area of the single stage high pressure turbine (Heider et al, 1993). A radially stacked mesh formed by 2D H-O-H grid surfaces extends from hub to casing. The O mesh wrapped around the airfoil is built with an automatic dual algebraic-optimization process in order to obtain better orthogonality and regularity of the grid cells. The mesh radial distribution is clustered near the hub, the blade tip and the casing to capture endwall boundary layers correctly. For the rotor of the single stage high pressure turbine, the gap left in the O mesh between the blade tip and the casing is completed by two subdomains formed by an O grid and a H grid (figure 1). Special care is paid to the mesh regularity in the gap region, with for example coinciding nodes between the interface of the blade O mesh and the gap O mesh.

The standard boundary conditions used usually for single blade row calculations are also applied at the turbine inlet and outlet during the stage computations : total pressure, total temperature and flow angles are imposed at the inlet while the static pressure is prescribed at the outlet. No-slip adiabatic boundary conditions are imposed at the walls. In the hub region of the high pressure turbine, the gap between the stator platform (stationary) and the rotor platform (rotating) are treated by considering mesh cells, located either in the stator mesh or in the rotor mesh, in which a linear variation of the rotating speed is imposed. The low pressure turbine rotors being shrouded, the same treatment is applied to modelise the gap between the stator platform and the rotor platform in all hub and tip regions of the low pressure turbine. The inner hub platform cavity and the outer tip platform cavity are not modelised.

High Pressure Turbine

A view of the high pressure turbine mesh at the hub is shown in figure 1. The overall grid points distribution is given on the following table.

Table 3. Mesh grid points distribution for the high pressure turbine

	H	O	H	O	H
Stator	19x31x101	197x45x101	17x47x101	-	-
Rotor	13x29x101	197x41x101	43x37x101	197x21x21	75x25x21
Total	2 176 350				

The thickness of the cell adjacent to the surface is fixed at 3μm for the hub, the blade and the tip, at 10μm for the gap and the ratio by which the cell size increases normal to the wall is 1.22 ; these values, which allow to get $y^+ \sim 1$ in most of the configurations, are required in order to obtain results which are independent from the mesh refinement (Heider et al, 1993, Heider & Arts, 1994).

The turbine flowfield and the 1% tip clearance region are presented in figure 2. Major vortex structures are located at the suction side of the stator and rotor blades. On the stator, the hub and casing passage vortices are clearly represented. On the rotor, the hub and casing passage vortices are stronger than the stator hub and casing passage vortices. The rotor tip

clearance vortex is the strongest vortex structure present on the high pressure turbine flowfield.

In figure 3, the predicted circumferentially averaged absolute swirl angle and absolute total pressure distributions are plotted versus span in comparison to experimental data. In general, the predicted results display a reasonable agreement with the experimental data.

The differences in values between calculated and measured angles at rotor exit are partly due to the fact that absolute angles are measured while relative angles are calculated. For the present flow configuration, the velocity triangle implies that a 10° discrepancy in the absolute frame is equivalent to 3° in the relative one ; this is coherent with the stator exit angle prediction level.

At the rotor inlet, the swirl angle values are slightly overestimated while the total pressure values are slightly underestimated. At the rotor outlet, the swirl angle values are slightly underestimated while the total pressure values are slightly overestimated. We can then conclude that the code provides stronger losses and angle deviations for the stator and weaker losses and angle deviations for the rotor. However, the differences between calculation results and experimental data are of the same order of magnitude as the differences between the results obtained by two distinguished experimental measurements at the rotor inlet.

The predicted total pressure profiles have the same shape as the measured ones. The predicted swirl angle profiles at the rotor inlet are quite similar to the measurements, while at the rotor outlet, they do not seem to bear much resemblance to the experimental data. Nevertheless, from a closer investigation of the swirl angle profiles, it appears that all the vortex structures are correctly captured. The main differences observed to the spanwise flow angle form are only due to the location of the hub and casing passage vortices. More precisely :

At the rotor inlet, we remark (on the absolute swirl angle profile) that :

- the stator hub passage vortex has moved from a 14% span location to a 10% span location,

- the stator casing passage vortex is correctly positioned to a 86% span location,

At the rotor outlet, we remark (on the absolute swirl angle profile) that :

- the rotor hub passage vortex has moved from a 39% span location to a 29% span location,

- the rotor casing passage vortex has moved from a 68% span location to a 73% span location,

- the tip clearance vortex is correctly positioned to a 87% span location.

From all these remarks, it appears that the code predicts the hub and casing passage vortices closer to the walls compared with the measurements. This difference in the vortex location is at the origin of the flow angle form discrepancies and is probably due to a thinner boundary layer resulted by the code near the hub and casing wall areas.

The mass flow rate difference between calculation and experimental data is 0.9%. No comparison has been made on the stage efficiency because the efficiency measurements have been judged incoherent with the information of the engine turbine component.

Low Pressure Turbine

The low pressure turbine mesh is similar to the high pressure turbine mesh without the OH clearance grid (because the low pressure turbine rotors are shrouded). The grid points distribution is given on the following table.

Table 4. Mesh grid points distribution for the low pressure turbine

	H	O	H
Stator 1	27x25x109	197x41x109	33x37x109
Rotor 1	19x25x109	197x41x109	25x37x109
Stator 2	15x25x109	197x41x109	27x37x109
Rotor 2	15x21x109	197x41x109	33x37x109
Stator 3	21x23x109	197x41x109	33x37x109
Rotor 3	15x21x109	197x41x109	33x37x109
Stator 4	21x23x109	197x41x109	33x37x109
Rotor 4	15x21x109	197x41x109	33x41x109
Total	8 440 306		

As for the high pressure turbine, the thickness of the cell adjacent to the surface is fixed at 3μm for the hub, the blade and the tip, and the ratio by which the cell size increases normal to the wall is 1.22.

The turbine flowfield is presented in figure 4. As for the high pressure turbine, the hub and casing passage vortices are clearly represented at the suction side of the stator and rotor blades. The major vortex structures are located on the first stage and more precisely on the stator 1 where the outer wall slope is the most important.

In figures 5, the predicted circumferentially averaged absolute swirl angle and absolute total pressure distributions at the rotor 4 outlet (turbine outlet) are plotted versus span in comparison to experimental data. The predicted results are quite close to the experimental data, especially for the absolute total pressure. Observing the absolute swirl angle profile, we can notice that the results are similar to that observed for the high pressure turbine as far as the vortices location (closer to the walls compared to the measurements) and the differences in values between

calculated (relative) and measured (absolute) angles are concerned.

In figures 6, the predicted circumferentially averaged static pressures at the hub and the tip are plotted in the planes located upstream and downstream to the stators (measurement stations 1-8) and in the plane located at the rotor 4 outlet (measurement station 9) in comparison to experimental data. The difference between calculation and experimental data is everywhere less than 5% ; so the reaction degree and the turbine work per stage are rather well estimated by the computation.

By using the static pressure, calculated or measured around a blade row, we can easily deduce the isentropic Mach number. Figures 7 show, for the stator 1, the predicted isentropic Mach number distributions at 15%, 50% and 85% span plotted versus the reduced curvilinear coordinate in comparison to experimental data. The calculated blade loading seems higher than the measured one at 15% and 85% span ; moreover the positive incidence measured on the profile shows that the pre-swirl blade generates a higher deviation than expected.

The mass flow rate and efficiency differences between calculation and experimental data are respectively 0.5% and 1%.

SUMMARY - CONCLUSIONS

A numerical study was undertaken to examine the potential of a multi-stage method based on a 3D Navier-Stokes code to predict the flowfield into turbine stages. Two turbine configurations were simulated ; a single stage high pressure turbine including tip clearance effects and a four stage low pressure turbine. Data from measurements were used to investigate the predictive capability of the code.

The numerical results have been shown to be in good agreement with experimental data, and the method to be sufficiently robust and rapid for industrial use.

Further effort is needed on the following topics :

- validation of the method, by confrontation with a larger number of different configurations,

- improvement of the multi-blade row modeling, by using a more elaborate approach to model the adjacent blade rows influence (Adamczyk, 1985),

- improvement of the turbulence modeling, by using a one or two transport equation turbulence model instead of the algebraic mixing-length turbulence model,

- improvement of the turbine environment description, by modeling the secondary flows in the inner hub and outer tip rotor platform cavities.

This will be the subject of future works.

ACKNOWLEDGMENTS

The authors gratefully acknowledge Snecma for the authorization to publish the present CFD calculation results and the results of the low pressure turbine tests. The authors also thank the consortium of the project 'tip clearance studies', for allowing to show some high pressure turbine measurements. The contribution of Mr Ph. Chanez and Mr Ph. Picot participating in the multi-stage simulation project and of Mr. E. Schwartz participating in the low pressure test result analysis is acknowledged.

REFERENCES

Adamczyk, J.J (1985) : Model Equation for Simulating Flows In Multistage Turbomachinery. ASME Paper 85-GT-226.

Heider, R.; Duboué, J.-M.; Petot, B.; Billonnet, G.; Couaillier, V.; Liamis, N. (1993) : Three-Dimensional Analysis of Turbine Rotor Flow including Tip Clearance. ASME Paper 93-GT-111.

Heider, R. & Arts, T. (1994) : Aerodynamic and Thermal Performance of a Three Dimensional Annular Transonic Nozzle Guide Vane (part I and II). AIAA Paper 94-2930.

Jameson, A., Schmidt, W., Turkel, E. (1981) : Numerical Solution of the Euler Equations by Finite Volume Methods Using Runge-Kutta Time-Stepping Schemes. AIAA Paper 81-1259.

Lerat, A., Sides, J., Daru, V. (1982) : An Implicit Finite-Volume Method for Solving the Euler Equations. Lecture Notes in Physics, vol. 170, Springer-Verlag 1982.

Liamis, N. & Couaillier, V. (1994) : Unsteady Euler and Navier-Stokes Flow Simulations with an Implicit Runge-Kutta Method. Proceedings of the Second ECCOMAS Computational Fluid Dynamics Conference, 5-8 September 1994, Stuttgart, Germany, John Wiley & Sons 1994.

Michel, R.; Quemard, C.; Durand, R. (1969) : Application d'un schéma de longueur de mélange à l'étude des couches limites turbulentes d'équilibre. ONERA NT 154.

Vuillot, A.-M.; Couaillier, V.; Liamis, N. (1993) : 3-D Turbomachinery Euler and Navier-Stokes Calculations with a Multidomain Cell-Centered Approach. AIAA Paper 93-2576.

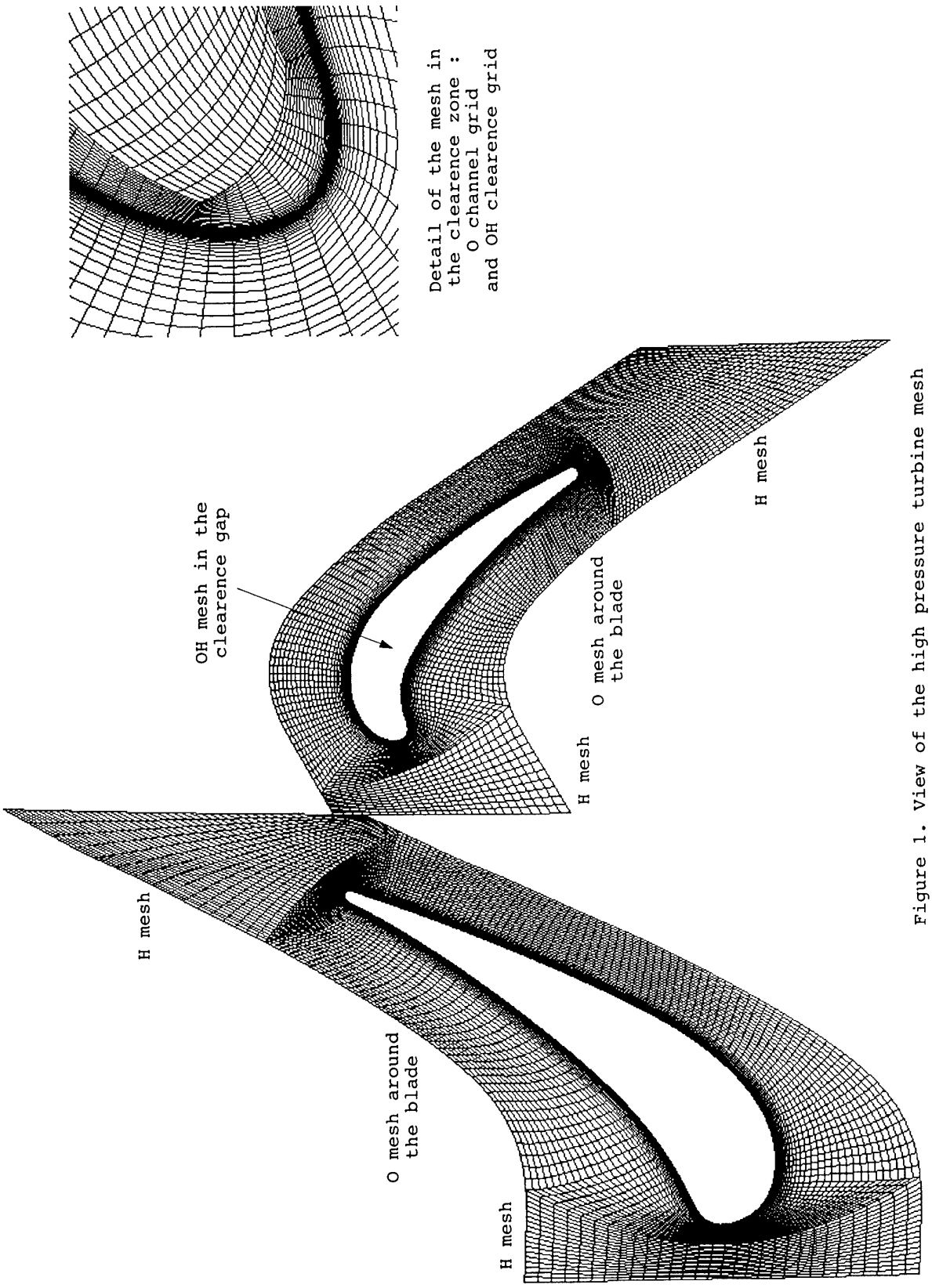

Figure 1. View of the high pressure turbine mesh

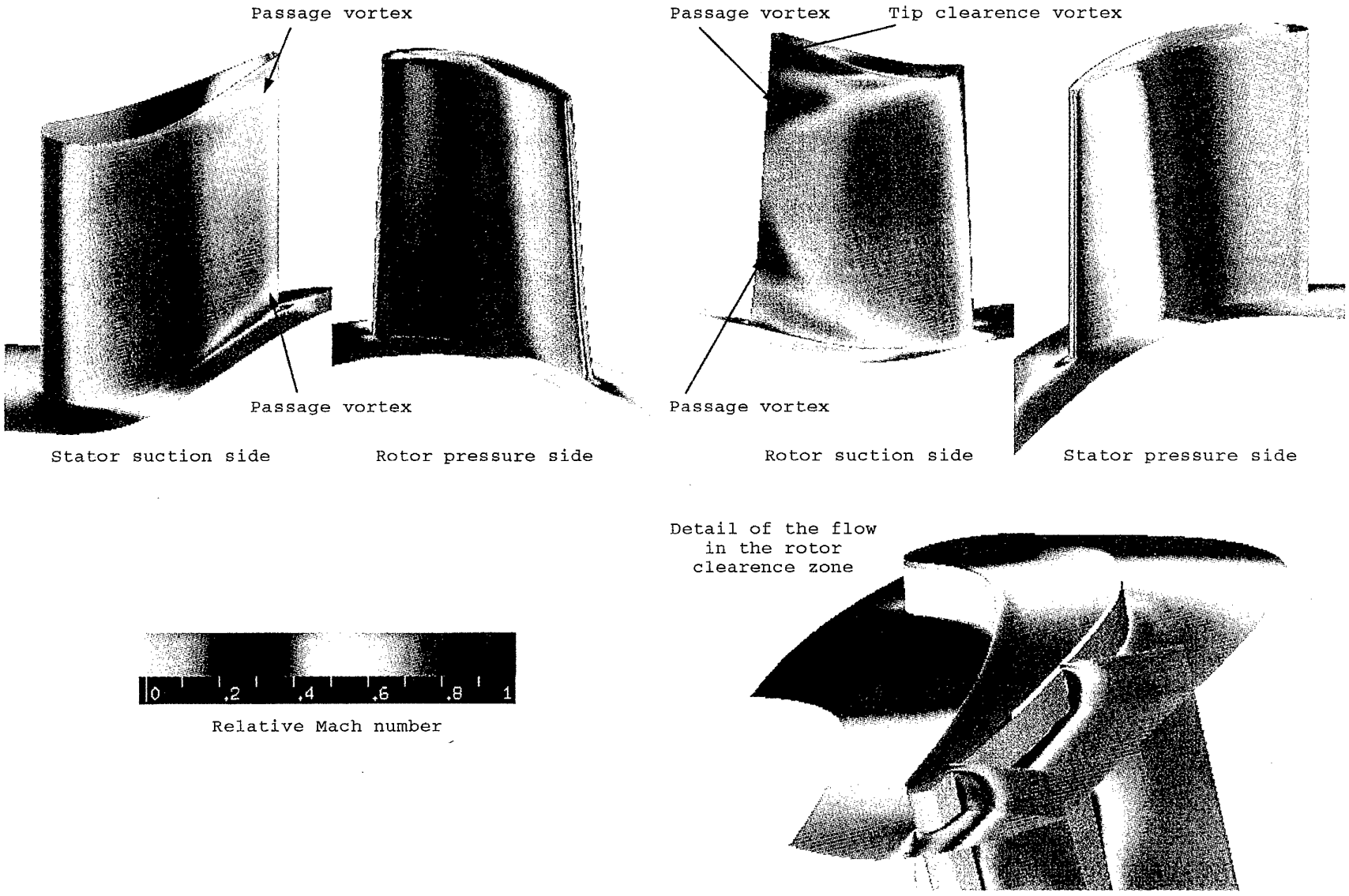

Figure 2. View of the high pressure turbine flow field

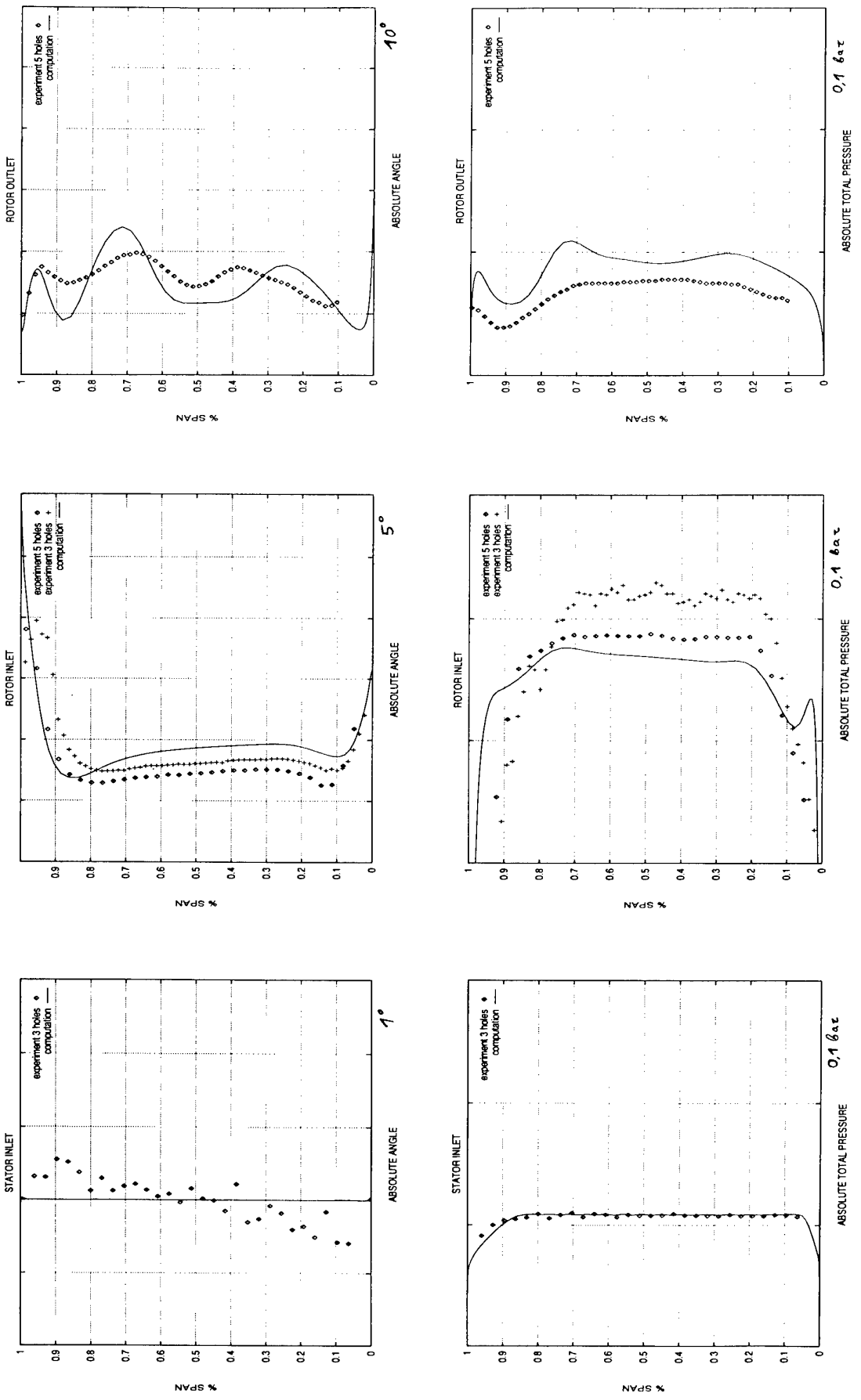

Figure 3. Total pressure and swirl angle distributions for the high pressure turbine

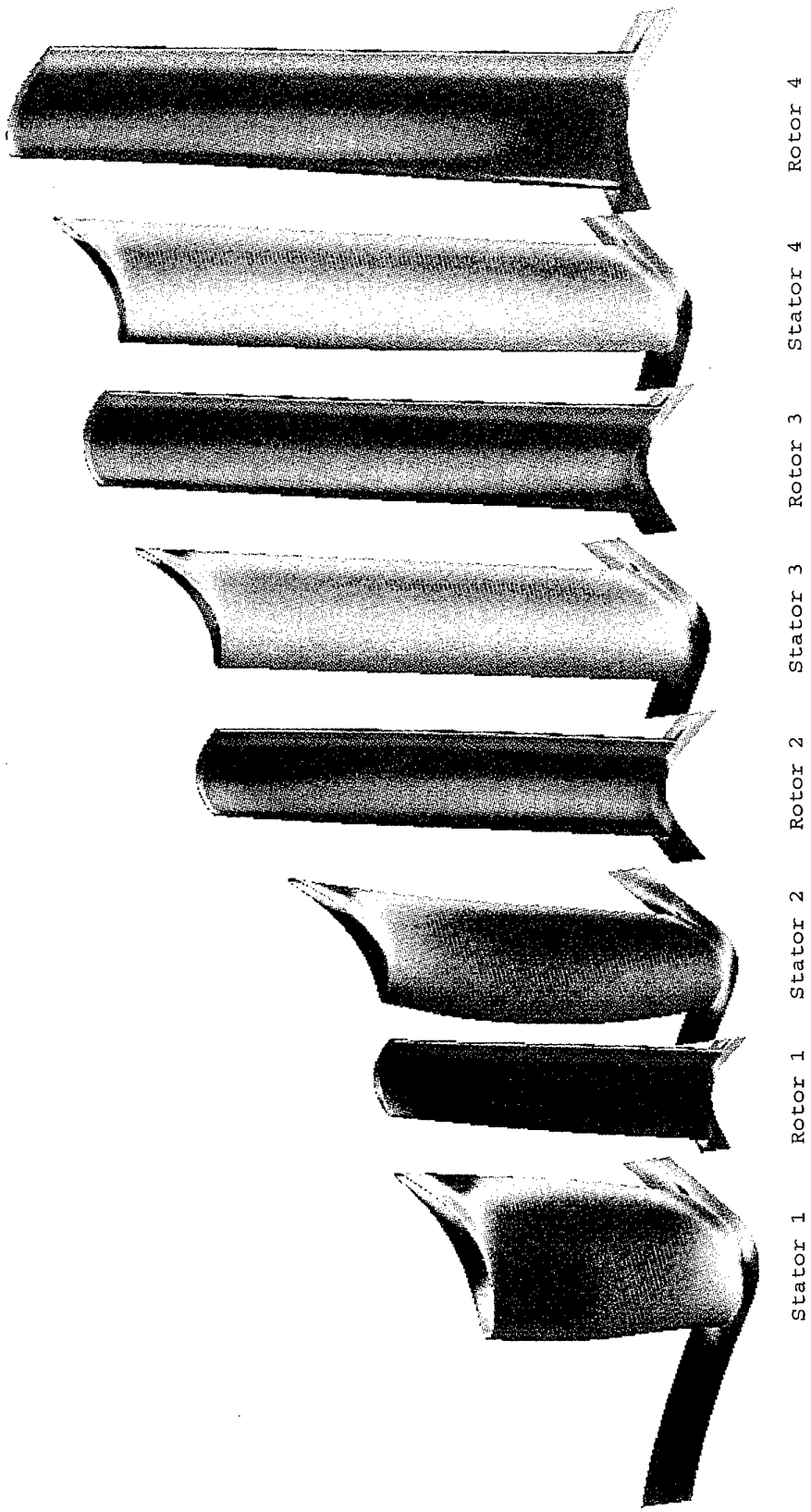

Figure 4. View of the low pressure turbine flow field

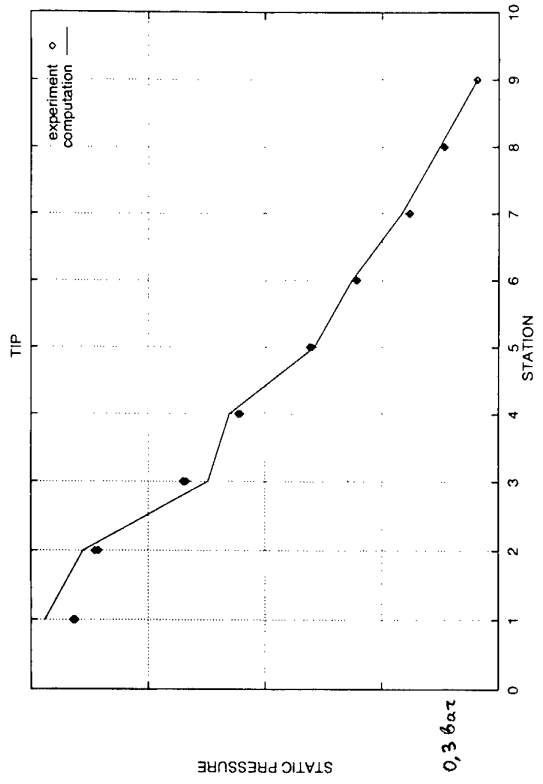

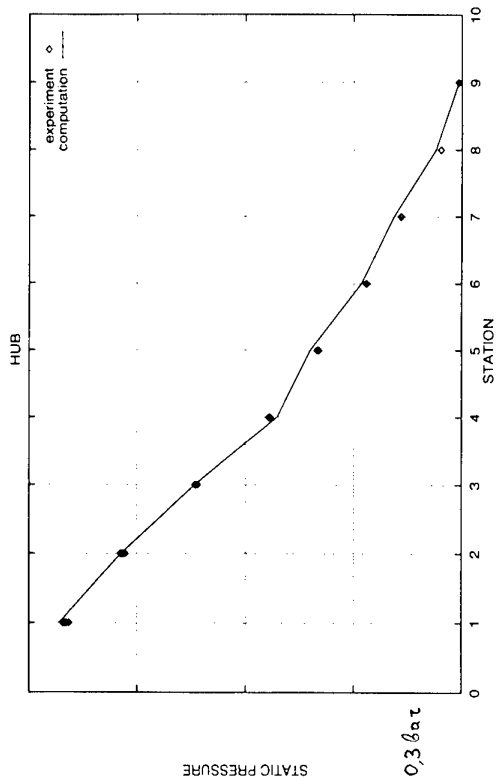

Figure 6. Static pressure distributions for the low pressure turbine

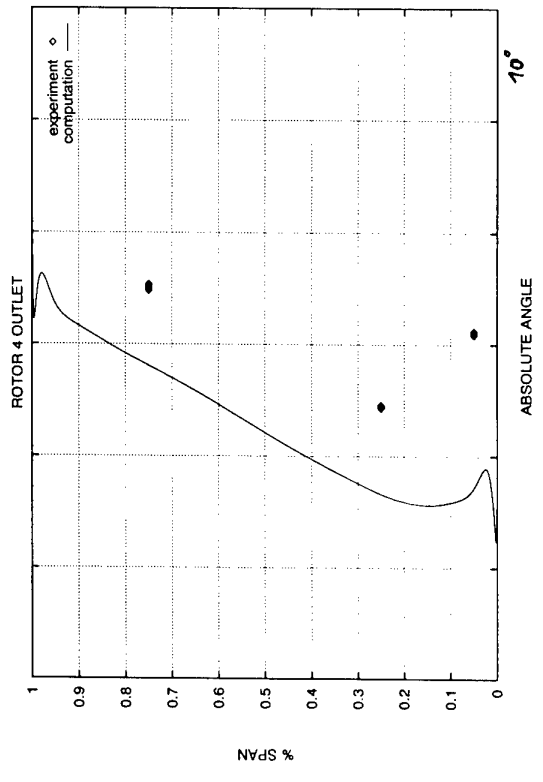

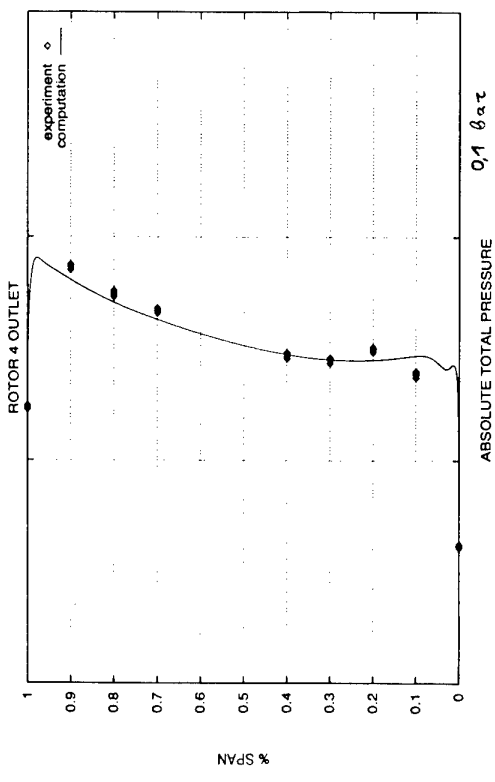

Figure 5. Total pressure and swirl angle distributions for the low pressure turbine

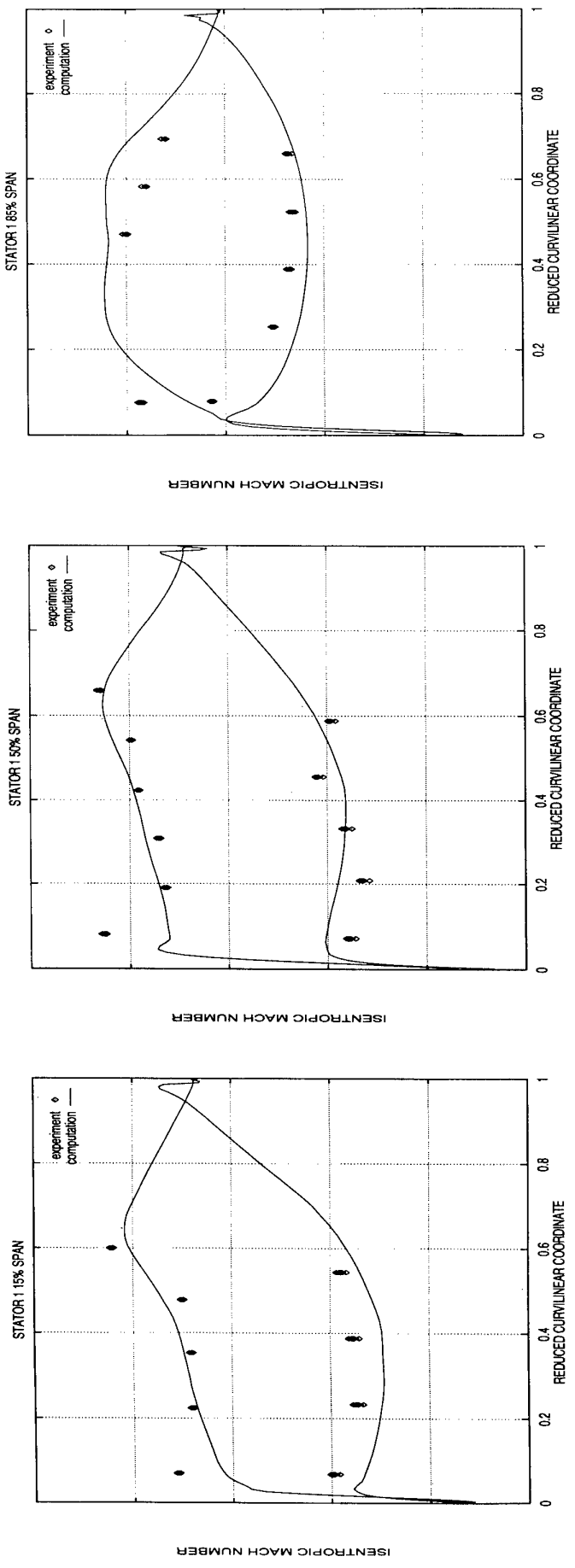

Figure 7. Isentropic Mach number distributions for the low pressure turbine

Meeting Discussions

Paper 31: **Advanced CFD Tools for Multi-Stage Turbine Analysis**

Authors: N. Liamis, J.-M. Duboué

Discussor: John J. Adamczyk

Question: Why is the first blade row simulation showing reverse loading near the trailing edge?

Authors's reply: The reverse loading near the trailing edge is due to geometrical aspects of the first turbine nozzle used in the rig. This phenomenon, only seen in the first blade row, is not a precision problem of the method.

Advanced Computational Fluid Dynamics in the Design of Military Turbines

N.J. Gwilliam and T.R. Kingston
Rolls Royce plc. - Bristol
Turbine Engine Systems
Whittle House - WH64
P.O. Box 3, Filton, Bristol
BS34 7QE

1.0 ABSTRACT

Today's design of turbine blade challenges the designer to meet the demanding requirements of overall increase in engine performance - more power for the same weight, greater engine efficiency and fuel economy. This has resulted in designs to cater for higher blade loading and faster rotational speeds. To achieve this, highlift shroudless designs are being adopted. One of the greatest challenges to the aerodynamic designer is the design of such blading so that the additional losses incurred, shock losses, greater secondary flows and suceptability to tip clearance are minimised. To do so, it is essential to be able to carry out an accurate three-dimensional analysis of the flow within the stage. This is achieved using computational fluid dynamics. This paper aims to describe and evaluate some of the tools available at Rolls Royce plc. for the numerical simulation of turbine flows. It was generated as part of a study to analyse a 'datum' and 'highlift' HP (high pressure) turbine, so as to establish both where losses occurred, and which CFD (Computational Fluid Dynamics) codes could best analyse the blading.

RESUME

De nos jours, la conception d'une aube de turbine présente de nouveaux défis aux ingénieurs en termes d'amélioration générale de la performance du moteur - plus de puissance pour le même poids, meilleur rendement du moteur et économie de combustible. Il en résulte une nouvelle génération de turbines avec une forte charge de l'aube et une vitesse rotationnelle élévée. Pour cela, il a fallu adopter les conceptions de forte-portance avec des aubes sans talon. Un des défis majeurs qui se pose aux spécialistes de l'aérodynamique est la conception d'une telle turbine de sorte que les pertes aerodynamiques (le choc, les phénomènes secondaires et le jeu au sommet de l'aube qui leur sont associés) soient minimisées. Pour cela, il est nécessaire de réaliser une analyse tri-dimensionnelle de l'écoulement dans un étage de turbine, obtenue en mettant au point un calcul numérique de dynamique des fluides par ordinateur. Dans cette communication, nous essaierons de décrire et d'évaluer certains codes disponibles chez Rolls-Royce plc pour la simulation numérique des écoulements dans l'environnement de la turbine. Cette communication a été rédigée dans le cadre d'une étude visant à analyser une turbine à haute pression avec une version de la turbine de réfèrence et une version à 'forte-portance', afin d'établir où se produisent les pertes, et quels codes peuvent les mieux analyser la turbine.

2. INTRODUCTION

Initially, design will commence with a through-flow program, with initial guesses for radial distributions of important parameters such as total pressure and absolute swirl angle. The solution will assume blockage, loss and turning in the blade design, and so the variation in streamtube, radius and height through the blade row may be determined. The blade is then divided into quasi-3D sections along these streamtubes, and sections are designed in isolation using 2D PVD programs and simple 2D analysis/design tools, such that the inlet, exit, loss and geometrical constraints are satisfied. The sections are then stacked radially and circumferentially so as to form the three-dimensional blade geometry. This geometry can be passed back to the throughflow program for the next iteration if desired.

Once stacked, the blade will be analysed in three dimensions using 3D CFD codes, and skewed so as to achieve matching between the design mass flow distribution and the analysis. In practice, at least three blade sections are normally designed blade-to-blade, which will be skewed. Experience indicates that five designed sections may be beneficial, too few will result in poor matching between analysis and design.

The 3D design of the blade is currently carried out using isolated blade row calculations, this implies the vane to rotor matching is only in throughflow calculations. It is important to determine the magnitude and importance of the interaction effects in HP turbines. To do so, new methods, both true unsteady and average unsteady have been developed. 3D multistage steady versions of existing codes have been developed which use overlapping grids to model deterministic stresses and bodyforces, which allow averaged-unsteadiness to be modelled. Also, a true unsteady code has been acquired and developed, which allows true unsteadiness to be calculated in relatively short calculation times.

2.1 Note on the Turbine Aerodynamic Environment

In an unshrouded HP turbine stage, some of the most important losses generated are undoubtedly through secondary flows and tip leakage. The NGV and rotor will both be affected by secondary flows generated by the endwall-blade interaction, in addition the shroudless rotor will have overtip leakage losses. A classical treatment of secondary flows is given by Üçer, Stow and Hisch [1]. In this model, there are two types of vortex downstream of a blade row. The principal vortex structure is the passage vortex, which occurs due to distortion of vortex filaments of the inlet boundary layer passing with the flow through a curved passage. In addition, there is also a trailing edge vortex sheet composed of trailing filament vortices, caused by the stretching of the inlet vortex when passing through a cascade with different velocities on the suction and pressure sides, and the trailing shed vorticity, due to the spanwise change of the blade circulation. A horseshoe vortex is created by the endwall boundary layer rolling up in front of a cylinder on a

Paper presented at the RTO AVT Symposium on "Design Principles and Methods for Aircraft Gas Turbine Engines", held in Toulouse, France, 11-15 May 1998, and published in RTO MP-8.

flat plate. This creates a vortical motion which is called a horseshoe vortex, due to its subsequent path on either side of the cylinder. In a turbine blade row, the pressure side of the vortex merges with and becomes part of the passage vortex. The suction surface side of the horseshoe vortex rotates in the opposite sense to the passage vortex, and runs down the suction surface to the trailing edge. It is dissipated in contact with the passage vortex.

Rotor tip gaps result in leakage flow over the tip of the blade from the pressure surface to the suction surface. The flow will depend on the gap size and on the pressure difference between surfaces, or blade loading. In HP turbine blades, the latter is usually high, and the resulting leakage flow affects blade efficiency. A vortex forms on the suction surface of the blade, due to the interaction between the tip leakage flow and the passage vortex. The dissipation and mixing of the leakage flow and vortex, introduces losses due to increased shear stresses and scrubbing. In addition there are secondary kinetic energy losses that are passed from the upstream to downstream bladerow.

Where the secondary fluid motion due to the vortex is in the same direction as the circumferential component of the primary flow, the net result is overturning of the flow, where more work is done by the fluid. However, where the secondary fluid motion is in the opposite sense, underturning of the flow occurs and work is lost.

Secondary flows increase losses by several means, there is a natural increase in the inlet endwall boundary layer up to the horseshoe separation lines. The separation bubble, caused by the separation of the horseshoe vortex, results in raised local shear stress levels. Corner losses on pressure and suction surfaces are due to increased surface shear stresses and mixing, from transportation of low energy boundary layer flow into the freestream. The dissipation of all vortices and complete mixing of the non-uniform outlet flow field downstream of the blade row both incur losses. The main loss in performance from secondary flows is due to the passage vortex. This transports low energy boundary layer fluid into the main stream, thus causing losses associated with this mixing, as well as increasing the velocity gradient, and hence shear stresses at the surfaces.

In addition, there are losses associated with tip leakage flows. A direct effect, due to the fact that the space associated with the tip gap undergoes no change in angular momentum, and is thus not available for doing work. And an indirect effect, the leakage flow implies unloading at the tip, resulting in a reduction in work done. The leakage flow also interacts with the main flow, which causes flow perturbation along with vortex formation and dissipation, resulting in mixing losses.

2.2 Blading

The blades analysed in this study were Rolls-Royce designed 'datum' and 'highlift' variants of a single stage HP turbine. The computational analyses were based upon 'cold-flow' conditions with unfilmed adiabatic surfaces (no heat transfer). The experimental data is based upon cold-flow rig tests carried out at Rolls-Royce Bristol, and has been normalised and scaled. The datum blading rig results indicate that it is exceptionally efficient, whereas the highlift variant, although good, could be improved. Rolls-Royce plc. aim to equal or better datum performance in highlift redesign, using CFD to optimise the turbine design.

3. THE CODES

Three main areas of CFD work were conducted: an isolated blade row study using two 3D codes (JA63 and SZ02); a 3D multistage (overlapping grids) steady study (using codes developed from both of the above); and a 3D unsteady study. The first study should give an accurate simulation of the flows present and allow the consequences of secondary flow losses and tip leakage to be evaluated. The second part uses overlapping grids to evaluate deterministic stresses and bodyforces, which simulates an average form of unsteadiness. These should indicate, in conjunction with the unsteady study, whether average unsteadiness is a reasonable assumption to make.

3.1 JA63

JA63 is developed from the BtoB3D computer program developed by W.N. Dawes at the Whittle Laboratory, Cambridge, for analysis of the flow through turbo-machines. The equations solved are the time dependent, Reynolds averaged Navier-Stokes equations. These represent the equations for the conservation of mass, energy, axial momentum, radial momentum and moment of momentum. The turbulent viscosity is modelled with a simple mixing length Baldwin-Lomax turbulence model.

These equations are solved in the relative plane using a cylindrical polar co-ordinate system with appropriate source terms to allow the solution to be obtained in a rotating co-ordinate system. The variables are stored at cell centres, and the program uses the finite volume explicit time-marching technique based on a two or four step Runge-Kutta with implicit residual smoothing to reach the steady state solution. The grid is a standard sheared, (or H) grid with I, J, K being the positional indices in the axial, circumferential and radial directions respectively.

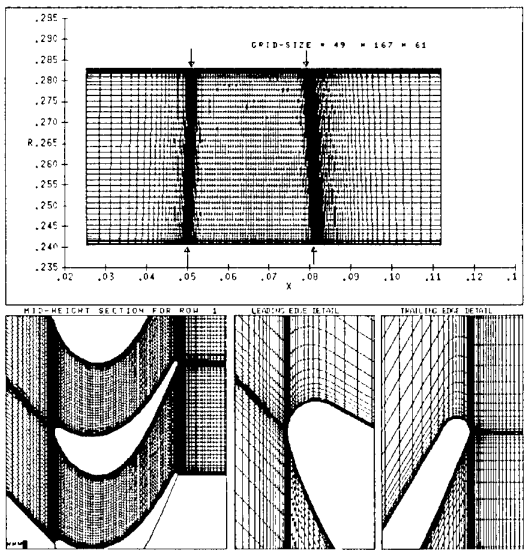

Figure 1 : JA63 Fine Grid. 167 x 49 x 61

For all cases, a 400,000 point grid was chosen for the NGV, and a 500,000 point grid for a rotor to allow for tip leakage modelling, and zero mesh exit angle grids were chosen for good shock resolution (Figure 1). The analyses took place overnight on a Silicon Graphics Origin 2000 compute server with two processors, or on a 256MByte B-class Hewlett-Packard workstation. The rotors in all cases are shroudless. The rotor grids modelled the tip clearance using eight points in the tip gap region. The sheared grid structure does not allow a fully square tip, and the tip of the blade must be slightly tapered, skewing the cells around it. With sufficient grid points the shape approaches a realistic geometry.

At Rolls-Royce Turbine Engineering, two styles of exit grid are used, one where the exit angle follows the flow, the other where the exit angle is zero. The latter facilitates superior shock capturing, a feature which is important in the analysis of HP blading.

3.2 SZ02

SZ02 is developed from the MEFP (Moore Elliptic Flow Program) code developed by Joan and John Moore at the Virginia Polytechnic Institute, it uses a box grid layout (Figure 2) and is based upon an implicit pressure correction method. This procedure is more expensive in computing time and memory, therefore, the size of the grid is more limited at present.

One of the advantages of SZ02 is that using the box grid is better than the sheared grid, particularly noticeable in the lack of skewed cells at the leading edge, and when using a tip gap. Since grid lines exist within the blade it is possible to have a flat tip, whereas only a tapered tip is possible in JA63. The SZ02 analyses were undertaken with grids of smaller magnitude than JA63, both due to memory requirements, and the fact that SZ02 is less grid sensitive.

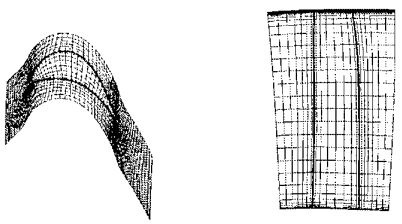

Figure 2 : Typical SZ02 Grid 79 x 33 x 41

3.3 3D Multistage "Overlapping" Steady.

3.3.1 Background

In the late 1980's, pioneering work by Adamczyk led to several companies developing multistage CFD with overlapping grids to calculate bodyforces and deterministic stresses. For example Pratt and Whitney presented two papers [2] and [3] at the 1995 International Gas Turbine and Aeroengine Congress and Exposition. Multi-row methods have been developed at Rolls-Royce plc. for the JA63 and SZ02 CFD codes. A full explanation of multistage modelling using bodyforces and deterministic stresses is given by Rhie, Gleixner, Spear, Fischberg and Zacharias in [2], which in turn is derived from work by Adamczyk.

The approach is a "continuous interface plane" where deterministic stresses are used to ensure continuous physical properties across interface planes. The average unsteady effects due to blades and vanes are incorporated the analysis and are approximated using deterministic stresses, along with the application of body forces. The latter are used to account for the 'potential' interaction between closely coupled rows. The deterministic stresses account for the 'average' wake blockage, and mixing effects both axially and radially. The idea is to incorporate periodic unsteady flow physics to provide a robust multistage design capability.

The method, involves running blade rows on separate processors, with information exchange between them. This should be more time and memory efficient than most unsteady calculations, which require large CPU power and run times. In the calculation of a blade row embedded in a multistage machine, the effect of adjacent blade rows is modelled by extending the usual grid to overlap the adjacent bladerows and introducing a circumferentially-averaged representation of the rows.

The region of overlap is only expected to embrace the complete downstream blade row (Figure 3), so as to capture wake decay. The exchange of information between processors is handled by PVM (parallel virtual machine) software. The PVM software is supervised during its running by PVC developed by Michael Giles of the Oxford University Computing Laboratory, which is a set of four routines, built on top of PVM, which restricts attention to a specific model of computation typical of many engineering parallel applications.

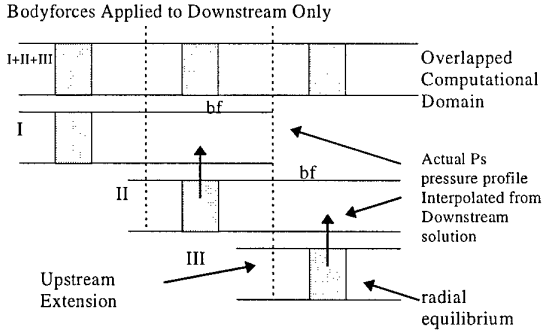

Figure 3 : Illustration of Overlapping Grid Principle

3.3.2 Running Overlapping Grids

The runs were performed on Hewlett-Packard 128MByte. and 256MByte. Workstations. The control file instructs PVC which machines the blade rows and supervisor are to be run on, and which channels information is to be exchanged over. A run file is necessary to start the processes. If a process runs out of control, then PVC will shut it down. Distributed multistage solutions with overlapping grids must be run so that both processors can easily access data. Memory requirements can potentially be high, but are much lower than a full 3D unsteady solution.

3.4 Unsteady Study

JA74 is developed from the UNSTREST code developed by Prof. John Denton of Cambridge University, and is aimed at eventually being able to calculate the 3D unsteady, viscous flow through a whole turbomachine. This will require far greater computer resources than are currently available. The number of blade passages that are practicable with current workstations is limited to about 20, but this can be divided between as many stages as required. The code is based upon Prof. John Denton's multistage steady calculation (MULTIP). Instead of the 'opposed difference' numerical scheme in MULTIP, which is not time accurate, a Ni scheme is used (a single step Lax-Wendroff method). This is a completely explicit scheme, but in the unsteady mode runs at CFL numbers significantly greater than unity (~1.5) on the smallest cells. JA74 is significantly quicker than other unsteady codes currently available offering rapid familiarisation, development and application. However, changes of a few grid points can vastly affect the length of run required.

It is important that the NGV and rotor grids have the same radial distribution at the intermediate plane. This will be a sliding interface plane, the changes from each blade row are interpolated on to the adjacent row. This is not a mixing plane, and the flow should pass through the interface without distortion provided sufficient grid points are available to prevent interpolation errors. The rotors are run shroudless, and a 3 point tip treatment has been set up with tapering.

For steady CFD, convergence is to a minimisation of residual changes, for unsteady CFD, convergence is to periodicity. The history plots, should result in a periodic waveform, and the mass flow plot in a constant mass flow, in line with that required. Once a fully converged solution is obtained, the solution may be run through one more sector, filing back flow files across the waveform, therefore producing a true unsteady picture which may be animated, or used to generate unsteady lift plots.

4. RESULTS AND DISCUSSION

The results were analysed by either CFD comparisons package, or by spreadsheet. The CFD analysis packages used were two Rolls-Royce plc. CFD post-processors and Visual3. Experimental data was available at axial traverse stations downstream of the NGV and rotor exit planes. For secondary flow behaviour, no experimental data was available, hence accuracy is based on expected general trends taken from [1].

It seems appropriate to mention some of the differences between CFD modelling and testing/reality. These should be borne in mind when considering the discussion below. The differences can be divided into those errors inherent in testing, and those inherent in physical modelling.

Physical Modelling.

- We know that the boundary layer, and turbulence models use algebraic modelling to simplify a complex situation to reduce running time and CPU requirements. These models will ultimately differ from the highly complex flows developed in reality. The subject is outside the scope of this paper, but its effects must be considered. In both JA63 and SZ02, the turbulence modelling will set the inlet turbulence level at some arbitrary level (usually 4%), which will be different to the inlet turbulence level in the rig, where it will be lower, and in the engine (where it will be much higher).

- Tip leakage flows are often poorly positioned. If the number of points in the tip clearance is too low, then the complex physical phenomena that occur here cannot be accurately modelled. However, even with the physics modelled well around the tip clearance region, its mixing with the flow is usually poor. Because there is a concentration of points in the tip clearance region, the tip clearance flow tends to stay there, whereas in reality it moves down and mixes out with the flow.

- Aerofoils analysed here are design aerofoils, not manufactured. Small differences, may lead to aerodynamic changes, particularly in the endwall and tip regions. This is difficult to account for. Also, the real annulus will not be smooth, as it is in the through-flow design, but will have bumps, and gaps where the blade is rotating.

Experimental Testing.

- Validating CFD with experimental data is full of ambiguities. Flows near endwalls and in tip leakage regions will inevitably have more errors inherent in measurements than the flow over the mid-span region. The angles of flows and therefore both total, static, temperature and angle readings will have a variable degree of error in these regions, so care must be taken in comparing data here. Tip wall statics in the rotor and vane exit planes will be affected by the vortices generated by the tip leakage and secondary flows.

- To measure the NGV exit flows, the rotor is moved back, so that the probe can be positioned. This is necessary, but the absence of the rotor introduces a redistribution of streamline curvature, which can affect the flowfield strongly.

- In the early eighties, a paper was published by Wyler [6] on the effects of probe blockages. The paper dealt with the intrusive effects of probes on enclosed and open flows, on subsonic, transonic and subsonic Mach numbers. It states that in transonic and subsonic flows, that the modification of the flow by the presence of a probe in a enclosed space will affect the readings. In the transonic region, a curved bow shaped shock will occur in front of the probe, and a pressure rise occur across it. Therefore, the readings taken by the probe will have some kind of error inherent due to this.

Bearing in mind the above, it is most reasonable to look for accurate prediction of flow features, and consistent predictions.

4.1 Isolated Blade Row Study

4.1.1 JA63

Zero exit angle grid gives better shock capture than the standard grid, where the exit angle follows the flow (see Figure 22). This is due to the better alignment of the mesh with the shocks. The primary flow features are closer to experimental results, especially the exit swirl angles. It should be noted that the wake appears slightly smeared with zero exit angle from the grid, nevertheless it is well defined, [5] reveals that both ONERA and NASA have observed similar results. An interaction exists between the shock and the wake issuing from the adjacent blade. The wake, which is strongly accelerated supersonically, undergoes a strong interaction with the shock, and a severe deceleration. This causes local thickening of the wake, and even separation bubbles. If the number of points in the grid is sufficiently high, then the exit angle of the grid no longer matters, but the number of points necessary for this would be greater than could be run routinely.

Coarser grid solutions do contain all of the flow features (see Figures 6 and 7), though resolution is not as good as with the fine grids. The fact that the gross flow features are predicted implies that there is nothing wrong in using such grids as an initial design tool, where the reduced run times allow rapid optimisation. However, the accuracy of the fine grid profile, for both swirl angle, and total pressure is better for detailed analyses, particularly around the tip region.

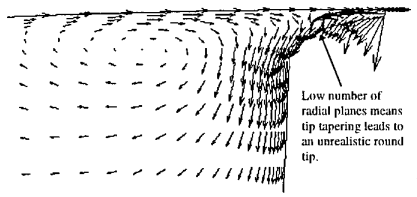

136,000 points

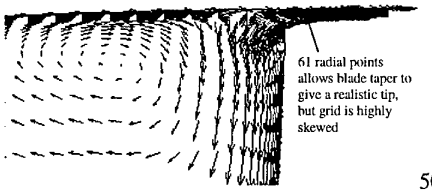

500,000 points.

Figure 6 : Illustration of Improved Tip Clearance Resolution with Increasing Number of Grid Points.

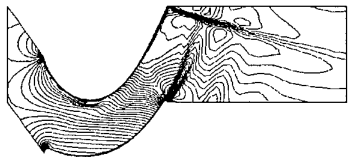

136,000 Points

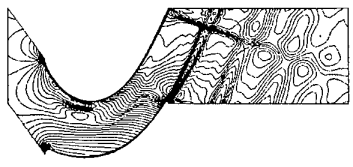

900,000 Points

Figure 7 : Increasing Shock Resolution with Increasing Number of Grid Points - Contours of Rel. Mach Number.

The rotor lift plots (Figure 8) illustrate that the highlift lift distributions are significantly different to the analyses performed at the original design conditions. The design analysis would have used the original design NGV exit profile, whereas the measured has the measured NGV traverse input. There is evidence that indicated that the effect of secondary flows is much stronger on the highlift NGV than on the datum, and this is presumed to account for this. On the suction surfaces of the highlift case, the shocks from the adjacent blade row may be seen, caused by the overall higher Mach number levels present.

The loss levels for JA63 are presented below (Figures 9 and 10). Here, the mass-averaged loss coefficients are defined as :

$$Y_{NGV} = \frac{P_{tin} - P_{exit}}{P_{exit} - p} \quad (1) \qquad Y_{rotor} = \frac{P_{rin} - P_{rexit}}{P_{rexit} - p} \quad (2)$$

where Y is the loss coefficient; P_{tin} is the total inlet pressure to the NGV; P_{exit} is the total exit pressure at the NGV exit plane; p is the static pressure; P_{tin} is the relative inlet pressure at the rotor inlet plane and P_{rexit} is the relative exit pressure at the rotor exit plane. It should be noted that this rotor loss coefficient assumes constant radius, and is not applicable if hade is present.

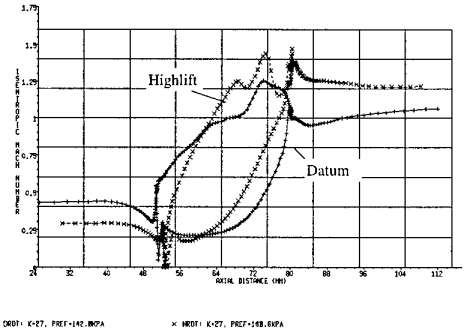

Prediction based on design condition.

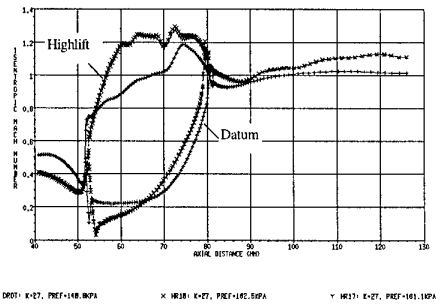

Prediction based on measured conditions.

Figure 8 : Blade Surface Mach Numbers for the Datum and Highlift Rotors - Blade Mid-Section

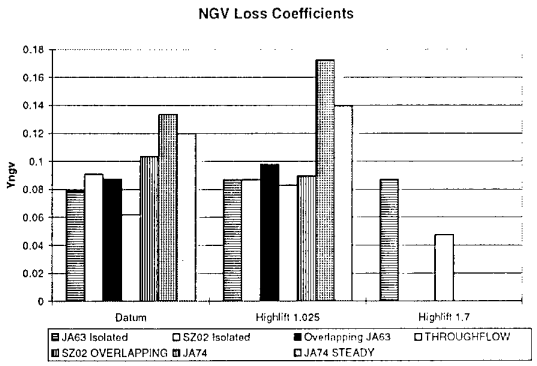

Figure 9 : Pressure Loss Coefficients, Datum and Highlift NGVs.

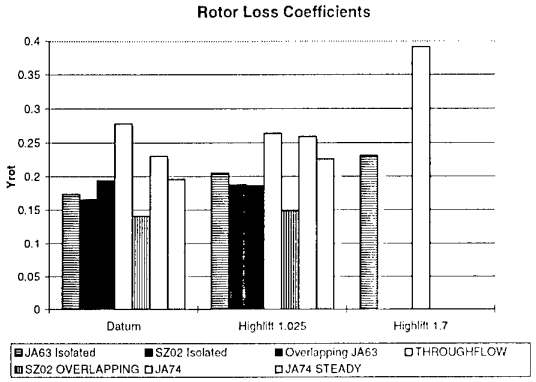

Figure 10 : Pressure Loss Coefficients, Datum and Highlift Rotors.

The highlift NGV is exhibiting a higher loss level than the datum. In the rotor plots, three cases are represented in Figure 10, the datum has tip clearance of 1.42%, the highlift has two tip clearances, 1.025% and 1.7%, representing two area traverses taken. As expected, the largest tip clearance gives the highest loss, indicating the usefulness of these codes for comparative purposes.

The isolated blade row analyses show that the radial profiles compare well to the test results (Figures 11 and 23). The losses predicted on the NGVs indicate that the highlift vane has far more loss on it than the datum, the transition should be identical for these predictions, making these comparisons valid. The extra loss is induced by secondary flow, contour plots (Figures 24 and 25) at the grid exit indicate that there is more turning on the wake than in the datum case. This is also evident in endwall streamlines (Figure 12), where a 'cleaner' aerodynamic design can be seen on the datum. The growth of the boundary layer is smaller, and the passage and contra-rotating horseshoe vortices are weaker. Turning, is quite similar for both builds, it appears from streamlines as if the shape of the leading edge of the highlift NGV is responsible. Comparing the streamline plots at the hub reveals that the highlift NGV's passage vortex starts rolling up much earlier than the datum, and is far stronger in magnitude. On the suction surface, the boundary layer thickens more quickly on the highlift derivative, and would imply that the contra-rotating side of the horseshoe vortex would also be stronger.

On the rotors, the streamlines (Figure 13) reveal that on the hub of the datum, the leading edge separation bubble caused

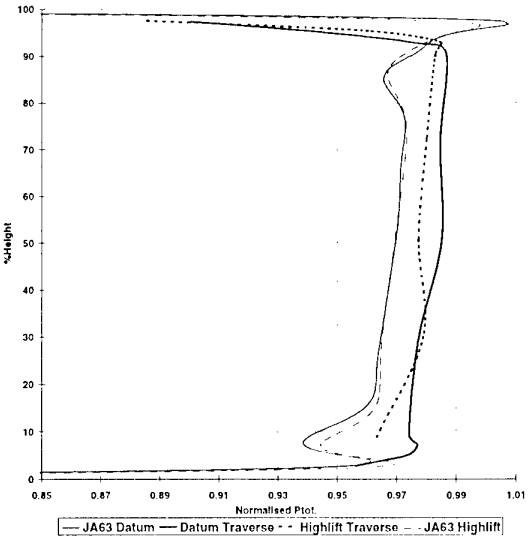

Figure 11 : Radial Variation of Normalised Absolute Total Pressure Ratio - Datum and Highlift NGV Exit Plane (~49mm)

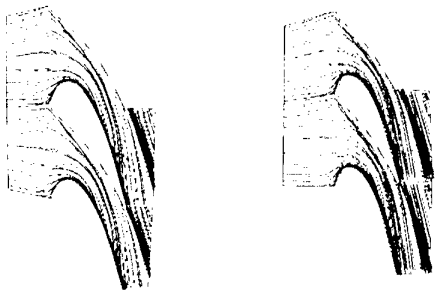

Datum Highlift

Figure 12 : NGV Endwall Streamlines - Hub.

Datum Rotor Hub Endwall Highlift 1.025% Tipcl

Figure 13 : Rotor Hub Endwall Streamlines.

by the endwall flows is relatively small, and the passage vortex appears to roll up with the suction surface contra-rotating horseshoe vortex early and neatly. In the highlift case, the leading edge separation bubble is much larger, it appears that the passage vortex is not merging with the horseshoe vortex, but separating, which implies that the dissipating effect of the counter-vortex will be lost. Such a large separation bubble is indicative of a very strong interaction between the blade and the endwall flows, and will result in raised local shear stress levels, which are due to the

higher stage loading present. Figure 14 shows suction surface vectors, which illustrate the higher secondary flows present on the highlift case, especially on the hub.

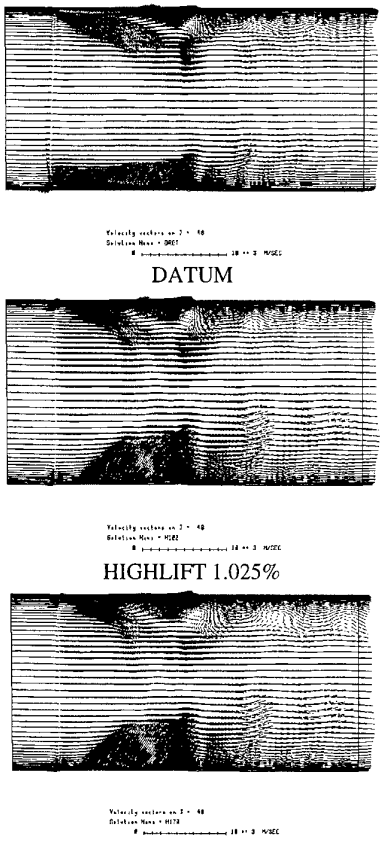

Figure 14 : Vector Diagrams on the Rotor Suction Surfaces.

4.1.2 SZ02

Results of a grid sensitivity study have indicated that the results of SZ02 are fairly grid independent. It follows that a fairly low resolution grid was chosen, however, the present elliptic grid smoothing does not always distribute the grid well where the number of node points is high. There may be benefits associated with finer grids, but points must be distributed precisely. The lift plots revealed a very similar picture to JA63 on both the NGV and the rotors. The loss coefficients reveal that a higher loss is predicted for the datum NGV at the exit plane than the highlift vane, though the overall loss through the vane passage is still lower. On examination of the endwall streamlines, it appears that the hub secondary flows on the highlift NGV are stronger than the datum, but the tip secondary flows (Figure 15), appear weaker than those in JA63 which usually better predicts secondary flows than SZ02. The primary flow radial profiles reveal a closer match between the highlift NGV and experiment, than for the datum NGV and traverse. The total pressure contours at the NGV exit indicate stronger secondary flows at the datum NGV tip, distorting the wake in this region, and weaker flows at the hub, consistent with the above.

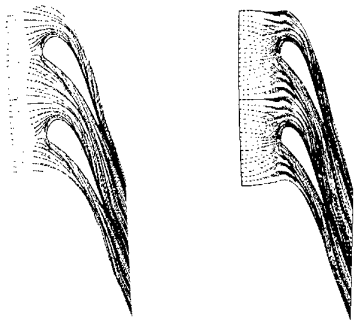

Datum Highlift

Figure 15 : NGV - Endwall Streamlines - Hub

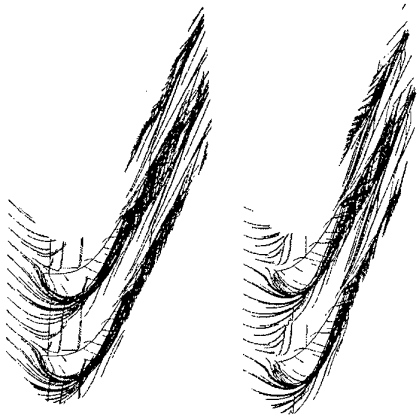

Datum Highlift

Figure 16 : Rotor - Endwall Streamlines - Tip

The loss coefficient plots (Figures 9 and 10) reveal very similar loss levels to JA63. The radial profiles also compare similarly. The endwall streamlines on the rotor paint a consistent picture with JA63, showing the same large separation bubble around the leading edge of the hub rotor section, and the stronger tip leakage vortex (Figure 16) accompanying the 1.42% tip clearance in the datum rotor, compared to the weaker 1.025% vortex modelled in the highlift case. The implicit code gives good results, of a similar quality to the explicit JA63 code, in addition, the effect of cooling holes and films can be modelled in SZ02, whereas they cannot in JA63, SZ02 is a very versatile code, its box grid is particularly useful for modelling novel features, and its ability to calculate heat transfer, is very impotant.

4.1.3 Implications for Design.

For the initial 3D design and skewing of the blade and vane, a relatively coarse mesh in JA63, should suffice, since the gross flow features are modelled. Once a good match has been achieved, then a fine grid analysis will be performed in order to establish if further skewing is necessary, and if flow features and performance are as desired. From the solution, it should be possible to predict whether a blade is going to have greater or less loss than another blade. Novel featues included to improve performance, and heat transfer can be modelled using SZ02. A fine grid analysis revealed that the highlift design had a higher loss both on the NGV and rotor, than the datum. This kind of information allows us to better predict performance in new designs before testing. A close

examination around the endwalls has revealed that the primary source of loss on the highlift NGV is secondary flow loss, and that higher secondary flows on the rotor contribute to the losses caused by the tip clearance. However, it must be remembered that a highlift design is more difficult, since the shape of the blade is constrained by the amount of lift it has to sustain.

4.2 3D Multistage Analysis and Design.

4.2.1 JA63 Multistage Analysis of Datum and Highlift Derivatives.

This is a straightforward adaptation of JA63, but will account for bodyforces and deterministic stresses, and represents a continuous interface plane approach. This has been validated by other Rolls-Royce plc. departments to be better than a modern mixing plane approach. The results in this case are not particularly different from isolated JA63, or a modern mixing plane approach, this might not be surprising, since the magnitude of the deterministic stresses may be fairly small at design point.

The results from the multistage version of JA63 are nevertheless good, and represent a continuous interface plane approach, with results similar to the SZ02 multistage interface plane shown in Figure 19. They do not appear to predict loss levels particularly different from the isolated blade row calculations (Figures 9 and 10), but efficiency predictions are slightly better.

The lift distributions reveal a similar picture to isolated blade row JA63 on the NGV. On the rotors, surface distributions differ slightly at the hub and tip, due to differences in the endwall boundary layer growth. The loss coefficient plots (Figures 9 and 10) show that the highlift NGV has a greater loss than the datum, but the rotor plots imply that the smaller tip clearance (1.025%) resulted in a similar, or slightly more efficient blade. The overlapping grids radial profile predictions are very good (Figures 17 and 18). The absolute swirl angle for the highlift rotor is a particularly impressive match. Endwall streamlines are similar to isolated JA63 predictions, but the highlift rotor with its 1.025% tip clearance, exhibits a weaker tip leakage flow. To validate whether loss calculations are correct, what is really needed is a 1.7% tip clearance prediction for the highlift case. Unfortunately, this run would not converge, and crashed successively. It is surmised that the gradients around the tip clearance became too large to sustain.

4.2.2 SZ02 Multistage Analysis of Datum and Highlift Derivatives.

Only a shrouded solution could be obtained. The problem appears to be in the high initial gradients around the tip leakage region, which are exchanged between blade rows, a problem which is being confronted. Improvement over the isolated blade row solutions is difficult to distinguish, with any comparisons being made difficult by the lack of tip clearance flow. The flow data is continuous at the interface plane (Figure 19). The comparison between the highlift NGV exit flow is impressive, but the datum is worse than in isolated blade row. In isolated blade row too, the solution is worse for the datum NGV, indicating a more complex flow, which it may not be possible to resolve closely using SZ02. High Mach numbers and shocks are inherent, and low secondary flows.

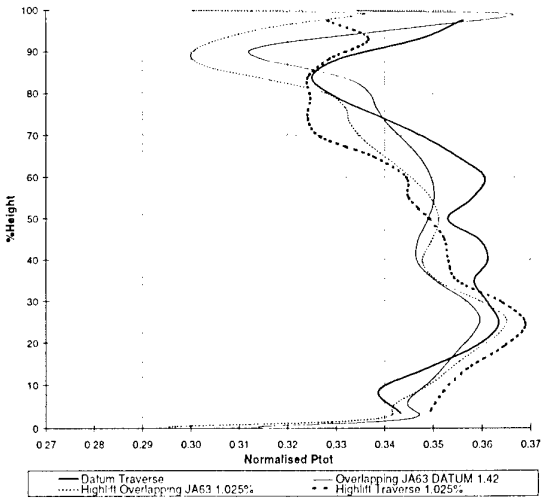

Figure 17 : Radial Variation of Normalised Absolute Total Pressure Ratio - Rotor Close Exit Plane (~111mm)

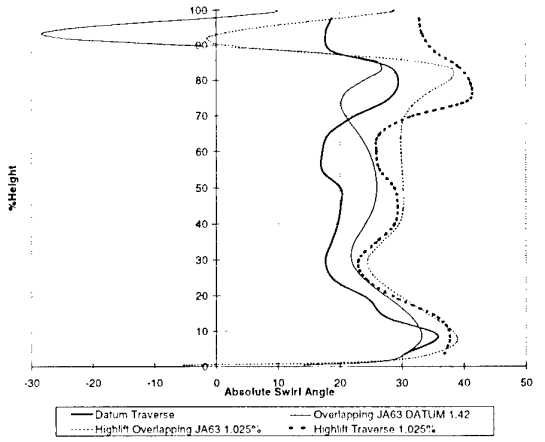

Figure 18 : Radial Variation of Absolute Swirl Angle - Datum and Highlift Rotor Close Exit Plane (~111mm)

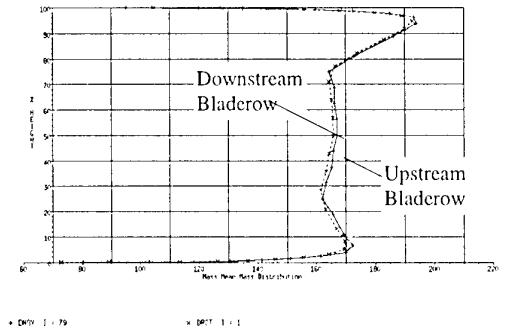

Figure 19 : SZ02 Overlapping Grids Continuous Interface Plane, mass flow distribution.

4.2.3 Multistage Steady with Overlapping Grids and Design

These methods tend to be expensive in memory compared to isolated blade row calculations. However, if considered relative to 3D unsteady calculations, they make very efficient use of memory, making them considerably more practical as a design tool. It is envisaged that these codes will play an increasingly important role in the design of multistage turbines. Convergence problems are common with this kind of modelling, and are linked to the passing of information between blade rows, where the early part of convergence tends to be problematic. The numerical scheme must be robust to cope with the swings in calculated variables.

The deterministic stresses will be small relative to the Reynolds stresses near the design point, and bodyforces, although present, may not significantly affect the solution, unless the unsteady loss is large enough. In turbines it is envisaged that the greatest potential application of such analysis is in the modelling of two or three stage turbines, and in the design of variable cycle engines, where interaction effects are likely to be much stronger. Certainly, the indication from these studies is that the magnitude of the deterministic stresses and the effect of bodyforces in HP unshrouded turbines is small at design point. The dominant effects are clearly the secondary flows and tip clearance.

4.4 JA74

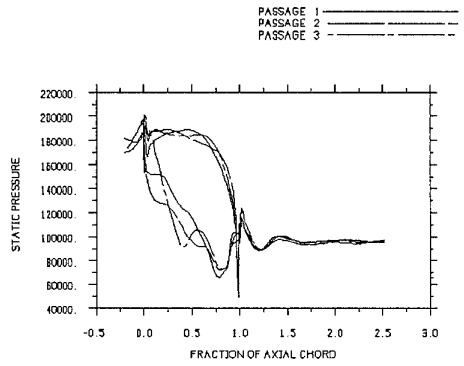

Figure 20 : Datum Mid-Span Unsteady Static Pressure Plots

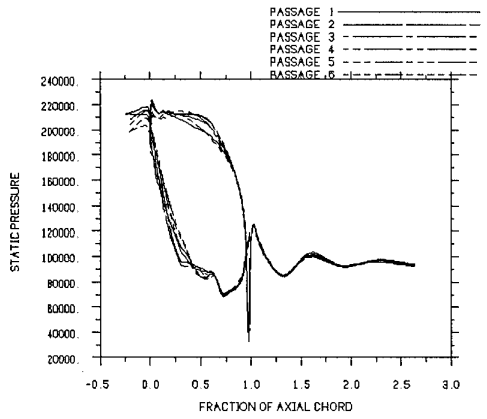

Figure 21 : Highlift Mid-Span Unsteady Static Pressure Plots

JA74's results are generally considered good, but care must be taken to ensure that smoothing is kept low, since numerical losses can be high, and damp out the real losses, particularly in the NGV, where the real losses are generally low compared to rotor losses. Where a tip clearance is present, it is has been found more difficult to keep smoothing levels low, hence NGV losses are overpredicted.

Unsteady phenomena depend on several factors, the most important of which is the ratio of blade numbers. The datum has a greater rotor:vane ratio than the highlift case. The unsteadiness on the datum rotor should be more pronounced. This is predicted by JA74, with the unsteady lift plots (Figures 20 and 21) from the datum solution exhibiting more variation than the highlift rotor. The fact that the datum is more efficient in test than the highlift indicates that the loss generated by these interaction effects is actually quite small. More unsteadiness does not necessarily mean more loss. The effect of the wake passing the rotor on both variants can be seen in the contour plots of entropy Figure 29). Comparisons with steady solutions with the same level of numerical smoothing have indicated that unsteady loss is similar in both variants, and may comprise 10 to 20% of the overall loss. However, this figure may be exaggerated due to loss overprediction, the dominant losses are still secondary flow and tip clearance related.

5.0 CONCLUSIONS

5.1 Isolated Blade Row Analyses

The JA63 and SZ02 codes in isolated blade row form allow a good simulation of the turbine flow field. Coarser JA63 grids (of the order of 130,000 grid points) are used by our designers in initial 3D design, to enable fast, cost-effective design. Once initial design is complete, finer grids can be used to analyse the blade flowfield in detail, and evaluate (comparatively) losses. SZ02 allows more complex geometrical features to be modelled, for example a tip cavity, or non-axisymmetric endwall, due to its versatile box grid. SZ02 also allows the calculation of heat transfer, which is imperative in the engine environment, and has the potential to represent film cooling and real annuli features, which should improve our simulation of the turbine environment.

5.2 Multistage Steady with Deterministic Stresses and Bodyforces

These multistage codes hold real potential in the field of turbine design. Unsteady calculations are still too expensive to contemplate as routine design tools, these methods allow us to predict the time average of the unsteady flow by averaging out the unsteady interaction effects. It is envisaged that they will play an increasingly important role in the design of multistage turbines. There are plans to include the modelling of real annuli, with non-uniformities present, tip and shroud leakage effects. These should improve our modelling capability, particularly in the boundary layer growth, and hence prediction of secondary flows. However, the accuracy of such calculations will be constrained by the limitations of turbulence and transition modelling for many years to come, as will all CFD methods.

5.3 Unsteady Study

Further studies are required to reduce numerical losses with a tip clearance present, so that better time accurate solutions can be obtained. Computationally, JA74 is significantly quicker than other true unsteady codes currently available, and offers rapid familiarisation, development and application, however, run times may still be long for multistage calculations, and are greater than could be run as part of routine design. Though average unsteadiness may be a reasonable assumption to make in stage prediction, only true unsteady codes will enable us to understand the loss mechanisms, and their origins.

5.4 Blading Analysis

Analysis of the datum and highlift NGVs implies that the highlift NGV has more loss, which is a result of stronger secondary flows at both the hub and tip. It appears that the shape of the endwall sections' leading edges are at least partly responsible. The stronger highlift NGV secondary flows may have resulted in some mismatch between rotor and NGV, since analyses including the traverse results for the NGV, rather than the design intent give significantly different lift distributions. The highlift rotor has higher losses than the datum, which are due to both stronger secondary flows, and consequently more susceptibility to tip leakage. It is secondary flow and tip leakage losses that dominate in the HP unshrouded turbine environment, unsteady losses are not inconsequential, but appear to be much smaller in magnitude.

5.5 General Summary

The work indicates that in the design of highlift HP turbines, secondary flow reduction is of prime importance. Tip leakage is a major form of loss, and strategies must be adopted to minimise its detrimental effects on performance. The isolated blade row predictions should enable us to do this in design, and since run times are short, should enable fast 3D design. The multistage steady tools will improve our design capabilities in multistage and variable cycle engine turbines. They will allow us to include interaction effects in our predictions, and to take them into account in our design process. The unsteady codes, like JA74 will enable us to better understand the interaction mehanisms, and in so doing establish strategies to reduce the losses associated with them.

6. ACKNOWLEDGEMENTS

This paper was generated through work funded by the Ministry of Defence. The authors gratefully acknowledge the permission of Rolls-Royce plc. to publish it, and would like to thank their colleagues in Turbines and Aerothermal Methods for their valuable contributions towards its content. The views expressed within this paper are entirely those of the authors, and do not necessarily represent those of Rolls-Royce plc.

7. REFERENCES

1. Thermodynamics and Fluid Mechanics of Turbomachinery, vol II.
A.S. Üçer, P. Stow and Ch. Hisch
NATO ASI Series.

2. Development and application of a multistage Navier-Stokes solver. Part 1: Multistage modelling using bodyforces and deterministic stresses.
C.M. Rhie, A.J. Gleixner, D.A. Spear, C.J. Fischberg, R.M. Zacharias
ASME report 95-GT-342.

3. Development and application of a multistage Navier-Stokes solver. Part II: Application to a high pressure compressor design.
C.R. Lejambre, R.M. Zacharias, B.P. Beiderman, A.J. Gleixner, C.J. Yetka.
ASME report 95-GT-342

4. An Experimental Investigation of Steady and Unsteady Flow Field in an Axial Turbine
M. Zaccaria and B. Lakshminarayana
NASA Contractor Report 4778

5.0 Validation du code "CANARI" par le calcul de l'Ecoulement Tridimensionnal Turbulent dans un Distributeur de turbine.
Béatrice ESCANDE et Laurent CAMBIER, O.N.E.R.A..
AGARD 1991

6.0 Probe Blockage Effects in Free Jets and Closed Tunnels
J.S. Wyler
Journal Of Engineering Power

7.0 Recent Progress in the Understanding of Basic Aspects of Secondary Flows in Turbine Blade Passages.
C.H. Sieverding
ASME report 84-GT-78

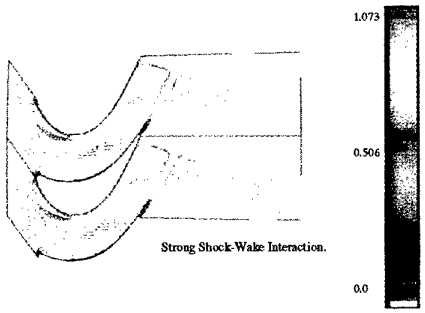

Figure 22 : Illustration of Shock Resolution Possible with Fine Zero Exit Angle Grids - Relative Mach No. Contours.

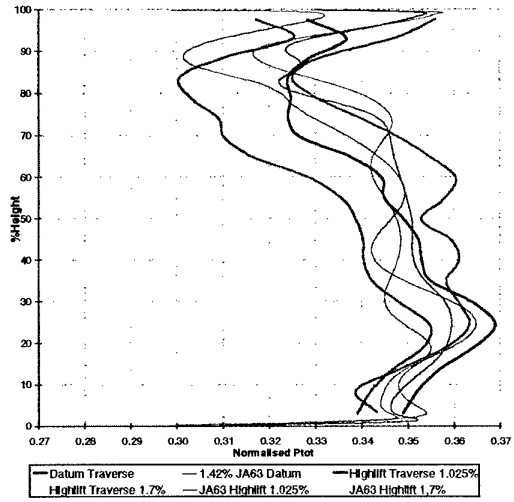

Figure 23 : Radial Variation of Normalised Absolute Total Pressure Ratio - Datum and Highlift Rotor Close Exit Plane (~111mm)

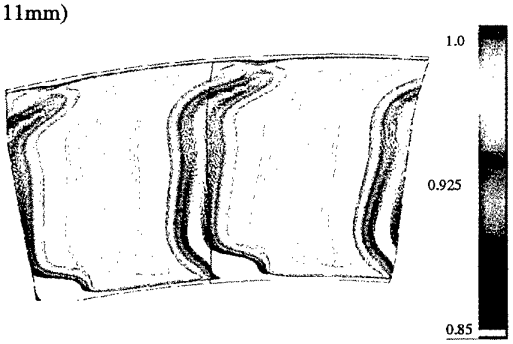

Figure 24 : Total Pressure Contours at the Datum NGV Exit Plane (49mm) - Scale Inlet Pressure to 15% loss

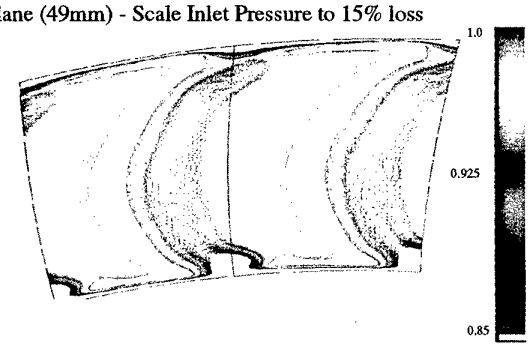

Figure 25 : Total Pressure Contours at the Highlift NGV Exit Plane (49mm) - Scale Inlet Pressure to 15% loss

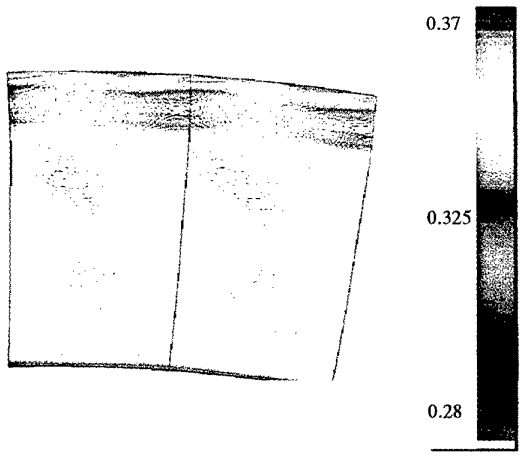

Figure 26 : Relative Total Pressure Contours at the Rotor Close Exit Plane (111mm) - Tip Clearance 1.42%

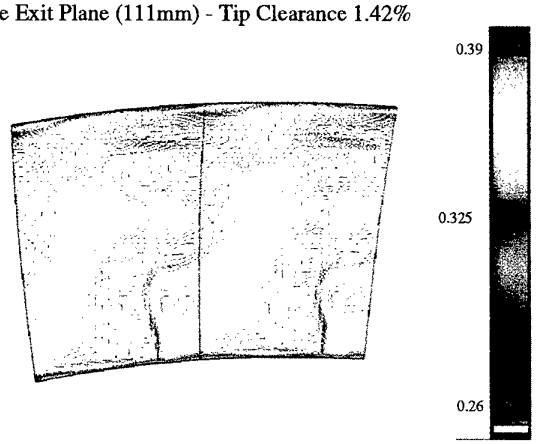

Figure 27 : Relative Total Pressure Contours at the Highlift Rotor Close Exit Plane (111mm) - Tip Clearance 1.025%

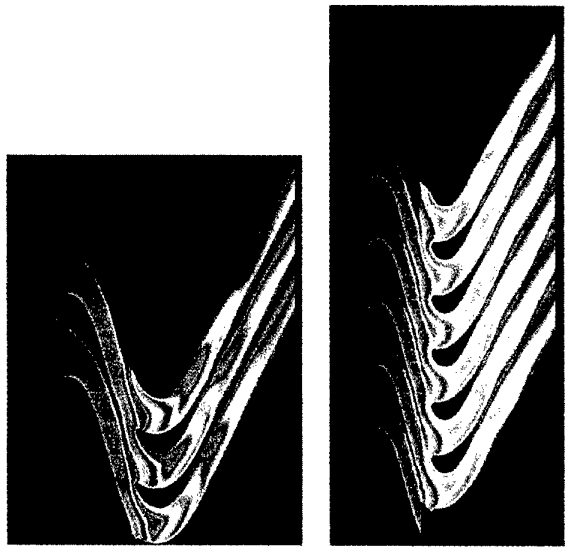

Figure 28: Entropy Contours Illustrating the NGV Wake Motion through the Rotor Passage.

Automatic Three-Dimensional Cyclic Crack Propagation Predictions with Finite Elements at the Design Stage of an Aircraft Engine

G. Dhondt
MTU Motoren- und Turbinen-Union München GmbH
Postfach 50 06 40
D-80976 München
Germany

1. SUMMARY

At MTU a method was devised to perform linear elastic three-dimensional (3-D) mixed-mode cyclic crack propagation calculations with the finite element method (FE) in a fully automatic way. The core of the method consists of an algorithm to modify an existing mesh consisting of 20-node 3-D brick elements to accommodate an arbitrarily shaped crack. Starting from the initial crack, the mixed-mode stress intensity factor (K) distribution is determined along the crack front and a crack increment is calculated leading to a new crack shape. This procedure is repeated about every 100 cycles until the desired crack length has been reached. Use of the superelement technique allows to perform more than 100 iterations within 24 hours for a realistic engine component.

2. INTRODUCTION

Loading the materials up to their limits significantly increases the danger of undetected crack initiation and propagation. In the past, numerical cyclic crack propagation calculations were nearly impossible due to the complicated geometry of aircraft engine components. One of the major obstacles is the modeling of the 3-D crack geometry. Indeed, since the actual component geometry nearly invariably leads to mixed-mode loading, an initially plane crack will grow out of the plane and assume an arbitrary shape with a crack front which constitutes an arbitrary 3-D curve. Generating a mesh which takes this actual 3-D crack shape into account is a formidable task. Repeating this task about every 100 cycles is virtually impossible. Here, only an automatic mesh generating procedure can be successful.

Recently, Riddell *et al.* [1] published an interesting comparison between existing crack propagation software. They considered NASA/FLAGRO [2-3], NASCRAC [4-5] and FRANC3D [6-7]. Only in-plane propagation was analyzed. Both NASA/FLAGRO and NASCRAC use a library of K-solutions or influence functions and model the crack front as elliptical quadrants or as straight lines. Thus, applications are limited to cases for which K-solutions are available in the data base. Although it was discovered that modeling the crack shape more accurately than by use of elliptical forms does not significantly improve the solution unless better crack propagation laws are used (e.g. including crack closure), this conclusion might apply to relatively simple specimen geometries only. The engine components treated in this article show that the crack front frequently significantly deviates from an elliptical or straight form. FRANC3D is a genuine 3-D boundary element code not restricting the crack geometry nor the loading, and is as such comparable to the methods proposed here. In the author's opinion, the boundary element method can be a valuable and attractive alternative to the finite element method for cyclic crack propagation calculations. Yet, engineering software is highly dominated by finite element codes for which a huge amount of experience is available which clearly hampers the introduction of alternative numerical procedures. The results in [1] concerning FRANC3D look very promising, although no mixed-mode problems were analyzed.

Another commercial software for mixed-mode crack propagation applications is ZENCRACK [8-9]. It operates on an existing finite element mesh and introduces the crack by replacing one or more brick elements by crack-blocks. There are straight crack blocks and quarter elliptical crack blocks. In [8] a mixed-mode crack propagation calculation is presented for a quarter circular crack under combined tension and torsion. The results are very encouraging, though it looks as if crack propagation is limited to the initially cracked elements.

The algorithms presented here [10-13] assume that a 3-D finite element mesh consisting of 20-node brick elements exists for the uncracked structure. In each iteration this mesh is automatically modified to accommodate the actual geometry of the crack. The crack shape can be fully arbitrary. Then, the K-distribution and a crack propagation increment are calculated using some generic finite element software and crack propagation law respectively. At that point a new crack front is established and the procedure starts over again. Compared to existing crack propagation software the method excels due to the generality of the crack propagation procedure (the propagation is dictated by the prevailing stress fields only) and its applicability to existing finite element meshes of the uncracked structure.

3. DESCRIPTION OF THE METHOD

One of the most difficult tasks in automatic crack propagation calculations is the insertion of the crack shape established at any iteration during the calculation into a 3-D mesh of the structure. The present method assumes that the uncracked structure has been meshed by means of 3-D 20-node brick elements. Apart from the element type no restrictions apply, i.e. the mesh may have been made at a time when crack propagation calculations were not an issue yet. The insertion of an arbitrarily shaped and arbitrarily oriented nonplanar crack is performed in two steps: first, the crack shape is inserted in the mesh. Then, the crack front is modeled.

The crack shape surely cuts a significant number of elements of the existing mesh. First, all elements being cut are identified. Then, they are cut and remeshed again using 20-node brick elements, taking care that the crack shape is tangent to the new elements [13]. This cutting procedure is very general and investigations have revealed its suitability for general 3-D meshing problems.

After the cutting, the crack front is inserted. Again, all elements cut by the front are identified and remeshed. At the crack front collapsed quarter point elements are inserted to generate the right stress and strain singularities. Using this mesh, the K-distribution along the crack front can be determined using some generic finite element software.

Paper presented at the RTO AVT Symposium on "Design Principles and Methods for Aircraft Gas Turbine Engines", held in Toulouse, France, 11-15 May 1998, and published in RTO MP-8.

By means of a crack propagation law (e.g. the Paris law) the crack propagation due to N cycles can be determined. During these N cycles the K-values are assumed to be constant. A large N reduces the amount of iterations needed to obtain a given crack propagation, but it also reduces the accuracy. On the other hand, it is unrealistic to make a finite element calculation every cycle. A good way to choose N is such that the maximum crack propagation along the crack front within the increment at stake does not exceed a given amount, e.g. 50 μm allowing N to vary from iteration to iteration. In this way, 100 calculations lead to a total crack propagation of about 4 to 5 mm. This procedures is more stable than keeping a constant N for all iterations since in the latter case the distance between the crack fronts continuously increases due to the increasing K-values as the crack length increases. This can eventually lead to unstable crack fronts. Once N is determined, the new crack front can be determined and the procedure starts over again.

Use of the superelement technique reduces the computation time drastically. To this end all elements not involved in the cutting procedure during the complete iteration process are collected into one superelement. Application of this procedure to models of real engine components containing 100,000 degrees of freedom or more leads to a reduction of the execution time by a factor of 40 or more.

4. CRACK IN A LOCKING PLATE SLOT OF A DISK

The procedure is first illustrated by means of the aircraft engine disk segment shown in Fig. 1.

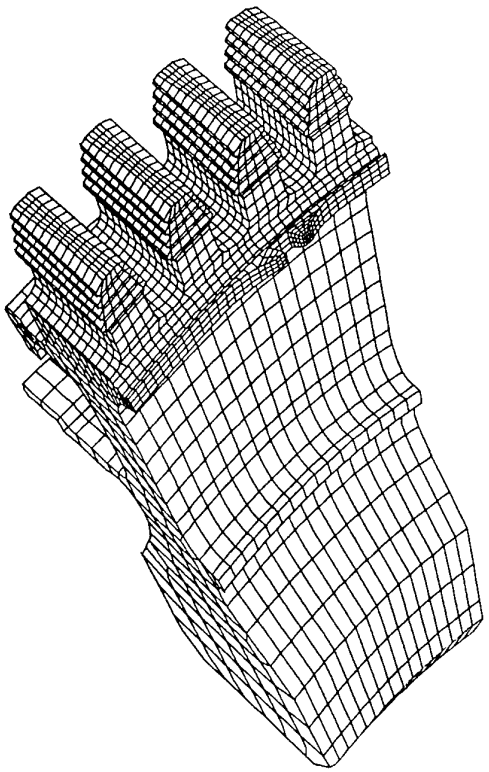

Figure 1. Aircraft engine disk segment

The disk contains fir tree notches in the rim area to insert the blades. These are kept in place by a circumferential locking plate fixed by rectangular locking plate slots, one of which is visible under the second disk lobe from the right in Fig. 1 (a disk lobe is the part of the disk between two fir tree notches). Due to the sharp edges of the locking plate slot the initiation of cracks in that region cannot be excluded. In this context, crack propagation calculations were performed for an assumed part circular crack along the upper left edge of the slot.

The mesh of the disk was given and consists of a fine mesh on top and a coarser mesh in the bore region, connected by multiple point constraints. A stress analysis revealed that the stress state along the initial crack was largely mode-I, leading due to the particular local geometry of the mesh to interelement crack propagation. Thus, mesh cutting was not necessary and the mesh modification was limited to the insertion of the crack front. Furthermore, under mode-I loading the plane crack remains plane and no crack shape curvature had to be taken into account. The mesh modifications at some intermediate stage is shown in Fig. 2. Notice the typical spider web structure around the crack front.

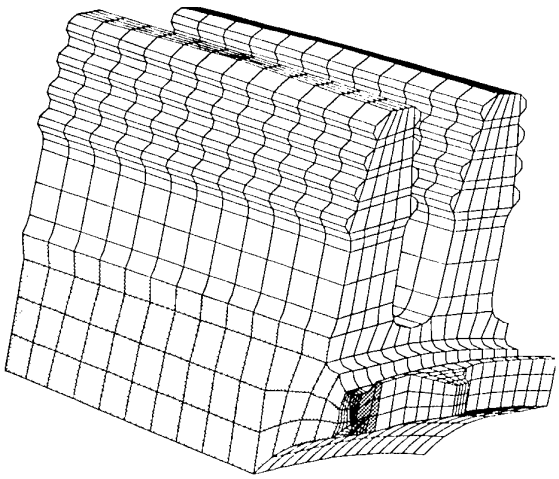

Figure 2. Details of the cracked locking plate slot

Figure 3 shows the evolution of the crack front during the crack propagation calculations. The maximum distance between two successive crack fronts is 50 μm. This guarantees the stability of the calculations. During the calculations it was observed that K along the lower boundary in Fig. 3 is relatively constant, whereas the K-values along the upper boundary decrease sharply at the start of the calculations to recover only at the end of the calculations. Thus, crack propagation is much slower in the notch at the top boundary (leading to a locally higher crack front line density) than along the lower boundary.

To check the accuracy of the finite element prediction, a crack propagation test was performed on the disk. It yielded 3500 cycles between the crack front positions denoted by an arrow in Figure 3. Figure 4, which shows the number of cycles as a function of the maximum crack length along the crack front, predicts 2800 cycles which is on the conservative side. This is reasonable since the crack propagation for this specific material exhibited some scatter and, therefore, the crack propaga-

tion law used in the numerical calculations was taken on the conservative side. The crack shape observed in the test fitted the predicted form very well.

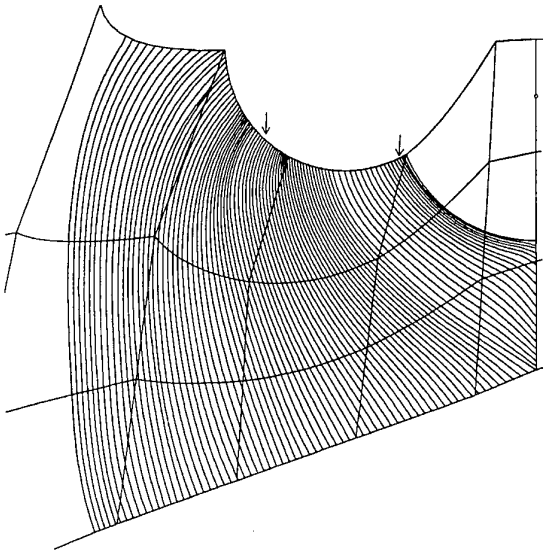

Figure 3. Crack propagation at the locking plate slot.

For most crack propagation calculations the number of cycles per crack length increment decreases as the crack propagates, since in general K increases for increasing crack length. This is not the case in Figure 4, since a constant K was observed along the lower edge of Figure 3. This also reveals the need for calculations with the real engine part geometry and the limits of textbook solutions.

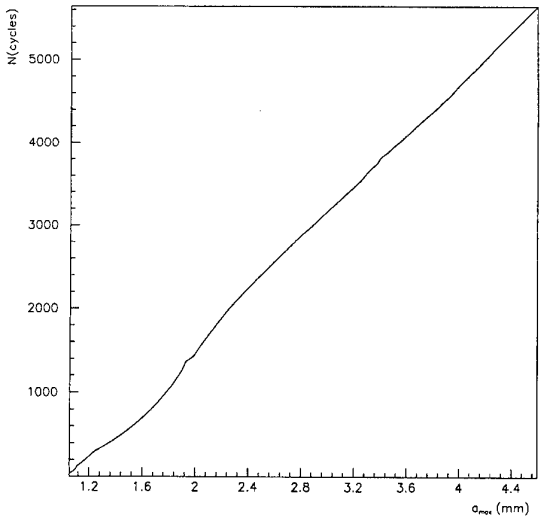

Figure 4. Cycles versus maximal crack front radius.

5. CRACK IN A TURBINE BLADE PLATFORM

The next example deals with a crack propagation calculation in a turbine blade platform. The mesh for the turbine blade and platforms is shown in Figure 5. The blade and platforms were meshed independently and are connected by means of multiple point constraints.

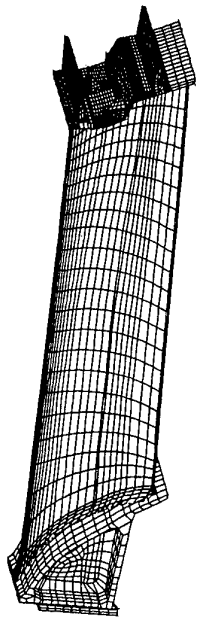

Figure 5. Turbine blade mesh.

Concern was expressed whether the relatively sharp corners in the upper platform could lead to propagation of initial cracks. To check this, a quarter circular initial crack was assumed at the top edge of the upper platform between the two gray element layers in Figure 6 (arrow denotes initial crack location).

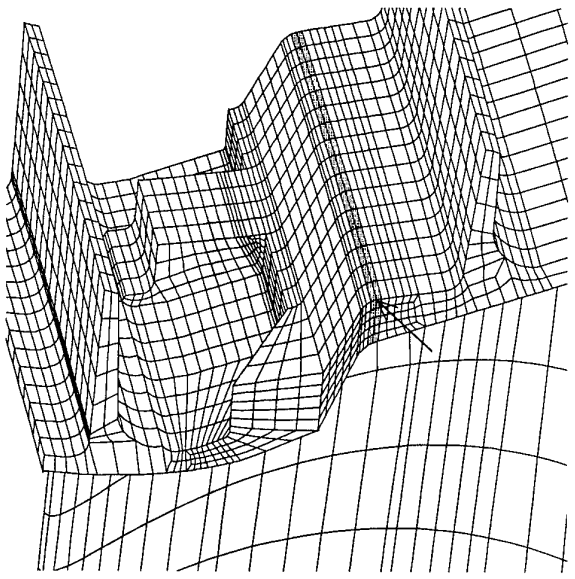

Figure 6. Initial crack location.

The stress field at the initial crack due to the centrifugal forces and thermal loads was essentially mode I, so the crack stays in its plane during the calculation. This means that here too the crack shape does not cut the elements of the original mesh, and only the crack front has to be inserted. The crack front during crack propagation is shown in Figure 7.

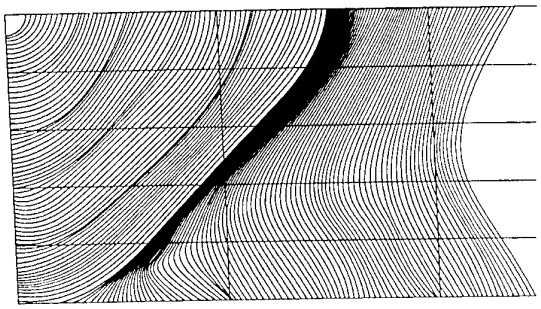

Figure 7. Crack propagation in the platform.

The upper and lower lines in Figure 7 are the upper and lower boundary of the upper platform. The crack starts as a quarter circular crack in the upper left corner of the figure and transforms into a slightly flatter equilibrium configuration half way through the platform thickness. Once it reaches the lower left corner of the platform the quarter circular form is no equilibrium configuration any more and the crack rapidly changes its shape into a slightly indented through crack. This is realized by a significant increase of the K-values at the lower boundary of the platform and a similar increase of the crack propagation rate. At the upper boundary the K values do not change and neither does the propagation rate. Here it should be emphasized that in Figure 7 and similar figures in the present article the maximum distance between two fronts is kept constant, and NOT the number of cycles. A higher line density means that the K-distribution along the crack front is not uniform and that the crack propagation rate along this front is higher where the line density is lower. Thus, the higher line density along the upper boundary in Figure 7 means that the crack propagation rate there is lower than at the lower platform boundary of the SAME crack front lines. This representation does not allow for a propagation rate comparison between different front lines, only along one and the same front line.

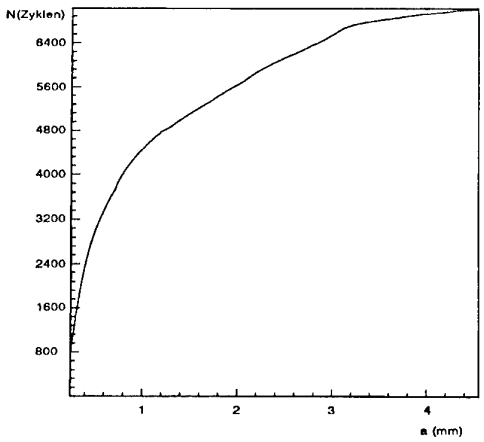

Figure 8. Cycles versus maximal crack length

The phenomenon of changing crack front equilibrium configurations is very interesting and frequently occurs when the crack crosses a sharp corner. Another nice example is given in [12]. It is one of the highlights of the present method that the crack shape is not prescribed. To the contrary, the shape establishes itself during propagation in equilibrium with the prevailing stress fields.

Figure 8 shows the number of cycles versus maximal crack length. Since the K-values continuously increase during propagation the number of cycles per unit crack increment decreases as the crack propagates. This curve is also very familiar from other crack propagation calculations. However, Figure 4 already demonstrated that this phenomenon is not self-evident and really depends on the local stress fields. Tests on the blade yielded a crack propagation rate of about 500 cycles/mm at the crack length of 1 mm, which is about the same order of magnitude as the curve in Figure 8.

6.CRACK IN THE BLADE ROOT NOTCH OF A DISK

In this section the disk segment of Figure 1 is revisited. This time, crack propagation is analyzed in one of the fir tree notches in the rim area of the disk. The disk lobes are not parallel to the disk axis. However, because of the stress field it is anticipated that cracks will grow in a plane containing the disk axis. Such a plane is not parallel to the mesh and thus the mesh has to be cut.

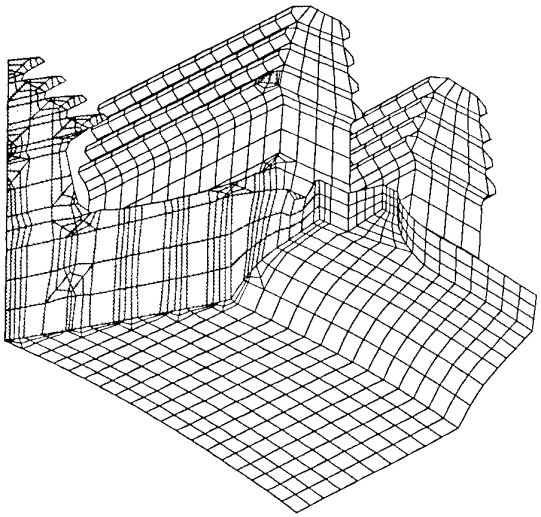

Figure 9. Crack plane before smoothing.

To this end all elements intersected by the crack plane were determined and remeshed to accommodate the plane. The mesh after cutting is shown in Figure 9. All new elements adjacent to the crack plane are genuine 20-node brick elements. However, some are rather small or long and narrow. Therefore, a smoothing algorithm was devised to improve the shape of these elements. The algorithm is based on a weighted Laplace smoothing and is described in detail in [13]. In general, a couple of smoothing iterations are needed to get satisfactory results. Application of the algorithm on the mesh in Figure 9 yielded Figure 10. Nearly all elements have a much better shape now, except a couple of elements in highly constrained regions, such as the fir tree area. However, this area is in the present context not relevant.

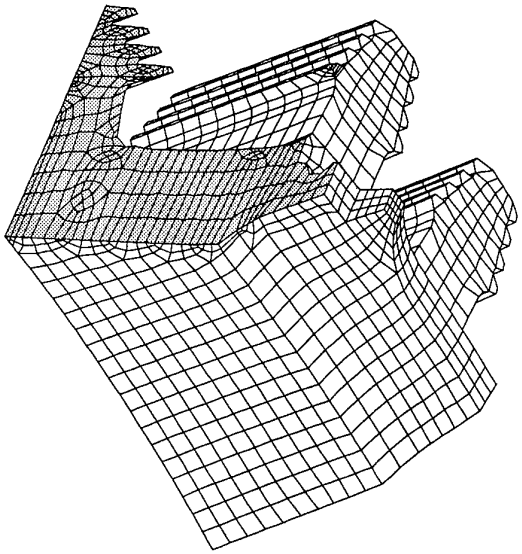

Figure 10. Crack plane after smoothing.

A small half circular crack was introduced in the fir tree notch (Fig. 11), and its propagation was calculated. Due to the relatively smooth stress field no unexpected phenomena occured. the half circular crack takes a somewhat flatter shape due to the stress gradient in the notch. The crack propagation is smooth and regular.

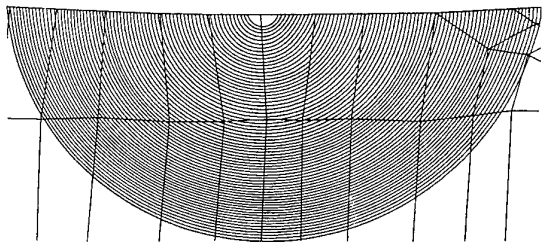

Figure 11. Crack propagation in the fir tree notch.

A similar crack was observed in tests. Between a crack length (radius) of 0.92 mm and a length of 2.6 mm 5300 cycles were counted. This agrees very well with the cycles predicted by the simulation, which yielded 5200 cycles. The curve expressing the number of cycles versus crack length (Figure 12) takes the usual square root shape.

This example differed from the previous ones in that the crack plane had to be introduced by cutting the mesh of the uncracked structure. However, the cutting is fully automatic and does not pose any restrictions on the mesh of the uncracked structure. Therefore, the present technique allows for a fast evaluation of the propagation of initial cracks, no matter their location and orientation. Thus, checking critical areas at a design stage for problems due to the propagation of microcracks is made affordable.

Since crack propagation in the disk notch region was in-plane due to the prevailing mode-I stress state, it is still not the most general case. This is the subject of the next section.

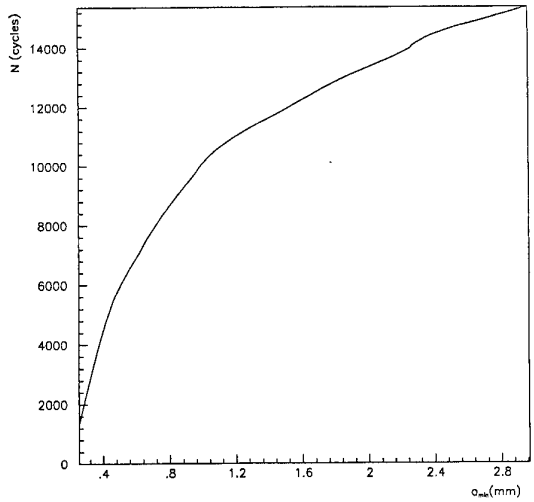

Figure 12. Cycles versus crack length for crack propagation in the fir tree notch.

7. MIXED-MODE CRACK PROPAGATION IN A 3-POINT BENDING SPECIMEN.

In the present section a genuine mixed-mode crack problem is treated. The geometry and loading correspond to a 3-point bending specimen, which is basically a beam-like specimen supported at its both ends and loaded by a point force in the middle. A plane initial crack with a straight front is introduced, containing the center point of the beam and making an angle of 45° with the midplane between the supports. The nonzero angle ensures the presence of mode II and mode III. The specimen height, length between the supports and thickness are 60 mm, 240 mm and 20 mm respectively. The initial crack has a depth of 20 mm and a maximum crack increment of 200 μm was defined. The mesh for the original crack configuration is shown in Figure 13. Figure 14 gives a close-up view of the crack tip region.

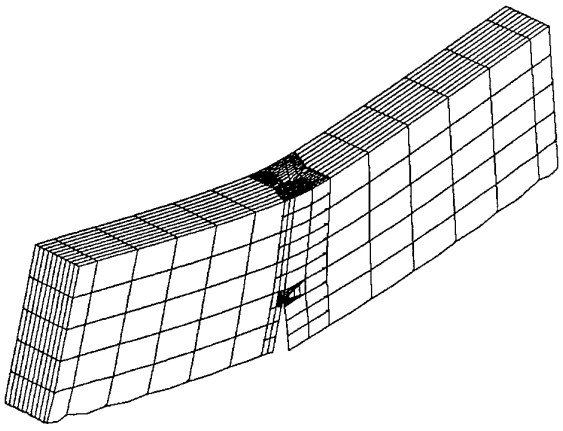

Figure 13. Mesh of the initially cracked structure

Several additional problems are caused by the presence of Mode II and mode III.

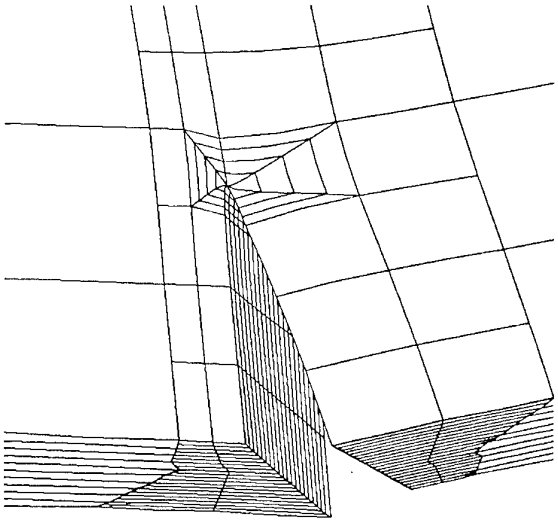

Figure 14. View of the crack tip region.

First of all, not all finite element software is able to calculate K_{II} and K_{III}. Therefore, an algorithm was devised to determine these values from the stresses in the nearby superconvergent reduced integration points. Detailed analyses [14] have revealed that this method yields reliable results.

Next, a crack propagation law and data are needed to calculate a propagation increment. The law should give information not only on the size of the increment but also on its direction. Indeed, due to mixed-mode the crack does not stay in its initial plane. Several criteria exist to determine the propagation direction and a thorough examination [15] has shown that the predictions are not all that different. In the present example the strain energy density criterion of Sih was used. The size of the crack propagation increment is another difficulty. As a first approximation an equivalent K-factor was determined which was subsequently used in the Paris mode I crack propagation law of the material concerned. For the present example the numerical values of the increment size were not so important, since only a qualitative evaluation of the method was envisaged. However, for future calculations it is clear that relevant crack propagation data are a prerequisite for the complete calculation to make sense.

Another problem constitutes the geometric description of the ensuing crack shape. Theoretically, the crack can take an arbitrarily curved shape and consequently a mathematical description is nearly impossible. In the present implementation a triangulation of the crack shape was deemed most suitable because of its flexibility, simplicity and availability. Assuming that the initial crack is triangulated by some commercial software (any good finite element preprocessor will do this job) or software available in the literature [16], each crack propagation increment is easily triangulated too, yielding a complete triangulation of the instantaneous crack shape. Furthermore, the cutting routines mentioned in section 3 are able to deal with any cutting shape for which a triangulation is available.

Finally, the problem of the finite dimensions of the crack shape arouse. So far, the cutting routines cannot handle cutting shapes which stop somewhere in the middle of a structure. Thus, the triangulated crack faces have to be extended in a synthetic way beyond the crack front for the cutting procedure to work. The way the shape is extended is immaterial, as long as the crack shape maintains a C^0 continuity. Appropriate extension routines were written, but the author hopes to be able to discard the need for such an extension in the near future.

Once the extension is obtained, the usual procedure applies: the structure is cut, the cut elements are replaced by new elements tangent to the crack shape. Subsequently, the crack front is introduced and the K-factors are calculated along the front. The crack propagation law yields a crack increment, the K-factor is assumed to stay constant during so many cycles as needed to obtain a predefined maximum propagation increment, and a new crack front is determined. The crack increment is triangulated and a new iteration, starting with the extension of the new crack shape, can start.

In total 70 iterations were performed yielding a total crack propagation of about 8 mm in height direction. The final crack shape is shown in Figure 15.

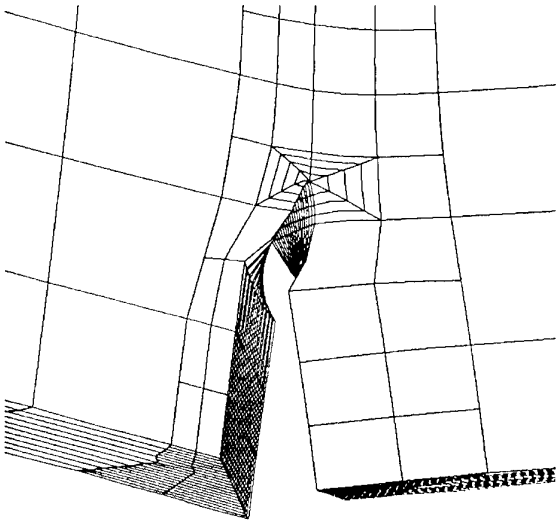

Figure 15. Crack propagation after 70 iterations.

To explain this crack propagation pattern, it is worthwhile to look at the K-distribution along the initial crack front as shown in Figure 16. The s-coordinate is the local distance along the crack front. The K_I values are symmetric with respect to a plane cutting the thickness in half and reach a maximum in the middle. The K_{II} values are antisymmetric with respect to the midplane and reach values at the free boundary of the same order of magnitude as K_I. Disregarding K_{III} for now, this leads to a strong mixed-mode I-II state at the free boundary transforming into a pure mode I state in the midplane. Since K_{III} does not occur in the Sih-criterion, this information indicates that the crack will curve strongly at the free boundary, whereas no curving will be noticed in the midplane. This agrees with our intuition and experimental evidence, indicating that the initial crack will try to grow towards the midplane between the supports, thereby acquiring a pure mode I state. It results in a twisted crack propagation surface as if a torque were applied to the crack. The K_{III} values are relatively constant and play a role in the determination of the crack increment size only. The K-distribution in Figure 16

agrees very well with calculations performed by Buchholz *et al.* for the same geometry and loading [7] using a virtual crack closure integral method.

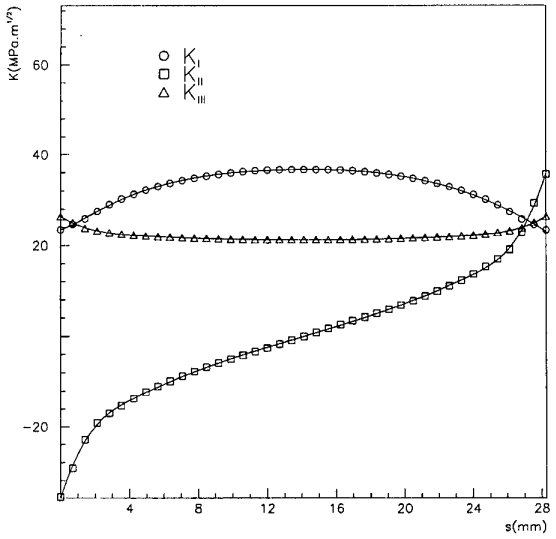

Figure 16. K-distribution along the initial front.

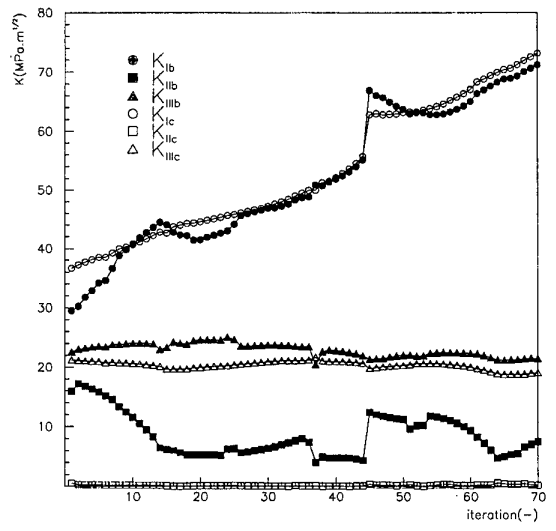

Figure 17. K-values at the center (c) and near the boundary (b) of the crack front during propagation.

Figure 17 shows how the K-values change during crack propagation. Mode I basically evolves into the dominant mode. This is partly due to a drastic increase in K_I and partly due to a slight decrease of K_{II}. Both effects lead to a decrease of the K_{II}/K_I ratio, and thus to a decrease of the crack curvature. The local increase of K_I and K_{II} near iteration 45 is probably due to the transgression of the complete crack front of a row of element boundaries of the uncracked mesh leading to a drastic change of the cracked mesh and has to be discarded. This is relatively obvious for mode I. Whether this applies to the complete K_{II} increase between iteration 45 and 60 is not obvious and requires further analysis. Finally, it is observed that K_{III} does not change significantly during propagation.

All these observations explain the curved crack propagation in Figure 15. The initial crack curves very strongly at the free surface, at each surface in another direction, leading to a final crack front which makes a smaller angle with the midplane between the supports. In fact, after 70 iterations the angle has decreased from 45° to 22°.

8. CONCLUSIONS.

The examples in the previous sections have shown that the present method is a powerful tool to predict the propagation of an arbitrarily shaped and oriented initial crack in a virgin component for which only an uncracked mesh with appropriate boundary conditions and loading are available. This is especially attractive for calculations at the design stage of a component, where it allows for a fast evaluation of fracture critical locations.

REFERENCES

1. Riddell, W.T., Ingraffea, A.R. and Wawrzynek, P.A.,"Experimental Observations and Numerical Predictions of Three-Dimensional Fatigue Crack Propagation", Eng. Fract. Mech., 1997, 58(4), 293-310.
2. Fatigue Crack Growth Computer Program NASA / FLAGRO Version 2.0 Structures and Mechanics Division, NASA/Lyndon B. Johnson Space Center, Houston, TX, 1992.
3. Forman, R.G., Shivakumar, V., Newman, J.C. Jr, Piotrowski, S.M. and Williams, L.C., "Development of the NASA / FLAGRO Computer Program". In Fracture Mechanics: Eighteenth Symposium, ASTM STP 945, ed. D.T. Read and R.P. Reed, American Society for Testing and Materials, Philadelphia, PA, 1988, 781-803.
4. NASCRAC User's Manual. Failure Analysis Associates, Palo Alto, CA, 1989.
5. NASCRAC Theory Manual, Failure Analysis Associates, Palo Alto, CA, 1989.
6. Wawrzynek, P.A., Martha, L.F., and Ingraffea, A.R., "A Computational Environment for the Simulation of Fracture Processes in Three Dimensions". In Analytical, Numerical and Experimental Aspects of Three Dimensional Fracture Processes, ed. A.J. Rosakis et al., ASME AMD-Vol 91. ASME, New York, 1988, 321-327.
7. Sousa, J.L., Martha, L.F., Wawrzynek, P.A. and Ingraffea, A.R., "Simulation of non-Planar Crack Propagation in Three-Dimensional Structures in Concrete and Rock". In Fracture of Concrete and Rock: Recent Developments, ed. S.P. Shaw, S.E. Swartz and B. Barr. Elsevier Applied Science, London, 1989, 254-264.
8. Timbrell, C., Claydon, P. and Cook, G., "Application of ABAQUS to Analysis of 3D Cracks and Fatigue Crack Growth Prediction". ABAQUS User's Conference Proceedings, June 1-3, 1994, Newport, R.I., USA, 527-541.
9. ZENCRACK software, Zentech International Limited, U.K.
10. Dhondt, G., "Zyklische Mode-I Rissfortschrittsberechnungen mit ABAQUS". In the Proceedings of the German ABAQUS User's Conference, Innsbruck, Sept. 1997, 1-17.
11. Dhondt, G., "Zyklische Mode-I-Rissfortschrittsberechnungen in Komplexen Bauteilen mit der Finite-Elemente-Methode" in the Proceedings of the DGLR Jahrestagung, München, 14-17 Oktober 1997, 381-390.
12. Dhondt, G., "Automatic 3-D Mode I Crack Propagation Calculations with Finite Elements", Int. J. Num. Meth. Engng., 1998, 41,739-757.

13. Dhondt, G., "Cutting of a 3-D Finite Element Mesh for Automatic Mode I Crack Propagation Calculations", to appear in Int. J. Num. Meth. Engng. (1998).
14. Dhondt, G., "On Corner Point Singularities along a Quarter Circular Crack Subject to Shear Loading", submitted for publication as a Report of Current Research to the Int. J. Fract.
15. Richard, H.A., "Bruchvorhersagen bei Überlagerter Normal- und Schubbeanspruchung von Rissen", VDI Forschungsheft 631/85, VDI Verlag, 1985.
16. Sloan, S.W. and Houlsby, G.T., "An Implementation of Watson's Algorithm for Computing 2-Dimensional Delaunay Triangulations", Soil Mechanics Report no. SM045/83, OUEL Report No. 1509/83, University of Oxford (1983).
17. Buchholz, F.-G., Wang, H., Lin, J. and Richard, H.A., "3D Fracture Analyses and Experimental Results on Three-Point Bend Specimens with Slant Cracks", in the Proc. of the Int. Conf. on Computational Engineering Science 98 (ICES 98), Atlanta, Georgia, USA, Oct. 6-9, 1998 (in press).

Meeting Discussions

Paper 33: **Automatic Three-Dimensional Cyclic Crack Propagation Predictions with Finite Elements at the Design Stage of an Aircraft Engine**

Author: G. Dhondt

Discussor: P. J. Bonacuse

Question: Is the author familiar with work of A. Ingraffea at Cornell? Compare.

Author's reply: Yes, first contacts have been established. Calculations comparing best methods are envisaged.

Discussor: Jörg Kumpfert

Question: What do you feel might be the lower limit of fracture toughness in the component you calculated?

Author's reply: It basically depends on the application. However, usually the calculations are performed up to K_{max} = 40 to 50 MPa m½. Smaller values will significantly decrease the life time.

FORCED RESPONSE PREDICTIONS FOR A HP TURBINE ROTOR BLADE

M. Vahdati[1], J. Green[2], J. G. Marshall[2] & M. Imregun[1]

[1]Imperial College, MED, Exhibition Road, London SW7 2BX, UK
[2]Rolls-Royce plc, P.O. Box 31, Moor Lane (ML-83), Derby DE24 8BJ, UK

1. SUMMARY

This paper presents two different strategies for the prediction of blade vibration levels under forced response. The first strategy is an uncoupled approach where the wake forces on the blade are obtained via a linearised aerodynamic model and fed into a reduced structural model. The aeroelastic solution is then performed either in the frequency or the time domain. The second approach is an integrated non-linear analysis that considers a multi-stage multi-passage and that includes the flexibility of the rotor blades. The analysis is then conducted in the time domain using non-linear unsteady aerodynamics. A case study was conducted for a HP turbine stage with 36 stator and 92 rotor blades. The response levels to a 36 engine order excitation were predicted using both the linearised uncoupled and non-linear integrated approaches and the findings were compared with available experimental data. Good overall agreement was reached for most of the cases studied.

2. INTRODUCTION

When the rotating blades go past flow defects created by the interaction of upstream and downstream blade rows, the ensuing unsteady aerodynamic forces can be large and may cause excessive vibration levels, hence the term forced response. What is of interest to the designer is the prediction of the fatigue life under this unsteady aerodynamic loading which can be due to wake passing from upstream blade rows (wake-rotor interaction), the potential field of upstream and downstream bladerows (potential-rotor interaction), or due to a combination of fluctuating back pressures. The problem of predicting the actual vibration amplitudes is further compounded by uncertainties in inherent structural damping values, interactions between the aerodynamic forcing and the blade motion, and the non-linear behaviour of the friction dampers at the blade roots. This last issue is discussed in some detail by Green & Marshall (1999).

In aero-engines it is usually not possible to move all resonances out of the running range due to the wide range of speed and conditions over which the machine must operate. The designer has to use judgement based on previous experience, but this is difficult due to case-to-case variability, non-linear structural effects and mistuning. The requirement for the prediction of actual blade vibration levels has led to significant amount research. The paper by Chiang & Kielb (1992), which presents an industrial design prediction system for forced response, also reviews much of the work in this area. A detailed overview of turbomachinery aeroelasticity methods, including forced response prediction techniques, is given by Marshall & Imregun (1995).

One of the significant computational difficulties in modelling rotor-stator flows is the relative motion between the rotor and the stator blades. The common approach used for modelling multi-stage flows is to employ several grids that move relative to each other. These grids are separated from each other by common boundaries, and the information is transferred from one grid to another by specifying appropriate conditions at these boundaries. The flow representation should incorporate the following features:

(i) the ability to model three dimensional flows and effects such as end-wall, tip leakage, etc. in a conservative fashion,
(ii) the ability to model both up- and down-stream pressure waves and their interactions,
(iii) the ability to model viscous effects from wakes, as they can contribute significantly towards the unsteady component of the flow.

Furthermore, it may be desirable to move the fluid mesh according to the instantaneous position of body under consideration so that the blade vibration can be included in the calculations. However, there are a number of reasons that make such complete non-linear models

Paper presented at the RTO AVT Symposium on "Design Principles and Methods for Aircraft Gas Turbine Engines", held in Toulouse, France, 11-15 May 1998, and published in RTO MP-8.

computationally very expensive. First, typical sector analyses are not applicable to stages with non-matching blade numbers and hence whole bladerow calculations are required; second, these models tend to take a long time to reach a periodic state, which further adds to the computational time. Lastly, if friction damping and/or mistuning are added to the model, there is no option but to calculate the entire stage in a coupled fashion (Vahdati & Imregun, 1996). An alternative is to consider the use of linearized methods which offer huge computational advantages. However forced response is not a fundamentally linear phenomenon. In every type of forced response there is a specified finite level of unsteadiness, and it is not clear *a priori* that linear perturbation methods should give accurate predictions. However, there is a growing body of evidence that linear models can be used successfully, at least for some cases (Suddhoo et al. 1991, Holmes & Chuang 1991, Hall & Clark 1991, Giles 1992).

The purpose of this paper is to illustrate the use of both linearised and non-linear approaches for the prediction of forced response. These techniques will be discussed below:

3. BRIEF BACKGROUND

3.1 Linearised Uncoupled Method

The aerodynamic part of the linearised method is based on 3D Euler equations. An inviscid non-linear steady-state flow is calculated first using a standard cell vertex finite volume scheme on a hexahedral mesh. The solution is time-marched using a 4-stage Runge-Kutta integrator, with standard second and fourth order adaptive smoothing. The flow solution is accelerated using local time-stepping and residual smoothing. The linearized equations are then formulated by assuming that the unsteadiness can be represented by small perturbations to the mean flow. The sources of unsteadiness that may be analysed are: prescribed upstream wakes, up/downstream potential fields, and prescribed blade motion. The unsteady linearized Euler equations are formulated and discretised in such a way that they have a similar form to the non-linear steady equations. These equations, at one prescribed frequency, are solved by adding a pseudo unsteady term, and then time-marched. Arbitrary blade numbers can be accommodated in this linearised scheme (Marshall & Giles, 1997).

The structural part is provided by a standard FE formulation (Armstrong & Edmunds, 1989). An eigen analysis is performed first to determine the normal vibration modes at the required engine speed. Next a Guyan reduction (Guyan 1965) of the full FE model is performed to reduce the computational effort in the next stage of the analysis. Only those nodes onto which the unsteady pressures are interpolated are retained after the reduction process. In addition, a non-linear friction damper can be incorporated into the model by using an experimentally-determined force-amplitude characteristic. Once the unsteady aerodynamic forces have then been integrated into the structural model, it is possible to simulate an engine acceleration through any resonance. Although all input parameters can be allowed to be time-dependent, the unsteady aerodynamic force is computed once only and hence it is assumed to have a constant distribution throughout the calculations. The structural response can be computed either in the time or the frequency domain. The time marching method of Thomas & Gladwell (1988), which employs an explicit scheme with time-step selection to accelerate the computation, was used in this study. However, it was found to be relatively expensive in spite of using a small-size structural model which was reduced using Guyan's technique. The harmonic balance method of Sanliturk & Ewins (1996), which represents the non-linear forces by their Fourier components, can be used to reduce the computational effort.

3.2 Non-linear Integrated Method

The non-linear aeroelasticity code, AU3D, is based on unstructured meshes and the aerodynamic part is an edge-based upwind solver. The flow geometry is described using general grids of 3D elements such as tetrahedra, bricks and wedges, a feature that offers great flexibility for modelling complex shapes. The time stepping is done in an implicit fashion and hence very large CFL numbers can be used without creating numerical instabilities in the solution algorithm. The code can be run in viscous mode via Reynolds-averaged Navier-Stokes equations with Baldwin-Barth turbulence model. It can also be run in inviscid mode, in which case the viscous losses are approximated via simple model. The so-called loss model is obtained by matching two steady-state solutions for the same blade passage, the first one being computed on the standard inviscid mesh and the second one on a fine viscous mesh. It is assumed that the unsteady viscous losses of the second mesh can be represented by the steady-state ones computed on the first mesh.

One of the main features of the AU3D code is its ability to undertake multi-passage multi-stage calculations. Given the computational expense of obtaining the initial steady-state solution for such cases, the following procedure was adopted:

(i) Compute a single-stage steady-state flow for a single stator blade.

(ii) Compute a single-stage steady-state flow for a single rotor blade.

(iii) Expand the solutions of steps (i) and (ii) to form a two-stage typical sector.

(iv) Compute a multi-stage steady-state flow for the typical sector by using the result of step (iii) as an

initial condition. This is the end of the start-up procedure.

(v) Proceed with the unsteady forced response calculations by using the results of step (iv) as a steady-state initial condition.

In the steady-state computations of steps (i)-(iv), the solution is integrated in time by using local time steps. This allows the mass flow to stabilize and the wake region to develop quickly. In the time-accurate computations of step (v), a minimum allowable time step length, based on the computational mesh, is used in the integration procedure.

The structural part of the non-linear method is also based on a 3D FE representation and the same non-linear friction damping model can be used.

4. CASE STUDY

The case of a high pressure turbine blade is used to demonstrate the capabilities of this method. This case is chosen as it is typical of modern design, and good data was available for this case from development engines. The HP stage consists of 36 nozzle guide vanes (NGVs) and 92 development standard blades. The rotor is shrouded, and can also accommodate an under-platform damper which introduces non-linear friction damping., though the present results will focus on the standard configuration only. The resonances of interest are 1st Torsion (1T) and second flap (2F) vibration modes which are excited by wake passing and occur at about 77% speed. To represent inherent structural damping, q-factors of 50 and 200 are used for 2F and 1T respectively, the values being obtained from laboratory bench testing. The results will be presented for both the linearised and non-linear methods and the displacements will be compared with gauge results from development engines.

The FE model, shown in **Fig. 1**, is common to both sets calculations. The Guyan reduction nodes were chosen to capture the unsteady aerodynamic forcing whilst maintaining a reasonable representation of the structure. The modeshapes of interest, 1T and 2F, are plotted in **Fig. 2.**

4.1 Linearised analysis

The aerodynamic damping exerted by the flow onto the rotor blade was calculated using the linear method for the same (77%) speed condition. Using the vibration mode shapes from the full FE model, it was found that the 2F and 1T modes had a q-factor of about 1500. This finding indicates that the aerodynamic damping is much smaller than the inherent material damping (q-factors of 50 and 200 for 2F and 1T). The low level of aerodynamic damping has two important consequences: (i) an uncoupled solution technique is valid for this case, and (ii) the predicted response levels will be very sensitive to the assumed q-factor values.

4.1.1 Determination of the unsteady aerodynamic forcing

The SLiQ code was used to determine the unsteady flow in the rotor due to the 1st harmonic of non-uniform flow in the nozzle. The analysis grid was formed with an inlet section covering the physical axial gap between the NGV and blade - i.e. the inlet plane was co-incident with the nozzle trailing edge. At the speed used for the steady flow condition, the implied forcing frequency is 4408 Hz for a 36 engine order (EO) excitation. The incoming 'wake' was first evaluated due to the combined potential and vortical fields. The flow from the nozzle is shown in **Fig. 3.**

The unsteady pressure distributions at mid-height of the rotor blade are plotted in **Fig. 4**, each blade passage showing an instantaneous flow solution. Here the static pressure is plotted - as this is what ultimately excites the structure. It can be seen that there is a significant level of unsteadiness in the rotor row (equivalent to about 10% of the steady lift).

4.1.2 Transient Dynamic Simulation Method

As shown in **Fig. 5**, the unsteady pressures were interpolated onto the FE mesh and the transient response to a 36 EO excitation was computed for by increasing the speed gradually. Such a sweep is necessary as the exact location of the resonance is not known, especially when a friction damper is used. The time history for inherent material damping is shown in **Fig. 6**. The 1T resonance is clearly seen as a sharp peak, followed by a flatter one for the 2F mode at a slightly higher speed (or frequency).

4.2 Non-linear analysis

Given the small axial gap, it was decided to perform a multi-stage computation to include all possible interactions. Given the blade numbers, a typical sector will consist of 9 stator and 23 rotor blades and it was decided to reduce the computational effort by decreasing the number of stator blades to 90, thus allowing a ratio of 2/5. The fact that the stator and rotor domains have different blade numbers is addressed by including the blade passages in the calculations so that the resulting bladerows have the same pitch. Therefore, the periodic boundaries are imposed only between the first and the last passages of each row.

4.2.1 Steady-flow Predictions.

As shown in **Fig. 7**, the aerodynamic mesh of the stator blade is unstructured in the axial and tangential directions (i. e. the cross-sectional plane) and structured in the radial direction. It is easily seen that it is possible to obtain very good leading and trailing edge definitions without

creating superfluous points away from the blades. The suitability this type of semi-unstructured mesh to turbomachinery applications is demonstrated by Sbardella et al. (1997).

The static pressure contours of the viscous stator domain are shown in **Fig. 8.** It can easily be seen that that there is a circumferential non-uniformity in the nozzle passage, a feature which will lead to unsteadiness in the rotor frame. Broadly speaking and ignoring temperature effects, this non-uniformity can be decomposed into two parts: (i) a pressure non-uniformity which gives rise to a purely inviscid interaction, and (ii) a velocity field (or wake) non-uniformity which is generated by viscous effects. The rotor domain is treated inviscidly and this approach can be justified by remembering that, although the wakes are generated by viscous effects, their subsequent interaction with the stator blades is, in the main, an inviscid process. The computational mesh and the steady-state flow are shown in **Fig. 9.**

4.2.2 Aeroelasticity calculations

The multi-stage calculations were performed in a coupled fashion in which the flow variables and the displacements are advanced in time simultaneously by exchanging boundary conditions. Consequently, features as fluid damping and blade motion are modelled automatically. In order to differentiate between the potential and wake effects, the stator domain was modelled via both inviscid (173,000 points) and viscous (305,000 points) meshes (**Fig. 10**). The contour plots of the static pressure are shown in **Fig. 11** for three different time instants. It is seen that there is a strong interaction between the stator blade shocks and the rotor blades. At a certain time instant, the oblique shock extending downstream of the trailing edge of the upper stator blade interacts with the expansion region near the leading edge of the second rotor blade, causing the shock wave strength to decay. At a later time, this shock hits the crown of the third rotor blade suction surface, causing large variations of pressure on this blade. It is immediately apparent that, as a result of shock-rotor interaction, the largest variation of rotor surface pressure occurs in the vicinity of the leading edge. Also, as can be seen from the instantaneous rotor static pressure profiles of **Fig. 12**, there is a considerable temporal variation of the pressure profile around the rotor blades and a significant movement of the shock.

A comparison of the viscous and inviscid stator domain calculations is shown in **Fig. 13**. It is seen that about 75% of the forcing is due to potential effects and that the (viscous) wake effects are responsible for the remaining 25%. The actual time history at the trailing edge of the shroud is shown in **Fig. 14**. The peak-to-peak amplitudes were computed to be 0.28 mm and 0.21 mm for the viscous and inviscid computations respectively. The response predictions from the linearised and non-linear approaches are compared to actual measured values in **Table 1**.

Table 1.
Comparison of measured and predicted peak-to-peak amplitudes (mm)

Method	1T	2F
Linearised	0.240	0.136
Non-linear	0.280	0.080
Measured mean	0.279	0.121
Measured max	0.397	0.128

5. CONCLUDING REMARKS

(i) Two different methodologies to compute the forced response of turbomachinery blades have been discussed in some detail and results have been presented for a high-pressure turbine. In general, there is good agreement with measured data. The linearized Euler method is an efficient and accurate method for obtaining response assessments within design cycle times. The integrated non-linear method requires an order of magnitude more computational effort and hence it will primarily be used as a numerical investigative tool.

(ii) Both linearised and non-linear computations indicated that the effects of fluid damping were small in this particular case, a feature which will make the results from both methods more comparable.

(iii) In this particular case, the major part of the forcing is observed to be coming from the inviscid (potential) effects. This is due to the fact that, for a significant part of the blade's height, the oblique shocks extending downstream of the trailing edge of the stator blades interact with the rotor blades.

(vi) The transient dynamic results from the linearised methods are broadly in very good agreement with the experimental data - in all cases the prediction is within the experimental scatter. The predicted amplitudes are in the range 0.1-0.4 mm at a point near the trailing edge of the blade surface, at the tip.

(v) The amplitudes at the 2F resonance, which occurs slightly higher in speed than the 1T resonance, tends to be about half the amplitude of the 1T mode. This is in agreement with the experimental results.

(vii) Both methods predict a 36 EO resonance in the 79-81% range speed for the 1T and 2F modes. The measured value is around 77% speed.

6. ACKNOWLEDGEMENTS

The authors would like to thank Rolls-Royce plc. for both sponsoring the work, supplying the experimental data and allowing its publication. They also thank Prof. M. B. Giles for support with the SLiQ code, Dr. R. M. Hall and Mr. R. Elliott for many very useful discussions.

7. REFERENCES

ARMSTRONG, I. & EDMUNDS. T.M., 1989, 'Fully Automatic Analysis in an Industrial Environment', 2nd NAFEMS International Conference, Stratford

CHIANG, H. D. & KIELB, R. E. 1992 An analysis system for blade forced response. *ASME paper* 92-GT-172

GILES, M.B. 1990, Stator/Rotor Interaction in a Transonic Turbine, *AIAA Journal of Propulsion* **6**(5) 621

GILES, M. B. 1992, 'An Approach for Multi-Stage Calculations Incorporating Unsteadiness', *ASME Paper* 92-GT-282

Green, J. S. * Marshall, J. G. 1999. Forced Response Prediction within the Design Process. 3rd European Conf. on Turbomachinery, 2-5 March 1999, London

GUYAN, R. J. 1965, Reduction of Mass and Stiffness Matrices, *AIAA Journal* **3**(2) 380

HALL, K.C., & CLARK, W.S. 1991, 'Prediction of Unsteady Aerodynamic Loads in Cascades using the Linearized Euler Equations on Deforming Grids', *AIAA* Paper 91-3378

HOLMES, D.G., & CHUANG, H.A. 1991, 'Two Dimensional Linearized Harmonic Euler Flow Analysis for Flutter and Forced Response', *Proceedings of 6th UAATP, Notre Dame*

HE, L. 1993, Three-Dimensional Time-Marching Inviscid and Viscous Solutions for Unsteady Flows around Vibrating Blades, *ASME Paper* 93-GT-92

MARSHALL, J.G. & GILES, M. B., 1997, 'Some Applications of a Time-Linearized Euler Method to Flutter and Forced Response in Turbomachinery', *8th ISUAAT, Stockholm*

RAI, M. M., An implicit conservative zonal boundary scheme for Euler equations calculations, Computers and Fluids, Vol. 14, No. 3, 1986, pp 295-319.

RAI, M. 1987, Unsteady 3D Navier-Stokes Simulations of Turbine Rotor-Stator Interaction, *AIAA Paper* 87-2038

SANLITURK, K. Y. & EWINS, D. J. 1996. Modelling 2D friction contact and its application using harmonic balance method. JSV, 193(2), 511-523

SBARDELLA, L, SAYMA, A. I. & IMREGUN, M., 1997. Semi-unstructured mesh generator for flow calculations in axial turbomachinery blading. 8th Int. Conf on Unsteady Aerodynamics and Aeroelasticity of Turbomachines, Stockhom,

SANLITURK, K.Y. & EWINS, D.J., 1996, 'Modelling 2D Friction Contact & its Application using the Harmonic Balance Method', JSV **193** (2) pp 511-523

SUDDHOO, A., GILES, M.B. & STOW, P., 1991, 'Simulation of Inviscid Blade Row Interaction Using a Linear and a Non-Linear Method', *ISABE Conference*

THOMAS R.M. & GLADWELL, I., 1988, Variable-Order Variable-Step Algorithms for Second-Order Systems Parts I&II, *International Journal for Numerical Methods in Engineering* **26** 39-80

VAHDATI, M. AND IMREGUN, M., 1996. A Non-linear Integrated Aeroelasticity Analysis of a Fan Blade Using Unstructured Dynamic Meshes. Journal of Mech. Eng. Sci, Part C, Vol 210, pp 549-563

Fig. 1 FE model of the rotor blade

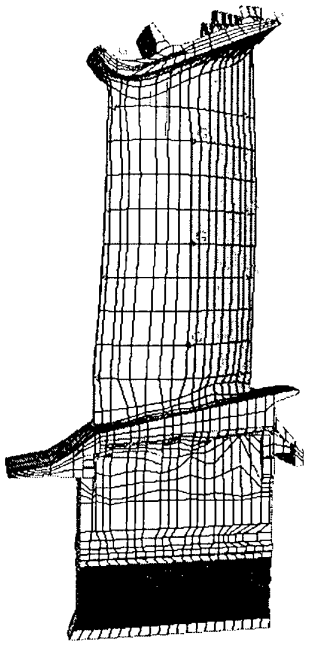

Fig. 2 Modes shapes for 1T and 2F

2nd Flap (5088 Hz)

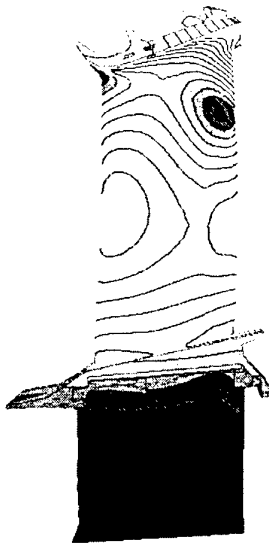

1st Torsion (5039 Hz)

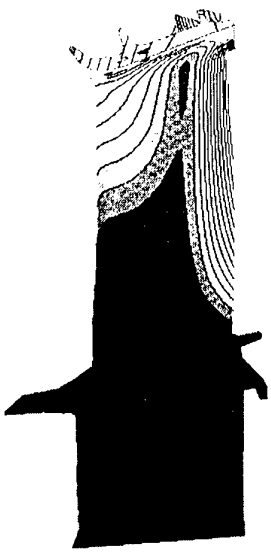

Fig. 3 Nozzle Flow

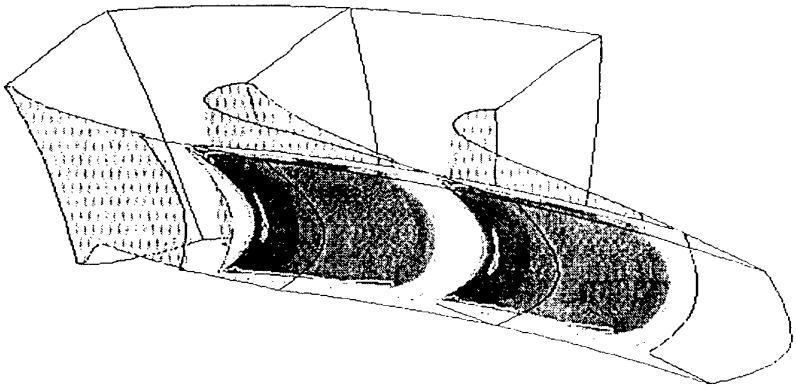

a) Static Pressure

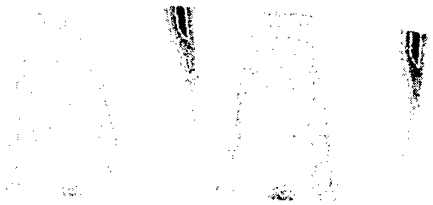

b) Total Pressure

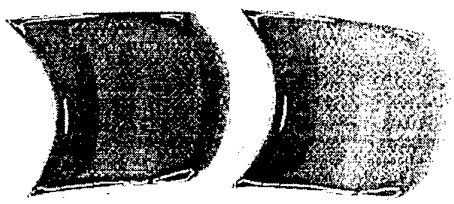

Fig. 4 Instantaneous pressure distributions at mid-height of the rotor blade

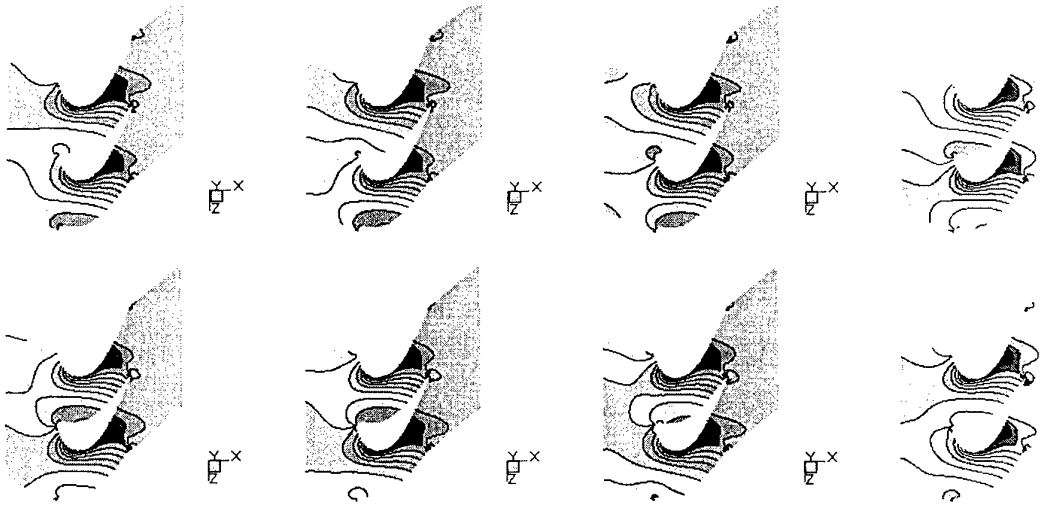

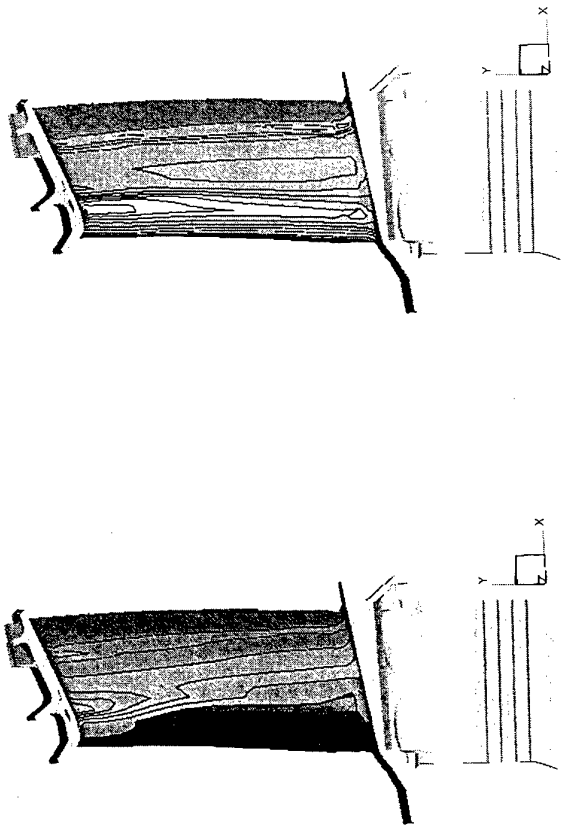

Fig. 5 Unsteady pressure on structural mesh

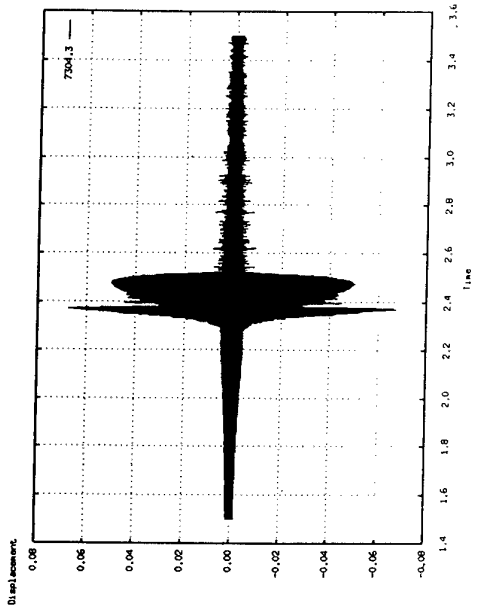

Fig. 6 Time history for inherent material damping only

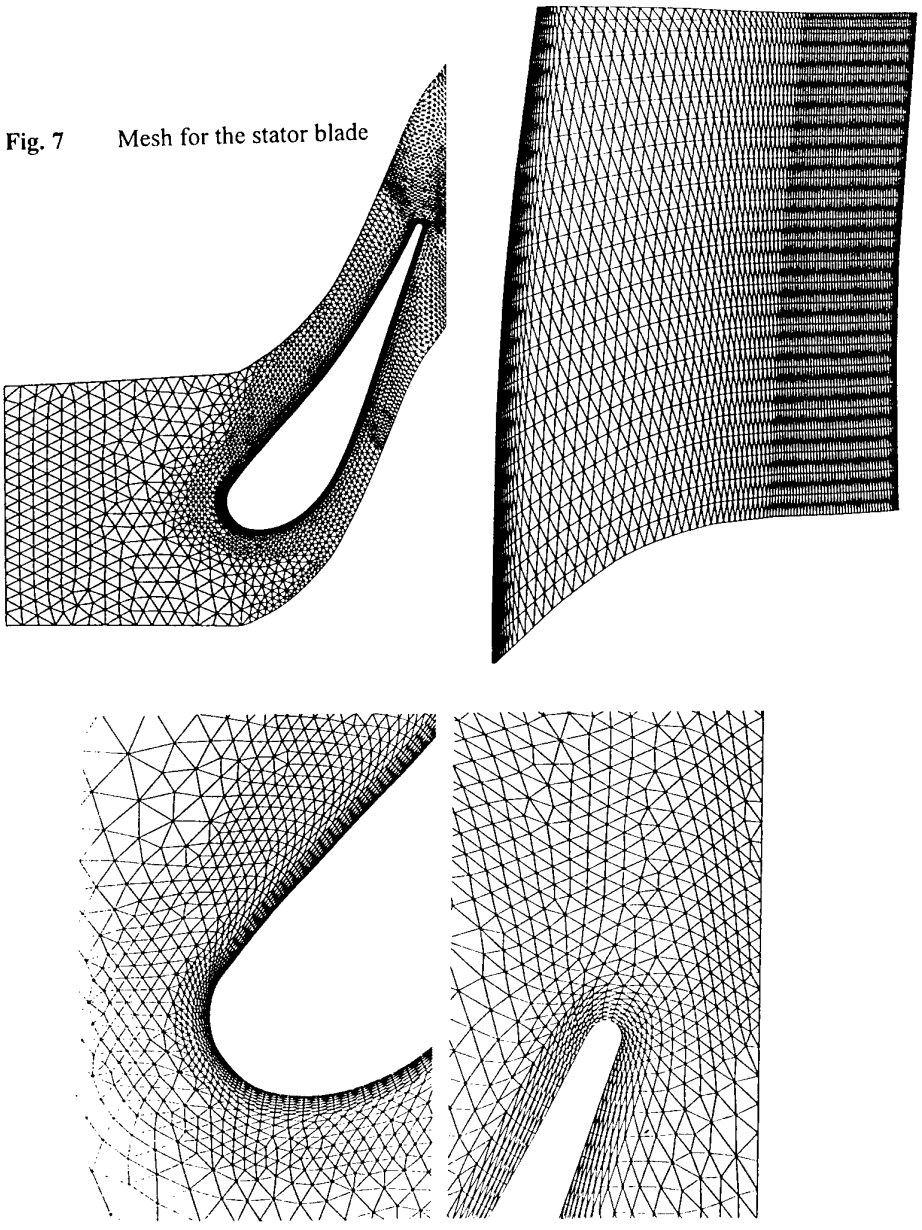

Fig. 7 Mesh for the stator blade

Fig. 8 Static pressure contours for the viscous stator domain

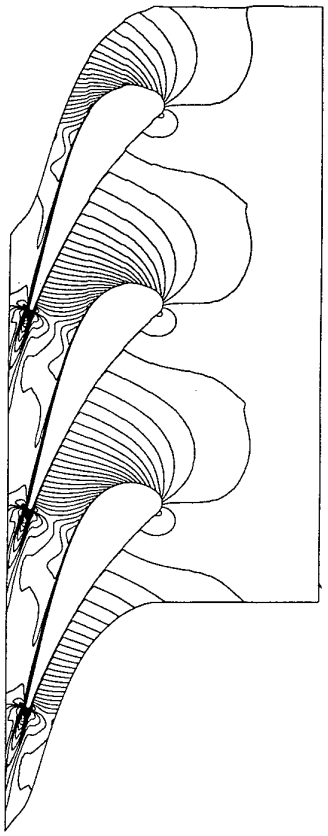

Fig. 9 Computational mesh and the steady-state flow for the rotor blade

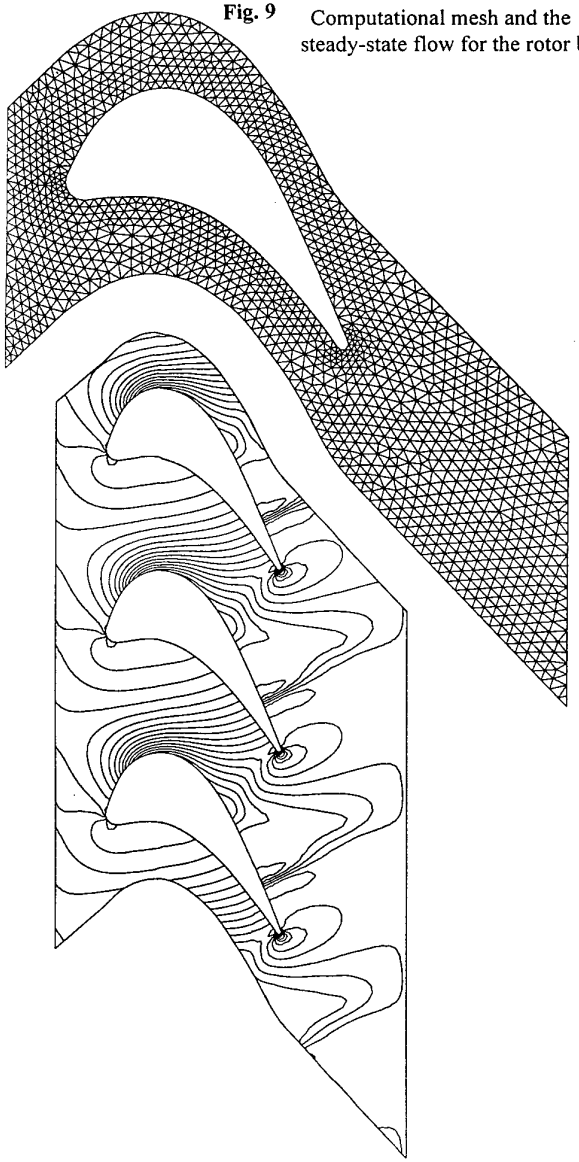

Fig. 10 Viscous and inviscid meshes for a typical sector of 2 stator and 5 rotor blades

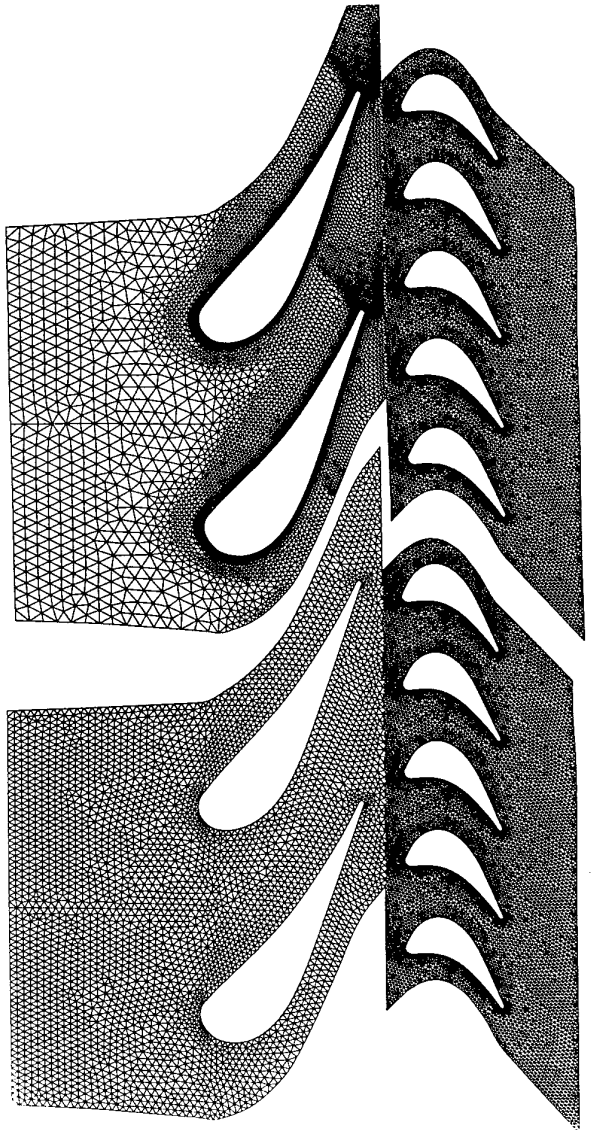

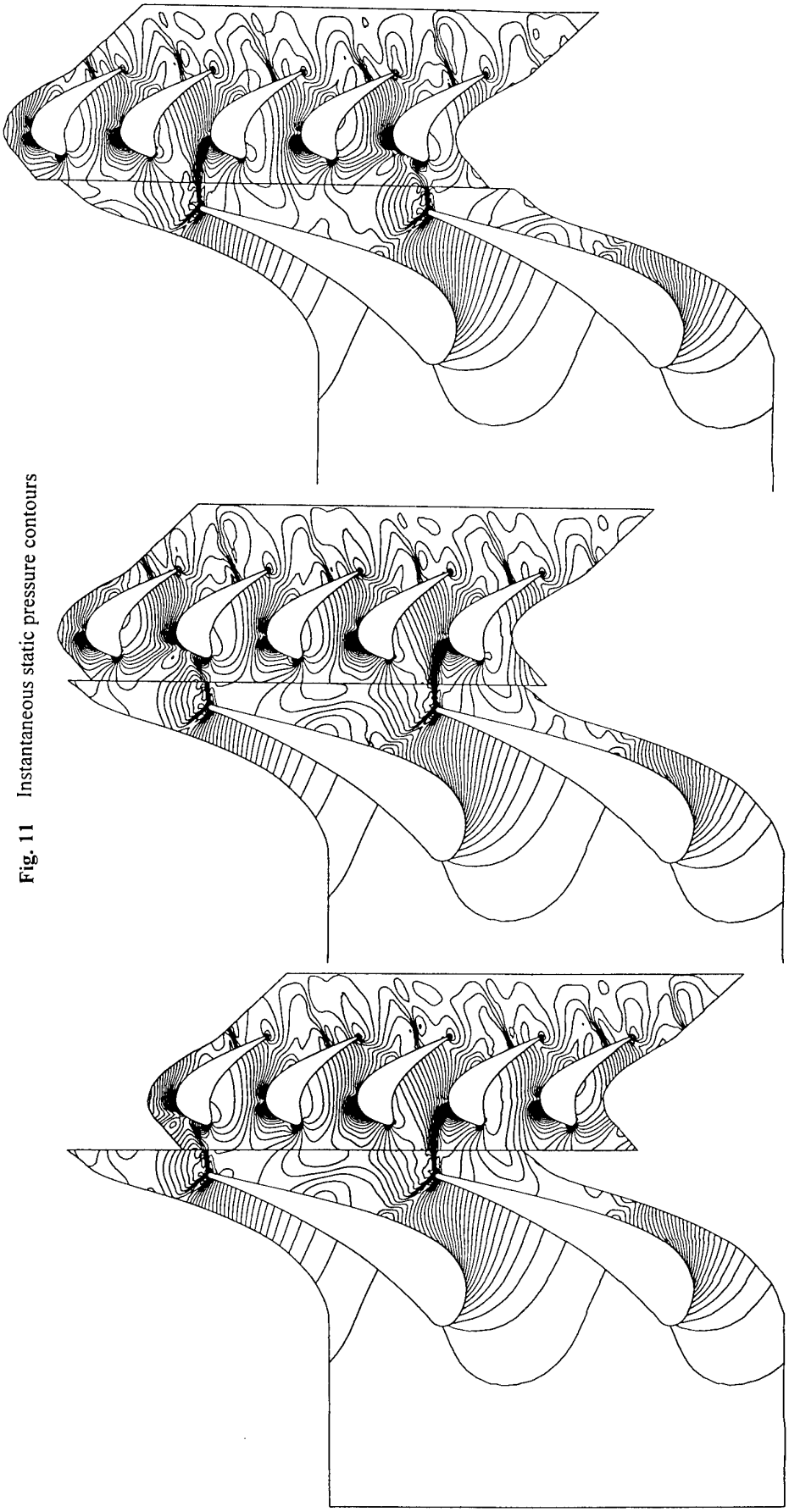

Fig. 11 Instantaneous static pressure contours

Fig. 12 Instantaneous rotor static pressure profiles

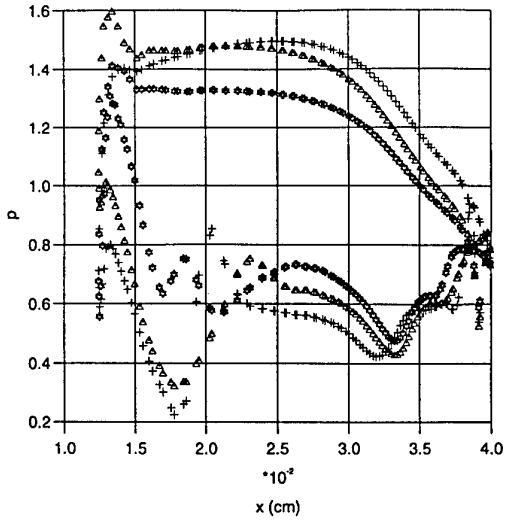

Fig. 13 Modal forces obtained from viscous and inviscid stator representations

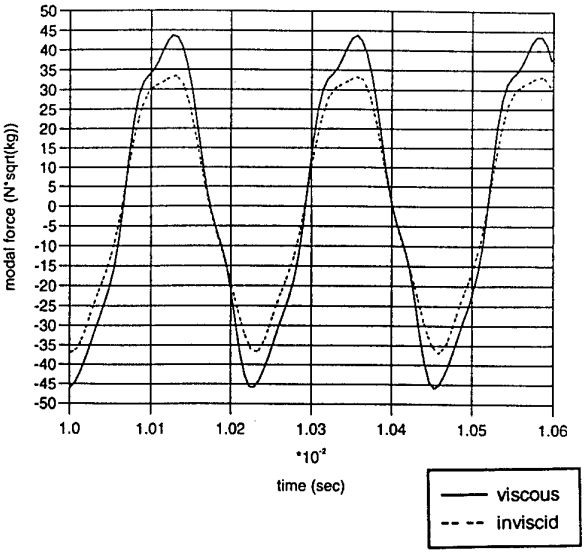

Fig. 14. Actual time history at the trailing edge of the shroud – Inviscid calculation

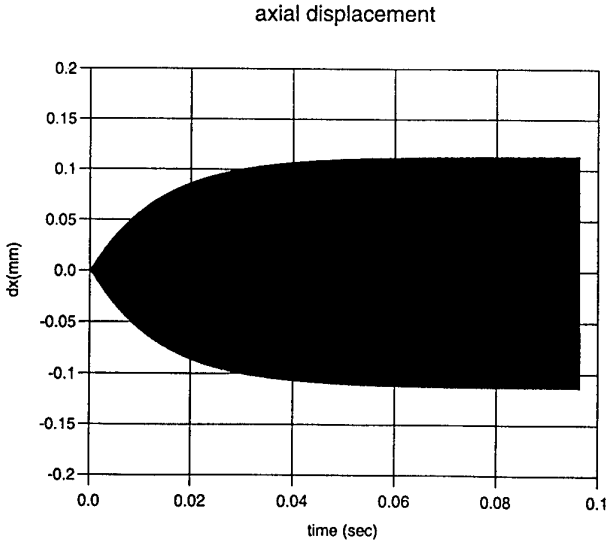

Aero-Thermo-Structural Design Optimization of Internally Cooled Turbine Blades

G. S. Dulikravich[1], T. J. Martin[2], B.H. Dennis[2], E. Lee[2] and Z.-X. Han[3]
Department of Aerospace Engineering, 233 Hammond Bldg.
The Pennsylvania State University
University Park, PA 16802
U.S.A.

1. SUMMARY

A set of robust and computationally affordable inverse shape design and automatic constrained optimization tools have been developed for the improved performance of internally cooled gas turbine blades. The design methods are applicable to the aerodynamics, heat transfer, and thermoelasticity aspects of the turbine blade. Maximum use of the existing proven disciplinary analysis codes is possible with this design approach. Preliminary computational results demonstrate possibilities to design blades with minimized total pressure loss and maximized aerodynamic loading. At the same time, these blades are capable of sustaining significantly higher inlet hot gas temperatures while requiring remarkably lower coolant mass flow rates. These results suggest that it is possible to design internally cooled turbine blades that will cost less to manufacture, will have longer life span, and will perform as good, if not better than, film cooled turbine blades.

2. INTRODUCTION

The objective of this paper is to present several methods for the inverse design and optimization of the external and internal geometric shapes of internally cooled gas turbine blades. The design methods are pertinent to aerodynamics, heat transfer, and the structural integrity of the blades that can also have thermal barrier coatings. The ultimate goal is to sketch a multidisciplinary design procedure that is capable of maximizing inlet turbine temperature, and enhancing the uniformity of temperature and stress/deformation fields in the blade material, while at the same time minimizing coolant mass flow rate, inlet-to-exit total pressure loss, and coolant supply pressure. The methodologies discussed in this paper were chosen because they have been perceived to be the most robust and computationally affordable, while making minimal assumptions concerning the actual physics of the problem. Although most of the examples are two-dimensional, the methods are directly applicable to three-dimensional blade configurations. In order to demonstrate that a variety of the existing proven disciplinary analysis computer codes can be used in this design environment, we have intentionally used our finite difference, finite volume, finite element, and boundary element codes. They were written in different programming languages. Some of the codes were written for single structured grids, others for multi-block grids, and yet other codes were written for non-structured grids.

Similarly, our hybrid optimization software package utilizes several standard gradient-based and non-gradient optimization algorithms with a special logic for automatic switching among these modules in order to arrive at the global minimum. Each of the codes and design methodologies will be discussed briefly with the objective of conveying the essential design concept.

[1] Associate Professor.
[2] Graduate Research Assistant.
[3] Visiting Scholar.
Associate Professor, BUAA, Beijing, P. R. China.

There is a strong interaction among a number of engineering disciplines when studying the internally cooled gas turbine blades. We will consider aerodynamics of the hot gas flow in detail, coolant aerodynamics and heat transfer very approximately, heat conduction in the blade material very accurately, and stress/deformation field of the blade equally accurately. In the design process explained in this paper, these individual disciplines will not be solved simultaneously because this approach would take an unacceptably long time even on a cluster of workstations running in parallel. For these pragmatic reasons we opted for a computationally affordable sequential, loosely coupled, design approach as follows.

First, an initial realistic shape of a turbine blade was generated and the hot gas flow-field around it was analyzed using computational fluid dynamics (CFD). Then, if an aerodynamic performance improvement was desired, an inverse shape design of the blade was performed subject to the desired surface pressure distribution while accounting for fluid compressibility, heat transfer, and turbulence. If the aerodynamic performance was to be maximized, the blade shape was optimized subject to constraints such as fixed axial chord length, inlet and exit flow angles, minimum allowable trailing edge radius, and hot gas mass flow rate.

Next, the interior of the blade needed to be designed so that blade temperature was as uniform and as high as the blade material and life expectancy would allow. Since hot surface temperature specified in the external CFD analysis and aerodynamic shape design were arbitrary, these temperatures were modified by reshaping and resizing the interior coolant flow passages. This involved a certain amount of empiricism when dealing with the coolant flow-field and heat transfer, and it utilized optimization. The result was a new configuration of coolant flow passages that would allow for increased turbine inlet hot gas temperature and decreased coolant mass flow rate. At the same time, this optimized interior blade geometry matched the blade hot surface convection heat transfer coefficient distribution predicted by the CFD code and made the temperature field throughout blade as uniform as possible thus minimizing blade thermal stresses.

3. EXTERNAL AERODYNAMIC SHAPE INVERSE DESIGN AND OPTIMIZATION

Although only a few are suitable for fully three-dimensional turbine blade geometry design, a variety of aerodynamic shape inverse design methodologies exist in the open literature [Dulikravich, 1995]. The reason why the particular inverse shape design procedure used in this work was chosen was to reduce the overall computing time while taking into account viscosity, turbulence, heat transfer, and compressibility.

3.1 Aerodynamic Shape Inverse Design

First, an inviscid flow-field was predicted around an initial guess for the shape of an airfoil. A four stage Runge-Kutta structured

Paper presented at the RTO AVT Symposium on "Design Principles and Methods for Aircraft Gas Turbine Engines", held in Toulouse, France, 11-15 May 1998, and published in RTO MP-8.

grid Euler solver was used with solid wall stationary boundary conditions on the airfoil surface until a combined average residual was reduced by four orders of magnitude, which was deemed to be an acceptably converged solution. An approximate factorized ADI algorithm was the basis of the steady-state solution of the Euler/Navier-Stokes code. A finite difference method on a block-structured non-orthogonal grid and explicitly added artificial dissipation terms were used in space discretization. Baldwin-Lomax turbulence modeling was used for turbulence closure in the Reynolds-averaged full Navier-Stokes solver.

Then, permeable wall boundary conditions were enforced causing a sudden increase in the combined average residual. The permeable wall boundary conditions are based on the signs of the eigenvalues of the Euler system of flow-field governing equations at the airfoil surface [Leonard; 1990; Leonard and Demeulenaere, 1997]. The permeable wall boundary conditions were enforced during every iteration with the Euler flow-field analysis code until the combined average residual decreased to the same level as it was when the initial flow-field was deemed converged (Fig. 1). At that moment, the airfoil normal surface coordinates were updated according to the geometry update formula.

$$\Delta n_{i-1}(\rho\tilde{W}_t)_{i-1} + \Delta s_i \frac{(\rho W_n)_i + (\rho W_n)_{i-1}}{2} = \Delta n_i(\rho\tilde{W}_t)_i$$

where

$$(\tilde{W}_t)_{i-1} = \left((W_t)_{i-1} + (W_t^{target})_{i-1}\right)/2$$

with a similar expression for $(\tilde{W}_t)_i$. Here, ρ is the local fluid density, W_n and W_t are the normal and tangential relative fluid velocity components at the airfoil surface, and Δn and Δs are the normal distance (local shape update value) and the local arc length of a surface grid cell, respectively. This transpiration concept (or quasi one-dimensional streamtube mass balance) equation was applied to the entire airfoil surface starting from the leading edge stagnation point. After the geometry update, the grid was regenerated in the domain near the airfoil and the flow-field variables were interpolated at the new grid points. This again caused a jump in the combined average residual. Euler equations with the characteristic surface boundary conditions were run again until the residual was reduced to the earlier level. At that moment, the geometry and the grid were updated again and the process continued. Usually, only 2-4 shape updates were needed (Fig. 1) with the Euler solver, depending on the magnitude of the geometry changes. The final surface pressure distribution almost duplicated the target surface pressure distribution.

The ultimate objective was to create the airfoil shape that was compatible with the actual viscous, turbulent flow with heat transfer. Therefore, the inverse shape design automatically proceeded by switching from the Euler mode to the full Navier-Stokes mode of the analysis code while enforcing solid wall boundary conditions on the shape just designed using the Euler solver. This step was necessary in order to develop boundary layer velocity profiles and possible flow separation regions before applying the final design step, which used the Navier-Stokes solver and impermeable moving wall boundary conditions [Leonard and Demeulenaere, 1997]. Here, the airfoil shape was updated and the new grid was generated during each iteration with the Navier-Stokes code. In this method, it was beneficial to keep the grid velocity term in the contravariant velocity components defined as

$$U = \frac{D\xi}{Dt} = \frac{\partial\xi}{\partial t} + u\frac{\partial\xi}{\partial x} + v\frac{\partial\xi}{\partial y}$$

$$V = \frac{D\eta}{Dt} = \frac{\partial\eta}{\partial t} + u\frac{\partial\eta}{\partial x} + v\frac{\partial\eta}{\partial y}.$$

The grid velocity term was calculated by following a space conservation law [Demirdzic and Peric, 1988]

$$\frac{\partial}{\partial t}\left(\frac{1}{J}\right) + \frac{\partial}{\partial\xi}\left(\frac{\partial\xi}{\partial t}\right) + \frac{\partial}{\partial\eta}\left(\frac{\partial\eta}{\partial t}\right) = 0$$

where J is the local Jacobian of the geometric transformation from the Cartesian x,y coordinates to the non-orthogonal curvilinear boundary conforming coordinates, ξ,η. The airfoil geometry was updated at every iteration by the same surface transpiration formula as in the case of the inviscid design, except that now $W_n = W_t = 0$ on the airfoil surface [Leonard, 1990].

The first example using this inverse shape design approach illustrated the redesign of a cascade of non-staggered NACA0012 airfoils at zero angle of attack with gap/chord ratio g/c = 2.0. The flow conditions were: Po1 = 286356 Pa, To1 = 1600 K, Pexit = 234910 Pa, dynamic viscosity $\mu = 5\times10^{-5}$ kg m^{-1} s^{-1}, specific gas constant R = 210 J kg^{-1} K^{-1}, ratio of specific heats γ = 1.4, reference length L = 0.1 m. This resulted in Prandtl number Pr = 0.72 and Reynolds number Re = 1 x 10^6 where the reference speed was the inlet stagnation speed of sound. The corresponding inlet Mach number was M = 0.5. Airfoil surface was treated as adiabatic. A single C-type grid was used with 193 x 33 = 6569 grid points. A target surface pressure distribution higher than the initial surface pressure distribution was imposed. Figure 2 indicates that the converged pressure distribution was in good agreement with the target pressure distribution and the final geometry was thicker than the initial airfoil. The flow-field was separated on the initial geometry starting from 80% of the chord (Fig. 3) while the final geometry had considerably smaller flow separation, which started at 96% of the chord (Fig. 4), because the transpiration method updated the geometry based on a streamtube approach. The convergence history of this iterative process (Fig. 1) depicts the first 1200 iterations performed with the inviscid version of the code while using permeable wall boundary conditions. During these 1200 iterations with the Euler solver, the airfoil geometry was updated three times (after 400, 800, and 1200 iterations). The Navier-Stokes solver with no-slip boundary conditions was then activated for 50 iterations to develop boundary layer velocity profiles. Finally, this was followed by the application of the Navier-Stokes code using a moving solid boundary formulation, that is, updating the airfoil shape and the grid after each iteration. This calculation was performed on an SGI Solid Impact R10000 workstation with a 175MHz processor and took 11 minutes, which was about 3.5 times as much computing time as required for one flow-field analysis with the Navier-Stokes code.

The second example involved the inverse shape design of a turbine cascade with high subsonic exit flow. The flow conditions were: Po1 = 600000 Pa, To1 = 1600 K, dynamic viscosity $\mu = 8\times10^{-5}$ kg m^{-1} s^{-1}, specific gas constant R = 210 J kg^{-1} K^{-1}, ratio of specific heats γ = 1.3, reference length L = 0.08 m. This resulted in Prandtl number Pr = 0.72 and Reynolds number Re = 1.18 x 10^6 where the reference speed was the inlet stagnation speed of sound. Exit static pressure, Pexit = 367420 Pa, was enforced thus making the exit isentropic Mach number M = 0.87. Temperature equal to 75% of To1 was enforced on the airfoil external surface. For better accuracy, an O-H-C multi-block grid (Fig. 5) was used where the total number of grid points was 11900. Figure 6 shows the initial, target, and final computed isentropic Mach number distributions on the airfoil surface versus airfoil contour arc length and the initial and final airfoil shapes. The Mach number distribution on the

new turbine airfoil was smoother in the nose and suction regions, and the Mach number dip on the pressure surface disappeared. Initial and final pressure contour lines are displayed in Figs. 7 and 8. This shape design consumed almost 3 hours of CPU time on the SGI workstation because this test case converged slower than the previous non-lifting case.

NOTE: The final version of this paper will also have examples of three-dimensional blade inverse shape design using Navier-Stokes equations (Fig. 9).

3.2 Aerodynamic Shape Optimization of a Supersonic Exit Cascade

When a global objective is to be reached (for example, minimum total pressure loss from inlet to exit of a turbine cascade), the flow-fields for a large number of cascade shapes must be analyzed. Since geometric variations explored may not be small, it is of utmost importance that a robust CFD code and a robust grid generation code are used. For this reason a robust compressible turbulent flow Navier-Stokes analysis code was used that utilized non-structured triangular grids [Han and Liu, 1997; Han et al., 1998]. The blade airfoil geometry was generated using eight parameters [Dennis and Dulikravich, 1997] that became design variables in the shape optimization process. The non-structured grid was generated using an advancing front method [Pirzadeh, 1993]. All boundary conditions in the flow solver were imposed using first order accuracy. The inlet and outlet boundary conditions were treated with locally 1-D non-reflection of waves passing out of the computational domain. Implementation of the 2-D non-reflection boundary conditions at inlet and exit boundaries would take many more operations than 1-D non-reflection boundary conditions. Periodic flow conditions were imposed with the phantom cells' values equal to the corresponding periodic real cells' values. The flow variables at the cells' vertices were calculated from surrounding cells centers' values with the distance weighted averaging method. The k-ε limiter and wall function were used in turbulence modeling.

As an example of the robust constrained aerodynamic shape optimization, the same cascade of turbine airfoils with a supersonic average exit Mach number M = 1.4 was created by lowering the exit static pressure to 101330 Pa (Fig. 9). By varying randomly the eight design variables (conic sections) controlling the airfoil shape, a population of 30 initial designs was formed. The design objective was: maximize lift, minimize total pressure loss, enforce an exit angle between -58 and -62 degrees. Using a constrained genetic algorithm and the non-structured turbulent compressible Navier-Stokes solver, after 10 generations the turbine airfoil cascade evolved to a significantly different shape (Fig. 10). The trailing edge radius converged to the minimum allowable value (as expected). The best design had an exit angle of -60.5 which is almost on the constraint boundary (it should converge to -60.0) (Fig. 11).

NOTE: The final version of this paper will have better converged results and more detailed discussion.

4. THERMAL SHAPE OPTIMIZATION

4.1 Interior Geometry Generation

The first step in the design of the multiple coolant flow passages was the description of the cooling wall thickness function; W(s), which determined the thickness of the wall between the hot gas and the coolant fluid. The abscissa, s, followed counter-clockwise along the metal/coating interface all the way around the airfoil, from trailing edge to trailing edge and formed a closed loop. W(s) was described by a piecewise-continuous β-spline curve that varied in the direction normal to the metal/coating interface to a distance controlled by one design variable per β-spline control vertex. One or more thermal barrier coatings with a specified thickness was added by generating additional congruent airfoil shapes inward to the outer airfoil surface. The coating thickness distribution was described using the β-splines so that it varied from point to point along the airfoil contour, allowing for greater thermal barrier protection in areas which were hotter, but thin in other areas that were more sensitive to spalation problems.

The x-coordinates of the intersections of the struts' centerlines with the outer turbine airfoil contour were defined as x_{Ssi} and x_{Spi}, for the suction and pressure sides, respectively. Figure 12 illustrates the complete geometric modeling of the coolant flow passages and thermal barrier coating. The range over which each strut could vary was specified and the number of coolant flow passages in the turbine airfoil was specified. Since the number of coolant passages may also be a design variable, a problem would arise when computing the gradient of the objective function in a typical gradient-based optimization algorithm. Additional coolant passages could not easily be added since the searching capabilities of the optimizer could never include all the possible combinations of passage locations and geometry. Therefore, a simple and straightforward approach was utilized by starting the optimization with a large number of passages (limited only by available computer memory and computer speed) and then automatically reducing the number of passages during the optimization procedure [Dulikravich and Kosovic, 1992; Dulikravich and Martin, 1994; Dulikravich, 1988]. Any particular coolant passage was eliminated whenever it was reduced to such a small size that it had a negligible effect on the heat flux at the hot outer boundary of the airfoil. In addition to the end-coordinates of the struts, the strut thickness, t_{Si}, and a filleting Lame curve exponents on the pressure and suction sides, e_{Sti} and e_{Sli}, respectively, were used to complete the geometric modeling of each strut (Fig. 12). The three-dimensional turbine blade was then generated by stacking the two-dimensional sections including a twist about the stacking axis, scaling of the sectional shapes, and yawing of the stacking axis.

4.2 A Model for Quasi-Conjugate Heat Transfer

It would be highly desirable, and it is theoretically feasible, to construct a conjugate heat transfer analysis [Li and Kassab, 1994] that simultaneously solves the fully three-dimensional turbulent compressible hot gas flow-field, the heat conduction within the turbine blade material, and the fully three-dimensional turbulent compressible coolant flow-field. At present, the computational time needed for this type of analysis is still too long for numerical optimization purposes. Therefore, a simpler semi-conjugate heat transfer analysis and optimization of the turbine blade was developed with the objective of avoiding extremely complex, computationally demanding, and unreliable task of repetitively predicting the fully three-dimensional turbulent compressible coolant flow-field [Stephens and Shih, 1997]. Specifically, the application of thermal boundary conditions on the coolant flow passage walls was greatly simplified by the specification of convective heat transfer coefficients and ambient fluid temperatures of the coolant fluid.

$$q'' = -k_M \frac{\partial T}{\partial n} = h_{cool,n}\left(T_w - T_{cool,n}\right)$$

Here, k_M is the coefficient of thermal conductivity of the metal blade. The convective heat transfer coefficient, h_{cool}, on the walls of the nth coolant passage was allowed to vary with the following parameters: velocity of the coolant, V_{cool}, coolant density, ρ_{cool}, the hydraulic diameter, D_h, temperature of the passage wall, T_w, bulk temperature of the coolant, T_{cool}, average wall roughness height, ε, temperature-dependency of the fluid properties, μ_{cool}, k_{cool}, c_{pcool}, thermal buoyancy, $g\beta$, and the geometric shape of the coolant passage. This list of 11 variables was replaced by 7 non-dimensional variables which were all based upon the bulk coolant flow properties [White, 1988, Chapter 5].

$$S_t = f\left(Re_D, Pr, \frac{\varepsilon}{D_h}, \frac{T_w}{T_{cool}}, Gr_D, Ec, shape\right)$$

where the non-dimensional numbers are:

Stanton number $St = \dfrac{h_{cool}}{\rho_{cool} c_{p_{cool}} V_{cool}}$,

Reynolds number $Re_D = \dfrac{\rho_{cool} V_{cool} D_h}{\mu_{cool}}$,

Prandtl number $Pr = \dfrac{\mu_{cool} c_{p_{cool}}}{k_{cool}}$,

Grashof number $Gr_D = \dfrac{g\beta(T_w - T_{cool}) D_h^{\,3}}{(\mu_{cool}/\rho_{cool})^2}$,

Eckert number $Ec = \dfrac{V_{cool}^2}{c_{Pcool}(T_w - T_{cool})}$,

Nusselt number $Nu_D = \dfrac{h_{cool} D_h}{k_{cool}}$, and

friction factor, $f = \dfrac{8\tau_w}{\rho_{cool} V_{cool}^{\,2}}$.

The following assumptions were made in order to simplify these correlations and to arrive at a usable functional relationship. The temperature differences in the coolant were assumed to be small enough to eliminate temperature-dependent physical properties. Thermal buoyancy and viscous dissipation effects were neglected as were the centripetal and Coriolis acceleration effects. Results of experimental data for this type of simplified forced convection heat transfer are quite common in the open literature. Correlations for rough surface tubes, such as those containing trip strips, are rather sparse. The Reynolds analogy is often used to produce a solution under these circumstances.

$$St\, Pr^{0.667} = \frac{f}{8}$$

The friction factor, f, was related to the pressure loss in the coolant passage by the well-known formula for fully developed pipe flows driven only by the pressure gradient

$$\Delta p = f \frac{L}{D} \rho_{cool} \frac{V_{cool}^{\,2}}{2}.$$

The value of the local friction factor could be taken from the Moody chart knowing the relative surface roughness, ε/D, of the particular section of the coolant passage and the corresponding local Reynolds number [Holman, 1981, p. 230]. For optimization purposes, the friction factor should be allowed to change during the optimization process. Therefore, an explicit formula given by Haaland was used [White, 1994, p. 317].

$$\frac{1}{f^{1/2}} = -1.8 \log_e\left[\frac{6.9}{Re_D} + \left(\frac{\varepsilon/D}{3.7}\right)^{1.11}\right]$$

This explicit expression is accurate to within 2% of the Moody chart, which itself is accurate to +/-15% versus experimental data for fully turbulent flows having Reynolds numbers in the range $10^3 < Re < 10^8$. During the numerical optimization procedure, the relative wall roughness in the turbulent flow coolant passage was a design variable [White, 1994] that was allowed to increase up to $\varepsilon/D = 0.1$. Large relative wall roughness values simulated the effect of placing pin fins and trip strips on the coolant passage walls. Because the coolant passages do not, in general, have a circular cross section, these heat transfer correlations were based on the local hydraulic diameters of the coolant passages, $D_h = 4A_h/P_h$, where A_h is the cross-sectional area and P_h is the wetted perimeter. Given the coolant mass flow rate, $\dot{m} = \rho_{cool} A_h V_{cool}$, the local average velocity of the coolant and the corresponding local Reynolds numbers were computed.

The coolant mass flow rate was allowed to vary during the optimization process so that it could be correlated with the limiting temperature on the hot surface of the turbine blade. Only the inlet coolant fluid temperature was specified and kept fixed.

The coolant streamwise pressure gradients were calculated for each coolant passage section given the empirical relationships previously described, $dp/dz = \Delta p/L$. These pressure gradients were used to determine the minimum required coolant supply pressure. That is, the static pressure, p_{cool}, at the inlet of the first coolant flow passage (at the root of the blade leading edge) was determined given the pressure losses in the entire coolant passage and the knowledge of a fixed static pressure, p_{static}, at the exit of the last coolant flow passage segment (assumed to be equal to the hot gas pressure at the blade trailing edge). Because the relationship between the coolant pressure loss and coolant inlet pressure was implicit, the bisection method was used to determine the root of the following function.

$$p_{eject}(\dot{m}, \varepsilon/D, p_{cool}) - p_{static} = 0$$

In this equation, the ejection static pressure, p_{eject}, was calculated given an initial guess to p_{cool} and the computed pressure losses, Δp. It was a function of the coolant mass flow rate, the coolant passage wall relative roughness, the inlet coolant pressure, as well as the blade and coating material properties and coolant passage geometry. In the case of trailing edge coolant ejection, the exit coolant static pressure, p_{static}, could be computed by a CFD prediction of the external hot flow through the turbine cascade. In the case of a closed loop cooling systems, p_{static} can be specified from an experimental evaluation.

The ambient (bulk) coolant temperatures in each of the coolant passages were allowed to be a non-linear function of heat flux, $T_{cool} = T_{cool}(Q)$. A quasi one-dimensional, steady state, incompressible, thermal energy equation was used to determine the bulk coolant temperatures and pressures along the entire length of the serpentine coolant flow passage.

$$\int \dot{m} c_p \frac{dT_{cool}}{dz} dz = \iint Q ds dz + \int \frac{\dot{m}}{\rho_{cool}} \frac{\Delta p}{T_N} dz$$

Here, Q is the heat flux through the coolant passage walls, s is the contour-following variable along the coolant wall perimeter, and z is the coolant streamwise direction. This equation was written for each coolant passage including 180 degree turn

sections and solved for the local streamwise temperature gradients, $(dT_{cool}/dz)_N$. For this purpose, we used blade outer hot surface temperatures and heat fluxes that were previously computed by the CFD analysis of the hot gas flow-field with blade wall temperatures guessed as 75% of the cascade inlet hot gas temperature. Because T_{cool} is a function of Q, the solution of the heat conduction equation in the blade material was non-linear due to the heat flux dependent ambient coolant temperature [Chyu et al., 1997] in the convection heat transfer boundary conditions. Subsequent solutions to the heat conduction provided better estimates of the heat flux, Q, and the iterative scheme proceeded until the computed heat fluxes converged. This was typically accomplished in a maximum of five solutions of the heat conduction problem in the entire airfoil.

This simplified approach to conjugate heat transfer did not fully account for all of the heat transfer characteristics in real rotating serpentine coolant flow passages which are very complex and three-dimensional, being affected by Coriolis and centripetal forces combined with thermal buoyancy [Han et al., 1994; Moshizuki et al., 1994]. Further study is needed in these areas before an empirical correlation between the heat transfer rate and rotation can be reliable within the ranges of Reynolds, Grashof, and rotation numbers encountered in a real turbine blade.

Thus, our present approach should be understood as an effective combination of the presently available experimentally obtained correlations combined with detailed computations of the hot gas flow-field and the heat conduction in the blade material with the ultimate goal of providing a computationally affordable preliminary optimization tool. This design tool should iteratively arrive at the optimized coolant flow passage geometry inside a cooled turbine blade so that coolant mass flow rate is reduced while increasing the hot gas inlet temperature and making the temperature field in the blade material as uniform as possible.

4.3 Heat Conduction Analysis

The mathematical model for steady heat conduction within an internally cooled turbine blade was represented by a boundary value problem over a multiply-connected domain resulting in a steady-state, nonlinear heat conduction equation. This equation was numerically integrated with the Boundary Element Method (BEM) because of its advantages over finite element and finite difference methods since the BEM did not require grid generation in the domain [Brebbia and Dominguez, 1989]. In addition, the BEM was found to be faster and more accurate than the other methods for this type of boundary value problems especially when very thin thermal barrier coatings were present.

4.4 Thermal Shape Optimization

The thermal design engineer does not know in advance the temperature and heat flux distributions on the external turbine blade surface. In order to develop the most effective thermal shape optimization strategy, three different thermal objective functions have been studied [Martin and Dulikravich, 1997]. It was observed that an objective function, F(Vi), based on integrated temperature difference was the most appropriate choice.

$$F(V_i)=\left\{\int_\Gamma (T-\overline{T})^2 d\Gamma\right\}$$

where Γ is the outer boundary of the blade. Here, the user specifies the desired average temperature, $\overline{T}$, within the material of the turbine blade. This temperature should be as high as possible while taking into account thermal creep and thermal cycle fatigue limitations of the blade material. The numerical optimization algorithm modified the geometry of the coolant passages in order to minimize the sum of squared differences between the local computed temperatures and the desired uniform temperature for each of the geometric perturbations. As this function was minimized, the temperature field within the turbine blade approached the desired value, $\overline{T}$, while reducing the temperature gradients and producing a more uniform temperature field.

4.5 Implicit Differentiation for Thermal Design Sensitivity Coefficients

The partial derivatives of the field variables (temperatures, temperature gradients, thermal conductivity, etc.) and boundary values (heat fluxes, heat transfer coefficients, etc.) with respect to a set of parameters, Vi, called design variables, are very useful when performing a parametric study of a particular design. These partial derivatives are called design sensitivity coefficients. The implementation of gradient-based numerical optimization algorithms for inverse thermal shape design and optimization require these partial derivatives as part of their operation. In general, there are four methods that can be used to determine sensitivity coefficients: 1) analytical differentiation, 2) numerical differentiation of the solution by finite differences, 3) direct implicit differentiation of the governing equations, and 4) the adjoint variable or control theory method. In the arena of modern applied numerical methods and computational fluid dynamics, analytic differentiation of the governing equations is still unreliable while the adjoint variable method requires a very complicated formulation of the optimization problem that needs to be developed uniquely for each objective function. Finite differencing, although the most common brute force method, is also the most expensive strategy of obtaining sensitivity coefficients. For example, if second-order central differencing is used, the governing system must be evaluated twice per every design variable per every optimization cycle iteration. When using the BEM, the implicit differentiation of the equations at the system level [Meric, 1995] offers a practical design sensitivity calculation because the factorization of coefficient matrices needs to be performed only once and stored. Kane and Saigal [1988] obtained the sensitivity coefficients by the implicit differentiation of the coefficient matrices formed by the boundary integral equations of two-dimensional sub-structural problems. This method has been extended to three-dimensional elasticity problems by Yamazaki et al. [1994]. Similarly, the system of boundary integral equations governing heat transfer in the blade material was differentiated with respect to the vector of design variables, V_i.

$$\frac{\partial c(x)}{\partial V_i}T(x)+c(x)\frac{\partial T(x)}{\partial V_i}+\int_{-1}^{1}\frac{\partial q^*(x,\xi)}{\partial V_i}T(\xi)|\vec{\eta}|d\xi$$

$$+\int_{-1}^{1}q^*(x,\xi)\frac{\partial T(\xi)}{\partial V_i}|\vec{\eta}|d\xi+\int_{-1}^{1}q^*(x,\xi)T(\xi)\frac{\partial|\vec{\eta}|}{\partial V_i}d\xi$$

$$=\int_{-1}^{1}\frac{\partial u^*(x,\xi)}{\partial V_i}q(\xi)|\vec{\eta}|d\xi+\int_{-1}^{1}u^*(x,\xi)\frac{\partial q(\xi)}{\partial V_i}|\vec{\eta}|d\xi$$

$$+\int_{-1}^{1}u^*(x,\xi)q(\xi)\frac{\partial|\vec{\eta}|}{\partial V_i}d\xi$$

The derivatives of the boundary conditions were found in the same way.

Dirichlet $\overline{\frac{\partial T}{\partial V_i}} = 0$ Neumann $\overline{\frac{\partial q}{\partial V_i}} = 0$

$$-k\frac{\partial q}{\partial V_i} - \frac{\partial k(T)}{\partial T}\frac{\partial T}{\partial V_i}q$$

Robin

$$= \frac{\partial h_{conv}}{\partial V_i}(T - T_{amb}) + h_{conv}\left(\frac{\partial T}{\partial V_i} - \frac{\partial T_{amb}}{\partial V_i}\right)$$

After discretization, but before the application of boundary conditions, the linear algebraic system can be expressed in the following form.

$$[C']\{T\} + [C]\{T'\} + [H']\{T\} + [H]\{T'\} = [G']\{Q\} + [G]\{Q'\}$$

Here, the apostrophe denotes differentiation with respect to the design variables. In our present research, implicit differentiation of the fundamental solution has been avoided by using a slightly more expensive method of finite differencing of the coefficient matrices [C'], [H'], and [G']. Thus, the equation used was

$$[H'] = \frac{[H(V_i + \Delta V_i)] - [H(V_i)]}{\Delta V_i}$$

Using this equation, the boundary needs to be integrated once for every design variable perturbation. The advantage of this approach over implicit differentiation of the fundamental solution is that it was very easy to program; particularly because it did not require the implementation of hyper-singular integration. Since most computing time is involved in the factorization of the coefficient matrix [A],

$$[A]^{-1}\left\{\frac{\partial X}{\partial V_i}\right\} = -[C']\{T\} - [H']\{T\} + [G']\{Q\} + \left\{\frac{\partial F}{\partial V_i}\right\}$$

rather than during the integration over the boundary, this method still provided a substantial reduction in computational time at the expense of the memory required to store two sets of BEM coefficient matrices. The linear system of equations was then solved for the unknown derivatives of temperature and flux $\partial T/\partial V_i$ and $\partial q/\partial V_i$. The gradient of the thermal objective function, as well as its design sensitivity, has been computed given the thermal sensitivity coefficients of $\partial T/\partial V_i$.

$$F(V_i) = \int_\Gamma 2(T - \overline{T})\frac{\partial T}{\partial V_i}d\Gamma$$

It should be pointed out that instead of using a thermal penalty function, the thermal constraint, $T_{max} = \overline{T}_{max}$, was placed directly into design sensitivity.

4.6 Evolutionary Hybrid Optimization

Since the design space for typical non-linear large-scale multidisciplinary optimization problems had an abundance of local minimums, it was advantageous to use a constrained evolutionary hybrid optimization approach [Foster and Dulikravich, 1997; Martin and Dulikravich, 1997] in order to avoid local minimums. The hybrid algorithm incorporated four of the most popular optimization approaches: the Davidon-Fletcher-Powell (DFP) gradient search method, a genetic algorithm (GA), the Nelder-Mead (NM) simplex method, and simulated annealing (SA). Each technique separately provided a unique approach to optimization with varying degrees of convergence, reliability, and robustness at different stages during an iterative optimization procedure. The new evolutionary hybrid scheme treated the existence of constraints in three ways: Rosen's projection method, a feasible search, and random design generation. Rosen's projection method [Haftka and Gurdal, 1992] provided search directions which guided the descent direction tangent towards active constraint boundaries. In the feasible search, designs that violated constraints were automatically restored to feasibility via the minimization of the active global constraint functions. If at any time this constraint minimization failed, a number of random designs were generated using a Gaussian-shaped probability density cloud about a desirable and feasible design until a new design was reached.

The feasible set of design variables from the current optimization cycle was saved into an array called the population matrix. This population was updated every iteration with new designs which were ranked according to the value of the objective function so that as the optimization process proceeded, the population evolved. The optimization problem was completed when the best design in the population was equivalent to a target design or when every optimizer failed to arrive at a better design simultaneously. This usually indicated that a global minimum had been found.

4.7 Results of Quasi-Conjugate Thermal Optimization

An example of the potential practical benefits of using this approach to design optimization of coolant flow passages based on the quasi-conjugate heat transfer optimization is demonstrated in Figs. 13-20. A symmetric Rankine oval shape (Fig. 13) was chosen to simulate a typical support strut airfoil. It was modeled as being made of stainless steel with thermal conductivity k = 30.0 W m^{-1} K^{-1} and having a 150 microns thick thermal barrier coating with thermal conductivity, k = 1.0 W m^{-1} K^{-1}. The strut airfoil was assumed to have four coolant flow passages that were initially symmetrically sized and located (Fig. 13). For specified temperatures (Fig. 14) on the outside surface of the strut airfoil, the structured grid Navier-Stokes code predicted the corresponding surface normal temperature derivatives from which the heat convection coefficient distribution (Fig. 15) was obtained using inlet hot gas temperature as the ambient temperature. The desired average temperature in the entire airfoil was specified to be $\overline{T}$ = 1300 K. There were 20 geometric design variables in this test case: 8 vertices of the b-spline for the blade wall thickness, 2 strut x-locations/strut, 1 strut thickness/strut, and 1 filleting parameter (Lame curve exponent)/strut. Using this flexible geometry treatment of the interior of the airfoil and using the quasi conjugate heat transfer optimization, the four coolant flow passages converged to their new shapes and locations (Fig. 13). The corresponding temperature distribution on the airfoil outer surface was more uniform than the initial surface temperature distribution. Even the leading edge stagnation point temperature was decreased slightly (Fig. 14). At the same time, the optimized coolant passages allowed for a significantly higher inlet hot gas temperature (Fig. 16) and a considerably lower coolant mass flow rate (Fig. 17) which is a remarkable result. Notice also that the final result was symmetric about x-axis. Coolant pressure loss increased (Fig. 18) during the quasi-conjugate optimization because of the increased optimized relative surface roughness (Fig. 19) required on the walls of each of the coolant passages. This in turn lead to the increased average convection heat transfer coefficient (Fig. 20) on the walls of each of the coolant passages. The entire design optimization process required two hours of a single processor time on Cray C-90 computer.

5. THERMOELASTICITY

NOTE: The final version of this paper will have three-dimensional blade thermo-elasticity optimization results.

6. ACKNOWLEDGMENTS

The authors are grateful for NASA-Penn State Space Propulsion Engineering Center Graduate Student Fellowship, National Science Foundation Grant DMI-9522854 monitored by Dr. George Hazelrigg, NASA Lewis Research Center Grant NAG3-1995 facilitated by Dr. John Lytle, and supervised by Dr. Kestutis Civinskas, and the ALCOA Foundation Faculty Research Fellowship facilitated by Dr. Yimin Ruan.

7. REFERENCES

Brebbia, C. A. and Dominguez, J. (19890 *Boundary Elements, An Introductory Course,* McGraw-Hill Book Company, New York.

Chyu, M. K., Ding, H., Downs, J. P., Van Sutendael, A. and Soechting, F. O. (June 1997) "Determination of Local Heat Transfer Coefficient Based on Bulk Mean Temperature Using a Transient Liquid Crystals Technique", ASME paper 97-GT-489, Orlando, FL.

Demirdzic, I. and Peric, M. (1988) "Space Conservation Law in Finite Volume Calculations of Fluid Flow ", *International Journal for Numerical Methods in Fluids*, Vol. 8, pp. 1037-1050.

Dennis, B. H. and Dulikravich, G. S. (September 1997) "Thermo-Elastic Analysis and Optimization Environment for Internally Cooled Turbine Airfoils", Symp. on Airbreathing Engines, Ed: F. S. Billig, Chattanooga, TN, Sept. 8-12, 1997, ISABE 97-7181, Vol. 2, pp. 1335-1341.

Dulikravich, G. S. (June 1988) "Inverse Design and Active Control Concepts in Strong Unsteady Heat Conduction", *Appl. Mechanics Reviews*, Vol. 41, No. 6, pp. 270-277.

Dulikravich, G. S. (January 1995) "Shape Inverse Design and Optimization for Three-dimensional Aerodynamics", *AIAA Invited Paper 95-0695*, AIAA Aerospace Sciences Meeting, Reno, NV.

Dulikravich, G. S. and Kosovic, B. (1992) "Minimization of the Number of Cooling Holes in Internally Cooled Turbine Blades", *International Journal of Turbo & Jet Engines*, Vol. 9, No. 4, pp. 277-283.

Dulikravich, G. S. and Martin, T. J. (1994) "Inverse Design of Super-Elliptic Cooling Passages in Coated Turbine Blade Airfoils", *AIAA Journal of Thermophysics and Heat Transfer*, Vol. 8, No. 2, pp. 288-294.

Dulikravich, G. S. and Martin, T. J. (1995) "Geometrical Inverse Problems in Three-Dimensional Non-Linear Steady Heat Conduction", *Engineering Analysis with Boundary Elements*, Vol. 15, pp. 161-169.

Dulikravich, G. S. and Martin, T. J. (1996) "Inverse Shape and Boundary Condition Problems and Optimization in Heat Conduction", Chapter 10 in *Advances in Numerical Heat Transfer*, Editors: W. J. Minkowycz and E. M. Sparrow, Taylor & Francis, pp. 324-367.

Foster, N. F. and Dulikravich, G. S. (January-February 1997) "Three-Dimensional Aerodynamic Shape Optimization Using Genetic and Gradient Search Algorithms", *AIAA Journal of Spacecraft and Rockets*, Vol. 34, No. 1, pp. 36-42.

Hafka, R. T. and Gurdal, Z. (1992) *Elements of Structural Optimization*, 3rd edition, Kluwer Academic Publishers, Boston, MA.

Han, J.-C., Zhang, Y. M., and Lee, C. P. (January 1994) "Influence of Surface Heating Condition on Local Heat Transfer in a Rotating Square Channel With Smooth Walls and Radial Outward Flow", *Journal of Turbomachinery*, Vol. 116, pp. 149-158.

Han, Z.-X., Fang, R. and Liu, Z.-J. (1998) "2-D Flowfields Calculation with Multi-Unstructured Grids", *Journal of Aerospace Power*, in press.

Han, Z.-X. and Liu, Z.-J. (November 1997) "Numerical Calculation of 2-D Inviscid Flow-Fields on Unstructured Grids", *J. of Engineering Thermophysics*, Vol. 18, No. 6.

Holman, J. P. (1981) "Heat Transfer", Fifth Edition, McGraw Hill Book Company.

Kane, J. H. and Saigal, S. (1988) "Design Sensitivity Analysis of Solids Using BEM", *Journal of Engineering Mechanics*, ASCE, Vol. 114, No. 10, pp. 1703-1722.

Leonard, O., 1990, "Subsonic and Transonic Cascade Design", AGARD R-780, pp. 7-1:7-18.

Leonard, O. and Demeulenaere, A. (1997) "A Navier-Stokes Inverse Method Based On a Moving Blade Wall Strategy", ASME paper 97-GT-416, Orlando, FL.

Li, H. and Kassab, A. J. (June 1994) "A Coupled FVM/BEM Approach to Conjugate Heat Transfer in Turbine Blades", *AIAA Paper 94-1981*, 6th AIAA/ASME Joint Thermophysics and Heat Transfer Conference, Colorado Springs, CO.

Pirzadeh, S. (1993) "Structured Background Grids for Generation of Unstructured Grids by the Advancing-Front Method", *AIAA J.*, Vol. 31, No. 2, pp. 257-265.

Martin, T. J. and Dulikravich, G. S. (September 1997) "Aero-Thermal Analysis and Optimization of Internally Cooled Turbine Blades", *XIII International Symposium on Airbreathing Engines (XIII ISABE)*, Chattanooga, TN, ISABE 97-7165, Vol. 2, pp. 1232-1250.

Meric, R. A. (1995) "Differential and integral sensitivity formulations and shape optimization by BEM", *Engineering Analysis with Boundary Elements*, Vol. 15, pp. 181-188.

Mochizuki, S., Takamura, J., Yamawaki, S., and Yang, W. J. (1994) "Heat Transfer in Serpentine Flow Passages With Rotation", *Journal of Turbomachinery*, Vol. 116, pp. 133-140.

Stephens, M. A. and Shih, T. I.-P. (June 1997) "Computation of Compressible Flow and Heat Transfer in a Rotating Duct with Inclined Ribs and a 180-Degree Bend", ASME paper 97-GT-192, Orlando, FL.

White, F. M. (1988) *Heat and Mass Transfer*, Addison-Wesley Publishing Company, Reading, MA, pp. 272.

White, F. M. (1994) *Fluid Mechanics*, Third Edition, McGraw-Hill Book Company, New York.

Yamazaki, K., Sakamoto, J., Kitano, M. (June 1994) 'Three-Dimensional Shape Optimization Using the Boundary Element Method", *AIAA J.*, Vol. 32, No. 6.

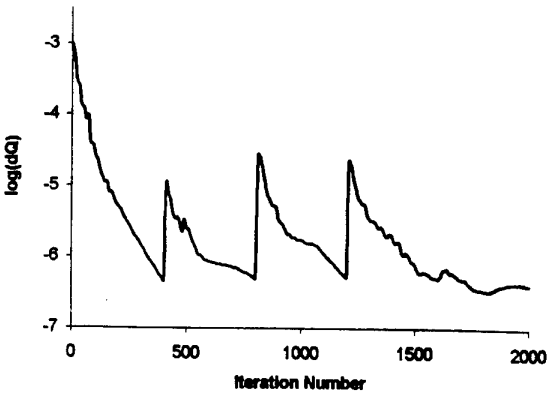

Fig. 1 Convergence history of the shape inverse design of symmetric airfoils in a non-lifting cascade.

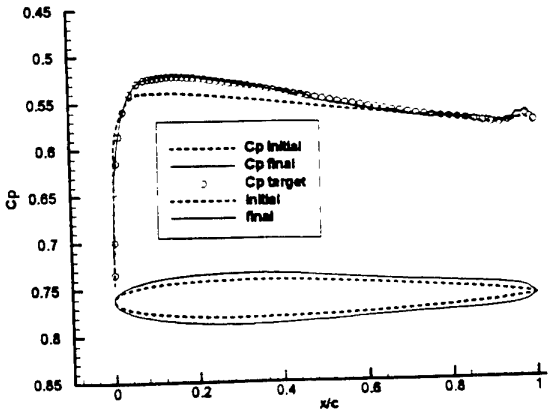

Fig. 2 Initial, target, and final isentropic surface Mach number distribution and initial and inversely designed symmetric airfoils in a non-lifting cascade.

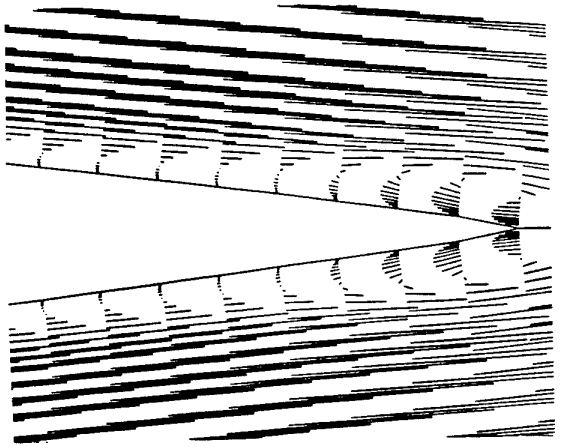

Fig. 3 Velocity field for the initial symmetric airfoils in a non-lifting cascade.

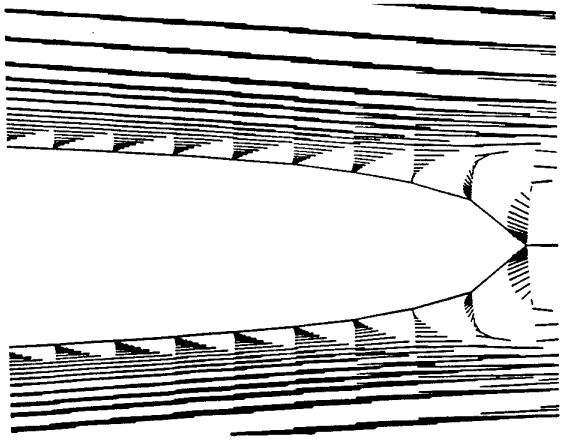

Fig. 4 Velocity field for the inversely designed symmetric airfoils in a non-lifting cascade.

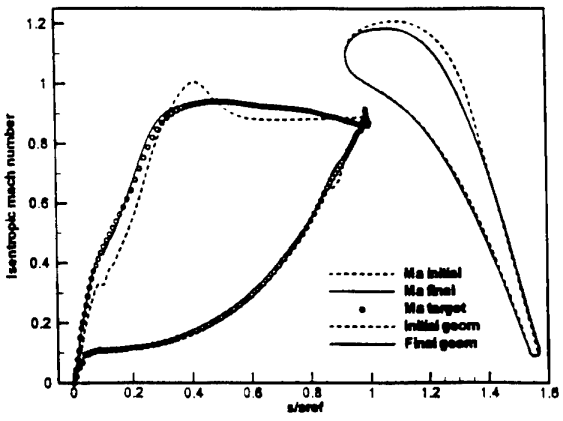

Fig. 5 Initial, target, and final isentropic surface Mach number distributions and initial and inversely designed high subsonic exit turbine cascade shapes.

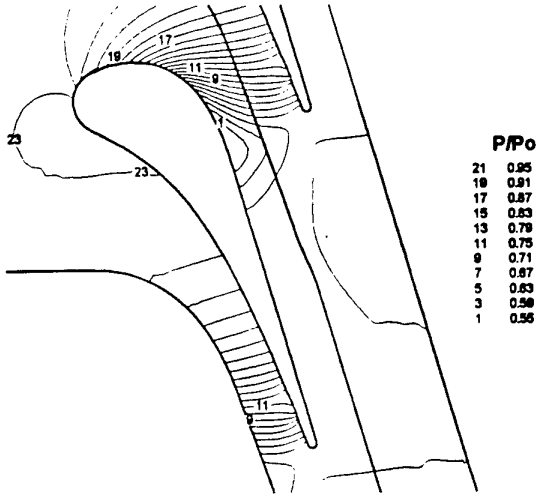

Fig. 6 Pressure field for an initial high subsonic exit turbine cascade obtained using Euler equations.

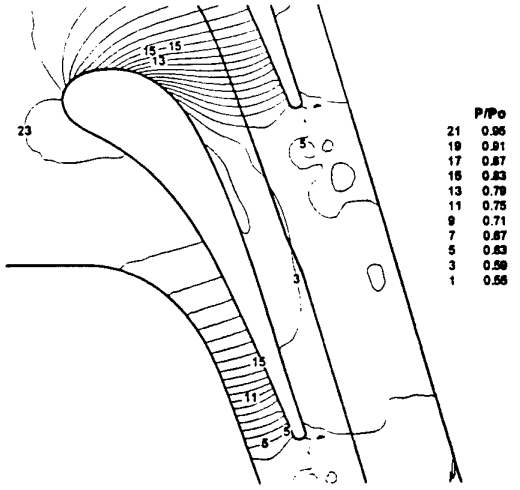

Fig. 7 Pressure field for the inversely designed high subsonic exit turbine cascade obtained using Euler equations.

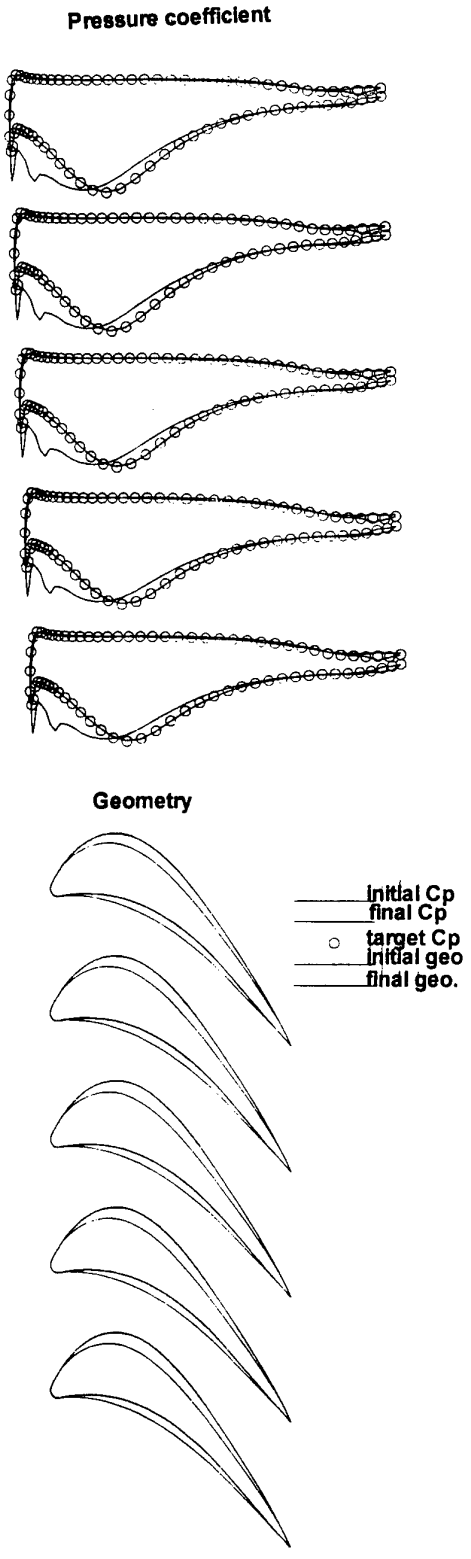

Fig. 8 Initial, target, and final isentropic surface Mach numbers for the sections of a three-dimensional turbine blade obtained using a Navier-Stokes solver.

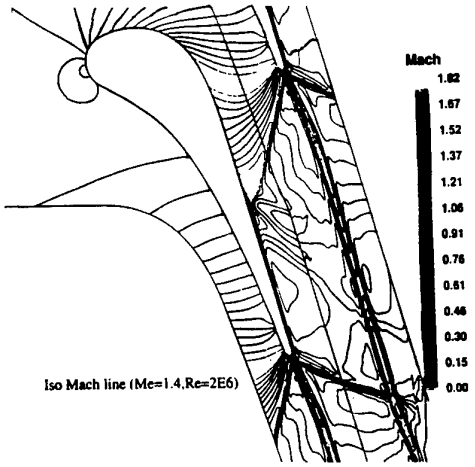

Fig. 9 Mach number field for an initial supersonic exit turbine cascade.

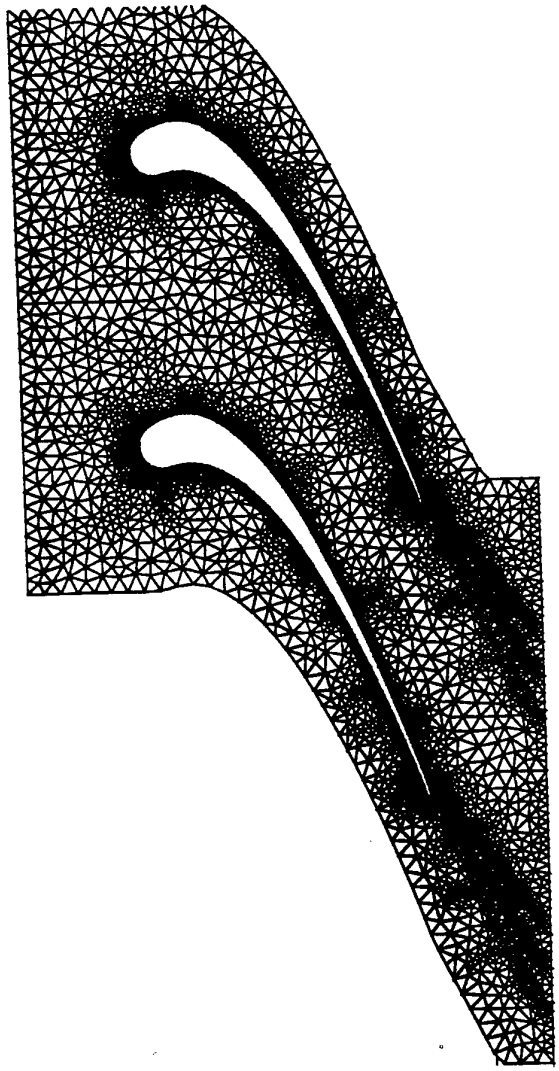

Fig. 10 Mach number field for a supersonic exit turbine cascade optimized using a genetic algorithm.

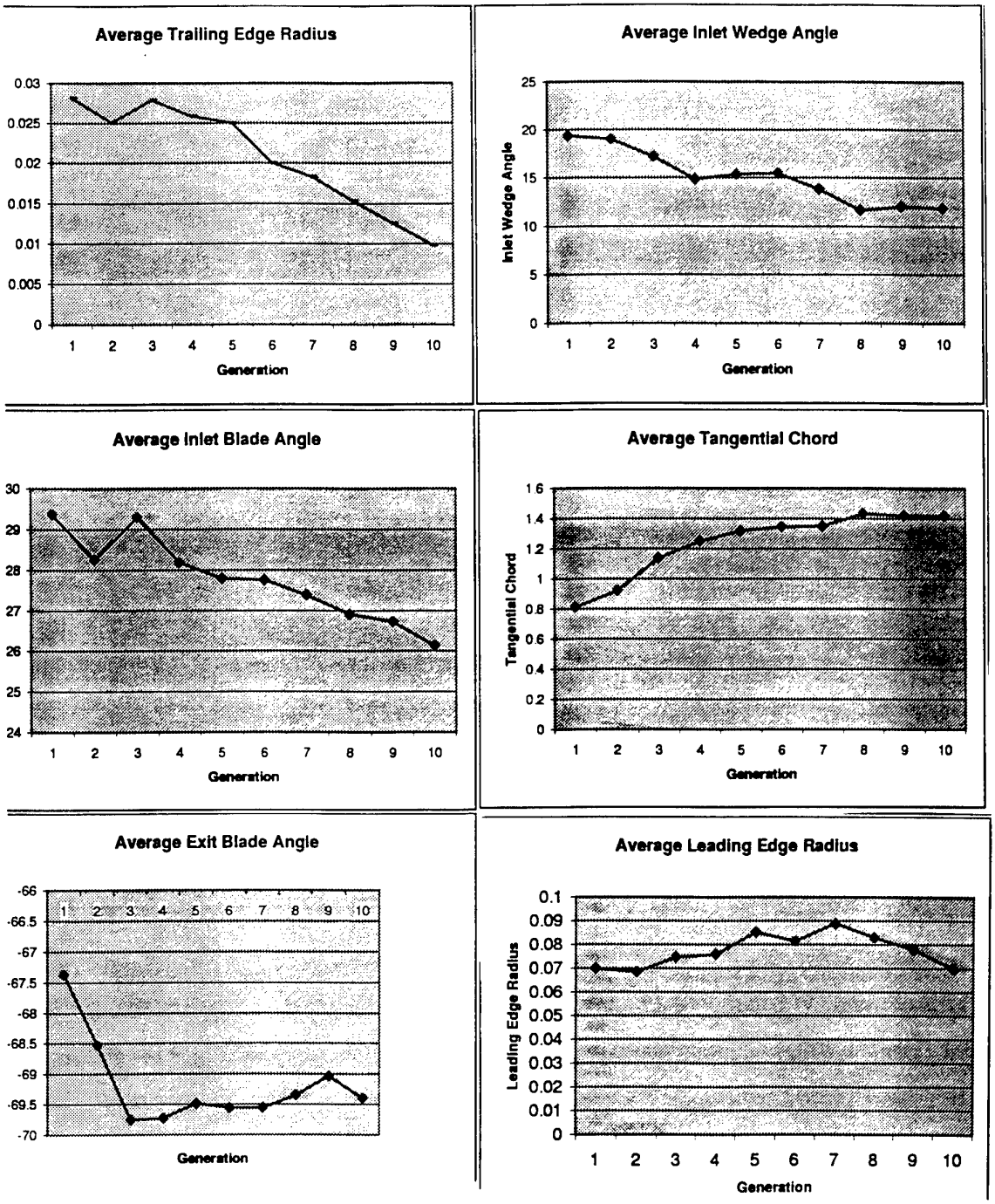

Fig. 11 Convergence histories of various parameters during constrained genetic algorithm optimization of a supersonic exit cascade using a non-structured Navier-Stokes solver.

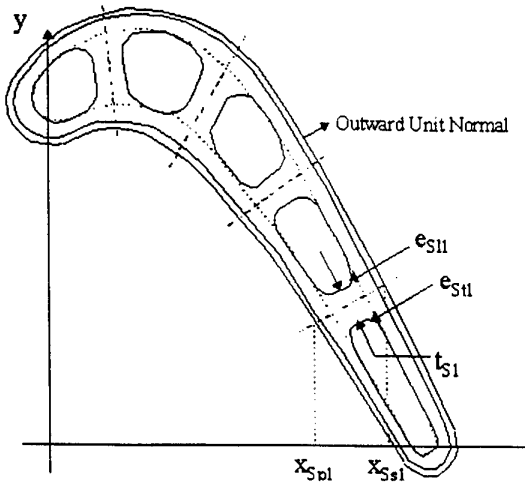

Fig. 12 Turbine airfoil geometry definition with multiple coolant passages, struts, and the thermal barrier coating/metal interface.

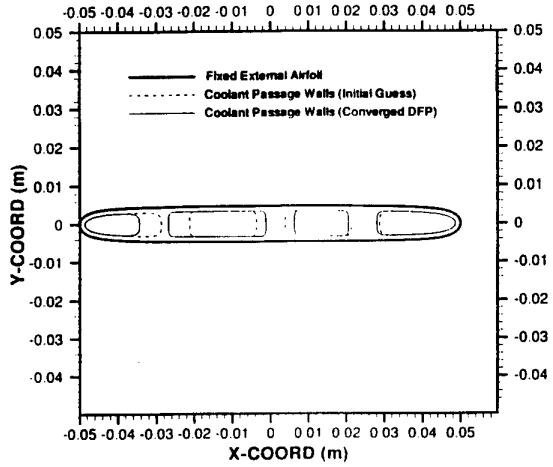

Fig. 13 Geometry of the coated internally cooled symmetric strut airfoil (initial guess and optimized interior).

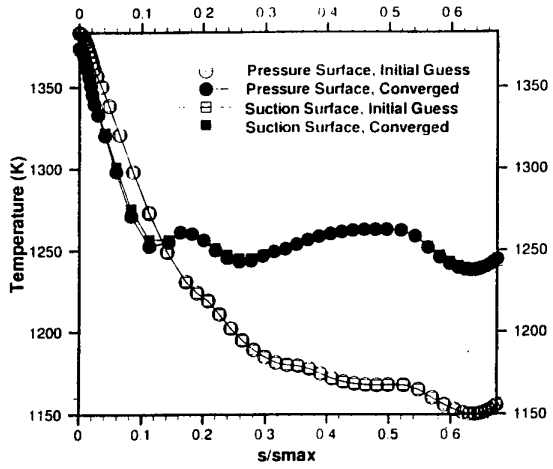

Fig. 14 Temperature distribution on the external surface of the symmetric strut airfoil (initial and optimized).

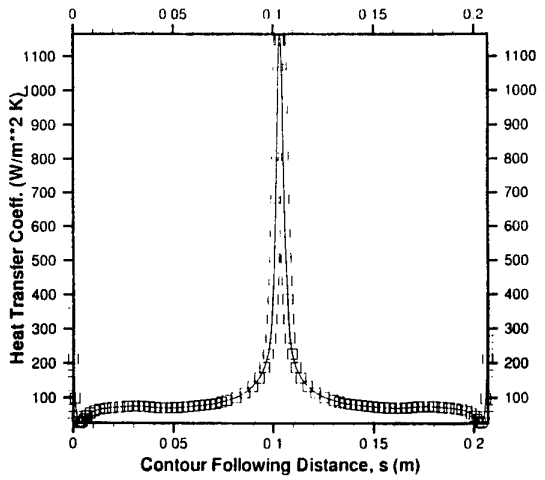

Fig. 15 Heat transfer coefficients on the external surface of the symmetric strut airfoil computed by a Navier-Stokes solver and specified as boundary conditions during thermal optimization.

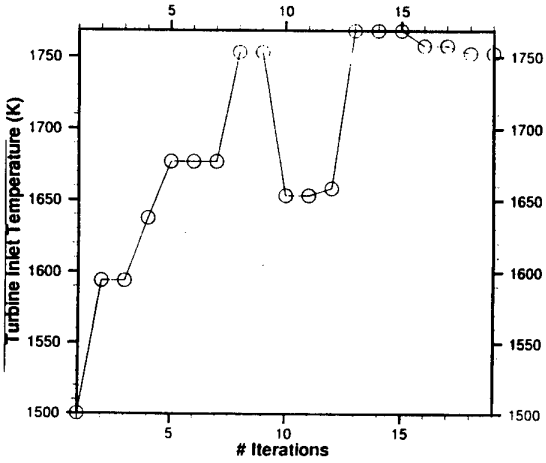

Fig. 16 Inlet hot gas temperature maximization history for the symmetric strut airfoil.

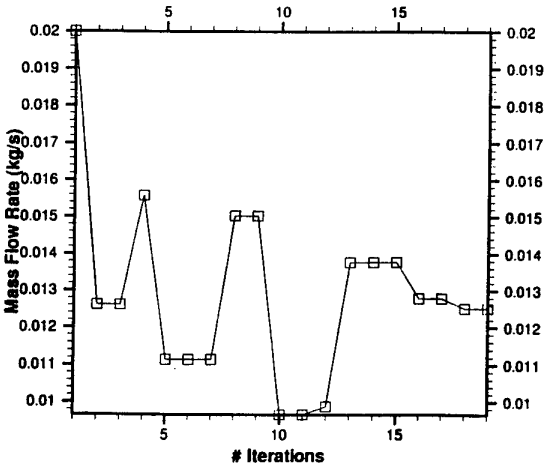

Fig. 17 Coolant mass flow rate minimization history for the symmetric strut airfoil.

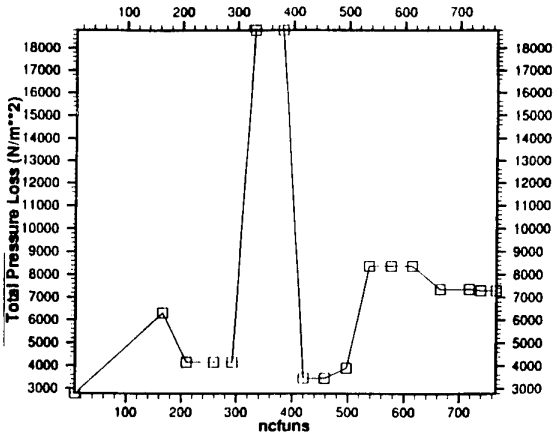

Fig. 18 Coolant pressure loss evolution during quasi-conjugate optimization of the interior of the symmetric strut airfoil.

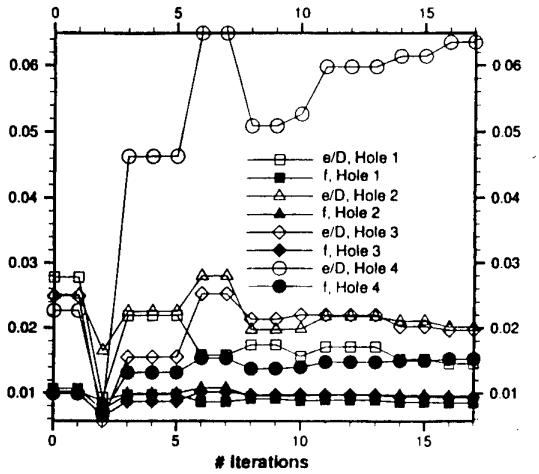

Fig. 19 Relative surface roughness evolution on the walls of the coolant flow passages during quasi-conjugate optimization of the interior of the symmetric strut airfoil.

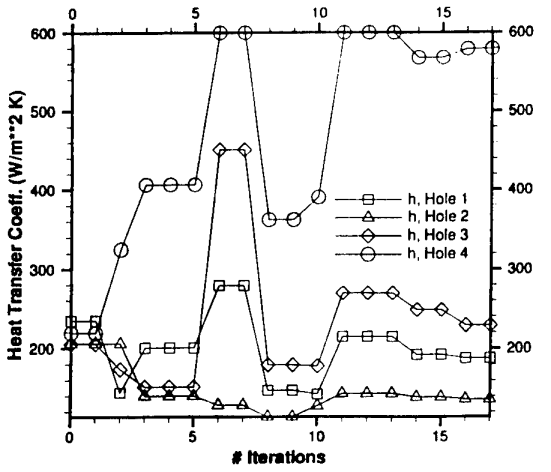

Fig. 20 Convection heat transfer coefficient evolution on the walls of the coolant flow passages during quasi-conjugate optimization of the interior of the symmetric strut airfoil.

The Benefits of a Rotating Rig for Research into Advanced Turbine Cooling Systems

R. Davenport
Specialist - Turbine Research
Rolls-Royce plc
Filton
Bristol
BS34 7QE
England

1. SUMMARY

Internal cooling of turbine blades is essential for efficient turbine engine performance and dictates the life of the component. Engine specific thrust and efficiency benefit from blade cooling although the use of cooling air imposes cycle penalties and can reduce aerodynamic efficiency. Cooling research aims to develop and validate design methods to give maximum cooling effectiveness for minimum cooling flow. The design methods need to be reliable reducing the risks in future projects thus helping to avoid in-service short falls and high maintenance costs.

Current design methods have been almost exclusively derived from experiments performed using simplified cooling geometries without the influence of rotation, which is perfectly feasible for nozzle guide vane designs but sadly lacking for rotor designs. However, it is important to pursue both static and rotating experiments to establish the effects of rotation and to determine design rules that allow corrections to static experimental data. All the experimental data can be used to validate CFD modelling which has difficulty in predicting heat transfer levels in highly turbulent 3D flows.

2. INTRODUCTION

Today engineers within the aero engine gas turbine and associated aeronautic industries are facing many challenges, which are set by

- The unremitting US and Pacific Rim competitive pressure
- Customer demands
- The increasingly stringent environmental, safety and reliability requirements
- The drive to reduce pre-production timescales and costs

For both industrial and aero gas turbines the ability to predict flow and heat transfer associated with blade cooling passages is essential if accurate blade metal temperatures and hence blade lives are to be calculated. A knowledge of the flow and heat transfer also enables efficient use of cooling flows reducing the aerodynamic penalties and will also be an important aspect in reducing engine emissions.

A further case in point is the development of twin engine aircraft's, and the advent of the 'Super Jumbo'. The requirements for reliable efficient operation of engines for a 180 minute Extended range Twin Operation (ETOP) or the costs involved to delayed or diverted 'Super Jumbo', are immense. Failure to deliver costs the gas turbine companies not just in terms of lost revenue, but in competitiveness and reputation. Furthermore with requirements changing regularly, industry has to be both proactive and reactive to its customer needs. This means that the 'time to market' must be minimised, which implies our designs need to be 'right first time'.

The objectives of the research are:

- Obtain a comprehensive experimental data-base
- Correlate the experimental data
- Improve current design methods
- Use experimental data to validate CFD codes
- Obtain CFD codes that can predict blade cooling passage heat transfer and flow accurately

It is a high priority to obtain design methods that incorporate the influence of rotation for relevant internal cooling geometries. Rotation has been shown to significantly reduce and enhance the heat transfer of simplified cooling geometries. Due to the complex nature of rotating experiments it would be extremely advantageous to have reliable CFD predictions, however, more detailed heat transfer data is required to validate the codes.

The research is expected to achieve the following:

- Increase turbine peak cycle temperature
- Improve specific thrust
- Improve specific fuel consumption
- Reduce blade cooling flows
- Reduce aerodynamic efficiency penalties of ejecting cooling flows
- Increase blade life

The lives of hot end components show a high sensitivity to metal temperatures; a decrease of 15°C to 25°C in metal temperature could double the life of an HP rotor blade.

Paper presented at the RTO AVT Symposium on "Design Principles and Methods for Aircraft Gas Turbine Engines", held in Toulouse, France, 11-15 May 1998, and published in RTO MP-8.

Information concerning the effects of rotation on actual engine geometries are of prime importance because there is no published data at the correct non-dimensional levels.

Most of the research in this area has been performed by Pratt and Whitney using NASA funding as part of the Hot Section Technology (HOST) programme, see reference 1. This work has studied a simplified coolant channel and obtained averaged heat transfer data using a steady-state method over a limited range of non-dimensionals. This work now forms part of the Integrated High Performance Turbine Engine Technology (IHPTET) programme which threatens to forge a US lead in advanced turbine technologies.

Further work in the US for General Electric (GE) has investigated the effect of aspect ratio on the buoyancy driven reverse flow near the leading wall of rotating cooling passages, reference 2. Due to the reversal of flow regions of zero to low velocity are created near the leading wall impairing the heat transfer in these regions. GE also have several projects using CFD to predict the effects of rotation. Reference 3 describes an analysis using a fully elliptic 3-D body fitted code based on pressure correction techniques.

European research in this field is performed at Darmstadt and Swansea. Professor DK Hennecke et al have been investigating the effects of rotation of impinging jets, reference 4, whilst Professor WD Morris at Swansea has designed a new research facility to investigate the effects of rotation on heat transfer, reference 5.

Current design methods are lacking in predicting the influence of rotation for any internal cooling geometry. This effect has been ignored and leads to uncertainties in the level and distribution of heat transfer within the cooling geometry.

There is a continuous development of cooling geometries using different concepts to increase cooling effectiveness and efficiency, however, this produces the need for new correlations that characterise the flow and heat transfer allowing the new concepts to be used in real solutions

This research programme not only provides detailed rotating heat transfer and flow data at more representative engine non-dimensionals, but also investigates today's relevant cooling geometries. State-of-the-art cooling concepts are modelled looking at multipass configurations leading to blade cooling systems that are characterised and applicable in new designs.

3. BACKGROUND

With the rotation of rotor blades, the air in the cooling passages experiences Coriolis and buoyancy forces, which dramatically alter both the level and distribution of heat transfer through the cross and radial secondary flows that are generated. The aim of the research rig is to provide experimental data from advanced blade cooling geometries to enable design methods to be improved by incorporating the effects of rotation upon internal heat transfer distributions. This would, in turn, allow more accurate blade temperatures to be calculated and hence more accurate and reliable life predictions.

To obtain experimental data at similar non-dimensional levels to that in the engine involved an analysis which matches Reynolds, Nusselt, Mach, Rotation and Rayleigh numbers in the cooling passages, which ultimately sets a model scale factor, coolant temperature and rotational speed. Inspection of current engine thermal designs and expected future trends enabled spinning rig design parameters to be fixed.

Cooling models are manufactured from perspex® which is transparent and has excellent thermal properties for the techniques used i.e. low thermal conductivity. To obtain the temperature measurement accuracy and large number of channels required, the decision to design and build a computer that could rotate at 5000rpm and take measurements from numerous thermocouples and transducers. There is still a requirement for a slip-ring to transfer the data to a host computer, however, all the data is digitised therefore any noise generated by the slip-ring is completely eliminated and the total number of channels significantly reduced.

Two methods of obtaining heat transfer data were used, surface thermocouples and liquid crystals. Surface thermocouples provide only single point information but has the advantage of providing a history of heat transfer coefficients (htc) during a transient test. Liquid crystals, on the other hand, provide a detailed surface distribution of htc allowing variations between ribs and around passage bends to be identified. However, there was a need to specially design video cameras to withstand the high 'g' (up to 20000g) field because they had to be positioned at the end of the arms, filming the liquid crystal on the surface of the model passages. Although the signals from the cameras are analogue, they are volt level and do not suffer from interference from the slip-ring and gave clear, steady pictures. The results from both methods are presented with the thermocouple values correlated using the parameter:

$$Nu = \mathrm{Re}^{1.1}\, Ro^{0.36} Ra^{-0.19}$$

4. NON DIMENSIONAL ANALYSIS

Before a rig design could be defined, it was important to identify what the non-dimensional analysis of the current blade designs would identify. The non-dimensional groups identified from the independent variables are as follows:

Identity	Definition	Physical Significance
Reynolds No. Re	$\rho u d / \mu$	$\frac{Inertia Forces}{Viscous Forces}$
Prandtl No. Pr	$\mu Cp / k$	$\frac{Momentum Diffusivity}{Heat Diffusivity}$
Mach No. M	$u / \sqrt{\gamma g R t}$	$\frac{Air Velocity}{Sonic Velocity}$
Grashof No. Gr	$r\Omega^2\rho^2 d^3 / \mu^2 . \Delta T / T$	$\frac{Buoyancy \times Inertia Forces}{Viscous Forces^2}$
Rayleigh No. Ra	$Gr.\Pr$	$\frac{Buoyancy \times Inertia \times Momentum Diff.}{Viscous Forces^2 \times Heat Diff.}$
Buoyancy No. Bg	Gr / Re^2	$\frac{Buoyancy Forces}{Inertia Forces}$
Buoyancy No. Br	Ra / Re^2	$\frac{Buoyancy Forces \times Momentum Diff.}{Inertia Forces \times Heat Diffusivity}$
Rotation No. Ro	$\Omega d / u$	$\frac{Coriolis Forces}{Inertia Forces}$

The dependent variables give rise to the following groups:

Identity	Definition	Physical Significance
Nusselt No. Nu	hd / k	$\frac{Characteristic Body Length}{Boundary Layer Equiv. Thickness}$
Stanton No. St	hA / mCp	$\frac{Heat Flux to Wall}{Enthalpy Flux past Wall}$

For internal blade cooling the aim is a complete simulation at high gas velocity, variable property mixed rotating convection. Therefore,

$$Nu = f_1[passageshape, \mathrm{Re}, \Pr, H/t, Gr, Ro, M] \quad \textbf{...Equation 1}$$

Making the following assumptions

1. Test geometrical scaled blade cooling passages at scale engine radius.
2. Prandtl number can be considered constant for air.

Hence, passage shape, H/t and Pr fall out of equation 1 giving:

$$Nu = f_2\left[\mathrm{Re}, Ro, \frac{\Delta T}{T}, M\right] \quad \textbf{.....Equation 2}$$

Now, for complete model to engine simulation each of the terms in equation 2 must have the same value in the model as in the engine. When this is achieved it follows that the Nusselt number in the model will equal that in the engine.

4.1 Engine to Model Analysis

For each of the terms in equation 2 it is possible to equate the model value to the engine value as follows:

$$\text{Ro gives} \left(\frac{\Omega d_h}{u}\right)_m = \left(\frac{\Omega d_h}{u}\right)_e \quad \textbf{..... Equation 3}$$

$$\text{Re gives} \left(\frac{W d_h}{A\mu}\right)_m = \left(\frac{W d_h}{A\mu}\right)_e \quad \textbf{.....Equation 4}$$

$$\text{M gives} \left(\frac{W\sqrt{T}}{AP}\right)_m = \left(\frac{W\sqrt{T}}{AP}\right)_e \textbf{ OR}$$

$$\left(\frac{u}{\sqrt{T}}\right)_m = \left(\frac{u}{\sqrt{T}}\right)_e \quad \textbf{.....Equation 5}$$

$$\frac{\Delta T}{T} \text{ gives} \left(\frac{\Delta T}{T}\right)_m = \left(\frac{\Delta T}{T}\right)_e \quad \textbf{.....Equation 6}$$

From equations 3 and 5

$$\frac{\Omega_m}{\Omega_e} \cdot \frac{d_m}{d_e} = \frac{u_m}{u_e} = \sqrt{\frac{T_m}{T_e}} \quad \textbf{.....Equation 7}$$

From equations 4 and 5

$$\frac{P_e}{P_m} = \frac{\mu_e}{\mu_m} \cdot \sqrt{\frac{T_e}{T_m}} \cdot \frac{d_m}{d_e} \quad \text{.....Equation 8}$$

For typical engine conditions:

Engine values

$$T_e = 855K$$
$$P_e = 2268.5kPa$$
$$\Delta T_e = 173K$$

Model values

$$T_m = 200K$$
$$P_m = 150kPa$$

Therefore from equation 8

$$\frac{d_m}{d_e} = \frac{2268.5}{150} \cdot \frac{1.413e^{-5}}{3.850e^{-5}} \cdot \sqrt{\frac{200}{855}} = 2.68$$

and equation 7

$$\frac{\Omega_m}{\Omega_e} = \frac{d_e}{d_m} \cdot \sqrt{\frac{T_m}{T_e}} = \frac{1}{2.68} \cdot \sqrt{\frac{200}{855}} = 0.18$$

and equation 6

$$\left(\frac{\Delta T}{T}\right)_m = \left(\frac{\Delta T}{T}\right)_e = \frac{173}{855} = 0.20$$

therefore for the model

$$\frac{T_w - T_g}{T_w} = 0.20$$

fixing the gas temperature at 200K leads to a required wall temperature of 250K.

These calculations indicate that the cooling model would be 2.5 to 3 times engine scale and would rotate at around one fifth engine speed ($\approx$3000 rpm) with a coolant supplied at 200K. An Excel® spreadsheet has been constructed to enable the thermodynamic design of the cooling model to be easily calculated by entering all the engine parameters at the design planes.

5. RIG DESIGN

To enable the rotating rig to provide enough future expansion, a maximum rig rotational speed of 4,000

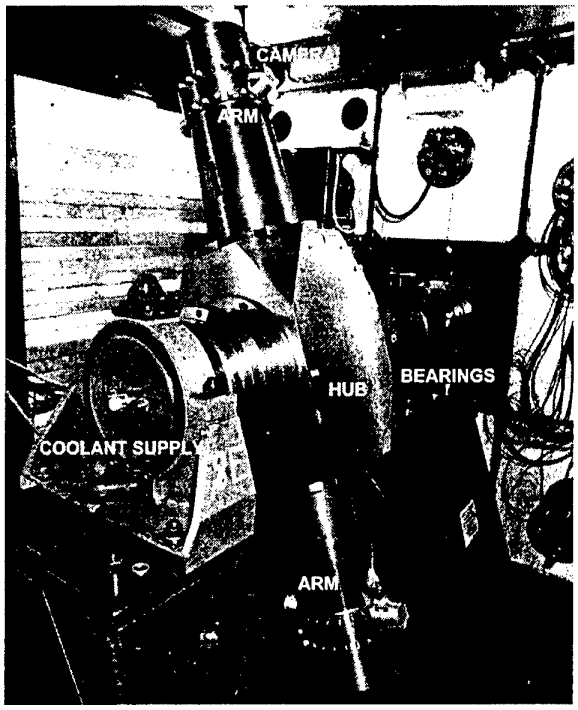

Figure 1

rpm was specified. This gave rise to a rig which has two 'arms' connected by a central hub which houses the rotating computer, shown by figure 1. Cooling models fit inside the arms which are hollow tubes with large threaded plates that screw into the end of the arms. The mean radius of rotation is 0.7m which coincides with the centreline of the cameras. The construction is cantilevered from a set of bearings which allows the front of the rig to be free of any obstructions at the point at which the coolant is introduced through two concentric face seals. It is important to have equal cooling to both arms to minimise any differential contraction of the components that experience cooling which could cause out of balance. The construction is all steel and weighs some 1.5 tonnes. A 'dummy' model, made of the same material and same mass, is placed in the end of the arm not occupied by the cooling model.

5.1 COOLANT SUPPLY SYSTEM

Figure 2 illustrates the cooling system required for the rig. To produce the correct buoyancy forces, the non dimensional analysis indicates that a coolant temperature of 200K and 0.1 kg/s are required. This has been achieved using a heat exchanger submersed in liquid nitrogen, using the level of liquid to control the exit temperature of the gas. It is important to clean and dry the air before cooling to avoid any solid particles from entering the cooling model. The entry pipework has a BS1042 orifice plate which is used to calibrate orifice plates in each of the supply lines feeding the two arms of the rotating rig.

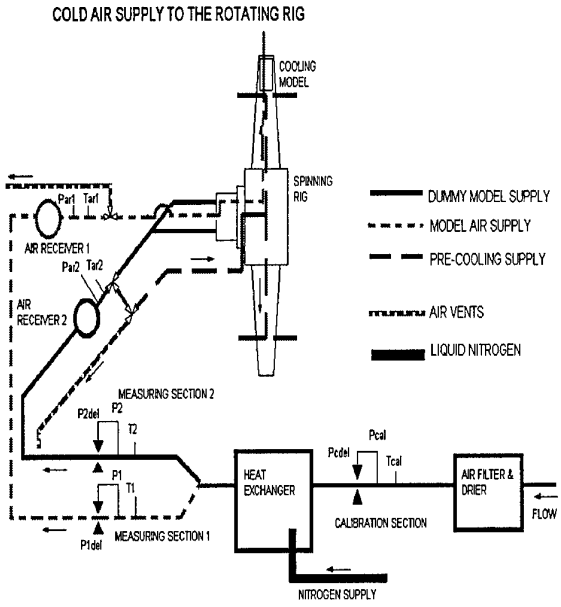

Figure 2

Coolant is supplied to each end of the arms through the inner pipe of a concentric pair of pipes which are fixed into the hub and connect to the inlet of the models. Prior to each test, coolant from line 2 is used to pre-cool the inner supply pipes by passing coolant through the cavity between the concentric pipes inside the rig arms.

5.2 SPINNING CELL

Due to the high energy levels of the rotating assembly, test work takes place in a containment cell. The walls of the cell are made from solid steel some 100mm thick with a lining comprising layers of 6mm plate and rubber. Extra containment is placed in the plane of rotation which is made from 100mm thick aluminium blocks, shown in figure 3. It is possible to lower the cell pressure to 30kPa reducing any windage losses during the spinning tests.

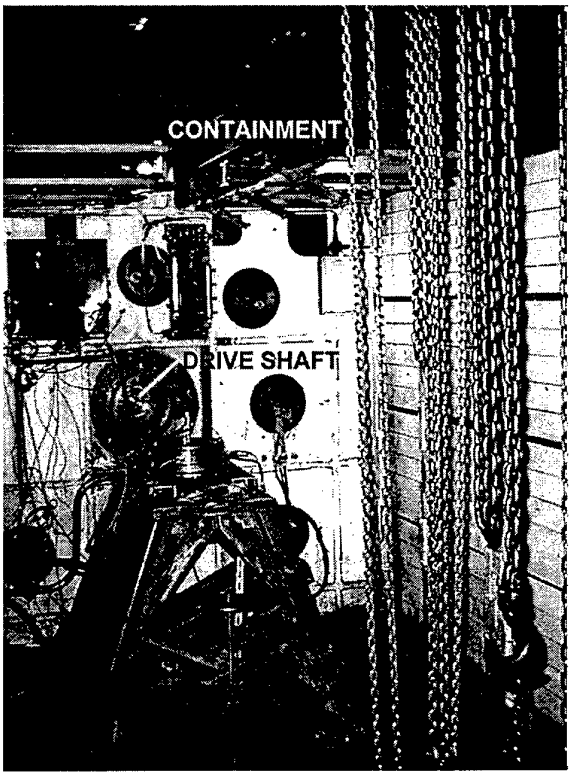

Figure 3

Two 500HP electric motors, shown in figure 4 are used to rotate the assembly.

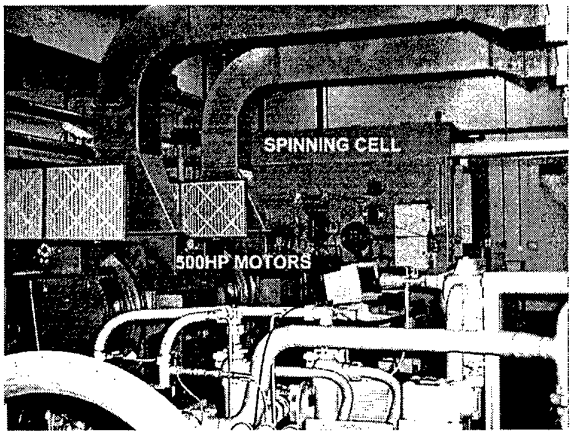

Figure 4

6. COOLING MODEL DESIGN AND INSTRUMENTATION

As indicated by the non dimensional analysis, typical model scales are between 2 and 4 that of engine scale. For HP turbines, engine blade heights are approximately 50mm, therefore, model cooling geometries are between 100mm and 200mm. This led to a total model envelope of 305mm by 177mm diameter being made available in the rig arms. Full engine geometries can be accommodated in this envelope incorporating film cooling rows, turbulators

and all other geometrical variations. The model includes an inlet plenum which feeds the coolant into a cavity which replicates the disk cover plate and disk geometry which leads to the bucket groove and then into the cooling passages. This helps to provide a flow at inlet to the cooling passages that is similar to that in the engine.

Perspex® is used to produce the models due to ease of machining, strength and good optical and thermal properties, see figure 5. Liquid crystals are applied to the cooling passage surfaces to enable full surface heat transfer distributions to be obtained. The crystal is illuminated using light emitting diodes (l.e.d.) positioned to provide an even light distribution allowing the video cameras to detect a change in light intensity when the liquid crystals reach a certain temperature.

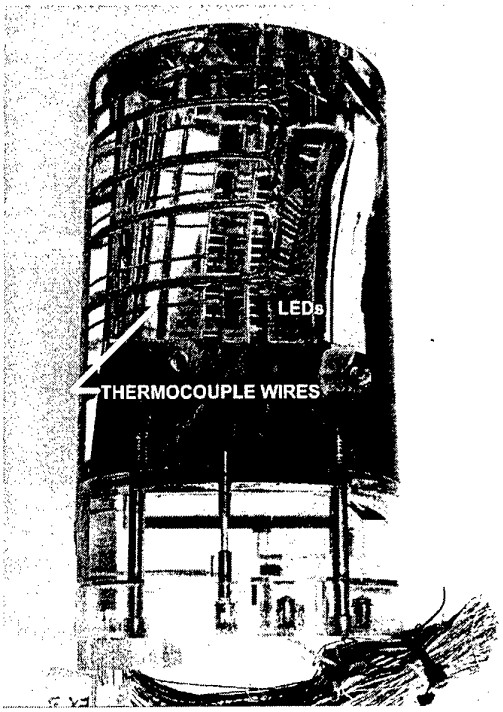

Figure 5

Surface and gas thermocouples are also placed on both the pressure and suction surfaces of the model with a single gas thermocouple on four radial planes and throughout all four cooling passages making a total of 48 temperature measurements. Pressure measurements were taken by kulite® transducers directly in the model and from tappings having hypodermic tubes feeding the pressures back to the centre of the rig. The pressures measured by the transducer in the model allowed all the pressures measured at the centre of the rig to be corrected for the effects of rotation.

7. DATA ACQUISITION COMPUTER

Heat transfer test work of a transient nature requires a large amount of instrumentation and slip-rings can introduce noise and limit the number of channels available. To eliminate these problems, a computer was designed and built that would monitor 64 thermocouples, 30 pressure measurements and thermal sensors for cold junction compensation. To transfer this quantity of data across a slip-ring would require nearly 200 channels. Noise is no longer a problem because all voltages are converted by the computer and sent across the slip ring in digital form. A typical gas and surface thermocouple trace is shown by figure 6. These data are available seconds after the test has been completed and allows a judgement about the validity of the test to be made quickly.

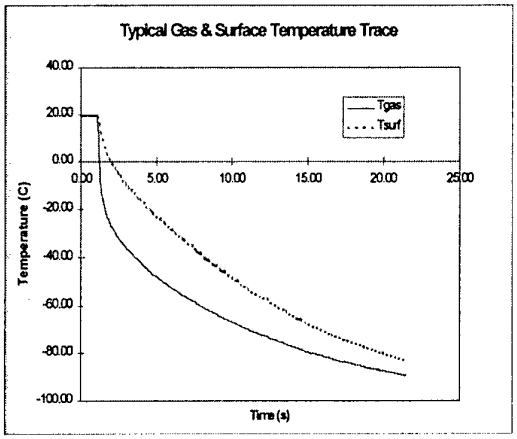

Figure 6

The computer fits into the central section or hub of the spinning rig in a cylindrical envelope measuring 153mm diameter x 432mm in length. Data acquisition is performed in a harsh environment for electronic components which have to withstand a rotational speed of 4,000 rpm, in a vacuum with a temperature variation of -20°C to 70°C. Temperature measurements are resolved to 0.1°C and can be read at 10000 readings/second. The design of the computer is modular with circuit boards that piggy back so that each board can be tested individually and replaced easily, see figure 7.

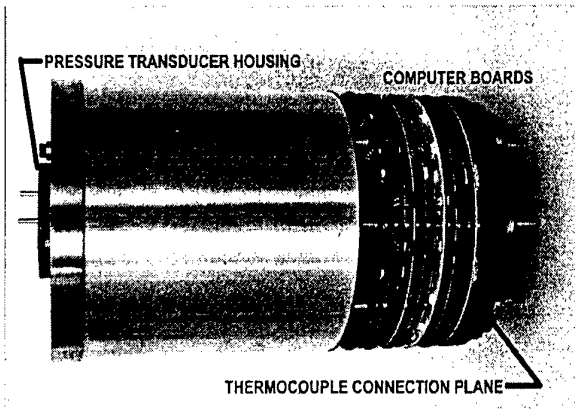

Figure 7

All the components are placed radially and are potted to help withstand the 'g' loading as they spin. The system can be expanded to read 128 thermocouple channels by inserting more boards without increasing the overall space envelope required. Thermistors are used to monitor the junction points between the thermocouple material and the computer connections giving an accuracy of ±0.2°C. Up to 20 heat flux gauges can also be read.

During each test the host computer collects data in real time from the spinning computer via a parallel data link and stores it in RAM which is then transferred to the hard disc. For high speed acquisition, >20kbytes/sec, channel data can be stored in the RAM of the spinning computer and downloaded at the end of the test. Raw data are converted to engineering units using calibrations held by the host computer and can then be plotted and displayed.

8. TEST ANALYSIS

Two types of experimental results are produced, surface thermocouple data that is analysed to provide a time history of heat transfer coefficient (htc) and liquid crystal video data that provides full surface htc distributions.

The basic geometry and equations are shown below.

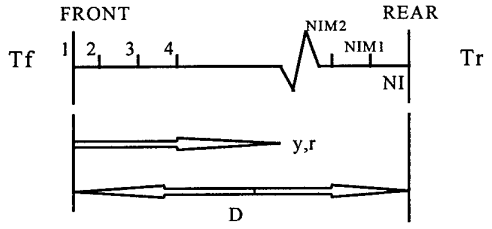

Tf = Gas temperature at front
Tr = Gas temperature at rear
TN = Gas temperature at node N

The governing equation is as follows

$$\frac{\partial(\rho C_p T)}{\partial t} = \frac{1}{r}\frac{\partial}{\partial y}\left\{rk\frac{\partial T}{\partial y}\right\} \quad \text{.....Equation 9}$$

with boundary conditions:

at y=0(front) $T_1 = T_1(t)$ .....**Equation 10**

or $k\left(\frac{\partial T}{\partial y}\right)_1 = h_f\left(T_f - T_1\right)$ ..**Equation 11**

at y=D(rear) $T_{NI} = T_{NI}(t)$ .....**Equation 12**

or $k\left(\frac{\partial T}{\partial y}\right)_{NI} = h_R\left(T_{NI} - T_R\right)$ ..**Equation 13**

The wall to which heat is transferred is assumed to be a homogeneous solid and that the heat transfer is predominantly one dimensional, therefore, the governing equation for transient conduction is equation 9. A 'semi-infinite' wall assumption is made setting a wall thickness at which the rear wall boundary condition has no effect on the conditions at the front surface or the rear wall has zero heat flux.

A simple finite different grid discretises the domain. The number of grids is fixed depending on the thickness of the wall and boundary conditions.

In the case where the surface is coated with liquid crystal, input data for that surface would be gas temperature transient, which is measured during the test, the time after which the surface reaches the liquid crystal change temperature, the initial temperature of the wall, the value of the change temperature of the crystal and the thermal properties of the wall (conductivity, specific heat and density). An iterative procedure, together with the heat flux boundary condition, is used to find the htc (assumed to be constant with time) which would give that surface temperature in the measured time.

Surface thermocouple input data would be the gas and wall temperature transients, measured in the test, and the thermal properties of the wall. The htc as a function of time can be determined directly from the surface heat flux rate calculated within the conduction domain.

9. TEST RESULTS

The test results that will be shown here are taken from a three pass multipass system that when combined with a leading edge passage makes a complete rotor cooling system. The model incorporates film cooling and ribbed passages, shown by figure 8. Results from surface thermocouples are presented for four sections of the 1st pass of the multipass at the hub, inner and outer sections of the 1st pass and at the outer section of the 2nd pass. Both suction and pressure surfaces are considered.

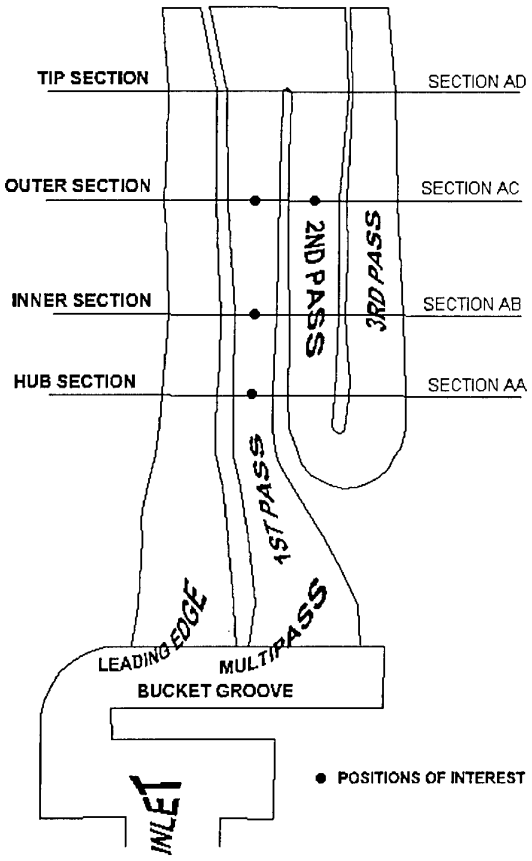

Figure 8

Results from hub section of the multipass system are shown by figure 9. Both pressure and suction surfaces indicate low levels of enhancement over smooth duct levels. A slight reduction in the enhancement as the correlation factor increases can be seen for the suction surface at this position.

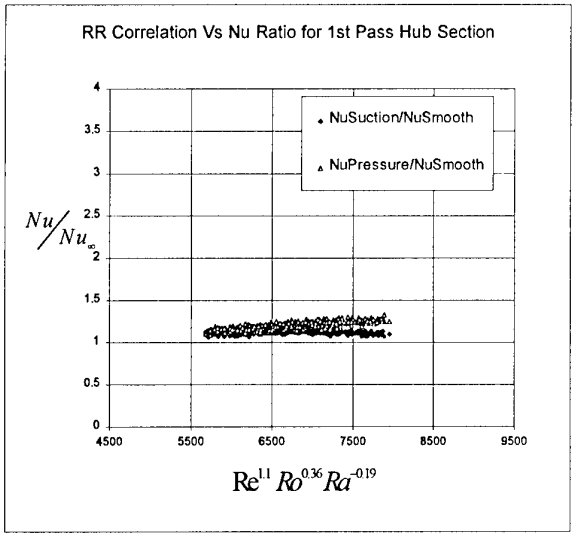

Figure 9

At the inner section the pressure and suction surfaces diverge considerably, however, both surfaces are still enhanced from that of the hub section, shown in figure 10. There is a slight trend shown by the suction surface of a decrease in enhancement factor.

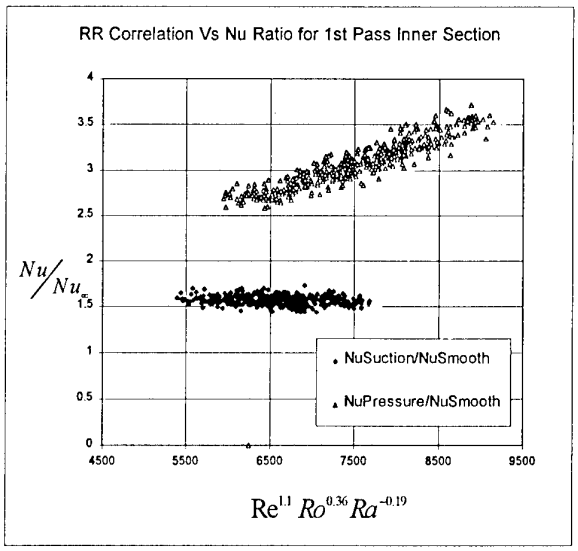

Figure 10

Further into the blade at the outer section the suction surface remains lower than the pressure surface but both are at similar levels to the previous section, shown by figure 11.

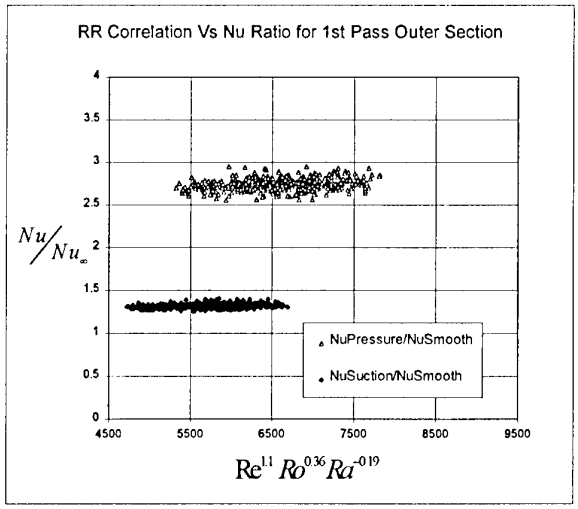

Figure 11

The final graph, figure 12, indicates that the suction surface enhancement factor recovers to a level above that of the pressure surface in the 2nd pass at the outer section. This could be because the bulk flow is now moving towards the engine centreline and also the secondary flows induced by the passage bend.

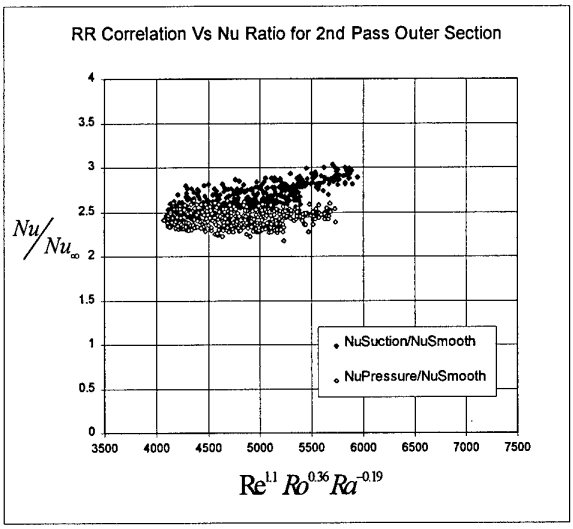

Figure 12

Liquid crystal results provide a more averaged result over the entire surface of the cooling passages. The htc values are averaged because the analysis method uses the surface temperature rise from time zero to the time at which the crystal changes state. The spatial resolution of the htc distribution is in pixels, a total video frame consists 512x512 pixels which gives a total number of data points of 262,144.

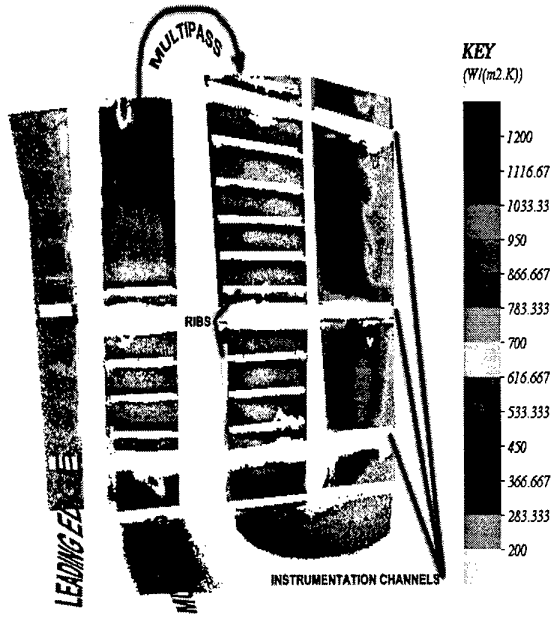

Figure 13

The htc distribution shown by figure 13 was obtained from the suction surface of the model with the rig spinning at 1700 rpm. The thinner white horizontal lines indicate ribs which are used to enhance the heat transfer in the passage. The effects can clearly be seen from the colours between the ribs. A large enhancement can be seen after the bend in the trailing edge region.

10. Conclusions

- This rig will enable the effects of rotation on new cooling geometries to be evaluated and incorporated into new design methods.
- This rig will enable full engine designs to be more effectively evaluated before production begins.
- Cooling air will be used more efficiently and effectively.
- Blade lives will be more predictable.

11. Acknowledgements

This paper was generated through work funded by the Defence Establishment Research Agency (DERA) and Rolls-Royce plc. The author wishes to gratefully acknowledge their permission to publish this paper and would also like to thank colleagues in the Turbine Technology Acquisition department for their valuable contributions towards it content. The views expressed within this paper are those of the author and do not necessarily represent those of either DERA or Rolls-Royce plc.

12. References

1. Effects of Rotation on Coolant Passage Heat Transfer Volume 2 - Coolant passages with Trips Normal and Skewed to the Flow.
2. *BV Johnson, JH Wagner, GD Steuber NASA-CR-4396 1993*
3. Effect of Aspect Ratio on the Buoyancy Driven Reverse Flow Near the Leading Wall of Rotating Cooling Passages.
   Tekriwal and Prabhat
   GE Corporate Research and Development
   ASME 96-GT-173 1996
4. Rotational Effects on Heat Transfer at Advanced Engine Conditions.
   FW Staub, AD Maddaus, PK Tekriwal
   GE Corporate Research and Development
   ASME 95-GT-417 1995
5. The Influence of Rotation on Impingement Cooling.
   CH Mattern, DK Hennecke
   Technical University Darmstadt
   ASME 96-GT-161 1996
6. Rotating Facility to Study Heat Transfer in the Cooling Passages of Turbine Rotor Blades.
   W.D. Morris
   University of Wales, Swansea
   Institute of Mechanical Engineers 1996
7. LDA Investigation of the Flow Development Through Rotating U-Ducts.
   SC Iacovides, H Jackson, DC Ji, BE Launder.
   UMIST, Manchester.
   ASME 94-GT-226 1994

Simulation of Crack Propagation in Engine Rotating Components Under Variable Amplitude Loading

P.J. Bonacuse
Materials Research Engineer
U. S. Army Research Laboratory

L. J. Ghosn
Resident Research Associate
Case-Western Reserve University

J. Telesman and A. M. Calomino
Materials Research Engineers
NASA Lewis Research Center

P. Kantzos
Senior Research Associate
Ohio Aerospace Institute

21000 Brookpark Rd., MS 49-7
Cleveland, OH 44135
U.S.A.

Abstract

The crack propagation life of tested specimens has been repeatedly shown to strongly depend on the loading history. Overloads and extended stress holds at temperature can either retard or accelerate the crack growth rate. Therefore, to accurately predict the crack propagation life of an actual component, it is essential to approximate the true loading history. In military rotorcraft engine applications, the loading profile (stress amplitudes, temperature, and number of excursions) can vary significantly depending on the type of mission flown. To accurately assess the durability of a fleet of engines, the crack propagation life distribution of a specific component should account for the variability in the missions performed (proportion of missions flown and sequence). In this report, analytical and experimental studies are described that calibrate/validate the crack propagation prediction capability for a disk alloy under variable amplitude loading. A crack closure based model was adopted to analytically predict the load interaction effects. Furthermore, a methodology has been developed to realistically simulate the actual mission mix loading on a fleet of engines over their lifetime. A sequence of missions is randomly selected and the number of repeats of each mission in the sequence is determined assuming a Poisson distributed random variable with a given mean occurrence rate. Multiple realizations of random mission histories are generated in this manner and are used to produce stress, temperature, and time points for fracture mechanics calculations. The result is a cumulative distribution of crack propagation lives for a given, life limiting, component location. This information can be used to determine a safe retirement life or inspection interval for the given location.

Introduction

The U. S. Army is changing its life management philosophy for critical rotating components in rotorcraft turbo-shaft engines. A 'safe-life' approach has been the Army's traditional means of determining component retirement lives. For 'safe-life,' a minimum calculated fatigue crack initiation life dictates when the component is retired from service. Although the 'safe-life' approach tends to be conservative and relatively easy to implement, it also suffers from several shortcomings, i.e.: 1) most components are retired with significant remaining crack initiation life, 2) unforeseen damage, such as scratches incurred during disassembly/assembly, is ignored, and 3) there is no established 'early warning' mechanism to identify changes in use and errors in life prediction.

The U. S. Air Force has pioneered a very different life management philosophy. The Air Force's methodology emphasizes planned inspections to detect damaged components while safely maximizing the use of undamaged components. This approach has often been termed retirement for cause (RFC). The RFC approach is based on fracture mechanics as the means of determining component lives. In RFC, preexisting flaws are assumed to exist at a size just below the detection threshold of the chosen inspection technique. The crack propagation life from this threshold to a fracture critical size is calculated for all high stress locations to determine the life limiting component location. Planned inspection intervals for these high stress locations are set to a fraction of the predicted life of the life limiting location to ensure that all propagating cracks are discovered well before they might cause component failure. The U. S. Army is adopting a tailored version of this approach.

Loading of rotorcraft engines, and in particular military rotorcraft engines, is typically far more variable than in fixed wing aircraft. Army rotorcraft perform a number of different missions with often very different loading histories. This variation in component loading can have a marked influence on the crack propagation life. For example, rapid excursions to high power settings can cause overloads that may retard crack growth rates. Conversely, many small stress excursions at high R-ratios can significantly shorten lives. This additional variability in load history can have a strong influence on the expected life distribution. Given that the Army utility helicopters are used in a variety of missions and the impending implementation of RFC, the effect of this variation on crack propagation life should be quantified.

A methodology is presented herein for predicting the distribution in the crack propagation lives of rotorcraft engine rotating components subjected to realistic mission loading histories. The methodology for determining the mission mix is based on direct Monte Carlo simulation of the engine loading given that the engine will likely be used in multiple aircraft performing a variety of missions. The development of this methodology is predicated upon the ability to accurately model

Paper presented at the RTO AVT Symposium on "Design Principles and Methods for Aircraft Gas Turbine Engines", held in Toulouse, France, 11-15 May 1998, and published in RTO MP-8.

fatigue crack growth under variable amplitude loading. The crack propagation life prediction code, FASTRAN II, was used to perform the life calculations. In order to calibrate and confirm the effectiveness of this code, an experimental program was devised and performed. Results are presented that validate the underlying crack propagation model.

Fatigue Crack Growth Under Variable Amplitude Loading

Models that predict load interactions for cracks propagating under variable amplitude loading, fall into two broad categories. The first group may be classified as overload plastic zone type models, which include the Willenborg [1] and Wheeler [2] models. These models calculate the effective crack driving force as a function of the ratio of the overload plastic zone size to the plastic zone size due to the current load amplitude as well as the location of the crack tip in relation to the overload plastic zone. Models of this type are widely used, especially by the engine companies who have invested significant effort in tailoring these models to their requirements.

The other class may be called crack closure models. They are based upon the original finding by Elber [3] who showed that crack regions behind the crack tip can close prior to reaching the minimum load. The stress intensity range over which the crack tip is open, termed ΔK_{eff}, is assumed to be the true crack driving force. The premature closure of the crack tip region is due to the crack growing through previously plastically deformed material which can come into contact behind the crack tip. The effective stress intensity factor range ($\Delta K_{eff} = K_{max} - K_o$) will therefore be somewhat smaller ($K_o \geq K_{min}$) than that computed without accounting for this effect. A model of this type is used in this work. The effective stress intensity factor range, ΔK_{eff}, is given by:

$$\Delta K_{eff} = Y \cdot (\sigma_{max} - \sigma_0)\sqrt{\pi a} \qquad \text{Eq. 1}$$

where a is the crack depth, Y is a geometric correction factor, σ_{max} is the maximum stress, and σ_o is the stress at crack closure. The cyclic crack growth rate, assuming a Paris Law, is related to the effective stress intensity range by (Eq. 2):

$$da/dN = C(\Delta K_{eff})^m \qquad \text{Eq. 2}$$

where C and m are material constants. The magnitude of the crack closure stresses (σ_o) is a function of the applied loading history, the crack tip constraint and the size and magnitude of the crack wake field behind the crack tip. A widely recognized crack propagation life prediction code, based upon the crack closure model, is FASTRAN II developed by Newman [4] at the NASA Langley Research Center.

The attractiveness of the crack closure model for engine applications is its ability to accurately predict crack growth of small flaws. Rotating engine components, such as disks, are highly stressed due to their high rotational speed. Because of these conditions, the critical crack size which results in failure is considerably smaller than typically encountered in airframe components. The crack closure models have been shown [5] to reliably predict the early stages of crack development where the crack wake is not yet fully developed and thus the ΔK_{eff} is greater than would be predicted by the overload plastic zone type models. Thus the authors believe that the crack closure models are appropriate where the critical crack sizes are relatively small i.e., lifing of engine rotating components.

The crack propagation analysis program FASTRAN II was used to estimate crack propagation lives in this study. The program contains a library of stress intensity solutions for a variety of crack geometries. The solution chosen for the sample problem examined in this report was a uniaxially loaded surface crack in a prismatic body (Figure 1). The overall dimensions of this prismatic body approximate the dimensions of the appropriate cross section of the second stage gas generator turbine disk in the UH-60 Blackhawk utility helicopter's T700 engine. This solution was also used to perform crack propagation calculations for the K_b bar specimens used in the experimental program. Stress amplitudes and temperatures were taken from calibrated thermal and stress analyses of this component. The failure criterion used by FASTRAN II to discontinue the crack propagation analysis was a calculated stress intensity factor range in excess of 90% of the input material fracture toughness (K_{IC}).

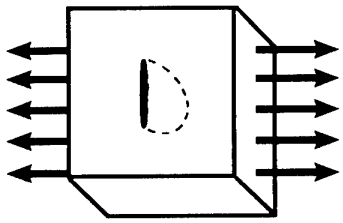

Figure 1: Schematic of prismatic body with surface crack.

The loading histories analyzed in this study were a randomized mix of utility helicopter mission histories. The U. S. Army has specified that the UH-60 Blackhawk helicopter performs ten different missions at three different ambient conditions yielding a total of 30 distinct engine histories (Table I). The purpose of specifying these mission profiles was to enable more realistic fatigue life calculations. It is well known that minor excursions (load ranges less than maximum minus minimum) cause additional damage both in crack initiation and propagation. Table I describes the specified portion of the overall engine life spent in each of these missions.

Table I: Army Mission Mix Specification

	Ambient Conditions			
Temp.	15°C	35°C	35°C	
Elevation	Sea Level	Sea Level	1220 m	
Mission				Totals
Troop Assault	5.10	5.80	0.50	11.40
Resupplying	3.30	3.80	0.30	7.40
Aeromed Evacuation	10.50	11.90	0.90	23.30
Replacing Units	3.00	3.40	0.30	6.70
Transport of Recon.	2.30	2.70	0.20	5.20
Reinforce/Reposition	4.70	5.40	0.40	10.50
Troop Extraction	2.60	3.00	0.20	5.80
Aerial Command Post	2.00	2.20	0.20	4.40
Sling Load	3.80	4.30	0.30	8.40
Training	7.60	8.60	0.70	16.90
Totals	44.90	51.10	4.00	100.0

All values in % of engine operating life

Calibration and Validation of Crack Growth Algorithm

To validate the accuracy of the FASTRAN II crack propagation analysis code for variable amplitude loading of a turbine disk alloy at elevated temperature, an experimental program (10 specimens) was performed. The purpose of the experimental program was twofold. The first was to generate relevant baseline data necessary to calibrate the crack closure model used by the FASTRAN II program. The second was to generate

variable amplitude loading experimental data that could be directly compared with FASTRAN II predictions.

Mechanical Testing Procedure

All specimens were cut from a single retired René 95 disk (Fig. 2). René 95 is a powder metallurgy, nickel-base superalloy that is used for most of the gas generator turbine rotating components in the UH-60 Blackhawk's T700 engine. The experiments were performed at 400°C to more closely simulate the engine operating environment at the fracture critical locations: the disk bore and bolt/cooling air holes.

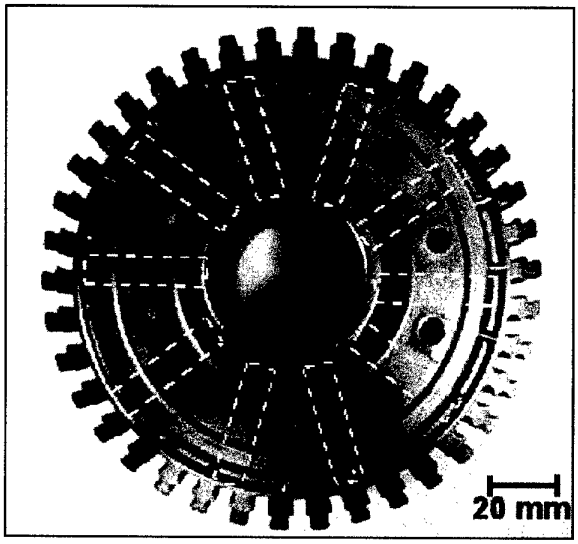

Figure 2: Fatigue crack growth specimen blank locations; T700 Stage 2 gas generator turbine disk.

Fatigue crack growth testing was performed with an axially loaded surface cracked specimen geometry, the K_b bar (Fig. 3). The K_b bar geometry was thought to be more representative of the actual flaws and high applied stresses expected in turbine disk applications than the more conventional compact tension specimen geometry. The gage section dimensions of the K_b bar specimen were nominally 10.2 mm wide by 4.3 mm thick. Crack lengths were monitored with a direct-current electric-potential (DCEP) technique. DCEP in this program was calibrated using marking cycles, heat tinting, and post failure crack length measurements. Testing was performed on a computer controlled, servo-hydraulic, test frame equipped with a clamshell furnace.

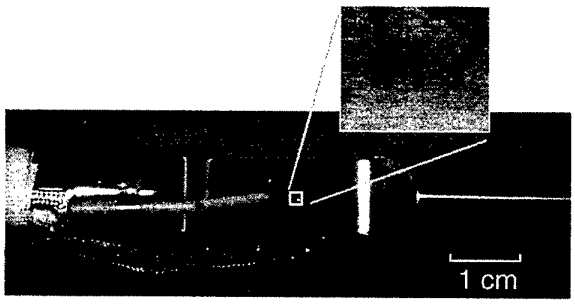

Figure 3: Kb Bar specimen instrumented for elevated temperature crack propagation experiment. Inset is a close up of an EDM notch with spot welded DCEP probes.

The cracks in the specimens were not allowed to propagate through the specimen thickness. The experiments were stopped at a crack depth where the accuracy of the analytical solution for the DCEP calibration was expected to degrade (approximately 50-60% through thickness).

Calibration Experiments

To properly calibrate the crack closure model, constant amplitude fatigue crack growth experiments were performed at three different R ratios ($R = \sigma_{min}/\sigma_{max}$): 0.05, 0.5 and 0.7. In Figure 4, the experimental data from these calibration experiments is displayed as a function of the applied crack driving force, ΔK_{app}. Figure 5 shows the same data set corrected for crack closure with Newman's formulation for the effective crack driving force, ΔK_{eff}. This formulation is used by the FASTRAN II software to estimate the effect of crack closure on the crack propagation rate. The stress intensity geometric correction formula for the K_b bar specimen was taken from Newman and Raju [6].

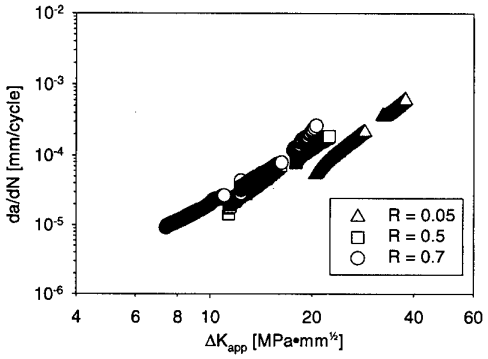

Figure 4: da/dN vs. ΔK_{app} for René 95 at 400°C.

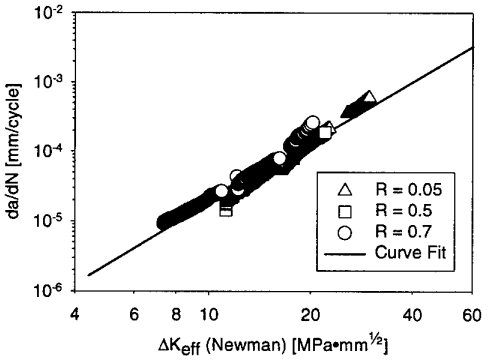

Figure 5: da/dN vs. ΔK_{eff} for René 95 at 400°C.

As seen in Figure 4, the R=0.05 data is considerably different than the 0.5 and 0.7 data, showing slower crack growth rates for the same ΔK_{app}. This difference is expected since at a 0.05 R-ratio, the crack closes at a higher applied stress than the minimum stress. But when the stress intensity factor range is corrected for the early closure of the crack faces ($\Delta K_{eff} = (K_{max} - K_{closure}) < (K_{max} - K_{min})$) using Newman's formulation [4], there is a better correlation between the three different R-ratios, (see Fig. 5). Hence, the ΔK_{eff} parameter plotted in Figure 5 represents a true measure of the actual crack driving force, independent of the applied load ranges. The curve fit of the crack growth rate versus the effective stress intensity factor range, determined from these three constant amplitude

experiments, is supplied to FASTRAN II for use in predicting the variable amplitude loading experiments.

Validation Experiments

The variable amplitude loading experimental program, consisted of 5 experiments. Three different repeating load sequences were applied to K_t bar test specimens at 400°C. Load sequence 1 (LS 1) (Fig. 6a) closely resembles the Army specified training mission. Load sequence 2 (LS 2) (Fig. 6b) is essentially the same as sequence 1 with a few additional large excursions (each roughly equivalent to a take-off - ground idle excursion). Load sequence 3 (LS 3) (Fig. 6c) was run to test the extremes of the crack closure model's predictive capability. It includes excursions covering various ranges of loading R ratio.

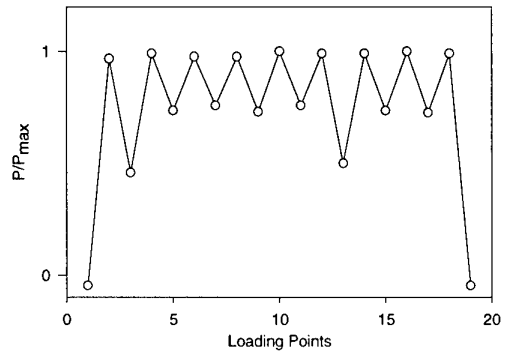

Figure 6a: Experimental Loading History 1 (LS 1).

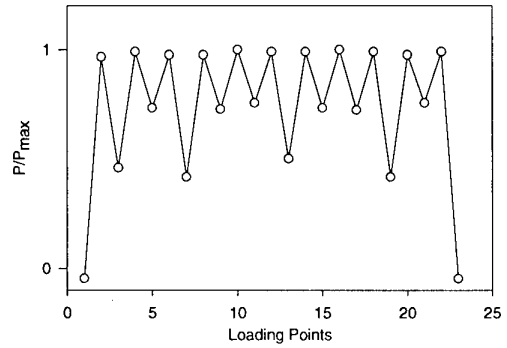

Figure 6b: Experimental Loading History 2 (LS 2).

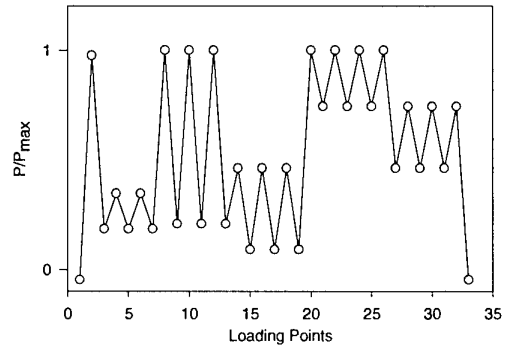

Figure 6c: Experimental Loading History 3 (LS 3).

The FASTRAN II analysis of the three loading spectra showed excellent agreement with the experimental results. Comparison of the experimentally observed crack depth versus the number of mission spectra repeats applied with the FASTRAN II predictions for each of the three spectra are shown in Figure 7. Only the data from one experiment for each loading spectrum is displayed. The predicted crack depths faithfully replicate those observed in the experiments. The predicted final crack depths were all within a factor of 1.5 of the experimentally observed values (Fig. 8).

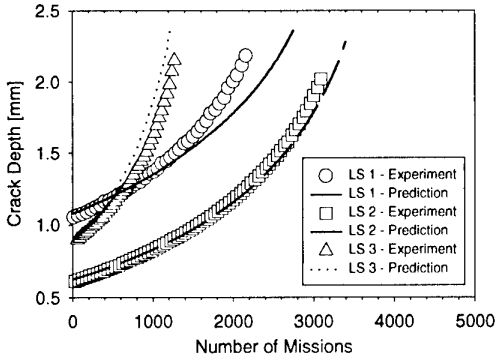

Figure 7: Correlation of FASTRAN II mission mix predictions with experimental crack depth data.

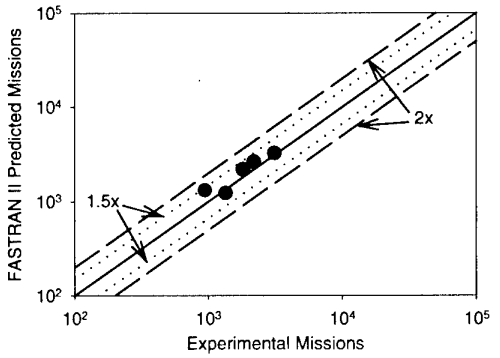

Figure 8: Experimental vs. predicted crack propagation lives for block loaded K_t bar FCG specimens.

In order to evaluate/demonstrate the need to correct the crack driving force for load interactions, the crack growth data were modeled using a Miner's type (linear) summation of all the different cyclic segments without regard for load interactions.. The crack growth rates for a given load excursion, at a given R ratio, were calculated using Walker's methodology [7] for evaluating the influence of the load ratio. The Walker model uses ΔK_{app} as the crack driving force. The results of the analysis, performed on the LS 3 spectrum (Fig. 6c) are presented in Figure 9. As shown, the crack growth rate calculated using this linear summation approach is substantially faster than was experimentally measured, amply demonstrating the presence of load interaction effects.

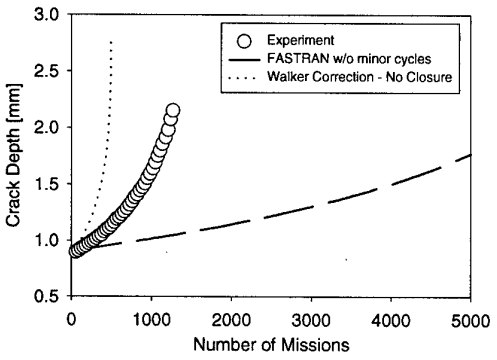

Figure 9: Influence of crack closure and minor cycles on the predicted crack propagation rate. The LS 3 spectrum was used in displayed results.

Also, an analysis of the minor cycles' influence on the crack growth behavior was performed. This analysis consisted of a FASTRAN II run with a single load excursion from the minimum stress to the maximum stress and back down to the minimum stress (all the minor cycles removed from the load history). As shown in Figure 9, the major excursion in the load histories could only account for a small fraction of the observed crack growth. Thus, the minor cycles' contribution to crack growth, for this particular spectrum, is significant.

Simulation of Mission Mix Histories

Given that the FASTRAN II crack propagation analysis code proved successful in predicting the crack growth behavior for the various spectrum loading sequences, it was deemed an appropriate tool for the study of mission mix history on the overall fatigue crack growth life.

There are several ways to interpret the Army's mission mix specification. The most literal interpretation is that each engine will experience the exact mission fractions and ambient conditions specified in the mission mix. In practice, this is highly improbable. It is far more likely that the mission mix is an estimate of the fleet usage. This would mean that an appropriate fraction of the fleet would experience the specified missions, for example, 0.5% of the fleet flying time (given a fleet of 2000 aircraft, one aircraft might fly this mission continuously or two aircraft half the time, etc.) will be used for the troop assault mission on a 35°C day from a base at 1220 m. Therefore, the more severe missions (as well as the more benign missions) are not spread evenly to all engines. This leads to a larger variance in the distribution of the expected crack propagation lives. In addition, the longer the interval between changes in mission for the engines, the larger the spread in the fatigue lives.

In describing this simulation technique several terms will be used that require unambiguous definition: A mission is a loading sequence that approximates the loading imposed on a component during a single rotorcraft flight, from engine start-up, through takeoff and flight maneuvers, to landing and engine shut-down. A block is defined as a number of sequentially repeated missions of the same type (e.g., any number of repeated Troop Assault missions all at sea level standard conditions would be considered a block). A block of missions is intended to simulate the repeated use of an engine for a specific mission while stationed with a unit. The block length is defined as simply the number of repeated missions in a block. A realization is defined as a sequence of blocks that terminates with component failure. A realization can be thought of as the simulated loading history of a single engine.

To determine the crack propagation life of a component, all potentially life limiting (high stress) locations are analyzed to predict the crack growth life from a flaw of a known size (as determined by the resolution and reliability of the inspection technique). The feature chosen for this crack propagation simulation was the bore of the second stage gas generator turbine disk. A crack propagating from this location would eventually lead to a catastrophic uncontained engine failure. To estimate the effect of the random mission mix loading, a direct Monte Carlo simulation technique was formulated. This method involved generating a number of blocks of mission loading sequences that were then fed into the FASTRAN II crack propagation analysis code (Fig. 10). This was repeated (16-64 realizations) with new randomly generated sequences of mission blocks to get a distribution of crack propagation lives.

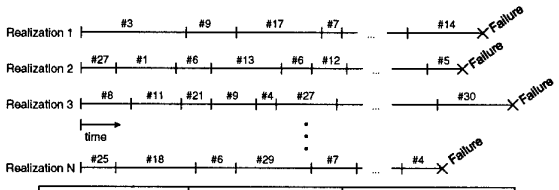

#1 Troop Assault SLS	#11 Troop Assault 35°C	#21 Troop Assault 35°C HA
#2 Resupply SLS	#12 Resupply 35°C	#22 Resupply 35°C HA
#3 Aeromed. Evac. SLS	#13 Aeromed. Evac. 35°C	#23 Aeromed. Evac. 35°C HA
#4 Replacing Units SLS	#14 Replacing Units 35°C	#24 Replacing Units 35°C HA
#5 Trans. of Recon SLS	#15 Trans. of Recon. 35°C	#25 Trans. of Recon. 35°C HA
#6 Reinforce/Repos. SLS	#16 Reinforce/Repos. 35°C	#26 Reinforce/Repos. 35°C HA
#7 Troop Extract. SLS	#17 Troop Extract. 35°C	#27 Troop Extract. 35°C HA
#8 Aerial Comm. Post SLS	#18 Aerial Comm. Post 35°C	#28 Aerial Comm. Post 35°C HA
#9 Sling Load SLS	#19 Sling Load 35°C	#29 Sling Load 35°C HA
#10 Training SLS	#20 Training 35°C	#30 Training 35°C HA

Figure 10: Schematic of random mission block loading. Note both the random selection of missions and the variation in the block length.

Several assumptions have been made to simplify the FASTRAN II simulation and to fill in for certain unknowns about the actual usage of the engine. First, it was assumed that the engines are "pooled" at the depot. By this it is meant that an engine returned to the depot for maintenance will not necessarily return to the original "owner" but will go to the first unit requiring an engine. This allows us to model the selection of each block of missions with an appropriately partitioned uniform random variable. The probability of selecting a particular mission and ambient condition is directly linked to the fraction of time the engine is expected to spend performing that mission/ambient condition combination as described by the Army mission mix specification (Table I).

Another, and perhaps oversimplifying, assumption is that, while stationed with a unit, the aircraft will perform one mission exclusively. For example, aircraft stationed at a training facility perform only the training mission. It was also assumed that the block length (number of missions between removal of the engines for overhaul at the depot) could be modeled as a Poisson process. The purpose of using a Poisson distributed random variable, as opposed to a fixed block length, was to more closely model the actual engine usage (the T700 has no scheduled overhaul interval). A Poisson process is defined as a discrete process where the intervals between events are exponentially distributed. The probability distribution is defined by (Eq. 3):

$$P(x) = \frac{\lambda^x}{x!} e^{-\lambda} \qquad \text{Eq. 3}$$

where P(x) is the probability that x events occur and λ is the mean number of events. This equation may be solved for the

number of events, x, and may be used to generate a Poisson distributed random variable. The Poisson distribution parameter, λ, for the purposes of this simulation, is equal to the mean block length and the random variable, x, will be defined as the Poisson distributed block length. The method of generating a Poisson distributed random variable was taken from Press et al. [8].

The simulation method was used to execute six runs of 16 realizations each using various values for the mean block length, λ (Table II). An additional run of 64 realizations with λ = 165 missions, was performed as a measure of the sample to sample variability. The first row of Table II, labeled λ = 1, was actually run with the block length fixed to one mission. This is roughly analogous to running the 30 missions, in proportion to the mission mix specification, on each of the engines.

Table II: Simulation Results

λ [missions/ block]	Realizations	Mean [hrs]	Standard Deviation [hrs]	-3σ Life [hrs]
1	16	8496	182.1	7950
33	16	8522	315.3	7576
66	16	8520	628.4	6472
99	16	8662	715.0	6517
132	16	8607	1176.1	5078
165	16	8578	1344.0	4546
165	64	8476	772.1	6160

The increase in the dispersion of the simulated crack propagation lives as the expected number of repeated missions between change of mission increases is clearly shown in Figure 11.

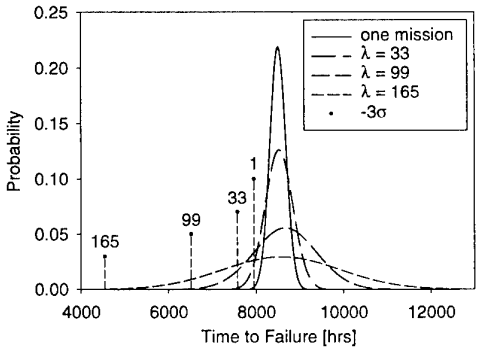

Figure 11: Normal distributions derived from simulation results. The labeled drop lines indicate life at mean minus 3 standard deviations for each distribution.

The last row of Table II shows the results of a repeat of the λ = 165 mission simulation with 64 realizations. The standard deviation in this sample was considerably smaller than in the 16 realization simulation run at the λ = 165 missions. The reason for this difference in the variance cannot be readily explained. However, it should be noted that the variance is likely to fluctuate from one sample to the next, especially when the sample size is relatively small. The difference in the simulated standard deviations may simply illustrate the sample to sample variation in the variance and may indicate that 16 realizations of the randomized mission loading sequence is inadequate to provide a reasonable estimate of the underling population's standard deviation. In spite of this discrepancy the trend of increasing variance with simulated block length seems to hold true.

Discussion

If one ignores the loading interaction that may occur in changing missions (variation in the maximum and minimum stresses from one type of mission to the next is small when compared to the variations in the loads within each mission), a linear summation approach might be used to calculate the mission mixed loading crack propagation life distribution. Given the calculated crack propagation lives for each of the missions, an analytical distribution function for the probability of failure can be derived if the following question can be answered: What fraction of the possible combinations of mission blocks, of Poisson distributed length, lead to failure in a given time, t? Numerical integration of the probability density function is possible but the number of combinations is daunting. For example: given a Poisson distribution parameter for the block length, λ, of 165 missions and assuming an average mission length of 1.46 hours per mission, at 3675 hours of component operation there would be approximately 15 blocks of missions flown, each block with one of the 30 possible missions. Assuming no distribution in the fatigue lives of the individual missions, i.e., each mission contributes exactly 1/(total mission cycles to failure for a specific mission) fractional damage to the component and assuming that each block is equally possible and independent, there can be 30^{15} or 1.4×10^{22} possible combinations. In calculating the probability of failure at longer operating times, the number of mission blocks increase and the number of possible combinations grows exponentially. With the additional complications that the missions are not equally probable, the length of the individual missions are not constant, and the number of missions per block is also variable, this becomes an increasingly difficult problem to solve in closed form. If it is assumed that the loading interaction that can occur in changing missions has a marked effect on fatigue crack growth, a closed form analytical solution does not seem feasible.

The results of this study indicate a strong dependence of the crack propagation life on the mission sequence and particularly on the mean block length (expected number of mission repeats between engine removal for overhaul). The expected crack propagation life variance caused by the mission mix loading will necessitate a reduction in the estimated lower bound crack propagation life. If not accounted for in the current component life estimates, retirement lives and/or inspection intervals will need to be shortened.

A basic assumption driving this simulation technique is that the mission sequence has strong effect on crack propagation rate. If it can be demonstrated that the effect of the mission sequence on the crack propagation rate is negligible, or that the mission loading in the prescribed mission mix is not conducive to significant 'mission to mission' load interactions, an analytical solution or a simplified (less computationally intensive) simulation technique might be utilized.

The intrinsic (material dependant) variability in the crack propagation life could also be incorporated into the simulation. This would require an additional random variable to account for the experimentally observed scatter in the crack propagation rate.

Given that the Army specified mission mix is an estimate of the actual usage, that the fleet usage is likely to evolve with time, and that there can be significant pilot to pilot variation in how the aircraft are flown, the contribution to the variability in crack propagation due to these loading variations can potentially be large. Accounting for this loading variability could lead to unacceptably short inspection intervals, increased inspection

costs, and a large impact on fleet readiness. To mitigate the loading history uncertainty, a strong argument can be made for onboard monitoring of the aircraft usage. This could allow for a "real-time" calculation of the available crack propagation life. A more aggressively used engine could be pulled for inspection or retirement, even though the original life estimates (based on the expected usage) would indicate that it was still safe to operate. Conversely, a lightly used engine might not be removed as often for costly inspection/overhaul or outright replacement.

Summary and Conclusions

The FASTRAN II crack propagation analysis code, which is based on the crack closure model, accurately predicts crack propagation in surface cracked K_b bar specimens under variable amplitude loading.

A method of estimating crack propagation life distribution of helicopter engine rotating components subjected to thirty different missions of varying severity, length, and probability of occurrence, has been developed. This method utilizes several random variables to generate simulated engine histories that are then fed into the FASTRAN II crack propagation analysis code.

There is a direct correlation between the mean number of missions between removal for inspection/overhaul and the variance in the predicted crack propagation lifetimes. Extra caution is therefore necessary when determining the retirement life or a safe inspection interval for critical rotating components. A more accurate accounting of the actual usage of the engines would also seem prudent. This might include onboard monitoring of engine usage.

References

1. Willenborg, J., Engle, R., and Wood, H., "A Crack Growth Retardation Model Using an Effective Stress Concept," AFFDL-TM-71-1-FRB, Wright-Patterson Air Force Base, Ohio, January 1971.

2. Wheeler, O. E., "Crack Growth Under Spectrum Loading," J. of Basic Eng. Trans. ASME, p. 181, March 1972.

3. Elber, W., "The Significance of Fatigue Crack Closure," *Damage Tolerance of Aircraft Structures, ASTM STP-486*, 1971, pp. 230-242.

4. Newman, J. C., *FASTRAN-II - A Fatigue Crack Growth Structural Analysis Program*, NASA TM-104159, Feb. 1992.

5. Newman, J. C., Jr., "Prediction of Fatigue Crack Growth under Variable Amplitude and Spectrum Loading Using a Closure Model," *Design of Fatigue and Fracture Resistant Structures, ASTM STP-761*, P. R. Abelkis and C. M. Hudson, eds., 1982, pp. 255-277.

6. Newman, J. C. and Raju, I. S., "Stress-Intensity Factor Equations for Cracks in Three-Dimensional Finite Bodies Subjected to Tension and Bending Loads," *Computational Methods in the Mechanics of Fracture*, S. N. Atluri, Ed., Elsevier Science, 1986, pp. 311-334.

7. Walker, K., "The Effect of Stress Ration During Crack Propagation and Fatigue for 2024-T3 and 7075-T6 Aluminum," *Effects of Environment and Complex Load History on Fatigue Life, ASTM STP 462*, American Society for Testing and Materials, 1970, pp. 1-14.

8. Press, W. H., Flannery, B. P., Teukolsky, S. A., and Vetterling, W. T., *Numerical Recipes*, Cambridge University Press, 1986.

Meeting Discussions

Paper 38: **Simulation of Crack Propagation in Engine Rotating Components Under Variable Amplitude Loading**

Author: P. J. Bonacuse

Discussor: G. Dhondt

Question: How did you determine the K. distribution in the real engine component?

Author's reply: Fastran II is 1-D code. Cracks were thought to be small enough at kfc, to neglect surface interactions. Stresses along the surface were also relatively uniform for the locations examined.

THEORY FOR THE USE OF FOREIGN GAS IN SIMULATING FILM COOLING

T.V. Jones
Department of Engineering Science
University of Oxford
Oxford OX1 3PU
U.K

1. SUMMARY

In the film cooling of turbines the coolant is significantly cooler than the freestream. Consequently the coolant is at a higher density and this plays an important role in determining the flowfield. In laboratory experiments with small temperature differences this density difference is simulated by using dense foreign gas. This paper analyses the effect of molecular properties on the thermal measurements so that they may be related to the cold air situation.

2. NOMENCLATURE

A,B,C - functions of position, eqn (15)
Cp -specific heat at constant pressure
f_1, f_2 - functions
$G_{x,y}$ - mass flux, $\rho u_{x,y}$
i - specific enthalpy
k - thermal conductivity
M - mole fraction
m - mass fraction
Nu_x - Nusselt number = $\dfrac{qx}{k_g(T_{aw}-T_w)}$
Pr - Prandtl number
q - heat flux
Re_x - Reynolds number based on freestream and x
T - Temperature
x - coordinate in freestream direction
y - coordinate perpendicular to surface
β $= \left(\dfrac{\partial B}{\partial y}\right)_b$
δ - viscous sublayer thickness
ε - diffusivity
ζ - thermal diffusion coefficient
η - film cooling effectiveness
λ - mass diffusion coefficient
ξ $= \varepsilon\rho$
ρ - density
μ - viscosity
ϕ $= -\left(\dfrac{\partial C}{\partial y}\right)_b$

Suffices
A - cold air coolant
aw - adiabatic wall
b - evaluated at the bottom of the turbulent region
c - coolant
FG - foreign gas coolant
g - freestream
w - evaluated at the wall

3. INTRODUCTION

The use of foreign gas in film cooling experiments has been prevalent throughout the history of the subject. The foreign gas has been employed in the coolant flows for the following reasons.

1. To act as a tracer gas to determine the distribution of coolant (Goldstein, 1971).
2. To enable coolants of different density to be injected while at the same time acting as a tracer gas. The experiment is essentially isothermal (Goldstein, 1971 and Pedersen et al, 1977).
3. To simulate coolants of different densities in heat transfer experiments (Teekaram et al., 1989).
4. To simulate coolants of different densities in aerodynamic experiments (Day et al., 1996).
5. Although not directly germaine to the present subject there is a class of experiments in which the mass transfer to heat transfer analogy is employed (Eckert, 1986).

Combinations of these techniques are employed whereby the mass transfer analogy is used with a foreign gas injection (e.g. Ammari, Hay and Lampard, 1989) or a tracer gas is used within a different foreign gas (e.g. Salcudean et al., 1994).

The objective of the present paper is to explore the interpretation of the third class of experiments, referred to as *case (3)* in the following.

Although there are situations where gases dissimilar to the freestream are injected for film cooling purposes this paper is concerned with the simulation of the gas turbine situation. In this case a significant ratio of coolant to freestream density occurs, resulting from their temperatures. The coolant temperature may be 1000K and the freestream 2000K giving density ratios of approximately two. In order to reproduce such large density ratios in a laboratory situation recourse to the use of heavy foreign gas as the coolant has been common. At present there is no general scaling parameter or procedure for the film cooling process and hence the need simulate the coolant density. The first tests of the use of foreign gas to simulate the injection of relatively cold air coolant were those of Teekaram,

Paper presented at the RTO AVT Symposium on "Design Principles and Methods for Aircraft Gas Turbine Engines", held in Toulouse, France, 11-15 May 1998, and published in RTO MP-8.

Forth and Jones (1989). In these experiments equivalent densities and mass flow rates were achieved by injecting CO_2 and air at different temperatures. The different thermal boundary conditions were taken into account by the normalisation of temperatures, inherent in the definition of film cooling effectiveness. Thus the mass flux and the momentum flux of coolant were reproduced and the assumption was that this generated the same flow field. At the same time little thought was given to the fact that the molecular properties of air and CO_2 were different, other than to note this difference and argue that the effects on the similarity of the parameters measured would be small. The experiments were performed to test this assumption and indeed showed good agreement between the air and CO_2 injection at the same coolant to freestream density ratio and injection to freestream velocity ratio. Since this time other workers have employed foreign gas to simulate density differences in heat transfer experiments (e.g. Han and co-workers 1993, 1995 and 1997).

In this paper analysis of the simulation of the thermal field is undertaken. This results in a justification for the close correspondence in the CO_2/air experiments and also gives formulae to correct experimental data for different gases.

4. SIMULATION OF COOLANT FLOWS

The boundary layer flow field in gas turbine film cooling is highly turbulent. The transport of species, momentum and enthalpy is thus dependent on the turbulent flow field generated by the coolant injection. The role of viscosity is secondary other than in the surface sublayer and perhaps within the injection geometry. Thus, if coolant of the same density although a different gas, is injected with the same velocity then the turbulent flowfield should be similar. Discharge coefficients of blade cooling holes are only Reynolds number dependent at low flow rates (Rowbury et al 1998). Also the thickness of a viscous sublayer under a flat plate turbulent boundary layer is dependent on Reynolds number to the tenth power. Hence the effects of Reynolds number changes due to foreign gas can be considered small in the first instance. Of course, freestream conditions and hence Reynolds number are assumed to be the same. It should be pointed out that the correspondence between flow fields referred to above obtains when both coolant density and mass flow (i.e. velocity) are simulated. Merely matching momentum flux is not a sufficient condition. Many workers do make the latter assumption and compare results for film cooling effectiveness and heat transfer coefficient in this case. It is obvious that such comparisons are approximate at best.

5. BASIC EQUATIONS

The basic boundary layer differential equations for flows of gas mixtures are given in Kays and Crawford (1993). For a binary mixture of an inert, foreign gas coolant in a freestream gas the mass concentration equation is,

$$G_x \frac{\partial m}{\partial x} + G_y \frac{\partial m}{\partial y} - \frac{\partial}{\partial y}\left(\lambda \frac{\partial m}{\partial y}\right) = 0 \qquad (1)$$

The energy equation is

$$G_x \frac{\partial i}{\partial x} + G_y \frac{\partial i}{\partial y} - \frac{\partial}{\partial y}\left(\varsigma \frac{\partial i}{\partial y}\right) = 0 \qquad (2)$$

m is the mass concentration of the coolant and i is the specific enthalpy of the mixture

i.e. $i = i_g (1-m) + i_c m.$ (3)

The local mass flux is G and λ and ς are the mass and thermal diffusion coefficients respectively. It has already been assumed that the diffusion coefficients are equal in arriving at these approximate governing equations. In the context of the present turbulent flow they refer to the turbulent quantities and their equality means that the turbulent Lewis number is unity. For gases this assumption is reasonable (Kays and Crawford 1993).

The thermal problem must generally be specified in terms of enthalpy, i, boundary conditions rather than in terms of temperature, T, which is the conventional method. The use of temperature arrives at the usual description of film cooling in terms of the film cooling effectiveness, η, where,

$$\eta = \frac{T_g - T_{aw}}{T_g - T_c}$$

suffices aw, g and c refer to the adiabatic wall, freestream and coolant respectively. The effectiveness is independent of the temperature boundary conditions as may be shown by superposition (Jones, 1991).

In the *case (1)* of experiments where a low concentration of tracer gas is employed the flow is essentially composed of a single gas and the energy equation may be written in terms of temperature.

$$G_x \frac{\partial T}{\partial x} + G_y \frac{\partial T}{\partial y} - \frac{\partial}{\partial y}\left(\varsigma \frac{\partial T}{\partial y}\right) = 0 \qquad (4)$$

The adiabatic wall case corresponds to that of an impermeable wall for the concentration equation. Thus at the wall (suffix w);

$$\left(\frac{\partial m}{\partial y}\right)_w = \left(\frac{\partial T}{\partial y}\right)_w = 0 \qquad (5)$$

The concentration field thus corresponds to the temperature field and,

$$\frac{m}{m_c} \equiv \frac{T - T_g}{T_c - T_g} \qquad (6)$$

giving the film cooling effectiveness as

$$\frac{m_w}{m_c} = \frac{T_{aw} - T_g}{T_c - T_g} = \eta \qquad (7)$$

In *case (2)* dense foreign gas is injected such that coolant density is significantly different to that of the freestream. This corresponds to the higher density of cold air injection. Again the majority of the flowfield and boundary conditions correspond for the adiabatic wall case and the film cooling effectiveness is given by eqn. (7). There is possibly an influence of different properties in the sublayer on the flowfield due to the molecular viscosity being different.

6. THERMAL FIELD FOR AN ADIABATIC WALL

The *case (3)* considered in this section obtains when the foreign gas is at a different temperature to the freestream. The adiabatic wall temperature is determined in an experiment and the effectiveness for the equivalent air case is sought. In this case the enthalpy boundary conditions relate to the mass fraction as Cp is not constant. From eqn. (3)

$$Cp = Cp_g(1-m) + Cp_c m \qquad (8)$$

In the following it is assumed that Cp's of air and foreign gas are independent of temperature. Hence Cp is only a function of concentration. This assumption is valid for the foreign gas experiments as these are conducted at modest temperature differences, the large density differences being simulated by the concentration of foreign gas as already described. For the air or engine cases, large temperature differences are present, however, the value of C_p can be taken as being essentially constant. Thermal conductivity is dependent on temperature and the local value is used for the engine situation. Again, the thermal conductivity is a function of concentration for the foreign gas experiment.

At the wall

$$\left(\frac{\partial i}{\partial y}\right)_w = \left(\frac{\partial Cp}{\partial y}\right)_w T_w + \left(\frac{\partial T}{\partial y}\right)_w Cp_w = Cp_w \left(\frac{\partial T}{\partial y}\right)_w = 0$$

as the wall is impermeable and adiabatic.

Thus the boundary conditions for i and m are identical if the isothermal case at T_g is subtracted from the case considered as this is also a zero heat transfer situation. Thus:-

	$\frac{i}{0}$	$\frac{m}{0}$
Freestream		
Coolant	$Cp_c(T_c - T_g)$	1
Wall	$C_{p_w}(T_{aw} - T_g)$	m_w

Thus $$\frac{Cp_w(T_g - T_{aw})}{Cp_c(T_g - T_c)} = \frac{m_w}{1}$$

but in this case $\left(\frac{T_g - T_{aw}}{T_g - T_c}\right) = \eta_{FG}$ i.e. the film cooling effectiveness measured with foreign gas. The film cooling effectiveness for cold air η_A with the same coolant density is given by setting $Cp_c = Cp_g$. Thus

$$m_w = \eta_A = \frac{Cp_w}{Cp_c}\eta_{FG} \qquad (9)$$

Cp_w is found from eqn (8), giving,

$$\eta_{FG} = \frac{Cp_c \eta_A}{Cp_g(1-\eta_A) + Cp_c \eta_A} \qquad (10a)$$

also,

$$\eta_A = \frac{C_{p_g}\eta_{FG}}{Cp_c(1-\eta_{FG}) + Cp_g \eta_{FG}} \qquad (10b)$$

The suffices *FG* and *A* refer to the cases for foreign gas and air respectively.

7. HEAT TRANSFER

The equivalence between the air and foreign gas enthalpy fields is not exact in *case (3)* when heat transfer is present as the sublayer molecular properties will be influential and different. However, as in the previous section it may be assumed that the turbulent flow field does correspond. If correspondence is thus sought for the turbulent region, the sublayer may be added subsequently. The temperature at the bottom of the turbulent layer is given by T_b as shown in Fig.1.

The heat transfer at b in Fig.1 is given by,

$$q_b = \xi_b \left(\frac{di}{dy}\right)_b \qquad (11)$$

where $\xi_b = \varepsilon_b \rho_b$

ε and ρ being the turbulent diffusivity and density respectively. As $\left(\frac{\partial m}{\partial y}\right)$ at the wall is zero it can be assumed that

$$\left(\frac{\partial C_p}{\partial y}\right)_b = \left(\frac{\partial C_p}{\partial y}\right)_w = 0 \qquad (12)$$

$$\text{Thus } q_b = \varepsilon_b \rho_b Cp_w \left(\frac{dT}{dy}\right)_b \qquad (13)$$

Assuming that heat transfer takes place by conduction through the sublayer of thickness δ.

$$q_b = k_b \left(\frac{T_b - T_w}{\delta}\right) \qquad (14)$$

where k is the conductivity.

The enthalpy field in the turbulent region will be of the form

$$i = A + BCp_c(T_c - T_g) + CCp_w(T_b - T_g) \qquad (15)$$

where A, B and C are functions of position.

This expression arises due to the linearity of the energy equation, eqn. (2), in enthalpy allowing superposition of the enthalpy fields for different boundary conditions given in Fig.2. A is the enthalpy field for isothermal conditions; B that for a coolant of unit enthalpy and zero enthalpy in the freestream and at the wall; C corresponds to unit enthalpy at the wall and zero freestream and coolant enthalpy.

Differentiating eqn. (15) with respect to y and using eqn. (11) gives the heat transfer rate as,

$$\frac{q}{\xi_b} = \beta Cp_c(T_c - T_g) - \phi Cp_w(T_b - T_g) \qquad (16)$$

where $\beta = \left(\frac{\partial B}{\partial y}\right)_b$ and $\phi = -\left(\frac{\partial C}{\partial y}\right)_b$

When the wall is adiabatic then $T_b = T_{bad} = T_{aw}$.

$$\text{Thus } \left(\frac{T_g - T_{aw}}{T_g - T_c}\right) = \frac{Cp_c \beta}{Cp_w \phi} = \eta_{FG}$$

When $Cp_c = Cp_w = Cp_g$ this equals η_A and therefore,

$$\eta_A = \frac{Cp_w}{Cp_c}\eta_{FG}$$

This equation is the same as found previously, eqn. (9). Substituting back in eqn. (16) for $T_g - T_c$ gives,

$$\frac{q}{\varepsilon_b \rho_b} = \phi Cp_w(T_{aw} - T_b) \qquad (17)$$

Eliminating T_b using eqn (14) gives

$$\frac{q}{(T_{aw} - T_w)} = \frac{\phi \varepsilon_b \rho_b Cp_w}{1 + \frac{\phi \varepsilon_b \rho_b Cp_w \delta}{k_w}} \qquad (18)$$

Thus the Nusselt number, Nu, becomes

$$Nu = \frac{qx}{k_g(T_{aw} - T_w)} = \frac{\phi \varepsilon_b \rho_b x}{k_g} \frac{Cp_w}{1 + \frac{\phi \varepsilon_b \rho_b \delta Cp_w}{k_w}} \qquad (19)$$

Dimensional reasoning shows that the term in eqn. (19) $\phi \varepsilon_b \rho_b x$ may be expressed as a function of freestream Reynolds number and coolant injection properties,

$$\frac{\phi \varepsilon_b \rho_b x}{\mu_g} = f_1\left(\mathrm{Re}_{xg}, \frac{\rho_c}{\rho_g}, \frac{u_c}{u_g}\right)$$

The term containing δ may be similarly expressed in terms of function f_2. Hence eqn. (19) becomes,

$$Nu = \frac{\mathrm{Pr}_g \frac{Cp_w}{Cp_g} f_1}{1 + \mathrm{Pr}_g \frac{Cp_w}{Cp_g} \cdot \frac{k_g}{k_w} f_2} \qquad (20)$$

Thus the ratio of Nusselt number for the cold air or engine case to that for the foreign gas simulation which is at the same Reynolds number and coolant to freestream density and velocity ratios becomes,

$$\frac{Nu_A}{Nu_{FG}} = \left(\frac{Cp_w}{Cp_g}\right)_{FG} \cdot \frac{1 + \left[\mathrm{Pr}_g \frac{Cp_w}{Cp_g} \frac{k_g}{k_w}\right]_{FG} f_2}{1 + \left[\mathrm{Pr}_g \frac{k_g}{k_w}\right]_A f_2} \qquad (21)$$

Again it is assumed that Cp for air is independent of temperature.

Analytical solutions for constant property flows matching the viscous sublayer to the turbulent region above are available and use may be made of these to obtain an approximate value of f_2.

Thus an estimate of the flowfield term f_2 in eqn (21) may be made from the heat transfer to a flat plate in a uniform flow. From standard texts (e.g. Kays and

Crawford, 1993) the constant property equation, for gases, is,

$$Nu_x = \frac{0.0287\,\mathrm{Re}_x^{0.8}\,\mathrm{Pr}}{0.169\,\mathrm{Re}_x^{-0.1}(13.2\,\mathrm{Pr}-8.66)+0.85} \qquad (22)$$

Pr is the Prandtl number and Re_x is the Reynolds number based on distance, x, from the leading edge. Eqn (22) may be rearranged to give,

$$Nu_x = \frac{\mathrm{Pr}\,f_1(\mathrm{Re}_x)}{1+\dfrac{2.62\,\mathrm{Pr}}{\mathrm{Re}_x^{0.1}-2.00}} \qquad (23)$$

The last term in the denominator corresponding to the thermal resistance of the sublayer represented by the term f_2Pr in eqns. (20) and (21). As can be seen the term is relatively insensitive to Reynolds number and as stated refers to the constant property case.

$$f_2 = \frac{2.62}{\mathrm{Re}_x^{0.1}-2.00} \qquad (24)$$

For $Re_x=10^5, f_2=2.25$ and for $Re_x=10^6, f_2=1.32$

Cp_{wFG} and k_{wFG} are determined from $\eta_A=m$ found from eqn.(10b). Cp_{wFG} is given by eqn.(8). k_{wFG} is approximately given by an equation of the same form, i.e.,

$$k = k_g(1-M)+k_cM \qquad (25)$$

but in this case M is the mole concentration determined from m. The value of k for the air case is determined by the relevant temperature.

It should finally be mentioned that the foregoing analysis has assumed that the local wall temperature represents, the isothermal wall situation. This is not exact, however, as Eckert (1992) points out "the upstream temperature or heat flux distribution has little effect on the local Stanton number in a turbulent boundary layer".

8. EXPERIMENTAL RESULTS

Heat transfer results are available for carbon dioxide injection and for injection using a gas mixture of sulphur hexafluoride and Argon. The mixture has the property that its ratio of specific heats is 1.4 i.e. the same as that of air. In this manner compressibility effects should also be reproduced although the analysis in this paper does not include compressibility. The properties are given in the Table 1 below

Gas	Density ratio	C_p ($KJ.k_g^{-1}$)	k ($W.m.^{-1}.k^{-1}$)	P_r	μ $K_g.m^{-1}.s^{-1}$
AIR (300K)	1.0	1.005	2.614×10^{-2}	0.711	1.85×10^{-5}
CO_2 (300K)	1.52	0.852	1.662×10^{-2}	0.768	1.499×10^{-5}
SF_6+A (300K)	1.77	0.564	1.67×10^{-2}	0.733	2.17×10^{-5}
AIR (1000K)	-	1.141	6.72×10^{-2}	0.709	4.177×10^{-5}
AIR (1800K)	-	1.286	0.111	0.701	6.07×10^{-5}

Table 1- Properties of Air, CO_2 and SF_6+A mixtures. (Air and SF_6 + A from Oldfield and Guo (1998)).

Eqn. (10b) gives the air film cooling effectiveness as a function of the measured foreign gas effectiveness and this is plotted in Fig.3 for CO_2 and SF_6+A mixtures. There is little correction for the CO_2 injection whereas the correction is significant for SF_6+A. The experimental results of Teekaram, Forth and Jones (1986) for CO_2 injection are given in Fig.4. These are compared with experimental results for the same injection density and velocity ratios but with air as the coolant. As can be seen the results are extremely close. In general the results for the CO_2 are slightly below that for air as would be predicted by eqn. (10b). However the experimental error obscures close analysis of the difference.

Examples of the correction necessary to give engine film cooling effectiveness and heat transfer coefficient are given in Figs. (5) and (6). In these cases SF_6+A was the foreign gas employed. The correction can be seen to be significant.

9. CONCLUSIONS

An approximate procedure has been set out for the correction of film cooling experimental results which employ foreign gas to achieve large coolant densities compared to the freestream. This takes into account the difference in specific heat and thermal conductivity. The correction has been shown to agree with the experimental observation that there is little correction necessary in the case of CO_2 injection. In general both film cooling effectiveness and Nusselt number require correction according to the formulae presented.

10. REFERENCES

Ammari, H.D., Hay, N. and Lampard, D., Effect of Density Ratio on the Heat Transfer Coefficient from a Film Cooled Flat Plate, ASME Paper 89-GT-176, 1989.

Day, C.R.B., Oldfield, M.L.G. and Lock G.D., The Influence of Film Cooling on the Efficiency of an Annular Nozzle Guide Vane Cascade, ASME Paper 97-GT-521, 1997.

Eckert, E.R.G., Similarity Analysis of Model Experiments for Film Cooling in Gas Turbines, Wärme-und Stoffubertragung 27, 217-223, 1992

Eckert, E.R.G., Analogies to Heat Transfer Processes, in Eckert, E.R.G., Measurements in Heat Transfer, 2nd Ed., Washington, Hemisphere, 1986.

Goldstein, R.J., Film Cooling, in Irvine, T.F., Hartnett, J.P., Advances in Heat Transfer, New York, Academic Press, 1971 pp 327-329.

Guo, S.M., Lai, C.C., Jones, T.V., Oldfield, M.L.G., Lock, G.D. and Rawlingson, A.J., The Application of Thin-Film Technology to Measure Turbine Vane Heat Transfer and Effectiveness in a Film-Cooled, Engine-Simulated Environment, to be published in Int J. of Heat and Fluid Flow.

Han, J.C., and co-workers in ASME Papers: 93-GT-134, 1993, 95-GT-11, 1995, and 97-GT-181, 1997.

Jones, T.V., Definitions of Heat Transfer Coefficients in the Turbine Situation, Turbomachinery: Latest Developments in a Changing Scene, I. Mech. E., pp201-206, 1991

Kays, W.M and Crawford, M.E., Convective Heat and Mass Transfer, 3rd Edition, McGraw-Hill Series in Mechanical Engineering, 1993.

Oldfield, M.L.G. and Guo, S., Aerothermal Properties of Foreign Gas (SF_6/Av) and Air: Recommended Formulae from 160-1000 K, Oxford University Report, OUEL 2141/97, 1997.

Pedersen, D.R., Eckhert, E.R.G., Goldstein, R.J. Film Cooling with Large Density Differences between Mainstream and the Secondary Fluid Measured by the Mass Transfer Analogy, J. Heat Transfer 99 pp 620-627, 1977.

Rowbury, D.A., Oldfield, M.L.G., Lock, G.D. and Dancer, S.N., Scaling of Film Cooling Discharge Coefficient Measurements to Engine Conditions, ASME Gas Turbine Conference to be held in Stockholm, 1998.

Salcudean, M., Gartshore, I., Zhang, K. and Barnea, Y., Leading Edge Film Cooling of a Turbine Blade Model through Single and Double Row Injection, ASME Paper 94-GT-2, 1994.

Teekaram, A.J., Forth, C.J.P. and Jones, T.V., The use of Foreign Gas to Simulate the Effect of Density Ratio in Film Cooling, ASME, J. of Turbomachinery Vol. III, pp 57-62, 1989

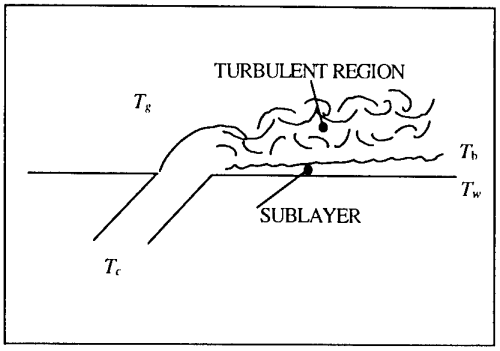

Fig.1. Schematic diagram showing turbulent region and sublayer

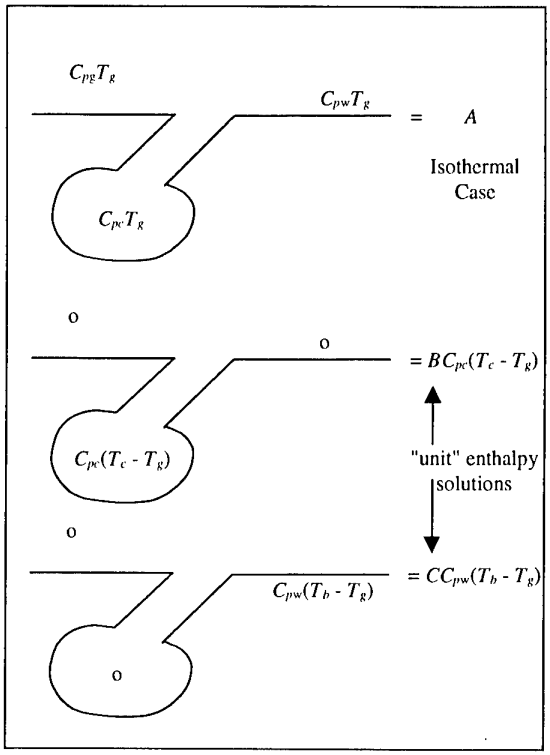

Fig.2. Boundary conditions which when superposed give the desired enthalpy boundary conditions of Fig.1.

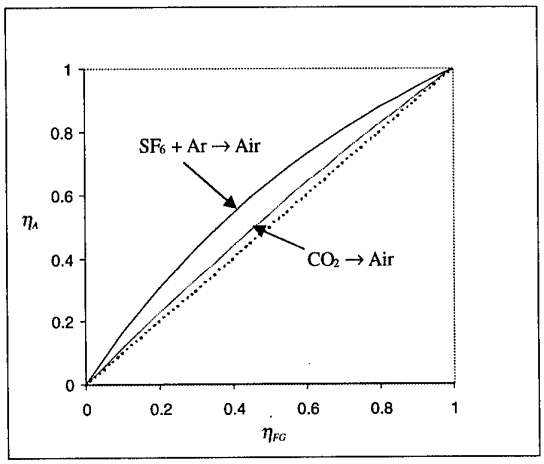

Fig.3. Film cooling effectiveness for cold air, η_A, versus the equivalent value for foreign gas, η_{FG}. Eqn (10b).

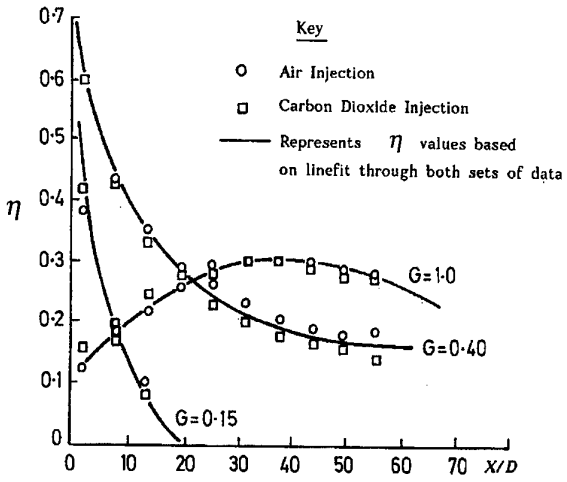

(a) Density ratio $\frac{\rho_c}{\rho_g} = 1.25$

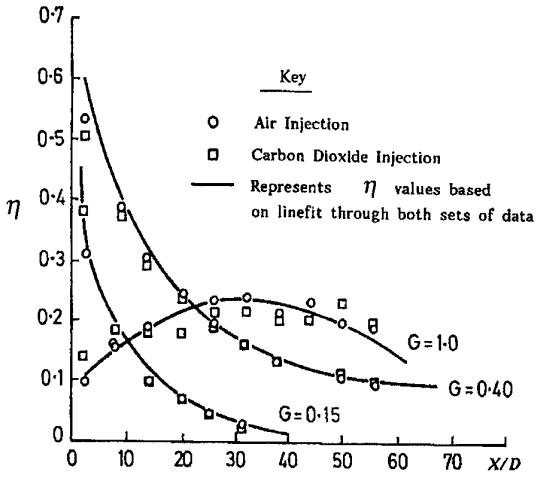

(b) Density ratio $\frac{\rho_c}{\rho_g} = 1.67$

Fig.4. Results for effectiveness η versus distance *X/D* downsream from a single row of 30° holes of diameter *D*. Carbon Dioxide and air injection results for the same density ratios. From Fig.3. it can be seen that the results for air are expected to be slightly above those for CO_2.

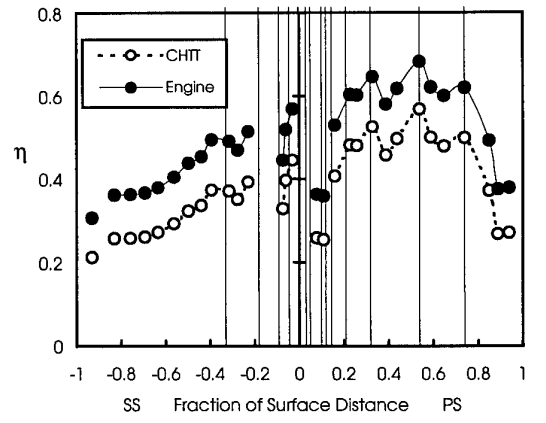

Fig.5. Film cooling effectiveness, η, on an NGV determined from experiments using SF_6 + A as the coolant and the value determined for the engine using eqn (10b). The lines show the positions of rows of film cooling holes.

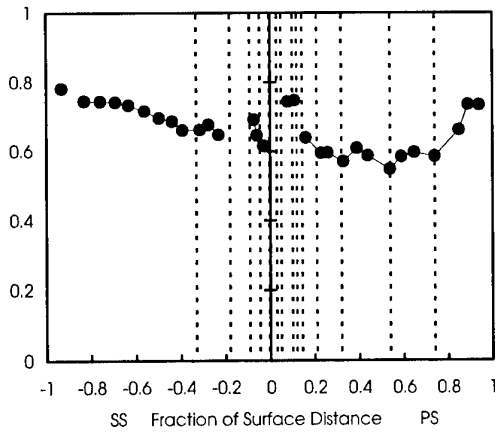

Fig.6 The ratio of Nusselt No. for the engine to that determined for SF_6 + A coolant in an experiment on an NGV from eqn (21). Dotted lines are rows of coolant injection holes.

The Potential of Advanced Materials on Structural Design of Future Aircraft Engines

J. Kumpfert, M. Peters, W.A. Kaysser

DLR - German Aerospace Center, Institute of Materials Research
D-51170 Cologne, Germany

SUMMARY

For a gas turbine engine manufacturer the direct operating costs (DOC) of aircraft engines is primarily reduced by control of fuel costs, maintenance costs, and through weight savings. All aspects are strongly influenced by the materials technology available and can improve the component efficiency significantly. The recent development of conventional high temperature titanium alloys has demonstrated the in-service capabilities of conventional materials due to better understanding of microstructure/property relationships. Beyond these capabilities new light-weight materials as titanium aluminides and titanium matrix composites (TMCs) may improve engine performance significantly. In particular TMCs can improve compressor efficiency by enabling new compressor design not feasible with any other material used today.

Increased turbine efficiency depends primarily on the gas turbine inlet temperature. To further increase the thrust-to-weight ratio and decrease the specific fuel consumption new aircraft engines will require gas turbine inlet temperatures well beyond 1600°C. Since new structural high temperature materials capable of service temperatures significantly above current high pressure turbine temperatures are not feasible in short-term other innovative technologies are required. This is in particular through the introduction of electron-beam physical vapor deposition (EB-PVD) thermal barrier coatings (TBCs).

Reduced emissions and lower specific fuel consumption (SFC) of next generation jet engines depend predominantly on new combustor design. Very low emission combustors require revolutionary materials as ceramic matrix composites (CMCs) to replace the metallic liner currently in use.

The potential payoff, processing, and properties of conventional high temperature titanium alloys, titanium aluminides, TMCs, TBCs, and CMCs are highlighted regarding applications in aircraft engines.

1. INTRODUCTION

During the design of a new engine many different design alternatives are considered. Their impact on the main engine characteristics like engine weight, specific fuel consumption (SFC), manufacturing costs, maintainability need to be investigated. For airlines as customers the direct operating costs (DOC) of an aircraft are an outstanding qualification parameter. The engine design dependent costs make up a portion of approximately 40% and above [1]. Hereby it is important to note, that the sensitivities of the DOC with respect to the engine characteristics mentioned above are quite different. While a 1% lower DOC of an 100-seater regional airplane requires an approximately 10% lower engine weight or engine price, only 5% reduction in SFC yields to the same drop in DOC [1]. This ranking is in particular of importance for civilian aircraft engines.

Apart from specific fuel consumption, the thrust-to-weight ratio is of considerable interest for military engines. The thrust-to-weight ratio has been significantly improved over the years accomplished through increased operating temperatures as well as improved structural efficiency]. It is very obvious that advanced materials play a major role here. In fact, modern aircraft engines represent some of the most demanding and sophisticated applications for structural materials in any engineering system manufactured today. This has been manifested by the steady increase in service temperature, product reliability and usage of lightweight materials [2].

But aircraft engines need not to be only economical on fuel, reliable, and capable of high specific thrust, they also have to be environmentally acceptable. This is of importance, since airplanes usually emit pollutants at altitudes, where the atmosphere is extremely sensitive. The greatest potential for reducing pollutant emissions lies in modification of the combustion chamber itself. In terms of emission nitrogen oxides and carbon dioxide are of prime concern. NOx is particularly a problem since emission increases with increasing pressure ratio and process temperature - both are obvious ways to increase engine performance. However, these influences can be overcompensated by very low emission combustors. Such combustors need to be operated without cooling air on the inner liner surface, which will therefore experience temperatures exceeding the temperature capability of any of the metals that could be realistically used [2]. From the perspective of the high temperature material systems known today, only ceramic matrix composites (CMCs) offer the potential to meet these extremely challenging demands. Therefore predominantly materials development will decide, whether future emission requirements of high pressure ratio aircraft engines can be satisfied.

This paper will address some aspects of advanced materials technologies such as recent conventional high temperature titanium alloys, titanium aluminides, titanium matrix composites (TMCs), thermal barrier coatings (TBCs), and ceramic matrix composites (CMCs) with special emphasis on design requirements of future aircraft engines. Fig. 1 shows a schematic allocation between different materials technologies and aircraft engine components leading to a significant payoff.

Paper presented at the RTO AVT Symposium on "Design Principles and Methods for Aircraft Gas Turbine Engines", held in Toulouse, France, 11-15 May 1998, and published in RTO MP-8.

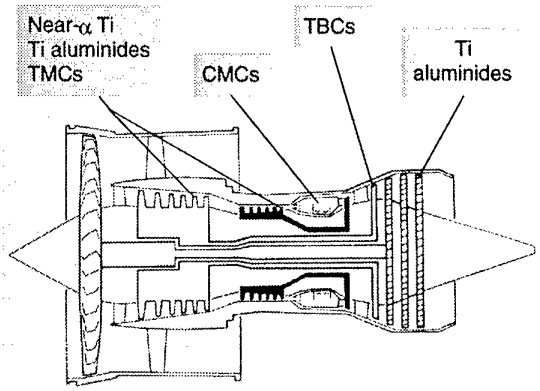

Fig. 1: Schematic allocations of advanced materials technologies and aircraft engine components leading to significant payoff.

2. New Light-Weight High Temperature Materials increase Component Efficiency

Near-alpha titanium alloys, titanium aluminides and titanium matrix composites (TMCs) represent the most important material classes with a high strength to weight ratio for current and future aircraft engines. The following chapter will address some of the improvements possible with high-temperature titanium alloys, titanium aluminides, as well as new design approaches possible with enabling technologies as represented by TMCs. An important discriminator between the different material classes is given by the respective maximum service temperature. The values given in Table 1 include environmental considerations, which considerably decrease the maximum service temperature of all titanium base alloys.

2.1. High-Temperature Titanium Alloys

There is probably no other metal system, which is closer related to aerospace applications than titanium base materials. Today titanium alloys represent one third of the weight of modern aircraft engines and - following Ni-base superalloys - are the second most used engine material. First applications of titanium alloys date back to the 1950s when they paved the way for the first fan-type gas turbine engines from Pratt & Whitney and Rolls Royce, first as compressor blades then disks. The large front fan of modern high by-pass engines as well as most of the stator and rotor blades and discs of the low and intermediate sections of the compressor with temperatures approaching 520°C are made of titanium alloys [3].

With only about half the density of steels or Ni-base superalloys, titanium alloys yield an excellent strength-to-weight ratio. Their corrosion resistance is outstanding, their abundance essentially unlimited. However, the reduction technology to reduce the ores to metal is energy and cost intensive, the prime reason for their relatively high price.

Over the last 4 decades a prime concern of engine manufacturers has been to increase the maximum service temperature of titanium alloys. Compared to the classical α+β titanium alloy Ti-6Al-4V, near-α titanium alloys contain less β stabilizing elements, which increases the volume fraction of the hcp α phase at the expense of the bcc β phase. Compared to bcc structures diffusion in hcp structures is much slower and deformation is more difficult due to limited number of slip systems. Both phenomena explain the superior elevated temperature behavior of near-α titanium alloys as shown in Fig. 2. As shown in Table 1 these alloys contain about 5 to 6% aluminum as their main alloying element with additions of neutral elements (Sn, Zr), but only small amounts β stabilizers, like Mo or Nb, to maintain strength and deformability. Silicon plays a key role in these alloys, since it is known now for more than 20 years, that small additions of about 0.1wt.%

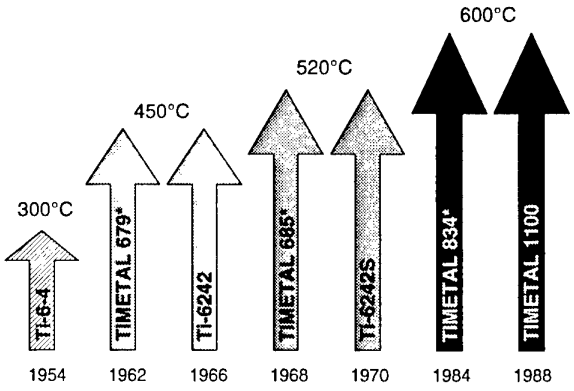

Fig. 2: Increase of maximum service temperature of conventional elevated temperature titanium alloys with respect to tensile and creep strength only. (*: all alloys developed by IMI have been renamed by Timet after the take-over of IMI by Timet).

Si to Ti-6242 effectively improves creep resistance [4]. Investigations in England revealed further increases of Si up to about 0.5 wt.% did not result in negative influences on mechanical behavior in more recently developed near-α titanium alloys. Therefore, to date all new high temperature titanium alloys reveal Si as an important alloying element thus raising the upper service temperature with respect to creep performance (Fig. 2).

Table I: Light-weight high temperature titanium base materials.

alloy type	short form	chemical composition (wt.% / * at.%)	max. service temperature
near-alpha	IMI 685	Ti-6Al-5Zr-0.5Mo-0.25Si	
titanium alloys	Ti-6242S	Ti-6Al-2Sn-4Zr-2Mo-0.1Si	
	IMI 834	Ti-5.8Al-4Sn-3.5Zr-0.7Nb-0.5Mo-0.35Si	480 - 520°C
Ti_3Al alloys	Alpha 2	Ti-24Al-11Nb*	
	Super-Alpha 2	Ti-25Al-10Nb-3V-1Mo*	520 - 550°C
Ti_2AlNb alloys	Orthorhombics	e.g.: Ti-22Al-25Nb*	650 - 700°C
TiAl alloys	Gamma alloys	e.g.: Ti-48Al-2Cr-2Nb*	720 - 800°C
TMCs	-	SiC fiber / Ti-base matrix	300 - 700°C

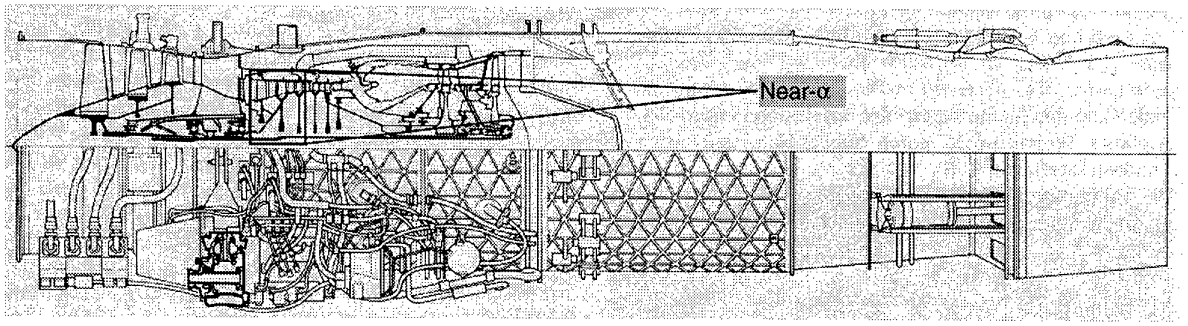

Fig. 4: For the high-performance military aircraft engine EJ200 (EUROJET, Munich, Germany) the last generation near-α titanium alloy TIMETAL 834 is in service in the high pressure compressor [12].

The two latest near-α alloys are TIMTEAL 834, formerly IMI 834, developed by Imperial Metal Industries Titanium Ltd. (IMI) and Rolls Royce and the US alloy TIMETAL 1100, developed by the Titanium Metals Cooperation of America (Timet) initially for Pratt & Whitney. Interestingly - despite of nearly identical chemistry - both alloys are recommended with quite different optimum microstructures. While TIMETAL 834 is usually thermomechanically processed in a way to produce a bi-modal type microstructure TIMETAL 1100 should be used in a fully lamellar structure (Fig. 3) [5, 6]. It could be shown, that lamellar structures prove to be superior in terms of

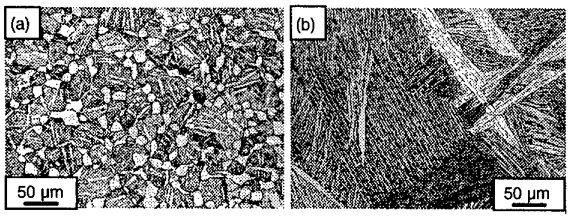

Fig. 3: Typical microstructures of the high-temperature near-α titanium alloys (a) TIMETAL 834 - bi-modal and (b) TIMETAL 1100 - fully lamellar.

yield and tensile strength, fracture toughness, fatigue crack growth and creep resistance, while finer bi-modal structures yield superior ductility and high-cycle fatigue strength [7, 8].

The new high temperature near-α titanium alloys have significantly improved the compressor efficiency in recently introduced engines such as the Trent 800 from Rolls Royce and the military engine EJ200 from Eurojet. The availability of new near-α titanium alloys capable of operating at about 500°C has allowed the use of light weight material for more stages of the compressor, since they reduce the amount of heavy Ni-base superalloys within the high pressure compressor (HPC). Recently developed high pressure compressor, as in the EJ 200, are employing near-α titanium alloys in the front and Ni-base superalloys in the stages exceeding ~520°C (Fig. 4). The high thrust-to weight ratio of the EJ 200 is in part a result of the high stage pressure ratio of the high pressure compressor, and the significant weight reductions by employing the last generation near-α titanium alloy TIMETAL 834 [9]. The main reason to employ Ni-base superalloys at service temperatures beyond 520°C is the severe oxidation problem of titanium alloys in general and also of near-α titanium alloys.

With respect to mechanical performance of titanium alloys, embrittlement of the subsurface zone by interstitial solution of mainly oxygen is considered to be the crucial factor rather than loss of load bearing cross section by oxide scale formation [10]. Improvement of oxidation resistance including minimizing embrittlement can essentially be achieved by addition of certain elements as aluminum or by surface modification techniques. However, as far as known from literature, oxidation resistant coatings have not yet been brought into real service. One major drawback of coated titanium alloys is their reduced fatigue life due to the brittleness of most coating systems. Recent investigations on magnetron-sputtered multilayer Ti-Al coatings demonstrated the capability to prevent the embrittlement of the subsurface zone, while keeping the low cycle fatigue live nearly unaffected [11]. Successful implementation of coatings could expand the service temperature range for near-α titanium alloys up to 600°C.

2.2 Titanium Aluminides

Increasing the aluminum content in Ti-base alloys leads to the formation of the intermetallic compounds Ti_3Al and TiAl. Besides aluminum Ti_3Al base alloys and TiAl base alloys contain β-stabilizing elements to yield sufficient ductility by stabilizing a multi-phase alloy. Examples of multi-phase alloys of each group, which were developed for applications in jet engines, are shown in Table 1. The most recent alloy family within the titanium aluminides is represented by the orthorhombic titanium alloys based on the intermetallic compound Ti_2AlNb. This class of material emerged in the early 90's based on the results on Ti_3Al-base titanium aluminides.

Titanium aluminides represent a new class of alloys, which provide a unique set of physical and mechanical properties that can lead to substantial payoffs in future aircraft engines [13]. Beside density reductions due the high aluminum content, Ti_3Al and in particular TiAl and Ti_2AlNb alloys exhibit

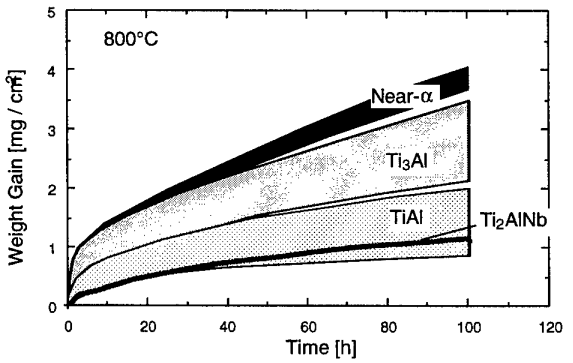

Fig. 5: Isothermal oxidation behavior of different classes of titanium base materials.

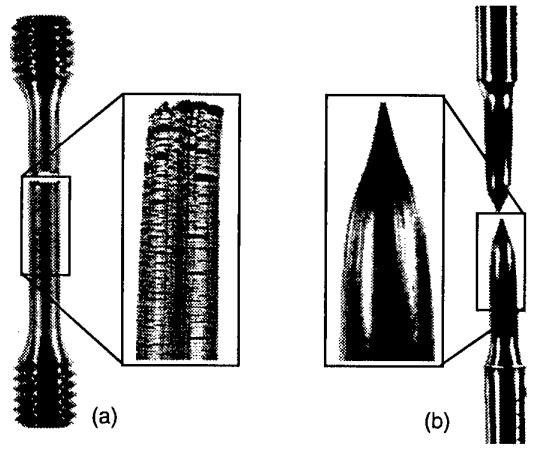

Fig. 6: Environmental embrittlement of an Ti_3Al base alloy (Ti-25Al-10Nb-3V-1Mo) during tensile testing at 700°C; (a) tested in air, (b) tested in vacuum.

significant higher oxidation resistance in comparison to near-α titanium alloys Fig. 5. The high oxidation resistance of the TiAl base alloys originates from the high volume fraction of protective alumina in the oxide scale. The critical aluminum content necessary to form a dense external Al_2O_3 scale, rather than a heterogeneous mixture of TiO_2 and Al_2O_3 is clearly above 50 at.% aluminum [14]. However, all TiAl base alloys considered today for practical application contain equal or less than 48 at.% aluminum to obtain sufficient ductility.

The addition of other elements in particular niobium has been found to significantly reduce the oxidation rate of TiAl base alloys [15]. The beneficial effect of niobium with respect to oxidation behavior could also be verified for the class of orthorhombic titanium alloys [16]. The orthorhombic alloy investigated exhibited an excellent oxidation behavior at 800°C and higher, compared to other titanium base materials (Fig. 5). This phenomena also leads to less pronounced environmental embrittlement of the orthorhombic material in comparison to the Ti_3Al base alloys, which were of significant interest in the 80's and early 90's with respect to applications in the aircraft engine. However, the influence of environmental embrittlement on mechanical properties is very pronounced for Ti_3Al base alloys. Fig. 6 shows that the brittle subsurface layer formed during high temperature exposure leads to deep surface cracks resulting in premature failure in comparison to a specimen tested in vacuum. Thus Ti_3Al base alloys show a large reduction in tensile ductility during tensile testing in air at temperatures as low as 550°C [17, 18]. Predominantly due to this pronounced phenomena work on Ti_3Al base alloys has been discontinued in favor of the orthorhombic titanium alloys.

Fig. 7 compares the specific yield strength, specific young's modulus and coefficient of thermal expansion (CTE) of near-α titanium alloys and titanium aluminides with the common Ni base alloy IN718, which found wide-spread use in aircraft engines.

An important advantage of titanium aluminides is the high strength retention at elevated temperatures. While near-α titanium alloys can reach strength values within the range of Ti_3Al / Ti_2AlNb base alloys at room temperature, the elevated temperature strength of the titanium aluminides clearly exceeds the values of the near-α titanium alloys (Fig. 7a). The wide strength ranges within each alloy family is primarily determined by microstructure variations, since the mechanical properties of almost all titanium base alloys are very sensitive to microstructure. Therefore microstructure control via thermal or thermomechanical processing is a key element with respect of implementation of new titanium base alloys into aircraft engines. For example TiAl base alloys exhibit usually relatively low strength, leading to specific strength values within the range of common Ni base alloys as IN718 in spite of the low density of TiAl. However, significantly improved understanding of microstructure/property relationships of TiAl base alloys in recent years led to advanced processing and high strength TiAl base materials [19]. Therefore without employing powder metallurgy specific strength of TiAl base materials approaching the upper strength level indicated in Fig. 7a can be obtained in laboratories. Current activities are aimed to verify the thermal stability of such microstructures and whether they can be exploited in large scale products.

Even more sensitive to microstructure are the mechanical properties of the Ti_3Al/Ti_2AlNb base alloys. While room temperature yield strength values can vary between 550 and 1450 MPa, tensile ductility was found to vary between 20%

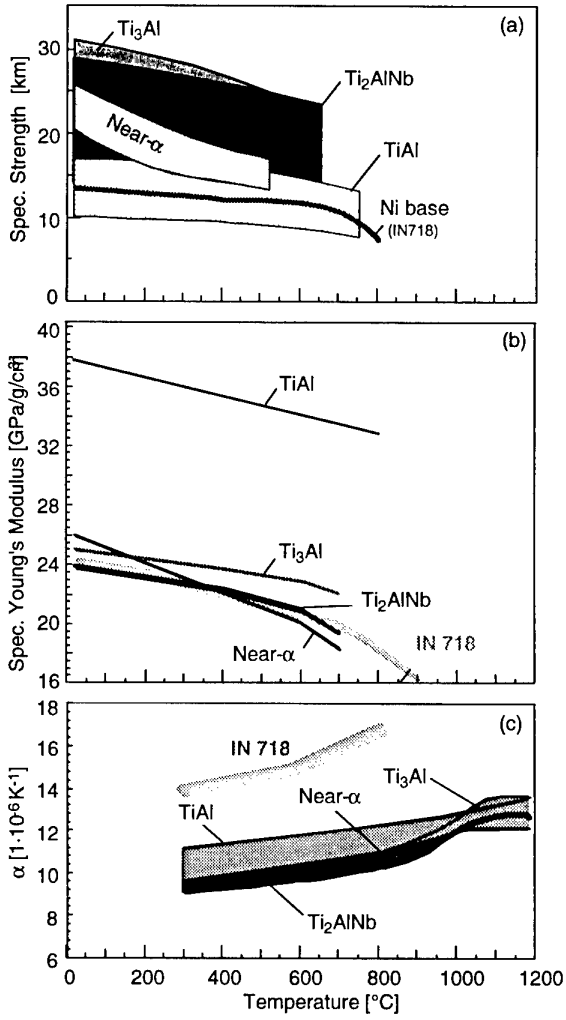

Fig. 7: Ranges of mechanical and physical properties of Near-α titanium alloys and titanium aluminides in comparison to the common Ni base alloy IN718.

and essentially zero [16, 20]. The reason for this wide range of mechanical properties depending on microstructure in Ti_3Al/Ti_2AlNb base alloys was determined to be a very pronounced age hardening effect. Again thermal stability of the individual microstructures is a key issue. It can be concluded, however, that orthorhombic titanium alloys clearly show higher specific strength at elevated temperature than TiAl base materials. Contrary the maximum service temperature of Ti_2AlNb base alloys is about 80°C lower in comparison to gamma TiAl materials due to the lower oxidation resistance at 700°C and below.

An important advantage of TiAl base alloys is the extraordinary high specific young's modulus, being more than 50% higher in comparison to Ti_3Al/Ti_2AlNb base alloys, near-α titanium alloys and IN718 (Fig. 7b). Many applications in aircraft engines can benefit from the high specific stiffness of gamma TiAl materials alone. Frames, cases, seal supports and other components that control clearances can therefore benefit from TiAl materials, even at low temperatures [21].

The greatest issue for design of TiAl components is damage tolerance. The low ductility of TiAl base alloys increases the possibility of damage, whether in-service or during handling (Fig. 8a). In addition the low fracture toughness of gamma TiAl alloys reduces the ability of the materials to resist the propagation of a pre-existing crack (Fig. 8b). A material with adequate toughness should be able to survive the presence of a crack even if its ductility is inadequate to prevent crack formation. Therefore the key to achieve successful design of aircraft engine components with titanium aluminides appears to lie in toughness, rather than ductility [22]. While TiAl base alloys exhibit typically fracture toughness values below 20 MPa√m, near-α titanium alloys, which are used in today's aircraft engines, show values at or above 40 MPa√m depending on microstructure.

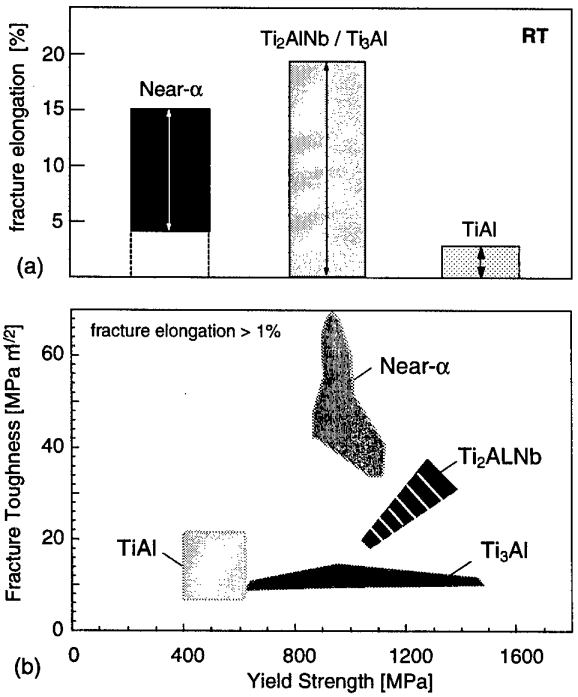

Fig. 8: Ranges of ductility (a) and fracture toughness (b) of advanced titanium base materials.

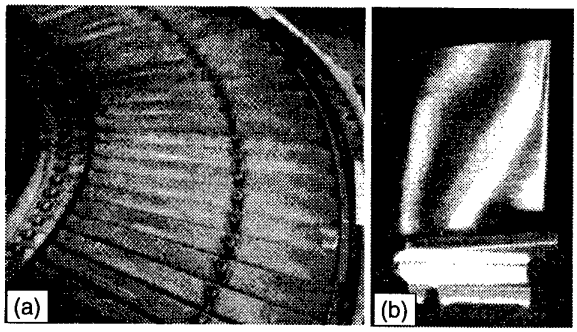

Fig. 9: High payoff applications for TiAl base alloys: (a) CF6-80C2 LPT stage 5 rotor after testing, (b) TiAl HPC blade [23].

Orthorhombic Ti_2AlNb base alloys appear to have better fracture toughness, higher ductility, higher specific yield strength and lower coefficient of thermal expansion than TiAl base alloys (Fig. 7). This property profile makes orthorhombic titanium aluminides attractive for applications in compressor casings [13]. If the orthorhombic alloys demonstrate damage tolerance behavior close to near-α titanium materials even rotating parts as compressor disks or impellers for smaller engines might be considered. In this case a complete new design - the all titanium compressor - might become reality, where all massive and heavy Ni base components are replaced by lighter titanium base materials. Such a design could reduce the weight of the HPC rotor alone by about 20%, not considering secondary effects [9]. In the case of TiAl base alloys the greatest payoff will come from low pressure turbine airfoils. Successful engine tests have been already performed with a full set of ninety-eight stage 5 low pressure turbine blades in a CF6-80C2 engine (Fig. 9). The expected weight reduction in the GE90 is up to 200kg by employing TiAl base alloys in the low pressure turbine [21]. Furthermore due to the high ignition resistance relative to near-α titanium alloys, gamma TiAl materials are also aggressively pursued as an airfoil material to replace Ni base alloys.

2.3 Titanium Matrix Composites (TMCs)

The primary driver for the development of titanium matrix composites (TMCs) has been the gas turbine engine industry. Recognizing that the structural limits of more conventional aerospace materials have largely been achieved, the primary goal of titanium (TMC) and titanium aluminide (IMC - will also be designated as TMC in this paper for simplicity) composite development effort is to provide 'revolutionary materials' which allow innovative and radical new component design. In comparison to the near-α titanium alloys and titanium aluminides TMCs offer important advantages in terms of specific strength and stiffness.

TMCs which have demonstrated properties suitable for aerospace applications consist of different titanium base alloys reinforced with 30-40 volume percent of continuous arrays of high strength (>3500 MPa) high modulus (380 GPa) ceramic SiC fibers. The choice of the titanium matrix determines the temperature capability of the TMC. For low temperature applications TMCs employ α+β or β titanium alloys (e.g. Ti-6-4, Ti-15AV-3Al-3Cr-3Sn) as matrix. Up to service temperatures of 500°C near-α titanium alloys are considered, while the development of titanium aluminide matrix alloys is driven by the goal to attain service temperatures up to 700°C. The class of

TMCs employing titanium aluminides as matrix offer the potential to replace nickel base superalloys. Since several important properties of TMCs are known to be significantly influenced by the matrix, the required matrix property profile is in particular complex in the case of high temperature TMCs. General requirements include; sufficient room temperature ductility (2.5-3%), high oxidation resistance, low environmental embrittlement at elevated temperatures, high chemical compatibility with the SiC fibers and low coefficient of thermal expansion to minimize residual stresses. In addition high creep resistance and high specific strength at elevated temperature of the matrix is important with regard to off-axis properties of the composite, i.e. loads not parallel to the fiber axis.

Within the group of titanium aluminides, orthorhombic titanium alloys based on the intermetallic phase Ti_2AlNb are currently most promising for high temperature TMCs. As can be seen in Fig. 7 and Fig. 8 orthorhombic titanium alloys exhibit high specific strength at elevated temperature, low coefficient of thermal expansion and high ductility at room temperature. In spite of their good oxidation resistance TiAl base alloys do not appear to be a suitable matrix in TMCs, since their high specific young's modulus, low room temperature ductility and high coefficient of thermal expansion leads to very high residual stresses in SiC/TiAl composites during processing [24]. Therefore it is difficult to produce crack free SiC/TiAl composites and also to avoid early crack formation in the matrix during loading. To summarize, orthorhombic alloys and near-α titanium alloys reinforced with SiC fibers are currently the most promising systems for intermediate and high temperature applications.

The quality of potential TMC engine applications is determined on one side by the choice of the composite system, however, the processing procedure also strongly influences the final product properties and costs. Among the different processing routes developed in recent years, TMCs are often fabricated using the foil/fiber/foil technique consisting of alternating layers of woven fiber mats and 100-150 µm thick titanium alloy foils which are stacked up and vacuum hot press or hot isostatic press consolidated into multilayer composites. An alternative approach, which was initially developed at the DLR, employing physical vapor deposition

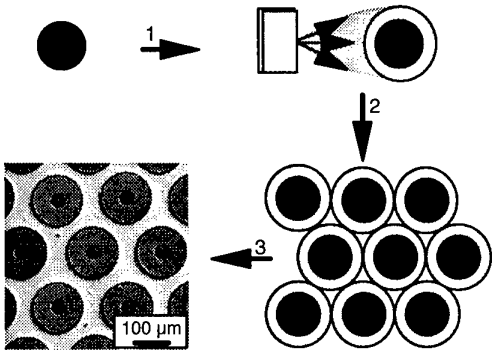

Fig. 10: Processing of TMCs via fiber coating technique: (1) PVD coating of fibers with titanium matrix, (2) lay-up of coated fibers in a hexagonal close packed arrangement, (3) consolidation via hot isostatic pressing (HIP).

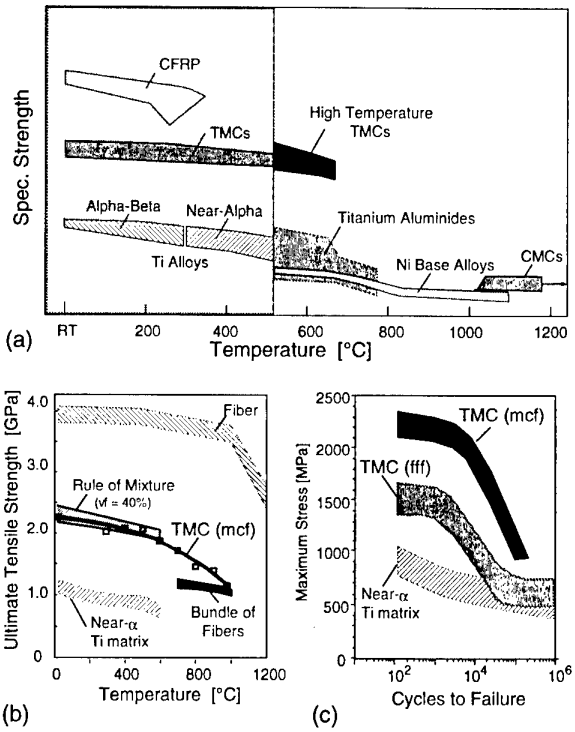

Fig. 11: Mechanical properties of TMCs: (a) specific tensile properties of TMCs and other advanced aviation materials, (b) ultimate tensile strength of TMCs produced via the matrix coated fiber technique (mcf), (c) longitudinal low cycle fatigue behavior of TMCs produced via foil/fiber/foil technique (fff) or via the matrix coated fiber technique (mcf); tests performed at room temperature (R=0.1, f=1Hz).

(PVD) to coat the fiber with matrix material and consolidate these coated fibers into multilayer composites has several advantages [25]. Most importantly, these technique results in very homogeneous fiber distribution combined with high reproducible quality (Fig. 10) [26]. An exact close packed hexagonal arrangement of the fibers prior to consolidation is an important prerequisite to avoid fiber damage during processing of TMCs [27].

The mechanical properties of TMCs are strongly dependent on factors such as processing technique, constituents (type of matrix alloy including its microstructure and fiber), fiber-to-matrix volume ratio, test procedure, and environment.

The specific strength capabilities of TMCs are shown qualitatively in Fig. 11a. In comparison to other advanced aviation materials TMCs offer the highest specific strength at elevated temperatures, which is an important property for next generation aircraft engines. At lower temperatures TMCs compete with carbon fiber reinforced plastics (CFRP) regarding specific strength values. Since the maximum service temperature of TMCs is primarily limited by environmental considerations the choice of matrix material determines the temperature service range of the composite (Fig. 11a). The full strength potential of TMCs can be attained by processing via the matrix coated fiber technique (mcf), resulting in longitudinal strength values within the rule of mixture (Fig 10b). Room temperature tensile properties of 2400 MPa could be reproducibly attained parallel to the fiber axis in a SiC/IMI834 composite with a fiber volume fraction of 40%. At very high temperatures ultimate tensile strength approaches the strength

of the loose fiber bundle, since the matrix strength tends towards zero and can be neglected [28].

Altough the axial properties of TMCs are clearly superior to existing materials, most applications will require a certain ratio of transverse to longitudinal properties. Since all TMCs produced currently exhibit a weak bond between fiber and matrix transverse properties as strength, modulus, and creep resistance are lower than in superalloys or unreinforced titanium alloys [29]. During transverse creep the bulk of the load has to be borne solely by a matrix filled with holes due to the weak interface [30]. Therefore at high operating temperatures ordered orthorhombic matrices are required, since they outperform near-α titanium alloys with respect to creep resistance and elevated temperature strength (Fig. 7) [31]. Approaches to improve the transverse creep properties of high temperature TMCs are: (1) lowering the volume fraction of the SiC fiber reinforcement; (2) designing a new fiber/matrix interface with a higher bond strength [32]; (3) formation of a creep-resistant matrix microstructure [33]. Current estimates suggest that fiber/matrix interface strength 2-4 times the level currently available may exist without adverse effects on the longitudinal properties of the composite [34]. In this context, however, it should be considered that the ratio of transverse to longitudinal properties in TMCs available today are already much higher than in polymer matrix composites [35].

For application of TMCs in next generation compressor rotors low cycle fatigue behavior is one of the most important criteria. Fig. 11c shows the longitudinal fatigue behavior TMC specimens (SiC/Near-α titanium) processed via the matrix coated fiber technique at room temperature [36]. It is obvious that the longitudinal fatigue behavior is significantly improved in comparison to the matrix material. Also in comparison to Ni base superalloys TMCs may be superior for higher stresses with lifetimes below 10^5 cycles on a density corrected basis [37]. It is also apparent that TMCs produced via the foil/fiber/foil technique (here: SiC/Ti-15-3) do usually lead to lower fatigue strength under the conditions tested [38]. Therefore a homogeneous fiber distribution, which can be attained by the matrix coated fiber technique, appears to beneficially influence the fatigue behavior.

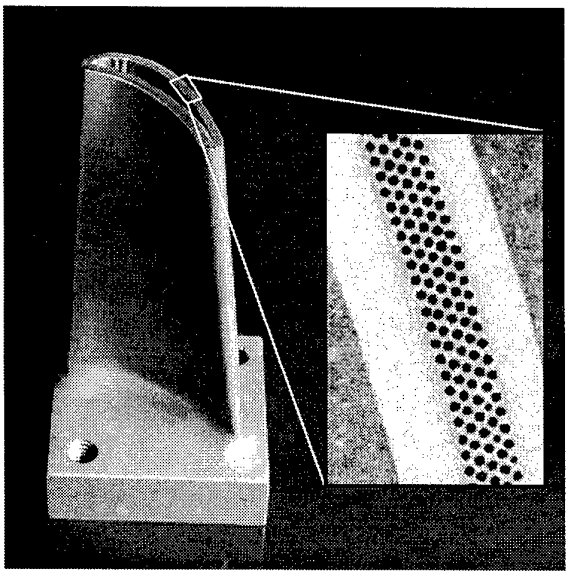

Fig. 12: Hollow TMC blade produced via the matrix coated fiber technique.

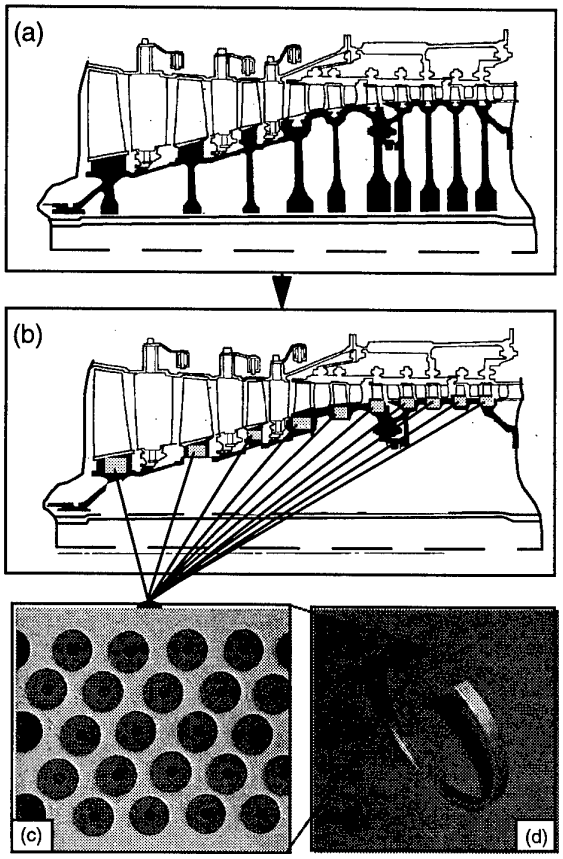

Fig. 13: Compressor design with TMCs; (a) conventional compressor design, (b) bling (bladed ring) design with TMCs, (c, d) fiber distribution in a TMC ring produced via the matrix coated fiber technique.

Potential aircraft engine applications for TMCs can be ranked depending on their potential payoff on one side and the risk as a consequence of component failure [39]. Structural non-rotating components as struts or fan frames, whose primary function is to maintain engine shape and clearances under the wide range of mission loadings, are of moderate to low risk and rely heavily on material stiffness. On large bypass engines such as the GE90, fan frame weight savings of 10-15% are possible [39]. TMC ducts or cases offer a 40% greater stiffness and a 25% weight reduction over the current unreinforced titanium structures [35]. Similarly, TMC links and actuators for moving exhaust flaps offer about 40% weight improvement over Ni base superalloys or stainless steel [40]. Rotating parts operated at low temperatures as fan airfoils represent low to moderate risk components since engines are designed to contain or otherwise to cope with their failure and prevent engine destruction. The fabrication of conventional fan blades with moderate curvature is feasible today (Fig. 12). TMC fan blades enable improved aerodynamic efficiency due to their high stiffness in comparison to conventional titanium fan blades. In addition the high specific strength of TMCs results in significant weight reduction and enables thinner blade root sections. In comparison to carbon fiber reinforced polymer (CFRP) fan blades, bird strike characteristics of TMC fan blades need special attention [41]. Ideal TMC applications are

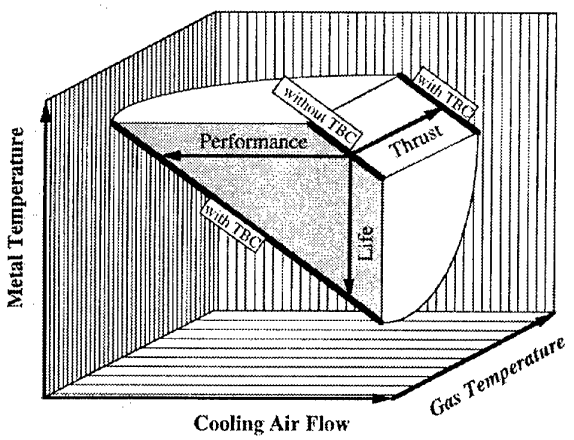

Fig. 14: Thermal barrier coatings (TBCs) allow increased engine performance and/or life extension.

subjected to highly directional loading at elevated temperatures. Therefore parts as blings (Fig. 13) or blums (bladed drums) are very high payoff components in terms of engine performance and weight savings. Rotor weight savings of high pressure compressor rotors might be above 50% if nickel-base superalloys can be replaced by high temperature TMCs. This type of application takes advantage of several strong points of TMCs: their ability to handle elevated temperatures, their relative low weight, and their high stiffness and strength in the direction of the fiber. However, rotating parts as blings are high risk components because their failure can destroy the engine. Reliable quality of the reinforced parts is therefore an important factor. The choice of the processing technique depends therefore on the balance of TMC quality and component cost.

Cost still remains a barrier issue to implementation of TMCs into high performance applications. So far, suppliers and end users have been unable to generate sufficient demand to yield an affordable TMC component [39]. To overcome this barrier TMC components with higher volume applications are being emphasized by a joint U.S. effort known as Titanium Matrix Composite Turbine Engine Component Consortium (TMCTECC) [42]. This $216-million, five-year program was launched in 1994 by U.S. aircraft engine manufactures, the Air Force, and the Advanced Research Projects Agency (ARPA).

3. Innovative Thermal Barrier Coatings (TBCs) increase Turbine Efficiency

Blades and vanes of the high pressure turbine section of aircraft engines are among the most highly stressed parts in engineering components. Internally cooled aerofoils of state-of-the-art Ni-base superalloys operate at temperatures of about 1000°C with short-term peaks yielding even 1100°C which is close to 90% of the alloys' melting points. These temperatures are maintained in service due to a highly sophisticated cooling technology by which however thermal energy is withdrawn from the aerofoils in the order of 1 MW/m^2 thus reducing the overall fuel efficiency of the engine. The necessity of a close control of materials temperatures can be expressed by the simple rule that blade life on creep is halved for every 10 to 15°C increase in temperature [43].

Future development of gas turbines clearly aims for increased gas turbine inlet temperatures (TIT) passing well beyond 1600°C. There is no doubt that this ambitious goal can only be met by usage of uneconomically extensive cooling techniques or by advanced high temperature materials [44] and in particular through the introduction of electron-beam physical vapour deposition (EB-PVD) thermal barrier coatings (TBCs) [45].

TBCs consist of thin ceramic layers of low thermal conductivity - typically partially stabilised zirconia - which are applied on aerofoil surfaces that just have a metallic corrosion resistant coating. The coating imparts good adhesion of the ceramic to the substrate. Application of the TBCs enables increasing engine performance/thrust by either increasing the gas temperature or reducing the cooling air flow. Alternatively the lifetime of the turbine blades can be extended by decreasing metal temperatures as schematically outlined in Fig. 14 [45, 46].

Plasma-sprayed (PS) TBCs have been widely applied to hot components like burner cans since the sixties while in recent applications to more pretentious parts like turbine blades EB-PVD technology is favoured. Contrary to plasma spraying, EB-PVD processing offers the opportunity to generate coatings having a unique columnar microstructure with 2 to 25 µm in diameter. The main advantage of this structure is its superior tolerance against straining and thermoshock, thus giving it a major edge in lifetime [47]. Furthermore, cooling hole closure will be prevented and aerodynamic design of the blades is maintained. In Table 1 the two processing methods are compared as far as thermal barriers for turbine blades are concerned.

During EB-PVD processing a high energy electron beam melts and evaporates a ceramic source ingot in a vacuum chamber. Ingots are bottom fed into the crucibles during evaporation to ensure continuous TBC growth. To achieve defined stoichiometry of the zirconia a controlled amount of oxygen is bled into the deposition chamber. Preheated substrates are positioned in the vapour cloud above where the vapour is deposited on substrates at deposition rates of 100 to 250 nm/s [48]. Typical columnar microstructures and aerodynamically smooth surfaces are obtained without the need for final polishing or conditioning of cooling holes. Due to the columnar microstructure the life time of the TBCs is prolonged and the damage tolerance improved. Typical characteristics and major advantages of thermally sprayed and on-evaporated TBCs are schematically outlined in Fig. 15 [49]. Fig. 16 shows a selection of EB-PVD TBCs on aircraft engine and stationary gas turbine blades produced at DLR on semi-commercial single-

Table 2: Plasma sprayed (PS) versus on-evaporated (EB-PVD) thermal barrier coatings (TBCs).

	PS	EB-PVD
Surface Finish	good but extra polish	excellent
Bond Coat Roughness	grit blasted	smooth
Bonding Mechanism	mechanical	chemical
Alloy Flexibility	high	limited
Typical Thickness	0.2-3mm	0.1-0.3mm
Cooling Hole Closure	poor	excellent
Coating Source	movable	fixed
Large Parts predicable	favourable	costly
Parts per Charge	1	1-10
Investment Costs (%)	100	100-400

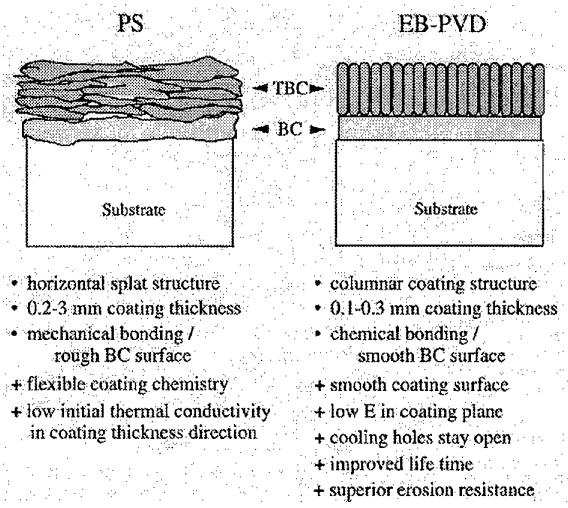

Fig. 15: A simplified comparison of properties for plasma sprayed (PS) and evaporated (EB-PVD) TBCs (schematic).

source 60kW Leybold and dual-source 150kW von Ardenne EB-PVD coaters.

Today first generation of thermal barriers are introduced onto aircraft engine airfoils, primarily to extent the lifetime of the blades. However, to exploit the full potential of TBCs further work has in particular to be directed to efforts which determine critical stresses more accurately based on detailed understanding of failure mechanisms of entire TBC systems with more confidence. The progress in the manufacture of more reliable TBC systems on single crystal materials will address the design of conveniently microstructured TBCs with superior strain tolerance on advanced bond coats with predictable formation of adherant thermally grown oxide scales. Furthermore, the tailoring of respective microstructures to differing substrates with regard to optimal adaption of their "porosity" and of the thermal expansion mismatch has to be taken into account. Here the disposal of appropriate EB-PVD technologies will enable the manufacture of unique microstructures for service-tolerant TBCs.

Future applications of TBCs aim at surface temperatures of 1250°C and above where aircraft engines as well as industrial turbines will operate. Today's state-of-the-art partialy stabilized zirconias (PYSZ), however, exhibit destabilisation of the tetragonal t' phase to monoclinic and cubic on extended exposure at temperatures above 1150°C, and sintering phenomena become predominant. Alternative ceramics will be needed with reduced sintering rates, better phase stability and lower thermal conductivity. The need for advanced ceramic materials will force EB-PVD processing development to overcome pertinent materials restrictions. Multiple-source high rate coaters will be a valuable tool in this context to enable the production of complex TBCs which are composed of "low" and "high" vapour pressure components. Advanced bond coat compositions may also attribute their share to the manufacture of safer TBC systems.

Generally, the coating market has become highly dynamized. New microstructures encompass compositionally graded, density graded and multilayered arrangements where, especially in the last case, a reduced heat conduction may allow the application of thinner overlays. CVD techniques can attribute their particular thin layer virtues. In any case basic and applied research capabilities have to focus on alternative materials and processing routes while earnestly guarding all cost requirements. Finally, non-destructive testing and life-prediction methodologies for TBC systems have to be furnished [50].

4. Ceramic Matrix Composites (CMCs) Enable Very-Low Emission Combustor

The greatest potential for reducing pollutant emissions lies in modification of the combustion chamber itself. Different approaches exist to minimize the pollutant emissions significantly and in particular NO_x. However, it is always very essential to control the fuel-air ratio in the hot zone of the combustor in a narrow range. With the current design of combustion chambers, this is very difficult to accomplish, since the metallic combustor liners are cooled on both sides. Reduction of the amount of cooling air to minimize the emissions would cause the metallic combuster liner to overheat.

The current approach is to make these new liners from ceramic matrix composites (CMCs) (Fig. 17). Higher efficiencies could be achieved through the use of damage-tolerant, oxidation- and temperature-resistant CMCs. Oxide-fiber-reinforced mullite-matrix composites are candidate materials with a strong potential for use in this application [52-54].

Contrary to the TMCs described above, fibers are not em-

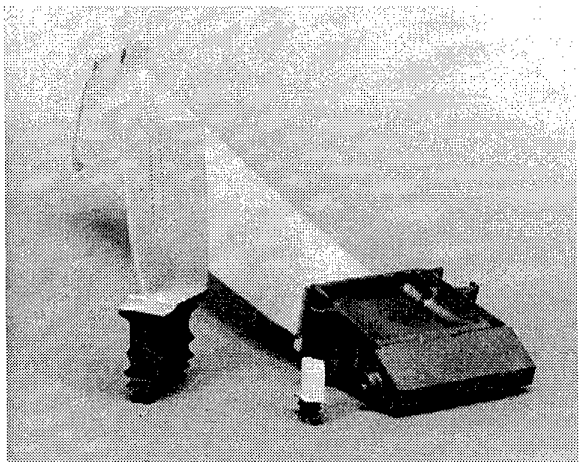

Fig. 16: EB-PVD TBCs on aircraft engine and stationary gas turbine blades.

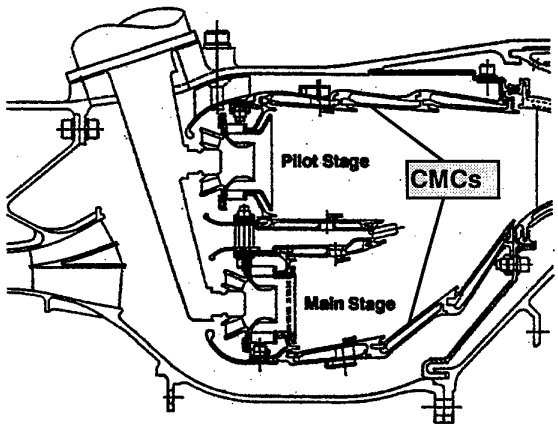

Fig. 17: Advanced combustor design with CMC shingles [51].

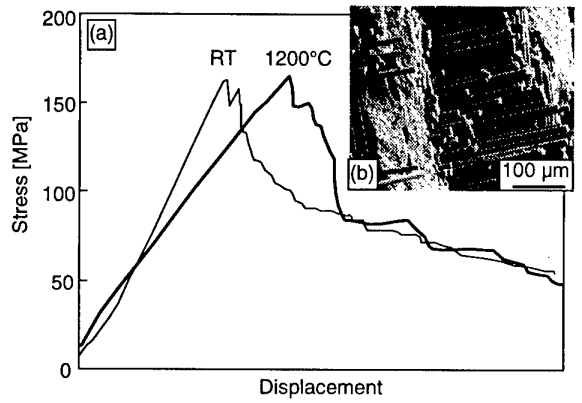

Fig. 18: Ceramic Matrix Composite (CMC): (a) strain/elongation plot of Nextel 720/mullite composite (b) fracture surface.

ployed to stiffen or strengthen the matrix material, but to increase primarily the damage tolerance behavior. Such a behavior becomes evident in Fig. 18, where the ceramic matrix composites exhibits pseudo-plasticity.

5. Conclusions

Advanced materials technologies are essential for future aircraft engine design.

- Near-α titanium alloys are the prime choice for elevated temperature applications up to 500°C in current aircraft engines.
- Titanium aluminides are at the edge for commercial applications and will further expand the range of application of light-weight high temperature components made of titanium base materials.
- Titanium matrix composites (TMCs) represent an enabling technology to realize new design approaches of future aircraft engine compressors.
- For thermally highly loaded rotating parts as high pressure turbine blades EB-PVD thermal barrier coatings (TBCs) exhibits the highest potential to increase turbine efficiency.
- To meet future emission requirements with high-pressure ratio engines ceramic matrix composites (CMC) shingles are a necessary prerequisite for newly designed combustion chambers.

Acknowledgments

The authors highly acknowledge valuable discussions with their colleagues H. Assler, H.J. Dudek, K. Fritscher, C. Leyens, H. Schneider, U. Schulz, and K. Weber.

References

1. J. Hertel, M. Albers: *The Impact of Engine and Aircraft Design Interrelations on DOC and its Application to Engine Design Optimization*, MTU FOCUS, 1, 1 (1995) 10-16.
2. J.C. Williams: *The Development of Advanced Gas Turbines: the Technical and Economic Environment*, Proc. Materials for Advanced Power Engineering 1994, ed. D. Coutsouradis, et al., Kluwer Academic Publishers (1994) (1994) 1831-1846.
3. P.-J. Winkler, M.A. Däubler, M. Peters: *Applications of Ti Alloys in the European Aerospace Industry*, Proc. Titanium '92: Science and Technology, ed. F.H. Frocs, I.L. Caplan, TMS, Warrendale, PA, USA (1992) 2877-2890.
4. S.R. Seagle, G.S. Hall, H.B. Bomberger: *High Temperature properties of Ti-6Al-2Sn-4Zrt-2Mo-0.09Si*, Metals Engg. Quartely, February, (1975) 48-54.
5. P.J. Bania: *Ti-1100: A New High Temperature Titanium Alloy*, Proc. Sixth World Conference on Titanium, ed. P. Lacombe, R. Tricot, G. Beranger, les editions de physique (1988) 825-830.
6. D.F. Neal: *Optimisation of Creep and Fatigue Resistance in High Temperature Ti Alloys IMI 829 and IMI 834*, Proc. Titanium: Sciene and Technology, ed. G. Lütjering, U. Zwicker, W. Bunk, DGM, Frankfurt, 1985 (1984) 2419-2424.
7. J. Kumpfert, D. Weinem, M. Peters, W.A. Kaysser: *Processing Window and Mechanical Behavior for Fine Grained Beat-Structure of the Near-Alpha-Titanium Alloy TIMETAL 1100*, Mater. Sci. Eng. A, (1998) in press.
8. M. Peters, Y.T. Lee, K.-J. Grundhoff, H. Schurmann, G. Welsch: *Influence of Processing on Microstructure and Mechanical Properties of Ti-1100 and IMI-834*, Proc. Microstructure/Property Relationships in Titanium Aluminides and Alloys, ed. Y.-W. Kim, R.R. Boyer, TMS, Warrendale, PA, USA (1991) (1990) 153-158.
9. M.A. Däubler, D. Helm: *Applications of IMI 834 in Aeroengines- A Collaborative IMI/MTU Programme*, Proc. Titanium 1990 - Products and Applications, ed. TDA, (1990)
10. C. Leyens, M. Peters, D. Weinem, W.A. Kaysser: *Influence of Long-Term Annealing on Tensile Properties and Fracture of Near-α Titanium Alloy Ti-6Al-2.75Sn-4Zr-0.4Mo-0.45Si*, Metall. Trans. A, 27A, (1996) 1709-1717.
11. C. Leyens, M. Peters, W.A. Kaysser: *Intermetallic Ti-Al Coatings for Protection of Titanium Alloys - Oxidation and Mechanical Behavior*, Proc. International Conference on Metallurgical Coatings and Thin Films, ed. (1997) in press.
12. K.v. Gersdorf, K. Grasmann, H. Schubert: *Flugmotoren und Strahltriebwerke*, Bernard & Graefe Verlag Bonn, Germany (1995) 416.
13. J.C. Williams: *Intermetallics for Structural Applications: Potential, Reality and the Road Ahead*, Proc. ISSI - Structural Intermetallics 1997, ed. M.V. Nathal, et al., TMS, Warrendale, PA (1997) 3-8.
14. G.H. Meier, D. Appalonia: *Oxidation of Ti-Base Alloys*, Proc. Oxidation of High-Temperature Intermetallics, ed. T. Grobstein, J. Doychak, TMS, Warrendale, PA, USA (1988) (1988) 185-193.
15. Y. Shida, H. Anada: *The Effect of Various Ternary Additives on the Oxidation Behavior of TiAl in High Temperature Air*, Ox.id. Met., 45, (1996) 197-219.
16. J. Kumpfert, C. Leyens: *Microstructure Evolution, Phase Transformations and Oxidation of an Orthorhombic Titanium Aluminide Alloy*, Proc. International Symposium on Structural Intermetallics - ISSI '97, ed. M.V. Nathal, et al., TMS, Warrendale, PA (1997) 895-904.
17. J. Kumpfert, M. Peters: *Gefüge, Textur und mechanische Eigenschaften einer Ti_3Al-Basislegierung*, Proc.

Symposium 7 - Materialwissenschaftliche Grundlagen, ed. F. Aldinger, H. Mugrabi, DGM, Frankfurt, Germany (1996) 423-428.

18. C.H. Ward, J.C. Williams, A.W. Thompson: *Dynamic Environmental Embrittlement of an α_2 Titanium Aluminide*, Scripta Metall., 28, (1993) 1017-1021.
19. Y.-W. Kim, D.M. Dimiduk: *Designing Gamma TiAl Alloys: Fundamentals, Strategy and Production*, Proc. ISSI - Structural Intermetallics 1997, ed. M.V. Nathal, et al., TMS, Warrendale, PA (1997) 531-544.
20. J. Kumpfert, C.H. Ward, M. Peters, W.A. Kaysser: *Thermomechanical Processing, Phase Transformations and Mechanical Properties of Ti-25Al-10Nb-3V-1Mo*, Proc. Synthesis/Processing of Lightweight Metallic Materials, ed. F.H. Froes, C. Suryanarayana, C.M. Ward-Close, TMS, Warrendale, PA, USA (1995) (1995) 85-96.
21. C.M. Austin, T.J. Kelly: *Progress in Implementation of Cast Gamma Titanium Aluminide*, Proc. Gamma Titanium Aluminides, ed. Y.-W. Kim, R. Wagner, M. Yamaguchi, TMS, Warrendale, PA, USA (1995) 21-32.
22. P.K. Wright: *Structural Intermetallics*, Proc. Structural Intermetallics, ed. R. Darolia, et al., TMS, Warrendale, PA, USA (1993) 885-893.
23. C.M. Austin, T.J. Kelly, K.G. McAllister, J.C. Chesnut: *Aircraft Engine Applications for Gamm Titanium Aluminide*, Proc. ISSI - Structural Intermetallics 1997, ed. M.V. Nathal, et al., TMS, Warrendale, PA (1997) 413-425.
24. R. Leucht, H.J. Dudek, K. Weber: *Additional ductile coatings for processing SiC-fibre Reinforced Gamma-TiAl Alloys*, J. Mater. Sci. Lett., 15, (1996) 1315-1318.
25. H.J. Dudek, R. Leucht, G. Ziegler: *Auger Electron Spectroscopy of the Interface of SiC Fiber Reinforced Titanium Alloys*, Proc. Titanium - Science and Technology, ed. G. Lütjering, U. Zwicker, W. Bunk, DGM, Frankfurt (1984) 1773-1780.
26. R. Leucht, K. Weber, H.J. Dudek, W.A. Kaysser: *Processing of SiC-Fibre Reinforced Titanium Parts*, Proc. ECCM-7, ed. Woodhead Publishing Ltd, Cambridge, UK (1996) 361-366.
27. J. Kumpfert, R. Leucht, K. Weber, H.J. Dudek: *Faserbruch bei Langfaserverstärkung in TMC-Ringen, DLR, Institute of Materials Research*, IB 334-95/01 (1995).
28. H. Assler, M. Gräber, P.W.M. Peters: *Modelling of Temperature Dependent Failure Process in Fibre Reinforced Titanium Alloy*, Proc. Firts International Conference on Damage and Failure of Interfaces - DFI-1, ed. Institute of Mechanics, Univ. of Technology, Vienna, Austria (1997) in print.
29. D.B. Miracle, M.G. Mendiratta: *Intermetallic Composites*. in: Intermetallic Compounds, J.H. Westbrook, R.L. Fleischer (eds.), John Wiley & Sons (1994) 287-300.
30. R. John, M. Khobaib, P.R. Smith: *Prediction of Creep-Rupture Life of Unidirectional Titanium Matrix Composites Subjected to Transverse Loading*, Metall. Trans. A, 27A, (1996) 3074-3080.
31. J. Kumpfert, H.J. Dudek, W.A. Kaysser: *Entwicklung neuer Titanmatrixverbundwerkstoffe für hohe Anwendungstemperaturen*, Proc. Hauptversammlung 1997 der DGM e.V., ed. (1997)
32. B. Maruyama, D.B. Gundel: *Spatially varied Interfaces*, Scripta Metall., 35, 3 (1996) 391-395.
33. S. Krishnamurthy, P.R. Smith, D.B. Miracle: *Modification of transverse creep behavior of an othorhombic titanium aluminide based Ti-22Al-23Nb/SiC$_f$ composite using heat treatment*, Mater. Sci. Eng. A, (1997) in print.
34. D.B. Miracle, P.R. Smith, J.A. Graves: *A Review of the Status and Developmental Issues for Continuously-Reinforced Ti-Aluminide Composites for Structural Applications*, Proc. Intermetallic Matrix Composites II, ed. J.A. Graves, R.R. Bowman, J.J. Lewandoswki, MRS, Pittsburgh, PA, USA (1994) (1994) 133-142.
35. S. Mall, T. Fecke, M.A. Foringer: *Introduction*. in: Titanium matrix Composites, S. Mall, T. Nicholas (eds.), Technomiy Publishing Company Inc., PA, USA (1998) 1-22.
36. H. Assler, J. Hemptenmacher, K.-H. Trautmann: *Iosthermal Low Cycle Fatigue of Titanium Matrix Composites*, Proc. Fourth Int. Conf. on Low Cycle Fatigue and Elasto-Plastic Behavior of Materials, ed. DVM, Berlin, Germany (1998) to be published.
37. J.M. Larsen, S.M. Russ, J.W. Jones: *An Evaluation of Fiber-Reinforced Titanium Matrix Composites for Advanced High-Temperature Aerospace Applications*, Metall. Trans. A, 26A, (1995) 3211-3223.
38. T.P. Gabb, J. Gayda, B.A. Lerch, G.R. Halford: *The Effect of Matrix Mechnical Properties on $[0]_8$ Unidircational SIC/Ti Composite Fatigue Resistance*, Scripta Metall., 25, (1991) 2879-2884.
39. S.A. Singerman, J.J. Jackson: *Titanium Metal Matrix Composites for Aerospace Applications*, Proc. Superalloys 1996, ed. R.D. Kissinger, et al., TMS, Warrendale, PA (1996) 579-586.
40. M. Lavitt: *First TMC Aircraft Part to Help Power F-22*, Aviation Week & Space Technology (1997) 74-75.
41. J. Frischbier, S. Sikorsky: *All-Composite Fan Blade for Advanced Ducted Engines*, MTU Focus, 2 (1992) 22-29.
42. S.W. Kandebo: *U.S., Europe Race for MMC Payoff, Aviation Week & Space Technology*, 8 (1994) 20-22
43. G.F. Harrison: Proc. European Propulsion Forum, ed. The Royal Aeronautical Society, London, UK (1993) 3.1-3.16.
44. K. Fritscher, M. Peters, H.J. Rätzer-Scheibe, U. Schulz: *Superalloys and Coatings*. in: Advance Aerospace Materials, H. Buhl (eds.), Springer, Berlin/Tokyo/Hong Kong (1992) 84-107.
45. J.T. DeMasi-Marcin, D.K. Gupta: *Protective Coating in the Gas Turbine Engine*, Surface and Coating Technology, 68/69 (1994) 1-9.
46. M. Peters, K. Fritscher, G. Staniek, W.A. Kaysser, U. Schulz: *Design and Properties of Thermal Barrier Coatings for Advanced Turbine Engines*, Materialwissenschaft und Werkstofftechnik, 28, (1997) 357-362.
47. S.M. Meier, D.M. Nissley, K.D. Sheffler, T.A. Cruse: *Thermal Barrier Coating Life Prediction Model Development*, ASME J. Eng. Gas Turbine Power, 114, (1992) 258-263.
48. B.A. Movchan: *EB-PVD Technology in the Gas Turbine Industry: Present and Future*, JOM, 48, 11/1996 40-45.
49. M. Peters, G. Staniek, K. Fritscher, U. Schulz, W.A. Kaysser: *Effective Thermal Barrier Caotings for Modern Turbine Engine Design*, Proc. 1997 European Propulsion Forum, ed. (1997) 179-188.
50. U. Schulz, K. Fritscher, C. Leyens, M. Peters, W.A. Kaysser: *Thermocyclic Behavior of Differently Stabi-*

lized and Structured EB-PVD Thermal Barrier Coatings, JOM-e, 49, 10/1997 (1997) 1-10.

51. I.E. Treager: *Aircraft Gas Turbine Engine Technology*, Glencoe, New York, NY, USA (1996) 187-197.
52. M. Schmücker, H. Schneider, K.K. Chawla, Z.R. Xu, J.S. Ha: *Thermal Degredation of Fiber Coatings in Mullite-Fiber-Reinforced Mullite Composites*, J. Amer. Ceram. Soc., 80, (1997) 97.
53. O. Reese, B. Sruhan, B. Kanka, H. Schneider: *Fabrication of Continuous Fiber-Reinforced Ceramics with a Nanosized Mullite Precursor*, Proc. High-Temperature Ceramic Matrix Composites II, ed. Amer. Ceram. Soc. (1995) 175-180.
54. J. Göring, H. Schneider: *Creep and Subcritical Crack Growth of Nextel 720 Alumino Silicate Fibers As Received and After Heat Treatment at 1300(degree)C*, Cermic Engeneering & Science Proceedings, 18, 3 (1997) 95-102.

Cycle-match engine models used in functional engine design - an overview

Marcus. S. Horobin
Rolls-Royce Mael
Performance Systems (GP1-11)
P.O. Box 3
Filton, Bristol BS34 7QE, UK

Abstract

The wider use of iterative thermodynamic (cycle-match) engine models across the functional design process offers many technical and organisational benefits which contribute to reduced risk in engine development programmes. The use of low and high order engine models for control-system design and validation is used to illustrate some of these advantages. The principles of the iterative technique are discussed with reference to the extra capabilities required of models used for control-system design and validation. Some related issues e.g. increased model capability, complexity and user-acceptability are also discussed.

1. Introduction

1.1 Background

In recent years, there has been a move in Rolls-Royce to work towards a Common Model approach in functional engine design and validation. This is primarily aimed at rationalising the computer models and providing interfaces between engine models and engine sub-systems e.g. control-system, secondary air-system. Constituent parts of the Whole Engine Model (WEM) may be programmed in various languages; interfaces are facilitated by the use of proprietary development environments (e.g. MATRIXx). This paper deals with the specific issues of using engine models for controller definition and validation.

1.2 Cycle-match models

Cycle-match models have been used for many years for engine performance modelling. They have gained universal acceptability among airframers and can be supplied to represent varying levels of thermodynamic detail - in both steady-state and dynamic terms. Usually these models are confined to the normal operating range of the engine, although overspeed, windmill and surge/stall modelling is sometimes included. Cycle match models employ iterative methods of solution which give certain advantages in terms of the physical processes that can be modelled, and in the approach taken in numerical integration. These points will be discussed later.

Cycle-match models are often used in a non time-dependent mode where the model produces a single solution representing steady operation of the engine - termed steady-state. This enables large sets of performance data to be generated without the overhead of transitions and settling time. This mode of operation is especially useful in generating and refining control schedules. Cycle-match models allow the definition of a point to be specified in terms of any parameter. For example, the model can be run to a prescribed level of thrust or stator outlet temperature (SOT). Clearly, the definition of the engine operating point must be unique. e.g. consider a reheated engine with main fuel flow (WFE), reheat fuel flow (WFRH) and final nozzle area (A8) as control variables. A valid operating point definition could be SOT+ fan working-line + thrust. The unique values of WFE, WFRH and A8, along with all other engine parameters (speed, pressures, temperatures, flows etc.) would consequently be generated. Specifying certain combinations of parameters (e.g. total FAR, fan working line + thrust) can generate a range of solutions. Beware, some programs might generate just one solution from a range of potential solutions. There is, of course, a difference between ill-considered program input (such as the example given above) and the true thermodynamic multiple solution e.g. specifying a jet-pipe temperature at low speed.

Running the model to a specified level of model output is particularly useful for complex engine cycles where a datum running line can be defined in terms of the thermodynamic constraints within the engine cycle. e.g. fan operating point, reheat entry Mach number, mixer pressure balance etc..

Transient simulation (i.e. over a time-base) is achieved by numerical integration of selected state variables - i.e. those engine parameters expressed in terms of their time-differential. Model bandwidth (the frequency range over which the model is dynamically representative) can vary between ~1Hz for models with only shaft dynamics, to 30-50Hz with volume dynamics included, and so integration timesteps can vary between 50ms for the lower order models to 1ms for high order models. Although numerical stability can dictate integration step time, iterative techniques allow the use of highly stable implicit (backward-looking), integration methods thus allowing model output frequency requirements to dictate the step length. A general rule is to select a step length of around 1/20 of the wavelength of the highest frequency event present. The amount of dynamic detail required in a model depends upon its application. For general engine operability and preliminary control viability studies, shaft dynamics may suffice; for more detailed studies greater dynamic fidelity may be required.

Cycle-match models allow the volume dynamics to be optional. For low frequency models, iteration is used to match the cycle at the speed dictated by the shaft dynamics - thus assuming instantaneous gas

Paper presented at the RTO AVT Symposium on "Design Principles and Methods for Aircraft Gas Turbine Engines", held in Toulouse, France, 11-15 May 1998, and published in RTO MP-8.

dynamics. Gas dynamics can be represented at various levels by consideration of conservation of flow, energy and momentum in defined volumes in the engine (e.g. compressor, duct, turbine etc.). Each level of dynamics modelling can be programmed separately for each defined volume, and those dynamic equations not selected to be solved are approximated as instantaneous events by iteration.

A note on terminology: 'Transient' is often used to describe models in the 5Hz range. 'Dynamic' or 'HIFEM' (High Frequency Engine Model) are terms used to describe models capable of 30-50Hz. Cycle match models are usually confined to modelling in 1D, (N.B. '0D' is a term sometimes used to describe models without the solution of the momentum equation which requires volume length to be specified). Events above ~50Hz require 2D or 3D modelling methods, although >1D representation may be employed for lower frequencies as required for accurate representation of steady-state component behaviour.

In the same way as the model running in steady-state mode, a model may be run to a prescribed profile of a control variable e.g. fuel flow vs. time. Again, iteration allows the model to run to a required profile of an engine output (e.g. thrust, shaft speed etc.). The required profiles of control input to achieve this output are therefore generated as a consequence.

1.3 Other model types

There are other types of engine thermodynamic modelling methods. A non-iterative method which has been sucessfully used for real-time (rt) and non-real-time (nrt) purposes relies on the solution of gas dynamics equations to achieve cycle matching. As explicit (forward-looking) integration methods must be used, integration step times are small to achieve acceptable numerical stability. However, the step time can result in being smaller than the model output frequency requirement commensurate with the level of dynamic representation. Non-iterative techniques only allow model running to control inputs, and so their use in Performance work is very limited. Solution is confined to time-based calculations with the exception of linearisation where time-based integration is not performed. With this type of model, steady-state mode (single point solution) is not feasible. (Linearisation is process of manipulation of a dynamic model to produce a transfer-function approximation - this will described in a later section). Furthermore, modelling of some physical processes are not possible without iteration e.g. certain pressure loss models, three stream mixing within fixed geometry. In order to get around problems such as these, known values of parameters from the previous time-step are used. In order to achieve accuracy and stability, timestep length may be driven down further. The necessity to solve the gas dynamic equations for cycle continuity may be an over-complication if, say, only 5Hz capability is required - especially if small integration steps are required for numerical stability. Whereas it is sometimes argued that a lower level of steady-state thermodynamic detail is required for some work, it is nevertheless a shortcoming of the method if some modelling capability is denied.

1.4 Functional design activities

'Functional Engineering' encompasses the traditional Performance and Controls activities. In the past there have been clear boundaries between the two areas but with engine cycles becoming more involved, and with there being many potential ways of defining the operating point of an engine, closer working relationships are required. The figure below shows the spectrum of activities which can be grouped under 'Functional Engineering'.

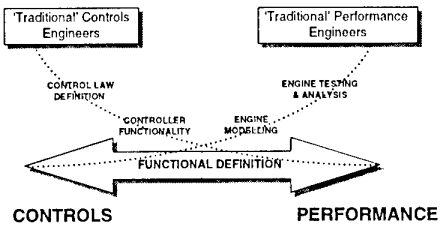

It is the 'middle-ground' activity from which a functional definition emerges. That is, a detailed understanding of the engine cycle and potential concepts of control. Modelling requirements in this area of work is centred around steady-state and low-order dynamic representation. High-order dynamic representation may be required for detailed control law design, detailed operability studies, and control-system validation where real-time modelling capability is required for hardware-in-the-loop (HITL) testing.

2. Requirements for the use of engine models

2.1 General

Consider the 'traditional' roles of the Performance Engineer and Controls Engineer, in terms of the engine functional definition. The Performance Engineer determines the appropriate way to control the engine to meet certain performance requirements within thermodynamic constraints. This will cover both transient and steady-state aspects of engine operation, and will make use of the type of model facilities described above. The Controls Engineer will determine suitable control laws to allow the engine to operate according to the constraints (e.g. control loops) identified. There is, of course, a considerable 'grey area' between the two, the extent of which increases with engine complexity. It is sometimes difficult to distinguish

between 'Performance Requirements for Engine Control' and 'Feasible Ways of Controlling Gas-Turbine Engines'. It is therefore important to remove as many of the working barriers between the two areas so that the functional definition process becomes co-operative, thus facilitating an iterative engineering approach. The final solution may be a compromise of the ideal as perceived by each area.

Each area, at present, uses different computing environments and tools owing to the differing engineering tasks. 'Pure' Performance work is generally based around development of the engine understanding through synthesis and analysis of engine test data. Where a control-system model is required to support this work, it is usually of a known, bespoke standard. In the past, control-system models, which have been required to run in the Performance computing environment, have been coded independently of any similar model existing in the Controls area. This has clear disadvantages in operational terms. Flexible performance data interfaces (including engine test database) and continuous engine model refinement are attributes of the Performance process. The 'Pure' Controls work is largely based on a given standard of engine. Specialist control-system development environments and tools are used to develop the detailed control-system definition. Standard controller design and analysis methods (including limited engine model manipulation) are attributes of the Controls process.

The Functional Engineering 'middle-ground' must encompass both processes and also be consistent with the pure Controls and Performance 'wings'. The Common Model Initiative (CMI) seeks to bring this about.

2.2 *The Common Model Initiative*

There are two fundamental elements:

- provision of a single engine program, used across Functional Engineering.
- provision of a single control-system model used across Functional Engineering

It is convenient (but not technically fundamental) to break down the first element into two parts:

- provision of model fully compatible with all Performance and Controls design and analysis tools and methods.
- provision of engine model real-time capability -- specifically for system integration testing (HITL) - but applicable to other applications e.g. pilot-in-the-loop (PITL)

A prime issue arising is the release and version control of the models. Engine models must be released to the Controls area; controller models must be released to the Performance area. A central repository containing all models may be the ideal, but network constraints may force the use of copies in each area; this needs careful handling.

A further extension of the principle would be to use actual Electronic Engine Controller (EEC) code with the performance model prior to HITL validiation testing.

The main challenges arise from the interface of different modelling tools. CORBA (Common Object-Requested Brokerage Architecture) methodology may be appropriate .

2.2.1 *Common Engine Model*

The figure below shows the range of applications and the suitability of iterative and non-iterative models to those tasks.

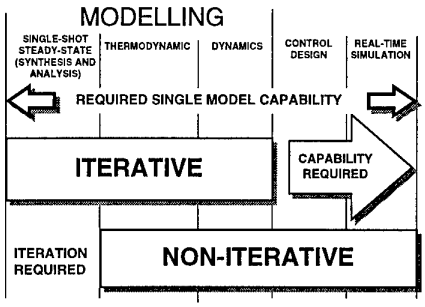

It is clear that the only methodology which has the potential to meet all requirements is the iterative (cycle-match) model. The steady-state performance work dictates an iterative approach. Iteration is *potentially* hazardous in real-time applications because of the variable solution time per timestep, however there are ways around the problem as discussed below. The capability to model physical processes in greater detail should enhance work in the controls and operability study areas.

Consider the specific requirements for an engine model to be used for control-law design:

1. compatibility with tools & environment
2. capability to generate linear models
3. adequate dynamic representation
4. adequately modelled control inputs
5. adequately modelled sensor stations
6. sufficient range of operation
7. acceptable user interface

It is currently an industry standard that cycle-match models are programmed in FORTRAN (although the emphasis is shifting towards C). As such, an engine model may be imported into proprietary development environments in the form of a user code block. Custom interface routines may be required. The interface routines should allow easy routing of additional signals if required.

Development environments such as MATLAB or MATRIXx have suites of tools (toolboxes) with which the model must be compatible. It is common practice for all dynamic elements in a system to be numerically integrated by the host environment. Several integration algorithms are available; the most appropriate for the particular dynamics present, can be chosen.

The generally accepted form of a dynamic system model is:

$$\left[y, \frac{dx}{dt}\right]_t = f[u, x]_t$$

where:

y	outputs	e.g.	thrust
dx/dt	state-derivative		shaft accel.
u	inputs		fuel flow
x	states		shaft speed

Knowing the states and their derivatives at time=t, their values for t+Δt can be determined by explicit integration.

e.g. Euler's method

$$x_{(t+\Delta t)} = x_t + \left.\frac{dx}{dt}\right|_t \cdot \Delta t$$

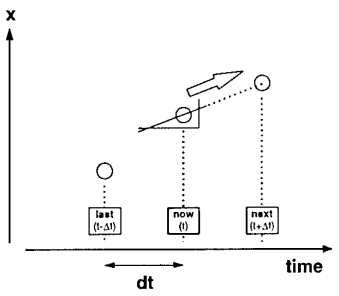

A first-order, explicit method such as Euler's would require very small timesteps (<0.1ms) to ensure stability when solving gas dynamic equations, although it would be adequate for shaft acceleration terms. Non-iterative methods which include gas dynamics modelling use higher order algorithms (e.g. Runge-Kutta, 4th-order) which ensure numerical stability at larger step lengths. Remember that the step length should not, in any case, be any larger than the step required to adequately represent the fastest dynamic mode present.

Hitherto, iterative engine models have not been considered in this form. It has been usual to provide an engine routine that performs its own numerical integration internally thus operating as a stand-alone package. There are merits and demerits to this approach. In the external/explicit integration form (as described above), state-variables are directly accessible as a program input and their derivatives as program output. It is in this form that a model can be linearised. This form is also compatible with the current practice of starting a simulation from an initial states vector [xo]. Such a vector would have been stored at the end of a previous run by the host environment. A cycle-match model set up in this external/explicit way is broadly equivalent in working terms to the non-iterative types. However, this should not be seen as the target, as there are potential benefits to be cashed from further exploitation of the iterative method. For example, initialisation at a steady-state condition can be achieved by running a cycle match model in steady-state mode, at any prescribed flight condition.

In the internal/implicit integration form, states are not accessible, and the direct calculation of their derivatives (from the dynamic equation) is not fundamental to the simulation process. In this form, the model is not linearisable, however there are benefits in terms of numerical stability and calculation rigour. An iterative model can be set up in either form, by modifications to its iterative matching scheme (*q.v*), thus giving the benefits/features of each approach. i.e. for full-range simulation, use implicit/internal; for linearisation use explicit/external (in this case integration is not performed). So, in addition to the steady-state mode, a dynamic simulation mode and linearisation modes are also required.

The implicit form of Euler's method is:

$$x_{(t+\Delta t)} = x_t + \left.\frac{dx}{dt}\right|_{t+\Delta t} \cdot \Delta t$$

... which can be re-written in the more useful form:

$$x_t = x_{(t-\Delta t)} + \left.\frac{dx}{dt}\right|_t \cdot \Delta t$$

At any particular timestep, the states at (t-Δt) are known and Euler's equation can be solved if the current state and state-derivative can be found. If the state-variable is made an iteration variable, then state-derivative can be obtained by looking backwards (rearranging implicit Euler equation):

$$\left.\frac{dx}{dt}\right|_t = \frac{x_t - x_{(t-\Delta t)}}{\Delta t}$$

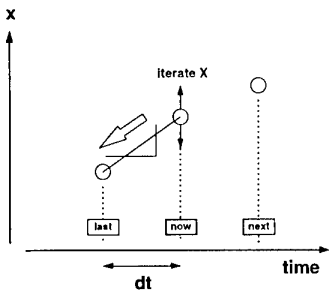

Another expression for the state-derivative is, of course, found in the relevant dynamic equation. Thus, a solution is sought for a particular value of state-variable which gives equality of the two expressions for state-derivative. On convergence, Euler's equation has been satisfied, and therefore integration implicitly performed. This idea will be developed in later sections.

In the early stages of a project, it is common to find that some control variables are not modelled as independent program input variables. For example, a variable mixer may be present in the engine concept, but early Performance studies do not need a geometry-to-thermodynamic-effect calculation. This is because the model can be matched by prescribing what such a feature has to achieve, rather than predicting the effect of a specified geometry. Clearly, in the case of control-system design, a geometry model is required, although some simplification may be acceptable at the preliminary stage.

Modelling of sensor stations should not present any problems as all common total gas conditions are calculated at all major interfaces through the engine. Static gas properties are not always modelled by default, however they can be easily provided.

The range of operation of engine models depends on the availability of component characteristic (chic) data. There are significant challenges in reliably modelling (in aerodynamic terms) sub-idle conditions, post compressor stall behaviour and overspeed conditions. For controls work, simplified dynamic starting and overspeed models may suffice, although it is in these particular areas that risk-reduction through smart control is being pursued, and therefore more rigorous models for engines operating in these regimes are becoming necessary.

2.2.2 *Common Control-system Model*

Integrated engine+controller models are seldom required in the extreme Performance activities, however for operability studies e.g. compressor stability assessment, a control-system model is essential. However, the emphasis is placed on the understanding engine behaviour in response to control-system action. Data interface requirements therefore differ - the Performance engineer wants full visibility of internal engine parameters and engine analysis tools. It is also the case that other sub-systems (e.g. secondary air-system, air and oil systems) should be represented in the best possible way. Being able to accurately predict to a detailed level the heat-to-oil/fuel and heat-to-surroundings using an integrated model would be useful in the assessment of stealth characteristics for example.

Clearly, if a controller model has been developed in a Controls development environment, it is desirable that this should also run in the Performance environment. Models constructed using Graphical User Interfaces (GUI) can be represented in pure code forms using proprietary code-writing tools; this facility offers potential for inter-environment use. C and ADA are common languages in this respect.

There are several issues that arise:

- interface of dissimilar languages (e.g. FORTRAN and C)
- ideally, the control-system and engine model should be separately configurable items
- the integrated model in this environment should be technically equivalent (in simulation terms) to the alternative scenario of the engine-model imported as a subservient element in the Controls environment (as previously discussed).
- steady-state initialisation

In the case of FORTRAN and C, there is no technological challenge in interfacing, more a case of careful handling of the different conventions used in the two languages. Naturally, the platform must support both languages.

There is an operational overhead if control-system and engine models have to be compiled into a single executable. The constituent parts of the integrated engine model are developed in parallel, and an the ability to maintain a 'mix-and-match' appoach (such as enjoyed in the Controls environment) is desirable.

Performance work often involves the prediction of nominal steady-state performance under the action of the control-system at, say, a particular power demand or rating (e.g. as expressed by a certain pilot-lever angle). Ideally the full, integrated model should be used to generate these points, however, the computing task can become a burden. Whereas the engine model can initialise at any condition by iteration (i.e. without a time-base), the control-system cannot. The steady condition must therefore be the result of a settled transient. Furthermore, if a matrix of flight points is required, the model must be 'flown' to each new point and allowed to settle. There are ways of alleviating this overhead. The transients are not of interest, so some dynamic terms can be muted or modified to reduce settling time. A problem can arise if this measure is taken to extremes, as the whole-system stability may be compromised and therefore prevent a steady condition being achieved! An alternative approach is to use a subset of the controller: the ratings structure, to establish the level of performance in terms of the engine rating parameters. The engine model can be run to such parameters (with due regard to engine limit loops) and converge on a steady-state solution (either on the prescribed rating or on an overriding limit) without any settling period. The engine condition thus obtained should be identical (within iteration tolerance) to that obtained by transient settling. However, there are some situations when this approach is not feasible -

even with iteration; the time-settling technique is sometimes essential e.g. engines with switching bleeds. The full model is, of course, the best means of determining the steady-state performance, if such a condition exists.

From the user's point of view, the two methods can be made to 'look' similar. The settling transient can be hidden and discarded after steady-state has been achieved.

3. Cycle-match representation of gas-turbine engines

3.1 component representation

The representation of steady-state component performance and interaction is well documented and is not covered in any detail herein.

3.2 representation of dynamics

The time-dependent behaviour of an engine is governed by three main groups of dynamics:

- Heat soakage (blade and carcass temperatures)
- Shaft dynamics
- Gas dynamics

The dynamics have effects in differing parts of the frequency spectrum. Shaft and heat-soakage dynamics are dominant in the 0-5Hz range, with some gas dynamics (mass and momentum) terms becoming significant in the 5-15Hz range. Energy dynamics are significant at higher frequencies only.

3.2.1 shaft dynamics

On most types of engine, shaft inertia is the dominant term in the acceleration characteristics. It is the shaft inertia which is responsible for the excursion of (high-pressure) compressor working line during acceleration and deceleration.

dynamic equation:

$$\frac{dN}{dt} = \frac{XP}{J.N}$$

where:

XP = excess power (net power for acceleration) i.e. turbine power - (compressor power + losses)

N = shaft rotational speed

J = polar moment of inertia

3.2.2 heat-soakage

An engine is a very large heat sink. Heat released from combustion contributes to a warming of engine parts as well as useful power to the turbine. (As much as 30% of fuel flow during an idle-max transient may be accounted for through consideration of heat soakage). There is therefore an effect on engine transient response, and compressor running line excursion for a given fuel input profile. Heat soakage dynamics have very little effect on the fundamental controllability of an engine, but may lead to significant changes in thrust (perhaps as much as 5%) over several minutes at a stabilised level of a controlled parameter such as LP shaft speed (NL).

The passage of heat directly affects tip clearances (esp. turbines) and thus component efficiency and compressor stall line. In particular reslam manoeuvres can be troublesome due to the large clearances (commensurate with the higher power level) which give significantly reduced surge-margins for the ensuing acceleration.

The passage of heat to oil (and therefore changes in viscosity) may affect starting performance where bearing drag may be significant. The 'losses' in the shaft dynamic equation can include such terms

3.2.3 gas dynamics

The 1D behaviour of gases in a defined volume can be modelled at various levels of detail by considering the continuity of mass, energy and momentum associated with the gas stream contained in that volume.

The density of the gas flowing through a volume or component is a time-varying property of that volume, i.e. there is a mass of gas which is being stored in the component. The mass flow in and mass flow out of the component must therefore differ at any instant during a transient. As gas stream conditions approach steady state, the difference between inlet and outlet flow becomes zero (accounting for any quasi-steady change in flow such as bleed taken from a compressor). So the outlet flow at an instant must be the inlet flow, minus the mass flow known to be being stored at the same instant. Similarly, momentum and energy must be conserved. The values of these parameters at component outlet, must be the inlet values minus the amount being stored at that instant.

Cycle match models allow the gas dynamics effects to be implemented as a 'trim' on the quasi-steady performance calculations. The 'actuator disc' approach is used to 'concentrate' the dynamics at a plane at the component exit (after the quasi-steady calculation)

Consideration of gas dynamics is essential for representative modelling of high frequency events such as compressor stall and fuel spiking. In both of these cases, the shaft and heat soakage dynamics are

largely irrelevant. Also engines with variable geometry may be capable of modulating power without shaft speed changes; the means of controlling the operating point of such engines may be heavily influenced by the gas dynamics present (rather than the conventional case where power level is largely dependent on shaft speed control). Full range engine transients have fundamentally low-frequency content (apart from the inital overfuelling) although there may be higher frequency dynamics present arising from the fuel system. Large volumes in an engine such as some industrial types, may require the consideration of gas dynamics to correctly represent manoeuvres in the lower frequency range.

The differential equations governing the 1D gas dynamics are given below. The Δ terms refer to (inlet - outlet).

mass

$$\frac{d\bar{\rho}}{dt} = \frac{\Delta W}{Volume}$$

momentum

$$\frac{d\overline{W}}{dt} = \frac{\Delta(pA + Wv)}{Length}$$

energy : enthalpy form

$$\frac{d}{dt}(\overline{\rho H - p}) = \frac{\Delta(W.H)}{Volume}$$

energy : entropy form

$$\frac{d}{dt}(\overline{\rho s}) = \frac{\Delta(W.s)}{Volume}$$

Some models may use simplified forms of these equations which assume low Mach number flow. A typical equation set is:

mass

$$\frac{dP}{dt} = R.T \times \frac{\Delta W}{Volume}$$

momentum

$$\frac{dW}{dt} = \frac{A \times \Delta P}{Length}$$

energy

$$\frac{dT}{dt} = \frac{\Delta(W.T).\gamma}{M} - \frac{T.\Delta W}{M}$$

$$\text{where } M = \frac{P.Volume}{R.T}$$

Heatsoak dynamics must be accounted for when considering the energy conservation equation.

The state variables in the equations above, refer to the average component properties although in some model implementations, the same equations are used in an 'actuator volume' sense. Rather than being applied to the average component properties, the gas dynamics are applied across a dummy volume at exit to the quasi-steady-state (qSS) process (the compressor in this example).

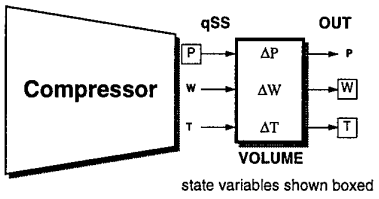

The position of the state variables (in this case P, W and T) relative to the volume are chosen to fit in with the model solution method.

3.2.4 other dynamic events

There may good reason to include other dynamic terms in an engine model in order to satisfactorily replicate engine behaviour, especially on analysis of gross transients such as fuel-spiking to map compressor stall line. Fuel ignition characteristics (often modelled as pure delays) can significantly affect control stability margins.

Having outlined the dynamics present in a gas turbine engine, we turn to the solution methods, which in turn will lead to an explanation of the method used in cycle-match models to linearise the dynamic terms.

3.3 outline of iterative solution method

Consider a simple gas-turbine engine model. The calculations can be broken into simple steps:

compressor
Pressure Ratio & Efficiency = f(N√T, W√T/P2)

combustion
T4 = f(T3, WFE, W4) pressure loss = f(W√T/P3)

turbine
W√T/P4 & Effy = f(ΔH/T, N√T4)

nozzle
entry W√T/P = constant

boundary conditions
WFE_req, P2, T2, PAMB, TAMB

A 3x3 multi-variable iterative scheme can be set up to generate steady-state performance given a value of fuel flow (WFE_req). Cycle match models may have very detailed matching schemes for steady-state synthesis - perhaps in in excess of 30x30. For steady-state test analysis, the matching scheme can be further extended to vary model assumptions (e.g. efficiencies) to match synthesised data to measured data.

calculation process:

- guess values of variables:
- compressor β (similar to outlet flow-function)
- fuel-air-ratio (FAR)
- compressor aerodynamic speed (N√T)

- perform compressor and can calcs.
- calculate W√T/P4
- equate compressor and turbine power - hence turbine ΔT
- read turbine chic for W√T/P4_chic and efficiency = f(N√T, ΔH/T)
- hence calc. turbine exit (nozzle entry) conditions
- calculate W√T/P5
- iterate to achieve constraints ('matching quantities') as below (within specified tolerance):

- WFE calculated = WFE_req
- W√T/P4 calculated = W√T/P4_turbine (from chic)
- W√T/P5 calculated = W√T/P5_nozzle

This 3x3 matching scheme is easily extended for a simulation with only shaft dynamics present. In this case, WFE_req is a function of time.

The extra variable is excess shaft power (XP); the extra matching quantity depends on which integration approach is being taken. (as discussed above).

The iterative/implicit approach requires the matching quantity to be:

$$\frac{N_{now} - N_{last}}{\Delta t} = \frac{XP}{J.N_{now}}$$

In the interests of iterative convergence, this is best rearranged with the XP power expressed in its consituent terms:

$$\frac{J.N_{now}}{\Delta t} + \frac{PW_c}{N_{now}} = \frac{J.N_{last}}{\Delta t} + \frac{PW_t}{N_{now}}$$

... where PW_c is the total power requirement (i.e. includes compressor power, losses and offtakes) and PW_t is the turbine power.

calculation process (implicit integration):
as for steady-state above but ...

- WFE_req_{now} input
- XP allowed to vary, hence turbine power known
- N√T is a variable, hence N_{now}
- iterate (at current timestep) until matched

The matching scheme can be extended further to include chosen dynamics for any component. For example, compressor gas dynamics can be included by adding 3 extra pairs of variables/matching-quantities as follows (low Mach no equations used for clarity) :

variables:
ΔP: 'stored' pressure in volume (cons. of mass)
ΔW: 'stored' flow in volume (cons. of momentum)
ΔT: 'stored' temperature in volume (cons. of energy)

matching quantities : (implicit integration)

conservation of mass

$$Volume.\frac{Pqss_{now}}{\Delta t.R.Tqss_{now}} + Wout_{now}$$

$$= Volume.\frac{Pqss_{last}}{\Delta t.R.Tqss_{now}} + Wqss_{now}$$

conservation of momentum

$$\text{Length}.\frac{\text{Wout}_{now}}{\Delta t} + \text{A}.\text{Pout}_{now} = \text{Length}.\frac{\text{Wout}_{last}}{\Delta t} + \text{A}.\text{Pqss}_{now}$$

conservation of energy

$$\frac{\text{M}.\text{Tout}_{now}}{\Delta t} + \gamma\text{out}_{now}.\text{Wout}_{now}.\text{Tout}_{now} + \text{Tout}_{now}.\text{Wqss}_{now} = \frac{\text{M}.\text{Tout}_{last}}{\Delta t} + \gamma\text{qss}_{now}.\text{Wqss}_{now}.\text{Tqss}_{now} + \text{Tout}_{now}.\text{Wout}_{now}$$

$$\text{where} \quad \text{M} = \frac{\text{Pqss}_{now}.\text{Volume}}{\text{R}.\text{Tqss}_{now}}$$

It has been said that the implicit approach gives a stable simulation by virtue of the backward-looking integration, but is not compatible with some Controls tasks owing to the lack of access to the state variables. The implicit/internal model has the interfaces shown below:

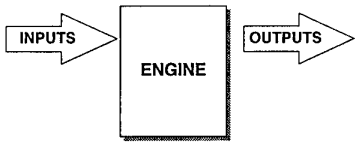

Linearisation of the dynamic terms is not possible with a matching scheme set up as above. For this, the explicit approach is required. In this case the iteration variables are the same, but the matching quantities are the state-variables themselves. Thus giving a model with the interfaces shown below:

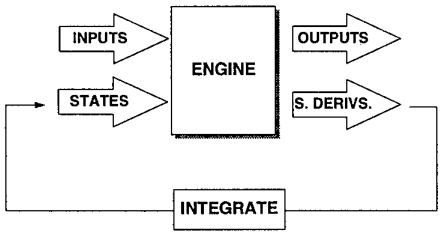

Consider the simple example with only shaft dynamics present. For the purposes of comparison, examine the calculation process for a simulation:

calculation process (explicit integration):
initial steady-state point as above.

- WFE_req_{now} input
- XP allowed to vary, hence turbine power known
- added matching quantity:

  N_{now} = N predicted from last step (forward integration)

- (the first timestep after the initial steady-state point, will match to initial N because XP on first case is zero)
- iterate (at current timestep) until match

Linearisation requires the model to be set up in this form, although integration is not performed.
The differences between the explicit and implicit simulation is shown below:

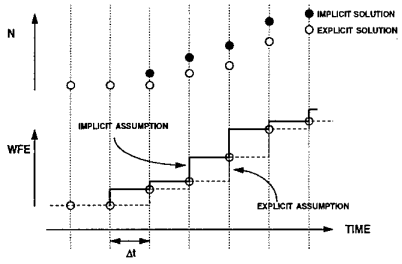

For a given fuel (WFE) input vs. time (lower axes), there is a slightly different response in state-variables (shaft speed is shown on upper axis). Both are approximations to reality, and with a small Δt, both responses should be indistinguishable. The truest response would be a combination of the two approaches (trapezoidal integration) which assumes a linear point-to-point on the input (rather than a stairstep)

3.4 linearisation

In order to analyse control-loop stability and hence optimise loop gains, methods are used which require the dynamic characterisation of the engine at a particular operating point as a transfer function.

The linearisation process provides this characterisation. The state-space convention can be used, which relates the engine's inputs, states, state-derivatives and outputs via a system of partial derivative matrices.

$$\frac{dx}{dt} = A[x] + B[u]$$
$$y = C[x] + D[u]$$

The linearisation process is therefore a generation of the partial derivative terms in each matrix. This is achieved by the parametric perturbation of states and inputs, observing the resultant effect on state derivatives and outputs.

Consider the low-order (shaft dynamics only) model above:

inputs: fuel flow (WFE)
(and other boundary conditions)

outputs : thrust (FN) etc.

state : shaft speed (N)

state derivative : shaft acceleration (Ndot)

The linearisation process:

- Establish a datum point (e.g. steady-state point run to specified fuel flow as example above : 3x3 scheme). Shaft acceleration for this point is, of course, zero. For the datum case we have :

  WFE = WFE_datum (specified)
  giving:
  N = N_datum
  Ndot= 0

- Extend matching scheme for shaft dynamics as for explicit integration (4x4 scheme)

- The A & C matrix elements can be found by generating a single solution for:

  WFE = WFE_datum
  N = (N_datum + ΔN)

With the 4x4 scheme, shaft speed is a specified matching quantity. The ensuing (thermodynamically sensible) matched point will have a non-zero value of excess power (XP), hence giving a non-zero value of Ndot. Similarly, FN will differ from the datum point.

- Similarly, B and D matrix elements can be derived by generating a single solution for:

  WFE = WFE_datum + ΔWFE
  N = N_datum

Clearly, the assumption is being made that the engine thermodynamics are linear over the perturbations applied. Typically, perturbations of 0.5% of point are used.

Linearisation of higher order models is achieved in exactly the same way. For full gas dynamics applied to the simple example, the steady-state matching scheme would be extended by 12 matching pairs (3 for each component - compressor, combustor, turbine, jet pipe).

3.5 real-time capability

So far, only non-real-time simulation has been considered. There are a number of model applications where a model must produce results in real-time. Ref. 1 usefully defines a Real-Time Engine Model (RTEM) as a 'transient computer program whose engine outputs are generated at a rate commensurate with the response of the physical system it represents'.

Example of real-time applications are :

- embedded models for flight systems
- engine models within aircraft simulators
- engine system integration testing

Ref. 1 covers the requirements of these applications in detail, and in terms of 4 criteria: consistency, bandwidth, versatility and execution speed. 'Consistency' is a term used in preference to 'accuracy' and refers to the ability of a model to represent the *reference* source of data - whatever that reference is. 'Reference' may change in various stages of the project: from the detailed performance prediction in the early stages, to engine test data later in a programme. 'Versatility' refers to the ability of the engine model to be refined/reworked in line with the evolving design. The model must be capable of simulating all aspects of engine behaviour that that the controller is capable of sensing or controlling - hence the bandwidth criteria. 'Execution speed' refers to the timestep at which the simulation must run in order to produce accurate [consistent], and numerically stable results. Of course, bandwidth and timestep are linked as described in section 1.2. The advantage of cycle-match models is that if a low bandwidth is required, then the model may be run stably at the large integration timesteps commensurate with the dynamics of interest. e.g. an aircraft simulator may only require outputs at 50ms.

The prime issue at stake here, is the use of iteration in a model on which is placed strict constraints on execution time. Clearly, no specific guarantees can be made on the number of iterations to match the cycle and so a limitation has to be imposed in order to give a model which has predictable execution times. It has been shown that a model limited to as few as 2 passes is viable. Truncation of iteration in this way may lead to loss of consistency, however this discrepancy is likely to be less than the difference between the iterative model (which is taken as the reference computer definition of the engine cycle) and a separate, non-iterating real-time model.

This being so, there are also potential run-time advantages to be cashed for some model applications. A model requiring 4 passes every

50ms uses less computing power than a non-iterative model running every 1ms (where 1ms may be required for stable running).The computing effort advantage amounts to a run time factor of around 10. The advantage is not so marked for applications requiring HIFEM RTEMs. An iterative model would run 2-4 passes at 1ms; a non-iterative model would typically run (1 pass) at 0.5ms or less. The comparison in this case may not be so spectacular!

Correct handling of gas dynamics in a non-iterative model may need extremely small timesteps, perhaps 0.1ms or less. Such a small timestep is not desirable for real-time work, a larger timestep is required. The usual way of ensuring numerical stability with a larger timestep is apply factors to selected volumes. Consequently, a larger timestep can be tolerated but at the expense of dynamic fidelity. The run time comparison for correct dynamics representation is therefore still in the iterative model's favour.

It must be said, however, with the advance in computing power, run-time advantages become less of an issue, it is the benefits of commonality and versatility that come to the fore.

Why stop at real time? There is perhaps the potential to further exploit Monte-Carlo type methodology to engine and controller design where ultra-fast non-linear models could be used effectively.

4. Production and validation of piecewise-linear models

The piecewise-linear form of engine model is an extension of the state-space linear model discussed in section 3.4. Essentially they comprise of a interpolated string of linear models. This type of model is used in the real-time applications mentioned above. It is not the purpose of this paper to compare the piecewise linear method to the aerothermal approach, but to illustrate how cycle-match models may complement their use. However it seems inevitable that the use of piecewise-linear models may dwindle as cycle-match models becomes more widely accepted in the real-time field of applications.

For a family of engines, a single piecewise-linear model structure may suffice; the constituent matrices will require trimming to a particular engine. This can be achieved by directly generating the matrices by linearisation of a non-linear model or through the use of system-identification (sysID) techniques which examine the response of a dynamic system (either real or modelled) to deduce the dynamics present. Care must be taken with sysID to avoid spurious recognition; direct linearisation may be safer.

A combination of the two techniques may be useful for model validation. Analagous to steady-state analysis-by-synthesis (the extended steady-state matching scheme mentioned in section 3.3), a technique may be developed which directly linearises the dynamic model, compares state-space matrices to those derived by sysID from the real engine. An iterative procedure can be applied to vary the dynamics assumptions in the model until a match is obtained with the matrices obtained from the engine. An improved dynamic model is thus obtained.

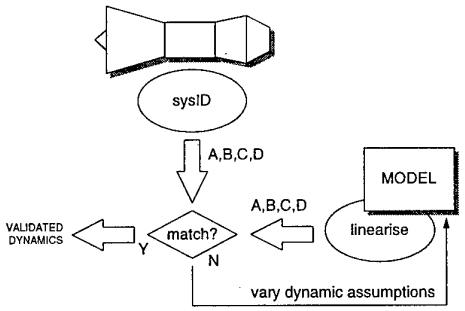

5. Conclusion

We have considered the capabilities and use of the cycle-match model with specific reference to the engine functional design process. The benefits of the wider use of cycle-match models can be summarised under the following headings:

capability
There is more and more emphasis on 'right-first-time' and 'no-surprises' in engine development. The most capable model methodology is sought. Iterative techniques offer rigorous aerothermal modelling, and their ability to run according to a wide range of constraints offer a flexible approach to prediction and analysis.

rationalisation of effort
It is clear that models should be built and developed by a single source of expertise. If these models can be applied across the whole spectrum of work, then a fragmented and duplicate approach can be eliminated.

model consistency
With a single model, discrepancies arising from different models are avoided.

reduced timescales
Cycle-match models are produced from the start of concept development. Availability of a Controls-compatible engine model at an early stage may contribute to reduced control-system development timescales, an early Performance-compatible controller model may facilitate early verification of Performance Requirements for Engine Control. A simultaneous engineering approach is therefore fostered which can also lead to reduced engine testing.

common toolset
Common tools will facilitate the population of the 'functional middle ground' referred to in section 2.1.

reduction in engine testing
Production and validation of piecewise-linear models presently requires dedicated engine testing. Direct linearisation of the reference cycle-match model may significantly reduce or even eliminate this testing. Furthermore, direct linearisation can yield altitude data, whereas special altitude tests in direct support of piecewise-linear models are rarely performed due to cost reasons.

6. References

1. **Aerospace Information Report:**
Real-Time Modeling Methods for Gas Turbine Engines (A.I.R. 4548)

7. Acknowledgements

The author acknowledges the input (implicit and explicit) of his colleagues. The author also acknowledges Rolls-Royce plc for permission to publish, however the views expressed do not necessarily reflect a company commitment.

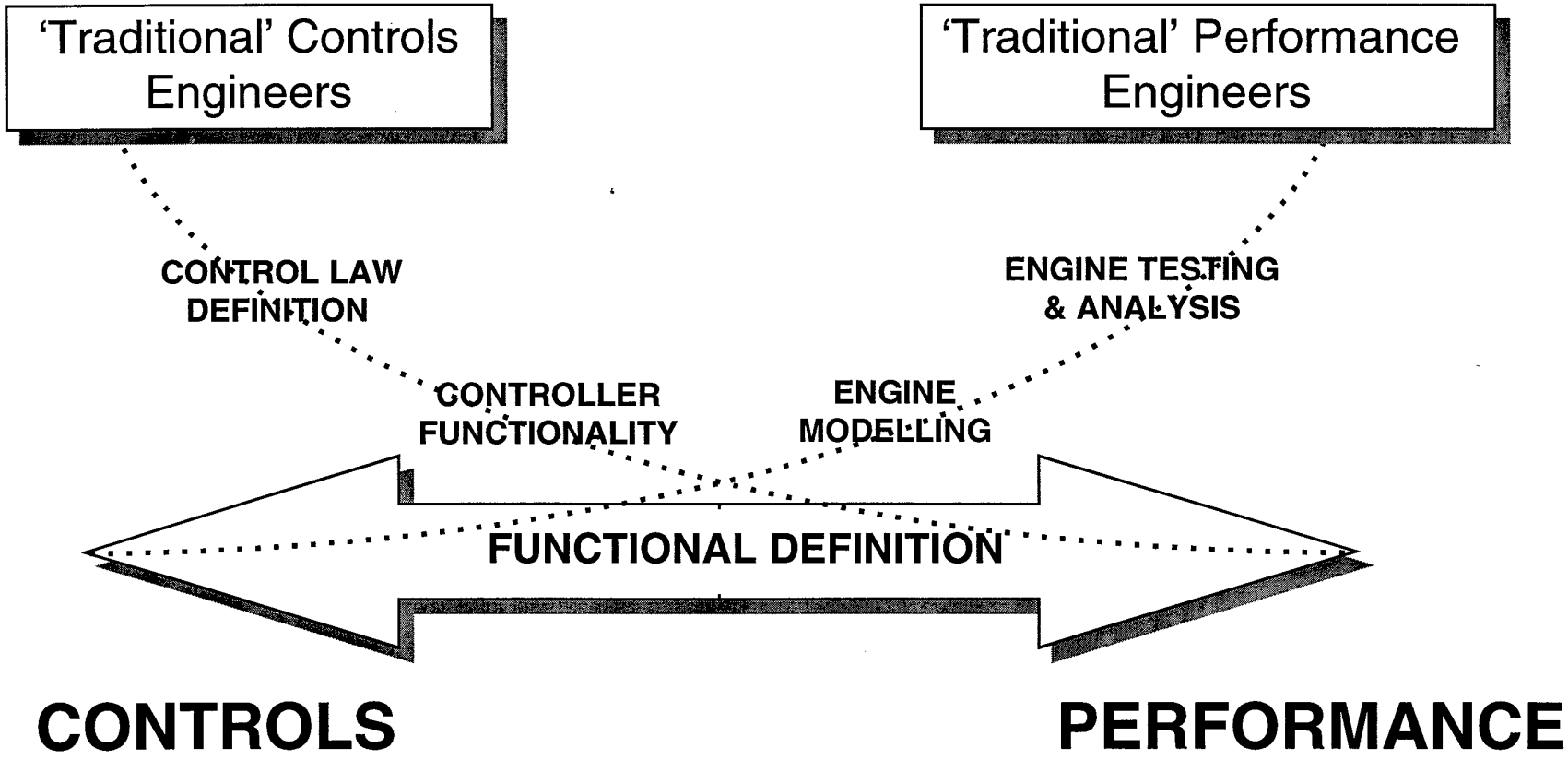
'Traditional' Controls Engineers
'Traditional' Performance Engineers
CONTROL LAW DEFINITION
ENGINE TESTING & ANALYSIS
CONTROLLER FUNCTIONALITY
ENGINE MODELLING
FUNCTIONAL DEFINITION
CONTROLS
PERFORMANCE

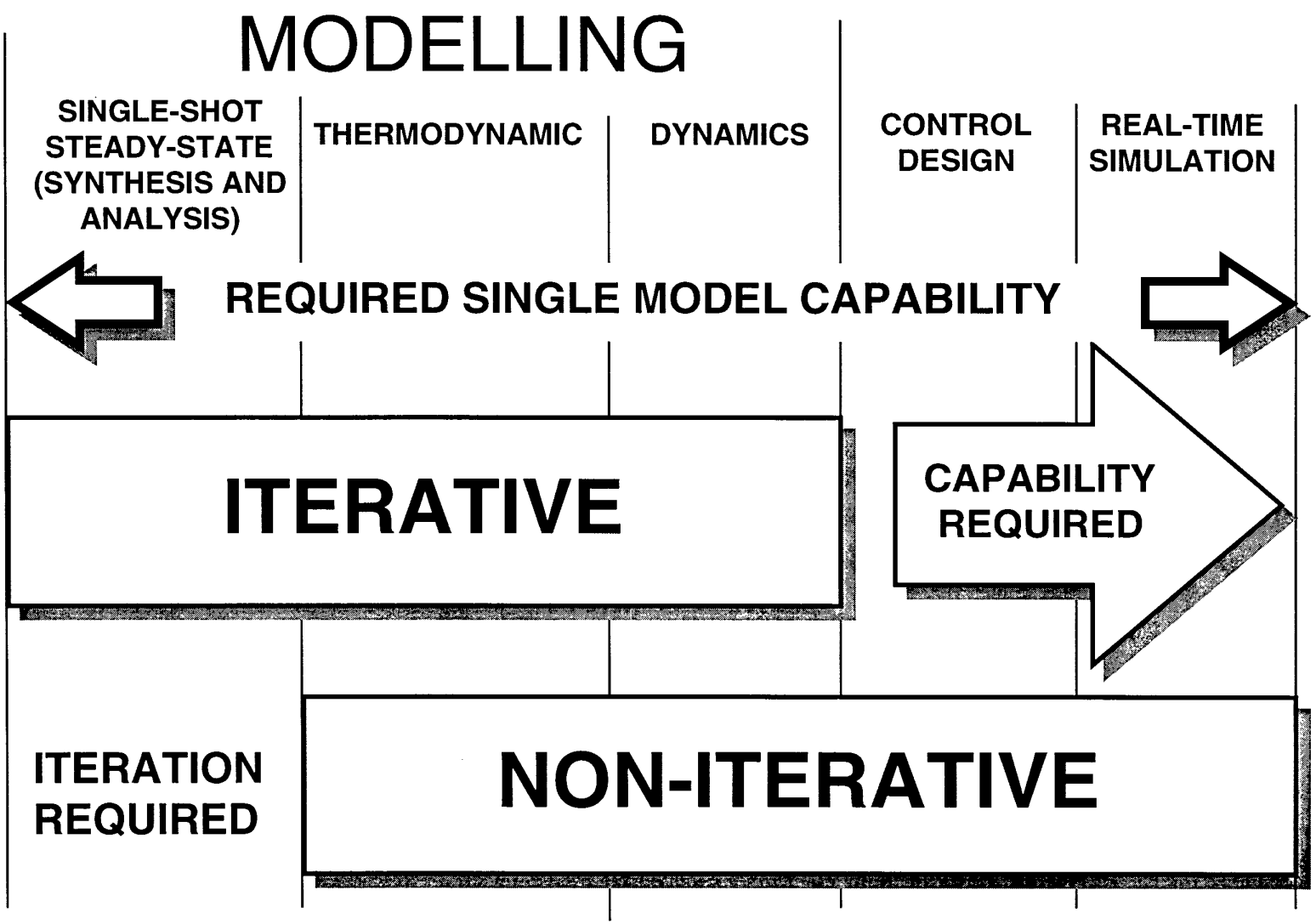
MODELLING
SINGLE-SHOT STEADY-STATE (SYNTHESIS AND ANALYSIS)
THERMODYNAMIC
DYNAMICS
CONTROL DESIGN
REAL-TIME SIMULATION
REQUIRED SINGLE MODEL CAPABILITY
ITERATIVE
CAPABILITY REQUIRED
ITERATION REQUIRED
NON-ITERATIVE

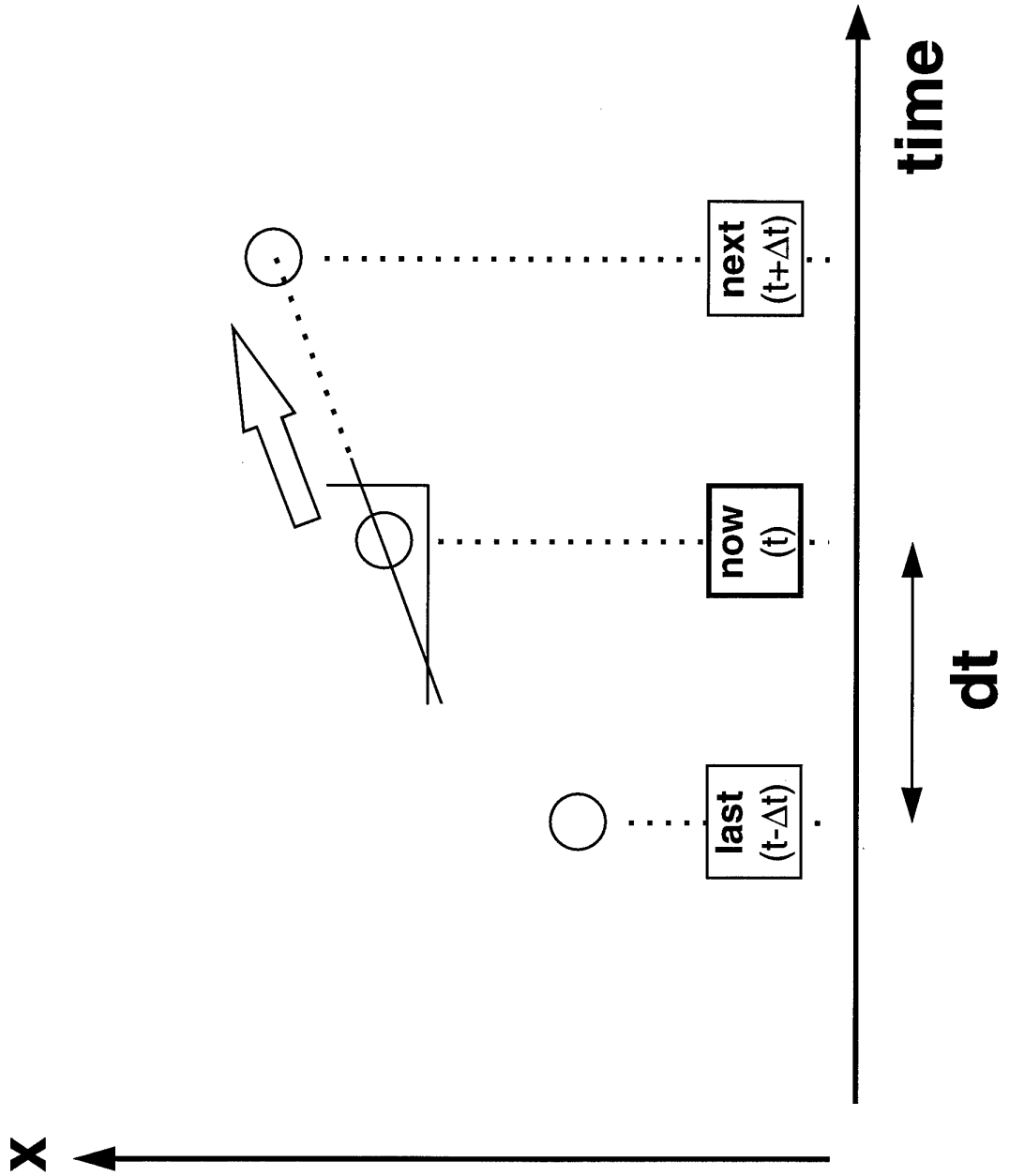
time
x
dt
last
(t-Δt)
now
(t)
next
(t+Δt)

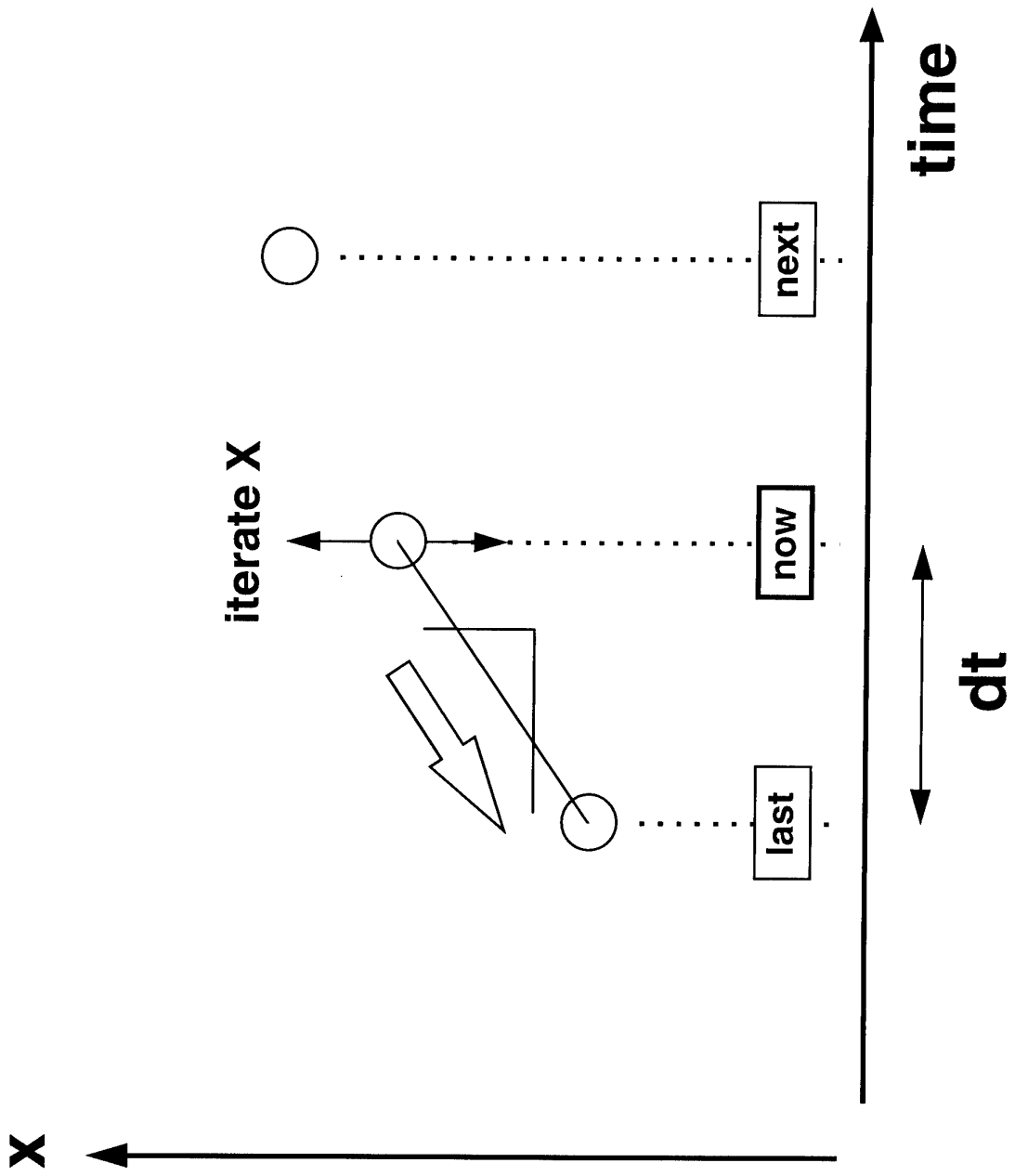
time
next
now
last
iterate X
dt
X

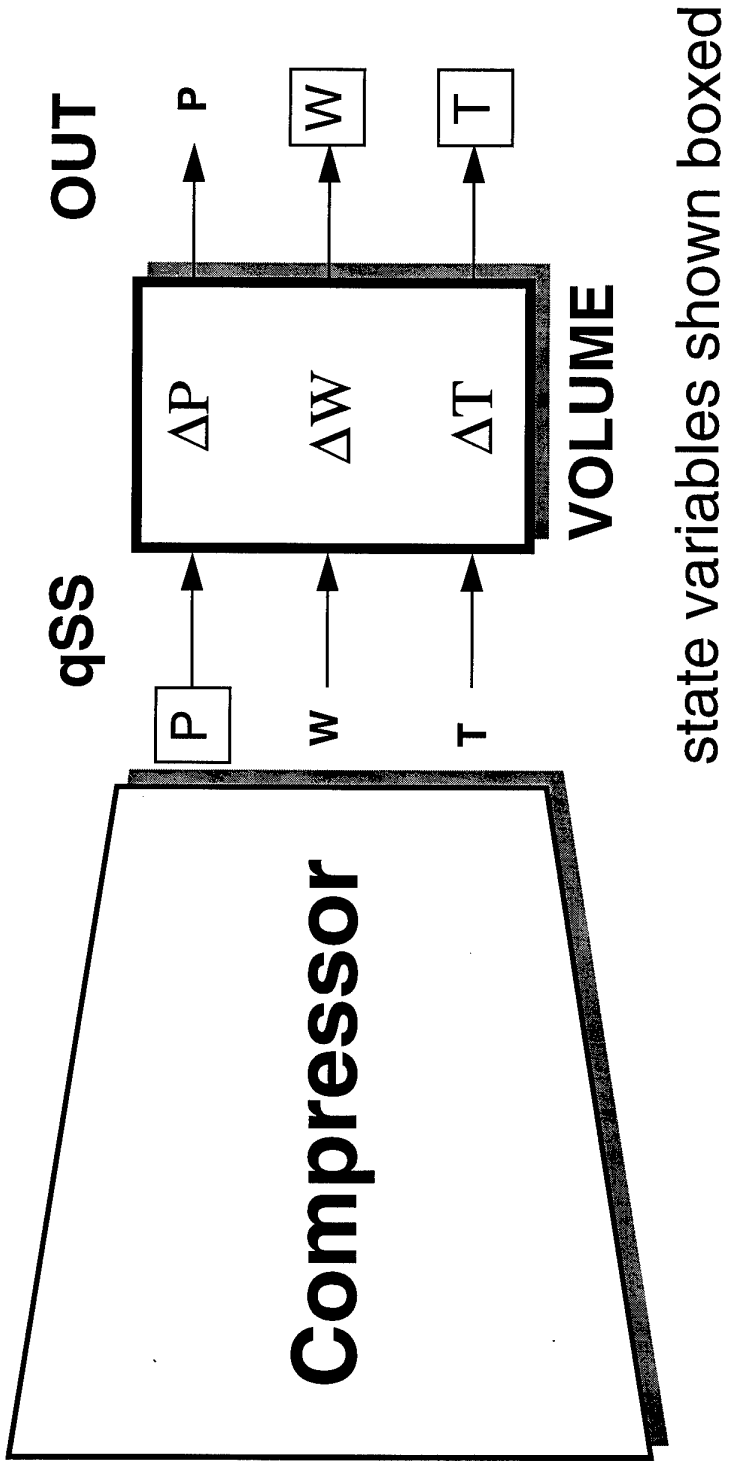
OUT
P
W
T
ΔP
ΔW
ΔT
VOLUME
qSS
P
W
T
Compressor
state variables shown boxed

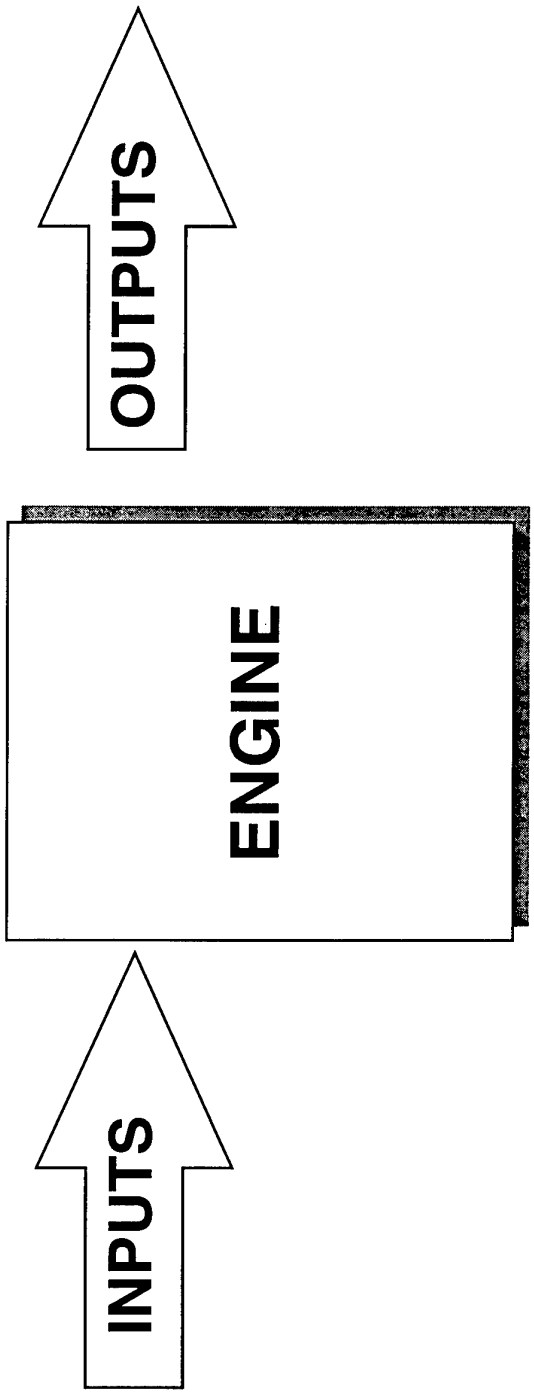
OUTPUTS
ENGINE
INPUTS

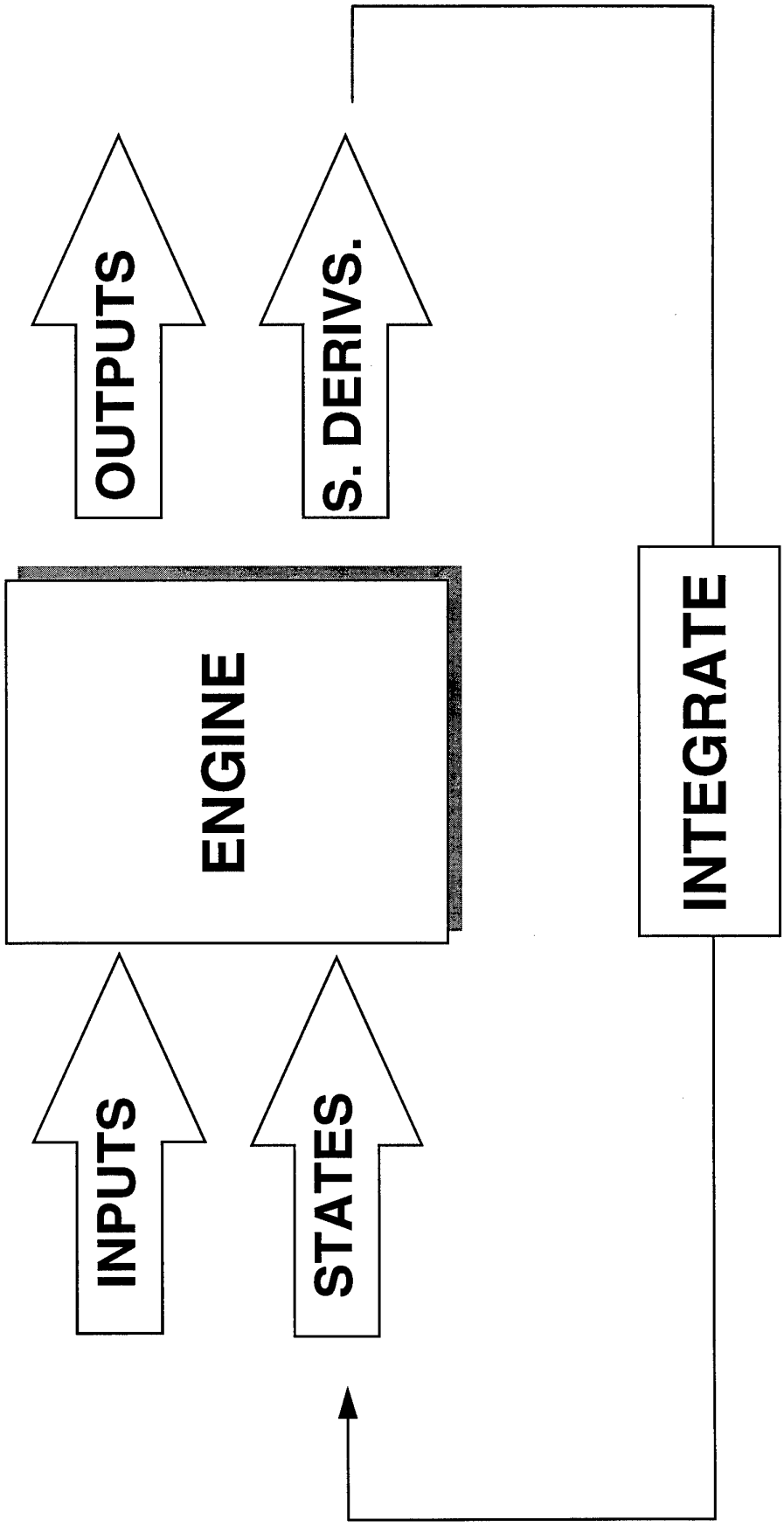
OUTPUTS
S. DERIVS.
ENGINE
INTEGRATE
INPUTS
STATES

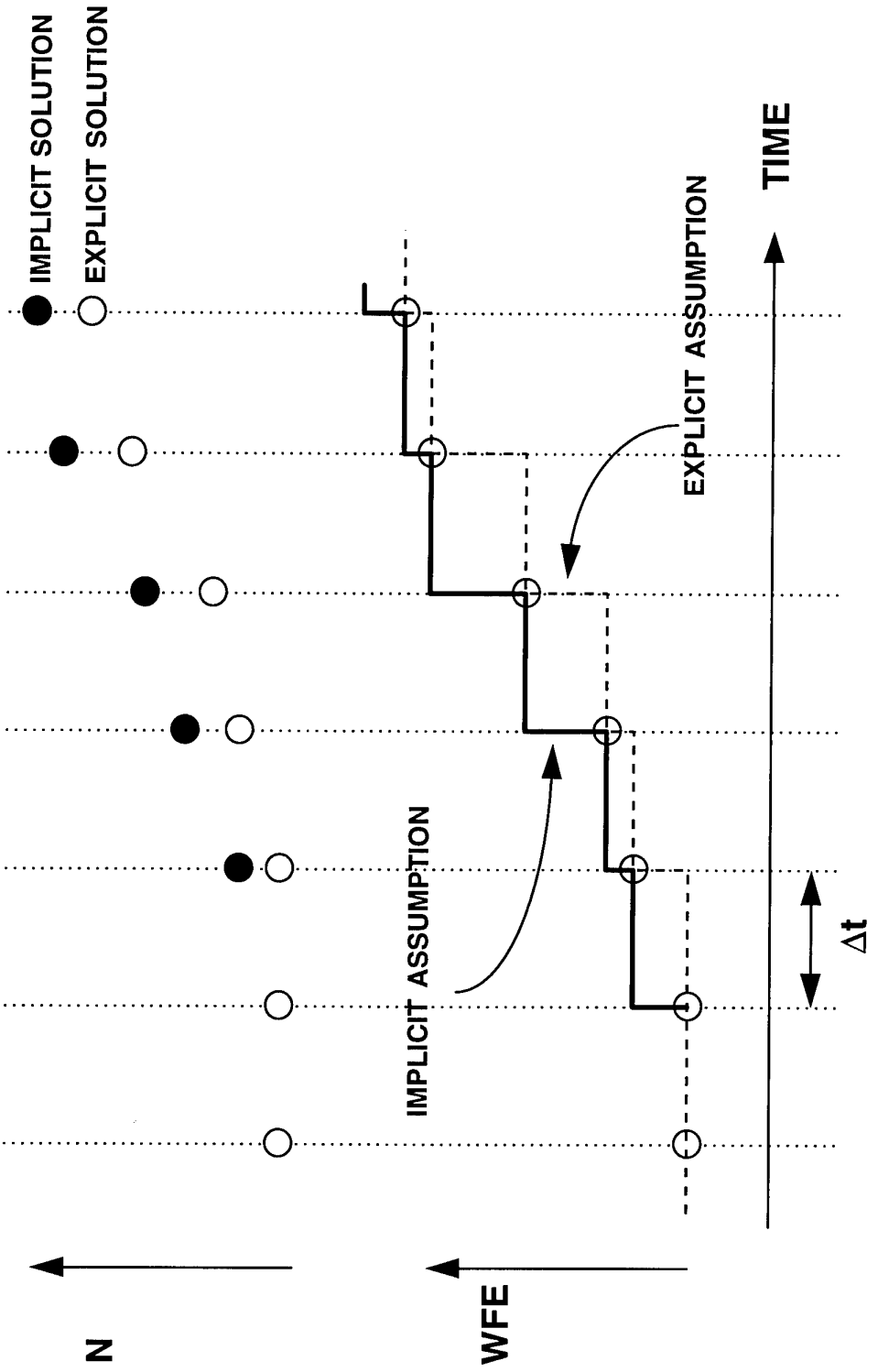
IMPLICIT SOLUTION
EXPLICIT SOLUTION
TIME
EXPLICIT ASSUMPTION
IMPLICIT ASSUMPTION
Δt
N
WFE

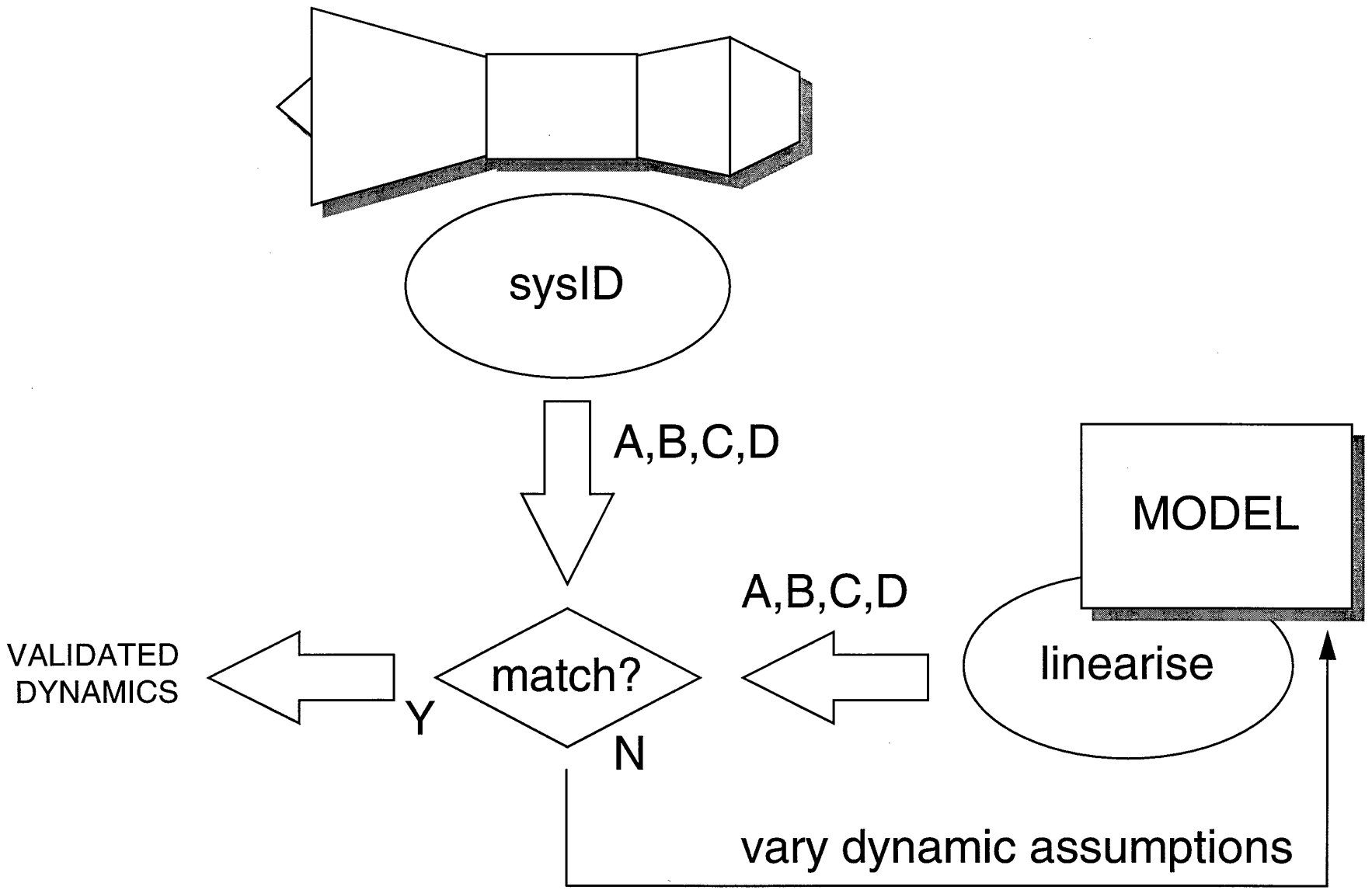
sysID
A,B,C,D
MODEL
A,B,C,D
VALIDATED
DYNAMICS
match?
Y
N
linearise
vary dynamic assumptions

Meeting Discussions

Paper 44: **Cycle-match Engine Models used in Functional Engine Design - an Overview**

Author: Marcus S. Horobin

Discussor: A. J. Cifone

Question: How can these codes or models be utilised by component designers to assist in decision-making, like component or total engine performance improvements, component interactions,etc?

Author's reply: Consideration of whole engine functional behaviour using these types of model can identify novel uses of engine features which have been provided for other specific or local purposes. For example, compressor variable geometry is primarily present to ensure compressor stability, however, whole engine studies might identify benefits from exploiting the flow modulating properties of inlet guide vanes. Consequently a challange is put to compressor designers to produce a robust design which will tolerate wide-range variation of geometry.

Post-session thought:

There is considerable advantage in the interfacing of cycle-match models with detailed component models. An information bottleneck can form where component boundary conditions are required for detailed component design. An integrated model would facilitate the iterative design process and help in the identification of the constraints placed on the component in an engine environment.

Smart Flow Control in Aircraft Engine Components & Component Interactions

S. Farokhi
Aerospace Engineering Department
The University of Kansas
Lawrence, KS 66045
USA

1. SUMMARY

Adverse flow environments pose challenging design constraints in aircraft engine components and component interactions. Some examples of such flow environments are: steep pressure gradients, random and periodic unsteadiness, shock wave interactions and 3-D boundary layer separation. These adverse flow environments and interactions promote the growth of various kinds of instability waves inherent in gas turbine engines, e.g., vorticity wave, entropy wave and acoustic or pressure wave instabilities. A series of smart subsonic and supersonic flow controllers are presented with applications to the design of aircraft gas turbine engine components. They are *on-demand* vortex generators capable of injecting co- and counter-rotating streamwise vortices in subsonic, transonic and supersonic flow. The strength and location of the vortex is a control variable and must be optimized via a closed-loop control algorithm. The subsonic smart VG assumes a ramp-type geometry (similar to Wheeler vortex generators) and the smart supersonic VG is a tailored cavity with a movable flap concealing the cavity. The movable flap is actuated inward to expose the cavity to transonic or supersonic flow. The depth of the cavity is controlled via a closed-loop feedback control system which ties the strength of the vortex to the "desired" performance as measured by one or more sensors. Candidate *cost functions* are proposed in the optimization routine for each component in a gas turbine engine.

2. INTRODUCTION

An aircraft airbreathing engine operates on the principle of air compression, fuel mixture and combustion and flow expansion in order to generate a propulsive force. In a gas turbine engine, the compression is achieved through inlet ram effects and subsequent mechanical compression through a compressor (axial, centrifugal or mixed). The expansion takes place in a turbine and a final expansion is achieved through a propulsive nozzle. The combustion of fuel/air mixture may be implemented in one or multiple stages. A common example of this (i.e., the multi-stage combustion) is the use of a conventional combustor (i.e., the primary burner) and a subsequent afterburner in military or supersonic aircraft. The dominant source of loss in each of these processes, i.e., compression, chemical reaction and combustion and expansion, is different. For example, in the inlets, boundary layer separation and the engine face distortion are to be controlled. In a compressor, the loss sources are found in the wall regions and the blade tips. In a turbine, the dominant loss source may be in the tip clearance flow and mixing losses in the free stream-coolant interaction. The combustors are limited by complete combustion, development of hot spots and NO_x formation. To control the negative attributes of the fluid flow/chemical reactions in these components, primarily in the engine off-design operation, a new set of flow effectors and sensors are needed. To recognize the mode of operation and to optimize performance, the flow effectors and sensors are to communicate in a closed-loop fashion using a smart control strategy. Among various kinds of flow effectors, e.g. resonating cavity, acoustic wave generator, oscillating flap, distributed suction, jet blowing, compliant surface, heating, cooling and vortex generators, the latter is the subject of current paper. Once manufacturing confidence is developed in the capability, reliability, maintainability and robustness of the smart systems (i.e., sensors, actuators and controllers), they will be implemented in the *design stage* of new aircraft and engine.

Among performance limiting factors involved in the operation of engine components in a gas turbine engine, we propose to concentrate on viscous-dominated three-dimensional flows. This, in fact, is a very large and diverse undertaking. Three-dimensional flow separation, reattachment, end-wall flows, tip clearance flow, corner vortex, shock-boundary layer interaction and vortex shedding in the wake of turbomachinery blades are a few of the examples found in a modern aircraft engine and propulsion installation. The random unsteadiness (i.e., the turbulence) that typically ensues from these viscous-dominated three-dimensional flows often take place in concentrated *patches*, or what is known as the spatial distortion, that again limit the engine performance.

A recent article by Gad-el-Hak [1] provides an excellent review of the status and outlook for flow and separation control. Modern developments in chaos control, microfabrication and neural networks are discussed, by Gad-el-Hak [1], in the context of flow control application. The first application of a smart vortex generator system on an airfoil in subsonic flow was made by Barrett and Barrett-Farokhi [2,3]. Blunt bodies of revolution, e.g. submarines, were also fitted with ramp-type vortex generators to control 3-D flow separation by Farokhi et al. [4,5]. A new design was introduced for vortex generators suitable for transonic and supersonic flows by Farokhi and Taghavi [6]. Initial performance characteristics of these supersonic vortex

Paper presented at the RTO AVT Symposium on "Design Principles and Methods for Aircraft Gas Turbine Engines", held in Toulouse, France, 11-15 May 1998, and published in RTO MP-8.

generators applied to a convergent-divergent rectangular nozzle is reported in references [7,8]. The flowfield measurements and performance of vortex generators of various geometry can be found in references [9,10]. The impact of riblet integration with vortex generator to reduce VG drag on low-speed airfoils is reported in references [11, 12].

2.1 Aircraft Engine Application

Dynamic interaction between a high-performance fighter aircraft inlet system and the fan/compressor limits the engine operating envelope. It is this environment of component interaction that lends itself readily to smart intervention of flow controllers like vortex generators. A smart vortex generator (SVG) system promises to reduce compressor-face (steady-state and dynamic) distortion levels thereby enhancing the stability margin of the compressor in a maneuvering aircraft. On turbomachinery blades, the passive version of subsonic and supersonic vortex generators can be used to control local separation and flow instabilities. The primary benefits in turbomachinery shall be a wider operating margin in off-design performance as well as higher stage loading possibilities which will reduce the number stages in compressors and turbines. The tip clearance flow could also be reduced by locally-aligned, passive vortex generators, on the blade, which can interact with the scraping vortex to relieve the pressure gradient zone near the blade tip. Active jet noise suppression using cavity vortex generators near the nozzle exit lip promises to reduce take-off and landing jet noise for high-speed civil transports. Mixing enhancement in a scramjet combustor can be promoted by integrating supersonic vortex generators in the inlet duct prior to fuel injection. Flow attachment on a vector thrust nozzle ramp can also be effected by smart supersonic vortex generators.

For the inlet-engine matching performance optimization, the rms-value of the pressure fluctuation at the engine face, for example, may serve as a cost function. In a convergent-divergent exhaust system, smart flow controllers are capable of attaching a separated flow on an expansion ramp of a 2D-CD nozzle which is either caused by a shock in an under-expanded nozzle or the expansion ramp deflection in a vector thrust mode. The cost function in a vector thrust nozzle may be chosen as the gross thrust coefficient in x, y or z-directions. Figure 1 shows the schematics of a supersonic inlet equipped with smart subsonic vortex generators integrated in the diffuser. The current practice of using vortex generators, as a means of flow control, in diffusers has the disadvantage of device drag and losses that are constantly borne by the installation. The smart VG system will serve as an *on-demand* controller with variable strength capability to encounter various off-design operations.

Due to very high frequency (i.e., of the order of blade passing frequency, $\omega.n_B$) actuation requirements of smart vortex generators on turbomachinery blading and the high-cycle fatigue characteristics of these actuators, only a passive version can be incorporated in compressors and turbines. The passive boundary layer control devices (i.e., VGs) are to be designed *into* the blades and shall, under optimum conditions, accrue the following (inter-related) benefits:

- withstand higher local diffusion rates at the engine off-design operation
- mitigate secondary flow losses in the blade tip region
- inject a streamwise vortex of arbitrary spin to control corner flow losses
- mitigate large radial flow in the wake of transonic blading
- improve compressor stability to inlet disturbances

The three-dimensional layout of the proposed flow controllers, i.e. both subsonic and supersonic VGs, on the turbomachinery blades is to be guided by performing accurate 3-D viscous computational fluid dynamics analysis of a single blade passage followed by the dynamic analysis of the compressor/turbine stage, i.e. the mutual interference problem. The blade surface streak pattern and its variation with operating conditions will serve as the initial value, or the guiding light, for the initial layout of the design and distribution of the flow control devices. The process, i.e. the blade design integrated with the passive flow control devices, by necessity has to be repeated to achieve an acceptable (or even an optimum) solution. To withstand higher local diffusion rates and *manage* the vortical flow on turbomachinery blades and flow passages, in short, shall be the goal of passive subsonic and supersonic VG integration in compressors and turbines.

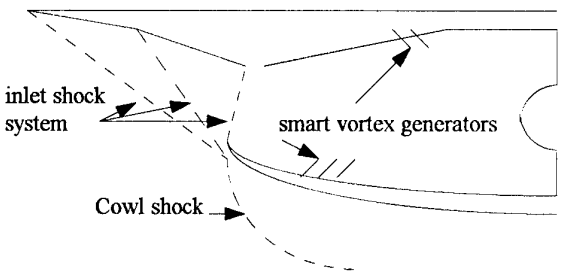

Fig. 1 Schematic of smart subsonic VGs in a supersonic inlet

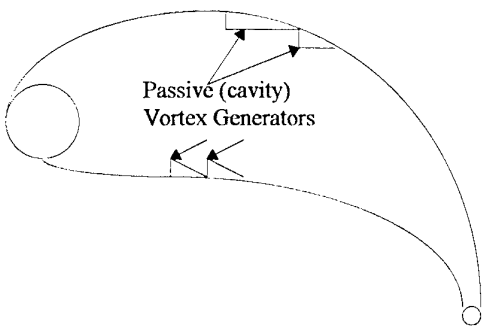

Fig. 2 Schematic of passive VGs on a turbine blade.

The mechanism for enhanced jet mixing, in an exhaust nozzle, is provided through streamwise vortex injection of the vortex generators in the shear layer which affects both the radiated noise intensity and the directivity pattern of high-speed jets. The shock-cell structure of an under-expanded jet, i.e., the cell spacing, is observed by Farokhi and Taghavi (unpublished schlieren studies) to be modified by the induced pressure field of longitudinal vortices. The supersonic VG system for the purposes of jet noise reduction/mixing enhancement should be integrated near the nozzle exit lip, as shown in Fig. 3.

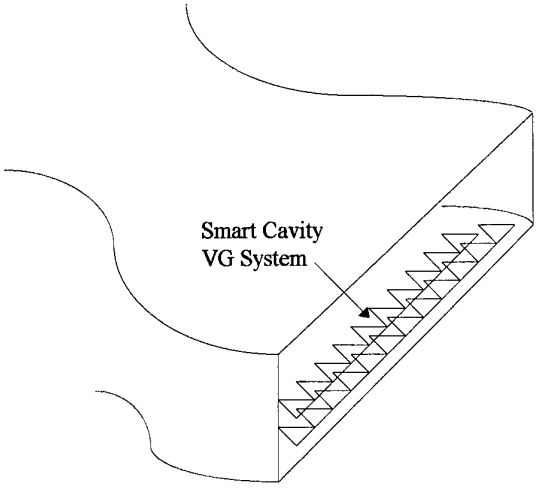

Fig. 3 Schematic of supersonic VG integration in a rectangular nozzle lip for the purpose of jet noise reduction and/or directivity management

2.2 Propulsion System Integration Applications

The main areas of concern are the exhaust system installation drag reduction in transonic speed regime and control surface vibration instability due to buffet and/or flutter. Boattail and base drag in military aircraft constitute a substantial percentage of the aircraft drag in transonic flight. Flow separation can be mitigated using smart vortex generators and the attendant penalties of drag rise or vibration can be reduced. In addition, a high-performance aircraft inlet system at supersonic speeds may encounter sub-critical instability, or buzz, which is caused by a periodic flow separation and reattachment on compression ramps. The shock oscillation associated with inlet buzz can be stabilized using smart vortex generators as well. A military aircraft in maneuver encounters flow separation on the windward side of its inlet with a potential ingestion of highly turbulent separated flow in the engine causing compressor stall or engine surge. In essence, all areas of flow separation in an engine or engine installation may be approached using a smart vortex generator system. As noted earlier, this does not include turbomachinery blading where high frequency actuation and high-cycle fatigue characteristics prevent the use of smart flow manipulators.

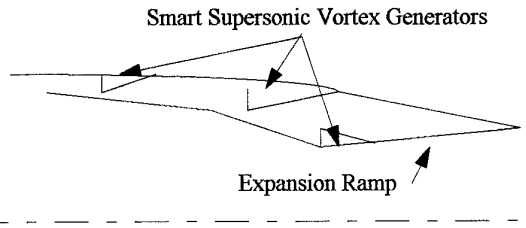

Fig. 4 Schematic of smart VGs outside (boattail) and inside a C-D supersonic nozzle.

3. A SMART VORTEX GENERATOR SYSTEM

The building blocks of a *smart* system are:

- sensor(s)
- processor(s)
- actuator(s)

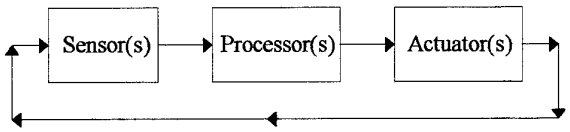

Fig. 5 Triad of a smart system

The requirements on the sensors and actuators are:

- robustness
- reliability/maintainability
- volume/weight
- power requirements
- cost

To meet these requirements, the current sensors in a modern aircraft engine can be used in the smart VG system, e.g. engine face rake, thermocouples, pressure transducers and shaft rpm-sensors. In addition, aircraft flight dynamic data (i.e., body angles and rates, flight speed and acceleration) can be incorporated in the control strategy of the smart aircraft system. The requirement on the processor, i.e. the computer memory/storage, number of processors and speed, strongly depends on the control strategy as well. The use of nonlinear adaptive control, e.g. as offered by neural networks, seems to be a promising approach in the development of smart flow control in aircraft engines. A parallel processor-equipped on-board computer offers the speed needed for the optimal use in neural network controller schemes.

4. EXPERIMENTAL RESULTS

Extensive studies on the subsonic vortex generator flowfield and design have been reported in the classical literature (e.g., references 10,13,14). Wheeler has designed modern vortex generators [15,16] which are characterized as *low profile* (i.e., device height, h, lies well within the boundary layer, δ) and consequently offer low device drag in passive mode operation. Aerodynamic characteristics of Wheeler VGs are studied by Lin, Selby and Howard [17] among other researchers. The water tunnel flow visualization of Wheeler doublet and wishbone VGs, as reported in [17], is shown in Figure 6.

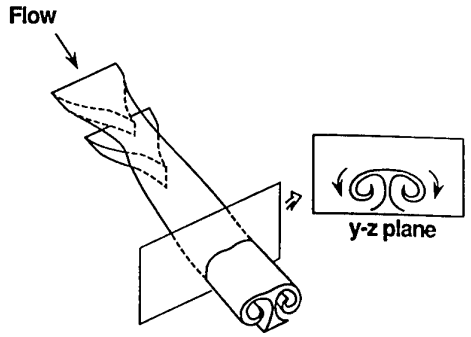

(a) Doublet VG in laminar boundary layer

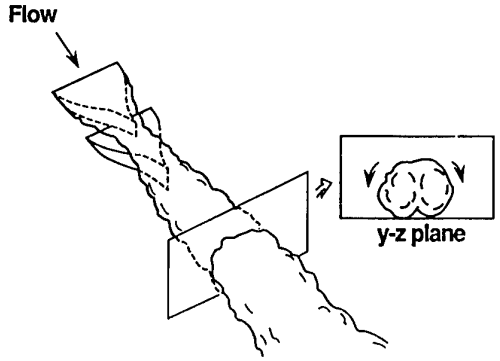

(b) Doublet VG in turbulent boundary layer

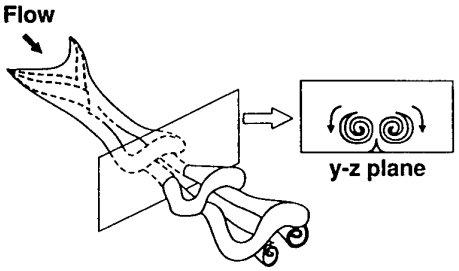

(c) Wishbone VG in laminar boundary layer

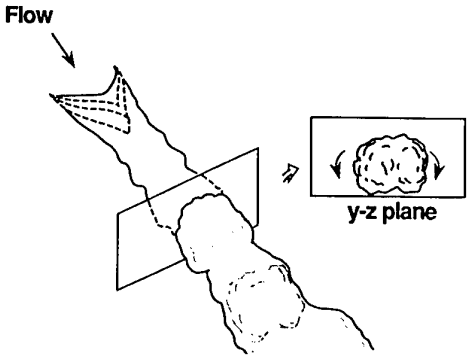

(d) Wishbone VG in turbulent boundary layer

Fig. 6 Flow structure downstream of doublet and wishbone vortex generators [17].

The laminar flowfield downstream of a doublet vortex generator, as shown in Fig. 6-a, indicates a mushroom structure evolution surrounding a pair of counter-rotating streamwise vortices. The wishbone VG in laminar flow gives birth to a periodic horseshoe vortex structure which is shed at a device-height Strouhal number of 1 (see Fig. 6-c). Although conventional engines will not operate with extensive laminar flow regions, the interest in laminar flow effects of submerged VGs may be found in micro-UAV (unmanned aerial vehicle) or high-altitude aircraft propulsion system applications. The turbulent flowfield of a doublet as well as a wishbone vortex generator is depicted in Fig. 6-b and 6-d. Similar turbulent wake structures evolve in both cases with counter-rotating vortex structures embedded in the device wake. The authors [17] report the vortex core in both VG examples rose to 2-3 device heights shortly after the vortex generators and then remained constant beyond that point. Wishbone vortex generators of height, $h=0.2\delta$, placed at 2δ upstream of separation point on a backward-facing separation ramp showed effective flow attachment capability in low-speed wind tunnel experiments [17].

A supersonic vortex generator capable of producing a pair of counter-rotating vortices (with a low device drag) is shown in Fig. 7. The cavity VG with its vertex pointing upstream expands the locally supersonic flow into the cavity (via Prandtl-Meyer expansion waves) and then as a result of interaction with the bottom ramp, the flow on the sides roll into streamwise vortices [6]. The low device drag at supersonic speeds is attributable to the *low-profile cavity* design creating weak expansion and compression waves turning the flow and generating vortical structures.

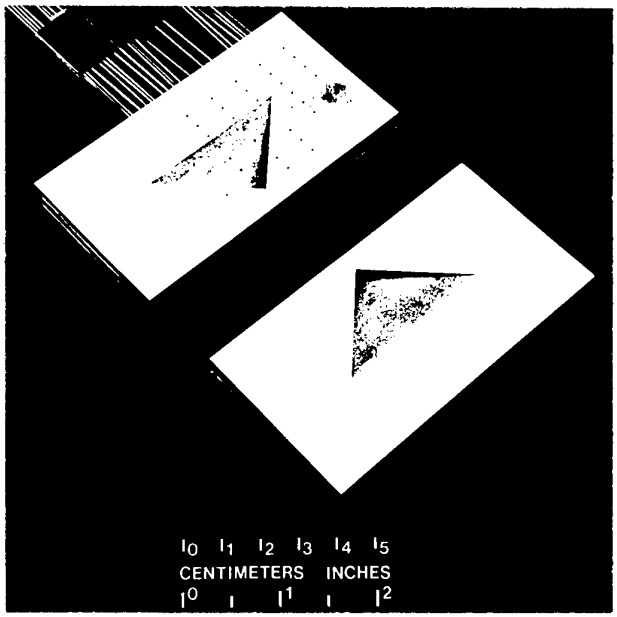

Fig. 7 A cavity supersonic vortex generator test article [7].

Pressure sensitive paint flow visualization studies in a two-dimensional, convergent-divergent supersonic nozzle equipped with a 60° cavity VG (with an 8° bottom plate ramp angle) is shown in Fig. 8. Nozzle pressure ratio (NPR) is the running parameter and ranges from the over-expanded case of 2 to the under-expanded case of 10. Flow is from top to bottom on each picture and the color scale in the center of the picture reveals: a) the shock formation in the low NPR cases (i.e., NPR of 2-4), b) the vortex cores which are generated near the vertex and curve in the streamwise direction shortly after they are created by the edges of the cavity, c) vortex interaction with the shock pushes the shock front further downstream and d) the area of the cavity center experiences a high pressure zone in response to *dipping streamlines* in the center of the cavity which create compression waves in the center.

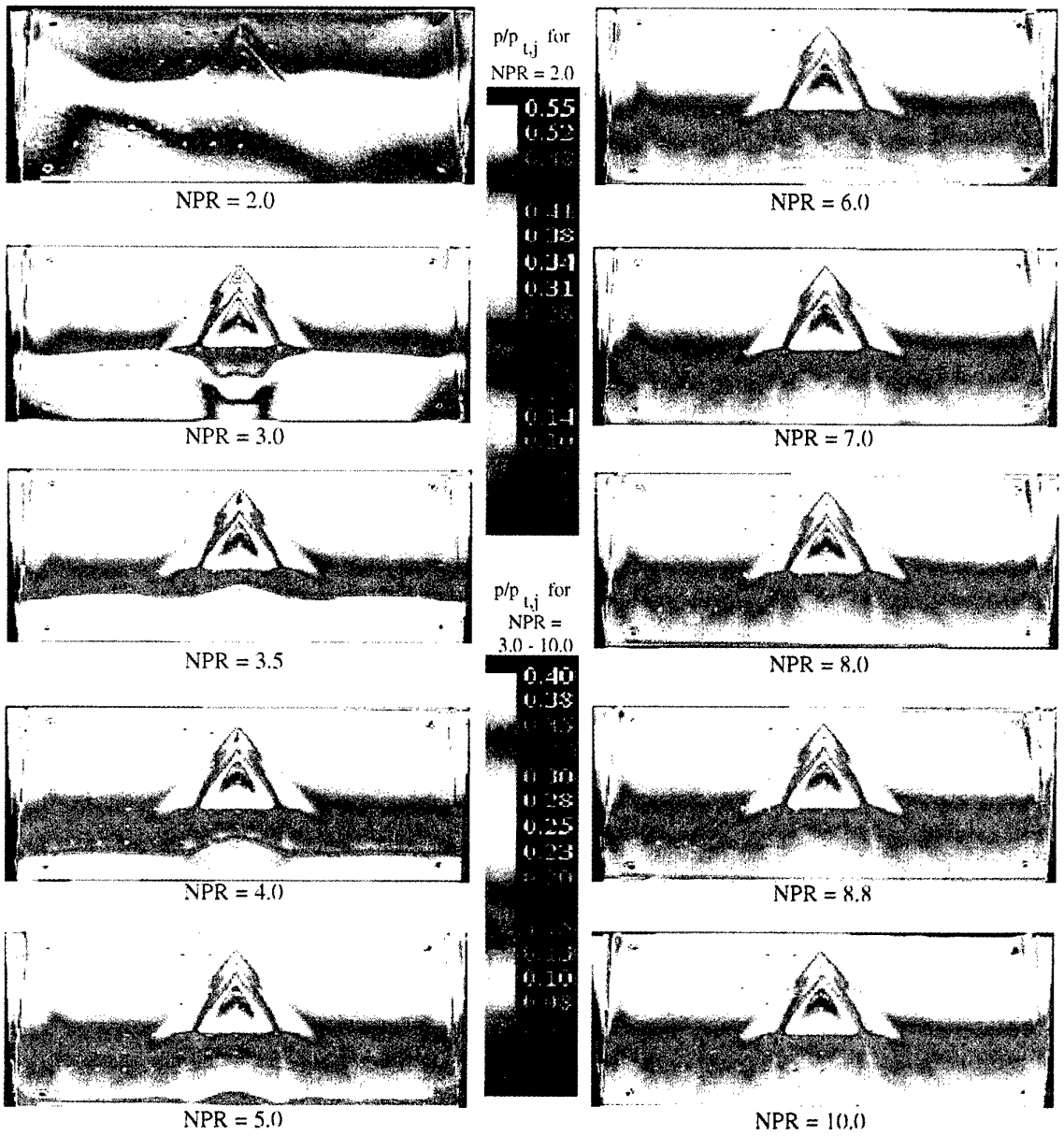

Fig. 8 Pressure sensitive paint study of a supersonic VG [8]

Subsonic vortex generators whose height can be controlled have been designed, fabricated and tested by Barrett [2] and Barrett-Farokhi [3] for a low-speed airfoil. A ramp-type vortex generator was equipped with a pneumatically-controlled bladder which adjusted the VG-height through a closed-loop control system. A six-component pyramid balance provided the aerodynamic performance information of the airfoil to the controller. The cost function in the optimization routine may be a)C_{lmax}, b) $(L/D)_{max}$ or c) another flight performance parameter. Figure 9 shows the schematic of the smart tetrahedral vortex generator (STVG) control system and the airfoil drag polar with the STVG in on or off position. The measured aerodynamic performance improvement on a NACA 4415 airfoil using the STVG system were:

a) C_{lmax} increase from 1.26 to 1.43,
b) α_{stall} increase from 12.5° to 14°,
c) a 30% increase in L/D at angles of attack beyond 12.5°
d) C_{do} increase of less than 0.1% in retracted VG position

Smart Wing Control & Performance

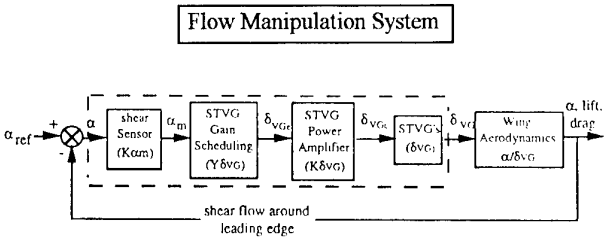

a) schematic of the STVG control system

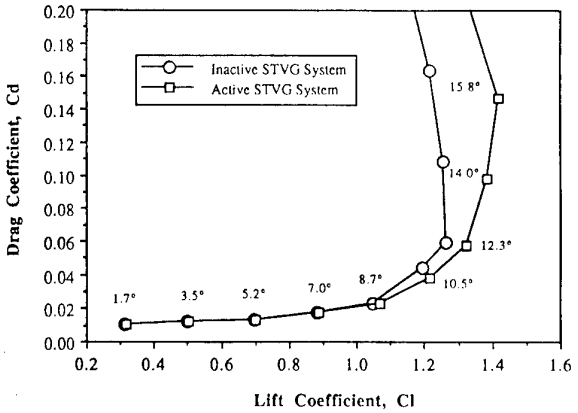

b) NACA 4415 drag polar

Fig. 9 STVG control system and airfoil performance in a wind tunnel with corrected data

A special type of smart tetrahedral vortex generator can be designed to not only actuate/control its deployment height (as in the previous example), but also optimize its orientation. The application of this type of STVG can be found in viscous flow control on bodies of revolution, e.g. aircraft fuselage or submarine hull. To enhance vehicle maneuverability, reduce acoustic signature or improve weapon delivery, the vortex flow about blunt-nosed bodies of revolution must be controlled. An extension of the STVG concept for planar applications (e.g., airfoils and wings) using a rotating ring, electromagnetic strips or a multi-element arrangement in a rosette design is summarized in Fig. 10. Here, it is not intended to present an exhaustive means of possible actuation mechanisms for an STVG, rather the aim is to introduce generalized concepts in versatile vortex generation systems with potential applications to other land, sea and air vehicles. Surface flow visualization studies on a wind tunnel model of an attack submarine at extreme heading angles revealed the flow attachment capability of the proposed concept [4,5].

Novel Concepts

on Smart Tetrahedral Vortex Generators

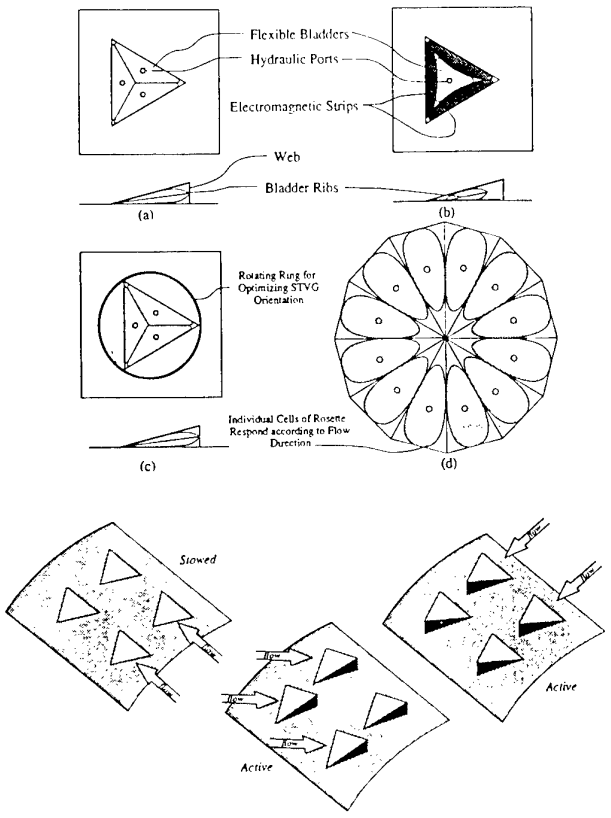

Fig. 10 Novel concepts in smart tetrahedral vortex generation

In an innovative approach to surface modification of an aerodynamic surface incorporating VGs, Wetzel [18] and Wetzel-Farokhi [11-12] introduced specially-oriented riblets downstream of vortex generators. This falls under the category of passive means of turbulent drag reduction, which in harmony with the spiraling flow of a vortex, introduces drag-reducing riblets locally-aligned with vortex flow. From various orientations of the riblet studies, the 45° yaw-in angle was chosen as the most effective in viscous drag reduction [18]. Some elementary results on airfoils are produced here to highlight the utility of surface treatment in conjunction with flow effectors, such as VGs and to further demonstrate the aerodynamic advantages accrued even in the face of adverse pressure gradient. Figure 11 shows the schematics of a low-speed airfoil wind tunnel model with leading edge roughness, wishbone vortex generators (placed at 20% chord) and two riblet configurations (straight and 45° yaw-in configuration) [18]. These were referred to as configurations B, C and D in Wetzel's dissertation. The wind tunnel tests were conducted at a Re_c of one million. As expected and evidenced in Fig. 12-a, the lift characteristic of the airfoil does not change with the riblets. However, the airfoil drag polar (Fig. 12-b) is influenced by the riblet and its orientation. In parts-c and -d, Fig. 12 shows the influence of inward-yawing riblets on drag reduction and L/D enhancement.

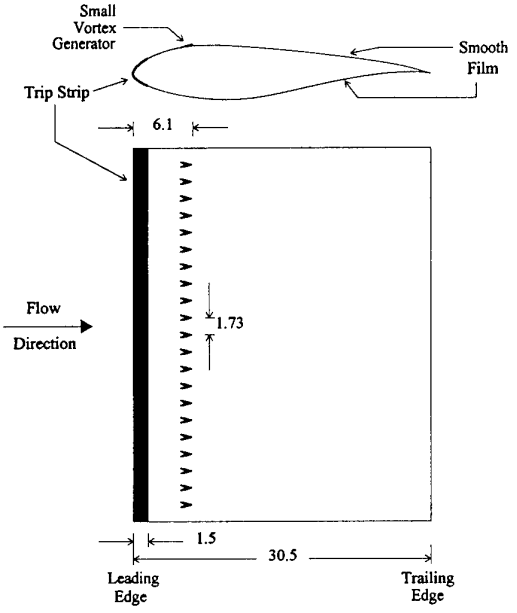

(a) Rough Configuration B

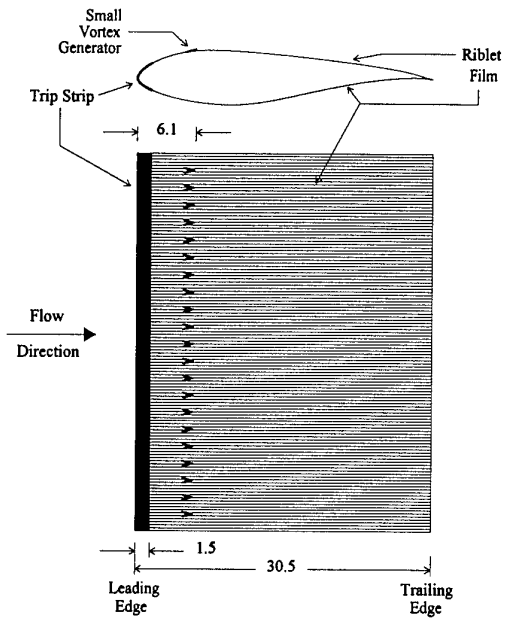

(b) Rough Configuration C

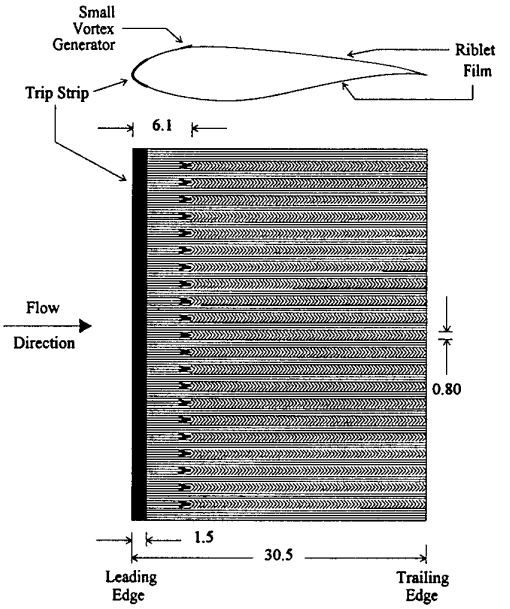

(c) Rough Configuration D

Fig. 11 A low-speed airfoil equipped with wishbone VGs and different riblet configurations [18].
(All Dimensions are in cm)

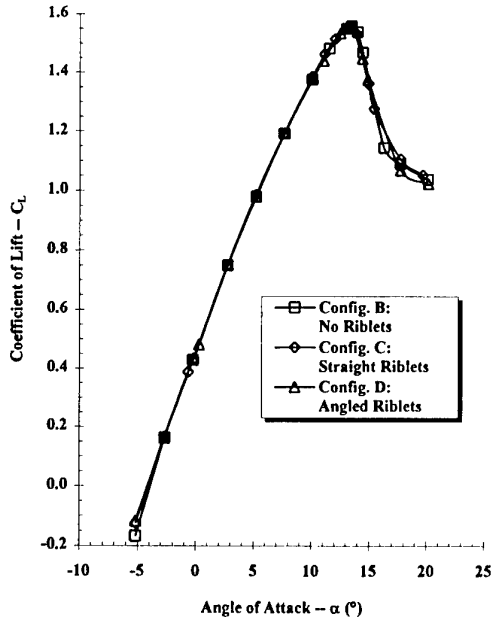

(a) Lift Characteristics

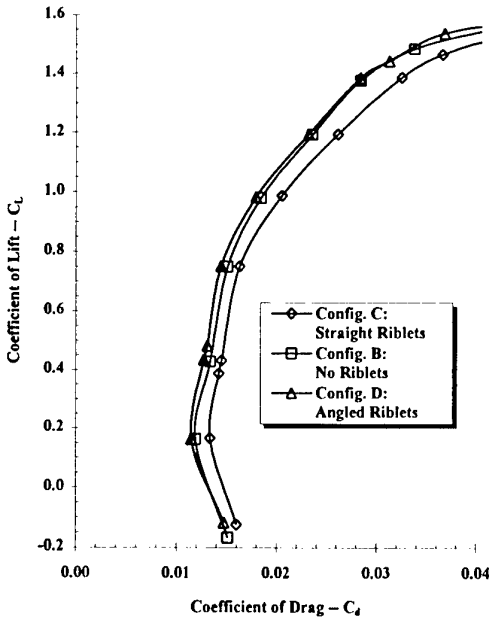

(b) Drag Characteristics

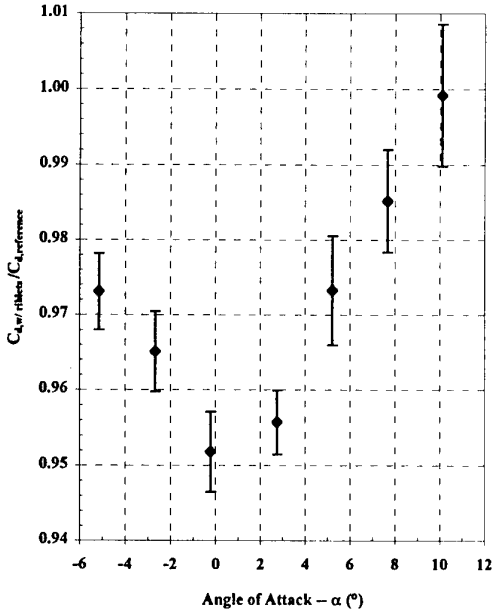

(c) Drag Ratio, Configurations B and D

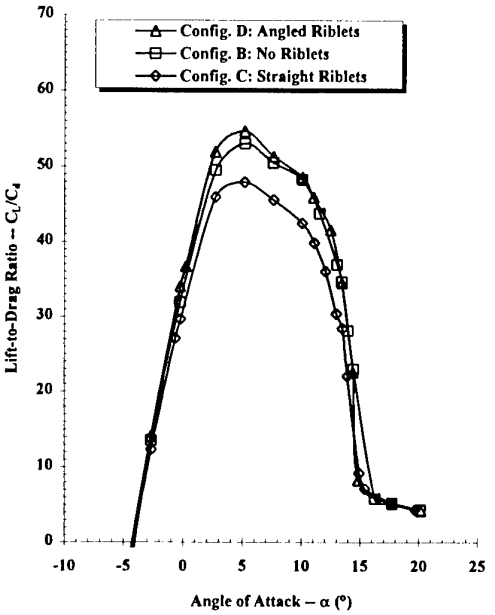

(d) Lift-to-Drag Ratio

Fig. 12 Influence of riblets on the aerodynamic characteristics of the S807 (NREL) airfoil with vortex generators, configuration B, C and D ($Re_c=10^6$).

To integrate the supersonic vortex generator in a convergent-divergent nozzle and to control the vortex strength, an expansion ramp with four rows of cavity VGs was designed as shown in Fig. 13. The expansion ramp is a part of a vectoring nozzle of rectangular geometry capable of adjusting the nozzle area ratio as well as the vectoring angle on the expansion ramps. The *smart* VG configuration is equipped with a deflecting flap (or a lid) which is actuated by a stepper motor. In each row four or five cavity VGs are integrated on to the expansion ramp. The vortex generators in a row are actuated in unison, as we are essentially dealing with a two-dimensional flow as well as the mechanical complexity of individual actuation of 18 vortex generators was prohibitive. The four rows of VGs are however, independently actuated, as the nozzle pressure ratio and the geometry are maintained. The feedback sensors for the experimental study are:

a) 8 Kulite (surface-mounted), high-frequency response, miniature pressure transducers (for separation and shock location control)

b) balance load cells in the axial and pitch directions of the vectoring C-D nozzle

c) microphone array (for jet noise control)

To signal the cavity exposure to the stepper motor and the extent of the VG depth, a *real time* sensor data stream into the controller is needed. The controller may serve several modes of performance optimization. For example, controllers can be developed (work in progress) with:

a) expansion ramp separation alleviation mode

b) gross thrust maximization mode (in -x or -z)

c) noise suppression/directivity management mode

d) acoustic feedback control mode (via frequency modulation of the VG flaps).

The coupling and inter-dependency between the performance optimization modes (for example, a and b, or a and c) shall be experimentally investigated. A tentative test matrix parameters and their range for the smart nozzle research are shown in Table 1.

Nozzle Pressure Ratio: 2.0, 2.5, 3.0, 5.0, 8.0, 10.0
Cavity Deployment Angle: 4°, 8°, 12°, 16°, 20°, 24°
Nozzle Area Ratio: 3, 4
Pitch Vector Angle (on the instrumented ramp): 0°, 20°
Individual & Multiple Row Deployments: 15

Table 1: Parameter range in smart nozzle research

The cost function in the optimization routine can be:

a) streamwise displacement of the shock in the nozzle
b) gross thrust component maximization, F_{gx}, F_{gz}
c) jet noise intensity/directivity management
d) dominant frequency cancellation in acoustic feedback control mode

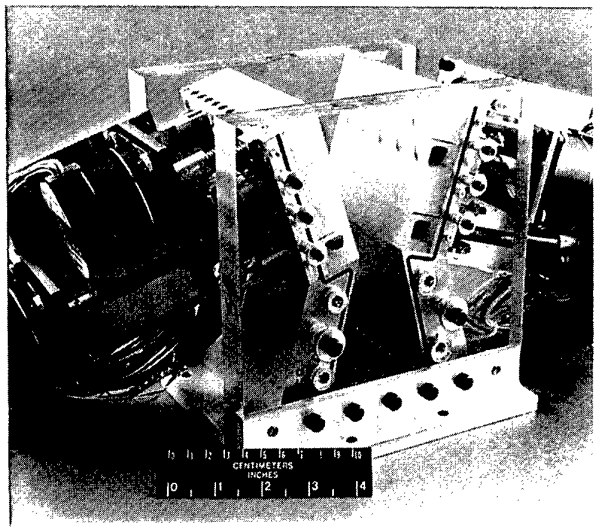

a) smart nozzle hardware assembly (4 stepper motors)

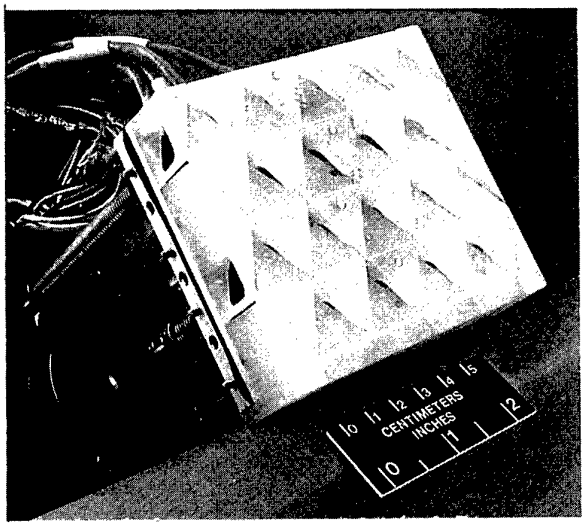

b) Four rows of VGs and 8 Kulite transducers

Fig. 13 Smart supersonic nozzle laboratory hardware

5. FUTURE WORK & RECOMMENDATIONS

The active flow control nozzle research by our team has reached the *smart* phase, as noted in the previous chapter. In addition, we are currently investigating the physics of streamwise vortex generation and evolution inside a turbulent supersonic boundary layer with neutral, positive and negative pressure gradient. This is aimed as a fundamental (theoretical and experimental) research for better understanding of the nature of viscous flow control in supersonic flow. In particular, the adverse and favorable pressure gradient environments to be modeled shall represent the aircraft inlet, nozzle, compressor and turbine blades. We believe the future development of smart components in aircraft gas turbine engines depend heavily on our understanding of the fundamental flow physics in realistic environments dominated by random and periodic unsteadiness, 3-D separation, corner flows and wall regions, blade tip and shock interactions.

6. ACKNOWLEDGMENT

The author wishes to acknowledge the invaluable contributions of his former and current students and colleagues at the University of Kansas, NASA-Langley Research Center and NASA-Lewis Research Center. In particular, professors Ray Taghavi and Ron Barrett, Dr. Kyle Wetzel and Mr. Richard Hazlewood have collaborated in smart vortex generator research. Mr. Daniel Cler of LaRC served as the project manager of active control nozzle research and he made valuable contributions to the program.

7. REFERENCES

1. Gad-el-Hak, M. "Modern Developments in Flow Control," *Applied Mechanics Reviews*, Vol. 49, No. 7, pp. 365-379, July 1996.

2. Barrett, R.M., "An Experimental Evaluation of Smart Tetrahedral Vortex Generators," Doctoral Dissertation, Aerospace Engineering Department, The University of Kansas, Lawrence, May 1993.

3. Barrett, R.M. and Farokhi, S., "Subsonic Aerodynamics and Performance of a Smart Vortex Generator System," *AIAA Journal of Aircraft*, Vol. 33, No. 2, pp. 393-398, March-April 1996.

4. Farokhi, S., Taghavi, R. and Barrett, R.M., "Pressure Drag Reduction Concepts on a Maneuvering Submarine," Invited Presentation, 10th European Drag Reduction Working Meeting, Berlin, Germany, March 19-20, 1997.

5. Farokhi, S., Taghavi, R., Barrett, R.M., Sherwood, T.S. and Mirsafian, S., " Active Vortex Management Concepts for Maneuvering Submarines," Proceedings of the Third International Symposium on Performance Enhancement for Marine Applications, Newport, Rhode Island, pp. 55-60, May 1997.

6. Farokhi, S. and Taghavi, R., "Smart Supersonic Vortex Generator," US Patent Number: 5,598,990, February 4, 1997.

7. Farokhi, S., Taghavi, R. Hazlewood, R., Cler, D. and Lamb. M., "A Novel Supersonic Vortex Generator," Paper presented at the Joint ASME/JSME Fluids Engineering Conference, Hilton Head, South Carolina, August 1995.

8. Cler, D., Lamb, R., Farokhi, S., Taghavi, R. and Hazlewood, R., "Application of Pressure-Sensitive Paint in Supersonic Nozzle Research," *AIAA Journal of Aircraft*, Vol. 33, No. 6, pp. 1109-1114, Nov.-Dec. 1996

9. Briedenthal, Jr. R.E. and Russell, D.A., "Aerodynamics of Vortex Generators," NASA-CR-182511, Dec. 1987.

10. Pearcey, H.H., "Shock-Induced Separation and Prevention by Design and Boundary Layer Control," in Lachmann, G.V., *Boundary Layer and Flow Control*, Vol. 2, pp. 1166-1344, 1961.

11. Wetzel, K.K. and Farokhi, S., "Development of High Lift-to-Drag, Low-Speed Airfoils with Coupled Vortex Generators and Riblets," Paper presented at the 13th AIAA Applied Aerodynamics Conference, San Diego, California, June 1995.

12. Wetzel, K.K. and Farokhi, S., "Interaction of Riblets and Vortex Generators on an Airfoil," Paper presented at the 14th AIAA Applied Aerodynamics Conference, New Orleans, June 1996.

13. Stephens, A.V. and Collins, G.A., "Turbulent Boundary Layer Control by Ramps or Wedges," ARL (Australia), Report A.85, 1954.

14. Tanner, L.H., Pearcey, H.H. and Tracy, C.M., "Vortex Generators; Their Design and Their Effects on Turbulent Boundary Layers," ARC (UK) Report 16487, 1954

15. Wheeler, G.O., "Means of Maintaining Attached Flow of a Flow Medium," U.S. Patent Number: 4,455,045, June 1984.

16. Wheeler, G.O., "Low Drag Vortex Generators", U.S. Patent Number: 5,058,837, October 1991.

17. Lin, J.C., Selby, G.V. and Howard, F.G., "Exploratory Study of Vortex Generating Devices for Turbulent Flow Separation Control," AIAA Paper Number 91-0042, 29th Aerospace Sciences Meeting, Reno, Nevada, January 1991.

18. Wetzel, K.K., "Interaction of Riblets and Vortex Generators on a Flat Plate and Airfoil," Ph.D. Dissertation, Aerospace Engineering Department, The University of Kansas, Lawrence, December 1995.

Meeting Discussions

Paper 45: **Smart Flow Control in Aircraft Engine Components and Component Interactions**

Author: S. Farokhi

Discussor: Walter O'Brien

Question: The flow control methods discussed are shown in one-dimenstional or external flow examples. Do you intend to do internal flow experiments (especially in adverse pressure gradients) where the effects of cascading and internal boundary layers can be examined?

Author's reply: Multi-dimensional flow control and adverse pressure gradient enviroments are more challenging and we intend to tackle these problems.

Question 2

Discussor: K.K. Chan

Question: Is there a size threshold for the VG devices to be effective?

Author's reply: In regular engines; i.e. macro-components, the proposed VG's could be tailed to fit, however in micro-engines, the flow control "rules" change.

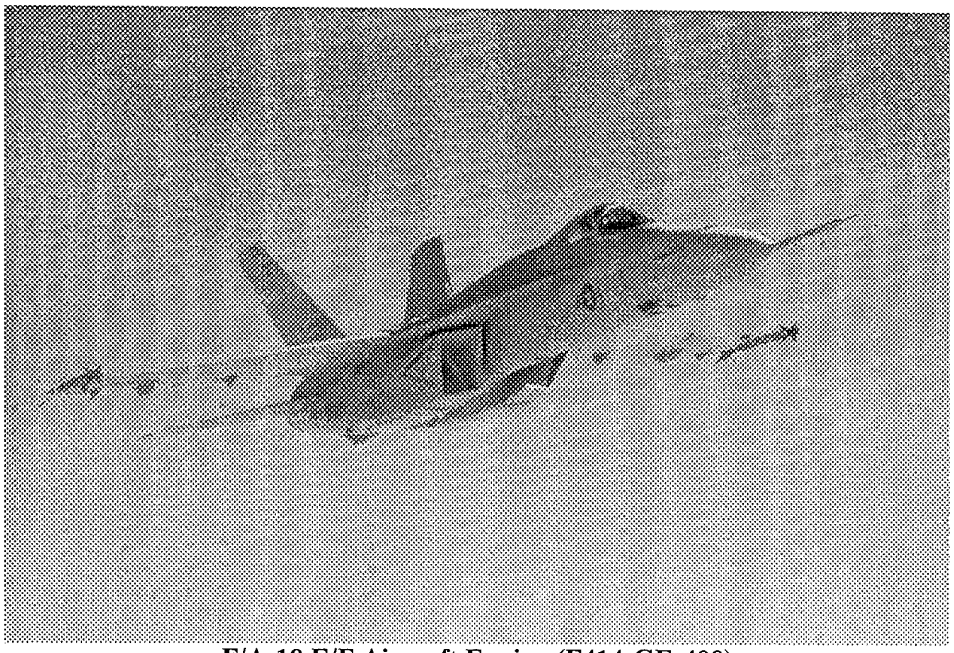

F/A-18 E/F Aircraft Engine (F414-GE-400) Design and Development Methodology

Robert Burnes
Don Blottenberger and Michael Elliott
Propulsion and Power Engineering
22195 Elmer Road
Building 106, Unit 4
Patuxent River, MD 20670, USA

Introduction

In the 1970's the United States Navy (USN) faced a dilemma. The F-4 Phantom and A-7 Corsair aircraft were aging rapidly and new threats were arising as technology advanced. To answer the call for a new attack fighter, the USN developed and deployed the F/A-18 aircraft. In 1987, the Secretary of Defense directed the USN to study advanced versions of the F/A-18 to face threats into the twenty-first century. This study resulted in the F/A-18 E/F. The F/A-18 E/F represents the next level in the evolution of the F/A-18 Attack Fighter as shown in Figure 1. From the beginning, the objective has remained stable; to define an affordable system taking full advantage of the cost benefits associated with a derivative system without compromise of mission capabilities.

Today with declining defense budgets, the F/A-18 E/F will be required to perform an increasing variety of missions as it replaces the F/A-18 C/D, A-6 and F-14 aircraft. Enhancements in the E/F include increased carrier recovery payload, larger mission radius, improved survivability and room for growth. The airframe is approximately 25 percent larger than earlier models to accommodate the increased internal fuel volume. To power the larger airframe and its inherent increase in drag is the General Electric F414-GE-400 engine. The F414 is the latest derivative of the F404, the engine in the F/A-18 A/B. Other F404 derivatives include the RM12 for the Swedish JAS39 Gripen, the F1D2 for the F117 Stealth Fighter, and the F412 which was being developed for the A-12 Avenger.

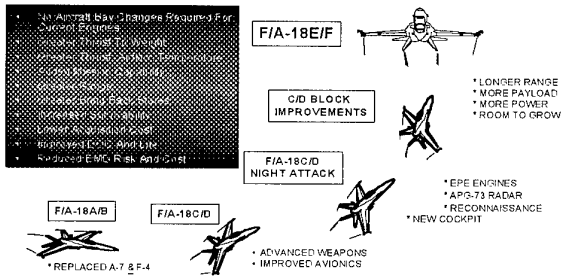

Evolution of the F/A-18 Attack Fighter
(Figure 1)

The A-12 Avenger program was a lesson learned for the USN. It was a fixed price, sole source development program where the F412 Engine was developed as Contractor Furnished Equipment (CFE). It, like the E/F program, was under a great deal of pressure as a required replacement for aging aircraft and its success was deemed necessary for the survival of Naval aviation. But the A-12's

Paper presented at the RTO AVT Symposium on "Design Principles and Methods for Aircraft Gas Turbine Engines", held in Toulouse, France, 11-15 May 1998, and published in RTO MP-8.

radical design and extensive state of art requirements did not allow for a risk-balanced design approach. The failure of the program provided the necessary catalyst for reform of the Navy's development philosophy. This carried through into the Power and Propulsion community for management and design of the F414-GE-400 engine. Affordability, Risk balance, risk management, full and open communication to the highest level, Cost-plus development, Integrated Product Teaming (IPT) and Government Furnished Equipment (GFE) were to be the cornerstones of the engine program.

The F414 engine has been developed under a cost plus award fee type contract to be GFE to Boeing, the airframer and integrator. The lesson learned by the F414 community was a Fixed Price type contract was too restrictive, inflexible and placed all the risk onto the contractor. A Cost Plus Award/Incentive Fee type contract was employed to help share the risk between the contractor and the government. Also, dissemination of USN requirements, risk sharing and an Integrated Product Team were more difficult in a CFE environment where the engine manufacturer was not a prime contractor. The USN wanted the flexibility to openly trade engine requirements using sound systems engineering processes at the engine level with participation of the airframe contractor. To ensure that integration with the weapon system was accomplished, an Interface Control Document and an Associate Contractor Agreement between Boeing and General Electric were required to define installation requirements and responsibilities.

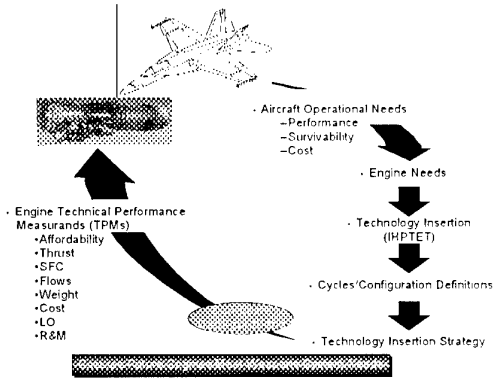

Configuration Strategy
(Figure 2)

Configuration & Requirements Definition

A conceptual design was developed before development could begin, considering the Navy's requirement for growth, performance and balanced risk, by a process similar to Figure 2. This conceptual illustration depicts how requirements and balanced technology insertions result in the functional design configuration. The aircraft operational needs are similar to those in Figure 1 and determine the overall engine performance required. Operational needs define requirements in terms of overall aircraft performance and support concepts (levels of maintenance, installation, fault isolation, etc). Engine-specific requirements are also considered. The baseline for F414 requirements was the engine had to be equal to or better in capability than the F404-GE-400. This encompassing requirement covered most of the design requirements, such as environmental concerns, transient times, reliability and maintainability, and was the fallback position for configuration trade studies. Mandated requirements were factored in, such as Live Fire Testing and Damage Tolerance Design, along with hundreds of F404 and F412 Lessons Learned. After all these, opportunities for improvement were determined still keeping in mind the balanced risk approach. Some of these included the addition of the Full Authority Digital Electronic Control (FADEC), Ceramic Matrix Composite (CMC) variable exhaust nozzle components and maintainer friendly, pro-longed life, augmentor.

For the first time in USN engine development, the F414 would be required to meet both vulnerability and susceptibility requirements. In the past, these capabilities, or lack of, were accepted as is, but this engine would be required to perform to Live Fire Test Requirements such as full engine blade containment, fuel ingestion and ballistic testing as well as meet radar cross section requirements to complete E&MD. Integration of these performance areas and the associated roll-up to the weapon system level provided the greatest challenge to a GFE development in that dissemination of subsystem requirements is difficult to determine and manage.

Once requirements were defined, an assessment of available technologies was used to develop a transition plan given the technologies' level of maturity, the level of acceptable risk and definition of cycles and required component performance. The resulting candidate configurations were then evaluated based on their technical performance capabilities and their suitability to Weapon System needs.

The F414 development plan (Figure 3) was essentially what General Electric proposed as Growth II+, with minor modifications. First, the Navy would require 10,000+ hours of development testing where 3500 test hours and 1500 ASMET durability hours would be required prior to First Flight in late 1995 to front load the test schedule. The Navy also changed the method and length of durability testing. For instance, prior to F414, flight qualification required 50-150 hours of Durability Proof Testing (DPT) at elevated temperatures as much as 35 degrees above maximum turbine temperatures. In this program, an Accelerated Simulated Mission Endurance Test (ASMET) run at Redline temps for 300 hours was required for flight qualification. For Limited Production Qualification (LPQ), a one thousand hour ASMET would be required instead of the traditional 300 hour DPT and 600 hour ASMET run on the F404-GE-402 program. F404 field influences also drove changes in development and design. F404 critical part failures of the early 90's drove the introduction of Damage Tolerant Design into the F414 Critical Parts for design margin over traditional Low Cycle Fatigue (LCF) methods. F404 investigations also revealed that Navy methods for LCF life verification were inadequate and could not prevent F404 field failures. From this the F414 developed a Life Methods Verification program which consisted of Crack Growth as well as LCF rotor spin testing in lieu of traditional spin pit and full engine testing. Additionally, a cost plus program environment alleviated any need that the Contractor would have for practice tests since any testing would now be used for part qualification. These changes allowed some efficiencies in full engine testing in that the originally proposed 14 ground test engines could be reduced to 12 plus an additional full engine's worth of spare hardware. A 50 percent spares lay-in for flight testing was also mandated for a total of 21 flight test engines to support seven aircraft.

Program Management

"An Integrated Design Approach". To truly incorporate an integrated design approach, Government and Contractor program management had to decide on team structure to allow for effective communication. This

philosophy led to the forming of Integrated Product Development Teams (IPDTs or IPTs). These teams formed a vehicle for concurrent engineering and effective communication. They are formed and disbanded as required,

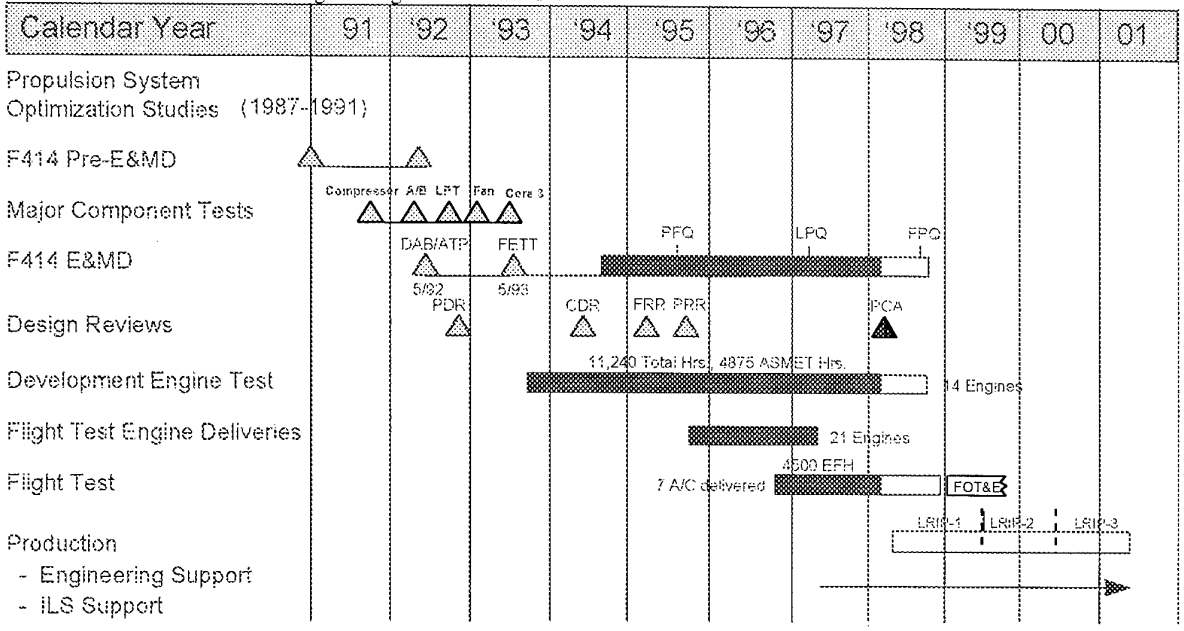

F414 Program Plan
(Figure 3)

co-located to the maximum extent, involve all stakeholders, and are led by co-leadership from areas including engineering, logistics, manufacturing, etc. To guide each team, each has a schedule, technical requirements, and common goals. They meet as necessary to review status of planned actions, current activities, schedule updates, risk assessments, and new issues. These teams may include sub-tier suppliers as well. The results include reduction in cycle time and improved quality and producibility. An example of successful IPDTs and Concurrent Engineering is the LPT blade design which resulted in cycle time reduction by twenty weeks and casting yield increases from traditional blade development by approximately 50% (Figure 4). This was primarily due to the use of concurrent engineering. Concurrent engineering is parallel design and integration efforts vice a series of design efforts.

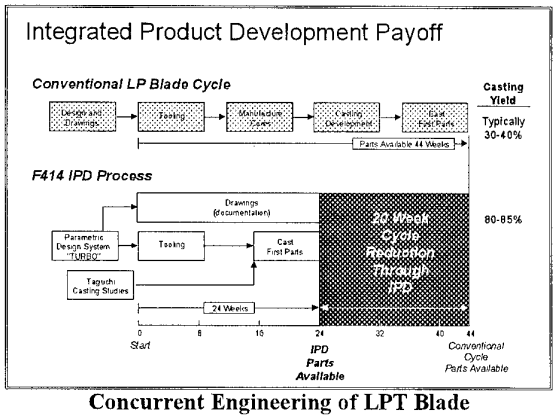

Concurrent Engineering of LPT Blade
(Figure 4)

One of the benefits resulting from Base Re-Alignment and Closure initiatives was to co-locate in one complex much of the Navy IPT. Now F414 program management, design and development, and flight test teams are generally co-located at the Patuxent River Naval Air Station. The BRAC 93 also created a funding line for construction of a Power Systems Evaluation Facility (PSEF) at Patuxent River where the government can run lube systems test, conduct small engine tests, and perform fuel/oil analysis.

12 Management Initiatives. At the onset of the program, GE F414 management, with years of development experience and the F412 program behind them, developed a set of Twelve Management Initiatives intended to lead the team to eventual success (Figure 5). Proposal to the Government Team resulted in buy-in at every level and ensured success. Technical requirements were defined eight months prior to the E&MD letter contract and the Engine model specification was negotiated and approved six months prior to the E&MD letter contract. The requirements definition and specification development required several negotiation conferences where every line of the specification was discussed to ensure that both Contractor and Navy personnel understood and agreed to the intended meaning. Compromise and/or clarification of the language was completed, or the item was deferred, until issue specialists could be consulted. This was a lesson learned from F404 experience during which misunderstanding and different interpretation of requirements resulted in legal action. To continue this level of Teaming, early and frequent design reviews were established to promote communication. This resulted in ~100 formal reviews and ~300 informal reviews. Of these, approximately eighty (80) percent were held prior to First Engine To Test (FETT).

Risk Management. For the F/A-18 E/F and F414, Risk Management and balanced risk started before any metal was turned. For example, the twelve management

initiatives were established as a set of guidelines to address risks and promote success. For risk mitigation and cost savings, all E&MD manufacturing sources were identified as future production sources. The added benefit of this approach was that it promoted personal ownership and a sense of Team participation at the supplier level. Proven materials and processes were incorporated in baseline early and next generation materials and processes were explored along parallel paths for risk abatement. As an example, advanced turbine materials were tested along with baseline parts in a rainbow wheel configuration throughout early development as risk mitigation for high turbine temperatures.

Leadership team and IPD teams deal with risk as part of daily business. A risk could be a potential redesign that would significantly increase weight and jeopardize a requirement or it could be a miscommunicated test result.

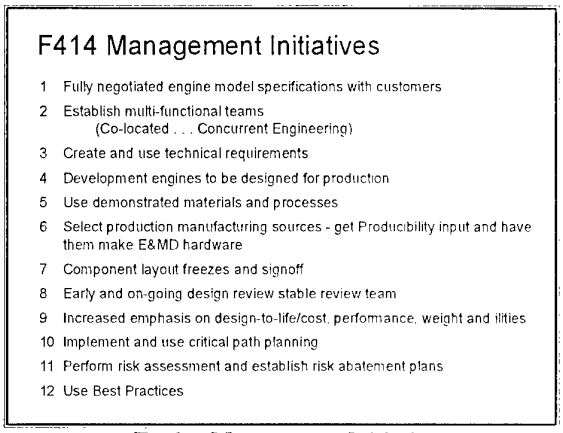

Twelve Management Initiatives
(Figure 5)

To deal with risk, a risk management process was developed that includes four basic principles. The first is risk identification. Certain risks surface obviously, like test failures, supplier problems, and design changes, while other risks must be brought to the surface by the IPD teams or leadership team. Tools used to identify risks include intuition, lessons learned from other programs like the F404, lessons learned from history of the F414, trends and forecasts, variation simulation and checklists. After identification, a risk analysis is performed to quantify the risk. An uncertainty and consequence level is established and overall risk level is quantified. Uncertainty of risk is the chance that the risk will happen. The consequence is the effect of the risk on the program requirements, be it technical, cost, schedule or political. Now that the risk is identified and analyzed, what must be done to minimize, manage or eliminate the risk? The third principle is risk planning. The responsible IPT can develop plans of action, redesigns, conduct trade studies, develop parallel paths, re-negotiate requirements or develop back-up plans to deal with the risk. The last principle is risk tracking and communication. Risk mitigation plans need to be monitored and reported, periodic team technical and programmatic reviews are needed and risk status must be reported to appropriate team members and management personnel. The risk management process is a continuous process that requires feedback through all steps to ensure effective communication and reduction of risk.

Through technology programs such as ManTech, Internal Research and Development activities and IHPTET or GE23A, transition opportunities are examined to maintain risk abatement options or reduce costs. The F414 has become known for successful technology transitions especially in areas such as Lean Processes.

Earned Value Management (EVM). An Open Plan (Critical path) planning system was used initially to setup the F414 cost and schedule, linking it to EVM. EVM is the Cost and Schedule Control System selected to satisfy the contractual requirements for cost accounting. For the F414, it measures GE against the cost and schedule baseline. The status is reviewed at monthly meetings where cost center managers from GE come together to report out on their individual cost center EVM numbers. In addition, every year the cost and schedule baseline is reviewed and revised at a "bottoms-up" review that incorporates funding changes and new schedule requirements into the baseline. The EVM measures contractor progress against the latest baseline.

Communication and Teaming. The foundation of the F414 engine program is unquestionably Communication and Teaming. At the F/A-18 E/F program level, full and open communication has always been a requirement. To function, the F414 program needed an immediate and continuous flow of information. Formal and informal avenues for communication were: a continually updated information management system which provides the USN with the same program management information as is used by GE Leadership; a risk advisory board which continually assesses program risk and evaluates means to mitigate that risk; a non-attributional Program Independent Analysis where Company or Government employees and officials can express concern areas which will then be investigated and presented to Navy program management; quarterly Program Management Reviews; monthly Technical Reviews; monthly Earned Value Management Reviews and daily communication.

To answer the Navy Requirement for an electronic Information Management System, GE provided an on-line Microsoft Office Compatible System called Distributed Engine Program Information and Control System or DEPICS. DEPICS is divided into Program Performance Measurands (PPMs) and Technical Performance Measurands (TPMs). PPMs track delivery of Contract Deliverable Requirements List items, Earned Value Management, Risk, Schedules and Plans, Support Equipment, and Formal Action Items just to name a few. TPMs track Test Schedule, Weight Status, Engine Performance, hardware Design To Cost (DTC) predictions, Reliability, Development and Material Review Board (MRB) actions and others. Each TPM or PPM contain multiple reports. For example, the Weight TPM has fourteen separate reports (by engine component or function) that role up into a system weight. Each item in these reports can be interrogated to understand potentials for change and variability.

To promote continual evaluation and reporting of Program Risk, the program requires F414 Team participation in the Program Risk Advisory Board (PRAB) process where management, engineering, logistics and test Team members must report on potential or existing risk items, all potential outcomes, uncertainty in the outcomes and consequences in terms of magnitude of the impact to Technical, Schedule and Cost performance. The PRAB meets quarterly at a minimum and outbriefs the Navy Program Manager.

The Program Independent Analysis (PIA) Team is an independent group which performs comprehensive evaluations of any and all areas that can affect program execution based on suggestions from Team members or observers. The intent is to provide a non-attributional means to constructively assess concern issues and the effectiveness of effort underway to address them and suggest alternate courses of action if required. The PIA meets quarterly and outbriefs the Navy Program Manager.

Throughout the design and development, technical reviews have been held monthly to provide the team with a detailed status of the design and identify/discuss any risk areas or current events. These technical reviews are attended by a cross functional group, including Boeing, General Electric and USN personnel from functional areas including engineering, logistics, manufacturing, testing, cost analysis, and program management. These reviews are most

	Fan	Core	Turbines	Afterburner	Controls
Design Base	• F404-400/-402 • F404/RM12 • F412	• F412 • F404-400/-402 • GE23A	• F404-400/-402 • F404/RM12 • GE23A	• F404-402 • F404/RM12 • F110-129 • F120	• F412 • F110-129
Technology Improvements	• +16% Airflow • Improved Bird Tolerance • Stage 2/3 Blisks • Improved durability	• Improved Stall Margin • Stage 1/2/3 Blisks • Improved Durability	• Improved Aerodynamics • Improved Materials • Improved Durability	• Improved Cooling • Improved Maintainability • Improved Durability	• Dual Channel Full Authority Digital Electronic Control (FADEC) • Electrical Throttle

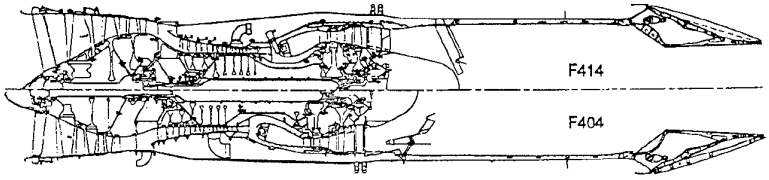

Comparison of F414 to F404
(Figure 6)

commonly held at General Electric in order to make available the detailed engineers to answer questions and concerns. However, reviews have been held at government facilities from time to time to take advantage of government facilities and for convenience. Within the last year, the technical reviews are presented by General Electric electronically through computer images. This allows the team to make animated presentations, show simulations "on screen" and serves to make better use of time.

With all these forums for communication, the best and most reliable is still the day to day discussions. For that, both government and contractor have to embrace the Teaming and IPT concepts. While the Contractor initially considered Teaming to mean Government interference and micro-managing, today very few decisions are made on either side with out peer discussions. Gone are the days when the only lines of communication were within the organization and information funneling. The Government F414 Team is managed using a Work Breakdown Structure (WBS) similar
to that of the Contractor. In this manner, tasking throughout the Team is coordinated. The benefit of this is the multi-disciplined avenues of communication. At all levels, the teams now communicate, GE Turbine expert to Navy Turbine expert discussing durability, GE and Navy F414 Chief Engineers discussing asset management and GE general manager and Navy PMA discussing program execution and system level risk. Each has the level of detail required to execute their function.

Government/Contractor Teaming is not only possible it's imperative in today's acquisition environment. Once past the original reluctance to share information at the lowest levels, the Navy and Contractor IPT's began to act as a true Team and utilize the tools that each member brought to the Team. An example of this is the redesign effort for the Combustor Fuel Manifold after its corrosion induced failure. Once the failure was identified during qualification testing, Navy materials personnel joined GE's Team working the problem with the sub-vendor and the redesign was qualified using another Navy facility while GE resumed the engine test to qualify the rest of the engine hardware. In past developments, the contractor would have been left to work the problem alone under intense government pressure never realizing that there were alternative design tools and qualification methods available. The resultant impacts would have been cost and unrecoverable test schedule delays. All investigations and redesigns of the F414 are handled similarly.

The Systems Engineering Process

The F414 engine program has taken a systems engineering approach to design and development. The approach entails a detailed analysis of requirements, functional analysis and allocation of requirements and resources, and synthesis of the system meeting those requirements and constraints. The requirements came from a changing military environment anticipated for the next several decades. There is an aging fleet of F-18 C/Ds and F14s. A new fighter with increased capability and less expensive operation and support costs was required. The F414 was designed and developed to propel just such a platform, the F-18 E/F, into the next century. Figure 6 displays the improvements from the F404 that the F414 design incorporated.

The last two steps in the systems engineering process, functional analysis and allocation and synthesis, encompass the design and development cycle. The design and development cycle include the preliminary design, component and rig testing at the component level, detailed design and testing of the resulting system. In analyzing and controlling the process, many tools have been used to aid in analyzing risk, technical and cost, and tracking status of the program. A few of these tools are configuration management, technical reviews, trade studies and risk management.

Configuration Management

Functional baseline configuration management was turned over to government control after the team, government and contractor, had agreed to a model specification. The functional baseline takes the form of a performance specification that details what capabilities the system must have to meet user requirements, how the system must integrate into the airframe and avionics systems, and how the contractor must test to demonstrate capabilities of the system. The agreed to specification was then included in the Engineering Manufacturing and Development contract and any changes had to go through the government functional baseline configuration

management process. This process is the Specification Change Notice (SCN) process and entails the contractor suggesting the specification change to the government and the government either accepting or denying the change. In a teaming environment there are few surprises and normally changes are agreed to in concept before the paperwork is submitted.

The allocated baseline is still under the control of General Electric. This means that although changes must be coordinated with the government, General Electric is free to

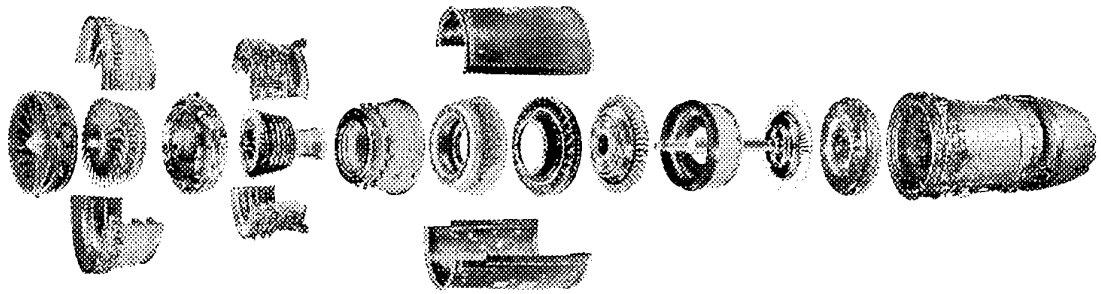

Expanded View of F414-GE-400 Engine
(Figure 7)

make changes to the allocated or physical configuration so far as all changes get qualified to functional specification guidelines. The government did have significant input into the establishment of the allocated baseline. A Preliminary Design Review (PDR) was held early in the EMD phase of development to form the original physical configuration baseline. Then, a few years later, a Critical Design Review (CDR) was held to reestablish the baseline. Throughout the process, GE held allocated configuration control and made changes to the baseline by way of Change In Designs (CIDs) which were coordinated with the government.

Physical Configuration Audit (PCA)

The Physical Configuration Audit (PCA) is the milestone used to establish confidence in the contractor's allocated baseline and readiness for production. It is typically accomplished near the end of EMD or early in production on production hardware. It involves reviewing the technical data package of a configuration item for completeness, correctness, flowdown, quality and proper documentation of manufacturing tracking. Traditionally it is the time when the government takes allocated configuration control and starts the government Engineering Change Proposal (ECP) process to change the newly established baseline. The F414 tailored the PCA process to best utilize its benefits. An integrated contractor/government team was formed to plan the PCA, organize the inspection teams and set exit criteria for the PCA. Forty (40) F414 Configuration Items (CIs) were selected for PCA from the list of over 2000 F414 CIs. The items were selected based on the following criteria: (1) F404 parts that showed manufacturing challenges; (2) F414 parts that had been changed during development; (3) Particularly complex parts; or (4) Randomly selected items from the population. Each individual PCA, completed at the corresponding manufacturing firm, included floor tracking and process examination as well as drawing to part comparisons and measurements. The teams included engineers, logisticians, Technical Data Package (TDP) experts, and quality personnel from the USN, GE and the sub-vendor, if different from GE.

The F414 PCA is on schedule for completion before the first LRIP delivery in July 1998. The team has identified and closed out several concerns that may have effected production or operation of the engine. In total, the team has closed out over 400 chits on the 40 configuration items.

Tailoring the PCA process to the F414 has proven highly beneficial at reducing manufacturing risk and improving communication between GE, the CI vendor and the USN. The F414 plans to continue funding for a follow-on PCA to begin in June 1998 and extend beyond the time that the USN will assume configuration control of the allocated baseline, sometime before full rate production.

Support Engineering

The F414 engine will be installed in F/A-18 E/F aircraft operated from Naval Air Stations (NAS), Carriers, and at forward bases overseas. With this extensive range of operation, support of the engine was a large concern. To deal with supportability cost and risk, support, maintenance and fleet personnel were included in the design and development process from the start of the program. Actual F404 maintainers and F414 Fleet Introduction Team (FIT) maintainers performed a maintenance demonstration where they went to GE and completely disassembled and reassembled an engine to demonstrate predicted maintenance times and to point out opportunities to improve the maintenance and support of the engine. It is also common for the technical layouts of hardware after official tests to be attended by support, maintenance and fleet personnel. It gives them a look at real hardware and gives the design engineers a conduit for communication with the people who will ultimately perform maintenance and support the engine.

The management philosophy was to initiate and maintain a Logistics Support Analysis (LSA) as early in the program as possible. This LSA influenced early design decisions and established a means of capturing Failure Modes and Effects Criticality Analysis (FMECA) data and Reliability Centered Maintenance (RCM) data to validate and/or update life and maintenance predictions. This data was gathered and updated several times through the E&MD effort and was fed into the comprehensive life management program.

The life management program, centered around the ASMET endurance tests, integrates a detailed analytical, theoretical and practical analysis of engine systems and components with the LSA, FMECA and RCM data to establish and maintain life limits, validate specification life and fatigue requirements, and provide input into the maintenance planning.

The maintenance planning includes buying and implementing support equipment, planning regular and

unscheduled maintenance tasks, and developing and implementing repair techniques as needed. Starting this planning and analysis early in the development process has allowed for the team to look at operation and maintenance of the engine and factor those costs and challenges into the early design of the engine. The result of this thinking was substantial savings from a common SE package used for both development and production.

Design Overview

The F414, shown in exploded view in Figure 7, is a 22,000 pound thrust class, low bypass, augmented turbofan engine. It consists of a front frame with Inlet Guide Vanes (IGVs), a three-stage Fan driven by a single stage Low Pressure Turbine (LPT), a seven-stage Compressor driven by a single stage High Pressure Turbine (HPT), an annular Combustor, an Afterburner (AB), and a Variable Exhaust Nozzle (VEN). Each major section is modularized and there is an accessories package.

The core: the Compressor, Combustor, and HPT, was developed initially for the F412 engine. The Combustor incorporates a multi-cooling hole, annular liner. The HPT is a single stage, with monocrystal blades and nozzles coated with thermal barrier coating (TBC) for increased fatigue life at temperature.

Blisk Technology
(Figure 8)

Blisk Incorporation

The "Blisks" used in the fan and in the compressor are a derivative of technology introduced by GE on the T700 engine program in the late 70s. A blisk is a single structure that combines the traditional disk and blades (Figure 8). When the F414 engine program was launched, engine weight was recognized as a major design consideration. Blisk designs were selected as a major weight reduction with added benefits. This weight savings results from eliminating the added weight of the blade and disk dovetail joint and the structural weight required to support it. As a benefit, performance was improved over conventional bladed disks by eliminating leakage paths through dovetails, ensuring non-interrupted hub flow paths and reducing interstage cavity windage losses. Eliminating dovetail leakage also lowers compressor rotor temperatures, thereby improving the rotor life. Another benefit was elimination of the fan stage 2 and 3 dovetails, where the F404 had experienced dovetail fretting problems resulting in major redesign efforts. Blisk airfoils are designed to minimize vibratory stresses at the leading edges where the airfoils are most likely to sustain foreign object damage (FOD). A detailed life cycle cost (LCC) analysis was completed using F404 field data on airfoil FOD incidents. LCC studies showed that blisks do not increase life cycle costs of the F414 engine. As for repairs, blisk airfoil repairs will range from simple clipping and blending of airfoil edges, to weld repair of more seriously damaged airfoils.

Damage Tolerant Design (DTD)

In 1992, the F404 experienced forced inspections, life reductions and bare firewalls after critical rotating part failures such as its stage 1 fan disk, and turbine cooling plate. This caused early part retirement, added fleet maintenance and unplanned spare parts procurement. The resultant dissatisfaction of fleet customers and the disturbing realization that there was not enough conservatism in our design methodologies to account for mission usage changes, materials properties variation, etc., changed the way USN Propulsion and Power managed critical part lives and directly influenced design of the F414 rotor components. DTD is a design methodology that requires a part to be designed to crack propagation life, assuming an inherent flaw in the material. This means that the crack propagation life must meet the specification life limits. Fracture mechanics crack growth rates and methods were demonstrated in spin pit testing where critical rotating parts had flaws introduced at critical locations. The F414 embraced DTD and included it into all critical part design. This meant accepting some additional weight in the disks and blisks as well as support structures for these components in trade for reduced stress levels. The payoff is greater confidence that the parts will meet specification life, higher resulting low cycle fatigue life, and more importantly, an inherent level of conservatism to guarantee a safer engine for the fleet. Figure 9 shows the hardware changed due to incorporation of DT and compares the Stage 1 fan disk with and without DT.

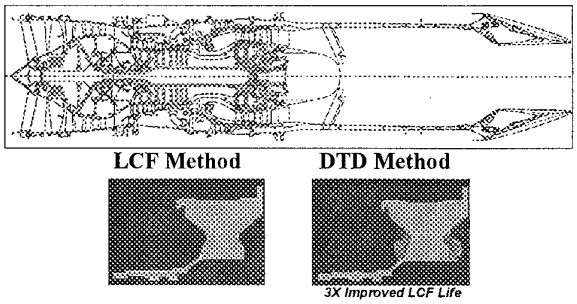

Fan Stage 1 Disk
DTD Hardware
(Figure 9)

Control Modes

Fuel flow is modulated to maintain the scheduled corrected Fan speed, and VEN area is modulated to maintain the scheduled Core Pressure Ratio (CPR). The primary benefits of this approach are accurate maintenance of stall margin and repeatable afterburning thrust as the engine deteriorates. As an engine deteriorates it will migrate onto compressor speed and turbine exit temperature control, similar to the F404 primary control mode. Backup control modes also exist in the event that critical parameters fail. The FADEC can also schedule the AB pilot fuel flow, extending the reliable AB lightoff envelope.

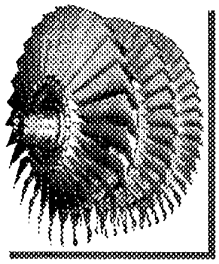

Fan Module

The F414 Fan has the highest pressure ratio of any three-stage Fan designed by GE Aircraft Engines for a production engine. This component is a derivative growth version of the F404 three-stage Fan with higher airflow. Damage tolerant design is applied to the disks for increased durability and reliability. The stage 1 rotor aspect ratio has been kept low to enhance bird strike and FOD resistance. The rotor is comprised of a bladed titanium disk for stage 1 with blades attached by dovetail joints. A tandem titanium blisk has been selected for Stage 2 and 3 based on weight, cost, performance and maintainability trade-off studies. The stator is comprised of an axially split casing and three stages of shrouded titanium vanes. The titanium casing has a silicone rubber abradable coating over each rotor to achieve clearance control and reduce blade rub stresses. This coating resulted as a lesson learned after the F404 experienced stage 2 blade tip cracking.

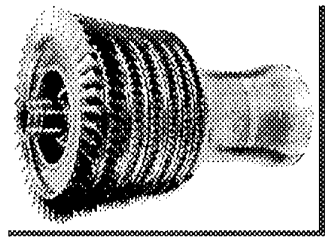

Compressor Module

The Compressor is a seven-stage design with the first three rotor stages changed to blisks. Inconel has been substituted widely for improved temperature capability and variable vane lever arms have been changed to Inconel to provide increased fatigue capability. The Inlet Guide Vane (IGV) and stage 1 blades were designed for enhanced bird ingestion capability by increasing the axial spacing between the vanes and blades based on F412 compressor design and demonstrated results in RM12 bird ingestion testing. The four rotor structural components; the stage 1/2 blisk, forward stub shaft, stage 3 blisk, and stages 4-7 spool, are bolted and rabbetted together at a single point. The Compressor stator is comprised of a steel forward case with anti-corrosion coating and a cast rear Inconel case. The cases have abradable coated flow path surfaces for rub tolerance and are split on a horizontal plane to allow access to the Compressor rotor blading. The IGV, stage 1, and stage 2 are shrouded variable vanes. Stage 3 through stage 6 vanes are comprised of 12 sectors per stage. Each sector has fixed vanes stabbed and brazed to the inner and outer bands.

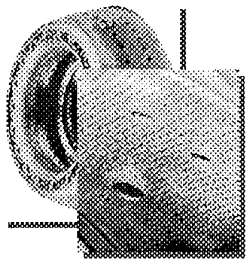

Combustor Module

The Combustor is derived from the F412 and F404 Combustors with major improvements including "ruggedization" features on fuel nozzles, improved fuel nozzle thermal management and an advanced multi-hole cooling pattern design. The Combustor system includes the Combustor liner, fuel nozzles and a single ignitor. Fuel nozzles include design modifications to reduce Combustor rumble, increase structural life and reduce carbon formation. The liner is an annular type with fuel injector cups and subassemblies: the inner liner, the outer liner, and the dome. The shells are multi-hole cooled to provide improved thermal control as demonstrated in the F412 and GE23A engines. The multi-hole pattern provides improved film and core cooling over the "nugget" designs therefore reducing liner temperatures, thermal gradients and cracking.

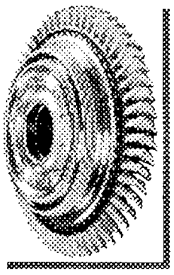

High Pressure Turbine Module

The HPT is based on the F412's single stage, monocrystal blade and vane design, with a physical vapor deposition thermal barrier coating (PVD TBC) on blades and vanes. Thin TBC has been added to the airfoils increasing durability and reducing the required cooling flow. The HPT nozzle assembly is a set of fabricated two-vane segments with the airfoils brazed to the inner and outer bands. Airfoil cooling is by internal impingement plus external film. The HPT rotor assembly consists of the disk with boltless blade retainers at the rim and bolted joints attaching the disk to the forward air seal/Compressor shaft. The aft shaft holds the No. 4 bearing between the high pressure and low pressure turbine rotors. The HPT blades are cast in a monocrystal material similar to the nozzle. The blade is cooled using high pressure Compressor discharge air which is ported through a combination of internal convection passages and external film holes. The HPT stator shroud and support design incorporates a thermally matched passive clearance control system. The F414 cooling plates improved the F404 design, which was apt to crack and propagate to failure as supported by field experience. The F414 improved the configuration by eliminating the bolts and altering the stress and temperature distribution to meet life requirements.

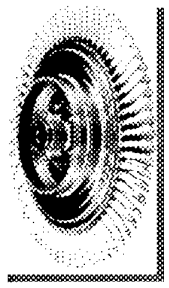

Low Pressure Turbine Module

The LPT nozzle is comprised of vanes cast in monocrystal material with TBC. LPT nozzle segments are cooled by fourth stage Compressor bleed air. This air is ported from the Compressor to the nozzle segments through the turbine cooling air tubes. The LPT rotor assembly comprises a disk with dovetailed blades, a forward seal/cooling plate, aft cooling plate, and an aft torque shaft assembly. The air cooled blades are cast in monocrystal material with TBC. The forward seals provide a passage for cooling air to cross between the turbine nozzle and the disk. The aft torque shaft assembly has a labyrinth seal on the aft side which controls flow and pressure in the C-sump. The torque shaft function is to transmit torque developed in the single stage rotor to the Fan driveshaft and as the attachment interface for C-sump rotating hardware. The LPT case is a one piece circumferential shell. The LPT shroud design has features which match the rotor thermal response for improved clearance control. The matching is done by thermally separating the shrouds from the case using separate shroud hangers and an increased mass case similar to the HPT.

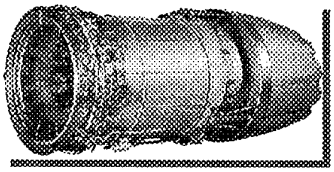

Afterburner Module

The Afterburner; augmentor and VEN, design is adapted from the F120 engine, using cooled radial flameholders and a central v-ring. The VEN is an improvement over the F404 design, using CMC material and improved features for maintainability. A flameholder system is used that can be serviced and maintained through the tailpipe without engine removal. Flexible fuel lines have been added to the AB fuel system.

The augmentor assembly consists of an AB case, an AB liner, a flameholder/spraybar system, a mixer and a contoured centerbody. The AB liner functionally provides a cooling wall between the case and hot combustion gas in the AB. The forward section provides the diffuser function. A lesson learned from the F404 was to design the liner for over two times the failed open nozzle pressures and to reduce or eliminate the liner aft dam cracking. To accomplish this, the F414 stiffened the liner and eliminated the aft dam damper wires. The air-cooled flameholder/spraybar system is based on GE's F120 design to accommodate the higher temperature environment of the F414.

The VEN is a converging-diverging type, very similar to the current F404 and RM12. It is a hinged flap design with fully modulating throat area. The VEN consists of primary flaps and seals, secondary flaps and seals and external flaps. The external flaps provide an external fairing that forms the boattail of the aircraft and is cooled by aircraft ambient flow.

Ceramic Matrix Composite (CMC) Seals

The original flap/seal primary and secondary configurations were identical to the F404. Early on in development, the calculations showed the F404's nozzle primary (converging) system would meet F414 life requirements with lower cooling flow, but the secondary (diverging) system would not. To significantly reduce part stress levels due to temperature gradients, a separate base sheet/structural backbone design was selected for the flaps and seals. This design also has added maintainability benefits by providing for flight line replacement of the life-limiting base sheet. However, simulated F414 mission testing on the AB prototype showed this design had inadequate life, even with the improved design and materials. A thermal stress model was constructed to match hardware conditions. Design iterations indicated a seal with a reverse curvature seal baseplate design would be able to solve the failure mechanism. Also, ceramic materials held strong promise for distortion-free operation in the secondary seal thermal environment. An AB prototype test was run with reverse curvature metallic seals in all locations except for one which carried a flat (uncurved) ceramic seal baseplate. The reverse curvature secondary seal design successfully met minimum life requirements with the hardware in serviceable conditions; suprisingly, the single ceramic part looked almost new. The condition of the ceramic seal at the end of the durability demonstration coupled with a considerable weight reduction potential provided incentive to make the entire set of flaps and seals out of CMC. Based on the results of that and additional operational and environmental tests, the CMC design was selected for the F414 secondary system.

Engine Control System

The F414 is controlled by a dual-channel, full-authority, digital electronic control (FADEC) system. This system controls Fan and Compressor variable geometry, VEN actuators, and fuel schedules for main and augmentor flow. This system also sends engine condition monitoring data to the aircraft's computers. The F414 FADEC incorporates advanced fault detection, isolation and accommodation algorithms to identify and adapt to system failures. The control system also has built-in test (BIT) software to provide electronic troubleshooting data to ground crews, thereby decreasing maintenance times. The FADEC architecture was chosen to provide the highest level of reliability and performance in a lightweight system. Each FADEC channel is a separate remote terminal (R/T). In addition, the aircraft to engine interface provides hardwired signals from each channel for all critical parameters since the aircraft 1553 bus is not flight critical. All sensors critical to control are dual coil or element and redundant signals are routed in separate harnesses. Each channel is a separate R/T on the 1553 bus and each has a dual redundant R/T interface. Through a cross channel data link the two channels exchange sensor and actuator feedback information. The cross channel data link is not needed however, for either channel operation and data link failure will not degrade the operation of either FADEC channel. This design approach allows the FADEC to start and operate on either channel. The F414 control system provides superior performance across the flight envelope, consistent performance as the engine deteriorates and more robust response to the loss of sensors in the gas path. Further, multi-variable control laws have been implemented in order to maintain control stability while achieving improved performance.

Thermal Management

In general, modern aircraft design concepts include the increase of aircraft heat load on the fuel to the engine. In order to address this issue, the thermal management bypass valve is engine mounted and control laws for bypass fuel flow management are contained in the FADEC. The algorithms use aircraft and engine fuel and oil temperatures along with engine speed to compute the necessary bypass fuel flow to maintain acceptable fuel system temperatures during the aircraft mission.

Static Structures

The F414 engine structure maintains the same basic structural, rotor support, and mounting arrangement as the proven F404 engine family configuration. The static structure of the engine provides load paths that transmit the maneuver generated inertial and gyroscopic forces, coupled with engine thrust to the engine mounts where they are reacted to by the airframe. Stiffness is also provided by the structure to maintain required radial clearances in the compressor and turbine. There are three major structural frames which provide support through struts for the inner engine flowpath, bearings and rotating hardware. The front frame is an anti-iced, bird strike tolerant structure which supports the No.1 bearing and controls the Fan inlet air with variable inlet guide vanes. The structural frame consists of a brazed fabrication of Inconel sheet, cast and wrought material, which has superior corrosion and strength properties. There are struts connecting the outer and inner structure which transmit bearing loads to the aft flange. The ice protection system within the front frame is similar to the proven RM12 and uses compressor bleed air and fan air in the front frame and centerbody.

The Midframe is the second structural frame and is a one piece structural titanium casting. This was changed

from Inconel (F404) to reduce weight while maintaining structural integrity. The third structural frame is the Turbine Frame. Another structural member is the Combustor case which consists of a cast diffuser and an inner case made of material with an additional 100 degrees F capability compared to the F404 case. The forged outer case provides increased damage tolerance. Another change from the F404 is the Outer Duct which is comprised of PMR-15 graphite composite material for reduced weight.

Bearing and Lube System

The mainshaft bearings, sumps and lube system are basic F404 designs with improvements based on lessons learned from fleet experience and other GE programs. There are three sumps (A, B and C Sump) that provide lubrication to five engine bearings. The A-Sump contains the No.1 Bearing which was modified from previous designs to incorporate a roller bearing to reduce LP system axial motion. The B-Sump contains the No.2 Ball Bearing and No.3 Ball Bearing. The C-Sump contains the No.4 Roller Bearing and No.5 Roller Bearing. One drastic difference in the bearing system for the F414 is that the No.4 Roller Bearing is inverted from the F404 design. This means that the inner race is mounted on the high speed shaft and outer race on the low speed shaft. This bearing is also larger then the F404, with increased load carrying capability. Due to these changes, the bearing is stiffer dynamically and runs with improved internal radial clearance control. This in turn reduces bearing loads and results in improved life for the bearing.

Test Program

The F414 test program incorporated F404 lessons learned and demonstrated certain important requirements early in the program to reduce risk, many before first flight. This gave the team more time to fix performance shortfalls and

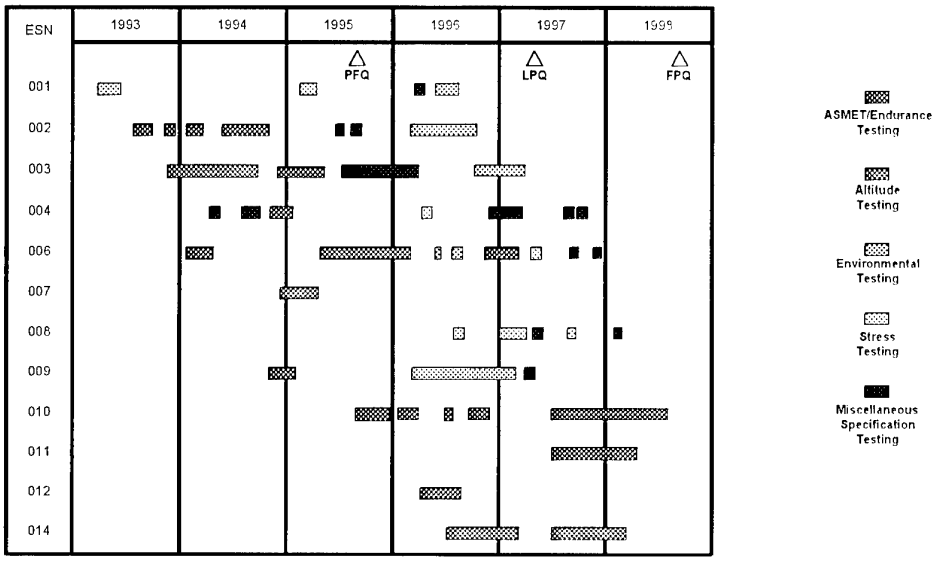

Engine Test Plan
(Figure 10)

helped to reduce costs by minimizing design changes late in the test program. The test program planned 6,523 test hours prior to first flight, including both official and assurance testing. Also, F412 compressor core assets were used in 1991, before the start of the E&MD program, due to similarity to the F414 design and availability of hardware to demonstrate air flows, efficiency and stall pressure ratio of the compressor.

The overall test program included 14 factory test engines running over 10,000 hours of testing (Figure 10). Testing was accomplished at a variety of sites, exploiting available facilities and special facilities. Environmental testing was run at NAWC-AD Trenton, survivability testing at NAWC-AD China Lake, gyroscopic testing at NAWC-AD Lakehurst, altitude testing at Arnold Engineering Test Facility and assorted tests including accelerated endurance testing at GE-Lynn.

Lessons learned from previous GE and USN test programs were incorporated into the F414 program. Backup engines were provided for all prime engines, and important requirement demonstration tests were run early in the test program. These tests included stress testing of components, durability and altitude testing. The results of these tests were then available to be incorporated into the life analysis. Another lesson learned led to an increase in the endurance testing to 300 hours required to release flight test engines.

In addition to lessons learned, many changes in philosophy were incorporated into the test program. Stairstep testing was included to identify high cycle fatigue problems. Stairstep testing was added in the beginning and end of all endurance and fatigue testing. ASMETs were added to the program and started at the beginning of E&MD to quickly identify durability problems. For all testing, part life was tracked for all critical hardware as they would be in the field to demonstrate the parts life tracking system.

F414 Lessons Learned

Target Fixation. Today's development programs require more testing and analysis to provide the confidence required to guarantee a low to moderate level of development risk. Gone are the days of a 300 or 600 hour Durability test with severities of 3 and 4 to 1. F404 and

other programs have shown the importance of minor throttle movement, afterburner hours and lightoffs and dwell times to accurate lifing. Multiple ASMET tests of 1000 hours or more is now the norm making development schedules tighter than ever before. A principle lesson learned through development testing is to avoid Target Fixation which focuses on milestones and specific tests vice the performance based requirements. For example, an immense amount of energy is focused towards completion of the official ASMET for Preliminary Flight Qualification, an alternate approach under a Cost type Contract with Contractor Teaming would be to define performance criteria such as demonstrated life instead of Test Completion. This life demonstration could take the form of a successful practice test and save the program schedule and cost. This approach could also be used to continue life testing as long as it was productive (i.e., a relevant configuration). The drawbacks to Target Fixation are more than just loss of opportunity. Target Fixation and the haste to meet milestones, takes priority over equally or more important tasks such as Learning tests. These are the temperature surveys, stress tests and the like which feed lifing analyses and reports. In future programs, the contractor should be required or incentivised to complete these learning tests early, much the same as they are incentivised for durability time. Since these learning tests and the resulting analyses often drives configurational changes as much as any durability test, an early determination of these changes allows the program to adequately plan for new part introduction for qualification purposes. Lastly, Target Fixation often obstructs the completion of necessary post-test inspections in the zeal to meet a milestone. On F414 this occurred on more than one occasion. One example was the discovery of Turbine blade shank cracking which also existed in previously run hardware and could have been found given the opportunity for further inspection. Fortunately this hardware was still available months and years after its testing had completed. Keeping hardware the completion of the development program will aid future investigations and can be used to aid field introduction activities such as Familiarization classes and repair development.

To combat Target Fixation and in the light of Acquisition Reform, future engine specifications should provide a list of performance requirements for milestone qualification instead of a list of tests that must be completed. This would allow the Team the leeway to determine the method to satisfy the requirements. It would also open several opportunities for advanced life exploration or demonstration as well as free-up precious schedule and assets. Tests types could still, and should, be required to develop a given performance. Detailing such required tests eliminates contractor speculation as to the mission usage and environmental constraints. But program focus must be on required performance vise test requirements.

Weight Management. Both Contractor and Government Team members agree that the area requiring the most attention by future programs is Weight Management. Managing to a weight requirement is difficult enough on a mature program, add to this the uncertainty of newly designed hardware and the variability among external plumbing and Controls hardware. Weight projection tools are nonexistent and weight typically loses in systems engineering trade studies. This is a lesson that is not easily learned. The F404 development program rated weight last in nearly all trade studies and ultimately had to pursue an extensive weight reduction program during Component Improvement Program (CIP). The F414 program has undergone three massive weight reduction initiatives and is still challenged for production.

Modeling and Simulation. As stated earlier, development testing requirements are increasing but the emphasis is on reducing the time and cost required for development. For this reason, the transition must be made from testing to modeling with test verification. At the start of the F414 development, much of the drafting was still done by hand. Later expansion into Computer Aided Design (Unigraphics) was initiated in interface configurations to supply data for electronic mockups and eventually Virtual Maintenance with the airframer models. Today, nearly the entire engine has been modeled and an analysis tool (Dyna3d) has been used, in conjunction with a rig test, to qualify the containment capability of the Fan. The F414 also has the most sophisticated steady state and transient performance models of any Navy engine program. Yet these have not been enough to mitigate schedule pressures. The future holds a continuation of this theme. Engine FADEC hardware and software are being integrated into manned flight simulators and hardware in the loop simulations are used to perform weapon system software integration testing. Navy component specialists, presently, are working with modeling and simulation tools to develop the ability to exercise the models the contractor uses to perform trade studies prior to directing the contractor and wasting valuable time and cost.

Given the success of Contractor/Government Teaming, there are several tools that continue the communication spirit and have become indispensable. GE developed a process tool for New Product Introductions (NPI) based on a series of tollgate reviews some of which requires customer involvement. With the exceptional Teaming to date, government personnel have a standing invitation to participate in the NPI process and often the customer tollgates are mere formalities. For engineering investigations, the Team uses TOPS8D for Team Oriented Problem Solving - 8 Discipline. TOPS8D is a rigorous approach that ensures proper systems engineering discipline is applied to complex problems. TOPS8D and the Team participation required, both government and contractor, have been instrumental in resolving issues such as compressor stator vane cracking. Six Sigma is a philosophy and tool to improve quality by improving processes resulting in savings to both the contractor and customer. Acquisition reform policies such as Single Process Initiatives and Commercial Practices are other means for mutual savings. Another tool, Quality Functional Deployment (QFD), is an important tool to check the customer's priorities during NPI's and at various points during development. Lastly, available tools for web based information systems and extended use of multi-media must be exploited to meet the real-time information exchange demands of major development programs.

Conclusion

In July of this year, the first production F414 will be delivered to the United States Navy. Later in September, the F414 will conclude its six year development program. This year marks a beginning more important than the end of F414 E&MD. The legacy of the program is its successful implementation of philosophies such as IPTs, Teaming, risk management, risk balance, and Concurrent Engineering and the lessons learned for future programs such as reliance on available tools like modeling, simulation and information technology.

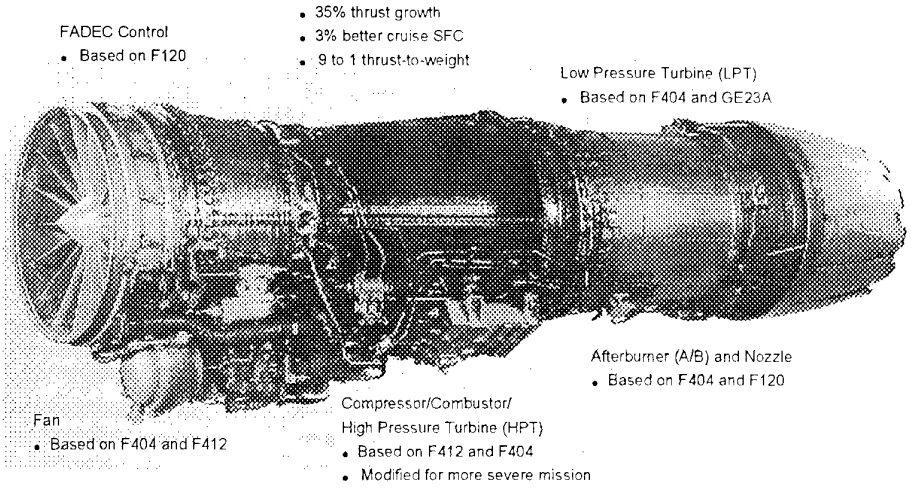

F414-GE-400 Engine
(Figure 11)

Special thanks to General Electric and Boeing for their pictures and inputs.

Meeting Discussions

Paper 46: **F/A-18 E/F Aircraft Engine (F414-GE-400) Design and Development Methodology**

Authors: Robert Burnes, Don Blottenberger, Michael Elliott

Discussor: G. William Gallops
Question: Are the single unit FADEC and composit fan duct an indication of relaxation of NAVY survivability requirements?

Author's reply: Yes and no.

REPORT DOCUMENTATION PAGE

1. Recipient's Reference	2. Originator's References	3. Further Reference	4. Security Classification of Document
	RTO-MP-8 AC/323(AVT)TP/9	ISBN 92-837-0005-8	UNCLASSIFIED/ UNLIMITED

5. Originator Research and Technology Organization
North Atlantic Treaty Organization
BP 25, 7 rue Ancelle, F-92201 Neuilly-sur-Seine Cedex, France

6. Title
Design Principles and Methods for Aircraft Gas Turbine Engines

7. Presented at/sponsored by
RTA Applied Vehicle Technology Panel (AVT) in Toulouse, France, 11-15 May 1998.

8. Author(s)/Editor(s)	9. Date
Multiple	February 1999
10. Author's/Editor's Address	**11. Pages**
Multiple	482

12. Distribution Statement There are no restrictions on the distribution of this document. Information about the availability of this and other RTO unclassified publications is given on the back cover.

13. Keywords/Descriptors

Aircraft engines	Computerized simulation	Turbojet engines
Gas turbine engines	Control equipment	Turboprop engines
Military aircraft	Combustion chambers	Turboshaft engines
Design	Cooling systems	Turboramjet engines
Performance	Operational effectiveness	Tactical aircraft
Reliability	Materials	Transport aircraft
Compressors	Vibration	Helicopters
Mathematical models	Turbofan engines	

14. Abstract

The symposium dealt with design approaches for military aircraft propulsion systems to provide enhanced operational flexibility, longer range, better fuel efficiency and improved affordability. All classes of gas turbines were addressed in nine sessions as follows:

- Engine Design and Analysis (Part I) (5 papers)
- Mechanical Systems (6 papers)
- Controls (4 papers)
- Combustors/Augmentors (4 papers)
- Compressor Systems (Part I) (5 papers)
- Compressor Systems (Part II) (3 papers)
- Turbines (Part I) (5 papers)
- Turbines (Part II) (4 papers)
- Engine Design and Analysis (Part II) (4 papers)

These proceedings also include a Technical Evaluation Report and a Keynote address published in French and English.

NORTH ATLANTIC TREATY ORGANIZATION

RESEARCH AND TECHNOLOGY ORGANIZATION
BP 25 • 7 RUE ANCELLE
F-92201 NEUILLY-SUR-SEINE CEDEX • FRANCE
Télécopie 0(1)55.61.22.99 • Télex 610 176

DIFFUSION DES PUBLICATIONS
RTO NON CLASSIFIEES

L'Organisation pour la recherche et la technologie de l'OTAN (RTO), détient un stock limité de certaines de ses publications récentes, ainsi que de celles de l'ancien AGARD (Groupe consultatif pour la recherche et les réalisations aérospatiales de l'OTAN). Celles-ci pourront éventuellement être obtenues sous forme de copie papier. Pour de plus amples renseignements concernant l'achat de ces ouvrages, adressez-vous par lettre ou par télécopie à l'adresse indiquée ci-dessus. Veuillez ne pas téléphoner.

Des exemplaires supplémentaires peuvent parfois être obtenus auprès des centres nationaux de distribution indiqués ci-dessous. Si vous souhaitez recevoir toutes les publications de la RTO, ou simplement celles qui concernent certains Panels, vous pouvez demander d'être inclus sur la liste d'envoi de l'un de ces centres.

Les publications de la RTO et de l'AGARD sont en vente auprès des agences de vente indiquées ci-dessous, sous forme de photocopie ou de microfiche. Certains originaux peuvent également être obtenus auprès de CASI.

CENTRES DE DIFFUSION NATIONAUX

ALLEMAGNE
Fachinformationszentrum Karlsruhe
D-76344 Eggenstein-Leopoldshafen 2

BELGIQUE
Coordinateur RTO - VSL/RTO
Etat-Major de la Force Aérienne
Quartier Reine Elisabeth
Rue d'Evere, B-1140 Bruxelles

CANADA
Directeur - Gestion de l'information
(Recherche et développement) - DRDGI 3
Ministère de la Défense nationale
Ottawa, Ontario K1A 0K2

DANEMARK
Danish Defence Research Establishment
Ryvangs Allé 1
P.O. Box 2715
DK-2100 Copenhagen Ø

ESPAGNE
INTA (RTO/AGARD Publications)
Carretera de Torrejón a Ajalvir, Pk.4
28850 Torrejón de Ardoz - Madrid

ETATS-UNIS
NASA Center for AeroSpace Information (CASI)
Parkway Center, 7121 Standard Drive
Hanover, MD 21076-1320

FRANCE
O.N.E.R.A. (Direction)
29, Avenue de la Division Leclerc
92322 Châtillon Cedex

GRECE
Hellenic Air Force
Air War College
Scientific and Technical Library
Dekelia Air Force Base
Dekelia, Athens TGA 1010

ISLANDE
Director of Aviation
c/o Flugrad
Reykjavik

ITALIE
Aeronautica Militare
Ufficio Stralcio RTO/AGARD
Aeroporto Pratica di Mare
00040 Pomezia (Roma)

LUXEMBOURG
Voir Belgique

NORVEGE
Norwegian Defence Research Establishment
Attn: Biblioteket
P.O. Box 25
N-2007 Kjeller

PAYS-BAS
NDRCC
DGM/DWOO
P.O. Box 20701
2500 ES Den Haag

PORTUGAL
Estado Maior da Força Aérea
SDFA - Centro de Documentação
Alfragide
P-2720 Amadora

ROYAUME-UNI
Defence Research Information Centre
Kentigern House
65 Brown Street
Glasgow G2 8EX

TURQUIE
Millî Savunma Başkanliği (MSB)
ARGE Dairesi Başkanliği (MSB)
06650 Bakanliklar - Ankara

AGENCES DE VENTE

NASA Center for AeroSpace Information (CASI)
Parkway Center
7121 Standard Drive
Hanover, MD 21076-1320
Etats-Unis

The British Library Document Supply Centre
Boston Spa, Wetherby
West Yorkshire LS23 7BQ
Royaume-Uni

Canada Institute for Scientific and Technical Information (CISTI)
National Research Council
Document Delivery,
Montreal Road, Building M-55
Ottawa K1A 0S2
Canada

Les demandes de documents RTO ou AGARD doivent comporter la dénomination "RTO" ou "AGARD" selon le cas, suivie du numéro de série (par exemple AGARD-AG-315). Des informations analogues, telles que le titre et la date de publication sont souhaitables. Des références bibliographiques complètes ainsi que des résumés des publications RTO et AGARD figurent dans les journaux suivants:

Scientific and Technical Aerospace Reports (STAR)
STAR peut être consulté en ligne au localisateur de ressources uniformes (URL) suivant:
http://www.sti.nasa.gov/Pubs/star/Star.html
STAR est édité par CASI dans le cadre du programme NASA d'information scientifique et technique (STI)
STI Program Office, MS 157A
NASA Langley Research Center
Hampton, Virginia 23681-0001
Etats-Unis

Government Reports Announcements & Index (GRA&I)
publié par le National Technical Information Service
Springfield
Virginia 2216
Etats-Unis
(accessible également en mode interactif dans la base de données bibliographiques en ligne du NTIS, et sur CD-ROM)

Imprimé par le Groupe Communication Canada Inc.
(membre de la Corporation St-Joseph)
45, boul. Sacré-Cœur, Hull (Québec), Canada K1A 0S7

NORTH ATLANTIC TREATY ORGANIZATION

RESEARCH AND TECHNOLOGY ORGANIZATION
BP 25 • 7 RUE ANCELLE
F-92201 NEUILLY-SUR-SEINE CEDEX • FRANCE
Telefax 0(1)55.61.22.99 • Telex 610 176

DISTRIBUTION OF UNCLASSIFIED
RTO PUBLICATIONS

NATO's Research and Technology Organization (RTO) holds limited quantities of some of its recent publications and those of the former AGARD (Advisory Group for Aerospace Research & Development of NATO), and these may be available for purchase in hard copy form. For more information, write or send a telefax to the address given above. **Please do not telephone.**

Further copies are sometimes available from the National Distribution Centres listed below. If you wish to receive all RTO publications, or just those relating to one or more specific RTO Panels, they may be willing to include you (or your organisation) in their distribution.

RTO and AGARD publications may be purchased from the Sales Agencies listed below, in photocopy or microfiche form. Original copies of some publications may be available from CASI.

NATIONAL DISTRIBUTION CENTRES

BELGIUM
Coordinateur RTO - VSL/RTO
Etat-Major de la Force Aérienne
Quartier Reine Elisabeth
Rue d'Evere, B-1140 Bruxelles

CANADA
Director Research & Development
Information Management - DRDIM 3
Dept of National Defence
Ottawa, Ontario K1A 0K2

DENMARK
Danish Defence Research Establishment
Ryvangs Allé 1
P.O. Box 2715
DK-2100 Copenhagen Ø

FRANCE
O.N.E.R.A. (Direction)
29 Avenue de la Division Leclerc
92322 Châtillon Cedex

GERMANY
Fachinformationszentrum Karlsruhe
D-76344 Eggenstein-Leopoldshafen 2

GREECE
Hellenic Air Force
Air War College
Scientific and Technical Library
Dekelia Air Force Base
Dekelia, Athens TGA 1010

ICELAND
Director of Aviation
c/o Flugrad
Reykjavik

ITALY
Aeronautica Militare
Ufficio Stralcio RTO/AGARD
Aeroporto Pratica di Mare
00040 Pomezia (Roma)

LUXEMBOURG
See Belgium

NETHERLANDS
NDRCC
DGM/DWOO
P.O. Box 20701
2500 ES Den Haag

NORWAY
Norwegian Defence Research Establishment
Attn: Biblioteket
P.O. Box 25
N-2007 Kjeller

PORTUGAL
Estado Maior da Força Aérea
SDFA - Centro de Documentação
Alfragide
P-2720 Amadora

SPAIN
INTA (RTO/AGARD Publications)
Carretera de Torrejón a Ajalvir, Pk.4
28850 Torrejón de Ardoz - Madrid

TURKEY
Milli Savunma Başkanliği (MSB)
ARGE Dairesi Başkanliği (MSB)
06650 Bakanliklar - Ankara

UNITED KINGDOM
Defence Research Information Centre
Kentigern House
65 Brown Street
Glasgow G2 8EX

UNITED STATES
NASA Center for AeroSpace Information (CASI)
Parkway Center, 7121 Standard Drive
Hanover, MD 21076-1320

SALES AGENCIES

NASA Center for AeroSpace Information (CASI)
Parkway Center
7121 Standard Drive
Hanover, MD 21076-1320
United States

The British Library Document Supply Centre
Boston Spa, Wetherby
West Yorkshire LS23 7BQ
United Kingdom

Canada Institute for Scientific and Technical Information (CISTI)
National Research Council
Document Delivery,
Montreal Road, Building M-55
Ottawa K1A 0S2
Canada

Requests for RTO or AGARD documents should include the word 'RTO' or 'AGARD', as appropriate, followed by the serial number (for example AGARD-AG-315). Collateral information such as title and publication date is desirable. Full bibliographical references and abstracts of RTO and AGARD publications are given in the following journals:

Scientific and Technical Aerospace Reports (STAR)
STAR is available on-line at the following uniform resource locator:
http://www.sti.nasa.gov/Pubs/star/Star.html
STAR is published by CASI for the NASA Scientific and Technical Information (STI) Program
STI Program Office, MS 157A
NASA Langley Research Center
Hampton, Virginia 23681-0001
United States

Government Reports Announcements & Index (GRA&I)
published by the National Technical Information Service
Springfield
Virginia 22161
United States
(also available online in the NTIS Bibliographic Database or on CD-ROM)

Printed by Canada Communication Group Inc.
(A St. Joseph Corporation Company)
45 Sacré-Cœur Blvd., Hull (Québec), Canada K1A 0S7

ISBN 92-837-0005-8